MULTIVARIATE STATISTICAL ANALYSIS OF GEOCHEMICAL DATA TO CONSTRAIN THE EVOLUTION, MINERALIZATION AND ALTERATION SIGNATURES OF IOCG AND BIF-HOSTED DEPOSITS

Marija Dmitrijeva

This thesis is submitted for the degree of Doctor of Philosophy

in the

School of Chemical Engineering and Advanced Materials,

Faculty of Engineering, Computer and Mathematical Sciences

at

The University of Adelaide



December 2019

TABLE OF CONTENTS

ABSTRACT ..... **.x**

DECLARATION ..... **xi**

ACKNOWLEDGEMENTS ..... **xiv**

PREFACE ..... **xvi**

CHAPTER 1: INTRODUCTION **1**

1.1 Research objectives and thesis structure 7

1.2 References 11

CHAPTER 2: A COPULA-BASED APPROACH TO THE IMPUTATION OF VALUES BELOW THEIR DETECTION LIMIT. **16**

Abstract 19

2.1 Introduction 20

2.2 Data 22

2.3 Implementation 23

2.3.1 Expectation-maximization algorithm 23

2.3.2 Fitting a copula to trivariate data 25

2.3.3 Metropolis-Hastings algorithm to draw random samples from a copula 27

2.3.4 Proposed copula-based algorithm 29

2.4 Results and Implications 33

2.5 Conclusions 34

Acknowledgements 35

References 35

CHAPTER 3: DISCRIMINATION AND VARIANCE STRUCTURE OF TRACE ELEMENT SIGNATURES IN FE-OXIDES: A CASE STUDY OF BIF-MINERALIZATION FROM THE MIDDLEBACK RANGES, SOUTH AUSTRALIA 40

Abstract 44

3.1 Introduction 45

3.2 Background 46

3.2.1 LA-ICP-MS Data Fabric 46

3.2.2 LA-ICP-MS Data Limitations 46

3.2.3 Compositional Data Adaptations for In-Situ LA-ICP-MS Data 47

3.3 Data Description 48

3.4 Statistical Analyses of Trace Element Data in Fe-Oxides 52

3.4.1 Treatment of Values Below Detection Limit 52

3.4.2 Univariate Analysis 53

3.4.2.1 Summary Statistics 53

3.4.2.2 Linear Mixed-Effects Regression 54

3.4.3 Multivariate Analysis 57

3.4.3.1 Principal Component Analysis 57

3.4.3.2 Linear Discriminant Function Analysis 57

3.5 Results 58

3.5.1 Data Assessment for Mineral Inclusions 58

3.5.2 Univariate Analysis of Fe-Oxides 58

3.5.2.1 Magnetite Trace Element Data 59

3.5.2.2 Hematite Trace Element Data 59

3.5.2.3 Hematite Trace Element Data Linear Mixed-Effects Models 60
3.5.3 Multivariate Analyses of Fe-Oxides 65
3.5.3.1 Principal Component Analysis 65
3.5.3.1 Linear Discriminant Analysis 67
3.6 Discussion 68
3.6.1 Trace Element Patterns of Fe-Oxides 71
3.6.2 Variance Structure of Hematite Data 72
3.6.3 Discrimination of Hematite Categories 73
3.7. Conclusions 74
Acknowledgements 75
References 76

CHAPTER 4: MULTIVARIATE STATISTICAL ANALYSIS OF TRACE ELEMENTS IN PYRITE: PREDICTION, BIAS AND ARTEFACTS IN DEFINING MINERAL SIGNATURES 80

Abstract 84
4.1 Introduction 85
4.2 Approach, Methods and Data Treatment 86
4.2.1 Data Acquisition 86
4.2.2 Data quality control, trimming and imputation 87
4.2.3 Multivariate analyses 89
4.3 Results 90
4.3.1 Summary of Trace Element Signatures in Pyrite 90
4.3.2 Principal component analysis, k-means clustering and dendrogram 91
4.3.3 Multiple linear regression 97
4.4 Discussion 98

4.4.1 Trace element signature of pyrite: prediction and bias for complex sulphide ores 98

4.4.2 Trapping of trace elements during ore overprinting 99

4.4.3 Impact of left-censored data on the interpretation of statistical analyses: artefacts and false interpretations 100

4.4.4 Implications and Significance 100

4.5 Conclusions 101

References 102

CHAPTER 5: DEFINING IOCG SIGNATURES THROUGH COMPOSITIONAL DATA ANALYSIS: A CASE STUDY OF LITHOGEOCHEMICAL ZONING FROM THE OLYMPIC DAM DEPOSIT, SOUTH AUSTRALIA 107

Abstract 110

5.1 Introduction 110

5.2 Geological background and rationale 111

5.3 Methods and Data 112

5.3.1 Sample Suite 112

5.3.2 Data processing 112

5.3.3 Multivariate Statistical Analyses 113

5.3.3.1 Hierarchical Clustering 113

5.3.3.2 Principal Component Analysis 114

5.3.4 Spatial 3D-modelling 114

5.3.5 Estimation of normative Cu-(Fe)-sulphide mineralogy 114

5.4 Results 115

5.4.1 Hierarchical Cluster Analysis 115

5.4.2 Principal Component Analysis results 116

5.4.3 Delimitation of the ODBC from Roxby Downs Granite 116
5.4.4 Element Distributions 118
5.4.4.1 Element pairs Ni-Co, Mn-CO2 and Nb-Ta 118
5.4.4.2 The U3O8-Se association 118
5.4.4.3 Granitophile elements (W-Sn-Mo) 119
5.4.4.4 Chalcophile and related elements (As-Sb and Au-Te) 120
5.5 Discussion 120
5.5.1 Definition of an IOCG signature through PCA 120
5.5.2 Lithogeochemistry of the Olympic Dam Breccia Complex 122
5.5.3 Vertical zonation 123
5.5.3 Geochemical trends and associations 123
5.6 Conclusions and outlook 123
Acknowledgements 123
References 124

CHAPTER 6: MINERALIZATION-ALTERATION FOOTPRINTS IN THE OLYMPIC DAM IOCG DISTRICT, SOUTH AUSTRALIA: THE ACROPOLIS PROSPECT 127

Abstract 130
6.1 Introduction 130
6.2 Geological background and rationale 132
6.3 Methods 133
6.3.1 Compositional data and imputation 133
6.3.2 Unsupervised machine learning 135
6.3.3 Supervised machine learning 137
6.3.4 Implicit 3D geological and numerical modelling 137

6.4 Results 137
6.4.1 Variation matrix and hierarchical clustering 137
6.4.2 Geological model 138
6.4.3 k-means clusters and PCA 140
6.4.4 Centered ternary diagrams 141
6.4.5 Alteration types, styles and intensities 142
6.4.6 Random forests model 142
6.5 Discussion 143
6.5.1 IOCG signatures at Acropolis prospect: a comparison with Olympic Dam 143
6.5.2 Alteration footprints 144
6.5.3 Exploration significance 145
6.6 Conclusions 147
Acknowledgements 147
References 147

CHAPTER 7: GEOCHEMICAL DATA ANALYSIS AND 3D MODELLING OF WIRRDA WELL PROSPECT, SOUTH AUSTRALIA: STRUCTURAL CONTROL ON IRON-OXIDE COPPER GOLD MINERALISATION 151

Abstract 155
7.1 Introduction 156
7.2 Geological background and rationale 161
7.3 Methods and data 164
7.3.1 Geochemical data and pre-processing 164
7.3.2 Statistical Analyses of Geochemical Data 168
7.3.2.1 Unsupervised statistical analyses 170
7.3.2.2 Supervised statistical analysis 172

7.3.2.3 Implicit numerical and geological modelling 175

7.3.2.4 Estimation of Cu(-Fe)-sulphide mineralogical zonation..... 175

7.4 Results..... 176

7.4.1 Geological Model of the Wirrda Well prospect 176

7.4.2 Multivariate statistical analysis 180

7.4.2.1 Variation matrix and dendrogram..... 180

7.4.2.2 Unsupervised classification: k-means clustering..... 182

7.4.2.3 Principal Component Analysis and Ternary Diagrams 184

7.4.2.4 Supervised classification depicts mineralisation signature in 3D.... 188

7.4.3 Numerical models for sulphide and metal distributions in the Wirrda Well prospect..... 192

7.5 Discussion..... 198

7.5.1 Structural control on the mineralisation at Wirrda Well 198

7.5.2 IOCG signatures: a comparison between Wirrda Well, Acropolis and Olympic Dam 200

7.6 Conclusions and Implications..... 204

Acknowledgments..... 205

References..... 206

CHAPTER 8: SUMMARY, RECOMMENDATIONS AND CONCLUDING REMARKS 216

8. Summary and Recommendations 217

8.1 Imputation of Left-Censored Values Using Copula Functions 219

8.2 Multivariate Analyses of Fe-oxides to Track BIF enrichment Process..... 220

8.3 Prediction of Nanoparticles Using the Multivariate Analyses of LA-ICP-MS data 221

8.4 Mineralisation signatures of the Olympic Dam IOCG district..... 224

8.5 Concluding remarks..... 227

References 229

CHAPTER 9: SUPPLEMENTARY AND ADDITIONAL MATERIAL 235

SUPPLEMENTARY MATERIAL A: For Chapter 2 236

Electronic Appendix A for Chapter 2 237

SUPPLEMENTARY MATERIAL B: For Chapter 3 243

Electronic Appendix A for Chapter 3 244

Electronic Appendix B for Chapter 3 245

Electronic Appendix C for Chapter 3 359

SUPPLEMENTARY MATERIAL C: For Chapter 4 362

Electronic Appendix A for Chapter 4 363

Electronic Appendix B for Chapter 4 366

Electronic Appendix C for Chapter 4 369

SUPPLEMENTARY MATERIAL D: For Chapter 5 372

Electronic Appendix A for Chapter 5 373

SUPPLEMENTARY MATERIAL E: For Chapter 6 374

Electronic Appendix A for Chapter 6 375

SUPPLEMENTARY MATERIAL F: For Chapter 7 376

Electronic Appendix A for Chapter 7 377

Electronic Appendix B for Chapter 7 379

Electronic Appendix C for Chapter 7 380

ADDITIONAL MATERIAL G: Petrography and Trace Element Signatures of Iron-Oxides in Deposits from the Middleback Ranges, South Australia: From Banded Iron Formation to Ore 382

ADDITIONAL MATERIAL H: Iron-oxides Constrain BIF Evolution in Terranes with Protracted Geological Histories: The Iron Count Prospect, Middleback Ranges, South Australia 384

ADDITIONAL MATERIAL I: Petrographic and Geochronological Constraints on The Granitic Basement to The Middleback Ranges, South Australia 386

ADDITIONAL MATERIAL J: Zircon at The Nanoscale Records Metasomatic Processes Leading to Large Magmatic–Hydrothermal Ore Systems 388

ADDITIONAL MATERIAL K: Hematite Geochemistry and Geochronology Resolve Genetic and Temporal Links Among Iron-Oxide Copper Gold Systems, Olympic Dam District, South Australia..... 390

ADDITIONAL MATERIAL L: Multivariate Statistical Analyses of LA-ICP-MS Trace Element Data for Iron-Oxides: Examples from Genetically Distinct Ore Deposits from South Australia..... 392

ADDITIONAL MATERIAL M: Copula Functions as a Tool for Statistical Modelling of Trace Element Signatures in Iron-Oxides: Examples from South Australian Ore Deposits 394

ADDITIONAL MATERIAL N: Defining IOCG Signatures Through Compositional Data Analysis: A Case Study of Lithogeochemical Zoning at Olympic Dam, South Australia…. 397

ADDITIONAL MATERIAL O: Mineralization Signatures of the Magnetite-Dominant Acropolis Prospect, Olympic Dam IOCG District, South Australia 403

ADDITIONAL MATERIAL P: 'Invisible' Au in Pyrite from Olympic Dam Deposit, South Australia: Bridging Textures with Statistical Analyses..... 406

ADDITIONAL MATERIAL Q: Why Detailed Mineralogy Is Important: Understanding Evolution of The Olympic Dam Iron-Oxide-Copper-Gold System, South Australia 410

CHAPTER 10: REFERENCES 414

ABSTRACT

Iron-oxide copper gold (IOCG) and banded iron formation (BIF)-hosted iron deposits are the dominant styles of mineralization in the Gawler Craton, South Australia. Multivariate geochemical datasets of various types and complexity collected from whole-rock samples and individual mineral grains from these deposits form a previously untapped source of information that can be applied to characterization and genetic modelling of such deposits. Moreover, such datasets carry major implications for new approaches to regional-scale exploration. Despite this, the ever-increasing complexity and size of geochemical datasets necessitates development of bespoke multivariate statistical analysis techniques as a prerequisite to any reproducible quantitative characterization of mineralization and/or alteration signatures, especially when detailed petrographic data are either limited or absent altogether.

Left-censored values, i.e., those concentrations that fall below minimum limit of detection (reflecting the analytical limitation of the instrument used for acquisition), are present in all types of geochemical datasets but are amplified in trace element datasets such as those obtained by laser ablation inductively coupled plasma mass spectrometry (LA-ICP-MS). A novel approach for imputation of values below detection limits using copula cumulative density functions (CDFs) is proposed. A case study involving imputation of left-censored data for Te in the presence of Au and Ag values is based upon fitting copula CDFs to the data and iteratively simulating new Te values from copula CDFs using the Metropolis-Hastings algorithm.

Within BIF-associated iron ores of the Middleback Ranges, iron oxides display interconversion and replacement reactions between magnetite by hematite and reprecipitation of new generations of platy hematite. Quantitative assessment of such interconversions, when correlated with available textural evidence, allows definition of geochemical signatures

associated with ore enrichment. Linear-mixed effects models support the statistically significant difference among prevailing textures. Such models can account for the high degree of correlation among the analyses within a single polished block and therefore respect the hierarchical structure of such data. The observed trace element signatures indicate the potential impact of hydrothermal fluids associated with the ~1.8 Myola Volcanics, ~1.6. Ga Hiltaba Suite granites and younger discordant mafic dykes on ore enrichment process in the Middleback Ranges.

Statistical analyses of a large LA-ICP-MS dataset for pyrite shows the independence of several minor and trace elements of economic interest or of relevance to optimized ore processing. Principal Component Analysis shows that Au is contained in zoned pyrite, along with As-Co(-Ni), thus suggesting the presence of invisible Au as both nanoinclusions and within the sulphide lattice. Nevertheless, PC2 essentially discriminates Co-As-Au from Ni, thus suggesting that Co-As zoning in pyrite is not always accompanied by Ni. The clearly defined (by PC1) Ag-Bi-Pb association is likely present in the form of discrete inclusions of telluride minerals. Other elements certainly hosted as minerals inclusions in pyrite and not in the crystal lattice include Zn, Sn, Mn, Ti, Sb and Cu.

Application of multivariate statistical analyses to whole-rock data from three different IOCG systems within the Olympic Dam district, coupled with geological 3D modelling, has resulted in recognition and specification of shared but subtly different mineralization and alteration signatures within each system. The novelty of such an approach lies in the direct comparison of lithological and mineralogical zonation with calculated parameters such as geochemical clusters and principal component scores, also taking into consideration an extended suite of elements representative of both protoliths and superimposed mineralization and alteration. Results showed that despite significant differences between the geological settings of individual IOCG systems (host lithologies, presence of mafic dykes, mineralization style etc.),

all three (the Olympic Dam deposit and the Acropolis and Wirrda Well prospects) can be readily characterized by the presence of ‘granitophile’ signatures thus confirming a common source of fluids for IOCG mineralization across the Olympic Cu-Au Province.

Multivariate statistical analysis is both flexible and adaptable and can readily complement and often outperform conventional approaches to interpreting different types of geochemical data. Although particularly applicable to larger, more complex datasets, this research also emphasizes the caution needed when working with datasets containing large proportions of left-censored values.

DECLARATION

I certify that this work contains no material which has been accepted for the award of any other degree or diploma in my name, in any university or other tertiary institution and, to the best of my knowledge and belief, contains no material previously published or written by another person, except where due reference has been made in the text. In addition, I certify that no part of this work will, in the future, be used in a submission in my name, for any other degree or diploma in any university or other tertiary institution without the prior approval of the University of Adelaide and where applicable, any partner institution responsible for the joint-award of this degree.

I acknowledge that copyright of published works contained within this thesis resides with the copyright holder(s) of those works.

I also give permission for the digital version of my thesis to be made available on the web, via the University's digital research repository, the Library Search and also through web search engines, unless permission has been granted by the University to restrict access for a period of time.

Signed Date 17/12/2019

ACKNOWLEDGEMENTS

The completion of my PhD degree was possible thanks to many wonderful people who have contributed to this thesis or supported me throughout this journey. I am grateful for your contributions large and small.

Foremost, I would like to thank my mother Oksana Demjanenko for the dedication and absolute commitment to the education of her children. My successes would have been impossible without the support I always receive from home. I also would like to thank my younger sisters, Daria, Lisa and Lika, for being the greatest motivators for me and also for making me a better person.

My sincere thanks to the 'Geoloogiaosakond' of the University of Tartu, which used to be my home away from home and where my interest in geology was nourished and grown thanks to many incredible geoscientists for over five years. I would like to kindly thank Jüri Plado, my undergraduate' and master's supervisor, for introducing me into the very first scientific challenges.

I am profoundly grateful for having an absolutely fantastic team of supervisors Cristiana Ciobanu, Nigel Cook, Kahty Ehrig and Andrew Metcalfe and for their hard work, persistence and criticism that not only improved my/our research outcome, but also greatly shaped my personality. My sincere thanks to Cristi for picking me as one of her students and exposing me to a variety of scientific problems ranging from nano-scale studies to geological modelling of ore deposits. Most importantly, I learnt that I will never be out of tasks. I would like to thank Nigel for countless hours of editing my manuscripts and Andrew for our long discussions about statistics, especially during the first and the hardest year of my degree. Finally, I would like to thank Kathy for giving me an opportunity to work on multiple IOCG systems by providing us

with incredibly interesting data. Altogether, I cannot express enough how grateful I am to my supervisors for the most productive, intense, yet creative time of my life.

The team of FOX students, Liam Courtney-Davis, Max Verdugo-Ihl and William Keyser are warmly thanked for being such great friends and colleagues. It was an absolute honour to work with you all and learn by your side. I thank you all for our numerous discussions, laughs and countless visits to the worst pub in South Australia - Schnithouse. I also would like to thank the extended crew, Mark, Alkis, Nick, Max Frenzel and Jing as well as other PhD students and postdocs from the School of Chemical Engineering.

My special regards go to the salsa people of Adelaide as well as members of the Adelaide University Salsamania Club for all the fun nights together and spontaneous visits to the O'Connell St bakery in the middle of night. I am especially thankful to Olivia, Saurabh, Celia, Nadil, Jung, Alvin and Pavan for their friendship. I also would like to thank my old-time friends Jaana Jõgeva, Jekaterina Nezdoli and Igor Ogibin for their encouragement and support all the way from the Northern Hemisphere.

Finally, I would like to express my greatest appreciation to my partner Aleksandr Ljamin for being by my side over the course of the doctorate studies. The amount of support received from you cannot be measured and your contribution to this degree is invaluable. I am eternally thankful.

PREFACE

This thesis comprises of a portfolio of articles and manuscripts which are either published or under review in international peer-reviewed journals, and one abridged thesis chapter to be submitted for publication. The journals in which these papers are published or have been submitted to are *'Computer and Geosciences*' (Chapter 2, intended submission) *'Mathematical Geosciences'* (Chapter 3, published), *'Minerals'* (Chapter 4, published), *'Ore Geology Reviews'* (Chapter 5, published), *'Journal of Geochemical Exploration'* (Chapter 6, published) *'Economic Geology'* (Chapter 7, submitted). All six chapters are closely related and summarize key findings and interpretations, to be read as standalone contributions. Recommendations have been made in Chapter 8, as a direct result of the key findings of this research, with the aim to explore certain aspects at a later date.

The three published articles, two submitted manuscripts and one thesis chapter which form the basis of this thesis are:

1. Dmitrijeva, M., Metcalfe, A.V., Ciobanu, C.L., Cook, N.J., Ehrig, K. (thesis chapter intended for later submission). A copula-based approach to the imputation of values below their detection limit.
2. Dmitrijeva, M. Metcalfe, A.V., Ciobanu, C.L. Cook, N.J., Frenzel, M., Keyser, W.M., Johnson, G., Ehrig, K. 2018. Discrimination and variance structure of trace element signatures in hematite: a case study of BIF-mineralization from the Middleback Ranges, South Australia Mathematical Geosciences, 50, 381-415.
3. Dmitrijeva, M., Cook, N.J., Ehrig, K., Ciobanu, C.L., Metcalfe, A.V., Kamenetsky, M., Kamenetsky, V.S., Gilbert, S., 2020, Multivariate statistical analysis of trace elements in pyrite: prediction, bias and artefacts in defining mineral signature. Minerals, 10, 61.

4. Dmitrijeva, M., Ehrig, K., Ciobanu, C., Cook, N., Verdugo-Ihl, M., Metcalfe, A., 2019a. Defining IOCG signatures through compositional data analysis: a case study of lithogeochemical zoning from the Olympic Dam deposit, South Australia. Ore Geology Reviews, 105, 86–101.
5. Dmitrijeva, M., Ciobanu, C., Ehrig, K., Cook, N., Metcalfe, A., Verdugo-Ihl, M., McPhie, J., 2019b. Mineralization-alteration footprints in the Olympic Dam IOCG district South Australia: The Acropolis prospect. Journal of Geochemical Exploration, 205, 106333
6. Dmitrijeva, M., Ciobanu, C.L., Ehrig, K., Cook, N.J., Verdugo-Ihl, M.R., Metcalfe, A.V., Kamenetsky, V.S., McPhie, J., in review, Geochemical data analysis and 3D modelling of Wirrda Well prospect, South Australia: structural control on iron-oxide copper gold mineralisation. Economic Geology.

Chapter 9 contains supplementary material for all chapters outlined above, as well as co-authored publication abstracts, conference abstracts and posters and co-authored conference abstracts that have been generated during PhD candidature.

The additional material is as follows:

A. Supplementary material for Chapter 2 (Thesis chapter).

B. Supplementary material for Chapter 3 (Mathematical Geosciences).

C. Supplementary material for Chapter 4 (Minerals).

D. Supplementary material for Chapter 5 (Ore Geology Reviews).

E. Supplementary material for Chapter 6 (Journal of Geochemical Exploration).

F. Supplementary material for Chapter 7 (Economic Geology, in review).

Co-authored article abstracts

G. Keyser, W., Ciobanu, C.L., Cook, N.J., Johnson, G., Feltus, H., Johnson, S., **Dmitrijeva, M.**, Ehrig, K., Nguyen, P.T., 2018. Petrography and trace element signatures of iron oxides in deposits from the Middleback Ranges, South Australia: From banded iron formation to ore. Ore Geology Reviews, 93, 337-360.

H. Keyser, W., Ciobanu, C.L., Cook, N.J., **Dmitrijeva, M.**, Courtney-Davies, L., Feltus, H., Gilbert, S., Johnson, G., Ehrig, K., 2019a. Iron-oxides constrain BIF evolution in terranes with protracted geological histories: The Iron Count prospect, Middleback Ranges, South Australia. Lithos, 324-325, 20-38.

I. Keyser, W., Ciobanu, C.L., Cook, N.J., Courtney-Davies, L., Kennedy, A., Wade, B.P. Ehrig, K., **Dmitrijeva, M.**, Kontonikas-Charos, A., Feltus, H., Johnson, G., 2019b. Petrographic and geochronological constraints on the granitic basement to the Middleback Ranges, South Australia. Precambrian Research, 324, 170-193.

J. Courtney-Davies, C., Ciobanu, C.L., Verdugo-Ihl, M.R., Slattery, A., Cook, N.J., **Dmitrijeva, M.**, Keyser, W.M., Wade, B.P., Domnick, U.I., Ehrig, K., Xu, J., Kontonikas-Charos, A. 2019. Zircon at The Nanoscale Records Metasomatic Processes Leading to Large Magmatic–Hydrothermal Ore Systems. Minerals, 9, 364.

K. Courtney-Davies, L., Ciobanu, C., Verdugo-Ihl, M.R. **Dmitrijeva, M.**, Cook, N., Ehrig, K., Wade, B. 2019. Hematite geochemistry and geochronology resolve genetic and temporal links among iron-oxide copper gold systems, Olympic Dam district, South Australia. Precambrian Research, 335, 105480.

First author conference abstracts (oral presentations)

L. **Dmitrijeva, M.,** Ciobanu, C.L., Metcalfe, A.V., Cook, N.J., Verdugo-Ihl, M.R., Keyser, W., Ehrig, K. 2017. Multivariate Statistical Analyses of LA-ICP-MS Trace Element Data for Iron-Oxides: Examples from Genetically Distinct Ore Deposits from South Australia. International Association of Mathematical Geosciences 2017, Perth, Australia, September 3rd-9th.

M. **Dmitrijeva, M.,** Ehrig, K., Ciobanu, C.L., Cook, N.J., Verdugo-Ihl, M.R., Metcalfe, A.V. Defining IOCG Signatures Through Compositional Data Analysis: A Case Study of Lithogeochemical Zoning at Olympic Dam, South Australia. 15th Quadrennial IAGOD Symposium, Salta, Argentina, August 28th-31st.

N. **Dmitrijeva, M.**, Ciobanu, C.L., Ehrig, K., Cook, N.J., Metcalfe, A.V., Verdugo-Ihl, M.R., McPhie, J. Mineralization Signatures of The Magnetite-Dominant Acropolis Prospect, Olympic Dam IOCG District, South Australia. Australasian Exploration Geoscience Conference 2019, Perth, Australia, September 2nd-5th.

First author conference abstracts (poster presentation)

O. **Dmitrijeva, M.**, Metcalfe, A.V., Ciobanu, C.L., Cook, N.J., Verdugo-Ihl, M.R., Keyser, W.M., Ehrig, K. Copula Functions as A Tool for Statistical Modelling of Trace Element Signatures In Iron-Oxides: Examples From South Australian Ore Deposits. International Association of Mathematical Geosciences 2017, Perth, Australia, September 3rd-9th.

P. **Dmitrijeva, M.**, Verdugo-Ihl, M.R., Ehrig, K., Ciobanu, C.L., Cook, N.J. 'Invisible' Au in Pyrite From Olympic Dam Deposit, South Australia: Bridging Textures With Statistical Analyses. TIGeR Conference 2019, Perth Australia, September 11th-13th.

Co-authored conference abstracts

Q. Cook, N.J., Ehrig, K., Ciobanu, C.L., Courtney-Davies, L., Verdugo-Ihl, M.R., Rollog, M., Schmandt, D., Owen, N., Macmillan, E., Kontonikas-Charos, A., Krneta, S., **Dmitrijeva., M.** Why Detailed Mineralogy is Important: Understanding Evolution of The Olympic Dam Iron-Oxide-Copper-Gold System, South Australia. 15th Quadrennial IAGOD Symposium, Salta, Argentina, August 28th-31st.

The final chapter of this thesis consists of a complete reference list of all publications cited within any of the manuscripts, chapters, supplementary and additional material submitted as a component of this thesis.

CHAPTER 1

INTRODUCTION

Iron-oxide copper-gold (IOCG) and banded iron formations (BIF)-hosted iron deposits are genetically and temporally distinct styles of mineralisation that represent significant mineral resources in South Australia. The two distinct types of deposit are found within the Eastern Gawler Craton, a complex ancient terrane with a protracted geological history (Fig. 1.1). Despite having formed via genetically distinct mechanisms, both deposit styles resulted in accumulation of Fe-oxides – by far the dominant minerals in these deposits. Their abundance, refractory character, ability to scavenge trace elements and incorporate them within their crystal lattice, and potential for correlation between geochemistry and grain-scale textures and geochronology (e.g., Courtney-Davies et al., 2019; Keyser et al., 2019), make iron oxides a valuable petrogenetic indicator that can constrain deposit evolution.

Mesoproterozoic magmatic-hydrothermal IOCG deposits of the Olympic Cu-Au Province (Skirrow et al., 2007; Reid, 2019) are associated with the emplacement of Gawler Silicic Large Igneous Province (SLIP; Allen et al., 2008) at ~1.6 Ga (Fig. 1.1). This event generated Hiltaba Suite (HS) intrusive rocks and their cogenetic equivalents, the Gawler Range Volcanics (GRV) (Blissett et al., 1993). Within the province, the IOCG deposits and prospects feature regional- and deposit-scale mineralogical alteration footprints (Kontonikas-Charos et al., 2014, 2017, 2018; Mauger et al., 2016), share complex ore and gangue mineral assemblages, and occur within a variety of host lithologies and with various controls on the mineralisation style: breccia-hosted, (Olympic Dam; Reeve et al., 1990; Ehrig et al., 2012), vein-hosted (Acropolis; Paterson, 1986; Creaser, 1989), skarn (Hillside; Ismail et al., 2014), or structurally controlled (Wirrda Well; Dmitrijeva et al., in review). In order to continue efficient exploration across the region and develop sustainable genetic models in space and time that account for the specific geological

settings, complexity and heterogeneity, a good understanding of their mineralisation signatures is required.

Archean-Palaeoproterozoic BIFs of the Middleback Ranges (Fig. 1.1), northeastern Eyre Peninsula, represent the major iron-ore producing region of South Australia. The Middleback Ranges is a ~50 km-long, N-S striking, belt comprising over 20 BIF-hosted iron ore deposits and prospects. The complex evolution of the Middleback Ranges spans multiple tectonothermal events over ~2 Ga and is consistent with an interpretation in which BIFs have interacted with surficial, magmatic and hydrothermal fluids resulting in the transformation and upgrading of Fe-rich sedimentary chemical precipitates into economic iron-rich horizons (Keyser et al., 2019). Such evolution is recorded in the textures, geochemical signatures and ages of iron-oxides (Keyser et al., 2018, 2019; Dmitrijeva et al., 2018). The geochemical signature from iron oxides in the Middleback Ranges carries implications for constraining ore enrichment process and regional geology as the iron oxide structures allow preservation of the signature of alteration by various sources, including ~1.6 Ga Hiltaba Suite granites.

Multi-element datasets of various size and complexity obtained from analysis of whole-rock samples or microanalysis of single mineral grains are widely utilised in applied ore deposit studies to constrain ore genesis, mineralisation and alteration, as well as the sequence of overprinting events. Often such studies lack multivariate analyses (e.g., Dare et al., 2014), and instead rely on simple bi- or trivariate diagrams that fail to acknowledge the multivariate and compositional nature of geochemical datasets. Such datasets are complex due to their multi-element nature, various sample origins, heterogeneous mineral textures and, not least, the analytical limitations of the methodologies used that often result in the presence of left-censored data. Advances in the acquisition of quantitative data by laser ablation inductively coupled plasma mass spectrometry

(LA-ICP-MS), or the ease of generation of large whole-rock geochemical datasets both allow unprecedented opportunity to characterise ore deposits, better constrain their spatio-temporal evolution, and, as well as enhance regional exploration programs in the absence of detailed mineralogical and petrographic data. Therefore, multivariate statistics - a quantitative, robust and reproducible approach for analysis of geochemical data is required.

Multivariate statistical analyses encompass a range of techniques spanning from data visualisation and exploratory analysis (e.g., boxplots, Tukey, 1977; parallel coordinates plot), linear and non-linear models (e.g., linear and quadratic regression), unsupervised algorithms (e.g., principal component, factor and discriminant analysis; Pearson, 1901; Spearman, 1904; Fisher, 1936), including clustering methods (hierarchical, k-means and/or fuzzy clustering), and supervised classification algorithms (e.g., random forests, Breiman et al., 1984; Breiman, 2001). The objective of multivariate analysis is to simultaneously analyse many variables and potentially discover patterns and structures within the data that are not observable by simple visualisation methods like bivariate plots or ternary diagrams. Data visualisation and unsupervised analysis aims at finding structures and patterns within the data, whereas the classification and modelling allows prediction of numerical or categorical response variables using a suite of explanatory variables. The majority of the currently employed algorithms were developed in the 20th Century, but remain, however, at the core of modern statistical analysis. In the context of the geochemical data analysis, the overarching aim is to aggregate samples/analyses into meaningful and interpretable clusters while revealing groups of variables (elements). Given the increasing cost of mineral exploration, classification and dependence modelling has advanced rapidly, as such techniques allow exclusion of redundant variables and creation of models based on smaller, higher analytical sensitivity

datasets with the potential for extrapolation and prediction of parameters of interest using large datasets with lesser number of measured elements and lower analytical sensitivity.

The most recent developments in statistical analyses include the specification of compositional data which, given their simplicial geometry, only carries relative information and requires a proper orthonormal coordinate representation to be analysed using the standard multivariate statistics (Aitchison, 1986; Egozcue et al., 2003). Advances in compositional data research also enhanced the recent developments of routines that deal with values that fall below minimum limits of detection, an important consideration given that many data analysis techniques require complete datasets. Such routines include imputation algorithms but are not limited to, model-based methods like expectation-maximisation (EM) and multiplicative lognormal replacement algorithm (Palarea-Albaladejo and Martin-Fernandez, 2013), as well as distance-based k-nearest neighbour where the information of the nearest complete observations is used to estimate the left-censored values (Hron et al., 2010).

Some multivariate analyses methods generally rely on assumption that the variables or their log-ratios have a multivariate normal distribution. This is not ideal because the distributional assumption may not be realistic for multivariate geochemical data. Therefore, a more flexible way of modelling geochemical data, such as copula functions, should be explored. Therefore, the expansion of currently available imputation methods, especially given the flexibility of modelling various distribution types using copula functions, could be necessary.

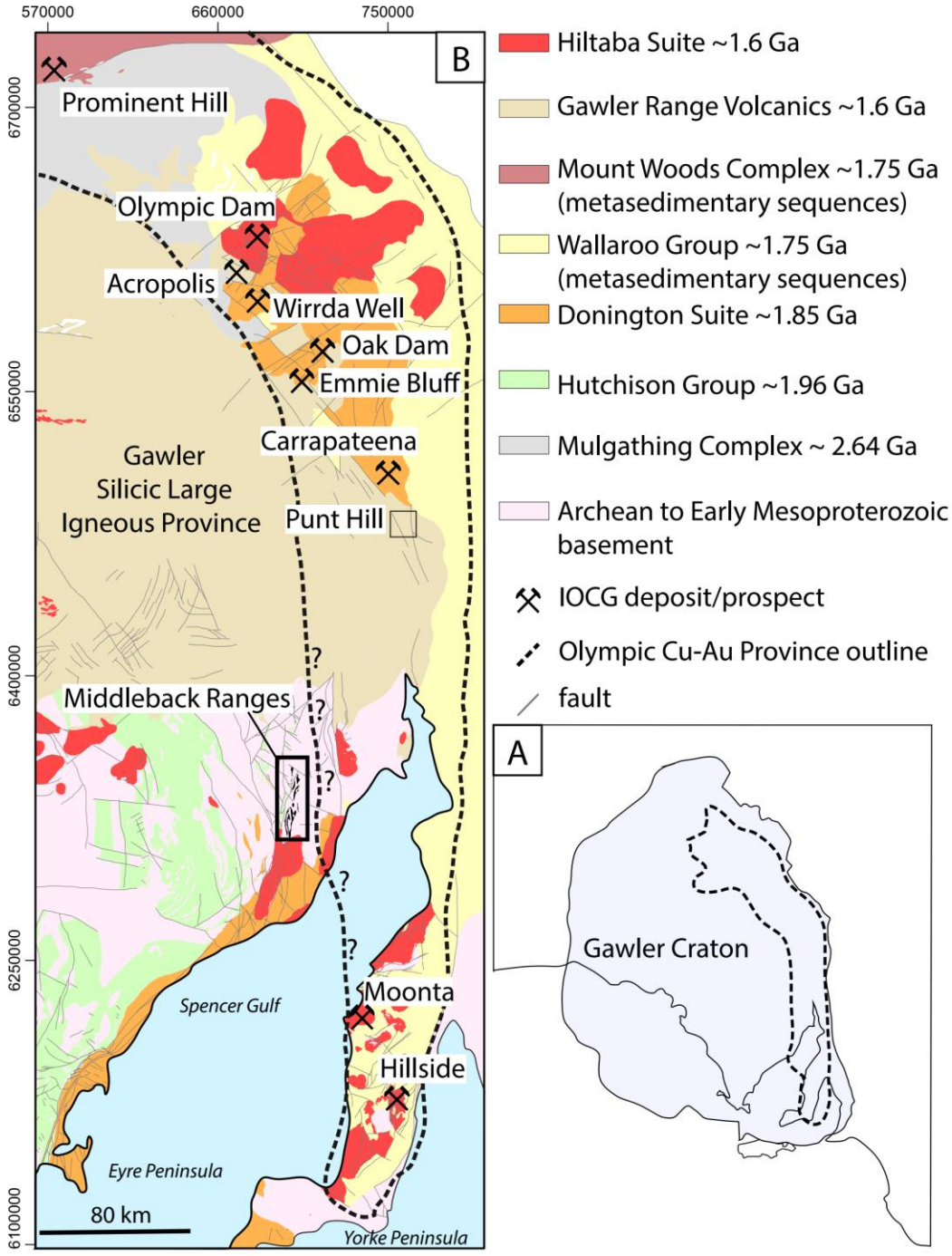


Figure 1.1. (A) Map showing the location of the Gawler Craton in South Australia and (B) geological map of the eastern Gawler Craton highlighting IOCG deposits and prospects hosted within the Olympic Cu-Au province and the Middleback Ranges. Map sourced from https://map.sarig.sa.gov.au.

1.1 RESEARCH OBJECTIVES AND THESIS STRUCTURE

This thesis is a contribution to the research project, 'Trace elements in iron-oxides: deportment, distribution and application in ore genesis, geochronology, exploration and mineral processing'. The broad objective of this project was to apply statistical analyses to whole-rock and mineral chemistry data to constrain the evolution, mineralisation and alteration signatures of IOCG and BIF-hosted ore deposits while testing the limitations and suitability of statistical analyses when applied to geochemical datasets.

This thesis aims to apply multivariate analyses to several whole-rock and LA-ICP-MS datasets from IOCG and BIF-hosted ore deposits in the absence of detailed mineralogical and petrographic information. The novelty in this project lies in the new approach of treating geochemical data, which considers their multi-element and compositional nature, while combining the results of statistical analyses with the geological and numeric 3D models, and, in some cases, also petrographic observations. Such a holistic approach, although including standard statistical analyses, has never been used to make inferences about the formation of IOCG and BIF-hosted ore deposits and their superimposed events. Despite statistical analyses having many wide applications across scientific disciplines, the approach used in this project is innovative, especially given the complementing 3D modelling and the size of the considered datasets.

The thesis is composed of two main parts which can be defined as: (i) application and development of multivariate analysis to LA-ICP-MS datasets; and (ii) large-scale studies of IOCG deposit/prospects based on the whole-rock geochemistry. Statistical analysis of trace element signatures in minerals is relevant for the characterisation of modes of occurrence of elements within a mineral (lattice-bound or inclusion-hosted) and thus may carry geometallurgical or

mineral processing implications. Analysis of trace element signatures in iron-oxides, coupled with textural categories of mineral grains, permits indication of highly localised ore enrichment settings of the Middleback Ranges, for example. The effect of the presence of left-censored data on the interpretations of the mineral trace elements signatures has been investigated, along with a new approach for imputation of left-censored data using copula functions. The individual case studies of this project expand the current knowledge about the Olympic Dam deposit and the Wirrda Well and Acropolis prospects. The 3D geology and numeric distribution of metals and mineralogical zones are shown for the first time for the Acropolis and Wirrda Well. Despite the dissimilarity with respect to hosting lithologies and the dominant Fe-oxide type, the obtained results allowed to compare and contrast the expressions of the mineralisation and alteration signatures within the three IOCG systems. These case studies demonstrated the genetic link and a common source of hydrothermal fluids for the IOCG systems in the district.

The main body of the thesis comprises six chapters which are either published (Chapters 3, 5, and 6), submitted for peer review (Chapters 4 and 7), or written as a stand-alone chapter in the form of a manuscript for later publication (Chapter 2). Each chapter represents an individual case study with its own individual datasets and data analyses methodologies. These are described in detail within additional supplementary materials for each component chapter and compiled as Chapter 9.

Left-censored values, i.e., those concentrations that fall below minimum limit of detection (primarily reflecting the analytical limitation of the instrument used for acquisition), are present in all types of geochemical datasets. A new algorithm for imputation of left-censored data that is based on copula, is proposed **Chapter 2**. The chapter describes a case study involving imputation of left-censored data for the element tellurium (Te) in the presence of measured values for silver

and gold, based upon fitting copula to the data and iteratively simulating new Te values from copula using the Metropolis-Hastings algorithm. This is a generalisation of using standard regression together with the expectation-maximisation algorithm. The proposed method has the advantages that it can model tail dependence and other non-Gaussian attributes.

Chapter 3 (Dmitrijeva et al., 2018) considers BIF-associated iron ores of the Middleback Ranges, in which iron oxides display interconversion and replacement reactions between magnetite by hematite and reprecipitation of new generations of platy hematite. Quantitative assessment of such interconversions, when correlated with available textural evidence, allows definition of geochemical signatures associated with ore enrichment. Linear-mixed effects models support the statistically significant difference among prevailing textures. Such models can account for the high degree of correlation among the analyses within a single polished block and therefore respect the hierarchical structure of such data. The observed trace element signatures indicate the potential impact of hydrothermal fluids associated with the ~1.8 Myola Volcanics, ~1.6. Ga Hiltaba Suite granites and younger discordant mafic dykes on ore enrichment process in the Middleback Ranges.

Chapter 4 (Dmitrijeva et al., 2020) presents a large body of trace element data for pyrite from Olympic Dam as an example demonstrating the predictability and potential bias in the interpretation on trace elements signatures in minerals. Statistical analysis of a large LA-ICP-MS dataset allows prediction of several minor and trace elements as inclusion-bound, a finding of interest for optimised ore processing. Pyrite is a major host for As, Co and probably also Ni, with Co and Ni being clearly indicating independent patterns of grain-scale zoning. Principal component analysis suggests that Au is contained in zoned pyrite, along with As-Co(-Ni), thus allowing to infer the presence of Au in form of electrum and telluride phases with only minor

proportion of it being attributed to the 'invisible' Au. Importantly, the study emphasizes the caution needed when working with datasets containing large proportions of left-censored values.

Multivariate analysis of whole-rock data from > 10,000 samples in **Chapter 5** (Dmitrijeva et al., 2019a) proved an effective way to underpin spatio-geochemical associations and define the geochemical signature of the Olympic Dam orebody. This giant deposit is hosted within the Olympic Dam Breccia Complex (ODBC), itself contained within the ~1.6 Ga Roxby Downs Granite. A combination of the commodity metals, i.e. Cu, U, Au, and Ag, and a range of associated trace elements were important for definition of the IOCG mineralisation signature. Numerical models were developed to show the geochemical gradients within the ODBC coupled with the zonation pattern of Cu(-Fe)-sulphides and the lithological classes in order to test whether trace elements, grouped according to multivariate analyses, match the observed mineralogical and alteration zonation. Vertical zonation with respect to Ni and Co, which are predominantly hosted by the pyrite-chalcopyrite zone, could be resolved, however the expected shallower enrichment of the ore with respect to Ag and Bi was not documented. The latter could by explained by an abundance of Ag-Bi-Pb tellurides within the pyrite at Olympic Dam. This case study raised several questions about the IOCG signatures of prospects adjacent to the Olympic Dam deposit, which display similar but non-identical mineralisation styles.

Chapter 6 (Dmitrijeva et al., 2019b) presents a 3D geological model and compositional data analysis of a whole-rock data set (4,864 samples) from the Acropolis prospect. This prospect contains vein-style mineralisation characterised by coarse-grained magnetite-apatite-sulphide assemblages with overprinting by hematite-sericite-chlorite. The IOCG mineralisation signature, as an association of REE-W-Sn-Sb-U, was shown to be present throughout the prospect, and overprints the Fe-V-Ni-Co 'magnetite' signature which was predominantly found within the veins.

The case study demonstrates the mineralisation and alteration styles of the prospect while showing the genetic relationships with the Olympic Dam deposit despite the significant differences with respect to mineralisation style.

As the third of three papers dealing with trace element signatures in IOCG deposits of the Olympic Cu-Au Province, **Chapter 7** (Dmitrijeva et al., in review) describes 3D geological and numeric models along with Cu(-Fe)-sulphide zonation and compositional data analysis of two whole-rock datasets from the Wirrda Well prospect (~29,000 and ~6,100 samples, respectively). The case study demonstrates that the prospect is comprised of two structural blocks which represent different levels of IOCG mineralisation, and which became disconnected from one another. The latter is evident from the distinct character in the mineralisation signature from Wirrda Well North and South, with a 'V-Ni-Co' signature being abundant in the northern block of the prospect. Most importantly, the case study also indicated that the pre-mineralisation dykes serve as fluid pathways with Cu(-Fe)-sulphides being concentrated along the dyke contacts.

A summary of the key findings, implications and recommendations of this research are presented in **Chapter 8**. This chapter defines several open questions and areas for potential future research. Additional supplementary material associated with Chapters 2-7, co-authored publications and conference abstracts and posters are compiled in **Chapter 9**. A complete reference list is given in **Chapter 10**.

1.2 References

Aitchison, J., 1986. The statistical analysis of compositional data. In: Monographs on Statistics and Applied Probability. Chapman & Hall, London 416 pp.

Allen, S., McPhie, J., Ferris, G., Simpson, C., 2008. Evolution and architecture of a large felsic igneous province in western Laurentia: the 1.6 Ga Gawler Range Volcanics, South Australia. Journal of Volcanaology and Geothermal Research 172, 132-147.

Blissett, A.H., Creaser, R.A., Daly, S.J., Flint, R.B., Parker, A.J., 1993. Gawler Range Volcanics. In: Drexel, J.F., Preiss, W.V., Parker, A.J. (Eds.), The Geology of South Australia. Vol. 1. The Precambrian, Geological Survey of South Australia, pp. 107–131

Breiman, L., 2001. Random forests. Machine Learning 45, 5–32.

Breiman, L., Friedman, J.H., Olshen, R.A., Stone, C.J., 1984. Classification and Regression Trees. Wadsworth, Belmont, pp. 358.

Courtney-Davies, L., Ciobanu, C.L., Verdugo-Ihl, M.R. Dmitrijeva, M., Cook, N.J., Ehrig, K., Wade, B., 2019. Hematite geochemistry and geochronology resolve genetic and temporal links among iron-oxide copper gold systems, Olympic Dam district, South Australia. Precambrian Research 335, 105480.

Dare, S.A.S., Barnes, S.-J., Beaudoin, G., Méric, J., Boutroy, E., Potvin-Doucet, C., 2014. Trace elements in magnetite as petrogenetic indicators. Mineralium Deposita, 49, 785–796.

Dmitrijeva, M. Metcalfe, A.V., Ciobanu, C.L. Cook, N.J., Frenzel, M., Keyser, W.M., Johnson, G., Ehrig, K., 2018. Discrimination and variance structure of trace element signatures in hematite: a case study of BIF-mineralisation from the Middleback Ranges, South Australia Mathematical Geosciences, 50, 381-415

Dmitrijeva, M., Ehrig, K., Ciobanu, C., Cook, N., Verdugo-Ihl, M., Metcalfe, A., 2019a. Defining IOCG signatures through compositional data analysis: a case study of lithogeochemical zoning from the Olympic Dam deposit, South Australia. Ore Geology Reviews, 105, 86–101.

Dmitrijeva, M., Ciobanu, C., Ehrig, K., Cook, N., Metcalfe, A., Verdugo-Ihl, M., McPhie, J., 2019b. Mineralisation-alteration footprints in the Olympic Dam IOCG district South Australia: The Acropolis prospect. Journal of Geochemical Exploration, 205, 106333

Dmitrijeva, M., Cook, N.J., Ehrig, K., Ciobanu, C.L., Metcalfe, A.V., Kamenetsky, M., Kamenetsky, V.S., Gilbert, S., 2020, Multivariate statistical analysis of trace elements in pyrite: prediction, bias and artefacts in defining mineral signature. Minerals, 10, 61

Dmitrijeva, M., Ciobanu, C.L., Ehrig, K., Cook, N.J., Verdugo-Ihl, M.R., Metcalfe, A.V., Kamenetsky, V.S., McPhie, J., in review, Geochemical data analysis and 3D modelling of Wirrda Well prospect, South Australia: structural control on iron-oxide copper gold mineralisation. Economic Geology.

Egozcue, J.J., Pawlowsky-Glahn, V., Mateu-Figueras, G., Barceló-Vidal, C., 2003. Isometric logratio transformations for compositional data analysis. Mathematical Geosciences, 35, 279–300.

Ehrig, K., McPhie, J., Kamenetsky, V., 2012. Geology and mineralogical zonation of the Olympic Dam iron oxide Cu-U-Au-Ag deposit, South Australia. Society of Economic Geologists, Special Publication, 16, 237–267.

Fisher, R.A., 1936. The Use of Multiple Measurements in Taxonomic Problems. Annals of Eugenics. 7 (2): 179–188.

Hron, K., Templ, M., Filzmoser, R., 2010. Imputation of missing values for compositional data using classical and robust methods. Computational Statistics and Data Analysis, 54, 3095-3107.

Ismail, R., Ciobanu, C.L., Cook, N.J., Teale, G.S., Giles, D., Schmidt Mumm, A., Wade, B., 2014. Rare earths and other trace elements in minerals from skarn assemblages, Hillside iron oxide–copper–gold deposit, Yorke Peninsula, South Australia. Lithos 184-187, 456-477.

Keyser K, Ciobanu, C.L., Cook, N.J., Johnson, G., Feltus, H., Johnson, S., Dmitrijeva, M., Ehrig, K., Nguyen, P.T., 2018. Petrography and trace element signatures of iron-oxides in deposits from the Middleback Ranges, South Australia: from banded iron formation to ore. Ore Geology Reviews, 93, 337–360.

Keyser, W.M., Ciobanu, C.L., Cook, N.J., Johnson, G., Dmitrijeva, M., Courtney-Davies, L., Feltus, F., Gilbert, S., Johnson, G., Ehrig, K., 2019. Iron-oxides constrain BIF evolution in terranes with protracted geological histories: The Iron Count prospect, Middleback Ranges, South Australia Lithos, 324–325, 20-38

Kontonikas-Charos, A., Ciobanu, C.L., Cook, N.J., 2014. Albitisation and redistribution of REE and Y in IOCG systems: insights from Moonta-Wallaroo, Yorke Peninsula, South Australia. Lithos, 208–209, 178–201.

Kontonikas-Charos, A., Ciobanu, C.L., Cook, N.J., Ehrig, K., Krneta, S., Kamenetsky, V.S., 2017. Feldspar evolution in the Roxby Downs Granite, host to Fe-oxide Cu-Au-(U) mineralisation at Olympic Dam, South Australia. Ore Geol. Rev. 80, 838–859.

Kontonikas-Charos, A., Ciobanu, C.L., Cook, N.J., Ehrig, K., Krneta, S., Kamenetsky, V.S., 2018. Rare earth element geochemistry of feldspars: examples from Fe-oxide Cu-Au systems in the Olympic Cu-Au Province, South Australia. Mineralogy and Petrology, 112, 145–172.

Mauger, A.J., Ehrig, K.J., Kontonikas-Charos, A., Ciobanu, C.L., Cook, N.J., Kamenetsky, V.S., 2016. Alteration at the Olympic Dam IOCG–U deposit: insights into distal to proximal feldspar and phyllosilicate chemistry from infrared reflectance spectroscopy. Australian Journal of Earth Sciences, 63, 959-972.

Palarea-Albaladejo, J., Martin-Fernandez, J.A., 2013. Values below detection limit in compositional chemical data. Analytica Chimica Acta, 764, 32-43.

Paterson, H.L., 1986. The Acropolis prospect. In: Paterson, H.L.C. (Ed.), Basement geology of the Stuart Shelf region, South Australia (vol. A1 – Olympic Dam/Stuart Shelf Excursion Guide, pp. 17–18). 8th Australian Geological Convention. Geological Society of Australia, Adelaide. Sydney, NSW

Pearson, K. 1901. On Lines and Planes of Closest Fit to Systems of Points in Space. Philosophical Magazine, 2, 559–572.

Reeve, J.S., Cross, K.C., Smith, R.N., Oreskes, N., 1990. Olympic Dam copper-uranium-gold-silver deposit. In: Hughes, F.E. (Eds.), Geology of the Mineral Deposits of Australia and Papua New Guinea: Austral. Inst. Min. Metal., Monograph 14, p. 1009-1035.

Reid, A., 2019. The Olympic Cu-Au Province, Gawler Craton: A Review of the Lithospheric Architecture, Geodynamic Setting, Alteration Systems, Cover Successions and Prospectivity. Minerals, 9, 371.

Skirrow, R.G., Bastrakov, E.N., Baroncii, K., Fraser, G.L., Creaser, R.A., Fanning, C.M., Raymond, O.L., Davidson, G.J., 2007. Timing of iron oxide Cu-Au-(U) hydrothermal activity and Nd isotope constraints on metal sources in the Gawler craton, South Australia. Economic Geology 102, 1441–1470.

Spearman, C., 1904. General Intelligence. Objectively Determined and Measured. The American Journal of Psychology, 5, 201-293

Tukey, J.W., 1977. Exploratory Data Analysis. Addison-Wesley. 688 pp.

CHAPTER 2

A COPULA-BASED APPROACH TO THE IMPUTATION OF VALUES BELOW MINIMUM LIMITS OF ANALYTICAL DETECTION

Marija Dmitrijeva[1], Andrew V. Metcalfe[2], Cristiana L. Ciobanu[1], Nigel J. Cook[1], Kathy Ehrig[3]

[1]*School of Chemical Engineering and Advanced Materials, The University of Adelaide, Adelaide, SA 5005, Australia*

[2]*School of Mathematical Sciences, The University of Adelaide, Adelaide, SA 5005, Australia*

[3]*BHP Olympic Dam, Adelaide, SA 5000, Australia*

Thesis Chapter

Statement of Authorship

Title of Paper	A copula-based approach to the imputation of values below their detection limit
Publication Status	☐ Published ☐ Accepted for Publication ☐ Submitted for Publication ☑ Unpublished and Unsubmitted w ork w ritten in manuscript style
Publication Details	Dmitrijeva., M., Metcalfe, A.V., Ciobanu, C.L., Cook, N.J., Ehrig, K. A copula-based approach to the imputation of values below their detection limit. Thesis Chapter.

Principal Author

Name of Principal Author (Candidate)	Marija Dmitrijeva		
Contribution to the Paper	Performed algorithm development and implementation, wrote the thesis chapter.		
Overall percentage (%)	55		
Certification:	This paper reports on original research I conducted during the period of my Higher Degree by Research candidature and is not subject to any obligations or contractual agreements with a third party that would constrain its inclusion in this thesis. I am the primary author of this paper.		
Signature		Date	17.12.19

Co-Author Contributions

By signing the Statement of Authorship, each author certifies that:

i. the candidate's stated contribution to the publication is accurate (as detailed above);

ii. permission is granted for the candidate in include the publication in the thesis; and

iii. the sum of all co-author contributions is equal to 100% less the candidate's stated contribution.

Name of Co-Author	Andrew V. Metcalfe		
Contribution to the Paper	Helped to define the direction of the paper, assisted with the algorithm development, coding and the interpretation of the results, contributed to the thesis chapter preparation.		
Overall percentage (%)	25		
Signature		Date	17.12.19

Name of Co-Author	Cristiana L. Ciobanu		
Contribution to the Paper	Assisted with the thesis chapter preparation.		
Overall percentage (%)	8		
Signature		Date	17.12.19

Name of Co-Author	Nigel J. Cook		
Contribution to the Paper	Assisted with the thesis chapter preparation.		
Overall percentage (%)	8		
Signature		Date	17.12.19

Name of Co-Author	Kathy Ehrig		
Contribution to the Paper	Assisted with the evaluation of the thesis chapter.		
Overall percentage (%)	4		
Signature		Date	17.12.19

A copula-based approach to the imputation of values below minimum limits of analytical detection

Marija Dmitrijeva[1], Andrew Metcalfe[2], Nigel J. Cook[1], Cristiana L. Ciobanu[1], Kathy Ehrig[3]

[1] School of Chemical Engineering and Advanced Materials, The University of Adelaide, Adelaide, SA 5005, Australia

[2] School of Mathematical Sciences, The University of Adelaide, Adelaide, SA 5005, Australia

[3] BHP Olympic Dam, Adelaide, SA 5001, Australia

Abstract

Left-censored values arise in all types of geochemical data and require quantitative methods for their imputation that preserve the structure of data as well as relationships among variables. Multivariate Gaussian distribution, which is embedded in many algorithms designed for left-censored data imputation, is restrictive and cannot account for asymmetries and tail-dependence which are often present in geochemical data. As an alternative, copula functions can be used to model the dependence among geochemical variables as they are more efficient and versatile for modelling multivariate distributions.

This work presents a case study of a trivariate copula fitted into data using a vine copula approach. Copula was fitted to a real three-element (Te-Au-Ag) whole-rock data where all measurements are measured above their detection limits. Three artificial detection limits L, (1, 0.8 and 0.5 ppm) were set up for Te values. The Te values < L were obtained from a fitted trivariate copula using Markov chain Monte Carlo simulation. For comparison purposes, Te values < L were also predicted using a standard regression. The expectation-maximization algorithm was used in both methods in order to iteratively obtain the best estimates for the left-censored values of Te, end errors were calculated

as the difference between observed and imputed values. There was little difference in the statistics of the errors, but the distribution of imputed values using the copula more closely resembles the distribution of the observations.

Introduction

Values falling below the minimum limits of detection (mdl) are present in all types of geochemical data, reflecting the analytical capabilities of the instrument used to acquire such data, often compounded by sample size. These <mdl values represent thresholds below which an instrument is not able to discriminate a signal from the background noise. Geochemical data can be obtained by a range of analytical instruments, e.g. microbeam technique such as laser-ablation inductively coupled plasma mass spectrometry (LA-ICP-MS) or electron probe micro-analyzer (EPMA), or various spectrometry methods designed for a particular set of elements, that can be combined to form 'whole-rock' data. In the case of microbeam methods, the number of <mdl values, and therefore the analytical sensitivity of the instrument, can be reduced by varying acquisition parameters, such as time for EPMA and, for instance, spot size for LA-ICP-MS. Similarly, better analytical sensitivity can be achieved for whole-rock data.

Geochemical datasets are used to define trends in complex geological applications, e.g., mineralization hosted in various lithologies (e.g. Dmitrijeva et al., 2019), multi-stage overprints (e.g. Verdugo-Ihl et al., 2017), mapping alteration and/or element mobility (e.g. Hood et al., 2018; 2019). The efficiency and speed at which geochemical data can be acquired allows the collection of large amounts, however the presence of values <mdl represents a major limitation since multivariate statistical analyses rely on complete datasets (e.g., Helsel, 2005). Various strategies have been suggested in order to overcame the issue of <mdl values. Such strategies include

exclusion of those elements containing more than a certain proportion of values <mdl (e.g., Makvandi et al. 2016), or replacing such data with an arbitrary value usually set to one half of the detection limit (e.g., Winderbaum et al. 2012). However, the former approach results in a significant loss of valuable information, and the latter lacks a mathematical basis, may introduce bias and can significantly underestimate data variability as the relative amount of replaced values increases.

A preferable approach is to use numerical imputation for values falling below the mdl. Methods for imputation include multiplicative log-normal replacement (Palarea-Albaladejo and Martín-Fernández, 2013) and regression procedures used in conjunction with the expectation-maximization (EM) algorithm (Honaker et al., 2011; Palarea-Albaladejo and Martín-Fernández, 2013). Such methods, which generally rely on the assumption that the variables, or their logarithms, have a multivariate normal distribution are not ideal because the distributional assumption may not be realistic for multivariate geochemical data. The prediction of values < mdl using algorithms that are based on normal distribution does not allow for asymmetry and heavy tails in complex geochemical data.

Vine copulas are flexible multivariate uniform distributions that allow modelling of complex dependence among the variables, i.e., elements, and therefore can be used to predict the values <mdl. The utilization of multivariate parametric and Archimedean copulas in missing data research has been briefly addressed (Houari et al., 2013; 2014; Di Lascio et al., 2014), however vine copulas have never been used or assessed for the imputation of <mdl in geochemical datasets. Vine copulas represent a cascade of pair-copulas constructions which decompose a multivariate probability density into a set of bivariate copulas where each pair can be chosen independently. The main advantage of vine copulas is its ability to take into account asymmetry and tail dependence.

In this contribution we introduce a copula-based method for imputation of values <mdl by using vine copulas. Firstly, we decompose a trivariate distribution of three typical trace elements of interest (Te, Au, and Ag) into a set of bivariate copulas and derive the conditional density function of the values < mdl for Te given the observed ones (Au and Ag). Secondly, we utilise the Metropolis-Hastings (M-H) algorithm, a method from the Markov chain Monte Carlo family of algorithms, in order to obtain a random sample from the conditional density function. In order to compare the outcome, we perform the prediction of values < mdl using the standard regression of Te onto Au and Ag. Finally, we compare the outcome of the predictions by calculating absolute and relative errors. The elements Te, Au and Ag are used as a test case to demonstrate the algorithm.

Data

The dataset used is this study is a 4083-sample subset from >10,000 whole-rock geochemical samples from the Olympic Dam deposit, South Australia, published by Ehrig et al. (2012). The objective is to compare imputed values <mdl with known observed values, so a subset of the data was taken based on the condition that all measured concentration values for Te, Au and Ag are above their respective detection limits, 0.2 ppm, 1 ppb and 0.1 ppm. Three artificial detection limits were set for Te: L_1 = 1; L_2 = 0.8; and L_3 = 0.5 ppm. Such an approach generated a step-wise reduction of Te <mdl values in the data from 1479 for L_1 = 1, through 1080 for L_2 = 0.8, to 471 for L_3 = 0.5 ppm. The Te <mdl values were predicted using two methods described in detail below: (i) standard regression; and (ii) sampling from a trivariate copula using the M-H algorithm. The distribution of imputed values was compared with the distribution of observations. The predicted and simulated values were further compared with the observed Te values ranging from the true

mdl of 0.2 ppm up to the L_1 = 1 ppm by calculating relative and absolute errors. The comparison necessarily excludes observations for which any of the elements are > mdl.

Implementation

This section describes and proposes a copula-based algorithm for the imputation of <mdl values using a trivariate Au-Te-Ag data. The copula-based algorithm bases on R packages 'copula' (Hofert et al., 2017) and 'VineCopula' (Schepsmeier et al., 2018). The building blocks of the agorithm are a trivariate copula function fitted to the data, the M-H algorithm (Chib and Greenberg, 1995) used for drawing new values from the copula, and finally, the E-M algorithm (Dempster et al., 1977) used for iteration.

Expectation-maximization algorithm

The Expectation-Maximization (EM) algorithm is an iterative method that can be used to find maximum likelihood estimates of parameters of some probability model, when some multivariate data have missing items that are replaced by their expected values. Here we use the E-M algorithm to estimate the values of Te, given the values for Au and Ag, and together the condition of Te being <mdl. We describe the E-M algorithm in the context of the standard multiple regression model, which is equivalent to fitting a Gaussian copula, for the particular case of trivariate data. The algorithm consists of two steps: the expectation E-step and the maximization M-step. Suppose there are *n* trivariate data (x_{1i}, x_{2i}, x_{3i}) for $i = 1,...,n$ and that for m of these data x_{3i} is recorded as below an mdl value of L.

Step 1. Replace values of x_{3i} that are below L by 0.5×L. This gives a dataset of n complete data

Step 2. Fit a regression model to this complete dataset

$x_{3i} = \beta_0 + \beta_1 \times x_{1i} + \beta_2 \times x_{2i} + \varepsilon_i$, where $\varepsilon_i \sim N(0, \sigma^2)$ for $i = 1, ..., n$ (1)

Step 3. Use the fitted regression model from Step 2 to predict the values of x_3 that have been replaced by 0.5×L, as follows. The estimates of the coefficients are $\hat{\beta}_0$, $\hat{\beta}_1, \hat{\beta}_2$ and the estimate of σ^2 is given by

$$\hat{\sigma}^2 = \frac{\sum \hat{\varepsilon}_i^2}{n-3},$$

where $\hat{\varepsilon}_i = x_{3i} - \hat{x}_{3i}$ and

$$\hat{x}_{3i} = \hat{\beta}_0 + \hat{\beta}_1 x_{1i} + \hat{\beta}_2 x_{2i}. \quad (2)$$

Let k be a typical datum with x_3 below L, $(x_{1k}, x_{2k}, 0.5 \times L)$, for $k = 1, ..., m$, and set

$$\hat{\mu}_k = \hat{\beta}_0 + \hat{\beta}_1 \times x_{1k} + \hat{\beta}_2 \times x_{2k} \quad (3)$$

Define

$$\hat{p} = \Phi\left(\frac{L - \hat{\mu}_k}{\hat{\sigma}}\right), \quad (4)$$

so

$$\Phi^{-1}(\hat{p}) = \frac{L - \hat{\mu}_k}{\hat{\sigma}}. \quad (5)$$

Then

$$\hat{x}_{3k} = \hat{\mu} - \hat{\sigma}\left(\frac{\phi\left(\Phi^{-1}(\hat{p})\right)}{\hat{p}}\right), \quad (6)$$

where $\Phi()$ and $\phi()$ are the cumulative density function and probability density function of a standard normal distribution (e.g. Norton et al., 2019). Replace all m values below L by the corresponding estimated $\hat{x}_{3k}$ values.

Step 4. Step 3 gives a revised complete dataset. Return to Step 2, except that 0.5L is now $\hat{x}_{3i}$ from Step 3 and iterate until the algorithm converges to give the final imputed values of $\hat{x}_{3k}$.

The algorithm is considered converged when the imputed value $\hat{x}_{3k}$ reach their final value, i.e. stop varying.

Fitting a copula to trivariate data

A bivariate copula is a bivariate uniform distribution. This construction includes all possible bivariate distributions, because any random variable can be transformed to a uniform distribution by a probability integral transform (PIT). The proof of PIT result is quite succinct and reproduced in Equations 7-9. Suppose a random variable X has a continuous cumulative distribution function (CDF), $F()$. Then, by definition of the CDF

$$P(a < X < b) = F(b) - F(a) . \quad (7)$$

Also, since $F()$ is a is defined as a monotonically increasing function,

$$P(a < X < b) = P(F(a) < F(X) < F(b)) , \quad (8)$$

therefore

$$P(F(a) < F(X) < F(b)) = F(b) - F(a) , \quad (9)$$

and since $0 \leq F(a), F(b) \leq 1$ in Eq. (8) defines $F(X)$ as a uniform random variable. Sklar's theorem (1959) is a formal proof that any multivariate distribution can be expressed as a copula, and that any copula, with any back-transformed marginal distribution, leads to a valid multivariate distribution.

In general, the PIT can be implemented empirically for data $\{x_i\}\ i = 1, \ldots, n$ by tranfroming each datum to the ratio of its rank to $n + 1$. That is

$$x_{1:n} \rightarrow i/(n+1) \tag{10}$$

where $x_{i:n}$ is the i[th] order statistic (the i[th] smallest value). This transformed datum is known as its pseudo-value. Alternatively, a probability distribution with CDF $F()$ can be fitted to the data, in which case the PIT is

$$x_i \rightarrow F(x_i). \tag{11}$$

Any multivariate probability distribution can be expressed as a product of bivariate copulas, and this expression is known as a vine or pair copula construction (Aas et al., 2009). In the case of three variables $f(x_1, x_2, x_3)$, the probability density function (PDF) can be written as:

$$f(x_1, x_2, x_3) = f_1(x_1) f_2(x_2) f_3(x_3) \times c_{13}(F_1(x_1) F_3(x_3)) c_{23}(F_2(x_2) F_3(x_3)) \times$$
$$c_{12|3}(F_{1|3}(x_1|x_3)(F_{2|3}(x_2|x_3)) \tag{12}$$

where $f_1()$, $f_2()$ and $f_3()$ are the marginal PDFs, $c_{13}()$ and $c_{23}()$ are bivariate copula PDFs for x_1 and x_3, x_2 and x_3, respectively, and $c_{12|3}()$ is a conditional bivariate copula PDF for x_1 and x_2 given x_3. This is generally simplified by assuming that the conditional copula $c_{12|3}()$ is well approximated by the unconditional copula $c_{12}()$. The arguments of the conditional copula $F_{1|3}(x_1|x_3)$ and $F_{2|3}(x_2|x_3)$ are obtained from the h function, which is defined as

$$h(w|u) = C(w|u) = \frac{\partial C(u,v)}{\partial v}, \tag{13}$$

where $C(u, w)$ is the copula CDF. Although this result is not intuitive, its proof is straightforward and is given below. It begins with the approximation:

$$C(w|u) \approx P(W < w | u - \delta < U < u). \tag{14}$$

The right hand-side of Eq. (14) is equal to

$$\frac{P(W<w)\cap u-\delta<U<u}{P(u-\delta<U<u)},$$

$$\frac{P(W<w\cap U<u)-P(W<w\cap U<u-\delta)}{P(u-\delta<U<u)},$$

$$\frac{C(w,u)-C(w,u-\delta)}{\delta}. \qquad (15)$$

Now we let $\delta \to 0$, Eq. (14) becomes exact, and ratio in Eq. (15) tends to the partial derivative $C(w|u)=\frac{\partial C(w,u)}{\partial u}$.

The vine copula construction is implemented by fitting bivariate copulas to element pairs $\left(x_{Te},x_{Au}\right)$, $\left(x_{Te},x_{Ag}\right)$ and $\left(x_{Au},x_{Au}\right)$, and using a numerical approximation for the partial derivative in Eq. (14). In this application the following copulas were considered: Gaussian, Student t, Clayton, Gumbel, Frank and Joe, whereas each copula was fitted to a pair of elements variables using maximum likelihood estimation. Frank copula was selected as a best suitable pair-copula for all the element pairs based upon the computed Akaike information criterion (AIC) (Akaike, 1973; Brechman, 2010, Schepsmeier et al., 2018). A parameter of Frank copula varied depending on the Te having mdl1 = 1, mdl2 = 0.8 or mdl3 = 0.5 ppm. The h function was obtained by numerical approximation (Brechmann and Schepsmeier, 2013).

Metropolis-Hastings algorithm to draw random samples from a copula

The fitted copula is a particular case of a trivariate distribution with PDF $f\left(x_1,x_2,x_3\right)$, and we require the expected value of the conditional distribution of X_3 given x_1,x_2 and $X_3<$ L. In general, this expectation cannot be expressed as an algebraic function of the parameters of the trivariate distribution. However, the expectation can be obtained to any required precision by

Monte-Carlo simulation. The conditional PDF for X_3 given values of x_{1k}, x_{2k} for x_1 and x_2, respectively is:

$$f(x_3 \mid x_{1k}, x_{2k}) = \frac{f(x_{1k}, x_{2k}, x_3)}{f(x_{1k}, x_{2k})} \tag{16}$$

for $k = 1,...,m$, which is proportional to $f(x_{1k}, x_{2k}, x_3)$. The value of $f(x_{1k}, x_{2k})$ is the normalizing constant, which makes the area under the PDF equal to one. The expected value of X_3 given x_{1k}, x_{2k} and $X_3 <$ L is found by drawing a large number, N, of random variates from $f(x_3 \mid x_{1k}, x_{2k})$, and taking the mean value of the x_{3_j} $j = 1,...,N$ that are < L. The precisions of the estimate of expectation increases with N, which is taken as 10^3 in this application (Fig. 1).

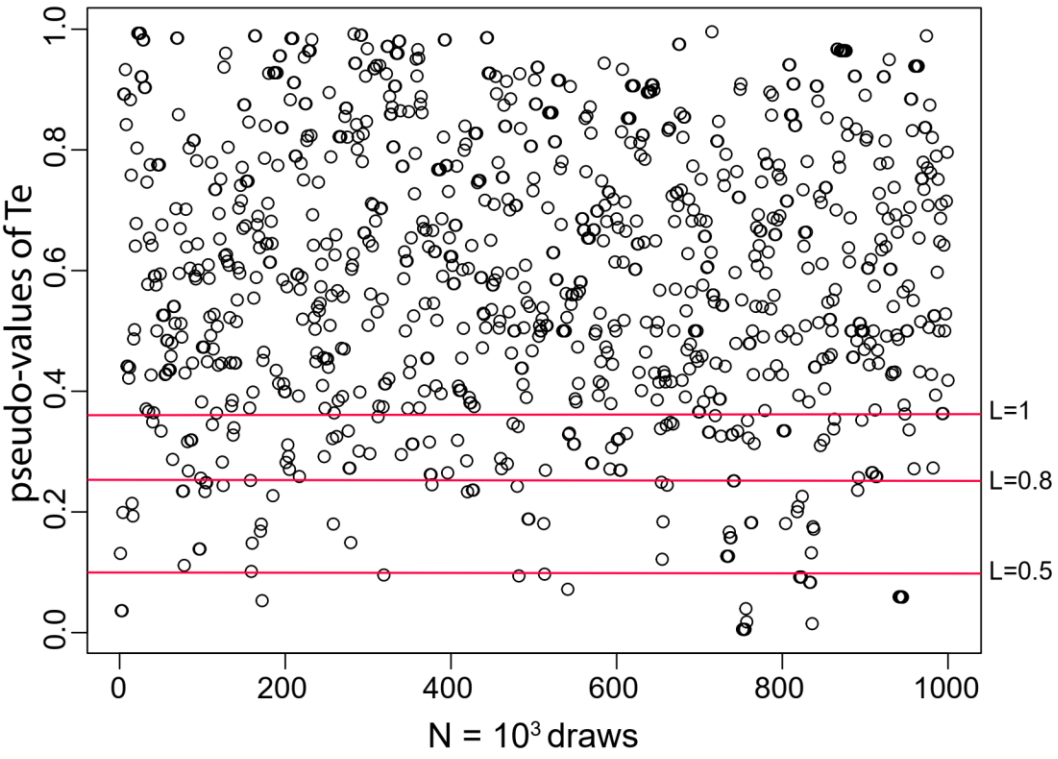


Figure 1. A result from a single iteration of the M-H algorithm showing 10^3 pseudo-values of Te sampled from a trivariate Au-Ag-Te copula. An imputed pseudo-value of Te was calculated as a mean of values below a particular L

The M-H algorithm is widely used for drawing random deviates from a probability distribution, and it has the substantial advantage of not requiring the values of the normalizing constant (e.g. Chib and Greenberg, 1995). In this univariate application the M-H algorithm can be written as follows. For each x_{1k}, x_{2k}:

Step 1. Take a plausible value of X_3, $x_{3,0}$, say as $x_{3,0}$, a starting point.

Step 2. For $i = 0,...N$ let $x^*_{3,i+1} = x_{3,i} + w_i$, where $w_i \sim N(0, \sigma^2)$ with σ around one quarter of the ranges of X_3. Calculate

$$q_i = \frac{f(x_{1k}, x_{2k}, x^*_{3,i+1})}{f(x_{1k}, x_{2k}, x_{3,i})} \tag{17}$$

if q_i >1 then $x_{3,i+1} = x^*_{3,i+1}$ else if q_i <1 draw u_i from $U[0,1]$

$$x_{3,i+1} = \begin{cases} x^*_{3,i+1} & \text{if} \quad q_i > u_i \\ x_{3,i} & \text{if} \quad q_i < u_i \end{cases} \tag{18}$$

Step 3. Return to Step 2 and iterate for N draws.

The M-H algorithm does not give a sequence of independent draws, but independence is not necessary to estimate the PDF. If independence s required the M-H algorithm can be-run and the final point of each run taken. The values of and N can be varied.

Proposed copula-based algorithm

An algorithm to simulate Te values from the density function $f\left(x_{Te} \mid x_{Au}, x_{Ag}\right)$ using the M-H algorithm is proposed below. A single iteration of the algorithm showing the below-mentioned steps is given in Appendix A.

Step 1. Replace the Te < mdl values by $(L - i/(m+1))$, where $i = 1,...,m$.

Step 2. Obtain pseudo-values for Te Au and Ag using the empirical PIT (see Eq. 10)

Step 3. Find and fit the optimal copula to the pseudo-values of Te-Au, Te-Ag and Au-Ag

Step 4. Having written a function to implement the M-H algorithm, (see lines 137-166; Appendix A), that generates random draws from the conditional distribution of pseudo values of Te given pseudo-values for Au, Ag, make 1000 random draws of pseudo-values of Te using the M-H algorithm and calculate the mean of those that are below the pseudo-values of L.

Step 5 Back transform pseudo-values of Te to Te in ppm. This requires the assumption of some parametric distribution for Te. The Weibull distribution is versatile for non-negative data and is used here, respectively. The Weibull distribution is fitted to Te values above L by a plotting method which allows for censored data. The plotting method equates $F(x_{1:n}) = i(n+1)$. In the case of the Weibull distribution

$$F(x) = 1 - e^{-(x/b)^a} \tag{19}$$

taking logarithms twice leads to

$$\ln(x_{1:n}) = \ln(b) + \frac{1}{a}\ln(-(1 - \frac{i}{n+1})) \tag{20}$$

so the $\ln(x_{1:n})$ are plotted against $\ln(-\ln(1-i/(n+1)))$ for $m+1 \le i \le n$,

and $1/a$ and $\ln(b)$ are estimated by the slope and the intercept. Finally, Te in ppm is given by

$$Te_{ppm} = \ln(b) + \frac{1}{a}\ln(-\ln(1 - Te)) \tag{21}$$

Where Te is a pseudo-value. Then return to Step 1 and replace the < L value with the values obtained in Step 6 and iterate until the algorithm converges. The algorithm's code for a single iteration with the corresponding steps is given in the Appendix A.

Table 1. Absolute and relative errors for standard regression and copula calculated for three different artificial mdls.

Model used to obtain <mdl Te values		SR DL=1	copula DL=1	SR DL=0.8	copula DL=0.8	SR DL= 0.5	copula DL = 0.5
Relative Errors							
$\sum_{i=1}^{m}(O_i - P_i)/m$	(22)	-0.036	-0.031	-0.003	0.005	0.082	0.150
$\sum_{i=1}^{m}(O_i - P_i)^2/m$	(23)	0.101	0.204	0.067	0.141	0.025	0.062
$\sum_{i=1}^{m}\lvert O_i - P_i\rvert^2/m$	(24)	0.345	0.352	0.303	0.306	0.214	0.217
Absolute Errors							
$\sum_{i=1}^{m}(O_i - P_i)$	(25)	0.055	0.073	0.051	0.060	0.047	0.071
$\sum_{i=1}^{m}(O_i - P_i)^2$	(26)	0.058	0.063	0.035	0.038	0.010	0.013
$\sum_{i=1}^{m}\lvert O_i - P_i\rvert^2$	(27)	0.203	0.213	0.158	0.165	0.087	0.093

SR- standard regression; O – observed value; P – predicted value

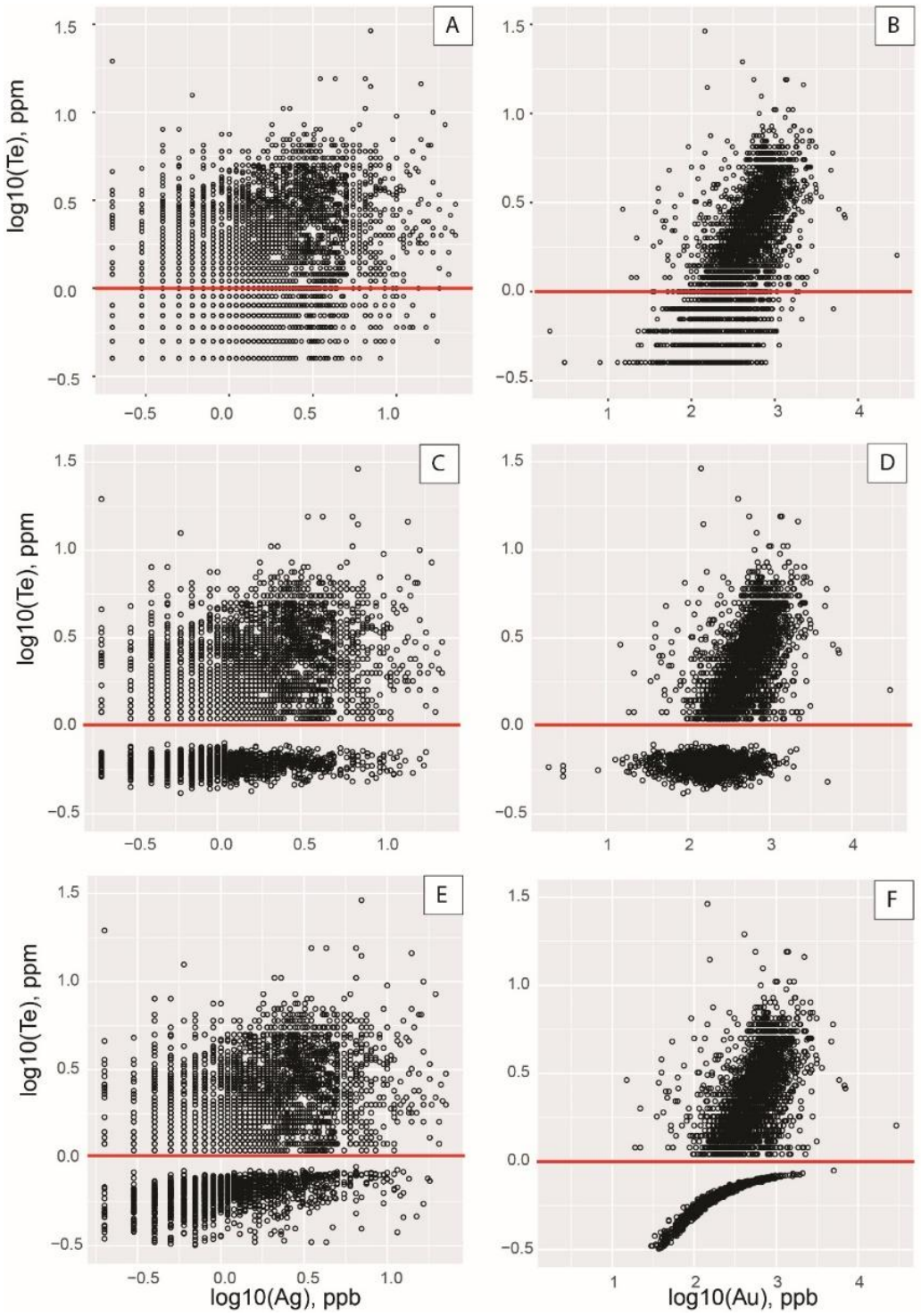


Figure 2. Scatterplots of Ag-Te and Au-Te showing the original data (n = 4083) (A-B). C-D displays Ag-Te and Au-Te scatterplots with the original data plotting above L = 1 threshold (red line), and values simulated from copula plotting below L. E-F displays original data above L and the Te values predicted using the standard regression plotting below L

Results and Implications

The absolute and relative errors, relative to the observed values for $L_1 = 1$, $L_2 = 0.8$ and $L_3 = 0.5$ ppm are presented in Table 1. The errors measure the performance of imputation using a copula and a standard regression. For $L_1 = 1$ ppm, the relative error obtained from copula is slightly lower than for standard regression, but for the other cases standard regression shows slightly lower errors. Nevertheless, the error differences in the statistics of the errors are negligible in most cases (Table 1). In contrast, the visualization of imputed values (Fig. 2) shows that the copula gives a distribution of imputed values that more closely resemble the distribution of the observations than does standard regression. Moreover, the copula does include standard regression as a special case. One of the properties of the given whole-rock data is a large number of discretised values, which increase as the values approach the real detection limits 0.2 ppm for Te, 1 ppb for Au and 0.1 ppm for Ag. Such discretization may serve as a limitation and potentially reduce the performance of copula-based imputation. Another limitation of the whole-rock geochemical data is the supposed fixed <mdl value for every element, which is the mean mdl value quoted by a laboratory. Given these limitations, copula-based approaches may be more suitable for trace element data for specific minerals obtained by LA-ICP-MS, in which each LA-ICP-MS datum contains a unique mdl value. The adaptation of the current algorithm for LA-ICP-MS data will require two modifications and a change of L from a single fixed value to a vector of mdl values $\boldsymbol{l}$. The first modification will include a change in the conditional statement, where a simulated Te pseudo-value is compared with the rank, i.e. pseudo-value of L_i. As for the whole-rock data, L_i, as well as its rank, is fixed (Eq. 10), then for LA-ICP-MS a vector of ranks of $\boldsymbol{l}$ needs to be used in the conditional statement (Step 4; Section 3.4; line 157, Appendix A). The second modification relates to the conversion of Te from pseudo-values to ppm (Step 5; Section 3.4), more specifically, the change is required in the

estimation of the parameters of the Weibull distribution (Eqs. 20-21; line 184, Appendix A). Provided that a trivariate vine copula with fitted bivariate Gaussian distribution to element pairs is essentially a trivariate normal distribution, it is evident that other optimal copulas, e.g. Student, Frank, Gumbel etc. might be a better fit than a Gaussian copula. Therefore, considering a large variety of copula families that are available and well-investigated (Joe, 1997; Nelsen, 2006), the copula-based imputation should be able to outperform standard regression for LA-ICP-MS data.

Conclusions

We propose a copula-based approach for imputation of data below mdl as a generalisation of standard regression. In both cases fitting and implementation is an iterative method using the E-M algorithm. The copula and standard regression were compared for the imputation of Te given complete Te, Au and Ag triples and artificially imposed mdl values for Te. There was no practical difference in terms of the statistics of the errors, but the distribution of imputed values using the copula more closely resembles the distribution of the observations than the distribution of imputed values obtained with standard regression.

Acknowledgements

This work is a contribution to the FOX project ‘Trace elements in iron-oxides: deportment, distribution and application in ore genesis, geochronology, exploration and mineral processing’, supported by BHP Olympic Dam and the South Australian Mining and Petroleum Services Centre of Excellence.

References

Aas, K., Czado, C., Frigessi, A., Bakken, H. 2009. Pair-copula constructions of multiple dependence. Insurance: Mathematics and Economics, 44, 182-198.

Akaike, H. 1973. Information theory and an extension of the maximum likelihood principle. In B. N. Petrov and F. Csaki (Eds.), Proceedings of the Second International Symposium on Information Theory Budapest, Akademiai Kiado, pp. 267-281.

Brechmann, E.C. 2010. Truncated and simplified regular vines and their applications. Diploma thesis, Technische Universitaet Muenchen, pp. 227.

Brechmann, E.C., Schepsmeier, U., 2013. CDVine: Modelling Dependence with C- and D-Vine Copulas in R. Journal of Statistical Software, 52, 3.

Chib, S., Greenberg, E. 1995. Understanding the Metropolis–Hastings algorithm. American Statistician 90, 1313-1321.

Dempster, A.P., Laird, N.M., Rubin, D.B. 1977. Maximum Likelihood from Incomplete Data via the EM Algorithm. Journal of the Royal Statistical Society, Series B, 9, 1–38.

Di Lascio, F.M.L., Giannerini, S., Reale, A, 2015. Exploring copulas for the imputation of complex dependent data. Statistical Methods and Applications, 24, 159-175.

Dmitrijeva, M., Ciobanu, C., Ehrig, K., Cook, N., Metcalfe, A., Verdugo-Ihl, M., and McPhie, J. 2019. Mineralization-alteration footprints in the Olympic Dam IOCG district South Australia: The Acropolis prospect: Journal of Geochemical Exploration, 205, 106333.

Ehrig, K., McPhie, J., Kamenetsky, V.S. 2012. Geology and mineralogical zonation of the Olympic Dam Iron Oxide Cu-U-Au-Ag deposit, South Australia. In: Society of Economic Geologists Special Publication, 16, 237-267.

Helsel, T. 2005. Nondetects and Data Analysis: Statistics for Censored Environmental Data. John Wiley & Sons, New York, pp. 250.

Hofert, M., Kojadinovic, I., Maechler, M., Yan, J. 2017. copula: Multivariate Dependence with Copulas. R package version 0.999-18 URL https://CRAN.R-project.org/package=copula

Honaker, J., King, G., Blackwell, M. 2011. Amelia II: A Program for Missing Data. Journal of Statistical Software, 45, 1–47.

Houari, R., Bounceur, A., Kechadi, M.T., Tari, A.A.K., Euler, R. 2013. Missing Data Analysis Using Multiple Imputation in Relation to Parkinson's Disease. https://doi.org/10.1145/3010089.3010117

Houari, R., Bounceur, A., Tari, A.A.K., Kechadi, M.T. 2014. Handling Missing Data problems with Sampling Methods. International Conference on Advanced Networking Distributed Systems and Applications (INDS).

Hood, S., Cracknell, M.J., Gazley, M.F. 2018. Linking protolith rocks to altered equivalents by combining unsupervised and supervised machine learning. Journal of Geochemical Exploration, 186, 270-280.

Hood, S., Cracknell, M.J., Gazley, M.F., Reading, A.M. 2019. Element mobility and spatial zonation associated with the Archean Hamlet orogenic Au deposit, Western Australia: Implications for fluid pathways in shear zone. Chemical Geology, 514, 10-26.

Joe, H. 1997. Multivariate Models and Dependence Concepts. Chapman & Hall, London, pp. 424.

Makvandi, S., Ghasemzadeh-Barvarz, M., Beaudoin, G., Grunsky, E.C., McClenaghan, M.B., Duchesne, C. & Boutroy, E., 2016. Partial least squares-discriminant analysis of trace element compositions of magnetite from various VMS deposit subtypes: Application to mineral exploration. Ore Geology Reviews, 78, 388–408.

Nelsen, R. 2006. An Introduction to Copulas. Springer Science & Business Media, pp. 272.

Norton, M., Khokhlov, V., Uryasev, S. 2019. Calculating CVaR and bPOE for common probability distributions with application to portfolio optimization and density estimation. Annals of Operations Research, submitted for publication, http://arxiv.org/abs/1811.11301.

Schepsmeier, U., Stoeber, J., Brechmann, E.C., Graeler, B., Nagler, T., Erhardt, T. 2018. VineCopula: Statistical Inference of Vine Copulas. R package version 2.1.8. https://CRAN.R-project.org/package=VineCopula

Sklar, A. 1959. Fonctions de répartition à n dimensions et leurs marges, Publications de l'Institut Statistique de l'Université de Paris, 8, 229-231.

Palarea-Albaladejo, J.; Martin-Fernandez, J.A. 2012. Values below detection limit in compositional chemical data. Analytica Chimica Acta, 764, 32-43.

Verdugo-Ihl, M.R., Ciobanu, C.L., Cook, N.J., Ehrig, K., Courtney-Davies, L., and Gilbert, S. 2017. Textures and U-W-Sn-Mo signatures in hematite from the Cu-U-Au-Ag orebody at Olympic Dam, South Australia: defining the archetype for IOCG deposits: Ore Geology Reviews, 91, 173–195.

Winderbaum, L., Ciobanu, C.L., Cook, N.J., Paul, M., Metcalfe, A., Gilbert, S. 2012. Multivariate analysis of an LA-ICP-MS trace element dataset for pyrite. Mathematical Geoscience, 44, 823–842.

CHAPTER 3

DISCRIMINATION AND VARIANCE STRUCTURE OF TRACE ELEMENT SIGNATURES IN FE-OXIDES: A CASE STUDY OF BIF-MINERALIZATION FROM THE MIDDLEBACK RANGES, SOUTH AUSTRALIA

Marija Dmitrijeva[1], Andrew V. Metcalfe[2], Cristiana L. Ciobanu[1], Nigel J. Cook[1], Max Frenzel[3], William M. Keyser[1], Geoff Johnson[4], Kathy Ehrig[5]

[1]*School of Chemical Engineering and Advanced Materials, The University of Adelaide, Adelaide, SA 5005, Australia*

[2]*School of Mathematical Sciences, The University of Adelaide, Adelaide, SA 5005, Australia*

[3]*Institute for Mineralogy, Freiberg University for Mining and Technology, Brennhausgasse 14, 09599 Freiberg, Germany*

[4]*SIMEC Mining, Level 2 169 Fullarton Road, Dulwich, SA 5005, Australia*

[5]*BHP Olympic Dam, Adelaide, SA 5000, Australia*

Article published in Mathematical Geosciences 4 (2018) 381-415

Statement of Authorship

Title of Paper	Discrimination and variance structure of trace element signatures in Fe-oxides: a case study from the Middleback Ranges, South Australia
Publication Status	☑ Published ☐ Accepted for Publication ☐ Submitted for Publication ☐ Unpublished and Unsubmitted work written in manuscript style
Publication Details	Dmitrijeva, M., Metcalfe, A.V., Ciobanu, C.L., Cook, N.J., Frenzel M., Keyser, W.M., Johnson, G., Ehrig, K. Discrimination and variance structure of trace element signatures in Fe-oxides: a case study from the Middleback Ranges, South Australia, Mathematical geosciences, 30, 381-415. https://doi.org/10.1007/s11004-018-9734-1

Principal Author

Name of Principal Author (Candidate)	Marija Dmitrijeva		
Contribution to the Paper	Performed some analytical work, carried out statistical data analysis and interpretation, wrote the manuscript.		
Overall percentage (%)	55		
Certification:	This paper reports on original research I conducted during the period of my Higher Degree by Research candidature and is not subject to any obligations or contractual agreements with a third party that would constrain its inclusion in this thesis. I am the primary author of this paper.		
Signature		Date	17.12.19

Co-Author Contributions

By signing the Statement of Authorship, each author certifies that:

i. the candidate's stated contribution to the publication is accurate (as detailed above);

ii. permission is granted for the candidate in include the publication in the thesis; and

iii. the sum of all co-author contributions is equal to 100% less the candidate's stated contribution.

Name of Co-Author	Andrew V. Metcalfe		
Contribution to the Paper	Helped to define the direction of the paper, assisted with the data interpretation, contributed to the manuscript preparation.		
Overall percentage (%)	1(		
Signature		Date	17.12.19

Name of Co-Author	Cristiana L. Ciobanu		
Contribution to the Paper	Helped to define the direction of the paper, assisted with the data interpretation, contributed to the manuscript preparation.		
Overall percentage (%)	10		
Signature		Date	17.12.19

Name of Co-Author	Nigel J. Cook		
Contribution to the Paper	Assisted with the manuscript preparation.		
Overall percentage (%)	5		
Signature		Date	17.12.19

Name of Co-Author	Max Frenzel		
Contribution to the Paper	Assisted with the statistical analyses.		
Overall percentage (%)	5		
Signature		Date	17.12.19

Name of Co-Author	William M. Keyser		
Contribution to the Paper	Performed some of the analytical work.		
Overall percentage (%)	5		
Signature		Date	17.12.19

Name of Co-Author	Geoff Johnson		
Contribution to the Paper	Assisted with sample collection and evaluation of the manuscript.		
Overall percentage (%)	5		
Signature		Date	17.12.19

Name of Co-Author	Kathy Ehrig		
Contribution to the Paper	Assisted with the evaluation of the manuscript.		
Overall percentage (%)	5		
Signature		Date	17.12.19

Math Geosci
https://doi.org/10.1007/s11004-018-9734-1

Discrimination and Variance Structure of Trace Element Signatures in Fe-Oxides: A Case Study of BIF-Mineralisation from the Middleback Ranges, South Australia

Marija Dmitrijeva[1] · Andrew V. Metcalfe[2] · Cristiana L. Ciobanu[1] · Nigel J. Cook[1] · Max Frenzel[1,3] · William M. Keyser[1] · Geoff Johnson[4] · Kathy Ehrig[5]

Received: 8 August 2017 / Accepted: 14 February 2018
© International Association for Mathematical Geosciences 2018

Abstract Uni- and multivariate statistical analyses of trace element laser-ablation inductively coupled plasma mass spectrometry data for Fe-oxides from banded iron formation (BIF) and BIF-hosted ores in 13 deposits/prospects of the Middleback Ranges, South Australia are presented. The obtained trace element signatures were considered within a petrographic-textural framework of iron-oxide evolution from magnetite through clean martite and porous martite to platy hematite, to evaluate changes in trace element concentrations with respect to the ore enrichment processes. Statistically valid distinctions among different hematite textures were indicated for most trace elements by linear mixed-effects models. Furthermore, the hematite data showed significant intra-class correlations between spot-analyses within individual polished blocks and correlations between polished blocks within individual deposits. The data are thus aggregated within their hierarchical levels. Two linear discriminant function analyses were performed to determine the combinations of trace elements that can distinguish hematite by textures and by location within the Middleback Ranges. Tin, a significant discriminator element in both models, reflects the regional influence

Electronic supplementary material The online version of this article (https://doi.org/10.1007/s11004-018-9734-1) contains supplementary material, which is available to authorized users.

✉ Marija Dmitrijeva
marija.dmitrijeva@adelaide.edu.au

[1] School of Chemical Engineering, The University of Adelaide, Adelaide, SA 5005, Australia

[2] School of Mathematical Sciences, The University of Adelaide, Adelaide, SA 5005, Australia

[3] Institute for Mineralogy, Freiberg University of Mining and Technology, Brennhausgasse 14, 09599 Freiberg, Germany

[4] SIMEC Mining, Level 2, 169 Fullarton Road, Dulwich, SA 5065, Australia

[5] BHP Olympic Dam, Adelaide, SA 5001, Australia

Published online: 03 April 2018

of granite-affiliated hydrothermal fluids on the clean martite. This granitic signature, therefore, postdates formation of magnetite BIFs and potentially represents a supergene ore enrichment stage. The combination of Ni, Co, Ti and Nb was discovered to be uniquely attributed to discrimination of the Northern and Southern Middleback Ranges, indicating very specific local settings unrelated to hematite textures. Both local and regional settings impacting on the trace element signatures of Fe-oxides throughout iron ore formation are recognised, suggesting distinct ore enrichment conditions within various segments of the belt.

Keywords Multivariate statistics · Laser-ablation inductively-coupled plasma-mass spectrometry · Principal component analysis · Linear mixed-effects models · Discriminant function analysis

1 Introduction

The two main Fe-oxides, magnetite and hematite, are dominant components of banded iron formations (BIF) and Fe-rich ores derived from BIF protoliths. The spatial associations of BIFs and iron-ores is a much-debated topic with respect to enrichment processes and their temporal evolution (Hagemann et al. 2016). This is because the evolution from BIF to Fe-rich ores is often suggested as a combination of hypogene and supergene processes that involves, besides diagenesis as a first "hypogene" stage following BIF deposition, a sequence of supergene processes. The latter are dependent upon the environment with high variation in pH and fO_2, as well as temperature/depth of erosion, host lithologies and structures controlling fluid focusing and chemistry. Such evolution can be tracked by transformation among Fe-oxides, textures, and relationships with Fe-hydroxides and gangue minerals.

Despite the recognised sub-groups of Precambrian BIFs (Algoma-, Lake Superior-, and Rapitan-type), BIF-hosted ores share strikingly similar textural and mineralogical features of Fe-oxides. This involves interconversion(s) among Fe-(hydr)-oxides, pseudomorphic replacements of magnetite by hematite (martitisation), and (re)-precipitation of hematite often as (micro)platy hematite (Hagemann et al. 2016; Taylor et al. 2001).

Trace element data of Fe-oxides from BIF and BIF-hosted ores are increasingly used to understand their formation conditions (Hensler et al. 2015), and differences in diagenetic, metamorphic or depositional environments during iron-ore enrichment process (Angerer et al. 2013; Bhattacharya et al. 2007). In general, in-situ trace element data are presented as two/three-component projections and/or multi-element spider diagrams, sometimes accompanied with calculated summary statistics (Dupuis and Beaudoin 2011; Wang et al. 2017).

Graphical representations of such data are generally followed by subjective interpretations rather than a confirmatory approach. Moreover, statistical analyses of trace element data in minerals lag behind the broad application of such data, and only a few studies have been conducted to date (Frenzel et al. 2016; Makvandi et al. 2016a, b; Winderbaum et al. 2012). As the size and complexity of trace element data grows, the number of possible two/three-component projections becomes inadequately large,

and therefore, a multivariate statistical approach is needed fully to extract information from sizable multi-trace element data.

In this study, statistical techniques are applied to texturally-defined hematite trace element data from BIFs and BIF-derived ore samples from the Middleback Ranges, South Australia. These include linear mixed-effects (LME) models, principal component analysis (PCA) and linear discriminant function analysis (LDA). Objectives are: (I) to assess numerically differences in trace element concentrations in textural categories of hematite; (II) to establish trace elements combinations specific to hematite textural categories; and (III) to investigate the variance structure of hematite data on different levels of hierarchy.

Each method follows a different approach: LME modeling resembles a fixed-effect linear regression with additional random-effect components; PCA is an unsupervised technique that requires no prior information and provides a summary of multivariate data; and LDA is a supervised technique that requires data to be assigned to certain classes upon which further classification is made. The internal features of trace element data obtained by laser ablation-inductively coupled plasma-mass spectrometry (LA-ICP-MS) are emphasised, including data quality control and statistical treatment of values below minimum limits of detection (BDL). The hierarchical structure of such data is specifically addressed by LME models, and the consequences of ignoring it are elucidated.

2 Background

2.1 LA-ICP-MS Data Fabric

Modern LA-ICP-MS datasets may number dozens or even hundreds of spot-analyses and/or linear trenches of various beam sizes in multiple mineral grains within a single sample. These multiple data points are sometimes treated as independent (Belissont et al. 2014), averaged out per grain (Makvandi et al. 2016a, b), per sample (Frenzel et al. 2016), or per deposit (Dupuis and Beaudoin 2011). The samples may cover a range of geological settings: from a single ore zone to a group of deposits, or even groups of deposits of different types. The final data are normally organised in a hierarchical manner and include analytical and geological information for every observation. Such datasets inherently contain several features that can impact the applicability and/or practicality of specific statistical methods and, therefore, serve as limitations.

2.2 LA-ICP-MS Data Limitations

A balanced survey design is defined as a data acquisition where an equal number of observations of the same variable is obtained in all possible groups. In statistical data analysis, balanced designs are preferred to ensure larger statistical power of tests. For studies of trace elements in minerals, it is not always possible to follow balanced design principles due to the limited availability of geological samples and/or analytical limitations. Consequently, LA-ICP-MS data are often unbalanced, meaning

that the number of observations belonging to different combinations of hierarchical levels is unequal (e.g. different numbers of analysis per texture per sample, different numbers of samples per locality etc.). Further difficulties arise from the choice of mineral grains to be analysed. As the choice of a grain is a subjective process, and each study is done on grains, or selected parts thereof, which may not be representative for the entire paragenetic sequence, the resulting data may be biased. In general, the choice of where to locate an individual spot analysis may also be constrained by the abundance of a mineral in a polished block, along with limitations of laser spot size, often making it difficult or impossible to obtain reliable compositional information on certain, particularly small, grains.

An additional factor affecting the quality of LA-ICP-MS data is the presence of variations in time-resolved ablation signals due to the presence of large inclusions or mixed patterns attributable to several phases. These realities must be acknowledged, and such data excluded, when performing data quality checks. Although impurities or contaminant phases cannot be predicted no matter how carefully the pre-analysis screening of grains is conducted, the true homogenous signal can be excised via data reduction software.

2.3 Compositional Data Adaptations for In-Situ LA-ICP-MS Data

Compositional data are defined as a D-part vector $x = [x_1, x_2, \ldots, x_D]$. The components of a compositional vector x are strictly positive real numbers carrying only relative information and summing up to a given constant, for instance, 100 wt% or one million ppm (Aitchison 1986; Pawlowsky-Glahn and Egozcue 2006). Although in-situ LA-ICP-MS trace element data do not satisfy the constant sum constraint because major components are never analysed, the theoretical sum total of all measured element concentrations is one million ppm, and consequently, trace element data represent a sub-composition (Aitchison et al. 2002).

In contrast to whole-rock compositions, trace elements are parts-per-million-level impurities existing in a mineral lattice, and only account for a small percentage of the bulk composition of a given grain. For instance, in the LA-ICP-MS analysis of Fe-oxide minerals, concentrations of a trace element are calculated by referencing against the signals from primary standard materials, using ^{57}Fe as an internal standard assuming the sample to contain 100 wt% Fe_2O_3 or Fe_3O_4 (for hematite and magnetite, respectively). Therefore, if a D-part composition includes a major element, for instance Fe, that dominates the composition and is relatively constant, then the log-ratio $\ln\left(\frac{Y_i}{\mathrm{Fe}}\right)$ differs from $\ln(Y_i)$ by the approximate constant ln(Fe) and has the same variance. Therefore, a log-ratio vector of trace element concentrations $\left[\ln\left(\frac{x_1}{X}\right), \ln\left(\frac{x_2}{X}\right), \ldots, \ln\left(\frac{x_D}{X}\right)\right]$ is equivalent to $[\ln(x_1), \ln(x_2), \ldots, \ln(x_D)]$ where $X = \sum_{i=1}^{D} x_i$ (Aitchison et al. 2002). Therefore, in this study, log-transformation (natural logarithm) of trace element data is performed prior to all the statistical analyses.

3 Data Description

The ~ 60 km-long Middleback Ranges, located in the northeast Eyre Peninsula, host a discontinuous sequence of iron ore deposits (Fig. 1). The iron ore deposits sampled in this study are hosted within the Lower Middleback Jaspilite unit of the Middleback Subgroup (Parker 1993; Szpunar et al. 2011), which in turn belongs to the regional Hutchinson Group metasediments (Szpunar et al. 2011). A summary of samples, host lithologies and number of spot analyses per sample are given is Table 1.

The sample suite predominantly consists of higher-grade iron ores composed largely of hematite and lower-grade iron ores dominated by magnetite and a variety of Fe-hydroxides (Fig. 2). To a lesser extent, the sample suite contains proto-ores, including siliceous hematite and/or magnetite dominated BIFs, as well as an altered amphibolite sample (chloritite containing magnetite).

Hematite, represented throughout the belt, was found in almost all samples as euhedral grains or pseudomorphs after magnetite either with clean inclusion-free surfaces (clean martite Mrt) or with well-developed porosity (porous martite p-Mrt) (Table 1; Fig. 2) (Keyser et al. 2018). The less dominant secondary platy hematite (pl-Hm) occurred predominantly in Iron Knight, Iron Monarch, Iron Prince and to a lesser extent in Iron Baron, Iron Queen and Iron Warrior. The majority of samples containing magnetite correspond to Iron Magnet, the main magnetite mineralisation of the Middleback Ranges. However, magnetite is present as inclusions in martite from samples throughout all the other deposits (Table 1). The various types of Fe-oxides as defined above are linked to a temporal evolution broadly considered as: magnetite → clean martite → porous martite → platy hematite (Fig. 2).

Detailed petrographic characterisation of samples used here (Table 1) is reported in Keyser et al. (2018). The backscatter electron images of Fe-oxide textures displays the coarse-grained euhedral magnetite (Mt) with interconversion to clean martite (Mrt) on grain margins (Iron Princess, sample MB1) (Fig. 2a), partial martitisation (Mrt) of euhedral magnetite (Mt) showing preserved relicts (Iron Chieftain, sample MB4) (Fig. 2b), porous martite (p-Mrt) with fine-grained goethite (Goe) forming within pores and along grain margins (Iron Queen, sample MB27) (Fig. 2c) and fine- and coarse-grained platy hematite (pl-Hm) with martite (Mrt) (Iron Prince, sample MB54) (Fig. 2d).

Details of LA-ICP-MS data acquisition processes are summarised in Appendix A. The dataset consists of 1098 spot-analyses on hematite and 508 analyses on magnetite (Table 1; Electronic Appendix B). The hematite texture for each spot analysis is recorded as clean martite (Mrt), porous martite (p-Mrt) or platy hematite (pl-Hm) ($n = 510$; $n = 376$ and $n = 212$, respectively) (Fig. 2). As shown in Table 1, samples generally contain only a subset of these different textural categories of hematite.

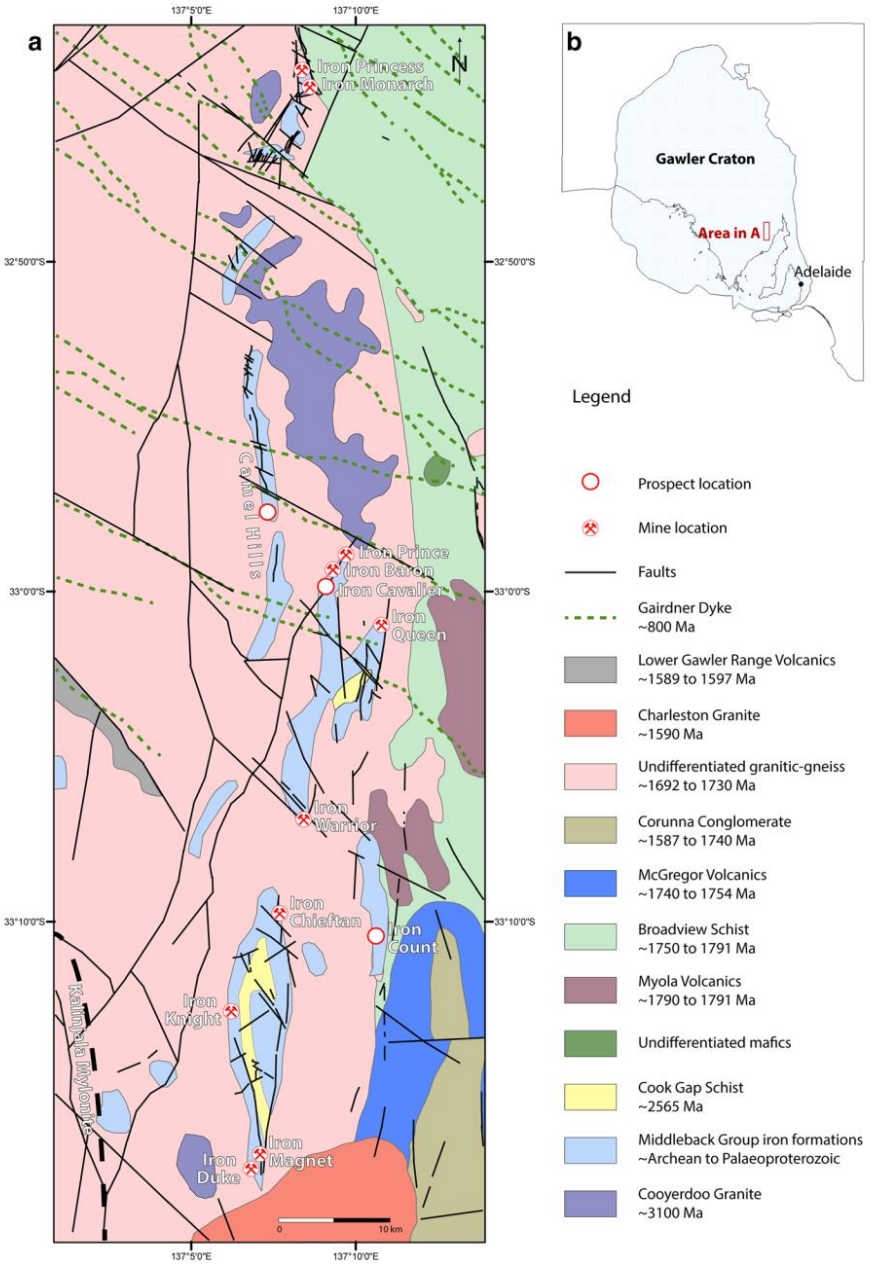


Fig. 1 **a** Locations of studied samples from iron ore deposits and prospects on a simplified basement geology map. **b** Location of Middleback Ranges. Map sourced from https://map.sarig.sa.gov.au/, modified after McAvaney (2012) and Szpunar et al. (2011)

Table 1 List of sampled Middleback Range deposits (from north to south)

Deposit	Sample no.	Sample lithology	Texture (s)	No. of spot-analyses
North				
Iron Princess	MB1	Massive martite-magnetite ore	Mrt	27
			Mt	20
	MB2	Banded carbonate-quartz-talc BIF	Mrt	13
			p-Mrt	18
			Mt	11
	MB65	Martite-goethite ore	p-Mrt	19
	MB66	Martite-goethite ore	p-Mrt	19
	MB68	Martite-goethite ore	p-Mrt	21
Iron Monarch	MB71	Massive banded siliceous BIF	Mrt	24
	MB72	Brecciated siliceous BIF	Mrt	6
	MB70a	Brecciated siliceous BIF	pl-Hm	19
	MB73	Massive banded siliceous BIF	pl-Hm	20
			p-Mrt	20
	MB74	Banded siliceous BIF	p-Mrt	19
	MB77a	Banded brecciated siliceous BIF	pl-Hm	19
			p-Mrt	19
	MB78	Brecciated siliceous BIF	p-Mrt	20
Middle				
Iron Prince	MB45	Massive martite ore	Mrt	12
	MB54	Massive martite ore	pl-Hm	14
			p-Mrt	11
	MB60	Vuggy friable specularite ore	pl-Hm	29
	MB57b	Hematite-goethite ore	p-Mrt	25
	MB59	Goethite ore	pl-Hm	2
Iron Baron	MB43	Massive martite ore	Mrt	16
	MB44a	Massive martite ore	Mrt	27
			pl-Hm	8
	MB99	Hematite-goethite ore	pl-Hm	20
	MB44b	Massive martite ore	p-Mrt	20
Camel Hills	MB13	BIF fragments in calcrete	Mrt	8
			p-Mrt	6
	MB14	Earthy limonite ore	p-Mrt	11
	MB16	Earthy banded siliceous BIF	Mrt	4
			p-Mrt	5
	MB18	Banded quartz-talc magnetite BIF	Mt	3

Table 1 continued

Deposit	Sample no.	Sample lithology	Texture (s)	No. of spot-analyses
Iron Cavalier	MB25	Banded martite-geothite ore	p-Mrt	24
	MB26	Earthy banded siliceous BIF	Mrt	4
			p-Mrt	14
			Mt	4
Iron Queen	MB27	Massive friable martite ore	Mrt	31
	MB28	Massive vuggy martite ore	Mrt	43
			pl-Hm	19
	MB29	Massive vuggy hematite-goethite ore	Mrt	19
			p-Mrt	20
Iron Warrior	MB10	Massive brecciated martite ore	Mrt	16
			p-Mrt	19
			Mt	27
	MB11	Vuggy brecciated massive martite ore	Mrt	19
			p-Mrt	20
			Mt	40
	MB12	Massive brecciated martite ore	Mrt	21
			Mt	40
	MB7	Chloritite	Mt	44
	MB8	Vuggy friable martite ore	pl-Hm	16
	MB9	Massive brecciated martite ore	p-Mrt	19
			Mt	20
Iron Count	MB23	Massive vuggy siliceous goethite-hematite ore	Mrt	25
	MB40a	Banded siliceous BIF	Mrt	12
	MB41a	Brecciated siliceous BIF	Mrt	21
	MB41b	Brecciated siliceous BIF with relict banding	Mrt	21
	MB40b	Massive martite ore	Mrt	8
			p-Mrt	7
			Mt	9
South				
Iron Chieftain	MB4	Vuggy massive hematite-goethite ore	Mrt	17
	MB5	Banded massive siliceous BIF	Mrt	12
			Mt	12
	MB21	Massive hematite-goethite ore	p-Mrt	20
Iron Knight	MB22b	Vuggy massive martite-goethite ore	Mrt	28
			Mt	20
	MB98	Hematite ore	pl-Hm	46

Table 1 continued

Deposit	Sample no.	Sample lithology	Texture (s)	No. of spot-analyses
Iron Magnet	MB33	Banded quartz-talc magnetite BIF	Mrt	19
			Mt	17
	MB34a	Quartz-talc magnetite BIF	Mrt	1
			Mt	14
	MB34b	Quartz-talc magnetite BIF	Mrt	12
			Mt	12
	MB35a	Banded talc magnetite BIF	Mrt	5
			Mt	51
	MB35b	Banded talc magnetite BIF	Mt	30
	MB36a	Massive talc-carbonate magnetite BIF	Mrt	19
	MB36b	Brecciated carbonate magnetite BIF	Mt	29
	MB92a	Banded carbonate magnetite BIF	Mt	35
	MB93	Magnetite BIF	Mt	35
	MB80a	Banded talc-quartz magnetite BIF	Mt	35
Iron Duke	MB20	Banded vuggy hematite-goethite ore	Mrt	20

Mt = Mt; Mrt = clean martite; p-Mrt = porous martite; pl-Hm = platy hematite

4 Statistical Analyses of Trace Element Data in Fe-Oxides

4.1 Treatment of Values Below Detection Limit

For multiple imputation for each of the categories of hematite, a covariance-based expectation–maximisation (EM) algorithm from the package "Amelia" (Dempster et al. 1977; Honaker et al. 2011) in R (R Core Team 2017) was chosen. The EM multiple imputation procedure approximates estimates of values below detection limits to underlying trace element distributions, assuming that the complete data are multivariate normal (Honaker et al. 2011).

Among the trace elements measured in hematite, only Ca had > 30% of BDL values, and was thus excluded from further statistical analyses. Raw concentrations of trace elements in categories of hematite were log-transformed to make data roughly distributed as multivariate lognormal. An approximate univariate normality was assumed for every trace element within each group of hematite. The informational prior matrix specifying a maximum, as a log-average detection limit for a group, a minimum, as a tenth of a log-average of detection limit for a group and a confidence level of 95% for every element was provided. The inspection of newly imputed values was checked by comparing the distributions of imputed values to those of observed values following the procedures of Honaker et al. (2011). Additional visualisation of imputed values in relation to observed ones was also performed (Fig. 3).

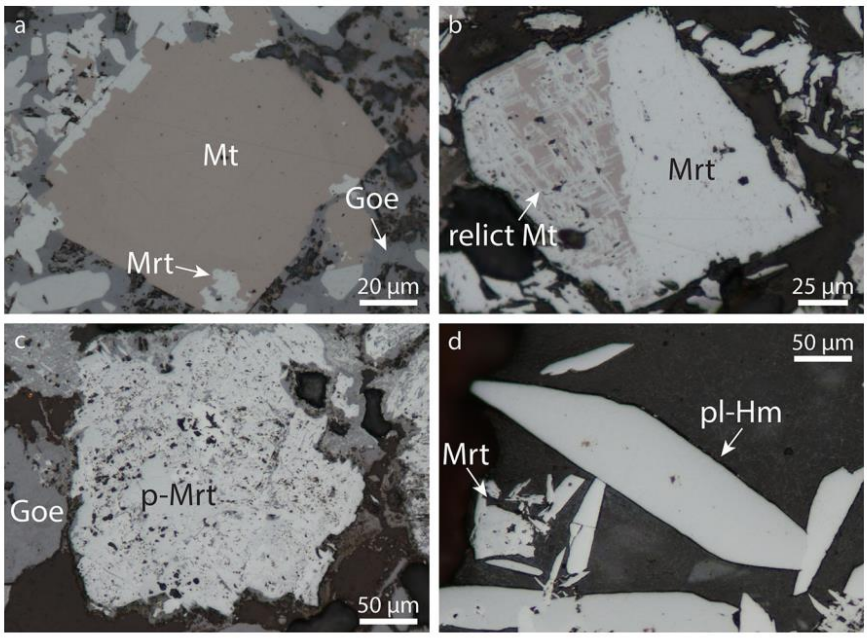


Fig. 2 Backscatter electron images of mineralogical and textural categories of iron ores, also showing the martitisation process and formation of microplaty hematite

The magnetite data have a significant number of elements with large proportion of values BDL or measured very close to it. Only elements that have > 30% of values above BDL were included in magnetite data set: Mg, Al, Si, Ti, V, Mn, Co, Ni, Zn, Ga, Sr, Y, La, Ce, W, Pb and U, and were deterministically imputed using half the detection limit. As a result, magnetite data has not been included in statistical analyses.

4.2 Univariate Analysis

4.2.1 Summary Statistics

To summarise the data, the geometric mean of raw data and 68% probability interval (PI) were calculated for every element in each of the textural categories of Fe-oxides. The geometric mean (GM) was chosen in preference to the arithmetic mean because it is less influenced by extreme outliers. The GM is equal to exponential of the arithmetic mean of the logarithm of the data. If the logarithm of the data is normally distributed then the GM represents the median of the original data. The 68% PI is calculated as exponential of the arithmetic mean of the logarithms of the data plus or minus the standard deviation of the logarithms of the data.

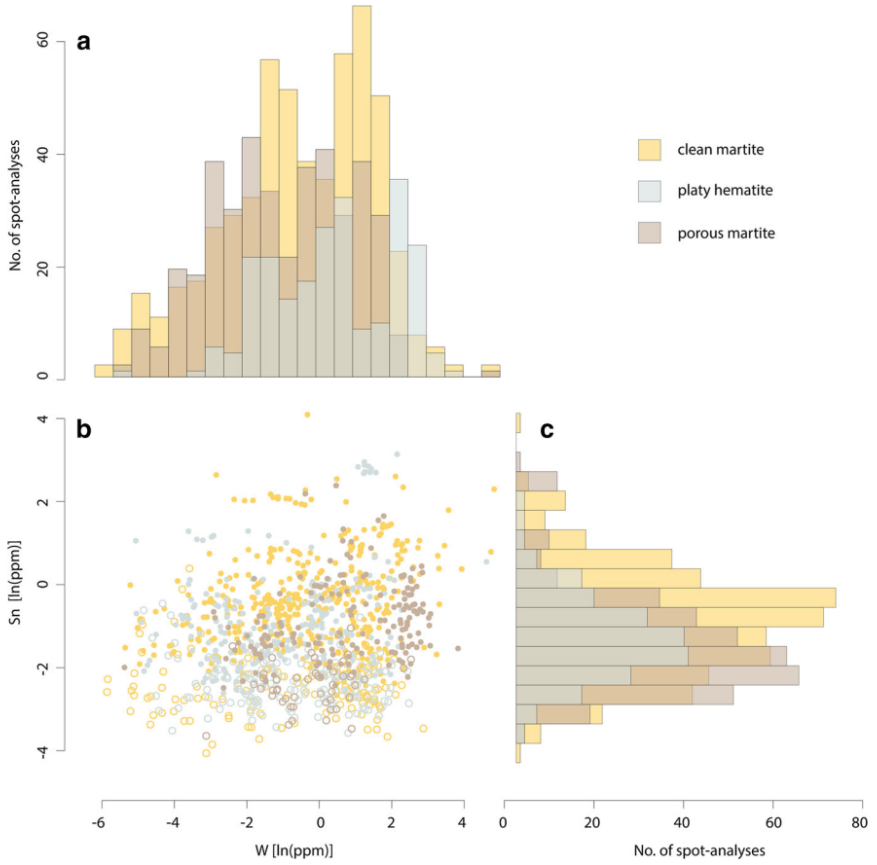


Fig. 3 Histograms and corresponding scatterplot of log-transformed concentrations of W and Sn in hematite displaying the effect of multiple EM imputation of BDL values. The imputed values are encoded as empty circles

4.2.2 Linear Mixed-Effects Regression

The LME models are an extension of the linear regression models allowing for more than one random component. In matrix terms, if there are additional υ random components, the model is

$$y = Xb + \sum_{i=1}^{\upsilon} U_i e_i + \varepsilon, \tag{1}$$

where y is a response vector of length $n \times 1$; b is a $k \times 1$ vector of unknown coefficients to be estimated; the X is known $n \times k$ matrix of predictor variables that define the mean response, e_i are $m_i \times 1$ vectors of random variation with mean 0 and variance σ_i^2; U_i are $n \times m_i$ matrices with known elements that define the variance structure; and

ε is an $n \times 1$ vector of random variation with mean 0 and variance σ^2. The product of Xb is the deterministic part of the model, and it components are the fixed effects. The components of the random variation are represented as random effects. The model can be summarised as

$$E[y] = Xb;\ \text{var}(y) = H\sigma^2, \tag{2}$$

where

$$H = \sum \phi_i U_i U_i' + I_n, \tag{3}$$

with

$$\phi_i = \sigma_i^2/\sigma^2, \tag{4}$$

where I_n is a $n \times n$ identity matrix. The objective is to estimate the b, σ^2 and the ϕ_i, and hence ${\sigma_i}^2$ (Corbeil and Searle 1976). The model can be fitted using maximum likelihood or restricted maximum likelihood (REML).

The hematite LA-ICP-MS data presented here require a mixed-effects modelling approach because there are multiple spot-analyses per polished block, and the trace element concentrations within a polished block are likely to be more closely related to each other than to concentration values from another polished block. Moreover, the polished blocks within the same deposit are likely to be more alike than polished blocks from different deposits. The conventional linear regression model does not take this association into account. The underlying question for these data is whether there is a relationship between trace element concentrations and corresponding Fe-oxide textures.

For the LME models, it is implicitly assumed that it is reasonable to consider the data as if deposits were randomly selected from all possible deposits within the Middleback Ranges; hand specimens were randomly collected from the selected deposits; and that laser measurements were performed at random locations within each textural category on the polished blocks made from hand specimens. The hierarchical structure of hematite LA-ICP-MS data is shown on Fig. 4. All spot analyses were assigned to a textural category (clean martite, porous martite, platy hematite) of an analysed grain. Therefore, a texture is the only fixed component for every spot-analysis. However, these data are unbalanced inasmuch as there are a different number of polished blocks from each deposit and also a different number of spot-analyses from each polished block. In addition, not all the textures are present within every polished block (Table 1). The R function lmer() (Bates et al. 2015) allows for these features of the data when estimating the components of variance and the effects of texture including statistical significance. The numerical components of the variance structure are calculated for each element allowing for the difference in textures. The model has the form

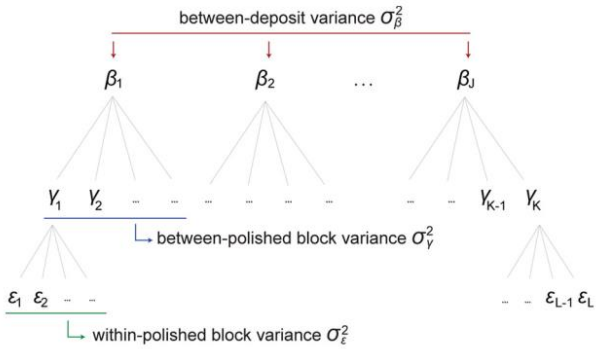


Fig. 4 Schematic representation of hierarchy of hematite trace element data: multiple individual spot-analyses ($l = 1, \ldots, L$) are nested within a polished block ($k = 1, \ldots, K$) that originate from a given deposit ($1, \ldots, J$) and three components of variance between-deposits variance ${\sigma_\beta}^2$ (red), between polished-block variance ${\sigma_\gamma}^2$ (green), and within-polished block variance σ_ϵ^2 (blue)

$$
\begin{aligned}
Y_{ijkl} &= \mu_i + \beta_j + \gamma_{k|j} + \epsilon_{ijkl}, \\
i &= 1, \ldots, I,\ j = 1, \ldots, J, k = 1, \ldots, K, l = 1, \ldots, L, \\
\beta_j &\sim N\left(0, \sigma_\beta^2\right),\ \gamma_{k|j} \sim N\left(0, \sigma_{k|j}^2\right),\ \epsilon_{ijkl} \sim N\left(0, \sigma_\epsilon^2\right). \qquad (5)
\end{aligned}
$$

The response Y_{ijkl} represents an element concentration for texture i, from deposit j, polished block k and spot analysis l. The index i runs from 1 to 3 (textures), j runs from 1 to 13 (deposits/prospects), and both k and l differ for different deposits and polished blocks. The four following parameters were estimated using the R function lmer():

1. the fixed effect parameter μ_i representing the mean concentration of a given trace element Y in a texturally-defined category of hematite on a log-scale;
2. the random effect parameter β_j representing the deviation of mean trace element concentration at each deposit from the total mean concentration of the texturally defined category; the estimated variance, σ_β^2, represents between-deposit variability;
3. the random effect parameter $\gamma_{k|j}$ representing the deviation of mean trace element concentration at each polished-block from the total mean within a deposit; the estimated variance ${\sigma_\gamma}^2$ represents between-polished block variability;
4. the residual term ϵ_{ijkl} with estimated variance σ_ϵ^2 corresponds to the unexplained error and represents within polished block variation.

Equation (5) distinguishes three main sources of variation in the response Y_{ijkl}: variation across deposit level σ_β^2; variation across polished blocks level σ_γ^2 (or within deposit level); and residual variation within a polished block σ_ϵ^2 (Fig. 4).

4.3 Multivariate Analysis

4.3.1 Principal Component Analysis

Principal component analysis is an exploratory technique used to reduce the number of dimensions in a multidimensional dataset. The first principal component (PC1) is a linear combination of the variables such that the variance is a maximum, subject to the constraint that the sum of squares of the coefficients, of the variables in the linear combination, equals 1. The second principal component (PC2) is a linear combination of variables such that the variance is a maximum, subject to two constraints. The two constraints are that the sum of squares of the coefficients equals 1, and that the vector of coefficients is orthogonal to the vector of coefficients of PC1. The process continues to give a number of PCs equal to the number of variables. The first principal component explains the majority of variance, defined as the sum of the variance of all the variables, and each successive component explains gradually less. The coefficients are referred to as principal component loadings. For each datum and PC, principal component score is calculated as the linear combination of the values of the original variables.

The results of PCA are usually shown as a biplot of scores (score of every sample on PC1 and PC2) and loadings (loadings of every element on PC1 and PC2) (Gabriel 1971). The score-plot is a projection of all data onto a plane that maximises the proportion of the total variance shown in the projection. The positioning of observations in proximity to each other on the score-plot reflects their chemical similarity. Similarly, the allocation of loadings mirrors correlation coefficients among trace elements. Therefore, elements grouped together on the loadings plot are positively correlated. If the trace element loadings are grouped diagonally opposite to each other, they are correlated negatively. It should be noted that biplot is only as good as the proportion of the total variance they depict. A good biplot will generally capture $\gg 50\%$ of the total variance (Gabriel 1971).

Prior to PCA, mean log-concentrations for each texture within each polished-block (clean martite $n = 30$, porous martite $n = 22$, platy hematite $n = 11$) were calculated. Furthermore, PCA was performed on correlation matrices (standardised covariance matrices) of textural categories of hematite. The rare earth elements (REE) were treated as a single sum (ΣREE), as these elements are highly correlated and their treatment as a group reduce their weight in PCA and make biplots easier to interpret.

4.3.2 Linear Discriminant Function Analysis

Similar to PCA, linear discriminant function analysis reduces the dimensionality of the data. However, while PCA maximises the proportion of the total variance displayed in a two- (or three-)dimensional projection of the data, LDA results in discriminant functions—linear combinations of variables that best separate known classes. Consequently, prior to classification, the k specific classes of data must be identified, textural category, or location in the Middleback Ranges. The $k - 1$ discriminant functions are then obtained by maximising a ratio of a measure of distances between classes to the variability within the class, subject to the discriminant functions being mutually

orthogonal. For a detailed account of the theory of LDA readers are referred to more comprehensive reviews (Johnson and Wichern 2007).

Linear discriminant analysis was used to distinguish a) three ($k = 3$) texturally defined hematite categories (model 1) and b) three ($k = 3$) locations of the Middleback Ranges: North, Middle and South (model 2) (Table 1) with respect to their trace element concentrations. The function lda() in the Venables and Ripley (2003) MASS R package was used to perform LDA. Similar to PCA, average trace element concentrations for each texture within each polished-block were used as input data for both models. The data were log-transformed and mean-centred prior to LDA.

5 Results

5.1 Data Assessment for Mineral Inclusions

The examination of time-resolved down-hole LA-ICP-MS profiles of all categories of hematite and magnetite showed the presence of gangue mineral inclusions: quartz, clay minerals, chlorite, Ca-, Mn-, and Sr-bearing carbonates, or accessory minerals such as Ti-(V)-bearing phases, apatite, monazite or zircon. In the absence of sulphur measurements, Ba-bearing inclusions were attributed to barite, and Pb-, Cu-, Zn-bearing inclusions were attributed to sulphides. Other potentially included phases, notably pyrite, could not be resolved.

LA-ICP-MS signal profiles with patterns or peaks indicating extreme contamination by phases other than Fe-oxides (apatite, silicates, sulphides etc.) were not included in this study dataset. However, some analyses of texturally defined hematite with flat ablation profiles display high concentrations of elements typical for gangue minerals: Mg (up to 1.3 wt%); Al (up to 1.2 wt%); Si (up to 2.8 wt%); and Mn (up to 0.8 wt%). Similarly, magnetite may contain Mg (up to ~ 1.5 wt%) and Si (up to ~ 3 wt%). The flatness of ablation signal profiles does not, however, necessarily rule out the presence of micro- to nanoscale inclusions.

5.2 Univariate Analysis of Fe-Oxides

The distribution patterns of trace elements in hematite and magnetite were investigated through box plots (Fig. 5a–d). The trace elements were selected and divided into four groups: (1) granitophile elements (REE, Y, U, Pb, W, Mo and Sn) (Fig. 5a); (2) lithophile elements (Si, Al, Mg, P) and Mn (Fig. 5b); (3) high field strength elements (HFSE) and transition metals (Ti, V, Ni, Cr and Co) (Fig. 5c); and (4) chalcophile elements (Zn, As, Cu, Sb) and Ga (Fig. 5d). In contrast to hematite, magnetite shows consistently low contents of all trace elements, and especially granitophile elements, with the sole exception of Mn (Fig. 5b). The contents of all the trace elements are highly variable across all groups of Fe-oxides and show significant overlaps.

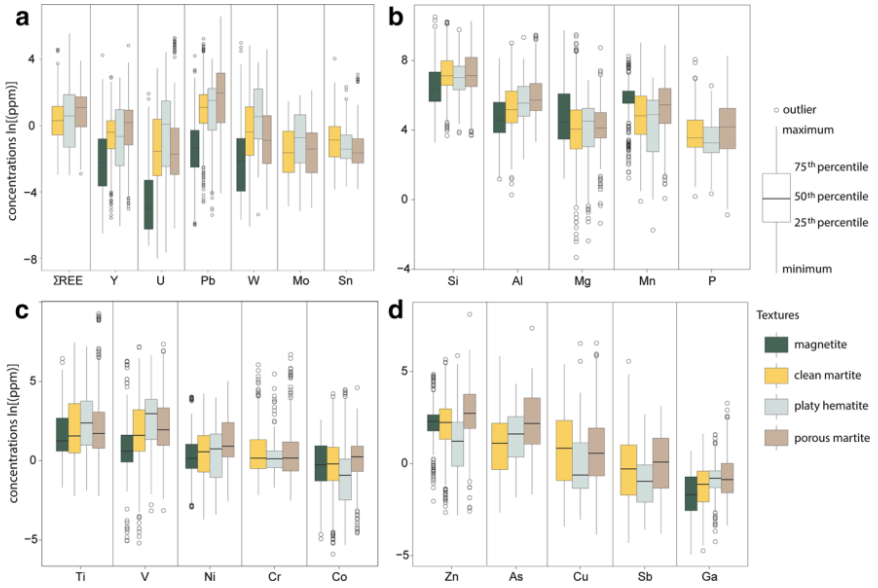


Fig. 5 Box-and-whisker diagrams of groups of trace element in magnetite and texturally defined hematite: **a** granitophile elements; **b** lithophile elements and Mn; **c** transition metals and high field strength elements; and **d** chalcophile elements and Ga

5.2.1 Magnetite Trace Element Data

The summary statistics for magnetite trace element data are reported in Table 2. Magnetite from low- to high-grade ores is characterised by the large variance and geometric means of lithophile elements Si, Mn, Mg and Al (Table 2). The elements Ti, V, Co, Ni, Zn, as well as Ga, have geometric means an order of magnitude smaller than the lithophile elements (Fig. 5c, d; Table 2). Granitophile elements (Pb, U and W) display very low concentrations in magnetite (Fig. 5a; Table 2), measured at sub-ppm levels only, and are thus markedly depleted compared to any of hematite categories.

5.2.2 Hematite Trace Element Data

The summary statistics of hematite from different textural categories are listed in Table 3. Out of all measured trace elements, Mg, Al, Si and Mn consistently have the highest geometric means (Table 3) in all types of hematite.

Porous martite has the largest geometric means for Mg, Al and Mn, and clean martite has the largest geometric mean for Si. Porous martite stands out compositionally by significantly larger geometric means for other elements (P, Cr, Co, Ni, Zn, Ga, As, Y, Sb, REE, Pb and Sr) compared to clean martite and platy hematite. In addition, Zr, Nb and Mo display geometric means slightly higher in platy hematite, whereas geometric means of Ti, V and W are larger compared to clean martite and porous martite (Table 3).

Table 2 Trace element composition of magnetite: range of minimum detection limit (DL) in ppm, proportion of values BDL (% BDL), geometric means (GM) and 68% probability interval (PI)

	DL range (ppm)	% BDL	GM (ppm)	68% PI (ppm)
Mg	–	0	121	22–656
Al	–	0	108	24–486
Si	54–184	6.3	666	166–2677
Ti	0.37–1.3	8.1	5.5	0.95–32
V	0.01–0.02	0.7	2.2	0.46–10
Mn	–	0	306	100–933
Co	0.01–0.04	2.9	0.69	0.14–3
Ni	0.1–0.38	4.1	1.3	0.31–5
Zn	0.26	0.3	9.1	3.42–24
Ga	0.01–0.07	7.7	0.19	0.05–0.62
Sr	0.005–0.02	12.5	0.07	0.01–0.42
Y	0.003–0.018	6.2	0.10	0.01–0.76
La	0.005–0.027	6.6	0.05	0.006–0.352
Ce	0.002–0.016	4.9	0.07	0.009–0.470
W	0.07–0.34	11.4	0.12	0.014–1.045
Pb	0.005–0.029	4.3	0.28	0.04–1.8
U	0.001–0.003	19.5	0.012	0.001–0.12

5.2.3 Hematite Trace Element Data Linear Mixed-Effects Models

The results of the LME models are shown in Table 4 and include the estimates of the means of log concentrations of trace elements in each category. The model allows for three components of variance induced by random effects: between-deposit σ_β^2, between-polished block σ_γ^2, and within-polished-block σ_ϵ^2, while overall variance encompasses all the components as (Figs. 4 and 6)

$$\sigma^2_{\text{overall}} = \sigma_\beta^2 + \sigma_\gamma^2 + \sigma_\epsilon^2. \tag{6}$$

In addition, the degree of clustering of the data at the polished block level and at the deposit level were estimated as intra-class correlations (ICC),

$$\text{ICC}_{\text{within-polished block}} = \left(\sigma_\beta^2 + \sigma_\gamma^2\right) / \left(\sigma_\beta^2 + \sigma_\gamma^2 + \sigma_\epsilon^2\right), \tag{7}$$

and

$$\text{ICC}_{\text{within-deposit}} = \sigma_\beta^2 / \left(\sigma_\beta^2 + \sigma_\gamma^2 + \sigma_\epsilon^2\right). \tag{8}$$

The estimates of standard deviations and corresponding ICCs are given in Table 4. It can be noticed, that there is a significant correlation among spot-analyses within

Table 3 Trace element composition of clean martite, porous martite and platy hematite: range of minimum detection limit (DL) in ppm, proportion of values BDL (% BDL), geometric means (GM) in ppm and 68% probability interval (PI)

	% of BDL	DL range clean martite (ppm)	GM clean martite (ppm)	68% PI clean martite (ppm)	DL range porous martite (ppm)	GM porous martite (ppm)	68% PI porous martite (ppm)	DL range platy hematite (ppm)	GM platy hematite (ppm)	68% PI platy hematite (ppm)
Mg	0.50	0.13–0.14	60.0	8.1–449	0.35	68.1	17.2–260	0.24	53.6	8.2–349
Al	–	–	185	45–752	–	379	113–1274	–	249	73.0–847
Si	3.5	69.9–135	1431	419–4884	107–155	1353	382–4786	122–147	1077	361–3210
P	11.4	4.9–22.7	43.1	12.1–149	5.1–14.5	59.8	12.0–284	4.5–12.6	29.0	8.2–101
Sc	32.0	0.02–0.42	0.20	0.04–0.77	0.05–0.45	0.26	0.06–1.1	0.05–0.19	0.22	0.07–0.63
Ti	7.2	0.34–1.1	7.2	0.89–57.3	0.54–1.8	9.2	0.98–86.8	0.32–1.2	10.6	1.6–68.5
V	0.27	0.11–0.23	5.8	0.77–44.2	–	9.6	1.4–65.3	0.05	13.5	2.3–80.1
Cr	29.5	0.23–1.9	1.6	0.37–6.8	0.41–2.2	1.7	0.31–8.9	0.39–1.8	1.3	0.41–3.9
Mn	0.10	–	115	20.4–658	–	188	39.2–897	0.35	65.7	9.5–453
Co	5.6	0.06–0.13	0.68	0.11–4.1	0.26–0.54	1.1	0.24–4.7	0.02–0.05	0.38	0.04–3.0
Ni	6.9	0.30–0.05	1.4	0.27–7.5	0.07–0.27	3.3	0.78–14.2	0.09–0.34	1.5	0.29–7.8
Cu	23.8	0.03–1.69	2.2	0.31–15.0	0.12–0.54	2.1	0.27–15.1	0.08–1.99	0.94	0.16–5.4
Zn	4.6	0.14–0.69	7.6	1.7–34.4	0.31–0.61	14.8	3.2–68.3	0.19–0.52	2.9	0.49–17.8
Ga	4.3	0.02–0.10	0.28	0.08–0.97	0.03–0.11	0.51	0.14–1.8	0.04–0.07	0.41	0.15–1.09
As	10.9	0.12–2.5	3.1	0.51–19.2	0.16–2.6	8.7	1.8–40.8	0.3–3.1	3.9	1.03–15.3
Sr	2.2	0.008–0.012	0.38	0.09–1.6	0.01	0.91	0.23–3.4	0.012–0.014	0.36	0.07–1.9
Y	1.9	0.004–0.009	0.54	0.12–2.4	0.01–0.02	0.81	0.14–4.4	0.006–0.017	0.39	0.05–3.1
Zr	14.1	0.008–0.085	0.11	0.01–0.73	0.01–0.07	0.15	0.01–1.3	0.022–0.053	0.29	0.04–1.9
Nb	15.4	0.005–0.037	0.03	0.004–0.17	0.004–0.02	0.03	0.005–0.21	0.003–0.011	0.05	0.009–0.3
Mo	9.32	0.01–0.19	0.19	0.03–0.89	0.01–0.08	0.20	0.04–0.88	0.02–0.05	0.39	0.06–2.3

Table 3 continued

	% of BDL	DL range clean martite (ppm)	GM clean martite (ppm)	68% PI clean martite (ppm)	DL range porous martite (ppm)	GM porous martite (ppm)	68% PI porous martite (ppm)	DL range platy hematite (ppm)	GM platy hematite (ppm)	68% PI platy hematite (ppm)
Sn	26.7	0.07–037	0.41	0.10–1.6	0.06–0.37	0.23	0.06–0.80	0.05–0.26	0.29	0.09–0.83
Sb	12.9	0.02–0.46	0.86	0.10–6.9	0.01–0.37	0.99	0.19–5.06	0.02–0.4	0.40	0.09–1.7
Ba	7.4	0.06–0.10	1.09	0.18–6.4	0.11	1.8	0.26–11.9	0.06–0.14	1.5	0.18–11.9
∑REE	–	–	1.3	0.33–5.4	–	2.2	0.52–9.2	–	1.6	0.26–9.4
W	2.4	0.009–0.088	0.61	0.08–4.6	0.01–0.04	0.40	0.06–2.5	–	1.6	0.31–8.7
Pb	1.3	0.0054–0.018	2.5	0.43–14.4	0.01–0.02	5.6	0.74–41.9	0.009–0.024	2.1	0.23–19.5
Th	25.8	0.002–0.137	0.013	0.002–0.081	0.002–0.051	0.02	0.003–2.6	0.002–0.013	0.02	0.003–0.13
U	2.4	0.001–0.011	0.21	0.02–2.7	0.003–0.028	0.2	0.02–2.6	0.003–0.004	0.63	0.26–9.4

Table 4 Estimates of standard deviation parameters and means of log concentrations of elements in clean martite, platy hematite and porous martite from LME fit

Element	Between-deposit standard deviation σ_β	Between-polished block standard deviation σ_γ	Within-sample standard deviation σ_ϵ	Within polished-block ICC	Within deposit ICC	Significance of variable "texture"	Mean clean martite	Mean platy hematite	Mean porous martite
Mg	0.67	1.21	1.15	0.64	0.27	***	4.25	3.78	4.89
Al	0.54	1.09	0.69	0.68	0.28	***	5.22	5.59	6.09
Si	0.21	0.83	0.96	0.58	0.20		7.26	7.46	7.36
P	0.63	0.76	0.95	0.63	0.30	***	3.79	3.77	4.42
Sc	0.62	0.99	0.84	0.66	0.29	***	− 1.70	− 1.31	− 1.10
Ti	0.00	1.98	1.09	0.57	0.00		2.28	2.21	2.40
V	0.98	1.54	0.95	0.70	0.31	***	1.47	2.55	2.55
Cr	0.50	1.13	0.92	0.65	0.26	**	0.35	0.54	0.74
Mn	0.64	1.31	0.99	0.66	0.27	***	4.59	4.32	5.72
Co	0.38	1.39	1.17	0.62	0.21	***	− 0.98	− 0.91	0.81
Ni	0.69	1.10	0.98	0.66	0.29	***	0.10	0.37	1.49
Cu	1.11	1.00	1.31	0.64	0.33		0.61	0.53	0.83
Zn	0.33	1.25	0.97	0.63	0.22	***	1.68	1.49	2.84
Ga	0.56	1.00	0.57	0.70	0.30	***	− 1.29	− 1.13	− 0.65
As	1.06	1.27	0.76	0.71	0.34	***	1.32	0.57	1.88
Sr	0.31	1.03	1.07	0.60	0.21	***	− 1.12	− 1.03	0.35
Y	0.95	0.92	1.03	0.66	0.33	***	− 0.56	− 0.75	− 0.03
Zr	0.77	1.49	1.17	0.66	0.28		− 1.99	− 1.68	− 1.75
Nb	0.00	1.70	0.99	0.57	0.00		− 3.18	− 3.12	− 3.25
Mo	0.94	1.07	0.91	0.68	0.33		− 1.55	− 1.52	− 1.57

Table 4 continued

Element	Between-deposit standard deviation σ_β	Between-polished block standard deviation σ_γ	Within-sample standard deviation σ_ϵ	Within polished-block ICC	Within deposit ICC	Significance of variable "texture"	Mean clean martite	Mean platy hematite	Mean porous martite
Sn	0.48	1.06	0.72	0.67	0.27	***	− 0.80	− 1.27	− 1.27
Sb	1.37	1.09	0.83	0.71	0.37	***	− 0.31	− 1.45	− 0.38
Ba	0.94	1.22	1.15	0.66	0.31	***	− 0.14	0.18	0.87
∑REE	0.69	1.07	0.88	0.66	0.30	***	0.31	0.50	1.07
W	1.15	1.29	1.13	0.68	0.33	o	− 0.54	− 0.43	− 0.81
Pb	1.08	1.43	1.01	0.69	0.32	***	0.71	0.63	1.93
Th	0.74	1.50	0.86	0.69	0.29	***	− 4.12	− 3.90	− 3.71
U	1.68	1.72	1.13	0.71	0.35	***	− 1.90	− 1.43	− 0.57

Significance codes [Pr(>Chisq)]: *** 0–0.001; **0.001–0.01; *0.01–0.05, ∘0.05–0.1, no symbol > 0.1 correspond to a p values obtained from likelihood-ratio test (LRT); the within-polished block ICC and within deposit ICC are calculated as in Eqs. (4) and (5)

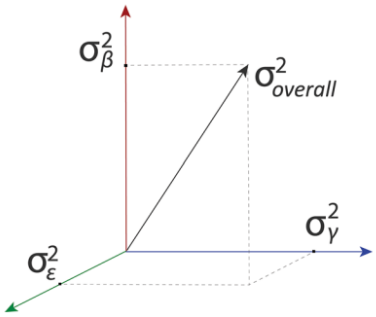


Fig. 6 Relationships between variance components of the linear mixed-effects model as in Fig. 4 and overall variance is as in Eq. (6)

polished blocks, while ICC between polished blocks of the same deposit is lower. The within-polished block ICCs are generally higher than 0.5 indicating high similarity among spot-analyses from the same polished block. Additionally, the within deposit ICC is slightly lower and does not exceed 0.3 for most of the elements. This suggests that some similarity among polished block from the same deposit exists.

The between-polished block standard deviation σ_γ is the largest component of variance for the majority of elements except Si, P, Cu, Sr, Y and Sb, while the between-deposit standard deviation σ_β is generally the smallest out of all estimated components of variance. However, for Sb the between-deposit standard deviation is the largest out of the variance components suggesting its abundance is highly variable amongst the deposits of Middleback Ranges. In addition, the estimates of between-deposit standard deviations of Ti and Nb were equal to zero indicating that variability between deposits is negligible.

A test of significance of the concomitant variable texture, using a likelihood-ratio test (LRT), showed that there is statistically significant evidence, mostly at $p < 0.001$ level, for a relationship between trace element concentrations and texture for the majority of elements. The exceptions are Si, Ti, Cu, Zr, Nb and Mo (Table 4), and W showed a p value approaching the 0.05 threshold.

5.3 Multivariate Analyses of Fe-Oxides

5.3.1 Principal Component Analysis

Biplots were used to simultaneously visualise scores and loadings of PCA. Figure 7 shows score-plots in the left-hand panels and loadings-plots in the right-hand panels. Only the twenty elements with the largest loadings on PC1 and PC2 for each textural category of hematite are included in the loadings-plots. The proportion of the total variance captured by the first two principal components is 57% for clean martite, 55% for porous martite, and 72% for platy hematite. Biplots of additional principal components are not displayed as they do not provide further insight.

All three textural categories of hematite show strong negative loadings of all trace elements on PC1 (Fig. 7b, d, f). This is due to the predominantly positive correlation coefficients among element concentrations (Electronic Appendix C). PC2 accounts for

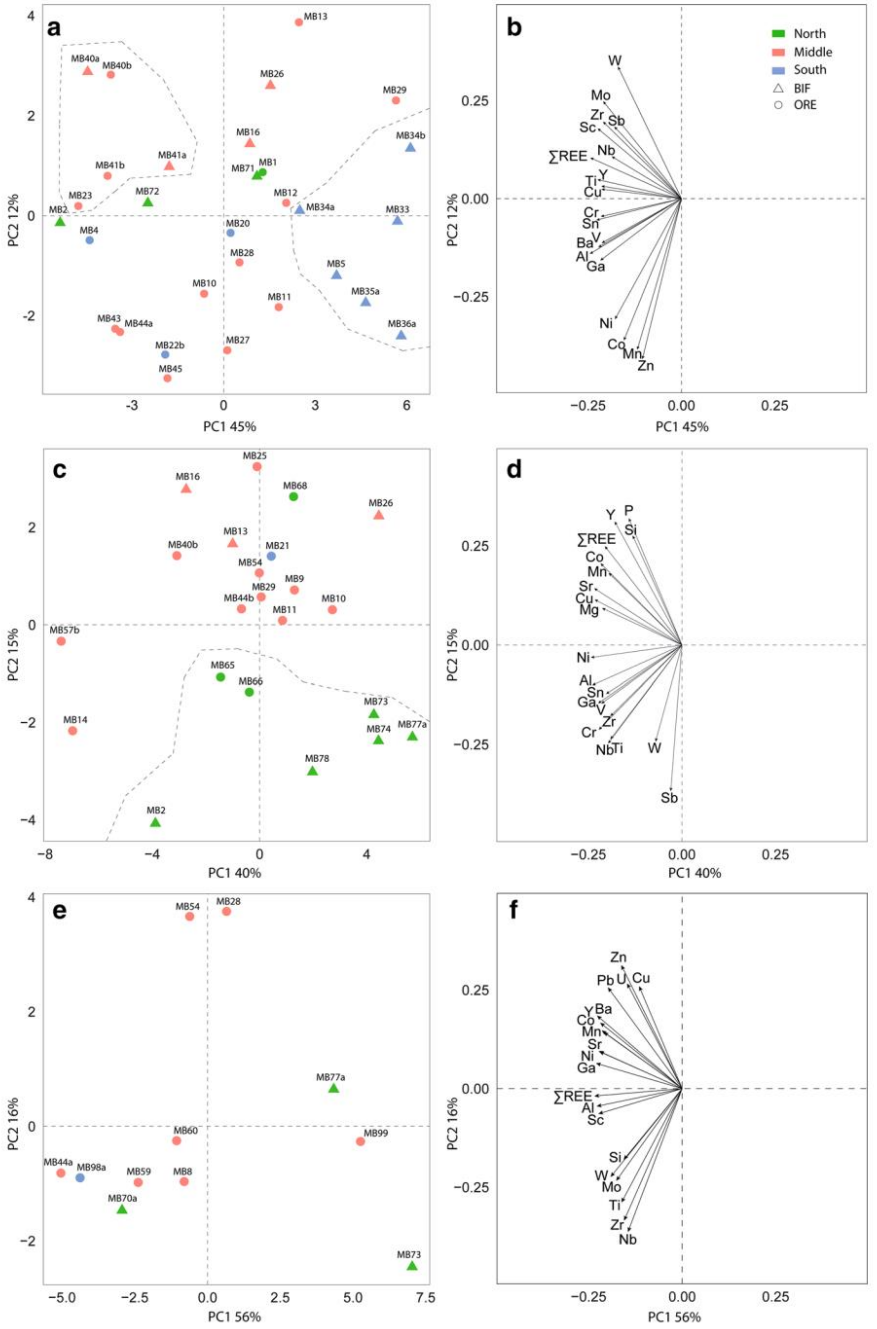


Fig. 7 Principal component analysis results of LA-ICP-MS data for clean martite ($n = 30$; **a**, **b**), porous martite ($n = 22$; **c**, **d**) and platy hematite ($n = 11$; **e**, **f**) from the North, Middle and South Middleback Ranges; the lithology types of samples are given in the legend

substantially less variance than PC1, and contains trace elements with both positive and negative loadings. Samples with similar geochemical signatures plot close to each other in these biplots.

PCA results of clean martite from different iron ore deposits are presented in Fig. 7a, b. The second principal component is characterised by high negative loadings of Ni, Co Mn, and Zn and high positive loadings of W, Mo, Sb, Sc and Zr (Fig. 7b). It can be noticed that clean martite originating from the Iron Magnet and Iron Chieftain deposits group together. These samples are characterised by low concentrations of W, Mo, Sc, Sb, Zr, ΣREE, and Nb suggesting depletion of these elements. In contrast, a group of clean martite from the Iron Count deposit shows high concentrations of these elements, and consequently plots diagonally opposite the Iron Magnet group. It can also be noticed that samples from the South are separated from the samples from the North and Middle. On the other hand, no systematic grouping can be seen for martite from Iron Warrior and Iron Queen.

The PCA results for porous martite also show a grouping of samples originating from the North Middleback Ranges (Fig. 7c) (except for sample MB68 from Iron Princess). Specifically, the porous martite of Iron Monarch and Iron Princess plot in proximity to each other and show low concentrations of ΣREE, Y, Si and P, elements often present in monazite/xenotime or apatite, and therefore probably attributable to contaminant phases.

The distribution of platy hematite samples on the score biplot (Fig. 7e) is extremely sporadic showing that platy hematite in deposits with presumed identical origin do not share geochemical signatures and have large variabilities within a single deposit. PC2 has high positive loadings of Pb, U, Zn and Cu, and high negative loadings of W, Mo, Si, Ti, Zr and Nb as indicated by the loadings-plot (Fig. 7f).

5.3.2 Linear Discriminant Analysis

The discriminant function coefficients, or weights for both fitted models are listed in Table 5. Corresponding misclassification rates obtained from fitting both models are reported in Table 6. The scores of trace elements on the two discriminant functions are calculated as the product of trace element concentrations and corresponding weights (Table 5; Figs. 8 and 9).

The results of the first LDA classification (Fig. 8) show which linear combinations of trace elements are important for the classification of texturally defined categories of hematite. The first discriminant function, DF1, contains the following elements with high absolute weights (> 0.6): Sn, Zn, Sb, Th, Pb, As and Ga, and discriminates porous martite and platy hematite from clean martite. The trace elements with the highest absolute weights on DF2 are ∑REE, Zn, Sn, Mn, Sb, Sr and Y. The DF 2 mostly discriminates platy hematite from porous martite (Fig. 8).

The results of the classification of the data by location yields linear combinations of those log-transformed trace element concentrations that are most important in distinguishing between samples from the North, Middle and South Middleback Ranges. The DF1, mostly discriminates between Middle on the one hand, and South and North on the other hand. It mostly reflects differences in Sn, Cu, Mn, Th, V, Nb, Ti, and Co

Table 5 Discriminant function matrix of two LDA models

Model 1: by texture				Model 2: by location			
DF1		DF2		DF1		DF2	
Sn	− 1.86	∑REE	− 1.29	Sn	− 1.15	Ga	− 1.25
Zn	− 0.99	Zn	− 0.83	Cu	− 0.83	Sc	− 0.80
Sb	− 0.79	Sn	− 0.79	Mn	− 0.73	Mo	− 0.75
Th	− 0.68	W	− 0.58	Th	− 0.70	Zn	− 0.62
Y	− 0.55	Ga	− 0.46	V	− 0.66	Sr	− 0.50
Co	− 0.52	Mo	− 0.38	∑REE	− 0.54	As	− 0.31
U	− 0.31	V	− 0.36	Sr	− 0.39	Y	− 0.30
Cu	− 0.25	Co	− 0.30	Ga	− 0.34	Sb	− 0.30
Ni	− 0.24	As	− 0.30	P	− 0.27	W	− 0.22
W	− 0.10	Mg	− 0.24	Al	− 0.26	Cr	− 0.20
Cr	− 0.07	Th	− 0.24	Zr	− 0.25	Ba	− 0.15
Ti	− 0.06	Ba	− 0.22	Zn	− 0.17	Zr	− 0.14
Al	− 0.04	Nb	− 0.19	Mg	− 0.09	Ti	− 0.12
Zr	− 0.02	U	− 0.19	W	− 0.06	P	− 0.11
Mo	0.03	Sc	− 0.07	Sc	0.05	V	− 0.05
Sr	0.03	P	0.08	Sb	0.07	Nb	0.06
Mg	0.05	Zr	0.08	U	0.11	Mg	0.10
Mn	0.30	Cu	0.14	Y	0.13	Ni	0.10
Si	0.30	Si	0.23	Cr	0.15	Si	0.11
P	0.34	Pb	0.28	Mo	0.20	Al	0.14
Sc	0.34	Ni	0.30	Pb	0.28	U	0.21
V	0.38	Cr	0.47	Si	0.34	Sn	0.21
Ba	0.45	Al	0.50	Ba	0.38	Mn	0.27
∑REE	0.47	Ti	0.56	Ni	0.59	Cu	0.45
Nb	0.50	Mn	0.63	As	0.61	∑REE	0.50
Pb	0.64	Sb	0.85	Nb	0.77	Pb	0.55
As	0.98	Sr	1.06	Ti	0.98	Co	0.64
Ga	1.29	Y	1.53	Co	0.98	Th	1.06

(Fig. 9). The second function, DF2, only distinguishes North from South, based on the concentrations of Ga, Sc, Mo, Zn, Co and Th.

Because of the distinct categorical variables used for classification in the two LDA models, the resultant discriminant functions are completely dissimilar.

6 Discussion

The Middleback Ranges show features common to other BIF-hosted iron ore deposits (Keyser et al. 2018). These include interbedded silicate, carbonate, and Fe-oxide layers,

Table 6 Classification matrix of two LDA models

Model 1: by textures					Model 2: by location				
Predicted group					Predicted group				
Actual group	Clean martite	Platy hematite	Porous martite	Misclassified	Actual group	Middle	North	South	misclassified
Clean martite	29	0	1	1	Middle	37	0	0	0
Platy hematite	0	9	2	2	North	1	14	0	1
Porous martite	1	0	21	1	South	0	0	11	0
	30	9	24	4		38	14	11	1

Total correctly classified 93% for Model 1, and 98% for Model 2

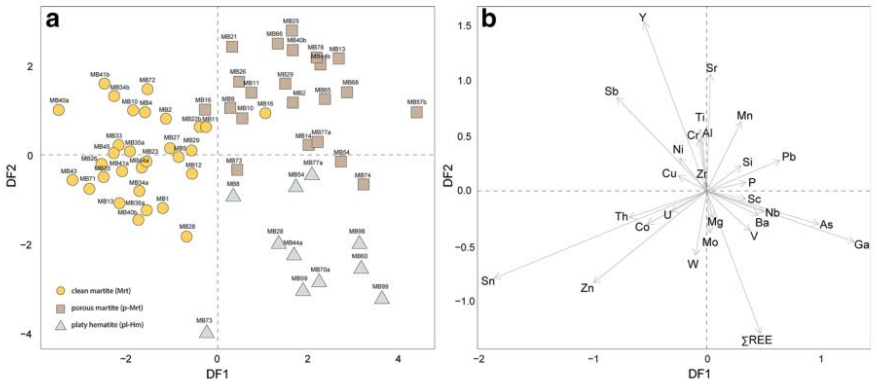


Fig. 8 Linear discriminant analysis (Model 1; Table 5) of LA-ICP-MS data for texturally defined hematite. Each data point corresponds to the trace element concentration for a textural category within a polished-block ($n = 63$); the distribution of hematite analyses from different textural categories (**a**), and element loadings of the discriminant function coefficients (**b**)

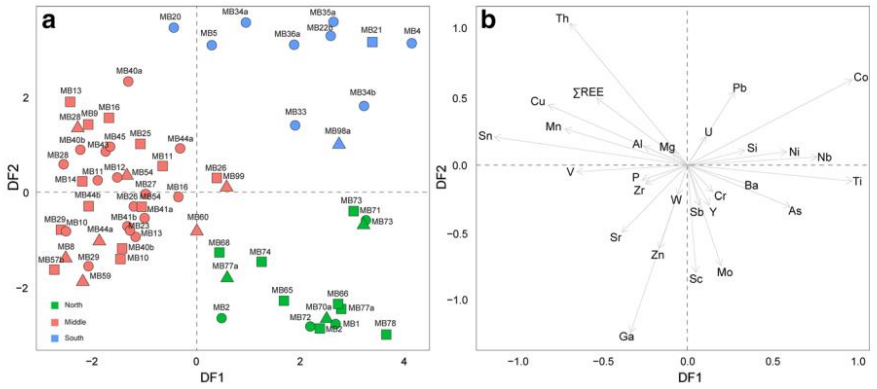


Fig. 9 Linear discriminant analysis of LA-ICP-MS dataset for hematite by location: North, Middle and South (Model 2; Table 5) (**a**), and loadings of the discriminant function coefficients (**b**). Legend for textural categories as in Fig. 8

the presence of complex fold structures (Davies 2000) and extensional local and major regional faults (Fig. 1). The structural control plays a fundamental role in formation of many BIF-derived ores, since faults are important pathways for fluid migration and leaching of gangue minerals (Dalstra and Rosière 2008). In addition to their structural complexity, Fe-deposits of the Middleback Ranges are characterised by interconversions of Fe-oxides typical of BIFs and BIF-derived iron ores, involving, for instance, transformation of magnetite to martite and the formation of platy hematite. These transformations allow one to constrain deposit evolution from initial deposition through ore enrichment and overprinting assuming that the history of post-depositional processes is preserved (Keyser et al. 2018). The post-depositional processes may include various burial and uplifting events, interaction with surficial waters and/or overprinting by hydrothermal fluids related to emplacement of intrusive bodies (e.g. ~ 1.6 Ga Hiltaba Suite (HS); ~ 800 Ma Gairdner Dyke Swarm).

In this study, the evolution of the Fe-oxides from BIFs to iron ore was examined with respect to changes in their trace element signatures assuming that the textural categorisation of hematite is the most significant basis to track these changes. Observed variations in trace element concentrations reflect a complex genetic history for these BIFs and ores (Keyser et al. 2018).

6.1 Trace Element Patterns of Fe-Oxides

The low trace element concentrations of magnetite from Iron Magnet deposit, and relict magnetite inclusions in martite indicate that magnetite is probably the earliest generation of Fe-oxide preserved in the Middleback Ranges (Keyser et al. 2018) and has not been affected by significant hydrothermal alteration. The elements, Si, Al, Mg and Mn, all compatible with BIF-depositional environments (Hagemann et al. 2016) are consistently measurable and are present at concentrations more than an order of magnitude higher than other cations substituting for Fe. The commonly high values of Si, Al, Mg and Mn are either indicators of inclusions or, alternatively, reflect initial incorporation of these elements to magnetite during diagenesis of pre-existing Fe-rich sediments.

New element-distribution patterns were introduced via martitisation. This is reflected in the enrichment of granitophile elements U, W, Pb, Y, and possibly $\sum$REE, Mo and Sn in all phases that post-date magnetite (Fig. 5). The sources of these granitophile elements are likely to have been surficial and/or hydrothermal fluids associated with granitoids that postdate BIF deposition and diagenetic magnetite formation: the ~ 1850 Ma Donington Suite, and/or the ~ 1585 Ma HS granites such as Charleston Granite (Creaser and Fanning 1993) (Fig. 1).

A further transition from clean martite to porous martite corresponds to the enhanced substitution for Fe by transitional metals (Cr, Mn, Co, Ni and Zn), chalcophiles such as As, along with some lithophile elements, notably Mg, Al, P, and REE (Table 4). On the other hand, concentrations of high field strength elements, Zr, Nb and Ti, as well as Mo, Sn and W in porous martite resemble the same levels as those in clean martite (Table 4). Martitisation and dissolution of the gangue minerals in the supergene environment could potentially result from interaction with fluids leaching adjacent Hiltaba-, and Myola-aged granitoids and younger discordant mafic rocks accompanied by high thermal gradient. The systematic difference in chemistry of clean and porous martite suggests their formation at different stages of ore enrichment.

Analysis of biplots (Fig. 7) suggests that a large proportion of the total variation within each hematite category is controlled by a single one-dimensional factor: the first principal component is clearly associated with the sequential addition of new trace elements to the Fe-oxides without depleting any existing components. This feature is also supported by the lack of highly negative correlations in the correlation matrices of the three categories of hematite (Electronic Appendix C).

The PCA scores (Fig. 7a, c, e) revealed the geochemical and/or spatial similarities for clean martite from Iron Magnet and Iron Chieftain sourced from magnetite BIFs. These samples show consistently low concentrations of granitophile elements, REE, W, Sc, Sb and Mo (Fig. 7a) reflecting the low concentrations of these elements in Iron

Magnet and Iron Chieftain BIFs. In contrast, clean martite from Iron Count has higher concentrations of granitophile elements. Such an association may reflect the influence of granitic fluids in overprinting ores and BIFs from Iron Count (Keyser et al. 2018; Fig. 1), but the comparative lack of influence from granites on magnetite BIFs in the South Middleback Range.

The geochemical/spatial similarity is also observed in porous martite from the North Middleback Ranges—samples originating from siliceous BIF from Iron Monarch plot in proximity to martite-goethite ores from Iron Princess (Fig. 7c). The northern Middleback Ranges are characterised by a specific As-, Ba-, Sb- and Mo-enriched signature that may reflect local hydrothermal activity potentially affiliated to emplacement of Hiltaba Suite (Keyser et al. 2018). In the case of platy hematite, the results of PCA are difficult to interpret based on current knowledge and number of samples: the samples do not tend to cluster together in any systematic way and, therefore, platy hematite with presumably identical origins does not display chemical similarity. Petrographic evidence shows, however, that microplaty hematite occurs in several distinct forms and associations, and likely grows throughout all of the various iron ore enrichment stages. For example, microplaty hematite can crystallise in open spaces from hydrothermal fluids, co-precipitate with and/or postdate Fe-hydroxides, or replace goethite during dehydration due to increased geothermal gradients (Morris 2012; Keyser et al. 2018).

6.2 Variance Structure of Hematite Data

Results of LME modelling (Table 4) have demonstrated that for trace elements, with the exceptions of Si, P, Cu, Sr and Y, the largest component of the total variance is that between polished-blocks within deposits, σ^2_γ. The Si-, P-, Cu-, Sr- and Y-bearing phases have been documented as typical components of inclusions in the downhole profiles (Sect. 4.1). The dominance of within-polished block standard deviation σ_ϵ of these elements could potentially originate either from nano- to micro-scale inclusions under the mineral surface, or from extensive zonation of mineral grains with respect to these elements.

The spot-analyses within polished blocks have high ICCs, where the class is a polished block (Table 4). The observed intra-class correlation among spot-analyses within a polished-block is not consistent with an assumption of independent observations which is often made when working with LA-ICP-MS datasets (Belissont et al. 2014). In contrast to independent observations, when a single observation provides no information about another one, spot-analyses on the same mineral within a given polished block are, effectively, replicants, and therefore, can be considered as clustered data. The finding that spot-analyses within the same polished block are relatively similar, and that to a lesser extent the same is true the within deposits, shows that treating the data as independent observations tend to overestimate the available information. The data are less informative than the same number of independent spot-analyses. If this is ignored in the statistical analyses, the statistical significance will be overestimated, leading to unsubstantiated claims.

Furthermore, the LME model makes the correct allowance for comparing textures. The method of using the means of spot-analyses on each polished block is not satis-

factory because: 1) the numbers of spot-analyses on each polished block differ, and 2) there is a positive correlation among polished blocks within deposits. A further advantage of using LME model is that it includes estimates of components of variance, which may themselves be of geological significance.

The results demonstrated here shed light onto multi-element discriminant diagrams (Dupuis and Beaudoin 2011) and why these are not always able to discriminate ore deposits when applied to new data (Zhou et al. 2017; Günther et al. 2017). In this case study, the largest component of variance of hematite data is due to the variance between polished blocks within deposits σ_{γ}^2. Because this conclusion might be applicable to any other hierarchical LA-ICP-MS dataset, it must be tested in the following studies.

6.3 Discrimination of Hematite Categories

The LDA was performed to find trace element combinations that provide the best discrimination between categories. Although the result of LME models demonstrated that the mean concentrations of most elements differ between textures (Table 4), there is also generally a considerable overlap between categories (Fig. 5). It follows that a discriminant function based on any single element will have poor discrimination power. As LDA combines information from all elements simultaneously, it provides significantly better discrimination. This assists in understanding the true differences in trace element signatures among texturally defined hematite.

The LDA shows that difference in trace element signatures is attributed to different hematite textures. Trace elements contributing to discrimination the most, for example, Sn, Zn, As, Ga, REE, Y and Sr, were shown to have statistically significant differences among textural categories in LME analyses (Table 4). The DF1 (Fig. 8) revealed that the two stages of martite, clean and porous, are distinct from each other in terms of the fluid chemistry in the supergene environment. Similarly, the distinguishing of platy hematite from porous martite is accented by DF2, and specifically, enrichment in W and REE and depletion of Sr and Y in porous martite relative to platy hematite (Table 4; Fig. 8).

The classification of hematite by location shows that trace element signatures of hematite are also useful in distinguishing among locations in the Middleback Ranges. Consequently, trace elements with the highest coefficients on the corresponding discriminant functions reflect the major geochemical differences between three locations within the belt, highlighting the significance of overprinting at the local scale (Keyser et al. 2018). Tin, Cu and ΣREE geochemical signatures of the Middle segment of the belt (Fig. 9) could be (partially) inherited from 1.8 Ga Myola Volcanics (Fig. 1) which host what has been recognised as a potential Fe-oxide Cu-Au Moola prospect in the Middleback Ranges (McIntyre, 2001). Both the southern and northern Middleback Ranges display geochemical signatures featuring relative enrichment in Ni, Co, Ti and Nb (Fig. 9), indicating the potential influence of younger discordant mafic rocks (Keyser et al. 2018).

Tin, Ga, As and Zn are discriminator elements with significantly large weights in both models (Figs. 8, 9; Model 1, 2 Table 5). Tin is a ubiquitous component in clean martite throughout the belt yet shows increased concentrations (Fig. 8; Table 4) and is

a discriminator element for the Middle segment of the belt (Fig. 9). This suggests that despite enrichment of Sn in some segments (i.e. Middle), the clean martite represented throughout the belt has an intrinsic Sn-enriched signature, potentially inherited from regional-scale processes, notably HS emplacement. In addition to a regional Sn signature, certain locations, for example, Iron Count, also show granite-affiliated signatures (W-Mo-Sb); see Sect. 6.1 (Fig. 7a) within clean martite that could potentially reflect a smaller scale overprinting process affecting Iron Count.

Of all the discriminator elements within the two LDA models, Ni and Co are uniquely attributed to hematite discrimination by location. In addition to Ti and Nb, that show no statistically significant difference among hematite textures (Table 4), nickel and Co are specifically attributed to separation between North and South Middleback Ranges from the Middle Middleback Ranges (Model 2 Table 5; Fig. 9). The enriched levels of transition metals, Ni and Co along with high field strength elements, Ti and Nb, in the North and South Middleback Ranges indicate highly localised settings in the supergene environment of ore enrichment at these locations.

The association between trace elements with potential affiliation to either and/or mafic and felsic intrusive rocks can be considered in the context of multiple stages of bi-modal magmatism and metamorphism (Creaser and Fanning 1993; Reid and Hand 2012; Pirajno and Hoatson 2012; Fig. 1). Assuming progressive development of keel-shaped, dome-and-basin structures along the belt strike (Peacock 2016), ore-enrichment environments would have variable exposure to sub-surface waters, and degrees of mixing with rainwaters washing over magmatic-rock hinterlands.

It is also noted that, in both models, the lithophile trace elements Si, Mg and Al do not have significant weights within the discriminant functions (Table 5). Although these elements have the highest concentrations in the Fe-oxides from BIFs and BIF-derived ores, they do not allow for discrimination by texture or location.

7 Conclusions

This reconnaissance study shows how a number of established statistical techniques can be used to advance research on the statistical treatment of multi-trace element mineral (LA-ICP-MS) datasets. Its main contribution lies in the quantitative assessment of the trace element geochemistry of different types of hematite in terms of their line of evolution. The investigation shows that if reinforced by strong petrographic control, statistical analyses may yield useful results on Fe-oxide evolution from BIFs to iron ore, with potential extrapolation to other minerals and ore systems. Another important result is the demonstration that the hierarchical structure of such data plays a fundamental role in the estimation of statistical significance when comparing different populations of trace element data.

Linear mixed-effects modelling offers much potential for the treatment of hierarchical trace element datasets. The statistical modelling of hierarchical LA-ICP-MS data must account for ICCs, and failure to do so will result in misleading statistical inferences. Of particular interest for LA-ICP-MS data is that the unbalanced data structure is handled by REML. The undertaking LME modelling of LA-ICP-MS datasets for other minerals would be valuable in understanding whether or not the trends in ICCs

demonstrated here are generally found in mineral trace element datasets. The LME model is an underused statistical technique in trace element geochemistry, this being the first study to apply it to a mineral trace element dataset, and is needed for the estimation of the variance components of hierarchical LA-ICP-MS datasets, which are typically unbalanced.

This case study has demonstrated how LDA can be used to discover elements associated with regional and local settings, even if the trace element concentrations are very low and show considerable overlaps among assumed populations. Furthermore, LDA offers a multivariate framework for investigation of mineral chemistry, however representative datasets and exhaustive petrographic characterisation are essential for generation and validation of discriminant models.

In addition to the above benefits of the statistical approach, the pre-treatment of LA-ICP-MS data is of crucial importance. This includes the exclusion of spot analyses failing strict quality controls and imputation of BDL values. In general, the estimation of BDL values plays an essential role, especially when further statistical analyses are based on the assumption of multivariate log-normal distributions. However, the choice of imputation technique depends on both the analyst and the intended use of the dataset, its size, internal features and limitations. To our best knowledge, the literature contains no systematic approach for imputation of BDL values of trace element data. Nevertheless, for trace element data originating from different known subpopulations, the imputation procedure should be performed separately for each sub-population as shown herein.

Last but not least, the multivariate statistical techniques should always be used together with as much external information as possible. Such information may include but not be limited to host lithology, prevailing mineral textures at various scales, formation temperatures and salinities determined from fluid inclusions, and geographic location. Only by using external data can useful insight be gained from the data yielding in proper interpretations.

Acknowledgements This research is a contribution to the project "Trace elements in Fe-oxides: deportment, distribution and application in ore genesis, geochronology, exploration and mineral processing", supported by BHP Olympic Dam and the South Australian Government Mining and Petroleum Services Centre of Excellence. We gratefully acknowledge the assistance of Phung Thi Nguyen, Holly Feltus, Steve Johnson, Benjamin Tinney and Thomas Line (Arrium Mining Ltd) during fieldwork.

Appendix A: Laser Ablation-Inductively Coupled Plasma-Mass Spectrometry Data Acquisition

LA-ICP-MS spot analyses of different textural types of hematite and magnetite from fifty-one one-inch polished blocks were performed, measuring the following isotopes: ^{24}Mg, ^{27}Al, ^{29}Si, ^{31}P, ^{43}Ca, ^{49}Ti, ^{51}V, ^{53}Cr, ^{55}Mn, ^{59}Co, ^{60}Ni, ^{65}Cu, ^{66}Zn, ^{69}Ga, ^{75}As, ^{88}Sr, ^{89}Y, ^{90}Zr, ^{93}Nb, ^{95}Mo, ^{118}Sn, ^{121}Sb, ^{137}Ba, ^{139}La, ^{140}Ce, ^{141}Pr, ^{146}Nd, ^{147}Sm, ^{153}Eu, ^{157}Gd, ^{159}Tb, ^{163}Dy, ^{165}Ho, ^{166}Er, ^{169}Tm, ^{172}Yb, ^{175}Lu, ^{182}W, ^{208}Pb, ^{232}Th and ^{238}U. Analysis was carried out at Adelaide Microscopy (The University of Adelaide) using a Resonetics LR (ASI) 193-nm Excimer laser microprobe coupled to an Agilent 7700cx Quadrupole ICP-MS. Total integration time for each spot was

70 s (s): with 30 s of background measurement followed by 40 s of ablation. Spot sizes of 29 and 43 μm were set depending on mineral grain size and trace element concentrations were calculated by referencing against signals from primary standards GSD-1G and BHVO-2G. Accuracy was monitored with reference materials GSD-1G and BHVO-2G by bracketed runs of up to 20 analyses to correct for instrument drift. Time-resolved signals were exported offline and examined for evidence of mineral inclusions and/or other mineral phases. Data reduction was performed using Glitter software (Van Achterbergh et al. 2001). The portion of the signal displaying constant counts as a function of acquisition time was selected for integration using ^{57}Fe as internal standard.

References

Aitchison J (1986) The statistical analysis of compositional data. Monographs on statistics and applied probability. Chapman and Hall Ltd. (Reprinted 2003 with additional material by The Blackburn Press), London. http://dx.doi.org/10.1007/978-94-009-4109-0

Aitchison J, Barceló-Vidal C, Pawlowsky-Glahn V (2002) Some comments on compositional data analysis in archaeometry, in particular the fallacies in Tangri and Wright's dismissal of logratio analysis. Archaeom 44:295–304. https://doi.org/10.1111/1475-4754.t01-1-00061

Angerer T, Hagemann SG, Danyushevsky LV (2013) High-grade iron ore at Windarling, Yilgarn Craton: a product of syn-orogenic deformation, hypogene hydrothermal alteration and supergene modification in an Archean BIF-basalt lithostratigraphy. Miner Depos 48:697–728. https://doi.org/10.1007/s00126-012-0450-3

Bates D, Maechler M, Bolker B, Walker S (2015) Fitting linear mixed-effects models using lme4. J Stat Softw 67:1–48. https://doi.org/10.18637/jss.v067.i01

Belissont R, Boiron MC, Luais B, Cathelinea M (2014) LA-ICP-MS analyses of minor and trace elements and bulk Ge isotopes in zoned Ge-rich sphalerites from the Noailhac-Saint-Salvy deposit (France): insights into incorporation mechanisms and ore deposition processes. Geochim Cosmochim Acta 126:518–540. https://doi.org/10.1016/j.gca.2013.10.052

Bhattacharya HN, Chakraborty I, Ghosh K (2007) Geochemistry of some banded iron formations of the Archean supracrustals, Jharkhand-Orissa region, India. J Earth Syst Sci 116:245–259. https://doi.org/10.1007/s12040-007-0024-4

Corbeil RR, Searle SR (1976) Restricted maximum likelihood (REML) estimation of variance components in the mixed model. Technometrics 18:31–38. https://doi.org/10.2307/1267913

Creaser RA, Fanning CM (1993) A U-Pb zircon study of the Mesoproterozoic Charleston Granite, Gawler Craton, South Australia. Aust J Earth Sci 40:519–526. https://doi.org/10.1080/08120099308728101

Dalstra HJ, Rosière CA (2008) Structural controls on high-grade iron ores hosted by banded iron formation: a global perspective. Rev Econ Geol 15:73–106. https://doi.org/10.5382/Rev.15.03

Davies MB (2000) Iron ore in South Australia. Primary industries and resources SA. Commod Rev 8:35

Dempster AP, Laird NM, Rubin DB (1977) Maximum likelihood from incomplete data via the EM algorithm. J R Stat Soc 39:1–38. https://doi.org/10.2307/2984875

Dupuis C, Beaudoin G (2011) Discriminant diagrams for iron oxide trace element fingerprinting of mineral deposit types. Miner Depos 46:319–335. https://doi.org/10.1007/s00126-011-0334-y

Frenzel M, Hirsch T, Gutzmer J (2016) Gallium, germanium, indium, and other trace and minor elements in sphalerite as a function of deposit type—A meta-analysis. Ore Geol Rev 76:52–78. https://doi.org/10.1016/j.oregeorev.2015.12.017

Gabriel KR (1971) The biplot graphical display of matrices with application to principal component analysis. Biometrika 58:453–467. https://doi.org/10.1093/biomet/58.3.453

Günther T, Klemd R, Zhang X, Horn I, Weyer S (2017) In-situ trace element and Fe-isotope studies on magnetite of the volcanic-hosted Zhibo and Chagangnuoer iron ore deposits in the Western Tianshan, NW China. Chem Geol 453:111–127. https://doi.org/10.1016/j.chemgeo.2017.02.001

Hagemann SG, Angerer T, Duuring P, Rosière CA, Figueiredo e Silva RC, Lobato LM, Hensler A-S, Walde DHG (2016) BIF-hosted iron mineral system: a review. Ore Geol Rev 76:317–359. https://doi.org/10.1016/j.oregeorev.2015.11.004

Hensler A, Hagemann SG, Rosière CA, Angerer T, Gilbert S (2015) Hydrothermal and metamorphic fluid-rock interaction associated with hypogene "hard" iron ore mineralisation in the Quadrilátero Ferrífero, Brazil: implications from in-situ laser ablation ICP-MS iron oxide chemistry. Ore Geol Rev 69:325–351. https://doi.org/10.1016/j.oregeorev.2015.02.023

Honaker J, King G, Blackwell M (2011) Amelia II: a program for missing data. J Stat Softw 45:1–47. https://doi.org/10.18637/jss.v045.i07

Johnson R, Wichern D (2007) Applied multivariate statistical analysis, 6th edn. Springer, New York

Keyser K, Ciobanu CL, Cook NJ, Johnson G, Feltus H, Johnson S, Dmitrijeva M, Ehrig K, Nguyen PT (2018) Petrography and trace element signatures of iron-oxides in deposits from the Middleback Ranges, South Australia: from banded iron formation to ore. Ore Geol Rev 93:337–360. https://doi.org/10.1016/j.oregeorev.2018.01.006

Makvandi S, Ghasemzadeh-Barvarz M, Beaudoin G, Grunsky EC, McClenaghan MB, Duchesne C, McClenaghan MB, Duchesne C (2016a) Principal component analysis of magnetite composition from volcanogenic massive sulfide deposits: case studies from the Izok Lake (Nunavut, Canada) and Halfmile Lake (New Brunswick, Canada) deposits. Ore Geol Rev 72:60–85. https://doi.org/10.1016/j.oregeorev.2015.06.023

Makvandi S, Ghasemzadeh-Barvarz M, Beaudoin G, Grunsky EC, McClenaghan MB, Duchesne C, Boutroy E (2016b) Partial least squares-discriminant analysis of trace element compositions of magnetite from various VMS deposit subtypes: application to mineral exploration. Ore Geol Rev 78:388–408. https://doi.org/10.1016/j.oregeorev.2016.04.014

McAvaney S (2012) The Cooyerdoo Granite: Paleo- and Mesoarchean basement of the Gawler Craton. MESA J 65:31–40

McIntyre JI (2001) Middleback Ranges Project—South Australia. EL 2763 Annual Report. Helix Resources N.L

Morris RC (2012) Microplaty hematite—Its varied nature and genesis. Aust J Earth Sci 59:411–434

Parker AJ (1993) The geology of South Australia, volume 1—The Precambrian. Geological Survey of South Australia, Bulletin, p 54

Pawlowsky-Glahn V, Egozcue JJ (2006) Compositional data and their analysis: an introduction. Geol Soc Lond Spec Publ 264:1–10. https://doi.org/10.1144/GSL.SP.2006.264.01.01

Peacock M (2016) Structural geology & high-grade iron ore mineralisation, Middleback Ranges, South Australia, Honours Thesis, The Australian National University

Pirajno F, Hoatson DM (2012) A review of Australia's Large Igneous Provinces and associated mineral systems: implications for mantle dynamics through geological time. Ore Geol Rev 48:2–54

R Core Team (2017) R: a language and environment for statistical computing. R Foundation for Statistical Computing, Vienna, Austria. https://www.R-project.org. Accessed 20 July 2017

Reid A, Hand M (2012) Mesoarchean to Mesoproterozoic evolution of the southern Gawler Craton, South Australia. Episodes 35:216–225

Szpunar M, Hand M, Barovich K, Jagodzinski E, Belousova E (2011) Isotopic and geochemical constraints on the Paleoproterozoic Hutchison Group, southern Australia: implications for Paleoproterozoic continental reconstructions. Precambrian Res 187:99–126. https://doi.org/10.1016/j.precamres.2011.02.006

Taylor D, Dalstra HJ, Harding AE, Broadbent GC, Barley ME (2001) Genesis of high-grade hematite orebodies of the Hamersley Province, Western Australia. Econ Geol 96:837–873. https://doi.org/10.2113/gsecongeo.96.4.837

Van Achterbergh E, Ryan CG, Jackson SE, Griffin WL (2001) Data reduction software for LAICP-MS. In: Sylvester JP (ed) Laser-ablation-ICPMS in the earth sciences; principles and applications. Mineralogical Association of Canada, Short Course Series, vol 29, pp 239–243

Venables WN, Ripley BD (2003) Modern applied statistics with S, 4th edn. Springer. https://doi.org/10.1007/978-0-387-21706-2

Wang M, Wang W, Liu K, Michalak PP, Wei K, Hu M (2017) In-situ LA-ICP-MS trace elemental analyzes of magnetite: the Tieshan skarn Fe–Cu deposit, Eastern China. Chem Erde 77:169–181. https://doi.org/10.1016/j.chemer.2016.11.002

Winderbaum L, Ciobanu CL, Cook NJ, Paul M, Metcalfe AV, Gilbert S (2012) Multivariate analysis of an LA-ICP-MS trace element dataset for pyrite. Math Geosci 44:823–842. https://doi.org/10.1007/s11004-012-9418-1

Zhou Z-J, Tang H-S, Chen Y-J, Chen Z-L (2017) Trace elements of magnetite and iron isotopes of the Zankan iron deposit, westernmost Kunlun, China: a case study of seafloor hydrothermal iron deposits. Ore Geol Rev 80:1191–1205. https://doi.org/10.1016/j.oregeorev.2016.09.020

CHAPTER 4

MULTIVARIATE STATISTICAL ANALYSIS OF TRACE ELEMENTS IN PYRITE: PREDICTION, BIAS AND ARTEFACTS IN DEFINING MINERAL SIGNATURES

Marija Dmitrijeva[1], Nigel Cook[1], Kathy Ehrig[2], Cristiana L. Ciobanu[2], Andrew V. Metcalfe[3], Maya Kamenetsky[4] Vadim Kamenetsky[4], Sarah Gilbert[5]

[1] *School of Chemical Engineering and Advanced Materials, The University of Adelaide, Adelaide, SA 5005, Australia*

[2] *BHP Olympic Dam, Adelaide, SA 5001, Australia*

[3] *School of Mathematical Sciences, The University of Adelaide, Adelaide, SA 5005, Australia*

[4] *School of Natural Sciences (Earth Sciences), University of Tasmania, Private Bag 79, Hobart TAS 7001, Australia*

[5] *Adelaide Microscopy, The University of Adelaide, Adelaide, SA 5005, Australia*

Submitted to *Minerals*, December 9th, 2019

Statement of Authorship

Title of Paper	Multivariate statistical analysis of trace elements in pyrite: prediction, bias and artefacts in defining mineral signatures
Publication Status	☐ Published ☐ Accepted for Publication ☑ Submitted for Publication ☐ Unpublished and Unsubmitted work written in manuscript style
Publication Details	Dmitrijeva, M., Cook, N.J., Ehrig, K., Ciobanu, C.L., Metcalfe, A.V., Kamenetsky, M., Kamenetsky, V.S., Gilbert, S. Multivariate statistical analysis of trace elements in pyrite: prediction, bias and artefacts in defining mineral signatures. Submitted to Minerals.

Principal Author

Name of Principal Author (Candidate)	Marija Dmitrijeva		
Contribution to the Paper	Performed the processing of the LA-ICP-MS data, statistical analysis. Prepared the manuscript.		
Overall percentage (%)	55		
Certification:	This paper reports on original research I conducted during the period of my Higher Degree by Research candidature and is not subject to any obligations or contractual agreements with a third party that would constrain its inclusion in this thesis. I am the primary author of this paper.		
Signature		Date	17.12.19

Co-Author Contributions

By signing the Statement of Authorship, each author certifies that:

i. the candidate's stated contribution to the publication is accurate (as detailed above);

ii. permission is granted for the candidate in include the publication in the thesis; and

iii. the sum of all co-author contributions is equal to 100% less the candidate's stated contribution.

Name of Co-Author	Nigel Cook		
Contribution to the Paper	Assisted with the interpretation of the data and preparation of the manuscript.		
Overall percentage (%)	15		
Signature		Date	17.12.19

Name of Co-Author	Kathy Ehrig		
Contribution to the Paper	Assisted with the data preparation and evaluation of the manuscript.		
Overall percentage (%)	8		
Signature		Date	17.12.19

Name of Co-Author	Cristiana L. Ciobanu		
Contribution to the Paper	Assisted with the interpretations of the data and manuscript preparation.		
Overall Percentage (%)	8		
Signature		Date	17.12.19

Name of Co-Author	Andrew V. Metcalfe		
Contribution to the Paper	Assisted with statistical analyses.		
Overall Percentage (%)	3		
Signature		Date	17.12.19

Name of Co-Author	Maya Kamenetsky		
Contribution to the Paper	Performed data collection.		
Overall Percentage (%)	5		
Signature		Date	17.12.19

Name of Co-Author	Vadim S. Kamenetsky		
Contribution to the Paper	Assisted with the manuscript evaluation.		
Overall Percentage (%)	3		
Signature		Date	17.12.19

Name of Co-Author	Sarah Gilbert		
Contribution to the Paper			
Overall Percentage (%)	3		
Signature		Date	17.12.19

minerals

MDPI

Article

Multivariate Statistical Analysis of Trace Elements in Pyrite: Prediction, Bias and Artefacts in Defining Mineral Signatures

Marija Dmitrijeva [1], Nigel J. Cook [1,*], Kathy Ehrig [2], Cristiana L. Ciobanu [1], Andrew V. Metcalfe [3], Maya Kamenetsky [4], Vadim S. Kamenetsky [4] and Sarah Gilbert [5]

1 School of Chemical Engineering and Advanced Materials, The University of Adelaide, Adelaide 5005, Australia; marija.dmitrijeva@adelaide.edu.au (M.D.); cristiana.ciobanu@adelaide.edu.au (C.L.C.)
2 BHP Olympic Dam, Adelaide 5001, Australia; kathy.ehrig@bhp.com
3 School of Mathematical Sciences, The University of Adelaide, Adelaide 5005, Australia; andrew.metcalfe@adelaide.edu.au
4 School of Natural Sciences (Earth Sciences), University of Tasmania, Private Bag 79, Hobart 7001, Australia; maya.kamenetsky@utas.edu.au (M.K.); dima.kamenetsky@utas.edu.au (V.S.K.)
5 Adelaide Microscopy, The University of Adelaide, Adelaide 5005, Australia; sarah.gilbert@adelaide.edu.au
* Correspondence: nigel.cook@adelaide.edu.au

Received: 9 December 2019; Accepted: 6 January 2020; Published: 10 January 2020



Abstract: Pyrite is the most common sulphide in a wide range of ore deposits and well known to host numerous trace elements, with implications for recovery of valuable metals and for generation of clean concentrates. Trace element signatures of pyrite are also widely used to understand ore-forming processes. Pyrite is an important component of the Olympic Dam Cu–U–Au–Ag orebody, South Australia. Using a multivariate statistical approach applied to a large trace element dataset derived from analysis of random pyrite grains, trace element signatures in Olympic Dam pyrite are assessed. Pyrite is characterised by: (i) a Ag–Bi–Pb signature predicting inclusions of tellurides (as PC1); and (ii) highly variable Co–Ni ratios likely representing an oscillatory zonation pattern in pyrite (as PC2). Pyrite is a major host for As, Co and probably also Ni. These three elements do not correlate well at the grain-scale, indicating high variability in zonation patterns. Arsenic is not, however, a good predictor for invisible Au at Olympic Dam. Most pyrites contain only negligible Au, suggesting that invisible gold in pyrite is not commonplace within the deposit. A minority of pyrite grains analysed do, however, contain Au which correlates with Ag, Bi and Te. The results are interpreted to reflect not only primary patterns but also the effects of multi-stage overprinting, including cycles of partial replacement and recrystallisation. The latter may have caused element release from the pyrite lattice and entrapment as mineral inclusions, as widely observed for other ore and gangue minerals within the deposit. Results also show the critical impact on predictive interpretations made from statistical analysis of large datasets containing a large percentage of left-censored values (i.e., those falling below the minimum limits of detection). The treatment of such values in large datasets is critical as the number of these values impacts on the cluster results. Trimming of datasets to eliminate artefacts introduced by left-censored data should be performed with caution lest bias be unintentionally introduced. The practice may, however, reveal meaningful correlations that might be diluted using the complete dataset.

Keywords: pyrite; trace elements; multivariate statistics; left-censored data; Olympic Dam

1. Introduction

Pyrite (FeS_2) is by far the most common sulphide mineral on Earth [1]. It is stable in geological environments ranging from low to high temperatures and at a wide range of pressures (e.g., [2]). Pyrite is also a robust, refractory mineral that can readily record successive stages of growth, which are expressed both by preserved textures and trace element signatures. Natural pyrite commonly incorporates a wide range of elements within its structure, notably As, Co and Ni, whereas several others, such as Cu, Tl and Ag, are more rarely reported at concentrations ranging from sub-ppm levels to as much as several wt.%. Interest in the trace element content of pyrite goes back to the 1940s [3–5], pre-dating electron probe microanalysis or other newer methods of trace element analysis with sensitivities in the ppm range, including laser ablation inductively coupled plasma mass spectrometry (LA-ICP-MS). Such chemically 'impure' pyrites may display subtly different physical properties (e.g., [6]) and elevated trace element contents may also impact on pyrite behaviour during mineral processing (e.g., [7]).

Trace element signatures in pyrite are used in ore deposit studies to constrain ore genesis, making pyrite one of the most studied minerals. Such signatures are used as tools to distinguish pyrite with different origins, to interpret fluid evolution, and to track the physicochemical conditions of hydrothermal mineral systems (e.g., [8–13], and many others).

Due to its relative abundance—commonly the dominant sulphide in many types of base and precious metal ores—pyrite is also an important, and in some cases the dominant host for several elements of economic importance, notably gold [14,15]. Pyrite can, however, also host a range of elements that are deleterious to processing, or which carry significance from an environmental perspective. Release of elements like Hg, or particularly Tl, [16–18] from pyrite can have major ramifications for environmental management around mine sites.

Advances in multi-element trace element analysis, particularly by LA-ICP-MS, have generated a substantial body of literature on the trace element chemistry of pyrite from a wide range of different deposits [19]. Moreover, trace element mapping by LA-ICP-MS has enabled the correlation of trace element signatures with mineral textures at the micron-scale. Although widely used and trusted, LA-ICP-MS does have the relative disadvantage of sampling relatively large volumes of material (compared, for example, to electron probe microanalysis)—a trade-off with the generally excellent sensitivity of the technique. Thus, LA-ICP-MS data cannot readily distinguish between those elements contained within the mineral lattice and elements present as inclusions of discrete minerals when those inclusions are too small and/or homogeneously distributed to be seen using other methods. Studies have emerged in recent years (e.g., [20–22]) showing, based on evidence from different minerals, that elements considered—or often taken for granted—as being lattice-bound in a given mineral, may actually occur in the form of included phases as fine particles (up to thousands of nm), or nanoparticles (<100 nm) that are only visible by using advanced transmission electron microscopy methods (e.g., [23–25]).

The ease of data generation by LA-ICP-MS has also led to datasets becoming larger, necessitating more sophisticated statistical techniques to recognize and interrogate patterns within the data. Multivariate statistical analysis can significantly complement the conventional ways of looking at mineral chemistry data by identifying associations among elements and grouping geochemical analyses into meaningful and interpretable clusters. Such an approach is reproducible, quantitative and not subjective (e.g., [26–29]).

Many data analysis techniques require complete data sets. A common problem, and one that is exacerbated when applying multivariate statistics to large datasets, is how to adequately treat concentration data that fall below the minimum detection limit (mdl). In geochemical data analysis, it is common to replace mdl values with a fraction of that value, for instance one half of mdl, or a fixed value, e.g., the mean or median, however, this approach is to be avoided as it changes the relative variation structure in compositions [30,31], especially when the number of affected samples is a significant percentage of the total. The exclusion of such values is not recommended either, as it results in significant loss of valuable information and bias when estimating parameters like mean and/or median.

For these reasons, sensible imputation of left-censored data is a preferred option. For geochemical (i.e., compositional) data, there are several available imputation algorithms which include, but are not limited to, model-based methods like expectation-maximisation (EM) and multiplicative lognormal replacement algorithm [30], as well as distance-based k-nearest neighbour where the information of the nearest complete observations is used to estimate the left-censored values [32].

This contribution addresses the trace element chemistry of pyrite in the giant Olympic Dam Cu–U–Au–Ag deposit, South Australia [33], the largest iron-oxide copper gold (IOCG) deposit on Earth. Published data for trace elements in pyrite from IOCG systems are relatively limited despite the fact that it is abundant and a potential host for metals of importance (e.g., [34–36]). There are also only few published examples of multivariate statistical analyses applied to pyrite data (e.g., [37,38]), although the potential application of multivariate statistical methods to issues of acid mine drainage has been recently recognised [39].

This study is significant in that it is based on a large suite of LA-ICP-MS analyses (almost 5000 analyses) of pyrite in relatively high-copper grade ores (>2% Cu) from across the deposit. Routine analysis of key minerals is undertaken by BHP Olympic Dam and this dataset was compiled from several individual batches acquired over a period of three years. Pyrite is the second most abundant sulphide in the Olympic Dam deposit, making up, on average, 0.46% of orebody (after chalcopyrite, 0.93%, and before bornite, 0.33% [33]). Across the deposit, pyrite typically occurs alone or is replaced by chalcopyrite, at sizes ranging from relict pyrite no more than a few microns in size, replaced by chalcopyrite, to cm-sized euhedral cubes.

The research presented below carries two main objectives. Firstly, we determine which elements occur in pyrite, and what are their typical concentration levels and ranges. Although it is impossible to quantify the proportion of a given element within the mineral lattice or as inclusions of discrete minerals, statistical analysis (Principal Component Analysis, PCA) allows identification of groups of elements with strong correlation with one another that can be further discussed in terms of their physical state within pyrite. For example, elevated concentrations of chalcophile group elements (Ag, Pb, Bi, Te, Se) that show a correlation with Au but not with As are likely to be present as discrete tellurides rather than being directly incorporated in the crystal lattice. Such prediction of mineral inclusions is impossible with bivariate plots alone, or from down-hole time-resolved LA-ICP-MS spot analysis depth profiles, if the inclusions are sufficiently small. We go on to discuss the implications these data may have for understanding deportment models for elements of economic interest (e.g., Au, Ag), deleterious elements of concern that need monitoring in the processing circuit (such as As), and also diverse elements that are of interest with respect to longer-term recovery potential (e.g., Co, Te, and Se).

Secondly, the large size of our dataset allows us to demonstrate how the common practice of excluding a percentage of analytical data because they yield values below mdl for multiple trace elements (left-censored values) can impact on the overall results and the interpretations reached. Values below detection limit are almost always present in geochemical datasets—yet are often neglected, poorly understood, or inadequately interpreted.

2. Approach, Methods and Data Treatment

2.1. Data Acquisition

Although Olympic Dam pyrite displays considerable diversity with respect to petrography, mineral assemblage and texture [33], acquisition of spot analyses for this study was intentionally done without recording pyrite textures. This approach was taken since choosing a particular location within a grain for a spot analysis can, often inadvertently, result in biased datasets which may include over- and undersampled textural varieties, and implicitly, their geochemical attributes.

To ensure that pyrite grains were analysed blindly (i.e., without bias or pre-selection on the basis of ore textures or ease of microanalysis), analyses of 145 samples of sulphide-bearing diamond drill

core samples, spatially located across the deposit, composited over 20 m-lengths (crushed/milled to 100% passing 1 mm) from Olympic Dam were considered. This implies that analysed pyrite grains can belong to any type of pyrite from anywhere in the deposit under the single constraint that they are from high-copper grade ores (>2% Cu). LA-ICP-MS spot analyses were acquired on randomly selected pyrite grains from these samples and analysed for a wide suite of elements. Due to the nature of the crushed/milled samples, there is no subjective bias in sample collection, thus making these data absolutely representative of pyrite in sulphide ores from Olympic Dam containing >2% Cu. A second advantage of using data acquired on crushed/milled drill core composites is the lack of intra-sample correlation, which is often the case for LA-ICP-MS data, where mineral grains derived from a single sample show highly similar chemistry (e.g., [35]). A third advantage is the fact that the samples have been milled, thus reducing—though not completely avoiding the issue of obtaining representative data on strongly zoned grains by analysis only of clean (inclusion-free) domains.

All analysis was undertaken RESOlution-LR 193 nm ArF excimer laser with a large format S155 ablation cell (Laurin Technic Inc., Narrabundah, Australia), coupled to an Agilent 7500cs Quadrupole ICP-MS at the University of Tasmania, Hobart, Australia. Laser spot size varied from 19 to 33 µm. Isotopes measured were ^{27}Al, ^{34}S, ^{47}Ti, ^{55}Mn, ^{57}Fe, ^{59}Co, ^{60}Ni, ^{65}Cu, ^{66}Zn, ^{75}As, ^{77}Se, ^{89}Y, ^{90}Zr, ^{95}Mo, ^{109}Ag, ^{111}Cd, ^{118}Sn, ^{121}Sb, ^{125}Te, ^{140}Ce, ^{157}Gd, ^{172}Yb, ^{178}Hf, ^{181}Ta, ^{182}W, ^{185}Re, ^{197}Au, ^{204}Pb, ^{205}Tl, ^{206}Pb, ^{207}Pb, ^{208}Pb, ^{209}Bi, ^{232}Th, ^{235}U and ^{238}U.

The ca. 5000 spot analyses were collected in 28 batches. Ablation consisted of 20 s of gas background collection followed by 40 s of spot ablation. Calibration routines considered both primary reference materials, STDGL3 and STDGL2b2 [40], depending on a particular batch, and the secondary GSD-1G (US Geological Survey) glass reference material. Standard measurements were performed at the beginning and at the end of each analysis round of ~20 to 25 spot analyses. All the data reduction was performed in LADR 1.0.09 [41]. Iron was the internal calibration element and ideal stoichiometry was assumed.

Four Pb isotopes were measured in order to fingerprint radiogenic and natural Pb in pyrite. The deposit is uranium-bearing and a greater part of the lead in the deposit is the radiogenic product of uranium decay. Nevertheless, galena with a clear non-radiogenic signature is also noted [42]. For this reason, Pb^{204}, Pb^{206}, Pb^{207} and Pb^{208} were measured separately, with data calculated based on a 1595 Ma age. Below, the notation ^{X}Pb is used to refer to all four lead isotopes unless specified otherwise.

2.2. Data Quality Control, Trimming and Imputation

Each time-resolved LA-ICP-MS depth profile was carefully checked for the presence of contaminating phases, e.g., REE- and U-bearing minerals, hematite, or Cu–(Fe)-sulphides, all of which commonly occur as inclusions in pyrite at Olympic Dam. As a second step to improve data quality, all rows containing anomalous/extreme values for all elements (but especially Cu), were excluded to make the data representative of pyrite without admixtures of Cu–(Fe)-sulphides. The Cu threshold was defined as >5000 ppm.

Sulphur was not considered in the subsequent data analysis; likewise, Cd, Sb and Tl which displayed only a very small number of values above mdl. A range of elements that are not expected to be incorporated into the pyrite lattice were also excluded from the data: Al, Ce, Gd, Hf, Ta, Th, Y, Yb and Zr. Other elements, notably U, W and Mo, were also not included in the data. These elements, characteristically associated with each other, are attributable to nano- and microinclusions of hematite, the dominant gangue mineral at Olympic Dam [33] and often as U–W–Sn–Mo-bearing hematite [43,44]. Nonetheless, when included into PCA, these elements strongly dominate the first principal component (PC1).

In order to investigate the effects of left-censored data on the statistical analyses and interpretation, the original dataset was trimmed to reduce the overall number of values that fall below the detection limit. Therefore, three datasets are considered further: a first comprising all 4926 spot analyses; and a second and third with 1501 and 525 analysis spots, respectively. The N = 4926 data contain 43%

of left-censored values overall, with at least half the elements having >50% of left-censored cases (Figure 1a). The N = 1501 data were obtained by trimming the N = 4926 dataset on the condition of retaining only those analyses that have less than six left-censored values per analysis (i.e., per row) resulting in a new sub-set that contains only 23% of left-censored cases overall (Figure 1b). Finally, the N = 525 data were obtained based on the condition of only retaining analyses that have three or less left-censored values per row—giving a still smaller subset with an overall of 12% of data being left-censored (Figure 1c). Such consecutive trimming results in the smaller datasets having more complete analyses—but, implicitly, slightly higher overall concentrations for all analysed elements.

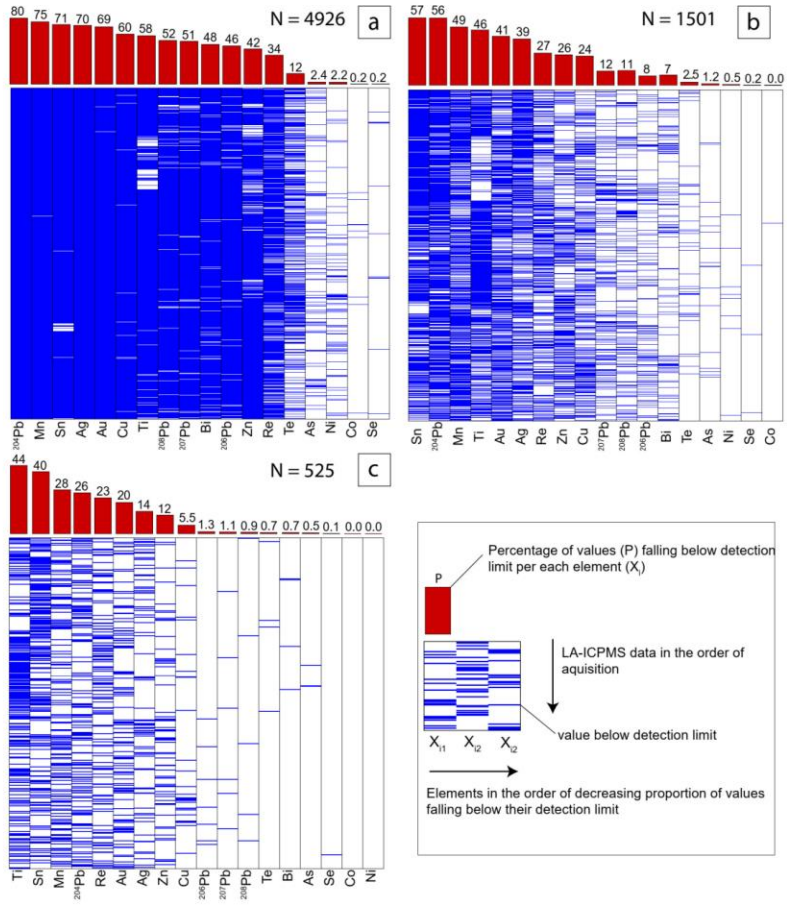


Figure 1. Schematic visualisation of measured and below mdl values for the (**a**) N = 4926, (**b**) N = 1501 and (**c**) N = 525 LA-ICP-MS pyrite datasets presented, from top to bottom, in the sequence of acquisition. The percentage of values being below detection limit is given for each element.

The imputation of left-censored data was done for each of the three datasets individually using multiplicative lognormal replacement from the R package 'zCompositions' [31]. We also attempted to employ an expectation-maximisation algorithm from the same package, a method that imputes values based on analyses without left-censored data. The algorithm did not produce the expected replacements due to the large amount of such values in the complete (N = 4926) dataset. The outcome

of multiplicative lognormal replacement was assessed via quantile–quantile and bivariate plots to assess the appropriateness of the replacement. An example of such assessment and comparison with deterministic imputation strategies (i.e., taking absolute mdl values, or replacing by a half and median) is given in Figure 2.

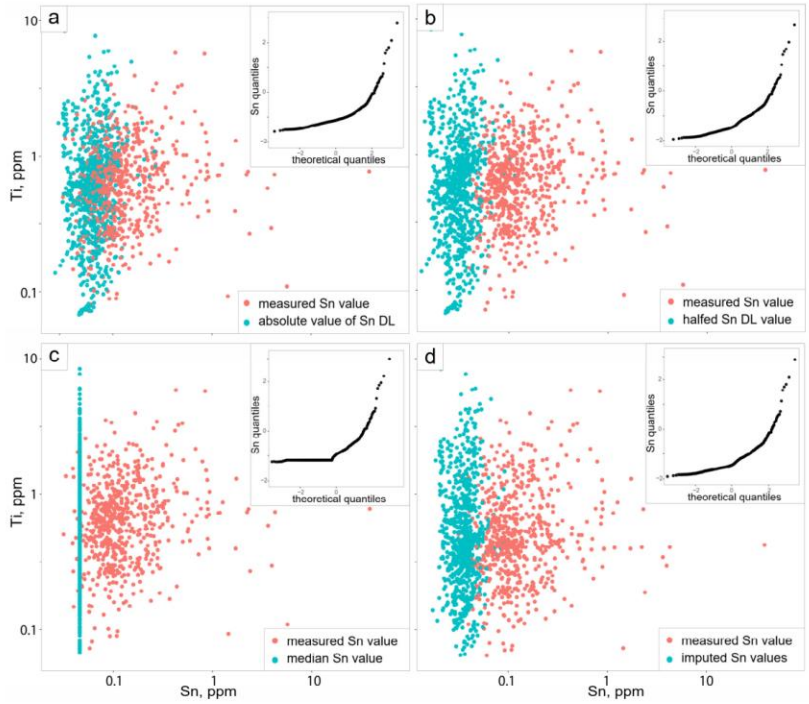


Figure 2. Quantile–quantile plots of Sn and bivariate plots of log-transformed Sn versus Ti in ppm from the N = 1501 dataset illustrating the effect of (**a**) taking absolute values of the detection limit, (**b**) division of a detection limit value by two, (**c**) fixed value imputation, e.g., median (calculated from the imputed dataset) and (**d**) multiplicative lognormal replacement. Note the similarity between b and d and the narrower range of imputed Sn values for d. Note that fixed value imputation results in asymmetric Sn distribution.

2.3. Multivariate Analyses

Multivariate statistical analyses were applied to each of the three datasets using the compositional data approach [45,46]. The techniques used included Principal Component Analysis (PCA) applied to the centred log-ratio(clr)-transformed data; k-means clustering applied to the isometric log-ratio(ilr)-transformed data, and hierarchical cluster dendrogram obtained from the Aitchison variation matrix generated for each of the thee datasets [46]. Additionally, multiple linear regression was fitted to obtain the quantitative relationships of Au to all the other elements.

Both clr- and ilr-transformations were performed using the R package 'compositions' [47]. The ilr transformation [48,49] was performed for each dataset using the R 'balanceBase()' function, which employed sequential binary partitioning of the D-part composition following the D-1 steps, whereas the steps of partitioning corresponded to the splits of the corresponding hierarchical dendrogram (Supplementary Material A; Tables S1–S3). The necessity of data transformations and Aitchison variation matrix is justified by the specific properties of geochemical data which only carry relative

information and sums up to a given constant, for instance, 100 wt.% or one million ppm [45]. Although trace element data accounts for a small percentage of the bulk composition and a log-ratio vector of trace element concentrations $\left[\ln \frac{x_1}{X}, \ln \frac{x_2}{X}, \ldots, \ln \frac{x_D}{X}\right]$ may be close to $[\ln(x_1, x_2, \ldots, x_D)]$, where $X = \sum_{i=1}^{D} x_i$ [50], the statistical analyses with log-transformed and raw data was avoided. This is because the PCA applied to the log-transformed data results in spurious patterns on biplots (e.g., [42,51]). However, visualisation of distributions for specific elements was done using boxplots applied to log-transformed concentrations.

The co-dependence between all possible pairs of elements will be investigated by using an Aitchison variation matrix (T), where the components of this D × D variation matrix are the variances of the log-ratios of all the possible pairs of elements, with $i, j = 1, \ldots, D$ and τ_{ij} obtained by

$$\tau_{ij} = var\left(\ln\left(\frac{x_i}{x_j}\right)\right) \quad (1)$$

Such variation matrix is used as a measure of similarity within elements for the hierarchical clustering algorithm. The results are presented as a dendrogram, reflecting the associations and geochemical affinities or dissimilarity among the groups of elements in a large dataset.

Under the compositional approach, both PCA and k-means clustering are efficient at underpinning element associations as groups, and clusters, i.e., analyses characterised by similar chemistry. These statistical analyses are often used for orebody characterisation and geochemical domaining [52], but the same methods are transferrable to LA-ICP-MS datasets. The k-means clustering is a versatile and simple iterative algorithm that aims at partitioning geochemical analyses into k predefined clusters. It is used for detecting groups of analyses within multivariate space which are not observable on bivariate plots. The optimal number of k can be found via applying k-means clustering a range of k values to data, and assessing the sum of squared errors versus a given range of k ('elbow' method).

Clustering results obtained with a user-defined number of k are further assessed for reproducibility of clusters and overall similarity of analyses within the clusters. For considered datasets, k was chosen as three due to the high reproducibility of these clusters >0.86 (Supplementary Material A; Figures S1–S3). Principal component analysis significantly complements k-means as it finds the maximum variability within the data by reducing dimensionality, resulting in a linear combination of elements as principal components (PCs). Given that principal components are orthogonal, they are applicable as meaningful petrological tools, e.g., recognition of different geochemical patterns allows underpinning mineralisation/alteration and host rock signatures [27,28]. The PCA was performed using singular value decomposition and a biplot was used for graphical representation of the PC loadings and scores [53]. The PC scores are calculated as the linear combinations of the original variables such that the variance of the first PCs is maximal, thus the first two PCs represent the majority of variance. The PC loadings represent associations among elements therefore displaying multi-element associations within the geochemical dataset.

Finally, multiple linear regression of a response variable log(Au) onto ilr-coordinates of the remaining elements was fitted into each dataset using the least squares method in the 'lmCoDaX()' function from the package 'robCompositions' [54]. This approach assumed that log(Au) is a real non-compositional response. For comparison purposes, two types of regressions were considered, classical and robust, as the latter is less affected by the presence of outliers. The purpose of regression models was to quantitatively assess the strength of relationship between Au and other elements.

3. Results

3.1. Summary of Trace Element Signatures in Pyrite

Although the use of standard descriptive characteristics like arithmetic mean, variance, or covariance are not appropriate for compositional data due to their scale invariance principle [55], we report the summary statistics as minimum, geometric mean, median and maximum to give an

idea of the ranges of the concentrations within pyrite. Extended summary tables containing the above-mentioned parameters and additional arithmetic mean and standard deviation calculated for each dataset and cluster are given in Supplementary Material B. As expected, the mean/median and geometric mean increase as the number of censored values decreases in datasets.

Table 1 contains the ranges of concentrations with the corresponding geometric mean and median values for the N = 1501 dataset. Overall, the elements with the highest median concentrations and maximum values are the ones which are regularly present above mdl: Co (median ~640 ppm), Ni (median ~70 ppm) and Se (median ~130 ppm). Their maximum values can reach up to ~ 4.5 wt.%, 0.4 wt.% and 0.1 wt.%, respectively (Table 1). Although Co and Ni do not have outliers in the upper tail of their distribution (Figures 3e, 4e and 5e), both elements have very variable concentrations, as shown by the large interquartile ranges and the presence of numerous outliers in the lower tail (Figures 3e, 4e and 5e). In contrast, Se varies the least among all the elements (e.g., Figure 4e). Arsenic has a median of ~25 ppm and only reaches up to 0.85 wt.% in pyrite. Copper has a relatively low median value of 2.74 ppm, however the maximum value is three orders of magnitude higher (0.5 wt.%). Zinc, Mn and Ti show fairly similar medians of 0.54, 0.38 and 0.43 ppm, respectively, whereas Mn has the largest maximum of ~800 ppm and a significant number of positive outliers in the upper tail (e.g., Figure 4e). Similar patterns are observed for Sn (median 0.045 ppm) and Ag (median 0.022 ppm). Gold and Re are the two elements with the lowest concentrations in pyrite. Gold is below mdl in ~70% of the cases (in N = 4926 data) and shows a median of only 0.005 ppm and a maximum value of ~15 ppm (Table 1). Rhenium concentrations are very low with a median of ~0.01 ppm, however it is above mdl in nearly 70% of analyses.

Table 1. Summary of the trace element composition of pyrite (in ppm) for the imputed N = 1501 dataset. Elements are arranged in order of decreasing median values.

	Co	Se	Ni	As	Te	Cu	Zn	Mn	Ti
minimum	0.28	4.0	0.015	0.35	0.009	0.096	0.12	0.060	0.049
maximum	44267	1075	4357	8586	815	5467	167	809	56
median	643	133	69	25	4.89	2.74	0.54	0.38	0.43
geom. mean	586	121	48	26	4.06	3.68	0.62	0.58	0.48
	^{206}Pb	^{204}Pb	^{207}Pb	^{208}Pb	Bi	Sn	Ag	Re	Au
minimum	0.001	0.043	0.001	0.0008	0.0003	0.017	0.001	0.0004	0.0003
maximum	765	467	490	466	156	611	223	0.72	14.9
median	0.29	0.23	0.12	0.10	0.12	0.045	0.022	0.014	0.005
geom. mean	0.40	0.36	0.16	0.14	0.12	0.064	0.037	0.011	0.008

Note: geom. mean—geometric mean.

3.2. Principal Component Analysis, K-Means Clustering and Dendrogram

The results of statistical analyses obtained from the N = 4926 dataset (Figure 3) are slightly different to those from both the N = 1501 (Figure 4) and N = 525 (Figure 5) datasets which demonstrate more similarities with respect to the groupings of elements on their PCA loadings and respective dendrograms. The obtained dendrograms from the trimmed data highlight a group of Ag–Bi–Pb–Au–Cu (Figures 4 and 5d). Despite the presence of many left-censored values within the N = 4926 dataset, the PC1 in all three datasets are dominated by the Bi–^{X}Pb–Ag signature, thus being the predominant feature of Olympic Dam pyrite.

However, as the trimmed datasets have fewer left-censored values, the groups on dendrograms and association of elements loading onto PC1 slightly change. In the N = 1501 and N = 525 datasets, the PC1 is dominated by all four Pb isotopes with Ag, Bi, Cu and minor Au loadings (Figure 4a,d and Figure 5a,d). In contrast, in the N = 4926 data, Bi is associated with ^{206}Pb, ^{207}Pb and ^{208}Pb while ^{204}Pb plots separately (Figure 3a,d).

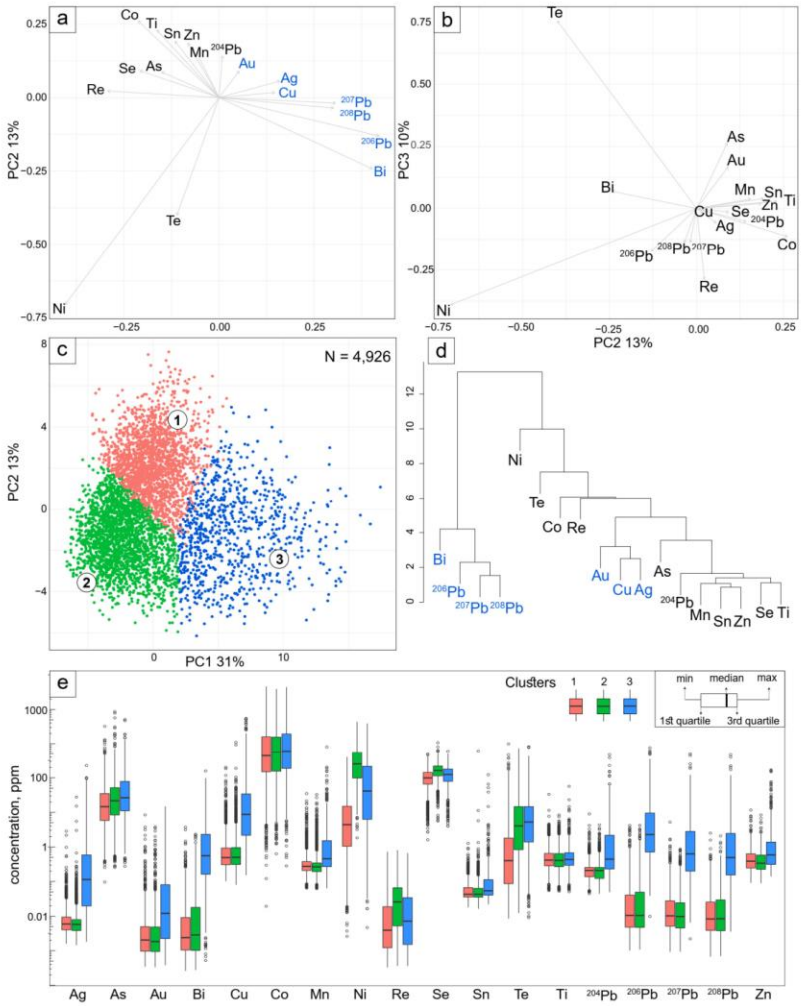


Figure 3. Principal component scores and loadings of centred log-ratio-transformed N = 4926 data. The projection of PC1 versus PC2 (**a**) and PC2 versus PC3 (**b**) shows loadings of the elements. Principal component scores are shown on the PC1 versus PC2 projection (**c**), on which each dot corresponds to an individual sample assigned to one of three clusters. Hierarchical cluster dendrogram (**d**) showing the association among the 18 elements with the height being a dissimilarity measure calculated from the variation matrix using Euclidean metrics (Table 2). (**e**) Box and whisker plot showing a range of concentrations for elements within each cluster. Note the correspondence among Cluster 3 and the Pb isotopes and Bi.

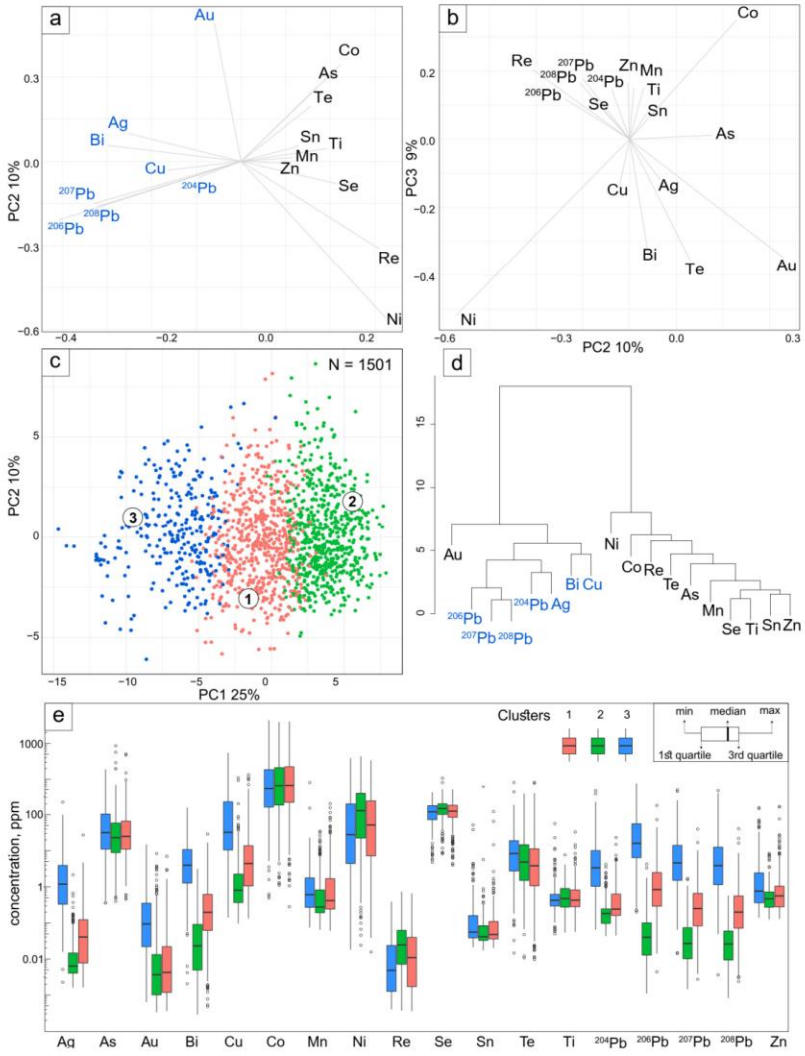


Figure 4. Principal component scores and loadings of centred log-ratio-transformed N = 1501 data. The projection of PC1 versus PC2 (**a**) and PC2 versus PC3 (**b**) shows loadings of the elements. Principal component scores are shown on the PC1 versus PC2 projection (**c**), on which each dot corresponds to an individual sample assigned to one of three clusters. Hierarchical cluster dendrogram (**d**) showing the association among the 18 elements with the height being a dissimilarity measure calculated from the variation matrix using Euclidean metrics (Table 3). (**e**) Box and whisker plot showing a range of concentrations for elements within each cluster. Note the correspondence among Cluster 3 and the Pb isotopes and Bi.

Another shared feature across the trimmed versions of the data is Ni, showing the highest disproportionality, i.e., least correlation with Bi, Ag, Au and Cu (e.g., $\tau_{NiBi} = 11.5$; $\tau_{NiAg} = 10.6$; $\tau_{NiAu} = 9.9$; Table 3), as well as ^{206}Pb, ^{207}Pb and ^{208}Pb. Cobalt is also always uncorrelated with Bi (e.g.,

$\tau_{CoBi} = 10.0$; Table 3). Additional patterns are shown in trimmed data (N = 1501 and N = 525), where Co, Ni as well as Re show negative association with ^{206}Pb, ^{207}Pb and ^{208}Pb and Ag. Such dissociation demonstrates Ni–Co being another dominant feature of Olympic Dam pyrite, as both are having the highest loadings onto PC1, thus opposing the Ag–Bi–^{X}Pb–Cu–Au group.

Although displaying less information than PC1, the PC2–PC3 projection represents a total of 18% of the data variability and shows different geochemical associations which are valid although not captured by the dendrograms or variation matrices. The dominant characteristic of PC2–PC3 projection is the dissociation between Ni and Co, which plot on the opposite sites of the loading plot in the original and all trimmed datasets (Figures 3b, 4b and 5b). Given that both elements are constantly present above their respective detection limits, it may be concluded that such Ni–Co dissociation reflects characteristic pyrite signatures, i.e., zonation patterns that are characterised by either intra-grain oscillatory zoning at a scale larger that the spot size used for LA-ICP-MS analysis, or selective (re)mobilisation of Co relative to Ni.

Two other important associations of the PC2–PC3 projection include the four Pb isotopes, ^{204}Pb, ^{206}Pb, ^{207}Pb and ^{208}Pb, which group together with Re and Se. Whereas the ^{X}Pb–Re–Se association typifies a molybdenite-Pb-chalcogenide signature, Co and As are likely to occur in the pyrite crystal lattice. Interestingly, As is not associated with Au in PC1–PC2; there is, however, a slight correlation in the PC2–PC3 projection.

The most highly correlated τ_{ij} values correspond to, as expected, the Pb isotopes (Tables 2–4). In the untrimmed data, ^{204}Pb shows the higher proportionality with Sn ($\tau_{204PbSn} = 1.4$) and Ag ($\tau_{204PbAg} = 1.8$) compared to the other Pb isotopes. However, the relationships among Pb isotopes change markedly in the trimmed data, where all four ^{X}Pb become strongly correlated. In the original data, there is a very strong proportionality between Ti–Se, Ti–Sn and Sn–Mn ($\tau_{TiSe} = 1.1$, $\tau_{TiSn} = 1.1$, $\tau_{SnMn} = 1.1$; Table 2) which is likely to be real as such a relationship is preserved in the trimmed data (Tables 3 and 4). Other consistently high correlations are attributed to Se which shows relationships with As and also with Re ($\tau_{SeAs} = 2.8$; $\tau_{SeRe} = 2.7$; Table 3) and Co which shows the highest correlation with Se and As (e.g., $\tau_{CoSe} = 4.2$; $\tau_{CoAs} = 4.1$; Table 3). In all the data, Au shows more correlation with Ag than with As (e.g., $\tau_{AuAg} = 4.6$; $\tau_{AuAs} = 5.6$ in Table 3; Tables 2–4).

Table 2. Variation matrix for the N = 4926 dataset with entries as the variances of log-ratios for each element pair. The underscored values indicate the weakest column-wise co-dependence.

	Au	**Bi**	**Cu**	**Co**	**Mn**	**Ni**	**Re**	**Se**	**Sn**	**Te**	**Ti**	**^{204}Pb**	**^{206}Pb**	**^{207}Pb**	**^{208}Pb**	**Zn**	**Ag**
As	4.1	7.4	4.6	4.4	3.0	7.6	5.9	2.6	2.7	5.3	2.8	3.1	7.4	5.7	5.8	2.7	4.5
Au		5.2	3.4	5.7	2.7	**9.0**	6.1	3.4	2.6	5.7	3.1	2.3	5.4	3.9	4.0	2.6	2.6
Bi			4.1	**9.6**	5.6	**12.3**	**10.1**	7.4	6.4	8.0	7.4	5.3	3.5	3.7	3.7	6.1	4.1
Cu				6.2	2.8	**9.1**	6.2	3.5	2.8	6.3	3.6	2.6	3.9	3.0	3.0	2.7	2.5
Co					4.3	8.7	6.4	4.1	4.1	8.4	4.1	4.5	**9.2**	7.2	7.3	4.2	5.8
Mn						7.4	4.0	1.4	1.1	5.1	1.3	1.5	5.2	3.5	3.5	0.9	2.8
Ni							6.9	5.6	7.1	8.4	7.2	7.5	**12.2**	**10.6**	**10.4**	7.3	**9.0**
Re								2.8	3.6	7.5	3.8	4.2	**9.4**	7.5	7.4	3.8	6.1
Se									1.0	4.9	1.1	1.7	6.7	4.8	4.8	1.2	3.3
Sn										5.1	1.1	1.4	5.8	4.1	4.1	0.9	2.8
Te											5.7	5.5	8.6	7.3	7.2	5.2	6.4
Ti												1.7	6.7	4.8	4.8	1.2	3.3
^{204}Pb													4.3	2.6	2.7	1.1	1.8
^{206}Pb														2.1	2.2	5.4	3.5
^{207}Pb															1.5	3.6	2.5
^{208}Pb																3.6	2.6
Zn																	2.6

Table 3. Variation matrix for the N = 1501 dataset with entries as the variances of log-ratios for each element pair. The underscored values indicate the weakest column-wise co-dependence.

	Au	Bi	Cu	Co	Mn	Ni	Re	Se	Sn	Te	Ti	^{204}Pb	^{206}Pb	^{207}Pb	^{208}Pb	Zn	Ag
As	5.6	7.5	6.5	4.1	4.1	6.9	5.9	2.8	3.1	4.0	3.0	4.3	8.7	7.2	7.1	3.3	6.7
Au		6.0	6.1	7.4	5.7	**9.9**	8.8	5.5	4.6	5.3	5.2	4.3	7.6	6.1	6.2	4.8	4.6
Bi			4.7	**10.0**	6.5	**11.5**	**10.8**	7.5	6.4	7.4	7.6	4.6	4.3	4.1	3.9	6.3	4.3
Cu				8.6	5.5	**9.8**	8.7	5.5	4.4	6.8	5.7	4.2	5.1	4.6	4.7	4.6	4.5
Co					5.4	8.4	6.5	4.2	4.8	6.7	4.4	5.8	**10.8**	8.9	8.9	5.0	8.3
Mn						7.0	5.0	2.4	2.4	4.2	2.5	3.5	7.6	5.8	5.6	1.8	6.6
Ni							6.3	4.5	6.1	6.8	5.9	7.7	**12.9**	**11.3**	**11.1**	6.4	**10.6**
Re								2.7	4.2	6.3	3.9	5.8	**11.6**	**9.7**	**9.6**	4.4	**9.3**
Se									1.5	3.5	1.2	3.0	8.2	6.4	6.3	1.6	5.9
Sn										3.8	1.6	2.8	7.2	5.6	5.5	1.5	5.6
Te											4.2	5.0	**9.3**	7.8	7.6	4.0	7.3
Ti												3.1	8.3	6.5	6.5	1.9	6.2
^{204}Pb													3.9	2.4	2.4	2.2	3.3
^{206}Pb														1.8	1.9	6.5	4.0
^{207}Pb															1.1	4.8	3.4
^{208}Pb																4.7	3.5
Zn																	5.3

Table 4. Variation matrix for the N = 525 dataset with entries as the variances of log-ratios for each element pair. The underscored values indicate the weakest column-wise co-dependence.

	Au	Bi	Cu	Co	Mn	Ni	Re	Se	Sn	Te	Ti	^{204}Pb	^{206}Pb	^{207}Pb	^{208}Pb	Zn	Ag
As	5.9	7.0	7.4	3.8	4.2	6.3	5.7	2.6	4.0	3.4	3.1	5.7	8.4	7.0	7.1	4.1	7.8
Au		4.8	6.3	8.2	6.8	**9.6**	**9.5**	5.7	5.3	5.0	5.4	5.1	6.7	5.7	5.8	5.4	4.8
Bi			4.7	**9.6**	6.9	**9.9**	**9.5**	6.1	5.9	6.3	6.2	3.7	4.2	3.4	3.5	5.5	3.9
Cu				**10.1**	6.7	**9.4**	**9.3**	5.5	5.0	6.6	5.8	5.2	5.6	5.2	5.4	4.8	5.7
Co					5.7	8.0	6.3	4.3	6.4	6.0	4.6	7.4	**10.9**	**9.2**	**9.3**	6.0	**9.9**
Mn						6.7	5.7	2.6	3.4	3.5	2.8	5.5	8.4	6.7	6.8	2.4	8.8
Ni							5.8	4.1	6.2	6.0	5.1	8.7	**12.1**	**10.2**	**10.3**	6.4	**11.0**
Re								2.8	5.6	5.5	4.0	7.6	**11.2**	**9.5**	**9.5**	5.2	**10.6**
Se									2.3	2.6	1.3	4.3	7.2	5.8	5.8	2.1	6.7
Sn										3.5	2.2	4.9	7.5	6.0	6.1	2.3	7.5
Te											3.2	5.6	8.4	7.0	7.0	3.7	7.6
Ti												4.6	7.5	6.0	6.1	2.5	7.0
^{204}Pb													2.4	1.1	1.1	3.5	3.6
^{204}Pb														0.9	1.2	5.9	3.7
^{204}Pb															0.4	4.5	3.4
^{204}Pb																4.4	3.4
Zn																	6.4

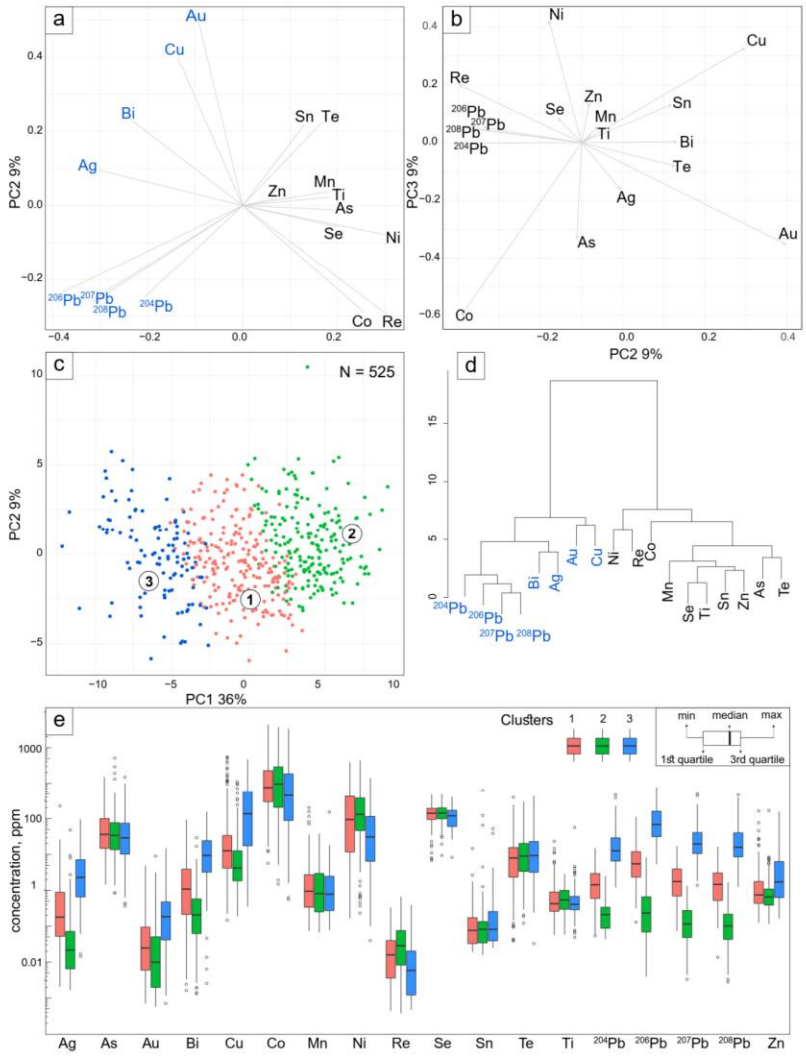


Figure 5. Principal component scores and loadings of centred log-ratio-transformed N = 525 data. The projection of PC1 versus PC2 (**a**) and PC2 versus PC3 (**b**) shows loadings of the elements. Principal component scores are shown on the PC1 versus PC2 projection (**c**), on which each dot corresponds to an individual sample assigned to one of three clusters (Supplementary Material B). Hierarchical cluster dendrogram (**d**) showing the association among the 18 elements with the height being a dissimilarity measure calculated from the variation matrix using Euclidean metrics (Table 4). (**e**) Box and whisker plot showing a range of concentrations for elements within each cluster. Note the correspondence among Cluster 3 and the Pb isotopes and Bi.

The k-means clustering was performed for each dataset individually using the dendrogram knots to derive ilr-coordinates. Because of that, the clusters are not directly comparable across three datasets, although the Cluster 3 dominated by Ag–Bi–^{X}Pb signature, is the only one that is consistently present

across all the data despite the left-censored values (Figure 3c,e, Figure 4c,e and Figure 5c,e). The results of k-mean clustering obtained from trimmed data (N = 1501 and N = 525) are similar to each other and slightly differ from the original data (N = 4926) (Supplementary Material B; Tables S4–S6). Within the original data, Clusters 1 and 2 are distinguished by Ni concentrations, whereas Ni is significantly enriched in Cluster 2 (median = 252 ppm; Supplementary Material B; Table S4) than in Cluster 1 (median = 4.4 ppm). Given that both Ni and Co are measured above mdl, the clustering strongly supports their different distribution in the analysed pyrite. The inverse positioning of Ni and Co on PC2–PC3 projection also confirms a wide range of Co/Ni ratios present within the data (e.g., Co/Ni ratio medians: Cluster 1–100; Cluster 2–2; Cluster 3–14; Supplementary Material B).

The results of k-means clustering of the trimmed datasets are, however, less interpretable. In both cases, the geochemical clusters are defined by the concentrations of Ag–Bi–^{X}Pb–Cu with Cluster 3 being the highest and Clusters 1 and 2 having consequently smaller values of these elements. Similarly, there is no obvious distinction among Clusters 1 and 2 in the trimmed data apart from the decrease in the concentration of Ag–Bi–^{X}Pb–Cu with Cluster 2 having the lowest values (Figures 4 and 5e).

3.3. Multiple Linear Regression

Table 5 shows the result of robust multiple linear regression of log(Au) onto the ilr-coordinates of seventeen elements in the form of the output of R routine linear model. The columns correspond to the estimated regression parameters (Estimate), their standard errors (Std. Error), t statistics obtained as parameter estimates divided by their standard errors (t value) and the *p*-values (Pr(>|t|)). The complete results of classic and robust regressions fitted into each of the datasets are given in Supplementary Material C. All fitted models were significant; however, they demonstrate adjusted R-squared values from 0.3 to 0.5, which is in accordance with highly variable data obtained via random spot analysis of pyrite grains.

Table 5. Results from robust multiple regression of the log(Au) for the ilr-coordinates of the remaining 17 elements in N = 1501 dataset. The extended results of classic and robust regressions fitted to the three datasets are in Supplementary Material C.

	Intercept	**Se**	**Ag**	**^{204}Pb**	**Te**	**Bi**	**^{206}Pb**	**Mn**	**Co**
Estimate	0.11	−0.33	0.18	0.10	0.07	0.05	−0.05	−0.03	−0.02
Std. Error	0.17	0.02	0.01	0.02	0.01	0.01	0.01	0.01	0.01
t value	0.67	−13.55	14.63	5.52	6.61	4.12	−3.07	−2.18	−2.01
Pr(>|t|)	0.505	0.000	0.000	0.000	0.000	0.000	0.002	0.030	0.045
significance		***	***	***	***	***	**	*	*
	Cu	**Ni**	**As**	**Sn**	**Re**	**^{208}Pb**	**^{207}Pb**	**Zn**	**Ti**
Estimate	−0.02	0.01	0.01	0.01	0.00	−0.01	0.00	0.00	0.00
Std. Error	0.01	0.01	0.01	0.02	0.01	0.02	0.02	0.02	0.02
t value	−1.57	0.75	0.71	0.36	−0.36	−0.28	0.15	0.04	0.11
Pr(>|t|)	0.117	0.451	0.481	0.719	0.719	0.777	0.879	0.968	0.911
significance	-	-	-	-	-	-	-	-	-

Notes: Multiple R-squared 0.46; Adjusted R-squared 0.46; significance codes [Pr(>|t|)]: *** 0–0.001; ** 0.001–0.01; * 0.01–0.05, '-' symbol >0.1 correspond to *p* values.

Throughout the original and trimmed datasets, Ag is consistently the best predictor for Au with the largest positive coefficient and t statistics (Table 5), suggesting that an increase in the Ag concentration within pyrite is always associated with increase in that of Au. Selenium is also a significant predictor of Au, however, in this case the coefficients are negative (e.g., estimate −0.33; Table 5), inferring an inverse relationship between Se and Au. Overall, Ag, Te and Bi are three elements that are good predictors of Au. Interestingly, ^{204}Pb and ^{206}Pb were assigned as significant predictors for Au in the N = 4926 and N = 1501 datasets, although ^{204}Pb exhibited a positive, and ^{206}Pb having a negative coefficient. However, none of the Pb isotopes were significant for Au prediction in the smaller (N = 525) dataset.

Arsenic and Ni are not important for Au prediction, whereas Co appears to be slightly significant with a negative coefficient in a few models (e.g., Table 5).

4. Discussion

4.1. Trace Element Signature of Pyrite: Prediction and Bias for Complex Sulphide Ores

As part of complex sulphide ore assemblages at Olympic Dam, pyrite is characterised by the presence of several trace elements of current or potential economic and/or metallurgical importance. Despite the intricate, grain-scale intergrowths between pyrite with chalcopyrite, three elements, As, Co, and Se, well known to be bound within the pyrite lattice at concentrations up to wt.% levels, give generally flat signals on the time-resolved LA-ICP-MS downhole profiles and have nearly overlapping mean and median values and are therefore not discriminative of any cluster (Supplementary Material B). The three elements, and to a lesser extent, also Te, are commonly present in pyrite from a variety of hydrothermal environments [56], including in IOCG deposits, as shown here for Olympic Dam, or known from Ernest Henry [34]. The two associations, Au–Co–As and Ag–Au, depicted by PC2 show element groups that could be lattice-bound but, intriguingly, may equally occur as fine particles and/or NPs. Indeed, Au–Ag–NPs have been reported from arsenic-free pyrite elsewhere and may be more common than presently known [24].

Pyrite is clearly an important host for Co at Olympic Dam. An understanding of the deportment of Co, an element recognised as characteristically enriched in IOCG systems relative to other magmatic-hydrothermal ore types [57], is important as this element represents both a potential target for future recovery but also because Co concentrations within copper concentrates need to be kept within acceptable limits. Even though carrollite and cobaltite inclusions in pyrite are known at Olympic Dam [33], the lack of significant large outliers in the Co concentration data for pyrite, together with the relatively stable Co signal on the LA-ICP-MS depth profiles strongly supports that it is exclusively lattice-bound. The variation in Co signal intensity observed in some depth profiles is readily attributed to the marked grain-scale zoning with respect to this element.

The same applies to Ni, although at concentrations which are appreciable lower. Interestingly, among all elements, Ni shows the greatest disproportionality, i.e., the least correlation with Bi, Ag, Au and Cu—inferring that Ni-rich bands are relatively depleted in these elements. The low Ni content gives a typical Co/Ni ratio of around 10. One interpretation of the very high Co/Ni ratio in Cluster 1 (median ~100; Supplementary Material B; Table S4), would be that pyrite assigned to this cluster contains individual Co-bearing mineral inclusions. Alternatively, and our preferred interpretation, is to attribute this to independent zoning patterns at the grain-scale, an argument also supported by their limited association (Figures 3b, 4b and 5b). It should be noted that the overall lack of correlation between Co and Ni at the scale of single mineral grain contrasts markedly with whole-rock data from Olympic Dam, in which Ni and Co correlate spatially, and together define the pyrite-chalcopyrite zone (in which the greater part of the pyrite occurs; [33]). Comparably wide ranges of Co/Ni are described from other IOCG and related systems [36,58].

The remarkably constant concentrations of Se (typically ~100–150 ppm; Supplementary Material B) are taken as indicating a lack of grain-scale zoning and homogenisation during any recrystallisation. Although reasonably homogenous across the clusters, As concentrations in pyrite, albeit at generally low absolute concentrations, show subtle variation suggesting grain-scale zoning, at least at the scale of the LA-ICP-MS spot analysis. Sub-micron scale compositional zoning is also most likely present within the analysed pyrite. There is a correlation between As and Co(–Ni) grains; although grain-scale zoning may not be coincident, those grains which are zoned with respect to one element are typically also zoned with respect to the other.

Despite the low average concentrations, ~25 ppm As (median of the N = 1501 dataset) in Olympic Dam pyrite, it is potentially the second largest host for As in the deposit after hematite [44], considering its proportion in the ore. The data presented here show that although pyrite contains measurable

gold, average contents are negligible, thus inferring that Olympic Dam pyrite is not 'arsenian' and that invisible gold in pyrite is not commonplace within the deposit. This is concordant with the well-documented occurrence of gold as native gold, electrum and less commonly, Au–Ag-tellurides throughout the deposit [33]. Invisible gold defined by the 'Au incorporation via As' paradigm cannot, however, be dismissed since the data show that a minority of pyrite grains analysed do contain Au—at noteworthy concentrations of maximum of 14 ppm (at the scale of the LA-ICP-MS crater) and furthermore that such pyrite is As-bearing. However, this type of 'invisible' gold is represented by a small proportion of Au since As is not a significant predictor for Au concentrations (Table 5; Supplementary Material C). The loading of Au in all three plots of PC1s plots perpendicular to As and to Bi–Ag–Pb, suggesting that PC1 predicts other possible host phases for Au, tellurides and electrum as nanoparticles/'invisible' Au.

A key characteristic of Olympic Dam pyrite is thus the prediction of tellurides of Ag–Au, Bi–Pb, Ag–Bi and Pb. Tellurium is distributed nearly equally across all the defined pyrite clusters (Figures 3e, 4e and 5e; Supplementary Material B), and never plots together with the Ag–Bi–Pb–(Au) signature. We can infer that Te occurs within the pyrite lattice, presumably at low concentration levels but forms telluride phases where present at higher concentrations. Despite the fact that Te is assigned to a distinct group from Ag–B–Pb–(Au) association, it might be concluded that Te forms Bi–Ag–Pb–(Au) telluride phases. The latter is also supported by Te being one of the most significant predictors of Au concentrations (Table 5; Supplementary Material C). Based on results of multiple linear regression analysis, electrum is one of the major hosts for Au, consistent with studies of gold mineralogy at Olympic Dam [33]. In addition, association of Au with telluride NPs, either Ag–Bi or Bi–Pb can be inferred as seen elsewhere [24]. Therefore, the idea that 'invisible Au' in pyrite is tied to As concentrations may be a bias of conducting analyses on pre-selected As-bearing pyrite grains.

4.2. Trapping of Trace Elements during Ore Overprinting

Sulphide ores in IOCG deposits, and particularly at Olympic Dam, can be also intimately associated with U-minerals [59–61] and Pb-minerals formed from the radiogenic decay and subsequent migration of U. Lead is an element not commonly incorporated within the pyrite lattice. At Olympic Dam and other IOCG systems in the same ore province, Pb has been shown to be partly non-radiogenic and partly radiogenic, introduced at the time of deposit formation and as a result of the decay of uranium, respectively [42,62]. Fractures within pyrite, as in other sulphides, can act as suitable traps for remobilised Pb to combine with available S, Se, and Te to form nanoparticulate galena, clausthalite [63] and altaite, and sometimes also anglesite. Upon healing and recrystallisation, these sub-micron- to nanoscale Pb-phases become effectively included within pyrite, or as preserved as linear Pb-bearing features within the grains that are observable by nanoSIMS isotope mapping [64,65]. The occurrence of such features likely indicates the role of trace element remobilisation and formation of inclusions during pyrite recrystallisation. Pyrite, a refractory mineral, is also likely to have acted as a physical trap for remobilised Ag, Bi, Pb and Te, which subsequently can form Ag–(Au)-tellurides, Bi–(Pb)–Ag-chalcogenides and other species.

Ores of the Olympic Dam deposit display evidence for multi-stage overprinting [33,43,44,59–61,66]. This has been observed for several mineral groups and is often expressed by the release of minor/trace impurities to form the same mineral with modified trace element signature and growth textures (e.g., hematite, uraninite), or formation of new minerals in close proximity to the parent phase. Ample evidence shows that sulphide minerals did not escape replacement, local-scale remobilisation and recrystallisation [60], even though key primary features are retained in Cu–Fe sulphides [67]. Pyrite, like hematite and uraninite, is better suited to retain signatures of the multi-stage overprint. There is also evidence for pseudomorphic replacement (coupled dissolution-reprecipitation reactions; CDRR) retained by ore minerals from the Olympic Dam deposit [43,44,59]. Often, as seen for both oxides and sulphides, CDR-assisted replacement results in precipitation of new minerals in close

spatial association with the replaced parent phase (e.g., sub-micron-scale molybdenite, scheelite, or uraninite NPs adjacent to replaced U–W–Sn–Mo-bearing hematite [43,44,68].

PC2 features high loadings of Sn, predicting inclusions of cassiterite in many of the analysed pyrites. Other elements expected to be present as inclusions are Cu (chalcopyrite), Zn (sphalerite), and Ti (rutile). Concentrations of the contaminant heavy metals Tl and Hg in Olympic Dam pyrite are insignificantly low. The prediction of such a diverse range of inclusions within pyrite may relate to the complex reworking of primary zoning patterns in pyrite which results in the formation of an eclectic range of mineral phases that could range in size from a few microns down to true nanoparticles. Such an interpretation is consistent with the small grain size and assemblage complexity of ores at Olympic Dam [33].

4.3. Impact of Left-Censored Data on the Interpretation of Statistical Analyses: Artefacts and False Interpretations

Replacement of mdl values by a fixed value, or alternatively, taking the absolute values of detection limits, are likely to impact most statistical inference (Figure 2a,c). Multiple imputation is the most reliable method to deal with left-censored data, however taking a notional 'half the mdl value' for LA-ICP-MS datasets also gives visually plausible distributions of individual analyses (Figure 2b,d). We have, however, not investigated the effect of the latter on the results of statistical analyses due to our preferred adoption of quantitative imputation.

The consequent reduction of left-censored values within the data allows changes in the geochemical clusters, element groups and the strength of relationships between elements (e.g., between Au and associated elements), to be systematically tracked. The prediction of log(Au) concentration using the elements from the original N = 4926 dataset are likely dubious (Supplementary Material C; Table S7) due to the significant percentage of left-censored values—and amply illustrated by the hard-to-interpret dendrogram and PC1–PC2–PC3 projection (Figure 3a–d). The prediction of log(Au), obtained model coefficients and significance of predictors is questionable because the vast majority of elements, including those which would never be expected to correlate with Au (e.g., Zn or Ti), appeared as statistically significant, thus overestimating the strength of the relationship between Au and other elements in the N = 4926 dataset. On the other hand, a group of elements Ag, Se, Te, Bi, Re, ^{204}Pb appear as significant predictors for log(Au) in both trimmed datasets (N = 1501 and N = 525), as well as in the original dataset, providing affirmation of the robustness of both types of multiple linear regressions (Supplementary Material C; Tables S8 and S9) and the genuine geochemical ties between Au and these elements. Similarly, throughout the statistical analyses, an association of Ag–Bi–^{X}Pb as Cluster 3 is recognised despite the data being incomplete (Figure 3a,c, Figure 4a,c and Figure 5a,c).

Despite the dubious predictions of Au using the original data, the N = 4926 dataset contains features that progressively disappear as the total number of analyses is reduced. Most importantly, the original dataset shows an inverse relationship between Ni and Co in Olympic Dam pyrite, elements which dominate the PC2 (Figure 3a), and likely indicates intra-grain heterogeneity in which absolute concentrations range over 2–3 orders of magnitude. K-means clustering applied to the original data revealed Cluster 1 which is specifically characterised by domains featuring very high Co/Ni ratios of ~100 (Supplementary Material B). Neither is this geochemical clustering, nor such a significant inverse Co–Ni relationship, identified from the k-means clustering of trimmed datasets. Moreover, within the trimmed data, the geochemical meaning of Clusters 1 and 2 is fundamentally changed.

Overall, the presence of a large percentage of left-censored data is shown to impact the results of statistical analysis and may consequently influence any interpretations drawn. The sequential trimming of data volume results in some of these features being dismissed as artefacts but also enables certain relationships among elements to be verified, thus allowing meaningful interpretations to be made.

4.4. Implications and Significance

One of the main implications of this study lies in the demonstration of how reduction of the left-censored data alters the results of statistical analyses, suggesting that a careful approach should be taken when trimming datasets. Possible pitfalls, like overestimation of dependence among variables, or overlooking the significant relationship among variables, should be avoided.

Mineral chemistry studies on pyrite from IOCG deposits are limited despite the abundance of pyrite in these deposits, the ability of pyrite to scavenge metals and metalloids, and its refractory character allowing discrimination between different mineralisation events. Another contribution of this work lies in the quantitative data analysis of trace element signatures in pyrite from Olympic Dam. Multivariate statistical analyses, when considering such a large multi-element dataset, allows inferences to be made about the role of inclusion versus lattice-bound trace elements, and where suspected, the identity of those inclusions. One example is the Ag–Bi–Pb–(Au) trace element signature in pyrite and prediction of various telluride species and electrum as inclusions. Although the proportion of Au attributed to inclusions of electrum versus tellurides in pyrite is not directly quantifiable, the prediction of Au-bearing phases is not possible from bivariate scatterplots alone.

Further work, however, would require nanoscale characterisation of Au–(As)-bearing pyrite which will allow improved discrimination of nanoparticle populations and interpretation of their formation from lattice-bound elements or by other mechanisms.

5. Conclusions

This study, carried out blind without preselection of pyrite grains by texture, shows that multivariate statistical analysis can enable prediction but also expose bias and artefacts when defining trace element signatures in minerals from complex sulphide ores. The combination of multivariate statistical analyses shows that Olympic Dam pyrite is characterised by: (i) a Ag–Bi–Pb signature predicting inclusions of tellurides (as PC1); and (ii) highly variable Co–Ni ratios likely representing an oscillatory zonation pattern in pyrite (as PC2). Pyrite is a major host for As, Co and probably also Ni. The three elements do not correlate well at the grain-scale, indicating high variability in zonation patterns. Arsenic is not a good predictor for invisible Au at Olympic Dam. Most pyrites contain only negligible Au, suggesting that invisible gold is not commonplace within the deposit. The data clearly show, however, that a small minority of pyrite grains analysed do contain Au—at noteworthy concentrations of tens and even hundreds of ppm, and moreover that this gold is correlated with Ag, Bi, Pb and Te. Such information is valuable for geometallurgical modelling and for derivation of qualitative deportment models of elements of interest.

The treatment of <mdl values in large datasets with abundant left-censored data is critical, especially given the fact how replacement by an absolute or fixed value, i.e., median, can skew the data. The trimming of datasets with left-censored values should be done with caution as it potentially may result in overly large and erroneous correlations or dilution of those due to the significant reduction of analyses. The number of mdl values impacts on the outcome of statistical analyses and replacement of <mdl values using multiple imputation is advised.

Supplementary Materials: The following are available online at http://www.mdpi.com/2075-163X/10/1/61/s1, Supplementary Material A: Sequential binary partitioning of the data into corresponding ilr-coordinates (Tables S1–S3). K-means clustering validation via Silhouette widths and 'elbow' plots (Figures S1–S3). Supplementary Material B: Summary Statistics (in ppm) for three clusters obtained via k-means algorithm (Tables S4–S6). Supplementary Material C: Results from regression of log(Au) for the ilr-coordinates of the remaining elements (Tables S7–S9).

Author Contributions: The research described was carried out by M.D. on datasets obtained by K.E., M.K. and V.S.K., with guidance provided by A.V.M. and S.G. The research was supervised by C.L.C. and K.E. and the paper written by M.D., N.J.C., C.L.C. and K.E. All authors have read and agreed to the published version of the manuscript.

Funding: This research was funded through the project "Trace elements in Fe-oxides: deportment, distribution and application in ore genesis, geochronology, exploration and mineral processing", supported by BHP Olympic Dam

and the South Australian Government Mining and Petroleum Services Centre of Excellence. N.J.C. acknowledges additional support from the ARC Research Hub for Australian Copper-Uranium (Grant IH130200033). V.K. acknowledges funding from the ARC Linkage Grant "The supergiant Olympic Dam U–Cu–Au–REE ore deposit: towards a new genetic model" (Linkage Grant LP130100438).

Acknowledgments: We appreciate the insightful comments of three anonymous reviewers, which have helped us better formulate results and interpretations.

Conflicts of Interest: The authors declare no conflict of interest.

References

1. Vaughan, D.J.; Corkhill, C.L. Mineralogy of Sulphides. *Elements* **2017**, *13*, 81–87. [CrossRef]
2. Craig, J.R.; Vokes, F.M.; Solberg, T.N. Pyrite: Physical and chemical textures. *Miner. Depos.* **1998**, *34*, 82–101. [CrossRef]
3. Carstens, C.W. Om geokjemiske undersøkelser av malmer. *Norsk Geol. Tidsskr.* **1941**, *21*, 213–221.
4. Fleischer, M. Minor Elements in Some Sulphide Minerals. In *Economic Geology Fiftieth Anniversary, Volume 1905–1955*; Bateman, A.M., Ed.; Economic Geology Publishing Company: Urbana, IL, USA, 1955; pp. 970–1024.
5. Hawley, J.E.; Nichol, I. Trace elements in pyrite, pyrrhotite and chalcopyrite of different ores. *Econ. Geol.* **1961**, *56*, 467–487. [CrossRef]
6. Gregory, D.D.; Lyons, T.W. The effects of trace element content on pyrite oxidation rates. In Proceedings of the American Geophysical Union Fall Meeting, New Orleans, LA, USA, 11–15 December 2017. 2017AGUFM.H41I1554G.
7. Abraitis, P.K.; Pattrick, R.A.D.; Vaughan, D.J. Variations in the Compositional, Textural and Electrical Properties of Natural Pyrite: A Review. *Int. J. Miner. Process.* **2004**, *74*, 41–59. [CrossRef]
8. Large, R.R.; Maslennikov, V.V.; Robert, V.; Danyushevsky, L.V.; Chang, Z.S. Multistage sedimentary and metamorphic origin of pyrite and gold in the giant Sukhoi Log deposit, Lena Gold Province, Russia. *Econ. Geol.* **2007**, *102*, 1233–1267. [CrossRef]
9. Large, R.R.; Danyushevsky, L.D.; Hollit, C.; Maslennikov, V.V.; Meffre, S.; Gilbert, S.; Bull, S.; Scott, R.; Emsbo, P.; Thomas, H.; et al. Gold and trace element zonation in pyrite using a laser imaging technique; implications for the timing of gold in orogenic and Carlin-style sediment-hosted deposits. *Econ. Geol.* **2009**, *104*, 635–668. [CrossRef]
10. Sung, Y.H.; Brugger, J.; Ciobanu, C.L.; Pring, A.; Skinner, W.; Nugus, M. Invisible gold in arsenian pyrite and arsenopyrite from a multistage Archaean gold deposit: Sunrise Dam, Eastern Goldfields Province, Western Australia. *Miner. Depos.* **2009**, *44*, 765–791. [CrossRef]
11. Cook, N.J.; Ciobanu, C.L.; Mao, J. Textural control on gold distribution in As-free pyrite from the Dongping, Huangtuliang and Hougou gold deposits, North China Craton (Hebei Province, China). *Chem. Geol.* **2009**, *264*, 101–121. [CrossRef]
12. Thomas, H.V.; Large, R.R.; Bull, S.W.; Maslennikov, V.; Berry, R.F.; Frazer, R.; Froud, F.; Moye, R. Pyrite and pyrrhotite textures and composition in sediments, laminated quartz veins, and reefs at Bendigo Gold Mine, Australia: Insights for ore genesis. *Econ. Geol.* **2011**, *106*, 1–31. [CrossRef]
13. Cook, N.J.; Ciobanu, C.L.; Meria, D.; Silcock, D.; Wade, B.P. Arsenopyrite–Pyrite Association in an Orogenic Gold Ore: Tracing Mineralization History from Textures and Trace Elements. *Econ. Geol.* **2013**, *108*, 1273–1283. [CrossRef]
14. Cook, N.J.; Chryssoulis, S.L. Concentrations of invisible gold in the common sulphides. *Can. Mineral.* **1990**, *28*, 1–16.
15. Reich, M.; Kesler, S.E.; Utsunomiya, S.; Palenik, C.S.; Chryssoulis, S.L.; Ewing, R.C. Solubility of gold in arsenian pyrite. *Geochim. Cosmochim. Acta* **2005**, *69*, 2781–2796. [CrossRef]
16. Deditius, A.P.; Reich, M. Constraints on the solid solubility of Hg, Tl, and Cd in arsenian pyrite. *Am. Mineral.* **2016**, *101*, 1451–1459. [CrossRef]
17. George, L.L.; Biagioni, C.; D'Orazio, M.; Cook, N.J. Textural and trace element evolution of pyrite during greenschist facies metamorphic recrystallization in the southern Apuan Alps (Tuscany, Italy): Influence on the formation of Tl-rich sulfosalt melt. *Ore Geol. Rev.* **2018**, *102*, 59–105. [CrossRef]
18. George, L.; Biagioni, C.; Lepore, G.O.; Lacalamita, M.; Agrosì, G.; Capitani, G.C.; Bonaccorsi, E.; D'Acapito, F. The speciation of thallium in (Tl, Sb, As)-rich pyrite. *Ore Geol. Rev.* **2019**, *107*, 364–380. [CrossRef]

19. Cook, N.J.; Ciobanu, C.L.; George, L.; Zhu, Z.-Y.; Wade, B.; Ehrig, K. Trace Element Analysis of Minerals in Magmatic-Hydrothermal Ores by Laser Ablation Inductively-Coupled Plasma Mass Spectrometry: Approaches and Opportunities. *Minerals* **2016**, *6*, 111. [CrossRef]
20. Ciobanu, C.L.; Verdugo-Ihl, M.R.; Slattery, A.; Cook, N.J.; Ehrig, K.; Courtney-Davies, L.; Wade, B.P. Silician magnetite: Si–Fe nanoprecipitates and other mineral inclusions in magnetite from the Olympic Dam deposit, South Australia. *Minerals* **2019**, *9*, 311. [CrossRef]
21. Xu, J.; Ciobanu, C.L.; Cook, N.J.; Slattery, A.D. Crystals from the Powellite–Scheelite Series at the Nanoscale: A Case Study from the Zhibula Cu Skarn, Gangdese Belt, Tibet. *Minerals* **2019**, *9*, 340. [CrossRef]
22. Keyser, W.; Ciobanu, C.L.; Cook, N.J.; Feltus, H.; Johnson, G.; Slattery, A.; Wade, B.P.; Ehrig, K. Mineralogy of Zirconium in Iron-Oxides: A Micron- to Nanoscale Study of Hematite Ore from Peculiar Knob, South Australia. *Minerals* **2019**, *9*, 244. [CrossRef]
23. Van Tendeloo, G.; Bals, S.; Van Aert, S.; Verbeeck, J.; Van Dyck, D. Advanced electron microscopy for advanced materials. *Adv. Mater.* **2012**, *24*, 5655–5675. [CrossRef]
24. Ciobanu, C.L.; Cook, N.J.; Utsunomiya, S.; Kogagwa, M.; Green, L.; Gilbert, S.; Wade, B. Gold-telluride nanoparticles revealed in arsenic-free pyrite. *Am. Mineral.* **2012**, *97*, 1515–1518. [CrossRef]
25. Ciobanu, C.L.; Cook, N.J.; Maunders, C.; Wade, B.P.; Ehrig, K. Focused ion beam and advanced electron microscopy for minerals: Insights and outlook from bismuth sulphosalts. *Minerals* **2016**, *6*, 112. [CrossRef]
26. Winderbaum, L.; Ciobanu, C.L.; Cook, N.J.; Paul, M.; Metcalfe, A.; Gilbert, S. Multivariate Analysis of an LA-ICP-MS Trace Element Dataset for Pyrite. *Mathem. Geosci.* **2012**, *44*, 823–842. [CrossRef]
27. Dmitrijeva, M.; Metcalfe, A.V.; Ciobanu, C.L.; Cook, N.J.; Frenzel, M.; Keyser, W.M.; Johnson, G.; Ehrig, K. Discrimination and Variance Structure of Trace Element Signatures in Fe-Oxides: A Case Study of BIF-Mineralisation from the Middleback Ranges, South Australia. *Math. Geosci.* **2018**, *50*, 381–415. [CrossRef]
28. Dmitrijeva, M.; Ehrig, K.; Ciobanu, C.L.; Cook, N.J.; Verdugo-Ihl, M.R.; Metcalfe, A. Defining IOCG signatures through compositional data analysis: A case study of lithogeochemical zoning from the Olympic Dam deposit, South Australia. *Ore Geol. Rev.* **2019**, *105*, 86–101. [CrossRef]
29. Dmitrijeva, M.; Ehrig, K.; Ciobanu, C.L.; Cook, N.J.; Verdugo-Ihl, M.R.; Metcalfe, A. Mineralization-alteration footprints in the Olympic Dam IOCG district, South Australia: The Acropolis prospect. *J. Geochem. Explor.* **2019**, *205*, 106333. [CrossRef]
30. Palarea-Albaladejo, J.; Martin-Fernandez, J.A. Values below detection limit in compositional chemical data. *Anal. Chim. Acta* **2013**, *764*, 32–43. [CrossRef]
31. Palarea-Albaladejo, J.; Martin-Fernandez, J.A. ZCompositions—R package for multivariate imputation of left-censored data under a compositional approach. *Chemom. Intell. Lab. Syst.* **2015**, *143*, 85–96. [CrossRef]
32. Hron, K.; Templ, M.; Filzmoser, P. Imputation of missing values for compositional data using classical and robust methods. *Comput. Stat. Data Anal.* **1986**, *54*, 3095–3107. [CrossRef]
33. Ehrig, K.; McPhie, J.; Kamenetsky, V.S. Geology and mineralogical zonation of the Olympic Dam Iron Oxide Cu–U–Au–Ag deposit, South Australia. In *Geology and Genesis of Major Copper Deposits and Districts of the World: A Tribute to Richard H. Sillitoe*; Society of Economic Geologists Special Publication: Littleton, CO, USA, 2012; Volume 16, pp. 237–267.
34. Foster, A.R.; Williams, P.; Ryan, C. Distribution of Gold in Hypogene Ore at the Ernest Henry Iron Oxide Copper-Gold Deposit, Cloncurry District, NW Queensland. *Explor. Mining Geol.* **2007**, *16*, 125–143. [CrossRef]
35. Rusk, B.; Oliver, N.; Cleverley, J.; Blenkinsop, T.; Dexian, Z.; Patrick, P.; Habermann, P. Physical and chemical characteristics of the Ernest Henry iron oxide copper gold deposit, Australia; implications for IOGC genesis. In *Hydrothermal Iron Oxide Copper-Gold & Related Deposits: A Global Perspective-Advances in the Understanding of IOCG Deposits*; Porter, T.M., Ed.; Global Perspective Series 3; PGC Publishing: Linden Park, Australia, 2010; pp. 201–218.
36. Reich, M.; Simon, A.C.; Deditius, A.; Barra, F.; Chryssoulis, S.; Lagas, G.; Tardani, D.; Knipping, J.; Bilenker, L.; Sánchez-Alfaro, P.; et al. Trace Element Signature of Pyrite from the Los Colorados Iron Oxide-Apatite (IOA) Deposit, Chile: A Missing Link Between Andean IOA And Iron Oxide Copper–Gold Systems? *Econ. Geol.* **2016**, *111*, 743–761. [CrossRef]

37. Gregory, D.D.; Cracknell, M.J.; Large, R.R.; McGoldrick, P.; Kuhn, S.; Maslennikov, V.V.; Baker, M.J.; Fox, N.; Belousov, I.; Figueroa, M.C.; et al. Distinguishing Ore Deposit Type and Barren Sedimentary Pyrite Using Laser Ablation-Inductively Coupled Plasma-Mass Spectrometry Trace Element Data and Statistical Analysis of Large Data Sets. *Econ. Geol.* **2019**, *114*, 771–786. [CrossRef]
38. Román, N.; Reich, M.; Leisen, M.; Morata, D.; Barra, F.; Deditius, A.P. Geochemical and micro-textural fingerprints of boiling in pyrite. *Geochim. Cosmochim. Acta* **2019**, *246*, 60–85. [CrossRef]
39. Elghali, A.; Benzaazoua, M.; Bussière, B.; Genty, T. Spatial Mapping of Acidity and Geochemical Properties of Oxidized Tailings within the Former Eagle/Telbel Mine Site. *Minerals* **2019**, *9*, 180. [CrossRef]
40. Danyushevsky, L.V.; Robinson, P.; Gilbert, S.; Norman, M.; Large, R.; McGoldrick, P.; Shelley, J.M.G. Routine quantitative multi-element analysis of sulphide minerals by laser ablation ICP-MS: Standard development and consideration of matrix effects. *Geochem. Explor. Environ. Anal.* **2011**, *11*, 51–60. [CrossRef]
41. Norris, A.; Danyushevsky, L. *Towards Estimating the Complete Uncertainty Budget of Quantified Results Measured by LA-ICP-MS*; Goldschmidt: Boston, MA, USA, 2018.
42. Schmandt, D.S. Mineralogical Distributions of Radionuclides in Copper–Uranium Ores from Olympic Dam, South Australia. Ph.D. Thesis, The University of Adelaide, Adelaide, Australia, 2019. Unpublished.
43. Ciobanu, C.L.; Wade, B.P.; Cook, N.J.; Schmidt Mumm, A.; Giles, D. Uranium-bearing hematite from the Olympic Dam Cu–U–Au deposit, South Australia; a geochemical tracer and reconnaissance Pb–Pb geochronometer. *Precambr. Res.* **2013**, *238*, 129–147. [CrossRef]
44. Verdugo-Ihl, M.R.; Ciobanu, C.L.; Cook, N.J.; Ehrig, K.; Courtney-Davies, L.; Gilbert, S. Textures and U–W–Sn–Mo signatures in hematite from the Cu–U–Au–Ag orebody at Olympic Dam, South Australia: Defining the archetype for IOCG deposits. *Ore Geol. Rev.* **2017**, *91*, 173–195. [CrossRef]
45. Aitchison, J. The Statistical Analysis of Compositional Data. In *Monographs on Statistics and Applied Probability*; Chapman & Hall: London, UK, 1986; p. 416. [CrossRef]
46. Pawlowsky-Glahn, V.; Egozcue, J.J.; Tolosana-Delgado, R. *Modeling and Analysis of Compositional Data*; Wiley: Chichester, UK, 2015; p. 272. [CrossRef]
47. van den Boogart, K.G.; Tolosana-Delgado, R.; Bren, M. Compositions: Compositional Data Analysis. R Package Version 1.40-2. 2018. Available online: https://CRAN.R-project.org/package=compositions (accessed on 8 January 2020).
48. Egozcue, J.J.; Pawlowsky-Glahn, V.; Mateu-Figueras, G.; Barceló-Vidal, C. Isometric logratio transformations for compositional data analysis. *Math. Geol.* **2003**, *35*, 279–300. [CrossRef]
49. Egozcue, J.J.; Pawlowsky-Glahn, V. Simplicial Geometry for Compositional Data. In *Compositional Data Analysis in the Geosciences: From Theory to Practice*; Buccianti, A., Mateu-Figueras, G., Pawlowsky-Glahn, V., Eds.; Special Publications; Geological Society: London, UK, 2006; Volume 264, pp. 145–159. [CrossRef]
50. Aitchison, J.; Barceló-Vidal, C.; Pawlowsky-Glahn, V. Some comments on compositional data analysis in archaeometry, in particular the fallacies in Tangri and Wright's dismissal of logratio analysis. *Archaeometry* **2002**, *44*, 295–304. [CrossRef]
51. Mathieu, L. Detecting magmatic-derived fluids using pyrite chemistry: Example of the Chibougamau area, Abitibi Subprovince, Québec. *Ore Geol. Rev.* **2019**, *114*, 103127. [CrossRef]
52. Caciagli, N. Multielement Geochemical Modelling for Mine Planning: Case Study from an Epithermal Gold Deposit. In *Compositional Data Analysis*; Martín-Fernández, J.A., Thió-Henestrosa, S., Eds.; Springer: Berlin, Germany, 2016; Volume 187, pp. 45–61. [CrossRef]
53. Gabriel, K.R. The biplot graphical display of matrices with application to principal component analysis. *Biometrika* **1971**, *58*, 453–467. [CrossRef]
54. Templ, M.; Hron, K.; Filzmoser, P. robCompositions: An R-Package for Robust Statistical Analysis of Compositional Data. In *Compositional Data Analysis. Theory and Applications*; Pawlowsky-Glahn, V., Buccianti, A., Eds.; John Wiley & Sons: Chichester, UK, 2018; pp. 341–355. [CrossRef]
55. Filsmozer, P.; Hron, K.; Templ, M. *Applied Compositional Data Analysis with Worked Examples in R*; Springer: New York, NY, USA, 2018; p. 280. [CrossRef]
56. Bowles, J.F.W.; Howie, R.A.; Vaughan, D.J.; Zussman, J. Non-silicates: Volume 5A. In *Rock-Forming Minerals*; Deer, W.A., Howie, R.A., Zussman, J., Eds.; Geological Society: London, UK, 2011; p. 920.
57. Barton, M.D. Iron oxide (–Cu–Au–REE–P–Ag–U–Co) systems. In *Treatise on Geochemistry*, 2nd ed.; Holland, H.D., Turekian, K.K., Eds.; Elsevier: Oxford, UK, 2014; pp. 515–541. [CrossRef]

58. Li, R.; Chen, H.; Xia, X.; Yang, Q.; Danyushevsky, L.D.; Lai, C. Using integrated in-situ sulphide trace element geochemistry and sulfur isotopes to trace ore-forming fluids: Example from the Mina Justa IOCG deposit (southern Perú). *Ore Geol. Rev.* **2018**, *101*, 165–179. [CrossRef]
59. Macmillan, E.; Cook, N.J.; Ehrig, K.; Ciobanu, C.L.; Pring, A. Uraninite from the Olympic Dam IOCG–U–Ag deposit: Linking textural and compositional variation to temporal evolution. *Am. Mineral.* **2016**, *101*, 1295–1320. [CrossRef]
60. Macmillan, E.; Ehrig, K.; Ciobanu, C.L.; Cook, N.J.; Pring, A. Replacement of uraninite by bornite via coupled dissolution-reprecipitation: Evidence from texture and microstructure. *Can. Mineral.* **2016**, *54*, 1369–1383. [CrossRef]
61. Macmillan, E.; Cook, N.J.; Ehrig, K.; Pring, A. Chemical and textural interpretation of late-stage coffinite and brannerite from the Olympic Dam IOCG–Ag–U deposit. *Mineral. Mag.* **2017**, *81*, 1323–1366. [CrossRef]
62. Owen, N.D. The Mineralogical Deportment of Radionuclides in South Australian Cu–Au–(U) Ores. Ph.D. Thesis, The University of Adelaide, Adelaide, Australia, 2019. Unpublished.
63. Owen, N.D.; Ciobanu, C.L.; Cook, N.J.; Slattery, A.D.; Basak, A.K. Nanoscale Study of Clausthalite-Bearing Symplectites in Cu–Au–(U) Ores: Implications for Ore Genesis. *Minerals* **2018**, *8*, 67. [CrossRef]
64. Rollog, M.; Cook, N.J.; Guagliardo, P.; Ehrig, K.; Ciobanu, C.L.; Kilburn, M. Detection of Trace Elements/Isotopes in Olympic Dam Copper Concentrates by nanoSIMS. *Minerals* **2019**, *9*, 336. [CrossRef]
65. Rollog, M.; Cook, N.J.; Guagliardo, P.; Ehrig, K.; Kilburn, M. Radionuclide distributions in Olympic Dam copper concentrates: The significance of minor hosts, incorporation mechanisms, and the role of mineral surfaces. *Minerals Eng.* **2020**, *148*, 106176. [CrossRef]
66. Owen, N.D.; Cook, N.J.; Rollog, M.; Ehrig, K.J.; Schmandt, D.S.; Ram, R.; Brugger, J.; Ciobanu, C.L.; Wade, B.; Guagliardo, P. REE-, Sr-, Ca-aluminum-phosphate-sulfate minerals of the alunite supergroup and their role as hosts for radionuclides. *Am. Mineral.* **2019**, *104*, 1806–1819. [CrossRef]
67. Ciobanu, C.L.; Cook, N.J.; Ehrig, K. Ore minerals down to the nanoscale: Cu–(Fe)-sulphides from the iron oxide copper gold deposit at Olympic Dam, South Australia. *Ore Geol. Rev.* **2017**, *81*, 1218–1235. [CrossRef]
68. Cook, N.J.; Ciobanu, C.L.; Ehrig, K.; Slattery, A.; Verdugo-Ihl, M.R.; Courtney-Davies, L.; Gao, W. Advances and opportunities in ore mineralogy. *Minerals* **2017**, *7*, 233. [CrossRef]



© 2020 by the authors. Licensee MDPI, Basel, Switzerland. This article is an open access article distributed under the terms and conditions of the Creative Commons Attribution (CC BY) license (http://creativecommons.org/licenses/by/4.0/).

CHAPTER 5

DEFINING IOCG SIGNATURES THROUGH COMPOSITIONAL DATA ANALYSIS: A CASE STUDY OF LITHOGEOCHEMICAL ZONING FROM THE OLYMPIC DAM DEPOSIT, SOUTH AUSTRALIA

Marija Dmitrijeva[1], Kathy Ehrig[2], Cristiana L. Ciobanu[1], Nigel J. Cook[1], Max R. Verdugho-Ihl[1], Andrew V. Metcalfe[3]

[1]*School of Chemical Engineering and Advanced Materials, The University of Adelaide, Adelaide, SA 5005, Australia*

[2]*BHP Olympic Dam, Adelaide, SA 5000, Australia*

[3]*School of Mathematical Sciences, The University of Adelaide, Adelaide, SA 5005, Australia*

Article published in Ore Geology Reviews 105 (2019) 86-101

Statement of Authorship

Title of Paper	Defining IOCG signatures through compositional data analysis: A case study of lithogeochemical zoning from the Olympic Dam deposit, South Australia. Ore Geology Reviews
Publication Status	☑ Published ☐ Accepted for Publication ☐ Submitted for Publication ☐ Unpublished and Unsubmitted work written in manuscript style
Publication Details	Dmitrijeva, M., Ehrig, K., Ciobanu, C.L., Cook, N.J., Verdugo-Ihl, M.R., Metcalfe, A.V. Defining IOCG signatures through compositional data analysis: A case study of lithogeochemical zoning from the Olympic Dam deposit, South Australia. Ore Geology Reviews, 105, 86-101. https://doi.org/10.1016/j.oregeorev.2018.12.013.

Principal Author

Name of Principal Author (Candidate)	Marija Dmitrijeva		
Contribution to the Paper	Performed statistical data analyses and interpretation, prepared the manuscript.		
Overall percentage (%)	55		
Certification:	This paper reports on original research I conducted during the period of my Higher Degree by Research candidature and is not subject to any obligations or contractual agreements with a third party that would constrain its inclusion in this thesis. I am the primary author of this paper.		
Signature		Date	17.12.19

Co-Author Contributions

By signing the Statement of Authorship, each author certifies that:

i. the candidate's stated contribution to the publication is accurate (as detailed above);

ii. permission is granted for the candidate in include the publication in the thesis; and

iii. the sum of all co-author contributions is equal to 100% less the candidate's stated contribution.

Name of Co-Author	Kathy Ehrig		
Contribution to the Paper	Helped to define the direction of the paper, assisted with the interpretation of the results and the manuscript evaluation.		
Overall percentage (%)	15		
Signature		Date	17.12.19

Name of Co-Author	Cristiana L. Ciobanu		
Contribution to the Paper	Helped to define the direction of the paper, assisted with the manuscript preparation and evaluation.		
Overall percentage (%)	9		
Signature		Date	17.12.19

Name of Co-Author	Nigel J. Cook		
Contribution to the Paper	Assisted with the manuscript preparation and evaluation.		
Overall percentage (%)	9		
Signature		Date	17.12.19

Name of Co-Author	Max R. Verdugo-Ihl		
Contribution to the Paper	Assisted with the estimation of the modal mineralogy at Olympic Dam.		
Overall percentage (%)	6		
Signature		Date	17.12.19

Name of Co-Author	Andrew V. Metcalfe		
Contribution to the Paper	Assisted with the statistical analyses and manuscript evaluation.		
Overall percentage (%)	6		
Signature		Date	17.12.19

Ore Geology Reviews 105 (2019) 86–101

Contents lists available at ScienceDirect

Ore Geology Reviews

journal homepage: www.elsevier.com/locate/oregeorev

Defining IOCG signatures through compositional data analysis: A case study of lithogeochemical zoning from the Olympic Dam deposit, South Australia

Marija Dmitrijeva[a,*], Kathy J. Ehrig[b], Cristiana L. Ciobanu[a], Nigel J. Cook[a], Max R. Verdugo-Ihl[a], Andrew V. Metcalfe[c]

[a] School of Chemical Engineering, The University of Adelaide, Adelaide, SA 5005, Australia
[b] BHP Olympic Dam, Adelaide, SA 5001, Australia
[c] School of Mathematical Sciences, The University of Adelaide, Adelaide, SA 5005, Australia

ARTICLE INFO

Keywords:
Principal component analysis
Hierarchical clustering
Whole-rock dataset
IOCG deposits
Lithogeochemical zoning
Olympic Dam

ABSTRACT

The Olympic Dam Cu-U-Au-Ag deposit is dominantly composed of mineralised hematite-breccias and occurs entirely within the Roxby Downs Granite. Multivariate statistical analysis of a large whole-rock, 15 m-interval geochemical dataset (10,565 samples) was undertaken to identify geochemical signatures characteristic of iron-oxide copper gold (IOCG)-style mineralization and constrain the conspicuous lithogeochemical zonation observed at Olympic Dam. Statistical analyses include principal component analysis on centred logratio (clr)-transformed data coupled with hierarchical clustering. Certain groups of elements that can be interpreted in terms of an evolving hydrothermal system relative to host lithologies are derived from data analysis: granitophile (U-W-Sn-Mo); siderophile (Ni-Co); chalcophile (Ag-Bi) and related elements (As-Sb and Au-Te). The distributions of elements within each group are investigated through three vertical cross-sections and are compared with known lithological and Cu-(Fe)-sulphide zonation. Throughout the Olympic Dam Breccia Complex, the IOCG signature is defined by multi-element combinations of the commodity metals Cu, U, Au, and Ag, coupled with a range of trace elements. Overall, the IOCG signature overlaps well with Fe-metasomatism despite mismatch which is likely due to discrete styles of mineralisation found only on the margins of the deposit and also to the presence of mineralised domains within Fe-poor zones. The IOCG signature is composed of two geochemical associations, which exhibit distinct spatial distributions. The first group, Cu-U_3O_8-Se-S, shows concentric zonation whereas the second group, Au-W-Mo-Sb-As, forms a vertical ~1800 m deep corridor in the southeastern lobe of the deposit. The specific Au-W-Mo-As-Sb signature could potentially be generic within IOCG systems across the Olympic Cu-Au province and if so, would provide a proxy model for near-mine exploration.

1. Introduction

A distinctive feature of many magmatic-hydrothermal ore deposits is the presence of systematic spatial distribution patterns, commonly expressed by zoned alteration assemblages and/or paragenetic sequences (e.g., Guilbert and Park, 1986). The spatial distribution of minerals, and hence the suite of elements that each contains, occurs due to fluid flow in and around intrusive bodies and conduits for hydrothermal fluids as a response to pH, Eh, temperature gradients and other factors. Investigation of the spatial distribution of mineral assemblages and mineral compositions in deposits formed by dynamic fluid/rock reactions as, for example, in skarn deposits (e.g., Meinert, 1997) is crucial for the development and validation of hypotheses concerning ore genesis that can underpin conceptual exploration models.

Magmatic-hydrothermal iron-oxide copper gold (IOCG) deposits (e.g. in Olympic Cu-Au Province, South Australia; the Cloncurry District, Queensland, or the Carajás Mineral Province, Brazil) represent an economically significant source of Cu, Au, Ag, and in some cases, also U. These deposits are also enriched in, and thus represent potential resources for rare earth elements (REE), and several minor elements, including Co, Nb, and Te (Barton, 2014). The IOCG clan encompasses a diverse group of deposits found in a range of geological settings, and formed from the Archean to Tertiary (e.g., Groves et al., 2010). Despite such a broad spectrum of IOCG systems in terms of age, regional setting, genetic characteristics, host rocks, and ore grade, they are all inherently associated with zoned alteration envelopes and contain significant, often dominant concentrations of Fe-oxides (Barton, 2014, and references therein). In conceptual models for IOCG systems, the expression of regional-scale hydrothermal alteration varies from distal alkali-rich to proximal hydrolytic sericite-chlorite assemblages (Hitzman et al.,

* Corresponding author.

https://doi.org/10.1016/j.oregeorev.2018.12.013
Received 8 October 2018; Received in revised form 8 December 2018; Accepted 17 December 2018
Available online 18 December 2018
0169-1368/ © 2018 Elsevier B.V. All rights reserved.

1992). Zonation patterns can be tracked at different scales, from alkali-rich metasomatism observable on the district-scale (e.g., Cloncurry, Queensland, Australia; Oliver et al., 2004; the Moonta area in the Gawler Craton, South Australia; Conor et al., 2010; Kontonikas-Charos et al., 2014), down to within individual deposits (e.g., Ernest Henry, Queensland; Mark et al., 2006). Such zonation patterns may also be expressed by changing compositions or concentrations of trace elements within minerals approaching the orebody (e.g., Ismail et al., 2014).

The Olympic Cu-Au Province, South Australia, is one of the best-endowed Proterozoic IOCG provinces on Earth and comprises deposits/prospects associated with a major tectono-magmatic event at ~1.6 Ga (Skirrow et al., 2007). Olympic Dam (OD) is by far the largest single deposit in the province and exhibits remarkable lateral and vertical mineralogical zonation with respect to Cu-(Fe)-sulphides among others (Ehrig et al., 2012). Sulphide distribution patterns are defined by an inwards transition from pyrite-chalcopyrite (Py-Cp), chalcopyrite-bornite (Cp-Bn) and bornite-chalcocite (Bn-Cc), observable also vertically from deeper to shallower levels. The deposit is well-suited for understanding geochemical patterns versus mineral zoning because of the relatively simple geological setting. The orebody is hosted within a breccia complex with various degrees of Fe-metasomatism, all enclosed within a host granite (e.g., Ehrig et al., 2012).

In this contribution, we address lithogeochemical zoning in the OD deposit with principal component analysis (PCA) and hierarchical clustering, using a large (10,565-sample) whole-rock geochemical dataset encompassing 39 elements. These exploratory multivariate statistical methods are required for making data-driven decisions on grouping variables, i.e., elements that define the specific geochemical signatures of IOCG systems, and to circumvent the large dimensionality of multi-element data. The combination of multivariate statistical methods and large whole-rock geochemical data offers potential insights that can constrain genetic models, identify potential sources of metals and fluids, and assert the nature, relative timing and mechanisms of superimposed overprinting events. Outcomes have application to other ore systems in comparable settings.

2. Geological background and rationale

The OD deposit is associated with rocks of the bimodal Gawler Silicic Large Igneous Province (SLIP) in the eastern Gawler Craton (Allen et al., 2008). The Gawler SLIP comprises intrusive rocks of the Hiltaba Suite (HS), and cogenetic extrusive equivalents assigned to the Gawler Range Volcanics (GRV). Within the OD deposit, the latter include intensively altered olivine-phyric and dolerite dykes (Huang et al., 2015; 2016) and breccias dominated by felsic volcanic fragments (Ehrig et al., 2012). Fresh dolerite dikes attributed to younger, 820 Ma Gairdner Large Igneous Province are also present (Huang et al., 2015). The deposit is entirely contained within the Olympic Dam Breccia Complex (ODBC) which is predominantly derived from the host Roxby Downs Granite (RDG) (Reeve et al., 1990). The southeastern areas of the ODBC contain the greatest density of sedimentary facies rocks at shallow depths immediately below the unconformity (McPhie et al., 2016). The deposit lies immediately below a major unconformity and is overlain by sedimentary rocks of the Stuart Shelf.

The ODBC comprises varied assemblages containing ore and gangue minerals of hydrothermal origin, as well as relict minerals derived from altered lithologies. The most widespread minerals (in order of abundance) are hematite, quartz, sericite, orthoclase, chlorite, siderite, fluorite, baryte, pyrite, chalcopyrite, bornite and chalcocite (Ehrig et al., 2012). Mineralogical studies of magmatic feldspars and accessory apatite from igneous rocks and hydrothermal minerals from the orebody (uraninite, hematite, REE-fluorocarbonates and Cu-(Fe)-sulphides) show preservation of primary characteristics despite being affected by superimposed fluid-rock interaction (Macmillan et al., 2016a,b,c; Krneta et al., 2016; Ciobanu et al., 2017; Kontonikas-Charos et al., 2017; Schmandt et al., 2017; Verdugo-Ihl et al., 2017). These studies show widespread evidence for rock-buffered reactions (replacement via coupling dissolution with reprecipitation rates; Putnis, 2002), inferring that reworking of mineral assemblages can take place on the scale of microns to meters if the porosity is not sustainably networked. This allows the hydrothermal alteration assemblages to preserve the gradational continuum observed within the ODBC. The continuum ranges from sericite-hematite alteration, becoming more pervasive and intense from peripheral, weakly-altered non-mineralized RDG to hematite-dominant breccias within the deposit centre (Ehrig et al., 2012; Mauger et al., 2016; Kontonikas-Charos et al., 2017).

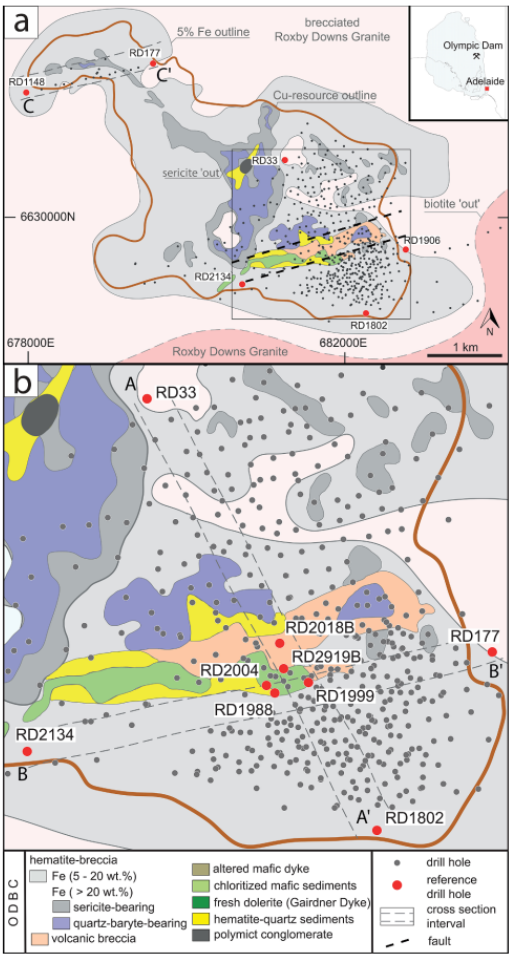


Fig. 1. Simplified geological map (coordinate system WGS 1984 UTM Zone 53S; after Ehrig et al., 2012) indicating the outline of the Olympic Dam Breccia Complex, drillhole collar locations, and cross-section CC' in the northwestern arm (a); the location of the cross-sections AA' and BB' in the southeastern lobe (b). The map is representative of geology projected at 350 m below the surface.

Economic concentrations of Cu-(Fe)-sulphides are predominantly contained within hematite-rich breccias and a strong association between Fe-metasomatism and Cu-mineralization is thus expected (Fig. 1a). The concentric zonation of Cu-(Fe)-sulphides is enveloped around an L-shaped, Cu-barren, high-Fe, quartz-baryte-bearing

hematite breccia that is mainly restricted to the central part of the ODBC (Fig. 1a; Reeve et al., 1990; Ehrig et al., 2012). These Cu-barren breccias were originally interpreted as hydrothermal fluid centres and maar-diatreme structures that represent nested eruption/collapse craters that subsequently incorporated and accommodated blocks of RDG, GRV, and assorted epiclastic and sedimentary facies (Reeve et al., 1990). The proposed model accounting for deposit zonation enveloping a central, highly-altered, low-sulphide zone (Fig. 5 in Reeve et al., 1990), became untenable following interpretation of closely-spaced drilling which intersected discovery of ~2 km-thick mineralised interval in the southeastern lobe of the deposit (Ehrig et al., 2012, 2017, and references therein). Further asymmetry is shown by presence of mineralization at a depth below ~1.5 km (and still open at 2.3 km) within felsic volcanic rocks on the SE margin of the deposit (Apukhtina et al., 2017). A shallow, maar-diatreme model would also require a subvolcanic environment, which although not completely ruled out by the RDG emplacement depth of 6–8 km [from petrographic studies of Creaser (1989) and feldspar-amphibole geothermobarometric estimates of Kontonikas-Charos et al. (2017)], does not explain why mineralization is hosted by altered granite. In addition, the central part of the deposit, considered in earlier studies as a fluid conduit (Reeve et al., 1990), is interpreted in the latest model as a result of vertical faults with multiple episodes of activation post-dating the lifespan of the ~1.6 Ga IOCG event (Cherry et al., 2018).

Therefore, deep mineralization intersected by drillhole RD1988 (Fig. 1b; Ehrig et al., 2012) suggests the presence of fluid centres deeper than previously recognised. Moreover, the RDG setting opens-up the idea that mineralisation could have been initiated at depth, from multiple fluid sources released from the granite cupola prior to its uplift. In magmatic-hydrothermal systems, vertical and lateral zonation with respect to mineral assemblages mirrors the spatial distribution of mineralization relative to the fluid source. Although it is difficult to reconcile both the concentric Cu-(Fe)-sulphide zonation with the occurrence of deep mineralization at the southeastern edge of the ODBC to a single simultaneous point of fluid entry, the present deposit zonation is most likely the result of both primary and superimposed effects. Faults (and their reactivation) and/or erosion of the upper parts of the deposit are considered particularly significant.

Altogether, the pronounced deposit zonation, coupled with an apparently simple granite-hosted setting, make OD an ideal target to test if there are other geochemical patterns that can be related to the Cu(-Fe)-sulphide zoning and if these display concentration gradients relative to potential fluid pathways. As a first step towards constraining geochemical gradients within the ODBC, we address the zonation patterns of metals with emphasis on lithological classes and Cu(-Fe)-sulphide mineral zonation patterns. The study aims to test whether certain trace elements, grouped according to multivariate statistical analyses, match the observed mineralogical and alteration zonation. Specifically, this work addresses the characteristic association of a distinct suite of 'granitophile' elements (U, W, Sn and Mo) identified at OD, and defining the distinct geochemical identity of the abundant primary oscillatory-zoned hematite (Ciobanu et al., 2013; Verdugo-Ihl et al., 2017). Understanding geochemical gradients not only allows inference of the hydrothermal evolution of the deposit, but also offers ways to distinguish between primary metallogenic patterns and trace element signatures attributable to superimposed processes.

3. Methods and data

3.1. Sample suite

The whole-rock multi-element geochemical dataset used for this study consists of 10,565 samples from 540 separate drillholes. Assay data were collected regularly from 15 m-long intervals along the drillcores and form a dense grid in the southeastern lobe of ODBC, and a transect in the northwestern arm of the deposit (Fig. 1a, b). A small number of drillholes which were sampled at 1, 2, 2.5 and 5 m-long intervals were recalculated to 15 m intervals. This study does not consider the northern domain of the ODBC due to the limited availability of whole-rock data. However, a single section across the extreme northwestern part of the ODBC is included.

All drill core samples were assayed for the same suite of elements by Bureau Veritas (Adelaide). Four-acid digestion (HCl-HNO_3-HF-$HClO_4$) and metaborate/tetraborate fusion were used to ensure total dissolution of all minerals. As given by Ehrig et al. (2012), analysis was achieved by four-acid digestion and inductively coupled plasma-optical emission spectroscopy (IP-OES) for Cu, Ag, As, Co, Ni, Pb, and Zn; lithium metaborate/tetraborate fusion and ICP-OES for Ba, Al, Ca, Ce, Fe, K, La, Mg, Mn, Na, P, Si, Sr, Ti, Y, and Zr; lithium metaborate/tetraborate fusion and inductively coupled plasma-mass spectroscopy for U_3O_8, Bi, Sb, and Mo; induction furnace-infrared spectrometry for CO_2 and S; and fire assay-flame atomic absorption spectrometry for Au. Essentially the same dataset is reported by Ehrig et al. (2012) and underpins the deposit-scale zonation patterns described therein. Summary statistics are provided in an appendix to Ehrig et al. (2012).

The sample suite covers the majority of lithologies present in the ODBC. A simplified classification for various hematite- and granite-breccias is based on the proportion of Fe wt. % and the presence/absence of aluminosilicates, mainly sericite (Table 1). Such an approach is appropriate to characterize the body of mineralized rocks within the ODBC.

The largest domain of sedimentary and volcanic rocks in the dataset (~2% and ~7% of the data, respectively) are present in the southeastern lobe of the ODBC (Fig. 1b). These lithologies form a WSW-ENE-trending lineament (Fig. 1) with vertical plunge down to depths of ~1 km. Quartz-baryte-bearing hematite breccias (~5% of data) are also dispersed in proximity to the volcanic and sedimentary rocks along the WSW-ENE lineament and are best developed in the middle part of the deposit (Fig. 1b). The sample suite also includes data for mafic dikes, which can be sub-divided into: (i) strongly altered rocks considered as mafic/ultramafic rocks coeval with 1.59 Ga magmatism; and (ii) fresher basaltic/dolerite rocks considered affiliated to the ~ 820 Ma Gairdner Dyke Swarm (Huang et al., 2015). Such mafic dikes, although intersected in 43 drillholes, are very minor constituent in the present dataset (< 2% of the data).

Geochemical signatures within the ODBC are investigated through three deposit-scale cross-sections, each covering drillholes within a 200 m-wide band (Fig. 1): a ~NW-SE cross-section crosscutting the southeastern part of the deposit (section AA'); a ~W-E profile placed along the strike of the domain of sedimentary and volcanic breccias in the SE lobe (section BB'); and a ~W-E profile along the length of the NW arm of the deposit (section CC').

3.2. Data processing

Left-censored values are measurements that fall below the minimum detection limit (mdl) and may thus introduce considerable inconsistence into the data (Helsel, 2006). In geochemical data analysis it is common to replace mdl values with a fraction of that value, for instance one half of mdl, however, this approach is to be avoided as it changes the relative variation structure in compositions (Palarea-Albaladejo and Martín-Fernández, 2013, 2015).

Within the OD dataset, the proportion of values below mdl varied depending on the measured element: it exceeded 50% for Cr, Ta, Tm, and V, and was close to 30% for Mn and Se. For all remaining elements, left-censored values were imputed using robust multiplicative log-normal replacement, a routine available from the 'zCompositions' package in R (Palarea-Albaladejo and Martín-Fernández, 2015). This method respects the geometry of the compositional data and preserves the ratios among D-part components in a composition, being thus a reasonable choice for an imputation technique.

Table 1
Simplified description of the main lithologies of the ODBC with corresponding nomenclature from literature; percentage of whole-rock data attributed to each lithological class is reported.

Lithology	Description	Percentage	Corresponding nomenclature and comments
Brecciated Roxby Downs Granite	Brecciated and altered granite with hematite as a matrix component of a clast-supported breccia	0.5	
Hematite breccia Fe (5–20 wt% Fe)	Hematite breccia with altered and progressively obliterated Roxby Downs Granite fragments; hematite is present as a matrix component, occasionally as pseudomorphic replacements after inherited granitic components	54	
Sericite-bearing hematite breccia Fe (> 20 wt%)	Hematite breccia with hematitic infill and almost fully hematitized and/or sericitised Roxby Downs Granite fragments; displays a more intense alteration and a strong association with sulphides	30	
Quartz-baryte-bearing hematite breccia (> 20 wt% Fe)	Hematite breccia with fragments of hematite and quartz which are placed within hematitic infill; Cu- and U-barren, the breccia lacks sulphides and aluminosilicates, although it comprises significant Au mineralization	5	As HEMQ in Ehrig et al. (2012)
Volcanic breccia	Hematite-rich breccia with intensely altered and reworked felsic and/or mafic-ultramafic clasts	7	The incorporated clasts are interpreted as relicts of felsic and mafic lavas of Gawler Range Volcanics (Ehrig et al., 2012)
Altered mafic-ultramafic dyke	Sericitised and/or chloritized, aphanitic, doleritic and porphyritic mafic dykes	1	~1590 Ma olivine-phyric basalts and dykes (Huang et al., 2016)
Fresh dolerite (Gairdner Dyke)	Green, Ti-magnetite-bearing dolerite dykes	0.5	Gairdner basaltic to doleritic dykes (Huang et al., 2015)
Chloritized mafic sediments	Laminated, chlorite-bearing sedimentary rock	1	As green sandstone and mudstone (McPhie et al., 2016); or KASH (Ehrig et al., 2012)
Hematite-quartz sediments	Laminated, hematite-rich sedimentary rock	1	As interbedded sandstone and red mudstone (McPhie et al., 2016) or KHEMQ (Ehrig et al., 2012)

3.3. Multivariate statistical analyses

3.3.1. Hierarchical clustering

Hierarchical cluster analysis of a 39-part sub-composition containing major and trace elements, Ag, Al, Au, As, Ba, Bi, Ce, Cl, Co, CO_2, Cu, F, Fe, Ga, K, Mg, Mn, Mo, Na, Nb, Nd, Ni, P, S, Sb, Se, Sb, Si, Sn, Sr, Ta, Te, Th, Ti, U_3O_8, W, Y, Zn, and Zr, was performed to explore the geochemical affinities among elements. In this study, correlation and covariance matrix of untransformed raw data were avoided due to the spurious effects of compositional data closure (Pearson, 1897; Aitchison, 1986). Instead, clustering was based on the variation matrix (Appendix A; Table 2). The entries of the matrix are the variances of the logratios of the elements (Aitchison, 1986)

$$\tau_{ij} = var(\ln(x_i/x_j)) \quad (1)$$

for i, j from 1 to 39. A small τ_{ij} indicates a small variance of $\ln(x_i/x_j)$, thus implying a degree of proportionality between elements x_i and x_j. In the variation matrix, perfect proportionality between two components is represented as zero. The variation matrix is preferred to the correlation matrix as a distance measure among the components of compositions (van den Boogaart and Tolosana-Delgado, 2013). Conversion of variation matrix into a distance matrix was done using Euclidean metric space, and it was followed by the complete linkage agglomeration method, which implies sequential merging of similar clusters as dictated by the distance measure.

Table 2
Variation matrix (Eq. (1)). The extended version of the variation matrix is in Appendix A.

Variable	Ag	Au	As	Ba	Bi	Ce	Co	Cu	Ga	Mo	Nb	Nd	Ni	S	Se	Sb	Sn	Ta	Te	Th	U_3O_8	W	Y	Zr
Au	1.9																							
As	2.0	1.7																						
Ba	3.1	3.0	1.4																					
Bi	1.0	1.8	1.5	2.5																				
Ce	1.0	1.2	1.2	2.0	0.9																			
Co	1.9	3.0	3.1	4.7	2.0	1.5																		
Cu	1.7	2.7	3.8	4.9	1.9	1.9	2.1																	
Ga	1.4	2.5	1.9	2.5	1.7	0.9	1.3	2.9																
Mo	1.5	1.3	0.9	1.7	1.2	0.8	2.5	2.5	1.7															
Nb	1.3	2.1	1.8	3.1	1.6	0.9	1.3	2.8	0.7	1.8														
Nd	0.9	1.5	1.3	2.2	0.9	**0.1**	1.3	1.9	0.7	1.0	0.7													
Ni	2.2	3.4	2.9	4.5	2.4	1.9	0.9	3.1	1.3	2.8	1.3	1.6												
S	1.5	1.8	2.1	3.0	1.4	1.0	1.4	1.4	2.0	1.2	1.6	1.1	2.1											
Se	2.0	2.7	3.0	4.8	2.3	1.9	1.9	2.4	2.3	2.8	1.6	1.8	2.2	1.9										
Sb	2.0	1.9	**0.4**	1.3	1.5	1.2	3.2	3.7	1.8	0.9	2.0	1.4	3.0	2.1	3.3									
Sn	1.4	1.8	1.1	2.2	1.4	0.8	2.1	3.1	1.1	1.1	0.9	0.7	2.2	1.6	2.4	1.2								
Ta	1.6	2.8	2.1	2.9	2.0	1.2	1.4	3.2	**0.3**	2.0	0.7	1.0	1.4	2.1	2.3	2.2	1.4							
Te	1.3	1.5	1.1	2.0	1.3	0.7	2.3	2.7	1.4	0.8	1.3	0.7	2.4	1.4	2.6	1.1	0.8	1.7						
Th	1.8	3.2	2.6	3.1	2.2	1.3	1.6	3.3	**0.2**	2.3	1.0	1.1	1.6	2.5	2.7	2.5	1.6	**0.4**	1.9					
U_3O_8	1.0	1.7	2.2	3.4	1.1	**0.6**	1.1	1.0	1.4	1.4	1.1	**0.6**	1.8	0.8	1.6	2.2	1.5	1.6	1.4	1.7				
W	1.5	1.2	0.8	1.8	1.3	0.8	2.6	2.8	1.9	**0.6**	1.7	1.0	2.9	1.3	2.6	0.8	0.9	2.2	0.8	2.6	1.5			
Y	1.1	2.3	1.9	2.7	1.3	**0.6**	1.0	2.2	**0.3**	1.6	**0.6**	**0.4**	1.2	1.4	1.9	1.8	1.0	**0.6**	1.2	**0.6**	0.8	1.6		
Zr	2.3	3.7	2.8	3.0	2.7	1.8	2.2	4.0	**0.4**	2.6	1.6	1.7	2.0	3.1	3.4	2.7	2.0	**0.6**	2.3	**0.3**	2.4	3.0	1.0	
Zn	2.1	3.5	2.5	3.3	2.4	1.7	1.8	3.6	1.0	2.5	1.6	1.5	1.7	2.7	3.1	2.5	1.9	1.1	2.1	1.1	2.1	2.7	1.2	1.2

*Numbers in bold indicate the strongest element pair codependence (≤0.6).

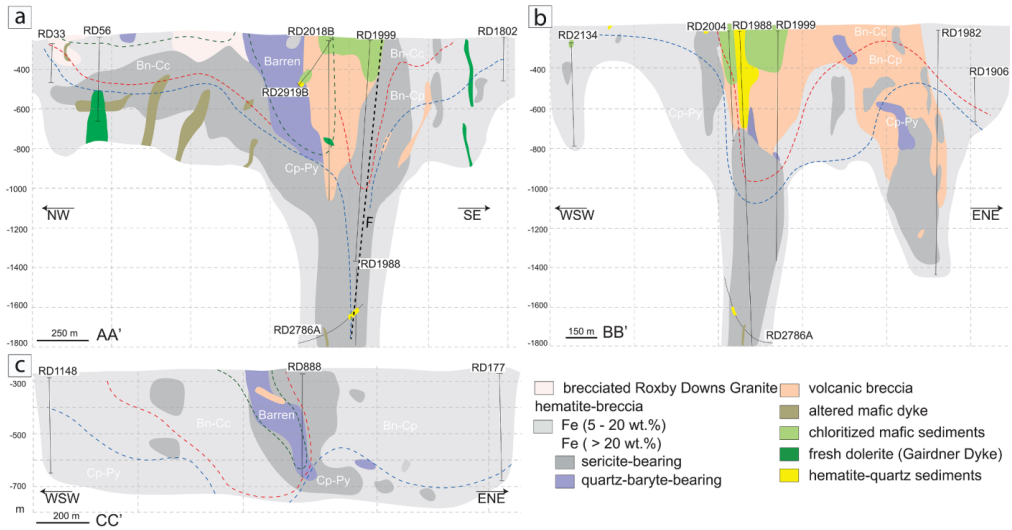


Fig. 2. Interpreted geological cross-sections featuring the distribution of lithological units in AA' (a), BB' (b) and CC' (c) with overlay of estimated Cu(-Fe)-sulphide zone boundaries (see Section 3.5). The cross-sections were reconstructed using core logging and the lithogeochemistry discussed in this study. The upper boundary of cross-sections represents the unconformity surface.

3.3.2. *Principal component analysis*

Principal Component Analysis (PCA) is frequently used for exploratory data analysis of multivariate data from geochemical studies to identify associations among elements that can be used to explain geological and geochemical processes (e.g. Grunsky, 2010; Grunsky et al., 2014; Chen et al., 2017). The method aims to find the maximum variation within the data by reducing its dimensionality and results in a linear combination of chemical elements defined as principal components (PCs). The outcomes of PCA are commonly presented as a biplot of scores (score of every sample on PC1 and PC2) and loadings (loadings of every element on PC1 and PC2) (Gabriel, 1971), whereas the positioning of loadings (i.e., elements), reflects geochemical affinities among the variables.

In this study, PCA was performed by singular values decomposition of centred logratio (clr) transformed data. The transformation is required to respect its simplicial geometry (Aitchison, 1986). The multivariate data analysis and corresponding calculations were performed in the R package 'compositions' (van den Boogaart et al., 2014).

3.4. *Spatial 3D-modelling*

Spatial modelling of continuous variables (i.e., element concentrations) was performed using the implicit 3D-modelling tool in Leapfrog Geo 3D software. The spatial models were derived by spheroidal interpolant function, i.e., semi-variogram, with a base range of 200 m and a constant drift. The cross-sections corresponding to lithological sections AA', BB' and CC' (Fig. 1) were derived as transects through the kriged surfaces of the SE-lobe and NW-arm. The location of cross-sections was chosen through the longest axis of densely populated drillholes (CC') and through the maximum lithological variability (BB').

3.5. *Estimation of normative Cu-(Fe)-sulphide mineralogy*

To approximate the deposit-scale sulphide-zonation, normative mineralogy calculations were used to estimate the proportion of sulphides based on whole-rock geochemical data, stoichiometric criteria and the predominant sulphide-assemblages. The employed approach considers the main S-bearing phases: baryte, pyrite, chalcopyrite, bornite and chalcocite; and native copper, following the following steps:

(1) Calculation of molar proportions for As, Ba, Cu, Ni, S, Sb and Zn;
(2) If the molar proportion of Ba ≥ S, then all S is converted to equivalent baryte and removed, otherwise equivalent amount of S in 1:1-ratio to Ba is removed;
(3) If S > 0 after step (2), then Sb and As are added to S (S*), whereas Ni and Zn are included with Cu (Cu*);
(4) The S*:Cu*-ratio is used to determine the sulphide-zone as following:
   a. If S*:Cu* > 2, then normative chalcopyrite is calculated (based on Cu*), which is then removed to subtract its equivalent from S* and then calculate normative pyrite with the remaining S* (→ 'Py-Cp-zone');
   b. Otherwise, if S*:Cu* > 0.8, then normative chalcopyrite is calculated by subtracting 0.8 from S*:Cu, dividing the difference by 1.2 and multiplying it by Cu*, after which the equivalent S* is removed, whereas normative bornite is then calculated by dividing the remaining S* by 4 (→ 'Cp-Bn-zone');
   c. Otherwise, if S*:Cu* > 0.5 (or < 0.8 if step 4d is not followed), then normative bornite is calculated by subtracting 0.5 from S*:Cu, dividing the difference by 0.3 and multiplying it by Cu* divided by 5, after which the equivalent S* is removed, whereas normative chalcocite corresponds to the remaining S* (→ 'Bn-Cc-zone');
   d. Otherwise, if (S*:Cu* ≤ 0.5), normative chalcocite corresponds to S*, which is removed from Cu*, after which the remaining Cu* corresponds to native copper. Since native copper is extremely sparse in the ODBC, the zone was amalgamated with 'Bn-Cc-zone';
   e. Regardless of the potential sulphide-zone, if Cu < 0.1 wt%, the zone is considered 'Barren'. The zones 'Py-Cp', 'Cp-Bn', 'Bn-Cc' and 'Barren' are used as categorical variables to project Cu(-Fe)-sulphide zonation onto cross-sections.

4. Results

The simplified geological cross-sections are given in Fig. 2a–c. All three cross-sections show interfaces between bornite-chalcocite ('Bn-Cc') and pyrite-chalcopyrite ('Py-Cp') zones and are thus representative of the complete ore zonation within the ODBC. In all cross-sections the 'Py-Cp' ore zone remains open at depth. The Cu(-Fe)-sulphide zonation (Fig. 2), which was calculated from the whole-rock data, broadly matches the patterns obtained from the MLA dataset reported by Ehrig et al. (2012).

CC' is a relatively shallow cross-section, down to a depth of only 800 m, and is based on a transect of just 15 equally-spaced drillholes in the NW arm (Fig. 2c). On the contrary, the southeastern cross-sections, AA' and BB', are deeper, intersect each other in drillhole RD1999 and are placed within the limits of the dense grid of drillholes (Fig. 1b). Cross-section BB' includes data from some of the deepest parts of the orebody, which remains open at a depth of ~1800 m (e.g., RD1988; Fig. 2b). The southeastern cross-sections feature greater lithological variability, containing sedimentary rocks and volcanic breccia as blocks ranging from shallow depths immediately below the unconformity to deeper parts of the ODBC (Fig. 2a, b). Although the interpretation of geological sections is reliable, based on the existing data, interpolation of continuous variables is inhibited due to the limited number of drillholes that continue below depths of ~1100 m in the southeastern lobe. The interpolant extents in the southeastern sections are therefore bounded at ~1100 m.

4.1. Hierarchical cluster analysis

The subset of the variation matrix displaying a 39-part sub-composition of the ODBC samples is shown in Table 2. The variation matrix reflects the degrees of proportionalities of elements and geochemical affinities among groups of elements. For instance, Ce shows the strongest co-dependency with Nd ($\tau_{CeNd} = 0.1$) followed by Ga and Th ($\tau_{GaTh} = 0.2$) and Sb and As ($\tau_{SbAs} = 0.4$). Tungsten shows a strong association with Mo ($\tau_{WMo} = 0.6$) and As ($\tau_{WAs} = 0.8$). In contrast, Ba shows the strongest disproportionality with Cu and Se ($\tau_{BaSe} = 4.8$; $\tau_{BaCu} = 4.9$). These associations are evident from the hierarchical clustering dendrogram (Fig. 3), which is based on the variation matrix (Appendix A; Table 2). The height of the dendrogram represents a measure of similarity among the elements and corresponds to a variation matrix. Therefore, merged groups of elements in the lower part indicate similarity.

Four distinct subgroups of elements can be distinguished. Group 1 encompasses K, Al, Zn, Zr, Ti, Si, Na, Th and Ga, along with Co and Ni, and represents the geochemical signatures of non-mineralized felsic and mafic intrusive rocks. In contrast, Groups 2, 3 and 4 are all elements characteristic of IOCG-style mineralization. Group 2 displays the association of Cu and U mineralization, also including Se. Group 3 specifically reflects a magmatic-hydrothermal granitic signature (Mo, W, and Sn, along with As, Sb, Au, and Te), whereby Au displays the

Table 3
Results from compositional principal component analysis. Bold numbers indicate elements with the largest loadings on principal components (> 0.19).

Eigenvalues of PC1 to PC3 Eigenvalues	PC1	PC2	PC3
λ	3.55	2.56	1.95
λ%	32	15	9
$\sum\lambda$%	32	48	57
Loadings of the elements on PC1-PC3			
Elements	**PC1**	**PC2**	**PC3**
Ag	−0.09	−0.06	0.13
Al	**0.26**	0.11	0.09
Au	**−0.25**	0.01	0.08
As	**−0.20**	**0.21**	−0.09
Ba	−0.16	**0.36**	**−0.29**
Bi	−0.15	−0.03	0.01
Ca	−0.07	−0.10	−0.17
Ce	−0.11	0.00	0.01
Cl	0.10	0.03	0.08
Co	0.05	**−0.27**	0.09
CO_2	0.17	**−0.35**	**−0.58**
Cu	−0.13	**−0.29**	0.17
F	−0.01	−0.01	−0.10
Fe	−0.11	−0.05	0.01
Ga	0.10	0.09	0.05
K	**0.33**	0.16	0.03
Mg	0.19	−0.01	0.08
Mn	**0.24**	**−0.34**	**−0.38**
Mo	−0.19	0.07	−0.14
Na	0.19	0.13	0.03
Nb	−0.01	−0.03	0.16
Nd	−0.07	−0.01	0.03
Ni	0.08	−0.16	0.12
P	−0.06	−0.06	0.11
S	−0.16	−0.19	−0.01
Sb	−0.18	**0.21**	−0.17
Se	−0.09	**−0.22**	**0.35**
Si	0.19	0.14	0.03
Sn	−0.10	0.07	−0.02
Sr	−0.09	0.11	−0.02
Ta	0.11	0.06	0.08
Te	−0.15	0.08	−0.04
Th	0.17	0.09	0.07
Ti	0.19	0.16	0.01
U_3O_8	−0.09	−0.17	0.11
W	**−0.23**	0.06	−0.11
Y	0.03	−0.02	0.06
Zr	**0.20**	0.17	0.01
Zn	−0.17	0.05	0.01

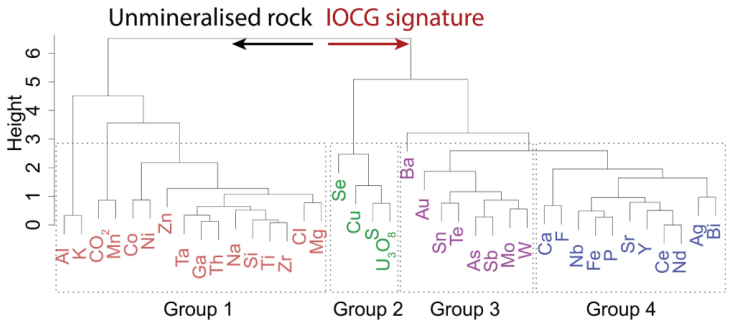


Fig. 3. Cluster dendrogram obtained from hierarchical cluster analysis of a 39-part geochemical sub-composition. The variation matrix (Appendix A; Table 2), which is based on pairwise logratios of the elements (Eq. (1)) , is used as a measure of dissimilarity.

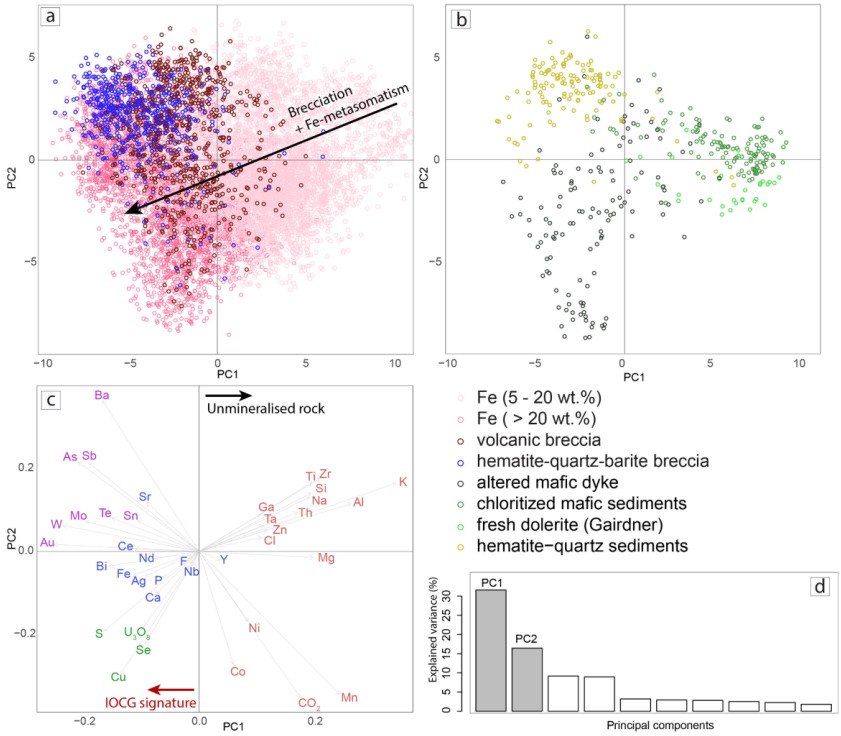


Fig. 4. The projected principal component scores of clr-transformed whole-rock data showing the dominant (a) and minor (b) lithological classes within the data (as in Table 1). Each data point represents a single sample. The principal component loadings (c) are color-coded to draw a comparison with the hierarchical dendrogram (Fig. 3). The scree plot illustrates the proportion of variance explained by each of the first ten principal components (d).

largest similarity with Ba. Finally, Group 4 encompasses a range of elements, including Ca, F, and REE (Ce and Nd) and the chalcophile elements Ag and Bi. The associations of elements presented in the dendrogram reflects the natural groups of elements mirrored by the combination of minerals.

4.2. Principal component analysis results

Principal component analysis of multi-element geochemical data after centred logratio transformation was used to examine relationship between elements in a 39-part sub-composition and reduce dimensionality.

The results of the PCA, including eigenvalues and loading of elements in PC1-3 are listed in Table 3. The graphs of the PC1-PC2 scores are split into two sub-charts to enhance the interpretability and visualization of the data. The biplot of PC1 and PC2 captures 31% and 16% of the total variation of the data, respectively (Fig. 4d). Because the sub-composition consists of both major and trace elements it is, therefore, assumed to reflect the major lithogeochemical variability, alteration patterns and geochemical affinities of trace elements. The PC1 is characterized by high positive loadings of K and Al. Both elements are largely hosted in RDG-derived K-feldspar, as well as in sericite and chlorite (the products of hydrothermal alteration of K-feldspar and micas). Elements associated with the mineralization in the ODBC, i.e., the IOCG-signature, appear on the opposite side of PC1; the largest loadings correspond to the association Au-W-Mo-As-Sb. The biplot (Fig. 4c) displays the multi-element associations of: (1) Ni-Co; (2) CO_2-Mn; (3) Zr-Th-Ti-Si-Na; (4) Cu-S-Se-U_3O_8; and (5) an element group comprising Ba, Sb, As, Mo, W and Au. We note that the element loadings displayed by PCs show subgroups of elements comparable to those suggested by the hierarchical cluster dendrogram (Fig. 3).

The two dominant sub-classes of hematite breccias, 5–20% and > 20% Fe, display a gradational change in whole-rock chemistry (Fig. 4a), whereas the least altered samples are those that show an association with granite-derived elements (e.g., K, Al and Si). In contrast, the whole-rock chemistry of breccias containing volcanic-clasts varies less, however this lithology is firmly tied to elements of Groups 1, 2 and 3 defining the IOCG signature.

Certain lithological classes display delineated clusters when plotted in PC1-PC2 space. Fresh dolerite and chloritized mafic sediments show a whole-rock chemistry that is distinct from that of altered mafic units. The latter stands out by the positive association with Group 2 elements. Quartz-baryte-bearing breccias, which is relatively depleted in Cu and U, are closely comparable with hematite-quartz sediments (Fig. 4a, b). The close resemblance between quartz-baryte-bearing breccia and hematite-quartz sediments is also underpinned by a correlation with the geochemical signature of the Ba, As, Sb, W, Mo and Au.

Based on the PCA results, a selection of groups of elements positively and inversely associated with the IOCG signature is presented below. These elements are split into groups and interpolated for each of the three sections, AA', BB' and CC'.

4.3. Delimitation of the ODBC from Roxby Downs Granite

The outline of the ODBC is defined by the logratio of K to Al, the distribution of PC1 scores, an isoline of Fe 20%, and the distribution of

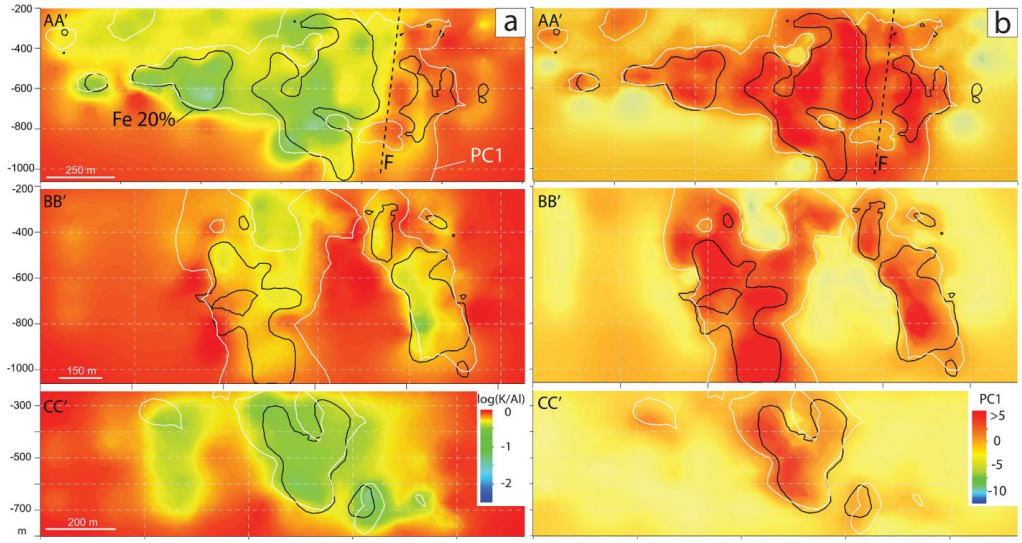


Fig. 5. Cross-sections AA', BB' and CC' illustrating kriged values of log-transformed molar ratio of K to Al (a) and PC1 scores derived from clr-transformed data (b). The kriged values are overlaid by isolines of 20 wt% Fe and PC1 scores that equal to zero.

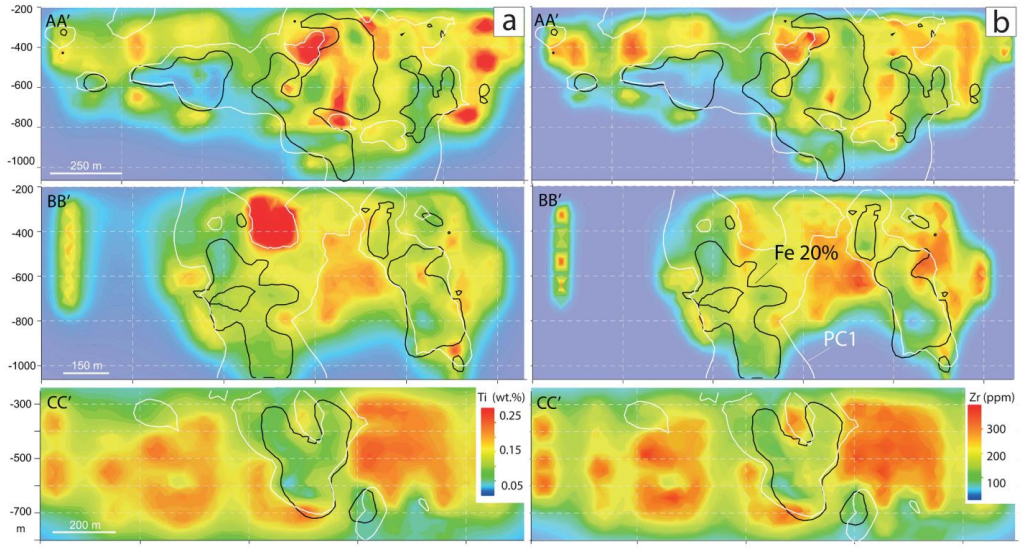


Fig. 6. Cross-sections AA', BB' and CC' showing the spatial distribution of Ti (in wt%) (a) and Zr (in ppm) (b) with an overlay of isolines of 20 wt% Fe and PC1 = zero.

Ti and Zr (Figs. 5 and 6). The logratio of K to Al maps out the extension of K-alteration enveloping the ODBC, while exhibiting the compositional variations of K and Al-bearing minerals (K-feldspar and sericite). Averaged out on the 15 m-interval whole-rock data, this logratio corresponds to the stoichiometry of K-feldspar if the logratio is equal to zero (Fig. 5a).

Similarly, the outline of ODBC is given by the kriged values of the PC1 scores, which are assigned to every sample in the dataset (Fig. 5b). In analogy with a clr-biplot, where principal component scores are displayed in two dimensions (Fig. 4a, b), the interpolation of scores in three dimensions allows investigation of their spatial distributions. An outline of PC1 scores equalling zero accurately delineates the ODBC from its host rocks. Samples with a positive score on PC1, i.e., placed within the outline, correspond to a lithogeochemical signature of IOCG mineralization within the ODBC, and correspond to negative values of $ln\left(\frac{K}{Al}\right)$. Notably, areas characterized by an occurrence of chloritized mafic sediments (sections BB' and CC'; Fig. 2) are defined by negative $ln\left(\frac{K}{Al}\right)$ and PC1.

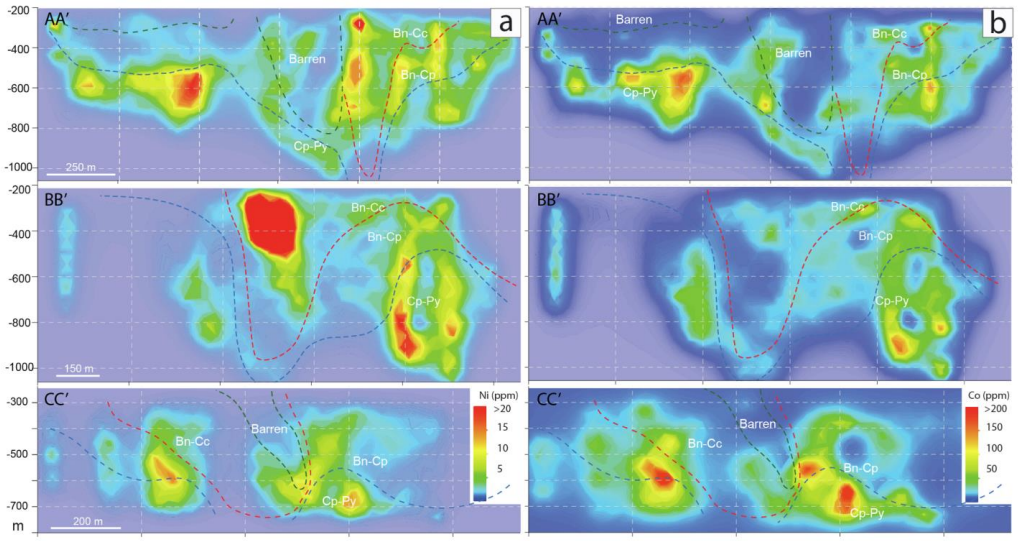


Fig. 7. Spatial distribution of (a) Ni and (b) Co (in ppm) in vertical cross-sections AA', BB' and CC'. The Cu(-Fe)-sulphide interfaces are estimates of modal mineralogy as in Fig. 2 (see Section 3.5).

The high field strength elements (HFSE), particularly, Ti and Zr, reflect the geochemical signature of the RDG (Figs. 4a, c and 6). The highest absolute concentrations of both elements occur outside the 20 wt% Fe outline and show an inverse association with Fe metasomatism in PC1, thus confirming that the ODBC is HFSE-depleted relative to the host granite. Furthermore, Ti points to the occurrences of mafic units, i.e., blocks of chloritized mafic sediments in shallower parts of section CC' and fresh Gairdner dolerite in section BB' (Fig. 6a).

4.4. Element distributions

4.4.1. Element pairs Ni-Co, Mn-CO_2 and Nb-Ta

Although Ni-Co and Mn-CO_2 fall within Group 1 on the dendrogram, these elements form an individual cluster observed in the PC1-PC2 projection (Fig. 4c). Such a slight yet noticable discrepancy could be attributed to the nature of these statistical analyses. The clustering algorithm partitions elements into the best possible homogenous groups by minimizing within-group similarities. On the other hand, PCA extracts the patterns that represent the highest variance in the data whereas it does not maximize the separation between the group.

Nickel and Co both show interrelation with Cu(-Fe)-sulphide zoning. Both elements are relatively enriched in the Py-Cp and Cp-Bn zones but are relatively depleted in the Bn-Cc zone (Fig. 7). Both elements can occur within pyrite and chalcopyrite, and as associated thiospinel and arsenic-sulphides of the arsenopyrite group, minerals which are rare or absent in bornite-chalcocite ores. Despite the significant spatial-geochemical similarities, the Ni-Co pair distribution has significant discrepancies that are attributed to zones of high-Ni and low-Co concentrations. These zones are specifically characterized by chloritized mafic sediments placed at shallow depths and as blocks in sections CC' and BB' (Fig. 7a).

The Mn-CO_2 pair displays a distribution resembling that of Ni-Co, but does not, however, correspond to Cu(-Fe)-zonation (Fig. 8). All four elements (Ni, Co, Mn and CO_2) typify the occurrences of fresh dolerite and altered mafic dykes, as for instance, in section BB', outside the positive PC1 values. In addition, these elements typify the occurrence of geochemical anomaly in volcanic and sericite-bearing hematite breccias in section CC' at a depth of ~800 m (Fig. 8). Despite the depletion in Group 3 elements (Au-W-Mo-Sb-As), this zone is placed within the PC1 values. Here, the pairs Ni-Co and Mn-CO_2 are highly correlated and correspond to samples containing Cu (~0.8 wt%) and U_3O_8 (~180 ppm) while showing an inverse association with Group 3 elements.

As revealed by the PCA, the ODBC exhibits a considerable decoupling between Nb and Ta. Not only is the latter reflected in PC1 (Fig. 4c) but also in the sections displaying the element distributions. Tantalum is a granite-derived element mostly concentrated outside of the Fe > 20 wt% outline and does not contribute to the IOCG signature. In contrast, Nb belongs to Group 2 elements and is concentrated in high-Fe zones, and especially in the altered mafic dyke from section AA' and at depth in section BB' (Fig. 9). Despite the strong decoupling of the two elements at higher concentrations, modest concentrations of Nb (up to 50 ppm) show patterns similar to Ta.

4.4.2. The U_3O_8-Se association

Group 2 contains the element pair U_3O_8-Se, which are closely associated as shown by the biplot, dendrogram, and variation matrix (Table 2). Group 2 is clearly related to the IOCG signature, as defined by PC1, but also displays a correlation with the granitophile elements. Notably, low U values, up to 200 ppm, are spatially correlated with granitophile elements (Figs. 10a and 11a–c). However, certain lithologies, such as quartz-baryte bearing breccias, appear relatively depleted in U despite being enriched in granitophile elements (Fig. 10a).

Despite U showing a good overlap with the Fe 20 wt% outline, high U values also exist outside the Fe contour, as seen in upper parts of section CC' and also section AA' (Fig. 10a). Notably, in the NW arm, U does not show an association with Fe metasomatism and even features relatively high values of 300 ppm on the eastern areas of AA' (Fig. 10a). As seen from cross-sections, U is strongly associated with Se although there are discrepancies in some areas, as for example, the high Se concentrations outside the IOCG outline (section CC'; Fig. 10b). In general, these elements are depleted in quartz-baryte bearing breccias in the central part of section BB' and also in chloritized mafic sediments (section CC'; Fig. 10).

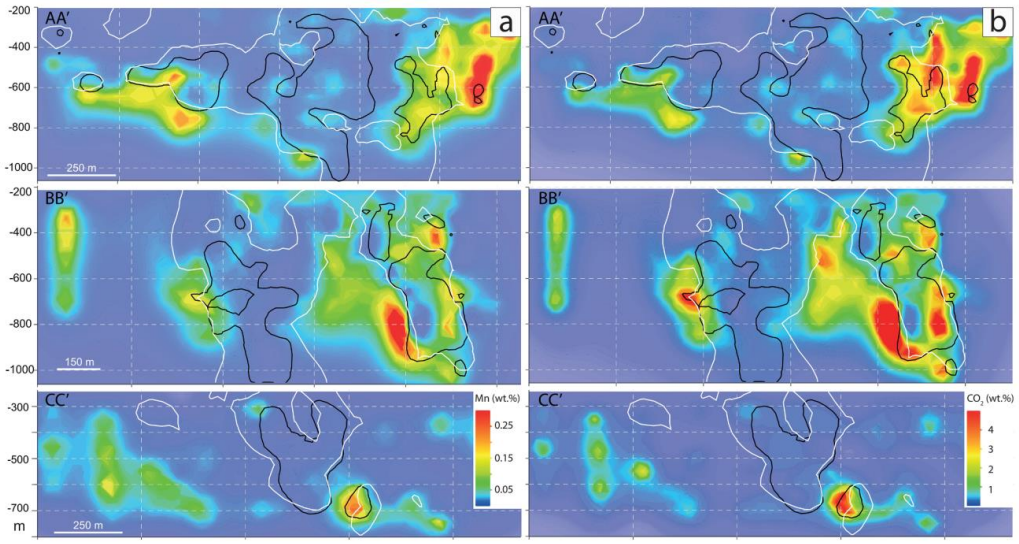


Fig. 8. Spatial distribution of (a) Mn and (b) CO_2 (in wt%) in cross-sections AA', BB' and CC' with overlay of 20 wt% Fe and PC1 = zero. Note the Mn-CO_2 geochemical anomaly in BB' at 800 m depth.

4.4.3. Granitophile elements (W-Sn-Mo)

Granitophile elements show close spatial-geochemical similarities as given by both PCA and the hierarchical dendrogram. Group 3 is specifically characterised by a lack of correlation with chloritized mafic sediments (Fig. 4b, c) and displays a strong relationship with Fe-metasomatism.

The granitophile elements, W, Sn and Mo, are ubiquitous throughout the ODBC and are consistently measurable above minimum limits of detection. Tungsten and Mo show a significant association with each other (τ_{WMo} = 0.6; Table 2), which is reflected in their spatial distributions. In contrast, the element pairs Sn and Mo (τ_{SnMo} = 1.1), and Sn and W (τ_{SnW} = 0.9) are slightly less associated although they still exhibit a remarkable spatial correlation (Fig. 11). Such a feature may be attributed to chalcopyrite, which is recognized as a systematic carrier of Sn (Ciobanu, 2015), whereas Mo and W are largely contained within hematite. Despite this, the absolute concentrations of granitophile elements are strongly linked to Fe-metasomatism and are thus always placed within the 20% Fe and PC1 outlines. This is readily reconciled by

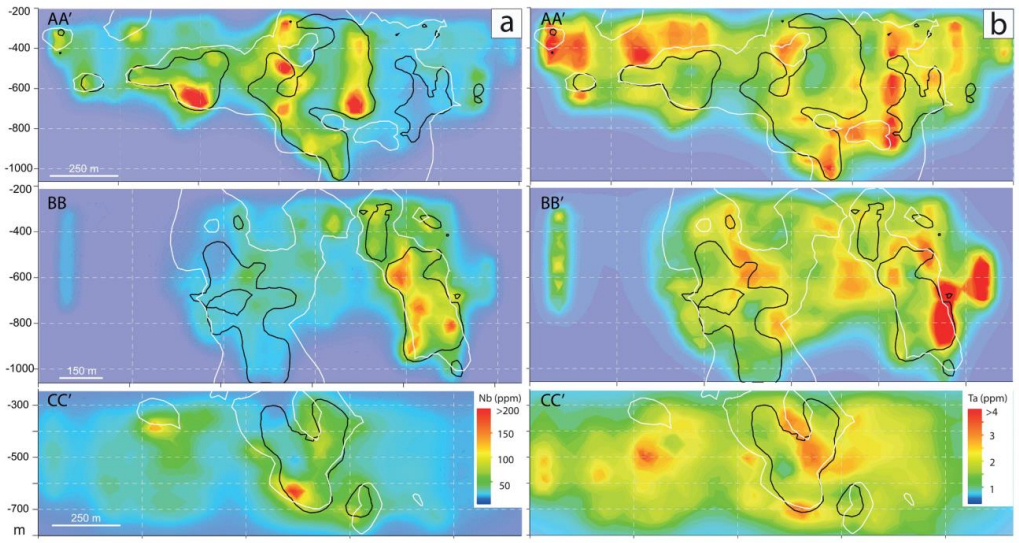


Fig. 9. The distribution of (a) Nb and (b) Ta (in ppm) in vertical cross-sections AA', BB' and CC' with the 20 wt% Fe and PC1 = zero isolines. Note the positive Ta anomalies outside of the PC1 = zero outline.

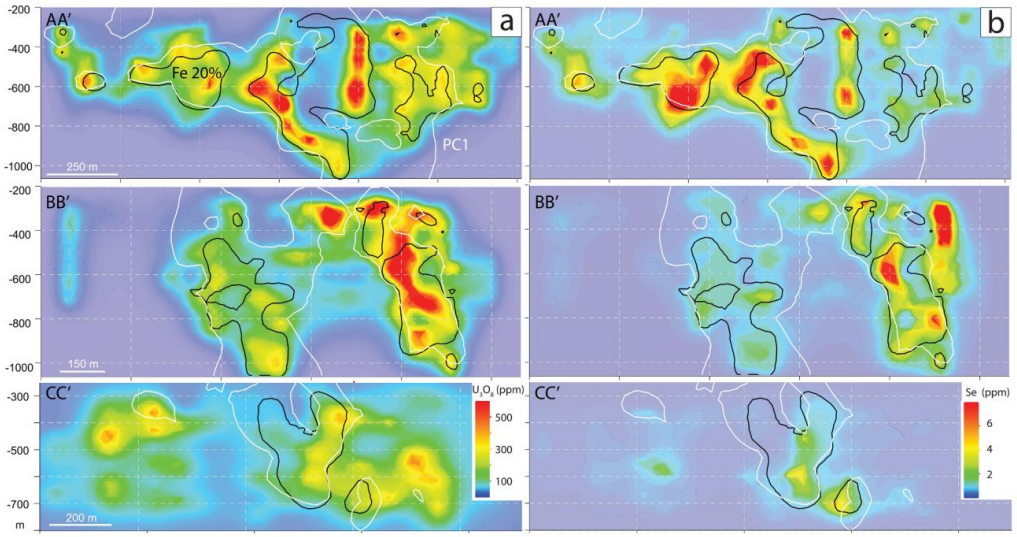


Fig. 10. Vertical cross-sections AA', BB' and CC' showing the distribution of (a) U_3O_8 and (b) Se (in ppm) with an overlay of 20 wt% Fe and PC1 = zero. Note the significant spatial correlation between U_3O_8 and Se.

the fact that these elements are almost exclusively hosted within hematite. The highest absolute concentrations of all granitophile elements are within drillhole RD1988 in the deepest part of section CC' (below 1400 m) and in the adjacent drillholes RD1999 and RD1960. In contrast, section AA' from the NW arm features local enrichment of granitophile elements at shallow levels and only very minor concentrations at depth (Fig. 11).

4.4.4. Chalcophile and related elements (As-Sb and Au-Te)

Although expected, the chalcophile elements Ag and Bi do not display a significant spatial correlation with one another. The cross-sections (Fig. 12) do not resolve a vertical zonation with respect to Ag and Bi, which contrasts with Ni-Co (showing a strong affiliation to the Py-Cp zone). Silver and Bi are present in all Cu-(Fe)-sulphide zones. Notably, both elements show a relative depletion in the quartz-hematite-bearing breccia (section AA'), and also in chlorite-bearing mafic sediments.

The other element pairs falling within Group 3 (As-Sb and Au-Te) are reasonably proportional, $\tau_{AsSb} = 0.4$ and $\tau_{AuTe} = 1.5$ (Table 2), thus exhibiting spatial correlation (section CC'; Figs. 13-14). All four elements are linked to Fe-metasomatism and correlate strongly with the granitophile elements, as seen in section CC', which shows enrichment in granitophile elements and As-Sb-Au-Te along the vertical mineralized corridor placed within the PC1 outline (Figs. 11, 13 and 14). However, Au is somewhat anomalous in that it displays low concentration in zones corresponding to quartz-baryte-bearing hematite breccias (section BB'; Fig. 14a). Nonetheless, shallow parts of the northern side of section AA' display relative enrichment in As and Te while showing high PC1 values and low Fe content (Figs. 13a and 14b). In the NW arm (section CC', Figs. 13 and 14), As-Sb and Au-Te, like the granitophile elements, show enrichment at shallow depths.

5. Discussion

5.1. Definition of an IOCG signature through PCA

Although the mineralogy of the OD deposit is well-characterised (Ehrig et al., 2012, 2017, and references therein), the low resolution-spacing multi-element whole-rock dataset analysed here lacks direct petrographic and mineralogical information. Inferences about the trace abundance mineralogical composition of individual samples can be made without the use of the mineral liberation analysis modal mineralogy dataset. This is due to the direct relationship between patterns and trends within the bulk geochemical data with the corresponding stoichiometries of ore- and rock-forming minerals (Aitchison, 1999). Overall, the PC1 reflects the averaged stoichiometric transition from RDG to hematite-dominant breccias, and displays a close overlap with geochemical changes associated with Fe-metasomatism (Fig. 5). Such a transition, as given by PC1, defines the specific IOCG mineralisation signature of the ODBC.

In magmatic-hydrothermal IOCG systems, such a signature is expected to contain the element association of Fe, Cu and Au defining the commodities exploited from the deposit, and/or minor elements that are characteristically anomalous in IOCG systems, notably U, REE, Ag and Co, but also including a broad range of other trace elements (Barton, 2014). The obtained IOCG signature encompasses the expected range of metals (Fig. 4c; Table 3). Notably, the range of metals that contribute to the IOCG signature are comparable to those of typical Cu ± Au ± Mo porphyry systems (Berger et al., 2008), since the IOCG signature evidently contains Mo, Ag, Ba, As, Sb and Te alongside Cu and Au (Fig. 4c). Overall, ore-forming processes in porphyry and IOCG systems likely share many similarities, such as magmatic affinity and enrichment in Fe (Richards and Mumin, 2013), and therefore these ore deposits will display a comparable range of metals. The similarities between the two groups of ore systems is intimately linked to crustal-scale processes, i.e., subduction and crustal extension, and input of metals from deep crust with mafic/mantle input (Skirrow et al., 2007; Groves et al., 2010; Richards et al., 2017).

The PCA results recognise two distinct associations (Au-W-Mo-Sb-As and S-Cu-Se-U_3O_8; Fig. 4c) within the IOCG signature. These associations are readily explained by their different spatial distribution. The Au-W-Mo-As-Sb group is spatially correlated with hematite and volcanic breccias, especially at depths below 1200 m, as well as in generally shallow quartz-baryte-bearing breccias (Figs. 11b, c, 13, and 14a). Although measured throughout the ODBC above the limits of detection, these elements are concentrated over the entire ~1800 m vertical extent of the mineralization and remain open at depth. The

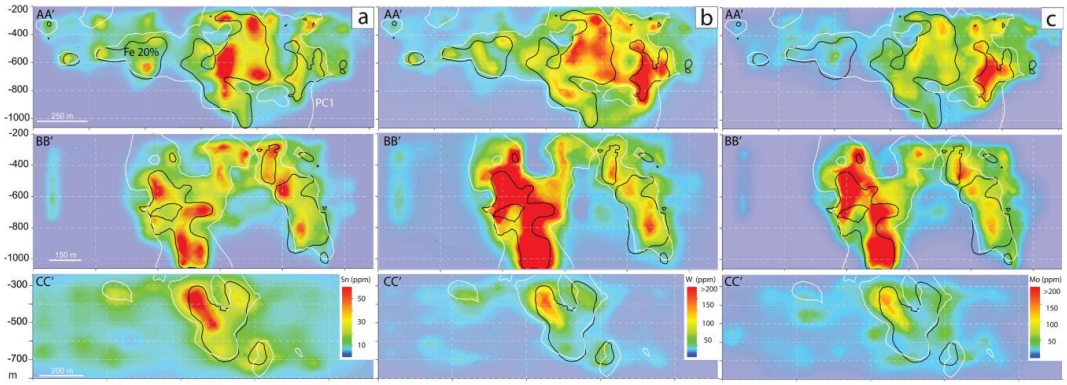


Fig. 11. The distribution of granitophile elements (a) Sn, (b) W, and (c) Mo in the vertical cross-sections AA', BB' and CC'. Note the great dependency of 20 wt% Fe outline and geochemical anomalies of granitophile elements.

concentration of elements along the vertical mineralized corridor is likely to be related to major structural feature such as a major subvertical WSW-ENE striking fault system (Fig. 1). On the other hand, the distribution of Cu mineralization, and to some extent also U, is known to be concentric (Ehrig et al., 2012), and as shown here, appears spatially independent from the Au-W-Mo-As-Sb association.

The Au-W-Mo-As-Sb signature can be attributed to a range of minerals, but is overwhelmingly related to compositionally-zoned hematite, which hosts most of the W, Mo and Sn throughout the deposit, as well as a significant part of the U (Verdugo-Ihl et al., 2017), and to sulphides hosting Sb and As: pyrite (As); tetrahedrite-tennantite (Sb-As); and cobaltite (As) (Ehrig et al., 2012). Gold is mostly in native form, alloyed with Ag (and rarely Cu), or as Au(± Ag)-tellurides, occurring as inclusions in sulphides and hematite.

Although mineral parageneses and ore-forming processes can only be inferred from whole rock data, the abundant body of metasomatic hematite endowed with W-Sn (± U-Mo) can be considered to represent a primary hydrothermal event in the ODBC. The Au-W-Mo-As-Sb association includes As, Sb and Au, elements which in some magmatic-hydrothermal systems (e.g., porphyry deposits) are considered as a shallow expression of mineralization (e.g., Richards and Mumin, 2013). Given that, we suggest the vertical 1800 m deep mineralized corridor anomalous in Au-W-Mo-As-Sb may represent a hydrothermal-fluid conduit. This is because the observed lithologies in the SE lobe (volcanic and sedimentary rocks) are all displaying the same IOCG signature and thus have been incorporated within the granite along a subvertical fault prior to, or during the onset of the mineralising system. On the other hand, the deep mineralized corridor may represent a subvertical fault system which hosts IOCG-signature bearing/mineralized breccias and sediments that were structurally incorporated into the ODBC from the shallower levels of the deposit. Thus, the occurrence of the mineralized corridor within a fault system may explain the geochemical signature documented along drillhole RD1988 which contains a wide variety of preserved, early paragenetic sequences

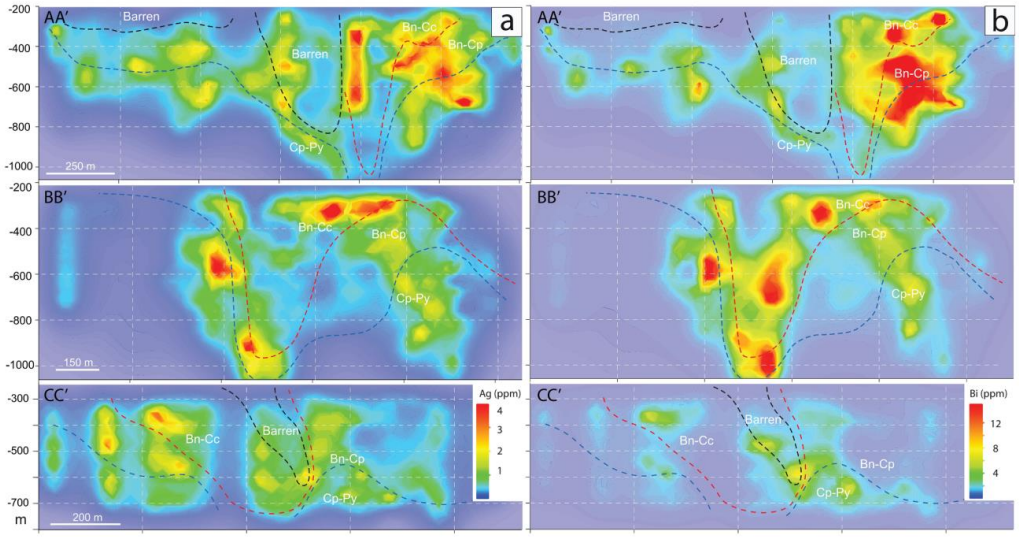


Fig. 12. Illustration of the vertical cross-sections AA', BB' and CC' showing the distributions of (a) Ag and (b) Bi with an overlay of interfaces of the estimated normative Cu-(Fe)-sulphide mineralogy (see Section 3.5).

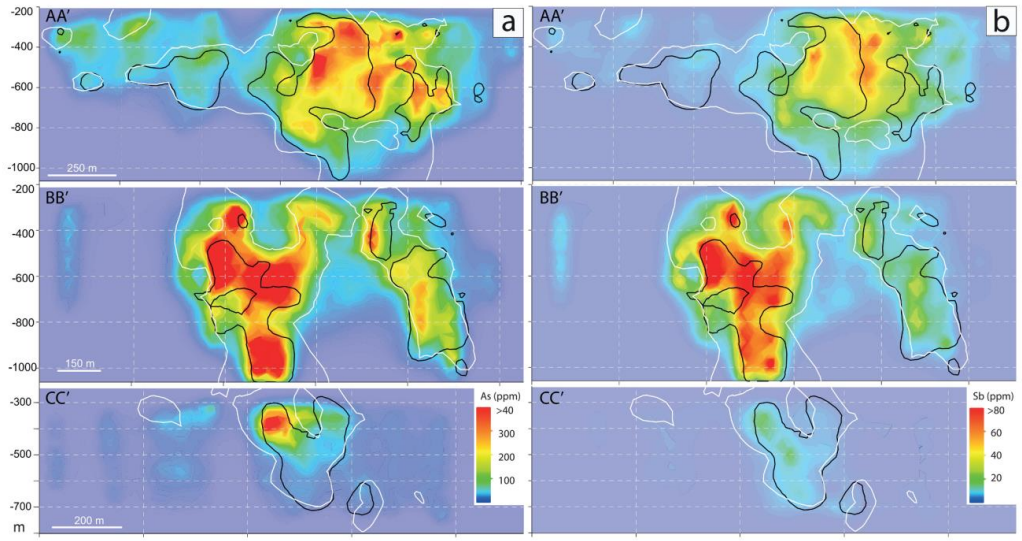


Fig. 13. Spatial distribution of (a) As and (b) Sb in vertical cross-sections AA', BB' and CC' with 20 wt% Fe and PC1 = zero outlines. Note the high spatial dependency between As and Sb geochemical anomalies and Fe-rich (> 20 wt%) zones.

combined with the expressions of superimposed multi-stage remobilization and redistribution of ore components. Overall, the Au-W-Mo-As-Sb association represents a significant pathfinder element group and is likely present in other IOCG deposits within the Olympic Cu-Au Province.

5.2. Lithogeochemistry of the Olympic Dam Breccia Complex

Although the extensive sampling grid covers the ODBC, no geochemical gradients could be recognised in PC1 other than those showing a match between certain breccia types/lithologies and the overall IOCG signature defined by the PC1 (Fig. 5b). Nevertheless, as shown here, the PCA is an effective tool to underpin multi-element signatures with lithological units.

Despite the close relationship between PC1 and > Fe 20 wt%, if compared to the cross-section (Fig. 5b), the distribution of positive PC1 values only partially overlaps with the distribution of > 20 wt% Fe hematite breccias and vice versa. This discrepancy may suggest that mineralization is not associated with Fe-metasomatism in some parts of the deposit. In turn it can be inferred that either (i) some sulphide accumulations do not coincide with Fe-metasomatism and represent the products of later sulphide remobilization, e.g., sulphide-rich veins on

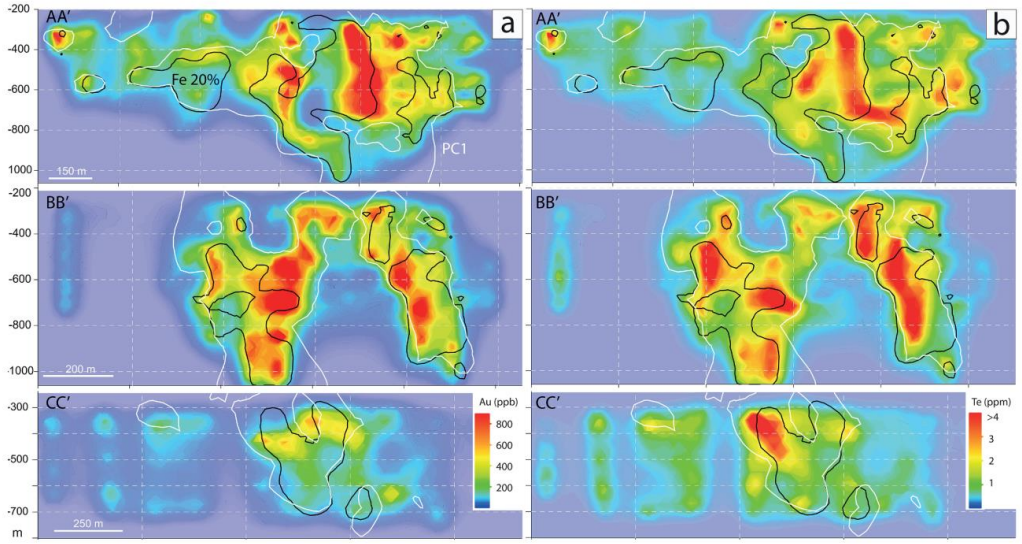


Fig. 14. Vertical cross-sections AA', BB' and CC' and corresponding distributions of (a) Au and (b) Te with an overlay of 20 wt% Fe and PC1 = zero.

the periphery of the ODBC in zones of only weak Fe-metasomatism, or (ii) that some Fe-rich pockets may pre- or postdate IOCG mineralization, e.g., preserved fragments of older Fe-rich sedimentary rocks. In addition, a distinct style of mineralization on the outer margins of the deposit, notably in the northwestern arm (Fig. 10a), may contribute to the observed discrepancy between PC1 and Fe.

The PC1 depicts the lack of IOCG signature in chlorite-bearing mafic sediments as given by the PC1-PC2 projection and the cross-sections (Fig. 5b). Although Cu-bearing minerals are present in chlorite-bearing mafic sediments (up to ~1.5 wt% Cu), the lack of an IOCG signature implies that the provenance of these sediments is unrelated to the IOCG mineralizing process. In contrast, hematite-quartz sediments are characterized by the IOCG signature. This may suggest that the latter sediments are partially sourced from ODBC rocks (McPhie et al., 2016), or nearby, eroded IOCG systems. Interestingly, altered mafic-ultramafic units, coeval with emplacement of RGD, within the ODBC also display IOCG signatures, and substantial enrichment in Cu and U. The latter supports the coeval bimodal magmatism immediately preceding initiation of hydrothermal activity that precipitated IOCG mineralization (Huang et al., 2016) (Fig. 5b).

5.3. Vertical zonation

Since the Cu-(Fe)-sulphides display vertical and lateral zonation, it is expected that certain chalcophile/siderophile elements should either reproduce such a zonation, or give additional gradients. Nickel and Co are closely associated with pyrite in the deeper pyrite-chalcopyrite parts of the ODBC (Fig. 7), in accordance with empirical observations of Ni- and Co-bearing minerals (pyrite, carrollite and cobaltite) within the Py-Cp zone (Ehrig et al., 2012). In contrast, the Bn-Cc zone features a relative depletion in Ni and Co at shallower depths (Fig. 7), corresponding to the low (often below minimum limits of detection) concentrations of Ni and Co in bornite and chalcocite (Ciobanu, 2015).

In contrast, Ag and Bi, are chalcophile elements and are readily partitioned into bornite (Bi > Ag) and chalcocite/digenite (Ag < Bi) (Cook et al., 2011). Therefore, Ag and Bi might be expected to display a relative enrichment at shallow levels within the ODBC. No such systematic patterns are, however, resolvable. Multiple explanations can be found for such discordance, possibly the most important being the sampling resolution, which may be inadequate to resolve the zonation in detail. Subordinate explanations include the presence of both Ag and Bi as discrete, sub-micron-scale inclusions of minor telluride and sulphosalt phases (e.g., hessite, tetradymite, wittichenite) in sulphides and other minerals throughout the deposit, and also the presence of Ag within chalcopyrite at depth in the absence of either chalcocite and bornite (Ciobanu, 2015).

5.4. Geochemical trends and associations

Oscillatory-zoned hematite, which is found throughout the 1800 m vertical extent of mineralization (Verdugo-Ihl et al., 2017), contains elevated concentrations of U, W, Sn and Mo. The same geochemical signature also occurs throughout the whole-rock samples in the ODBC, however, whole-rock data show a spatial separation between U and the remaining granitophile elements. As seen in Fig. 10a, concentrations of up to 200 ppm U correlate with W-Sn-Mo but that correlation diminishes at higher U concentrations. The three main U-bearing minerals are uraninite, brannerite and coffinite (Macmillan et al., 2016a, 2017), together accounting for ~80–85% of total U. These minerals are dispersed throughout the ODBC, occur as inclusions in hematite, sulphides and most other minerals, and also display extensive evidence of breakdown, replacement, remobilization and re-concentration (Macmillan et al., 2016a, 2017). Although these processes are readily recognizable in drillcore specimens and polished mounts, their scale and impact on deposit-scale U distributions are less well constrained and are only partially resolved by the whole-rock dataset. Moreover, the radioactive decay of U-bearing minerals and migration of daughter radionuclides and radiogenic lead is also observed at the scale of nanometres upwards (Rollog et al., 2019).

Analyses of the whole-rock data exhibit a remarkably strong U_3O_8-Se-Cu-S association throughout the ODBC (Fig. 10), in which Se and U_3O_8 are particularly strongly correlated. A partial explanation for such a trend is found within the preferential partitioning of Se into Cu(-Fe)-sulphides (e.g., Cook et al., 2011; George et al., 2016), where it substitutes for S. Selenide minerals are generally rare at OD but the most abundant of these, clausthalite (PbSe) can readily form via interaction between sulphide-hosted Se and remobilized radiogenic Pb as shown in other IOCG deposits from the Gawler Craton (Owen et al., 2018).

A further geochemical trend is attributed to the positive anomaly of CO_2, Mn, Co, Ni and Nb in section BB'. This zone, which is also mineralized and contains ~50 wt% Fe based on whole-rock data, differs significantly from the remaining data set. This is due to this association being attributed to a pyrite-magnetite-apatite-siderite assemblage which can be regarded as a geochemical signature specific to deep, peripheral, relatively-reduced Fe-oxide alteration.

6. Conclusions and outlook

Application of PCA and hierarchical clustering to large whole-rock data sets is an effective way to underpin spatio-geochemical associations and delineate an orebody in a disseminated mineral system. Recognition of multi-element geochemical signatures is important in the ODBC because despite the presence of generally common elements (Fe, Cu and Au), there are other accompanying indicator elements such as W, Mo, As and Sb. Trace elements contributing to the multi-element IOCG signature are likely to be common within other IOCG systems in the Olympic Cu-Au Province and can be utilized as vectors in near-mine exploration.

Further work should address IOCG signatures within prospects adjacent to OD displaying similar but not identical mineralization style, e.g., at Wirrda Well and Acropolis (Krneta et al., 2017), to understand the fundamental mineralogical, geochemical and genetic controls on trace element distribution patterns. Considerable opportunity therefore exists for testing whether granitophile signature are unique to the ODBC, or are ubiquitous throughout IOCG deposits of the Olympic Cu-Au Province, and potentially, also elsewhere.

The PC1 gives neither solid gradients nor defines zonation within the ODBC. Similarly, the individual trace element dispersion patterns within the ODBC cannot capture the zonation due to the low-resolution of the whole-rock data, complex partitioning patterns dependent on a range of factors, and superimposed processes that have modified primary distribution patterns. Therefore, considering the complexity of ore assemblages in response to multiple episodes of mineral dissolution and (re)precipitation, trace element signatures in individual minerals, e.g., Cu(-Fe)-sulphides, or Fe-oxides, may prove more efficient at constraining the spatiotemporal evolution of the ODBC. The variations in trace element signatures in individual minerals may provide systematic geochemical tracers that can be interpreted in terms of prograde and retrograde hydrothermal fluid evolution. Such an approach, if coupled with careful textural and compositional characterisation of relevant minerals, can be used to define vertical/lateral zonation to underpin the evolution of the system in space and time.

Acknowledgments

This work is a contribution to the FOX project 'Trace elements in iron-oxides: deportment, distribution and application in ore genesis, geochronology, exploration and mineral processing', supported by BHP Olympic Dam and the South Australian Mining and Petroleum Services Centre of Excellence. N.J.C. acknowledges additional support from the ARC Research Hub for Australian Copper-Uranium (Grant IH130200033). Constructive comments from an anonymous reviewer

and Editor-in-Chief Franco Pirajno are highly appreciated.

Appendix A. Supplementary data

Supplementary data to this article can be found online at https://doi.org/10.1016/j.oregeorev.2018.12.013.

References

Aitchison, J., 1986. The statistical analysis of compositional data. Monographs on Statistics and Applied Probability. Chapman & Hall, London http://dx.doi.org/10.1007/978-94-009-4109-0.

Aitchison, J., 1999. Logratios and natural laws in compositional data analysis. Math. Geol. 31, 563–580. https://doi.org/10.1023/A:1007568008032.

Allen, S.R., McPhie, J., Ferris, G., Simpson, C., 2008. Evolution and architecture of a large felsic Igneous Province in western Laurentia: the 1.6 Ga Gawler Range Volcanics, South Australia. J. Volcanol. Geotherm. Res. 172, 132–147. https://doi.org/10.1016/j.jvolgeores.2005.09.027.

Apukhtina, O.B., Kamenetsky, V.S., Ehrig, K., Kamenetsky, M.B., Maas, R., Thompson, J., McPhie, J., Ciobanu, C.L., Cook, N.J., 2017. Early, deep magnetite-fluorapatite mineralization at the Olympic Dam Cu-U-Au-Ag deposit, South Australia. Econ. Geol. 112, 1531–1542. https://doi.org/10.5382/econgeo.2017.4520.

Barton, M.D., 2014. Iron oxide (–Cu–Au–REE–P–Ag–U–Co) systems. In: Holland, H.D., Turekian, K.K. (Eds.), Treatise on Geochemistry,, second ed. Elsevier, Oxford, pp. 515–541 https://doi.org/10.1016/B978-0-08-095975-7.01123-2.

Berger, B.R., Ayuso, R.A., Wynn, J.C., Seal, R., 2008. Preliminary model of porphyry copper deposits. In: USGS Numbered Series Open-file Report, pp. 55 https://doi.org/10.3133/ofr20081321.

Chen, S., Hattori, K., Grunsky, E.C., 2017. Multielement statistical evidence for uraniferous hydrothermal activity in sandstones overlying the Phoenix uranium deposit, Athabasca Basin, Canada. Mineral. Deposita 53, 493–508. https://doi.org/10.1007/s00126-017-0756-2.

Cherry, A., Ehrig, K., Kamenetsky, V.S., McPhie, J., Crowley, J., Kamenetsky, M., 2018. Precise geochronological constraints on the origin, setting and incorporation of ca. 1.59 Ga surficial facies into the Olympic Dam Breccia Complex, South Australia. Precambr. Res. 315, 162–168. https://doi.org/10.1016/j.precamres.2018.07.012.

Ciobanu, C.L., 2015. Trace element signatures in sulphides at Olympic Dam and satellite prospects: a reconnaissance study for ore vectoring using Cu-(Fe)-sulphides in Iron Oxide Copper Gold Deposits. Unpublished Report. The University of Adelaide.

Ciobanu, C.L., Wade, B.P., Cook, N.J., Schmidt Mumm, A., Giles, D., 2013. Uranium-bearing hematite from the Olympic Dam Cu-U-Au deposit, South Australia: a geochemical tracer and reconnaissance Pb-Pb geochronometer. Precambr. Res. 238, 129–147. https://doi.org/10.1016/j.precamres.2013.10.007.

Ciobanu, C.L., Cook, N.J., Ehrig, K., 2017. Ore minerals down to the nanoscale: Cu-(Fe)-sulphides from the iron oxide copper gold deposit at Olympic Dam, South Australia. Ore Geol. Rev. 81, 1218–1235. https://doi.org/10.1016/j.oregeorev.2016.08.015.

Conor, C., Raymond, O., Baker, T., Teale, G., Say, P., Lowe, G., 2010. Alteration and mineralisation in the Moonta-Wallaroo Cu–Au mining field region, Olympic domain, South Australia. In: Porter, M. (Ed.), Hydrothermal Iron Oxide Copper-Gold and Related Deposits: A Global Perspective 3. PGC Publishing, Adelaide, pp. 1–24.

Cook, N.J., Ciobanu, C.L., Danyushevsky, L.V., Gilbert, S., 2011. Minor and trace elements in bornite and associated Cu–(Fe)-sulfides: a LA-ICP-MS study. Geochim. Cosmochim. Acta 75, 6473–6496. https://doi.org/10.1016/j.gca.2011.08.021.

Creaser, R.A., 1989. The Geology and Petrology of Middle Proterozoic Felsic Magmatism of the Stuart Shelf, South Australia. Unpublished Ph.D. thesis. La Trobe University, Melbourne, Australia.

Ehrig, K., McPhie, J., Kamenetsky, V., 2012. Geology and mineralogical zonation of the olympic dam iron oxide Cu-U-Au-Ag deposit, South Australia. Soc. Econ. Geol. Spec. Pub. 16, 237–267.

Ehrig, K., Kamenetsky, V., McPhie, J., Cook, N.J., Ciobanu, C.L., 2017. Olympic Dam iron-oxide Cu-U-Au-Ag deposit. In: Phillips, G.N. (Ed.), Australian Ore Deposits. AusIMM, Melbourne, pp. 601–610.

Gabriel, K.R., 1971. The biplot graphical display of matrices with application to principal component analysis. Biometrika 58, 453–467. https://doi.org/10.1093/biomet/58.3.453.

George, L.L., Cook, N.J., Ciobanu, C.L., 2016. Partitioning of trace elements in co-crystallized sphalerite–galena–chalcopyrite hydrothermal ores. Ore Geol. Rev. 77, 97–116.

Groves, D.I., Bierlein, F.P., Meinert, L.D., Hitzman, M.W., 2010. Iron Oxide Copper-Gold (IOCG) deposits through earth history: implications for origin, lithospheric setting, and distinction from other epigenetic iron oxide deposits. Econ. Geol. 105, 641–654. https://doi.org/10.2113/gsecongeo.105.3.641.

Grunsky, E., 2010. The interpretation of geochemical survey data. Geochem. Explor. Env. A. 10, 27–74. https://doi.org/10.1144/1467-7873/09-210.

Grunsky, E., Mueller, U.A., Corrigan, D., 2014. A study of the lake sediment geochemistry of the Melville Peninsula using multivariate methods: applications for predictive geological mapping. J. Geochem. Explor. 141, 15–41. https://doi.org/10.1016/j.gexplo.2013.07.013.

Guilbert, J.M., Park, C.F., 1986. The Geology of Ore Deposits. W.H. Freeman and Co, London, pp. 985.

Helsel, D., 2006. Fabricating data: How substituting values for nondetects can ruin results, and what can be done about it. Chemosphere 65, 2434–2439. https://doi.org/10.1016/j.chemosphere.2006.04.051.

Hitzman, M.W., Oreskes, N., Einaudi, M.T., 1992. Geological characteristics and tectonic setting of Proterozoic iron oxide (Cu-U-Au-REE) deposits. Precambr. Res. 58, 241–287. https://doi.org/10.1016/0301-9268(92)90121-4.

Huang, Q., Kamenetsky, V.S., McPhie, J., Ehrig, K., Meffre, S., Maas, R., Thompson, J., Kamenetsky, M., Chambefort, I., Apukhtina, O., Hu, Y., 2015. Neoproterozoic (ca. 820–830 Ma) mafic dykes at Olympic Dam, South Australia: links with the Gairdner Large Igneous Province. Precambr. Res. 271, 160–172. https://doi.org/10.1016/j.precamres.2015.10.001.

Huang, Q., Kamenetsky, V.S., Ehrig, K., McPhie, J., Kamenetsky, M., Cross, K., Meffre, S., Agangi, A., Chambefort, I., Direen, N.G., Maas, R., Apukhtina, O., 2016. Olivine-phyric basalt in the Mesoproterozoic Gawler silicic large igneous province, South Australia: examples at the Olympic Dam Iron Oxide Cu–U–Au–Ag deposit and other localities. Precambr. Res. 281, 185–199. https://doi.org/10.1016/j.precamres.2016.05.019.

Ismail, R., Ciobanu, C.L., Cook, N.J., Teale, G.S., Giles, D., Schmidt Mumm, A., Wade, B., 2014. Rare earths and other trace elements in minerals from skarn assemblages, Hillside iron oxide–copper–gold deposit, Yorke Peninsula, South Australia. Lithos 184–187, 456–477. https://doi.org/10.1016/j.lithos.2013.07.023.

Kontonikas-Charos, A., Ciobanu, C.L., Cook, N.J., 2014. Albitization and redistribution of REE and Y in IOCG systems: insights from Moonta-Wallaroo, Yorke Peninsula, South Australia. Lithos 208–209, 178–201. https://doi.org/10.1016/j.lithos.2014.09.001.

Kontonikas-Charos, A., Ciobanu, C.L., Cook, N.J., Ehrig, K., Krneta, S., Kamenetsky, V.S., 2017. Feldspar evolution in the Roxby Downs Granite, host to Fe-oxide Cu-Au-(U) mineralisation at Olympic Dam, South Australia. Ore Geol. Rev. 80, 838–859. https://doi.org/10.1016/j.oregeorev.2016.08.019.

Krneta, S., Ciobanu, C.L., Cook, N.J., Ehrig, K., Kontonikas-Charos, A., 2016. Apatite at Olympic Dam, South Australia: a petrogenetic tool. Lithos 262, 470–485. https://doi.org/10.3390/min8080342.

Krneta, S., Ciobanu, C.L., Cook, N.J., Ehrig, K., Kontonikas-Charos, A., 2017. The Wirrda Well and Acropolis prospects Gawler Craton, South Australia: insights into evolving fluid conditions through apatite chemistry. J. Geochem. Explor. 181, 276–291. https://doi.org/10.1016/j.gexplo.2017.08.004.

Macmillan, E., Cook, N.J., Ehrig, K., Ciobanu, C.L., Pring, A., 2016a. Uraninite from the Olympic Dam IOCG-U-Ag deposit: linking textural and compositional variation to temporal evolution. Am. Mineral. 101, 1295–1320. https://doi.org/10.2138/am-2016-5411.

Macmillan, E., Ciobanu, C.L., Ehrig, K., Cook, N.J., Pring, A., 2016b. Chemical zoning and lattice distortion in uraninite from Olympic Dam, South Australia. Am. Mineral. 101, 2351–2354. https://doi.org/10.1180/minmag.2017.081.006.

Macmillan, E., Ehrig, K., Ciobanu, C.L., Cook, N.J., Pring, A., 2016c. Replacement of uraninite by bornite via coupled dissolution-reprecipitation: evidence from texture and microstructure. Can. Mineral. 54, 1369–1383. https://doi.org/10.3749/canmin.1600031.

Macmillan, E., Cook, N.J., Ehrig, K., Pring, A., 2017. Chemical and textural interpretation of late-stage coffinite and brannerite from the Olympic Dam IOCG-Ag-U deposit. Mineral. Mag. 81, 1323–1366. https://doi.org/10.1180/minmag.2017.081.006.

Mark, G., Oliver, N.H.S., Williams, P.J., 2006. Mineralogical and chemical evolution of the Ernest Henry Fe-oxide-Cu-Au ore system, Cloncurry district, northwest Queensland, Australia. Mineral. Deposita 40, 769–801. https://doi.org/10.1007/s00126-005-0009-7.

Mauger, A.J., Ehrig, K.J., Kontonikas-Charos, A., Ciobanu, C.L., Cook, N.J., Kamenetsky, V.S., 2016. Alteration at the Olympic Dam IOCG–U deposit: insights into distal to proximal feldspar and phyllosilicate chemistry from infrared reflectance spectroscopy. Austral. J. Earth Sci. 63, 959–972. https://doi.org/10.1080/08120099.2016.1264474.

McPhie, J., Orth, K., Kamenetsky, V., Kamenetsky, M., Ehrig, K., 2016. Characteristics, origin and significance of Mesoproterozoic bedded clastic facies at the Olympic Dam Cu–U–Au–Ag deposit, South Australia. Precambr. Res. 276, 85–100. https://doi.org/10.1016/j.precamres.2016.01.029.

Meinert, L., 1997. Application of skarn deposit zonation models to mineral exploration. Explor. Min. Geol. 6, 185–208.

Oliver, N.H.S., Cleverley, J.S., Mark, G., Pollard, P.J., Fu, B., Marshall, L.J., Rubenach, M.J., Williams, P.J., Baker, T., 2004. The role of sodic alteration in the genesis of iron oxide-copper-gold deposits, eastern Mt Isa Block, Australia. Econ. Geol. 99, 1145–1176. https://doi.org/10.2113/99.6.1145.

Owen, N.D., Ciobanu, C.L., Cook, N.J., Slattery, A., Basak, A., 2018. Nanoscale study of clausthalite-bearing symplectites in Cu-Au-(U) ores: implications for ore genesis. Minerals 8, 67. https://doi.org/10.3390/min8020067.

Palarea-Albaladejo, J., Martín-Fernández, J.A., 2013. Values below detection limit in compositional chemical data. Anal. Chim. Acta 764, 32–43. https://doi.org/10.1016/j.aca.2012.12.029.

Palarea-Albaladejo, J., Martín-Fernández, J.A., 2015. zCompositions—R package for multivariate imputation of left-censored data under a compositional approach. Chemometr. Intell. Lab. Syst. 143, 85–96. https://doi.org/10.1016/j.chemolab.2015.02.019.

Pearson, K., 1897. Mathematical contributions to the theory of evolution: on a form of spurious correlation which may arise when indices are used in the measurements of organs. Proc. R. Soc. London 60, 489–498. https://doi.org/10.1098/rspl.1896.0076.

Putnis, A., 2002. Mineral replacement reactions: from macroscopic observations to microscopic mechanisms. Mineral. Mag. 66, 689–708. https://doi.org/10.1180/0026461026650056.

Reeve, J.S., Cross, K.C., Smith, R.N., Oreskes, N., 1990. Olympic Dam copper-uranium-gold-silver deposit. In: Hughes, F.E. (Eds.), Geology of the Mineral Deposits of Australia and Papua New Guinea: Austral. Inst. Min. Metal., Monograph 14, p. 1009–1035.

Richards, J.P., Mumin, A.H., 2013. Magmatic-hydrothermal processes within an evolving

Earth: Iron oxide-copper-gold and porphyry Cu ± Mo ± Au deposits. Geology 41, 767–770. https://doi.org/10.1130/G34275.1.
Richards, J.P., López, G.P., Zhu, J.J., Creaser, R.A., Locock, A.J., Mumin, A.H., 2017. Contrasting tectonic settings and sulfur contents of magmas associated with cretaceous porphyry Cu ± Mo ± Au and intrusion-related iron oxide Cu-Au deposits in Northern Chile. Econ. Geol. 112, 295–318. https://doi.org/10.2113/econgeo.112.2.295.
Rollog, M., Cook, N.J., Guagliardo, P., Ehrig, K.J., Kilburn, M., 2019. In situ spatial distribution mapping of radionuclides in minerals by nanoSIMS. Geochem. Explor. Environm. Anal. https://doi.org/10.1144/geochem2018-038. (in press).
Schmandt, D.S., Cook, N.J., Ciobanu, C.L., Ehrig, K.J., Wade, B.P., Gilbert, S., Kamenetsky, V.S., 2017. Rare earth element fluorocarbonate minerals from the Olympic Dam Cu-U-Au-Ag deposit, South Australia. Minerals 7, 202. https://doi.org/10.3390/min7100202.
Skirrow, R.G., Bastrakov, E.N., Barovich, K., Fraser, G.L., Creaser, R.A., Fanning, C.M., Raymond, O.L., Davidson, G.J., 2007. Timing of iron oxide Cu-Au-(U) hydrothermal activity and Nd isotope constraints on metal sources in the Gawler craton, South Australia. Econ. Geol. 102, 1441–1470. https://doi.org/10.2113/gsecongeo.102.8.1441.
van den Boogaart, K.G., Tolosana-Delgado, R., 2013. In: Analyzing Compositional Data with R. Springer, pp. 258 https://doi.org/10.1007/978-3-642-36809-7.
van den Boogaart, K.G., Tolosana-Delgado, R., Bren, M., 2014. Compositions: Compositional Data Analysis. R package version 1.40-1. https://doi.org/10.1016/j.cageo.2006.11.017.
Verdugo-Ihl, M.R., Ciobanu, C.L., Cook, N.J., Ehrig, K., Courtney-Davies, L., Gilbert, S., 2017. Textures and U-W-Sn-Mo signatures in hematite from the Cu-U-Au-Ag orebody at Olympic Dam, South Australia: defining the archetype for IOCG deposits. Ore Geol. Rev. 91, 173–195. https://doi.org/10.1016/j.oregeorev.2017.10.007.

CHAPTER 6

MINERALIZATION-ALTERATION FOOTPRINTS IN THE OLYMPIC DAM IOCG DISTRICT, SOUTH AUSTRALIA: THE ACROPOLIS PROSPECT

Marija Dmitrijeva[1], Cristiana L. Ciobanu[1], Kathy Ehrig[2], Nigel J. Cook[1], Andrew V. Metcalfe[3] Max R. Verdugho-Ihl[1], Jocelyn McPhie[4]

[1] *School of Chemical Engineering and Advanced Materials, The University of Adelaide, Adelaide, SA 5005, Australia*

[2] *BHP Olympic Dam, Adelaide, SA 5000, Australia*

[3] *School of Mathematical Sciences, The University of Adelaide, Adelaide, SA 5005, Australia*

[4] *School of Natural Sciences and Centre of Excellence in Ore Deposits (CODES), University of Tasmania, Hobart, Tasmania 7001, Australia*

Article published in Journal of Geochemical Exploration 209 (2019) 106333

Statement of Authorship

Title of Paper	Mineralization-alteration footprints in the Olympic Dam IOCG district, South Australia: The Acropolis prospect. Journal of Geochemical Exploration
Publication Status	☑ Published ☐ Accepted for Publication ☐ Submitted for Publication ☐ Unpublished and Unsubmitted w ork w ritten in manuscript style
Publication Details	Dmitrijeva, M., Ciobanu, C.L., Ehrig, K., Cook, N.J., Metcalfe, A.V., Verdugo-Ihl, M.R., McPhie, J. Mineralization-alteration footprints in the Olympic Dam IOCG district, South Australia: The Acropolis prospect. Journal of Geochemical Exploration, 205, 10633. https://doi.org/10.1016/j.gexplo.2019.106333

Principal Author

Name of Principal Author (Candidate)	Marija Dmitrijeva		
Contribution to the Paper	Performed statistical data analyses, geological modelling, interpreted the results and prepared the manuscript.		
Overall percentage (%)	55		
Certification:	This paper reports on original research I conducted during the period of my Higher Degree by Research candidature and is not subject to any obligations or contractual agreements with a third party that would constrain its inclusion in this thesis. I am the primary author of this paper.		
Signature		Date	17.12.19

Co-Author Contributions

By signing the Statement of Authorship, each author certifies that:

i. the candidate's stated contribution to the publication is accurate (as detailed above);

ii. permission is granted for the candidate in include the publication in the thesis; and

iii. the sum of all co-author contributions is equal to 100% less the candidate's stated contribution.

Name of Co-Author	Cristiana L. Ciobanu		
Contribution to the Paper	Helped to define the direction of the paper, assisted with the interpretation of the results and the manuscript evaluation.		
Overall percentage (%)	15		
Signature		Date	17.12.19

Name of Co-Author	Kathy Ehrig		
Contribution to the Paper	Helped to define the direction of the paper, assisted with the manuscript preparation and evaluation.		
Overall percentage (%)	6		
Signature		Date	17.12.19

Name of Co-Author	Nigel J. Cook		
Contribution to the Paper	Assisted with the manuscript preparation and evaluation.		
Overall percentage (%)	6		
Signature		Date	17.12.19

Name of Co-Author	Andrew V. Metcalfe		
Contribution to the Paper	Assisted with the statistical analyses and manuscript evaluation.		
Overall percentage (%)	6		
Signature		Date	17.12.19

Name of Co-Author	Max R. Verdugo-Ihl		
Contribution to the Paper	Assisted with the estimation of the modal mineralogy at Olympic Dam.		
Overall percentage (%)	6		
Signature		Date	17.12.19

Name of Co-Author	Jocelyn McPhie		
Contribution to the Paper	Assisted with the geological interpretation of the Acropolis prospect.		
Overall percentage (%)	6		
Signature		Date	17.12.19

Journal of Geochemical Exploration 205 (2019) 106333

Contents lists available at ScienceDirect

Journal of Geochemical Exploration

journal homepage: www.elsevier.com/locate/gexplo

Mineralization-alteration footprints in the Olympic Dam IOCG district, South Australia: The Acropolis prospect

Marija Dmitrijeva[a,*], Cristiana L. Ciobanu[a], Kathy J. Ehrig[b], Nigel J. Cook[a], Andrew V. Metcalfe[c], Max R. Verdugo-Ihl[a], Jocelyn McPhie[d]

[a] School of Chemical Engineering and Advanced Materials, The University of Adelaide, Adelaide, SA 5005, Australia
[b] BHP Olympic Dam, Adelaide, SA 5001, Australia
[c] School of Mathematical Sciences, The University of Adelaide, Adelaide, SA 5005, Australia
[d] ARC Centre of Excellence in Ore Deposits, School of Natural Sciences, University of Tasmania, Hobart, TAS 7005, Australia

ARTICLE INFO

Keywords:
Acropolis prospect
Magnetite-dominant IOCG
K-means clustering
PCA
Implicit 3D modelling

ABSTRACT

The Acropolis prospect, 20 km southwest from the Olympic Dam Cu-U-Au-Ag deposit, South Australia, is a vein-style magnetite (± apatite ± hematite) system. A whole-rock dataset comprising 4864 core samples from 14 drillholes was analysed using multivariate statistical analyses to understand and identify geochemical signatures of mineralization, as well as the expressions and extents of hydrothermal alteration. Statistical analysis included unsupervised (principal component analysis, hierarchical and *k*-means clustering) and supervised (random forests) machine learning algorithms. The geology of the Acropolis prospect is presented as a 3D geological model complemented by cross-sections. The results of statistical analyses are overlaid and interpreted relative to the geological model, and encompass a projection of sodic and propylitic alteration as PC3, and mineralization signature as PC1.

Although the mineralization footprint of the Acropolis prospect partially overlaps with a Hiltaba Suite granite, it is not centred on the granite body. A distinct 'magnetite' signature of Fe-V-Ni-Co is developed in the southwestern part of Acropolis and represents samples containing > 60 wt% Fe. In contrast, the 'hematite' signature displays an association of REE, W, Sn, Sb, U, Th, Ca and P, and is present throughout the Acropolis prospect with the exception of drillhole ACD5, which is non-mineralized. Interpolated values of Cu (> 200 ppm) indicate an offset from Fe-rich veins, thus supporting a genetic model in which Cu-bearing mineralization overprints Cu-Au-deficient magnetite-dominant veins. The results obtained provide insights into the evolution from magnetite to hematite-dominant IOCG systems and may provide a proxy for exploration of shallow and economically significant IOCG deposits in the eastern Gawler Craton.

1. Introduction

Iron-oxide copper gold (IOCG) deposits encompass a diverse group of mineralization styles found in a range of geological settings, and formed from the Archean to Tertiary (Groves et al., 2010). In the last three decades, IOCG systems spanning a continuum from magnetite- to hematite-rich end-members have been subject to many studies aimed at defining common mineralogical and geochemical characteristics and ore genesis (Hitzman et al., 1992; Hitzman, 2000; Williams et al., 2005; Corriveau, 2005; Barton, 2014 and references therein). These deposits are well known for their broad alteration haloes – particularly alkali-(calcic) alteration, and also for their marked deposit-scale zoning, as seen for the IOCG systems at Olympic Dam deposit, South Australia (Ehrig et al., 2012 and references therein; Mauger et al., 2016; Dmitrijeva et al., 2019), or Ernest Henry, Queensland (Mark et al., 2006).

Conceptualization of IOCG-style mineralization and ore genesis has become increasingly problematic, however, particularly since diverse end-members have been added to this group. These include Cu-Au-poor ore systems, such as the Kiruna and El Laco types, which were initially considered as magnetite-apatite deposits of magmatic origin (Geijer, 1931; Frietsch, 1978; Park, 1961), albeit of very different ages (1888 ± 6 Ma, Romer et al., 1994, vs. 2.1 ± 0.1 Ma, Maksaev et al., 1988). As more Kiruna-type magnetite-apatite deposits were identified, notably in the Chilean Iron Belt (El Algarrobo, Ruiz et al., 1968; El Romeral, Bookstrom, 1977), and as detailed geochemical studies

* Corresponding author.
E-mail address: marija.dmitrijeva@adelaide.edu.au (M. Dmitrijeva).

https://doi.org/10.1016/j.gexplo.2019.106333
Received 16 April 2019; Received in revised form 13 June 2019; Accepted 8 July 2019
Available online 17 July 2019
0375-6742/ © 2019 Elsevier B.V. All rights reserved.

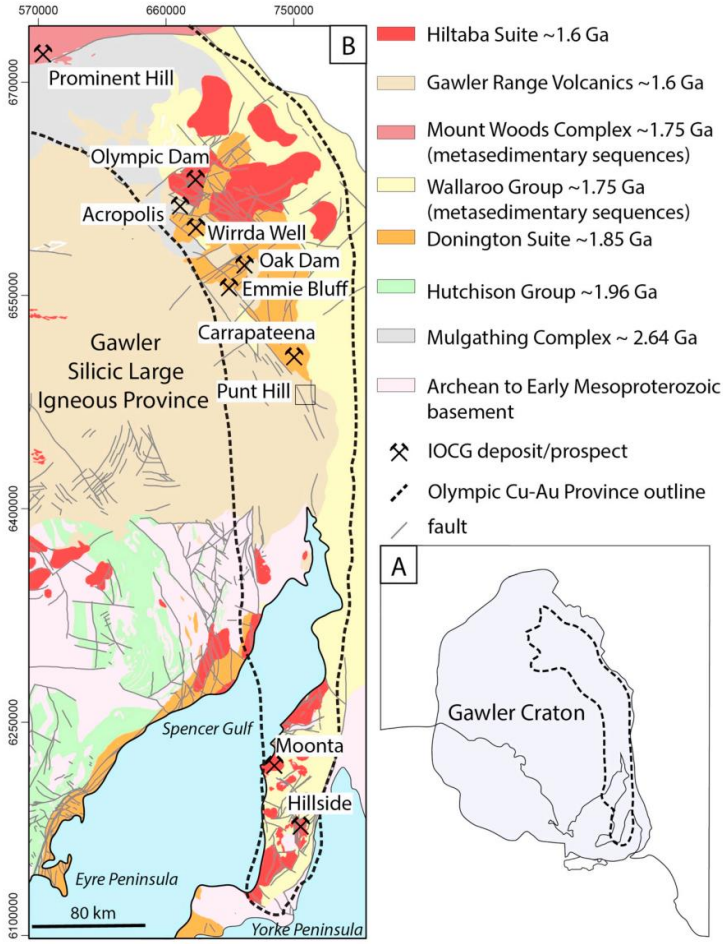


Fig. 1. (A) Sketch showing the location of the Gawler Craton in South Australia and (B) geological map of the eastern Gawler Craton highlighting IOCG deposits and prospects hosted within the Olympic Cu–Au province. Map sourced from https://map.sarig.sa.gov.au.

allowed improved discrimination of magmatic and hydrothermal generations of Fe-oxides (Dare et al., 2014; Knipping et al., 2015a), such deposits were considered kin to IOCG systems, and were redefined as a distinct subgroup, the iron-oxide apatite (IOA) type.

The magnetite-apatite association is, however, also part of early, alkali-calcic alteration within IOCG systems and has been well documented in mineralogical studies from deposits of the Olympic Cu–Au province, South Australia (e.g., Ismail et al., 2014; Krneta et al., 2016, 2017a, 2017b). Therefore, magnetite-apatite is not as discriminative between IOA and IOCG, as is the lack of alkalic (Na–K) alteration in the deposit footprint reported for some IOA deposits (e.g., Los Colorados, Chile; Knipping et al., 2015b).

One of the best endowed IOCG terranes on Earth is the Mesoproterozoic Olympic Cu–Au province, Eastern Gawler Craton, South Australia, in which mineralization relates to ~1.6 Ga magmatism comprising both bimodal volcanics (Gawler Range Volcanics; GRV) and igneous rocks (Hiltaba Suite granitoids) (Fig. 1; Skirrow et al., 2007).

Drilling of geophysical targets over the past 40 years has led to the discovery of multiple satellite prospects within a 5–100 km-radius from Olympic Dam deposit (Fig. 2). Among these, the Acropolis prospect represents a geophysical target at least 3 times the size of Olympic Dam. This prospect represents a relatively Cu-Au-poor example of magnetite-dominant mineralization that is mainly hosted within GRV. The Acropolis prospect is broadly considered contemporaneous with Olympic Dam based upon comparable mineral assemblages and geochronology (Krneta et al., 2017b; Cherry et al., 2018).

In this contribution, we present a 3D geological model and apply compositional data analysis to the whole-rock data set (4864 samples) to characterize the mineralization and alteration styles of the Acropolis prospect. Machine learning techniques are increasingly used in geochemistry to obtain data-driven geological insights from large datasets (e.g., Grunsky, 2010). Given the increased volume and multi-element character of modern data sets, a quantitative and reproducible approach to data analysis is required.

Application of statistical analysis to deposit-scale whole-rock datasets from Olympic Dam (Dmitrijeva et al., 2019) allowed recognition of a characteristic IOCG signature which, apart from common elements Fe, Cu and Au, also comprises indicator elements such as W, Mo, As and Sn.

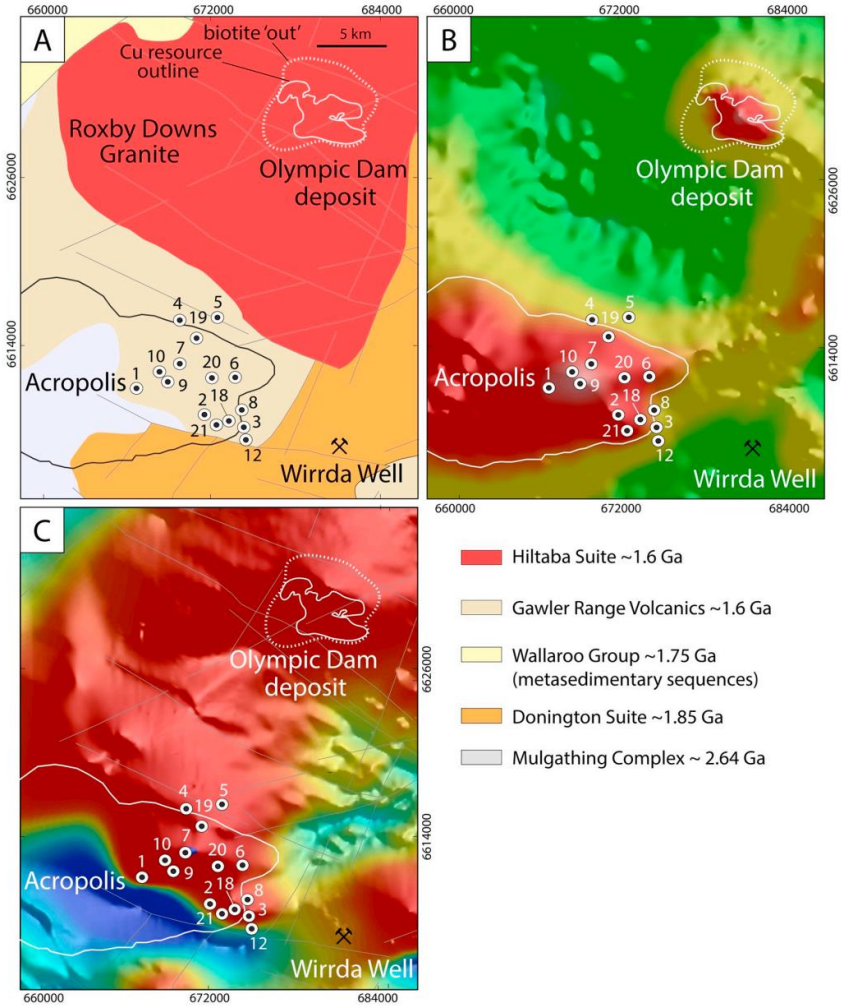


Fig. 2. (A) Geological map of the Olympic Dam area showing adjacent Acropolis and Wirrda Well prospects. The fifteen 'ACD' drillholes (circles) are indicated by their numbers only for simplicity. (B) Bouguer and (C) total magnetic intensity anomalies showing geophysical expression of Acropolis relative to Olympic Dam. Map sourced from https://map.sarig.sa.gov.au.

In the present contribution, an analogous approach is taken by applying unsupervised (principal component analysis, hierarchical and *k*-means clustering), and supervised (random forests, RF) machine learning algorithms to whole-rock data from Acropolis. Coupled with an implicit geological model, these techniques allow visualization of the associations of key elements, alterations and mineralization within three-dimensional space, also facilitating direct comparison with the Olympic Dam deposit.

Our overarching aim is to understand the genetic relationships between Olympic Dam and nearby prospects using Acropolis as an example to track the evolution of IOCG systems from magnetite- to hematite-rich end-members.

2. Geological background and rationale

The Olympic Cu-Au(−U) province is a 700-km-long N-S striking metallogenic belt along the eastern margin of the Gawler Craton (Fig. 1). Cu-Au(−U) metallogeny is represented by IOCG-style mineralization associated with a major magmatic event, the Gawler Silicic Large Igneous Province (SLIP), at ~1.6 Ga (Fig. 1B) that generated Hiltaba Suite intrusive rocks and their cogenetic equivalents, the Gawler Range Volcanics (GRV) (Blissett et al., 1993). Host lithologies for IOCG systems vary from Hiltaba Suite-affiliated granites (e.g., Olympic Dam within the Roxby Downs Granite RDG), older sedimentary rocks (e.g., Hillside within Wallaroo Group) and GRV lavas (e.g., Prominent Hill), and older ~1.85 Ga Donington Suite Granitoids (e.g., Wirrda Well and Carrapateena).

Copper-Au(−U) mineralization is strongly linked to regional-scale

hydrothermal alteration of Hiltaba Suite granitoids and other lithologies (Kontonikas-Charos et al., 2014, 2017, 2018a; Mauger et al., 2016), and also to iron metasomatism and sericite alteration that increases towards the deposit. Iron metasomatism may be expressed as hematite-dominant breccias, mineralized with respect to disseminated Cu(−Fe)-sulphides, and displaying pervasive replacement of precursor minerals (e.g., Olympic Dam, Ehrig et al., 2012; Prominent Hill, Schlegel and Heinrich, 2015). At Olympic Dam, the mineralization enclosed within the Olympic Dam Breccia Complex (ODBC), in turn hosted in RDG, exhibits a remarkable lateral and vertical zonation with respect to Cu-(Fe)-sulphides (Ehrig et al., 2012, and references therein). A primary geochemical footprint of the Cu-U-Au-Ag mineralization can be recognised and is characterized by an abundance of hematite with a distinct 'granitophile' element (U-W-Sn-Mo) signature (Verdugo-Ihl et al., 2017). Statistical analysis of a large whole-rock dataset (10,565 samples; Dmitrijeva et al., 2019) indicated that the IOCG signature that geochemically defines the ODBC does not only comprise the common elements Fe, Cu and Au, but also includes indicator elements such as W, Mo, Sn and As, highlighting the importance of a 'granitophile element' signature.

Olympic Dam contains by far the largest resource in the Gawler Craton discovered to date. Several other prospects in the immediate vicinity of Olympic Dam have been explored, including the Acropolis prospect, ~20 km SW from Olympic Dam, which is characterized by a large positive Bouguer anomaly of 4 mGal and a dipolar magnetic anomaly with a maximum peak of 58,000 nT with negative readings towards the southwest (Fig. 2; Dentith, 2003). Nevertheless, both potential field anomalies have an overlapping positive peak in the vicinity of the ACD10, ACD7 and ACD9 drillholes. The prospect has been intersected by drillholes beneath ~480 m of barren sedimentary cover across a 50 km^2 area, at least twice the size of the ODBC (Fig. 2). In this study, the whole-rock geochemical data comprises 4864 drill core samples collected from 14 diamond drill cores sampled at 1 m-intervals to appropriately characterize the lithological variability of the vein-style mineralization at Acropolis. Drillhole ACD15 did not intersect basement and has not been considered. Unlike the ODBC, the Acropolis prospect represents vein-style mineralization with weakly-developed brecciation (Cross, 1993) within the felsic sericite-hematite altered GRV (Mortimer et al., 1988; Ehrig et al., 2017). The volcanic rocks consist mainly of rhyolitic, dacitic and andesitic lavas, as well as minor ignimbrites (McPhie, 2016). Within the area, the basement is composed of Donington Suite Granitoids (~1840 Ma; Jagodzinski, 2005) which, in certain zones, also host mineralization. Weakly-brecciated granite intersected in drillhole ACD7 (Fig. 3A), and containing minor mineralization has been attributed to the Hiltaba Suite (Paterson, 1986; Creaser, 1989).

As described in early publications (Paterson, 1986; Cross, 1993), mineralization at Acropolis comprises a network of veins with massive, coarse-grained magnetite - apatite - sulphides (pyrite-chalcopyrite) ± biotite ± K-feldspar assemblage locally overprinted to different extents by hematite-sericite-chlorite assemblage; barite, fluorite and phlogopite can also be associated with sulphides (Fig. 3B, C). A transition from high-temperature (> 400 °C) magnetite-dominant to lower temperature hematite-dominant (150–300 °C) mineralization has been inferred based on fluid inclusions from magnetite-rich assemblage and magnetite oxygen isotopes studies (Oreskes and Einaudi, 1992). Samples containing higher concentration of sulphide minerals, particularly chalcopyrite, are associated with hematite-sericite-chlorite assemblages replacing early magnetite-apatite (Krneta et al., 2017a, 2017b). U−Pb apatite geochronology indicates that the Fe-oxide-apatite assemblage at Acropolis formed shortly after deposition of the host GRV lavas at ~1.59 Ga (Mortimer et al., 1988; Cherry et al., 2018), thus being broadly contemporaneous with hematite mineralization at Olympic Dam (Ciobanu et al., 2013; Courtney-Davies et al., 2016, 2019; Apukhtina et al., 2017). The geochemical signatures expressed by apatite, which record a transition from magmatic, through early magnetite-associated hydrothermal to hematite-sericite-associated, suggests genetic and spatio-temporal communalities between hydrothermal mineralization in the Olympic Dam deposit and the Acropolis prospect (Krneta et al., 2017a, 2017b).

Despite similarities with the styles of alteration at Olympic Dam (Ehrig et al., 2017), the predominant magnetite-bearing vein-style mineralization and host felsic volcanics at Acropolis makes the prospect a valuable target for understanding geochemical footprints of IOCG systems within the same district. The observed replacement of magnetite by hematite is also of interest since this is known to carry a 'granitophile'-element signature (Verdugo-Ihl et al., 2017; Dmitrijeva et al., 2019), therefore offering the opportunity to underpin the variations in IOCG geochemical signatures by comparison with Olympic Dam.

An approach similar to that used by Dmitrijeva et al. (2019) is undertaken here. This study aims to derive the geochemical signatures of the Acropolis prospect from whole-rock data across 14 drillholes using hierarchical clustering and principal component analysis (PCA). The following groups of elements are specifically addressed: 'granitophile' (U-W-Sn-Mo), high-field strength (Th-Zr-Ta-Nb), chalcophile (Bi), rare earth (Ce, Nd, Y and Yb) and other indicator elements (Cd, Co, Mo, Ni, Sb, Sc, Ti, V and Zn). Because of intense alteration, including pervasive iron metasomatism, high lithological variability and potentially, the impact of superposed geological events, recognition of primary lithologies in core logging is difficult in Acropolis prospect. To circumvent this, we utilize *k*-means cluster analysis as a data-driven supplement to subjective visual core logging, thus providing lithogeochemical clusters, which encompass protolith chemistry and superimposed geochemical signatures. The derived classes are subsequently used to train and test a RF model to predict the lithogeochemistry using geochemical elements as predictor variables. Such use of data-derived lithogeochemical clusters, featuring distinct characteristics, are shown to readily assist discrimination of hematite versus magnetite-dominant mineralization and alteration types in the Acropolis system. A holistic understanding of genetic relationships between Olympic Dam and its nearby prospects, including Acropolis, may shed light on the fundamental processes that form hematite and magnetite-dominant IOCG members within the same district.

3. Methods

The work-flow diagram (Fig. 4) illustrates the successive stages of data preparation, clustering, classification, validation and interpretation.

3.1. Compositional data and imputation

Each whole-rock sample was analysed at Intertek/Genalysis, Adelaide, using fire assay - flame atomic absorption spectrometry for Au; induction furnace - infrared spectrometry for C and S; four acid digestion - inductively coupled plasma optical emission spectrometry (ICP-OES) for Cu, Ni, Pb, Zn; four acid digestion – inductively coupled plasma mass spectrometry (ICP-MS) for Ag, As, Cd, Co, Ge, In, Li, Re, Se, Te, Tl; lithium metaborate fusion ICP-OES for Al, Ca, Cr, Fe, K, Mg, Mn, Na, P, Sc, Si, Ti, V; and lithium metaborate fusion ICP-MS for REE, Be, Bi, Cs, Ga, Hf, Mo, Nb, Rb, Sb, Sn, Sr, Ta, Th, U, W, Y, Zr. The data were examined for the presence of values below detection limits, thus certain trace elements were not included in the final subset of the data. Specifically, Ag, As, Au, Be, C, Cr, Cs Ga, Ge, In, Re, Pb, Te and Tl, for which ~30% of values were below the limit of detection, were excluded. Given the high level of correlation among the REE elements, only Ce, Nd, Y, and Yb were considered. Therefore, the remaining set of 36 elements represent a range of analytes: Al, Ba, Bi, Ca, Cd, Ce, Co, Cu, Fe, K, Li, Mg, Mn, Mo, Na, Nb, Nd, Ni, P, Rb, S, Sb, Sc, Si, Sn, Sr, Ta, Th, Ti, U, V, W, Y, Yb, Zn, Zr. The left-censored values of the remaining data were imputed prior to data analysis using the robust multiplicative lognormal replacement method implemented in the R package

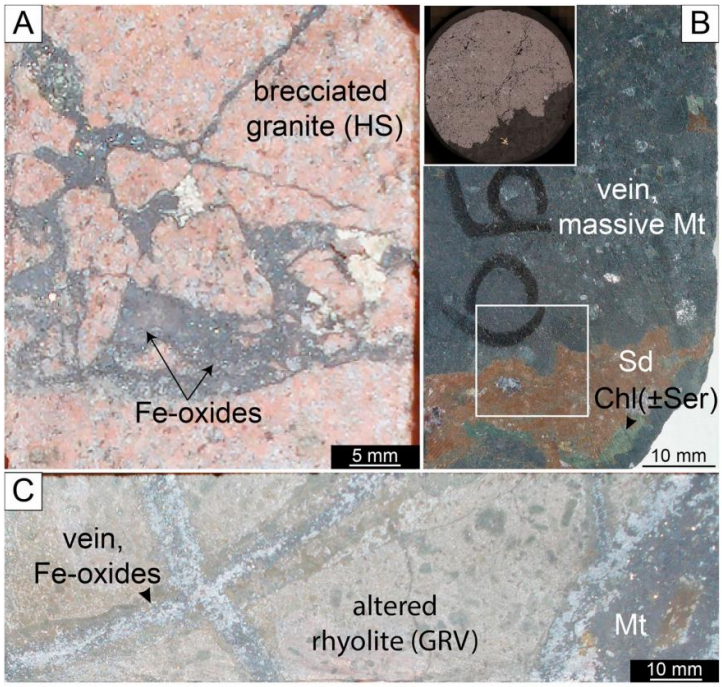


Fig. 3. Representative lithologies and mineralization in Acropolis. (A) Crackle breccia in granite of Hiltaba Suite (HS) with Fe-oxides infill. (B) Coarse-grained vein magnetite (Mt). Note presence of gangue minerals comprising siderite (Sd) with minor chlorite (Chl) and sericite (Ser). Inset shows a reflected light photomicrograph of Mt. (from area marked by the white rectangle). (C) Altered GRV rhyolite with crosscutting veinlets of Fe-oxides and gangue minerals (white). Note coarser Mt. is present in wider veins (right corner).

'zCompositions' (Palarea-Albaladejo and Martín-Fernández, 2015).

Geochemical data have specific mathematical properties where the components of a compositional D-part vector $x = [x_1, x_2, \ldots, x_D]$ are strictly positive real numbers carrying only relative information and summing up to a given constant, for instance, 100 wt% or one million ppm (Aitchison, 1986; Pawlowsky-Glahn and Egozcue, 2006). To respect such properties of the geochemical data, a compositional approach to multivariate statistical analyses is undertaken at every step of data analysis. To investigate the bivariate relationship among all the pairwise geochemical data components, Aitchison variation matrix (Aitchison, 1986) was produced where every entry of the matrix is the variance of the element pair log-ratio:

$$\tau_{ij} = var(\ln(x_i/x_j)) \quad (1)$$

for i, j, from 1 to 36. Such a variation-matrix, where highly-correlated elements display low τ_{ij}, is preferred over the correlation and/or covariance matrix of untransformed raw data because of the geometric properties of compositions (Pearson, 1897).

Multivariate statistical analyses of compositions require specific data representations such as isometric log-ratio (ilr), centred log-ratio (clr) or additive log-ratio transformations. These transformations, applied to raw geochemical data, result in ilr- and clr-coordinates that belong to Euclidean vector space thus allowing application of multivariate statistical techniques with no problems of compositional closure. Isometric log-ratio coordinates were obtained using the principles of compositional balances. The information extracted from the cluster dendrogram was used to generate balances (i.e., isometric log-ratio (ilr) coordinates) of 36-part composition (Egozcue and Pawlowsky-Glahn, 2005, 2006).

Calculation of balances consists of sequential binary partition, in which the 36-part composition is split into two non-overlapping variables following $D - 1$ steps. This results in 35 ilr-coordinates which are appropriate for characterization of this data (Table 1). The clr coefficients of the compositions were obtained by dividing each component of a composition by the geometric mean of the composition and then taking the natural logarithm.

One way to display compositions is their representation in a simplex. A ternary diagram, which is a 3-part simplex, is thus an

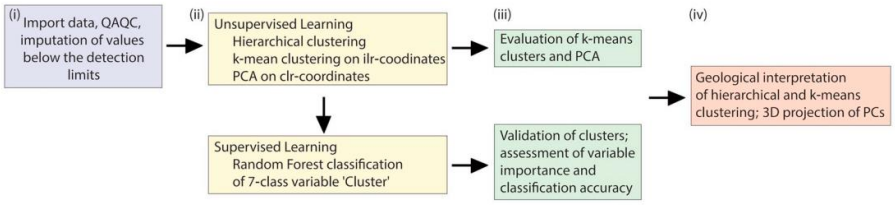


Fig. 4. Workflow diagram showing the steps for data analysis. (i) preparation, quality assurance and quality control (QAQC) and imputation, (ii) PCA, k-means clustering and RF classification, (iii) results validation and evaluation, and (iv) interpretation. Abbreviations: clr - centred log-ration, ilr - isometric log-ratio, PCA - principal component analysis, RF - random forests.

Table 1
Sequential binary partitioning used to obtain 35 ilr-coordinates of 36 geochemical variables. The procedure of partitioning is based on the hierarchical dendrogram (Fig. 5). Composite variables within a balance are the geometric mean of all components.

Balance	Binary partition
b1	[Ba, Nb, Ta, Zr, Al, Si, Na, K, Rb, Mn, Cd, Th, U, Sr, Y, Yb, Ce, Nd | S, Ca, P, Li, Mg, Sn, Sc, Ti, Zn, Sb, W, Cu, Mo, Bi, Fe, V, Co, Ni]
b2	[Ba, Nb, Ta, Zr, Al, Si, Na, K, Rb | Mn, Cd, Th, U, Sr, Y, Yb, Ce, Nd]
b3	[Ba | Nb, Ta, Zr, Al, Si, Na, K, Rb]
b4	[Nb, Ta | Zr, Al, Si, Na, K, Rb]
b5	[Nb | Ta]
b6	[Zr, Al, Si | Na, K, Rb]
b7	[Zr | Al, Si]
b8	[Al | Si]
b9	[Na | Ka, Rb]
b10	[K | Rb]
b11	[Mn | Cd, Th, U, Sr, Y, Yb, Ce, Nd]
b12	[Cd | Th, U, Sr, Y, Yb, Ce, Nd]
b13	[Th, U | Sr, Y, Yb, Ce, Nd]
b14	[Th | U]
b15	[Sr | Y, Yb, Ce, Nd]
b16	[Y, Yb | Ce, Nd]
b17	[Y | Yb]
b18	[Ce | Nd]
b19	[S | Ca, P, Li, Mg, Sn, Sc, Ti, Zn, Sb, W, Cu, Mo, Bi, Fe, V, Co, Ni]
b20	[Ca, P, Li, Mg, Sn, Sc, Ti, Zn, Sb, W | Cu, Mo, Bi, Fe, V, Co, Ni]
b21	[Ca, P | Li, Mg, Sn, Sc, Ti, Zn, Sb, W]
b22	[Ca | P]
b23	[Li, Mg | Sn, Sc, Ti, Zn, Sb, W]
b24	[Li | Mg]
b25	[Sn, Sc, Ti | Zn, Sb, W]
b26	[Sn | Sc, Ti]
b27	[Sc | Ti]
b28	[Zn | Sb, W]
b29	[Sb | W]
b30	[Cu, Mo | Bi, Fe, V, Co, Ni]
b31	[Cu | Mo]
b32	[Bi | Fe, V, Co, Ni]
b33	[Fe, V | Co, Ni]
b34	[Fe | V]
b35	[Co | Ni]

appropriate visualization tool for compositional data. For visualization of geochemical data on such a ternary diagram, it is often preferred to sum up several geochemical variables to represent a specific geological process (Ordóñez-Calderón et al., 2017). Such amalgamation is, however, not compatible with geometric properties of composition (Egozcue and Pawlowsky-Glahn, 2005). To circumvent this, three new composite variables were obtained as geometric means of the elements that belong to a geochemically meaningful group specified by the dendrogram (Fig. 5). Furthermore, centred ternary diagrams were generated by scaling a 3-part sub-composition relative to its centre. Firstly, a centre of the data is obtained by a closed vector of geometric means:

$$cen(X) = C(g(X_1), g(X_2), ..., g(X_D)), \quad (2)$$

and, secondly, the centring of the data is achieved by perturbing each component of a composition by the inverse of the centre:

$$x_i = C\left[\frac{x_{i1}}{g(X_1)}, \frac{x_{i2}}{g(X_2)}, ..., \frac{x_{iD}}{g(X_{D1})}\right]. \quad (3)$$

The above-mentioned centring procedure is equivalent to scaling of data with respect to its mean in Euclidean space. The main purpose of compositional centring is to avoid multiplication by arbitrary scalars which are often used to re-scale variables of different magnitudes such as trace versus major elements.

3.2. Unsupervised machine learning

Unsupervised machine learning algorithms are used to effectively find structures and patterns within the data without the pre-defined categorical variables (Caciagli, 2016; Ordóñez-Calderón et al., 2017). In geochemistry, structures and patterns normally reflect lithology and geochemical processes such as mineralization and/or alteration (Grunsky, 2010). In this case study, a range of unsupervised algorithms such as hierarchical clustering, *k*-means cluster analysis and PCA is used to characterize lithogeochemistry, alteration and mineralization at the Acropolis prospect. Firstly, a cluster dendrogram based on Aitchison's variation matrix (Table 2) is constructed. The dendrogram displays the agglomeration of the elements where the height of the dendrogram reflects a measure of similarity among the elements.

Secondly, iterative *k*-means cluster analysis is applied to balances representing ilr-coordinates of the 36-part simplex. *k*-means cluster analysis aims at partitioning geochemical samples into a *k* pre-specified non-overlapping clusters based on a set of variables i.e., elements (MacQueen, 1967). Each cluster is defined by a centroid, whereas clustering is achieved by minimizing the intra-cluster variation around it. The optimal number of *k* clusters is determined and assessed using a

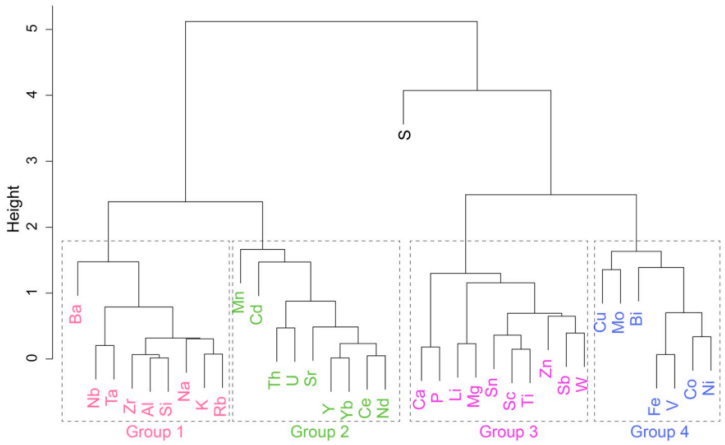


Fig. 5. Hierarchical cluster dendrogram showing the association among the selected 36 elements (Appendix A). The height of the dendrogram is a dissimilarity measure calculated from the pairwise log-ratio matrix of the 36 elements using Euclidean metrics and Eq. (1) (see Section 3.1).

Table 2
A subset of variation matrix with entries as the variances of the log-ratios of each element pair. The highlighted values indicate the strongest (green) and weakest (yellow) column-wise codependence.

	Bi	Ca	Ce	Co	Cu	Fe	K	Mo	Na	Nb	Nd	Ni	P	S	Sb	Sc	Si	Sn	Ta	Th	Ti	U	V	W	Y	Yb	Zn	Zr
Al	1.4	1.5	0.4	1.0	2.5	1.5	0.2	2.2	0.2	0.4	0.5	1.9	1.2	3.3	0.4	0.3	0.0	0.7	0.6	0.7	0.3	0.6	1.4	0.7	0.4	0.3	0.9	0.1
Bi		1.6	1.4	0.9	1.6	1.2	1.9	1.6	1.7	1.7	1.6	1.2	1.7	3.0	1.3	1.2	1.3	1.0	2.8	2.0	1.1	1.2	1.4	1.2	1.5	1.5	1.1	1.5
Ca			0.9	1.1	2.5	1.1	1.9	2.3	1.4	1.8	0.9	1.8	0.2	4.1	1.1	0.9	1.5	1.1	2.7	1.8	1.1	1.2	1.2	1.3	1.2	1.2	1.3	1.8
Ce				0.9	2.0	1.1	0.8	1.4	0.6	0.6	0.1	1.7	0.7	3.0	0.5	0.3	0.4	0.4	1.2	0.7	0.4	0.5	1.3	0.6	0.2	0.2	0.8	0.5
Co					1.1	0.5	1.4	1.0	1.5	1.8	1.0	0.3	1.3	2.0	0.8	0.5	0.9	0.6	2.6	1.0	0.6	0.6	0.6	0.8	1.2	1.2	0.4	1.0
Cu						1.3	2.7	1.4	3.1	2.9	2.2	1.1	2.4	1.9	2.1	1.9	2.3	1.5	4.0	2.6	2.1	1.5	1.4	2.0	2.5	2.4	1.8	2.6
Fe							1.5	1.3	1.9	2.9	1.2	0.7	1.1	2.7	0.8	0.6	1.3	0.6	3.9	1.0	0.9	0.7	0.1	0.9	1.5	1.4	0.7	1.4
K								2.8	0.3	0.4	0.8	2.5	1.8	3.7	0.6	0.7	0.2	0.8	0.6	1.1	0.5	1.0	1.8	1.1	0.4	0.4	1.1	0.3
Mo									2.7	2.8	1.7	1.3	2.0	1.8	1.6	1.2	2.0	1.1	4.3	1.8	1.3	0.8	1.5	1.4	2.1	2.1	1.5	2.1
Na										0.6	0.7	2.6	1.5	3.7	0.6	0.6	0.2	1.1	0.8	0.9	0.5	1.0	2.1	0.9	0.5	0.4	1.2	0.3
Nb											0.5	2.9	1.5	3.7	0.9	0.9	0.4	0.8	0.2	1.3	0.6	1.4	3.0	1.3	0.2	0.2	1.2	0.5
Nd												1.9	0.8	3.3	0.6	0.3	0.5	0.4	1.1	0.8	0.3	0.6	1.4	0.8	0.1	0.1	0.9	0.7
Ni													2.0	2.2	1.9	0.8	1.8	0.9	4.2	2.0	1.1	1.0	0.7	1.6	2.1	2.1	1.1	2.0
P														3.8	0.9	0.9	1.2	0.8	2.2	1.5	0.9	0.9	1.3	1.0	1.0	1.1	1.1	1.4
S															3.8	2.7	3.3	2.7	5.1	3.2	2.6	2.4	3.2	3.4	3.7	3.5	3.3	3.6
Sb																0.5	0.4	0.5	1.5	0.6	0.5	0.5	1.0	0.4	0.5	0.5	0.6	0.6
Sc																	0.4	0.4	1.5	0.8	0.1	0.4	0.6	0.5	0.5	0.5	0.5	0.4
Si																		0.6	0.5	0.6	0.3	0.5	1.3	0.7	0.4	0.3	0.8	0.0
Sn																			1.6	1.2	0.3	0.5	0.8	0.5	0.4	0.4	0.7	0.7
Ta																				1.0	1.2	2.0	3.8	1.8	0.7	0.7	2.1	0.4
Th																					0.9	0.5	1.3	1.0	0.9	0.7	0.9	0.5
Ti																						0.6	0.7	0.7	0.3	0.3	0.5	0.4
U																							1.0	0.5	0.8	0.7	0.6	0.5
V																								1.1	1.6	1.6	0.8	1.5
W																									0.9	0.8	0.6	0.7
Y																										0.0	0.8	0.5
Yb																											0.8	0.4
Zn																												0.9

plot of the sum of squared errors (SSE) versus a number of clusters ("elbow" method). Additionally, the cluster robustness is tested via a bootstrapping algorithm that returns the Jaccard similarity value j_i, varying between 0 and 1. Commonly, a well-sustained cluster shows at least 0.75 of Jaccard similarity value. Finally, the separation distance between seven clusters was assessed using Silhouette analysis. Silhouette coefficient s_i determines how well each object lies within its cluster; a high average Silhouette value is indicative of good clustering (Rousseeuw, 1987).

As a final step, the patterns within the multi-element geochemical data are explored through PCA, which aims to find the maximum variability within the data by reducing dimensionality and results in a linear combination of elements as principal components (PCs). PCA was performed via singular value decomposition of centred log-ration (clr) transformed data. The above-mentioned algorithms and their visualization were implemented using the R packages 'compositions', 'fpc', 'ggtern' and 'ggplot2' (Wickham, 2016; Hennig, 2018; Hamilton, 2018; van den Boogart et al., 2018).

3.3. Supervised machine learning

The objective of supervised learning is the prediction of numerical or categorical response variables using a suite of explanatory variables (e.g., chemical elements). Random forests (Breiman, 2001) are supervised ensemble algorithms that extend classification and regression tree methodology. Individual trees within a RF encompass a series of hierarchical decision nodes that are utilized to predict response variable (Breiman et al., 1984) and identify the most influential explanatory variables.

A RF model is set up to classify samples into 7-class categorical variables ('Cluster'), derived from *k*-means cluster analysis, using elements. To fit the model, 30% of the data were randomly selected to form a training set. Construction of an individual decision tree starts with a bootstrap of *n* cases from the training set. Once a bootstrap sample is obtained, tree construction starts by selecting a subset of 7 elements that are randomly selected from the total of 36 elements. The number of elements selected is typically set to the square root of the total number of elements. This process is repeated for 700 bootstrapped samples leading to 700 decision trees. Having constructed 700 trees, each observation is classified into one of the seven categories by each tree. The observation is then classed into the category that occurs most frequently among the 700 individual classifications (majority vote).

The remaining 70% of the data forms the validation set which is not shown to the RF classifier during the training process and thus used to validate the model and check its accuracy. The overall model performance is evaluated using the prediction accuracy and percentage of correctly classified samples, obtained from the classification of 'Cluster' variable using the validation set. A relative importance of the predictive power of each variable is measured using the mean decrease Gini index. Gini index represents a quality of a split for every variable of a tree whereas the index is calculated every time a split of a node is made. The Gini index is always smaller for the two descendent nodes than the parent node. Adding up the Gini index decrease for each individual variable over all trees in the forest gives a fast variable importance assessment where high mean decrease Gini indicates a higher node 'purity' and therefore higher variable importance.

Random forests generate results that appear as accurate as outputs of other supervised classifiers, such as support vector machines, k-nearest neighbours, (Cracknell and Reading, 2014) and discriminant analysis or, in case of whole-rock geochemical data, outperform above-mentioned algorithms (O'Brien et al., 2015; Ordóñez-Calderón and Gelcich, 2018).

3.4. Implicit 3D geological and numerical modelling

This study has completed 3D modelling of the major faults, intrusions and lithological groups across the area intersected by drillholes using the Leapfrog 3D 4.5.0 implicit modelling software. Geological model and numeric interpolants were created to understand mineralization and alteration signatures relative to lithologies in Acropolis. The geological model was built by assuming fault-bounded blocks. Such faults were introduced to correlate marker GRV units showing displacements (data from drillhole logging; McPhie, 2016). No other constraints were considered. The geochemical similarity of GRV lavas allows differentiation of some of the felsic units and correlation of GRV andesite and ignimbrites across drillholes. Within GRV dacites, only three dacite units were distinguished and correlated across the drillholes based on their Ti/Zr and Ti/Al ratios. In contrast, the GRV rhyolites are geochemically indistinguishable. Numeric models of continuous variables PC1, PC3, Cu > 200 ppm and Fe > 25 wt% were constructed using spheroidal interpolant function, i.e., semi-variogram with a base range of 1800 m. For numeric interpolants isotropy of the environment was assumed.

4. Results

4.1. Variation matrix and hierarchical clustering

The obtained variation matrix comprised of the variances of the pair-wise log-rations τ_{ij} is given in Table 2. The extended variation matrix is in Appendix A. The variation matrix identifies the key geochemical associations within the data, whereas the small τ_{ij} values correspond to a high geochemical affinity among elements and vice versa. For instance, the smallest τ_{ij} values characterize element pairs which are predominantly hosted within silicate minerals such as K-feldspar, albite and sericite ($\tau_{AlSi} = 0.01$; $\tau_{SiK} = 0.2$ and $\tau_{AlNa} = 0.2$). Similarly, there is a high degree of proportionality among pairs of rare earth elements, Ce, Nd, Y and Yb (Table 2) with τ_{ij} values < 0.2. Among the elements representing the mineralization signature, Fe features a very strong association with V ($\tau_{FeV} = 0.1$), but also displays a strong affinity with Ni, Sb, Sc, Sn, Ti, U, W and Zn ($\tau_{ij} < 1.0$; Table 2). Similarly, Ca is strongly associated with P. In contrast to other high-field strength elements (HFSE), Ta shows the strongest disproportionality with mineralization and indicator elements Cu ($\tau_{TaCu} = 4.0$), Fe ($\tau_{FeTa} = 3.9$), Mo ($\tau_{MoTa} = 4.3$), Ni ($\tau_{TaNi} = 4.2$) and S ($\tau_{TaS} = 5.1$).

Fig. 5 presents the cluster dendrogram which is derived from the variation matrix in Table 2. The vertical axis of the dendrogram is a measure of similarity among the elements and it is directly related to the variation matrix (Table 2). The dendrogram suggests four geochemical groups. Group 1, comprising Ba, Zr, Al, Si, Na, K and Rb represents a geochemical signature of felsic host rocks, such as granites and GRV lavas, and is also indicative of silicate minerals which are the products of hydrothermal alteration. Additionally, Ta and Nb are incorporated into Group 1 which is readily explained by their strong disproportionality with Fe, Mo, Ni, and Cu (Table 2) and presence within minerals of magmatic origin, notably titanite. The mineralization signature is represented by Groups 2, 3 and 4, whereby Group 2 shows some affinity with Group 1 suggesting a complex elemental partitioning of Mn, Cd, Sr, U, Th, and REE, which could be associated with minerals within host rocks and in mineralized veins. Interestingly, the Ca—P pair is grouped within Group 2 whereas REE are placed within Group 1, suggesting that apatite is not the major host for REE. Group 4 is a cluster of elements associated with Fe-rich mineralization reflecting the strong co-dependence among Fe, V, Ni and Co, along with Cu, Mo and Bi. Group 3, which encompasses W, Sb, Zn, Ti, Sc, Mg, Li, Ca and P is evidently associated with Group 4 and represents a range of indicator elements for mineralization. Combined, Groups 3 (Ca, P, Li, Mg, Sn, Sc, Ti, Zn, Sb and W) and 4 (Cu, Mo, Bi, Fe, V, Co and Ni) form an indicative IOCG-signature within the magnetite-dominant mineralization in Acropolis. Finally, S which features as a stand-alone element on the dendrogram, is certainly associated with Groups 3 and 4, however its position on the dendrogram is likely to be biased by the

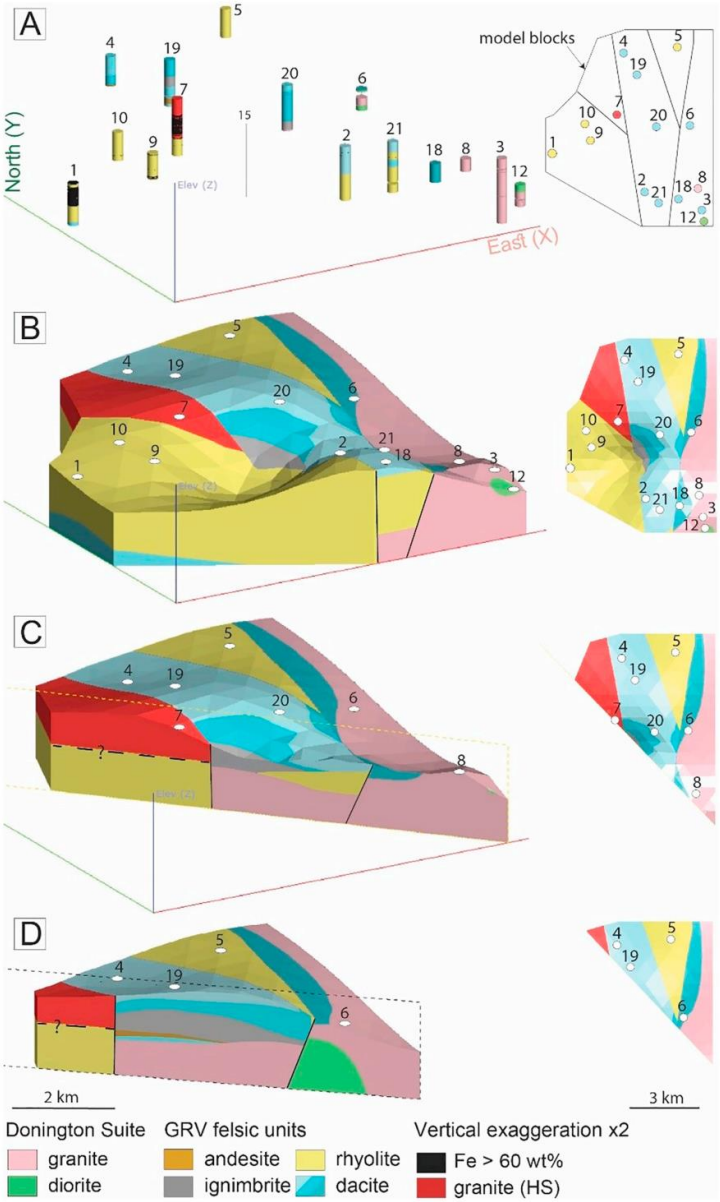


Fig. 6. Location and geology of the fifteen ACD drillholes (A) and geological model of Acropolis shown as 3D diagrams in oblique views (left) and plan views (right) (B-D). The sequence of sections from B to D are intended to show the occurrence of Hiltaba Suite (HS) granite relaitve to the GRV sequences and basement Donington Suite rocks. Faults are inferred from drillhole logging (McPhie, 2016). Due to the oblique rotation, colors used in the legend only approximate the colors of the model.

large number of imputed below detection limit (BDL) values.

4.2. Geological model

A 3D geological model provides a visual and simplified summary of Acropolis prospect geology (Fig. 6). Information from logging of 15 drillholes (McPhie, 2016) allows an empirical classification of the logging data into meaningful geological units distributed across five fault-bounded blocks. Four cross-sections through the geological model have been derived (Fig. 7). The eastern block is composed of Donington Suite Granitoids (Fig. 7A, B), whereas the central part of the model represents GRV lithologies comprising andesite, ignimbrite and dacites (Fig. 7B, C,

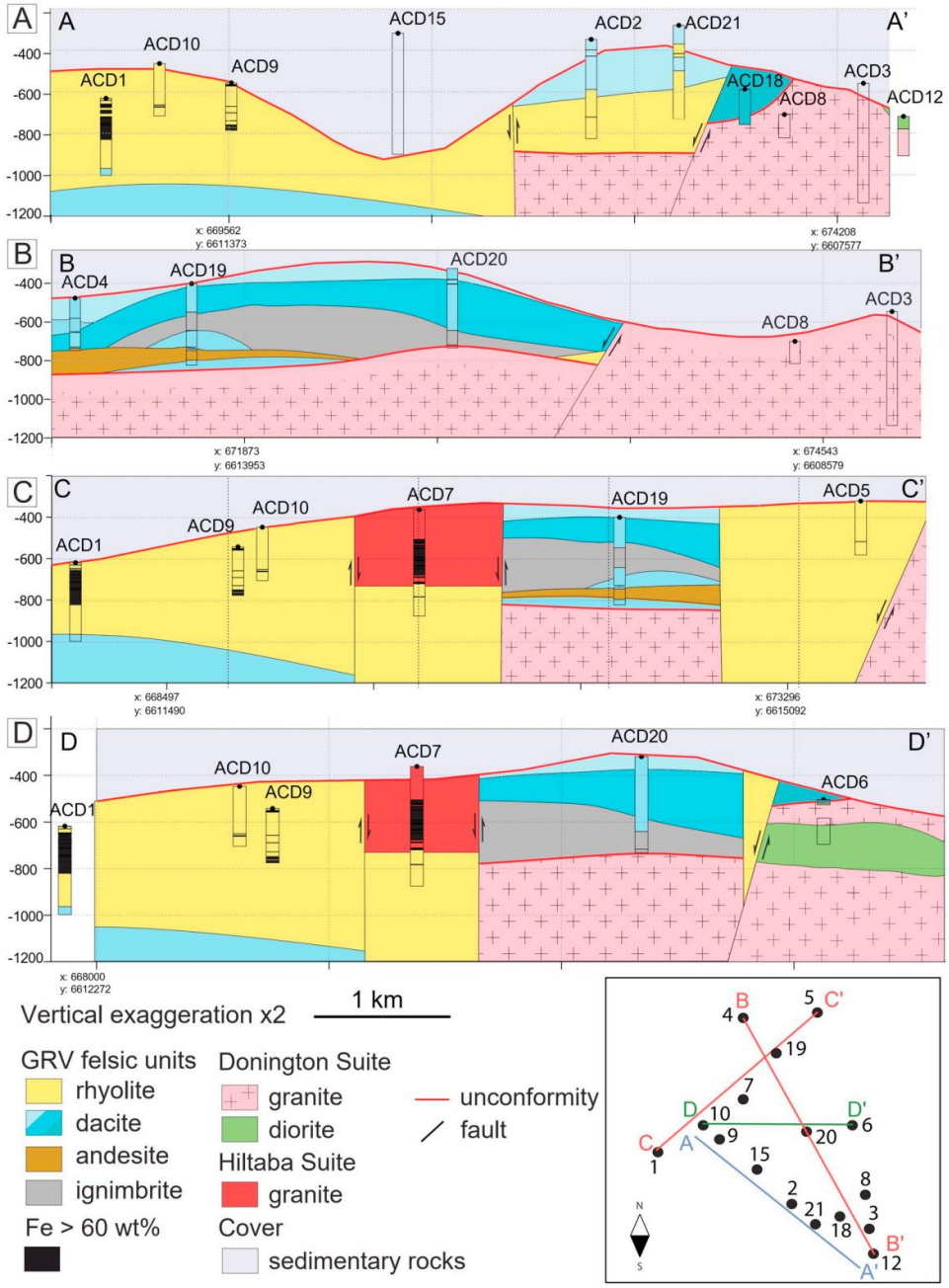


Fig. 7. Cross-sections through the geological model of Acropolis showing host rock lithologies and all ACD drillholes studied here. Note that Fe-oxide mineralization occurs in rhyolite but also in Hiltaba Suite (HS) granite and to some extent also in the basement rocks (A-D). Location or cross-section is shown in the inset (bottom right).

D) with the basement composed of the Donington Suite granite. The western part of the model is composed of undifferentiated rhyolite. Faulted contacts were assumed between the Hiltaba-granite (upper levels in drillhole ACD7), and rhyolites based on the limited data available (Figs. 6 and 7C, D).

The andesite is correlated across ACD4 and ACD19, whereas the ignimbrite unit, intersected in ACD19 and ACD20 only, is extrapolated laterally (Fig. 7B). The dacite overlying ignimbrite is correlated acrosss three drillholes (ACD4, ACD19 and ACD20) and bounded by a subvertical fault to the south-east. Similarly, the topmost dacite (ACD2 and ACD21) is overlying rhyolite but shows faulted contact to another dacite unit. The latter extends across ACD6 and ACD18 and shows a nonconformable relationship with the basement Donington granite (Fig. 7A, B). The Hiltaba granite is dropped down considering that it is bounded by a normal fault (Fig. 7C, D).

4.3. k-means clusters and PCA

The robustness of the k-means clusters was determined using a bootstrapping algorithm and within clusters sum of squares plot ("elbow" plot) which suggest that the geochemical data may be split into between 6 and 8 geologically meaningful groups (Fig. 8A). The "elbow" plot was obtained by running k-means clustering on the dataset for a range of values for k from 1 to 10 (Fig. 8A). Despite the typical challenge of selecting an optimal number of clusters, a number of seven was considered to be optimal for Acropolis data. The goal of *k*-means clustering was to classify the data, especially chemically similar felsic rocks, with various degrees of mineralization and alteration. The derived seven lithogeochemical clusters contain information about mineralogy, alteration and mineralization. The Silhouette widths s_i (Fig. 8B; Table 3) obtained for each cluster (i = 1, 2, …, 7) shows that clusters 2, 4, 5 and 6 display a very good intra-cluster cohesion while cluster 1 shows the lowest s_i value. Cluster stability calculated as Jaccard similarity values j_i indicated that cluster 1 is the least stable with j_1 = 0.57 whereas clusters 2, 3, 5, 6 and 7 are the most stable ones with j_i > 0.7.

The lithological-geochemical description of the seven obtained clusters is given in Table 3. *k*-means clustering is especially efficient at identifying unmineralized rhyolites (Cluster 1) and Fe-rich veins (Cluster 6). Donington granite and diorite with significant sodic alteration (median Na = 1.2 wt%) and low Cu content (median = 85 ppm) represent Cluster 2. In contrast, Cluster 5, which also encompass Donington granite and diorite, has a larger Fe proportion (median = 20 wt%) compared to 8 wt% of Fe in Cluster 2, and also the highest median Cu concentration (530 ppm) among all clusters.

Clusters 3 and 7 are comprised by rhyolites and dacites with relatively high Fe content of 30 wt% and 25 wt%, respectively, resulting in higher measured density of 3.1 kg/m^3. However, the main distinction between Clusters 3 and 7 is attributed to Cu content, which is significantly higher in Cluster 7 (median 280 ppm), compared to a median value of 137 ppm in Cluster 3 (Table 3).

Cluster 4 comprises 1384 whole-rock samples and is the largest obtained by the *k*-means procedure. Therefore, it is the most diverse cluster and includes rhyolites, dacites, Hiltaba Suite-affiliated granite and minor Donington granite samples. Cluster 4 stands out from Clusters 5 and 7 as being relatively Cu poor (median 180 ppm) and differs from Cluster 3 by the lower Fe content (median = 10 wt%).

Projection of the seven clusters onto PCs provides their visual assessment and geochemical affinities (Fig. 9). The PC scores of PC1, PC2 and PC3 are listed in Table 4; these are the coordinates of each sample in a corresponding PC projection (Fig. 9A, C). First and foremost, a projection of PC1–2 (Fig. 9A, B) shows the distinct Cluster 6 and its strong association with IOCG-signature elements of Groups 2, 3 and 4. On the other hand, Clusters 1, 2, 4 and 5 show an affinity with Group 1 elements (Rb, K, Ba, Si, Al, Zr and Na) representing felsic host rocks along with their alteration products (Fig. 9A).

One of the most interesting features depicted by the PC1-PC2 projection is the position of Clusters 3 and 7 in relation to Fe-rich veins (represented by Cluster 6) and host rocks (Clusters 1, 2, 4, and 5). Clusters 3 and 7 show an association with IOCG-signature elements and thus likely representing altered and/or partially mineralized/veined samples, rather than the magnetite-dominant mineralization itself.

Whereas the PC1-PC2 projection provides information about the most dominant process depicted by the samples data, the projection of samples onto PC2-PC3 provides additional insight into the geochemical meaning of the obtained clusters, and therefore the geological processes

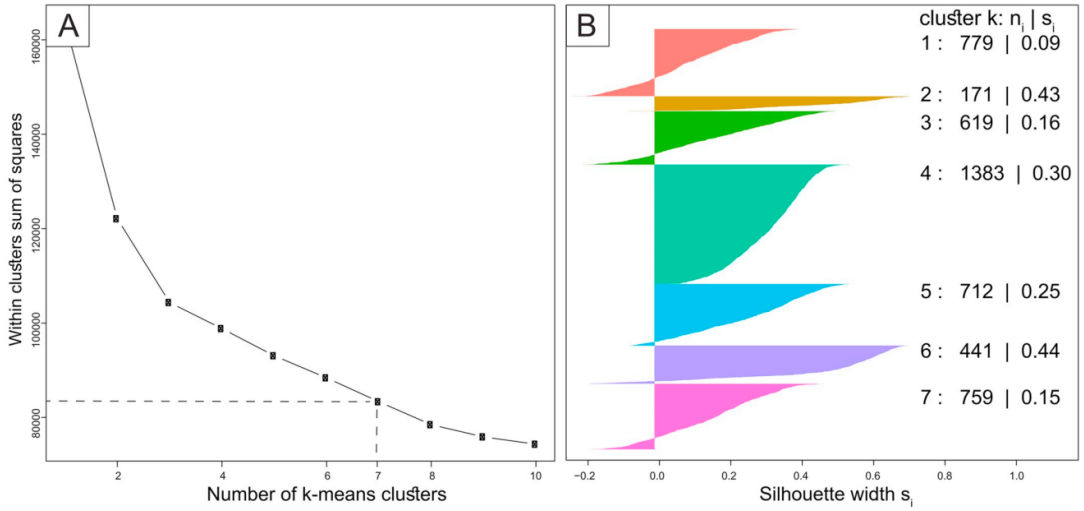


Fig. 8. (A) Sum of squared errors versus and the number of clusters k = 1, …, 10 showing that 6 to 8 clusters are optimal for *k*-means cluster analysis. (B) Values of Silhouette widths (s) plotted for each geochemical analysis within a cluster (clusters are color-coded and numbered). Cluster number i (i = 1, …, 7), a number of analyses (n_i) and average s_i per cluster are given on the right side.

Table 3
Characteristics of seven clusters obtained from *k*-means cluster analysis.

Cluster	n_i, samples	Jaccard similarity value, j_i	Silhouette value, s_i	Predominant cluster lithology and median values of Fe, K and Cu	Median density, kg/m^3	Median magnetic susceptibility, $\times 10^{-3}$ SI
1	779	0.57	0.09	Altered, least-veined rhyolites and minor dacites with 5% Fe, 5–6% K and 35 ppm Cu.	2.6	0.86
2	171	0.74	0.43	Altered Donington granite and diorite with pronounced sodic alteration; 8% Fe, 3.5% K and 85 ppm Cu	2.7	0.94
3	619	0.84	0.16	Altered and intensively veined rhyolites and dacites with 30% Fe, 2.7% K and 137 ppm Cu	3.1	1.52
4	1384	0.69	0.30	Altered and moderately veined rhyolites, dacites, HS and Donington granite with 10% Fe, 5% K and 180 ppm Cu	2.7	1.91
5	712	0.74	0.25	Altered Donington granite and diorite with minor dacites; 20% Fe, 4% K and high Cu content (530 ppm)	2.9	28
6	441	0.93	0.44	Fe-rich veins; Fe > 60%, K < 0.1% and high Cu content (430 ppm)	4.2	306
7	759	0.75	0.15	Altered and veined rhyolites, dacites and ignimbrites with Fe 25% and K 2% and 280 ppm Cu	3.1	28

n_i = number of whole-rock samples within each cluster. Calculated cluster stability and Silhouette values are from Fig. 8b. Median densities and median values of Fe, K are in wt%.

involved. For instance, the PC2-PC3 projection differentiates Cluster 5 from the others as the most Cu-Mo-rich cluster of samples (Fig. 9C). Interestingly, Cluster 2, which is comprised of weakly mineralized Donington granite and diorite (Table 3), shows an affinity with Fe-V-Co-Ni along with Li, Mg, Mn, Zn, Ca, Na, Ti and Sc. Such a geochemical signature can be readily explained by propylitic and sodic alteration assemblage of calc-silicate minerals, i.e., epidote-chlorite-albite, and the presence of Fe-rich (micro)veinlets throughout Donington Suite Granitoid host rocks. Another interesting feature of the PC2-PC3 projection is the Nb−Ta signature, which not only characterizes a portion of samples of Fe-rich veins (Cluster 6) but can also be attributed to a portion of least mineralized rhyolites (Cluster 1). This suggests the presence of Nb-Ta-bearing minerals in both felsic host rocks and also within mineralized veins. The latter interpretation is supported by the hierarchical dendrogram (Fig. 5), which grouped Na−Ta together with Group 1 elements representing felsic host rock signatures.

The information provided by the projections can be summarized as follows: PC1 depicts a contrast between felsic host rocks versus mineralized Fe-rich veins associated with a group of IOCG-signature elements. The spatial projection of PC1 scores indicates the mineralization signatures within drillholes ACD7, ACD9 and ACD1, along with a less pronounced signature in ACD3 and ACD12 (Fig. 10A). Similarly, the PC3 scores, which represent sodic and propylitic alteration (negative values) display the alteration signature in the eastern part of the Acropolis prospect, specifically within ACD6 and ACD20 (Fig. 10B). The three-dimensional outlines of Fe > 20 wt% and Cu > 200 ppm provide additional comparison with the lithologies, PC scores and also Clusters 2, 3 and 6 (Fig. 10C). Such a comparison allows for an understanding of mineralization signatures with respect to host lithologies and lithogeochemical clusters.

4.4. Centred ternary diagrams

Using the information extracted from the hierarchical dendrogram (Fig. 5) and PCA results (Fig. 9), a 3-part sub-composition consisting of composite variables was generated and visualized on a ternary diagram (Fig. 11). Composite variables represent geometric means of Ba, Zr, Al, Si, Na, K and Rb (Group 1), Ca, P, Li, Mg, Sn, Sc, Ti, Zn, Sb and W (Group 3), and Cu, Mo, Bi, Fe, V, Co and Ni (Group 4).

Niobium and Ta were not included within the Group 1 composite variable due to their complex distribution; Group 2 was also disregarded on similar grounds. The purpose of the ternary diagrams was to visualize data in a new 3-part geochemical space and provide visual comparison between logged lithologies and the seven clusters obtained. A projection of clusters on a ternary diagram efficiently reproduce and significantly complements the results of PCA (Fig. 9).

In the space of 3-part sub-composition, chemical distinctions among the clusters are evident as Groups 1, 3 and 4 represent end-members within the Acropolis geochemical data (Fig. 11A). The diagram shows that Cluster 3 is associated with Group 3 variables (Ca, P, Li, Mg, Sn, Sc, Ti, Zn, Sb and W), which are the indicator and target elements of the Fe-rich veins. Additionally, the diagram shows that Clusters 5, 6 and 7 are the most Cu- and Fe- rich, which corresponds accurately with the cluster descriptions (Table 3) and the results of PCA (Fig. 9A, B). Finally, the diagram efficiently demonstrates that samples belonging to Clusters 1 and 2 are the least veined/mineralized as they plot towards the Group 1 apex (Ba, Zr, Al, Si, Na, K and Rb).

Logged lithologies were plotted on two additional ternary diagrams (Fig. 11B, C) in order to provide a visual comparison with the seven clusters. These ternary diagrams certainly provide additional insight into the geochemical meaning of the clusters, such as clusters being largely independent of the rock protolith and instead reflecting the geochemical signatures defined by a 3-part sub-composition ('CuMo-BiFeCoNiV', 'BaZrAlSiNaRbK' and 'CaPLiMgScTiZnWSnSb'; Fig. 11). Due to the diverse styles of alteration, mineralization and degrees of overprinting, unequivocal recognition of the primary protolith is not

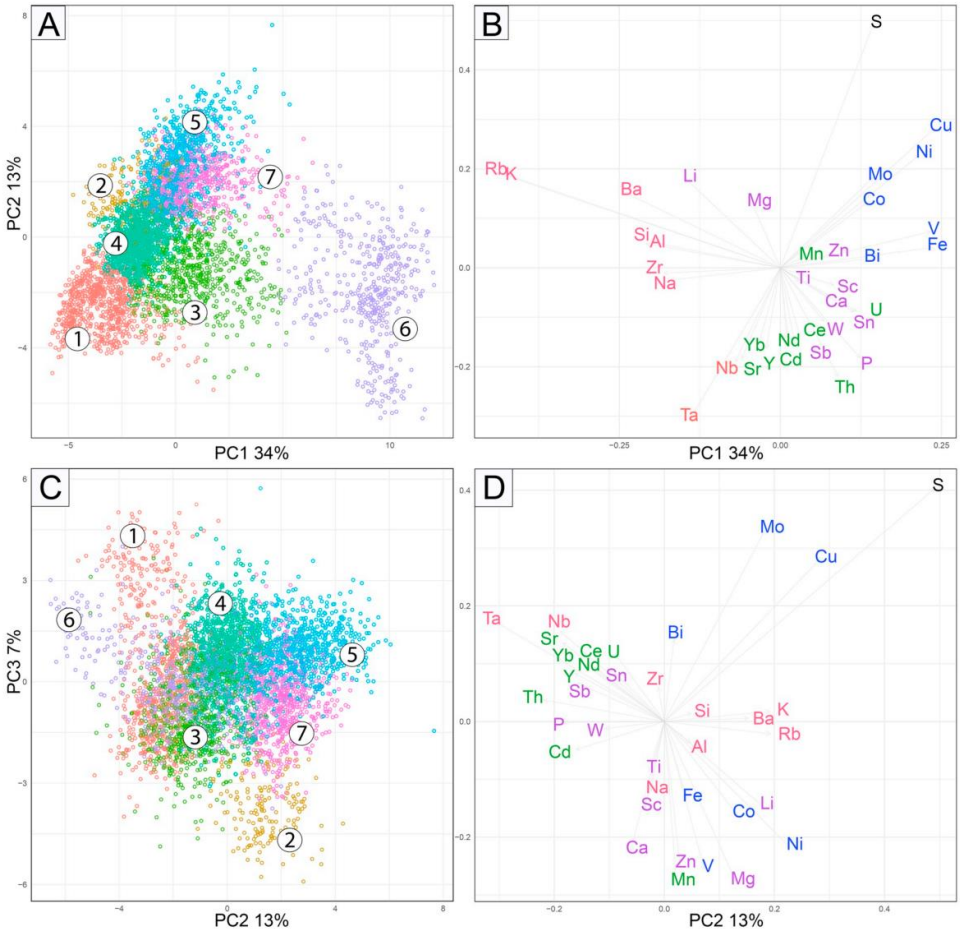


Fig. 9. Principal component scores and loadings of centred log-ratio-transformed data. The projection of PC1 versus PC2 (A) and PC2 versus PC3 (C) shows seven clusters (color-coded and numbered) obtained from the k-means cluster analysis (Table 3). Each data point (circle) represents an individual sample. The loadings of the elements on PC1 versus PC2 (B) and PC2 versus PC3 (D) projections (Table 4) color-coded according to the hierarchical dendrogram in Fig. 6.

supported. This is a common issue when trying to characterize a deposit with such a protracted geological history and complex alteration overprints (e.g. Ordóñez-Calderón and Gelcich, 2018).

4.5. Alteration types, styles and intensities

A plot of [Na/Al] + Ca vs. K/Al (Fig. 12A) was constructed to demonstrate the extent of potassic, sericitic and sodic alteration in rocks from the Acropolis prospect. Recognition of a specific alteration type is not possible from the whole-rock data alone as different alteration types display substantial overlap. Nevertheless, Cluster 2 corresponding to sodic alteration within Donington Suite Granitoids clearly stands out. Propylitic alteration is, unfortunately, not resolvable from the bivariate plots due to the presence of multiple Ca-Mg-Fe-bearing minerals in differing proportions.

The magnetic susceptibility of whole-rock data features a trend corresponding to individual magnetite- and hematite-dominant samples (Fig. 12B). The magnetic susceptibility values $> 10 \times 10^{-3}$ SI are likely to represent samples containing magnetite. Given the 95% ellipsoid outlines, a majority of the clusters comprise samples that contain both hematite and magnetite, with the exception of Clusters 1 and 3. Cluster 3 is likely to represent geochemical signature of hematite mineralization, whereas Cluster 1 corresponds to the least veined/mineralized rhyolites as discussed above.

4.6. Random forests model

The validation subset of 3405 geochemical samples was used to test the RF model trained on 1459 samples. In the case of seven-category classification of the whole-rock samples the model accuracy is 91% (Table 5). Such a relatively high model accuracy justifies the seven clusters obtained via k-means for splitting geochemical data into geochemical domains. The model indicated that samples of Donington Suite Granitoids (Cluster 2) and Fe-rich veins (Cluster 6) are the least misclassified clusters. In contrast, Clusters 3 and 4 have showed at least 10% of misclassified observations.

The variable importance indicated by the RF model is presented in Fig. 13 with S, Cu and Fe being the most important for geochemical

Table 4
Results of PCA given as the proportions of explained variance by first, second and third principal components, with loadings (coordinates of the elements on the PCs projection; Fig. 9b, d).

Eigenvalues of PC1 to PC3			
Eigenvalues	PC1	PC2	PC3
λ	3.43	2.11	1.55
λ%	34	13	7
Σλ%	34	48	55

Loadings of the elements on PC1-PC3			
Elements	PC1	PC2	PC3
Al	−0.18	0.04	−0.03
Ba	**−0.24**	0.15	0.00
Bi	0.13	0.01	0.14
Ca	0.07	−0.06	**−0.22**
Cd	0.01	−0.15	−0.04
Ce	0.03	−0.13	0.10
Co	0.13	0.13	−0.16
Cu	**0.23**	**0.28**	**0.27**
Fe	**0.23**	0.04	−0.13
K	**−0.43**	0.19	0.01
Li	−0.14	0.17	−0.14
Mg	−0.04	0.12	**−0.27**
Mn	0.03	0.02	**−0.27**
Mo	0.14	0.18	**0.33**
Na	−0.17	−0.02	−0.11
Nb	−0.07	−0.18	0.15
Nd	0.01	−0.14	0.10
Ni	**0.21**	**0.22**	**−0.21**
P	0.12	−0.18	−0.00
Rb	**−0.44**	0.19	−0.02
S	0.14	**0.49**	**0.40**
Sb	0.02	−0.15	0.06
Sc	0.08	−0.03	−0.14
Si	**−0.20**	0.04	0.01
Sn	0.11	−0.08	0.08
Sr	−0.06	−0.18	0.13
Ta	−0.13	**−0.30**	0.17
Th	0.08	**−0.21**	0.03
Ti	0.02	−0.02	−0.08
U	0.11	−0.08	0.11
V	**0.23**	0.07	**−0.25**
W	0.06	−0.10	−0.01
Y	−0.02	−0.16	0.08
Yb	−0.03	−0.15	0.10
Zn	0.08	0.02	**−0.24**
Zr	−0.18	−0.01	0.06

Numbers in bold indicate absolute loadings of the elements with > 0.2 implying a high correlation of a particular element with its respective PC.

classification. Given that statistical analyses are sensitive to discretization, S importance is likely an artefact due to the imputation of the BDL values. In fact, if the RF model is fitted without S, the classification performance is hardly affected and Cu and Fe remain important.

5. Discussion

5.1. IOCG signatures at Acropolis prospect: a comparison with Olympic Dam

The kriged values of PC1 display a mineralized domain in the western part of the prospect (ACD1, ACD7 and ACD9), and within Donington Granitoids from the southeastern corner of the prospect (ACD3 and ACD12) (Figs. 6; 10). Similar to the IOCG footprint in the Olympic Dam deposit, the multi-element signature of mineralization at Acropolis encompasses a range of indicator trace elements alongside the IOCG-defining metals Fe and Cu (Table 4; Fig. 5). The major distinction between mineralization signatures in the two deposits is, however, the deficiency in Au at Acropolis (one of the metals that remained below minimum detection limits in ~70% of geochemical analyses). Furthermore, in Acropolis, Cu is present at only sub-economic concentrations with values from 200 to 1000 ppm distributed throughout all drillholes with the exceptions of the unmineralized ACD5 and ACD15 (Fig. 10C). Nevertheless, Cu strongly contributes to the IOCG signature (Figs. 5 and 9B) and is an important geochemical variable for classification of the data (Fig. 11).

Sulphide-poor assemblages comprising magnetite ± apatite followed by hematite ± sulphide-richer Cu—Au mineralization (as known from Acropolis; e.g., Krneta et al., 2017a, 2017b) are also known from other IOCG deposits (e.g., Ernest Henry, Mark et al., 2006; Tjårrojåkka, Sweden, Edfelt and Martinsson, 2003). Based on results of the present study, it is evident that although Fe-oxide and Cu(—Fe)-sulphide mineralization are associated, they clearly offset each other in some measure reaffirming that patterns observed in whole-rock data correspond, to some extent, with petrographic observations (Krneta et al., 2017a, 2017b; Fig. 10C). Although it is not possible to accurately resolve mineralogical assemblages from the whole-rock data, it is evident that the most Cu-rich samples (Clusters 5; Fig. 9A; B) contain 'only' 20 wt% Fe (Table 3), therefore high Cu content is not necessarily related to the elevated Fe values, which can reach up to 60 wt% in Fe-rich veins (Cluster 6; Figs. 9A, B and 10C). In both Olympic Dam and Acropolis, a high threshold of Fe (> 60 wt%) correlates with lower Cu content.

Despite the relative lack of direct petrographic control over these data, inferences about the mineralogy of the Acropolis prospect can readily be made due to the direct relationships between the stoichiometries of rock- and ore-forming minerals with the whole-rock geochemical data (Aitchison, 1986). Both PC1 and PC2 clearly distinguish elements hosted by or within sulphides (Mo, Cu, S) from oxide-hosted elements (Fe and V) (Fig. 9D), thus supporting the petrographic observations that chalcopyrite is not always associated with the magnetite-dominant assemblage (Krneta et al., 2017a, 2017b). Unlike in Olympic Dam deposit, where Mo is predominantly hosted within U-W-Sn-Mo-bearing hematite, it is predominantly associated with sulphides in Acropolis.

The projection of loadings on PC1–2 illustrates that Co—Ni are grouped with Cu—Mo, thus suggesting a Cu-bearing mineral, likely carrollite (or other thiospinels), as one of the main Co—Ni hosting minerals (Fig. 9B). On the PC2–3 projection, the Co—Ni group appears close to Fe-Vi, probably reflecting that a relatively high proportion of Co and Ni is also hosted by magnetite (Fig. 9D). In Olympic Dam, Co and Ni show correlation with the pyrite-chalcopyrite ore zone which was interpreted to reflect the abundance of these elements in pyrite (Dmitrijeva et al., 2019). Nickel is, however, a good proxy for distinguishing mafic lithologies at Olympic Dam (Dmitrijeva et al., 2019). Vanadium, on the other hand, displays a very strong association with Cluster 6 corresponding to magnetite ($\tau_{FeV} = 0.1$; Table 2; Fig. 12B) and therefore is likely associated with early magnetite, rather than hematite.

The presence of a Nb—Ta signature in the mineralized veins at Acropolis can be attributed to high-Ti magnetite with trellis-like exsolution of ilmenite ± rutile (Krneta et al., 2017a, 2017b), leading to this element pair also typifying mineralization. At OD, Ti-rich magnetite is typical of magmatic magnetite in host granite, whereas the early, hydrothermal magnetite is silician (Si-magnetite; Verdugo-Ihl et al., 2019; Ciobanu et al., 2019). The hematite in the Olympic Dam orebody is Ti-poor and varies in content with other HFSE such as Nb (Verdugo-Ihl et al., 2019). Early hematite associated with Si-magnetite is, however, HFSE-rich, (Verdugo-Ihl et al., 2019), particularly with respect to Ti. As the Si-magnetite + HFSE-hematite from the weakly-mineralized granite forming an outer shell at Olympic Dam have been considered to form at ≥400 °C (Verdugo-Ihl et al., 2019), we consider the Ti-rich magnetite veins at Acropolis to be not only early but also representing a

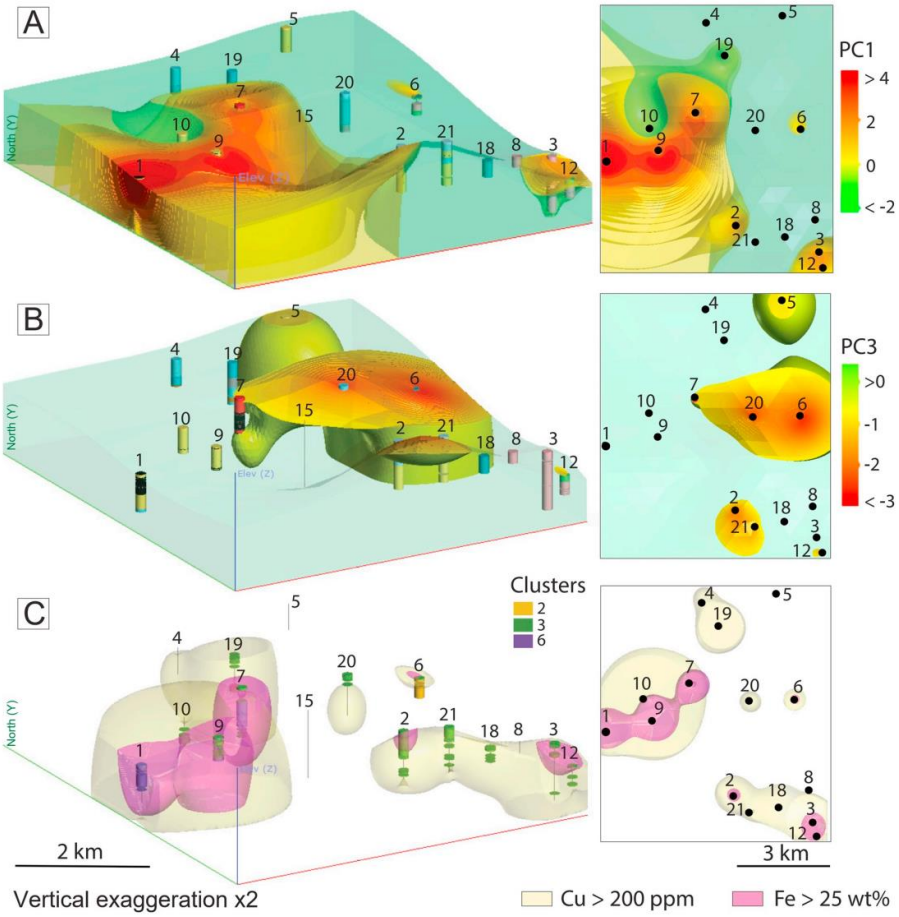


Fig. 10. (A, B) PC1 and PC3 scores (krigged values) plotted in oblique (left) and plan view (right) showing the IOCG signature and alteration footprint, respectively, at Acropolis. Note that the IOCG signature is not centred on the Hiltaba Suite granite as shown in Fig. 6 although it does overlap with it (ACD7). The legend for lithologies as in Fig. 6. (C) Plots in oblique (left) and plan view (right) showing isosurfaces of Fe > 25 wt% and Cu > 200 ppm with an overlay of geochemical clusters relevant for sodic and propylitic alteration (Cluster 2), 'hematite' (Cluster 3) and 'magnetite' signature (Cluster 6). Note the mismatch between the areas with Cu- and Fe-rich concentrations e.g., in ACD4 and ACD19.

high-temperature stage.

The elements W, Sn and Sb (hosted by iron-oxides), along with U, Th, Sr, P and REE (hosted for the most part by a diverse range of U-, Th- and REE-minerals) are also a part of the IOCG signature. These elements are, however, less dominant on PC1 compared to Group 4 elements (Cu-Mo-Bi-Fe-V-Ni-Co). The association between REE, P and Sr may reflect a Sr-bearing REE-phosphate mineral, probably akin to the compositionally-broad, paragenetically-late family of Sr-Ca-REE-Al-phosphate-sulphates of the Alunite Supergroup described from Olympic Dam (Owen et al., in review).

5.2. Alteration footprints

In the Acropolis prospect, visual discrimination of the felsic rocks, that host mineralization, can be highly uncertain given the petrographic similarities between multiple effusive/eruptive episodes within the GRV and also the impact of overprinting alteration (McPhie, 2016; Fig. 3). The lithogeochemical 7-class variable 'Clusters' are thus better suited to characterize and discriminate altered and mineralized host lithologies. This is because: (i) clusters can be associated with zones of distinct geochemical characteristics with respect to alteration and mineralization; and (ii) they are natural groups within the data which can be directly related with specific geological processes. Given the high accuracy of classification using RF, it is clear that seven clusters represent valid natural groups for these data, which can be validated by petrographic study.

Based on the magnetic susceptibility values, the majority of the geochemical clusters include both magnetite- and hematite-dominant assemblages (Fig. 12B), with the exceptions of Clusters 1 and 3. Whereas Cluster 1 corresponds to the least mineralized rhyolites (Table 3), Cluster 3 represents veined/mineralized rhyolites and dacites which are characterized by Group 2 and 3 sub-compositions of Ca-P-Li-Mg-Sc-Ti-Zn-W-Sn-Sb (Fig. 11A), along with REE, Sr, U and Th (Fig. 9B). Such a signature, which is evidently associated with hematite-

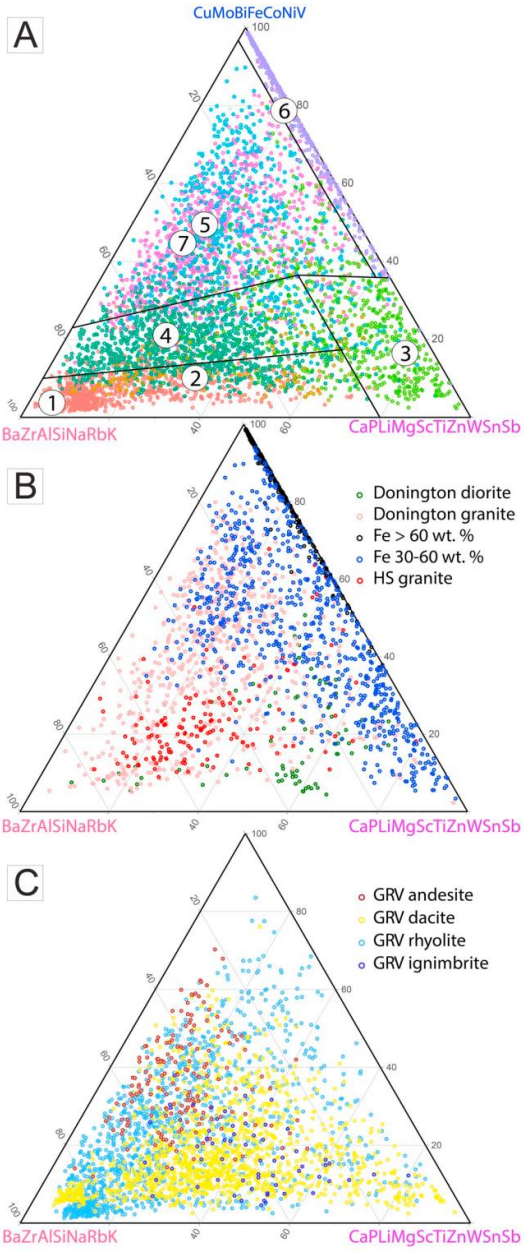


Fig. 11. Centred ternary diagrams of the whole-rock reduced to three sub-compositions as in the dendrogram presented as Fig. 5. (A) The seven geochemical clusters (color-coded and numbered) obtained from k-means analysis are distinguishable in the 3-component simplex although with some overlap e.g., Clusters 5 and 7; lines separating clusters are fitted visually. (B, C) The same diagram as in (A) with samples separated by lithologies as per logging. This shows how k-means geochemical clusters in (A) are better suited to discriminate altered lithologies.

dominant alteration, e.g. 'hematite signature', is likely the geochemical footprint of a hematite-dominant alteration overprinting an early Cu-deficient magnetite assemblage. The projection of Cluster 3 in Leapfrog (Fig. 10C) indicates that such a signature does not form halos around Fe-rich veins (Cluster 6), but is ubiquitous throughout the Acropolis prospect. This confirms that the conspicuous granitophile signature at Olympic Dam (Ciobanu et al., 2013; Courtney-Davies et al., 2016; Verdugo-Ihl et al., 2017; Dmitrijeva et al., 2019) is also recognised at Acropolis, particularly in areas where hematite is present.

The felsic rocks that host mineralization at Acropolis are affected by intense and overlapping alteration which has resulted in major compositional changes to the rocks (Fig. 12A). Potassic and sericitic alteration are both ubiquitous and are recognised in the vast majority of samples throughout the prospect area (Fig. 12A). Sodic alteration is, however, relatively minor, having been obliterated by a superimposed, subsequent stage of potassic alteration (Kontonikas-Charos et al., 2017) and is mostly present within Cluster 2 (predominantly in ACD6), which represents Donington Suite Granitoids (Fig. 10C) with an increased proportion of Na (ACD6; median = 1.2 wt%). In contrast, the Na content of GRV dacites and rhyolites have median values of ~0.1 wt%, whereas Hiltaba Suite granites (ACD7) and the remaining samples of Donington Suite Granitoids appear without pronounced sodic alteration (median Na values are 0.12 wt% and 0.07 wt%, respectively). Projection of the whole-rock samples on PC2-PC3 (Fig. 9D) indicates an association of Na-Ca-Li-Mn-Mg-Ti-Sc that can be interpreted as an expression of propylitic and sodic alteration with a Fe-V-Co-Ni signature present within minor veins. The extent of propylitic and sodic alteration is demonstrated in Fig. 10B as an interpolant of negative PC3 values, for the eastern zone of the Acropolis prospect.

5.3. Exploration significance

The Fe-V-Ni-Co element association is a signature of early, high-temperature 'magnetite' formation at Acropolis and should be recognisable in magnetite-bearing IOCG mineralization within the Olympic IOCG province. Despite being relatively deficient with respect to Cu and Au, the IOCG geochemical signature for Acropolis still comprises Cu and Fe along with granitophile elements W-Sn-Mo-U, Sb, Bi and REE, which are characteristic for the hematite-dominant mineralization signature at Olympic Dam. The presence of a superimposed granitophile element-bearing signature marks formation of hematite and represents an unequivocal correlation between Acropolis, Olympic Dam and many other IOCG deposits in South Australia. Such a signature has not been widely reported from other IOCG terranes, with the exception of the Carajás district, Brazil (Courtney-Davies et al., 2016). The idea that a high abundance of apatite in Acropolis may account for IOA-type mineralization is not supported by the current data since Ca and P show no strong correlation with Cluster 6, which represents magnetite (Fig. 12B).

The magnetite veins at Acropolis may represent either the preserved root of Cu–Au mineralization that has been eroded away, or alternatively, the upper part of undiscovered mineralization since the IOCG signature (PC1 plot), although partially coincident, is not centred on the Hiltaba granite. Although the Olympic Dam district lacks basement outcrop at surface, comparisons can be made with generic IOCG alteration models based on observations elsewhere, notably from the Great Bear magmatic zone, northwestern Canada (Montreuil et al., 2013; Corriveau et al., 2016). For example, in the latter case, amphibole- and magnetite-bearing, calcic-iron alteration assemblages are recognised as distinct facies forming along zones of weakness produced by albitisation (Corriveau et al., 2016). It is also acknowledged that alteration and element mobility in IOCG systems, including those elements considered 'immobile', is orders of magnitude higher than in many other types of hydrothermal systems (Montreuil et al., 2013). In the case of the Olympic Cu–Au province, regional-scale albitization followed by potassic alteration and then by dominant metasomatic iron

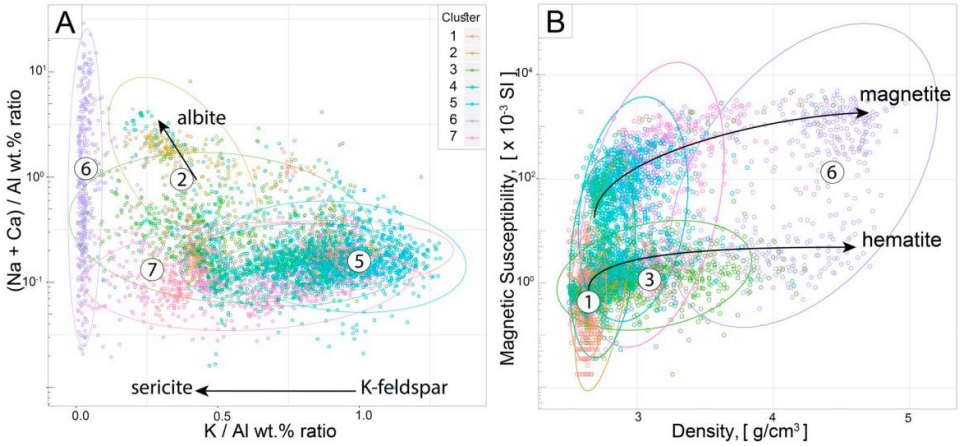


Fig. 12. Alteration trends from whole-rock analyses (A) and magnetic susceptibility versus density (B) color-coded and numbered according to a cluster membership and outlined by 0.95 confidence ellipses. (A) The typical K-feldspar to sericite alteration is represented by transition from Cluster 5 to Clusters 1 and 7. In contrast Na + Ca alteration shows the albitization (Cluster 2). Cluster 6 representing 'magnetite' signature (Fe-V-Ni-Co) spreads across Na + Ca alteration but is invariant to sericite alteration. (B) Clusters 1, 3 and 6 showing two distinct trends reflecting magnetite-dominant versus hematite dominant mineralization. The petrophysical data is limited to samples with measurements of both properties.

Table 5
Confusion matrix of the fitted Random Forest model onto validation set (n = 3405 samples). True classes are arranged by columns, whereas predicted classes are within rows.

	1	2	3	4	5	6	7
1	491	0	2	23	0	0	0
2	0	113	0	1	1	0	0
3	4	0	378	7	15	7	18
4	44	1	32	874	15	0	12
5	0	0	7	26	453	0	13
6	0	0	4	0	0	306	1
7	0	0	12	33	10	7	495
True class total	539	114	435	964	494	320	539
Percentage misclassified	8%	0.8%	15%	10%	9%	4%	8%
Model accuracy	91%						

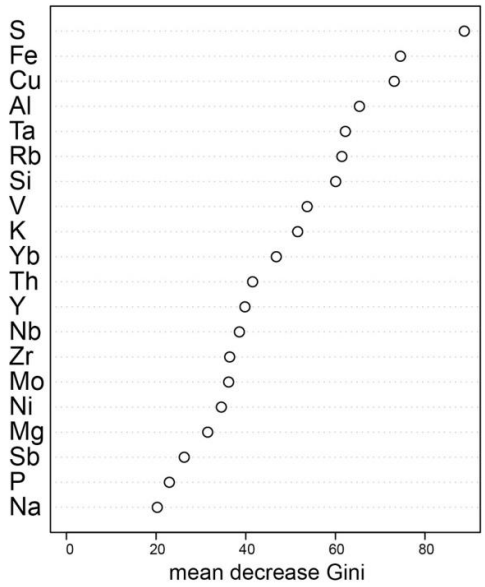


Fig. 13. Plot showing variable importance as 'mean decrease Gini index' obtained from fitted random forests model. The twenty most important elements are odered according to this index showing that S, Fe and Cu are the most important variables for classification whereas P and Na are the least important.

alteration are recognised in the Moonta area, further south from the Olympic Dam district (Conor et al., 2010; Kontonikas-Charos et al., 2014). At Olympic Dam, these stages are also recognised but they are partially telescoped with one another (Mauger et al., 2016; Kontonikas-Charos et al., 2017). Alkali-calcic alteration with key calc-silicates (clinozoisite/zoisite; actinolite, calcic garnet) are present in the weakly-mineralized granite from the outer shell at Olympic Dam as shown from mineralogical studies down to the nanoscale (Cook et al., 2017; Kontonikas-Charos et al., 2018a, 2018b; Ciobanu et al., 2019). Analogous mineralogical studies at Acropolis will prove whether the comparable geochemical trends with Olympic Dam are supported by similar mineralogy. As in any hydrothermal system, the role played by protoliths would impact on the mineralogical expression within the same general alteration scheme, e.g., if limestones are present, skarn assemblages with calc-silicates as mentioned above will be formed, e.g., at Island Dam in the Olympic Dam district (Keyser et al., 2017), or at Hillside at the southern shore of the Yorke Peninsula (Ismail et al., 2014).

The recognition of magnetite-dominant members of the IOCG systems are of critical importance in establishing the 3D-spatial frameworks of entire IOCG systems and can help target discovery of fertile and hematite-dominant mineralization. This is particularly significant in the eastern Gawler Craton where basement and contained mineralization do not outcrop and are instead buried by several hundred metres of barren sedimentary cover. Overall, an improved understanding of the genesis and full extent of zonation in IOCG systems is fundamental for their effective exploration, both at the local and regional scales.

6. Conclusions

This contribution demonstrates that application of supervised and unsupervised machine learning techniques is effective for investigation of mineralization and alteration signatures of a large data set, and for understanding the key geochemical associations among component elements in the absence of detailed petrographic and mineralogical information. Reinforced by the RF model, a categorical variable 'Cluster', obtained from k-means algorithm, is appropriate for characterization of a deposit with a protracted history such as the Acropolis deposit, and others of same age in the same metallogenetic province. The seven clusters derived here represent geochemically meaningful domains.

Within the prospect, Fe and Cu mineralization are slightly offset – consistent with the observation of Cu-deficient magnetite-apatite veins in the western part of the Acropolis and overprinting Cu-endowed hematite-dominant assemblages that extend throughout the prospect area represented as Cluster 3. This conclusion is supported by the low magnetic susceptibility of Cluster 3 and a range of the indicator elements which are typically hosted within a hematite-dominant assemblage: Ca, P, U, Th, REE, W, Sn and Sb. In contrast, magnetite mineralization (Cluster 6) is typified by a Fe-V-Ni-Co signature, although Co—Ni are also co-hosted within chalcopyrite, which is not always in association with magnetite. The Fe-V-Ni-Co signature is an indicator of early and likely high-temperature IOCG mineralization and is a significant proxy for exploration of fertile hematite-dominant IOCG deposits at shallower crustal levels. However, at Acropolis, hematite-dominant assemblages are superimposed onto sulphide-poor magnetite ± apatite mineralization.

Variable alteration style and intensity are ubiquitous at Acropolis. Sodic and propylitic alteration are relatively minor (or at least poorly preserved) and are mostly developed within Donington Suite Granitoids in the eastern block of the prospect. Sodic and propylitic alteration are likely obliterated by ubiquitous potassic and sericitic alteration which are pervasive throughout the prospect.

Acknowledgements

This work is a contribution to the FOX project 'Trace elements in iron-oxides: deportment, distribution and application in ore genesis, geochronology, exploration and mineral processing', supported by BHP Olympic Dam and the South Australian Mining and Petroleum Services Centre of Excellence. N.J.C. acknowledges additional support from the ARC Research Hub for Australian Copper-Uranium (Grant IH130200033). Two anonymous reviewers are thanked for their comments that greatly improved the manuscript. The Leapfrog Geo support team is also warmly thanked for their assistance with geological modelling.

Appendix A. The variation matrix

	Ba	Bi	Ca	Cd	Ce	Co	Cu	Fe	K	Li	Mg	Mn	Mo	Na	Nb	Nd	Ni	P	Rb	S	Sb	Sc	Si	Sn	Sr	Ta	Th	Ti	U	V	W	Y	Yb	Zn	Zr
Al	0.7	1.4	1.5	0.9	0.4	1.0	2.5	1.5	0.2	0.5	0.7	1.1	2.2	0.2	0.4	0.5	1.9	1.2	0.2	3.3	0.4	0.3	0.0	0.7	0.4	0.6	0.7	0.3	0.6	1.4	0.7	0.4	0.3	0.9	0.1
Ba		2.0	1.9	2.0	1.2	1.5	3.0	1.8	0.3	1.6	1.3	1.6	2.9	0.8	1.1	1.2	2.7	2.4	0.6	3.2	1.2	1.1	0.6	1.3	1.0	1.5	1.9	1.0	1.5	2.0	1.6	1.0	1.0	1.4	0.7
Bi			1.6	2.2	1.4	0.9	1.6	1.2	1.9	1.2	1.3	1.9	1.6	1.7	1.7	1.6	1.2	1.7	1.8	3.0	1.3	1.2	1.3	1.0	1.8	2.8	2.0	1.1	1.2	1.4	1.2	1.5	1.5	1.1	1.5
Ca				2.6	0.9	1.1	2.5	1.1	1.9	1.3	0.9	1.6	2.3	1.4	1.8	0.9	1.8	0.2	1.9	4.1	1.1	0.9	1.5	1.1	1.1	2.7	1.8	1.1	1.2	1.2	1.3	1.2	1.2	1.3	1.8
Cd					1.4	1.7	2.9	2.3	1.4	1.7	2.1	1.7	2.2	1.2	1.5	1.5	2.7	2.2	1.4	3.5	1.2	1.5	0.9	1.5	1.2	1.5	1.1	1.3	1.3	2.6	1.5	1.2	1.2	1.2	0.9	
Ce						0.9	2.0	1.1	0.8	0.8	0.7	1.3	1.4	0.6	0.6	0.1	1.7	0.7	0.7	3.0	0.5	0.3	0.4	0.4	0.3	1.2	0.7	0.4	0.5	1.3	0.6	0.2	0.2	0.8	0.5
Co							1.1	0.5	1.4	0.7	0.9	1.2	1.0	1.5	1.8	1.0	0.3	1.3	1.4	2.0	0.8	0.5	0.9	0.6	1.2	2.6	1.0	0.6	0.6	0.6	0.8	1.2	1.2	0.4	1.0
Cu								1.3	2.7	2.3	2.3	2.1	1.4	3.1	2.9	2.2	1.1	2.4	3.0	1.9	2.1	1.9	2.3	1.5	2.6	4.0	2.6	2.1	1.5	1.4	2.0	2.5	2.4	1.8	2.6
Fe									1.5	1.2	1.0	1.7	1.3	1.9	2.9	1.2	0.7	1.1	1.9	2.7	0.8	0.6	1.3	0.6	1.5	3.9	1.0	0.9	0.7	0.1	0.9	1.5	1.4	0.7	1.4
K										1.1	1.0	1.4	2.8	0.3	0.4	0.8	2.5	1.8	0.1	3.7	0.6	0.7	0.2	0.8	0.7	0.6	1.1	0.5	1.0	1.8	1.1	0.4	0.4	1.1	0.3
Li											0.2	1.5	1.9	0.8	1.1	0.9	1.1	1.3	1.0	3.2	1.1	0.6	0.6	0.9	0.9	1.7	1.3	0.7	0.9	1.1	1.2	0.8	0.8	0.8	0.6
Mg												1.3	2.0	0.9	1.2	0.7	1.2	1.3	1.0	2.9	0.9	0.6	0.6	0.9	0.8	2.0	1.3	0.5	1.1	0.9	1.0	0.7	0.7	0.7	0.9
Mn													2.0	1.8	1.7	1.5	1.9	2.1	1.3	2.5	1.3	1.2	1.2	1.5	1.5	2.4	1.7	1.2	1.5	1.7	1.4	1.6	1.6	1.2	1.4
Mo														2.7	2.8	1.7	1.3	2.0	2.9	1.8	1.6	1.2	2.0	1.1	2.1	4.3	1.8	1.3	0.8	1.5	1.4	2.1	2.1	1.5	2.1
Na															0.6	0.7	2.6	1.5	0.3	3.7	0.6	0.6	0.2	1.1	0.5	0.8	0.9	0.5	1.0	2.1	0.9	0.5	0.4	1.2	0.3
Nb																0.5	2.9	1.5	0.4	3.7	0.9	0.9	0.4	0.8	0.9	0.2	1.3	0.6	1.4	3.0	1.3	0.2	0.2	1.2	0.5
Nd																	1.9	0.8	0.8	3.3	0.6	0.3	0.5	0.4	0.4	1.1	0.8	0.3	0.6	1.4	0.8	0.1	0.1	0.9	0.7
Ni																		2.0	2.4	2.2	1.9	0.8	1.8	0.9	2.3	4.2	2.0	1.1	1.0	0.7	1.6	2.1	2.1	1.1	2.0
P																			1.9	3.8	0.9	0.9	1.2	0.8	1.1	2.2	1.5	0.9	0.9	1.3	1.0	1.0	1.1	1.1	1.4
Rb																				3.7	0.7	0.6	0.2	0.8	0.8	0.6	1.3	0.5	1.2	1.9	1.2	0.5	0.5	1.0	0.3
S																					3.8	2.7	3.3	2.7	3.6	5.1	3.2	2.6	2.4	3.2	3.4	3.7	3.5	3.3	3.6
Sb																						0.5	0.4	0.5	0.6	1.5	0.6	0.5	0.5	1.0	0.4	0.5	0.5	0.6	0.6
Sc																							0.4	0.4	0.6	1.5	0.8	0.1	0.4	0.6	0.5	0.5	0.5	0.5	0.4
Si																								0.6	0.4	0.5	0.6	0.3	0.5	1.3	0.7	0.4	0.3	0.8	0.0
Sn																									0.8	1.6	1.2	0.3	0.5	0.8	0.5	0.4	0.4	0.7	0.7
Sr																										1.2	0.7	0.7	0.6	1.7	0.9	0.5	0.4	0.9	0.4
Ta																											1.0	1.2	2.0	3.8	1.8	0.7	0.7	2.1	0.4
Th																												0.9	0.5	1.3	1.0	0.9	0.7	0.9	0.5
Ti																													0.6	0.7	0.7	0.3	0.3	0.5	0.4
U																														1.0	0.5	0.8	0.7	0.6	0.5
V																															1.1	1.6	1.6	0.8	1.5
W																																0.9	0.8	0.6	0.7
Y																																	0.0	0.8	0.5
Yb																																		0.8	0.4
Zn																																			0.9

References

Aitchison, J., 1986. The statistical analysis of compositional data. In: Monographs on Statistics and Applied Probability. Chapman & Hall, London. https://doi.org/10.1007/978-94-009-4109-0. 416 pp.

Apukhtina, O.B., Kamenetsky, V.S., Ehrig, K.J., Kamenetsky, M.B., Maas, R., Thomson, J., McPhie, J., Ciobanu, C.L., Cook, N.J., 2017. Early, deep magnetite-fluorapatite mineralization at the Olympic Dam Cu-U-Au-Ag deposit, South Australia. Econ. Geol. 112, 1531–1542. https://doi.org/10.5382/econgeo.2017.4520.

Barton, M.D., 2014. Iron oxide (–Cu–Au–REE–P–Ag–U–Co) systems. In: Holland, H.D., Turekian, K.K. (Eds.), Treatise on Geochemistry, second ed. Elsevier, Oxford, pp.

515–541. https://doi.org/10.1016/B978-0-08-095975-7.01123-2.
Blissett, A.H., Creaser, R.A., Daly, S.J., Flint, R.B., Parker, A.J., 1993. Gawler range volcanics. In: Drexel, J.F., Preiss, W.V., Parker, A.J. (Eds.), The Geology of South Australia. vol. 1. The Precambrian, Geological Survey of South Australia, pp. 107–131.
Bookstrom, A., 1977. The Magnetite Deposits of E1 Romeral, Chile. Econ. Geol. 72, 1101–1130. https://doi.org/10.2113/gsecongeo.72.6.1101.
Breiman, L., 2001. Random forests. Mach. Learn. 45, 5–32. https://doi.org/10.1023/A:1010933404324.
Breiman, L., Friedman, J.H., Olshen, R.A., Stone, C.J., 1984. Classification and Regression Trees. Wadsworth, Belmont. pp. 358. https://doi.org/10.1002/cyto.990080516.
Caciagli, N., 2016. Multielement geochemical modelling for mine planning: case study from an epithermal gold deposit. In: Martín-Fernández, J.A., Thió-Henestrosa, S. (Eds.), Compositional Data Analysis. Springer Proceedings in Mathematics & Statistics. 187. pp. 45–61. https://doi.org/10.1007/978-3-319-44811-4_4.
Cherry, A.R., Kamenetsky, V.S., McPhie, J., Thompson, J.M., Ehrig, K.J., Meffre, S., Kamenetsky, M.B., Krneta, S., 2018. Tectonothermal events in the Olympic IOCG Province constrained by apatite and REE-phosphate geochronology. Austral. J. Earth Sci. 65, 643–659. https://doi.org/10.1080/08120099.2018.1465473.
Ciobanu, C.L., Wade, B.P., Cook, N.J., Schmidt Mumm, A., Giles, D., 2013. Uranium-bearing hematite from the Olympic Dam Cu-U-Au deposit, South Australia; a geochemical tracer and reconnaissance Pb-Pb geochronometer. Precambrian Res. 238, 129–147. https://doi.org/10.1016/j.precamres.2013.10.007.
Ciobanu, C.L., Verdugo-Ihl, M.R., Slattery, A., Cook, N.J., Ehrig, K.J., Courtney-Davies, L., Wade, B.P., 2019. Silician magnetite: Si–Fe-nanoprecipitates and other mineral inclusions in magnetite from the Olympic Dam Deposit, South Australia. Minerals 9, 311. https://doi.org/10.3390/min9050311.
Conor, C.C.H., Raymond, O., Baker, T., Teale, G.S., Say, P., Lowe, G., 2010. Alteration and mineralisation in the Moonta-Wallaroo copper-gold mining field region, Olympic Domain, South Australia. In: Porter, T.M. (Ed.), Hydrothermal Iron Oxide Copper-Gold & Related Deposits: A Global Perspective, v. 3—Advances in the Understanding of IOCG Deposits. PGC Publishing, Adelaide, pp. 1–24.
Cook, N.J., Ciobanu, C.L., Ehrig, K., Slattery, A., Verdugo-Ihl, M.R., Courtney-Davies, L., Gao, W., 2017. Advances and opportunities in ore mineralogy. Minerals 7, 233; doi.org/https://doi.org/10.3390/min7120233.
Corriveau, L., 2005. Iron oxide copper-gold (± Ag ± Nb ± P ± REE ± U) deposits: a Canadian Perspective: Geological Association of Canada, Mineral Deposits Division. Special Publication 5 (2007), 307–328.
Corriveau, L., Montreuil, J.F., Potter, E., 2016. Alteration facies linkages among iron oxide copper-gold, iron oxide-apatite, and affiliated deposits in the Great Bear Magmatic Zone, Northwest Territories, Canada. Econ. Geol. 111, 2045–2072.
Courtney-Davies, L., Zhu, Z., Ciobanu, C., Wade, B., Cook, N., Ehrig, K., Cabral, A., Kennedy, A., 2016. Matrix-matched iron-oxide laser ablation ICP-MS U-Pb geochronology using mixed solution standards. Minerals 6, 85. https://doi.org/10.3390/min6030085.
Courtney-Davies, L., Tapster, S., Ciobanu, C., Cook, N.J., Verdugo-Ihl, M.R., Ehrig, K.J., Kennedy, A.K., Gilbert, S.E., Condon, D.J., Wade, B.P., 2019. A multi-technique evaluation of hydrothermal hematite U-Pb isotope systematics: implications for ore deposit geochronology. Chem. Geol. 513, 54–72. https://doi.org/10.1016/j.chemgeo.2019.03.005.
Cracknell, M.J., Reading, A.M., 2014. Geological mapping using remote sensing data: a comparison of five machine learning algorithms, their response to variations in the spatial distribution of training data and the use of explicit spatial information. Comput. Geosci. 63, 22–33. https://doi.org/10.1016/j.cageo.2013.10.008.
Creaser, R.A., 1989. The Geology and Petrology of Middle Proterozoic Felsic Magmatism of the Stuart Shelf, South Australia (Ph.D thesis). La Trobe University, Melbourne, pp. 434.
Cross, K.C., 1993. Acropolis and Wirrda Well. In: Drexel, J.F., Preiss, W.V., Parker, A.J. (Eds.), The Geology of South Australia. Vol. 1, the Precambrian. Geological Survey of South Australia, South Australia, pp. 138.
Dare, S., Barnes, S.-J., Beaudin, G., 2014. Did the massive magnetite "lava flows" of El Laco (Chile) form by magmatic or hydrothermal processes? New constraints from magnetite composition by LA-ICP-MS. Min Dep 50, 607–617. https://doi.org/10.1007/s00126-014-0560-1.
Dentith, M., 2003. Geophysical signatures of South Australian mineral deposits: miscellaneous and minor deposits. ASEG Extended Abstracts (3), 257–281. https://doi.org/10.1071/ASEGSpec12_20.
Dmitrijeva, M., Ehrig, K., Ciobanu, C., Cook, N., Verdugo-Ihl, M., Metcalfe, A., 2019. Defining IOCG signatures through compositional data analysis: a case study of lithogeochemical zoning from the Olympic Dam deposit, South Australia. Ore Geol. Rev. 105, 86–101. https://doi.org/10.1016/j.oregeorev.2018.12.013.
Edfelt, A., Martinsson, O., 2003. The Tjårrojåkka Fe-oxide Cu (–Au) occurrence, Kiruna area, northern Sweden. In: Eliopoulos, D. (Ed.), Mineral Exploration and Sustainable Development. Millpress, Rotterdam, pp. 1069–1072.
Egozcue, J.J., Pawlowsky-Glahn, V., 2005. Groups of parts and their balances in compositional data analysis. Math. Geol. 37, 795–828. https://doi.org/10.1007/s11004-005-7381-9.
Egozcue, J.J., Pawlowsky-Glahn, V., 2006. Simplicial geometry for compositional data. In: Buccianti, A., Mateu-Figueras, G., Pawlowsky-Glahn, V. (Eds.), Compositional Data Analysis in the Geosciences: From Theory to Practice. vol. 264. Geological Society, London, pp. 145–159. https://doi.org/10.1144/GSL.SP.2006.264.01.11. Special Publications.
Ehrig, K., McPhie, J., Kamenetsky, V., 2012. Geology and mineralogical zonation of the Olympic Dam iron oxide Cu-U-Au-Ag deposit, South Australia. Soc. Econ. Geol. Spec. Pub. 16, 237–267. https://doi.org/10.5382/SP.16.11.
Ehrig, K. Kamenetsky, V.S., McPhie, J. Apukhtina, O., Ciobanu, C., Cook, N., Kontonikas-Charos, A., Krneta, S. 2017. The IOCG-IOA Olympic Dam Cu-U-Au-Ag deposit and nearby prospects, South Australia. Proceedings, 14th Biennial SGA Meeting 'Mineral Resources to Discover' Québec City, Canada, vol. 3, p. 823–826.
Frietsch, R., 1978. On the magmatic origin of iron ores of the Kiruna type. Econ. Geol. 73, 478–485. https://doi.org/10.2113/gsecongeo.73.4.478.
Geijer, P., 1931. The iron ores of the Kiruna type: geographical distribution, geological characters, and origin. Sver. Geol. Unders., Ser 39.
Groves, D.I., Bierlein, F.P., Meinert, L.D., Hitzman, M.W., 2010. Iron Oxide Copper-Gold (IOCG) deposits through earth history: implications for origin, lithospheric setting, and distinction from other epigenetic iron oxide deposits. Econ. Geol. 105, 641–654. https://doi.org/10.2113/gsecongeo.105.3.641.
Grunsky, E., 2010. The interpretation of geochemical survey data. Geochem. Explor. Env. A. 10, 27–74. https://doi.org/10.1144/1467-7873/09-210.
Hamilton, N., 2018. ggtern: An Extension to 'ggplot2', for the Creation of Ternary Diagrams. R Package Version 3.0.0. https://CRAN.R-project.org/package=ggtern.
Hennig, C., 2018. fpc: Flexible Procedures for Clustering. R package version 2.1-11.1.. https://CRAN.R-project.org/package=fpc.
Hitzman, M.W., 2000. Iron oxide-Cu-Au deposits: what, where, when, and why. In: Porter, T.M. (Ed.), Hydrothermal Iron Oxide Copper-Gold & Related Deposits: A Global Perspective. vol. 1. Australian Mineral Foundation, Adelaide, pp. 9–25.
Hitzman, M.W., Oreskes, N., Einaudi, M.T., 1992. Geological characteristics and tectonic setting of Proterozoic iron oxide (Cu-U-Au-REE) deposits. Precambrian Res. 58, 241–287. https://doi.org/10.1016/0301-9268(92)90121-4.
Ismail, R., Ciobanu, C.L., Cook, N.J., Teale, G.S., Giles, D., Schmidt Mumm, A., Wade, B., 2014. Rare earths and other trace elements in minerals from skarn assemblages, Hillside iron oxide–copper–gold deposit, Yorke Peninsula, South Australia. Lithos 184–187, 456–477. https://doi.org/10.1016/j.lithos.2013.07.023.
Jagodzinski, E.A., 2005. Compilation of SHRIMP U–Pb Geochronological Data – Olympic Domain, Gawler Craton, South Australia, 2001–2003. Geoscience Australia, Canberra, pp. 197 Record 2005/20.
Keyser, W.M., Ciobanu, C.L., Cook, N.J., Courtney-Davies, L., Ehrig, K., Gilbert, S., McPhie, J., 2017. Links between sedimentary protoliths and IOCG Links between sedimentary protoliths and IOCG-skarn skarn alteration, Island Dam, South Australia. In: Proceedings of the 14th SGA Biennial Meeting, Quebec City, QC, Canada, 20–23 August 2017, pp. 935–938.
Knipping, J., Bilenker, J., Simon, A., Reich, M., Barra, F., Deditius, A., Wälle, M., Heinrich, C., Holtz, F., Munizaga, R., 2015a. Trace elements in magnetite from massive iron oxide-apatite deposits indicate a combined formation by igneous and magmatic-hydrothermal processes. Geochim. Cosmochim. Acta 171, 15–38. https://doi.org/10.1016/j.gca.2015.08.010.
Knipping, J.L., Bilenker, L.D., Simon, A.C., Reich, M., Barra, F., Deditius, A.P., Lundstrom, C., Bindeman, I., Munizaga, R., 2015b. Giant Kiruna-type deposits form by efficient flotation of magmatic magnetite suspensions. Geology 43, 591–594. https://doi.org/10.1130/G36650.1.
Kontonikas-Charos, A., Ciobanu, C.L., Cook, N.J., 2014. Albitization and redistribution of REE and Y in IOCG systems: insights from Moonta-Wallaroo, Yorke Peninsula, South Australia. Lithos 208–209, 178–201. https://doi.org/10.1016/j.lithos.2014.09.001.
Kontonikas-Charos, A., Ciobanu, C.L., Cook, N.J., Ehrig, K., Krneta, S., Kamenetsky, V.S., 2017. Feldspar evolution in the Roxby Downs Granite, host to Fe-oxide Cu-Au-(U) mineralisation at Olympic Dam, South Australia. Ore Geol. Rev. 80, 838–859. https://doi.org/10.1016/j.oregeorev.2016.08.019.
Kontonikas-Charos, A., Ciobanu, C.L., Cook, N.J., Ehrig, K., Krneta, S., Kamenetsky, V.S., 2018a. Rare earth element geochemistry of feldspars: examples from Fe-oxide Cu-Au systems in the Olympic Cu-Au Province, South Australia. Miner. Petrol. 112, 145–172. https://doi.org/10.1007/s00710-017-0533-z.
Kontonikas-Charos, A., Ciobanu, C.L., Cook, N.J., Ehrig, K., Ismail, R., Krneta, S., Basak, A., 2018b. Feldspar mineralogy and rare earth element (re)mobilization in iron-oxide copper gold systems from South Australia: a nanoscale study. Mineral. Mag. 82, S173–S197. https://doi.org/10.1180/minmag.2017.081.040.
Krneta, S., Ciobanu, C.L., Cook, N.J., Ehrig, K., Kontonikas-Charos, A., 2016. Apatite at Olympic Dam, South Australia: a petrogenetic tool. Lithos 262, 470–485. https://doi.org/10.1016/j.lithos.2016.07.033.
Krneta, S., Ciobanu, C.L., Cook, N.J., Ehrig, K.J., Kontonikas-Charos, A., 2017a. Rare Earth Element Behaviour in Apatite from the Olympic Dam Cu–U–Au–Ag Deposit, South Australia. Minerals 7, 135. https://doi.org/10.3390/min7080135.
Krneta, S., Cook, N.J., Ciobanu, C.L., Ehrig, K.J., Kontonikas-Charos, A., 2017b. The Wirrda Well and Acropolis prospects, Gawler Craton, South Australia: Insights into evolving fluid conditions through apatite chemistry. J. Geochem. Explor. 181, 276–291. https://doi.org/10.1016/j.gexplo.2017.08.004.
MacQueen, J., 1967. Some methods for classification and analysis of multivariate observations. In: Le Cam, L.M., Neyman, J. (Eds.), Proceedings of the Fifth Berkeley Symposium on Mathematical Statistics and Probability. vol 1. Berkeley University of California Press, pp. 281–297.
Maksaev, V., Gardeweg, M., Ramírez, C.F., Zentilli, M., 1988. Aplicación del método trazas de fisión (fission track) a la datación de cuerpos de magnetita de El Laco e Incahuasi en el Altiplano de la Región de Antofagasta: Congreso Geológico Chileno, 5th. vol. 1. Antofagasta, Actas, pp. B1–B23.
Mark, G., Oliver, N.H.S., Williams, P.J., 2006. Mineralogical and chemical evolution of the Ernest Henry Fe oxide–Cu–Au ore system, Cloncurry district, northwest Queensland, Australia. Mineral. Deposita 40, 769–801. https://doi.org/10.1007/s00126-005-0009-7.
Mauger, A.J., Ehrig, K.J., Kontonikas-Charos, A., Ciobanu, C.L., Cook, N.J., Kamenetsky, V.S., 2016. Alteration at the Olympic Dam IOCG–U deposit: insights into distal to proximal feldspar and phyllosilicate chemistry from infrared reflectance spectroscopy. Austral. J. Earth Sci. 63, 959–972. https://doi.org/10.1080/08120099.2016.1264474.

McPhie, J., 2016. Acropolis Report. BHP Billiton Olympic Dam.
Montreuil, J.-F., Corriveau, L., Grunsky, E.C., 2013. Compositional data analysis of IOCG systems, Great Bear magmatic zone, Canada: to each alteration types its own geochemical signature. Geochem-Explor. Env. A. 13, 229–247. https://doi.org/10.1144/geochem2011-101.
Mortimer, G.E., Cooper, J.A., Paterson, H.L., Cross, K., Hudson, G.R.T., Uppill, R.K., 1988. Zircon U–Pb Dating in the Vicinity of the Olympic Dam Cu–U–Au Deposit, Roxby Downs, South-Australia. Econ. Geol. 83, 694–709. https://doi.org/10.2113/gsecongeo.83.4.694.
O'Brien, J.J., Spry, P.G., Nettleton, D., Xu, R., Teale, G.S., 2015. Using Random Forests to distinguish gahnite compositions as an exploration guide to Broken Hill-type Pb–Zn–Ag deposits in the Broken Hill domain, Australia. J. Geochem. Explor. 149, 74–86. https://doi.org/10.1016/j.gexplo.2014.11.010.
Ordóñez-Calderón, J.C., Gelcich, S., 2018. Machine learning strategies for classification and prediction of alteration facies: examples from the Rosemont Cu-Mo-Ag skarn deposit, SE Tucson Arizona. J. Geochem. Explor. 194, 167–188. https://doi.org/10.1016/j.gexplo.2018.07.020.
Ordóñez-Calderón, J.C., Gelcich, S., Oliveira, J.F., 2017. Applied data analytics on multielement geochemistry for pre-mining characterization of geological and geometallurgical attributes: examples of the Rosemont Cu-Mo-Ag skarn deposit, Tucson, Arizona. In: CoDaWork 2017 - Abbadia San Salvatore (IT).
Oreskes, N., Einaudi, M.T., 1992. Origin of hydrothermal fluids at Olympic Dam; preliminary results from fluid inclusions and stable isotopes. Econ. Geol. 87, 64–90. https://doi.org/10.2113/gsecongeo.87.1.64.
Owen, N.D., Cook, N.J., Rollog, M., Ehrig, K.J., Schmandt, D.S., Ram, R., Brugger, J., Ciobanu, C.L., Wade, B., Guagliardo, P., 2019. REE-, Sr- Ca-aluminum-phosphate-sulfate minerals of the alunite supergroup and their role as hosts for radionuclides. Am. Mineral (accepted).
Palarea-Albaladejo, J., Martín-Fernández, J.A., 2015. zCompositions—R package for multivariate imputation of left-censored data under a compositional approach. Chemometr. Intell. Lab. Syst. 143, 85–96. https://doi.org/10.1016/j.chemolab.2015.02.019.
Park, C.F., 1961. A magnetite "flow" in northern Chile. Econ. Geol. 56, 431–436. https://doi.org/10.2113/gsecongeo.56.2.431.
Paterson, H.L., 1986. The Acropolis prospect. In: Paterson, H.L.C. (Ed.), Basement geology of the Stuart Shelf region, South Australia (vol. A1 – Olympic Dam/Stuart Shelf Excursion Guide, pp. 17–18). 8th Australian Geological Convention. Geological Society of Australia, Adelaide. Sydney, NSW.
Pawlowsky-Glahn, V., Egozcue, J.J., 2006. Compositional data and their analysis: an introduction. In: Buccianti, A., Mateu-Figueras, G., Pawlowsky-Glahn, V. (Eds.), Compositional Data Analysis in the Geosciences: From Theory to Practice. 264. Geological Society, London, pp. 1–10 Special Publications.
Pearson, K., 1897. Mathematical contributions to the theory of evolution: on a form of spurious correlation which may arise when indices are used in the measurements of organs. Proc. R. Soc. London 60, 489–498. https://doi.org/10.1098/rspl.1896.0076.
Romer, R.L., Martinsson, O., Perdahl, J.-A., 1994. Geochronology of the Kiruna Iron Ores and Hydrothermal Alteration. Econ. Geol. 89, 1249–1261. https://doi.org/10.2113/gsecongeo.89.6.1249.
Rousseeuw, P.J., 1987. Silhouettes: a graphical aid to the interpretation and validation of cluster analysis. J. Comput. Appl. Math. 20, 53–65. https://doi.org/10.1016/0377-0427(87)90125-7.
Ruiz, F.C., Ortiz, F., Moraga, A., Aguilar, A., 1968. Genesis of the Chilean iron ore deposits of Mesozoic age. International Geological Congress 7, 323–338.
Schlegel, T.U., Heinrich, C.A., 2015. Alteration and lithology control Cu mineralization at Prominent Hill iron oxide-copper-gold deposit, Gawler craton, South Australia. Econ. Geol. 110, 1953–1994. https://doi.org/10.2113/econgeo.110.8.1953.
Skirrow, R.G., Bastrakov, E.N., Barovich, K., Fraser, G.L., Creaser, R.A., Fanning, C.M., Raymond, O.L., Davidson, G.J., 2007. Timing of iron oxide Cu-Au-(U) hydrothermal activity and Nd isotope constraints on metal sources in the Gawler craton, South Australia. Econ. Geol. 102, 1441–1470. https://doi.org/10.2113/gsecongeo.102.8.1441.
van den Boogart, K.G., Tolosana-Delgado, R., Bren, M., 2018. Compositions: Compositional Data Analysis. R Package Version 1.40-2. https://CRAN.R-project.org/package=compositions.
Verdugo-Ihl, M.R., Ciobanu, C.L., Cook, N.J., Ehrig, K., Courtney-Davies, L., Gilbert, S., 2017. Textures and U-W-Sn-Mo signatures in hematite from the Cu-U-Au-Ag orebody at Olympic Dam, South Australia: defining the archetype for IOCG deposits. Ore Geol. Rev. 91, 173–195. https://doi.org/10.1016/j.oregeorev.2017.10.007.
Verdugo-Ihl, M.R., Ciobanu, C.L., Cook, N.J., Ehrig, K.J., Courtney-Davies, L., 2019. Defining Early Stages of IOCG Systems: Evidence From Iron-Oxides in the Outer Shell of the Olympic Dam Deposit. South Australia, Mineral. Depositahttps://doi.org/10.1007/s00126-019-00896-2. (in press).
Wickham, H., 2016. ggplot2: Elegant Graphics for Data Analysis. Springer-Verlag, New York. https://doi.org/10.1007/978-0-387-98141-3.
Williams, P.J., Barton, M.D., Johnson, D.A., Fontboté, L., Haller, A., Mark, G., Oliver, N.H.S., Marschik, R., 2005. Iron-oxide–copper–gold deposits: geology, space–time distribution, and possible modes of origin. Economic Geology 100th Anniversary 371–406 (Volume).

CHAPTER 7

GEOCHEMICAL DATA ANALYSIS AND 3D MODELLING OF WIRRDA WELL PROSPECT, SOUTH AUSTRALIA: STRUCTURAL CONTROL ON IRON-OXIDE COPPER GOLD MINERALISATION

Marija Dmitrijeva[1], Cristiana L. Ciobanu[1], Kathy Ehrig[2], Nigel J. Cook[1], Max R. Verdugho-Ihl[1], Andrew V. Metcalfe[3], Vadim Kamenetsky[4], Jocelyn McPhie[4]

[1] *School of Chemical Engineering and Advanced Materials, The University of Adelaide, Adelaide, SA 5005, Australia*

[2] *BHP Olympic Dam, Adelaide, SA 5001, Australia*

[3] *School of Mathematical Sciences, The University of Adelaide, Adelaide, SA 5005, Australia*

[4] *School of Natural Sciences and Centre of Excellence in Ore Deposits (CODES), University of Tasmania, Hobart, Tasmania 7001, Australia*

Submitted to *Economic Geology*, December 15th, 2019

Statement of Authorship

Title of Paper	Geochemical Data Analysis and 3D Modelling of Wirrda Well Prospect, South Australia: Structural Control on Iron-Oxide Copper Gold Mineralisation
Publication Status	☐ Published ☐ Accepted for Publication ☑ Submitted for Publication ☐ Unpublished and Unsubmitted w ork w ritten in manuscript style
Publication Details	Dmitrijeva, M., Ciobanu, C.L., Ehrig, K., Cook, N.J., Verdugo-Ihl, M.R., Metcalfe, A.V., Kamenetsky, V.S., McPhie, J. Geochemical Data Analysis and 3D Modelling of Wirrda Well Prospect, South Australia: Structural Control on Iron-Oxide Copper Gold Mineralisation. Submitted to Economic Geology

Principal Author

Name of Principal Author (Candidate)	Marija Dmitrijeva		
Contribution to the Paper	Performed statistical data analyses, geological modelling, interpreted the results and wrote the manuscript.		
Overall percentage (%)	55		
Certification:	This paper reports on original research I conducted during the period of my Higher Degree by Research candidature and is not subject to any obligations or contractual agreements with a third party that would constrain its inclusion in this thesis. I am the primary author of this paper.		
Signature		Date	17.12.19

Co-Author Contributions

By signing the Statement of Authorship, each author certifies that:

i. the candidate's stated contribution to the publication is accurate (as detailed above);

ii. permission is granted for the candidate in include the publication in the thesis; and

iii. the sum of all co-author contributions is equal to 100% less the candidate's stated contribution.

Name of Co-Author	Cristiana L. Ciobanu		
Contribution to the Paper	Helped to define the direction of the paper, assisted with the interpretation of the results and the manuscript evaluation.		
Overall percentage (%)	15		
Signature		Date	17.12.19

Name of Co-Author	Kathy Ehrig		
Contribution to the Paper	Assisted with the manuscript preparation and evaluation.		
Overall percentage (%)	5		
Signature		Date	17.12.19

Name of Co-Author	Nigel J. Cook		
Contribution to the Paper	Assisted with the manuscript preparation and evaluation.		
Overall percentage (%)	5		
Signature		Date	17.12.19

Name of Co-Author	Max R. Verdugo-Ihl		
Contribution to the Paper	Assisted with the estimation of the modal mineralogy at the Wirrda Well prospect.		
Overall percentage (%)	5		
Signature		Date	17.12.19

Name of Co-Author	Andrew Metcalfe		
Contribution to the Paper	Assisted with the statistical analyses and manuscript evaluation.		
Overall percentage (%)	5		
Signature		Date	17.12.19

Name of Co-Author	Vadim Kamenetsky		
Contribution to the Paper	Assisted with the geological interpretation of the Wirrda Well prospect		
Overall percentage (%)	5		
Signature		Date	17.12.19

Name of Co-Author	Jocelyn McPhie
Contribution to the Paper	Assisted with the geological interpretation of the Wirrda Well prospect
Overall percentage (%)	5
Signature	
Date	17.12.19

Geochemical data analysis and 3D modelling, Wirrda Well prospect, South Australia: structural control on iron-oxide copper gold mineralization

Marija Dmitrijeva[1*], Cristiana L. Ciobanu[1], Kathy Ehrig[2], Nigel J. Cook[1], Max R. Verdugo-Ihl[1], Andrew V. Metcalfe[3], Vadim S. Kamenetsky[4], Jocelyn McPhie[4]

[1] *School of Chemical Engineering and Advanced Materials, The University of Adelaide, Adelaide, SA 5005, Australia*

[2] *BHP Olympic Dam, Adelaide, SA 5001, Australia*

[3] *School of Mathematical Sciences, The University of Adelaide, Adelaide, SA 5005, Australia*

[4] *School of Natural Sciences and Centre of Excellence in Ore Deposits (CODES), University of Tasmania, Hobart, Tasmania 7001, Australia*

*corresponding author email: marija.dmitrijeva@adelaide.edu.au

Abstract

The Wirrda Well prospect, characterized by two distinct residual gravity anomalies: Wirrda Well North (WWN); and Wirrda Well South (WWS), is located in the Olympic Dam district, South Australia. The prospect, bounded by an unmineralized ~1.6 Ga Hiltaba Suite granite in the east, features ~1.6 Ga iron-oxide copper gold (IOCG) mineralization hosted by ~1.84 Ga Donington Suite granites crosscut by abundant mafic dykes. The majority of these dykes are considered to be of Donington affiliation, but post -mineralization dykes are also documented at Wirrda Well. The latter are attributed to a relatively unaltered ~1590 Ma picrite and ~820 Ma Gairdner Dyke Swarm (GDS) dolerites. Unsupervised (Principal Component Analysis, Hierarchical and *k*-means

Clustering) and supervised (Random Forests) statistical analyses were applied in combination to two geochemical datasets. A three-dimensional (3D) geological model of the Wirrda Well prospect and geochemical interpolations for Fe, Cu and U distributions were created and combined with the results of statistical analysis and an estimate of normative Cu(-Fe)-sulfide mineralogical zonation. WWN and WWS correspond to two blocks displaying significant mineralogical and geochemical differences. The 3D modelling shows metal anomalies along the pre-mineralization dykes, interpreted as structural control for IOCG mineralization, albeit less pronounced in the south. Dyke orientation indicates the two areas represent distinct structural blocks resulting from dismemberment prior to emplacement of the youngest, GDS dykes. WWN is characterized by a Fe-V-Ni-Co signature defined as 'magnetite'-type whereas WWS contains higher-grade Cu-Au(±Bi-Ag) mineralization and has a marked Mo-W-U(±Sn) signature defined as 'hematite' type, considered of granitic affiliation in the Olympic Dam District. Wirrda Well is a good example of structurally controlled IOCG mineralization, whereby contacts between mafic dykes and host granites provided permeable structures for fluid focusing and metal deposition.

Keywords: IOCG; Wirrda Well prospect; Implicit 3D modelling; K-means clustering; PCA; Random Forest

Introduction

Iron oxide copper-gold (IOCG) deposits are characterized by the presence of magnetite and hematite as major minerals paragenetically associated with Cu-Au ores (Barton, 2014, and references therein). Although either of the other Fe-oxides can be dominant, commonly both Fe-oxides and their interconversion products are present throughout a given IOCG deposit or

province, e.g., Cloncurry district (Queensland, Australia; Mark et al., 2006), or the Great Bear Magmatic Zone (Northwest Territories, Canada; Corriveau et al., 2016).

The Olympic Cu-Au Province is a world-class IOCG terrane located along the eastern margin of the Gawler Craton, South Australia (Skirrow et al., 2007). This metallogenetic province hosts several dozen deposits and prospects, including the >10 billion tonne Olympic Dam Cu–U–Au–Ag deposit (BHP, 2019). The IOCG event is associated with the emplacement of Gawler Silicic Large Igneous Province (SLIP) at ~1.6 Ga, comprising Hiltaba Suite intrusions and their cogenetic equivalents, the Gawler Range Volcanics (GRV) (Blissett et al., 1993; Allen et al., 2008). IOCG mineralization of different styles, e.g., breccias, veins, and skarns, is hosted by various basement rocks, including granites of different ages, metasedimentary and volcanic rocks. Despite such a wide diversity, deposits/prospects in the Olympic Cu-Au Province share geochemical and mineralogical characteristics, including: (i) regional- and deposit-scale alkali-calcic alteration (Conor et al., 2010; Kontonikas-Charos et al., 2014, 2017, 2018; Mauger et al., 2016); and (ii) preservation of primary U-W-Sn-Mo-bearing hematite considered as a 'granitophile' mineral signature typifying the ~1.6 Ga event throughout the Olympic Cu-Au Province (Ciobanu et al., 2013; Verdugo-Ihl et al., 2017; Dmitrijeva et al. 2019a; Courtney-Davies et al., 2019).

Olympic Dam (Fig. 1) is a hematite-dominant IOCG deposit entirely enclosed within a breccia complex formed mostly from alteration of the Hiltaba Suite-affiliated Roxby Downs Granite (RDG; Reeve et al., 1990). Deposit-scale zonation with respect to Cu-(Fe)-sulfides: pyrite-chalcopyrite through chalcopyrite-bornite to bornite-chalcocite towards central and shallower levels is recognized throughout the entire orefield (Ehrig et al., 2012, and references therein). In contrast, Acropolis, a prospect in the Olympic Dam district (Fig. 1) comprises veins and stockworks containing magnetite+hematite+sulfides (pyrite+chalcopyrite) predominantly hosted

within felsic GRV lavas as recognized in early works (Paterson, 1986; Creaser, 1989; Cross, 1993; McPhie et al., in review). Recent petrological and geochemical studies of fluorapatite and Fe-oxides, U-Pb dating of hematite and statistical analysis of whole rock datasets defining mineralization+alteration footprints at Acropolis (Thompson et al., 2016; Krneta et al., 2017b; Courtney-Davies et al., 2019; Dmitrijeva et al., 2019b) enabled the prospect to be closely tied to ~1.6 Ga IOCG-style mineralization as known from Olympic Dam.

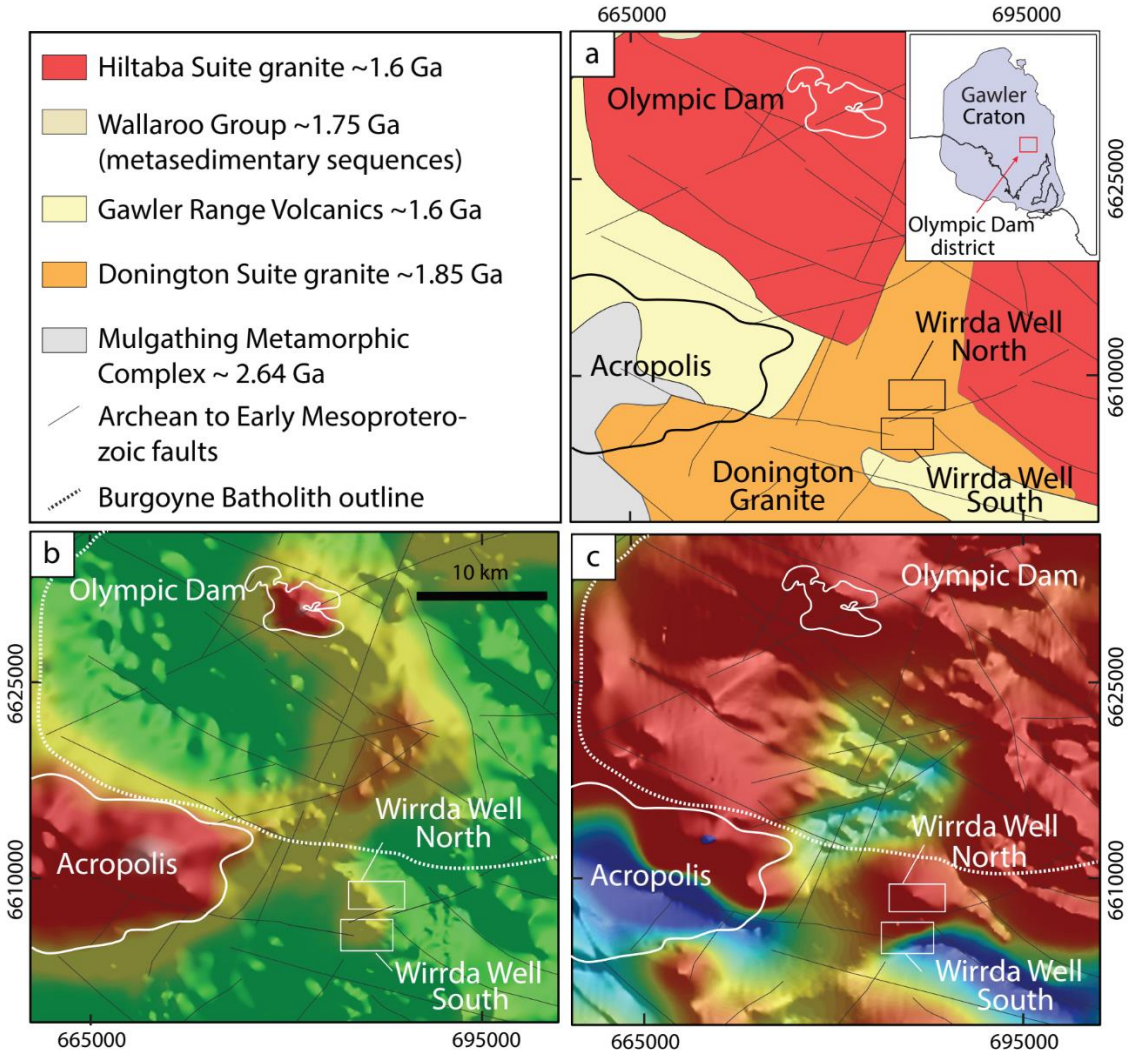


Figure 1. (A) Geological map of the Olympic Dam district showing the Acropolis and Wirrda Well prospects. Wirrda Well North (WWN) and South (WWS) are indicated by rectangles. (B) Bouguer and (C) total magnetic intensity (TMI) maps, comparing IOCG prospects with the Olympic Dam deposit. The

approximate outline of the Burgoyne Batholith is interpreted from potential field anomalies and Ehrig (2013). Maps sourced from https://map.sarig.sa.gov.au.

One of the less studied IOCG prospects in the district is Wirrda Well, ~25 km SSE from Olympic Dam deposit (Fig. 1). The prospect is hosted by sheared granites of the Donington Suite emplaced at ~1840 Ma (Jagodzinski, 2005). Exploration programs carried out at Wirrda Well have defined two mineralized fields, Wirrda Well North and Wirrda Well South (hereafter WWN and WWS) and also recognized the presence of magnetite in addition to hematite at this prospect (Cross, 1993; Ehrig, 2013).

The application of unsupervised and supervised statistical analyses to large whole-rock datasets has been able to define alteration and mineralization signatures typical of IOCG hydrothermal systems in the Olympic Dam district (Dmitrijeva et al., 2019a, 2019b). Geological modeling, coupled with the results of statistical analysis and diagnosis of mineralogical zoning can assist in direct interpretation of mineralization/alteration patterns in three-dimensional space. Here we utilize such an approach by applying a range of statistical analyses to two geochemical datasets of different analytical sensitivity from the Wirrda Well prospect. This research contributes to building a 3D geological model for the Wirrda Well prospect and aims to characterize geochemical signatures that allow comparison with Olympic Dam deposit and Acropolis prospect in the same district. Understanding the common geochemical trends between different styles of IOCG mineralization in the Gawler Craton is important not only for constraining the sequence of magmatic-hydrothermal processes involved in their formation but also for optimizing exploration programs in the region.

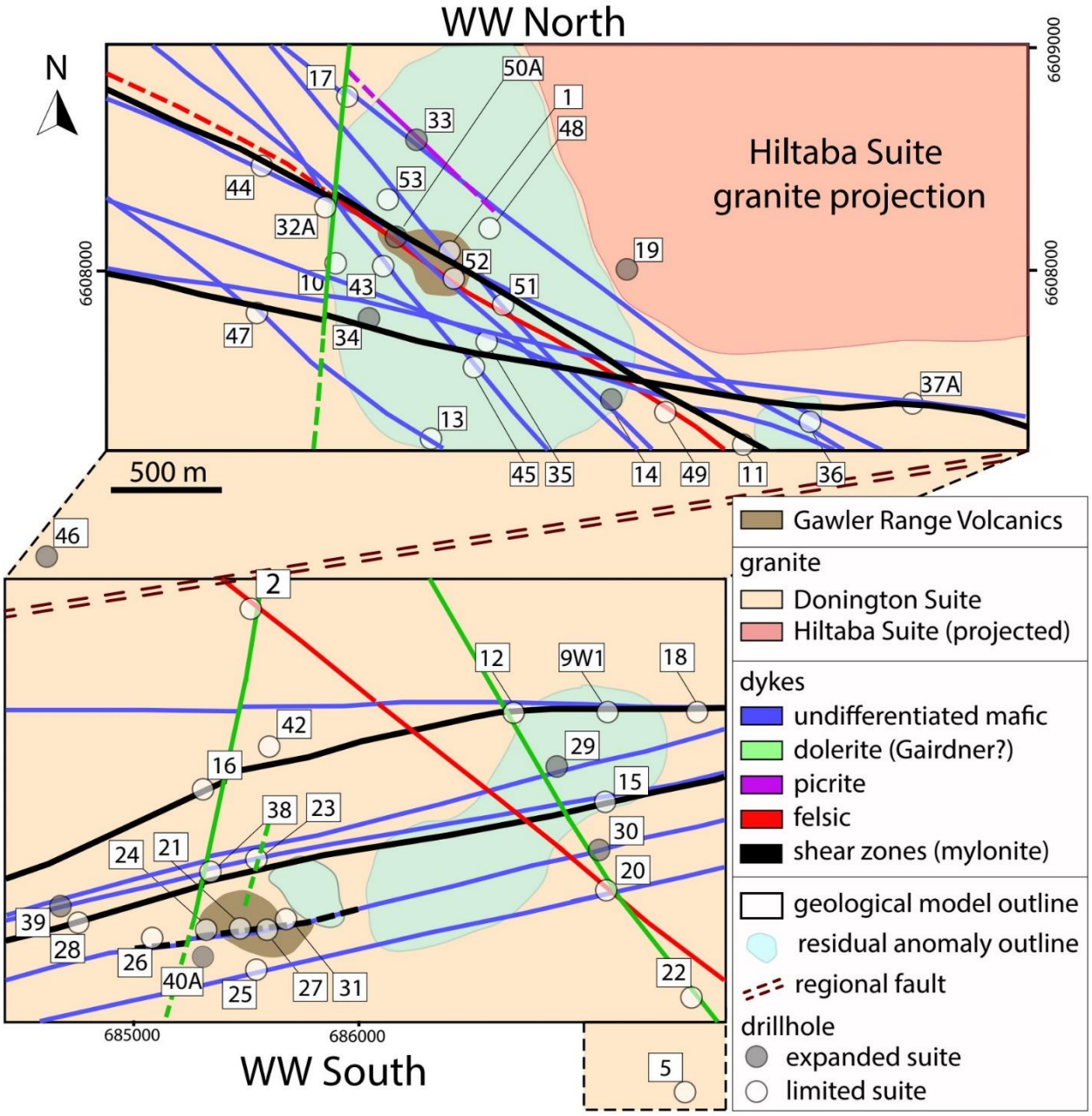


Figure 2. Geological map of Wirrda Well North and South showing locations of the 48 'WRD' drillholes (boxed numbers) and crosscutting dykes. Dyke orientations are interpreted from the geological model (Fig. 5). The regional fault is positioned according to Fig. 1. Residual gravity anomaly outlines are from Ehrig (2013).

Geological background and rationale

The Wirrda Well prospect is intersected by 48 drillholes (Fig. 2) under Late Proterozoic Stuart Shelf sediments of thickness between 350 and 600 m. Potential field anomaly consists of nearly coincident gravity (6 mGal) and magnetic highs (1800 nT) (Fig. 1; Vella, 1997). Despite the dense drillhole data grid, covering an area of 16 km^2 across both WWN and WWS, modelling of ground magnetic data constrained by petrophysical measurements could not account for the observed anomaly (Vella, 1997). Geochemical and logging data from Wirrda Well indicate a majority (~70%) of rocks hosting mineralization are composed of Donington Suite granite. Mafic dykes of undifferentiated age and provenance, henceforth referred to as 'undifferentiated' (Figs. 2; 3A, b) make up ~10%. The remaining ~20% consists of other lithologies, including picrites, dolerites, Hiltaba Suite-affiliated granite and GRV, all considered non-mineralized. Picrites penecontemporaneous with the IOCG event (U-Pb apatite dating yielding 1596 ± 17 Ma; Huang et al., 2016), intersected in drillhole WRD33, are 'unmineralized' and crosscut mineralized rocks. Minor, felsic GRV rocks are found along faulted contacts within both WWN and WWS (Fig. 3A). Another 'unmineralized' lithology is a medium-grained, K-feldspar granite attributed to Hiltaba Suite (LA-ICP-MS U-Pb zircon age yielding 1622 ±18 Ma; M. Kamenetsky unpublished data) intersected in drillhole WRD19 (Fig. 3A). This is likely a component granite of the Burgoyne Batholith that produces gravity lows towards the northeast (Ehrig, 2013). Throughout the prospect, Donington Suite granite features widespread shear-induced foliation and mylonitisation (Fig. 3C; Courtney-Davies et al., 2019). Such fabrics are also developed within/along contacts to mafic dykes apart from picrites (Ehrig, 2013).

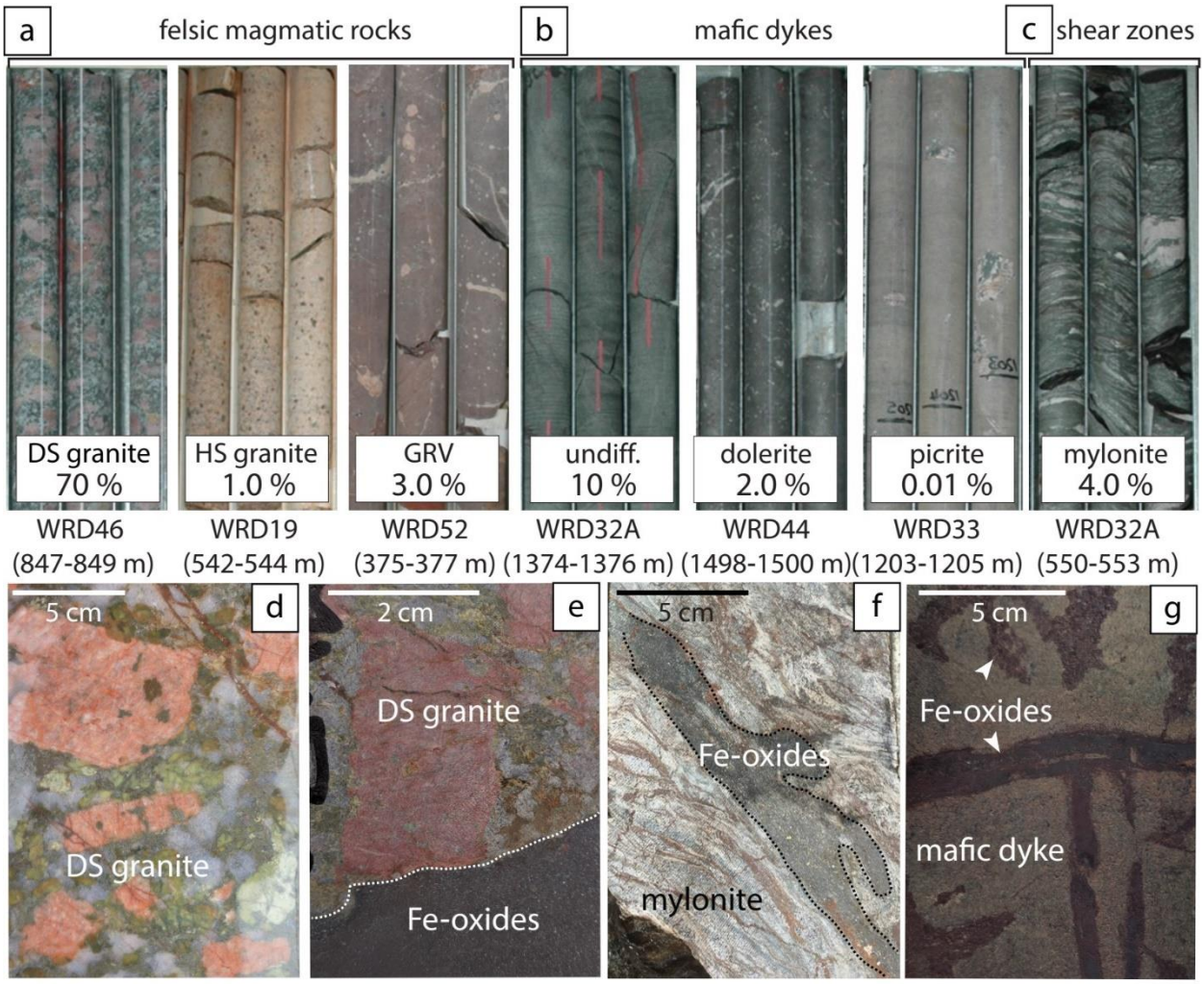


Figure 3. Photographs of representative lithologies from the selection of one-meter drillcores from the Wirrda Well prospect. (A) felsic magmatic rocks, (B) mafic dykes, and (C) shear zone mylonite. Photographs of hand specimens showing (D) Donington Suite (DS) granite, note the alteration of plagioclase; (E, F) Fe-oxides within and along micro-shears in altered and mylonitized DS, respectively (G) Fe-oxide-bearing veinlets within undifferentiated mafic dyke.

Mineralization at Wirrda Well, initially considered a single body of granitic breccia (Parker, 1990), was reinterpreted as breccia pipes developed along shear zones and contacts between Donington Suite granite and pre-mineralization mafic dykes (Ehrig, 2013). Copper sulfide + iron oxide mineralization within each breccia pipe displays a transition from magnetite to hematite upwards, as well as from pyrite-chalcopyrite through chalcopyrite-bornite to bornite-chalcocite

(Ehrig, 2013). Both patterns are comparable with those in the Olympic Dam deposit (Ehrig et al., 2012). Geochemical signatures of fluorapatite record a transition from magmatic to hydrothermal stages comparable to that documented from Olympic Dam (Krneta et al., 2017a, 2017b). Oscillatory-zoned W-Sn-Mo-U-rich hematite, the defining and commonly dominant mineral in IOCG mineralization across the Olympic Dam district (Ciobanu et al., 2013; Verdugo-Ihl et al., 2017; Keyser et al., 2017; Courtney-Davies et al., 2019), has recently been documented from Wirrda Well. Uranium-Pb hematite dating has yielded a mineralization age of 1598.9 ± 6.3 Ma (drillhole WRD46; Courtney-Davies et al., 2019), thus supporting spatial-temporal links between IOCG mineralization within the Olympic Dam district. Silician magnetite, one of the earliest hydrothermal iron oxides formed during alkali-calcic alteration of host granites recognized in the weakly mineralized outer shell of Olympic Dam, is also present at depth in the Wirrda Well prospect (drillhole WRD33; Verdugo-Ihl et al., 2019; Ciobanu et al., 2019; Courtney-Davies et al., 2019).

Multivariate statistical analyses of large deposit/prospect-scale datasets from Olympic Dam (10,565 samples) and Acropolis (4,864 samples) have indicated a multi-element mineralization signature, comprising of Fe, Cu and Au and also indicator elements such as W, Mo, Sn and As (Dmitrijeva et al., 2019a, 2019b). These studies have highlighted the importance and exploration significance of a 'granitophile element' signature within the IOCG systems from the Olympic Dam district. In this contribution we combine advanced geochemical data analysis of two large whole-rock datasets for Wirrda Well with implicit 3D geological and numerical modelling. The two datasets are: (i) a larger dataset obtained from 48 drillholes with standard analytical sensitivity (the 'limited suite'; analysis of 29,172 samples for 32 elements); and (ii) a smaller dataset obtained from 10 of the 48 drillholes analyzed at higher analytical sensitivity (the 'extended suite'; analysis

of 6,155 samples for 33 elements) collected from a subset of samples from dataset (i). Unsupervised statistical analysis includes variation matrix, *k*-means and principal component analysis, all applied to the 6,155-samples dataset in order to obtain mineralogical-geochemical endmembers, i.e., clusters. Further, the supervised classification using random forests is used to predict the cluster memberships for the 29,172 sample limited suite data thus allowing to overcome the absence of certain elements in dataset (i) which are important for characterization of South Australian IOCG mineralizing systems (e.g., W, Mo, Sn, Bi, As, Sb, Ag).

Methods and Data

Geochemical data and pre-processing

Whole-rock multi-element geochemical data for the Wirrda Well prospect comprises two distinct datasets with limited and extended suites, respectively. Each whole-rock sample within the limited element suite was analyzed at Bureau Veritas (Adelaide) whereas the extended element suite analyses were completed at Intertek/Genalysis (Adelaide). Assay data was obtained using a range of analytical techniques. These were: a combination of four-acid digestion and inductively coupled plasma-optical emission spectroscopy for Cu, Ag, As, Co, Ni, and Zn; ICP-OES for Ba, Al, Ca, Ce, Fe, K, La, Mg, Mn, Na, P, Si, Sr, Ti, Y, and Zr; lithium metaborate/tetraborate fusion and inductively coupled plasma-mass spectroscopy for U3O8, Bi, Sb, and Mo; induction furnace-infrared spectrometry for CO2 and S; and fire assay-flame atomic absorption spectrometry for Au. A comprehensive summary of both datasets with respect to minimum detection limits (mdl) and the proportion of analyses falling below mdl for each element is presented in Table 1.

The limited elemental suite comprises analyses of 29,172 drill core samples for 32 elements (Ag, Al, As, Au, Ba, Bi, Ca, Ce, Cu, Co, CO_2, Cr, Fe, K, La, Mg, Mn, Mo, Na, Ni, P, Pb, S, Sb,

Sc, Si, Sr, Th, Ti, U, V, Y, Zn, and Zr). Of these elements, Bi, Sb, Sr, Th, and Y have a significant proportion of non-measured values and Ag, As, and Mo have >60% and Pb >45% of values below mdl, therefore limiting the number of analyses with fully quantitative data to the 26 remaining elements. The limited elemental suite data were collected from one-meter intervals within 48 drillholes that are roughly evenly distributed across the prospect (Fig. 3). Coupled with geological logging for each drillhole, the limited elemental suite data are used as a basis for geological and numerical modelling. Additionally, specific gravity (bulk dry density) and magnetic susceptibility are reported for the majority of the 29,172 samples, thus allowing these parameters to be included in statistical analysis and geological modelling.

Table 1. Elements represented in the limited (29,172 samples analyzed for 32 elements) and extended (6,155 samples analyzed for 33 elements) suite datasets, with respective minimum detection limits (mdl) and the proportion of values falling below mdl for each element. Values in bold highlight those elements used to form the compiled elemental suite (6,155 observations of 51 elements) in 10 drillholes. If the element was not included in the set of elements for all analyses, then the proportion of not-measured instances are indicated.

Element	Limited Suite, mdl	% below mdl	Extended Suite, mdl ppm	% below mdl
Ag	1 ppm	81	**0.1**	10
Al	**0.01 %**	-		
As	10 ppm	77	**1**	2
Au	**0.02 ppm**	46		
Ba	**0.02 %**	13		
Be			**0.5**	-
Bi	3	60% not measured	**0.05**	0.4
Ca	**0.01 %**	0.05		
Cd			**0.05**	22
Ce	0.01 %	12	**0.5**	-

Cu	**50 ppm**	4	1	86% not measured
Co	5 ppm	3	**0.1**	-
CO_2	**0.05 %**	23		
Cr	**20 ppm**	42		
Cs			**0.05**	0.1
Fe	**0.01 %**	-		
Ga			**0.1**	-
Ge			**0.1**	3.0
Hf			**0.1**	0.1
In			**0.05**	8
K	**0.01 %**	0.1		
Li			**0.1**	-
Lu			**0.02**	-
Mg	**0.01 %**	0.02		
Mn	**0.01 %**	5.4		
Mo	5 ppm	67	**1**	7
Na	**0.01 %**	0.2		
Nb			**0.1**	0.6
Nd			**0.1**	-
Ni	**5 ppm**	11	1	88% not measured
Pb	10 ppm	49	5	30% not measured
P	**0.01 %**	1.7		
Rb			**0.1**	0.04
S	**0.01 %**	9.4		

Sb	1 ppm	60 % Not measured	**0.5**	13
Sc	**5 ppm**	6.33		
Se			**1**	56
Si	**0.01 %**	-		
Sn			**1**	0.1
Sr	20 ppm	6% Not measured	**0.5**	-
Ta			**0.1**	2.9
Te			**0.1**	42
Th	4 ppm	57% Not measured	**0.05**	-
Ti	**0.01 %**	0.3		
Tl			**0.02**	0.03
U	4	2.5	**0.5**	-
V	**20 ppm**	2.7		
W			**1**	0.22
Y	5 ppm	60% not measured	**0.5**	-
Yb			**0.05**	-
Zn	**5 ppm**	0.1	1	86% not measured
Zr	**20 ppm**	1.3		

The extended element suite geochemical data comprises 6,155 analyses covering a total of 33 elements (Ag, As, Be, Bi, Cd, Ce, Co, Cs, Cu, Ga, Ge, Hf, In, Li, Lu, Mo, Nb, Nd, Ni, Rb, Sb, Se, Sn, Sr, Ta, Te, Th, Tl, U, W, Y, Yb, and Zn). These data were obtained on a sub-set of the samples analyzed for the limited element suite. They are, however, restricted to ten drillholes: WRD14, -19, -29, -30, -33, -34, -39, -40A, -46, and -50A (Fig. 3). The extended element suite does cover a greater number of components and includes the entire range of lithologies. As such, it is fully

representative of endmember host rocks, such as Donington and Hiltaba Suite granites, undifferentiated mafic dykes, picrite, dolerite and GRV. Importantly, the extended element suite also differs in that mdl values are significantly lower, thus, the reported concentrations are of higher analytical sensitivity than in the limited elemental suite. Additionally, loss of ignition (LOI) is reported.

In order to extract the maximum information from the two geochemical datasets, analyses of the limited element suite were combined with the extended suite data to form a joint geochemical dataset consisting of 6,155 analyses of 51 elements in ten drillholes (Table 1; Fig. 3). If the element was present in both datasets (e.g., Co) then the data with the higher analytical sensitivity was preferred. The 51 elements thus combine the limited suite elements: Al, Au, Ba, Ca, Cu, CO_2 Cr, Fe, K, Mg, Mn, Na, Ni, P, S, Sc, Si, Ti, V, Zn, Zr; with those of the extended suite: Ag, As, Be, Bi, Cd, Ce, Co, Cs, Ga, Ge, Hf, In, Li, Lu, Mo, Nb, Nd, Rb, Sb, Se, Sn, Sr, Ta, Te, Th, Tl, U, W, Y, and Yb (Table 1). This dataset is hereafter referred to as the 'compiled suite' dataset. The limited (29,172 analyses of 21 elements) and compiled (6,155 analysis of 51 elements) datasets are used in combination and are processed using a range of unsupervised and supervised statistical analysis methods.

Statistical Analyses of Geochemical Data

Unsupervised and supervised statistical analyses are widely used in ore deposit geochemistry to gain maximum insights from large whole-rock geochemical datasets (Ordóñez-Calderón et al., 2017). Such data can be a robust proxy for mineralogy, and thus if processed using quantitative methods can help identify distinct groups characterizing an orebody and its host rocks (Bachmann et al., 2019), or alternatively, can aid in recognition of hidden or subtle associations among elements that represent indicators for a particular style of mineralization (Dmitrijeva et al., 2019a).

Because two independent geochemical datasets are used in combination, a four-stage workflow diagram highlighting the steps of data analysis is provided as Fig. 4.

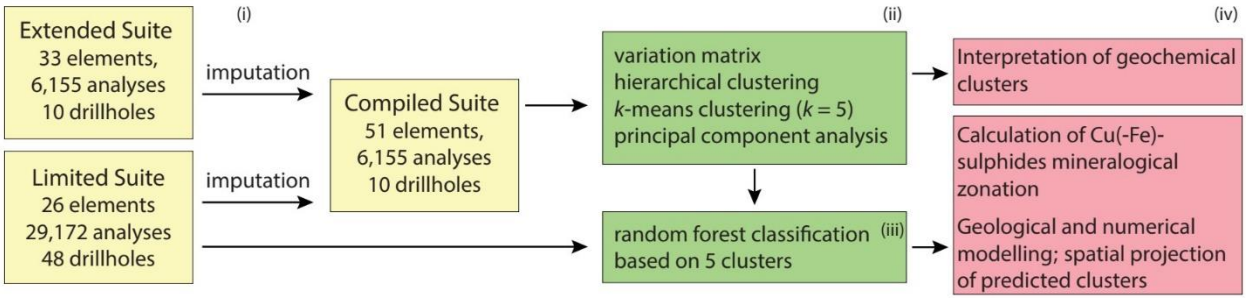


Figure 4. Workflow diagram showing the sequence of data analysis procedures. (i) imputation of values falling below the minimum detection limit (see section 3.1) and assembly of compiled suite data; (ii) unsupervised data analysis applied to the compiled suite data followed by (iii) random forests classification of limited suite data, and (iv) interpretation and visualization of the results.

The element concentrations are analyzed as proportions of the total of the measured elements per each sample. Therefore, a compositional approach to statistical analyses is undertaken at every step (Aitchison, 1986; Pawlowsky-Glahn and Egozcue, 2006). Specifically, the centered log-ratio transformation (clr):

$$clr(\boldsymbol{x}) = [ln\left(\frac{x_1}{g(\boldsymbol{x})}\right), ln\,(\frac{x_2}{g(\boldsymbol{x})}), \dots, ln\,(\frac{x_D}{g(\boldsymbol{x})})]$$

is used for principal component analysis, whereas each component of a composition x_i $(i = 1, \dots, D)$ is divided by the geometric mean of the composition $g(\boldsymbol{x})$ and then the natural logarithm is taken. The isometric logratio transformation (ilr) (Egozcue et al., 2003; Egozcue and Pawlowsky-Glahn, 2006) is used for the k-means cluster analysis. The ilr transformation was obtained using the concept of balances, whereas balances are calculated by a sequential binary partition of the D-part composition following the D-1 steps. The arbitrary $ilr_{R/S}$ coordinate

separated the compositions in a group, R with r elements from the composition in a group S, with s elements:

$$ilr_{R/S} = \sqrt{\frac{rs}{r+s}} ln\left(\frac{g(y_R)}{g(y_S)}\right)$$

where the $g(\boldsymbol{y_R})$ is the geometric mean of the r variables and $g(\boldsymbol{y_S})$ is the geometric mean of the s variables.

As a first stage of data analysis, values falling below mdl were imputed (Fig. 4). For both datasets, imputation was done using the robust multiplicative lognormal replacement method implemented in the R package 'zCompositions' (Palarea-Albaladejo and Martín-Fernández, 2015). This imputation technique preserves the ratios among the components of a composition, thus being a valid choice to replace values below mdl values. Further stages of data analysis include the application of unsupervised and supervised statistical analyses to the compiled and limited suite datasets, respectively (Fig. 4).

Unsupervised statistical analyses

Unsupervised statistical analyses aim to establish patterns intrinsic to the data without any associated response variable. Variation matrix, hierarchical and k-means clustering, coupled with Principal Component Analysis (PCA), were integrated together and applied to the compiled suite data (6,155 analyses of 51 elements + LOI) (Fig. 4), allowing definition of geochemical endmembers. Unsupervised statistical analyses and visualization of results were implemented using a set of software packages available in R: 'compositions'; 'ggplot2'; and fpc' (Wickham, 2016; Hennig, 2018; van den Boogart et al., 2018).

Firstly, relationships among elements were investigated using the Aitchison variation matrix (Aitchison, 1986). The elements of this variation matrix are the variances of the log-ratios between variables calculated as $\tau_{ij} = var\left(\ln\left(x_i/x_j\right)\right)$ for i, j from 1 to 51. Further, the variation matrix was converted into a distance matrix $d_{ij} = \sqrt{\sum_{k=1}^{51}(\tau_{ik} - \tau_{jk})^2}$ for i, j from 1 to 51 and used as a dissimilarity measurement for hierarchical clustering. The resulting cluster dendrogram displays the hierarchical agglomeration of element groups where the vertical position of the split shows the relative distance between each group.

Secondly, the k-means algorithm was employed to classify geochemical data into clusters. k-means clusters can be interpreted in terms of geometallurgical domains and are at the starting point of orebody characterization (Caciagli, 2016; Bhuiyan et al., 2019). Interpretation of clusters is possible because these can discriminate geochemistry of alteration and mineralization assemblages from that of host lithologies to a degree that might be difficult to identify using a combination of visual logging, geological mapping, or consideration of geochemical data in conventional ways. For example, at Acropolis, clusters obtained via the k-mean algorithm distinguished 'magnetite'- versus 'hematite'-geochemical signatures (Dmitrijeva et al., 2019b) with good correlation to mineralogical-petrological data for the two Fe-oxides (Courtney-Davies et al., 2019). The goal of the k-means clustering is to partition geochemical analyses into pre-specified, non-overlapping k clusters based on the squared Euclidean distance between geochemical analyses as a measure of dissimilarity. Each cluster is formed around a starting point, i.e., centroid, which is further iteratively recalculated as the within-cluster sum of squared errors (SSE) for each cluster is minimized. Although the algorithm requires the user to specify a numerical value for k, selection of optimal k is facilitated by: (i) plotting the total within-cluster SSE against the number of clusters ('elbow' method); and (ii) assessment of the stability of each cluster using the bootstrapping

method and calculation of Jaccard similarity values j_i for each cluster. The Jaccard similarity represents the robustness of a cluster and is commonly above 0.75 for a well-sustained cluster (Hennig, 2018). Additionally, the Silhouette analysis provides a visual assessment of how well each object lies within its cluster, i.e., cluster homogeneity, whereby a high average Silhouette value s_i is an indication of good clustering (Rousseeuw, 1987). Prior to k-means clustering, geochemical data require a transformation that projects such data onto Euclidean space. The latter was achieved by obtaining the ilr-coordinates (i.e., balances) of the compiled suite data by sequential binary partitioning (Egozcue and Pawlowsky-Glahn, 2005). The steps of partitioning are based on the hierarchical cluster dendrogram and provided in Appendix Table A1. The sequential binary partitioning consisted of splitting the 51-part composition into 50 non-overlapping balances, where for example, the b45 or 45th balance is a composite variable obtained as a ratio of geometric means CuS / BiAuAgMoTeU (Appendix Table A1).

The final step of unsupervised statistical analysis is PCA, a method generally used for revealing hidden data structures while exploring the significant associations amongst geochemical variables (Caciagli, 2016). Principal components are a new set of variables calculated from the linear combinations of the original variables. A biplot is used for a graphical representation of the chosen principal components where elements and geochemical analyses are plotted as loadings and scores. Provided that the selected principal components capture the significantly large proportion of the variance, the biplot can provide insight into the multivariate data structure. Notably, in ore deposit geochemistry, PC1 normally delineates the host rock geochemical signatures from the main mineralization signatures (Chen et al., 2017). The subsequent components are orthogonal among themselves and may be the product of other geochemical processes like superimposed alteration

(Grunsky, 2010). PCA was performed on the clr-transformed compiled suite data by using a singular value decomposition.

Supervised statistical analysis

Random Forests (RF) is one of the most widely used supervised statistical techniques, allowing prediction of categorical or numerical response variable using a set of predictor variables i.e., geochemical elements (Breiman et al., 1984, Breiman, 2001). Random Forests is an ensemble method that uses multiple decision trees, in which each tree encompasses a series of hierarchical decision nodes that are utilized to predict response variables based on the majority of votes cast by all decision trees (Breiman et al., 1984). A range of classification problems in geoscience can be solved using RF algorithms: predictive modelling tools for lithologic mapping (Kuhn et al., 2018), geometallurgical modelling (Bhuiyan et al., 2019), and/or prediction of ore deposit type based on mineral chemistry (e.g., Gregory et al., 2019). Generally, the RF algorithm consists of two subsequent steps: classifier training using the relatively small training set, and subsequent validation of the predictions using the test set to evaluate performance of the predictive model.

Implementation of the RF classification was achieved using the package 'randomForest' in R (Liaw and Wiener, 2002). The limited suite data (29,172 samples of 32 elements) includes the 6,155 samples that were also analyzed for the expanded suite of elements. Therefore, the 'compiled suite' dataset (6,155 analyses of 52 elements) is used as a training set for the RF model in which the five-level categorical variable 'cluster' derived from *k*-mean algorithm is a response variable. The goal of RF classification is to select the best performing RF model and to predict 'cluster' variables for the remaining 23,017 samples which lack high-precision measurements of those elements which are important indicator elements in IOCG deposits of the Gawler Craton (notably Mo, Sn, W, Ag, Bi, and REE, as well as As and Sb). To train the RF model, the following set of

predictor variables was chosen: Cu, Co, Ni, Pb, Zn, Ba, La, Ce, Fe, Al, Si, K, Ca, Mg, Mn, Na, P, Ti, Zr, Cr, V, Sc, U, S, CO_2, and Au. This choice of elements is based on their presence at quantifiable concentrations in the 23,017-samples test set. In order to improve RF model performance, specific gravity and magnetic susceptibility were added into the list of predictor variables.

The RF method averages results from 500 decision trees with 500 being a default setup of the algorithm. Each decision tree is obtained from the training set by randomly selecting a subset of eight elements from 28 predictors (26 elements + specific gravity and magnetic susceptibility). The number of elements in the subset is a parameter of the RF and eight gave the highest model accuracy over a range from 5 to 14. Thus, the process of building decisions trees was repeated for 500 bootstrapped samples whereby each geochemical analysis was classified into one of the five categories of the 'Cluster' by each tree. Finally, a geochemical analysis was assigned to a category 'cluster' that occurs most frequently amongst the 500 separate classifications (majority vote).

The remaining 23,017 samples form a test set which is not shown to the RF classifier during the training process. Fitting the RF model into a testing set resulted in the prediction of the category 'Cluster' for 23,017 samples. Because it is impossible to estimate the RF model accuracy for the predictions made, overall model performance was evaluated using the bootstrap aggregation. Bootstrapping consisted of randomly selecting and generating a training sub-set of 6,000 analyses from the total of 23,017 samples for which category 'Clusters' have just been predicted. This is because a sub-set with a size of 6,000 comprises nearly a quarter of the data. The bootstrapped 6,000-sample sub-set was used as a training set to cross-validate the 'Cluster' for the remaining 17,017 samples. A total of ten bootstrapped training and test pair-datasets were derived, and model accuracy was calculated for each as a proportion of correctly classified samples. The model

accuracy, represented as a confusion matrix of correctly classified and misclassified samples, is one of the outcomes of the RF classification. Additionally, the mean decrease in the Gini index, a measure of the contribution of a given variable to correctly classify training data, was used to determine the relevance of different elements during RF classifier training. Finally, PCA was applied to the limited suite data in order to compare the position of the 'clusters' in the PC1-PC2 projection with that of the compiled suite dataset.

Implicit numerical and geological modelling

Geological and numerical models for the Wirrda Well prospect were developed using Leapfrog Geo 4.5.1 implicit modelling software to assist in understanding the structure and geometry of the prospect. Numerical modelling of the continuous variables Cu (ppm), Fe (wt.%) and U (ppm) was done using spheroidal kriging with 'no drift' and 1500 m base range in both the both WWN and WWS. In the absence dyke strike directions measured in oriented drill core, isotropy of continuous variables was assumed. A spatial trend with orientation along the strike of the 'undifferentiated' mafic dykes was applied to all numerical models. The model is constrained by the fit obtained at the orientation along which the dykes are aligned.

Estimation of Cu(-Fe)-sulfide mineralogical zonation

The normative Cu(-Fe)-sulfide mineralogy was estimated from the limited suite data thus covering the entire set of 48 drillholes. Five main S-bearing phases were considered: barite, pyrite, chalcopyrite, bornite and chalcocite. Four mineralogical categories, i.e. Cu(-Fe)-sulfide zones were derived from the calculations: 'Py-Cp', 'Cp-Bn', 'Bn-Cc' and 'Barren'. The category 'Barren' was defined as <300 ppm Cu irrespective of the calculated zone. The remaining zones were obtained using methods methodologies as given by Dmitrijeva et al. (2019a). The four resulting categories

representing the mineralogical zonation in both WWN and WWS were projected in 3D space thus allowing for a comparison with the geological and numerical models.

Results

Geological Model of the Wirrda Well prospect

The three-dimensional model shown as Fig. 5 adequately describes the observed geometry of the Wirrda Well prospect by combining logging data and 29,172 geochemical analyses of 32 elements from 48 drillholes. This model aims at resolving the geometry, strike and interrelationships amongst the undifferentiated mafic dykes, which are present throughout both WWN and WWS, and is combined with numerical modelling (i.e., kriging) of Cu, Fe and U grades, as well as calculated parameters such as *k*-mean clusters and Cu(-Fe)-sulfide mineralogical zonation.

The surface topography of the prospect was derived as the collars of the drillholes. Wirrda Well North and South were modelled separately due to the scarcity of drillhole data and the significant geochemical differences between the two. Donington Suite granite is the main geological unit hosting the mineralization within both areas. The Hiltaba Suite granite intersected below the Donington Suite granite in WRD19, was modelled as a separate block in the northeastern area of WWN, as suggested by the geophysical anomaly (Ehrig, 2013). Prior to geological modelling, a discrimination of mafic dykes based on their Al/Zr and Ti/Zr was attempted. The dykes showed some variation in terms of these ratios and were classified into four groups based on a visual discrimination on the corresponding scatterplot (high Al/Zr, low Al/Zr, high Ti/Zr, and low Ti/Zr). However, due to brecciation and shearing of the dykes and their contacts, it was impossible to make a clear chemical or spatial discrimination (Fig. 5A). These dykes were thus further modelled

using the interval selection tool to create hanging- and footwall surfaces. Sets of geometrical, 'vein-like' shapes were created in Leapfrog to approximate their dip and strike, which is broadly concordant with the apparent orientation of samples in the drillholes (Fig. 5A). Nevertheless, the samples of the undifferentiated mafic dykes fit onto identical planes, thus suggesting strong structural control on their emplacement despite the slight differences in their Al/Zr and Ti/Zr ratios.

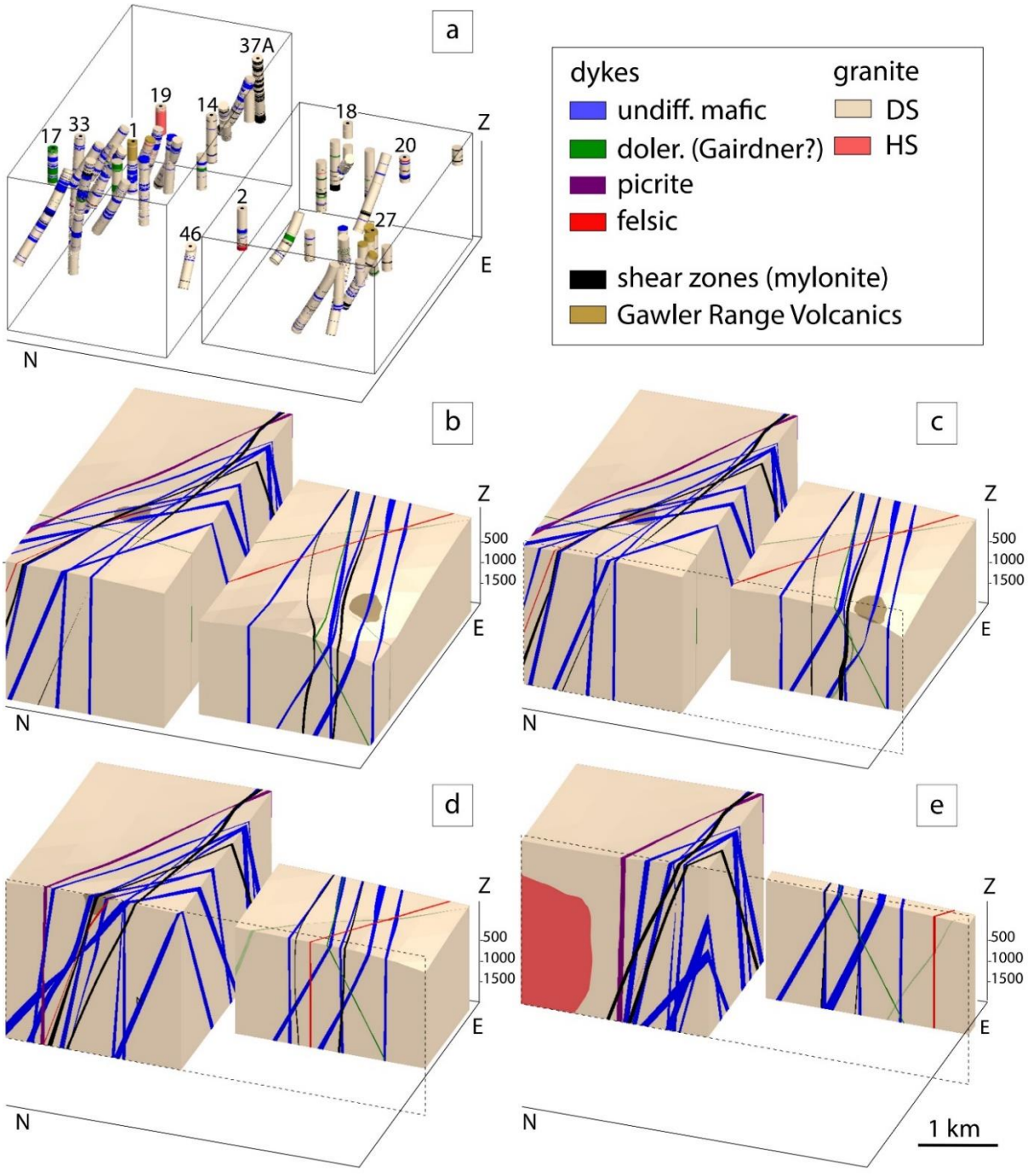


Figure 5. (A) Location and geology of the 48 'WRD' drillholes and (B-E) geological model of Wirrda Well North and South shown in oblique view with plunge 30° and azimuth 70°. The sequence of the sections intends to show the orientation and interrelationship among the undifferentiated mafic dykes, Donington and the Hiltaba granites.

Table 2. Variation matrix (sub-matrix) of 31 elements from the Compiled Suite data. The full variation matrix is given in Appendix Table B1.

	Ag	Al	As	Au	Bi	CO_2	Cu	Co	Cr	Fe	K	Li	Mn	Mo	Na	Nb	Ni	S	Sc	Sb	Se	Si	Sn	Ta	Te	Th	Ti	U	V	W
Al	2.6																													
As	1.9	1.4																												
Au	2.0	2.8	2.0																											
Bi	2.5	2.9	1.8	2.6																										
CO_2	6.8	5.2	4.7	6.4	5.5																									
Ce	1.7	1.0	1.1	1.7	2.4	5.1																								
Cu	1.8	3.1	2.4	2.1	2.0	6.0																								
Co	2.1	1.4	0.8	2.1	2.3	4.5	2.2																							
Cr	2.7	1.0	1.4	2.7	3.1	5.5	3.0	1.4																						
Fe	1.6	1.5	0.7	1.8	2.4	4.3	2.0	0.5	1.4																					
K	3.3	0.2	2.2	3.6	4.0	6.1	4.1	2.2	1.4	2.3																				
Li	2.1	0.3	1.1	2.2	2.6	5.3	2.4	0.9	0.7	1.0	0.7																			
Mn	4.1	2.4	2.3	3.8	3.5	1.6	3.4	1.7	2.6	1.7	3.2	2.2																		
Mo	1.8	1.8	1.4	2.1	2.2	5.7	1.8	1.5	2.1	1.1	2.5	1.3	3.0																	
Na	2.6	0.4	1.4	2.7	3.1	5.6	3.4	1.7	1.2	1.6	0.6	0.7	2.8	2.0																
Nb	2.4	0.5	1.4	2.5	2.9	5.2	3.0	1.5	1.5	1.4	0.7	0.7	2.5	1.8	0.6															
Ni	2.1	1.3	1.1	2.3	3.0	4.5	2.5	0.4	1.1	0.3	2.0	0.8	1.7	1.6	1.5	1.5														
S	3.4	3.9	3.1	3.5	3.7	5.0	1.9	2.0	3.8	1.9	4.9	3.1	2.6	2.7	4.5	3.5	2.0													
Sc	2.0	0.6	0.8	2.3	2.7	4.5	2.5	0.6	0.7	0.5	1.1	0.3	1.7	1.3	0.8	0.9	0.4	2.7												

Sb	1.7	1.1	0.6	1.9	2.1	4.1	2.3	0.8	1.2	0.5	1.8	0.9	1.8	1.3	1.2	1.1	0.7	2.7	0.6																		
Se	1.7	0.8	1.0	1.9	2.6	4.8	2.4	0.8	1.2	0.7	1.3	0.6	2.2	1.4	0.9	0.8	0.7	2.7	0.5	0.7																	
Si	2.3	0.1	1.1	2.5	2.6	4.9	2.9	1.2	1.0	1.2	0.4	0.3	2.2	1.6	0.3	0.4	1.1	3.6	0.5	0.8	0.6																
Sn	1.8	0.8	0.8	1.8	2.5	4.7	2.2	0.7	1.0	0.6	1.3	0.6	1.9	1.4	0.9	0.8	0.6	2.4	0.4	0.5	0.6	0.6															
Ta	2.7	0.2	1.6	2.9	3.0	5.4	3.5	1.6	1.3	1.7	0.4	0.6	2.6	2.0	0.4	0.3	1.6	4.2	0.8	1.2	0.9	0.2	0.9														
Te	1.6	2.3	1.3	1.6	2.3	4.7	2.1	1.2	2.2	0.8	3.2	1.7	2.5	1.4	2.3	2.0	1.3	2.4	1.4	1.1	1.3	1.9	1.2	2.4													
Th	2.2	0.7	1.5	2.7	3.1	5.4	3.4	1.7	1.7	1.4	1.0	0.9	2.8	1.8	0.5	0.6	1.6	4.1	1.0	1.2	0.8	0.4	1.1	0.5	2.0												
Ti	2.4	0.2	1.1	2.5	2.9	5.0	2.7	1.0	0.7	1.1	0.6	0.2	2.1	1.6	0.6	0.7	0.9	3.3	0.3	0.9	0.7	0.3	0.5	0.5	2.0	1.0											
U	1.3	1.8	1.2	1.4	2.4	5.4	2.0	1.1	1.9	0.8	2.5	1.2	2.7	1.3	1.9	1.5	1.1	2.4	1.2	1.0	0.9	1.5	0.9	1.9	0.9	1.5	1.6										
V	2.2	1.3	1.0	2.4	3.0	4.6	2.5	0.6	1.0	0.3	2.0	0.8	1.9	1.5	1.5	1.5	0.3	2.4	0.2	0.7	0.8	1.1	0.6	1.6	1.4	1.6	0.7	1.3									
W	1.9	1.4	0.7	1.8	1.9	4.1	2.0	0.7	1.4	0.6	2.1	1.1	1.8	1.4	1.5	1.3	0.9	2.2	0.7	0.5	0.9	1.1	0.4	1.5	1.0	1.6	1.1	1.0	0.8								
Zr	2.6	0.1	1.4	2.8	3.0	5.1	3.2	1.4	1.2	1.5	0.3	0.5	2.4	1.8	0.4	0.4	1.3	3.8	0.6	1.1	0.8	0.1	0.8	0.2	2.2	0.6	0.3	1.8	1.3	1.4							

Modeling results show that the orientations of undifferentiated dykes vary between WWN and WWS and are defined as NW-SE and WSW-ENE-striking, respectively. The mylonite samples, which are associated with the intervals of sheared/mylonitized dykes were similarly modelled as crosscutting linear, 'vein-like' features. The picrite from drillhole WRD33 (two intervals comprising 24 whole-rock samples) was also modelled as a vein, however its orientation was assumed to lie along the strike of the undifferentiated dykes. The GRV units are intersected in the uppermost part of the drillholes (Figs. 2; 5) and were modelled as 'erosional surfaces' which are the software equivalent for unconformity.

Multivariate statistical analysis

Variation matrix and dendrogram

The variation matrix (Table 2; Appendix Table B1) and hierarchical cluster analysis of elements from the compiled suite shows groups of elements that can be linked to host-rock geochemistry, mineralization and hydrothermal alteration. Six separate groups can be identified on the hierarchical dendrogram (Fig. 6). The first group, the CO_2-Mn pair forms its own node on the dendrogram. That is confirmed by the variation matrix, where CO_2 shows the greatest dissimilarity with the majority of the elements including IOCG indicator elements like Cu ($\tau_{CuCO2} = 6$), Au ($\tau_{AuCO2} = 6.4$) and Ag $\left(\tau_{AgCO2} = 6.8\right)$, and also elements typifying silicates: $\tau_{AlCO2} = 5.4$, $\tau_{ZrCO2} = 5.1$ (Table 2). Manganese is the only element which shows the largest proportionality with CO_2, $\tau_{MnCO2} = 1.6$ suggesting that carbonates are the largest hosts of Mn. Group 2 is formed exclusively by elements typically hosted within silicate minerals that represent the products of hydrothermal alteration or primary magmatic silicates. Group 2 can be subdivided

into high-field strength elements ‘Ta-Hf-Zr-Nb-Th’ and the remaining set of ‘Ba-Na-Sr-Cs-Tk-K-Rb-Al-Si’ (Fig. 6).

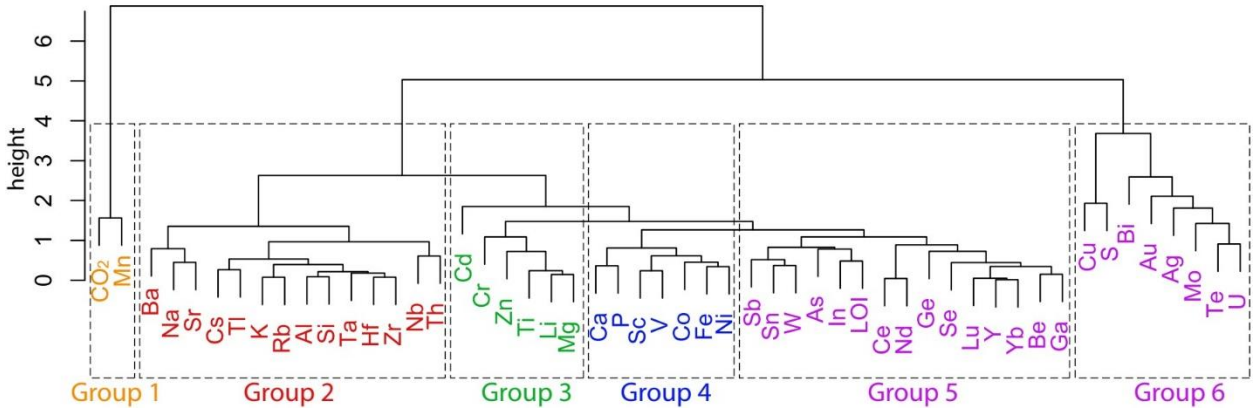


Figure 6. Hierarchical cluster dendrogram showing the six geochemical ‘Groups’ formed by 51 elements and loss of ignition (LOI). The height of the dendrogram is a dissimilarity measure calculated from the pairwise log-ratio matrix (Table 2; Appendix Table B1) of the 52 variables using Euclidean metrics.

The following Groups 3, 4 and 5 form a single tree on the dendrogram, however are clearly distinct as the height of the tree decreases. The Group 3 ‘Cd-Cr-Zn-Ti-Li-Mg’ typifies the geochemical signature of mafic rocks and the products of their alteration: $\tau_{CrMg} = 0.7$, $\tau_{CrTi} = 0.7$, $\tau_{CrSc} = 0.7$ (Table 2; Appendix Table B1). The adjacent Group 4 is composed of ‘Ca-P-Sc-Fe-Ni-Co-V’ an association that likely represents ‘magnetite-apatite association’ formed during early alkali-calcic alteration within some IOCG-kin deposits with little Cu+Au mineralization (e.g., Williams et al., 2005). Group 4 shows a high degree of proportionality among its elements, in which $\tau_{FeV} = 0.3$, $\tau_{FeNi} = 0.3$, $\tau_{FeCo} = 0.5$, and $\tau_{CaP} = 0.4$. Groups 5, one of the largest groups on the dendrogram, is composed of ‘Sb-Sn-W-As-In-LOI-Ce-Nd-Ge-Se-Lu-Y-Yb-Be-Ga’ elements. This group includes Sn-W, i.e., ‘granitophile’ elements, As-Sb, and REE, all of which are found within IOCG mineralization from the Gawler Craton and elsewhere. Finally, Group 6 represents a distinct node on the dendrogram and includes elements which represent the

commodity metals Cu-Au-U-Ag along with the trace elements Bi, Mo and Te that are closely associated with Cu-(Fe)-sulfides.

Table 3. Characteristics of five clusters obtained from k-means cluster analysis applied to compiled suite data

Cluster	N, samples	Jaccard similarity value, j_i	Silhouette value, s_i	Lithological and geochemical characteristics of the cluster	Median Cu, ppm	Median Au, ppb	Median density, kg/m^3	Median magnetic susceptibility, $\times 10^{-3}$ SI
1	1566	0.77	0.11	Mineralized DS granite and undifferentiated mafic dykes	2600	60	2.98	4.23
2	1319	0.90	0.31	Unmineralized DS granite	500	11	2.81	2.12
3	733	0.72	0.28	Hematite-dominant samples	7150	100	3.12	9.25
4	1891	0.85	0.25	Unmineralized DS granite and HS granite	250	13	2.73	1.01
5	646	0.81	0.16	Magnetite-dominant samples	150	10	3.82	55.18

N = number of whole-rock samples within each cluster. Calculated Silhouette values are from Fig. 7B.

Unsupervised classification: k-means clustering

A k value of five was chosen to partition the ilr-coordinates of the compiled suite data into geochemically meaningful clusters. The ‘elbow’ plot showing the relationship between the within-cluster sum of squared errors and a number of k suggests that the inflection point can be defined

at $k = 5$ (Fig. 7A). The resulting clusters k_i, $(i = 1, 2, \ldots, 5)$ are well-delineated and show high Silhouette width s_i with Clusters 2, 3 and 4 show the highest $s_i > 0.2$ (Fig. 7B; Table 3). The Jaccard similarity value, j_i calculated for each cluster shows overall high cluster stability and only clusters 1 and 3 have $j_i < 0.8$ (Table 3).

The obtained clusters reflect and capture mineralization, hydrothermal alteration and the protolith rocks at the Wirrda Well prospect. The complete distinction among mafic and felsic lithologies within the prospect is difficult due to the effects of overprinting alteration.

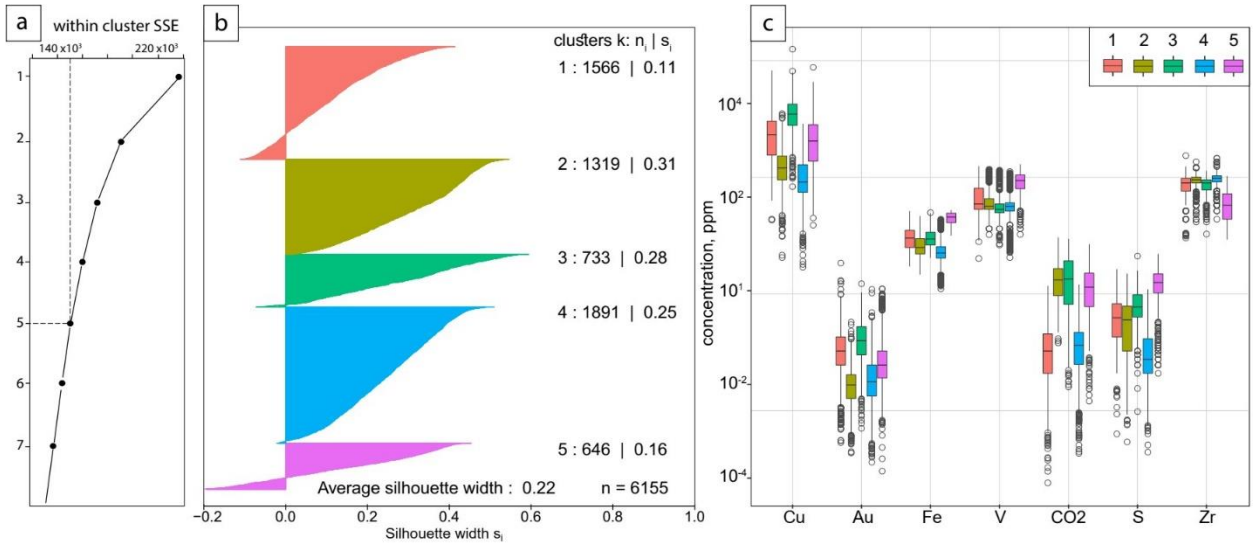


Figure 7. (A) within cluster sum of squared errors plotted against the number of clusters $k = 1, \ldots, 7$ demonstrating that 5 or 6 clusters are optimal for the k-mean procedure; (B) Silhouette width values plotted for 5 obtained clusters (color-coded). The cluster i $(i = 1, \ldots, 5)$, the number of analyses within a cluster (n_i) and the average Silhouette width (s_i) are given to the right; (C) boxplots for clusters obtained from the k-means procedure showing ranges of elements for each cluster. Median values of Cu and Au are also given in Table 3.

Nevertheless, those samples representing the least mineralized Donington Suite granite and unmineralized Hiltaba Suite granite fall within Cluster 4, which also contains the largest number of analyses $n_4 = 1891$. Samples from Cluster 4 also display the lowest median density of 2.73 kg/m^3 and the lowest median magnetic susceptibility values of 1.01 $\times 10^{-3}$ SI (Table 3). All these

features correspond to the typical petrophysical properties of felsic igneous rocks. In contrast, Clusters 1 and 2 are slightly denser and more magnetic (Table 3) and represent the Donington Suite granite samples and undifferentiated mafic dykes. Cluster 1 contains the highest proportion of undifferentiated mafic dykes and also shows a significantly higher concentrations of Cu and Au compared to Clusters 2 and 4 (Fig. 7C). Cluster 2, although similar to Cluster 1 with respect to petrophysical attributes, is not mineralized and shows Cu and Au concentrations similar to those of the granite-dominated Cluster 4. Cluster 2 is also distinguished by the relatively high proportion of Mn-CO_2 (Fig. 7C).

Finally, Clusters 3 and 5 represent the mineralization and are characterized by the highest median densities and median magnetic susceptibilities (Table 3). Cluster 5, which shows a mean magnetic susceptibility of 55 x 10^{-3} SI and also the highest proportion of Fe and V amongst all the clusters represents the magnetite-dominant samples at the Wirrda Well prospect (Fig. 7C). In contrast, Cluster 3, contains the highest concentrations of Cu and Au while still showing a relatively high Fe proportion and therefore high density and magnetic susceptibility (Table 3). Additional insights into the geochemical meaning of each cluster is provided by the PCA biplots which precisely capture the geochemical signatures of each cluster.

Principal Component Analysis and Ternary Diagrams

Biplots (Figs. 8 and 9) represent the results of PCA applied to the ‘compiled suite’ dataset. A total variability of 54% is explained by the first three components: PC1=29%, PC2 = 15% and PC3 = 8%. The PC1-PC2 projection (Fig. 8A) displays principal component loadings of elements forming the geochemical groups comparable with those on the dendrogram (Fig. 6). PC1 separates elements into mineralization associated Group 6 (Cu-Bi-Au-Ag-Mo-Te-U) and geochemical signatures of host rocks and their alteration products represented by Groups 2 and 3. Notably,

however, PC1 does not differentiate between mafic and felsic host rocks, even if elements of Group 2 that can be considered felsic rock affiliated, have higher loadings onto PC1 than mafic affiliated elements of Group 3 (Cd-Cr-Zn-Ti-Li-Mg) (Fig. 8A). The PC1-PC2 projection also distinguishes the mineralization-associated Group 6 from Group 4 (Fe-Ni-V-Co). Additionally, PC2 efficiently shows the CO_2-Mn pair of elements as a distinct, stand-alone geochemical association thus confirming the high degree of disproportionality of CO_2 with the remaining geochemical variables.

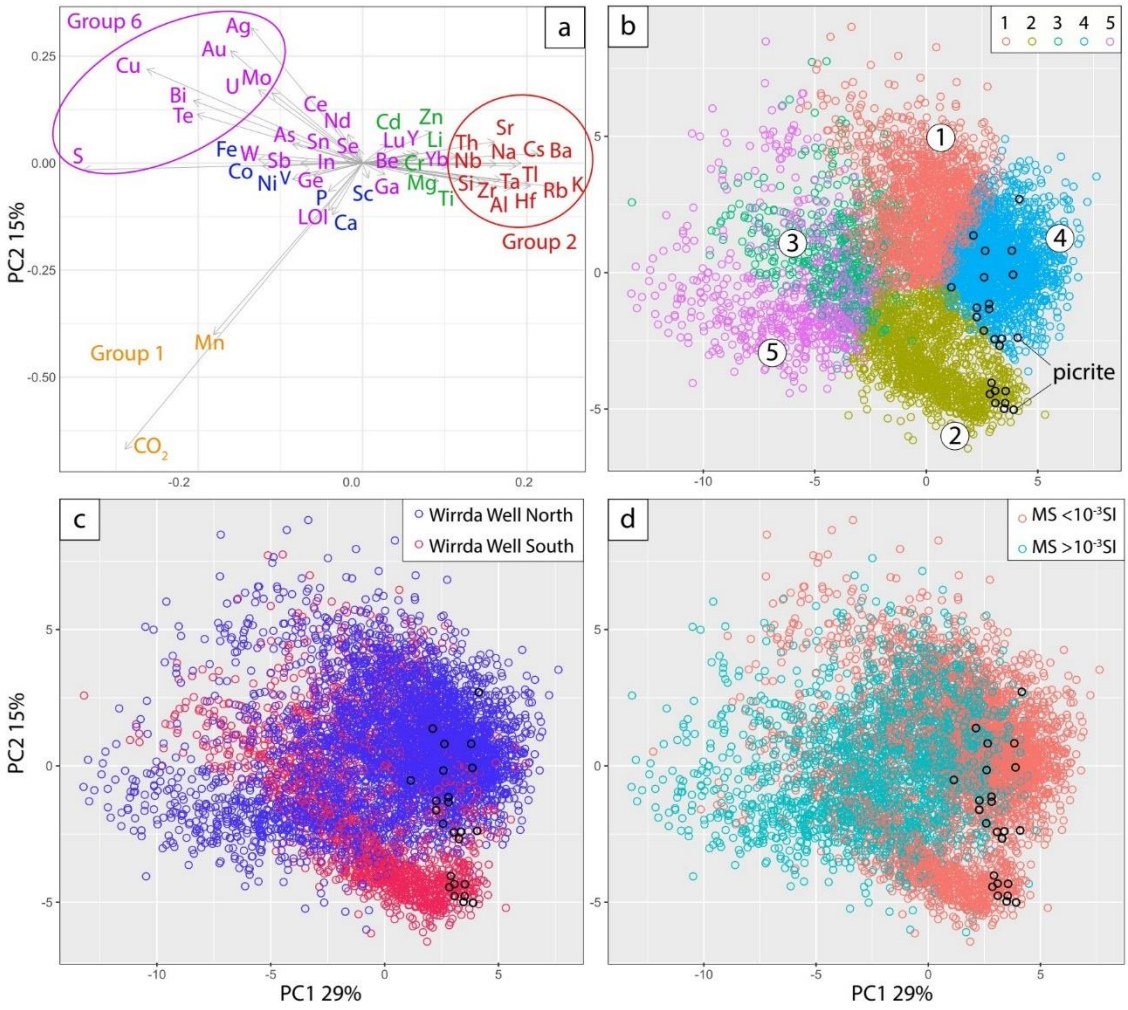


Figure 8. PC1-PC2 projection showing (A) principal component loadings (color-coded according to the hierarchical dendrogram in Fig. 6) obtained from the centered log-ratio-transformed compiled suite data. Principal component scores showing (B) the distribution of five clusters (color-coded and numbered), (C) samples from the Wirrda Well North and South, and (D) two magnetic susceptibility (MS) categories in PC1-PC2 projection. Each point (circle) represents a single sample. The loadings of the elements, i.e. coordinates within the projection (A), are given in Appendix Table C1.

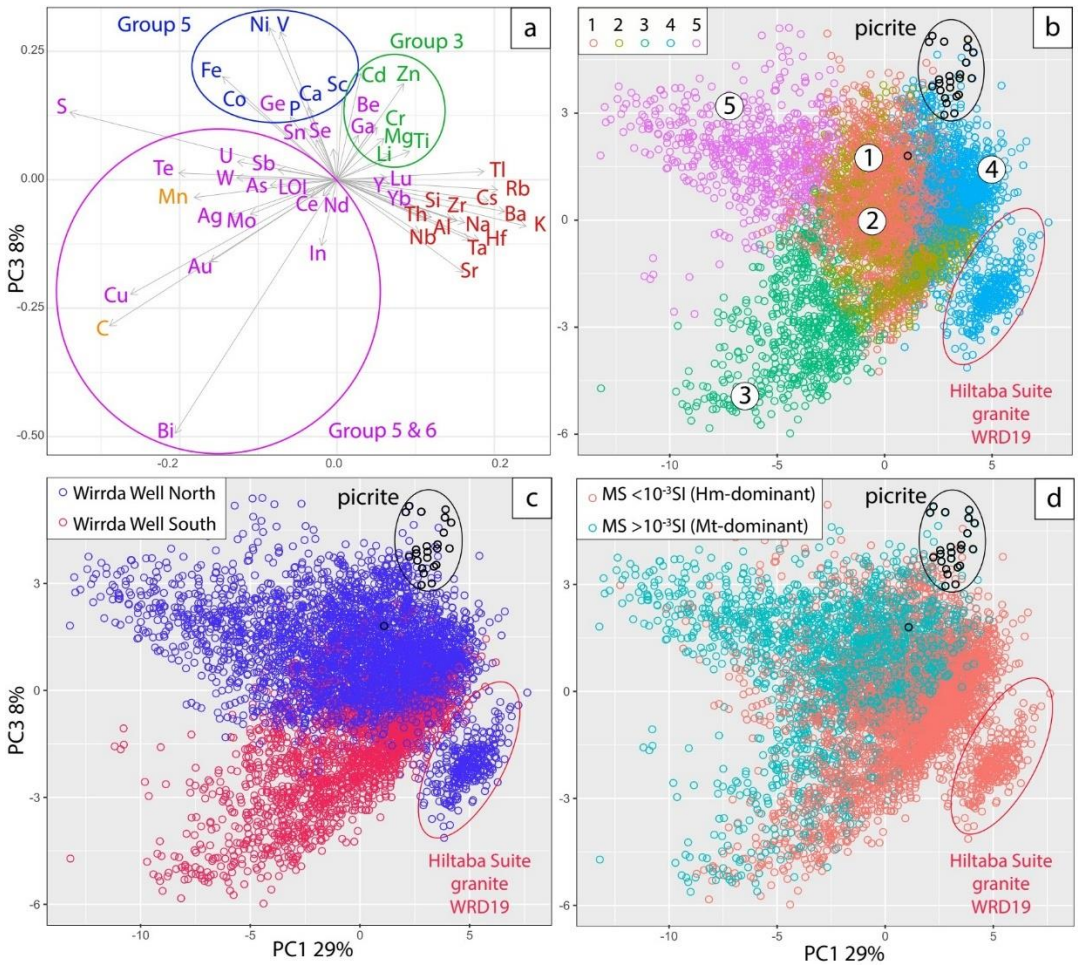


Figure 9. (A) Principal component loadings (color-coded according to the hierarchical dendrogram in Fig. 6) obtained from the centered log-ratio-transformed compiled suite data. PC1-PC3 projection of the principal component scores shows (B) the distribution of five clusters (colour-coded and numbered), (C) distinctions between the samples from the Wirrda Well North and South, and (D) two magnetic susceptibility (MS) categories indicating highly magnetic versus least magnetic samples. Each point (circle) represents a single sample. Note the high loadings of Group 3 elements onto picrite samples, and also the clustering of samples from the Hiltaba granite drillhole (WRD19) away from other sample groups. The loadings of the elements, i.e. coordinates within the PC1-PC3 projection (A), are given in Appendix Table C1.

The PC1-PC2 projection of 5 clusters obtained by *k*-means provides better insight into their geochemical signatures. The projection (Fig. 8B) confirms that Cluster 4 is unmineralized and predominantly composed of granites. In contrast Clusters 1 and 2 are likely to include more mafic samples, whereas Cluster 1 is characterized by elements of Groups 5 and 6, which indicate the

signature of IOCG mineralization. The latter is confirmed by Cu and Au concentration in Cluster 1 (Fig. 7C), which show median values of 2600 ppm and 60 ppb, respectively (Table 3). Similarly, Cluster 3 is characterized by loadings of 'Cu-Bi-Au-Ag-Mo-Te-U' (Group 6), whereas the median Cu values are the highest (~7150 ppm). Cluster 3 therefore represents higher-grade Cu mineralization.

Although the PC3 only captures 8% of the data variability, it provides additional insights into the mineralization at Wirrda Well prospect. The PC1-PC3 projection of element loadings (Fig. 9A) delineates Group 5 (Fe-V-Ni-Co) from the IOCG mineralization signature represented by Groups 5 and 6. The PC1-PC3 projection also separates the Hiltaba Suite granite from the Donington Suite granite thus indicating significant primary magmatic geochemical differences between them. Additionally, the projection highlights the picrites and those elements typifying their geochemical signatures, Zn-Cd-Cr (Zn ~1,000 ppm). Finally, the projection successfully discriminates the magnetite-dominant Fe-V-Co-Ni-bearing signature of Cluster 5 from the mineralized, hematite-dominant, IOCG-signature-bearing Cluster 3. The latter discrimination is also highlighted by the differences in magnetic susceptibilities (Fig. 9D) and the significant differences between WWN and WWS; with the latter strongly associated with Cluster 3.

The degree of associations between certain clusters and geochemical groups can be investigated via ternary diagrams. The two ternary diagrams (Fig. 10) are obtained by scaling and centring of three-part sub-compositions using the compositional data principles (van den Boogaart and Tolosano-Delgado, 2013). The sub-compositions are formed as geometric means of geochemical groups (Fig. 6): Group 1 representing carbonates (Mn-CO_2), Group 2 representing silicates (Ba-Na-Sr-K-Rb-Al-Tl-Cs-Si), Group 4 representing magnetite-bearing samples (Fe-V-Ni-Co) and Group 6 representing the Cu-Au mineralization and U-Mo 'granitophile' signature (Cu-S-Bi-Au-

Ag-Mo-Te-U). The distribution of samples in the 3-part sub-compositions thus confirms the association of the 'magnetite' and 'granitophile' signatures with Cluster 3 and 5, respectively (Fig. 10A). Finally, the diagrams demonstrate that samples belonging to Cluster 4 are least mineralized granite as compared to Cluster 1 which plots towards Group 6 (Cu-Au mineralization and 'granitophile' signatures) thus representing mineralized samples (Fig. 10B).

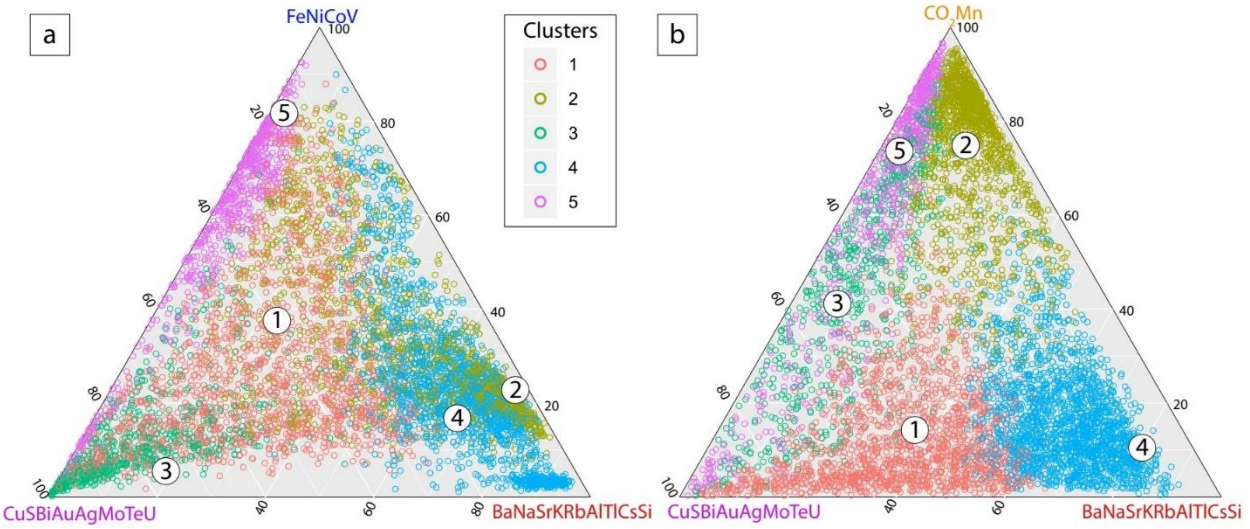


Figure 10. Centered ternary diagrams of the compiled suite element data color-coded according to five geochemical clusters and reduced to the three sub-compositions (Groups) as in the dendrogram (Fig. 6). (A) Group 4 (Fe-V-Ni-Co), Group 2 (Ba-Na-Sr-K-Rb-Al-Tl-Cs-Si) and Group 6 (Cu-S-Bi-Au-Ag-Mo-Te-U) distinguish the 'hematite' (Cluster 3) and 'magnetite' (Cluster 5) signatures. (B) Group 1 (CO_2-Mn), Group 2 and Group 6 indicate least altered Cluster 4 and the association of CO_2-Mn signature with Clusters 2 and 5.

Supervised classification depicts mineralization signature in 3D

The five-level response variable 'Cluster' was predicted for limited suite data and resulted in 88% model accuracy. The confusion matrix representing the results of the model fitted onto a bootstrapped sample (21,264 samples) is presented in Table 4. Cluster 4, representing the unmineralized Donington and Hiltaba Suite granites is the least misclassified. In contrast, the iron-oxide and Cu mineralization signatures from Clusters 3 and 5 are the most misclassified. The mean

decrease in Gini, a measure of the contribution of a given element to correctly classify data, was used to determine the relevance of different elements during Random Forests classification (Fig. 11A).

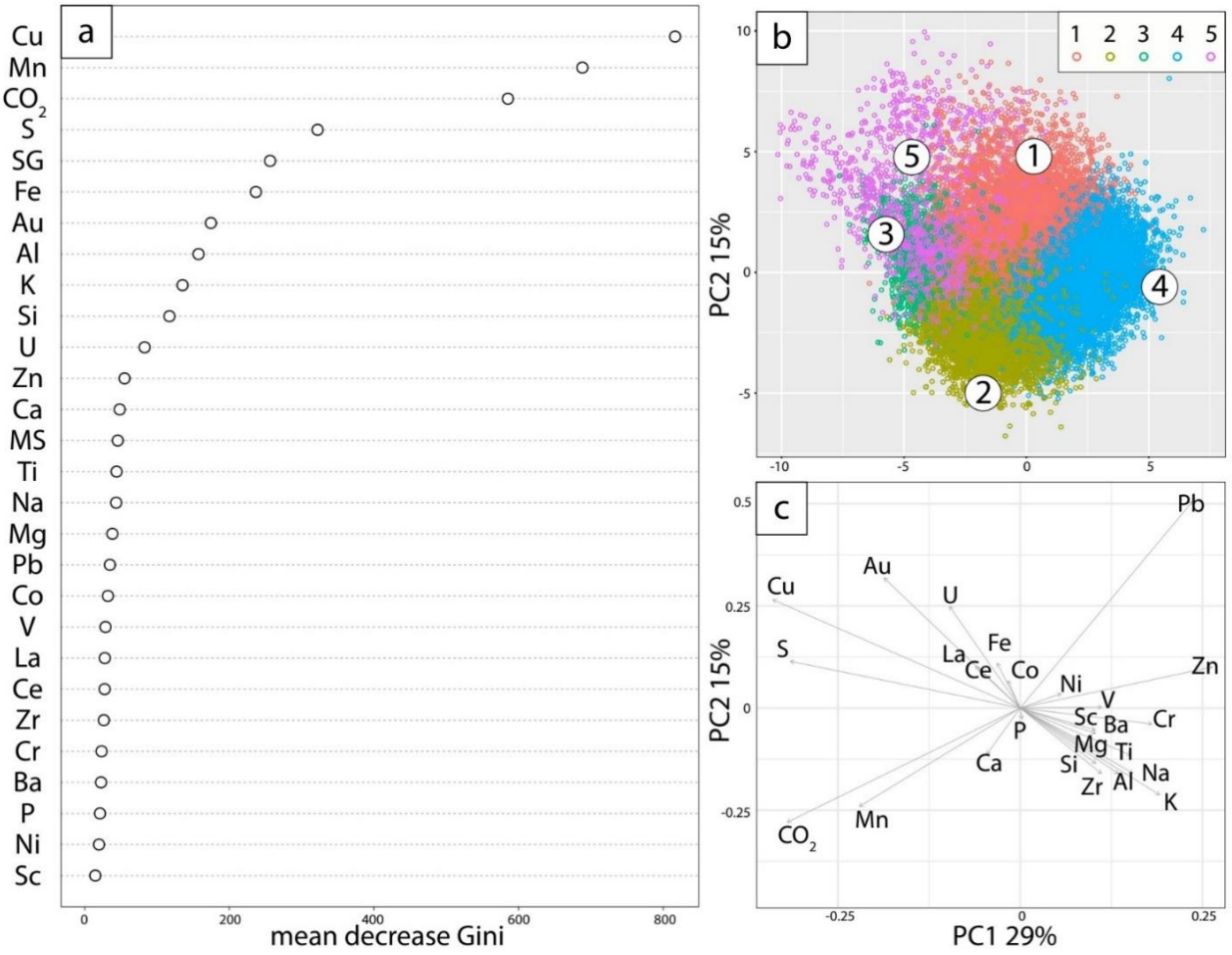


Figure 11. (A) Diagram showing the variable importance as 'mean decrease Gini index' obtained from classification using the random forest model. The 28 predictors are ordered according to their contribution into correct classification of the training data. Copper, Fe, Au and specific gravity (SG) are amongst the most important for the classification, whereas Ni and Sc are the least important. (B) Principal component scores and (C) loadings obtained from the PCA of the limited suite data. Each sample (circle) is color-coded according to the predicted cluster from the random forest model. MS – magnetic susceptibility.

Table 4. Confusion matrix of the RF classification of five-level response variable 'Cluster' onto bootstrapped test sample (n = 21,264). True classes are arranged by columns, predicted classes are within rows.

Cluster	1	2	3	4	5
1	5833	87	49	270	81
2	159	5010	131	179	17
3	157	78	958	0	26
4	562	244	1	11137	0
5	87	56	47	0	1095
n, total	6798	5475	1186	11586	1219
n, misclassified	965	465	228	449	124
percentage misclassified, %	14.1	8.5	19.2	3.9	10.2
model accuracy, %	88				

Copper, Mn-CO_2, Au and Fe were among the most important variables for RF classification. Additionally, density and magnetic susceptibility are also of high importance. Scandium, Ni and P are the least important variables. The PCA was applied to the limited suite data in order to check the predicted clusters on the PC1-PC2 projection and verify the PCA results on the compiled suite dataset (Fig. 11B, C). The projection of predicted variable 'cluster' (Fig. 11B) directly corresponds to those obtained from the compiled suite data (Fig. 8B), thus additionally validating the RF classification. Moreover, element loadings obtained from the limited suite elements (Fig. 11C) match those from the compiled suite data (Fig. 8A).

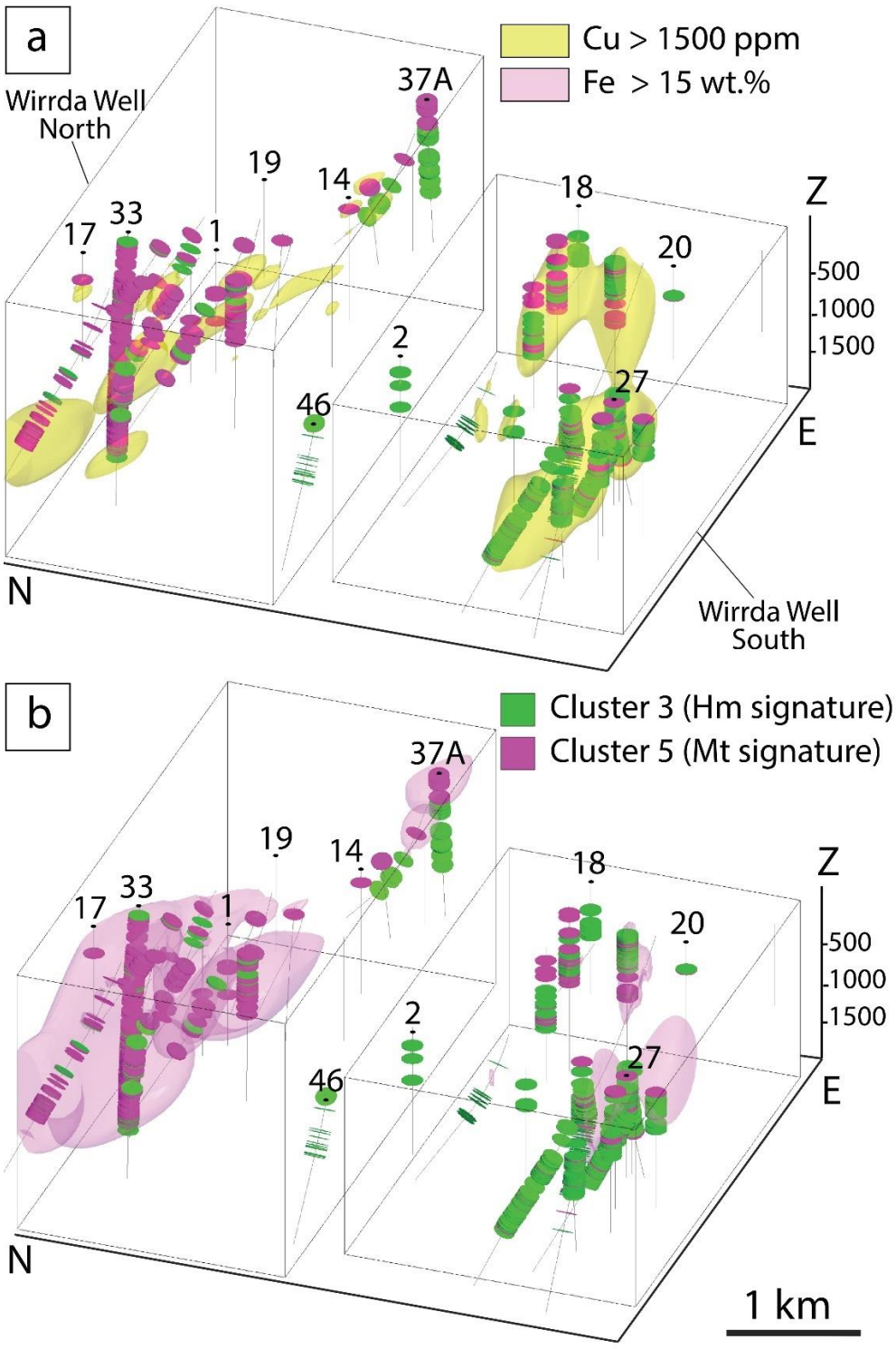


Figure 12. Oblique view (plunge 30° azimuth 70°) of Wirrda Well North and South showing isosurfaces of Fe > 15 wt% and Cu > 1500 ppm with an overlay of geochemical clusters relevant for 'hematite' signature (Cluster 3) and 'magnetite' signature (Cluster 5). Note the high degree of spatial correlation between Cu and 'hematite' signature (Cluster 3) in Wirrda Well South.

Clusters 3 and 5 are the most important outcome of the k-means classification since they depict two distinct iron-oxide assemblages. Hematite-dominant, IOCG-signature-bearing and Cu-Au-mineralized samples in Cluster 3 are also characterized by 'granitophile' elements like U, Mo and W (Fig. 9A). The projection of Cluster 3 in both WWN and WWS thus indicates the distribution of Cu-Au mineral assemblages. The shell of Cu > 1500 ppm shows a strong overlap with the extent of Cluster 3 (Fig. 12A) and is especially well developed in WWS. Cluster 3 is also present in WWN, albeit patchy as Cu mineralization is less developed and shows a marked NW-SE orientation. The Fe >15 wt.% outline shows a mismatch with the Cu >1500 ppm shell, especially in WWS, thus indicating that higher-grade Cu mineralization was not associated with the strongest Fe-metasomatism. Cluster 5, which typifies the Fe-V-Ni-Co signature and low Cu-Au content is weakly developed in the WWS, however it is the dominant cluster in WWN. Also, Cluster 5 shows significant overlap with samples containing >15 wt.% Fe (Fig. 12B).

Numerical models for sulfide and metal distributions in the Wirrda Well prospect

The calculated Cu(-Fe)-sulfide zones as 'pyrite-chalcopyrite (Py-Cp)', chalcopyrite-bornite -(Cp-Bn)', 'bornite-chalcocite (Bn-Cc)' and 'Barren (Cu <300 ppm)' allow representation of mineralogical zonation of the Wirrda Well prospect (Fig. 13). The mineralization threshold was set to a value of Cu < 300 ppm which is considerably lower compared to the Olympic Dam 'Barren' zone defined as 0.1 wt.% Cu. Wirrda Well South displays vertical zonation comprising a transition from deep 'Py-Cp' through a well-developed 'Cp-Bn' zone to a shallower Bn-Cc zone, as for instance in drillhole WRD12 (Fig. 13). The shallow parts of the drillholes WRD31, WRD27, WRD21 and WRD24 which contain GRV units are unmineralized. In contrast, WWN shows a distinct pattern of mineralogical zonation. Firstly, WWN features a less-developed 'Cp-Bn' zone and significantly more 'barren' samples. Secondly, in some of the drillholes the mineralogical

zonation shows patchy ‘Py-Cp’ intervals distributed within Bn-Cc zones (WRD50A, WRD34 and WRD14; Fig. 13).

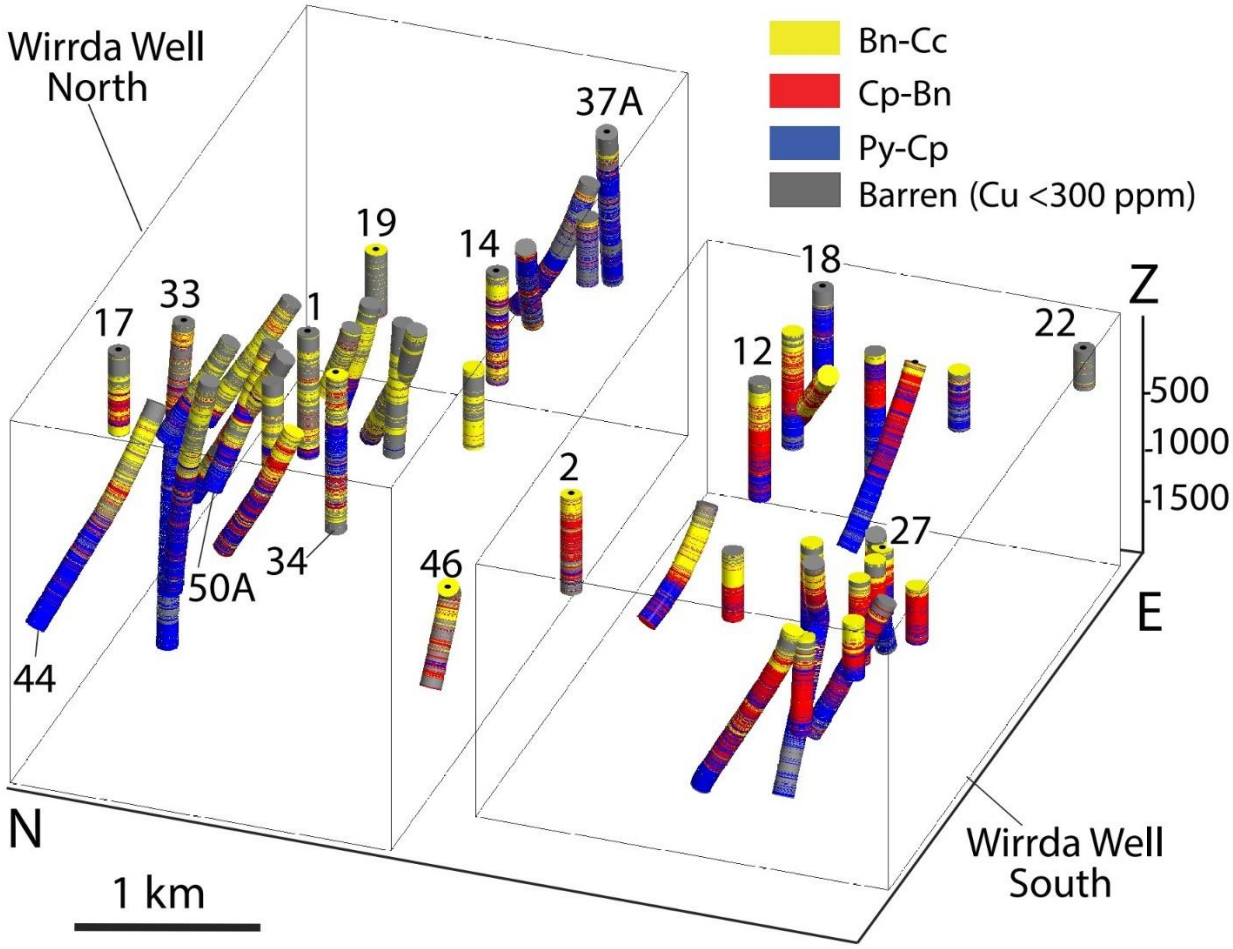


Figure 13. Estimated normative Cu(-Fe)-sulfide mineralogy distribution patterns in Wirrda Well North and South, oblique view with plunge 30° and azimuth 70°. Note the smooth vertical transition from ‘Py-Cp’ through ‘Cp-Bn’ to ‘Bn-Cc’ in the WWS, and the patchy zoning in WWN.

The numerical distribution models for Fe, Cu and U in WWN and WWS are presented in a plan view at the -600 RL and a cross section. Outlines of Cu >1500 ppm and Fe 15 wt.% were projected as dashed lines to highlight patterns of anomalous metal concentration.

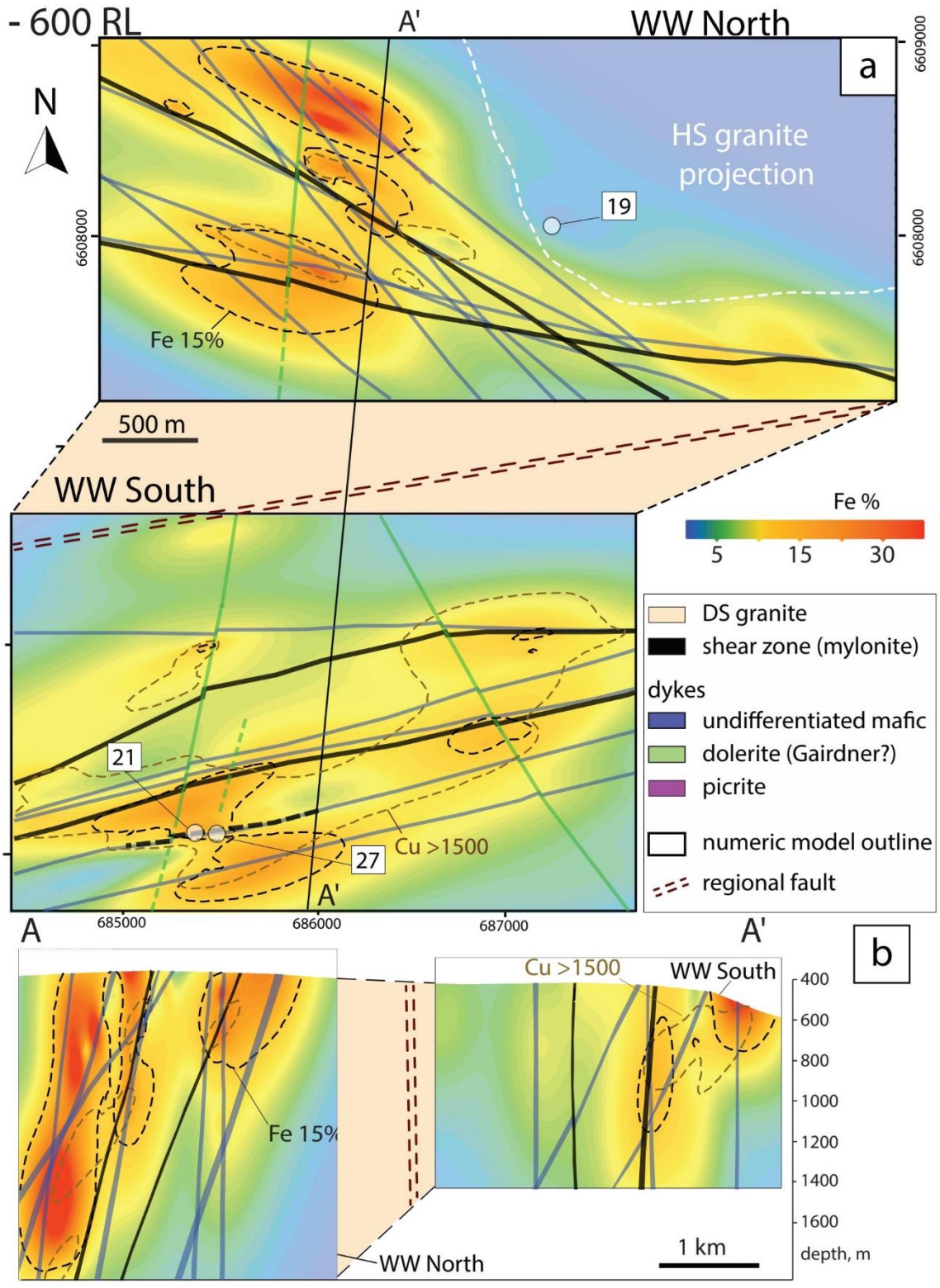


Figure 14. Spatial distribution of Fe in Wirrda Well North and South obtained via kriging in (A) plan view and (B) in cross-section A–A'. Note the reference drillholes. See text for further explanation.

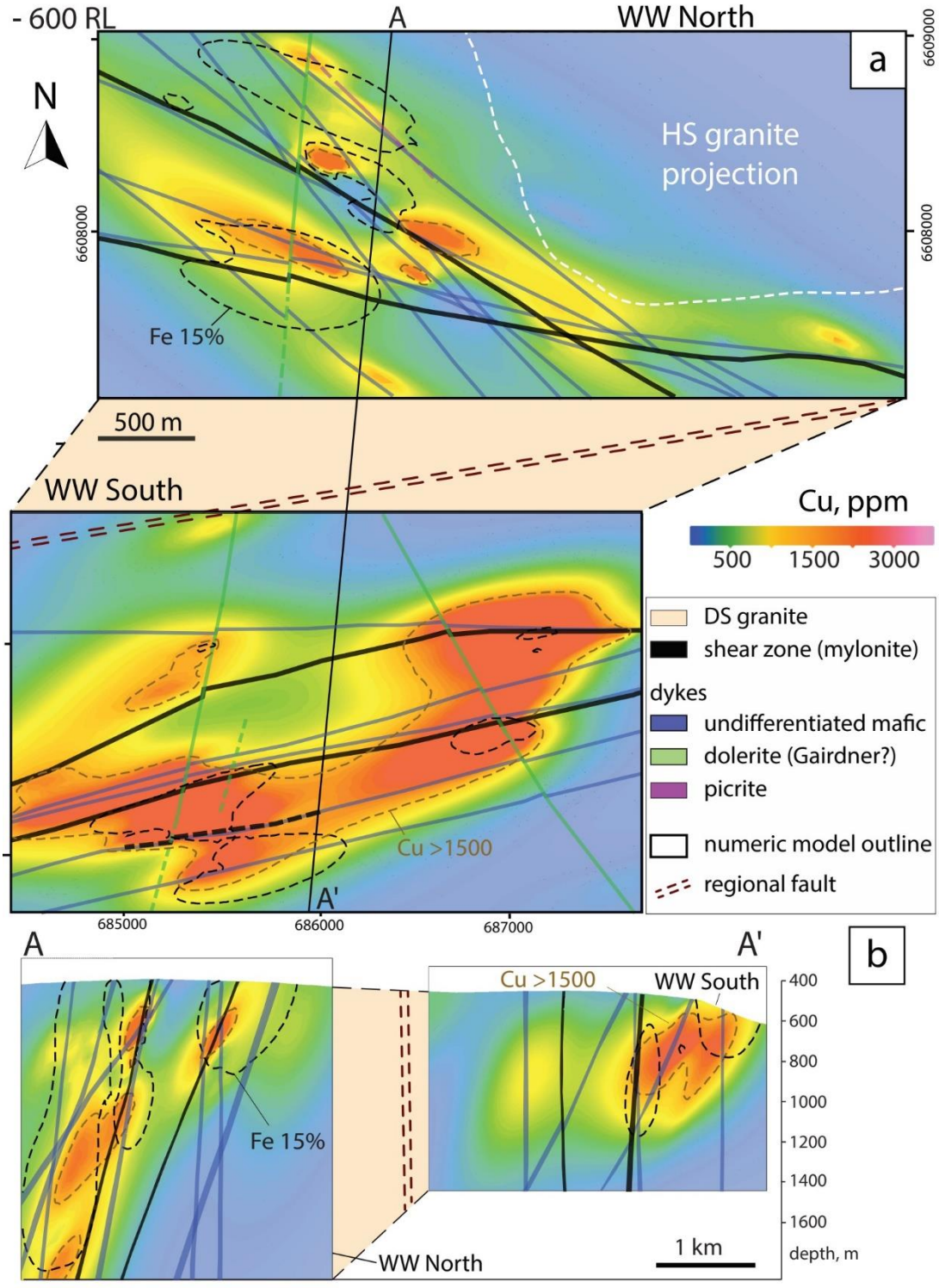


Figure 15. Distribution of Cu in (A) plan view of Wirrda Well North and South and in (B) cross-section A–A'. See text for further explanation.

Iron distribution in WWN and WWS is show patterns oriented along the planes of undifferentiated dykes, particularly in WWN (Fig. 14). Iron concentrations exceeding 10 wt.% are present throughout the prospect, concordant with Fe metasomatism (pervasive Fe alteration of lithologies). Notably, drillhole WRD19, which predominantly intersects Hiltaba Suite granite, displays Fe contents <5 wt.%, concordant with either fresh or sericite altered granite. In WWS, the Fe distribution is less traceable along the dykes than in WWN (Fig. 14). Moreover, in this case, the highest Fe anomaly is offset by shear/mylonite planes crosscutting mafic dykes, implying post-mineralization reactivation of these planes (Fig. 14B).

Comparable to Fe, the distribution of Cu also shows orientation broadly concordant with the dykes and shear zones, albeit with differences between WWN and WWS (Fig. 15). Highest concentrations of Cu occur at the intersections between mafic dykes and shear zones in WWN (Fig. 15A). Anomalies of Cu and Fe, i.e., 1500 ppm Cu and 15 wt.% Fe, are spatially coincident, as observed in both plan view and cross-section (Fig, 15A, B). However, in WWS, there is a marked mismatch between Cu distribution and high Fe content, particularly observable at depth where the Cu forms a broad halo almost irrespective of dyke geometries (Fig. 15B). In plan-view, Cu also forms a broad halo, which although elongate along the dyke direction, is less controlled by their exact geometry, thus contrasting with the Cu distribution in the north (Fig. 15A). It is notable that the shallower Cu anomaly in WWS is concordant with the upward Cu(-Fe)-sulfide distribution dominated by bornite and chalcocite (higher Cu content) in WWS rather than chalcopyrite in WWN.

Uranium is the only ‘granitophile’ element that is measured in the present sample suite at concentrations on average <100 ppm. In plan-view, U shows a distribution broadly similar to that of Fe and Cu (Fig. 16), with a tendency to concentrate at intersections of dykes and/or shear zones.

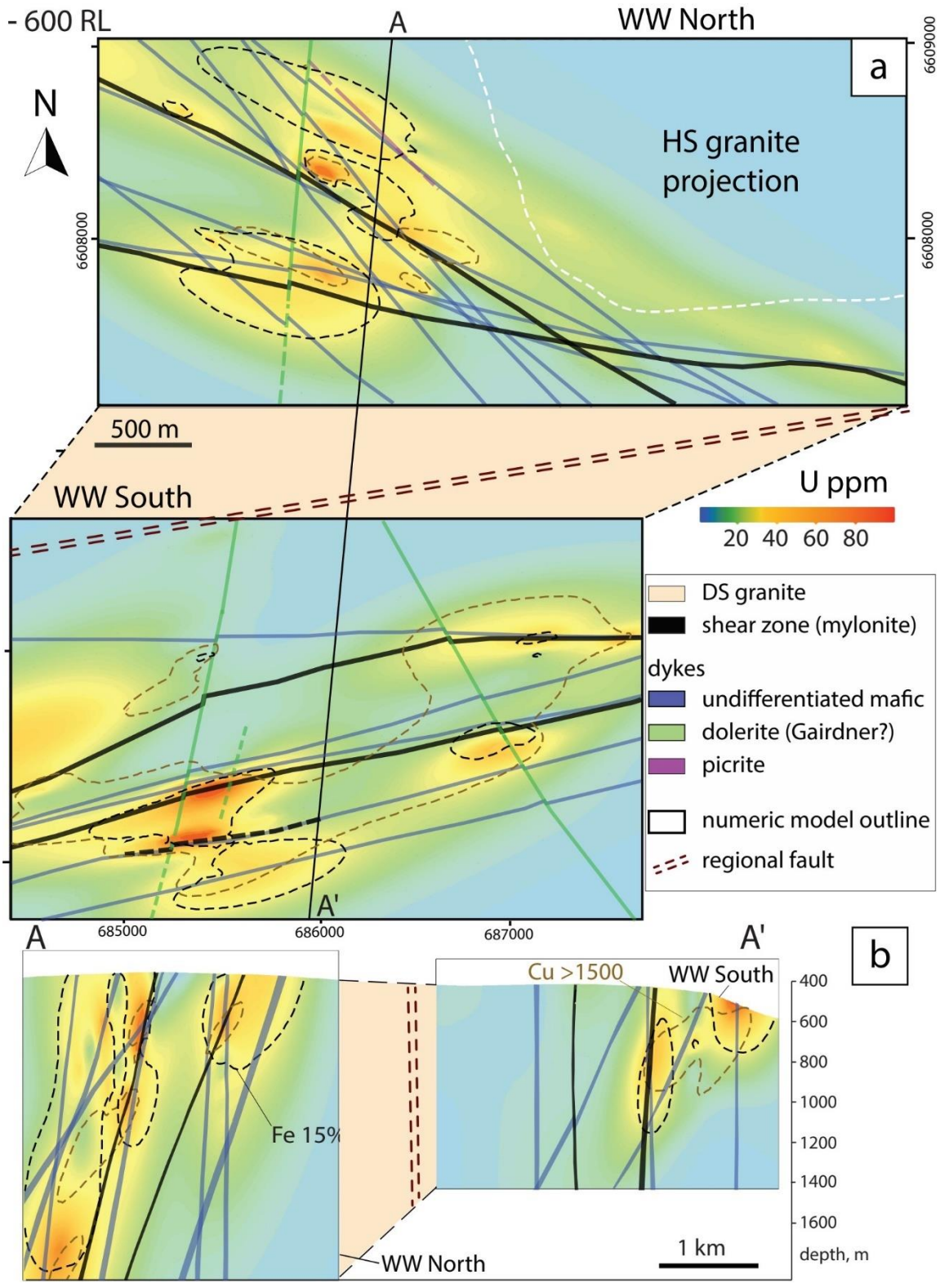


Figure 16. Distribution of U in Wirrda Well North and South in (A) plan view and (B) cross-section A–A'. See text for further explanation.

Background U concentrations (~20 ppm) are present throughout the prospect, including in the drillhole intersecting the Hiltaba Suite granite (WRD19). Higher U values (> 40 ppm) are located within the Fe >15 wt.% outline (Fig. 16). In the eastern side of WWS, an area of U with values ~ 30 ppm is not associated with elevated Cu or Fe content, instead forming a separate zone of elevated U (Fig 16A).

Discussion

Structural control on the mineralization at Wirrda Well

The dense network of mafic dykes and shear zones crosscutting the dykes at low angles (Fig. 5) controlling metal distributions at Wirrda Well (Figs. 14-16) indicates the presence of permeable structures at the contacts with/and within mylonitized granite. Considering that most of the mafic dykes are older than the ~1.6 Ga IOCG mineralization, such structures provided conduits for focusing of IOCG fluids and metal deposition. Remobilization of ductile Cu-(Fe)-sulfides during reactivation of these structures is supported by highest-grade Cu concentrations occurring at dyke/shear zone junctions (Fig. 15). Mylonitisation of Donington granite along shear zones produced new generations of Fe-oxides, Cu-Fe-sulfides, monazite and siderite at Wirrda Well (Courtney-Davies et al., 2019). This is likely to have the same effects for lithologies more ductile than granite such as the mafic dykes.

Given the differences in dyke orientation and metal distributions (Figs. 2, 14-16), the two mineralized areas can be considered as two distinct structural blocks that became separated by movement on one of the E-W regional faults and subsequent rotation relative to each other, i.e., WNW- and SSW-striking dykes in WWN and WWS, respectively (Fig. 2). Vertical offset between these blocks can thus account for the deeper and shallower mineralization at WWN and WWS,

respectively (Figs. 14-16). The minimum age of the deposit dismemberment can be constrained by emplacement of the ~820 Ma, approximately NW-SE-striking GDS dolerites that crosscut both mineralized areas but show no control on metal distribution.

Table 5. Geochemical signatures of the mineralization in the Olympic Dam deposit and the Acropolis and Wirrda Well prospects according to the current study and Dmitrijeva et al. (2019a, b). A dominant signature represents elements with the strongest loading onto a PC1 obtained from a particular IOCG system. Subordinate signature corresponds to elements that have significant, however not dominant loadings onto corresponding PC1.

IOCG mineralization signature	**Olympic Dam**	**Wirrda Well**	**Acropolis**
'hematite' (granitophile)		**dominant**	
	Au-W-Mo-As-Sb	Cu-Au-Bi (Southern lobe)	Sn-Sb-W
		subordinate	
	Te-Bi-Cu-Sn-Ag-LREE-Sr-U-Ca-P	Ag-Mo-W-U-As-Sb-LREE (Southern lobe)	LREE-U-Th-Sr-Ca-P
'magnetite'		**dominant**	
	na	Fe-V-Ni-Co (Northern lobe)	Fe-V-Ni-Co
		subordinate	
		Ca-P-Sc (Northern lobe)	Cu-Mo-Bi

*na -not applicable

Vertical zonation of sulfides is smooth in WWS and may have a primary, hypogene origin as documented from preserved textures within the Cu-(Fe)-sulfides at Olympic Dam (Ciobanu et al., 2017). In contrast, a combination of hypogene and superimposed secondary processes accounts for the vertical Cu(-Fe)-sulfide distribution at WWN (Fig. 13) since newly-formed sulfides were documented along shear zones at Wirrda Well (Courtney-Davies et al., 2019).

Overall, metal distribution, differences in dyke orientation between WWN and WWS, and mylonitisation along shear zones indicate multi-stage reactivation of permeable structures accounting for formation of breccia pipes (Ehrig, 2013). Metal enrichment along lithological contacts and shear zones with low angle to these contacts is attributable to valve-pumping fault mechanisms allowing inflow of fluids throughout a protracted tectonothermal history. Wirrda Well can thus be considered a structurally-controlled type of breccia pipe mineralization whereby faults and their impact on metal zonation patterns are more prominent than at Olympic Dam, where mineralogical and geochemical zoning is traceable in 3D space (Ehrig et al., 2012; Dmitrijeva et al., 2019a).

IOCG signatures: a comparison between Wirrda Well, Acropolis and Olympic Dam

Granites (Donington and Hiltaba Suite) within Wirrda Well, characterized by the geochemical signature comprising lithophile elements (Al, Ba, K, Na, Si) and HFSE (Ta, Zr, Nb) (Group 2; Fig. 6), are comparable with those from Acropolis (GRV lavas, Donington and Hiltaba Suite granites) and Olympic Dam deposit (Hiltaba Suite granite). At Wirrda Well, however, although an overall geochemical similarity exits for the felsic lithologies (Cluster 4; Fig. 8B), the higher loadings of samples on the Group 2 elements discriminate among the Donington and Hiltaba Suite granites (Fig. 9B-C). The Hiltaba granite at Wirrda Well lacks a Cu-Bi-Au-Ag-Mo-Te-U mineralization signature (Fig. 6). Moreover, the Hiltaba granite at Wirrda Well has mean and median Fe values

of 2.4 and 2.9 wt.%, respectively, which along with the numerical models of Fe distribution (Fig. 14A) suggest no enrichment in Fe relatively to fresh rock. Nonetheless, as known from Olympic Dam, mineral replacements via coupled dissolution-reprecipitation reactions can lead to granite alteration that is not reflected in the whole-rock data (Kontonikas-Charos et al., 2017). Comparably, the Hiltaba Suite granite at Acropolis, crosscut by Fe-oxide veins, also lacks a 'granitophile' signature.

Alkali (sodic and potassic) alteration is present throughout all lithologies at Wirrda Well, including the Hiltaba granite. Unlike in the Olympic Dam deposit, where potassic alteration displays a strong spatial relationship with intense Fe-metasomatism (Dmitrijeva et al., 2019a), the higher Fe-grade zones at Wirrda Well are controlled by dyke intersections. Comparable superimposed and laterally extensive alteration halos not centered on the Fe-rich zones were documented in the Acropolis prospect (Dmitrijeva et al., 2019b). The Mn-CO_2 pair, corresponding to the unmineralized Cluster 2 (Figs. 8B-C; 10B; 11B), represents the presence of carbonates, i.e., Mn-bearing siderite, and suggests that a proportion of carbonates likely resulted from post-mineralization events notably in WWS.

The geochemical associations defining the signatures of IOCG mineralization vary across the Olympic Dam district. Despite this, all three hydrothermal systems are typified by a broader range of elements prominently featuring the association W-Sn-Mo (part of the 'granitophile' group of elements; Verdugo-Ihl et al., 2017; in press; Courtney-Davies et al., 2019), as well as the omnipresent association U-LREE. The mineralization signature depicted by statistical analysis of whole rock data varies depending on the predominant Fe-oxide type. For example, the IOCG signature in the Olympic Dam deposit lacks V, Ni and Co or such signature remains undiscovered. These elements are, however, associated with hydrothermal magnetite signature at both Wirrda

Well and Acropolis (Table 5). Notable with respect to the broad range of metals considered for the IOCG clan of deposits (Williams et al., 2005, and references therein) is the presence of W and Sn in association with Mo and U, part of the 'granitophile' group as defined from petrological studies which, in the Olympic Dam district is tied to the hematite signature (Verdugo-Ihl et al., 2017; in press; Courtney-Davies et al., 2019; Dmitrijeva et al., 2019a, 2019b).

This study shows that the Wirrda Well prospect shares geochemical signatures with those in both the Acropolis and Olympic Dam deposits, thus providing a link between magnetite- and hematite-dominant IOCG hydrothermal systems in the eastern Gawler Craton (Table 5). The Fe-V-Ni-Co signature noted in Acropolis and WWN can be attributed to high-temperature, early stage fluids. The statistical analyses applied here were not specifically targeted to discriminate between lithologies such as mafic dykes, which may be responsible for the high Ni concentrations noted in the whole rock dataset. This element may be a contaminant from the dykes rather than within magnetite since is low in the Wirrda Well silician magnetite, albeit still higher than in the same type of magnetite from the outer shell at Olympic Dam (Courtney-Davies et al., 2019; Verdugo-Ihl et al., in press; Ciobanu et al., 2019). In contrast, the 'magnetite' signature defined from statistical analysis of whole rock data for Acropolis (Fe-V-Ni-Co) does not include Ti (Table 5), despite this element reaching up to 1 wt.% in hydrothermal titanomagnetite (Courtney-Davies et al., 2019).

Based on the alteration footprints and geophysical expression, distinct depths of formation can be discussed for the two prospects. WWN shows structurally controlled deeper zones (small pore volume), resulting in a confined hydrothermal system with narrow mineralization along fluid conduits (Fig. 13) and a weak geophysical expression (Fig. 1B, C). This is consistent with formation in a relatively deep setting, as also documented for the IOCG mineralizing system at

Olympic Dam (Verdugo-Ihl et al., in press; Courtney Davies et al., in review). In contrast, the laterally extensive geophysical expression of Acropolis (Fig. 1B, C), mimicked by the scale of alteration halos (Dmitrijeva et al., 2019b), is typical of shallow formation whereby fluids are linked to surficial fracture networks (Meinert, 1997). Nevertheless, the two prospects do not directly represent a 'vertical' continuum of IOCG mineralization but rather display signatures indicative of hot fluids, i.e., >600 °C for titaniferous magnetite at Acropolis (Buddington and Lindsley, 1964) and at least 400 °C in silician magnetite from WWN containing nm-scale inclusions of tchermackite (Ciobanu et al., 2018).

The 'hematite' signature recognizable from whole rock data for all three IOCG deposits/prospects (Table 5) is most pronounced in the WWS. In the Olympic Dam deposit, such a signature is strongly associated with both Cu-Au mineralization since the orebody outline can be defined by the extents of Fe-metasomatism (Ehrig et al., 2012) and the IOCG mineralization signature (Dmitrijeva et al., 2019a). In contrast, in both Acropolis and WWS, the spatial extent of the 'hematite' signature is markedly offset from the expression of intense Fe-metasomatism (Table 5). Although mineralization in the Wirrda Well prospect is linked to the 1.6 Ga magmatic-hydrothermal event, the dated U-bearing hematite is from the western side of the prospect (WW46), outside the two mineralized areas (Courtney-Davies et al., 2019), rather than the presently outlined Hiltaba Suite intrusion, which, lacks an IOCG signature. Such relationships imply that another Hiltaba Suite intrusion, which supplied hydrothermal fluids, must underlie the prospect. Such a 'granitophile' signature may have value as an indicative vector towards proximal IOCG mineralization in the district.

Conclusions and Implications

1. The Wirrda Well prospect contains two distinct areas with IOCG-style mineralization: WWN and WWS. These display geochemical differences: (i) predominantly 'magnetite'-signature for WWN; and marked Mo-W-U(±Sn), a 'hematite' signature associated with higher-grade Cu-Au-(±Bi-Ag) mineralization for WWS.
2. Pre-mineralization mafic dykes provide permeable structures for fluid focusing and metal deposition since Fe, Cu, and to some extent U, are concentrated along dyke contacts to host granites. Dismemberment of the mineralized area/orebody into WWN and WWS occurred post-mineralization yet prior to the ~820 Ma Gairdner event. The new geological and numerical models show that Wirrda Well is one of the best examples of structurally controlled mineralization within the Olympic Dam district.
3. Although the geological setting, mineralogy and geochemistry of the Wirrda Well prospect show some dissimilarities to Olympic Dam and Acropolis, there is nevertheless sufficient geochemical similarities to confirm a common origin for hydrothermal fluids responsible for IOCG mineralization.

Statistical analyses of large prospect-scale geochemical datasets from the three IOCG hydrothermal systems in the Olympic Dam district provide a novel approach that can optimally explain relationships between magnetite- and hematite-dominant IOCG mineralization in the Gawler Craton, with potential application elsewhere.

This case study demonstrates how a combination of supervised and unsupervised algorithms can efficiently characterize an orebody and derive the geochemical signatures of mineralization. The unsupervised techniques applied to the extended suite dataset are essential for understanding the geochemical associations among the elements and formulation of the key 'Clusters' which

typify the geochemical endmembers of the data. The supervised RF algorithm applied to the limited suite data yields valid predictions when extrapolating the 'Clusters', thus being a reliable and cost-effective tool for ore deposit characterization. The efficiency of RF is especially relevant as those elements that are characteristic of IOCG mineralization in the Gawler Craton (e.g., W, Mo, Sn, Bi, As, Sb, and Ag) were absent in the limited suite data. On this basis, the combined approach represents an example of efficient 'orebody' characterization and can be used for brownfields exploration around IOCG deposits, and potentially for regional-scale exploration. In addition to providing detailed characterization of mineralization signatures, the three-dimensional geological modeling and geochemical interpolation, when combined with advanced statistical analyses of geochemical data, can facilitate understanding of ore genesis in time and space.

Acknowledgments

This work is a contribution to the FOX project 'Trace elements in iron-oxides: deportment, distribution and application in ore genesis, geochronology, exploration and mineral processing', supported by BHP Olympic Dam and the South Australian Mining and Petroleum Services Centre of Excellence. K.E. acknowledges the Wirrda Well exploration team, led by Mick Carew, who designed, drilled and logged the Wirrda Well drill core. Maya Kamenetsky (CODES, University of Tasmania) kindly provided her unpublished zircon ages from WRD19. V.K. and J.M. acknowledge funding from the ARC Linkage Grant "The supergiant Olympic Dam U-Cu-Au-REE ore deposit: towards a new genetic model". N.J.C. acknowledges additional support from the ARC Research Hub for Australian Copper-Uranium (Grant IH130200033). The Leapfrog Geo support team is also kindly thanked for their assistance with the development of the geological model.

References

Aitchison, J., 1986, The statistical analysis of compositional data. Monographs on Statistics and Applied Probability. Chapman & Hall, London, 416 p.

Allen, S., McPhie, J., Ferris, G., and Simpson, C., 2008, Evolution and architecture of a large felsic igneous province in western Laurentia: the 1.6 Ga Gawler Range Volcanics, South Australia: Journal of Volcanology and Geothermal Research, v. 172, p. 132-147.

Bachmann, K., Menzel, P., Tolosana-Delgado, R., Schmidt, C., Hill., and M. Gutzmer, J., 2019, The use of assay data as a foundation for a geometallurgical model-The case of the Thaba Chromite Mine, South Africa: Journal of Geochemical Exploration, v. 201, p. 99-112.

Barton, M.D., 2014. Iron oxide (–Cu–Au–REE–P–Ag–U–Co) systems. in Holland, H.D. and Turekian, K.K., ed., Treatise on Geochemistry, 2nd ed.: Elsevier, Oxford, p. 515–541.

BHP. 2019. BHP Annual Report 2019, (https://www.bhp.com/-/media/documents/investors/annual-reports/2019/bhpannualreport2019.pdf)

Bhuiyan, M., Esmaieli, K., and Ordóñez-Calderón, J.C., 2019, Application of Data Analytics Techniques to Establish Geometallurgical Relationships to Bond Work Index at the Paracutu Mine, Minas Gerais, Brazil: Minerals, v. 9, p. 302.

Blissett, A.H., Creaser, R.A., Daly, S.J., Flint, R.B., and Parker, A.J., 1993, Gawler Range Volcanics, in Drexel, J.F., Preiss, W.V. and Parker, A.J. ed., The Geology of South Australia. vol. 1 The Precambrian, Geological Survey of South Australia, p. 107–131

Breiman, L., 2001, Random forests: Machine Learning, v. 45, p. 5–32.

Breiman, L., Friedman, J.H., Olshen, R.A., and Stone, C.J., 1984, Classification and Regression Trees. Wadsworth, Belmont. 358 p.

Buddington, A.F., and Lindsley, D.H., 1964, Iron-titanium oxide minerals and synthetic equivalents: Journal of Petrology, v. 5, p. 310–357.

Caciagli, N., 2016, Multielement geochemical modelling for mine planning: case study from an epithermal gold deposit, in Martín-Fernández, J.A. and Thió-Henestrosa, S. ed., Compositional Data Analysis: Springer Proceedings in Mathematics & Statistics. p. 45–61.

Chen, S., Hattori, K., and Grunsky, E.C., 2017, Multielement statistical evidence for uriniferous hydrothermal activity in sandstones overlying the Phoenix uranium deposit, Athabasca Basin, Canada: Mineralium Deposita, v. 53, p. 493-508.

Ciobanu, C.L., Wade, B.P., Cook, N.J. Schmidt Mumm, A., and Giles, D., 2013, Uranium-bearing hematite from the Olympic Dam Cu-U-Au deposit, South Australia; a geochemical tracer and reconnaissance Pb-Pb geochronometer: Precambrian Research, v. 238, p. 129–147.

Ciobanu, C.L., Cook, N.J., Ehrig, K., 2017, Ore minerals down to the nanoscale: Cu-(Fe)-sulphides from the iron oxide copper gold deposit at Olympic Dam, South Australia: Ore Geology Reviews, v. 81, p. 1218–1235.

Ciobanu, C.L., Verdugo-Ihl, M.R., Slattery, A., Cook, N.J., Ehrig, K.J., and Courtney-Davies L., 2018, Nanoscale study of silician magnetite from IOCG systems: examples from the Olympic Dam District, South Australia: Quadrennial International Association on the Genesis of Ore Deposits symposium, 15th, Salta, Argentina, 2018, Proceedings, p. 185–186.

Ciobanu, C.L., Verdugo-Ihl, M.R., Slattery, A., Cook, N.J., Ehrig, K.J., Courtney-Davies, L., and Wade, B.P., 2019, Silician Magnetite: Si–Fe-Nanoprecipitates and Other Mineral Inclusions in Magnetite from the Olympic Dam Deposit, South Australia: Minerals, v. 9, p. 311.

Conor, C.H.H., Raymond, O., Baker, T., Teale, G., Say, P., and Lowe. G., 2010, Alteration and mineralization in the Moonta-Wallaroo copper-gold mining field region, Olympic Domain, South Australia. in Porter, T.M., ed., Hydrothermal Iron Oxide Copper-Gold and Related Deposits: a Global Perspective, v. 3, PGC Publishing, Adelaide, p. 147–170.

Courtney-Davies, L., Ciobanu, C., Verdugo-Ihl, M.R., Dmitrijeva, M., Cook, N., Ehrig, K., and Wade, B., 2019., Hematite geochemistry and geochronology resolve genetic and temporal links among iron-oxide copper gold systems, Olympic Dam district, South Australia: Precambrian Research, v. 335, p. 105480.

Courtney-Davies, L., Ciobanu, C.L., Tapster, S.R., Cook, N.J., Ehrig, K.J., Crowley, J.L., Verdugo-Ihl, M.R., Wade, B.P., and Condon, D.J., in review, Opening the Magmatic-Hydrothermal Window: High-Precision U-Pb Geochronology of the Mesoproterozoic Olympic Dam Cu-U-Au-Ag Deposit, South Australia: Economic Geology.

Corriveau, L., Montreuil, J.F., and Potter, E., 2016, Alteration facies linkages among iron oxide copper-gold, iron oxide-apatite, and affiliated deposits in the Great Bear Magmatic Zone, Northwest Territories, Canada: Economic Geology, v. 111, p. 2045–2072.

Creaser, R.A. 1989, The Geology and Petrology of Middle Proterozoic Felsic Magmatism of the Stuart Shelf, South Australia: Unpublished PhD thesis, Melbourne, Australia, La Trobe University, 434 p.

Cross, K., 1993, Acropolis and Wirrda Well prospects, in Drexel, J.F., Preiss, W.V., and Parker, A.J., ed., The geology of South Australia. vol. 1, The Precambrian: Geological Survey of South Australia, Bulletin 54, p. 138

Dmitrijeva, M., Ehrig, K., Ciobanu, C., Cook, N., Verdugo-Ihl, M., and Metcalfe, A., 2019a, Defining IOCG signatures through compositional data analysis: a case study of lithogeochemical zoning from the Olympic Dam deposit, South Australia: Ore Geology Reviews, v. 105, p. 86–101.

Dmitrijeva, M., Ciobanu, C., Ehrig, K., Cook, N., Metcalfe, A., Verdugo-Ihl, M., and McPhie, J., 2019b, Mineralization-alteration footprints in the Olympic Dam IOCG district South Australia: The Acropolis prospect: Journal of Geochemical Exploration, v. 205, p. 106333.

Egozcue, J.J., Pawlowsky-Glahn, V., Mateu-Figueras, G., and Barceló-Vidal, C., 2003, Isometric logratio transformations for compositional data analysis: Mathematical Geosciences, v. 3, p. 279–300.

Egozcue, J.J., and Pawlowsky-Glahn, V., 2005, Groups of parts and their balances in compositional data analysis: Mathematical Geosciences, v. 37, p. 795–828.

Egozcue, J.J., and Pawlowsky-Glahn, V., 2006, Simplicial geometry for compositional data, in Buccianti, A., Mateu-Figueras, G., and Pawlowsky-Glahn, V., ed., Compositional Data Analysis in the Geosciences: From Theory to Practice: Geological Society, London, Special Publications v. 264, p. 145–159.

Ehrig, K., McPhie, J., and Kamenetsky, V., 2012, Geology and mineralogical zonation of the Olympic Dam iron oxide Cu-U-Au-Ag deposit, South Australia: Society of Economic Geologists Special Publication v. 16, p. 237–267.

Ehrig, K., 2013, Geology of the Wirrda Well IOCG deposit. Powerpoint presentation, 10th Annual SA Exploration and Mining Conference, Adelaide. (http://saemc.com.au/archive/2013/13ehrig.pdf)

Gregory, D.D., Cracknell, M.J., Large, R.R., McGoldrick, P., Kuhn, S., Maslennikov, V.V., Baker, M.J., Fox, N., Belousov, I., Figueroa, M.C., Steadman J.A., Fabris, A.J., and Lyons, T.W., 2019., Distinguishing Ore Deposit Type and Barren Sedimentary Pyrite Using Laser Ablation-Inductively Coupled Plasma-Mass Spectrometry Trace Element Data and Statistical Analysis of Large Data Sets: Economic Geology, v. 114, p. 771-786.

Grunsky, E., 2010, The interpretation of geochemical survey data: Geochemistry: Exploration, Environment, Analysis, v. 10, p. 27-74.

Groves, D.I., Bierlein, F.P., Meinert, L.D., and Hitzman, M.W., 2010, Iron Oxide Copper-Gold (IOCG) deposits through earth history: implications for origin, lithospheric setting, and distinction from other epigenetic iron oxide deposits: Economic Geology, v. 105, p. 641–654.

Hennig, C., 2018, fpc: Flexible Procedures for Clustering. R package version 2.1-11.1. (https://CRAN.R-project.org/package=fpc).

Huang, Q., Kamenetsky, V.S., Ehrig, K., McPhie, J., Kamenetsky, M., Cross, K., Meffre, S., Agangi, A., Chambefort, I., Direen, N.G., Maas, R., and Apukhtina, O., 2016, Olivine-phyric basalt in the Mesoproterozoic Gawler silicic large igneous province, South Australia: examples at the Olympic Dam iron oxide Cu–U–Au–Ag deposit and other localities: Precambrian Research, v. 281, p. 185–199.

Jagodzinski, E.A., 2005, Compilation of SHRIMP U–Pb Geochronological Data – Olympic Domain, Gawler Craton, South Australia, 2001–2003: Geoscience Australia, Canberra, p. 197.

Keyser, W.M., Ciobanu, C.L., Cook, N.J., Courtney-Davies, L., Ehrig, K., Gilbert, S., and McPhie, J., 2017, Links Between Sedimentary Protoliths and IOCG-Skarn Alteration, Island Dam, South Australia: SGA Biennial Meeting, 14th, Quebec City, QC, Canada, 2017, Proceedings, p. 935–938.

Kontonikas-Charos, A., Ciobanu, C.L., and Cook, N.J., 2014, Albitization and redistribution of REE and Y in IOCG systems: insights from Moonta-Wallaroo, Yorke Peninsula, South Australia: Lithos, v. 208–209, p. 178–201.

Kontonikas-Charos, A., Ciobanu, C.L., Cook, N.J., Ehrig, K., Krneta, S., and Kamenetsky, V.S., 2017, Feldspar evolution in the Roxby Downs Granite, host to Fe-oxide Cu-Au-(U) mineralization at Olympic Dam, South Australia: Ore Geology Reviews, v. 80, p. 838–859.

Kontonikas-Charos, A., Ciobanu, C.L., Cook, N.J., Ehrig, K., Krneta, S., and Kamenetsky, V.S., 2018, Rare earth element geochemistry of feldspars: examples from Fe-oxide Cu-Au systems in the Olympic Cu-Au Province, South Australia. Mineralogy and Petrology, v. 112, p. 145–172.

Krneta, S., Ciobanu, C.L., Cook, N.J., Ehrig, K.J., and Kontonikas-Charos, A., 2017a, Rare Earth Element Behaviour in Apatite from the Olympic Dam Cu–U–Au–Ag Deposit, South Australia: Minerals, v. 7, p. 135.

Krneta, S., Cook, N.J., Ciobanu, C.L., Ehrig, K.J., and Kontonikas-Charos, A., 2017b, The Wirrda Well and Acropolis prospects, Gawler Craton, South Australia: Insights into evolving fluid conditions through apatite chemistry: Journal of Geochemical Exploration, v. 181, p. 276–291.

Kuhn, S., Cracknell1, M.J., and Reading, A.M., 2018, Lithologic mapping using Random Forests applied to geophysical and remote-sensing data: A demonstration study from the Eastern Goldfields of Australia: Geophysics, v. 83, p. B183-B193.

Liaw, A., and Wiener, M., 2002, Classification and Regression by randomForest: R News, v. 2, p. 18-22

Mauger, A.J., Ehrig, K.J., Kontonikas-Charos, A., Ciobanu, C.L., Cook, N.J., Kamenetsky, V.S., 2016, Alteration at the Olympic Dam IOCG–U deposit: insights into distal to proximal feldspar and phyllosilicate chemistry from infrared reflectance spectroscopy. Australian Journal of Earth Sciences, v. 63, p. 959–972.

Mark, G., Oliver, N.H.S., and Williams, P.J., 2006, Mineralogical and chemical evolution of the Ernest Henry Fe oxide–Cu–Au ore system, Cloncurry district, northwest Queensland, Australia: Mineralium Deposita, v. 40, p. 769–801.

McPhie, J. Ehrig, K., Kamenetsky, M., Crowley, J., and Kamenetsky, V.S., . in review. Geology of the Acropolis prospect, South Australia, constrained by high-precision CA-TIMS ages: Australian Journal of Earth Sciences.

Meinert, L.D., 1997, Application of skarn deposit zonation models to mineral exploration: Exploration and Mining Geology, v. 6, p. 185-208.

Ordóñez-Calderón, J.C., Gelcich, S., Oliveira, J.F., 2017, Applied data analytics on multielement geochemistry for pre-mining characterization of geological and geometallurgical attributes: examples of the Rosemont Cu-Mo-Ag skarn deposit, Tucson, Arizona. In: CoDaWork 2017 - Abbadia San Salvatore (IT).

Parker, A.J., 1990, Gawler Craton and Stuart Shelf - regional geology and mineralization, in Hughes, F.E., ed., Geology of the Mineral Deposits of Australia and Papua New Guinea: Australasian Institute of Mining and Metallurgy, Monograph Series, v. 14, p. 999–1008.

Paterson. H.L., 1986, The Acropolis prospect, in Paterson H.L.C., ed., Basement geology of the Stuart Shelf region, South Australia (vol. A1 – Olympic Dam/Stuart Shelf Excursion Guide, pp. 17–18). 8th Australian Geological Convention, Geological Society of Australia, Adelaide. Sydney, NSW.

Pawlowsky-Glahn, V., and Egozcue, J.J., 2006, Compositional data and their analysis: an introduction, in Buccianti, A., Mateu-Figueras, G. and Pawlowsky-Glahn, V. ed., Compositional Data Analysis in the Geosciences: From Theory to Practice: Geological Society of London, Special Publication, v. 264, p. 1–10.

Palarea-Albaladejo, J., and Martín-Fernández, J.A., 2015, zCompositions—R package for multivariate imputation of left-censored data under a compositional approach: Chemometrics and Intelligent Laboratory Systems, v. 143, p. 85–96.

Reeve, J.S., Cross, K.C., Smith, R.N., and Oreskes, N., 1990, Olympic Dam copper-uranium-gold-silver deposit, in Hughes, F.E., ed., Geology of the Mineral Deposits of Australia and Papua New Guinea: The Australasian Institute of Mining and Metallurgy, v. 14, p. 1009–1035.

Rousseeuw, P.J., 1987, Silhouettes: a graphical aid to the interpretation and validation of cluster analysis. Journal of Computational and Applied Mathematics, v. 20, p. 53–65.

Skirrow, R.G., Bastrakov, E.N., Baroncii, K., Fraser, G.L., Creaser, R.A., Fanning, C.M., Raymond, O.L., and Davidson, G.J., 2007, Timing of iron oxide Cu-Au-(U) hydrothermal activity and Nd isotope constraints on metal sources in the Gawler craton, South Australia: Economic Geology, v. 102, p. 1441‑1470.

Thompson, J., Meffre, S., Maas, R., Kamenetsky, V., Kamenetsky, M., Goemann, K., and Danyushevsky, L., 2016, Matrix effects in Pb/U measurements during LA-ICP-MS analysis of the mineral apatite: The Journal of Analytical Atomic Spectrometry, v. 31, p. 1206–1215.

van den Boogart, K.G., Tolosana-Delgado, R., and Bren, M., 2018. Compositions: Compositional Data Analysis. R Package Version 1.40-2. (https://CRAN.R-project.org/package=compositions).

Vella, L., 1997, Interpretation and modelling, based on petrophysical measurements, of the Wirrda Well potential field anomaly, South Australia: Exploration Geophysics, v. 28, p. 299-306.

Verdugo-Ihl, M.R., Ciobanu, C.L., Cook, N.J., Ehrig, K., Courtney-Davies, L., and Gilbert, S., 2017, Textures and U-W-Sn-Mo signatures in hematite from the Cu-U-Au-Ag orebody at Olympic Dam, South Australia: defining the archetype for IOCG deposits: Ore Geology Reviews, v. 91, p. 173–195.

Verdugo-Ihl, M.R., Ciobanu, C.L., Cook, N.J., Ehrig, K.J., and Courtney-Davies, L., in press. Defining Early Stages of IOCG Systems: Evidence from Iron-Oxides in the Outer Shell of the Olympic Dam Deposit, South Australia, Mineralium Deposita.

Wickham, H., 2016. ggplot2: Elegant Graphics for Data Analysis. Springer-Verlag, New York. (https://doi.org/10.1007/978-0-387-98141-3).

Williams, P.J., Barton, M.D., Johnson, D.A., Fontboté, L., Haller, A., Mark, G., Oliver, N.H.S., and Marschik, R., 2005, Iron-oxide–copper–gold deposits: geology, space–time distribution, and possible modes of origin. Economic Geology, 100th Anniversary Volume, p. 371-406.

CHAPTER 8

SUMMARY, RECOMMENDATIONS AND CONCLUDING REMARKS

8. SUMMARY AND RECOMMENDATIONS

In this thesis and its component chapters, multivariate analyses were applied to mineral and whole-rock geochemical data in the context of characterisation of ore deposits/prospects and constraining ore-forming processes. Multivariate analyses have become increasingly used in ore deposit geochemistry to gain maximum insights from large whole-rock and trace element in mineral geochemical datasets. Used correctly, such data can be a robust proxy for mineralogy, mineralisation and alteration and thus, if processed using quantitative methods, can result in distinct groups accurately characterizing an orebody and its host rocks. The thesis aims at demonstrating the advantages of such a combined approach applied to hydrothermal IOCG deposits within a single district thus allowing a direct comparison of lithological and mineralogical zonation with calculated parameters such as geochemical clusters and principal component scores while considering the entire set of elements. The current work also addressed the effect of left-censored data on the interpretations of the multivariate analyses of LA-ICP-MS data and presented first steps for development of a new approach for imputation of such values.

Despite the many fundamental differences between mineral chemistry and whole-rock datasets, the same multivariate analyses are appropriate, however, the interpretation of the results of statistical analyses depends on data type and on additional information such as mineral textures, sample locations, density and magnetic susceptibility. The whole-rock data correspond to mineralogical composition of a sample and reflect the proportions and stoichiometries of ore- and rock-forming minerals thus making interpretation of mineralisation/alteration signatures obtained via multivariate analyses a relatively straightforward task. On the other hand, interpretation of the statistical analyses applied to LA-ICP-MS trace element datasets can be more sophisticated. This is because some elements can be found as nano- to micron-scale inclusions e.g., tellurides in pyrite, as in the large LA-ICP-MS dataset from Olympic Dam

(Dmitrijeva et al., 2020), whereas others can be lattice-hosted, or both. The fundamental processes controlling the mode of occurrences of elements are unique for each mineral type and particular deposit/prospect, thus making the interpretation of multivariate analyses applied to LA-ICP-MS data more challenging.

Statistical inference is usually based on an assumption of a simple random sample from a population. The geological sampling is, however, non-random and focuses on specimens that are likely to contribute to explanation of geochemical processes. However, the multivariate analysis describes the relationship between elements in such specimens and there is no compelling reason to suspect that estimation of these relationships will be biased by sampling strategy. Moreover, aspects of the sampling strategy that are likely to have an effect have been accounted for using hierarchical models (Dmitrijeva et al., 2018).

Additional considerations should be taken with respect to variable selection for a model. As the number of predicting elements in a model increases, the model complexity and variance increases whereas the model accuracy decreases (Guyon and Elisseeff, 2003). To avoid that, a variable selection e.g., recursive feature elimination, could be used to build a simpler and more stable model by finding and ranking a relative importance of each predictor (Mitchell, 1998). For example, in geochemical data, rare earth elements are often redundant since they behave similarly in many geological environments.

The multivariate analysis approach employed in this work could be complemented by a variety of algorithms. The results from the chosen k-means clustering could be compared with other clustering algorithms such as self-organising maps (Kohonen, 2001; Torppa et al., 2019), k-nearest neighbours, fuzzy c-means clustering (e.g. Hanesch et al., 2001) etc. Additional consideration of the spatial nature of the whole-rock data would certainly improve the clustering approach. Spatial clustering as an alternative to a linear method such as k-means

algorithm, would provide a mathematically more valid framework of clustering whole-rock data. Similarly, the chosen classification method for this work was random forests. The results could be compared with other classification methods, e.g., support vector machines, linear and quadratic discriminant analysis, to find the best classification model for a particular dataset coupled with a cross-validation and bootstrapping to measure performance of models.

8.1. IMPUTATION OF LEFT-CENSORED VALUES USING COPULA FUNCTIONS

Multivariate statistical analyses are tailored to draw inferences from complete datasets. In practice, many of the multivariate data are incomplete because some elements are below their minimum detection limit (mdl), i.e. they are left-censored data. Handling the left-censored data is therefore a challenge, and an important step in data pre-processing. The challenge is to impute the missing data without changing the data distribution and the relationships among the variables. In this thesis we used copula functions for imputation of left-censored data, as they allow to model mathematically flexible multivariate distributions that can account for account for asymmetry, tail-dependence and non-linear relationships among the variables. Such properties of the data cannot, in general, be fully accounted for by the standard regression model and the expectation-maximisation (E-M) algorithm (e.g., Palarea-Albaladejo and Martín-Fernández, 2013; Honaker et al., 2011). Given that copula functions are able to model any complex multivariate distributions, they are less restrictive and more mathematically flexible than the standard regression model, and therefore should result in a better fit to data.

We demonstrate a case study of trivariate data Te-Au-Ag for which Te, Au and Ag are all above mdl, with artificial mdl applied to Te. This enabled a comparison between imputed and measured values. An optimal copula, based on a range of six copula forms, was obtained using a maximum likelihood criterion. The trivariate probability density function of Te-Au-Ag was decomposed into a product of univariate marginal distributions with a cascade of the Frank

copulas for Te-Au and Te-Ag, and a conditional Frank copula of Ag-Au | Te. Three different artificial detection limits (1.0, 0.8 and 0.5 ppm) were set for Te, with all three being higher than the actual detection limit of 0.2 ppm. For each artificial detection limit, values of Te below that limit were imputed by average of a large number of Monte-Carlo draws from the conditional distribution of Te, given the values of Au and Ag together with Te being below mdl. The imputed Te values were compared with those from standard regression and the measured values.

8.2. MULTIVARIATE ANALYSES OF FE-OXIDES TO TRACK BIF ENRICHMENT PROCESS

Multivariate analysis of Fe-oxide LA-ICP-MS data from deposits/prospects of the Middleback Ranges complements the large body of published petrographic, geochronological and mineral chemistry data for these ores and their host rocks (Keyser et al., 2018, 2019a, 2019b, 2020). Multivariate analyses of hematite (~1,000 spots) and magnetite (~500 spots), coupled with petrographic classification of the analysed grains, allowed evolution from magnetite through clean and porous martite to platy hematite to be tracked. Quantitative assessment of Fe-oxide trace element signatures was conducted using linear mixed-effects models, a mathematically more appropriate type of regression that takes into account the hierarchies present in the LA-ICP-MS data (Dmitrijeva et al., 2018). The hierarchical structure of LA-ICP-MS data consists of a high-degree of similarity among the spots within individual samples, as well as a certain degree of similarity among the samples from the same deposit/prospect.

BIFs from the Middleback Ranges undergo textural and geochemical changes as they pass through ore enrichment processes. Multivariate analyses highlight the differences among hematite sampled from various parts of the Middleback Ranges. Elements typically associated with an IOCG geochemical signature, such as Cu, REE, and Sn-W-Mo signature, are documented for hematite from the Iron Count deposit in the Middle segment of the Middleback

Ranges. The western limit of the Olympic Cu-Au Province is relatively ill-defined (Fig. 1.1). Despite the northeastern Eyre Peninsula being considered highly prospective for IOCG-style mineralisation (Wise, 2019), no significant discoveries have been made in the area to date. The presence of a clear 'granitophile' signature in BIF iron-oxides demonstrates that the area was exposed to metal-bearing hydrothermal fluids and thus offers affirmation of the high IOCG prospectively potential. The geochemical signature of Fe-oxides within the southern and northern segments of the Middleback Ranges (Ni-Co-Ti-Nb) highlights the strongly localised nature of post-depositional processes that have impacted on these rocks – as well as the likelihood of contributions from igneous rocks of different ages, e.g., ~1.79 Wertigo Granite, 1.6 Ga Hiltaba Suite granite, and ~800 Ma Gairdner Dyke Swarm dolerites.

8.3. Prediction of Nanoparticles Using Multivariate Analysis of LA-ICP-MS data

The LA-ICP-MS dataset from Olympic Dam pyrite (Dmitrijeva et al., 2020) is possibly one of the least biased mineral chemistry dataset of this type obtained so far, thus providing not only a robust assessment of trace element signatures, but also the opportunity to assess the effects of left-censored data on interpretation and statistical inference. Multivariate analyses showed a range of trace element signatures, such as: (i) Ag-Bi-Pb signature predicting inclusions of tellurides mechanically trapped in pyrite grains as micron- and nanoscale inclusion; (ii) highly variable oscillatory zonation patterns with respect to Ni and Co; and (iii) Au-Co-As signature predicting the presence of 'invisible' Au, within Olympic Dam ores, even if not commonplace. The case study also demonstrated that the idea of 'invisible' Au in pyrite is likely being tied to pre-selected samples containing higher-As-Au concentrations. Such sampling strategy ignores the presence of other element associations representing lattice-bound elements or micron- and nanoscale inclusions which are important for interpretation of ore-forming processes. The prediction of nanoparticles of telluride and electrum phases from LA-ICP-MS data carry an

important implication in that they confirm the multi-stage overprinting, local-scale remobilisation and recrystallisation of several mineral groups (e.g., Ciobanu et al., 2013; Verdugo-Ihl et al., 2017; Macmillan et al., 2016a, 2016b, 2017). Another significant implication of such predictions is undoubtedly related to the mineral processing, which given the low lost, followed by a good quality control of the LA-ICP-MS data, is a significant addition to the geometallurgical modelling.

The prediction of telluride and electrum phases along with the high degree of interest with respect to 'invisible' Au in Olympic Dam pyrite raised questions with respect to nanoscale characterisation of such pyrite. Preliminary studies of one sample with particularly high contents of As and Au has shown the presence of the predicted phases within As-(Co-Ni) rich bands (Fig. 8.1), thus complementing and confirming the interpretations made from the LA-ICP-MS data. The association between Au and Bi-(Pb)-tellurides depicted at the nanoscale (Fig. 8.1), as well as in the LA-ICP-MS data, suggests the strong affinity between Au and chalcophile elements, as has been documented for As-free pyrite elsewhere (Ciobanu et al., 2012). The presence of such nanoparticles confirms the interpretations made from the LA-ICP-MS data showing that pyrite has experienced complex reworking and partial recrystallisation.

The fundamental processes controlling the mode of occurrences of elements are unique for each mineral type and a particular site of interest, thus making interpretation of multivariate analyses applied to LA-ICP-MS data more challenging. However, investigation of minerals at the nanoscale can assist in the interpretation of the trace element signatures in minerals meaning that the topic of trace element signatures in pyrite and their implications for ore forming processes are yet to be understood.

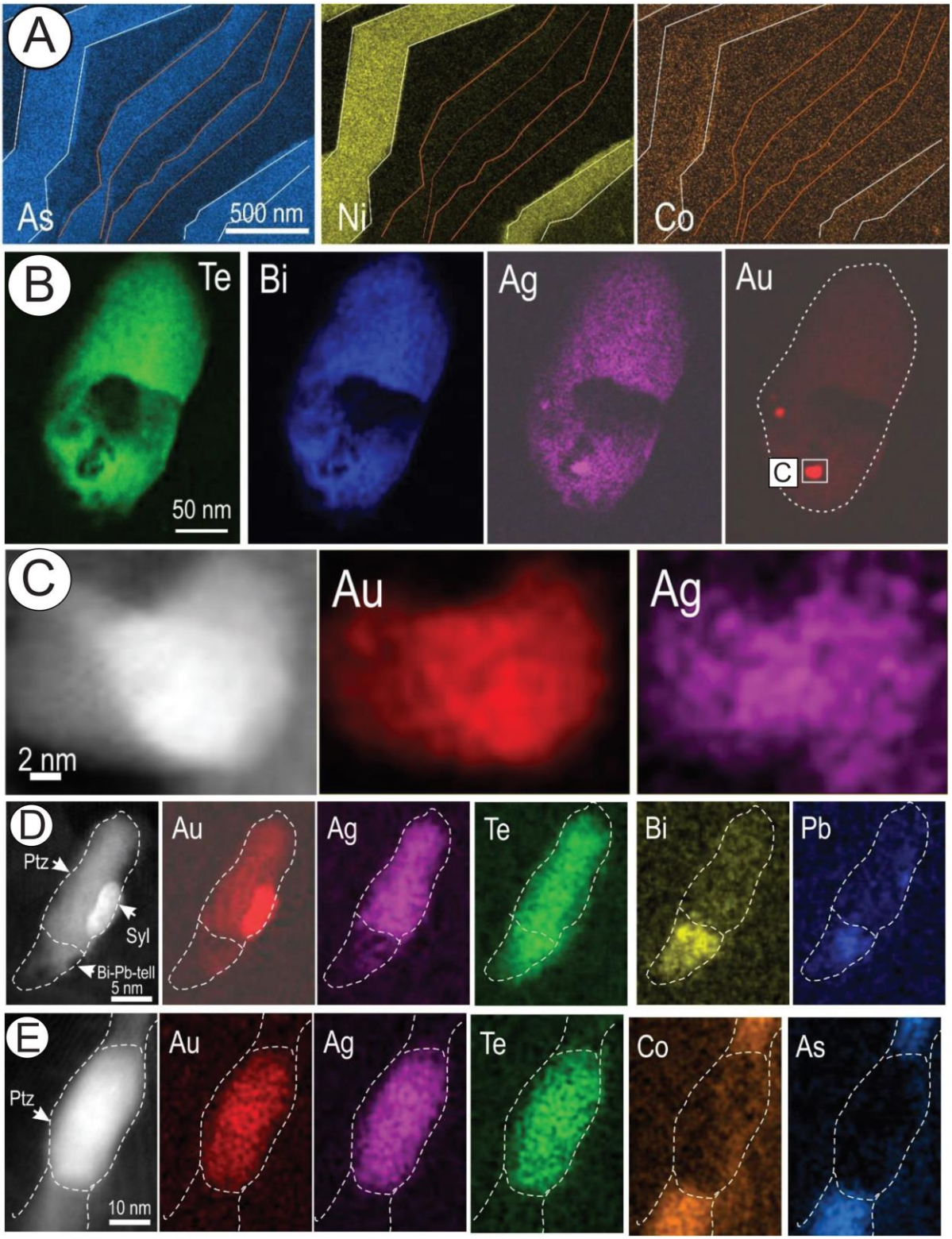


Figure 8.1. STEM-EDX maps of pyrite in a foil showing primary As(-Co-Ni) zonation (A) and various types of inclusions: volynskite (B) with electrum nanoparticle (C), two Au-Ag-tellurides (petzite, Ptz and sylvanite, Syl) and Bi-Pb sulphotelluride at the edge (D) and petzite (E).

8.4. MINERALISATION SIGNATURES OF THE OLYMPIC DAM IOCG DISTRICT

The three case studies focussing on whole-rock geochemistry of the Olympic Dam deposit and the adjacent Acropolis and Wirrda Well prospects build upon previous deposit-scale studies of these systems (Paterson, 1986; Reeve et al., 1990; Ehrig et al., 2012), as well as detailed studies of petrography, mineral chemistry and geochronology (e.g., Krneta et al., 2017; Macmillan et al., 2016a, 2017; Verdugo-Ihl et al., 2017; Courtney-Davies et al., 2019).

This work allowed 3D geological models of the Acropolis and Wirrda Well prospects to be derived for the first time. In addition, numerical models for multiple elements in the Olympic Dam deposit are shown. Findings give an overview of the IOCG mineralisation signatures within the Olympic Dam district and provide evidence for the shared genetic links between magnetite- and hematite-dominant IOCG ores in the district despite the distinct host rocks and varying styles of the mineralisation. Recognizing IOCG geochemical signatures and their variation across such a varied range of IOCG systems, i.e., structurally controlled and breccia- or vein-hosted, is important for their efficient exploration undercover.

Mineralogical zonation patterns were not accurately resolvable from the 15 m-spaced whole-rock data from Olympic Dam. Further mineralogical study allowed an explanation of zonation patterns for Au-Te and Ag-Bi. Specifically, the lack of deposit-scale zonation with respect to Ag-Bi could be explained by abundant inclusions of telluride minerals mechanically trapped within pyrite (Dmitrijeva et al., 2020), and potentially within associated Cu-(Fe)-sulphides. The Au-Te association also evidently represents Au-bearing telluride phases that are distributed throughout the deposit irrespectively of ore zone. The IOCG mineralisation signature of the Olympic Dam deposit was defined as an association of Au-W-Mo-As-Sb (Table 8.1), which is predominantly concentrated along the vertical ~ 1.8 km-deep corridor in the southeastern lobe of the deposit. The intense Fe-metasomatism and Au-W-Mo-As-Sb signature are, however,

spatially offset from the high-grade Cu mineralisation, which forms concentric vertical and lateral zonation.

Similar, albeit slightly more varying mineralisation signatures were obtained from the adjacent Wirrda Well and Acropolis prospects (Table 8.1; Dmitrijeva et al., 2019b, in review). The spatial projection of mineralisation signatures demonstrated a slight offset from the Fe-rich samples (e.g., Wirrda Well) and magnetite-bearing veins (e.g., Acropolis), thus showing a broad halo of overprinting around these prospects. The 'magnetite' signature (Fe-V-Ni-Co) was documented in both prospects, however it is lacking, or remains undiscovered in the Olympic Dam deposit (Table 8.1). The 'hematite' signature (W-Sn-Mo-U; Verdugo-Ihl et al., 2017), accompanied by a range of elements (e.g., Cu, Au, Bi, As, Sb, REE, etc.) typically showing elevated signatures in IOCG systems (Barton, 2014), was discovered throughout the prospects including in the drillholes relatively distant to the high-grade Cu-Au mineralisation (Dmitrijeva et al., in review). Most importantly, such signatures, as well as the mineralisation are not centred on the Hiltaba Suite granites thus suggesting the presence of a deep and 'fertile' source of the hydrothermal fluids.

Although the broad similarity among the three ore systems has been shown in previous studies, inferring common geneses, the importance of structural controls on mineralisation at the Wirrda Well prospect, where faults have a prominent impact on mineralogical zonation and Cu grade distribution has not been addressed previously. The abundant pre-mineralisation mafic dykes, in both Wirrda Well North and South, represent fluid pathways or corridors with Cu mineralisation concentrated along the dyke contacts thus implying a significant importance of faults in their potential to conduit fluids in IOCG systems. The strong structural control on mineralisation in Wirrda Well implies a confined system with laterally restricted mineralisation suggesting a relatively deep setting (Dmitrijeva et al., 2019 in review). In contrast, the large lateral extents of the IOCG signature as well as geophysical expression at Acropolis, suggests

a higher fluid to rock ratio resulting from the greater permeability of the extrusive lithologies, i.e., Gawler Range Volcanics.

The approach demonstrated in the three case studies (Dmitrijeva et al., 2019a, b and in review) could still benefit from additional layers of information such as gravity, magnetic and magnetotelluric inversions, on a smaller scale (Goodwin and Skirrow, 2019; Wise, 2019) and, fluid flow pathways, architecture and depositional gradients of the IOCG mineral systems on a regional scale (e.g., Skirrow et al., 2019).

Table 8.1. Geochemical signatures of the mineralisation in the Olympic Dam deposit and the Acropolis and Wirrda Well prospects Dmitrijeva et al. (2019a, b, in review). A dominant signature represents elements with the strongest loading onto a PC1 obtained from a particular IOCG system. Subordinate signature corresponds to elements that have significant, however not dominant loadings onto corresponding PC1.

IOCG mineralisation signature	Olympic Dam	Wirrda Well	Acropolis
'hematite' (granitophile)		**dominant**	
	Au-W-Mo-As-Sb	Cu-Au-Bi (Southern lobe)	Sn-Sb-W
		subordinate	
	Te-Bi-Cu-Sn-Ag-LREE-Sr-U-Ca-P	Ag-Mo-W-U-As-Sb-LREE (Southern lobe)	LREE-U-Th-Sr-Ca-P
'magnetite'		**dominant**	
	na	Fe-V-Ni-Co (Northern lobe)	Fe-V-Ni-Co
		subordinate	
		Ca-P-Sc (Northern lobe)	Cu-Mo-Bi

*na -not applicable

Further work could address mineralisation signatures outside of the Olympic Dam district, potentially expanding to IOCG systems in the northern and southern parts of the Olympic Cu-

Au Province. Ample research opportunities exist for mineral prospectively mapping of the South Australian IOCG province (e.g., Skirrow et al., 2019), with potential for incorporation of the fractal geometry of ore systems (e.g., Wang et al., 2012; Haddad-Martim et al., 2018). The spatial distribution of structurally controlled deposits, such as IOCGs, display fractal geometry (e.g., Carajás province; Haddad-Martim et al., 2018) and include the consistency of trends of over a wide range of scales. The fractal nature of such trends suggests that regional structural mineralisation controls, such as permeability, can be inferred from micron-scale patterns of minerals. Such scale invariance is given by (micro-)faults being the dominant factor controlling fluid flows. Therefore, the geometric trends can be assessed at the micron-scale (e.g., minerals orientation in thin section) as well as at the orebody and regional scales. Thus, fractals could be used to model the spatial distribution of ore deposits, which have non-random distributions as they are formed via interplay of certain geological processes that controlled their occurrence. The research of fractal geometry of ore deposits is not new; however, it has not been applied to the IOCG deposits of the Gawler Craton thus potentially being an innovative tool for the mineral prospectively mapping.

8.5. CONCLUDING REMARKS

New insights into three IOCG systems within the Olympic Dam district are given. These findings complement the wealth of information obtained from iron-oxide minerals within the Olympic Dam deposit in recent years (Ciobanu et al., 2013, 2019; Dmitrijeva et al., 2019a; Verdugo-Ihl et al., 2017, 2019, in press). The research also provides examples of frameworks for multivariate analyses of geochemical datasets in the context of applied ore deposit studies. Importantly, the methodologies described are applicable to ore deposit research outside of the eastern Gawler Craton. The research also contributes by proposing a novel algorithm for imputation of the left-censored data using copula functions.

Key conclusions from the conducted research in this thesis include:

1. Multivariate analyses provide further insight to univariate analysis and bivariate correlations for investigation of mineralisation and alteration signatures of a large whole-rock as well as LA-ICP-MS dataset, and for understanding the key geochemical associations among elements in the absence of detailed petrographic and mineralogical information.
2. Olympic Dam pyrite is characterised by: (i) a Ag-Bi-Pb signature predicting inclusions of tellurides; and (ii) highly variable Co-Ni ratios likely representing complex oscillatory zonation patterns. Pyrite is the main host for Co, whereas electrum and telluride phases mechanically trapped within pyrite grains may be a subordinate host for Au in the deposit.
3. Left-censored data significantly impacts the statistical inference and therefore the interpretation of geochemical signatures. The first steps towards the development of new algorithm for imputation of such data was proposed using copula probability density functions and Monte-Carlo simulation.
4. Multivariate analyses of iron oxides from BIF deposits and prospects suggests highly localised settings attributed to ore enrichment processes in the Middleback Ranges. The identified trace elements associations suggest affiliation of fluids to both mafic and felsic intrusive rocks and can be considered in the context of multiple stages of ore enrichment. Cu, REE, and Sn-W-Mo signature in the Iron Count prospect suggest that the area is prospective for the IOCG mineralisation.
5. In Olympic Dam the IOCG mineralisation signature is composed of two geochemical associations (i) Cu-U_3O_8-Se-S showing concentric zonation and (ii) Au-W-Mo-Sb-As forming a vertical ~1800 m-deep corridor in the southeastern lobe. The ore body and extends of potassic alteration are well-defined by principal component scores and Fe

wt.% outlines, however slight mismatch between the mineralisation signatures and Fe-metasomatism indicates (i) later sulphide remobilisation, e.g., sulphide-rich veins on the periphery of the ODBC in zones of only weak Fe-metasomatism, or (ii) that some Fe-rich pockets may pre- or postdate IOCG mineralisation, e.g., preserved fragments of older Fe-rich sedimentary rocks.

6. Geological and numerical 3D modelling indicates that Cu, Fe and U distribution in the Wirrda Well prospect is controlled by low-angle crosscutting shear zones. The prospect is composed of two distinct vertically-offset structural blocks that show deeper and shallower mineralisation at Wirrda Well North and South, respectively, as reflected by geochemical signatures from these blocks.
7. Acropolis, a vein-style mineralisation, shows a broad and laterally extensive mineralisation signatures as well as sodic, propylitic, potassic and sericitic alteration halo. Mineralisation signatures are represented by hematite-dominant assemblage: Ca, P, U, Th, REE, W, Sn and Sb, that overprint early and high-temperature IOCG mineralisation typified by 'Fe-V-Ni-Co' signature mostly present in veins.
8. Granitophile signature as 'W-Mo-Sn±U' as well as mineralisation signature comprised of Cu-Au-Bi-Ag-As-Sb-REE is omnipresent in IOCG systems within the district indicating a genetic link and common source of fluids forming the mineralisation.

REFERENCES

Barton, M.D., 2014. Iron oxide (–Cu–Au–REE–P–Ag–U–Co) systems. In: Holland, H.D., Turekian, K.K. (Eds.), Treatise on Geochemistry, second ed. Elsevier, Oxford, pp. 515–541.

Ciobanu, C.L., Cook, N.J., Utsunomiya, S., Kogagwa, M., Green, L., Gilbert, S., Wade, B. 2012. Gold telluride nanoparticles revealed in arsenic-free pyrite, American Mineralogist, 97, 1515-1518.

Ciobanu, C.L., Wade, B.P., Cook, N.J., Schmidt Mumm, A., Giles, D., 2013. Uranium-bearing hematite from the Olympic Dam Cu–U–Au deposit, South Australia: a geochemical tracer and reconnaissance Pb–Pb geochronometer. Precambrian Research. 238, 129–147.

Ciobanu, C.L., Verdugo-Ihl, M.R., Slattery, A., Cook, N.J., Ehrig K., Courtney-Davis, L., Wade, B.P. 2019 Silician Magnetite: Si–Fe-Nanoprecipitates and Other Mineral Inclusions in Magnetite from the Olympic Dam Deposit, South Australia. Minerals, 9, 311.

Courtney-Davies, L., Ciobanu, C., Verdugo-Ihl, M.R. Dmitrijeva, M., Cook, N., Ehrig, K., Wade, B. 2019. Hematite geochemistry and geochronology resolve genetic and temporal links among iron-oxide copper gold systems, Olympic Dam district, South Australia. Precambrian Research, 335, 105480.

Creaser, R.A., 1989. The Geology and Petrology of Middle Proterozoic Felsic Magmatism of the Stuart Shelf, South Australia (PhD thesis) La Trobe University, Melbourne p. 434.

Dmitrijeva, M. Metcalfe, A.V., Ciobanu, C.L. Cook, N.J., Frenzel, M., Keyser, W.M., Johnson, G., Ehrig, K. 2018. Discrimination and variance structure of trace element signatures in hematite: a case study of BIF-mineralisation from the Middleback Ranges, South Australia Mathematical Geosciences, 50, 381-415.

Dmitrijeva, M., Ehrig, K., Ciobanu, C., Cook, N., Verdugo-Ihl, M., Metcalfe, A., 2019a. Defining IOCG signatures through compositional data analysis: a case study of lithogeochemical zoning from the Olympic Dam deposit, South Australia. Ore Geology Reviews, 105, 86–101.

Dmitrijeva, M., Ciobanu, C., Ehrig, K., Cook, N., Metcalfe, A., Verdugo-Ihl, M., McPhie, J., 2019b. Mineralisation-alteration footprints in the Olympic Dam IOCG district South Australia: The Acropolis prospect. Journal of Geochemical Exploration, 205, 106333

Dmitrijeva, M., Cook, N.J., Ehrig, K., Ciobanu, C.L., Metcalfe, A.V., Kamenetsky, M., Kamenetsky, V.S., Gilbert, S. 2020, Multivariate statistical analysis of trace elements in pyrite: prediction, bias and artefacts in defining mineral signature. Minerals, 10, 61.

Dmitrijeva, M., Ciobanu, C.L., Ehrig, K., Cook, N.J., Verdugo-Ihl, M.R., Metcalfe, A.V., Kamenetsky, V.S., McPhie, J., in review, Geochemical data analysis and 3D modelling of Wirrda Well prospect, South Australia: structural control on iron-oxide copper gold mineralisation. Economic Geology.

Ehrig, K., McPhie, J., Kamenetsky, V., 2012. Geology and mineralogical zonation of the Olympic Dam iron oxide Cu-U-Au-Ag deposit, South Australia. Society of Economic Geologists Special Publication, 16, 237–267.

Goodwin, J.A., Skirrow, R.G., 2019. Producing magnetite and hematite alteration proxies using 3D gravity and magnetic inversion. Geoscience Australia Record 2019/03, 27 p.

Guyon, I., Elisseeff, A., 2003. An introduction to variable and feature selection. Journal of Machine Learning Research, 3, 1157–1182.

Haddad-Martim, P.M., Carranza, E.J.M., de Souza Filho, C.R. 2018. The Fractal Nature of Structural Controls on Ore Formation: The Case of the Iron Oxide Copper-Gold Deposits in the Carajás Mineral Province, Brazilian Amazon. Economic Geology, 113, 1499-1524.

Hanesch, M., Scholger, R., Dekkers M.J. 2001. The application of fuzzy C-means cluster analysis and non-linear mapping to a soil data set for the detection of polluted sites. Physics and Chemistry of the Earth, Part A: Solid Earth and Geodesy, 26, 885-891.

Honaker, J., King, G., Blackwell, M. 2011. Amelia II: a program for missing data. Journal of Statistical Software, 45, 1-47.

Keyser, W., Ciobanu, C.L., Cook, N.J., Johnson, G., Feltus, H., Johnson, S., Dmitrijeva, M., Ehrig, K., Nguyen, P.T., 2018. Petrography and trace element signatures of iron oxides in deposits from the Middleback Ranges, South Australia: From banded iron formation to ore. Ore Geology Reviews, 93, 337-360.

Keyser, W., Ciobanu, C.L., Cook, N.J., Dmitrijeva, M., Courtney-Davies, L., Feltus, H., Gilbert, S., Johnson, G., Ehrig, K., 2019a. Iron-oxides constrain BIF evolution in terranes with protracted geological histories: The Iron Count prospect, Middleback Ranges, South Australia. Lithos, 324-325, 20-38.

Keyser, W., Ciobanu, C.L., Cook, N.J., Courtney-Davies, L., Kennedy, A., Wade, B.P. Ehrig, K., Dmitrijeva, M., Kontonikas-Charos, A., Feltus, H., Johnson, G., 2019b. Petrographic and geochronological constraints on the granitic basement to the Middleback Ranges, South Australia. Precambrian Research, 324, 170-193.

Keyser, W., Ciobanu, C.L., Cook, N.J., Wade, B.P., Kennedy, A., Kontonikas-Charos, A., Ehrig, K., Feltus, H., Johnson, G. 2020. Episodic mafic magmatism in the Eyre Peninsula: Defining syn- and post-depositional BIF environments for iron deposits in the Middleback Ranges, South Australia. Precambrian Research, 337, 105535.

Kohonen, T. 2001. Self-Organizing Maps, 3ed. Springer Series in Information Sciences, pp. 30

Krneta, S., Cook, N.J., Ciobanu, C.L., Ehrig, K.J., Kontonikas-Charos, A., 2017. The Wirrda Well and Acropolis prospects, Gawler Craton, South Australia: Insights into evolving fluid conditions through apatite chemistry. Journal of Geochemical Exploration, 181, 276–291.

Macmillan, E., Cook, N.J., Ehrig, K., Ciobanu, C.L., Pring, A. 2016a. Uraninite from the Olympic Dam IOCG-U-Ag deposit: linking textural and compositional variation to temporal evolution. American Mineralogist, 101, 1295-1320.

Macmillan, E., Ehrig, K., Ciobanu, C.L., Cook, N.J., Pring, A. 2016b. Replacement of uraninite by bornite via coupled dissolution-reprecipitation: evidence from texture and microstructure. Canadian Mineralogist, 54, 1369-1383.

Macmillan, E., Cook, N.J., Ehrig, K., Pring, A. 2017. Chemical and textural interpretation of late-stage coffinite and brannerite from the Olympic Dam IOCG-Ag-U deposit. Mineralogical Magazine, 81, 1323-1366.

Mitchell, M., 1998. An introduction to genetic algorithms. In: A Bradford Book. The MIT Press, 158 pp.

Palarea-Albaladejo, J., Martín-Fernández, J.A., 2013. Values below detection limit in compositional chemical data Analytica Chimica Acta, 764, 32-43.

Paterson. H.L., 1986. The Acropolis prospect H.L.C. Paterson (Ed.), Basement geology of the Stuart Shelf region, South Australia (vol. A1 – Olympic Dam/Stuart Shelf Excursion Guide, pp. 17–18). 8th Australian Geological Convention, Geological Society of Australia, Adelaide. Sydney, NSW.

Reeve, J.S., Cross, K.C., Smith, R.N., Oreskes, N., 1990. Olympic Dam copper-uranium-gold-silver deposit. In: Hughes, F.E. (Eds.), Geology of the Mineral Deposits of Australia and Papua New Guinea: Australasian Institute of Mining and Metallurgy, Monograph 14, 1009–1035.

Savu-Krohn, C., Rantitsch, G., Auer, P., Melcher, F., Graupner, T., 2011. Geochemical fingerprints of coltan ores by machine learning of uneven datasets. Natural Resources Research, 20, 177–191.

Skirrow, R.G., Murr, J., Schofield, A., Huston, D.L., van der Wielen, S., Czarnota, K., Coghlan, R., Highet, L.M., Connolly, D., Doublier, M., Duan, J., 2019. Mapping iron oxide Cu-Au (IOCG) mineral potential in Australia using a knowledge-driven mineral systems-based approach. Ore Geology Reviews, 113, 103011.

Torppa, J. Nykänen, V., Molnár, F. 2019. Unsupervised clustering and empirical fuzzy memberships for mineral prospectivity modelling. Ore Geology Reviews, 107, 58-71.

Verdugo-Ihl, M.R., Ciobanu, C.L., Cook, N.J., Ehrig, K., Courtney-Davies, L., Gilbert, S. 2017. Textures and U-W-Sn-Mo signatures in hematite from the Cu-U-Au-Ag orebody at Olympic Dam, South Australia: defining the archetype for IOCG deposits. Ore Geology Reviews, 91, 173-195.

Verdugo-Ihl, M.R., Ciobanu, C.L., Slattery, A., Cook, N.J., Ehrig, K., Courtney-Davis, L. 2019. Copper-Arsenic Nanoparticles in Hematite: Fingerprinting Fluid-Mineral Interaction. Minerals, 9, 388.

Verdugo-Ihl, M.R., Ciobanu, C.L., Cook, N.J., Ehrig, K., Courtney-Davis, L. in press. Defining early stages of IOCG systems: evidence from iron oxides in the outer shell of the Olympic Dam deposit, South Australia. Mineralium Deposita

Wang, G., Carranza, E.J.M., Zuo, R., H, Y., Du, Y., Pang, Z., Sun, Y., Qu, J. 2012. Mapping of district-scale potential targets using fractal models. Journal of Geochemical Exploration, 122, 34-46.

Wise, T. 2019. Prospectively modelling of the Olympic Cu–Au Province. MESA Journal 90, pages 36–41.

CHAPTER 9

SUPPLEMENTARY AND ADDITIONAL MATERIAL

SUPPLEMENTARY MATERIAL A

FOR CHAPTER 2 – A COPULA-BASED APPROACH

TO THE IMPUTATION OF VALUES BELOW

MINIMUM LIMITS OF ANALYTICAL DETECTION

APPENDIX A: PSEUDO-CODE OF A SINGLE ITERATION OF THE PROPOSED COPULA-BASED ALGORITHM DISPLAYING A FIVE-STEP APPROACH FOR SIMULATION OF LEFT-CENSORED DATA; L =1.

ELECTRONIC APPENDIX A FOR CHAPTER 2

```
# load libraries

library(VineCopula)
library(CDVine)
library(copula)
library(dplyr)

# read in data

data <- read.csv('OlympicDamElementsSubset.csv', header=T,sep=',')
dataComplete <- data %>% filter(Ag>0, Au>0, Bi>0, In>0,
                                Mo>0, Sb>0, Se>0, Sn>0, Te>0)


# subset

TeAuAg <- dataComplete[,c('Te','Au','Ag')]

# define L

L = 1

# reshuffle the data so rows with Te < L will be first

below <- TeAuAg[which(TeAuAg$Te<=L),]
above <- TeAuAg[which(TeAuAg$Te>L),]
TeAuAg <- rbind(below,above)
y <- TeAuAg$Te
length <- length(y)


## Step 1

# replace the values below L by
```

```r
# arbitrary values

for (i in 1:length(y)){
    if (y[i]<=L){
        y[i] = 1*(L-(i/(nrow(below))))
        print(i)
    }
}

# compile new data frame

Te_2AuAg <- as.data.frame(cbind(y,TeAuAg$Au,TeAuAg$Ag))
colnames(Te_2AuAg) <- c('Te_2','Au','Ag')

## Step 2

# obtain pseudo values for Te Au and Ag using the PIT

udat <- as.data.frame(pobs(Te_2AuAg))


## Step 3

# Find and fit the optimal copula to the pseudo values of Te-Au, Te-Ag and Au-Ag pairs

BiCopSelect(udat[,1],udat[,2],familyset = 1:6,indeptest = T)
# DL = 1; Frank copula par = 6.010272
# DL = 0.8; Frank copula par =  6.050401
# DL = 0.5; Frank copula par =  5.852314


# Te & Ag

BiCopSelect(udat[,1],udat[,3],familyset = 1:6)
# DL = 1; Frank copula par = 2.151466
# DL = 0.8; Frank copula par =  2.18767
# DL = 0.5; Frank copula par = 2.194253
```

```
72.
73. # Au & Ag
74.
75. BiCopSelect(udat[,2],udat[,3],familyset = 1:6)
76. # Frank copula par = 2.692378
77.
78. # define m and n where
79. # n is the total number of rows
80. # m is the number of rows where Te < L
81.
82. m <- sum(TeAuAg$Te<=L)
83. n <- nrow(TeAuAg)
84.
85. ## Step 4
86. # function pdf_calc() generates random draws from the conditional distribution of
87. # pseudo values of Tegiven pseudo values for Au, Ag
88.
89. pdfcalc=function(x,given){
90.         pdfc = dCopula(cbind(x,given[,1][1]),copula = frankCopula(6.010272),log = TRUE)+
91.             dCopula(cbind(x,given[,2][1]),copula = frankCopula(2.151466),log = TRUE)+
92.             dCopula(cbind(BiCopHfunc(given[,1][1], x, family=5, par=6.010272)$hfunc2,
93.                           BiCopHfunc(given[,2][1], x, family=5, par=2.151466)$hfunc2),
94.             copula=frankCopula(2.692378),log=TRUE)-
95.             dCopula(cbind(given[,1][1],given[,2][1]),copula = frankCopula(2.692378),log = TRUE)


96.         return(pdfc)
97.     }
98.
99. # creating a dummy dataframe 'udat_new'
100.
101.udat_new <- data.frame()
102.
103.# if a particular Te value is less than m-th Te value
104.# then these rows containing such value are bind into an object 'udat_new'
105.# object 'given' contains Au Ag values for Te values being < L
106.
107.for (j in 1:4083){
```

```
    if (udat$Te_2[j] < sort(udat$Te_2)[m]) {

        udat_new <- rbind(udat_new,udat[j,])
        j = j+1

        given <- udat_new[,2:3]
    }
}

# setting up the parameters
# for the Metropolis-Hastings simulation

# Make 1000 random draws of Te using the M-H algorithm and calculate
# the mean of those that are below the pseudo values of L

K=1000
x <- matrix(rep(0.5,3*K),nrow=K,ncol=1)
x[1,1] <- runif(1)

# creating new data frame where the results will be stored

imputed <- data.frame()

# looping through the rows of given Ag and Au values

for (j in 1:nrow(given)){

# Sampling Te values from the tr-variate copulas using the Metropolis-Hasting algorithm

for (k in 2:K){
    currentx = x[k-1,]
    sampled <- rnorm(1, mean=0,sd=0.3) #sd to 0.1
    proposedx = currentx + sampled

    if (proposedx >0 & proposedx <1){

        ratio = exp(pdfcalc(proposedx,given)-pdfcalc(currentx,given))
```

```
145.
146.        if(runif(1) < ratio){
147.            x[k,] = proposedx # accept move with probabily min(1,A)
148.        }
149.    }
150.    else{
151.        x[k,] = currentx  # otherwise "reject" move and stay
152.    }
153.}
154.
155.    xnew <- c()
156.    for (i in 1:length(x)){
157.            if(x[i] < m/(n+1)){ # m/(n+1) is the rank of L
158.                xnew <- c(xnew,x[i])
159.            }
160.    }
161.
162.    print(length(xnew))
163.    impPO <- mean(xnew)
164.    imputed <- rbind(imputed,impPO) # contains pseudo-observations of sampled Te values
165.    print(j)
166.}
167.
168.## Step 5
169.# Back transform pseudo values of Te to Te in ppm. This requires the assumption of some parametric


170.# distribution for Te, whereas here the Weibull distribution is used.
171.# The Weibull distribution is fitted to Te values above L by a plotting method
172.# which allows for censored data.
173.
174.TeOverL <- Te_2AuAg[which(Te_2AuAg$Te_2>L),]
175.yy <- log(sort(TeOverL$Te_2))
176.pp <- log(-log(1-(m+ c(1:(n-m)))/4084))
177.dat <- as.data.frame(cbind(yy,pp))
178.m1 <- lm(yy ~ pp, data= dat)
179.
180.# extracting log of b as the estimates
```

```
# and calculating the reciprocal of a using the Weibull distribution

logb <- m1$coefficients[1]
recipa <- (log(L)-logb )/(log(-log(1-(m+0.5)/(n+1))))

# obtain Te values in ppm

imputedppm <- exp(logb + recipa* log(-log(1 - imputed$value)))
```

SUPPLEMENTARY MATERIAL B

FOR CHAPTER 3 – DISCRIMINATION AND VARIANCE STRUCTURE OF TRACE ELEMENT SIGNATURES IN FE-OXIDES: A CASE STUDY OF BIF-MINERALISATION FROM THE MIDDLEBACK RANGES, SOUTH AUSTRALIA

APPENDIX A: LASER ABLATION-INDUCTIVELY COUPLED PLASMA-MASS SPECTROMETRY DATA ACQUISITION

APPENDIX B: TRACE ELEMENT CONCENTRATIONS (IN PPM) IN IRON-OXIDES FROM SAMPLES FROM THE MIDDLEBACK RANGES (LA-ICP-MS DATA)

APPENDIX C: PEARSON CORRELATION COEFFICIENTS OF TRACE ELEMENTS IN CLEAN MARTITE, POROUS MARTITE AND PLATY HEMATITE

ELECTRONIC APPENDIX A FOR CHAPTER 3

Appendix A: Laser ablation-inductively coupled plasma-mass spectrometry data acquisition

LA-ICP-MS spot analyses of different textural types of hematite and magnetite from fifty-one one-inch polished blocks were performed, measuring the following isotopes: 24Mg, 27Al, 29Si, 31P, 43Ca, 49Ti, 51V, 53Cr, 55Mn, 59Co, 60Ni, 65Cu, 66Zn, 69Ga, 75As, 88Sr, 89Y, 90Zr, 93Nb, 95Mo, 118Sn, 121Sb, 137Ba, 139La, 140Ce, 141Pr, 146Nd, 147Sm, 153Eu, 157Gd, 159Tb, 163Dy, 165Ho, 166Er, 169Tm, 172Yb, 175Lu, 182W, 208Pb, 232Th and 238U. Analysis was carried out at Adelaide Microscopy (The University of Adelaide) using a Resonetics LR (ASI) 193-nm Excimer laser microprobe coupled to an Agilent 7700cx Quadrupole ICP-MS. Total integration time for each spot was 70 seconds (s): with 30 s of background measurement followed by 40 s of ablation. Spot sizes of 29 and 43 µm were set depending on mineral grain size and trace element concentrations were calculated by referencing against signals from primary standards GSD-1G and BHVO-2G. Accuracy was monitored with reference materials GSD-1G and BHVO-2G by bracketed runs of up to 20 analyses to correct for instrument drift. Time-resolved signals were exported offline and examined for evidence of mineral inclusions and/or other mineral phases. Data reduction was performed using Glitter software (Van Achterbergh et al. 2001). The portion of the signal displaying constant counts as a function of acquisition time was selected for integration using 57Fe as internal standard.

ELECTRONIC APPENDIX B FOR CHAPTER 3

Electronic Appendix B. Trace element concentrations (in ppm) in iron-oxides from samples from the Middleback Ranges (LA-ICP-MS data)

Position	Deposit	Lithology	Sample no.	Analysis no.	Texture	Mg	Al	Si	P	Ca	Sc	Ti	V	Cr	Mn
Middle	Warrior	ORE	MB10	MB10Hm-1	porous martite	23.52	105.16	1337.17	7.35	45.91	<0.082	1.17	8.37	<0.59	126.53
Middle	Warrior	ORE	MB10	MB10Hm-10	porous martite	42.20	88.95	998.76	81.76	<36.25	<0.08	1.50	2.35	<0.6	354.89
Middle	Warrior	ORE	MB10	MB10Hm-11	porous martite	67.49	95.64	653.05	63.22	<44.1	<0.079	1.78	2.00	0.64	174.88
Middle	Warrior	ORE	MB10	MB10Hm-12	porous martite	38.60	93.85	567.89	40.43	<37.11	<0.074	2.17	1.25	0.51	177.01
Middle	Warrior	ORE	MB10	MB10Hm-13	porous martite	31.21	134.39	879.56	49.45	77.14	<0.082	1.33	17.09	0.66	298.54
Middle	Warrior	ORE	MB10	MB10Hm-14	porous martite	39.08	194.31	919.93	58.90	<42.47	<0.073	2.33	25.58	<0.59	295.72
Middle	Warrior	ORE	MB10	MB10Hm-15	porous martite	104.83	274.80	2307.20	35.62	49.96	0.19	3.21	15.88	1.19	286.11
Middle	Warrior	ORE	MB10	MB10Hm-16	porous martite	68.24	305.39	1047.92	32.91	94.19	<0.079	4.21	42.98	<0.64	231.69
Middle	Warrior	ORE	MB10	MB10Hm-18	porous martite	77.37	256.12	1079.82	18.46	83.76	<0.06	4.05	7.00	<0.49	111.17
Middle	Warrior	ORE	MB10	MB10Hm-19	porous martite	16.19	79.38	1736.55	16.15	<39	<0.083	4.34	4.29	1.05	95.76
Middle	Warrior	ORE	MB10	MB10Hm-2	porous martite	28.66	123.80	789.51	9.63	<53.82	<0.098	3.11	1.68	<0.69	125.59
Middle	Warrior	ORE	MB10	MB10Hm-20	porous martite	282.29	711.94	2367.98	31.03	<45.48	<0.079	5.18	6.04	0.77	100.03
Middle	Warrior	ORE	MB10	MB10Hm-3	porous martite	76.41	123.54	1381.80	22.18	<50.28	<0.071	3.55	85.67	1.57	320.12
Middle	Warrior	ORE	MB10	MB10Hm-4	porous martite	12.45	318.55	1554.87	67.88	<38.21	<0.061	3.56	19.71	<0.52	123.60
Middle	Warrior	ORE	MB10	MB10Hm-5	porous martite	11.99	99.64	2033.70	12.82	101.73	<0.071	0.81	6.83	<0.6	63.88
Middle	Warrior	ORE	MB10	MB10Hm-6	porous martite	13.03	233.52	1908.86	76.98	35.63	<0.07	2.51	2.64	<0.55	64.34
Middle	Warrior	ORE	MB10	MB10Hm-7	porous martite	58.43	121.62	655.92	<5.18	86.98	0.11	2.17	1.28	1.44	145.03
Middle	Warrior	ORE	MB10	MB10Hm-8	porous martite	33.92	220.78	951.11	87.57	<33.25	<0.062	1.70	34.95	<0.64	151.98
Middle	Warrior	ORE	MB10	MB10Hm-9	porous martite	51.72	118.61	1540.43	55.23	30.76	<0.064	1.52	4.53	<0.5	202.33
Middle	Warrior	ORE	MB10	MB10Mt-1	magnetite	35.08	90.98	489.63	<7.12	56.62	<0.095	1.45	0.65	<0.68	224.64
Middle	Warrior	ORE	MB10	MB10Mt-10	magnetite	20.14	117.73	462.09	20.33	<78.89	<0.105	1.31	5.39	0.78	260.68
Middle	Warrior	ORE	MB10	MB10Mt-11	magnetite	54.15	91.00	554.93	<6.26	<50.42	0.09	1.25	0.63	<0.64	354.55
Middle	Warrior	ORE	MB10	MB10Mt-12	magnetite	76.12	90.53	422.58	16.75	57.97	<0.092	1.03	0.67	<0.74	316.56
Middle	Warrior	ORE	MB10	MB10Mt-13	magnetite	522.19	92.51	714.85	11.30	1216.94	<0.092	1.87	0.62	<0.67	345.37
Middle	Warrior	ORE	MB10	MB10Mt-14	magnetite	78.30	93.66	384.82	<6.33	<54.18	0.18	1.66	0.60	<0.66	246.48
Middle	Warrior	ORE	MB10	MB10Mt-15	magnetite	253.06	108.33	342.53	24.32	426.47	<0.102	1.06	1.09	<0.74	354.53
Middle	Warrior	ORE	MB10	MB10Mt-16	magnetite	100.67	95.50	3665.24	11.91	<47.07	<0.096	1.11	0.56	0.66	273.25
Middle	Warrior	ORE	MB10	MB10Mt-17	magnetite	18.60	58.30	107.74	<6.56	<39.37	<0.086	3.24	1.20	<0.64	373.43
Middle	Warrior	ORE	MB10	MB10Mt-18	magnetite	23.15	96.74	417.84	9.80	55.49	<0.068	1.27	0.77	<0.65	194.18
Middle	Warrior	ORE	MB10	MB10Mt-19	magnetite	194.63	84.93	6108.31	25.38	105.49	<0.089	4.58	2.16	<0.59	784.37
Middle	Warrior	ORE	MB10	MB10Mt-2	magnetite	84.74	93.71	294.47	8.13	<59.89	<0.094	1.48	0.41	<0.63	283.96
Middle	Warrior	ORE	MB10	MB10Mt-20	magnetite	11.34	61.01	309.30	10.46	<43.75	<0.077	1.25	0.98	<0.64	316.64
Middle	Warrior	ORE	MB10	MB10Mt-3	magnetite	13.61	88.19	260.75	<7.83	135.07	<0.094	2.36	0.67	1.04	352.76
Middle	Warrior	ORE	MB10	MB10Mt-4	magnetite	21.06	94.34	195.77	<6.49	116.86	<0.079	2.05	0.68	0.79	299.41
Middle	Warrior	ORE	MB10	MB10Mt-5	magnetite	37.66	89.23	691.28	8.45	57.99	0.10	2.24	0.65	<0.67	360.11
Middle	Warrior	ORE	MB10	MB10Mt-6	magnetite	27.30	126.64	360.70	8.90	70.72	<0.094	1.48	3.95	<0.69	184.84
Middle	Warrior	ORE	MB10	MB10Mt-7	magnetite	171.89	93.14	768.83	13.19	<49.96	<0.093	1.06	1.24	<0.81	384.82
Middle	Warrior	ORE	MB10	MB10Mt-8	magnetite	64.14	90.63	221.27	<6.59	<49.09	<0.108	0.84	0.37	<0.62	203.32
Middle	Warrior	ORE	MB10	MB10Mt-9	magnetite	87.45	89.01	181.19	<6.15	<47.91	<0.087	1.27	0.47	<0.7	323.84
Middle	Warrior	ORE	MB11	MB11Hm-10	clean martite	19.42	168.59	453.20	33.62	<91.37	<0.146	2.79	52.46	<1.17	154.98
Middle	Warrior	ORE	MB11	MB11Hm-11	clean martite	4.88	326.10	1386.21	21.08	<80.53	<0.137	1.13	2.07	<1.27	95.30

Analysis no.	Co	Ni	Cu	Zn	Ga	As	Sr	Y	Zr	Nb	Mo	Sn	Sb	Ba	La	Ce	Pr
MB10Hm-1	1.04	2.05	4.30	32.77	0.31	4.50	0.36	1.29	0.04	0.01	0.11	0.16	1.13	1.20	0.23	0.41	0.04
MB10Hm-10	0.07	0.49	<0.137	15.68	0.63	1.90	0.29	2.53	0.01	0.01	0.18	0.20	0.75	0.51	0.48	0.59	0.05
MB10Hm-11	0.12	1.05	0.36	7.87	0.23	5.96	0.52	1.97	0.03	0.01	0.11	0.18	0.97	1.21	0.52	1.02	0.09
MB10Hm-12	0.32	0.61	0.89	9.84	0.17	2.80	0.33	1.17	0.01	<0.00	0.07	0.20	0.68	0.43	0.25	0.36	0.05
MB10Hm-13	0.45	2.89	<0.147	15.83	0.62	1.78	0.33	1.49	0.02	0.02	0.16	0.17	0.67	1.75	0.29	0.41	0.06
MB10Hm-14	0.77	3.63	0.49	20.27	0.32	3.35	0.41	1.79	0.01	0.02	0.11	0.10	1.62	3.00	0.51	0.55	0.05
MB10Hm-15	2.66	6.66	6.52	57.64	0.24	4.15	1.04	1.33	0.10	0.02	0.52	0.16	1.95	5.28	0.29	0.44	0.02
MB10Hm-16	0.58	7.32	0.19	42.60	0.36	5.73	0.46	1.19	0.09	0.02	0.10	0.28	5.09	3.93	0.22	0.44	0.04
MB10Hm-18	1.06	0.88	2.44	44.93	0.19	7.70	0.78	2.96	0.04	0.01	0.06	0.29	1.60	3.00	1.29	1.65	0.13
MB10Hm-19	0.25	0.60	1.71	26.75	0.74	4.49	0.47	1.47	0.01	<0.00	0.12	0.22	0.30	0.27	0.19	0.33	0.03
MB10Hm-2	0.93	0.69	0.26	7.82	0.16	4.86	0.53	0.70	0.03	<0.00	<0.033	0.12	1.69	0.70	0.21	0.43	0.06
MB10Hm-20	1.23	2.43	19.75	85.33	0.60	9.55	0.62	1.05	0.07	0.08	0.03	0.29	2.02	3.65	0.27	0.50	0.03
MB10Hm-3	0.32	1.78	<0.169	32.80	0.29	5.37	0.49	0.72	0.03	0.02	0.06	0.40	1.52	0.98	0.21	0.33	0.03
MB10Hm-4	0.51	2.38	0.34	67.13	0.39	2.52	0.28	1.74	0.34	0.03	0.07	0.27	0.80	3.73	0.33	0.41	0.05
MB10Hm-5	0.12	1.04	0.42	4.79	0.46	7.99	0.27	2.06	0.07	0.00	0.02	0.17	0.21	3.86	0.54	0.55	0.05
MB10Hm-6	0.11	0.32	2.61	37.70	0.58	4.03	0.19	1.81	<0.0164	<0.00	0.04	0.20	0.18	0.32	0.26	0.34	0.03
MB10Hm-7	1.20	0.92	8.04	53.39	0.53	6.11	0.49	0.65	<0.0124	0.02	0.03	0.25	1.20	2.31	0.17	0.32	0.04
MB10Hm-8	0.86	6.91	<0.126	18.27	0.37	3.70	0.32	0.48	0.06	0.02	1.06	0.12	3.76	4.35	0.18	0.24	0.01
MB10Hm-9	0.50	1.32	0.88	15.42	0.33	6.63	0.63	3.20	0.06	0.01	0.13	0.24	1.04	1.13	1.03	1.24	0.11
MB10Mt-1	0.64	0.53	<0.182	9.51	0.17	1.98	0.16	0.30	<0.0159	0.01	0.08	0.13	0.52	0.08	0.09	0.14	0.01
MB10Mt-10	6.25	1.11	0.60	11.38	0.50	2.00	0.22	0.82	0.07	0.05	0.13	<0.12	0.61	1.46	0.28	0.41	0.03
MB10Mt-11	0.97	0.90	<0.183	8.96	0.19	0.81	0.03	0.64	<0.0149	0.00	0.01	0.26	0.11	0.92	0.06	0.14	0.01
MB10Mt-12	2.59	0.33	<0.172	4.48	0.15	0.63	0.09	1.28	0.03	0.00	0.01	0.20	0.04	0.73	0.10	0.11	0.01
MB10Mt-13	0.87	0.62	<0.155	8.84	0.08	1.60	0.43	2.05	0.03	0.02	<0.038	0.12	0.10	2.19	0.16	0.26	0.02
MB10Mt-14	0.42	0.53	<0.177	4.50	0.16	0.60	<0.00	0.16	0.02	0.01	<0.038	0.22	0.03	0.25	0.05	0.05	0.00
MB10Mt-15	1.54	0.69	<0.218	10.38	0.18	1.95	0.11	0.85	0.01	<0.00	0.07	0.18	0.14	2.43	0.14	0.25	0.01
MB10Mt-16	0.57	0.55	<0.193	5.39	0.14	0.89	0.01	0.07	<0.0157	<0.00	0.03	0.18	0.09	<0.065	0.02	0.02	<0.0026
MB10Mt-17	6.01	1.36	<0.18	5.84	0.22	0.67	<0.0087	0.07	0.01	0.01	0.08	0.31	0.02	0.23	0.04	0.05	0.00
MB10Mt-18	0.36	0.49	<0.18	9.67	0.29	1.08	0.52	0.31	<0.0143	0.00	0.05	0.25	0.30	0.12	0.04	0.10	0.01
MB10Mt-19	9.37	<0.28	<0.166	7.83	0.21	3.23	0.04	1.58	0.05	0.01	<0.027	0.15	0.06	1.43	0.24	0.63	0.04
MB10Mt-2	1.33	0.59	<0.168	3.59	0.07	0.95	0.02	0.66	0.05	<0.0062	0.04	0.15	0.01	0.29	0.10	0.12	0.02
MB10Mt-20	4.92	0.67	1.19	9.47	0.38	0.39	0.01	0.01	<0.0139	0.00	0.03	0.23	0.10	0.07	0.01	0.02	<0.00
MB10Mt-3	3.69	0.47	<0.187	9.31	0.35	<0.22	0.03	0.01	<0.00	<0.00	0.07	0.29	<0.035	0.06	<0.00	0.00	<0.00
MB10Mt-4	0.96	0.31	<0.167	4.09	0.29	0.46	0.01	0.04	<0.0155	0.01	<0.047	0.19	<0.037	<0.00	0.01	0.02	0.00
MB10Mt-5	2.38	0.49	<0.188	5.00	0.18	0.90	<0.0093	0.07	<0.0164	0.00	<0.028	0.17	<0.0227	<0.00	0.02	0.03	0.01
MB10Mt-6	1.37	1.28	2.62	16.93	0.18	2.63	0.16	0.22	<0.0153	<0.0061	0.01	0.25	0.46	0.67	0.07	0.13	0.02
MB10Mt-7	3.70	0.39	<0.154	7.61	0.43	1.70	0.04	0.43	0.01	<0.0066	<0.029	0.25	0.05	0.67	0.11	0.18	0.02
MB10Mt-8	0.69	0.82	<0.186	2.87	0.19	0.37	0.01	0.02	<0.0156	0.01	<0.027	0.14	<0.031	<0.065	0.03	0.02	0.00
MB10Mt-9	0.71	<0.172	0.30	4.78	0.14	0.39	0.02	0.15	<0.00	<0.00	0.03	0.15	<0.00	0.20	0.04	0.10	0.00
MB11Hm-10	0.26	3.77	1.56	40.43	0.49	1.84	0.32	0.34	0.06	0.02	0.04	0.26	1.23	2.42	0.25	0.33	0.02
MB11Hm-11	0.48	0.49	5.36	82.73	0.30	1.07	0.20	0.49	<0.02	<0.00	0.02	0.21	0.07	0.28	0.14	0.25	0.02

Analysis no.	Nd	Sm	Eu	Gd	Tb	Dy	Ho	Er	Tm	Yb	Lu	W	Pb208	Th	U
MB10Hm-1	0.23	0.04	0.04	0.08	0.01	0.08	0.02	0.07	0.01	0.11	0.02	0.38	6.21	<0.00	0.02
MB10Hm-10	0.21	0.07	0.05	0.15	0.02	0.07	0.03	0.11	0.01	0.10	0.01	0.43	1.85	<0.00	0.01
MB10Hm-11	0.46	0.06	0.08	0.15	0.01	0.14	0.04	0.10	0.01	0.10	0.01	1.14	3.27	0.00	0.02
MB10Hm-12	0.19	0.07	0.05	0.06	0.01	0.06	0.03	0.05	0.00	0.05	0.00	0.24	1.57	<0.00	0.01
MB10Hm-13	0.19	0.05	0.03	0.07	0.01	0.04	0.02	0.08	0.01	0.07	0.01	0.71	1.63	0.00	0.01
MB10Hm-14	0.38	0.08	0.03	0.13	0.01	0.08	0.02	0.08	0.02	0.05	0.02	1.50	2.71	<0.00	0.02
MB10Hm-15	0.14	<0.00	0.03	0.04	0.01	0.07	0.02	0.08	0.00	0.06	0.01	1.14	3.36	0.00	0.03
MB10Hm-16	0.24	0.03	0.03	0.04	0.01	0.08	0.02	0.08	0.01	0.06	0.01	1.06	3.14	<0.00	0.04
MB10Hm-18	0.57	0.10	0.12	0.19	0.03	0.21	0.05	0.17	0.02	0.14	0.02	0.61	4.49	<0.00	0.04
MB10Hm-19	0.18	0.07	0.05	0.14	0.02	0.10	0.03	0.10	0.01	0.10	0.02	0.18	2.13	0.00	0.01
MB10Hm-2	0.28	0.10	0.05	0.09	0.02	0.08	0.02	0.04	0.01	0.07	0.00	0.06	2.35	<0.00	0.01
MB10Hm-20	0.17	0.03	0.05	0.08	0.01	0.07	0.02	0.07	0.01	0.09	0.01	2.15	4.83	0.01	0.11
MB10Hm-3	0.16	0.01	0.03	0.08	0.00	0.06	0.01	0.05	0.01	0.03	0.01	0.83	2.45	0.00	0.06
MB10Hm-4	0.22	0.09	0.07	0.12	0.02	0.09	0.03	0.12	0.01	0.06	0.02	1.00	2.70	0.01	0.02
MB10Hm-5	0.34	0.06	0.07	0.11	0.01	0.15	0.03	0.21	0.03	0.21	0.04	0.52	6.02	<0.00	0.02
MB10Hm-6	0.19	0.03	0.06	0.09	0.02	0.12	0.05	0.11	0.02	0.17	0.03	0.13	1.83	<0.00	0.01
MB10Hm-7	0.09	0.07	0.03	0.04	0.00	0.07	0.01	0.08	0.01	0.08	0.01	0.29	3.18	<0.00	0.02
MB10Hm-8	0.09	0.02	0.02	0.03	0.00	0.02	0.01	0.03	0.01	0.06	0.00	1.10	2.05	0.01	0.02
MB10Hm-9	0.59	0.08	0.10	0.17	0.02	0.13	0.05	0.17	0.03	0.17	0.02	1.36	3.82	0.00	0.02
MB10Mt-1	0.06	<0.00	0.01	0.03	0.00	0.02	0.00	0.02	0.00	0.04	0.00	<0.0245	0.11	<0.00	<0.00
MB10Mt-10	0.15	0.09	0.04	0.04	0.01	0.06	0.02	0.06	0.01	0.07	0.01	<0.00	0.23	<0.00	<0.00
MB10Mt-11	0.04	<0.00	0.02	0.03	0.01	0.03	0.00	0.03	0.00	0.03	0.01	0.06	0.31	<0.00	<0.00
MB10Mt-12	0.07	<0.018	0.02	0.05	0.01	0.06	0.01	0.04	<0.0038	0.01	0.00	0.02	0.09	0.01	<0.00
MB10Mt-13	0.12	0.03	0.04	0.06	0.01	0.09	0.03	0.10	0.01	0.04	0.01	0.08	0.98	<0.00	0.00
MB10Mt-14	0.01	0.02	<0.0044	0.01	0.00	0.01	0.00	0.01	0.00	0.02	<0.0022	0.01	0.10	<0.00	<0.0057
MB10Mt-15	0.08	0.07	0.04	0.05	0.01	0.04	0.01	0.02	0.01	0.02	0.01	0.22	0.76	<0.00	<0.00
MB10Mt-16	<0.00	<0.0173	<0.0044	0.01	<0.0023	0.01	0.00	0.00	<0.00	<0.00	<0.0022	0.73	0.60	0.02	0.00
MB10Mt-17	0.01	0.01	<0.0043	<0.0165	<0.0031	0.00	0.00	<0.00	<0.0021	<0.00	<0.00	0.14	1.31	<0.00	0.00
MB10Mt-18	0.05	0.03	0.02	0.01	0.00	0.01	0.00	0.01	0.00	0.01	0.00	0.44	7.13	0.01	0.03
MB10Mt-19	0.29	0.09	0.06	0.04	0.00	0.11	0.02	0.11	0.01	0.07	0.01	0.33	0.41	0.00	<0.00
MB10Mt-2	0.07	0.01	0.02	0.06	0.00	0.04	0.00	0.02	0.00	0.03	0.00	0.19	0.23	<0.00	0.00
MB10Mt-20	<0.00	<0.0154	0.00	<0.015	<0.002	<0.0083	<0.00	<0.00	0.00	<0.00	<0.00	0.71	1.40	<0.00	0.00
MB10Mt-3	<0.00	0.01	<0.00	<0.0195	0.00	<0.00	<0.00266	<0.00	0.00	<0.00	<0.00	0.19	0.30	<0.00	0.00
MB10Mt-4	0.01	0.01	<0.0044	<0.00	<0.00	<0.00	<0.00	0.00	0.00	<0.00	<0.00	0.44	1.64	<0.00	0.00
MB10Mt-5	<0.0155	<0.0181	<0.0046	<0.00	<0.00237	<0.00	<0.0024	0.00	<0.00	0.00	<0.0023	0.05	0.22	<0.00	<0.00
MB10Mt-6	0.10	0.02	0.01	0.03	0.01	0.03	0.00	0.01	0.01	0.03	0.00	0.21	0.25	<0.00	0.00
MB10Mt-7	0.06	<0.00	0.01	0.03	0.00	0.02	0.01	0.03	<0.0023	0.01	<0.00	0.06	0.89	<0.00	0.00
MB10Mt-8	0.01	0.01	<0.0044	<0.00	<0.00319	<0.00	0.00	<0.0069	<0.00	0.01	<0.0022	1.13	13.77	<0.00	0.01
MB10Mt-9	0.03	<0.0162	0.01	<0.0158	0.00	0.01	0.00	0.01	0.00	0.00	<0.00206	0.54	0.25	<0.00	0.01
MB11Hm-10	0.07	0.05	0.03	0.05	<0.0053	0.01	0.01	0.03	0.00	0.02	0.01	1.37	6.78	0.00	0.05
MB11Hm-11	0.12	0.05	0.03	0.05	0.01	0.05	0.01	0.06	0.01	0.02	0.01	0.00	3.01	<0.00	0.01

Position	Deposit	Lithology	Sample no.	Analysis no.	Texture	Mg	Al	Si	P	Ca	Sc	Ti	V	Cr	Mn
Middle	Warrior	ORE	MB11	MB11Hm-12	clean martite	8.82	146.41	1102.08	21.81	<85.56	<0.148	3.42	2.72	<1.11	68.73
Middle	Warrior	ORE	MB11	MB11Hm-13	clean martite	10.06	159.32	1894.12	47.56	126.70	0.29	1.86	1.51	1.20	35.67
Middle	Warrior	ORE	MB11	MB11Hm-14	clean martite	101.57	340.73	1169.73	<8.72	<84.53	0.22	11.87	6.86	<1.23	257.71
Middle	Warrior	ORE	MB11	MB11Hm-15	clean martite	8.94	125.51	426.40	13.37	70.83	<0.152	1.26	5.74	<1.26	41.33
Middle	Warrior	ORE	MB11	MB11Hm-16	clean martite	10.43	136.66	803.74	167.90	<98.74	<0.146	1.71	0.68	<1.29	54.05
Middle	Warrior	ORE	MB11	MB11Hm-17	clean martite	5.88	134.08	1074.82	<8.71	<78	<0.143	3.38	1.02	<1.16	88.03
Middle	Warrior	ORE	MB11	MB11Hm-18	clean martite	3.00	136.15	870.02	<7.9	130.66	<0.126	2.71	0.84	<1.24	62.96
Middle	Warrior	ORE	MB11	MB11Hm-19	clean martite	27.83	233.24	427.13	24.05	<81.07	<0.14	5.21	74.68	4.64	211.25
Middle	Warrior	ORE	MB11	MB11Hm-2	clean martite	16.49	330.98	1632.37	<9.64	<106.01	<0.139	2.06	28.09	1.25	111.43
Middle	Warrior	ORE	MB11	MB11Hm-20	clean martite	28.21	139.83	1008.03	34.57	<79.47	<0.142	2.19	0.44	<1.23	69.73
Middle	Warrior	ORE	MB11	MB11Hm-3	clean martite	13.41	171.91	813.46	<8.7	<113.29	<0.143	1.01	2.86	<1.06	30.26
Middle	Warrior	ORE	MB11	MB11Hm-4	clean martite	12.69	176.04	1380.38	74.95	<99.55	<0.148	3.19	10.95	<1.26	64.80
Middle	Warrior	ORE	MB11	MB11Hm-5	clean martite	12.99	141.02	1714.74	<8.41	<94.43	<0.128	0.95	0.41	<1.01	79.78
Middle	Warrior	ORE	MB11	MB11Hm-6	clean martite	5.83	173.66	1101.68	11.32	<80.44	<0.138	1.50	2.47	<1.09	71.77
Middle	Warrior	ORE	MB11	MB11Hm-7	clean martite	29.17	192.67	647.31	27.79	<98.83	<0.156	4.22	91.31	1.36	251.86
Middle	Warrior	ORE	MB11	MB11Hm-8	clean martite	43.01	235.38	749.67	57.63	<84.43	0.39	7.40	142.91	1.73	340.89
Middle	Warrior	ORE	MB11	MB11Hm-9	clean martite	23.67	253.59	1268.65	81.14	<95.05	0.29	1.79	79.78	<1.23	177.40
Middle	Warrior	ORE	MB11	MB11HmPorous-1	porous martite	46.58	308.91	871.32	21.65	<113.11	<0.16	3.03	21.53	8.06	181.44
Middle	Warrior	ORE	MB11	MB11HmPorous-10	porous martite	94.57	184.07	975.72	<10.84	<85.75	<0.155	2.76	5.60	<1.34	238.54
Middle	Warrior	ORE	MB11	MB11HmPorous-11	porous martite	75.99	204.43	941.79	12.23	166.57	<0.142	4.94	59.98	5.69	286.96
Middle	Warrior	ORE	MB11	MB11HmPorous-12	porous martite	15.19	182.85	1553.28	16.06	<72.96	<0.133	15.14	7.48	<1.04	52.45
Middle	Warrior	ORE	MB11	MB11HmPorous-13	porous martite	11.36	199.05	2162.17	25.68	<83.33	0.26	15.07	3.14	<1.13	26.66
Middle	Warrior	ORE	MB11	MB11HmPorous-14	porous martite	55.92	191.67	830.75	<8.05	336.99	<0.127	3.11	9.29	1.52	197.06
Middle	Warrior	ORE	MB11	MB11HmPorous-15	porous martite	50.49	222.82	792.98	14.22	<84.68	0.15	4.98	16.37	2.02	239.55
Middle	Warrior	ORE	MB11	MB11HmPorous-16	porous martite	75.82	381.11	1649.75	<9.28	<92.36	<0.16	7.06	47.86	2.57	188.82
Middle	Warrior	ORE	MB11	MB11HmPorous-17	porous martite	70.17	376.36	672.77	15.42	<72.97	0.18	5.37	70.62	3.26	212.85
Middle	Warrior	ORE	MB11	MB11HmPorous-18	porous martite	89.28	421.50	1508.81	29.27	<85.2	0.20	7.89	41.06	<1.19	321.87
Middle	Warrior	ORE	MB11	MB11HmPorous-19	porous martite	115.63	324.32	2216.40	35.65	232.87	<0.134	2.30	9.15	<0.96	125.43
Middle	Warrior	ORE	MB11	MB11HmPorous-2	porous martite	82.30	247.60	525.19	<11.42	<131.26	0.19	3.10	5.57	<1.49	257.04
Middle	Warrior	ORE	MB11	MB11HmPorous-20	porous martite	111.35	729.08	1415.31	13.84	171.71	<0.155	5.91	629.83	4.60	553.50
Middle	Warrior	ORE	MB11	MB11HmPorous-3	porous martite	78.73	439.57	550.04	<10.49	<98.54	0.31	335.94	34.02	<1.52	302.85
Middle	Warrior	ORE	MB11	MB11HmPorous-4	porous martite	24.42	178.02	1194.90	708.65	230.12	0.22	6.52	8.11	<1.44	216.16
Middle	Warrior	ORE	MB11	MB11HmPorous-5	porous martite	50.11	298.63	921.65	20.64	137.08	<0.16	0.91	96.51	14.24	324.94
Middle	Warrior	ORE	MB11	MB11HmPorous-6	porous martite	55.21	337.51	754.76	<8.98	178.99	<0.155	1.11	13.79	9.26	203.78
Middle	Warrior	ORE	MB11	MB11HmPorous-7	porous martite	53.91	190.21	605.87	36.60	125.81	<0.171	1.06	6.96	<1.24	411.50
Middle	Warrior	ORE	MB11	MB11HmPorous-8	porous martite	85.96	347.62	1846.87	28.45	<107.03	0.34	9.69	261.38	<1.31	143.73
Middle	Warrior	ORE	MB11	MB11HmPorous-9	porous martite	103.65	559.48	1275.54	44.85	124.71	0.61	2.99	76.67	<1.33	990.13
Middle	Warrior	ORE	MB11	MB11Mg-1	magnetite	45.35	175.66	851.32	<10.64	<121.2	0.17	27.66	3.64	<1.24	128.21
Middle	Warrior	ORE	MB11	MB11Mg-10	magnetite	31.33	220.76	<152.38	31.08	252.51	<0.17	2.38	13.14	<1.29	196.32
Middle	Warrior	ORE	MB11	MB11Mg-11	magnetite	141.06	101.89	15293.28	<10.73	<103.95	<0.189	6.18	1.28	<1.52	544.98
Middle	Warrior	ORE	MB11	MB11Mg-12	magnetite	31.52	127.86	200.22	24.50	<97.68	<0.163	6.39	49.39	<1.45	294.10
Middle	Warrior	ORE	MB11	MB11Mg-13	magnetite	133.53	85.50	1471.57	15.50	<101.82	<0.166	3.91	15.51	<1.62	486.10
Middle	Warrior	ORE	MB11	MB11Mg-14	magnetite	55.97	140.21	11833.82	<11.46	<99	<0.143	6.59	18.51	<1.4	328.28

Analysis no.	Co	Ni	Cu	Zn	Ga	As	Sr	Y	Zr	Nb	Mo	Sn	Sb	Ba	La	Ce	Pr
MB11Hm-12	0.79	0.59	10.64	121.65	0.39	6.96	0.26	1.84	0.01	0.00	0.01	0.26	0.36	0.83	0.16	0.24	0.02
MB11Hm-13	0.41	0.43	3.54	47.41	0.31	2.84	0.33	1.09	<0.02	0.02	<0.05	<0.195	0.25	0.84	0.18	0.32	0.03
MB11Hm-14	0.82	1.41	0.94	38.80	0.50	10.36	0.92	2.35	0.04	0.00	0.03	<0.189	2.05	6.82	0.84	1.25	0.11
MB11Hm-15	0.31	<0.27	0.40	17.88	0.32	2.31	0.08	0.60	0.02	0.00	0.01	<0.205	0.16	<0.00	0.20	0.25	0.02
MB11Hm-16	0.14	<0.227	1.57	15.54	0.31	2.89	0.07	1.15	<0.0202	0.01	0.09	<0.191	0.18	0.24	0.13	0.18	0.02
MB11Hm-17	0.45	0.76	4.20	86.01	0.17	2.22	0.16	0.66	0.03	0.00	0.03	0.30	<0.056	0.07	0.06	0.10	0.02
MB11Hm-18	0.52	0.49	5.12	83.05	0.19	2.40	0.12	0.33	<0.0196	0.01	0.02	0.31	0.27	0.28	0.06	0.11	0.01
MB11Hm-19	0.63	4.18	2.81	80.11	0.43	1.35	0.28	0.38	0.23	0.04	0.12	<0.194	1.03	3.86	0.25	0.27	0.02
MB11Hm-2	0.50	1.62	6.58	61.55	0.46	6.64	0.36	3.12	0.02	0.01	<0.052	<0.217	2.02	1.83	0.35	0.61	0.08
MB11Hm-20	0.29	0.50	1.36	11.00	0.20	2.15	0.11	0.86	<0.00	<0.00	0.06	<0.213	0.22	0.18	0.08	0.14	0.02
MB11Hm-3	0.66	1.19	2.51	75.26	0.46	1.82	0.09	1.54	0.03	0.00	0.05	<0.198	0.31	0.15	0.12	0.22	0.03
MB11Hm-4	0.23	0.48	2.98	9.88	0.40	1.65	0.19	1.70	0.03	0.01	0.03	0.35	0.44	0.75	0.19	0.24	0.06
MB11Hm-5	0.39	0.31	1.55	3.96	0.14	2.13	0.04	0.53	<0.028	<0.00	<0.035	<0.188	<0.045	<0.00	0.04	0.09	0.01
MB11Hm-6	0.65	0.34	7.65	116.93	0.55	2.33	0.23	1.31	0.01	<0.0076	0.04	0.26	0.55	2.43	0.09	0.25	0.02
MB11Hm-7	0.70	4.81	3.85	86.21	0.32	1.99	0.31	0.71	0.14	0.05	0.06	<0.193	1.75	5.16	0.40	0.42	0.03
MB11Hm-8	0.38	8.60	<0.22	16.77	0.25	2.81	0.52	0.62	0.22	0.09	0.10	<0.187	2.28	6.91	0.49	0.47	0.03
MB11Hm-9	0.73	3.01	8.57	104.36	0.23	2.62	0.44	0.86	0.15	0.02	0.20	<0.184	1.14	2.87	0.26	0.42	0.02
MB11HmPorous-1	0.87	1.19	1.45	22.85	0.35	8.89	0.77	2.37	0.05	0.03	0.09	<0.198	2.51	4.03	0.74	1.15	0.12
MB11HmPorous-10	2.81	1.43	0.83	19.53	0.23	5.26	0.35	0.71	0.01	<0.00	<0.043	<0.23	1.00	5.03	0.30	0.45	0.03
MB11HmPorous-11	2.07	2.80	3.51	71.99	0.47	8.90	1.03	2.72	0.09	0.01	0.28	<0.188	2.80	2.82	0.95	1.55	0.12
MB11HmPorous-12	0.50	1.25	4.45	49.11	0.33	4.30	0.22	1.61	<0.018	0.02	0.05	0.23	0.50	0.64	0.21	0.29	0.03
MB11HmPorous-13	0.25	1.13	4.80	26.62	0.18	8.33	0.21	2.79	0.04	0.05	0.05	0.36	0.56	0.31	0.31	0.49	0.04
MB11HmPorous-14	1.71	0.70	1.60	12.16	0.37	6.50	0.73	0.57	0.06	0.04	<0.047	0.37	0.71	3.84	0.42	0.49	0.03
MB11HmPorous-15	1.42	2.21	1.27	40.64	0.23	7.71	0.69	1.51	0.07	0.01	<0.00	0.21	2.90	4.63	0.62	0.97	0.10
MB11HmPorous-16	2.56	3.89	6.10	48.85	0.24	10.03	0.68	1.79	0.19	0.04	0.28	<0.21	2.68	4.81	0.55	1.11	0.09
MB11HmPorous-17	0.98	4.44	1.76	42.57	0.60	6.28	0.69	0.89	0.24	0.04	<0.054	<0.21	2.58	3.75	0.39	1.07	0.05
MB11HmPorous-18	2.05	3.64	3.48	71.50	0.55	6.82	0.68	1.34	0.08	0.02	0.07	<0.209	2.19	3.76	0.64	1.78	0.10
MB11HmPorous-19	0.77	2.25	0.82	52.78	0.60	7.03	1.12	2.73	0.02	0.02	0.09	<0.174	2.13	5.15	1.03	1.21	0.10
MB11HmPorous-2	1.89	1.48	0.74	19.50	0.44	7.33	0.50	1.03	<0.025	0.00	<0.045	<0.23	1.41	4.90	0.38	0.64	0.07
MB11HmPorous-20	2.00	20.19	1.38	100.85	0.65	5.14	0.57	0.62	0.20	0.08	0.12	<0.2	8.73	9.62	0.36	0.60	0.03
MB11HmPorous-3	14.01	1.54	15.13	75.81	0.79	7.30	0.79	1.68	0.01	0.01	0.03	0.39	2.37	2.21	0.51	0.88	0.09
MB11HmPorous-4	0.26	1.29	0.52	25.98	0.24	9.73	0.58	5.64	0.04	0.07	0.03	<0.202	1.68	2.07	1.40	1.31	0.10
MB11HmPorous-5	1.14	4.56	0.45	42.72	0.25	5.65	0.42	0.58	0.06	0.04	0.04	<0.19	2.67	2.36	0.30	0.35	0.02
MB11HmPorous-6	0.68	0.95	1.57	26.42	0.53	8.63	0.83	1.58	0.05	0.01	<0.037	0.24	1.73	5.87	0.56	0.91	0.11
MB11HmPorous-7	0.46	0.62	4.32	46.35	0.46	4.23	0.62	0.77	<0.022	0.00	<0.039	<0.193	0.87	2.29	0.39	0.47	0.04
MB11HmPorous-8	1.60	6.27	1.65	42.78	0.27	7.55	1.15	2.28	0.12	0.02	0.33	0.30	2.08	5.37	0.80	1.31	0.10
MB11HmPorous-9	2.65	6.30	6.74	64.55	0.39	7.39	0.90	2.13	0.12	0.01	0.20	0.34	2.96	3.25	1.27	4.26	0.31
MB11Mg-1	1.21	0.80	1.26	33.66	0.29	2.85	0.18	0.32	<0.034	0.00	0.04	<0.205	0.68	1.33	0.21	0.28	0.02
MB11Mg-10	5.37	2.11	<0.3	26.12	0.27	1.27	0.15	0.21	<0.00	0.02	0.01	0.27	0.76	0.75	0.06	0.07	0.00
MB11Mg-11	6.68	0.55	<0.23	7.84	0.23	2.28	0.05	1.19	0.05	<0.00	1.57	<0.22	0.22	1.15	0.26	0.54	0.04
MB11Mg-12	5.21	1.97	0.52	20.57	0.24	3.07	0.23	0.46	0.03	<0.0101	0.05	<0.22	1.20	0.92	0.23	0.60	0.05
MB11Mg-13	3.10	0.64	<0.23	13.83	0.10	3.36	0.15	1.37	<0.00	<0.00	1.72	<0.22	0.48	1.78	0.43	0.90	0.09
MB11Mg-14	1.22	0.41	1.16	23.76	0.32	4.59	0.41	0.86	<0.00	0.01	3.06	<0.22	0.73	2.87	0.29	0.59	0.07

Analysis no.	Nd	Sm	Eu	Gd	Tb	Dy	Ho	Er	Tm	Yb	Lu	W	Pb208	Th	U
MB11Hm-12	0.22	0.06	0.05	0.08	0.02	0.08	0.03	0.12	0.01	0.09	0.02	0.10	3.82	0.01	0.02
MB11Hm-13	0.17	0.03	0.05	0.05	0.01	0.08	0.03	0.07	0.01	0.09	0.02	0.20	3.20	0.01	0.05
MB11Hm-14	0.47	0.10	0.16	0.23	0.03	0.30	0.06	0.19	0.03	0.23	0.02	0.23	17.62	0.00	0.22
MB11Hm-15	0.06	0.03	0.02	0.04	0.01	0.01	0.01	0.03	0.00	0.03	<0.0057	0.07	0.75	<0.0049	0.02
MB11Hm-16	0.13	0.03	0.05	0.08	<0.0029	0.09	0.03	0.07	0.02	0.04	0.01	0.04	1.40	<0.00	0.01
MB11Hm-17	0.09	0.04	0.01	<0.021	0.01	0.03	0.01	0.04	0.00	0.04	<0.0027	<0.0133	2.42	0.00	0.00
MB11Hm-18	0.06	<0.021	<0.0078	0.05	0.00	0.02	0.01	<0.0087	0.00	0.02	0.00	0.05	2.41	<0.00	0.01
MB11Hm-19	0.15	0.01	0.02	0.06	0.00	0.03	0.01	0.02	0.01	0.06	0.00	1.63	9.08	0.02	0.05
MB11Hm-2	0.41	0.13	0.14	0.16	0.03	0.28	0.08	0.22	0.04	0.28	0.03	0.31	5.59	<0.00	0.10
MB11Hm-20	0.12	<0.023	0.04	0.04	0.01	0.08	0.02	0.05	0.01	0.08	0.01	<0.00	0.74	0.00	0.01
MB11Hm-3	0.24	0.04	0.05	0.05	0.01	0.08	0.03	0.14	0.02	0.11	0.02	0.04	2.00	0.00	0.01
MB11Hm-4	0.21	0.04	0.07	0.15	0.02	0.14	0.04	0.15	0.02	0.16	0.03	0.11	1.95	0.01	0.02
MB11Hm-5	0.03	0.01	0.04	0.04	0.01	0.05	0.01	0.04	<0.0027	0.06	0.00	0.03	0.86	<0.00	0.01
MB11Hm-6	0.13	0.06	0.05	0.06	<0.004	0.13	0.03	0.09	0.01	0.08	0.01	0.06	3.97	0.00	0.02
MB11Hm-7	0.13	0.04	0.02	0.05	0.01	0.04	0.02	0.03	0.01	0.09	0.02	2.16	10.78	0.02	0.08
MB11Hm-8	0.23	0.02	0.02	<0.041	0.01	0.05	0.01	0.03	0.00	0.06	0.01	3.00	13.72	0.03	0.11
MB11Hm-9	0.11	0.04	0.04	0.04	0.01	0.08	0.02	0.06	0.01	0.04	0.02	1.50	9.03	0.01	0.08
MB11HmPorous-1	0.45	0.14	0.11	0.19	0.02	0.18	0.05	0.17	0.02	0.21	0.02	0.49	11.18	0.02	0.31
MB11HmPorous-10	0.17	0.03	0.03	0.02	0.01	0.06	0.01	0.09	0.01	0.07	0.01	0.26	10.24	0.01	0.04
MB11HmPorous-11	0.55	0.23	0.14	0.33	0.04	0.36	0.07	0.23	0.04	0.18	0.03	1.00	15.09	0.02	0.35
MB11HmPorous-12	0.15	<0.034	0.04	0.05	0.02	0.08	0.02	0.09	0.02	0.11	0.01	0.31	3.48	0.02	0.03
MB11HmPorous-13	0.22	0.09	0.07	0.07	0.01	0.19	0.05	0.14	0.03	0.20	0.02	0.78	4.01	0.03	0.09
MB11HmPorous-14	0.13	<0.02	0.03	0.04	0.00	0.03	0.01	0.07	0.01	0.09	0.01	0.69	11.41	0.00	0.08
MB11HmPorous-15	0.35	0.08	0.10	0.19	0.02	0.15	0.03	0.13	0.03	0.17	0.02	0.41	11.57	0.02	0.13
MB11HmPorous-16	0.47	0.14	0.09	0.14	0.02	0.12	0.04	0.11	0.02	0.11	0.02	1.13	16.80	0.03	0.14
MB11HmPorous-17	0.24	0.09	0.06	0.06	0.01	0.11	0.02	0.06	0.01	0.08	0.01	0.87	15.02	0.01	0.14
MB11HmPorous-18	0.57	0.09	0.10	0.18	0.02	0.14	0.02	0.13	0.02	0.12	0.02	0.51	17.27	0.01	0.19
MB11HmPorous-19	0.39	0.19	0.14	0.14	0.01	0.19	0.05	0.17	0.03	0.09	0.02	0.41	19.87	0.02	0.19
MB11HmPorous-2	0.31	0.07	0.07	0.11	0.02	0.15	0.02	0.10	0.01	0.09	0.02	0.18	11.89	0.01	0.09
MB11HmPorous-20	0.08	0.03	0.01	0.05	<0.003	0.03	0.01	0.01	0.01	0.05	0.01	2.34	20.40	0.01	0.33
MB11HmPorous-3	0.42	0.14	0.09	0.25	0.03	0.17	0.05	0.17	0.04	0.14	0.02	0.11	5.47	0.01	0.18
MB11HmPorous-4	0.57	0.15	0.13	0.17	0.03	0.20	0.06	0.30	0.04	0.19	0.05	0.65	4.69	0.01	0.02
MB11HmPorous-5	0.04	<0.0232	0.03	0.05	0.00	0.02	0.02	0.04	<0.0029	0.05	0.01	0.84	14.21	<0.00	0.20
MB11HmPorous-6	0.33	0.05	0.10	0.15	0.03	0.17	0.03	0.11	0.02	0.12	0.02	0.33	11.17	<0.00	0.24
MB11HmPorous-7	0.13	0.03	0.04	<0.041	0.01	0.10	0.02	0.07	<0.0052	0.04	0.01	0.20	13.86	0.00	0.07
MB11HmPorous-8	0.52	0.10	0.10	0.10	0.03	0.20	0.04	0.15	0.03	0.16	0.04	1.40	25.57	0.01	0.46
MB11HmPorous-9	1.67	0.40	0.23	0.39	0.06	0.34	0.07	0.26	0.03	0.20	0.03	1.08	33.44	0.04	0.49
MB11Mg-1	0.15	0.01	0.01	0.04	0.01	0.02	0.01	0.02	0.00	0.03	0.01	0.04	0.18	<0.00	0.00
MB11Mg-10	0.05	0.05	0.01	0.04	<0.01	0.00	0.00	0.02	0.00	0.03	0.01	<0.0121	0.07	0.00	0.00
MB11Mg-11	0.14	0.05	0.04	0.07	0.01	0.09	0.01	0.05	0.00	0.05	<0.0054	0.15	0.14	<0.00	0.00
MB11Mg-12	0.27	0.10	0.07	0.01	0.01	0.07	0.01	0.04	0.01	0.04	0.01	0.10	0.21	<0.00	0.00
MB11Mg-13	0.40	0.03	0.08	0.15	0.02	0.10	0.02	0.05	0.01	0.03	0.00	0.11	4.48	<0.00	0.01
MB11Mg-14	0.23	0.03	0.04	0.05	0.01	0.04	0.00	0.02	0.00	0.02	0.01	0.54	0.80	<0.00	<0.0022

Position	Deposit	Lithology	Sample no.	Analysis no.	Texture	Mg	Al	Si	P	Ca	Sc	Ti	V	Cr	Mn
Middle	Warrior	ORE	MB11	MB11Mg-15	magnetite	408.66	101.09	1671.16	20.62	926.04	<0.17	5.64	9.10	<1.48	341.15
Middle	Warrior	ORE	MB11	MB11Mg-16	magnetite	26.50	167.65	<164.44	<11.98	<105.92	<0.189	1.90	1.05	<1.61	415.47
Middle	Warrior	ORE	MB11	MB11Mg-17	magnetite	14.57	161.95	270.97	22.65	<93.93	<0.165	2.51	1.20	2.33	343.76
Middle	Warrior	ORE	MB11	MB11Mg-18	magnetite	20.73	139.50	274.31	<9.79	115.68	0.18	2.15	1.17	1.55	266.63
Middle	Warrior	ORE	MB11	MB11Mg-19	magnetite	70.11	166.74	279.10	15.55	<113.84	<0.191	<1.32	1.12	2.31	361.46
Middle	Warrior	ORE	MB11	MB11Mg-2	magnetite	46.53	125.88	382.71	<12.25	171.05	<0.173	4.61	12.16	3.26	274.35
Middle	Warrior	ORE	MB11	MB11Mg-20	magnetite	32.58	165.62	173.23	<10.7	<96.96	<0.179	3.04	1.20	<1.37	266.45
Middle	Warrior	ORE	MB11	MB11Mg-21	magnetite	26.55	166.07	265.09	<10.83	<132.17	<0.171	1.15	1.29	<1.41	336.14
Middle	Warrior	ORE	MB11	MB11Mg-22	magnetite	20.97	173.41	<184.04	<13.9	<145.71	<0.192	1.70	7.70	<1.53	340.60
Middle	Warrior	ORE	MB11	MB11Mg-23	magnetite	68.10	154.07	472.72	<10.02	134.61	0.33	3.19	1.55	1.76	237.98
Middle	Warrior	ORE	MB11	MB11Mg-24	magnetite	52.35	166.86	376.17	<11.17	<132.9	<0.148	1.67	0.90	<1.48	419.98
Middle	Warrior	ORE	MB11	MB11Mg-25	magnetite	50.94	136.14	978.99	<10.92	197.13	<0.181	32.37	23.07	<1.38	332.64
Middle	Warrior	ORE	MB11	MB11Mg-26	magnetite	87.34	128.68	803.68	17.89	<125.18	<0.158	5.24	3.16	<1.58	458.13
Middle	Warrior	ORE	MB11	MB11Mg-27	magnetite	25.59	257.10	410.08	<10.32	<122.02	<0.157	2.64	8.99	<1.35	299.00
Middle	Warrior	ORE	MB11	MB11Mg-28	magnetite	56.59	232.60	2001.35	18.23	<104.23	<0.16	4.83	4.43	<1.25	325.27
Middle	Warrior	ORE	MB11	MB11Mg-29	magnetite	284.55	73.16	788.19	<9.83	147.08	<0.162	2.96	0.90	<1.34	365.68
Middle	Warrior	ORE	MB11	MB11Mg-3	magnetite	792.86	163.65	2116.91	11.94	157.39	<0.189	3.04	4.16	1.79	399.24
Middle	Warrior	ORE	MB11	MB11Mg-30	magnetite	77.02	212.06	845.17	44.12	<122.08	<0.167	2.68	104.52	2.08	911.52
Middle	Warrior	ORE	MB11	MB11Mg-31	magnetite	294.38	114.81	2338.64	14.41	444.88	<0.192	6.42	1.50	<1.55	646.81
Middle	Warrior	ORE	MB11	MB11Mg-32	magnetite	18.52	102.65	<134.46	<9.27	196.19	<0.152	3.86	1.08	1.39	358.87
Middle	Warrior	ORE	MB11	MB11Mg-33	magnetite	44.24	215.53	919.14	20.81	<104.48	0.41	8.13	30.11	2.84	219.87
Middle	Warrior	ORE	MB11	MB11Mg-34	magnetite	19.43	172.69	273.95	9.79	<102.2	<0.145	3.27	3.21	1.60	212.57
Middle	Warrior	ORE	MB11	MB11Mg-35	magnetite	50.92	170.91	<148.52	12.72	102.66	<0.167	2.47	0.95	1.63	246.10
Middle	Warrior	ORE	MB11	MB11Mg-36	magnetite	35.82	175.61	389.02	16.55	<107.59	<0.167	3.34	1.53	<1.53	434.76
Middle	Warrior	ORE	MB11	MB11Mg-37	magnetite	52.51	230.89	177.52	42.45	90.54	<0.153	2.36	4.94	<1.21	537.94
Middle	Warrior	ORE	MB11	MB11Mg-38	magnetite	11.84	146.24	<146.88	25.89	84.86	<0.171	2.19	4.62	<1.48	294.76
Middle	Warrior	ORE	MB11	MB11Mg-39	magnetite	18.64	168.85	485.82	<9.7	<87.87	<0.163	1.57	5.14	<1.5	302.73
Middle	Warrior	ORE	MB11	MB11Mg-4	magnetite	78.22	2034.02	2932.97	56.38	<112.37	0.22	29.31	132.94	4.55	1193.19
Middle	Warrior	ORE	MB11	MB11Mg-40	magnetite	34.26	170.29	<170.42	<12.11	<109.01	<0.192	1.37	1.33	<1.74	394.71
Middle	Warrior	ORE	MB11	MB11Mg-5	magnetite	13.47	249.92	359.78	<9.25	<103.81	<0.156	85.56	6.05	<1.31	355.13
Middle	Warrior	ORE	MB11	MB11Mg-6	magnetite	17.95	193.94	263.16	<11.62	<134.05	<0.185	5.37	1.54	<1.39	386.42
Middle	Warrior	ORE	MB11	MB11Mg-7	magnetite	24.29	147.05	550.81	<10.91	<135.38	<0.159	3.39	25.83	<1.28	267.72
Middle	Warrior	ORE	MB11	MB11Mg-8	magnetite	19.58	201.01	<166.65	<12.19	<117.64	0.23	3.49	4.76	<1.38	298.38
Middle	Warrior	ORE	MB11	MB11Mg-9	magnetite	23.12	193.91	304.14	<10.32	334.89	<0.176	2.64	5.06	<1.43	268.50
Middle	Warrior	ORE	MB12	MB12HmClean-1	clean martite	19.82	69.94	751.31	11.28	<105.37	<0.132	2.47	48.14	1.47	155.67
Middle	Warrior	ORE	MB12	MB12HmClean-10	clean martite	18.18	90.29	238.38	54.70	<136.09	0.69	2.56	23.07	<1.66	60.55
Middle	Warrior	ORE	MB12	MB12HmClean-11	clean martite	13.89	20.01	<127.94	<10	<108.87	0.41	<0.96	2.06	1.68	3.88
Middle	Warrior	ORE	MB12	MB12HmClean-12	clean martite	22.50	51.88	263.42	18.91	<120.5	0.57	<1	0.30	<1.3	10.28
Middle	Warrior	ORE	MB12	MB12HmClean-13	clean martite	162.01	205.89	1542.43	27.74	<94.21	0.46	47.30	48.54	2.09	938.18
Middle	Warrior	ORE	MB12	MB12HmClean-14	clean martite	34.21	104.63	373.79	66.97	<95.65	0.52	2.97	1.83	1.48	388.57
Middle	Warrior	ORE	MB12	MB12HmClean-15	clean martite	174.87	204.51	393.27	<9.18	<85.99	0.28	<1.05	1.87	<1.28	64.09
Middle	Warrior	ORE	MB12	MB12HmClean-16	clean martite	62.20	149.59	831.88	58.80	<89.3	0.52	6.93	13.50	1.49	93.25
Middle	Warrior	ORE	MB12	MB12HmClean-17	clean martite	42.59	163.34	589.44	204.37	<82.74	1.97	2.87	4.55	<1.12	215.52

Analysis no.	Co	Ni	Cu	Zn	Ga	As	Sr	Y	Zr	Nb	Mo	Sn	Sb	Ba	La	Ce	Pr
MB11Mg-15	4.01	<0.34	<0.25	16.01	0.28	3.87	0.60	1.17	0.07	0.35	2.84	<0.26	0.41	2.30	0.56	0.89	0.08
MB11Mg-16	3.02	1.56	<0.251	7.18	0.30	<0.43	0.01	0.00	<0.0286	0.00	0.01	<0.24	<0.084	<0.00	0.00	<0.0058	<0.0048
MB11Mg-17	10.99	1.21	<0.24	9.96	0.31	0.37	0.01	<0.0103	<0.00	<0.00	<0.00	<0.222	<0.086	0.08	0.00	0.00	<0.0042
MB11Mg-18	0.63	0.70	<0.26	6.46	0.30	<0.36	<0.0138	0.01	0.01	<0.00	0.05	<0.218	<0.074	<0.00	0.02	0.01	0.00
MB11Mg-19	1.19	1.30	<0.29	9.10	0.44	2.41	0.03	0.12	<0.00	0.02	<0.052	<0.25	<0.077	0.26	0.07	0.10	<0.007
MB11Mg-2	2.51	1.61	<0.27	14.25	0.27	1.45	0.17	0.34	<0.028	0.03	<0.05	<0.23	1.17	1.37	0.21	0.26	0.01
MB11Mg-20	0.68	1.35	<0.24	11.58	0.33	0.80	0.12	0.04	<0.0249	0.00	0.02	0.27	0.11	0.31	0.01	0.02	0.00
MB11Mg-21	3.50	0.71	<0.27	7.50	0.41	<0.28	0.01	0.02	0.04	0.01	<0.059	0.23	0.09	0.34	0.02	0.01	0.00
MB11Mg-22	3.23	1.06	<0.29	13.98	0.38	0.75	0.09	0.10	0.04	0.01	0.07	<0.29	<0.101	<0.00	0.07	0.23	0.01
MB11Mg-23	2.57	1.33	<0.24	9.10	0.51	2.56	0.07	0.52	0.04	0.01	0.07	<0.22	0.86	0.11	0.09	0.20	0.03
MB11Mg-24	5.22	1.05	<0.27	7.57	0.26	0.50	0.02	0.03	<0.00	0.02	<0.041	0.23	<0.075	0.12	0.01	0.02	<0.0039
MB11Mg-25	3.99	1.96	<0.23	12.18	0.32	2.93	0.11	0.40	0.02	0.03	<0.046	0.26	0.71	0.90	0.18	0.26	0.03
MB11Mg-26	5.11	1.33	<0.24	8.10	0.23	1.01	0.01	0.12	<0.0249	0.01	0.05	<0.22	0.28	0.31	0.05	0.10	0.01
MB11Mg-27	2.09	1.34	<0.26	12.13	0.43	1.13	0.09	0.15	0.05	0.00	0.05	0.36	0.82	1.43	0.10	0.11	<0.0041
MB11Mg-28	6.07	1.05	<0.22	24.70	0.37	2.00	0.20	0.17	0.02	<0.00	<0.055	0.36	0.19	1.27	0.10	0.29	0.03
MB11Mg-29	7.12	0.61	<0.218	8.49	0.09	<0.37	<0.00	0.05	0.03	<0.009	<0.04	0.20	<0.079	0.09	0.02	0.02	0.00
MB11Mg-3	4.58	1.10	<0.31	12.62	0.45	1.66	0.06	0.09	<0.00	0.01	<0.05	<0.25	<0.102	0.26	0.07	0.09	<0.0046
MB11Mg-30	3.36	3.04	1.90	17.97	0.17	3.16	0.24	0.74	0.29	0.02	<0.042	0.33	1.14	2.52	0.41	0.74	0.06
MB11Mg-31	1.63	0.26	0.54	8.97	0.22	3.10	0.14	0.82	0.05	0.02	12.31	0.22	<0.09	2.30	0.70	1.00	0.08
MB11Mg-32	0.84	0.70	<0.27	8.25	0.15	<0.34	0.01	0.01	<0.022	<0.00	0.01	<0.2	<0.059	<0.00	<0.00	<0.0045	<0.00
MB11Mg-33	1.96	1.49	0.42	34.17	0.14	2.50	0.42	0.38	<0.00	<0.009	0.05	<0.22	1.78	0.69	0.08	0.19	0.01
MB11Mg-34	0.56	1.58	<0.21	9.12	0.29	0.43	0.06	0.01	<0.00	<0.00	0.02	<0.21	<0.078	0.30	0.01	<0.0045	0.00
MB11Mg-35	0.25	1.50	0.29	3.63	0.42	0.43	<0.014	<0.0106	<0.00	<0.01	<0.064	<0.24	<0.095	<0.00	0.01	0.00	<0.00
MB11Mg-36	3.03	0.80	0.55	5.05	0.38	0.93	0.03	0.25	<0.0248	0.00	0.04	<0.23	<0.098	0.10	0.12	0.45	0.02
MB11Mg-37	2.81	0.52	7.54	11.98	0.85	8.59	0.02	1.65	<0.00	<0.00	0.10	0.23	0.41	<0.00	0.28	0.51	0.07
MB11Mg-38	4.78	0.87	<0.26	10.41	0.36	0.48	0.01	0.02	<0.0254	<0.01	0.05	<0.24	0.12	0.27	0.02	0.03	<0.0043
MB11Mg-39	2.00	0.81	0.30	12.93	0.30	1.80	0.03	0.19	0.02	0.01	0.06	0.30	0.31	<0.00	0.04	0.08	0.01
MB11Mg-4	5.25	10.61	8.79	65.42	0.79	7.20	0.88	1.30	0.24	0.02	<0.044	0.40	2.85	7.31	0.96	2.15	0.18
MB11Mg-40	4.24	0.79	0.43	6.10	0.33	<0.33	<0.00	0.00	0.02	0.01	0.05	<0.28	0.08	<0.00	<0.00	0.00	<0.00
MB11Mg-5	13.13	1.35	0.54	36.91	0.33	1.09	0.08	0.14	0.05	0.04	<0.042	0.34	0.22	<0.00	0.04	0.16	0.01
MB11Mg-6	8.43	0.53	<0.25	8.15	0.39	<0.4	0.02	0.01	0.01	<0.0105	<0.047	<0.23	0.07	0.16	0.01	<0.0055	<0.0045
MB11Mg-7	4.99	1.87	<0.21	17.20	0.32	1.52	0.17	0.30	0.05	0.01	<0.067	0.49	0.76	0.86	0.11	0.15	0.01
MB11Mg-8	7.78	1.16	<0.24	15.17	0.43	1.63	0.05	0.10	0.03	0.01	<0.05	<0.25	0.42	<0.00	0.03	0.05	0.02
MB11Mg-9	2.68	1.26	<0.21	16.55	0.34	1.32	0.09	0.23	0.02	<0.00	0.05	0.28	0.48	0.19	0.07	0.10	0.01
MB12HmClean-1	0.53	1.48	<0.24	4.42	0.06	1.17	0.24	0.60	0.44	0.06	0.07	0.34	0.14	3.09	0.43	0.49	0.05
MB12HmClean-10	0.06	<0.3	0.38	3.53	<0.032	3.44	0.86	0.59	0.24	0.01	0.35	1.28	0.12	<0.00	0.19	0.33	0.05
MB12HmClean-11	<0.024	<0.169	<0.25	0.59	<0.049	0.25	0.10	0.05	0.02	0.00	0.15	<0.207	<0.07	0.19	0.02	0.03	0.00
MB12HmClean-12	<0.029	<0.3	0.38	2.34	0.05	1.91	0.15	0.14	<0.00	<0.00	0.10	<0.238	0.09	<0.00	0.02	0.07	0.02
MB12HmClean-13	0.52	12.20	0.30	25.70	0.73	5.76	0.60	5.67	0.52	0.10	0.19	0.60	11.71	8.46	2.02	1.56	0.14
MB12HmClean-14	2.67	1.02	0.71	14.77	0.11	1.45	1.08	0.40	<0.00	<0.0086	<0.055	0.34	0.16	0.38	0.14	0.28	0.03
MB12HmClean-15	0.09	0.88	<0.29	2.01	0.09	<0.25	0.07	1.86	0.03	<0.00	0.20	<0.203	<0.074	0.26	2.26	1.81	0.12
MB12HmClean-16	0.62	1.10	4.69	18.22	0.10	2.24	0.85	2.02	0.06	0.05	0.15	0.79	0.57	0.88	0.91	1.24	0.12
MB12HmClean-17	2.35	1.99	1.76	8.09	0.30	5.68	3.03	2.03	0.11	0.27	0.13	0.56	0.82	1.14	0.52	1.13	0.11

Analysis no.	Nd	Sm	Eu	Gd	Tb	Dy	Ho	Er	Tm	Yb	Lu	W	Pb208	Th	U
MB11Mg-15	0.36	0.08	0.06	0.11	0.02	0.09	0.02	0.06	0.01	0.05	0.01	0.06	0.08	<0.00	<0.00
MB11Mg-16	<0.00	<0.0313	<0.0114	<0.00	<0.0042	<0.00	<0.00	<0.00	<0.004	<0.00	<0.0058	0.11	0.09	0.00	0.00
MB11Mg-17	<0.00	<0.00	<0.00	<0.027	<0.00	<0.00	<0.0037	0.01	<0.0034	<0.00	0.00	0.07	5.92	0.00	0.03
MB11Mg-18	<0.00	<0.0274	<0.0071	0.02	<0.00	<0.015	<0.00	0.01	<0.00	<0.00	<0.00	0.25	2.46	<0.00	0.05
MB11Mg-19	0.02	0.01	0.01	<0.0319	<0.00	0.01	0.01	0.00	<0.004	0.01	0.00	0.56	6.10	<0.00	0.02
MB11Mg-2	0.07	0.03	0.02	0.02	0.00	0.04	0.01	0.03	0.00	0.05	0.01	0.26	5.40	0.00	0.16
MB11Mg-20	<0.00	<0.00	<0.007	<0.038	<0.0036	<0.015	0.00	<0.00	0.00	<0.00	<0.0036	0.51	4.09	0.00	0.05
MB11Mg-21	0.01	0.01	<0.0093	0.02	<0.00	0.01	<0.00	<0.00	0.00	0.01	<0.0033	0.71	5.04	0.01	0.04
MB11Mg-22	0.03	0.04	<0.0088	<0.034	0.01	0.01	0.01	0.01	0.00	<0.035	0.01	1.24	4.52	0.01	0.06
MB11Mg-23	0.10	<0.0242	0.03	0.04	0.01	0.04	0.01	0.07	0.00	<0.014	0.01	<0.02	0.10	<0.00	0.00
MB11Mg-24	0.02	<0.00	0.01	<0.00	<0.00	0.01	<0.0035	<0.00	0.00	0.01	<0.00	0.01	0.20	<0.00	<0.00
MB11Mg-25	0.16	0.01	0.01	0.01	<0.0038	0.03	0.01	0.02	0.00	<0.017	0.00	0.01	0.54	<0.00	0.00
MB11Mg-26	0.02	<0.0272	0.01	0.03	0.00	0.01	0.01	<0.01	0.00	0.01	0.00	0.43	0.60	0.00	0.02
MB11Mg-27	0.03	<0.0265	<0.00	0.01	0.00	<0.0146	0.00	0.02	<0.0034	<0.00	<0.00	0.49	5.49	0.01	0.03
MB11Mg-28	0.20	<0.024	0.02	0.03	<0.0032	0.04	0.01	0.01	0.00	0.01	0.00	0.04	0.67	<0.00	0.01
MB11Mg-29	<0.00	<0.00	<0.0064	<0.035	<0.0033	<0.0137	<0.0034	<0.0102	<0.00	<0.00	<0.0046	<0.00	0.42	0.00	0.00
MB11Mg-3	0.02	<0.03	0.00	<0.03	<0.00	0.02	<0.0041	0.01	<0.0038	<0.0178	0.00	0.13	2.92	<0.00	0.05
MB11Mg-30	0.22	0.07	0.03	0.12	<0.006	0.05	0.02	0.05	0.01	0.05	0.01	0.14	5.70	0.00	0.04
MB11Mg-31	0.35	0.01	0.06	<0.046	0.01	0.05	0.02	0.05	0.01	0.05	0.00	0.07	0.30	<0.00	0.00
MB11Mg-32	<0.00	0.01	0.00	<0.034	<0.00	<0.00	<0.00	<0.00	<0.00308	<0.0144	<0.00	0.70	4.08	<0.00	0.03
MB11Mg-33	0.10	0.02	0.01	0.06	<0.0033	0.01	0.01	0.03	0.00	0.02	0.00	0.12	1.80	0.01	0.01
MB11Mg-34	0.01	<0.00	<0.00	<0.00	0.00	<0.00	<0.00	<0.0141	0.00	0.01	<0.00	0.20	3.97	<0.00	0.02
MB11Mg-35	<0.00	<0.00	<0.0101	<0.048	<0.00	<0.00	<0.00	<0.00	0.00	0.01	0.00	0.15	3.97	0.00	0.02
MB11Mg-36	0.24	0.07	0.02	0.04	0.01	0.04	0.01	0.03	<0.00	0.06	0.00	0.04	1.11	<0.00	<0.0031
MB11Mg-37	0.33	0.16	0.05	0.18	0.03	0.13	0.04	0.14	0.02	0.12	0.04	0.20	0.70	<0.00	0.01
MB11Mg-38	0.01	<0.00	<0.0071	<0.048	<0.0037	0.02	0.00	0.01	<0.00	<0.00	0.00	1.46	6.28	<0.00	0.11
MB11Mg-39	0.03	0.04	0.02	<0.027	0.00	0.01	0.00	0.02	<0.0048	0.01	0.00	0.62	2.76	0.00	0.01
MB11Mg-4	0.84	0.29	0.11	0.28	0.03	0.16	0.03	0.12	0.01	0.11	0.01	<0.0156	0.02	<0.00	0.00
MB11Mg-40	<0.00	<0.00	0.00	<0.03	0.00	<0.00	<0.00	<0.00	<0.00	<0.00	<0.004	0.38	6.33	<0.00	0.09
MB11Mg-5	0.07	0.01	0.02	0.03	<0.00	0.02	0.00	<0.0106	0.00	<0.0153	0.00	0.04	0.46	<0.00	0.01
MB11Mg-6	<0.00	<0.00	<0.0075	<0.029	<0.0039	<0.0161	0.00	<0.012	<0.0052	0.01	<0.00	0.01	0.06	<0.00	<0.0035
MB11Mg-7	0.06	<0.041	0.02	<0.029	0.00	0.03	<0.0056	0.03	0.00	0.02	0.00	0.01	18.56	<0.00	0.02
MB11Mg-8	<0.027	<0.00	0.01	0.02	0.00	0.03	0.00	0.00	0.00	0.01	0.00	0.05	16.17	<0.00	0.13
MB11Mg-9	0.06	0.01	0.02	0.03	0.00	0.05	0.01	0.03	0.00	0.02	0.00	0.04	1.01	<0.00	0.03
MB12HmClean-1	0.12	<0.023	0.02	0.08	<0.0031	0.08	0.02	0.08	0.01	0.07	0.01	5.20	5.57	0.03	0.37
MB12HmClean-10	0.18	0.03	0.03	0.05	0.01	0.10	0.02	0.04	0.01	0.05	0.00	1.02	12.29	0.03	0.08
MB12HmClean-11	0.03	<0.00	0.01	<0.0253	0.01	<0.00	0.00	0.01	0.00	0.01	<0.0033	0.55	0.35	<0.00	0.08
MB12HmClean-12	0.07	<0.00	<0.0081	<0.031	<0.0042	0.02	0.00	0.01	0.00	0.02	<0.0041	0.50	0.99	<0.00	0.03
MB12HmClean-13	0.71	0.10	0.15	0.28	0.04	0.22	0.09	0.28	0.03	0.29	0.05	2.10	17.21	0.03	0.11
MB12HmClean-14	0.17	0.03	0.04	<0.024	0.01	0.06	0.02	0.03	0.01	0.04	0.01	0.01	45.05	<0.0054	0.03
MB12HmClean-15	0.46	0.03	0.02	0.08	0.01	0.13	0.06	0.34	0.06	0.45	0.11	9.73	0.40	<0.00	0.11
MB12HmClean-16	0.54	0.18	0.04	0.19	0.03	0.17	0.06	0.20	0.02	0.22	0.03	5.88	8.62	0.01	0.17
MB12HmClean-17	0.54	0.19	0.10	0.25	0.02	0.19	0.04	0.14	0.02	0.20	0.03	0.99	18.48	0.00	0.12

Position	Deposit	Lithology	Sample no.	Analysis no.	Texture	Mg	Al	Si	P	Ca	Sc	Ti	V	Cr	Mn
Middle	Warrior	ORE	MB12	MB12HmClean-18	clean martite	1.51	22.17	<126.76	11.29	110.08	0.49	2.37	2.20	<1.47	7.05
Middle	Warrior	ORE	MB12	MB12HmClean-19	clean martite	15.90	156.99	426.92	106.77	<98.75	1.52	1.96	18.90	<1.26	115.88
Middle	Warrior	ORE	MB12	MB12HmClean-2	clean martite	1.61	34.90	662.42	<10.37	115.67	<0.169	<0.82	0.15	<1.35	2.90
Middle	Warrior	ORE	MB12	MB12HmClean-20	clean martite	1.75	36.40	216.77	<10.14	<76.94	0.31	<0.77	2.76	<1.22	34.40
Middle	Warrior	ORE	MB12	MB12HmClean-21	clean martite	13.90	59.66	544.31	22.36	<93.66	0.41	3.00	24.44	1.76	83.63
Middle	Warrior	ORE	MB12	MB12HmClean-3	clean martite	71.35	160.06	698.41	87.11	<101.68	2.13	1.70	3.96	<1.26	308.81
Middle	Warrior	ORE	MB12	MB12HmClean-4	clean martite	11.38	62.44	267.62	17.93	<93.43	0.70	1.04	21.84	<1.13	69.27
Middle	Warrior	ORE	MB12	MB12HmClean-5	clean martite	0.85	38.64	<125.24	<10.49	<106.31	0.54	<0.71	0.68	<1.29	3.70
Middle	Warrior	ORE	MB12	MB12HmClean-6	clean martite	112.48	89.56	579.35	<9.77	<100.14	0.50	2.33	27.65	2.12	107.83
Middle	Warrior	ORE	MB12	MB12HmClean-7	clean martite	44.42	211.38	534.09	323.09	<106.59	2.53	2.80	3.18	1.30	257.99
Middle	Warrior	ORE	MB12	MB12HmClean-8	clean martite	69.20	73.95	1834.20	18.00	<92.47	0.20	2.40	17.71	<1.07	165.09
Middle	Warrior	ORE	MB12	MB12HmClean-9	clean martite	2.04	27.38	182.84	40.85	<84.69	0.61	<1.06	0.45	<1.43	10.39
Middle	Warrior	ORE	MB12	MB12Mg-1	magnetite	87.16	104.71	5639.29	24.11	<120.92	0.22	2.78	6.11	<1.39	358.30
Middle	Warrior	ORE	MB12	MB12Mg-10	magnetite	15.83	55.93	344.21	<12.33	105.81	<0.194	4.27	6.97	3.52	368.86
Middle	Warrior	ORE	MB12	MB12Mg-11	magnetite	14.34	61.00	<138.62	<10.1	<101.85	<0.164	2.75	1.00	<1.31	359.80
Middle	Warrior	ORE	MB12	MB12Mg-12	magnetite	107.10	73.81	416.10	<10.87	<93.23	0.19	2.17	0.96	<1.41	405.30
Middle	Warrior	ORE	MB12	MB12Mg-13	magnetite	110.10	87.37	3229.39	<10.73	<115.48	0.25	1.21	0.69	<1.34	558.65
Middle	Warrior	ORE	MB12	MB12Mg-14	magnetite	30.61	66.38	<146.11	15.98	<97.75	0.24	2.70	0.99	<1.4	398.93
Middle	Warrior	ORE	MB12	MB12Mg-15	magnetite	32.76	128.53	278.24	<11.36	<109.75	0.18	8.00	5.51	<1.47	362.58
Middle	Warrior	ORE	MB12	MB12Mg-16	magnetite	28.21	57.46	483.38	16.29	115.57	<0.176	3.72	0.92	<1.42	423.74
Middle	Warrior	ORE	MB12	MB12Mg-17	magnetite	14.83	64.85	271.05	16.91	<108.69	<0.166	2.80	1.12	<1.34	396.00
Middle	Warrior	ORE	MB12	MB12Mg-18	magnetite	29.99	69.50	496.66	14.20	<92.67	0.18	2.25	0.86	<1.5	481.30
Middle	Warrior	ORE	MB12	MB12Mg-19	magnetite	107.03	87.05	4703.61	28.46	<125.56	<0.196	32.26	1.03	<1.64	442.47
Middle	Warrior	ORE	MB12	MB12Mg-2	magnetite	23.80	74.98	<140.35	15.71	<116.01	<0.138	<0.97	0.75	<1.21	302.51
Middle	Warrior	ORE	MB12	MB12Mg-20	magnetite	78.67	70.30	332.12	<11.54	155.74	<0.165	2.27	1.02	<1.67	132.18
Middle	Warrior	ORE	MB12	MB12Mg-21	magnetite	31.13	71.35	197.48	<12.19	<110.75	<0.173	1.50	1.05	<1.28	279.66
Middle	Warrior	ORE	MB12	MB12Mg-22	magnetite	53.87	71.97	346.65	<12.24	<121.76	0.18	4.10	0.84	3.26	304.91
Middle	Warrior	ORE	MB12	MB12Mg-23	magnetite	110.53	68.19	538.20	34.91	<129.92	<0.169	3.34	0.88	<1.28	282.50
Middle	Warrior	ORE	MB12	MB12Mg-24	magnetite	97.52	71.87	292.42	<12.16	157.90	<0.168	2.48	0.94	1.28	362.93
Middle	Warrior	ORE	MB12	MB12Mg-25	magnetite	207.56	75.41	5558.03	20.49	<122.02	0.25	3.70	1.02	1.37	558.21
Middle	Warrior	ORE	MB12	MB12Mg-26	magnetite	176.38	77.27	6379.98	<12.19	<127.07	0.23	3.26	0.83	<1.58	356.80
Middle	Warrior	ORE	MB12	MB12Mg-27	magnetite	63.96	66.24	4606.86	<11.23	<115.61	<0.173	1.38	0.86	<1.39	465.00
Middle	Warrior	ORE	MB12	MB12Mg-28	magnetite	123.57	80.40	2301.63	<10.87	<105.59	<0.195	3.43	1.09	<1.66	365.95
Middle	Warrior	ORE	MB12	MB12Mg-29	magnetite	17.48	57.74	<163.35	<13.16	<123.04	<0.214	2.02	1.12	<1.5	426.38
Middle	Warrior	ORE	MB12	MB12Mg-3	magnetite	37.45	69.06	<143.77	<11.64	<122.99	<0.163	1.70	0.91	<1.28	429.47
Middle	Warrior	ORE	MB12	MB12Mg-30	magnetite	30.97	56.52	<166.6	<13.38	<118.35	<0.199	3.51	2.10	<1.63	382.30
Middle	Warrior	ORE	MB12	MB12Mg-31	magnetite	121.53	92.11	2994.42	31.28	148.90	0.29	4.06	1.49	<1.51	453.20
Middle	Warrior	ORE	MB12	MB12Mg-32	magnetite	30.65	59.50	<140.13	<10.43	117.74	<0.169	1.96	0.80	<1.43	501.55
Middle	Warrior	ORE	MB12	MB12Mg-33	magnetite	74.03	57.01	1908.92	<13.14	229.38	<0.198	1.65	0.96	<1.57	434.68
Middle	Warrior	ORE	MB12	MB12Mg-34	magnetite	86.15	57.64	1680.22	<11.21	<98.53	<0.174	3.45	1.05	<1.48	311.76
Middle	Warrior	ORE	MB12	MB12Mg-35	magnetite	24.19	55.14	284.05	<12.23	<129.27	0.30	1.69	0.80	<1.5	502.57
Middle	Warrior	ORE	MB12	MB12Mg-36	magnetite	57.75	128.84	2472.77	14.77	132.43	<0.211	3.58	1.18	<1.41	386.71

Analysis no.	Co	Ni	Cu	Zn	Ga	As	Sr	Y	Zr	Nb	Mo	Sn	Sb	Ba	La	Ce	Pr
MB12HmClean-18	0.05	0.57	<0.28	1.01	0.04	<0.21	0.05	0.09	0.05	0.01	0.12	<0.194	<0.043	0.09	0.06	0.07	0.01
MB12HmClean-19	0.60	0.89	4.56	11.56	0.11	3.50	1.79	1.21	0.09	0.00	0.14	0.68	0.65	1.06	0.38	0.64	0.07
MB12HmClean-2	<0.024	0.28	<0.23	0.97	<0.063	<0.35	0.11	0.09	<0.00	<0.00	0.20	<0.19	<0.031	0.10	0.02	0.03	<0.004
MB12HmClean-20	0.05	0.44	<0.27	0.62	<0.054	<0.38	0.05	1.82	<0.00	<0.00	0.31	<0.208	<0.082	0.16	1.89	1.26	0.07
MB12HmClean-21	0.43	0.54	<0.26	5.57	0.07	1.51	0.40	0.95	0.25	0.03	<0.044	<0.202	0.39	1.12	0.39	0.55	0.06
MB12HmClean-3	2.49	2.24	2.47	11.76	0.44	7.54	2.92	1.35	0.02	<0.017	<0.063	0.22	0.17	0.23	0.48	0.93	0.12
MB12HmClean-4	0.90	0.84	0.53	7.14	0.11	3.45	0.91	0.85	0.03	0.01	0.02	<0.206	0.33	0.18	0.26	0.45	0.07
MB12HmClean-5	<0.033	<0.26	<0.27	0.94	0.14	0.37	0.01	0.06	<0.00	<0.00	0.11	0.20	<0.043	0.11	0.01	0.03	0.01
MB12HmClean-6	0.51	1.13	0.30	3.66	0.15	2.23	0.45	1.70	0.19	0.01	0.04	0.28	0.40	2.48	0.67	0.87	0.09
MB12HmClean-7	3.45	1.75	4.27	16.11	0.42	2.79	3.50	1.88	0.02	0.01	0.09	<0.21	0.11	1.48	0.74	0.95	0.07
MB12HmClean-8	0.40	2.54	<0.25	8.54	0.11	3.95	1.50	5.29	0.42	0.04	0.03	0.19	0.42	6.82	1.47	2.20	0.22
MB12HmClean-9	<0.041	0.34	<0.24	<0.51	<0.044	0.55	0.27	0.10	0.02	<0.00	0.09	<0.191	0.25	0.27	0.06	0.09	0.01
MB12Mg-1	4.24	1.57	<0.3	8.81	0.19	2.39	0.50	0.63	0.16	0.04	0.05	0.33	0.55	3.57	0.46	0.52	0.05
MB12Mg-10	2.64	1.50	<0.27	10.62	0.07	1.45	0.07	0.26	0.03	<0.00	0.07	<0.24	0.21	0.55	0.14	0.17	0.02
MB12Mg-11	5.45	0.45	<0.25	8.14	0.14	0.41	0.05	0.14	<0.00	<0.00	0.04	<0.228	0.20	0.15	0.06	0.10	0.01
MB12Mg-12	1.44	0.92	<0.24	6.15	0.06	<0.31	0.01	0.04	0.01	0.00	<0.045	<0.2	<0.075	0.08	0.06	0.04	0.01
MB12Mg-13	1.66	0.51	<0.26	9.86	<0.056	1.17	0.16	0.18	<0.03	0.01	0.03	<0.24	<0.086	1.00	0.10	0.18	0.02
MB12Mg-14	3.43	0.89	<0.29	6.27	<0.061	<0.42	<0.0145	0.05	<0.00	<0.0103	0.03	<0.22	<0.078	<0.00	0.07	0.08	0.00
MB12Mg-15	2.91	2.20	0.36	3.66	0.29	<0.34	<0.00	0.01	<0.0269	0.00	0.04	<0.24	<0.08	<0.00	0.01	0.01	0.00
MB12Mg-16	1.66	1.13	<0.26	5.47	<0.049	<0.29	<0.0142	0.02	0.18	0.27	0.07	0.48	<0.048	<0.00	0.01	0.01	<0.00
MB12Mg-17	4.71	1.22	<0.3	10.76	<0.071	<0.39	0.08	0.04	<0.00	<0.00	<0.047	0.41	<0.071	0.20	0.02	0.03	0.00
MB12Mg-18	3.65	1.07	<0.29	9.20	<0.05	0.55	0.03	0.07	<0.00	0.01	<0.047	<0.229	0.09	<0.00	0.02	0.02	0.00
MB12Mg-19	3.35	2.01	<0.35	10.72	0.18	2.91	0.29	0.80	0.11	<0.00	0.03	0.44	0.25	9.99	0.46	0.78	0.05
MB12Mg-2	0.66	0.87	<0.3	5.90	<0.046	<0.45	<0.00	0.01	0.02	<0.00	<0.00	<0.22	<0.086	<0.00	0.01	0.01	<0.00
MB12Mg-20	0.39	1.55	<0.28	4.16	<0.071	<0.36	<0.00	<0.0136	0.02	<0.00	<0.047	0.42	<0.079	<0.00	<0.00	<0.0054	0.00
MB12Mg-21	0.82	1.01	<0.29	4.73	0.06	<0.39	0.07	<0.0074	<0.00	<0.00	0.02	0.30	<0.058	0.10	<0.00	0.00	<0.00
MB12Mg-22	1.28	1.54	<0.32	4.85	0.06	<0.39	0.44	0.02	0.11	0.25	<0.049	0.36	<0.09	0.23	0.02	0.03	<0.00
MB12Mg-23	1.97	1.64	<0.33	3.35	0.10	<0.32	<0.00	0.03	<0.00	<0.00	<0.047	0.32	<0.079	<0.00	0.02	0.02	0.00
MB12Mg-24	2.22	2.25	<0.3	6.34	<0.073	<0.41	<0.00	0.02	<0.027	<0.00	0.06	0.24	<0.05	<0.00	0.02	0.03	0.00
MB12Mg-25	5.12	1.31	0.75	10.14	0.14	2.93	0.37	0.92	0.06	0.00	<0.049	0.48	0.36	2.04	0.33	0.69	0.05
MB12Mg-26	3.14	1.04	<0.28	4.15	<0.068	3.92	0.23	0.69	0.05	0.00	<0.05	<0.25	0.23	2.20	0.51	0.65	0.04
MB12Mg-27	6.66	1.29	<0.29	10.38	<0.051	1.84	0.13	0.25	0.03	0.00	<0.00	<0.23	0.13	1.48	0.14	0.22	0.02
MB12Mg-28	3.45	0.66	<0.29	3.13	0.05	1.82	0.15	0.22	0.02	0.00	0.03	<0.23	0.34	1.73	0.32	0.30	0.02
MB12Mg-29	7.37	1.17	<0.28	8.25	0.07	0.68	0.02	0.03	<0.00	<0.00	<0.054	<0.24	0.18	<0.00	0.01	0.03	0.00
MB12Mg-3	2.36	<0.38	<0.26	7.00	<0.055	<0.38	<0.00	0.03	0.02	0.01	<0.046	0.29	<0.049	0.11	0.02	0.03	0.00
MB12Mg-30	1.42	0.70	<0.35	8.19	0.07	<0.36	0.01	0.03	<0.0319	<0.00	<0.08	0.39	<0.085	0.09	0.01	0.01	0.00
MB12Mg-31	2.22	0.80	1.18	4.98	<0.066	1.89	1.02	0.19	0.12	<0.00	<0.047	0.24	<0.092	1.13	0.20	0.20	0.02
MB12Mg-32	8.57	1.09	<0.28	6.81	0.12	<0.39	<0.00	0.01	<0.00	<0.00	0.06	0.22	<0.083	<0.00	0.03	0.02	<0.0043
MB12Mg-33	7.30	0.47	<0.3	9.92	0.12	2.21	0.08	0.25	0.05	0.04	<0.078	0.29	0.27	3.31	0.30	0.29	0.03
MB12Mg-34	1.91	1.43	<0.3	6.82	<0.052	0.85	0.18	0.13	0.01	<0.0107	0.08	0.28	0.09	0.27	0.07	0.08	0.01
MB12Mg-35	3.62	0.79	<0.33	10.67	<0.052	<0.34	<0.00	<0.008	0.01	<0.00	0.03	0.47	<0.073	<0.00	0.01	0.00	<0.00
MB12Mg-36	7.37	2.55	<0.36	10.59	0.33	4.45	0.18	0.62	0.07	0.03	<0.048	<0.23	0.51	1.24	0.72	0.77	0.04

Analysis no.	Nd	Sm	Eu	Gd	Tb	Dy	Ho	Er	Tm	Yb	Lu	W	Pb208	Th	U
MB12HmClean-18	0.03	<0.00	0.01	0.02	<0.0033	0.01	0.00	0.00	<0.00317	<0.0148	0.00	0.54	0.45	0.00	0.06
MB12HmClean-19	0.32	0.15	0.04	0.13	0.02	0.07	0.02	0.11	0.01	0.07	0.02	1.41	17.11	0.01	0.15
MB12HmClean-2	0.01	<0.00	<0.0066	0.01	<0.00	<0.02	<0.0035	<0.00	0.00	<0.022	0.00	6.57	0.19	<0.00	0.14
MB12HmClean-20	0.42	0.05	0.01	0.06	0.01	0.15	0.03	0.27	0.04	0.26	0.05	17.68	0.18	0.01	0.14
MB12HmClean-21	0.15	0.06	0.03	0.05	0.01	0.09	0.03	0.09	<0.0034	0.06	0.02	1.78	1.92	0.03	0.17
MB12HmClean-3	0.52	0.10	0.09	0.27	0.02	0.16	0.03	0.10	0.01	0.09	0.02	0.02	115.47	0.01	0.08
MB12HmClean-4	0.41	0.14	0.06	0.15	0.02	0.14	0.02	0.08	0.01	0.13	0.02	0.81	102.14	0.00	0.09
MB12HmClean-5	0.03	0.01	<0.0111	0.01	0.00	0.01	0.00	0.01	<0.00315	<0.00	<0.0033	1.09	0.11	<0.00	0.22
MB12HmClean-6	0.32	0.07	0.07	0.09	0.02	0.11	0.03	0.13	0.02	0.13	0.03	1.63	3.68	0.03	0.15
MB12HmClean-7	0.40	0.09	0.06	0.14	0.01	0.15	0.03	0.08	0.01	0.14	0.01	0.24	17.23	0.00	0.09
MB12HmClean-8	0.84	0.11	0.18	0.25	0.04	0.32	0.09	0.30	0.06	0.41	0.07	2.88	8.31	0.17	0.28
MB12HmClean-9	0.06	<0.026	0.01	<0.036	<0.0048	0.01	0.01	0.01	<0.00	0.02	<0.0033	0.19	1.93	<0.00	0.05
MB12Mg-1	0.19	0.03	0.04	<0.026	0.00	0.03	0.01	0.04	0.01	0.04	0.01	0.10	2.56	<0.006	0.03
MB12Mg-10	0.06	0.03	0.02	<0.041	0.00	0.01	0.01	0.02	0.00	0.03	0.00	1.77	25.86	0.01	0.29
MB12Mg-11	0.04	0.01	0.02	0.02	0.00	0.00	0.01	<0.0111	0.00	0.02	0.00	0.01	<0.027	<0.00	<0.00
MB12Mg-12	<0.00	<0.0276	0.00	<0.00	<0.0037	0.00	0.00	<0.00	<0.00	<0.0162	<0.0036	0.05	3.03	0.02	0.03
MB12Mg-13	0.05	<0.00	<0.0075	0.02	0.00	<0.00	<0.0039	<0.00	0.00	0.01	0.01	0.03	0.23	<0.00	0.01
MB12Mg-14	<0.00	<0.00	<0.00	<0.0285	0.00	<0.00	<0.0039	<0.00	<0.00	<0.00	0.01	0.21	4.08	0.00	0.09
MB12Mg-15	<0.00	0.01	<0.00	0.01	<0.0039	<0.00	<0.00	<0.012	<0.00	<0.00	0.00	0.11	3.91	<0.00	0.06
MB12Mg-16	<0.0241	<0.0282	0.01	<0.039	0.00	<0.00	0.00	0.00	<0.00	<0.00	<0.0037	0.13	2.97	<0.00	0.05
MB12Mg-17	0.01	<0.041	<0.00	0.01	<0.00	0.00	<0.00	<0.00	0.00	<0.0172	<0.0038	1.51	2.04	0.01	0.06
MB12Mg-18	0.01	<0.00	0.00	<0.04	<0.00	0.00	0.00	<0.0118	0.00	0.01	0.00	0.72	3.67	0.00	0.07
MB12Mg-19	0.11	0.01	0.02	<0.031	<0.0042	0.03	0.01	0.04	0.01	0.09	0.02	0.05	0.68	<0.00	0.01
MB12Mg-2	<0.00	<0.00	0.00	0.01	0.00	0.01	<0.0036	0.00	<0.00	0.01	0.00	0.11	0.10	<0.00	0.00
MB12Mg-20	0.01	<0.0293	0.00	0.01	<0.0039	<0.00	<0.00	<0.00	<0.00	<0.00	0.00	0.77	0.48	<0.0065	0.01
MB12Mg-21	0.01	<0.027	<0.00	<0.038	<0.00	<0.00	<0.00	<0.0112	<0.00	<0.00	<0.00	0.11	0.19	0.01	0.00
MB12Mg-22	<0.0258	<0.00	<0.0077	<0.03	0.00	<0.0164	<0.00	<0.00	<0.00	0.00	0.00	0.02	<0.044	0.00	<0.0037
MB12Mg-23	<0.025	<0.00	<0.00	<0.0287	0.00	<0.00	0.00	<0.00	<0.00	<0.00	0.00	0.59	0.06	<0.00	<0.00
MB12Mg-24	<0.00	<0.00	0.00	<0.00	<0.00	0.01	0.00	<0.00	<0.00	<0.00	<0.0039	<0.00	0.12	<0.0065	<0.0036
MB12Mg-25	0.24	0.05	0.03	<0.042	0.01	0.04	0.01	0.05	0.01	0.08	0.02	0.08	0.11	0.00	0.00
MB12Mg-26	0.10	0.01	0.01	0.01	0.00	0.02	0.01	0.04	<0.004	0.05	0.01	1.32	1.02	0.01	0.01
MB12Mg-27	0.04	0.01	0.00	<0.029	0.00	0.01	<0.007	0.01	0.00	0.01	0.00	<0.00	0.05	<0.00	<0.00
MB12Mg-28	0.13	<0.00	0.01	<0.029	<0.0039	0.02	<0.004	0.01	<0.0037	0.04	0.01	0.00	0.02	<0.00	<0.00
MB12Mg-29	<0.028	<0.00	<0.0085	<0.033	0.00	<0.00	<0.00	0.00	<0.0042	0.00	<0.0043	<0.00	0.58	<0.00	0.01
MB12Mg-3	<0.00	<0.0285	<0.0073	<0.00	<0.0038	0.01	0.00	0.00	0.00	<0.00	<0.00	0.08	0.22	<0.00	<0.0038
MB12Mg-30	<0.00	<0.00	<0.00	<0.06	<0.00	<0.0191	<0.00	<0.00	0.00	<0.0206	<0.0045	<0.00	<0.025	<0.00	<0.00
MB12Mg-31	0.05	0.04	<0.0104	0.02	<0.0038	<0.016	<0.0039	0.03	0.00	0.03	0.00	0.03	<0.037	<0.00	<0.00
MB12Mg-32	<0.00	<0.028	<0.00	<0.00	<0.0037	0.01	<0.00	<0.00	<0.00	<0.00	0.00	0.80	5.36	<0.00	0.01
MB12Mg-33	0.05	<0.048	<0.0123	0.01	<0.0064	<0.0186	0.00	<0.0139	0.00	0.03	0.01	2.00	1.57	0.00	0.00
MB12Mg-34	<0.00	<0.03	0.00	<0.03	0.00	<0.00	<0.004	<0.0173	0.00	<0.0176	0.01	0.71	0.20	<0.00	0.00
MB12Mg-35	<0.00	0.01	0.00	0.03	<0.004	0.00	<0.00	<0.0122	<0.0038	<0.00	<0.00	1.03	0.47	<0.00	<0.0037
MB12Mg-36	0.21	0.01	<0.0076	0.05	0.01	0.05	0.01	0.11	<0.0065	0.07	0.02	<0.021	0.38	<0.00	0.00

Position	Deposit	Lithology	Sample no.	Analysis no.	Texture	Mg	Al	Si	P	Ca	Sc	Ti	V	Cr	Mn
Middle	Warrior	ORE	MB12	MB12Mg-37	magnetite	59.96	60.15	4481.04	<10.78	<104.08	<0.176	1.98	1.10	<1.46	451.56
Middle	Warrior	ORE	MB12	MB12Mg-38	magnetite	8.67	51.16	<133.1	<10.11	93.51	<0.156	1.36	10.38	<1.28	256.83
Middle	Warrior	ORE	MB12	MB12Mg-39	magnetite	16.70	70.29	<156.58	<12.65	<111.09	<0.204	3.04	0.90	<1.35	403.56
Middle	Warrior	ORE	MB12	MB12Mg-4	magnetite	58.78	74.04	571.25	28.91	<104.39	<0.175	2.29	1.34	<1.37	340.14
Middle	Warrior	ORE	MB12	MB12Mg-40	magnetite	27.93	55.45	292.42	20.14	<119.81	<0.173	2.10	0.99	<1.67	430.29
Middle	Warrior	ORE	MB12	MB12Mg-5	magnetite	26.47	78.93	<156.65	<11.43	<111.77	<0.169	1.77	0.83	1.64	460.97
Middle	Warrior	ORE	MB12	MB12Mg-6	magnetite	93.77	80.12	6366.25	<11.51	<110.32	<0.168	2.12	0.82	<1.5	497.49
Middle	Warrior	ORE	MB12	MB12Mg-7	magnetite	19.89	62.88	261.53	<10.81	178.48	<0.188	1.39	0.56	<1.3	375.73
Middle	Warrior	ORE	MB12	MB12Mg-8	magnetite	185.82	145.00	9454.69	<11.95	<108.05	<0.196	1.98	0.79	<1.42	484.39
Middle	Warrior	ORE	MB12	MB12Mg-9	magnetite	9.61	47.67	<159.13	17.56	<124.29	<0.174	2.03	0.39	<1.48	238.03
North	Princess	ORE	MB1	MB1Hm-1	clean martite	20.51	149.53	394.23	58.48	169.36	<0.168	4.92	3.55	2.02	6.90
North	Princess	ORE	MB1	MB1Hm-10	clean martite	94.99	134.87	594.32	11.45	<95.6	<0.132	1.90	1.95	2.88	9.32
North	Princess	ORE	MB1	MB1Hm-11	clean martite	85.59	144.12	1371.71	33.11	<103.86	0.27	1.66	3.23	1.71	7.56
North	Princess	ORE	MB1	MB1Hm-12	clean martite	99.84	149.64	990.39	23.48	144.31	0.16	1.49	3.78	3.55	9.35
North	Princess	ORE	MB1	MB1Hm-13	clean martite	2.81	100.33	296.22	23.30	<86.42	<0.165	0.88	3.36	2.57	2.05
North	Princess	ORE	MB1	MB1Hm-15	clean martite	12.43	146.03	477.73	27.56	<114.8	0.15	<1.04	3.72	2.67	8.55
North	Princess	ORE	MB1	MB1Hm-16	clean martite	68.99	163.32	421.44	55.04	116.73	0.50	<0.74	3.03	1.37	7.05
North	Princess	ORE	MB1	MB1Hm-17	clean martite	72.89	113.64	424.72	31.66	<100.99	<0.12	0.94	2.36	<1.1	14.61
North	Princess	ORE	MB1	MB1Hm-18	clean martite	71.32	169.37	4687.94	101.69	<106.32	0.15	1.09	2.78	1.64	11.55
North	Princess	ORE	MB1	MB1Hm-19	clean martite	103.98	156.83	1025.07	24.16	<90.94	<0.157	<1	3.18	3.04	19.51
North	Princess	ORE	MB1	MB1Hm-2	clean martite	33.75	122.46	1049.37	27.17	<119	0.22	1.09	3.55	<1.03	13.59
North	Princess	ORE	MB1	MB1Hm-20	clean martite	25.93	110.97	1248.05	41.40	155.31	0.18	<0.88	2.44	2.86	10.85
North	Princess	ORE	MB1	MB1Hm-3	clean martite	33.57	118.05	981.95	27.79	<108.69	0.23	2.24	2.23	2.71	6.88
North	Princess	ORE	MB1	MB1Hm-4	clean martite	26.99	168.14	1859.62	37.21	<110.91	<0.159	1.42	3.45	2.79	11.27
North	Princess	ORE	MB1	MB1Hm-5	clean martite	81.13	113.13	2919.72	19.89	<112.53	0.33	<1	3.06	7.66	5.80
North	Princess	ORE	MB1	MB1Hm-6	clean martite	27.51	119.44	661.76	36.24	<131.01	0.20	2.47	3.00	3.59	3.81
North	Princess	ORE	MB1	MB1Hm-7	clean martite	45.77	140.33	22450.74	42.12	179.70	<0.161	<0.92	3.55	7.17	12.13
North	Princess	ORE	MB1	MB1Hm-8	clean martite	43.81	135.20	9542.45	22.79	<99.79	<0.154	3.91	3.34	5.77	7.69
North	Princess	ORE	MB1	MB1Hm-9	clean martite	229.39	123.55	1437.03	13.09	<76.73	0.27	2.56	2.86	1.78	44.69
North	Princess	ORE	MB1	MB1Mg-1	magnetite	148.71	145.45	1596.55	<13	215.71	0.18	<0.96	2.57	1.55	21.79
North	Princess	ORE	MB1	MB1Mg-10	magnetite	120.34	160.42	608.23	17.79	<133.44	<0.153	<0.77	2.14	1.54	26.60
North	Princess	ORE	MB1	MB1Mg-11	magnetite	134.11	146.76	281.82	<11.28	<128.42	<0.164	<0.91	2.00	1.30	23.40
North	Princess	ORE	MB1	MB1Mg-12	magnetite	175.50	149.01	669.09	14.78	192.81	<0.163	<1.29	2.27	<1.21	19.64
North	Princess	ORE	MB1	MB1Mg-13	magnetite	762.24	1056.01	1811.38	19.59	130.24	<0.198	<1.09	2.26	1.98	25.29
North	Princess	ORE	MB1	MB1Mg-14	magnetite	161.46	97.85	557.43	21.78	<121.33	<0.142	<1.03	1.89	1.92	19.21
North	Princess	ORE	MB1	MB1Mg-15	magnetite	466.69	154.14	1234.48	12.72	<116.08	0.23	<0.92	2.04	1.81	22.92
North	Princess	ORE	MB1	MB1Mg-16	magnetite	304.88	165.29	6734.31	1529.14	<148.14	0.82	<1.34	1.86	<1.67	97.12
North	Princess	ORE	MB1	MB1Mg-17	magnetite	159.64	113.57	387.01	<10.59	<95.38	<0.147	<0.94	1.91	2.47	17.95
North	Princess	ORE	MB1	MB1Mg-18	magnetite	216.48	99.05	1882.38	<11.04	<91.99	0.14	<0.88	2.30	5.22	17.47
North	Princess	ORE	MB1	MB1Mg-19	magnetite	223.71	145.10	1568.40	24.74	225.83	<0.169	<0.97	2.23	3.58	17.92
North	Princess	ORE	MB1	MB1Mg-2	magnetite	244.04	152.18	666.29	<11.34	<141.22	0.13	<0.75	1.96	<1.21	17.47
North	Princess	ORE	MB1	MB1Mg-20	magnetite	328.47	146.01	817.88	32.37	<83.36	<0.14	<0.98	2.14	<1.18	22.21
North	Princess	ORE	MB1	MB1Mg-3	magnetite	102.80	128.56	806.43	15.13	<170.71	0.33	<1.11	2.56	3.50	21.14

Analysis no.	Co	Ni	Cu	Zn	Ga	As	Sr	Y	Zr	Nb	Mo	Sn	Sb	Ba	La	Ce	Pr
MB12Mg-37	4.79	1.33	0.51	9.74	<0.068	2.07	0.18	0.29	0.10	<0.0107	0.01	0.35	0.13	1.68	0.30	0.32	0.02
MB12Mg-38	2.06	1.27	0.82	6.87	0.10	0.67	0.23	0.41	0.07	<0.00	0.02	0.27	0.27	0.42	0.20	0.26	0.01
MB12Mg-39	5.62	1.34	<0.28	12.26	0.06	0.53	0.06	0.16	<0.00	<0.00	<0.051	0.45	0.09	<0.00	0.07	0.08	0.01
MB12Mg-4	4.02	1.41	0.30	11.42	<0.061	0.95	0.40	0.10	<0.00	0.01	<0.046	0.23	<0.06	<0.00	0.05	0.06	<0.0044
MB12Mg-40	2.92	0.88	<0.27	7.48	0.14	<0.34	<0.00	0.02	<0.038	<0.00	<0.068	0.37	<0.095	0.07	0.02	0.01	<0.0045
MB12Mg-5	1.98	1.22	<0.29	12.88	0.06	<0.38	0.03	<0.0079	0.01	<0.0105	0.05	<0.26	<0.05	<0.00	0.00	<0.0077	<0.00
MB12Mg-6	1.44	1.06	<0.26	13.37	<0.066	1.75	0.44	0.25	0.11	0.02	0.05	<0.24	0.22	1.89	0.14	0.19	0.02
MB12Mg-7	2.41	0.56	<0.28	9.21	0.06	<0.37	0.03	0.07	<0.00	<0.00	<0.044	0.21	0.14	<0.103	0.04	0.06	0.01
MB12Mg-8	1.89	1.77	<0.35	8.80	<0.054	3.14	0.56	0.47	0.13	0.05	<0.00	<0.27	0.29	4.78	0.40	0.64	0.07
MB12Mg-9	3.66	0.71	<0.27	7.56	<0.047	0.73	0.11	0.23	<0.00	<0.00	<0.051	<0.24	0.29	<0.00	0.09	0.12	0.02
MB1Hm-1	0.53	5.14	0.80	3.58	0.19	3.95	0.15	0.18	0.12	0.00	0.77	<0.21	1.15	0.84	0.07	0.10	0.03
MB1Hm-10	<0.039	3.06	<0.181	1.17	0.15	2.43	0.14	0.03	0.05	0.00	0.79	<0.177	0.20	1.47	0.04	0.04	0.00
MB1Hm-11	0.13	7.02	0.61	3.27	0.26	4.70	0.12	0.24	0.15	0.01	1.31	<0.184	1.20	1.75	0.27	0.31	0.05
MB1Hm-12	0.08	5.12	0.60	2.72	0.14	3.59	0.12	0.18	0.09	<0.0092	0.78	<0.178	0.58	1.04	0.15	0.21	0.02
MB1Hm-13	0.06	6.72	<0.212	1.26	0.28	2.56	0.07	0.12	0.07	0.00	1.36	<0.18	0.57	1.09	0.08	0.09	0.01
MB1Hm-15	0.61	5.91	1.35	2.59	0.11	5.31	0.22	0.16	0.13	0.00	1.36	<0.197	1.28	1.86	0.16	0.22	0.03
MB1Hm-16	0.08	2.76	0.50	1.30	0.10	3.61	0.17	0.15	0.14	<0.00	0.43	<0.177	0.84	0.98	0.18	0.22	0.03
MB1Hm-17	1.67	27.96	0.42	3.59	0.31	5.55	0.18	0.30	0.05	<0.0083	0.24	0.20	1.90	0.98	0.09	0.12	0.03
MB1Hm-18	0.31	7.14	0.33	1.08	0.17	3.88	0.27	0.49	0.14	0.01	0.73	0.23	1.30	1.82	0.19	0.26	0.03
MB1Hm-19	0.48	7.91	0.50	4.18	0.23	5.42	0.19	0.28	0.11	<0.0126	1.23	0.42	1.66	2.71	0.30	0.33	0.03
MB1Hm-2	1.14	18.25	2.29	2.49	0.35	5.99	0.17	0.34	0.07	0.01	0.77	<0.175	2.13	1.78	0.44	0.46	0.05
MB1Hm-20	0.87	4.65	11.11	3.31	0.17	5.47	0.34	0.26	0.12	0.01	1.26	0.21	2.16	1.13	0.38	0.45	0.06
MB1Hm-3	<0.04	5.12	<0.23	0.81	0.24	2.96	0.19	0.11	0.03	<0.00	1.21	0.19	0.74	0.63	0.08	0.12	0.02
MB1Hm-4	0.14	3.62	0.42	0.46	0.19	3.27	0.11	0.22	0.04	<0.01	1.82	0.26	0.99	1.80	0.18	0.24	0.03
MB1Hm-5	0.10	2.99	3.07	0.84	0.21	4.63	0.19	0.31	0.06	0.01	1.02	<0.181	1.93	1.02	0.26	0.31	0.04
MB1Hm-6	0.05	4.35	1.15	2.82	0.14	2.98	0.11	0.19	0.05	0.00	1.17	<0.211	1.22	0.73	0.14	0.12	0.03
MB1Hm-7	0.86	6.77	0.29	3.46	0.22	4.19	0.21	0.21	<0.038	0.00	1.06	<0.202	1.72	0.91	0.15	0.20	0.03
MB1Hm-8	0.85	7.89	<0.235	1.71	0.19	3.29	0.10	0.06	0.07	0.00	0.93	<0.18	3.24	1.35	0.03	0.04	0.01
MB1Hm-9	0.60	7.19	1.63	5.14	0.22	3.61	0.18	0.24	0.06	<0.0083	0.54	<0.176	1.42	0.60	0.17	0.19	0.03
MB1Mg-1	3.70	54.08	<0.205	17.78	0.38	0.70	0.16	0.01	0.01	<0.00	0.03	<0.219	0.20	0.26	0.02	0.04	0.00
MB1Mg-10	4.01	54.35	<0.26	17.10	0.49	2.29	0.20	0.01	<0.00	<0.00	0.03	<0.204	0.67	0.26	0.03	0.02	0.00
MB1Mg-11	3.36	52.58	<0.26	22.18	0.30	0.75	0.26	0.01	<0.00	<0.00	<0.00	<0.188	0.24	0.21	0.03	0.04	<0.0044
MB1Mg-12	4.05	55.48	<0.27	13.43	0.50	<0.36	0.03	0.01	<0.00	<0.00	0.03	<0.24	0.18	<0.00	0.02	0.01	0.00
MB1Mg-13	4.57	54.56	<0.22	12.15	0.64	3.01	0.19	0.16	0.05	0.00	0.04	<0.198	1.04	0.53	0.09	0.09	0.02
MB1Mg-14	3.72	50.00	<0.25	13.36	0.41	0.64	0.02	0.01	0.01	<0.00	<0.00	0.31	0.26	<0.106	0.01	0.01	0.00
MB1Mg-15	3.90	49.63	0.53	16.03	0.31	2.52	0.86	0.09	<0.036	0.00	0.03	<0.19	0.23	0.26	0.05	0.04	0.01
MB1Mg-16	3.66	43.97	<0.32	37.53	0.48	8.24	0.34	3.25	0.06	<0.00	0.16	<0.29	1.87	1.53	1.26	1.67	0.22
MB1Mg-17	3.71	47.87	0.41	13.89	0.30	0.69	0.12	<0.0101	<0.00	<0.00	0.03	<0.185	0.16	<0.00	0.01	0.03	<0.0042
MB1Mg-18	4.11	51.68	0.32	18.18	0.39	0.68	0.13	0.01	0.01	<0.00	<0.00	<0.192	0.21	0.08	0.00	0.01	<0.0044
MB1Mg-19	3.27	51.53	0.32	10.02	0.37	0.83	0.03	0.03	0.01	<0.00	<0.05	<0.229	0.47	<0.00	0.03	0.03	0.01
MB1Mg-2	3.53	47.30	<0.213	13.99	0.46	0.39	0.04	0.02	<0.00	<0.00	<0.00	<0.168	0.30	0.23	0.03	0.02	0.00
MB1Mg-20	3.41	54.26	2.45	11.20	0.17	1.34	0.04	0.06	0.01	<0.00	<0.04	<0.169	0.32	0.16	0.05	0.04	0.00
MB1Mg-3	3.57	51.41	<0.27	17.51	0.37	0.60	0.21	0.02	0.01	<0.00	<0.054	<0.24	0.27	0.08	0.03	0.02	0.01

Analysis no.	Nd	Sm	Eu	Gd	Tb	Dy	Ho	Er	Tm	Yb	Lu	W	Pb208	Th	U
MB12Mg-37	0.07	0.02	0.01	<0.03	0.00	0.02	<0.00	0.02	0.00	0.05	0.01	0.03	0.12	<0.00	<0.00
MB12Mg-38	0.04	0.03	0.01	<0.037	<0.0049	0.02	0.00	0.03	0.00	0.05	0.01	0.07	0.27	<0.00	<0.0062
MB12Mg-39	0.05	0.02	<0.008	0.05	<0.0041	0.01	<0.0042	<0.018	0.00	0.01	<0.0041	0.67	14.81	<0.0065	0.02
MB12Mg-4	0.02	<0.00	0.01	<0.00	0.00	<0.0221	0.00	<0.00	0.00	<0.0169	0.00	<0.00	<0.034	0.00	<0.00
MB12Mg-40	<0.025	<0.00	<0.0076	<0.0293	<0.00	<0.00	0.00	0.00	0.00	<0.0175	<0.0039	0.68	1.13	0.00	0.01
MB12Mg-5	<0.0251	<0.00	<0.00	<0.029	<0.0039	0.01	<0.004	<0.012	<0.00	<0.0173	<0.00	0.12	0.40	<0.00	0.00
MB12Mg-6	0.09	<0.029	0.01	<0.04	<0.00	0.00	<0.0055	<0.0167	0.00	0.02	0.01	0.02	0.05	<0.00	0.00
MB12Mg-7	0.02	<0.027	0.01	<0.00	<0.0036	<0.00	0.00	0.02	<0.00	<0.00	0.00	1.22	5.71	<0.00	0.03
MB12Mg-8	0.19	0.04	0.03	0.03	0.01	0.01	0.01	0.03	0.00	0.06	0.01	1.01	0.58	0.00	0.01
MB12Mg-9	0.09	<0.044	0.02	<0.031	0.00	0.01	<0.0042	<0.0128	0.00	0.04	0.00	0.76	0.89	0.03	0.15
MB1Hm-1	0.07	0.03	0.01	0.03	0.00	0.02	0.00	0.01	0.00	0.01	<0.0038	3.36	1.54	0.00	0.15
MB1Hm-10	0.03	<0.0252	<0.00	0.01	<0.0034	<0.00	<0.00	<0.00	<0.00	<0.00	<0.00	3.22	2.39	<0.00	0.05
MB1Hm-11	0.14	0.02	0.02	0.03	0.00	0.02	0.00	0.01	0.00	0.02	0.00	3.73	1.78	0.00	0.25
MB1Hm-12	0.06	0.03	0.01	0.03	<0.0034	0.01	0.01	0.02	<0.00	<0.015	0.00	3.30	1.75	<0.00	0.17
MB1Hm-13	0.07	0.01	0.00	0.03	<0.0037	0.02	0.00	<0.0113	0.00	0.00	0.00	2.71	0.99	0.00	0.11
MB1Hm-15	0.10	0.03	<0.0071	0.05	0.00	0.01	0.01	<0.0113	0.00	0.00	0.00	5.06	2.05	<0.0063	0.22
MB1Hm-16	<0.14	0.02	0.01	0.02	0.00	0.00	0.00	<0.0099	0.00	0.01	<0.0044	4.48	1.74	0.00	0.17
MB1Hm-17	0.08	0.01	0.02	0.01	0.00	0.04	<0.0031	0.02	0.00	0.01	0.00	2.03	2.34	0.00	0.22
MB1Hm-18	0.22	0.04	0.03	0.04	0.00	0.05	0.01	0.02	0.00	0.02	0.00	3.45	2.41	0.00	0.23
MB1Hm-19	0.24	0.03	0.03	0.02	<0.0033	0.01	0.00	0.02	0.00	0.04	0.00	4.41	2.26	<0.00	0.21
MB1Hm-2	0.32	0.02	0.03	0.07	0.01	0.03	0.01	0.03	0.00	0.03	<0.00	2.44	2.15	<0.00	0.99
MB1Hm-20	0.22	0.05	0.03	0.04	<0.003	0.02	0.01	0.02	0.00	0.03	0.01	4.18	5.16	0.01	0.30
MB1Hm-3	0.08	0.03	0.02	0.04	0.00	0.01	<0.0035	<0.0105	<0.00	<0.0152	0.00	2.62	3.66	0.00	0.15
MB1Hm-4	0.18	0.01	0.00	0.05	<0.0037	<0.015	0.00	0.02	0.00	0.01	0.00	9.57	1.62	<0.00	0.14
MB1Hm-5	0.16	0.10	0.02	<0.026	0.01	0.02	0.01	0.01	0.00	0.01	0.00	4.51	1.83	<0.00	0.31
MB1Hm-6	0.10	0.04	0.02	0.03	0.00	0.01	0.01	0.01	0.00	0.01	<0.00	3.13	0.99	<0.00	0.25
MB1Hm-7	0.15	0.04	0.02	0.03	<0.004	0.03	0.00	0.01	0.00	<0.018	<0.0055	4.90	1.64	<0.00	0.23
MB1Hm-8	0.03	0.01	0.00	0.05	0.00	0.01	0.00	0.01	<0.00	<0.00	<0.00	1.80	2.70	<0.00	0.12
MB1Hm-9	0.14	<0.033	0.01	0.04	0.01	0.01	<0.0031	<0.00	0.00	0.01	0.00	2.89	1.27	0.00	0.18
MB1Mg-1	<0.026	0.01	<0.0077	<0.03	<0.00	0.01	<0.00	0.00	<0.00	<0.00	<0.0039	0.10	0.32	<0.00	0.00
MB1Mg-10	0.04	0.01	<0.0153	0.01	<0.004	<0.00	<0.00	<0.00	0.00	<0.00	<0.00	1.18	0.24	<0.00	<0.00
MB1Mg-11	0.03	<0.00	<0.00	<0.028	<0.00	<0.0154	<0.00	<0.00	<0.00	<0.00	0.00	0.16	0.50	<0.00	0.00
MB1Mg-12	<0.00	0.01	0.00	<0.032	<0.00	<0.00	<0.0043	0.01	<0.00	<0.019	0.00	0.16	0.13	<0.00	0.00
MB1Mg-13	0.06	0.01	0.01	0.02	<0.0045	0.02	0.00	0.01	0.00	<0.0201	<0.0044	0.27	0.81	<0.00	0.08
MB1Mg-14	0.02	0.01	<0.00	<0.0281	<0.00	<0.00	<0.00	<0.00	<0.00	0.01	<0.00	0.06	0.23	<0.00	0.00
MB1Mg-15	0.05	0.01	<0.0073	<0.049	<0.00	0.02	<0.00	0.02	<0.00	0.01	<0.0037	0.32	1.54	<0.00	0.02
MB1Mg-16	0.96	0.24	0.21	0.37	0.05	0.31	0.05	0.17	0.02	0.11	0.02	1.01	3.09	<0.00	0.17
MB1Mg-17	0.02	<0.00	<0.0098	0.01	<0.00	<0.0147	<0.00	<0.00	0.00	<0.00	<0.00	0.18	0.10	<0.00	0.00
MB1Mg-18	<0.00	<0.0286	<0.0074	<0.00	<0.00	<0.00	<0.00	<0.00	0.00	<0.00	<0.0037	0.30	0.16	<0.00	<0.0051
MB1Mg-19	<0.027	0.01	0.00	<0.00	<0.0073	0.00	<0.00	<0.00	0.00	0.00	0.00	0.04	0.08	<0.00	0.00
MB1Mg-2	<0.022	<0.0257	0.00	<0.025	<0.00	<0.00	0.00	<0.00	<0.00	<0.00	<0.00	0.08	0.79	<0.00	0.01
MB1Mg-20	0.04	0.01	0.00	<0.043	0.00	<0.00	0.00	0.01	0.00	<0.00	0.00	0.10	0.23	<0.00	0.01
MB1Mg-3	0.02	<0.034	<0.0089	0.01	<0.00	0.00	<0.00	<0.0141	0.00	0.00	<0.0045	0.31	0.17	<0.00	0.01

Position	Deposit	Lithology	Sample no.	Analysis no.	Texture	Mg	Al	Si	P	Ca	Sc	Ti	V	Cr	Mn
North	Princess	ORE	MB1	MB1Mg-4	magnetite	134.50	88.92	768.79	27.61	494.38	<0.184	<0.98	2.38	1.49	20.43
North	Princess	ORE	MB1	MB1Mg-5	magnetite	134.26	114.24	305.60	21.07	<146.58	<0.175	0.77	2.21	<1.35	21.76
North	Princess	ORE	MB1	MB1Mg-6	magnetite	89.15	107.10	413.95	29.96	<151.21	<0.15	0.94	1.88	<1.36	17.96
North	Princess	ORE	MB1	MB1Mg-7	magnetite	135.58	72.48	168.45	41.29	265.21	<0.181	<1.18	1.90	<1.2	19.27
North	Princess	ORE	MB1	MB1Mg-8	magnetite	408.81	131.72	4292.66	<12.16	<130.2	0.21	<0.96	2.04	<1.27	22.61
North	Princess	ORE	MB1	MB1Mg-9	magnetite	122.82	101.01	490.51	22.24	<120.81	<0.145	1.20	2.13	<1.08	28.17
South	Chieftain	ORE	MB21	MB21HmPorous-1	porous martite	48.69	638.81	3442.89	378.19	106.07	0.53	6.66	2.72	1.18	526.41
South	Chieftain	ORE	MB21	MB21HmPorous-10	porous martite	38.36	90.29	1155.24	68.21	121.71	0.17	2.25	1.35	<0.67	236.82
South	Chieftain	ORE	MB21	MB21HmPorous-11	porous martite	34.02	88.89	1002.22	62.65	<46.63	0.12	6.38	1.17	<0.59	226.56
South	Chieftain	ORE	MB21	MB21HmPorous-12	porous martite	39.95	38.60	999.41	44.07	67.16	<0.062	15.71	1.29	<0.66	214.11
South	Chieftain	ORE	MB21	MB21HmPorous-13	porous martite	35.00	123.83	1251.63	68.24	108.50	<0.078	2.13	1.59	<0.51	192.47
South	Chieftain	ORE	MB21	MB21HmPorous-14	porous martite	40.77	333.40	1907.69	297.94	<46.68	0.21	2.21	6.14	0.94	295.36
South	Chieftain	ORE	MB21	MB21HmPorous-15	porous martite	45.69	291.03	2545.41	318.11	<53.44	<0.088	3.87	2.06	0.62	291.36
South	Chieftain	ORE	MB21	MB21HmPorous-16	porous martite	25.81	90.63	966.19	52.57	<44.37	0.12	6.67	2.13	<0.59	149.84
South	Chieftain	ORE	MB21	MB21HmPorous-17	porous martite	52.66	923.24	5647.00	922.59	<42.1	0.54	5.76	1.51	1.09	518.82
South	Chieftain	ORE	MB21	MB21HmPorous-18	porous martite	39.89	58.06	1212.22	63.61	86.21	<0.07	26.35	0.95	0.71	252.45
South	Chieftain	ORE	MB21	MB21HmPorous-19	porous martite	89.85	495.33	3735.72	371.16	97.52	0.33	85.63	4.40	<0.58	625.94
South	Chieftain	ORE	MB21	MB21HmPorous-2	porous martite	55.76	350.60	1835.46	81.24	63.59	0.19	4.31	17.42	1.32	259.21
South	Chieftain	ORE	MB21	MB21HmPorous-20	porous martite	61.61	358.84	1348.70	72.20	69.61	0.20	2.42	3.60	1.89	445.38
South	Chieftain	ORE	MB21	MB21HmPorous-3	porous martite	16.29	199.39	758.24	34.08	56.86	0.10	2.46	1.18	<0.53	184.19
South	Chieftain	ORE	MB21	MB21HmPorous-4	porous martite	125.28	1050.03	6513.75	769.87	<81.58	1.04	4.61	4.52	<0.89	920.18
South	Chieftain	ORE	MB21	MB21HmPorous-5	porous martite	59.46	1042.74	3762.01	463.91	<54.1	0.54	3.11	3.83	1.16	536.41
South	Chieftain	ORE	MB21	MB21HmPorous-6	porous martite	46.81	110.16	1183.07	59.54	56.86	<0.072	0.64	1.21	1.05	216.29
South	Chieftain	ORE	MB21	MB21HmPorous-7	porous martite	113.92	43.36	1937.34	84.20	116.25	<0.059	1.41	1.46	<0.42	251.27
South	Chieftain	ORE	MB21	MB21HmPorous-8	porous martite	91.81	36.16	1801.92	75.54	65.73	<0.067	1.02	1.07	0.97	204.20
South	Chieftain	ORE	MB21	MB21HmPorous-9	porous martite	111.77	64.42	1308.55	56.14	<52.31	0.18	2.90	1.31	<0.55	233.38
South	Knight	ORE	MB22b	MB22bHm-1	clean martite	286.72	872.29	1064.30	12.84	<39.55	0.33	69.72	373.50	3.13	518.32
South	Knight	ORE	MB22b	MB22bHm-10	clean martite	395.81	900.85	874.96	12.04	162.71	<0.11	40.85	64.13	2.48	314.26
South	Knight	ORE	MB22b	MB22bHm-11	clean martite	252.40	960.14	849.09	22.32	202.00	<0.091	46.98	192.36	9.12	386.69
South	Knight	ORE	MB22b	MB22bHm-12	clean martite	199.25	765.28	731.58	13.75	53.69	<0.104	37.23	12.72	0.81	328.46
South	Knight	ORE	MB22b	MB22bHm-13	clean martite	184.62	879.23	404.65	14.73	46.68	0.09	44.64	11.06	1.26	495.24
South	Knight	ORE	MB22b	MB22bHm-14	clean martite	100.98	808.46	354.27	7.15	65.10	<0.109	43.39	33.38	3.90	241.05
South	Knight	ORE	MB22b	MB22bHm-15	clean martite	427.96	994.59	1037.88	10.95	<53.99	0.18	51.43	29.36	3.19	445.27
South	Knight	ORE	MB22b	MB22bHm-16	clean martite	216.29	943.08	504.13	<5.36	147.82	<0.085	51.16	9.40	26.89	379.50
South	Knight	ORE	MB22b	MB22bHm-18	clean martite	149.78	747.25	1068.10	<6.37	<58.39	<0.104	70.69	21.64	1.46	424.01
South	Knight	ORE	MB22b	MB22bHm-19	clean martite	235.89	774.81	1971.65	25.12	<55.64	0.20	20.49	1309.07	3.99	729.35
South	Knight	ORE	MB22b	MB22bHm-2	clean martite	120.32	791.53	807.05	21.95	58.76	0.13	49.45	118.31	<0.83	378.63
South	Knight	ORE	MB22b	MB22bHm-20	clean martite	186.83	1095.32	977.03	17.62	<37.84	0.23	70.57	8.28	<0.64	279.47
South	Knight	ORE	MB22b	MB22bHm-3	clean martite	114.92	543.93	711.32	9.43	53.44	0.53	47.20	141.76	1.33	207.18
South	Knight	ORE	MB22b	MB22bHm-4	clean martite	159.74	835.63	735.80	<5.85	<52.13	0.19	56.32	24.58	<0.79	479.87
South	Knight	ORE	MB22b	MB22bHm-5	clean martite	136.93	1080.12	278.24	13.51	70.23	0.18	67.72	3.15	<0.56	61.22
South	Knight	ORE	MB22b	MB22bHm-6	clean martite	371.40	863.48	829.41	22.15	51.13	0.16	52.19	497.25	1.30	570.21
South	Knight	ORE	MB22b	MB22bHm-7	clean martite	142.91	635.86	1385.80	13.45	<33.56	0.21	63.16	527.94	6.70	1037.48

Analysis no.	Co	Ni	Cu	Zn	Ga	As	Sr	Y	Zr	Nb	Mo	Sn	Sb	Ba	La	Ce	Pr
MB1Mg-4	4.21	48.28	<0.24	11.40	0.48	0.97	0.14	0.08	0.03	<0.00	0.07	<0.213	0.53	0.10	0.08	0.08	0.01
MB1Mg-5	4.16	49.72	<0.25	18.83	0.52	0.58	0.14	<0.008	<0.0271	<0.0108	<0.05	<0.192	0.23	0.17	0.03	0.03	0.01
MB1Mg-6	4.11	44.86	0.38	13.81	0.32	0.52	0.08	0.01	<0.00	<0.00	<0.044	<0.181	0.35	<0.00	0.04	0.03	0.00
MB1Mg-7	3.95	50.12	<0.249	8.50	0.44	1.03	0.08	0.08	<0.00	<0.0116	0.03	<0.216	0.51	<0.122	0.04	0.02	0.01
MB1Mg-8	3.82	49.50	0.23	16.22	0.36	2.55	0.18	0.02	<0.00	<0.00	<0.047	<0.208	0.69	0.44	0.02	0.04	0.01
MB1Mg-9	3.91	50.73	0.22	11.09	0.23	0.63	0.05	0.03	<0.024	<0.00	<0.00	<0.2	0.36	0.08	0.04	0.05	0.01
MB21HmPorous-1	6.78	19.76	7.76	83.63	0.16	149.35	0.48	6.75	0.43	0.06	0.78	0.17	0.73	0.21	2.47	4.00	0.40
MB21HmPorous-10	0.75	1.47	1.44	13.32	0.04	37.81	1.28	1.43	0.10	0.01	0.53	<0.085	0.72	0.05	0.62	1.14	0.14
MB21HmPorous-11	0.35	1.47	1.02	11.20	0.09	22.71	0.98	1.24	0.08	0.01	0.65	<0.067	0.44	0.43	0.52	1.02	0.10
MB21HmPorous-12	0.45	0.82	0.67	8.19	0.11	22.61	0.88	1.14	0.07	0.00	0.38	<0.077	0.63	0.16	0.42	0.83	0.10
MB21HmPorous-13	1.03	1.88	2.32	11.64	0.06	41.54	1.17	1.23	0.15	<0.0044	0.53	0.13	0.92	0.50	0.68	1.17	0.15
MB21HmPorous-14	4.85	17.10	4.26	94.25	0.08	70.96	1.09	4.38	0.13	0.03	0.67	0.10	0.67	0.20	1.24	1.94	0.24
MB21HmPorous-15	3.57	14.20	2.88	71.39	0.17	57.01	1.44	4.54	0.13	0.04	0.78	<0.087	0.56	0.30	1.36	2.12	0.24
MB21HmPorous-16	0.40	1.48	0.83	6.61	0.07	29.65	1.03	0.86	0.07	0.00	0.55	0.13	1.05	0.31	0.43	0.72	0.08
MB21HmPorous-17	12.38	55.45	9.57	292.13	0.09	107.77	0.46	13.11	0.34	0.01	1.14	<0.078	0.39	0.16	3.27	5.32	0.62
MB21HmPorous-18	0.20	0.67	0.29	12.54	0.05	8.27	1.26	1.63	0.01	0.01	0.72	<0.061	0.23	0.29	0.52	0.99	0.13
MB21HmPorous-19	4.99	17.21	3.45	82.97	0.13	65.52	1.70	7.83	0.31	0.05	0.95	0.18	0.43	0.42	2.00	3.20	0.35
MB21HmPorous-2	3.14	4.93	6.89	33.68	0.06	59.78	1.76	1.90	0.37	0.04	0.83	0.19	0.65	0.90	0.85	1.42	0.13
MB21HmPorous-20	6.62	4.25	8.39	30.65	0.17	78.34	1.25	1.77	0.47	0.03	1.77	0.15	1.36	0.49	0.80	1.39	0.14
MB21HmPorous-3	3.11	2.27	3.75	14.73	0.14	64.02	0.07	0.44	0.23	0.02	0.24	0.09	1.23	<0.00	0.26	0.60	0.06
MB21HmPorous-4	10.47	36.16	7.76	174.97	0.15	147.59	0.84	13.43	1.02	0.06	1.29	0.35	0.39	0.33	3.21	5.99	0.65
MB21HmPorous-5	8.00	28.09	8.99	144.23	0.11	128.32	1.09	8.20	0.77	0.11	1.31	0.44	0.72	0.20	2.32	4.13	0.43
MB21HmPorous-6	0.89	2.39	1.87	11.29	0.07	35.12	1.27	1.57	0.08	0.02	0.64	0.07	0.76	0.52	0.62	1.24	0.13
MB21HmPorous-7	0.34	1.90	1.53	8.20	0.09	13.13	2.02	2.33	0.01	0.01	0.55	0.08	0.51	2.33	2.32	2.76	0.27
MB21HmPorous-8	0.42	0.89	1.03	8.63	0.06	13.34	1.25	1.80	0.12	0.02	0.65	<0.067	0.62	1.19	1.23	1.61	0.17
MB21HmPorous-9	0.81	1.53	0.61	6.63	0.11	29.58	1.39	1.60	0.08	0.02	0.46	0.14	0.81	0.49	0.72	1.23	0.14
MB22bHm-1	8.60	13.60	2.07	11.53	0.46	3.51	0.78	1.20	0.06	0.06	0.06	0.51	0.55	24.79	0.43	0.52	0.05
MB22bHm-10	1.66	1.05	1.84	9.93	0.23	3.40	0.80	0.77	<0.023	0.02	<0.056	0.78	0.53	9.42	0.43	0.48	0.04
MB22bHm-11	3.23	10.94	2.11	13.98	0.51	4.37	1.41	0.64	0.01	0.00	0.09	0.65	0.20	24.29	0.31	0.34	0.02
MB22bHm-12	6.28	5.46	1.24	10.90	0.37	4.47	0.63	1.18	0.04	0.01	0.03	0.69	0.45	9.15	0.36	0.62	0.06
MB22bHm-13	68.24	4.42	11.26	11.97	0.30	2.30	0.27	0.47	0.03	0.01	<0.024	0.55	0.35	10.95	0.12	0.19	0.03
MB22bHm-14	1.96	2.08	0.31	8.00	0.33	1.72	0.24	0.63	<0.0162	<0.0064	0.07	0.47	0.22	7.58	0.32	0.36	0.03
MB22bHm-15	3.40	3.86	4.34	7.10	0.43	3.00	0.69	0.83	<0.00	0.01	0.04	0.56	0.45	17.42	0.25	0.36	0.04
MB22bHm-16	56.70	1.81	39.64	17.50	0.31	3.02	0.73	0.45	0.03	0.01	0.07	0.74	0.16	12.67	0.15	0.17	0.02
MB22bHm-18	7.68	1.43	5.29	17.18	0.30	3.04	1.14	0.69	0.04	0.01	0.06	0.68	0.23	19.48	0.23	0.35	0.03
MB22bHm-19	4.96	64.58	3.07	15.39	1.08	3.56	0.88	1.27	0.41	0.05	0.30	0.23	0.96	47.97	0.66	0.68	0.05
MB22bHm-2	4.37	7.81	1.06	16.09	0.41	4.19	0.66	1.08	0.04	0.02	0.06	0.58	0.36	20.35	0.50	0.56	0.05
MB22bHm-20	2.88	6.91	2.13	17.04	0.48	6.92	0.75	0.72	0.30	2.12	1.69	1.19	0.11	16.14	0.25	0.25	0.03
MB22bHm-3	0.66	12.16	0.36	10.00	0.15	3.29	1.10	0.99	0.76	0.02	3.65	0.66	0.71	2.16	0.31	0.46	0.07
MB22bHm-4	2.39	3.89	7.42	11.21	0.34	4.35	1.05	1.59	<0.0203	0.01	0.08	0.61	0.78	17.02	0.46	0.77	0.11
MB22bHm-5	0.23	0.52	<0.139	15.74	0.22	0.56	0.02	0.06	<0.00	0.02	0.01	0.75	0.05	0.58	0.02	0.05	0.00
MB22bHm-6	1.65	22.98	0.45	15.71	0.46	1.85	0.40	0.66	0.05	0.01	0.09	0.63	0.35	17.02	0.39	0.39	0.03
MB22bHm-7	3.05	40.08	2.26	15.80	0.49	3.12	0.65	0.83	0.26	0.03	0.20	0.28	0.84	33.76	0.48	0.42	0.03

Analysis no.	Nd	Sm	Eu	Gd	Tb	Dy	Ho	Er	Tm	Yb	Lu	W	Pb208	Th	U
MB1Mg-4	0.07	<0.0306	0.00	0.01	0.00	0.01	0.00	0.02	<0.00	<0.00	0.00	0.28	0.22	<0.00	0.01
MB1Mg-5	0.02	0.02	0.00	<0.03	<0.0057	<0.00	<0.00	0.00	<0.00	<0.00	0.00	0.31	0.32	<0.00	<0.00
MB1Mg-6	0.02	0.01	<0.0125	<0.00	<0.00	0.01	<0.0038	0.00	<0.00	<0.00	0.00	0.27	0.35	<0.00	0.01
MB1Mg-7	0.01	<0.033	<0.0084	0.01	0.00	0.01	0.00	<0.0134	<0.00	<0.00	<0.006	0.04	0.29	<0.00	0.03
MB1Mg-8	<0.026	0.01	<0.00	<0.00	0.00	<0.0164	<0.00	<0.00	0.00	<0.0178	0.00	0.54	0.25	<0.00	0.01
MB1Mg-9	0.07	0.03	0.01	<0.03	0.00	<0.00	<0.00	0.01	<0.00	0.01	<0.00	0.29	0.60	<0.00	0.01
MB21HmPorous-1	1.75	0.31	0.30	0.49	0.07	0.49	0.11	0.37	0.04	0.24	0.05	0.23	84.42	0.10	1.09
MB21HmPorous-10	0.57	0.13	0.11	0.17	0.03	0.15	0.04	0.09	0.01	0.10	0.01	0.06	30.40	0.02	1.33
MB21HmPorous-11	0.48	0.11	0.08	0.11	0.03	0.11	0.02	0.05	0.01	0.04	0.01	0.08	22.60	0.02	1.09
MB21HmPorous-12	0.43	0.09	0.09	0.15	0.01	0.10	0.02	0.06	0.00	0.05	0.00	0.05	18.10	0.03	1.05
MB21HmPorous-13	0.59	0.14	0.09	0.19	0.02	0.13	0.02	0.10	0.01	0.09	0.01	0.11	28.53	0.03	1.51
MB21HmPorous-14	0.98	0.23	0.19	0.33	0.03	0.34	0.07	0.21	0.03	0.16	0.03	0.07	43.43	0.06	0.78
MB21HmPorous-15	1.11	0.23	0.20	0.43	0.04	0.29	0.08	0.25	0.03	0.21	0.03	0.15	47.60	0.03	1.61
MB21HmPorous-16	0.33	0.06	0.05	0.09	0.01	0.10	0.02	0.07	0.01	0.06	0.01	0.07	61.41	0.02	1.43
MB21HmPorous-17	2.73	0.59	0.46	0.88	0.12	0.82	0.19	0.59	0.07	0.43	0.07	0.07	76.57	0.05	0.58
MB21HmPorous-18	0.52	0.13	0.11	0.17	0.02	0.16	0.03	0.11	0.01	0.06	0.01	0.05	5.86	<0.00309	1.29
MB21HmPorous-19	1.68	0.45	0.31	0.54	0.07	0.57	0.12	0.43	0.05	0.37	0.06	0.33	60.78	0.07	1.82
MB21HmPorous-2	0.53	0.10	0.07	0.20	0.02	0.15	0.04	0.13	0.01	0.11	0.01	0.21	43.58	0.09	1.72
MB21HmPorous-20	0.62	0.18	0.09	0.15	0.02	0.13	0.04	0.10	0.01	0.10	0.02	0.17	65.74	0.10	1.17
MB21HmPorous-3	0.28	0.08	0.04	0.08	0.01	0.07	0.01	0.04	0.00	0.03	0.00	0.10	60.79	0.09	0.21
MB21HmPorous-4	2.78	0.75	0.63	0.87	0.12	0.89	0.22	0.67	0.08	0.50	0.10	0.23	80.47	0.12	1.43
MB21HmPorous-5	1.89	0.37	0.33	0.68	0.10	0.56	0.13	0.41	0.05	0.34	0.06	0.24	71.46	0.16	1.63
MB21HmPorous-6	0.56	0.14	0.11	0.20	0.02	0.15	0.03	0.10	0.02	0.08	0.01	0.12	20.41	0.02	1.54
MB21HmPorous-7	1.16	0.15	0.16	0.30	0.04	0.24	0.05	0.15	0.03	0.16	0.02	0.10	12.57	0.01	1.41
MB21HmPorous-8	0.72	0.13	0.11	0.18	0.02	0.13	0.04	0.10	0.01	0.12	0.02	0.13	14.33	0.02	1.41
MB21HmPorous-9	0.62	0.11	0.11	0.15	0.02	0.16	0.03	0.12	0.02	0.09	0.02	0.16	36.62	0.02	1.29
MB22bHm-1	0.23	0.05	0.06	0.09	0.01	0.09	0.02	0.07	0.01	0.06	0.01	0.32	5.55	0.01	8.14
MB22bHm-10	0.12	<0.017	0.01	0.03	0.01	0.04	0.01	0.03	0.00	0.04	0.01	1.16	3.96	0.02	1.99
MB22bHm-11	0.10	0.01	0.01	0.05	0.00	0.04	0.01	0.01	0.00	0.01	0.00	0.38	5.46	<0.0032	3.65
MB22bHm-12	0.32	0.12	0.06	0.12	0.02	0.12	0.02	0.09	0.01	0.07	0.01	0.08	3.46	<0.00	1.71
MB22bHm-13	0.09	0.03	0.02	<0.021	<0.0027	<0.0114	0.01	0.04	0.00	0.02	<0.00	0.09	2.20	0.00	0.50
MB22bHm-14	0.14	0.05	0.03	0.03	0.01	0.03	0.01	0.03	0.01	0.02	<0.0022	0.08	3.01	0.01	2.53
MB22bHm-15	0.15	0.05	0.03	0.08	0.01	0.07	0.01	0.03	0.01	0.04	0.01	0.12	3.35	0.02	1.55
MB22bHm-16	0.08	<0.00	0.01	0.03	0.00	0.02	0.01	0.02	0.00	0.03	0.00	0.07	2.52	0.00	0.58
MB22bHm-18	0.22	0.03	0.03	0.04	0.01	0.06	0.00	0.04	0.01	0.05	0.00	0.05	3.39	0.00	1.18
MB22bHm-19	0.20	0.02	0.03	0.04	0.01	0.09	0.03	0.06	0.01	0.05	0.01	1.05	10.64	0.05	18.03
MB22bHm-2	0.20	0.03	0.03	0.07	0.01	0.08	0.01	0.06	0.01	0.05	0.01	0.44	6.75	0.02	8.19
MB22bHm-20	0.10	0.02	0.01	0.02	0.01	0.03	0.01	0.03	0.01	0.01	0.00	0.58	4.53	0.02	0.57
MB22bHm-3	0.20	0.07	0.05	0.11	0.01	0.09	0.02	0.07	0.01	0.07	0.01	2.54	5.77	0.03	7.68
MB22bHm-4	0.42	0.10	0.09	0.10	0.02	0.20	0.02	0.06	0.01	0.06	0.01	0.17	4.87	0.00	3.31
MB22bHm-5	0.01	0.03	0.00	<0.0224	0.00	0.01	0.00	<0.0053	<0.00164	<0.0077	<0.00168	0.03	0.23	0.00	0.10
MB22bHm-6	0.07	0.02	0.01	0.03	0.00	0.03	0.01	0.03	0.01	0.05	0.01	0.30	6.01	0.02	9.27
MB22bHm-7	0.13	<0.0114	0.01	0.04	<0.0026	0.04	0.01	0.03	0.01	0.03	0.01	0.96	7.77	0.04	14.51

Position	Deposit	Lithology	Sample no.	Analysis no.	Texture	Mg	Al	Si	P	Ca	Sc	Ti	V	Cr	Mn
South	Knight	ORE	MB22b	MB22bHm-8	clean martite	164.12	759.44	1116.39	30.60	<35.96	0.50	69.99	304.11	6.38	370.39
South	Knight	ORE	MB22b	MB22bHm-9	clean martite	304.65	760.82	2074.36	13.28	109.77	0.23	23.86	1293.22	12.92	675.44
South	Knight	ORE	MB22b	MB22bMt-1	magnetite	1294.42	1017.60	1415.68	<6.8	58.05	0.23	54.20	3.69	<0.76	1368.44
South	Knight	ORE	MB22b	MB22bMt-10	magnetite	896.50	1127.54	1229.82	<6.26	52.28	<0.113	64.74	4.26	<0.79	702.13
South	Knight	ORE	MB22b	MB22bMt-11	magnetite	351.72	984.62	398.75	<6.04	60.12	<0.106	78.89	7.37	1.39	817.95
South	Knight	ORE	MB22b	MB22bMt-12	magnetite	15.72	208.37	187.25	17.74	<47.54	0.23	4.02	429.40	<0.73	151.12
South	Knight	ORE	MB22b	MB22bMt-13	magnetite	27.97	338.58	362.30	<6.52	53.55	0.42	8.59	505.77	3.89	220.45
South	Knight	ORE	MB22b	MB22bMt-14	magnetite	978.92	804.25	1063.76	<5.67	40.36	<0.092	52.82	2.88	<0.71	1096.63
South	Knight	ORE	MB22b	MB22bMt-15	magnetite	808.86	785.47	1372.91	<8.01	<64.7	<0.133	61.02	168.68	<0.97	781.72
South	Knight	ORE	MB22b	MB22bMt-16	magnetite	365.41	852.47	1334.78	<6	<50.32	0.10	79.15	170.40	<0.74	309.97
South	Knight	ORE	MB22b	MB22bMt-17	magnetite	6.38	428.71	172.80	<5.37	31.13	0.31	5.79	532.17	6.05	173.95
South	Knight	ORE	MB22b	MB22bMt-18	magnetite	4.70	1169.63	367.64	<6.05	60.54	<0.113	5.81	407.57	6.31	208.07
South	Knight	ORE	MB22b	MB22bMt-19	magnetite	21.83	1162.25	508.06	9.41	<49.76	<0.104	5.64	349.07	8.27	722.73
South	Knight	ORE	MB22b	MB22bMt-2	magnetite	585.69	1045.49	1233.06	8.85	<49.05	<0.12	83.61	169.69	<0.79	440.92
South	Knight	ORE	MB22b	MB22bMt-20	magnetite	977.84	900.89	1776.12	26.31	<40.14	0.13	55.78	518.16	3.01	674.39
South	Knight	ORE	MB22b	MB22bMt-3	magnetite	1232.06	1286.49	2254.65	18.13	<48.65	0.19	57.95	2.31	<0.88	440.27
South	Knight	ORE	MB22b	MB22bMt-4	magnetite	493.71	989.44	1834.47	15.59	<55.9	0.24	66.49	135.57	1.45	884.58
South	Knight	ORE	MB22b	MB22bMt-5	magnetite	439.81	822.20	639.98	11.64	<57.85	<0.089	49.98	5.84	<0.72	437.77
South	Knight	ORE	MB22b	MB22bMt-6	magnetite	595.75	1033.87	1800.78	8.98	<51.2	<0.096	48.41	44.06	0.87	589.73
South	Knight	ORE	MB22b	MB22bMt-7	magnetite	452.51	631.59	794.62	<6.36	110.13	<0.109	35.02	64.50	2.19	754.87
South	Knight	ORE	MB22b	MB22bMt-8	magnetite	230.88	792.74	426.44	<6.57	<55.88	<0.116	40.68	14.62	1.85	688.20
South	Knight	ORE	MB22b	MB22bMt-9	magnetite	2561.29	1173.17	2875.44	<5.83	187.95	<0.091	56.45	2.64	<0.69	1292.47
Middle	Cavalier	BIF	MB26	MB26Hm-1	porous martite	25.80	336.93	10956.88	64.43	<31.75	<0.063	6.54	1.39	<0.49	68.03
Middle	Cavalier	BIF	MB26	MB26Hm-10	porous martite	10.88	291.28	17582.19	44.17	<39.49	0.10	5.81	1.47	<0.51	26.55
Middle	Cavalier	BIF	MB26	MB26Hm-11	porous martite	17.74	311.66	3161.77	36.79	42.65	<0.061	5.91	1.57	<0.41	39.20
Middle	Cavalier	BIF	MB26	MB26Hm-12	porous martite	8.28	352.93	5518.01	18.83	40.89	0.10	8.25	2.42	<0.46	21.79
Middle	Cavalier	BIF	MB26	MB26Hm-14	porous martite	1322.88	78.54	6525.68	100.54	132.60	<0.099	34.82	0.52	<0.56	111.16
Middle	Cavalier	BIF	MB26	MB26Hm-15	porous martite	53.35	226.98	1824.61	131.36	144.73	<0.077	9.12	1.40	<0.56	192.58
Middle	Cavalier	BIF	MB26	MB26Hm-16	porous martite	821.88	34.22	20987.82	72.47	<63.45	0.24	<0.54	0.09	<0.62	52.66
Middle	Cavalier	BIF	MB26	MB26Hm-17	porous martite	33.41	242.46	3837.67	100.28	123.16	<0.075	7.30	1.38	1.31	162.85
Middle	Cavalier	BIF	MB26	MB26Hm-18	porous martite	15.89	274.18	16847.52	45.16	<29.37	0.18	10.34	1.30	<0.44	31.56
Middle	Cavalier	BIF	MB26	MB26Hm-3	porous martite	73.04	177.98	4734.40	16.05	<33.66	0.11	4.67	0.69	<0.52	11.37
Middle	Cavalier	BIF	MB26	MB26Hm-5	porous martite	13.71	353.28	4389.47	18.04	<35.82	0.11	12.96	1.83	<0.59	25.60
Middle	Cavalier	BIF	MB26	MB26Hm-6	porous martite	117.60	289.38	25065.20	190.84	<40.19	0.11	7.25	1.36	<0.7	283.89
Middle	Cavalier	BIF	MB26	MB26Hm-7	porous martite	35.99	275.47	14053.03	95.34	<43.32	0.10	3.57	1.44	0.84	118.91
Middle	Cavalier	BIF	MB26	MB26Hm-8	porous martite	40.57	274.55	6642.95	132.21	67.32	0.07	3.80	1.47	<0.55	139.63
Middle	Queen	ORE	MB27	MB27Hm-1	clean martite	42.94	188.86	357.35	8.42	<73.71	<0.108	5.80	2.43	<0.76	384.32
Middle	Queen	ORE	MB27	MB27Hm-10	clean martite	122.51	305.47	906.50	42.89	<55.12	0.13	5.65	2.24	<0.77	1163.40
Middle	Queen	ORE	MB27	MB27Hm-11	clean martite	192.59	274.90	1116.14	41.69	219.61	0.27	6.23	9.39	<0.92	926.37
Middle	Queen	ORE	MB27	MB27Hm-12	clean martite	92.48	194.15	418.06	24.86	<54.72	<0.092	5.25	1.88	<0.66	169.82
Middle	Queen	ORE	MB27	MB27Hm-14	clean martite	31.50	175.15	258.90	24.40	<49	<0.084	4.88	1.68	<0.72	229.89
Middle	Queen	ORE	MB27	MB27Hm-16	clean martite	58.79	214.78	1768.72	14.87	<72.62	<0.1	5.54	1.86	<0.82	351.29
Middle	Queen	ORE	MB27	MB27Hm-17	clean martite	90.68	261.65	518.74	40.30	<62.82	<0.095	4.93	2.15	1.04	552.93

Analysis no.	Co	Ni	Cu	Zn	Ga	As	Sr	Y	Zr	Nb	Mo	Sn	Sb	Ba	La	Ce	Pr
MB22bHm-8	13.98	11.84	14.48	12.95	0.41	3.99	0.80	1.37	0.23	0.03	0.13	0.44	0.28	19.76	0.61	0.82	0.07
MB22bHm-9	8.62	67.66	3.68	11.44	0.95	3.59	0.72	1.03	0.41	0.05	0.33	0.37	0.99	50.81	0.58	0.52	0.06
MB22bMt-1	5.42	0.28	<0.175	2.85	0.16	3.26	0.71	0.03	0.02	0.28	<0.026	0.44	0.05	0.07	0.00	0.01	<0.00
MB22bMt-10	2.33	0.58	0.20	12.58	0.41	1.36	0.40	0.11	<0.0164	0.03	<0.028	0.48	0.12	0.84	0.05	0.07	0.00
MB22bMt-11	4.34	2.02	0.33	9.27	0.32	0.33	0.11	0.04	<0.016	0.01	<0.047	0.51	<0.042	1.98	0.01	0.02	0.00
MB22bMt-12	1.48	3.39	<0.188	5.37	0.13	0.92	0.11	0.26	0.25	0.01	0.51	0.28	0.59	0.23	0.09	0.14	0.01
MB22bMt-13	2.72	1.19	<0.231	13.96	0.13	2.15	0.11	0.42	1.07	0.01	0.43	0.44	1.29	0.31	0.06	0.14	0.01
MB22bMt-14	4.06	0.40	0.22	6.39	0.24	5.24	0.96	0.04	0.10	1.37	0.05	0.68	0.15	0.36	0.01	0.02	<0.00
MB22bMt-15	6.62	9.28	<0.197	15.10	0.38	1.84	0.32	0.39	0.34	3.90	0.15	1.10	0.08	6.16	0.23	0.22	0.02
MB22bMt-16	1.74	3.19	0.92	18.08	0.13	1.79	0.22	0.30	0.07	0.17	0.04	0.43	0.38	2.45	0.09	0.14	0.01
MB22bMt-17	1.18	7.06	<0.16	4.79	0.18	0.24	0.08	0.22	1.38	0.06	0.93	0.20	0.14	0.83	0.46	0.32	0.03
MB22bMt-18	1.28	13.21	<0.184	3.44	0.07	<0.174	0.13	0.06	3.40	0.04	1.29	0.18	0.04	1.28	0.04	0.07	0.00
MB22bMt-19	1.59	3.87	0.62	33.18	0.11	0.44	0.02	0.03	2.10	0.01	0.23	0.24	0.21	<0.00	0.00	0.02	0.00
MB22bMt-2	0.73	4.77	<0.2	14.54	0.26	1.42	0.09	0.31	0.03	0.59	<0.051	0.80	0.23	0.64	0.06	0.10	0.01
MB22bMt-20	2.85	19.16	0.84	11.62	0.49	14.34	0.85	0.36	0.06	0.07	0.15	0.42	0.53	11.57	0.21	0.23	0.02
MB22bMt-3	0.57	<0.19	2.69	24.56	0.33	15.93	0.15	0.14	0.06	0.70	0.04	0.92	0.50	0.50	0.01	0.03	0.01
MB22bMt-4	0.29	5.58	<0.157	17.77	0.37	10.85	0.03	0.96	0.18	1.55	<0.026	0.81	0.16	0.44	0.20	0.38	0.04
MB22bMt-5	4.32	4.25	2.26	8.94	0.30	1.75	1.05	0.12	<0.00	0.01	0.01	0.48	0.19	27.94	0.06	0.09	0.01
MB22bMt-6	2.28	5.89	<0.19	15.60	0.15	5.71	0.10	0.35	<0.0151	0.03	<0.026	0.56	0.46	0.27	0.02	0.05	0.00
MB22bMt-7	4.22	3.26	2.33	7.98	0.32	1.15	0.61	0.27	0.04	0.04	0.03	0.52	0.22	3.02	0.18	0.21	0.01
MB22bMt-8	2.11	1.52	<0.235	4.57	0.18	0.77	1.37	0.09	0.02	<0.0065	0.15	0.60	0.09	0.74	0.04	0.07	0.01
MB22bMt-9	0.35	0.41	<0.181	26.33	0.14	35.51	0.02	0.04	0.03	0.08	<0.043	0.77	0.21	0.06	0.01	0.01	0.00
MB26Hm-1	0.55	1.20	1.04	3.74	0.43	0.34	0.26	0.60	0.02	<0.00	<0.0247	0.09	<0.014	1.12	0.30	0.25	0.02
MB26Hm-10	0.34	0.82	0.66	4.78	0.35	0.33	0.15	0.74	0.01	<0.00	<0.018	0.07	<0.0143	0.24	0.44	0.40	0.05
MB26Hm-11	0.39	0.83	0.47	4.18	0.41	0.38	0.15	0.48	0.01	0.01	<0.0254	0.09	<0.0141	0.13	0.30	0.24	0.02
MB26Hm-12	0.32	0.81	0.47	4.25	0.41	0.25	0.13	0.73	<0.00	0.01	<0.029	0.11	0.03	0.05	0.46	0.34	0.03
MB26Hm-14	0.31	0.62	0.82	3.10	0.07	3.79	0.39	1.42	0.04	0.01	0.02	0.10	0.24	0.68	0.61	0.77	0.07
MB26Hm-15	0.47	0.99	0.19	1.62	0.29	0.95	0.59	1.09	0.03	0.01	0.03	0.38	0.06	1.30	0.66	0.82	0.10
MB26Hm-16	0.07	0.29	0.23	3.62	<0.033	1.36	0.24	0.90	0.03	0.02	0.01	0.27	0.12	0.56	0.29	0.29	0.03
MB26Hm-17	0.46	0.85	0.33	3.76	0.40	1.24	0.45	1.01	0.07	0.02	0.03	0.14	0.10	1.03	0.71	0.89	0.08
MB26Hm-18	0.34	0.78	1.06	6.65	0.42	0.39	0.26	1.41	<0.0103	0.01	<0.0177	0.08	0.03	0.29	0.75	0.88	0.10
MB26Hm-3	0.36	1.20	0.32	4.23	0.17	<0.164	0.06	1.24	<0.0107	<0.00	<0.026	<0.072	<0.021	0.08	0.73	0.87	0.09
MB26Hm-5	0.20	0.89	0.38	5.29	0.47	0.25	0.06	1.40	0.01	<0.0064	<0.028	0.09	0.04	0.15	0.88	0.95	0.11
MB26Hm-6	0.49	1.13	1.30	4.81	0.36	0.99	0.71	2.13	0.16	<0.00	<0.024	0.16	<0.038	0.80	0.91	0.95	0.11
MB26Hm-7	0.51	0.75	0.76	5.17	0.55	0.87	0.42	0.75	<0.016	0.01	0.01	0.08	0.03	0.53	0.59	0.51	0.05
MB26Hm-8	0.65	0.65	0.66	2.85	0.42	0.90	0.50	0.59	0.06	<0.0044	0.03	0.17	<0.022	0.36	0.69	0.69	0.06
MB27Hm-1	3.33	2.23	1.50	9.54	1.90	0.80	0.48	0.56	0.05	0.01	0.23	0.48	0.16	1.36	0.10	0.17	0.02
MB27Hm-10	2.86	6.94	11.00	29.75	2.28	<0.22	4.12	1.49	<0.0169	<0.00	0.17	0.64	<0.041	0.53	0.17	0.17	0.04
MB27Hm-11	3.62	3.84	10.00	25.83	2.08	0.61	2.67	2.38	0.11	0.04	0.33	0.76	<0.051	2.30	0.31	0.41	0.07
MB27Hm-12	2.30	1.31	0.20	7.18	1.99	0.60	0.14	0.21	0.04	<0.0062	0.28	0.46	<0.044	0.46	0.06	0.09	0.01
MB27Hm-14	2.18	1.49	0.23	7.18	1.82	0.65	0.13	0.24	0.02	<0.00	0.14	0.37	0.13	0.69	0.06	0.09	0.01
MB27Hm-16	1.53	3.04	4.65	17.72	2.00	<0.21	0.63	0.59	0.01	<0.00	0.05	0.54	<0.0266	0.07	0.06	0.05	0.02
MB27Hm-17	2.13	3.67	9.36	27.84	2.04	0.76	1.07	1.14	<0.00	0.01	0.17	0.56	0.09	0.29	0.11	0.11	0.03

Analysis no.	Nd	Sm	Eu	Gd	Tb	Dy	Ho	Er	Tm	Yb	Lu	W	Pb208	Th	U
MB22bHm-8	0.35	0.08	0.05	0.08	0.01	0.11	0.02	0.07	0.01	0.08	0.02	0.42	7.15	0.04	7.11
MB22bHm-9	0.20	0.05	0.03	0.04	0.01	0.04	0.02	0.05	0.01	0.06	0.01	0.89	10.07	0.12	14.95
MB22bMt-1	<0.00	<0.00	0.00	<0.016	<0.00216	<0.00	<0.00	0.00	<0.00204	<0.00	<0.00	35.75	2.76	0.17	0.38
MB22bMt-10	0.04	0.01	0.00	<0.0245	0.00	<0.0096	<0.0024	<0.0072	0.00	0.01	0.00	23.04	3.43	0.20	0.30
MB22bMt-11	0.00	0.01	0.00	<0.00	0.00	<0.00	0.00	<0.007	0.00	<0.00	<0.0031	22.29	3.04	0.22	0.57
MB22bMt-12	0.06	0.01	0.01	0.04	0.00	0.03	0.01	0.01	0.00	0.04	0.00	16.22	1.37	0.05	0.04
MB22bMt-13	0.12	0.03	0.01	<0.023	0.01	0.05	0.01	0.02	0.01	0.03	<0.0031	0.02	11.47	0.02	<0.00
MB22bMt-14	0.01	0.01	<0.0039	<0.00	<0.002	0.01	<0.00	0.00	<0.0027	<0.0127	<0.00276	13.24	2.43	0.18	0.49
MB22bMt-15	0.08	0.01	0.01	0.05	0.00	<0.0116	0.00	0.03	0.00	0.02	0.00	0.04	31.78	0.01	<0.00
MB22bMt-16	0.06	0.01	0.01	<0.016	0.00	0.03	0.00	0.02	0.00	0.01	<0.002	19.77	0.90	0.03	0.11
MB22bMt-17	0.11	0.01	0.01	0.03	<0.0019	0.01	0.01	0.01	0.00	0.01	0.00	25.16	3.36	0.19	0.48
MB22bMt-18	0.02	<0.00	<0.00	0.01	<0.0022	<0.00	0.00	0.00	<0.00	0.01	<0.0037	17.05	2.86	0.16	0.59
MB22bMt-19	0.01	0.01	<0.006	<0.0161	<0.00217	<0.0154	0.00	0.00	0.00	0.01	<0.00	14.85	3.75	0.38	0.19
MB22bMt-2	0.05	0.02	<0.0047	0.03	<0.0024	0.03	0.01	0.02	0.00	0.01	0.00	0.01	26.80	0.02	<0.00
MB22bMt-20	0.03	0.03	0.01	0.01	0.00	0.02	0.01	0.01	0.00	0.01	0.01	40.72	1.50	0.02	0.19
MB22bMt-3	0.02	0.01	0.00	0.02	0.00	0.01	0.00	0.00	0.00	<0.00	0.00	36.63	2.19	0.09	0.14
MB22bMt-4	0.15	0.01	0.03	0.04	0.01	0.06	0.01	0.04	0.01	0.05	0.01	0.40	0.27	<0.00	0.09
MB22bMt-5	0.07	0.01	<0.0068	<0.00	0.00	0.02	0.00	<0.0062	0.00	0.01	0.00	0.49	0.66	<0.00	0.37
MB22bMt-6	0.04	0.02	<0.0042	0.02	<0.003	0.02	0.00	0.03	0.00	0.01	0.00	0.04	0.23	0.00	0.11
MB22bMt-7	0.08	0.02	0.01	<0.034	0.00	<0.0094	0.01	0.02	0.00	0.02	0.00	0.98	1.50	<0.00	0.99
MB22bMt-8	0.01	0.01	<0.0046	<0.025	0.00	0.01	<0.0047	0.01	<0.00	0.01	<0.0023	0.37	4.13	0.01	0.96
MB22bMt-9	0.01	<0.00	0.00	<0.015	<0.0029	<0.00	0.00	0.00	0.00	0.00	0.00	0.26	0.18	<0.00	0.36
MB26Hm-1	0.09	0.01	0.01	0.03	0.00	0.04	0.01	0.03	<0.0014	0.02	0.00	0.05	0.03	<0.00	0.01
MB26Hm-10	0.20	0.05	0.01	0.01	0.01	0.02	0.01	0.03	0.00	0.01	0.00	0.07	0.08	0.00	0.01
MB26Hm-11	0.08	<0.0114	0.01	0.04	0.00	0.01	0.00	0.03	0.00	0.00	<0.0014	0.17	0.11	<0.00	0.01
MB26Hm-12	0.09	0.01	0.01	0.01	0.01	0.04	0.01	0.01	0.00	0.01	0.00	0.19	0.06	0.00	0.02
MB26Hm-14	0.35	0.13	0.04	0.06	0.02	0.11	0.02	0.08	0.01	0.02	0.01	1.19	0.33	0.01	0.10
MB26Hm-15	0.38	0.11	0.03	0.10	0.01	0.07	0.02	0.07	0.01	0.04	0.01	0.36	0.31	0.00	0.05
MB26Hm-16	0.19	0.06	0.02	0.09	0.01	0.08	0.01	0.05	0.00	0.05	0.01	4.17	0.23	0.01	0.25
MB26Hm-17	0.42	0.04	0.04	0.07	0.02	0.09	0.02	0.04	0.00	0.01	0.00	0.28	0.51	0.00	0.06
MB26Hm-18	0.41	0.09	0.05	0.13	0.02	0.05	0.02	0.06	0.01	0.02	0.00	0.16	0.09	<0.00	0.01
MB26Hm-3	0.37	0.08	0.04	0.10	0.01	0.05	0.01	0.05	0.00	0.03	0.01	0.03	0.05	0.00	0.01
MB26Hm-5	0.54	0.06	0.04	0.06	0.01	0.06	0.02	0.07	0.01	0.02	0.00	0.04	0.09	0.00	0.01
MB26Hm-6	0.55	0.08	0.07	0.12	0.02	0.12	0.04	0.08	0.02	0.06	0.01	0.05	0.22	0.00	0.01
MB26Hm-7	0.20	0.03	0.01	0.02	0.00	0.04	0.01	0.02	0.00	0.01	0.01	0.22	0.22	0.01	0.04
MB26Hm-8	0.26	0.04	0.02	0.05	0.00	0.03	0.02	0.02	<0.0015	0.01	0.00	0.20	0.21	<0.0028	0.01
MB27Hm-1	0.13	0.03	0.02	<0.035	0.01	0.04	0.01	0.05	0.01	0.06	0.00	0.31	7.81	<0.0046	0.29
MB27Hm-10	0.19	0.15	0.09	0.17	0.03	0.20	0.04	0.11	0.01	0.07	0.00	0.05	0.82	<0.00	0.06
MB27Hm-11	0.32	0.12	0.08	0.28	0.03	0.25	0.06	0.22	0.03	0.15	0.02	0.50	2.36	0.01	0.26
MB27Hm-12	0.08	0.03	0.02	0.09	0.02	0.05	0.01	0.03	0.00	0.01	<0.0022	0.03	9.40	<0.00	0.27
MB27Hm-14	0.08	0.03	0.02	0.10	0.00	0.05	0.00	0.02	<0.0021	0.01	<0.00	0.12	8.10	<0.00	0.14
MB27Hm-16	0.03	0.02	0.02	0.03	0.01	0.04	0.02	0.04	0.00	0.04	0.00	0.01	0.21	<0.00	0.03
MB27Hm-17	0.15	<0.028	0.03	0.12	0.01	0.09	0.02	0.07	0.01	0.02	0.01	0.10	0.79	<0.00	0.09

Position	Deposit	Lithology	Sample no.	Analysis no.	Texture	Mg	Al	Si	P	Ca	Sc	Ti	V	Cr	Mn
Middle	Queen	ORE	MB27	MB27Hm-18	clean martite	109.10	339.24	1724.60	61.85	<53.96	0.33	4.25	2.62	1.47	670.58
Middle	Queen	ORE	MB27	MB27Hm-19	clean martite	118.94	257.47	670.07	37.26	<63.47	0.21	5.43	2.05	1.02	527.38
Middle	Queen	ORE	MB27	MB27Hm-2	clean martite	222.30	598.94	1400.26	98.32	<67.69	0.20	5.35	32.29	<0.83	1217.09
Middle	Queen	ORE	MB27	MB27Hm-20	clean martite	79.85	197.51	8960.37	<6.04	<60.95	<0.08	4.33	1.68	<0.66	361.37
Middle	Queen	ORE	MB27	MB27Hm-3	clean martite	37.27	178.75	194.67	13.43	<58.71	<0.109	5.01	2.07	<0.78	413.71
Middle	Queen	ORE	MB27	MB27Hm-4	clean martite	272.55	795.06	952.84	82.52	<57.79	0.56	4.95	6.45	<0.73	3189.29
Middle	Queen	ORE	MB27	MB27Hm-5	clean martite	98.75	274.07	1058.73	40.85	<56.57	<0.1	8.48	2.16	2.02	419.71
Middle	Queen	ORE	MB27	MB27Hm-6	clean martite	96.13	301.90	608.14	24.26	136.47	0.09	7.22	2.65	0.96	759.77
Middle	Queen	ORE	MB27	MB27Hm-7	clean martite	122.73	372.76	8608.20	58.23	<49.5	0.25	5.55	2.24	<0.7	823.25
Middle	Queen	ORE	MB27	MB27Hm-8	clean martite	30.08	149.29	<71.27	<6.1	<59.04	<0.103	5.36	1.82	<0.68	161.14
Middle	Queen	ORE	MB27	MB27Hm-9	clean martite	57.52	214.01	356.32	12.01	<48.19	<0.078	3.60	1.77	<0.83	418.91
Middle	Queen	ORE	MB28	MB28HmClean-1	clean martite	7.20	110.30	425.46	108.36	<46.64	<0.078	2.73	2.46	0.84	47.91
Middle	Queen	ORE	MB28	MB28HmClean-10	clean martite	5.45	83.96	474.24	227.42	39.32	0.07	3.68	3.29	0.59	41.05
Middle	Queen	ORE	MB28	MB28HmClean-11	clean martite	3.35	54.05	361.27	393.72	<42.85	<0.079	1.78	1.07	<0.6	27.67
Middle	Queen	ORE	MB28	MB28HmClean-12	clean martite	11.88	145.26	324.65	123.84	41.46	0.10	1.97	2.78	<0.53	51.98
Middle	Queen	ORE	MB28	MB28HmClean-13	clean martite	9.64	128.71	805.93	140.79	67.76	<0.069	1.62	19.54	<0.53	46.74
Middle	Queen	ORE	MB28	MB28HmClean-14	clean martite	10.94	167.69	388.91	20.37	<52.79	<0.075	4.49	29.72	<0.5	71.52
Middle	Queen	ORE	MB28	MB28HmClean-15	clean martite	67.76	253.83	998.63	76.09	88.93	0.13	6.58	20.00	<0.59	111.66
Middle	Queen	ORE	MB28	MB28HmClean-16	clean martite	4.31	165.35	364.17	19.07	97.15	0.13	5.58	1.38	<0.4	54.00
Middle	Queen	ORE	MB28	MB28HmClean-17	clean martite	13.51	214.33	679.96	49.72	<34.78	0.33	5.83	36.58	1.19	103.28
Middle	Queen	ORE	MB28	MB28HmClean-18	clean martite	166.72	150.82	1537.29	201.51	128.29	0.11	13.66	4.38	0.74	119.57
Middle	Queen	ORE	MB28	MB28HmClean-19	clean martite	9.85	145.09	498.40	230.23	<31.4	<0.06	10.18	9.93	<0.45	48.29
Middle	Queen	ORE	MB28	MB28HmClean-2	clean martite	14.15	127.32	438.09	268.24	<57.25	0.30	2.96	18.46	0.91	101.51
Middle	Queen	ORE	MB28	MB28HmClean-20	clean martite	8.00	136.80	634.23	36.97	74.84	0.18	1.41	45.49	0.95	82.38
Middle	Queen	ORE	MB28	MB28HmClean-3	clean martite	28.96	172.29	532.85	216.23	<47.6	<0.074	2.64	30.61	<0.56	49.11
Middle	Queen	ORE	MB28	MB28HmClean-4	clean martite	20.40	205.35	800.07	221.08	147.77	<0.102	1.25	80.73	<0.81	189.85
Middle	Queen	ORE	MB28	MB28HmClean-5	clean martite	4.63	91.17	723.68	237.72	29.51	<0.042	2.83	8.53	<0.33	29.05
Middle	Queen	ORE	MB28	MB28HmClean-7	clean martite	5.88	95.08	1335.19	235.59	<39.83	<0.069	3.36	1.11	<0.56	17.72
Middle	Queen	ORE	MB28	MB28HmClean-8	clean martite	5.15	102.12	462.87	306.67	<41.65	0.14	2.77	1.62	0.82	28.60
Middle	Queen	ORE	MB28	MB28HmClean-9	clean martite	11.66	201.05	596.67	116.35	<37.17	0.14	2.86	43.42	<0.58	63.05
Middle	Queen	ORE	MB28	MB28HmPlaty-10	platy hematite	11.31	170.33	1558.96	63.28	<31	0.18	3.89	25.03	0.90	91.48
Middle	Queen	ORE	MB28	MB28HmPlaty-11	platy hematite	14.25	174.57	716.55	43.47	679.20	0.07	6.80	36.54	<0.47	80.39
Middle	Queen	ORE	MB28	MB28HmPlaty-12	platy hematite	10.74	121.31	632.69	292.39	69.54	0.15	3.30	16.15	<0.39	88.95
Middle	Queen	ORE	MB28	MB28HmPlaty-13	platy hematite	18.81	167.94	1636.39	37.35	58.31	0.11	0.82	50.59	0.60	115.71
Middle	Queen	ORE	MB28	MB28HmPlaty-14	platy hematite	14.53	189.31	476.24	52.56	47.59	0.07	1.71	65.43	<0.42	115.29
Middle	Queen	ORE	MB28	MB28HmPlaty-15	platy hematite	24.44	207.54	8044.05	57.04	49.64	0.11	1.78	82.21	0.96	131.63
Middle	Queen	ORE	MB28	MB28HmPlaty-16	platy hematite	20.63	236.20	1560.80	63.83	66.98	<0.053	0.74	43.17	<0.48	124.55
Middle	Queen	ORE	MB28	MB28HmPlaty-17	platy hematite	13.15	140.01	2030.35	331.49	57.62	<0.073	1.68	19.61	<0.57	99.19
Middle	Queen	ORE	MB28	MB28HmPlaty-18	platy hematite	8.75	139.38	372.67	128.44	79.91	<0.063	2.25	10.18	0.49	48.61
Middle	Queen	ORE	MB28	MB28HmPlaty-19	platy hematite	4.13	155.16	874.26	14.35	56.60	0.11	5.07	7.47	0.50	54.10
Middle	Queen	ORE	MB28	MB28HmPlaty-2	platy hematite	8.68	111.12	480.44	286.55	42.54	<0.054	3.98	2.95	0.69	88.15
Middle	Queen	ORE	MB28	MB28HmPlaty-20	platy hematite	8.37	146.93	336.76	69.11	<38.5	0.11	3.63	8.12	0.82	83.65
Middle	Queen	ORE	MB28	MB28HmPlaty-3	platy hematite	9.67	119.57	167.51	55.12	143.57	0.11	1.01	30.82	<0.56	74.35

Analysis no.	Co	Ni	Cu	Zn	Ga	As	Sr	Y	Zr	Nb	Mo	Sn	Sb	Ba	La	Ce	Pr
MB27Hm-18	1.43	6.11	14.52	33.18	1.81	0.95	1.82	2.25	<0.00	0.01	0.07	0.55	0.14	0.20	0.20	0.27	0.04
MB27Hm-19	2.12	3.65	6.13	16.89	1.82	<0.19	1.30	1.02	<0.00	0.00	0.24	0.66	<0.033	0.72	0.13	0.14	0.03
MB27Hm-2	6.29	6.70	13.44	34.08	1.70	1.70	2.96	3.27	0.14	0.03	1.39	0.75	0.28	2.83	0.43	0.71	0.10
MB27Hm-20	2.29	4.31	1.62	11.07	2.07	1.14	0.82	0.38	0.02	0.01	0.06	0.48	0.06	0.23	0.07	0.12	0.03
MB27Hm-3	3.32	2.24	0.40	7.19	1.57	0.26	0.45	0.32	0.02	<0.00	0.12	0.50	<0.045	0.22	0.07	0.10	0.02
MB27Hm-4	9.79	14.21	23.74	72.75	1.91	0.32	32.16	4.51	0.08	0.01	1.11	1.02	0.04	1.29	0.60	0.47	0.11
MB27Hm-5	1.53	3.54	7.04	20.22	2.05	0.93	0.88	1.33	<0.00	0.01	0.13	0.54	0.12	0.68	0.13	0.21	0.02
MB27Hm-6	6.94	3.98	6.92	24.24	1.97	1.06	1.34	1.96	0.02	0.02	0.18	0.36	0.05	1.70	0.24	0.35	0.05
MB27Hm-7	1.85	5.78	13.72	34.01	1.95	<0.22	2.51	2.34	<0.00	<0.00	0.11	0.62	0.04	0.23	0.25	0.24	0.05
MB27Hm-8	0.98	1.46	<0.163	6.64	1.75	<0.194	0.02	0.06	0.02	0.01	0.03	0.42	<0.043	0.05	0.02	0.04	0.01
MB27Hm-9	3.18	1.63	3.02	12.39	1.90	0.33	0.62	0.57	0.04	<0.0064	0.38	0.44	0.10	0.35	0.09	0.11	0.03
MB28HmClean-1	0.10	0.72	3.64	7.43	0.38	2.04	0.19	0.77	0.02	0.02	0.06	0.29	0.15	0.54	0.16	0.28	0.04
MB28HmClean-10	0.10	1.37	2.43	4.78	0.33	1.29	0.34	0.91	0.02	0.00	0.13	0.31	0.05	0.26	0.11	0.19	0.03
MB28HmClean-11	0.04	2.13	0.57	5.02	0.31	1.39	0.07	0.37	0.07	0.01	0.05	0.15	0.09	0.55	0.07	0.15	0.03
MB28HmClean-12	0.33	1.71	5.58	28.16	0.35	1.43	0.48	0.27	0.02	0.01	<0.029	0.30	0.13	0.52	0.11	0.15	0.02
MB28HmClean-13	0.16	2.06	1.76	4.87	0.32	1.40	0.20	0.79	0.04	0.02	0.09	0.28	0.06	2.43	0.23	0.32	0.03
MB28HmClean-14	0.94	1.78	74.36	158.82	0.29	1.49	0.65	0.59	0.05	<0.00	0.07	0.29	0.13	4.76	0.22	0.39	0.04
MB28HmClean-15	0.42	1.42	26.29	36.61	0.48	1.43	0.76	1.30	0.21	0.03	0.11	1.11	0.11	5.27	0.43	0.64	0.07
MB28HmClean-16	0.49	0.56	46.46	136.49	0.39	0.98	0.27	0.18	0.03	0.01	0.02	0.35	0.03	0.92	0.06	0.08	0.02
MB28HmClean-17	0.45	2.61	32.52	62.10	0.31	1.85	0.68	0.78	0.19	0.00	0.12	0.24	0.14	3.79	0.25	0.50	0.06
MB28HmClean-18	0.70	1.66	2.25	14.12	0.53	2.50	0.54	1.24	0.02	0.00	0.22	0.17	0.19	2.61	0.51	0.64	0.07
MB28HmClean-19	0.18	0.95	1.22	10.84	0.44	1.39	0.05	0.80	0.01	0.01	0.10	0.33	<0.026	0.61	0.16	0.26	0.03
MB28HmClean-2	0.11	1.22	4.62	9.06	0.29	2.45	0.88	1.11	0.14	0.02	0.11	0.30	0.13	2.75	0.33	0.60	0.07
MB28HmClean-20	0.30	1.57	8.54	25.83	0.18	0.70	0.64	1.27	0.57	0.04	0.13	0.14	0.14	5.46	0.36	0.46	0.10
MB28HmClean-3	0.19	2.72	13.81	6.53	0.38	1.09	0.43	0.95	0.02	0.01	0.11	0.34	0.09	4.62	0.24	0.29	0.03
MB28HmClean-4	0.38	4.82	6.21	13.43	0.32	1.12	0.72	2.84	0.08	0.02	0.23	0.14	0.06	11.52	0.49	0.80	0.10
MB28HmClean-5	0.12	1.57	1.29	5.29	0.38	0.84	0.10	0.83	<0.0081	0.00	0.13	0.36	0.10	0.71	0.08	0.10	0.02
MB28HmClean-7	0.08	1.10	0.15	4.52	0.31	1.39	<0.00	0.60	<0.00	0.00	0.05	0.26	0.06	<0.00	0.05	0.07	0.01
MB28HmClean-8	0.18	2.42	2.59	6.88	0.34	1.61	0.09	0.62	0.03	0.03	0.16	0.34	0.19	0.61	0.13	0.26	0.04
MB28HmClean-9	0.31	2.89	2.74	6.32	0.32	1.48	0.23	0.95	0.02	<0.00	0.10	0.47	0.10	5.07	0.35	0.49	0.08
MB28HmPlaty-10	0.33	3.32	9.17	32.76	0.47	1.56	0.30	3.50	<0.00	0.01	0.23	0.29	0.11	6.76	0.34	0.61	0.08
MB28HmPlaty-11	0.38	2.36	14.77	56.34	0.72	0.97	4.25	0.72	0.08	0.01	0.04	0.29	0.08	51.34	0.30	0.41	0.05
MB28HmPlaty-12	0.74	2.09	0.97	7.67	0.22	0.99	0.18	0.76	0.06	0.01	0.12	0.23	0.04	3.76	0.24	0.28	0.04
MB28HmPlaty-13	0.57	3.45	6.41	18.87	0.34	0.94	0.58	1.57	0.09	0.01	0.16	0.20	0.09	8.05	0.46	0.64	0.08
MB28HmPlaty-14	0.40	3.00	4.25	9.75	0.26	0.80	0.66	1.96	0.11	0.04	0.09	0.24	0.04	6.47	0.40	0.69	0.09
MB28HmPlaty-15	1.63	5.40	1.75	9.98	0.48	1.79	0.32	1.72	0.11	0.01	0.09	0.15	0.04	11.60	0.44	0.62	0.10
MB28HmPlaty-16	0.48	3.91	1.01	14.00	0.42	0.76	0.20	0.96	0.02	<0.0036	0.12	0.09	0.06	9.63	0.52	0.45	0.07
MB28HmPlaty-17	0.39	1.38	2.15	10.78	0.39	1.33	0.33	0.84	0.06	0.01	0.12	0.29	0.03	4.49	0.24	0.33	0.04
MB28HmPlaty-18	0.46	1.08	38.15	68.05	0.32	1.19	0.47	0.32	0.04	0.01	0.05	0.39	0.11	1.25	0.14	0.23	0.04
MB28HmPlaty-19	0.36	1.06	7.44	33.57	0.39	0.60	0.24	0.16	0.05	0.02	0.13	0.09	<0.02	0.48	0.03	0.07	0.01
MB28HmPlaty-2	0.53	1.18	3.53	13.60	0.36	1.29	0.25	1.09	0.02	0.02	0.09	0.22	0.07	1.07	0.15	0.26	0.04
MB28HmPlaty-20	0.37	1.30	41.91	74.42	0.22	1.12	0.73	1.37	0.14	0.02	0.17	0.26	0.07	3.45	0.22	0.46	0.06
MB28HmPlaty-3	0.15	2.74	2.15	7.54	0.21	0.81	0.66	0.53	0.29	0.06	0.12	0.18	0.05	2.70	0.25	0.29	0.03

Analysis no.	Nd	Sm	Eu	Gd	Tb	Dy	Ho	Er	Tm	Yb	Lu	W	Pb208	Th	U
MB27Hm-18	0.26	0.10	0.04	0.24	0.02	0.13	0.03	0.14	0.02	0.13	0.01	0.16	1.33	<0.00	0.12
MB27Hm-19	0.13	0.04	0.03	0.11	0.01	0.08	0.03	0.07	0.01	0.08	0.01	0.08	1.08	<0.00	0.05
MB27Hm-2	0.49	0.18	0.09	0.34	0.05	0.40	0.10	0.29	0.05	0.30	0.04	0.86	11.30	<0.0049	0.79
MB27Hm-20	0.12	0.05	0.03	0.08	0.01	0.08	0.02	0.06	0.01	0.01	0.00	0.12	6.58	<0.00	0.14
MB27Hm-3	0.05	0.04	0.01	<0.045	0.01	0.05	0.01	0.05	0.01	0.03	0.00	0.01	2.97	<0.00	0.07
MB27Hm-4	0.62	0.17	0.12	0.38	0.09	0.49	0.12	0.34	0.04	0.34	0.06	0.35	4.10	<0.00	0.28
MB27Hm-5	0.13	0.08	0.02	0.13	0.02	0.12	0.03	0.04	0.01	0.06	0.01	0.22	0.63	<0.00	0.08
MB27Hm-6	0.22	0.07	0.05	0.13	0.02	0.11	0.04	0.16	0.02	0.07	0.01	0.42	1.60	<0.00	0.06
MB27Hm-7	0.30	0.08	0.06	0.24	0.03	0.21	0.06	0.20	0.02	0.08	0.03	0.04	0.86	<0.00	0.11
MB27Hm-8	0.02	0.01	<0.0044	0.02	0.00	0.02	0.00	0.01	<0.00211	0.00	<0.00	0.01	0.99	<0.00	0.08
MB27Hm-9	0.14	0.08	0.03	0.07	0.02	0.07	0.02	0.06	0.01	0.03	0.00	0.05	5.97	<0.00	0.11
MB28HmClean-1	0.23	0.10	0.05	0.13	0.02	0.07	0.01	0.07	0.01	0.04	0.01	0.26	1.35	0.00	0.19
MB28HmClean-10	0.15	0.04	0.04	0.09	0.02	0.11	0.02	0.04	0.01	0.08	0.00	0.10	1.11	0.00	0.39
MB28HmClean-11	0.13	0.04	0.02	0.05	0.01	0.05	0.02	0.04	0.00	0.04	0.01	0.09	0.93	<0.00	0.06
MB28HmClean-12	0.16	0.04	0.02	0.04	0.00	0.02	0.01	0.03	0.01	0.00	0.00	0.08	2.87	<0.0034	0.33
MB28HmClean-13	0.19	0.05	0.05	0.15	0.01	0.08	0.02	0.08	0.01	0.05	0.01	0.32	4.42	<0.00	1.70
MB28HmClean-14	0.27	0.07	0.05	0.06	0.01	0.08	0.01	0.05	0.01	0.04	0.01	0.30	14.69	0.00	2.16
MB28HmClean-15	0.37	0.08	0.07	0.12	0.02	0.13	0.03	0.05	0.01	0.08	0.02	0.63	8.42	0.01	3.68
MB28HmClean-16	0.08	0.02	0.02	0.02	0.01	0.02	0.00	0.01	0.01	0.02	0.00	0.23	7.51	0.01	0.06
MB28HmClean-17	0.29	0.12	0.04	0.14	0.02	0.12	0.02	0.07	0.01	0.08	0.01	0.60	8.29	0.01	2.32
MB28HmClean-18	0.36	0.15	0.06	0.12	0.02	0.11	0.02	0.05	0.01	0.02	0.01	0.17	3.95	<0.00	0.19
MB28HmClean-19	0.11	0.05	0.03	0.04	0.01	0.06	0.02	0.04	0.01	0.03	0.01	0.20	1.12	0.00	0.25
MB28HmClean-2	0.36	0.15	0.07	0.14	0.02	0.13	0.03	0.07	0.01	0.12	0.02	0.46	3.93	0.01	1.65
MB28HmClean-20	0.42	0.06	0.07	0.11	0.02	0.10	0.02	0.07	0.01	0.08	0.01	0.82	5.28	0.01	5.81
MB28HmClean-3	0.16	0.08	0.07	0.12	0.01	0.11	0.02	0.07	0.01	0.06	0.02	0.44	6.85	0.00	2.93
MB28HmClean-4	0.57	0.16	0.14	0.24	0.03	0.23	0.06	0.17	0.02	0.17	0.03	0.91	13.16	0.00	4.86
MB28HmClean-5	0.09	0.03	0.05	0.06	0.01	0.09	0.03	0.07	0.01	0.02	0.01	0.02	0.83	<0.0023	0.14
MB28HmClean-7	0.07	0.03	0.03	0.05	0.01	0.05	0.01	0.04	0.01	0.03	0.00	0.03	0.30	<0.00	0.00
MB28HmClean-8	0.15	0.05	0.06	0.06	0.01	0.06	0.02	0.05	0.01	0.08	0.01	0.33	1.60	0.00	0.21
MB28HmClean-9	0.33	0.21	0.05	0.09	0.02	0.08	0.02	0.08	0.01	0.04	0.01	0.38	7.32	0.00	2.32
MB28HmPlaty-10	0.44	0.17	0.12	0.19	0.03	0.27	0.06	0.24	0.03	0.21	0.02	0.22	5.59	<0.00	0.90
MB28HmPlaty-11	0.19	0.10	0.03	0.06	0.01	0.06	0.02	0.05	0.01	0.06	0.01	0.49	9.99	0.01	2.56
MB28HmPlaty-12	0.15	0.05	0.04	0.08	0.01	0.05	0.02	0.04	0.01	0.05	0.01	0.36	5.61	0.00	1.86
MB28HmPlaty-13	0.45	0.10	0.08	0.15	0.02	0.14	0.03	0.14	0.02	0.11	0.01	1.07	10.28	0.01	5.29
MB28HmPlaty-14	0.37	0.15	0.06	0.13	0.02	0.15	0.04	0.08	0.03	0.13	0.02	0.90	7.45	0.01	4.42
MB28HmPlaty-15	0.30	0.10	0.07	0.10	0.02	0.11	0.03	0.13	0.02	0.10	0.01	1.00	15.07	<0.00	5.88
MB28HmPlaty-16	0.26	0.04	0.03	0.06	0.02	0.06	0.01	0.07	0.01	0.04	0.00	1.55	11.79	0.00	5.17
MB28HmPlaty-17	0.19	0.04	0.05	0.09	0.01	0.07	0.02	0.06	0.01	0.06	0.01	0.31	6.10	0.00	1.65
MB28HmPlaty-18	0.18	0.04	0.02	0.10	0.01	0.05	0.01	0.03	0.00	0.03	0.01	0.34	5.41	0.00	0.45
MB28HmPlaty-19	0.03	0.01	0.01	0.02	0.01	0.02	0.01	0.02	0.00	0.01	0.00	0.12	3.04	0.00	0.61
MB28HmPlaty-2	0.18	0.04	0.04	0.07	0.01	0.08	0.01	0.07	0.01	0.04	0.00	0.15	2.13	0.00	0.46
MB28HmPlaty-20	0.38	0.13	0.06	0.15	0.02	0.17	0.03	0.10	0.01	0.06	0.01	0.24	5.91	0.01	1.54
MB28HmPlaty-3	0.14	0.07	0.03	0.06	0.01	0.05	0.02	0.06	0.01	0.04	0.01	1.46	3.49	0.01	5.40

Position	Deposit	Lithology	Sample no.	Analysis no.	Texture	Mg	Al	Si	P	Ca	Sc	Ti	V	Cr	Mn
Middle	Queen	ORE	MB28	MB28HmPlaty-4	platy hematite	12.58	162.11	449.86	33.09	47.00	0.14	2.33	25.72	<0.5	65.88
Middle	Queen	ORE	MB28	MB28HmPlaty-5	platy hematite	21.63	191.27	1116.59	27.49	82.19	0.10	0.72	44.51	1.45	143.30
Middle	Queen	ORE	MB28	MB28HmPlaty-6	platy hematite	10.55	162.05	360.63	31.82	<33.36	0.20	2.51	27.05	0.76	81.35
Middle	Queen	ORE	MB28	MB28HmPlaty-7	platy hematite	8.80	146.50	373.54	27.91	136.76	0.11	3.35	4.87	<0.4	60.37
Middle	Queen	ORE	MB28	MB28HmPlaty-8	platy hematite	8.36	109.10	651.14	239.47	35.94	0.12	3.36	12.74	<0.48	80.49
Middle	Queen	ORE	MB28	MB28HmPlaty-9	platy hematite	21.15	224.19	1551.32	50.04	206.70	0.10	1.86	68.83	<0.5	124.64
Middle	Queen	ORE	MB29	MB29HmClean-1	clean martite	0.28	50.23	398.58	<9.69	223.09	<0.114	1.04	0.31	<0.95	5.05
Middle	Queen	ORE	MB29	MB29HmClean-10	clean martite	0.93	49.04	<107.59	26.45	<104.58	<0.156	<0.83	1.13	<1.06	3.48
Middle	Queen	ORE	MB29	MB29HmClean-11	clean martite	0.72	116.11	630.16	13.68	134.31	0.50	0.89	1.08	<1.01	8.47
Middle	Queen	ORE	MB29	MB29HmClean-12	clean martite	<0.144	51.34	<101.77	36.36	<88.05	<0.131	<0.86	0.89	<1.14	2.69
Middle	Queen	ORE	MB29	MB29HmClean-13	clean martite	2.01	51.97	<102.47	<9.52	<100.11	<0.122	<0.77	1.17	<0.88	6.31
Middle	Queen	ORE	MB29	MB29HmClean-14	clean martite	<0.135	46.65	175.41	10.36	<93.55	<0.131	1.96	1.07	<1.12	1.64
Middle	Queen	ORE	MB29	MB29HmClean-15	clean martite	0.44	60.62	2001.51	<9.28	<93.87	<0.142	0.92	0.43	<0.96	6.24
Middle	Queen	ORE	MB29	MB29HmClean-17	clean martite	4.98	390.18	460.93	35.07	<99.66	1.17	5.65	1.55	<1.16	19.36
Middle	Queen	ORE	MB29	MB29HmClean-18	clean martite	<0.141	52.20	212.18	<9.48	<84.55	0.30	1.25	1.30	<0.9	4.50
Middle	Queen	ORE	MB29	MB29HmClean-19	clean martite	2.62	48.44	351.21	<7.81	150.64	<0.117	5.49	1.60	2.03	2.76
Middle	Queen	ORE	MB29	MB29HmClean-2	clean martite	<0.137	47.52	334.17	11.76	<98.7	<0.129	<0.77	0.24	<1.04	3.35
Middle	Queen	ORE	MB29	MB29HmClean-20	clean martite	0.81	145.76	275.27	26.07	<94.75	<0.129	1.15	0.54	<1.03	7.39
Middle	Queen	ORE	MB29	MB29HmClean-3	clean martite	2.86	46.40	<112.27	16.24	<110.79	<0.166	0.81	0.46	1.42	4.75
Middle	Queen	ORE	MB29	MB29HmClean-4	clean martite	2.22	47.56	179.23	<10.69	162.67	<0.135	<0.71	0.60	<1.1	7.19
Middle	Queen	ORE	MB29	MB29HmClean-5	clean martite	2.33	116.94	22072.96	18.71	<104.32	0.51	1.37	0.59	<1.03	13.31
Middle	Queen	ORE	MB29	MB29HmClean-6	clean martite	6.32	85.04	276.32	52.61	157.56	<0.132	647.50	0.65	1.17	8.04
Middle	Queen	ORE	MB29	MB29HmClean-7	clean martite	0.35	47.15	248.53	19.99	180.65	<0.129	1.03	0.40	0.95	3.14
Middle	Queen	ORE	MB29	MB29HmClean-8	clean martite	0.20	49.41	316.81	<10.1	109.11	<0.133	1.53	1.12	<1.12	4.34
Middle	Queen	ORE	MB29	MB29HmClean-9	clean martite	0.27	51.86	343.83	<9.73	<88.79	<0.138	1.75	1.14	1.09	4.85
Middle	Queen	ORE	MB29	MB29HmPorous-1	porous martite	35.30	798.91	1235.90	106.58	<111.76	2.13	13.41	3.17	<1.01	754.57
Middle	Queen	ORE	MB29	MB29HmPorous-10	porous martite	22.83	972.31	1418.95	181.72	214.63	3.83	12.50	3.81	2.58	713.60
Middle	Queen	ORE	MB29	MB29HmPorous-11	porous martite	37.53	1238.43	1578.49	269.35	113.01	5.27	17.50	4.47	1.79	637.06
Middle	Queen	ORE	MB29	MB29HmPorous-12	porous martite	36.58	703.39	1333.13	96.62	<88.86	2.34	11.47	3.00	1.28	543.37
Middle	Queen	ORE	MB29	MB29HmPorous-13	porous martite	58.16	1080.66	1340.55	317.01	139.50	4.58	14.73	3.84	1.76	627.83
Middle	Queen	ORE	MB29	MB29HmPorous-14	porous martite	37.58	668.01	1112.06	104.14	<80.05	2.18	11.08	2.70	2.35	721.01
Middle	Queen	ORE	MB29	MB29HmPorous-15	porous martite	33.36	726.27	1246.09	103.72	109.69	2.36	10.88	2.96	<0.96	736.15
Middle	Queen	ORE	MB29	MB29HmPorous-16	porous martite	28.98	770.21	1408.15	116.00	206.67	1.92	11.14	3.20	<0.9	669.61
Middle	Queen	ORE	MB29	MB29HmPorous-17	porous martite	26.97	747.56	1242.94	110.99	228.32	2.40	12.71	3.20	<0.99	498.89
Middle	Queen	ORE	MB29	MB29HmPorous-18	porous martite	39.19	979.98	1217.15	179.27	<93.53	3.13	12.07	4.55	2.61	632.11
Middle	Queen	ORE	MB29	MB29HmPorous-19	porous martite	43.24	1266.32	1512.47	165.82	207.22	4.22	11.29	5.31	3.13	682.18
Middle	Queen	ORE	MB29	MB29HmPorous-2	porous martite	93.71	5556.18	3311.33	400.36	628.61	31.73	13.01	9.42	11.68	366.40
Middle	Queen	ORE	MB29	MB29HmPorous-20	porous martite	120.78	7275.29	3806.89	489.63	695.93	40.33	16.90	11.23	16.57	275.17
Middle	Queen	ORE	MB29	MB29HmPorous-3	porous martite	0.26	46.80	<107.31	<9.62	<98.55	<0.142	1.30	1.14	<0.94	5.05
Middle	Queen	ORE	MB29	MB29HmPorous-4	porous martite	44.60	646.21	1399.13	78.19	<115.9	2.19	12.11	3.40	1.43	752.09
Middle	Queen	ORE	MB29	MB29HmPorous-5	porous martite	30.83	818.33	1104.16	120.76	<75.76	3.14	12.16	4.73	<0.79	682.14
Middle	Queen	ORE	MB29	MB29HmPorous-6	porous martite	36.24	1033.72	1430.71	162.58	238.21	3.09	20.87	3.97	1.75	674.01
Middle	Queen	ORE	MB29	MB29HmPorous-7	porous martite	30.06	681.11	1161.63	110.72	276.30	2.19	13.71	3.09	1.14	597.86

Analysis no.	Co	Ni	Cu	Zn	Ga	As	Sr	Y	Zr	Nb	Mo	Sn	Sb	Ba	La	Ce	Pr
MB28HmPlaty-4	1.60	1.90	34.06	143.03	0.41	2.09	1.50	0.85	0.06	0.00	0.10	0.28	0.12	15.44	0.25	0.49	0.06
MB28HmPlaty-5	0.68	3.13	0.59	8.86	0.34	0.80	0.36	1.85	0.03	0.02	0.14	0.23	<0.023	10.32	0.65	0.85	0.07
MB28HmPlaty-6	0.47	2.71	14.80	59.02	0.31	0.60	0.27	0.79	0.04	0.00	0.13	0.29	0.05	5.84	0.18	0.27	0.03
MB28HmPlaty-7	0.61	0.66	46.12	151.85	0.32	1.67	0.58	0.58	0.03	0.01	0.07	0.34	0.10	1.64	0.16	0.35	0.06
MB28HmPlaty-8	0.38	1.06	4.68	23.55	0.28	0.93	0.32	1.05	0.03	0.01	0.13	0.18	0.10	2.70	0.18	0.30	0.03
MB28HmPlaty-9	0.90	5.43	6.57	22.58	0.28	0.99	1.16	0.85	0.05	0.00	0.09	0.15	0.08	12.38	0.39	0.52	0.05
MB29HmClean-1	<0.0221	<0.15	<0.135	<0.25	0.12	0.38	0.01	0.01	0.02	0.00	0.06	<0.169	0.17	0.04	0.00	0.00	0.00
MB29HmClean-10	<0.0244	0.13	<0.127	<0.25	0.11	<0.47	0.02	0.21	0.09	0.01	0.08	<0.185	2.12	0.05	0.24	0.22	0.02
MB29HmClean-11	<0.0162	0.07	0.43	0.45	0.21	0.58	0.21	0.09	0.08	0.00	0.04	<0.162	0.48	<0.00	0.10	0.09	0.01
MB29HmClean-12	<0.028	<0.078	<0.144	1.00	0.15	<0.39	<0.0132	0.01	0.11	0.01	0.07	0.21	1.45	<0.00	0.01	0.01	<0.00295
MB29HmClean-13	<0.0231	<0.137	<0.16	0.55	0.13	0.48	0.04	0.08	0.08	0.01	0.07	0.63	1.00	<0.00	0.06	0.08	0.01
MB29HmClean-14	<0.028	<0.159	<0.13	1.13	0.09	<0.36	0.01	0.02	0.07	0.02	0.05	<0.17	0.65	<0.00	0.00	0.01	0.00
MB29HmClean-15	<0.029	<0.138	0.74	0.84	0.20	0.87	0.11	0.29	0.05	0.00	0.11	<0.174	0.60	0.32	0.20	0.14	0.01
MB29HmClean-17	<0.025	<0.148	7.42	0.69	0.12	1.01	0.83	0.49	0.26	0.03	0.12	0.27	1.21	0.19	0.81	0.66	0.05
MB29HmClean-18	0.04	<0.158	<0.15	0.55	0.13	<0.4	<0.00	0.03	0.15	0.03	0.07	<0.183	0.68	<0.00	0.01	0.01	<0.00298
MB29HmClean-19	<0.015	<0.125	<0.115	0.45	0.15	0.57	0.08	0.45	0.30	0.05	0.09	<0.145	1.36	<0.00	0.76	0.58	0.05
MB29HmClean-2	<0.0173	<0.118	<0.141	0.25	0.07	<0.45	<0.00	0.02	0.04	0.00	0.05	<0.174	0.81	<0.00	0.01	0.01	<0.0045
MB29HmClean-20	<0.0167	<0.114	0.41	<0.27	0.18	<0.41	0.06	0.01	0.04	0.00	<0.044	<0.181	1.59	<0.00	0.00	0.02	0.00
MB29HmClean-3	0.02	<0.197	0.27	<0.28	0.24	1.91	0.09	0.56	0.03	0.00	0.04	<0.194	1.06	0.05	0.88	0.51	0.05
MB29HmClean-4	<0.0303	<0.119	<0.16	0.49	0.10	1.03	0.02	0.45	0.02	<0.00	0.05	<0.185	0.75	0.14	0.69	0.41	0.02
MB29HmClean-5	0.01	<0.083	0.45	0.75	0.09	1.29	0.46	0.42	0.10	<0.00	0.09	<0.19	1.12	1.11	2.09	1.93	0.14
MB29HmClean-6	0.02	<0.081	1.38	61.29	0.13	0.53	0.43	0.62	0.27	0.04	0.06	0.56	0.73	0.79	0.71	0.50	0.06
MB29HmClean-7	0.01	<0.138	<0.151	0.37	0.16	1.78	0.17	0.43	0.03	0.01	0.07	<0.172	1.23	0.09	0.55	0.43	0.02
MB29HmClean-8	0.05	<0.078	<0.136	0.39	0.07	0.60	0.03	0.06	0.05	0.01	<0.053	<0.17	0.64	0.05	0.06	0.06	0.00
MB29HmClean-9	<0.0163	<0.079	<0.153	<0.22	0.11	0.47	0.03	0.12	0.09	0.01	0.05	<0.17	0.80	<0.103	0.17	0.14	0.01
MB29HmPorous-1	2.03	4.83	2.88	19.54	0.41	0.65	3.54	0.09	0.41	0.03	0.08	<0.184	<0.126	0.33	0.14	2.46	0.05
MB29HmPorous-10	2.06	0.12	4.84	27.00	0.41	1.64	5.44	0.44	0.25	0.03	0.09	<0.151	0.99	0.62	0.28	2.90	0.06
MB29HmPorous-11	1.93	0.25	6.82	50.11	0.26	1.77	5.48	0.69	0.46	0.02	0.12	<0.146	1.44	0.69	0.21	2.72	0.06
MB29HmPorous-12	2.09	5.52	2.12	28.05	0.46	0.67	4.56	0.07	0.13	0.01	0.04	0.18	<0.098	0.70	0.08	2.12	0.04
MB29HmPorous-13	1.95	<0.073	7.22	49.35	0.27	1.93	4.79	0.69	0.40	0.03	0.29	0.27	1.55	1.04	0.18	2.63	0.07
MB29HmPorous-14	1.85	6.73	1.87	26.91	0.45	0.59	5.15	0.05	0.20	0.02	0.08	<0.15	0.16	0.59	0.12	2.39	0.03
MB29HmPorous-15	2.12	5.17	3.17	22.42	0.51	0.85	4.06	0.12	0.17	0.02	0.11	0.16	0.17	0.42	0.11	2.62	0.04
MB29HmPorous-16	1.76	0.31	3.25	15.59	0.17	1.30	3.95	0.21	0.50	0.04	0.12	<0.153	2.11	0.46	0.15	2.41	0.04
MB29HmPorous-17	1.03	0.17	1.86	3.48	0.22	1.19	4.43	0.15	0.19	0.01	0.14	<0.141	1.16	0.43	0.17	3.01	0.04
MB29HmPorous-18	2.32	7.39	4.90	35.17	0.48	0.91	4.44	0.72	0.23	0.01	0.08	<0.159	0.15	0.74	0.38	3.45	0.09
MB29HmPorous-19	2.26	8.51	9.66	73.29	0.55	1.50	4.79	1.29	0.36	0.03	0.06	0.29	<0.082	0.07	0.45	3.55	0.09
MB29HmPorous-2	0.45	<0.191	10.20	4.77	0.23	3.04	29.16	0.26	0.68	0.01	0.16	<0.173	0.32	2.11	0.78	3.39	0.19
MB29HmPorous-20	0.70	0.35	14.19	3.32	0.26	3.36	34.97	0.31	0.92	0.02	0.28	<0.138	0.14	2.47	0.23	2.34	0.10
MB29HmPorous-3	0.01	<0.116	<0.134	0.42	0.10	0.44	0.00	0.03	0.25	0.02	0.07	<0.185	1.39	0.05	0.03	0.02	0.00
MB29HmPorous-4	2.25	2.95	1.25	24.65	0.44	0.53	4.63	0.06	0.28	0.01	0.08	<0.195	<0.13	0.38	0.08	2.07	0.03
MB29HmPorous-5	1.57	0.13	3.18	7.08	0.21	1.35	4.41	0.55	0.44	0.08	0.16	0.15	1.43	0.57	0.23	2.65	0.06
MB29HmPorous-6	2.07	0.45	4.55	36.63	0.30	1.75	5.01	0.54	0.20	0.02	0.13	0.18	1.89	0.85	0.36	2.85	0.05
MB29HmPorous-7	1.72	0.94	1.42	10.18	0.16	0.61	4.24	0.11	0.25	0.01	0.14	<0.137	0.77	0.31	0.13	2.38	0.04

Analysis no.	Nd	Sm	Eu	Gd	Tb	Dy	Ho	Er	Tm	Yb	Lu	W	Pb208	Th	U
MB28HmPlaty-4	0.26	0.07	0.06	0.09	0.01	0.13	0.02	0.07	0.01	0.08	0.01	0.24	17.01	0.00	1.61
MB28HmPlaty-5	0.45	0.08	0.05	0.10	0.01	0.13	0.03	0.14	0.01	0.10	0.01	0.99	11.34	0.01	4.69
MB28HmPlaty-6	0.18	0.05	0.03	0.08	0.00	0.06	0.01	0.04	0.01	0.05	0.01	0.49	7.73	<0.00	3.20
MB28HmPlaty-7	0.29	0.11	0.06	0.09	0.02	0.09	0.02	0.05	0.01	0.02	0.01	0.08	9.04	<0.00	0.46
MB28HmPlaty-8	0.21	0.04	0.05	0.08	0.01	0.07	0.01	0.07	0.01	0.06	0.01	0.20	4.43	<0.00274	0.80
MB28HmPlaty-9	0.26	0.08	0.04	0.06	0.01	0.08	0.02	0.06	0.01	0.06	0.01	0.99	17.96	<0.00	5.08
MB29HmClean-1	0.00	<0.00	<0.0048	0.01	<0.00	<0.00	<0.00	<0.0079	0.00	<0.00	0.00	0.13	0.04	<0.00	<0.00252
MB29HmClean-10	0.08	<0.00	<0.0075	0.04	0.00	0.02	0.00	<0.0151	0.00	0.01	0.00	2.47	0.55	0.00	0.02
MB29HmClean-11	0.03	0.00	<0.0086	0.00	<0.00	0.01	0.00	0.01	0.00	0.01	0.00	1.58	0.80	0.00	0.01
MB29HmClean-12	0.00	<0.00	<0.005	0.00	0.00	0.01	0.00	<0.00	<0.00	0.01	<0.00	0.38	0.10	<0.00	0.00
MB29HmClean-13	0.03	0.00	0.00	<0.0277	<0.00264	0.01	<0.00	0.01	0.00	<0.0166	<0.00	1.63	0.10	0.00	0.01
MB29HmClean-14	<0.00	<0.00	0.00	<0.00	<0.00	<0.011	0.00	<0.00	<0.00252	<0.0118	<0.00263	0.16	0.06	<0.00	<0.00264
MB29HmClean-15	0.02	0.01	0.01	<0.0197	<0.0027	0.02	<0.0027	0.00	0.00	0.01	<0.0026	2.42	0.76	<0.00	0.01
MB29HmClean-17	0.16	0.01	0.01	0.04	0.00	0.06	0.01	0.03	0.00	<0.0127	<0.0028	3.85	3.92	0.02	0.05
MB29HmClean-18	0.00	<0.00	<0.0071	0.00	<0.00264	<0.00	<0.0027	<0.0143	0.00	<0.0118	<0.00	0.10	0.05	<0.00	0.00
MB29HmClean-19	0.17	<0.025	0.02	0.06	0.00	0.07	0.00	0.04	0.01	0.04	0.01	4.71	1.22	0.01	0.02
MB29HmClean-2	0.01	<0.00	<0.0053	<0.00	0.00	<0.0116	0.00	0.01	<0.00	0.00	<0.0039	0.14	0.06	<0.00	0.00
MB29HmClean-20	0.00	<0.00	<0.00	<0.00	<0.0027	<0.00	<0.00274	0.00	<0.00	<0.012	0.00	0.24	0.38	<0.00	<0.0027
MB29HmClean-3	0.21	0.01	0.01	0.03	0.00	0.02	0.01	0.02	0.00	0.02	0.00	4.96	1.73	<0.00	0.02
MB29HmClean-4	0.10	<0.0209	0.01	0.01	<0.004	0.01	0.01	0.03	0.01	0.02	0.00	5.05	2.03	0.00	0.00
MB29HmClean-5	0.59	0.05	0.03	0.10	0.00	0.02	0.01	0.03	0.00	0.02	<0.0028	4.51	6.10	0.01	0.05
MB29HmClean-6	0.14	<0.02	<0.0073	0.02	<0.00	0.03	0.01	0.03	0.01	0.04	<0.0038	5.22	1.77	<0.0046	0.02
MB29HmClean-7	0.10	0.01	0.01	0.03	0.00	0.02	0.01	0.03	0.00	0.02	0.00	3.70	0.71	0.00	0.02
MB29HmClean-8	0.02	<0.0194	<0.005	<0.0195	<0.0037	<0.00	0.00	<0.0116	0.00	<0.00	0.00	0.69	0.18	<0.00	0.00
MB29HmClean-9	0.03	<0.0195	0.00	0.01	0.00	0.01	0.00	0.01	0.00	0.01	<0.0026	0.68	0.38	<0.00	0.00
MB29HmPorous-1	0.24	0.04	0.01	0.01	0.00	0.04	0.00	0.02	<0.0026	0.01	0.00	3.32	12.76	0.06	0.14
MB29HmPorous-10	0.22	0.02	0.02	0.06	0.01	0.04	0.01	0.03	0.01	0.04	0.01	6.09	13.57	0.02	0.15
MB29HmPorous-11	0.20	0.05	0.02	0.06	0.01	0.04	0.01	0.06	0.01	0.07	0.02	7.12	15.04	0.05	0.93
MB29HmPorous-12	0.13	0.03	0.01	0.04	0.00	0.02	<0.0024	0.01	<0.00221	<0.0103	0.00	2.56	10.95	0.01	0.20
MB29HmPorous-13	0.24	0.07	0.02	0.08	0.01	0.08	0.01	0.08	0.00	0.05	0.00	7.17	14.60	0.02	0.96
MB29HmPorous-14	0.12	0.04	0.01	0.02	0.00	0.02	<0.0023	0.02	0.00	<0.0102	0.00	2.92	16.04	0.02	0.14
MB29HmPorous-15	0.14	0.05	0.01	0.03	0.00	0.01	0.01	0.01	<0.0023	0.01	0.00	2.52	11.56	0.02	0.19
MB29HmPorous-16	0.16	0.03	0.01	0.03	0.00	0.03	0.01	0.01	0.00	0.03	0.00	3.94	12.30	0.03	0.16
MB29HmPorous-17	0.16	0.06	0.01	0.03	0.00	0.02	<0.00	0.02	0.00	0.01	0.00	4.67	11.95	0.00	0.11
MB29HmPorous-18	0.48	0.11	0.04	0.05	0.01	0.02	0.02	0.06	0.01	0.04	0.01	2.68	15.08	0.03	0.19
MB29HmPorous-19	0.40	0.08	0.04	0.09	0.01	0.10	0.02	0.07	0.01	0.09	0.02	2.45	15.12	0.04	0.17
MB29HmPorous-2	0.75	0.14	0.03	0.10	0.01	0.07	0.01	0.04	0.00	0.03	0.01	2.06	51.62	0.07	0.54
MB29HmPorous-20	0.33	0.10	0.04	0.07	0.02	0.10	0.02	0.04	0.00	0.04	0.00	2.00	55.83	0.06	0.72
MB29HmPorous-3	0.01	<0.0202	0.00	<0.029	0.00	0.01	<0.0028	0.01	0.00	<0.0122	<0.00	0.31	0.18	<0.00	0.00
MB29HmPorous-4	0.11	0.02	0.01	<0.022	<0.003	0.03	0.00	0.01	<0.0028	0.01	<0.0042	2.88	10.90	0.03	0.12
MB29HmPorous-5	0.19	0.08	0.02	0.06	0.01	0.04	0.01	0.02	0.00	0.06	0.01	4.55	11.89	0.02	0.19
MB29HmPorous-6	0.22	0.08	0.03	0.05	0.01	0.07	0.00	0.05	0.00	0.03	0.00	4.37	18.66	0.03	0.23
MB29HmPorous-7	0.17	0.03	0.01	0.04	0.01	0.01	0.00	0.02	0.00	0.01	<0.0022	4.05	11.61	0.03	0.15

Position	Deposit	Lithology	Sample no.	Analysis no.	Texture	Mg	Al	Si	P	Ca	Sc	Ti	V	Cr	Mn
Middle	Queen	ORE	MB29	MB29HmPorous-8	porous martite	46.85	627.99	1301.41	80.01	185.62	1.84	10.74	2.67	<0.88	684.61
Middle	Queen	ORE	MB29	MB29HmPorous-9	porous martite	32.28	1071.65	1448.49	192.29	<80.5	4.36	13.72	3.48	0.89	730.99
North	Princess	BIF	MB2	MB2Hm-1	porous martite	98.44	532.80	439.66	<10.16	214.30	0.59	471.89	34.98	1.82	115.82
North	Princess	BIF	MB2	MB2Hm-10	porous martite	360.81	869.92	2565.66	<14.61	<132.74	<0.218	633.50	39.43	50.43	381.86
North	Princess	BIF	MB2	MB2Hm-11	porous martite	155.80	969.62	964.12	<12.7	325.35	0.24	639.34	40.54	61.14	134.92
North	Princess	BIF	MB2	MB2Hm-12	porous martite	147.57	639.87	801.78	12.45	181.92	0.41	769.27	42.59	40.01	173.08
North	Princess	BIF	MB2	MB2Hm-13	porous martite	168.62	731.74	1147.59	11.41	<90.92	0.58	811.20	51.37	23.13	103.89
North	Princess	BIF	MB2	MB2Hm-14	porous martite	190.58	1136.12	3601.44	22.71	<102.5	0.32	670.82	44.59	14.17	89.95
North	Princess	BIF	MB2	MB2Hm-15	porous martite	89.66	928.36	1183.26	22.84	183.94	0.40	580.44	37.02	336.00	50.21
North	Princess	BIF	MB2	MB2Hm-17	porous martite	97.84	759.37	3164.94	18.93	127.93	0.61	684.12	42.60	337.66	93.84
North	Princess	BIF	MB2	MB2Hm-19	porous martite	74.82	618.91	808.62	14.01	251.52	0.69	496.12	31.55	631.71	188.43
North	Princess	BIF	MB2	MB2Hm-2	porous martite	566.26	1636.33	3779.15	21.63	362.08	0.52	551.29	54.66	9.94	239.55
North	Princess	BIF	MB2	MB2Hm-20	porous martite	408.17	1127.94	1637.37	32.81	<102.05	1.27	945.26	40.23	261.55	263.05
North	Princess	BIF	MB2	MB2Hm-3	porous martite	1268.56	2812.29	15469.76	<12.02	271.40	1.06	1102.73	64.48	1.59	141.83
North	Princess	BIF	MB2	MB2Hm-4	porous martite	239.55	822.04	1413.78	9.93	225.64	0.34	484.77	32.24	32.80	74.26
North	Princess	BIF	MB2	MB2Hm-5	porous martite	202.85	901.08	1970.34	38.09	<115.39	1.29	668.53	35.76	808.42	56.24
North	Princess	BIF	MB2	MB2Hm-6	porous martite	129.90	595.92	1075.63	26.70	<115.68	0.23	517.47	41.24	11.39	101.76
North	Princess	BIF	MB2	MB2Hm-7	porous martite	1133.10	2423.86	4885.10	14.96	<119.13	0.40	642.24	49.11	3.26	452.10
North	Princess	BIF	MB2	MB2Hm-8	porous martite	188.83	948.14	1246.77	15.67	172.88	0.41	593.63	46.31	12.35	151.39
North	Princess	BIF	MB2	MB2Hm-9	porous martite	118.44	533.27	603.65	15.22	<124.42	0.24	360.29	37.50	1.51	177.06
North	Princess	BIF	MB2	MB2Mg-1	magnetite	350.87	548.08	1175.44	21.89	253.25	1.89	15.40	10.54	<1.16	324.55
North	Princess	BIF	MB2	MB2Mg-11	magnetite	167.61	81.96	442.69	11.62	8219.72	1.45	28.08	14.09	<1.2	503.32
North	Princess	BIF	MB2	MB2Mg-12	magnetite	196.74	168.04	609.55	31.88	178.95	1.62	32.72	13.94	<1.21	467.67
North	Princess	BIF	MB2	MB2Mg-13	magnetite	83.90	327.59	736.01	<10.09	2100.93	0.72	15.83	13.57	1.21	179.46
North	Princess	BIF	MB2	MB2Mg-15	magnetite	117.69	143.57	713.00	<11.73	845.80	0.87	59.85	9.41	<1.46	337.59
North	Princess	BIF	MB2	MB2Mg-3	magnetite	105.36	162.84	440.56	<9.96	<102.78	1.24	101.44	5.74	1.05	488.73
North	Princess	BIF	MB2	MB2Mg-4	magnetite	33.89	126.48	594.84	<10.18	<96.62	2.48	21.40	10.25	<1.04	70.08
North	Princess	BIF	MB2	MB2Mg-5	magnetite	131.35	193.41	757.10	<11.51	<111.11	1.38	47.39	14.29	1.38	50.44
North	Princess	BIF	MB2	MB2Mg-6	magnetite	31.08	176.97	684.94	13.91	197.29	2.38	33.76	13.45	<1.12	94.51
North	Princess	BIF	MB2	MB2Mg-8	magnetite	570.96	91.02	470.44	12.16	575.39	1.65	6.55	4.22	<1.06	3780.18
North	Princess	BIF	MB2	MB2Mg-9	magnetite	96.44	98.70	531.36	26.71	1538.42	1.31	7.04	15.26	<1.1	270.48
South	Magnet	BIF	MB33	MB33Hm-1	clean martite	203.54	15.47	686.82	245.16	<89.36	<0.114	<0.65	0.33	1.04	231.32
South	Magnet	BIF	MB33	MB33Hm-10	clean martite	96.25	31.77	159.05	<8.89	126.64	0.42	34.03	1.82	<1.01	3.92
South	Magnet	BIF	MB33	MB33Hm-11	clean martite	85.89	18.60	421.79	33.29	<102.67	0.16	0.69	0.72	1.82	259.97
South	Magnet	BIF	MB33	MB33Hm-12	clean martite	24.37	13.56	116.17	<7.65	<79.92	0.18	<0.75	0.61	1.21	299.74
South	Magnet	BIF	MB33	MB33Hm-13	clean martite	24.24	7.95	327.66	10.08	<76.58	0.20	<0.61	0.34	<1	263.45
South	Magnet	BIF	MB33	MB33Hm-14	clean martite	54.84	30.17	1037.90	24.31	<94.71	0.20	73.73	1.11	1.31	3.01
South	Magnet	BIF	MB33	MB33Hm-15	clean martite	77.58	30.92	1445.72	19.79	207.63	<0.136	160.29	1.24	<0.98	162.54
South	Magnet	BIF	MB33	MB33Hm-16	clean martite	13.85	39.45	14816.53	35.92	267.57	<0.151	11.94	1.73	<1.04	3.14
South	Magnet	BIF	MB33	MB33Hm-17	clean martite	2.01	31.01	<135.1	32.18	168.22	<0.163	87.03	1.28	<1.45	1.81
South	Magnet	BIF	MB33	MB33Hm-18	clean martite	1.60	30.64	171.24	14.60	<92.15	<0.125	109.88	1.64	<0.98	1.67
South	Magnet	BIF	MB33	MB33Hm-19	clean martite	19.06	13.08	617.72	14.57	<82.81	<0.127	<0.69	0.49	<0.9	267.42
South	Magnet	BIF	MB33	MB33Hm-2	clean martite	309.57	12.88	815.21	84.67	<103.44	<0.117	<0.55	0.38	<0.89	271.09

Analysis no.	Co	Ni	Cu	Zn	Ga	As	Sr	Y	Zr	Nb	Mo	Sn	Sb	Ba	La	Ce	Pr
MB29HmPorous-8	1.77	6.05	1.51	29.50	0.40	0.57	4.49	0.06	0.11	0.02	0.09	<0.149	0.10	0.52	0.10	2.22	0.04
MB29HmPorous-9	2.60	4.47	4.75	32.93	0.53	0.76	4.75	0.28	0.38	0.02	0.13	<0.127	0.17	0.73	0.14	2.75	0.04
MB2Hm-1	1.75	4.84	1.79	9.19	3.41	49.92	1.16	0.33	0.56	1.33	0.26	0.85	7.43	1.50	0.29	0.44	0.03
MB2Hm-10	7.65	23.49	57.17	11.57	4.00	61.98	1.91	0.55	0.66	1.43	0.53	0.86	9.57	4.06	0.49	0.69	0.09
MB2Hm-11	4.57	15.30	57.79	9.16	4.02	66.45	3.09	0.81	7.79	1.82	0.19	1.20	11.52	3.87	0.48	0.74	0.07
MB2Hm-12	1.10	5.26	0.68	13.42	3.95	37.59	1.47	0.89	12.82	1.71	0.53	0.88	8.32	2.80	0.40	0.60	0.06
MB2Hm-13	1.11	5.61	0.64	13.85	3.75	44.77	1.07	0.48	0.42	1.08	0.60	1.12	8.16	2.85	0.61	0.85	0.09
MB2Hm-14	1.16	7.48	0.43	14.46	4.58	51.33	0.98	0.27	0.73	0.83	0.57	0.52	15.31	2.97	0.29	0.42	0.05
MB2Hm-15	2.86	10.28	4.37	19.62	4.60	67.23	0.98	0.42	3.89	1.76	0.28	0.92	17.07	3.99	0.21	0.42	0.03
MB2Hm-17	22.03	46.32	4.42	14.85	4.29	91.40	1.69	4.25	71.92	0.98	0.92	0.72	21.03	4.60	0.68	1.09	0.14
MB2Hm-19	1.47	4.97	<0.24	13.31	4.70	58.26	1.46	6.42	214.99	0.37	0.17	0.73	14.12	3.46	0.14	0.27	0.03
MB2Hm-2	0.42	5.49	0.26	14.19	3.84	78.64	1.45	0.47	0.37	1.82	0.31	1.67	10.59	2.77	0.49	0.76	0.08
MB2Hm-20	0.27	6.32	1.15	12.92	4.16	55.99	1.09	13.82	149.10	3.14	1.21	1.89	11.14	4.49	0.68	1.41	0.17
MB2Hm-3	0.53	4.21	0.27	12.43	3.07	29.37	1.00	0.76	1.40	2.78	0.97	1.67	18.57	8.44	1.57	2.07	0.21
MB2Hm-4	2.99	10.94	20.47	19.09	3.25	39.69	0.76	0.46	0.47	0.41	0.17	0.54	5.74	1.44	0.42	0.67	0.05
MB2Hm-5	0.23	5.69	0.82	10.67	3.54	62.96	1.04	26.32	301.08	2.52	0.50	1.10	10.55	2.96	0.70	1.52	0.22
MB2Hm-6	0.78	5.34	2.71	9.88	3.46	57.11	0.89	0.61	2.42	2.78	0.84	0.87	10.33	2.10	0.80	1.09	0.11
MB2Hm-7	0.35	9.99	0.71	25.30	3.89	38.58	0.71	0.79	1.54	1.62	2.17	0.78	9.26	4.28	0.82	1.08	0.13
MB2Hm-8	1.02	7.14	1.56	8.68	3.80	75.81	1.31	0.49	1.82	3.57	1.09	1.86	15.00	3.30	0.67	0.91	0.11
MB2Hm-9	2.27	33.77	7.79	10.64	3.76	49.47	1.12	0.27	0.44	0.87	0.38	0.89	8.10	1.95	0.24	0.33	0.03
MB2Mg-1	0.04	3.33	0.35	15.33	0.38	3.16	0.17	0.96	0.64	0.09	2.64	0.25	0.82	1.94	0.69	1.17	0.15
MB2Mg-11	0.11	2.73	<0.19	5.47	0.28	4.62	2.09	1.12	0.85	0.23	2.43	0.42	1.12	5.35	1.42	1.91	0.19
MB2Mg-12	0.64	4.28	0.41	8.55	0.18	4.32	0.15	0.91	1.24	0.17	2.48	0.58	1.68	2.71	0.81	1.18	0.11
MB2Mg-13	0.01	1.80	<0.195	12.43	0.43	4.02	0.39	1.08	0.06	0.16	2.67	<0.18	0.86	3.90	0.80	1.19	0.12
MB2Mg-15	0.25	3.20	0.30	8.76	0.07	6.05	0.40	1.21	0.58	0.44	2.90	<0.24	1.48	2.66	0.86	1.11	0.11
MB2Mg-3	0.34	6.22	0.60	15.47	0.19	1.57	0.12	0.42	0.42	0.04	2.55	<0.2	0.49	1.01	0.28	0.40	0.05
MB2Mg-4	<0.046	4.09	<0.22	5.70	0.24	4.44	0.15	1.18	0.97	0.15	3.61	<0.184	1.11	2.50	1.00	1.44	0.16
MB2Mg-5	<0.047	2.09	0.44	5.94	0.12	5.46	0.22	0.88	0.83	0.23	2.13	0.31	1.23	1.83	0.84	1.04	0.11
MB2Mg-6	0.04	1.36	<0.201	7.76	0.16	8.77	0.91	1.31	0.47	0.22	3.02	<0.187	0.85	6.16	1.81	2.39	0.26
MB2Mg-8	<0.033	5.63	<0.239	7.00	<0.061	2.32	0.04	1.72	0.54	0.03	5.04	0.26	0.54	1.38	0.44	0.64	0.07
MB2Mg-9	0.09	3.24	<0.24	8.65	0.16	2.48	0.21	1.00	0.86	0.08	2.51	<0.177	0.69	2.49	1.05	1.49	0.15
MB33Hm-1	0.63	1.08	0.16	4.06	0.06	0.41	1.45	1.81	0.03	<0.00	<0.00	0.20	<0.097	0.93	0.49	0.53	0.07
MB33Hm-10	0.04	<0.135	0.14	0.55	0.03	1.23	0.22	0.05	3.58	0.07	0.18	<0.178	0.48	0.16	0.05	0.03	0.00
MB33Hm-11	0.72	1.02	2.51	6.67	0.06	<0.3	1.67	0.05	<0.00	<0.00	0.08	<0.162	<0.071	0.42	0.02	0.03	0.00
MB33Hm-12	0.56	0.91	<0.121	3.20	<0.033	<0.3	0.04	<0.0063	0.01	<0.0058	<0.00	<0.158	0.07	0.24	0.00	0.00	0.00
MB33Hm-13	0.56	1.13	<0.143	4.11	0.07	<0.35	0.15	0.05	0.03	<0.00	<0.037	<0.152	<0.077	0.32	0.03	0.03	<0.00
MB33Hm-14	<0.021	<0.127	<0.145	1.38	<0.025	<0.34	0.06	0.05	0.80	0.04	0.25	<0.163	0.36	<0.00	0.05	0.03	0.00
MB33Hm-15	0.21	<0.132	<0.12	2.15	<0.026	0.55	0.28	0.43	0.88	0.03	0.06	<0.17	0.35	0.63	0.02	0.07	0.01
MB33Hm-16	0.03	<0.081	0.55	1.32	0.06	<0.35	0.09	0.03	0.18	0.08	0.22	<0.19	0.54	<0.00	0.02	0.02	0.00
MB33Hm-17	<0.03	<0.105	<0.171	<0.36	<0.02	<0.43	0.22	0.13	0.65	0.02	0.12	<0.222	0.13	<0.00	0.03	0.06	0.01
MB33Hm-18	<0.0152	<0.074	<0.168	0.48	0.09	<0.33	<0.00	0.03	0.72	0.06	0.14	<0.161	0.08	<0.00	0.01	0.02	<0.00271
MB33Hm-19	0.81	0.86	<0.105	4.10	<0.031	<0.34	0.08	0.03	0.01	<0.00	0.03	<0.163	<0.078	0.22	0.02	0.03	0.00
MB33Hm-2	0.81	1.38	<0.156	3.64	0.06	<0.32	0.66	0.85	<0.0219	<0.00	<0.028	<0.169	<0.059	0.28	0.25	0.22	0.03

Analysis no.	Nd	Sm	Eu	Gd	Tb	Dy	Ho	Er	Tm	Yb	Lu	W	Pb208	Th	U
MB29HmPorous-8	0.17	0.04	0.02	<0.018	0.00	0.01	0.00	0.02	<0.00	0.01	<0.00	2.63	10.59	0.04	0.26
MB29HmPorous-9	0.21	0.04	0.01	0.03	0.01	0.04	0.01	0.02	0.00	0.02	0.00	2.82	13.54	0.03	0.54
MB2Hm-1	0.14	0.05	0.02	0.05	0.01	0.07	0.01	0.03	0.00	0.04	<0.00324	2.53	7.48	0.18	0.72
MB2Hm-10	0.35	0.04	0.04	0.11	0.02	0.08	0.02	0.04	0.01	0.06	0.00	3.44	21.09	0.29	1.14
MB2Hm-11	0.29	0.10	0.03	0.07	0.01	0.13	0.02	0.07	0.02	0.08	0.02	4.02	17.10	0.24	0.79
MB2Hm-12	0.21	0.06	0.04	0.05	0.01	0.12	0.03	0.10	0.01	0.11	0.01	4.09	8.82	0.27	1.30
MB2Hm-13	0.34	0.11	0.03	0.11	0.01	0.08	0.02	0.04	0.00	0.07	0.01	6.81	11.53	0.32	0.88
MB2Hm-14	0.15	0.04	0.01	0.04	0.01	0.04	0.01	0.04	0.01	0.02	<0.0046	9.70	19.11	0.15	0.93
MB2Hm-15	0.21	0.05	0.02	0.11	0.01	0.04	0.01	0.03	0.00	0.04	0.01	3.02	23.71	0.36	0.82
MB2Hm-17	0.37	0.20	0.06	0.36	0.05	0.52	0.10	0.28	0.07	0.52	0.08	4.05	40.41	0.59	3.54
MB2Hm-19	0.20	0.09	0.10	0.24	0.04	0.43	0.18	0.75	0.14	1.35	0.28	0.80	14.77	0.49	4.34
MB2Hm-2	0.37	0.13	0.01	0.21	0.02	0.07	0.01	0.05	0.01	0.05	0.01	6.68	9.62	0.19	0.54
MB2Hm-20	0.79	0.35	0.27	0.87	0.16	1.18	0.32	1.07	0.20	1.35	0.27	4.69	14.24	0.94	7.79
MB2Hm-3	0.71	0.15	0.05	0.18	0.03	0.15	0.02	0.08	0.00	0.07	0.00	101.11	6.77	0.66	0.97
MB2Hm-4	0.17	0.09	0.02	0.08	0.01	0.08	0.02	0.03	0.01	0.02	0.00	1.40	11.01	0.24	0.56
MB2Hm-5	1.02	0.61	0.35	1.58	0.35	2.49	0.59	2.33	0.35	3.13	0.49	2.75	13.60	1.91	13.55
MB2Hm-6	0.61	0.26	0.05	0.11	0.02	0.09	0.02	0.05	0.01	0.06	0.01	3.56	12.96	0.52	1.66
MB2Hm-7	0.42	0.06	0.09	0.25	0.03	0.18	0.02	0.10	0.01	0.12	0.01	6.06	11.26	0.39	1.31
MB2Hm-8	0.39	0.13	0.04	0.15	0.02	0.13	0.01	0.05	0.02	0.06	0.01	4.58	15.57	0.32	1.53
MB2Hm-9	0.09	0.04	0.02	0.05	<0.0101	0.05	0.01	0.02	0.00	<0.02	<0.0044	2.55	10.76	0.12	0.56
MB2Mg-1	0.67	0.18	0.04	0.15	0.04	0.17	0.03	0.11	0.01	0.05	0.01	0.01	0.35	0.00	0.01
MB2Mg-11	0.83	0.27	0.09	0.18	0.03	0.13	0.03	0.08	0.01	0.07	0.01	0.02	<0.036	<0.00	<0.0037
MB2Mg-12	0.49	0.17	0.05	0.19	0.03	0.14	0.02	0.06	0.01	0.05	0.01	0.01	<0.025	<0.00	<0.0036
MB2Mg-13	0.63	0.14	0.07	0.15	0.03	0.12	0.03	0.08	0.01	0.05	0.01	1.04	0.49	0.01	0.00
MB2Mg-15	0.52	0.16	0.04	0.21	0.03	0.18	0.04	0.06	0.01	0.05	0.01	1.73	0.43	<0.00	0.02
MB2Mg-3	0.22	0.09	0.01	0.07	0.01	0.08	0.01	0.03	0.00	0.04	0.00	0.04	1.27	<0.00	0.01
MB2Mg-4	0.85	0.22	0.05	0.32	0.04	0.23	0.03	0.06	0.02	0.06	0.01	0.02	0.53	<0.0078	<0.0036
MB2Mg-5	0.48	0.11	0.06	0.19	0.02	0.15	0.03	0.07	0.01	0.05	0.02	<0.00	0.23	<0.0106	<0.0153
MB2Mg-6	1.07	0.22	0.09	0.29	0.04	0.26	0.04	0.10	0.01	0.05	0.01	<0.00	0.13	<0.00	<0.0034
MB2Mg-8	0.35	0.13	0.08	0.20	0.04	0.30	0.05	0.14	0.02	0.14	0.02	<0.0161	0.31	0.01	0.01
MB2Mg-9	0.73	0.16	0.05	0.19	0.04	0.21	0.03	0.08	0.01	0.02	0.00	19.59	1.97	0.14	0.38
MB33Hm-1	0.23	0.04	0.04	0.12	0.01	0.11	0.03	0.09	0.02	0.09	0.01	0.04	0.22	0.00	0.00
MB33Hm-10	0.02	<0.00	0.01	0.01	0.00	<0.00	<0.00	<0.00	0.00	0.01	0.00	6.27	0.32	0.01	0.00
MB33Hm-11	0.02	<0.00	<0.00	0.01	<0.0024	<0.00	<0.00	<0.00	<0.00	<0.00	0.00	0.01	0.11	0.00	0.02
MB33Hm-12	<0.00	<0.00	<0.0043	<0.017	<0.0023	<0.0133	<0.00	<0.0072	<0.00217	<0.00	<0.00321	0.01	0.04	<0.00	<0.00223
MB33Hm-13	0.01	<0.00	<0.00	<0.024	<0.00227	<0.0094	0.00	<0.00	<0.0022	<0.00	<0.00225	<0.0109	0.13	<0.00	0.00
MB33Hm-14	0.02	0.01	0.01	0.01	<0.0024	<0.00	0.00	<0.00	<0.00	0.01	<0.00	0.88	0.15	<0.0044	0.02
MB33Hm-15	0.03	0.01	0.01	0.05	0.00	0.03	0.01	0.02	0.00	0.05	0.01	0.18	0.61	0.00	0.00
MB33Hm-16	0.01	<0.00	0.00	0.03	<0.00265	<0.00	<0.00	<0.00	<0.00	0.01	<0.00263	1.59	0.09	0.01	0.01
MB33Hm-17	<0.00	<0.00	0.00	0.01	<0.00	<0.0141	<0.00	0.01	0.00	<0.0152	0.00	0.35	0.05	<0.00	0.00
MB33Hm-18	<0.00	<0.0252	0.00	<0.018	<0.00	0.01	0.00	<0.0076	<0.00	<0.0108	<0.00	0.12	0.09	<0.00	0.00
MB33Hm-19	0.02	<0.00	0.00	<0.00	<0.0033	0.01	0.00	0.00	0.00	<0.00	<0.00	0.05	0.27	<0.00	<0.00228
MB33Hm-2	0.14	0.04	0.03	0.05	0.00	0.03	0.00	0.06	0.01	0.04	0.01	<0.0115	0.14	0.00	0.01

Position	Deposit	Lithology	Sample no.	Analysis no.	Texture	Mg	Al	Si	P	Ca	Sc	Ti	V	Cr	Mn
South	Magnet	BIF	MB33	MB33Hm-20	clean martite	0.79	30.93	125.55	12.36	<81.56	<0.119	4.31	1.18	<1	0.91
South	Magnet	BIF	MB33	MB33Hm-3	clean martite	0.63	28.72	197.92	10.08	<91.87	0.14	1.47	1.00	<0.9	1.77
South	Magnet	BIF	MB33	MB33Hm-4	clean martite	32.99	1.32	363.63	31.75	<103.21	0.15	0.55	0.27	<0.94	280.30
South	Magnet	BIF	MB33	MB33Hm-5	clean martite	586.21	2.49	1242.12	16.36	<92.13	<0.113	<0.63	0.41	1.22	275.90
South	Magnet	BIF	MB33	MB33Hm-6	clean martite	410.85	22.33	847.56	23.27	<95.4	<0.132	1.06	0.40	1.03	297.99
South	Magnet	BIF	MB33	MB33Hm-7	clean martite	161.10	58.66	3072.66	31.04	124.18	<0.13	<0.71	0.64	<0.94	260.55
South	Magnet	BIF	MB33	MB33Hm-8	clean martite	20.68	31.42	319.93	13.24	215.05	<0.133	0.98	0.58	<0.87	244.57
South	Magnet	BIF	MB33	MB33Mg-1	magnetite	9.24	28.52	21345.31	<10.25	<105.38	<0.135	50.70	1.54	<1.26	109.93
South	Magnet	BIF	MB33	MB33Mg-10	magnetite	490.38	34.28	1480.92	13.50	151.47	0.19	<0.66	0.43	<1.31	340.31
South	Magnet	BIF	MB33	MB33Mg-11	magnetite	136.52	20.60	577.29	<11.27	<125.64	<0.179	1.11	0.46	<1.37	332.87
South	Magnet	BIF	MB33	MB33Mg-12	magnetite	58.66	24.34	<127.1	11.19	<98.4	<0.169	<0.64	0.31	<1.2	318.02
South	Magnet	BIF	MB33	MB33Mg-13	magnetite	256.11	23.35	952.37	<9.28	<100.22	<0.155	0.84	0.50	<1.01	334.56
South	Magnet	BIF	MB33	MB33Mg-14	magnetite	104.69	17.34	<105.8	<8.71	<90.82	<0.121	0.66	0.43	<0.94	315.81
South	Magnet	BIF	MB33	MB33Mg-15	magnetite	23.17	23.19	<108.45	<9.05	<92.15	<0.143	<0.66	0.27	<1.14	329.45
South	Magnet	BIF	MB33	MB33Mg-16	magnetite	71.86	18.38	1394.83	13.84	<86.01	<0.15	<0.66	0.49	1.67	279.74
South	Magnet	BIF	MB33	MB33Mg-19	magnetite	84.72	13.40	516.51	<10.8	<117.57	<0.17	1.06	0.68	<1.33	262.77
South	Magnet	BIF	MB33	MB33Mg-2	magnetite	34.44	22.47	157.76	<11.57	<127.17	<0.18	<0.8	0.72	1.41	296.82
South	Magnet	BIF	MB33	MB33Mg-20	magnetite	14.80	26.97	306.14	18.56	<87.52	<0.135	2.00	0.95	<1.13	215.93
South	Magnet	BIF	MB33	MB33Mg-3	magnetite	325.08	14.96	836.41	<12.03	<127.92	<0.172	<0.78	0.41	<1.26	311.85
South	Magnet	BIF	MB33	MB33Mg-5	magnetite	42.19	18.57	1427.10	<12.16	<129.28	0.35	<0.77	0.34	<1.23	339.27
South	Magnet	BIF	MB33	MB33Mg-6	magnetite	443.30	26.89	1138.96	26.14	162.09	<0.185	<0.9	0.38	<1.47	210.24
South	Magnet	BIF	MB33	MB33Mg-7	magnetite	21.82	25.30	146.76	13.03	<122.3	<0.148	<0.75	0.49	<1.31	283.54
South	Magnet	BIF	MB33	MB33Mg-8	magnetite	43.46	18.88	9837.58	11.82	<131.51	0.22	<0.91	0.63	<1.45	251.87
South	Magnet	BIF	MB33	MB33Mg-9	magnetite	1817.53	20.27	6510.89	14.47	<113.91	<0.165	<1.14	0.50	<1.43	309.01
South	Magnet	BIF	MB35a	MB35aMt-1	magnetite	988.41	10.01	238.65	<6.88	267.03	<0.099	2.04	0.72	<0.84	547.46
South	Magnet	BIF	MB35a	MB35aMt-10	magnetite	22.08	25.60	203.13	<6.18	79.09	<0.081	1.26	0.50	<0.73	473.50
South	Magnet	BIF	MB35a	MB35aMt-11	magnetite	16.69	16.75	<72.79	9.94	105.07	<0.102	1.10	0.55	<0.72	485.86
South	Magnet	BIF	MB35a	MB35aMt-13	magnetite	37.65	14.89	660.21	12.22	204.99	<0.1	1.34	0.60	<0.78	408.46
South	Magnet	BIF	MB35a	MB35aMt-14	magnetite	59.05	8.49	604.76	<4.68	545.24	0.08	2.19	0.61	<0.53	287.03
South	Magnet	BIF	MB35a	MB35aMt-15	magnetite	113.48	15.54	539.05	130.39	260.58	<0.108	1.54	0.66	<0.8	482.17
South	Magnet	BIF	MB35a	MB35aMt-16	magnetite	196.49	11.31	736.09	<7.18	122.04	<0.116	1.09	0.57	<0.82	310.65
South	Magnet	BIF	MB35a	MB35aMt-17	magnetite	1892.64	14.50	4401.98	12.77	<64.53	<0.134	0.82	0.45	<1.07	305.77
South	Magnet	BIF	MB35a	MB35aMt-18	magnetite	20.22	20.42	295.68	<6.17	<44.97	0.11	1.17	0.44	<0.81	484.66
South	Magnet	BIF	MB35a	MB35aMt-19	magnetite	71.87	25.08	<78.82	<6.72	<51.78	<0.109	1.28	0.32	<0.77	569.46
South	Magnet	BIF	MB35a	MB35aMt-2	magnetite	143.08	9.55	476.75	13.07	<43.27	<0.079	2.05	0.65	<0.79	288.59
South	Magnet	BIF	MB35a	MB35aMt-20	magnetite	60.68	14.83	357.48	<6.38	28.21	<0.099	0.68	0.30	<0.6	438.81
South	Magnet	BIF	MB35a	MB35aMt-21	magnetite	21.59	20.40	924.73	12.19	<66.24	<0.09	0.89	0.44	<0.87	488.78
South	Magnet	BIF	MB35a	MB35aMt-22	magnetite	588.12	14.21	1920.97	<7.83	<69.81	<0.119	1.98	0.30	<0.94	411.17
South	Magnet	BIF	MB35a	MB35aMt-23	magnetite	69.19	11.05	301.58	<6	<64.58	<0.096	0.76	0.41	<0.67	259.80
South	Magnet	BIF	MB35a	MB35aMt-24	magnetite	15.51	16.18	204.66	<6.45	87.15	<0.094	0.97	0.46	0.92	490.19
South	Magnet	BIF	MB35a	MB35aMt-26	magnetite	10.00	12.98	1468.36	16.31	65.74	<0.085	71.95	0.50	<0.67	446.66
South	Magnet	BIF	MB35a	MB35aMt-28	magnetite	15.56	14.64	358.05	<7.13	43.59	<0.106	1.00	0.42	<0.9	436.11
South	Magnet	BIF	MB35a	MB35aMt-3	magnetite	63.41	17.48	671.79	50.82	487.96	<0.099	2.62	0.86	<0.69	401.40

Analysis no.	Co	Ni	Cu	Zn	Ga	As	Sr	Y	Zr	Nb	Mo	Sn	Sb	Ba	La	Ce	Pr
MB33Hm-20	<0.0152	<0.105	<0.14	0.16	<0.029	0.32	<0.0086	0.02	0.17	0.04	0.23	0.31	0.11	<0.00	0.01	0.01	<0.00
MB33Hm-3	<0.0136	<0.163	<0.122	<0.21	<0.029	<0.3	<0.00	0.03	0.26	0.08	0.36	<0.146	1.72	<0.00	0.02	0.02	0.00
MB33Hm-4	0.73	0.95	0.22	3.80	<0.039	0.44	0.26	0.08	<0.00	<0.00	0.04	0.19	<0.084	0.09	0.05	0.08	0.01
MB33Hm-5	0.58	1.18	<0.144	2.81	0.12	<0.32	0.03	0.03	<0.00	<0.00	<0.0271	<0.155	0.09	0.77	0.04	0.02	0.00
MB33Hm-6	0.55	0.53	<0.149	4.34	0.04	<0.37	0.25	0.04	<0.016	0.00	<0.0286	<0.162	0.11	0.17	0.01	0.01	<0.0039
MB33Hm-7	0.75	0.97	2.96	2.72	0.03	0.52	0.55	0.19	0.06	<0.00	0.01	0.17	<0.079	0.68	0.15	0.13	0.01
MB33Hm-8	0.38	0.73	<0.129	3.88	<0.028	<0.3	0.13	0.05	0.04	<0.00	<0.027	<0.149	<0.073	0.22	0.02	0.02	0.00
MB33Mg-1	0.16	<0.115	<0.142	1.22	<0.032	0.99	0.34	0.73	3.73	0.05	0.19	<0.175	1.29	0.36	0.11	0.14	0.02
MB33Mg-10	0.49	0.84	<0.178	4.20	<0.034	0.48	0.04	0.03	0.01	<0.00	0.02	<0.211	<0.134	0.57	0.05	0.04	0.00
MB33Mg-11	0.57	1.04	<0.18	4.40	0.10	<0.37	0.01	0.01	<0.0215	<0.00	<0.038	0.25	0.15	0.22	0.01	0.01	<0.00
MB33Mg-12	0.61	0.81	<0.155	4.10	0.04	<0.4	0.02	0.02	<0.00	<0.0077	<0.05	<0.199	<0.105	0.11	0.01	0.01	0.00
MB33Mg-13	0.53	0.66	<0.158	5.32	0.06	0.42	0.03	0.04	<0.00	<0.00	<0.00	<0.174	<0.091	0.88	0.03	0.01	0.00
MB33Mg-14	0.68	0.87	<0.137	4.85	0.07	<0.38	<0.0127	0.02	<0.0163	<0.0064	<0.029	<0.178	<0.08	0.26	0.02	0.01	<0.00
MB33Mg-15	0.82	0.90	<0.139	3.27	<0.031	<0.33	<0.0133	0.01	<0.00	<0.00	0.02	<0.185	<0.087	<0.00	0.01	0.00	0.00
MB33Mg-16	0.63	0.67	<0.153	4.56	0.13	<0.31	<0.0091	<0.00	<0.0166	<0.00	<0.00	0.25	0.15	0.08	<0.00	0.00	<0.00
MB33Mg-19	0.93	0.79	0.91	6.55	0.11	<0.41	0.67	0.04	<0.00	<0.00	0.02	<0.218	0.12	0.66	0.04	0.04	0.00
MB33Mg-2	0.61	1.16	<0.158	5.60	<0.038	<0.48	0.00	0.02	<0.0208	<0.00	<0.00	<0.197	<0.123	<0.00	0.01	0.01	<0.00
MB33Mg-20	0.14	<0.13	<0.115	1.97	0.03	0.52	0.50	0.64	0.22	0.08	0.31	<0.166	1.64	0.25	0.06	0.10	0.01
MB33Mg-3	0.63	1.37	<0.209	2.69	0.07	<0.37	0.01	0.01	<0.00	<0.00	0.03	<0.21	<0.122	0.06	0.00	0.00	<0.00
MB33Mg-5	0.64	1.17	<0.158	3.55	0.07	<0.45	0.02	0.01	<0.00	0.00	<0.00	<0.207	<0.133	<0.00	0.01	0.01	<0.00
MB33Mg-6	0.67	0.97	<0.188	4.46	0.12	<0.47	0.12	0.06	0.03	<0.00	0.03	<0.227	<0.13	0.41	0.04	0.04	0.00
MB33Mg-7	0.51	1.18	<0.153	4.55	<0.04	<0.43	0.02	0.01	<0.0275	<0.0076	0.02	<0.197	<0.123	0.05	0.01	0.01	0.00
MB33Mg-8	0.57	0.87	<0.173	3.46	0.07	<0.49	0.03	0.02	<0.00	<0.0089	<0.041	<0.219	0.18	0.06	0.02	0.01	<0.0039
MB33Mg-9	0.55	0.85	<0.171	4.95	0.07	<0.46	0.04	<0.0065	<0.00	<0.0085	<0.039	<0.213	<0.099	<0.00	<0.0046	<0.00	<0.0037
MB35aMt-1	0.25	0.59	<0.198	15.59	0.04	<0.23	0.33	0.26	0.02	0.01	<0.05	<0.091	<0.022	0.29	0.09	0.09	0.01
MB35aMt-10	0.09	0.50	<0.211	11.82	0.03	<0.18	<0.0089	0.05	<0.0158	<0.00	0.02	<0.098	<0.021	<0.00	0.04	0.03	0.00
MB35aMt-11	0.19	0.64	<0.168	11.59	0.05	0.20	<0.0122	0.09	<0.0154	<0.0061	0.04	<0.091	0.03	<0.00	0.04	0.02	0.00
MB35aMt-13	0.10	0.29	<0.178	9.87	<0.052	0.57	0.18	0.19	<0.0157	0.01	<0.027	0.14	0.06	0.61	0.18	0.14	0.01
MB35aMt-14	0.11	0.42	0.42	4.79	0.06	2.60	0.55	0.98	0.01	0.04	0.01	0.07	0.35	2.69	0.76	0.68	0.06
MB35aMt-15	0.14	0.67	<0.212	11.16	0.06	0.35	0.08	0.22	0.02	0.00	<0.042	<0.106	0.05	0.07	0.12	0.13	0.01
MB35aMt-16	0.22	0.46	<0.199	11.03	<0.056	0.28	0.17	0.08	0.03	0.03	0.10	0.13	<0.034	0.25	0.11	0.09	0.00
MB35aMt-17	0.33	0.28	<0.26	14.88	<0.058	0.42	0.32	0.14	0.03	0.01	<0.048	<0.121	0.08	0.57	0.16	0.17	0.01
MB35aMt-18	0.09	0.50	<0.188	12.50	<0.049	<0.219	<0.00	<0.0074	<0.00	<0.00	0.03	<0.108	<0.033	<0.00	<0.0036	<0.00	<0.00
MB35aMt-19	0.10	0.53	<0.208	11.84	<0.038	0.34	0.02	0.28	<0.0165	<0.0065	<0.04	0.14	0.05	0.05	0.24	0.17	0.02
MB35aMt-2	0.21	0.52	0.25	13.03	0.10	<0.125	0.13	0.01	<0.016	0.02	0.14	0.11	0.03	0.06	0.01	0.01	<0.00
MB35aMt-20	0.07	0.70	<0.15	11.65	0.05	<0.14	0.03	<0.0067	0.01	<0.00	0.05	<0.104	<0.0213	0.11	<0.00	0.00	<0.00
MB35aMt-21	0.12	0.41	<0.195	11.47	0.08	<0.18	<0.00	0.01	<0.0153	<0.00	0.05	<0.089	<0.058	<0.00	0.00	0.01	<0.00
MB35aMt-22	0.16	0.46	<0.187	15.59	0.05	<0.26	0.08	0.02	0.01	0.00	<0.032	0.13	<0.035	<0.00	0.01	0.01	<0.00311
MB35aMt-23	0.22	0.45	0.36	7.13	<0.028	1.21	0.25	0.93	<0.0149	0.03	0.09	0.22	0.23	0.93	0.42	0.37	0.04
MB35aMt-24	0.08	0.33	<0.18	9.92	0.05	<0.132	<0.00	<0.0063	<0.00	<0.00	0.03	<0.085	<0.049	<0.00	<0.0044	0.00	<0.0025
MB35aMt-26	0.13	0.23	<0.159	10.91	0.04	<0.166	0.02	0.05	<0.016	0.01	<0.027	0.12	0.06	<0.00	0.04	0.03	0.00
MB35aMt-28	0.08	0.39	<0.175	12.20	0.09	<0.24	0.01	0.01	<0.00	<0.00	0.04	0.15	<0.041	<0.00	<0.0036	<0.0035	<0.00
MB35aMt-3	0.16	0.67	<0.196	10.61	0.12	1.18	0.45	0.51	<0.023	0.01	0.04	0.10	0.14	0.74	0.32	0.32	0.02

Analysis no.	Nd	Sm	Eu	Gd	Tb	Dy	Ho	Er	Tm	Yb	Lu	W	Pb208	Th	U
MB33Hm-20	<0.0152	<0.00	<0.00	0.01	<0.0024	<0.00	<0.00	0.00	<0.00	<0.00	0.00	0.11	0.04	<0.00	<0.00235
MB33Hm-3	0.01	<0.00	<0.00	<0.0228	<0.00	<0.009	0.00	0.01	<0.00207	<0.0097	<0.00	1.21	0.10	<0.00	<0.0021
MB33Hm-4	0.03	0.01	<0.0062	<0.017	<0.00	0.02	<0.00	0.01	0.00	<0.0103	0.00	0.02	0.19	0.00	<0.0032
MB33Hm-5	0.01	0.01	<0.00	0.01	0.00	0.01	0.00	<0.0073	<0.0022	<0.00	<0.00	0.02	0.29	<0.00	0.00
MB33Hm-6	0.02	<0.026	<0.0066	<0.0183	0.00	<0.0102	0.00	<0.0077	<0.00	0.01	<0.00	<0.00	0.15	<0.00	0.00
MB33Hm-7	0.06	0.01	<0.0047	0.03	<0.00	0.01	0.00	0.00	0.00	<0.011	0.00	0.06	0.98	<0.0045	0.02
MB33Hm-8	0.01	<0.00	0.01	<0.0174	<0.0033	0.00	<0.00	0.00	<0.00	<0.0105	<0.0023	0.03	0.22	<0.00	0.00
MB33Mg-1	0.06	0.04	0.01	0.04	0.00	0.04	0.02	0.04	0.01	0.05	0.01	0.64	2.35	0.04	3.15
MB33Mg-10	0.01	0.01	<0.00	<0.0243	0.00	0.00	0.00	0.00	<0.00	<0.0146	0.00	0.13	1.55	0.00	2.97
MB33Mg-11	<0.00	<0.0244	<0.0108	<0.00	0.00	<0.00	<0.00	0.00	0.00	<0.0147	<0.0033	1.01	0.77	0.03	0.93
MB33Mg-12	<0.00	<0.00	0.00	<0.00	<0.0043	0.00	<0.00	0.00	<0.00	0.00	<0.003	1.78	0.73	0.01	2.45
MB33Mg-13	<0.00	<0.00	<0.0051	<0.00	0.00	<0.00	0.00	<0.00	<0.00256	0.01	0.00	0.47	0.08	<0.00	0.90
MB33Mg-14	<0.016	<0.00	0.00	<0.0264	<0.00251	0.01	<0.00	0.01	0.00	<0.00	0.00	0.27	1.13	0.00	4.99
MB33Mg-15	<0.00	0.01	<0.007	<0.00	<0.00	<0.00	<0.00	0.00	<0.00	<0.00	<0.00	0.76	4.63	0.03	6.92
MB33Mg-16	<0.028	<0.00	0.00	<0.033	<0.00255	<0.00	<0.0026	<0.008	<0.00	<0.0113	<0.00253	0.29	1.23	<0.00	0.15
MB33Mg-19	<0.02	0.01	0.01	<0.0234	0.00	0.00	<0.0032	<0.0099	<0.00	<0.014	<0.0031	0.22	0.78	<0.00	0.88
MB33Mg-2	0.01	0.01	0.00	<0.00	<0.00	<0.0187	<0.00	<0.01	<0.00	0.01	0.00	0.15	2.83	0.01	2.52
MB33Mg-20	0.09	0.04	0.02	0.04	0.00	0.04	0.01	0.04	0.00	0.09	0.01	0.18	0.90	0.00	0.89
MB33Mg-3	0.01	<0.00	<0.0089	<0.0247	<0.0033	0.01	<0.0048	<0.0105	<0.00	<0.00	0.00	0.56	0.25	<0.00	0.12
MB33Mg-5	<0.00	0.01	0.00	0.01	0.00	<0.00	<0.00	<0.0104	<0.00315	0.00	0.00	0.18	0.11	<0.00	0.01
MB33Mg-6	0.01	<0.00	0.00	<0.0257	0.00	<0.00	0.00	<0.00	<0.00	0.00	0.00	0.10	0.12	0.00	0.01
MB33Mg-7	0.01	<0.00	0.00	0.01	<0.003	<0.00	<0.00	0.00	<0.00	<0.0133	<0.00	0.02	0.13	<0.0093	0.02
MB33Mg-8	0.01	0.01	0.00	0.01	<0.00	0.00	0.00	<0.00	<0.00	0.01	<0.00	0.09	0.10	<0.0073	0.01
MB33Mg-9	<0.00	<0.0246	<0.0063	<0.0247	<0.0033	<0.00	<0.00	<0.00	0.00	<0.0148	<0.00	0.16	0.14	0.01	0.03
MB35aMt-1	0.03	0.02	0.00	<0.031	0.00	0.02	0.01	0.02	0.00	0.03	0.01	<0.02	0.03	<0.0112	<0.00
MB35aMt-10	0.01	0.01	<0.0062	0.01	<0.0032	<0.00	0.00	0.00	<0.0021	0.00	<0.00	0.01	0.18	<0.00	<0.0053
MB35aMt-11	0.04	<0.00	<0.00	<0.00	<0.00219	0.01	<0.00	0.00	<0.00	0.00	<0.00	0.01	0.05	<0.00	<0.01
MB35aMt-13	0.06	<0.017	0.01	0.04	<0.00	0.02	0.00	0.01	<0.00	0.00	0.00	<0.031	0.05	0.00	<0.0073
MB35aMt-14	0.24	0.04	0.05	0.03	0.00	0.04	0.02	0.05	0.00	0.04	0.00	0.01	0.07	<0.01	0.00
MB35aMt-15	0.08	<0.019	0.01	<0.018	0.00	0.01	0.00	0.01	<0.00	<0.0109	<0.0033	<0.0197	0.10	<0.00	0.00
MB35aMt-16	0.02	0.01	0.01	<0.027	<0.00	0.01	0.00	<0.00	<0.0025	0.01	0.00	<0.02	0.06	<0.00	0.00
MB35aMt-17	0.05	<0.0215	0.01	0.02	<0.00	<0.0116	0.00	0.01	0.00	0.01	0.00	0.03	0.21	0.00	<0.0067
MB35aMt-18	<0.0163	<0.0191	<0.00	<0.0186	0.00	<0.00	0.00	<0.00	0.00	<0.00	<0.00	0.03	0.10	<0.0088	<0.00
MB35aMt-19	0.05	<0.00	0.01	0.01	0.00	<0.0097	0.00	0.01	0.00	0.02	<0.0032	2.05	0.29	0.02	0.08
MB35aMt-2	<0.00	<0.0173	<0.0044	<0.00	<0.00227	<0.00	0.00	0.00	<0.00	<0.00	0.00	0.46	0.48	0.07	0.08
MB35aMt-20	<0.00	<0.00	0.00	<0.00	<0.00227	<0.00	<0.0023	<0.007	<0.00	<0.00	<0.00	0.52	0.11	0.06	0.06
MB35aMt-21	<0.00	<0.0235	<0.00	<0.00	<0.00218	0.00	<0.00	<0.00	<0.00	<0.00	<0.00	0.06	0.30	0.00	0.00
MB35aMt-22	0.01	<0.0288	0.00	<0.00	<0.00267	0.01	<0.0027	0.00	<0.00	<0.0119	<0.00259	1.03	0.22	0.15	0.08
MB35aMt-23	0.11	<0.0162	0.02	0.05	0.01	0.05	0.02	0.05	0.01	0.05	0.01	0.97	0.23	0.04	0.06
MB35aMt-24	<0.00	0.01	<0.0059	<0.0159	<0.00	0.00	<0.00	0.00	<0.00202	<0.00	<0.00	0.18	0.05	0.01	0.01
MB35aMt-26	0.02	0.01	<0.0044	0.01	<0.00322	<0.0094	<0.00	<0.00	<0.00	<0.00	0.00	0.37	0.10	0.07	0.03
MB35aMt-28	<0.0163	0.01	<0.00	<0.00	<0.00	<0.0103	0.00	<0.00	0.00	<0.00	<0.00243	0.52	0.44	0.06	1.37
MB35aMt-3	0.10	0.03	0.01	0.03	0.00	0.01	0.01	0.03	0.00	0.02	<0.0023	0.30	0.06	0.00	0.02

Position	Deposit	Lithology	Sample no.	Analysis no.	Texture	Mg	Al	Si	P	Ca	Sc	Ti	V	Cr	Mn
South	Magnet	BIF	MB35a	MB35aMt-30	magnetite	62.30	17.23	704.70	<7.39	<66.33	<0.107	22.81	0.43	<0.75	343.95
South	Magnet	BIF	MB35a	MB35aMt-31	magnetite	25.16	18.13	3771.65	<7.29	<62.07	<0.121	1.59	0.40	<0.86	481.58
South	Magnet	BIF	MB35a	MB35aMt-32	magnetite	21.88	19.77	109.91	<6.29	<59.39	<0.122	1.99	0.40	<0.72	472.96
South	Magnet	BIF	MB35a	MB35aMt-33	magnetite	14.20	18.47	519.97	<6.53	<60.97	<0.11	0.91	0.42	<0.89	485.07
South	Magnet	BIF	MB35a	MB35aMt-34	magnetite	518.90	13.27	1326.77	7.53	209.00	<0.112	2.28	0.74	<0.84	333.67
South	Magnet	BIF	MB35a	MB35aMt-35	magnetite	17.18	20.06	<72.93	<6.64	<48.22	<0.096	2.45	0.76	<0.77	451.00
South	Magnet	BIF	MB35a	MB35aMt-36	magnetite	25.89	26.37	120.85	7.09	51.64	0.11	2.56	0.85	<0.63	488.33
South	Magnet	BIF	MB35a	MB35aMt-38	magnetite	50.19	14.45	222.59	13.35	<51.32	<0.096	2.82	0.54	<0.7	460.40
South	Magnet	BIF	MB35a	MB35aMt-39	magnetite	123.53	12.09	300.76	<6.82	63.45	<0.102	1.31	0.37	<0.79	453.04
South	Magnet	BIF	MB35a	MB35aMt-4	magnetite	65.62	11.66	259.92	140.02	547.77	<0.086	1.02	0.78	<0.63	459.86
South	Magnet	BIF	MB35a	MB35aMt-40	magnetite	33.16	16.07	136.72	<5.93	<35.78	<0.077	1.33	0.49	1.12	429.92
South	Magnet	BIF	MB35a	MB35aMt-6	magnetite	52.32	13.65	1317.86	8.96	637.67	<0.093	1.97	0.69	<0.78	364.42
South	Magnet	BIF	MB35a	MB35aMt-7	magnetite	165.80	12.78	233.35	<5.95	2141.25	<0.106	21.83	0.69	1.08	522.62
South	Magnet	BIF	MB35a	MB35aMt-8	magnetite	21.55	14.41	173.60	20.67	<51.36	<0.107	1.43	0.60	<0.7	477.51
South	Magnet	BIF	MB35a	MB35aMt-9	magnetite	22.01	19.43	491.26	7.56	262.33	<0.117	1.27	0.75	<0.94	416.21
South	Magnet	BIF	MB35b	MB35bMt-1	magnetite	1096.97	304.34	17833.97	12.64	254.46	<0.097	96.94	8.34	5.98	2637.31
South	Magnet	BIF	MB35b	MB35bMt-12	magnetite	27.19	10.99	616.57	320.05	850.19	<0.103	5.86	7.30	<0.88	156.27
South	Magnet	BIF	MB35b	MB35bMt-13	magnetite	126.21	87.22	1426.23	8.29	63.42	<0.088	9.13	7.05	<0.64	289.87
South	Magnet	BIF	MB35b	MB35bMt-14	magnetite	45.07	66.89	753.48	8.06	<55.63	<0.082	5.86	3.75	<0.66	262.34
South	Magnet	BIF	MB35b	MB35bMt-15	magnetite	59.27	69.41	148.33	<6.29	78.69	0.10	8.31	4.86	0.71	430.43
South	Magnet	BIF	MB35b	MB35bMt-20	magnetite	149.91	146.84	3307.91	<5.33	<38.92	<0.086	6.65	2.03	<0.72	364.52
South	Magnet	BIF	MB35b	MB35bMt-21	magnetite	344.44	198.07	4361.91	<7.75	<57.69	<0.1	6.58	2.07	<0.61	555.62
South	Magnet	BIF	MB35b	MB35bMt-22	magnetite	268.22	139.03	3659.27	<7.9	69.20	<0.114	7.26	1.80	<0.88	357.15
South	Magnet	BIF	MB35b	MB35bMt-23	magnetite	228.01	99.37	2516.59	<7.02	93.32	<0.094	4.63	2.24	<1.01	259.72
South	Magnet	BIF	MB35b	MB35bMt-24	magnetite	40.38	120.34	265.24	10.08	<42.57	0.13	5.56	1.90	<0.62	359.08
South	Magnet	BIF	MB35b	MB35bMt-25	magnetite	37.71	117.74	<77.36	<7.05	<65.15	<0.103	6.10	1.95	<0.98	361.74
South	Magnet	BIF	MB35b	MB35bMt-26	magnetite	71.97	125.75	889.46	<7.45	72.66	<0.103	5.23	1.79	1.81	353.58
South	Magnet	BIF	MB35b	MB35bMt-27	magnetite	43.81	81.62	174.05	7.51	<32.08	<0.071	4.36	1.76	0.71	345.26
South	Magnet	BIF	MB35b	MB35bMt-28	magnetite	44.62	119.68	216.41	10.98	110.60	0.14	5.29	1.85	<0.81	363.85
South	Magnet	BIF	MB35b	MB35bMt-29	magnetite	188.65	141.24	3114.23	13.15	<59.95	<0.104	5.10	1.56	0.77	412.85
South	Magnet	BIF	MB35b	MB35bMt-3	magnetite	357.26	80.52	1024.23	<5.99	<46.68	<0.083	19.66	7.40	<0.58	321.94
South	Magnet	BIF	MB35b	MB35bMt-30	magnetite	80.48	102.74	278.68	<7.58	<49.23	<0.105	4.36	1.53	<0.97	326.50
South	Magnet	BIF	MB35b	MB35bMt-31	magnetite	35.38	81.53	<88.15	11.31	103.30	<0.115	4.44	1.90	<0.77	317.05
South	Magnet	BIF	MB35b	MB35bMt-32	magnetite	68.33	123.63	342.81	<6.5	<52.72	<0.099	5.65	1.51	<0.56	363.81
South	Magnet	BIF	MB35b	MB35bMt-33	magnetite	43.09	129.49	176.12	<7.78	<72.89	0.18	5.91	1.61	<0.93	368.26
South	Magnet	BIF	MB35b	MB35bMt-34	magnetite	19.38	72.95	232.19	<7.8	<49.88	<0.105	3.52	1.47	<0.85	320.23
South	Magnet	BIF	MB35b	MB35bMt-35	magnetite	184.16	127.47	2324.05	7.38	65.64	<0.107	5.41	1.86	<0.76	352.27
South	Magnet	BIF	MB35b	MB35bMt-36	magnetite	90.04	99.20	303.73	<7.1	<59.97	<0.097	5.74	1.75	1.77	366.09
South	Magnet	BIF	MB35b	MB35bMt-37	magnetite	614.31	177.05	8727.49	<6.12	<51.44	<0.089	40.74	13.80	1.23	411.97
South	Magnet	BIF	MB35b	MB35bMt-38	magnetite	54.56	76.03	203.96	18.55	97.57	<0.09	47.12	18.83	0.80	453.88
South	Magnet	BIF	MB35b	MB35bMt-39	magnetite	40.53	84.35	203.76	15.65	<36.16	<0.093	47.02	15.96	<0.76	467.06
South	Magnet	BIF	MB35b	MB35bMt-4	magnetite	40.18	134.50	72.55	<6.08	95.85	0.09	22.13	8.17	0.70	350.23
South	Magnet	BIF	MB35b	MB35bMt-40	magnetite	26.37	37.25	<77.1	<7	54.20	<0.111	44.61	18.43	<0.8	430.95

Analysis no.	Co	Ni	Cu	Zn	Ga	As	Sr	Y	Zr	Nb	Mo	Sn	Sb	Ba	La	Ce	Pr
MB35aMt-30	0.10	0.42	0.24	21.78	0.04	0.42	0.05	0.09	<0.0183	0.03	0.01	<0.112	<0.035	0.41	0.14	0.07	0.01
MB35aMt-31	0.20	0.27	<0.212	12.87	0.06	0.42	0.03	0.12	0.03	<0.00	<0.045	<0.124	0.03	0.06	0.09	0.09	0.01
MB35aMt-32	0.14	1.16	<0.207	11.28	0.07	<0.28	<0.00	0.02	<0.00	0.00	0.03	<0.104	0.01	0.06	0.01	0.01	<0.00
MB35aMt-33	0.12	0.80	<0.199	10.04	0.09	<0.21	<0.0095	0.05	<0.0169	<0.00	0.03	<0.091	<0.023	0.06	0.02	0.02	<0.0028
MB35aMt-34	0.18	0.55	<0.227	16.72	0.05	0.37	0.28	0.07	<0.018	0.01	0.09	<0.105	0.05	0.45	0.05	0.05	0.00
MB35aMt-35	0.24	0.27	<0.156	11.05	0.07	<0.142	<0.009	<0.01	<0.00	<0.00	0.05	<0.09	<0.02	<0.00	0.00	0.00	<0.00
MB35aMt-36	0.25	0.64	<0.147	12.56	0.05	<0.173	0.01	<0.0078	<0.00	<0.0052	<0.023	<0.068	<0.031	<0.00	0.00	0.00	0.00
MB35aMt-38	0.20	0.76	<0.159	8.67	0.08	<0.179	<0.00	0.01	<0.0152	0.00	<0.045	0.09	<0.029	0.24	0.02	0.01	0.00
MB35aMt-39	0.14	0.72	0.38	13.29	0.04	<0.195	<0.00	<0.0069	<0.00	<0.00	0.01	<0.108	<0.0314	<0.00	<0.00	<0.0033	0.00
MB35aMt-4	0.20	1.04	<0.129	11.24	<0.027	0.39	0.79	0.54	0.04	<0.00	<0.0314	<0.073	<0.03	1.12	0.61	0.48	0.04
MB35aMt-40	0.18	0.69	<0.128	10.22	0.12	<0.172	0.01	0.04	<0.0132	<0.00	<0.00	<0.082	<0.035	0.21	0.03	0.04	0.00
MB35aMt-6	0.26	0.60	<0.164	11.29	0.11	0.85	0.60	0.86	0.05	0.03	0.03	<0.082	0.14	2.32	0.52	0.44	0.04
MB35aMt-7	0.20	0.53	0.20	12.49	0.09	0.30	2.70	0.81	0.04	<0.0059	<0.026	<0.096	0.05	0.67	0.33	0.27	0.02
MB35aMt-8	0.13	0.85	<0.167	15.61	0.04	<0.112	0.01	0.00	<0.00	<0.0064	0.04	<0.094	<0.031	<0.00	0.01	0.01	<0.00
MB35aMt-9	0.27	0.64	<0.173	10.92	0.08	0.21	0.26	0.11	0.01	<0.0072	0.02	<0.11	<0.042	0.12	0.08	0.05	0.00
MB35bMt-1	2.41	6.65	8.07	22.79	0.25	3.80	1.09	0.74	0.03	0.20	0.35	3.88	0.19	1.30	0.90	1.29	0.11
MB35bMt-12	0.41	2.76	<0.159	5.62	0.35	1.06	0.99	0.91	0.42	0.08	2.06	0.13	0.15	0.24	0.91	1.01	0.11
MB35bMt-13	0.57	2.85	<0.182	8.66	0.31	0.77	0.27	0.56	0.13	0.18	0.55	<0.087	0.08	0.92	1.30	1.22	0.10
MB35bMt-14	0.55	1.44	<0.185	10.88	0.30	0.65	0.13	0.38	0.13	0.03	0.96	0.18	0.01	0.18	0.25	0.35	0.04
MB35bMt-15	0.78	1.81	<0.145	12.77	0.18	0.30	0.05	0.18	<0.00	<0.00	0.03	0.09	<0.029	0.06	0.07	0.07	0.01
MB35bMt-20	0.91	1.61	<0.175	12.01	0.16	0.28	0.07	0.09	<0.0136	0.01	0.78	0.09	<0.026	<0.056	0.11	0.14	0.01
MB35bMt-21	1.15	0.92	<0.184	14.51	0.15	0.58	0.09	0.19	0.04	0.03	<0.04	0.17	<0.0225	0.42	0.50	0.56	0.04
MB35bMt-22	1.21	1.76	<0.211	12.92	0.32	0.33	0.06	0.10	0.02	0.01	0.09	<0.121	<0.036	0.38	0.11	0.11	0.01
MB35bMt-23	0.78	1.01	<0.188	8.65	0.19	0.59	0.18	0.11	0.07	0.03	0.35	<0.102	0.05	0.07	0.10	0.10	0.01
MB35bMt-24	0.83	1.23	<0.153	13.24	0.13	<0.144	<0.0084	<0.00	<0.00	<0.00	0.12	<0.098	<0.041	<0.00	<0.00	0.00	<0.00
MB35bMt-25	1.07	1.82	<0.189	13.34	0.06	0.16	0.01	<0.0076	<0.018	<0.00	0.03	<0.105	0.05	0.12	0.01	<0.0036	<0.00
MB35bMt-26	0.95	1.37	<0.212	13.47	0.18	<0.23	0.02	0.03	0.02	0.00	<0.033	<0.113	<0.037	0.25	0.04	0.04	0.01
MB35bMt-27	0.98	1.33	0.27	11.19	0.21	<0.094	0.10	0.05	0.02	0.01	<0.02	0.09	<0.016	0.07	0.01	0.01	0.00
MB35bMt-28	1.07	1.15	<0.187	10.19	0.25	<0.151	<0.00	<0.0071	<0.00	<0.00	0.06	<0.101	<0.023	0.07	0.01	0.01	0.00
MB35bMt-29	0.97	1.07	<0.21	13.51	0.09	0.31	0.06	0.08	0.01	0.01	0.04	0.15	0.04	0.23	0.09	0.10	0.01
MB35bMt-3	1.32	4.78	<0.181	10.86	0.29	<0.16	0.02	<0.0042	0.01	<0.00	0.06	<0.086	<0.0275	<0.00	0.00	0.01	<0.0024
MB35bMt-30	0.85	1.06	<0.202	12.55	0.18	<0.3	<0.0109	0.06	0.04	0.02	<0.047	0.18	0.01	0.06	0.01	0.02	0.00
MB35bMt-31	0.90	1.08	<0.215	11.01	0.13	<0.155	0.06	0.03	0.02	<0.00	<0.048	0.55	<0.038	<0.00	0.01	0.01	0.00
MB35bMt-32	1.04	1.23	<0.167	10.51	0.17	<0.163	<0.0088	0.02	0.01	<0.0062	0.03	<0.103	0.04	0.21	0.01	0.01	0.00
MB35bMt-33	1.05	1.36	<0.181	12.91	0.16	<0.19	<0.00	<0.0082	<0.0195	<0.00	0.07	0.15	<0.027	<0.00	<0.0058	0.01	<0.00
MB35bMt-34	1.08	1.17	<0.214	10.16	0.16	<0.232	0.01	0.01	<0.028	<0.00	0.08	<0.109	<0.038	<0.00	0.00	0.01	0.00
MB35bMt-35	0.99	0.79	<0.176	15.26	0.15	0.27	0.05	0.06	0.03	0.01	0.07	<0.105	<0.022	0.07	0.07	0.09	0.01
MB35bMt-36	0.83	1.27	<0.21	11.79	0.22	0.16	0.01	0.01	<0.00	0.01	0.07	0.12	0.02	0.07	0.00	0.01	<0.00
MB35bMt-37	1.05	7.17	<0.137	11.47	0.14	<0.14	0.06	0.11	0.06	0.00	0.08	<0.098	<0.0216	0.13	0.04	0.05	0.00
MB35bMt-38	1.02	5.28	<0.171	12.23	0.15	<0.137	<0.00	<0.0073	0.01	<0.00	0.07	<0.099	<0.039	<0.00	0.00	0.00	0.00
MB35bMt-39	1.02	4.27	<0.194	14.56	0.23	<0.145	<0.00	<0.0069	0.03	<0.0064	0.09	0.09	<0.022	<0.00	<0.00	<0.00	<0.0039
MB35bMt-4	1.16	4.08	<0.185	14.16	0.29	<0.176	<0.00	0.02	<0.00	0.02	0.08	0.14	0.03	<0.00	0.04	0.04	0.00
MB35bMt-40	1.09	7.35	<0.181	14.32	0.37	<0.185	<0.00	0.00	0.01	<0.007	0.09	<0.112	<0.024	<0.00	0.00	<0.00	<0.00

Analysis no.	Nd	Sm	Eu	Gd	Tb	Dy	Ho	Er	Tm	Yb	Lu	W	Pb208	Th	U
MB35aMt-30	0.01	<0.0199	<0.0051	<0.028	<0.0026	<0.00	0.00	0.01	<0.00	<0.00	<0.0036	1.25	0.31	0.08	0.07
MB35aMt-31	0.03	0.01	0.00	<0.00	<0.0026	<0.0108	0.00	0.01	0.00	<0.0117	0.00	2.00	0.39	0.54	0.12
MB35aMt-32	<0.0163	<0.00	<0.0049	0.01	<0.00	<0.00	0.00	<0.0077	0.00	0.00	<0.0024	0.97	0.28	0.07	0.07
MB35aMt-33	<0.00	<0.00	<0.00	<0.0179	0.00	0.00	0.00	0.00	0.00	<0.0107	0.00	0.47	0.29	0.32	0.16
MB35aMt-34	0.02	0.01	<0.0071	<0.00	<0.00	<0.0106	<0.00	0.01	<0.00	<0.0115	0.00	0.12	0.04	0.01	0.01
MB35aMt-35	<0.00	<0.0175	<0.0045	<0.0241	<0.00	<0.00	<0.00	<0.00	<0.00	<0.00	<0.0022	0.69	0.19	0.11	0.02
MB35aMt-36	<0.00	<0.00	<0.00	<0.00	0.00	<0.00	<0.00	<0.0058	<0.00	0.00	<0.00	0.42	0.12	0.18	0.05
MB35aMt-38	0.02	<0.00	<0.0042	<0.0228	<0.00	<0.0089	<0.00	<0.0067	0.00	<0.00	<0.0021	0.60	0.13	0.13	0.08
MB35aMt-39	0.01	<0.00	<0.0065	<0.0248	<0.00	<0.00	<0.00	<0.0073	<0.00223	<0.00	<0.00229	0.17	0.07	<0.00	<0.0024
MB35aMt-4	0.13	0.02	0.01	0.03	0.00	0.02	0.01	0.04	0.00	0.06	0.01	0.01	0.29	<0.00	0.00
MB35aMt-40	0.01	0.01	<0.0037	0.01	0.00	<0.00	0.00	<0.0082	0.00	<0.0084	0.00	3.97	0.27	1.18	0.06
MB35aMt-6	0.12	0.04	0.02	0.04	0.01	0.05	0.01	0.04	0.01	0.06	<0.002	0.88	0.40	1.69	0.17
MB35aMt-7	0.09	0.01	0.02	<0.027	<0.0021	0.01	0.01	0.06	0.00	0.06	0.01	0.08	<0.0179	<0.00	<0.00
MB35aMt-8	<0.0152	<0.00	0.00	0.01	<0.00	<0.00	0.00	0.00	<0.00	<0.00	0.00	1.45	0.09	0.00	0.09
MB35aMt-9	0.03	<0.00	0.01	0.02	0.00	0.01	<0.0026	0.01	<0.00	<0.00	0.00	0.14	0.01	<0.00	0.00
MB35bMt-1	0.36	0.09	0.03	<0.041	0.01	0.03	0.01	0.05	0.00	0.08	0.01	0.22	0.03	0.01	0.04
MB35bMt-12	0.53	0.03	0.05	0.10	0.01	0.06	0.03	0.05	0.01	0.10	0.01	0.02	0.22	0.00	0.00
MB35bMt-13	0.24	<0.023	0.04	0.03	0.01	0.04	0.02	0.07	0.01	0.11	0.02	<0.00	0.03	<0.00	<0.00295
MB35bMt-14	0.11	0.03	0.01	<0.017	0.00	0.03	0.01	0.01	0.00	0.02	0.00	0.18	0.02	0.00	0.01
MB35bMt-15	0.03	<0.00	<0.0043	<0.023	<0.0038	0.01	<0.0022	0.01	0.00	0.00	<0.0021	0.01	0.09	<0.0063	0.00
MB35bMt-20	0.05	<0.00	0.01	<0.0206	<0.00	<0.00	0.00	0.01	0.00	0.01	0.00	0.17	0.03	0.05	0.00
MB35bMt-21	0.13	<0.018	0.01	0.03	<0.0024	0.00	0.00	0.02	0.00	0.02	0.00	0.08	0.05	0.01	0.01
MB35bMt-22	0.02	0.01	<0.0075	<0.0201	<0.0027	0.01	<0.0028	<0.00	0.00	0.01	<0.0037	0.57	0.23	<0.0095	0.00
MB35bMt-23	0.05	<0.00	<0.0049	<0.0187	<0.0035	<0.00	<0.00	0.01	0.00	0.02	<0.0034	0.42	0.24	<0.00	<0.0052
MB35bMt-24	<0.00	<0.00	<0.00	<0.0159	<0.00	<0.00	<0.00217	<0.00	<0.00203	<0.00	<0.00	0.53	0.52	<0.0134	0.01
MB35bMt-25	0.01	<0.00	0.00	<0.0192	<0.00258	<0.00	<0.00	<0.008	0.00	0.00	<0.00251	0.48	0.07	0.07	0.03
MB35bMt-26	0.01	0.01	<0.0053	<0.0202	<0.00	<0.00	<0.00	0.00	<0.00	<0.0122	0.00	0.25	0.09	0.00	0.00
MB35bMt-27	<0.0111	<0.00	0.00	<0.00	<0.0017	0.00	0.00	0.01	0.00	0.01	0.00	<0.026	<0.049	0.00	<0.0059
MB35bMt-28	0.02	0.01	0.00	<0.0257	0.00	<0.0101	0.00	0.01	<0.0033	<0.00	<0.00	0.02	0.04	<0.0104	0.00
MB35bMt-29	0.05	<0.021	<0.0054	<0.029	<0.00275	0.01	0.00	0.01	0.00	<0.00	0.00	1.08	0.12	0.00	0.00
MB35bMt-3	<0.0134	<0.00	<0.0057	0.01	<0.00	<0.0085	<0.00	<0.0063	<0.00	<0.00	0.00	0.06	<0.016	<0.00	0.00
MB35bMt-30	<0.018	<0.00	0.01	<0.0291	0.00	<0.00	0.00	0.01	0.00	0.02	0.00	90.22	0.34	0.00	<0.00
MB35bMt-31	0.01	<0.00	0.00	0.01	<0.0028	0.00	<0.0029	<0.00	<0.00	0.00	0.00	149.41	0.27	0.00	0.00
MB35bMt-32	0.01	<0.00	<0.0044	<0.0236	0.00	<0.0092	<0.00	<0.0069	0.00	<0.00	0.00	0.40	0.19	0.01	0.01
MB35bMt-33	<0.0183	<0.00	0.00	<0.03	<0.00281	<0.00	<0.00	0.00	<0.00	<0.0126	<0.00273	0.57	0.06	<0.00	0.01
MB35bMt-34	<0.00	<0.0214	<0.0095	<0.029	<0.004	0.01	<0.00	<0.00	<0.0038	<0.00	<0.00	112.81	0.45	<0.00	<0.0086
MB35bMt-35	0.03	0.01	<0.0078	<0.00	<0.0023	<0.00	0.00	0.00	<0.00	0.00	0.00	0.12	0.09	<0.00	0.00
MB35bMt-36	0.01	<0.00	<0.0052	0.01	<0.0037	<0.00	<0.00	0.01	0.00	<0.00	0.00	0.46	0.08	0.00	0.01
MB35bMt-37	0.02	0.01	0.00	<0.00	<0.00	0.01	0.00	0.01	0.00	0.02	0.00	26.27	0.46	<0.0112	<0.00
MB35bMt-38	<0.00	0.01	<0.00	<0.0151	<0.00	<0.00	0.00	<0.00	<0.00	<0.00	<0.00	21.22	0.45	0.02	<0.0073
MB35bMt-39	<0.0153	<0.00	<0.0065	<0.017	<0.0033	<0.0137	<0.00	<0.00	0.00	<0.0105	<0.00	28.58	0.65	0.01	0.00
MB35bMt-4	<0.014	<0.00	0.00	0.02	<0.00	<0.00	0.00	<0.00	<0.00	0.00	<0.00	0.10	<0.045	0.51	<0.00
MB35bMt-40	0.01	<0.00	<0.0049	<0.0188	0.00	<0.00	<0.00	<0.0078	<0.00	0.00	<0.00246	0.16	0.12	0.01	0.01

Position	Deposit	Lithology	Sample no.	Analysis no.	Texture	Mg	Al	Si	P	Ca	Sc	Ti	V	Cr	Mn
South	Magnet	BIF	MB35b	MB35bMt-7	magnetite	354.14	78.76	574.91	10.85	778.79	<0.074	20.63	8.99	0.89	795.60
South	Magnet	BIF	MB35b	MB35bMt-8	magnetite	57.12	84.66	191.14	<5.83	<40.02	0.15	20.93	8.37	1.34	344.31
South	Magnet	BIF	MB36a	MB36aHmClean-1	clean martite	1566.09	11.81	760.65	<7.36	4074.21	<0.102	0.88	0.42	<0.78	471.36
South	Magnet	BIF	MB36a	MB36aHmClean-10	clean martite	1812.50	20.47	3301.24	<5.67	<38.9	0.10	<0.57	0.59	<0.72	320.21
South	Magnet	BIF	MB36a	MB36aHmClean-11	clean martite	1909.67	16.56	1624.65	<5.79	125.24	<0.092	<0.43	0.42	<0.64	845.43
South	Magnet	BIF	MB36a	MB36aHmClean-12	clean martite	84.34	7.79	757.62	<4.92	<41.49	<0.094	0.70	0.43	<0.6	285.59
South	Magnet	BIF	MB36a	MB36aHmClean-13	clean martite	30.71	15.37	<69.93	<5.92	72.39	<0.096	35.95	0.35	<0.64	539.90
South	Magnet	BIF	MB36a	MB36aHmClean-14	clean martite	152.80	10.68	590.13	<5.97	321.30	<0.095	<0.52	0.47	0.90	335.26
South	Magnet	BIF	MB36a	MB36aHmClean-15	clean martite	27.22	14.81	201.35	<6.84	<37.16	<0.115	1.70	0.42	<0.9	467.86
South	Magnet	BIF	MB36a	MB36aHmClean-16	clean martite	13215.41	11.64	1056.74	25.55	362.42	<0.103	1.33	0.48	<0.75	5509.06
South	Magnet	BIF	MB36a	MB36aHmClean-17	clean martite	8048.10	17.23	1875.34	8.78	113.46	0.10	1.01	0.44	<0.74	2296.43
South	Magnet	BIF	MB36a	MB36aHmClean-18	clean martite	17.66	11.16	124.93	<6.08	<51	<0.111	<0.51	0.30	<0.81	660.12
South	Magnet	BIF	MB36a	MB36aHmClean-19	clean martite	316.53	15.27	1578.81	9.20	86.42	<0.108	1.17	0.48	<0.93	521.64
South	Magnet	BIF	MB36a	MB36aHmClean-2	clean martite	40.15	20.39	134.45	21.50	<54.6	<0.096	0.57	0.40	<0.75	335.57
South	Magnet	BIF	MB36a	MB36aHmClean-20	clean martite	20.95	13.30	<74.46	11.32	<40.67	<0.11	<0.66	0.42	<0.66	574.65
South	Magnet	BIF	MB36a	MB36aHmClean-3	clean martite	27.19	18.45	115.80	<6.19	<42.57	<0.097	0.82	0.53	<0.74	422.29
South	Magnet	BIF	MB36a	MB36aHmClean-4	clean martite	695.94	16.48	1049.62	7.56	304.64	0.16	<0.67	0.45	<0.71	549.50
South	Magnet	BIF	MB36a	MB36aHmClean-6	clean martite	39.01	14.61	587.51	105.13	<60.4	<0.102	0.68	0.35	<0.8	667.66
South	Magnet	BIF	MB36a	MB36aHmClean-7	clean martite	291.12	15.50	91.92	5.62	<41.81	<0.084	0.77	0.32	<0.71	706.10
South	Magnet	BIF	MB36a	MB36aHmClean-8	clean martite	63.93	9.36	327.14	<6.03	<44.51	<0.102	<0.57	0.38	<0.68	195.33
South	Magnet	BIF	MB36a	MB36aHmClean-9	clean martite	12.61	13.20	486.17	<6.54	<62.68	<0.109	1.52	0.32	<0.89	281.99
South	Magnet	BIF	MB36b	MB36bMt-1	magnetite	20.91	10.51	<67.43	<6.83	78.59	<0.107	<0.52	0.48	<0.71	1368.01
South	Magnet	BIF	MB36b	MB36bMt-13	magnetite	16.26	6.15	<63.73	<5.74	<46.5	<0.086	24.29	0.64	<0.7	1626.27
South	Magnet	BIF	MB36b	MB36bMt-15	magnetite	13.42	6.54	<67.04	<5.95	<50.53	<0.088	<0.42	0.38	<0.63	1527.99
South	Magnet	BIF	MB36b	MB36bMt-17	magnetite	11.76	5.49	96.44	12.41	42.45	<0.075	<0.58	1.46	0.78	314.40
South	Magnet	BIF	MB36b	MB36bMt-19	magnetite	13.56	7.24	996.70	13.12	<41.85	<0.096	<0.47	0.74	<0.72	1285.44
South	Magnet	BIF	MB36b	MB36bMt-20	magnetite	35.23	12.76	212.76	10.88	92.65	<0.102	2.60	0.69	1.68	415.96
South	Magnet	BIF	MB36b	MB36bMt-3	magnetite	8.24	5.11	<86.44	<7.59	<61.59	0.16	0.96	1.81	<0.89	116.35
South	Magnet	BIF	MB36b	MB36bMt-6	magnetite	7.40	14.50	298.46	<5.65	131.62	<0.085	36.50	3.56	<0.71	1508.79
South	Magnet	BIF	MB36b	MB36bMt-9	magnetite	19.82	5.16	<64.52	109.77	362.53	<0.095	<0.37	1.10	<0.71	557.33
Middle	Baron	ORE	MB44b	MB44bHmPorous-1	porous martite	52.95	109.47	4559.64	39.50	279.53	0.31	1.64	50.70	2.51	120.60
Middle	Baron	ORE	MB44b	MB44bHmPorous-10	porous martite	55.07	133.88	4121.57	15.48	117.17	0.22	2.69	65.00	2.82	129.80
Middle	Baron	ORE	MB44b	MB44bHmPorous-11	porous martite	24.49	282.50	1078.19	22.93	<100.55	0.59	27.15	836.11	2.71	473.44
Middle	Baron	ORE	MB44b	MB44bHmPorous-12	porous martite	913.75	230.66	494.63	<8.7	<108.1	<0.18	383.12	211.41	86.12	1040.02
Middle	Baron	ORE	MB44b	MB44bHmPorous-13	porous martite	416.20	255.54	<155.33	16.06	<101.06	0.62	439.89	223.96	70.72	538.35
Middle	Baron	ORE	MB44b	MB44bHmPorous-14	porous martite	783.26	287.30	<153.04	<9.55	<134.05	0.95	598.55	72.20	19.62	1461.39
Middle	Baron	ORE	MB44b	MB44bHmPorous-15	porous martite	1664.94	419.33	661.36	<8.89	<94.2	0.81	988.46	326.57	104.28	1409.34
Middle	Baron	ORE	MB44b	MB44bHmPorous-16	porous martite	247.22	842.36	7935.80	195.71	522.04	<0.199	22.84	667.78	28.15	147.27
Middle	Baron	ORE	MB44b	MB44bHmPorous-17	porous martite	816.17	434.46	1081.20	26.59	<130.78	0.42	1193.79	167.21	47.52	1352.55
Middle	Baron	ORE	MB44b	MB44bHmPorous-18	porous martite	814.83	284.16	216.00	14.21	<107.17	0.61	400.08	60.09	12.37	1682.57
Middle	Baron	ORE	MB44b	MB44bHmPorous-19	porous martite	802.28	243.19	216.22	<8.36	<108.6	0.40	496.45	47.64	39.38	1613.69
Middle	Baron	ORE	MB44b	MB44bHmPorous-2	porous martite	48.46	98.96	4493.71	<9.37	251.80	0.35	2.22	45.09	<1.24	118.25
Middle	Baron	ORE	MB44b	MB44bHmPorous-20	porous martite	715.68	247.85	<152.13	19.97	194.17	0.34	440.85	48.99	20.58	1729.10

Analysis no.	Co	Ni	Cu	Zn	Ga	As	Sr	Y	Zr	Nb	Mo	Sn	Sb	Ba	La	Ce	Pr
MB35bMt-7	0.80	4.25	1.50	10.01	0.29	1.36	0.67	1.03	0.02	0.27	0.53	<0.08	0.19	0.52	1.63	1.89	0.12
MB35bMt-8	1.27	4.16	<0.16	12.90	0.26	<0.175	0.01	<0.0059	<0.00	<0.00	<0.024	<0.088	<0.0269	<0.00	0.01	0.01	<0.0023
MB36aHmClean-1	0.71	0.29	<0.168	2.64	0.07	0.55	1.23	1.50	0.02	0.03	<0.054	<0.09	0.11	1.93	0.79	0.74	0.07
MB36aHmClean-10	0.87	0.28	0.19	5.60	0.06	0.28	0.38	0.07	0.06	0.02	0.09	<0.084	0.08	0.21	0.12	0.07	0.01
MB36aHmClean-11	0.64	0.71	<0.162	6.98	<0.029	<0.145	0.16	0.01	<0.02	<0.00	0.04	<0.094	0.02	<0.00	0.00	0.01	<0.00
MB36aHmClean-12	0.82	0.40	<0.173	4.13	0.09	0.33	0.32	0.08	0.03	0.02	0.10	<0.086	0.05	0.74	0.19	0.13	0.01
MB36aHmClean-13	0.67	0.44	<0.164	7.86	0.07	<0.167	<0.0085	<0.0045	<0.00	0.00	0.03	0.14	<0.02	<0.00	0.00	0.00	<0.00
MB36aHmClean-14	0.66	0.78	0.20	3.80	0.07	0.41	2.36	0.08	0.02	0.01	0.04	0.11	0.12	1.15	0.18	0.14	0.01
MB36aHmClean-15	0.51	0.44	<0.171	7.09	<0.035	<0.148	<0.0087	<0.0065	<0.00	<0.00	<0.027	<0.094	<0.02	<0.063	0.02	0.01	<0.00
MB36aHmClean-16	0.92	0.22	<0.205	6.33	0.10	<0.22	1.17	0.23	<0.00	0.02	0.08	<0.101	0.07	1.72	0.27	0.23	0.02
MB36aHmClean-17	0.54	0.52	<0.141	7.32	0.07	0.30	0.16	0.12	<0.00	0.01	0.05	<0.094	<0.043	0.82	0.14	0.11	0.01
MB36aHmClean-18	0.58	0.29	<0.18	7.18	<0.032	<0.192	0.02	0.07	0.01	0.01	<0.038	0.13	0.04	<0.064	0.09	0.06	0.01
MB36aHmClean-19	0.72	0.37	<0.195	9.85	0.08	<0.24	0.13	0.06	0.02	0.00	<0.03	<0.109	0.05	0.37	0.13	0.06	0.01
MB36aHmClean-2	0.62	0.80	<0.175	7.82	<0.038	<0.121	<0.00	<0.0046	<0.0157	<0.00	0.02	<0.085	<0.046	<0.00	0.00	<0.00	0.00
MB36aHmClean-20	0.53	<0.19	<0.23	6.01	0.10	<0.196	<0.00	<0.0082	<0.0159	<0.00	0.03	<0.098	<0.0209	<0.00	0.01	0.00	<0.00
MB36aHmClean-3	0.85	0.31	<0.15	9.30	0.05	<0.192	0.06	<0.0077	0.01	0.00	<0.026	<0.089	<0.028	0.17	0.00	<0.00299	<0.00
MB36aHmClean-4	0.90	<0.19	<0.197	7.60	0.10	<0.125	0.16	0.11	0.03	<0.00	0.03	<0.096	0.04	0.29	0.17	0.10	0.01
MB36aHmClean-6	0.71	0.37	<0.221	6.63	0.06	0.36	0.38	0.35	<0.00	<0.00	<0.0262	0.12	<0.029	0.81	0.23	0.19	0.02
MB36aHmClean-7	0.62	0.45	<0.171	5.89	0.10	<0.143	0.02	0.01	0.01	<0.0055	<0.024	<0.081	<0.032	<0.00	0.03	0.02	0.00
MB36aHmClean-8	0.65	0.21	<0.188	2.95	0.07	0.33	0.25	0.12	0.06	0.01	0.07	<0.099	<0.05	1.04	0.16	0.14	0.01
MB36aHmClean-9	0.77	0.47	0.22	3.89	0.05	0.48	0.29	0.40	0.15	0.06	0.06	<0.099	0.21	2.33	0.63	0.44	0.02
MB36bMt-1	1.01	0.37	<0.197	8.36	0.03	0.16	0.04	0.12	<0.00	0.00	0.07	<0.087	0.03	0.42	0.05	0.04	0.01
MB36bMt-13	0.97	0.71	<0.174	10.50	0.08	<0.186	0.05	0.01	<0.00	<0.00	0.01	<0.084	<0.0189	<0.00	0.02	0.01	<0.0024
MB36bMt-15	1.01	0.76	<0.159	15.07	<0.039	<0.176	<0.0084	0.01	<0.0149	<0.00	<0.026	<0.083	<0.0198	<0.086	<0.0031	0.01	<0.0025
MB36bMt-17	0.62	1.30	<0.14	2.50	0.06	0.78	0.45	0.58	0.04	0.01	0.03	<0.082	0.16	2.68	0.41	0.33	0.03
MB36bMt-19	1.27	0.93	<0.175	8.46	0.09	0.40	0.26	0.63	<0.0154	0.00	0.05	<0.108	0.14	2.76	0.48	0.33	0.03
MB36bMt-20	0.86	<0.174	0.33	9.39	<0.037	1.30	0.55	0.12	<0.021	0.01	0.03	<0.089	0.67	0.28	0.08	0.08	0.00
MB36bMt-3	0.54	0.71	<0.241	3.92	0.09	0.91	0.43	0.36	0.02	0.01	0.01	<0.116	0.12	2.34	0.28	0.21	0.02
MB36bMt-6	1.48	0.49	<0.174	7.69	0.08	0.35	0.62	0.15	0.59	0.06	0.13	0.09	1.83	2.09	0.04	0.04	0.01
MB36bMt-9	0.79	0.49	<0.18	4.28	0.04	0.48	1.16	0.87	0.05	0.01	<0.024	<0.094	0.09	1.82	0.50	0.40	0.06
MB44bHmPorous-1	1.73	15.15	58.96	14.27	0.38	4.06	2.27	3.19	0.04	<0.00	0.35	<0.163	0.48	23.45	0.71	1.41	0.17
MB44bHmPorous-10	2.03	28.21	89.87	8.49	1.07	7.64	4.14	3.58	0.11	0.02	0.28	<0.211	0.29	86.65	0.78	1.66	0.20
MB44bHmPorous-11	2.36	51.02	7.63	1.96	0.48	1.32	0.50	0.69	0.19	0.39	0.10	1.07	0.10	15.49	0.52	0.55	0.08
MB44bHmPorous-12	26.66	3.96	2.53	25.26	1.59	3.28	0.39	0.28	0.03	<0.0116	<0.037	3.13	0.15	4.93	0.15	0.27	0.02
MB44bHmPorous-13	9.60	1.83	1.95	18.64	1.35	3.32	0.26	0.28	<0.00	0.00	<0.00	3.48	0.18	0.89	0.09	0.28	0.03
MB44bHmPorous-14	0.07	1.18	0.46	36.97	1.42	5.40	0.38	0.36	0.02	0.08	<0.04	3.04	0.53	0.83	0.16	0.36	0.05
MB44bHmPorous-15	1.53	2.25	6.05	28.53	1.76	4.25	0.90	0.31	0.03	<0.0079	<0.036	2.80	0.20	8.07	0.18	0.60	0.04
MB44bHmPorous-16	6.36	152.81	168.83	6.39	3.02	19.05	5.77	6.04	0.35	0.08	0.58	<0.24	1.03	189.78	3.18	3.98	0.40
MB44bHmPorous-17	8.04	5.34	5.02	37.13	1.96	5.88	1.29	1.26	0.03	0.02	0.05	3.50	0.26	20.18	0.72	1.23	0.13
MB44bHmPorous-18	0.17	2.43	<0.22	44.42	1.50	1.42	0.18	0.23	0.01	0.06	<0.037	2.64	0.27	0.98	0.13	0.28	0.04
MB44bHmPorous-19	0.05	0.46	<0.21	44.76	1.06	1.38	0.10	0.06	<0.0209	<0.0082	<0.037	2.77	0.17	0.21	0.01	0.07	0.01
MB44bHmPorous-2	2.34	12.36	58.98	14.34	0.43	5.37	2.34	3.36	0.04	<0.00	0.31	<0.157	0.37	24.00	0.78	1.46	0.20
MB44bHmPorous-20	0.07	1.87	<0.24	44.86	1.10	0.73	0.07	0.06	<0.00	0.06	<0.038	2.86	<0.069	0.92	0.04	0.05	0.00

Analysis no.	Nd	Sm	Eu	Gd	Tb	Dy	Ho	Er	Tm	Yb	Lu	W	Pb208	Th	U
MB35bMt-7	0.47	0.04	0.07	0.08	0.02	0.06	0.02	0.10	0.01	0.09	0.02	0.01	0.14	<0.00	0.00
MB35bMt-8	0.01	<0.0153	<0.00	<0.00	<0.002	<0.0083	<0.00	<0.00	0.00	0.00	<0.00	0.15	0.15	0.01	0.02
MB36aHmClean-1	0.35	0.06	0.06	0.08	0.01	0.07	0.03	0.06	0.01	0.04	0.01	0.38	0.54	0.02	0.02
MB36aHmClean-10	0.05	<0.00	<0.0038	<0.0146	<0.00276	<0.00	<0.00	0.00	<0.00	<0.00	0.00	0.05	0.08	0.01	0.01
MB36aHmClean-11	0.01	<0.0153	<0.0039	<0.00	0.00	<0.00	<0.00	<0.0062	<0.00	<0.009	0.00	<0.0091	0.03	<0.0036	0.00
MB36aHmClean-12	0.01	<0.00	<0.0037	0.01	0.00	0.01	0.00	0.01	<0.0018	<0.00	<0.00261	0.14	0.15	<0.00	0.01
MB36aHmClean-13	<0.00	<0.00	<0.006	<0.00	<0.00	<0.009	<0.00	<0.00	<0.00	<0.00	<0.00211	0.01	<0.027	<0.00	<0.00194
MB36aHmClean-14	0.04	<0.00	<0.0072	<0.00	<0.00	0.01	0.00	0.01	0.00	0.00	<0.00209	0.12	0.22	<0.00	0.00
MB36aHmClean-15	<0.00	<0.00	0.00	<0.00	0.00	<0.00	<0.00	<0.00	<0.00211	<0.0099	<0.00	0.01	0.02	<0.00	<0.00
MB36aHmClean-16	0.10	0.02	0.02	0.02	0.00	0.01	0.01	0.03	0.00	<0.0103	0.00	0.14	0.14	<0.00	0.01
MB36aHmClean-17	0.02	<0.016	0.01	<0.022	<0.0021	<0.00	0.00	0.01	0.00	0.01	0.00	0.08	0.09	<0.00	0.00
MB36aHmClean-18	0.03	<0.0169	0.00	<0.0167	0.00	<0.00	<0.0023	0.00	<0.00	<0.01	<0.00	0.06	0.04	<0.00	<0.00
MB36aHmClean-19	<0.016	0.01	0.01	0.01	<0.00	<0.00	<0.00	0.01	<0.00	0.00	0.00	0.04	0.09	<0.00	0.00
MB36aHmClean-2	<0.00	0.01	<0.0062	<0.00	<0.0022	<0.00	<0.00	0.00	<0.00	<0.00	<0.00218	<0.0101	<0.0139	<0.00	<0.00
MB36aHmClean-20	<0.00	<0.0172	<0.0044	<0.017	<0.00227	<0.00	<0.00231	<0.0099	<0.00	<0.0143	<0.00	<0.0144	<0.00	<0.00	<0.00
MB36aHmClean-3	<0.0139	<0.00	<0.0042	<0.016	0.00	<0.0125	0.00	0.00	<0.00	<0.00	<0.00208	<0.00	0.02	<0.00	0.00
MB36aHmClean-4	0.02	<0.00	0.01	<0.024	0.00	0.00	<0.00	<0.0101	0.00	0.02	<0.0022	0.02	0.18	<0.00	<0.0029
MB36aHmClean-6	0.07	0.02	0.01	<0.028	0.00	0.01	0.01	0.01	0.00	0.02	0.00	0.05	0.08	<0.00	0.00
MB36aHmClean-7	0.01	0.01	0.00	<0.0149	<0.00	<0.00	<0.00	<0.0062	<0.0019	<0.0089	<0.00	0.00	0.03	<0.0036	<0.00
MB36aHmClean-8	0.05	<0.00	<0.0043	<0.0167	0.00	<0.00	0.00	0.01	<0.00	0.01	<0.0022	0.15	0.21	<0.004	0.01
MB36aHmClean-9	0.12	<0.0173	0.00	0.04	<0.0032	0.03	0.01	0.03	<0.0022	<0.0102	0.01	0.42	0.59	0.01	0.03
MB36bMt-1	0.01	<0.00	0.00	0.01	<0.00	0.01	0.00	<0.00	<0.00191	0.01	<0.00196	0.01	0.06	<0.00	<0.0032
MB36bMt-13	<0.0132	<0.0154	<0.004	<0.0213	<0.00203	<0.00	<0.00	<0.00	<0.00	0.01	0.00	0.30	0.22	<0.00	0.02
MB36bMt-15	<0.00	0.01	<0.0072	0.01	0.00	<0.00	<0.00215	<0.00	<0.00	<0.00	0.00	<0.00	0.05	<0.00	<0.0034
MB36bMt-17	0.10	0.02	0.01	<0.023	0.00	0.01	0.01	0.02	0.00	0.02	<0.0017	<0.0172	0.11	<0.0086	0.00
MB36bMt-19	0.09	0.02	0.01	0.02	0.00	0.01	0.01	0.02	0.00	0.02	0.00	0.29	1.12	0.00	0.00
MB36bMt-20	0.03	<0.00	0.00	0.03	0.00	0.01	<0.00217	0.01	0.00	0.01	<0.00	0.23	1.01	<0.0051	0.00
MB36bMt-3	0.08	<0.00	0.01	0.04	<0.0038	0.03	<0.0027	<0.0083	<0.0025	<0.012	0.00	0.18	0.32	<0.0057	0.00
MB36bMt-6	0.01	<0.015	0.01	0.02	0.00	<0.0083	0.00	0.00	0.00	0.00	<0.0028	<0.033	0.21	<0.00	0.00
MB36bMt-9	0.29	0.03	0.03	0.06	0.01	0.05	0.01	0.03	0.00	0.04	0.01	0.32	0.45	0.05	0.06
MB44bHmPorous-1	0.92	0.25	0.13	0.16	0.04	0.28	0.06	0.20	0.03	0.20	0.03	0.09	10.97	0.01	0.09
MB44bHmPorous-10	0.91	0.23	0.14	0.31	0.05	0.31	0.07	0.16	0.04	0.16	0.02	0.18	12.23	0.01	0.12
MB44bHmPorous-11	0.21	0.04	0.03	0.06	0.01	0.03	0.01	0.05	<0.0029	0.07	0.01	7.93	5.27	0.00	0.02
MB44bHmPorous-12	0.13	0.09	0.02	0.03	0.00	0.03	0.01	0.02	0.00	<0.014	0.00	0.05	2.45	<0.0073	0.01
MB44bHmPorous-13	0.16	0.03	0.02	0.07	0.01	0.01	0.00	0.02	0.00	0.01	0.00	0.03	1.71	<0.00	0.00
MB44bHmPorous-14	0.29	0.06	0.03	0.05	0.01	0.04	0.01	0.03	0.01	0.01	0.00	0.05	1.58	0.03	0.17
MB44bHmPorous-15	0.24	0.06	0.04	0.03	0.00	0.03	0.01	0.04	0.00	0.01	0.00	0.04	2.95	0.02	0.03
MB44bHmPorous-16	1.84	0.28	0.20	0.40	0.06	0.41	0.10	0.30	0.03	0.25	0.06	3.08	53.69	0.02	0.33
MB44bHmPorous-17	0.45	0.16	0.06	0.17	0.01	0.14	0.02	0.08	0.02	0.08	0.01	0.14	8.77	0.00	0.05
MB44bHmPorous-18	0.14	0.02	0.02	0.06	0.00	0.02	0.01	0.04	0.00	0.02	0.01	0.40	1.58	<0.00	0.02
MB44bHmPorous-19	0.05	<0.023	<0.00	<0.0322	0.00	<0.0126	<0.00	0.01	0.00	0.01	0.00	0.01	0.69	<0.00	0.00
MB44bHmPorous-2	0.88	0.24	0.15	0.28	0.04	0.36	0.06	0.21	0.04	0.19	0.02	0.14	11.39	0.01	0.08
MB44bHmPorous-20	0.02	<0.00	0.00	<0.023	<0.00	<0.00	0.00	<0.0095	0.00	<0.00	0.00	0.03	0.64	0.00	0.14

Position	Deposit	Lithology	Sample no.	Analysis no.	Texture	Mg	Al	Si	P	Ca	Sc	Ti	V	Cr	Mn
Middle	Baron	ORE	MB44b	MB44bHmPorous-3	porous martite	44.70	97.83	4423.93	35.63	117.76	0.44	<0.79	44.89	<1.25	123.77
Middle	Baron	ORE	MB44b	MB44bHmPorous-4	porous martite	63.89	165.42	5465.34	52.66	357.93	0.72	6.70	95.64	3.63	222.92
Middle	Baron	ORE	MB44b	MB44bHmPorous-5	porous martite	52.55	128.26	5598.32	62.10	270.87	0.50	3.57	65.78	3.57	230.28
Middle	Baron	ORE	MB44b	MB44bHmPorous-6	porous martite	42.06	93.11	3620.53	15.23	127.92	<0.154	0.75	79.18	<1.28	103.72
Middle	Baron	ORE	MB44b	MB44bHmPorous-7	porous martite	45.33	105.93	4258.75	26.09	224.06	<0.14	<0.81	49.00	<1.35	125.76
Middle	Baron	ORE	MB44b	MB44bHmPorous-8	porous martite	49.90	154.30	5037.69	39.76	149.46	0.36	3.71	73.56	3.07	160.15
Middle	Baron	ORE	MB44b	MB44bHmPorous-9	porous martite	39.61	101.61	3921.05	<8.36	109.71	<0.157	2.61	48.01	<1.46	124.29
Middle	Prince	ORE	MB60	MB60HMPlaty-10	platy hematite	408.11	677.97	629.80	9.46	1850.86	0.25	21.44	50.71	1.06	1069.82
Middle	Prince	ORE	MB60	MB60HMPlaty-11	platy hematite	308.41	695.46	483.66	<4.49	965.35	0.33	23.28	68.91	1.30	396.86
Middle	Prince	ORE	MB60	MB60HMPlaty-12	platy hematite	198.27	693.34	439.68	21.57	512.72	0.60	15.01	56.39	1.85	270.93
Middle	Prince	ORE	MB60	MB60HMPlaty-13	platy hematite	208.04	976.87	964.34	27.50	529.06	<0.064	1360.44	33.29	0.57	352.54
Middle	Prince	ORE	MB60	MB60HMPlaty-14	platy hematite	547.17	381.60	349.89	5.11	2060.05	0.07	16.89	67.61	1.29	565.33
Middle	Prince	ORE	MB60	MB60HMPlaty-15	platy hematite	138.91	995.66	674.70	15.46	843.21	0.12	1044.19	58.61	0.57	528.24
Middle	Prince	ORE	MB60	MB60HMPlaty-16	platy hematite	17.93	1403.86	884.98	8.39	<37.72	2.10	<0.37	17.52	<0.55	26.34
Middle	Prince	ORE	MB60	MB60HMPlaty-17	platy hematite	359.22	387.85	334.29	17.46	940.57	<0.081	6.25	40.47	0.80	370.40
Middle	Prince	ORE	MB60	MB60HMPlaty-2	platy hematite	27.06	2199.56	2297.34	<4.98	62.24	2.56	<0.32	30.46	0.93	19.37
Middle	Prince	ORE	MB60	MB60HMPlaty-4	platy hematite	153.34	209.26	358.94	5.43	261.30	<0.057	33.33	37.68	4.58	147.08
Middle	Prince	ORE	MB60	MB60HMPlaty-5	platy hematite	65.48	953.11	559.38	10.53	97.34	0.24	2.04	19.27	0.80	162.01
Middle	Prince	ORE	MB60	MB60HMPlaty-6	platy hematite	290.07	593.04	362.17	<5.28	630.08	0.15	6.13	61.24	1.08	449.31
Middle	Prince	ORE	MB60	MB60HMPlaty-7	platy hematite	20.68	916.26	576.40	<9.29	95.18	1.25	<0.8	39.51	2.46	55.49
Middle	Prince	ORE	MB60	MB60HMPlaty-8	platy hematite	135.21	1060.29	1138.52	15.53	336.04	0.80	0.99	13.20	<0.58	209.16
Middle	Prince	ORE	MB60	MB60HMPlaty-9	platy hematite	364.45	672.27	499.62	7.75	929.00	0.20	10.65	40.33	1.91	460.43
North	Princess	ORE	MB65	MB65Hm-1	porous martite	31.16	624.32	626.71	28.37	<59.59	0.30	1.84	2.20	<0.82	85.39
North	Princess	ORE	MB65	MB65Hm-10	porous martite	114.66	3511.39	2150.73	316.47	230.65	3.48	13.96	2.47	2.53	426.01
North	Princess	ORE	MB65	MB65Hm-11	porous martite	33.54	291.44	1121.06	94.38	217.20	0.51	1.27	2.44	2.20	33.75
North	Princess	ORE	MB65	MB65Hm-12	porous martite	96.56	1341.19	1245.72	97.57	158.93	1.76	2.12	1.96	2.34	351.01
North	Princess	ORE	MB65	MB65Hm-13	porous martite	27.14	504.10	1720.34	69.25	54.63	0.21	0.50	2.01	0.76	172.43
North	Princess	ORE	MB65	MB65Hm-14	porous martite	24.59	365.72	1293.24	130.16	124.79	0.48	1.64	1.92	<0.57	69.36
North	Princess	ORE	MB65	MB65Hm-15	porous martite	25.88	286.99	646.67	20.82	129.97	0.32	12.87	1.56	<0.72	58.68
North	Princess	ORE	MB65	MB65Hm-16	porous martite	67.44	1890.74	1451.80	127.63	144.77	1.59	4.05	2.48	1.57	181.61
North	Princess	ORE	MB65	MB65Hm-17	porous martite	48.78	730.88	963.21	44.36	<35.73	0.36	1.41	2.57	<0.7	100.73
North	Princess	ORE	MB65	MB65Hm-18	porous martite	36.01	161.87	782.73	130.03	144.34	0.32	4.92	1.67	<0.7	11.61
North	Princess	ORE	MB65	MB65Hm-19	porous martite	17.76	339.74	718.97	61.99	<49.93	0.91	45.90	11.52	52.54	45.97
North	Princess	ORE	MB65	MB65Hm-2	porous martite	36.72	789.99	1239.36	86.73	75.95	0.94	2.59	2.80	4.42	180.85
North	Princess	ORE	MB65	MB65Hm-20	porous martite	25.27	346.57	1132.53	53.45	82.43	0.09	<0.56	2.70	2.31	38.84
North	Princess	ORE	MB65	MB65Hm-4	porous martite	56.15	483.30	1968.75	260.79	184.95	0.75	<0.65	2.41	0.71	103.35
North	Princess	ORE	MB65	MB65Hm-5	porous martite	27.29	654.69	3436.46	178.06	384.91	0.79	3.16	4.56	10.90	85.62
North	Princess	ORE	MB65	MB65Hm-6	porous martite	29.75	348.96	975.48	23.49	64.61	0.68	2.97	7.42	2.09	76.73
North	Princess	ORE	MB65	MB65Hm-7	porous martite	31.40	386.86	1187.89	41.23	129.48	0.32	1.47	2.71	2.30	86.19
North	Princess	ORE	MB65	MB65Hm-8	porous martite	40.84	712.22	1126.98	101.02	76.48	0.77	7.40	4.15	5.69	127.24
North	Princess	ORE	MB65	MB65Hm-9	porous martite	21.00	468.54	1134.54	56.22	<45.46	0.32	19.54	2.43	<0.74	157.30
North	Princess	ORE	MB66	MB66Hm-1	porous martite	267.84	187.11	252.05	57.48	<137.16	0.34	2.38	1.95	<1.64	168.99
North	Princess	ORE	MB66	MB66Hm-10	porous martite	456.86	160.92	431.25	146.78	<111.62	<0.186	7.21	3.40	<1.61	324.77

Analysis no.	Co	Ni	Cu	Zn	Ga	As	Sr	Y	Zr	Nb	Mo	Sn	Sb	Ba	La	Ce	Pr
MB44bHmPorous-3	1.14	8.75	56.95	12.43	0.36	4.81	2.29	3.36	0.05	0.01	0.44	<0.18	0.41	22.35	0.64	1.39	0.20
MB44bHmPorous-4	3.77	11.72	56.51	15.39	0.52	5.67	2.90	5.22	0.15	0.03	0.24	0.19	0.65	28.55	1.00	2.30	0.30
MB44bHmPorous-5	2.57	12.86	60.43	20.14	0.52	5.77	2.65	6.26	0.13	0.02	0.17	0.16	0.49	24.47	1.03	2.31	0.31
MB44bHmPorous-6	1.69	7.95	43.32	13.76	0.16	4.49	1.69	2.60	0.04	<0.0075	0.33	<0.164	0.27	15.88	0.72	1.13	0.15
MB44bHmPorous-7	0.87	7.45	52.98	13.40	0.30	3.06	1.90	3.41	<0.02	0.01	0.56	0.19	0.45	14.07	0.64	1.21	0.15
MB44bHmPorous-8	1.66	10.48	74.81	13.81	0.46	5.45	2.80	4.52	0.11	0.01	0.80	0.34	0.42	23.17	0.84	1.93	0.22
MB44bHmPorous-9	1.73	5.95	50.36	12.11	0.37	2.87	1.43	3.61	0.06	0.03	0.51	<0.187	0.26	13.89	0.54	1.15	0.17
MB60HMPlaty-10	0.53	5.30	0.41	10.11	0.41	8.23	0.87	0.44	1.31	0.08	2.04	0.23	0.28	2.23	0.29	0.69	0.07
MB60HMPlaty-11	0.45	6.33	0.34	4.01	0.62	8.07	0.47	0.53	1.14	0.17	2.37	<0.08	0.27	3.22	0.32	0.70	0.08
MB60HMPlaty-12	0.37	2.79	0.30	4.98	0.47	5.94	0.43	0.42	1.03	0.08	2.06	<0.085	0.17	2.44	0.25	0.56	0.05
MB60HMPlaty-13	0.47	2.67	4.92	219.74	0.59	8.54	0.53	0.37	0.72	0.44	2.79	3.66	0.20	1.51	0.37	0.83	0.10
MB60HMPlaty-14	0.22	2.62	0.13	2.85	0.32	2.97	1.08	0.27	1.08	0.05	2.07	0.12	0.09	2.80	0.22	0.32	0.04
MB60HMPlaty-15	0.40	5.16	1.52	351.64	0.50	7.30	0.54	0.34	3.12	0.17	2.30	0.52	0.15	2.52	0.32	0.74	0.06
MB60HMPlaty-16	0.25	0.16	<0.086	1.77	0.42	4.50	0.15	0.12	0.23	<0.00	1.72	0.27	0.49	1.33	0.29	0.78	0.10
MB60HMPlaty-17	0.22	3.81	0.26	2.27	0.29	4.53	0.32	0.23	0.79	0.03	2.39	0.14	0.13	4.30	0.17	0.37	0.04
MB60HMPlaty-2	0.15	1.01	0.43	1.90	0.57	4.93	0.19	0.12	0.34	<0.0047	1.83	0.14	0.30	1.19	0.26	0.51	0.07
MB60HMPlaty-4	0.16	0.67	<0.095	1.39	0.15	0.62	0.18	0.07	0.72	0.06	0.39	<0.054	0.08	1.61	0.06	0.10	0.01
MB60HMPlaty-5	0.42	3.41	0.26	2.60	0.52	6.38	0.23	0.30	0.22	0.01	3.78	<0.062	0.15	1.62	0.33	0.80	0.07
MB60HMPlaty-6	0.48	6.15	<0.134	2.53	0.46	4.68	0.55	0.32	0.86	0.02	1.92	<0.072	0.13	1.42	0.18	0.49	0.05
MB60HMPlaty-7	0.34	2.15	<0.232	3.26	0.53	6.10	0.31	0.16	0.25	<0.009	2.47	<0.144	0.24	1.33	0.20	0.63	0.07
MB60HMPlaty-8	0.38	3.27	0.15	3.31	0.69	17.29	0.83	0.45	0.11	0.00	4.21	0.13	0.47	1.48	0.51	1.21	0.16
MB60HMPlaty-9	0.30	4.07	0.18	3.48	0.46	6.04	0.59	0.31	0.80	0.07	2.58	<0.081	0.24	1.57	0.24	0.57	0.06
MB65Hm-1	2.23	11.61	8.50	9.90	0.33	52.31	0.97	0.51	7.58	0.05	4.33	0.12	4.76	2.56	0.23	3.29	0.06
MB65Hm-10	6.78	17.57	57.52	29.07	0.63	49.54	4.20	4.14	13.81	0.01	4.55	0.11	4.39	12.30	1.50	27.00	0.65
MB65Hm-11	1.77	3.67	0.79	5.46	0.23	19.57	0.64	1.27	2.72	0.05	1.76	<0.103	3.65	0.95	0.83	1.75	0.15
MB65Hm-12	2.13	24.80	22.49	14.36	0.57	38.94	2.62	1.89	5.66	0.02	1.95	<0.105	4.46	4.56	0.62	16.63	0.36
MB65Hm-13	2.15	15.41	7.28	10.21	0.73	34.17	1.76	0.67	2.59	0.01	1.49	<0.083	9.30	5.58	0.37	9.54	0.20
MB65Hm-14	1.00	12.44	3.35	6.10	0.45	18.93	1.16	0.96	2.32	0.02	0.46	<0.092	3.77	4.33	0.63	3.80	0.17
MB65Hm-15	0.79	16.53	0.36	3.91	0.50	16.64	0.72	1.57	8.25	0.00	1.55	<0.088	3.70	2.08	0.24	0.80	0.05
MB65Hm-16	4.91	23.16	32.22	21.42	0.51	55.87	1.47	5.68	26.06	0.01	5.22	0.11	8.10	4.80	0.49	15.16	0.24
MB65Hm-17	3.59	19.19	6.41	13.58	0.74	55.57	1.11	1.29	17.47	0.02	5.57	0.11	5.04	1.27	0.25	2.54	0.08
MB65Hm-18	0.51	7.65	0.58	1.76	0.33	18.57	0.32	1.22	0.56	0.04	0.63	<0.087	4.19	1.58	0.64	1.27	0.13
MB65Hm-19	1.64	3.10	1.66	4.34	0.44	19.00	0.68	1.56	17.30	0.09	1.97	<0.098	3.22	2.05	0.28	1.02	0.07
MB65Hm-2	1.83	13.56	15.09	10.49	0.61	44.60	1.88	1.09	3.53	0.03	1.46	<0.106	3.44	3.85	0.53	12.33	0.26
MB65Hm-20	1.38	17.16	0.56	6.83	0.83	175.34	1.44	0.32	0.40	0.00	1.69	<0.084	5.99	2.18	0.20	0.47	0.04
MB65Hm-4	1.55	14.43	8.29	7.82	0.57	36.83	2.13	1.93	1.85	0.01	0.95	<0.08	2.15	5.76	0.94	8.90	0.28
MB65Hm-5	2.23	19.23	13.95	9.28	0.70	50.74	1.38	3.89	20.98	0.03	3.79	<0.109	7.03	4.41	0.44	8.71	0.17
MB65Hm-6	2.52	13.32	<0.199	9.49	0.49	37.90	1.25	0.64	8.62	0.04	4.86	0.10	6.43	1.94	0.25	0.54	0.05
MB65Hm-7	2.59	15.68	2.31	14.74	0.55	44.26	1.39	0.50	5.35	<0.00	2.87	<0.095	7.95	1.45	0.21	1.29	0.05
MB65Hm-8	3.08	6.77	12.39	10.34	0.24	29.92	1.03	1.93	16.09	0.06	8.37	0.15	5.15	0.69	0.60	2.96	0.12
MB65Hm-9	2.10	15.74	3.19	7.41	0.70	42.92	2.22	0.69	3.18	0.01	2.18	<0.098	4.93	5.21	0.38	6.13	0.17
MB66Hm-1	0.62	22.19	2.19	39.52	0.15	26.90	0.31	0.20	0.21	0.01	0.40	<0.26	7.60	1.92	0.04	0.07	0.01
MB66Hm-10	0.71	25.30	2.81	107.77	0.16	35.17	0.16	0.16	0.13	0.02	0.67	<0.22	7.88	0.96	0.03	0.08	0.01

Analysis no.	Nd	Sm	Eu	Gd	Tb	Dy	Ho	Er	Tm	Yb	Lu	W	Pb208	Th	U
MB44bHmPorous-3	0.94	0.28	0.17	0.23	0.05	0.30	0.07	0.23	0.03	0.13	0.03	0.12	10.60	0.01	0.08
MB44bHmPorous-4	1.34	0.32	0.21	0.60	0.06	0.40	0.10	0.35	0.04	0.32	0.05	0.24	14.76	0.03	0.16
MB44bHmPorous-5	1.61	0.47	0.21	0.60	0.09	0.41	0.13	0.40	0.05	0.31	0.06	0.18	12.65	0.03	0.12
MB44bHmPorous-6	0.57	0.25	0.10	0.17	0.04	0.15	0.05	0.20	0.02	0.16	0.03	0.26	9.35	<0.00	0.04
MB44bHmPorous-7	0.68	0.18	0.09	0.27	0.04	0.21	0.06	0.22	0.02	0.21	0.03	0.09	8.35	0.01	0.07
MB44bHmPorous-8	1.27	0.43	0.20	0.38	0.06	0.44	0.10	0.35	0.04	0.31	0.03	0.16	11.67	0.01	0.12
MB44bHmPorous-9	0.63	0.19	0.12	0.25	0.04	0.25	0.06	0.16	0.03	0.18	0.02	0.08	7.16	0.01	0.07
MB60HMPlaty-10	0.29	0.10	0.03	0.15	0.01	0.08	0.01	0.02	0.00	0.03	0.01	2.50	11.57	0.11	5.99
MB60HMPlaty-11	0.37	0.17	0.04	0.06	0.01	0.07	0.01	0.04	0.00	0.04	0.00	2.48	10.52	0.13	4.39
MB60HMPlaty-12	0.34	0.07	0.04	0.14	0.02	0.05	0.01	0.05	0.00	0.02	0.01	1.72	7.83	0.06	4.16
MB60HMPlaty-13	0.41	0.11	0.04	0.07	0.01	0.07	0.01	0.05	0.00	0.03	<0.0021	1.93	14.27	0.03	4.50
MB60HMPlaty-14	0.09	0.03	0.01	<0.022	0.00	0.01	0.01	0.03	0.01	0.02	0.00	2.59	7.94	0.10	5.06
MB60HMPlaty-15	0.38	0.12	0.02	0.08	0.01	0.03	0.01	0.02	0.00	0.04	0.01	2.36	15.33	0.06	6.49
MB60HMPlaty-16	0.33	0.09	0.03	<0.017	0.01	0.05	0.01	0.02	0.00	0.03	0.00	0.99	5.96	0.01	6.36
MB60HMPlaty-17	0.16	0.03	0.01	0.03	0.00	0.04	0.01	0.02	0.00	0.02	0.00	2.24	6.70	0.04	2.77
MB60HMPlaty-2	0.33	0.04	0.02	0.05	0.00	0.01	0.00	0.01	0.00	0.02	0.00	0.92	4.76	0.02	3.85
MB60HMPlaty-4	0.01	0.01	0.00	<0.0105	<0.00	0.01	<0.0014	0.01	0.00	0.01	0.00	0.88	2.67	0.02	1.96
MB60HMPlaty-5	0.39	0.08	0.03	0.06	0.01	0.05	0.01	0.02	0.01	0.04	0.01	1.36	8.25	0.02	4.04
MB60HMPlaty-6	0.19	0.04	0.02	0.05	0.01	0.05	0.00	0.02	0.01	0.02	0.00	2.30	8.58	0.07	3.90
MB60HMPlaty-7	0.29	0.16	0.02	0.09	<0.005	0.06	0.01	0.03	0.00	0.01	<0.006	1.36	7.39	<0.0069	3.91
MB60HMPlaty-8	0.64	0.21	0.04	0.11	0.02	0.08	0.02	0.05	0.00	0.07	0.01	1.30	16.07	0.02	5.15
MB60HMPlaty-9	0.26	0.09	0.04	0.07	0.01	0.08	0.01	0.02	0.01	0.02	0.00	2.19	9.38	0.05	3.54
MB65Hm-1	0.37	0.09	0.04	0.16	0.01	0.06	0.01	0.03	0.00	0.02	0.01	5.27	29.51	0.01	2.88
MB65Hm-10	3.34	1.02	0.39	0.93	0.17	0.87	0.17	0.52	0.08	0.56	0.07	7.15	62.93	0.16	8.44
MB65Hm-11	0.89	0.16	0.12	0.14	0.03	0.10	0.02	0.07	0.01	0.04	0.01	2.85	9.52	0.03	1.03
MB65Hm-12	2.02	0.57	0.16	0.45	0.09	0.39	0.08	0.23	0.04	0.20	0.03	5.19	48.43	0.04	2.43
MB65Hm-13	1.26	0.32	0.09	0.16	0.04	0.25	0.03	0.10	0.02	0.15	0.01	3.52	47.79	0.02	1.10
MB65Hm-14	0.63	0.26	0.10	0.16	0.02	0.16	0.02	0.07	0.01	0.05	0.01	3.36	18.78	0.02	0.99
MB65Hm-15	0.41	0.12	0.05	0.11	0.04	0.20	0.04	0.15	0.02	0.13	0.02	2.00	9.97	0.03	2.01
MB65Hm-16	1.35	0.53	0.24	0.58	0.16	0.89	0.18	0.68	0.09	0.56	0.10	4.64	24.85	0.17	6.40
MB65Hm-17	0.43	0.20	0.06	0.30	0.04	0.27	0.05	0.14	0.02	0.16	0.02	2.06	30.15	0.12	7.35
MB65Hm-18	0.58	0.17	0.10	0.24	0.03	0.12	0.03	0.08	0.02	0.07	0.01	2.22	3.96	0.02	0.50
MB65Hm-19	0.30	0.08	0.07	0.23	0.03	0.20	0.04	0.13	0.01	0.14	0.02	4.33	15.41	0.04	3.15
MB65Hm-2	1.31	0.36	0.12	0.32	0.06	0.33	0.07	0.13	0.02	0.19	0.02	3.82	44.48	0.03	1.46
MB65Hm-20	0.18	0.06	0.03	0.07	0.01	0.03	0.01	0.01	0.01	0.01	<0.0019	0.46	30.25	0.00	3.32
MB65Hm-4	1.43	0.48	0.20	0.56	0.06	0.30	0.05	0.19	0.02	0.11	0.02	2.60	42.12	0.02	0.89
MB65Hm-5	0.80	0.35	0.15	0.44	0.08	0.59	0.13	0.39	0.06	0.33	0.05	4.71	26.78	0.10	4.92
MB65Hm-6	0.29	0.08	0.05	0.16	0.02	0.10	0.02	0.06	0.00	0.05	0.01	3.26	34.12	0.04	4.06
MB65Hm-7	0.27	0.12	0.04	0.11	0.02	0.06	0.01	0.03	0.01	0.06	0.01	3.87	44.43	0.03	2.90
MB65Hm-8	0.72	0.23	0.09	0.21	0.03	0.28	0.06	0.18	0.02	0.18	0.01	7.44	22.16	0.09	9.83
MB65Hm-9	0.86	0.23	0.08	0.30	0.04	0.19	0.03	0.11	0.01	0.11	0.01	2.57	46.30	0.02	2.58
MB66Hm-1	0.07	<0.024	<0.0063	<0.024	<0.0033	0.02	0.00	0.03	0.00	0.04	0.00	0.05	69.94	0.01	0.06
MB66Hm-10	0.04	0.02	0.01	0.02	<0.0034	0.02	0.00	0.02	<0.0045	<0.015	0.00	0.19	200.53	0.00	0.09

Position	Deposit	Lithology	Sample no.	Analysis no.	Texture	Mg	Al	Si	P	Ca	Sc	Ti	V	Cr	Mn
North	Princess	ORE	MB66	MB66Hm-11	porous martite	115.76	233.60	299.45	190.63	<119.61	0.52	16.72	7.64	5.42	350.09
North	Princess	ORE	MB66	MB66Hm-12	porous martite	780.43	221.67	378.38	213.80	<115.42	<0.166	5.71	2.73	1.92	404.86
North	Princess	ORE	MB66	MB66Hm-13	porous martite	585.11	252.95	794.72	128.47	139.67	0.48	17.30	7.39	4.32	428.43
North	Princess	ORE	MB66	MB66Hm-14	porous martite	1513.52	305.87	704.11	163.74	189.02	0.29	14.78	7.01	2.37	831.09
North	Princess	ORE	MB66	MB66Hm-15	porous martite	689.49	1975.47	3992.73	174.26	<113.63	0.23	21.23	12.15	5.86	462.76
North	Princess	ORE	MB66	MB66Hm-16	porous martite	187.64	197.61	484.99	163.31	121.44	0.28	18.55	7.20	<1.99	241.80
North	Princess	ORE	MB66	MB66Hm-17	porous martite	243.39	168.63	175.21	80.58	127.00	<0.194	6.74	4.45	2.90	200.24
North	Princess	ORE	MB66	MB66Hm-18	porous martite	779.31	221.46	899.58	79.76	<114.03	0.34	9.78	4.38	1.68	1128.81
North	Princess	ORE	MB66	MB66Hm-19	porous martite	255.60	293.07	1076.97	92.17	265.01	0.57	15.56	7.03	<2.14	312.68
North	Princess	ORE	MB66	MB66Hm-2	porous martite	109.64	248.32	236.44	178.37	<129.94	0.28	6.52	4.03	2.10	188.79
North	Princess	ORE	MB66	MB66Hm-20	porous martite	193.59	262.37	620.69	171.08	<74.62	0.36	6.16	5.25	2.27	251.19
North	Princess	ORE	MB66	MB66Hm-3	porous martite	170.53	255.25	443.24	142.81	<148.01	0.44	14.38	8.81	6.20	337.92
North	Princess	ORE	MB66	MB66Hm-4	porous martite	54.64	434.04	477.70	707.69	<113.45	0.26	9.94	4.08	2.13	431.14
North	Princess	ORE	MB66	MB66Hm-6	porous martite	295.20	461.54	1295.35	211.98	<125.55	0.20	13.36	7.49	3.61	409.44
North	Princess	ORE	MB66	MB66Hm-7	porous martite	580.29	85.96	214.26	100.92	<123.57	0.21	10.36	7.42	4.05	382.62
North	Princess	ORE	MB66	MB66Hm-8	porous martite	330.01	232.00	269.91	79.35	116.48	<0.17	16.23	4.87	2.18	472.25
North	Princess	ORE	MB66	MB66Hm-9	porous martite	113.74	271.91	539.16	261.85	<105.89	0.31	7.82	3.84	3.31	206.26
North	Monarch	BIF	MB70a	MB70aHmPlatyPorous-1	platy hematite	75.84	1324.93	1549.53	41.25	64.34	<0.126	112.15	22.71	1.55	20.16
North	Monarch	BIF	MB70a	MB70aHmPlatyPorous-10	platy hematite	151.87	657.36	941.53	84.79	986.66	<0.118	107.47	18.22	11.39	15.23
North	Monarch	BIF	MB70a	MB70aHmPlatyPorous-11	platy hematite	129.86	675.07	10243.89	27.29	2186.99	0.18	128.24	21.63	18.68	10.82
North	Monarch	BIF	MB70a	MB70aHmPlatyPorous-13	platy hematite	81.84	568.70	524.82	17.02	56.00	0.40	95.90	29.78	1.39	16.73
North	Monarch	BIF	MB70a	MB70aHmPlatyPorous-14	platy hematite	181.22	741.86	881.58	16.30	207.45	0.39	23.18	16.65	1.22	14.68
North	Monarch	BIF	MB70a	MB70aHmPlatyPorous-15	platy hematite	36.53	895.17	706.18	<8.2	68.05	0.21	20.17	23.81	<1.07	10.01
North	Monarch	BIF	MB70a	MB70aHmPlatyPorous-16	platy hematite	121.46	805.91	1207.91	51.32	<73.36	0.27	20.68	40.00	1.25	62.21
North	Monarch	BIF	MB70a	MB70aHmPlatyPorous-17	platy hematite	34.19	752.35	933.84	<5.34	<42.9	0.43	54.94	76.03	0.64	11.08
North	Monarch	BIF	MB70a	MB70aHmPlatyPorous-18	platy hematite	42.09	779.45	1229.87	87.83	<47.2	0.80	106.51	32.93	1.58	65.36
North	Monarch	BIF	MB70a	MB70aHmPlatyPorous-19	platy hematite	45.41	817.67	5861.35	79.86	70.43	0.53	57.99	21.23	1.54	67.43
North	Monarch	BIF	MB70a	MB70aHmPlatyPorous-2	platy hematite	66.74	1024.98	1518.02	117.17	<42.03	0.38	13.95	27.10	3.45	122.07
North	Monarch	BIF	MB70a	MB70aHmPlatyPorous-20	platy hematite	50.60	580.92	1159.99	109.24	68.46	0.16	83.05	39.85	1.23	42.81
North	Monarch	BIF	MB70a	MB70aHmPlatyPorous-3	platy hematite	42.00	577.96	740.36	8.51	58.28	0.22	69.23	40.91	2.45	15.88
North	Monarch	BIF	MB70a	MB70aHmPlatyPorous-4	platy hematite	105.09	1454.42	1701.27	15.23	<61.12	0.28	67.04	222.96	1.11	18.54
North	Monarch	BIF	MB70a	MB70aHmPlatyPorous-5	platy hematite	97.94	849.57	934.44	16.30	<58.95	0.35	44.76	21.01	<0.84	19.97
North	Monarch	BIF	MB70a	MB70aHmPlatyPorous-6	platy hematite	93.12	282.86	295.51	<6.69	<61.21	0.42	70.27	11.82	<0.82	10.93
North	Monarch	BIF	MB70a	MB70aHmPlatyPorous-7	platy hematite	48.72	1259.21	1474.09	30.33	<53.82	0.95	59.87	44.40	1.42	31.04
North	Monarch	BIF	MB70a	MB70aHmPlatyPorous-8	platy hematite	20.16	479.87	466.48	<8.78	111.45	0.42	90.88	32.16	<0.98	8.09
North	Monarch	BIF	MB70a	MB70aHmPlatyPorous-9	platy hematite	164.38	613.60	1659.69	42.07	275.33	<0.115	96.77	17.67	18.69	23.27
North	Monarch	BIF	MB73	MB73HmPlaty-1	platy hematite	1.38	28.77	<138.8	<11.74	<119.49	<0.168	3.93	3.96	<1.57	1.86
North	Monarch	BIF	MB73	MB73HmPlaty-10	platy hematite	0.61	20.07	4414.50	21.87	145.38	<0.174	3.37	0.95	<1.56	1.54
North	Monarch	BIF	MB73	MB73HmPlaty-11	platy hematite	1.40	45.38	612.04	<9.97	<104.11	<0.164	7.60	1.64	<1.39	2.55
North	Monarch	BIF	MB73	MB73HmPlaty-12	platy hematite	0.55	23.39	1209.24	19.77	<106.09	<0.174	3.25	1.36	<1.65	1.31
North	Monarch	BIF	MB73	MB73HmPlaty-13	platy hematite	0.86	32.91	17508.84	42.49	167.35	<0.198	4.22	1.36	<1.69	3.83
North	Monarch	BIF	MB73	MB73HmPlaty-14	platy hematite	1.37	26.66	8822.57	26.50	<105.61	<0.167	5.79	1.51	<1.55	3.90
North	Monarch	BIF	MB73	MB73HmPlaty-15	platy hematite	2.76	74.78	2133.46	<10.43	<119.46	<0.177	5.36	1.95	<1.5	15.87

Analysis no.	Co	Ni	Cu	Zn	Ga	As	Sr	Y	Zr	Nb	Mo	Sn	Sb	Ba	La	Ce	Pr
MB66Hm-11	0.45	21.16	4.36	84.78	0.37	43.76	0.46	0.29	0.40	0.03	0.69	<0.25	12.50	2.64	0.05	0.15	0.02
MB66Hm-12	0.44	24.10	3.26	124.58	0.36	36.53	0.13	0.34	0.03	0.02	0.67	0.31	6.54	1.03	0.02	0.06	0.01
MB66Hm-13	0.93	21.98	4.13	97.73	0.33	41.95	0.58	0.37	0.52	0.05	0.79	<0.25	12.99	2.60	0.05	0.19	0.03
MB66Hm-14	0.81	26.63	13.22	130.50	0.26	34.03	0.22	0.40	0.20	0.08	0.92	<0.26	11.34	3.59	0.07	0.12	0.02
MB66Hm-15	1.06	23.22	26.37	474.45	0.49	42.12	0.61	0.22	0.63	0.09	1.58	3.12	15.71	3.09	0.05	0.14	0.01
MB66Hm-16	0.80	19.20	4.32	79.37	0.26	37.98	0.48	0.41	0.26	0.04	0.61	<0.29	11.43	3.82	0.03	0.11	0.01
MB66Hm-17	1.06	24.80	3.01	80.39	0.15	35.02	0.53	0.28	0.18	0.05	0.68	0.35	10.68	1.23	0.07	0.10	0.02
MB66Hm-18	0.52	21.94	2.44	56.22	0.31	20.58	0.82	0.22	0.19	0.03	0.42	<0.25	7.20	1.89	0.07	0.13	0.02
MB66Hm-19	0.71	25.41	3.06	50.09	0.29	33.33	0.64	0.33	0.16	0.06	0.60	0.45	10.96	3.19	0.07	0.15	0.02
MB66Hm-2	0.58	20.75	4.11	78.39	0.21	35.48	0.23	0.19	0.23	0.03	0.94	<0.29	7.33	0.57	0.03	0.04	0.01
MB66Hm-20	0.83	25.28	3.87	82.92	0.30	51.88	0.23	0.25	0.08	0.02	1.05	0.27	22.94	1.38	0.04	0.11	0.02
MB66Hm-3	0.97	26.46	3.81	78.83	0.48	39.17	0.63	0.33	0.42	0.06	0.69	<0.32	13.42	3.15	0.08	0.22	0.04
MB66Hm-4	0.69	26.59	6.83	322.57	0.53	72.95	0.14	0.17	0.15	0.02	2.91	<0.24	13.44	2.99	0.02	0.07	0.00
MB66Hm-6	1.84	30.31	5.99	101.50	0.55	45.03	0.61	0.42	0.42	0.07	1.02	<0.27	13.89	4.19	0.08	0.26	0.04
MB66Hm-7	1.49	22.68	4.33	154.12	0.26	34.92	0.38	0.26	0.32	0.08	0.65	<0.26	13.44	3.05	0.02	0.08	0.01
MB66Hm-8	0.86	24.76	3.15	65.66	0.17	24.11	0.36	0.19	0.14	0.02	0.38	0.24	4.91	1.81	0.04	0.10	0.01
MB66Hm-9	0.50	21.34	2.93	91.73	0.17	36.86	0.26	0.14	0.45	0.03	1.01	<0.25	10.91	1.91	0.03	0.07	0.01
MB70aHmPlatyPorous-1	0.54	2.90	0.23	17.19	0.58	18.11	1.10	0.27	0.96	0.11	0.57	0.41	7.69	1.74	0.82	3.16	0.39
MB70aHmPlatyPorous-10	0.69	4.18	0.68	6.05	0.53	75.29	25.64	0.67	1.05	0.17	0.57	0.29	14.19	15.40	18.16	19.45	3.55
MB70aHmPlatyPorous-11	1.40	7.34	0.35	8.68	0.46	6.19	26.21	0.47	1.34	0.12	1.08	0.23	5.68	2.13	3.04	60.23	1.12
MB70aHmPlatyPorous-13	0.76	5.18	0.83	14.55	0.34	7.96	0.86	0.37	1.52	0.20	1.27	0.22	5.54	2.27	2.46	15.22	0.72
MB70aHmPlatyPorous-14	1.11	3.75	0.33	4.63	0.42	12.65	4.35	0.30	1.35	0.15	0.48	0.14	7.90	0.94	1.28	2.41	0.64
MB70aHmPlatyPorous-15	0.34	1.24	<0.25	4.48	0.40	4.51	0.44	0.11	0.91	0.10	2.81	0.33	3.25	0.37	0.19	4.64	0.16
MB70aHmPlatyPorous-16	1.04	11.19	0.47	9.11	0.63	12.37	5.39	0.49	1.36	0.10	0.80	0.19	8.13	13.82	5.27	6.28	1.31
MB70aHmPlatyPorous-17	0.68	3.98	0.30	3.83	0.58	9.69	1.07	0.42	1.38	0.10	1.39	0.21	6.61	0.62	0.66	19.99	0.62
MB70aHmPlatyPorous-18	1.28	15.33	<0.21	12.73	0.57	12.80	2.77	0.86	2.07	0.20	1.58	0.21	7.95	5.08	3.19	85.44	1.35
MB70aHmPlatyPorous-19	1.38	15.50	0.22	21.02	0.65	11.33	2.62	0.86	1.41	0.14	2.14	0.27	8.20	4.68	2.80	4.19	1.04
MB70aHmPlatyPorous-2	1.21	27.76	0.46	19.73	0.97	34.53	6.80	0.56	0.86	0.07	0.96	0.18	11.77	9.53	10.18	11.84	2.04
MB70aHmPlatyPorous-20	1.57	20.28	0.28	6.84	0.72	14.17	1.74	1.19	1.54	0.20	1.43	<0.111	7.05	2.88	1.75	7.44	0.87
MB70aHmPlatyPorous-3	1.31	3.87	<0.205	3.51	0.31	8.53	1.39	0.42	1.19	0.25	0.92	0.16	7.82	0.67	0.69	4.70	0.79
MB70aHmPlatyPorous-4	1.43	10.50	<0.23	3.40	0.37	13.85	3.75	0.61	0.90	0.13	5.69	0.21	6.17	4.11	1.90	22.92	0.63
MB70aHmPlatyPorous-5	1.89	3.15	0.38	3.16	0.45	15.89	1.49	0.49	1.21	0.13	2.50	0.19	8.47	0.82	1.20	50.28	0.78
MB70aHmPlatyPorous-6	0.19	0.72	<0.184	1.77	0.19	6.06	0.25	0.18	0.54	0.08	2.12	0.41	4.06	<0.065	0.20	1.84	0.20
MB70aHmPlatyPorous-7	1.32	5.33	0.74	6.37	0.59	12.77	1.25	0.53	0.87	0.18	3.36	0.24	5.04	1.96	1.89	13.71	0.60
MB70aHmPlatyPorous-8	0.30	1.44	0.39	1.89	0.17	4.74	1.30	0.25	0.89	0.22	0.65	0.19	3.85	2.19	2.04	6.09	0.61
MB70aHmPlatyPorous-9	2.87	5.82	<0.2	7.62	0.57	39.91	16.96	0.34	1.31	0.15	0.90	0.24	9.51	3.15	3.68	3.69	0.80
MB73HmPlaty-1	0.03	<0.29	<0.23	<0.37	<0.048	0.32	0.03	0.03	0.27	0.05	0.31	<0.25	0.07	<0.00	0.01	0.00	0.00
MB73HmPlaty-10	<0.055	0.27	<0.29	<0.36	0.07	<0.35	<0.0136	<0.0072	0.14	0.03	0.25	<0.23	0.09	<0.00	0.00	0.01	<0.00
MB73HmPlaty-11	<0.033	<0.31	<0.23	<0.37	<0.044	1.69	<0.0128	0.01	0.45	0.06	0.19	<0.23	0.50	0.31	0.00	0.00	0.00
MB73HmPlaty-12	<0.035	<0.175	<0.28	<0.39	<0.057	<0.35	<0.0136	0.01	0.40	0.04	0.30	<0.24	<0.066	<0.00	0.01	0.02	0.00
MB73HmPlaty-13	0.02	0.30	<0.28	<0.39	<0.05	1.14	0.05	0.12	0.72	0.05	0.30	<0.25	0.20	0.22	0.08	0.06	0.01
MB73HmPlaty-14	<0.036	<0.00	<0.26	<0.37	<0.054	<0.41	<0.00	0.02	0.56	0.04	0.22	<0.24	<0.084	<0.00	0.01	0.01	0.00
MB73HmPlaty-15	0.09	<0.27	<0.26	<0.41	0.20	1.19	0.01	0.02	0.40	0.03	0.33	0.30	0.33	<0.143	0.00	0.01	<0.00

Analysis no.	Nd	Sm	Eu	Gd	Tb	Dy	Ho	Er	Tm	Yb	Lu	W	Pb208	Th	U
MB66Hm-11	0.12	0.03	0.02	0.06	0.01	0.04	<0.0037	0.03	0.00	0.05	0.01	0.26	204.69	0.01	0.37
MB66Hm-12	0.03	0.02	<0.0094	0.03	0.00	0.01	0.01	<0.0106	0.00	0.06	<0.00	0.07	266.41	<0.00	0.09
MB66Hm-13	0.17	0.07	0.01	0.06	0.02	0.05	0.01	0.03	0.01	0.02	0.01	0.22	217.77	0.02	0.41
MB66Hm-14	0.07	0.05	0.02	0.08	0.01	0.01	0.02	0.03	0.00	0.07	0.01	0.23	159.94	0.01	0.24
MB66Hm-15	0.07	0.07	0.02	0.04	0.00	0.03	0.01	0.03	0.01	0.04	0.02	0.25	491.74	0.01	0.63
MB66Hm-16	0.10	<0.03	0.02	<0.029	0.01	0.03	0.01	0.04	0.01	0.05	0.01	0.15	166.92	0.01	0.26
MB66Hm-17	0.09	0.01	0.02	0.04	<0.0038	0.04	0.01	0.03	0.00	0.05	0.01	0.29	97.26	0.01	0.16
MB66Hm-18	0.09	0.04	0.03	0.07	0.01	0.03	0.01	0.03	0.00	0.02	0.01	0.11	96.53	0.00	0.12
MB66Hm-19	0.12	0.03	<0.0212	0.05	0.01	0.04	<0.0046	0.03	0.00	0.04	0.01	0.22	140.55	0.01	0.27
MB66Hm-2	0.07	<0.026	0.02	0.06	<0.0035	0.02	0.00	<0.015	0.00	0.03	0.00	0.13	182.29	<0.00	0.10
MB66Hm-20	0.11	0.02	0.02	0.02	0.01	0.03	0.01	0.02	0.01	0.08	0.01	0.21	205.87	0.01	0.16
MB66Hm-3	0.19	0.10	0.02	<0.029	<0.004	0.05	0.01	0.06	0.00	0.03	0.01	0.23	145.04	0.02	0.40
MB66Hm-4	0.05	0.02	0.03	0.05	0.00	0.04	0.00	0.01	<0.0029	0.02	0.01	0.15	772.43	0.00	0.16
MB66Hm-6	0.17	0.04	0.05	0.08	0.02	0.08	0.01	0.03	0.01	0.03	0.01	0.31	212.46	0.01	0.38
MB66Hm-7	0.07	0.03	0.01	0.03	<0.00	0.03	0.01	0.04	<0.0036	0.04	0.01	0.12	221.98	<0.00	0.24
MB66Hm-8	0.06	0.01	<0.0088	0.06	<0.00	0.03	<0.0033	0.03	0.00	0.04	0.00	0.15	102.88	0.02	0.15
MB66Hm-9	0.08	<0.025	0.02	0.05	0.00	0.02	<0.0034	0.01	0.01	0.01	<0.0047	0.11	195.43	<0.00	0.16
MB70aHmPlatyPorous-1	1.55	0.26	0.05	0.18	0.03	0.11	0.02	0.04	0.01	0.06	0.01	6.08	3.62	0.03	0.71
MB70aHmPlatyPorous-10	9.10	0.77	0.11	0.42	0.03	0.27	0.02	0.10	0.01	0.09	0.01	3.32	16.21	0.13	0.53
MB70aHmPlatyPorous-11	3.88	0.89	0.11	0.22	0.05	0.23	0.04	0.12	0.01	0.17	0.01	9.82	2.73	0.07	0.99
MB70aHmPlatyPorous-13	2.02	0.34	0.07	0.16	0.02	0.15	0.02	0.06	0.01	0.11	0.01	11.73	3.44	0.06	1.34
MB70aHmPlatyPorous-14	2.45	0.53	0.08	0.21	0.04	0.18	0.03	0.13	0.02	0.13	0.01	6.83	1.39	0.03	0.51
MB70aHmPlatyPorous-15	0.67	0.16	0.02	0.15	0.01	0.09	0.00	0.03	0.00	0.03	0.00	10.80	0.77	0.01	0.63
MB70aHmPlatyPorous-16	4.09	0.60	0.14	0.26	0.03	0.27	0.03	0.11	0.01	0.13	0.01	7.31	8.57	0.10	1.06
MB70aHmPlatyPorous-17	3.07	0.62	0.10	0.25	0.04	0.14	0.03	0.12	0.02	0.13	0.01	14.72	1.95	0.05	2.52
MB70aHmPlatyPorous-18	5.18	1.03	0.19	0.52	0.07	0.43	0.05	0.17	0.02	0.21	0.04	9.89	14.57	0.09	1.22
MB70aHmPlatyPorous-19	3.75	0.55	0.15	0.40	0.05	0.26	0.03	0.11	0.03	0.13	0.02	9.49	17.10	0.05	0.85
MB70aHmPlatyPorous-2	5.61	0.53	0.10	0.23	0.03	0.17	0.03	0.06	0.01	0.09	0.01	3.21	35.38	0.22	0.45
MB70aHmPlatyPorous-20	3.43	0.69	0.16	0.33	0.07	0.39	0.05	0.15	0.03	0.25	0.02	10.27	12.91	0.05	1.38
MB70aHmPlatyPorous-3	2.40	0.54	0.09	0.21	0.03	0.13	0.01	0.09	0.01	0.10	0.01	9.09	2.94	0.06	1.36
MB70aHmPlatyPorous-4	2.62	0.43	0.10	0.19	0.04	0.23	0.04	0.08	0.02	0.17	0.02	46.02	3.44	0.07	4.34
MB70aHmPlatyPorous-5	2.75	0.59	0.11	0.29	0.05	0.25	0.04	0.11	0.03	0.11	0.03	7.56	2.59	0.08	0.85
MB70aHmPlatyPorous-6	0.82	0.19	0.03	0.11	0.02	0.06	0.01	0.03	0.01	0.04	0.00	5.38	0.58	0.01	0.37
MB70aHmPlatyPorous-7	2.33	0.34	0.08	0.24	0.02	0.13	0.01	0.07	0.01	0.06	0.01	16.44	5.71	0.08	1.92
MB70aHmPlatyPorous-8	2.01	0.32	0.07	0.14	0.03	0.14	0.02	0.04	0.01	0.05	0.01	10.88	2.94	0.10	1.45
MB70aHmPlatyPorous-9	2.66	0.40	0.09	0.27	0.02	0.18	0.02	0.08	0.01	0.06	0.01	4.94	4.46	0.05	0.58
MB73HmPlaty-1	<0.024	<0.0276	0.00	0.01	<0.0037	0.01	<0.0038	<0.00	<0.0035	0.01	<0.0036	0.21	<0.049	<0.00	0.04
MB73HmPlaty-10	<0.00	0.01	0.01	<0.0266	<0.0036	<0.00	<0.00	0.00	<0.00	<0.00	<0.0035	0.28	<0.034	<0.00	0.00
MB73HmPlaty-11	<0.00	<0.0253	<0.00	<0.0252	<0.0034	<0.00	<0.0069	<0.00	<0.00322	0.01	<0.00	0.73	0.17	<0.00	0.03
MB73HmPlaty-12	<0.00	0.01	<0.00	<0.038	<0.0036	<0.00	<0.00	0.00	<0.00	<0.00	<0.0035	0.31	<0.041	<0.0061	0.01
MB73HmPlaty-13	0.04	<0.00	<0.0074	0.03	0.00	<0.0159	0.00	<0.00	0.00	<0.00	0.00	3.49	0.25	<0.0066	0.04
MB73HmPlaty-14	<0.041	0.01	<0.0072	0.04	<0.0037	<0.00	<0.00	0.01	<0.00	<0.00	0.00	0.39	0.05	<0.00	0.01
MB73HmPlaty-15	0.01	0.01	0.00	0.01	0.00	<0.00	0.00	<0.00	<0.00	<0.00	0.00	1.76	0.94	<0.006	0.09

Position	Deposit	Lithology	Sample no.	Analysis no.	Texture	Mg	Al	Si	P	Ca	Sc	Ti	V	Cr	Mn
North	Monarch	BIF	MB73	MB73HmPlaty-16	platy hematite	0.78	25.88	2038.57	11.91	<88.67	<0.163	3.55	1.56	<1.36	2.81
North	Monarch	BIF	MB73	MB73HmPlaty-17	platy hematite	0.48	29.48	<147.18	<11.73	<96.19	<0.156	5.32	1.26	<1.65	2.17
North	Monarch	BIF	MB73	MB73HmPlaty-18	platy hematite	0.79	19.07	14974.31	<10.14	<114.67	<0.167	2.03	1.11	<1.54	1.71
North	Monarch	BIF	MB73	MB73HmPlaty-19	platy hematite	0.28	149.88	<131.18	11.28	105.12	<0.175	1.75	5.78	<1.39	10.21
North	Monarch	BIF	MB73	MB73HmPlaty-2	platy hematite	0.56	25.86	8520.47	13.37	221.05	<0.169	4.42	1.73	<1.65	2.17
North	Monarch	BIF	MB73	MB73HmPlaty-20	platy hematite	1.78	27.32	2766.11	27.79	<119.98	<0.188	4.44	1.56	<1.43	1.02
North	Monarch	BIF	MB73	MB73HmPlaty-3	platy hematite	1.48	25.45	156.67	<12.58	174.00	<0.19	4.52	1.36	<1.79	2.40
North	Monarch	BIF	MB73	MB73HmPlaty-4	platy hematite	3.36	22.18	<126.16	<9.89	<106.06	<0.152	4.21	1.20	<1.33	2.00
North	Monarch	BIF	MB73	MB73HmPlaty-5	platy hematite	1.08	30.16	228.46	<10.26	<115.11	<0.167	5.69	1.46	<1.54	2.20
North	Monarch	BIF	MB73	MB73HmPlaty-6	platy hematite	0.34	21.54	345.50	<10.44	<110.68	<0.173	3.43	1.26	<1.51	1.72
North	Monarch	BIF	MB73	MB73HmPlaty-7	platy hematite	0.70	24.86	<133.33	<11.32	<121.92	<0.165	4.12	1.29	1.42	2.49
North	Monarch	BIF	MB73	MB73HmPlaty-8	platy hematite	12.95	113.22	11920.80	21.08	<121.72	<0.192	2.91	4.91	<1.56	109.54
North	Monarch	BIF	MB73	MB73HmPlaty-9	platy hematite	1.13	25.07	1487.65	<10.66	224.42	<0.177	4.27	1.19	1.78	1.53
North	Monarch	BIF	MB73	MB73HmPorous-1	porous martite	9.54	122.53	1118.34	<10.7	<109.02	0.18	1.64	6.33	<1.25	44.52
North	Monarch	BIF	MB73	MB73HmPorous-10	porous martite	10.06	50.01	<127.68	<9.39	<104.02	<0.151	<0.8	2.99	<1.5	33.85
North	Monarch	BIF	MB73	MB73HmPorous-11	porous martite	34.79	58.99	<130.59	16.53	<117.1	0.15	<0.68	0.97	1.65	93.93
North	Monarch	BIF	MB73	MB73HmPorous-12	porous martite	12.00	117.53	<136.42	<10.23	<111.99	<0.153	1.39	7.73	<1.53	83.89
North	Monarch	BIF	MB73	MB73HmPorous-13	porous martite	21.00	95.90	260.00	<9.92	80.64	<0.15	0.83	5.60	1.62	79.45
North	Monarch	BIF	MB73	MB73HmPorous-14	porous martite	48.89	71.22	7522.36	<10.95	<90.29	<0.189	2.60	6.28	<1.53	124.78
North	Monarch	BIF	MB73	MB73HmPorous-15	porous martite	47.77	81.72	3337.75	15.31	<99.9	<0.156	0.97	11.50	1.32	213.07
North	Monarch	BIF	MB73	MB73HmPorous-16	porous martite	112.84	95.40	1638.51	<11.74	<115.29	<0.191	<1.1	35.68	2.01	198.88
North	Monarch	BIF	MB73	MB73HmPorous-17	porous martite	3.40	145.06	244.45	<11.91	<128.36	<0.19	7.96	32.12	<1.7	17.27
North	Monarch	BIF	MB73	MB73HmPorous-18	porous martite	7.25	133.94	<145.53	14.35	<102.61	<0.184	2.77	22.18	2.05	61.03
North	Monarch	BIF	MB73	MB73HmPorous-19	porous martite	36.27	133.49	983.34	23.33	<115.1	<0.195	8.04	6.86	<1.58	307.97
North	Monarch	BIF	MB73	MB73HmPorous-2	porous martite	62.71	75.28	8933.43	27.16	118.54	0.17	0.81	4.32	<1.37	98.89
North	Monarch	BIF	MB73	MB73HmPorous-20	porous martite	27.74	54.95	414.96	<10.6	<106.83	<0.162	<0.66	5.29	<1.51	61.77
North	Monarch	BIF	MB73	MB73HmPorous-3	porous martite	17.40	68.98	159.39	<10.28	<120.48	0.21	<0.9	7.94	1.34	24.19
North	Monarch	BIF	MB73	MB73HmPorous-4	porous martite	133.24	61.33	758.91	30.75	<114.91	<0.199	<0.82	2.27	<1.38	97.91
North	Monarch	BIF	MB73	MB73HmPorous-5	porous martite	6.55	106.45	271.34	<11.45	<122.86	<0.153	2.64	6.05	<1.33	62.82
North	Monarch	BIF	MB73	MB73HmPorous-6	porous martite	2.49	80.73	4758.39	<10.88	<118.57	<0.18	2.67	3.75	<1.3	7.12
North	Monarch	BIF	MB73	MB73HmPorous-7	porous martite	93.99	76.51	487.48	<10.16	117.45	<0.158	<0.98	1.40	<1.34	68.42
North	Monarch	BIF	MB73	MB73HmPorous-8	porous martite	41.32	150.68	566.86	11.07	280.24	<0.155	<0.75	3.60	<1.22	239.88
North	Monarch	BIF	MB73	MB73HmPorous-9	porous martite	20.74	58.79	147.29	<9.87	<101.57	<0.16	<0.92	2.24	1.76	47.57
North	Monarch	BIF	MB74	MB74HmPorous-10	porous martite	5.88	212.52	13044.61	<12.56	<135.08	<0.2	10.48	4.46	<1.49	6.04
North	Monarch	BIF	MB74	MB74HmPorous-11	porous martite	28.79	351.11	3041.50	34.49	<213.92	<0.31	11.59	5.39	2.59	5.98
North	Monarch	BIF	MB74	MB74HmPorous-12	porous martite	58.47	860.07	723.52	43.59	<199.85	<0.27	9.33	10.19	4.78	9.34
North	Monarch	BIF	MB74	MB74HmPorous-13	porous martite	7.72	219.26	568.00	13.46	<128.49	<0.203	10.58	6.57	<1.87	4.13
North	Monarch	BIF	MB74	MB74HmPorous-14	porous martite	2.30	185.78	158.31	29.14	<115.9	0.19	8.95	6.50	<1.73	2.43
North	Monarch	BIF	MB74	MB74HmPorous-15	porous martite	15.32	267.13	191.30	36.44	352.35	<0.184	7.34	4.17	1.58	9.00
North	Monarch	BIF	MB74	MB74HmPorous-16	porous martite	35.07	211.61	218.73	19.05	<139.54	<0.192	13.75	6.86	<1.64	6.19
North	Monarch	BIF	MB74	MB74HmPorous-17	porous martite	35.15	237.57	5397.52	67.76	<119.62	0.24	9.82	6.40	2.64	15.23
North	Monarch	BIF	MB74	MB74HmPorous-18	porous martite	16.80	223.69	762.19	<12.35	<98.8	0.29	11.16	3.75	2.04	3.89
North	Monarch	BIF	MB74	MB74HmPorous-19	porous martite	28.68	513.76	437.31	<11.22	<102.55	<0.183	5.55	17.60	1.92	10.48

Analysis no.	Co	Ni	Cu	Zn	Ga	As	Sr	Y	Zr	Nb	Mo	Sn	Sb	Ba	La	Ce	Pr
MB73HmPlaty-16	<0.025	0.29	0.31	0.68	<0.077	<0.38	0.04	0.02	0.69	0.04	0.20	<0.24	0.18	<0.00	0.01	0.01	<0.0058
MB73HmPlaty-17	0.05	<0.185	<0.29	<0.52	<0.043	<0.45	0.01	0.02	0.54	0.07	0.26	<0.26	0.13	<0.109	0.01	0.00	<0.00
MB73HmPlaty-18	0.02	<0.115	<0.22	<0.36	<0.053	<0.41	<0.00	<0.0067	0.45	0.06	0.13	0.27	0.15	<0.00	0.02	0.02	<0.00
MB73HmPlaty-19	0.07	1.02	<0.24	0.65	0.11	0.67	0.02	<0.0068	0.30	0.02	1.88	0.31	0.09	0.21	<0.00	<0.0047	<0.00
MB73HmPlaty-2	<0.037	<0.19	0.36	<0.38	0.07	<0.4	0.01	<0.0076	0.32	0.06	0.31	<0.25	<0.086	<0.00	<0.0054	<0.0053	0.01
MB73HmPlaty-20	0.04	<0.225	0.40	<0.27	0.11	<0.37	0.03	<0.017	0.39	0.07	0.29	<0.26	0.19	0.16	0.02	<0.0105	0.00
MB73HmPlaty-3	0.06	<0.31	<0.27	<0.37	0.09	<0.38	0.09	0.03	0.64	0.07	0.09	<0.24	0.33	<0.00	<0.0074	0.01	0.01
MB73HmPlaty-4	<0.0222	<0.223	0.25	<0.32	<0.059	0.30	<0.00	<0.0065	0.33	0.05	0.22	<0.21	<0.079	<0.00	<0.022	0.02	<0.00
MB73HmPlaty-5	<0.053	<0.206	<0.24	<0.35	<0.045	<0.3	<0.00	0.03	0.67	0.03	0.17	<0.23	0.14	<0.00	0.01	0.01	0.00
MB73HmPlaty-6	<0.044	<0.34	<0.29	<0.26	<0.048	<0.36	<0.00	<0.0074	0.48	0.04	0.15	<0.24	0.07	<0.00	<0.00	0.01	<0.00
MB73HmPlaty-7	<0.00	<0.209	<0.26	0.40	0.08	<0.34	<0.00	0.02	0.72	0.06	0.18	<0.22	0.24	<0.00	0.01	<0.0049	<0.008
MB73HmPlaty-8	0.21	1.56	0.71	1.79	0.12	3.34	0.13	0.11	0.44	0.06	0.66	<0.23	0.78	0.97	0.03	0.05	<0.0045
MB73HmPlaty-9	<0.044	0.26	<0.28	<0.4	<0.059	<0.42	<0.0141	0.00	0.57	0.02	0.18	0.28	0.10	<0.00	<0.0053	<0.0146	0.00
MB73HmPorous-1	0.82	1.17	<0.22	1.88	0.21	6.67	0.37	0.22	0.56	0.03	0.75	<0.185	2.77	1.11	0.06	0.09	0.01
MB73HmPorous-10	1.01	2.02	0.23	0.92	0.19	1.88	0.11	0.02	0.38	0.01	0.15	<0.209	0.41	0.11	0.00	0.02	<0.0075
MB73HmPorous-11	1.93	1.46	0.30	2.85	0.14	2.76	0.42	<0.0139	<0.00	<0.00	0.05	<0.206	0.48	<0.00	0.01	0.01	0.00
MB73HmPorous-12	1.35	1.43	<0.29	4.61	0.13	4.55	0.23	0.08	0.35	0.05	0.50	<0.23	1.38	0.21	0.03	0.03	<0.0042
MB73HmPorous-13	1.57	1.72	3.26	8.09	0.16	8.22	1.01	0.31	0.33	<0.00	0.63	<0.22	1.77	2.23	0.12	0.14	0.01
MB73HmPorous-14	0.67	2.59	0.29	2.49	0.13	9.49	0.73	0.15	0.59	0.01	0.34	0.27	2.36	0.64	0.09	0.12	0.01
MB73HmPorous-15	1.59	2.28	0.31	7.32	0.14	12.83	0.45	0.51	0.78	0.01	0.65	<0.21	3.33	2.89	0.27	0.33	0.04
MB73HmPorous-16	1.58	2.29	<0.3	6.17	0.09	13.72	0.63	0.60	1.04	<0.00	1.18	<0.25	2.88	3.40	0.32	0.41	0.03
MB73HmPorous-17	0.12	1.03	<0.3	2.29	0.09	3.57	0.29	0.08	0.40	0.05	1.25	<0.25	2.08	0.29	0.04	0.05	0.00
MB73HmPorous-18	0.66	0.32	<0.31	3.03	0.14	11.12	0.64	0.31	1.50	<0.02	1.28	<0.25	4.28	0.62	0.19	0.22	0.02
MB73HmPorous-19	1.03	1.62	<0.28	1.87	0.33	4.16	0.19	0.25	0.47	0.03	0.99	<0.23	1.22	1.59	0.14	0.15	0.01
MB73HmPorous-2	1.45	2.32	<0.3	3.84	0.10	9.86	0.47	0.57	2.53	<0.0094	1.71	<0.208	2.04	1.51	0.20	0.23	0.02
MB73HmPorous-20	0.74	1.73	1.18	2.60	0.14	2.19	0.69	0.02	<0.024	<0.00	0.09	<0.24	0.38	0.22	0.00	0.02	<0.00
MB73HmPorous-3	0.42	0.54	0.42	0.87	0.15	2.22	0.33	0.03	1.94	<0.00	0.71	<0.199	0.97	0.19	0.01	0.03	0.00
MB73HmPorous-4	1.72	1.69	5.66	12.56	<0.071	9.02	0.57	0.34	0.06	<0.0098	1.70	<0.203	1.23	0.62	0.11	0.14	0.01
MB73HmPorous-5	0.56	0.67	<0.31	3.12	0.26	1.98	0.10	0.12	2.06	0.04	0.85	0.21	0.74	0.42	0.05	0.06	0.01
MB73HmPorous-6	0.11	0.68	<0.27	<0.36	0.18	1.33	0.07	0.01	0.23	0.05	0.36	<0.21	0.38	<0.00	<0.0051	0.01	0.00
MB73HmPorous-7	1.15	0.86	6.34	9.88	0.19	5.43	0.36	0.06	0.03	<0.00	0.40	<0.194	1.42	0.55	0.02	0.03	0.00
MB73HmPorous-8	0.95	2.16	3.16	2.58	0.16	3.52	0.22	0.15	0.38	0.01	0.75	<0.19	1.11	0.67	0.07	0.09	0.01
MB73HmPorous-9	1.39	1.10	<0.26	1.63	0.21	2.74	0.34	0.02	0.30	0.00	0.17	<0.21	0.44	0.11	0.01	0.01	<0.0041
MB74HmPorous-10	<0.04	0.33	<0.31	<0.61	0.21	1.06	0.12	0.09	0.33	0.12	0.49	<0.25	0.33	0.70	0.08	0.11	0.03
MB74HmPorous-11	<0.083	0.37	<0.54	<0.4	<0.119	2.62	0.29	128.11	0.39	0.13	0.17	0.49	1.48	0.78	0.12	0.36	0.10
MB74HmPorous-12	0.42	1.79	<0.41	2.42	0.24	4.29	0.64	0.25	0.32	0.11	0.41	<0.37	2.43	0.53	0.18	0.28	0.10
MB74HmPorous-13	0.03	0.66	<0.34	0.49	0.27	1.37	0.16	0.04	0.24	0.17	0.20	0.46	0.73	0.10	0.05	0.10	0.04
MB74HmPorous-14	<0.027	0.23	0.38	<0.46	0.14	0.34	<0.0151	<0.0114	0.18	0.13	0.46	<0.23	0.24	<0.114	0.01	0.02	0.02
MB74HmPorous-15	<0.046	<0.33	<0.27	<0.53	0.10	1.23	0.29	9.50	0.35	0.12	0.39	<0.25	1.11	1.42	0.14	0.29	0.07
MB74HmPorous-16	0.04	0.58	<0.32	<0.47	0.17	3.96	0.44	0.18	0.30	0.12	0.10	<0.27	1.76	0.56	0.14	0.32	0.13
MB74HmPorous-17	0.07	<0.26	0.36	<0.46	0.11	6.54	0.93	0.56	0.24	0.11	0.07	0.34	2.25	1.43	1.71	1.80	0.36
MB74HmPorous-18	<0.039	<0.28	<0.26	<0.46	0.20	0.97	0.09	0.09	0.45	0.13	0.21	<0.25	0.85	0.91	0.08	0.09	0.05
MB74HmPorous-19	0.21	1.40	<0.26	1.56	0.27	1.90	0.40	0.09	0.36	0.10	0.44	<0.22	1.60	0.51	0.18	0.36	0.10

Analysis no.	Nd	Sm	Eu	Gd	Tb	Dy	Ho	Er	Tm	Yb	Lu	W	Pb208	Th	U
MB73HmPlaty-16	<0.033	<0.00	<0.00	0.01	<0.00	<0.00	<0.0037	0.00	<0.00	<0.00	<0.00	0.50	0.12	0.01	0.01
MB73HmPlaty-17	0.01	<0.00	<0.0127	0.01	0.00	<0.00	<0.00	<0.00	0.00	<0.0239	0.00	0.31	<0.025	<0.00	0.01
MB73HmPlaty-18	0.01	<0.0249	0.00	0.06	<0.0047	<0.00	<0.00	<0.0103	<0.00	<0.00	<0.00	0.48	<0.031	0.01	0.01
MB73HmPlaty-19	0.01	<0.0253	<0.0065	<0.00	<0.00	<0.00	<0.0035	<0.00	<0.00	<0.015	<0.0033	6.70	0.62	0.00	0.50
MB73HmPlaty-2	<0.00	<0.0284	<0.00	0.04	<0.00	<0.00	<0.00	<0.0117	0.00	<0.0169	0.00	0.22	0.01	<0.00	0.03
MB73HmPlaty-20	<0.00	<0.00	<0.00	<0.028	<0.00	<0.00	<0.00	0.01	<0.00	<0.0168	<0.00	1.04	0.03	0.01	0.04
MB73HmPlaty-3	<0.00	<0.00	0.01	<0.061	0.00	0.02	<0.00	<0.0113	<0.0035	<0.00	<0.00	0.53	0.04	<0.00	0.01
MB73HmPlaty-4	<0.00	<0.00	0.01	0.01	<0.0045	<0.0133	<0.00	<0.00	0.00	<0.00	<0.00	0.36	<0.03	<0.00	0.00
MB73HmPlaty-5	<0.00	<0.0258	<0.00	<0.036	<0.0034	0.01	<0.00	<0.00	0.00	0.01	<0.0034	0.31	0.03	<0.00	0.01
MB73HmPlaty-6	0.01	<0.0274	0.00	<0.00	0.00	0.01	<0.0065	<0.00	<0.0035	<0.0163	<0.0036	0.16	<0.042	<0.00	0.00
MB73HmPlaty-7	<0.0226	<0.00	<0.0067	<0.026	<0.0035	<0.00	0.00	0.00	0.00	0.01	<0.0034	0.27	<0.023	<0.00	0.00
MB73HmPlaty-8	0.05	0.03	<0.0075	<0.041	0.00	0.01	<0.00	0.01	<0.00	0.02	0.01	2.37	1.72	0.01	0.39
MB73HmPlaty-9	0.01	<0.00	<0.00	<0.00	<0.0037	<0.00	<0.00	<0.00	<0.00	0.02	<0.00	0.14	0.01	0.00	0.00
MB73HmPorous-1	0.04	<0.025	0.01	<0.025	0.01	0.03	0.00	0.01	0.00	0.02	<0.00	4.74	2.28	0.01	0.72
MB73HmPorous-10	0.02	<0.00	<0.0063	<0.024	0.00	0.01	<0.00	<0.00	<0.00	<0.0145	0.00	0.15	0.88	<0.00	0.15
MB73HmPorous-11	<0.0223	<0.0258	<0.0067	<0.044	<0.0034	0.01	<0.00	<0.00	<0.00	<0.00	<0.0034	0.06	2.02	0.00	0.08
MB73HmPorous-12	0.01	<0.00	<0.0099	<0.027	<0.00	<0.015	<0.0037	0.00	<0.0077	<0.0162	<0.0051	2.95	5.28	0.01	0.29
MB73HmPorous-13	0.07	0.05	0.02	<0.043	<0.0047	0.03	0.01	<0.0104	0.01	0.04	0.00	2.26	3.21	0.01	0.51
MB73HmPorous-14	0.05	0.01	0.01	<0.048	0.00	0.04	<0.00	0.02	0.00	0.01	0.00	1.80	3.81	<0.0111	0.47
MB73HmPorous-15	0.19	0.06	0.04	<0.035	0.01	0.07	0.02	0.02	0.01	0.06	<0.0047	1.56	7.93	<0.0057	1.21
MB73HmPorous-16	0.19	0.05	0.05	0.07	0.00	0.07	0.01	0.03	0.01	0.04	0.01	1.79	6.47	0.00	1.57
MB73HmPorous-17	0.03	0.02	0.01	<0.029	<0.0038	0.01	<0.00	0.01	0.00	0.01	0.00	11.45	1.68	0.02	1.17
MB73HmPorous-18	0.16	<0.028	0.02	0.08	0.01	0.04	0.01	0.03	0.01	0.02	0.00	6.68	2.81	0.01	1.73
MB73HmPorous-19	0.04	<0.029	0.01	0.04	<0.0039	0.03	0.01	0.02	0.00	0.03	0.00	3.21	4.38	0.00	0.58
MB73HmPorous-2	0.12	<0.037	0.01	0.06	0.01	0.02	0.01	0.02	0.00	0.02	0.01	0.98	3.55	0.00	0.68
MB73HmPorous-20	0.01	0.01	<0.00	<0.00	0.00	0.01	<0.00	<0.00	0.00	<0.00	<0.0035	0.44	2.63	<0.00	0.09
MB73HmPorous-3	0.02	0.01	0.01	<0.037	<0.00	<0.00	0.00	<0.0108	<0.0047	<0.022	<0.00	0.50	1.12	<0.00	0.99
MB73HmPorous-4	0.04	0.01	0.01	<0.027	<0.0037	0.02	0.01	0.01	<0.00	0.02	0.00	0.97	3.80	0.00	0.32
MB73HmPorous-5	0.08	<0.00	<0.0159	<0.027	0.00	0.02	0.01	0.01	<0.0035	<0.00	<0.00	1.91	2.14	<0.0063	0.45
MB73HmPorous-6	0.01	<0.00	0.01	<0.00	0.00	<0.021	0.00	<0.00	<0.00	<0.00	0.00	1.84	0.44	0.00	0.14
MB73HmPorous-7	0.03	0.01	0.01	<0.024	<0.0045	<0.00	<0.0033	<0.0099	<0.00	0.01	<0.0032	0.34	2.20	0.01	0.13
MB73HmPorous-8	0.02	<0.00	0.02	0.02	0.00	0.01	0.00	0.01	<0.0045	<0.0213	0.01	1.48	4.77	0.01	0.51
MB73HmPorous-9	0.02	0.01	<0.00	<0.046	<0.005	0.01	<0.0052	0.00	<0.00	<0.00	<0.00	0.15	1.22	0.00	0.11
MB74HmPorous-10	0.04	<0.031	0.02	<0.053	<0.0058	0.04	0.00	0.01	<0.00	<0.00	0.00	1.61	0.19	<0.00	0.06
MB74HmPorous-11	0.86	0.63	1.34	3.21	0.73	7.93	2.29	9.40	1.38	11.06	1.90	1.07	0.32	0.03	0.32
MB74HmPorous-12	0.36	0.15	0.05	0.10	0.01	0.05	0.01	0.03	<0.0085	0.03	<0.0062	1.56	0.73	0.01	0.39
MB74HmPorous-13	0.33	0.04	0.01	<0.034	0.00	<0.019	0.00	0.01	<0.00	0.01	0.00	1.91	0.24	0.00	0.15
MB74HmPorous-14	0.10	<0.00	0.01	<0.00	0.01	0.01	<0.00	0.00	0.00	<0.00	<0.0039	1.26	<0.038	<0.00	0.03
MB74HmPorous-15	0.25	0.17	0.16	0.24	0.08	0.52	0.13	0.54	0.08	0.47	0.08	1.23	0.42	<0.00	0.20
MB74HmPorous-16	0.62	0.20	0.04	0.07	0.02	0.03	0.01	0.03	0.01	0.02	0.00	0.45	0.26	0.01	0.28
MB74HmPorous-17	0.94	0.24	0.07	0.18	0.02	0.09	0.02	0.06	0.01	0.04	0.02	0.81	1.03	0.01	0.29
MB74HmPorous-18	0.15	0.04	0.01	0.04	0.01	0.03	0.00	0.02	0.00	<0.0179	<0.004	0.74	0.23	<0.00	0.04
MB74HmPorous-19	0.32	0.05	0.03	0.07	0.00	0.06	0.01	0.04	0.01	0.01	0.01	2.84	0.93	0.02	0.26

Position	Deposit	Lithology	Sample no.	Analysis no.	Texture	Mg	Al	Si	P	Ca	Sc	Ti	V	Cr	Mn
North	Monarch	BIF	MB74	MB74HmPorous-2	porous martite	56.19	310.22	222.99	54.90	<175.74	<0.213	5.94	65.83	<2.24	9.46
North	Monarch	BIF	MB74	MB74HmPorous-20	porous martite	43.75	531.10	416.27	30.35	<105.55	0.29	10.09	11.93	<1.57	7.47
North	Monarch	BIF	MB74	MB74HmPorous-3	porous martite	11.82	324.15	243.80	24.34	144.61	<0.196	7.14	130.41	<1.69	3.58
North	Monarch	BIF	MB74	MB74HmPorous-4	porous martite	<0.35	108.08	267.36	21.05	<135.06	<0.183	10.72	3.39	<1.41	1.07
North	Monarch	BIF	MB74	MB74HmPorous-5	porous martite	32.72	364.90	948.63	300.60	197.29	<0.184	6.34	7.80	<1.6	20.28
North	Monarch	BIF	MB74	MB74HmPorous-6	porous martite	24.37	378.90	13697.46	30.45	<156.54	0.45	2.75	5.05	<1.55	3.09
North	Monarch	BIF	MB74	MB74HmPorous-7	porous martite	22.75	251.67	16653.01	15.87	<166.63	<0.22	6.45	5.28	<2.06	2.52
North	Monarch	BIF	MB74	MB74HmPorous-8	porous martite	50.36	283.01	5687.93	81.91	<149.25	0.31	17.35	7.03	<1.72	17.74
North	Monarch	BIF	MB74	MB74HmPorous-9	porous martite	43.97	399.60	867.69	68.06	196.40	0.27	23.73	5.96	<1.46	26.76
North	Monarch	BIF	MB77a	MB77aHmPlaty-1	platy hematite	883.76	251.98	2936.51	<11.76	2086.90	0.33	<0.82	32.46	2.54	248.07
North	Monarch	BIF	MB77a	MB77aHmPlaty-10	platy hematite	21.81	79.70	<135.04	<9.83	<110.3	<0.155	<1.05	1.59	<1.5	19.54
North	Monarch	BIF	MB77a	MB77aHmPlaty-11	platy hematite	1.36	27.51	8056.68	26.34	114.69	<0.192	1.63	0.12	<1.48	1.66
North	Monarch	BIF	MB77a	MB77aHmPlaty-12	platy hematite	15.32	76.91	<126.68	<9.76	124.03	<0.159	<0.92	0.89	1.39	11.02
North	Monarch	BIF	MB77a	MB77aHmPlaty-13	platy hematite	36.85	462.11	2246.64	93.61	207.19	0.89	<1.18	44.27	<1.8	180.04
North	Monarch	BIF	MB77a	MB77aHmPlaty-14	platy hematite	1.60	76.67	<137.36	20.47	<94.4	0.26	17.63	2.94	<1.29	1.73
North	Monarch	BIF	MB77a	MB77aHmPlaty-15	platy hematite	79.15	102.28	<132.49	<9.94	126.42	<0.158	2.08	2.44	<1.39	25.64
North	Monarch	BIF	MB77a	MB77aHmPlaty-16	platy hematite	98.14	57.12	1890.56	22.45	255.80	<0.195	<0.95	1.92	<1.64	29.35
North	Monarch	BIF	MB77a	MB77aHmPlaty-17	platy hematite	<0.24	10.33	273.64	26.14	<105.68	0.21	<1.08	<0.059	<1.65	<0.35
North	Monarch	BIF	MB77a	MB77aHmPlaty-18	platy hematite	0.93	24.99	3610.09	<10.7	163.96	<0.156	<0.93	6.04	<1.44	16.28
North	Monarch	BIF	MB77a	MB77aHmPlaty-19	platy hematite	591.27	39.62	644.92	56.34	2131.34	<0.167	24.47	3.46	<1.54	177.82
North	Monarch	BIF	MB77a	MB77aHmPlaty-2	platy hematite	103.35	67.22	1595.73	<10.22	<126.82	0.25	<0.93	0.73	1.77	15.66
North	Monarch	BIF	MB77a	MB77aHmPlaty-20	platy hematite	513.25	30.84	<127.2	<9.57	2313.39	<0.156	<0.81	1.03	<1.54	123.32
North	Monarch	BIF	MB77a	MB77aHmPlaty-4	platy hematite	5.17	64.56	795.85	<12.63	<154.31	<0.179	<1.01	1.60	<1.65	10.69
North	Monarch	BIF	MB77a	MB77aHmPlaty-5	platy hematite	143.98	30.21	410.59	48.27	438.03	0.29	0.94	0.53	<1.35	27.31
North	Monarch	BIF	MB77a	MB77aHmPlaty-6	platy hematite	11.73	71.84	583.96	<9.91	<110.63	<0.174	<0.9	3.95	1.72	14.71
North	Monarch	BIF	MB77a	MB77aHmPlaty-7	platy hematite	43.67	85.21	6216.80	<10.17	200.47	<0.187	0.84	5.36	<1.44	19.60
North	Monarch	BIF	MB77a	MB77aHmPlaty-8	platy hematite	27.22	57.03	<122.65	11.18	<109.8	<0.144	<0.89	1.14	<1.34	12.66
North	Monarch	BIF	MB77a	MB77aHmPlaty-9	platy hematite	8.37	47.76	256.19	21.16	<121.64	<0.164	1.69	2.13	<1.34	1.14
North	Monarch	BIF	MB77a	MB77aHmPorous-1	porous martite	7.01	84.12	<151.52	<11.96	<130.15	<0.191	<0.77	1.54	<1.54	16.46
North	Monarch	BIF	MB77a	MB77aHmPorous-10	porous martite	12.38	266.67	16108.38	93.00	<115.35	<0.175	3.54	2.80	<1.42	87.71
North	Monarch	BIF	MB77a	MB77aHmPorous-11	porous martite	19.09	194.86	5190.55	12.62	<106.49	0.23	<1.09	1.99	2.10	22.33
North	Monarch	BIF	MB77a	MB77aHmPorous-12	porous martite	2.98	83.29	200.71	14.07	201.23	<0.147	1.14	1.87	1.99	9.28
North	Monarch	BIF	MB77a	MB77aHmPorous-13	porous martite	6.44	80.28	399.87	12.38	<88.01	<0.162	1.09	1.16	<1.54	12.47
North	Monarch	BIF	MB77a	MB77aHmPorous-14	porous martite	0.71	27.52	306.57	27.53	<86.92	<0.171	<0.97	0.04	<1.44	5.86
North	Monarch	BIF	MB77a	MB77aHmPorous-15	porous martite	19.92	84.87	179.32	119.39	<102.01	<0.185	<0.86	0.30	<1.6	21.28
North	Monarch	BIF	MB77a	MB77aHmPorous-16	porous martite	3.81	45.72	<136.67	31.82	<111.1	<0.175	2.73	0.56	<1.44	7.26
North	Monarch	BIF	MB77a	MB77aHmPorous-17	porous martite	35.66	81.99	<127.71	22.61	195.03	<0.153	2.58	1.91	<1.47	9.32
North	Monarch	BIF	MB77a	MB77aHmPorous-18	porous martite	2.10	73.07	5075.82	<9.41	<82.33	<0.188	14.03	3.46	<1.4	8.35
North	Monarch	BIF	MB77a	MB77aHmPorous-2	porous martite	43.63	143.21	437.16	22.22	<140.73	<0.167	2.82	2.70	<1.39	34.50
North	Monarch	BIF	MB77a	MB77aHmPorous-20	porous martite	16.20	80.95	6921.80	<10.43	<97.38	0.32	<1.08	1.31	2.23	29.61
North	Monarch	BIF	MB77a	MB77aHmPorous-3	porous martite	6.27	77.14	147.28	11.45	<124.54	<0.193	<0.95	1.35	<1.29	17.34
North	Monarch	BIF	MB77a	MB77aHmPorous-4	porous martite	1.80	93.39	426.52	<11.03	<125.98	<0.188	<1.31	2.47	<1.55	7.39
North	Monarch	BIF	MB77a	MB77aHmPorous-5	porous martite	13.11	49.23	212.78	16.07	170.62	0.22	<0.75	0.94	<1.67	9.70

Analysis no.	Co	Ni	Cu	Zn	Ga	As	Sr	Y	Zr	Nb	Mo	Sn	Sb	Ba	La	Ce	Pr
MB74HmPorous-2	0.25	1.07	1.94	1.67	0.09	3.26	0.77	0.32	0.20	0.07	0.43	<0.3	2.12	0.73	0.30	0.34	0.12
MB74HmPorous-20	<0.06	1.31	0.63	<0.39	0.38	5.79	0.55	0.27	0.64	0.15	0.22	<0.25	3.30	0.43	0.35	0.39	0.18
MB74HmPorous-3	0.16	0.37	0.69	0.78	0.05	1.98	0.19	0.05	0.25	0.07	0.51	<0.29	0.87	0.10	0.03	0.07	0.03
MB74HmPorous-4	<0.026	<0.18	<0.29	<0.31	0.16	<0.37	0.01	0.01	0.02	0.07	0.23	0.23	<0.078	0.11	0.01	0.02	0.00
MB74HmPorous-5	0.11	0.54	4.56	1.12	<0.079	3.43	0.79	1.95	0.26	0.08	0.18	0.37	1.70	2.96	1.31	2.00	0.28
MB74HmPorous-6	<0.047	0.66	<0.31	0.49	0.22	1.31	4.95	0.27	0.34	0.14	1.00	<0.26	0.54	11.21	17.64	15.15	2.05
MB74HmPorous-7	0.04	0.44	<0.4	<0.48	0.14	1.08	0.19	0.08	0.21	0.11	0.33	0.36	0.51	0.50	0.05	0.12	0.04
MB74HmPorous-8	<0.044	<0.31	0.77	<0.55	0.14	3.53	0.91	0.68	0.31	0.17	0.13	<0.28	2.32	1.26	1.03	1.29	0.25
MB74HmPorous-9	<0.054	<0.31	0.37	0.88	0.17	9.58	0.86	0.88	0.41	0.26	<0.083	0.38	2.78	3.78	0.94	1.36	0.18
MB77aHmPlaty-1	0.59	0.77	1.09	11.55	0.24	10.95	1.52	0.61	0.03	0.01	0.25	<0.24	3.75	0.57	0.19	0.71	0.08
MB77aHmPlaty-10	1.51	1.03	10.31	6.30	0.16	17.37	1.70	0.03	<0.00	<0.00	0.02	<0.22	3.17	0.69	0.02	0.05	<0.00
MB77aHmPlaty-11	0.04	0.83	<0.27	0.75	0.08	1.18	0.02	0.03	<0.00	<0.00	<0.00	<0.22	0.25	<0.099	0.01	0.04	<0.00
MB77aHmPlaty-12	0.51	0.69	1.00	1.62	0.13	9.16	0.51	0.02	0.04	0.01	0.04	<0.207	2.14	0.33	0.03	0.06	0.01
MB77aHmPlaty-13	1.69	2.12	1.67	31.95	0.13	14.09	1.42	1.14	0.08	0.03	0.39	<0.26	4.91	2.06	0.56	1.29	0.15
MB77aHmPlaty-14	0.07	<0.21	<0.29	<0.5	<0.04	2.46	0.04	0.05	0.82	0.37	0.21	<0.23	0.81	0.11	0.03	0.03	0.00
MB77aHmPlaty-15	<0.043	1.18	<0.24	3.16	0.24	4.29	0.07	0.06	<0.025	<0.00	0.24	<0.204	0.98	0.19	0.06	0.09	0.01
MB77aHmPlaty-16	0.08	0.32	0.31	3.08	0.25	3.85	0.12	0.05	<0.026	0.01	0.07	<0.26	1.08	0.15	0.04	0.07	0.01
MB77aHmPlaty-17	<0.027	0.48	0.30	<0.32	0.11	<0.41	<0.00	0.00	<0.026	<0.00	<0.047	<0.24	0.09	<0.00	0.00	0.00	<0.00
MB77aHmPlaty-18	0.07	0.26	<0.25	1.15	0.30	3.92	0.16	0.06	0.04	0.00	<0.057	<0.22	1.36	0.73	0.04	0.05	0.00
MB77aHmPlaty-19	0.43	1.10	0.44	23.47	0.31	9.95	0.35	0.44	0.06	<0.00	0.49	<0.24	2.71	0.34	0.20	0.21	0.03
MB77aHmPlaty-2	0.04	0.79	<0.22	<0.36	0.26	10.47	0.36	0.03	0.02	0.01	<0.057	<0.205	2.41	0.20	0.05	0.04	<0.00
MB77aHmPlaty-20	0.04	0.29	<0.3	0.88	0.08	1.38	0.13	0.06	0.02	<0.0091	0.04	<0.211	0.24	<0.00	0.01	0.02	<0.0039
MB77aHmPlaty-4	0.50	1.01	<0.31	3.27	0.28	14.53	0.49	0.04	0.02	<0.0115	<0.052	<0.26	3.22	0.19	0.06	0.05	0.01
MB77aHmPlaty-5	0.03	0.41	<0.29	3.09	0.17	2.96	0.16	0.08	<0.024	0.00	0.06	<0.218	0.60	0.09	0.03	0.06	0.01
MB77aHmPlaty-6	0.31	0.98	0.25	2.10	0.26	17.21	0.29	0.07	<0.046	0.02	0.16	<0.2	3.33	<0.00	0.06	0.11	0.02
MB77aHmPlaty-7	0.07	1.07	0.59	1.02	0.27	11.77	0.24	0.09	<0.00	<0.00	0.07	<0.22	2.60	0.10	0.04	0.11	0.02
MB77aHmPlaty-8	0.66	<0.157	0.72	0.59	<0.051	6.12	0.23	0.03	<0.022	<0.00	<0.00	<0.21	1.41	0.22	0.01	0.02	<0.00
MB77aHmPlaty-9	0.04	0.72	0.28	<0.42	0.21	1.98	0.12	0.04	<0.00	<0.0097	0.12	<0.207	0.49	<0.00	0.03	0.05	0.00
MB77aHmPorous-1	0.63	1.25	0.44	3.79	0.25	19.54	0.69	0.05	0.03	<0.00	0.10	<0.27	4.50	0.18	0.03	0.06	<0.0063
MB77aHmPorous-10	1.52	4.23	<0.31	35.19	0.33	18.83	0.65	0.94	0.16	0.03	1.91	<0.24	4.83	1.15	0.26	0.37	0.04
MB77aHmPorous-11	0.80	1.80	0.99	5.23	0.33	29.24	2.16	0.04	0.07	0.01	0.57	0.29	5.53	1.10	0.06	0.08	0.02
MB77aHmPorous-12	0.59	1.19	1.65	2.99	0.30	14.27	0.31	0.16	<0.00	0.02	0.15	0.27	2.15	0.17	0.19	0.24	0.03
MB77aHmPorous-13	0.57	1.12	<0.22	1.67	0.27	29.11	0.55	<0.0099	<0.00	<0.00	<0.06	<0.23	6.00	0.25	0.04	0.02	<0.00
MB77aHmPorous-14	0.05	0.92	<0.27	0.60	0.15	23.81	0.02	0.01	<0.0221	<0.00	<0.056	<0.205	7.22	0.18	0.03	0.02	<0.00
MB77aHmPorous-15	0.19	<0.25	0.30	<0.45	0.07	58.78	0.03	0.01	0.01	<0.00	<0.044	<0.25	17.15	0.25	0.05	0.05	<0.0094
MB77aHmPorous-16	0.06	1.46	0.37	0.97	0.24	17.97	0.44	<0.00	0.09	0.02	<0.043	<0.25	4.98	0.09	0.02	0.03	0.00
MB77aHmPorous-17	0.40	<0.31	<0.26	2.79	0.36	24.42	2.06	0.02	0.05	0.02	0.16	<0.23	4.78	0.64	0.03	0.07	0.00
MB77aHmPorous-18	0.14	2.16	<0.27	1.88	0.21	20.98	0.31	0.03	0.36	0.14	0.39	<0.23	4.02	0.29	0.04	0.08	0.01
MB77aHmPorous-2	0.30	2.18	<0.24	4.13	0.31	16.13	0.32	0.21	0.12	0.01	0.68	<0.22	5.03	0.46	0.10	0.15	0.02
MB77aHmPorous-20	2.32	0.55	0.60	4.06	0.16	20.52	1.01	0.07	<0.0232	<0.00	<0.042	<0.25	5.56	<0.00	0.04	0.07	0.00
MB77aHmPorous-3	0.63	1.59	0.33	4.16	0.18	24.57	1.35	0.05	<0.00	0.13	<0.043	<0.23	4.43	0.70	0.03	0.09	<0.004
MB77aHmPorous-4	0.24	0.94	<0.25	1.56	0.40	24.14	0.16	0.10	<0.043	0.03	0.26	<0.25	6.80	0.26	0.06	0.12	0.01
MB77aHmPorous-5	0.27	0.67	<0.28	1.60	0.21	14.22	0.33	0.03	0.03	<0.00	<0.043	<0.23	3.72	0.18	0.05	0.06	0.01

Analysis no.	Nd	Sm	Eu	Gd	Tb	Dy	Ho	Er	Tm	Yb	Lu	W	Pb208	Th	U
MB74HmPorous-2	0.58	0.11	0.05	0.06	0.01	0.02	<0.0066	0.03	0.00	0.05	0.00	5.37	0.64	0.01	1.39
MB74HmPorous-20	1.09	0.24	0.09	0.10	0.02	0.08	0.02	0.04	0.01	0.05	0.00	1.12	0.45	0.02	0.54
MB74HmPorous-3	0.07	0.03	0.01	0.01	<0.00	<0.017	0.00	0.02	0.01	<0.018	<0.004	6.26	0.21	<0.00	0.54
MB74HmPorous-4	<0.00	<0.00	<0.0073	<0.04	<0.0038	<0.0156	<0.00	<0.00	<0.00	<0.0168	<0.0037	0.67	<0.056	<0.00	0.01
MB74HmPorous-5	1.25	0.51	0.23	0.28	0.03	0.28	0.05	0.15	0.02	0.19	0.03	0.80	1.08	0.02	0.31
MB74HmPorous-6	5.68	0.53	0.36	0.51	0.06	0.32	0.02	0.08	<0.0038	0.03	<0.00	1.40	4.42	0.15	0.02
MB74HmPorous-7	0.15	0.16	0.01	<0.05	<0.0048	0.02	0.00	0.01	0.01	<0.00	<0.0047	0.93	<0.045	<0.00	0.05
MB74HmPorous-8	1.09	0.24	0.10	0.24	0.03	0.12	0.04	0.13	0.01	0.04	0.01	1.00	1.06	0.01	0.30
MB74HmPorous-9	0.80	0.14	0.09	0.20	0.03	0.22	0.03	0.10	0.01	0.05	0.01	1.07	1.31	0.01	0.32
MB77aHmPlaty-1	0.31	0.08	0.03	0.08	0.01	0.07	0.02	0.05	0.00	0.02	0.01	1.93	3.32	0.01	0.33
MB77aHmPlaty-10	<0.023	<0.00	<0.0068	<0.00	<0.005	<0.0145	<0.00	<0.00	<0.00	0.01	<0.00	0.27	2.74	<0.00	<0.0033
MB77aHmPlaty-11	0.03	<0.00	<0.0067	<0.0258	0.00	<0.0143	<0.0035	<0.00	<0.00	0.01	<0.00	0.20	0.51	0.00	0.01
MB77aHmPlaty-12	0.46	<0.00	<0.0064	0.02	0.00	0.01	<0.0034	<0.0101	<0.00	<0.015	<0.00324	1.45	1.24	0.00	0.01
MB77aHmPlaty-13	0.57	0.21	0.05	0.15	0.03	0.19	0.03	0.06	0.01	0.08	<0.0059	1.41	5.74	0.00	0.51
MB77aHmPlaty-14	<0.00	0.01	0.01	0.02	0.00	<0.00	0.00	0.00	<0.00	<0.00	<0.0049	12.59	0.38	0.03	0.06
MB77aHmPlaty-15	<0.023	<0.00	0.01	<0.00	<0.0036	<0.0149	<0.0052	0.01	<0.00	<0.00	<0.00	1.47	1.07	<0.00	0.02
MB77aHmPlaty-16	0.05	0.02	0.01	0.02	0.00	0.01	<0.00	<0.0118	0.00	<0.00	<0.00	0.46	0.34	<0.00	0.05
MB77aHmPlaty-17	<0.00	<0.00	<0.00	<0.00	<0.00	0.01	<0.00	<0.0119	<0.00	0.01	<0.0038	0.04	0.06	<0.00	<0.00
MB77aHmPlaty-18	0.01	0.01	<0.00	0.01	<0.0033	0.01	0.00	0.00	<0.00	0.01	<0.0033	0.43	0.52	<0.00	0.07
MB77aHmPlaty-19	0.10	0.02	0.01	0.03	0.00	0.01	<0.0039	0.02	0.00	0.03	0.00	0.90	1.50	0.00	0.02
MB77aHmPlaty-2	0.01	<0.00	<0.0064	0.02	0.00	<0.00	0.00	0.01	<0.00	0.01	<0.00	1.20	1.15	0.02	0.02
MB77aHmPlaty-20	<0.00	<0.026	<0.0093	<0.025	<0.00	<0.0141	0.00	0.01	<0.00	0.01	<0.0034	2.44	0.45	<0.00	0.00
MB77aHmPlaty-4	0.05	<0.0322	<0.00	0.02	<0.0043	0.01	<0.0044	0.02	<0.0041	<0.0191	<0.0042	1.21	1.89	<0.0073	<0.004
MB77aHmPlaty-5	<0.023	0.01	<0.0121	<0.038	<0.00	0.01	0.00	0.01	0.00	0.02	<0.0035	0.47	0.77	0.01	0.01
MB77aHmPlaty-6	0.05	0.02	0.00	0.01	0.00	0.01	0.00	<0.00	0.00	0.01	0.00	0.96	1.01	<0.00	0.03
MB77aHmPlaty-7	<0.024	<0.00	<0.007	<0.027	<0.0036	<0.00	<0.0037	<0.00	0.00	0.01	<0.0036	1.02	1.27	<0.00	0.03
MB77aHmPlaty-8	0.01	<0.00	<0.0061	0.04	<0.0032	0.01	<0.00	<0.00	<0.00	<0.00	<0.00	0.49	0.55	<0.00	0.01
MB77aHmPlaty-9	0.02	<0.027	<0.0099	<0.00	0.01	0.01	0.00	0.00	0.00	<0.0162	<0.0036	1.60	0.26	0.00	0.01
MB77aHmPorous-1	0.02	0.01	0.01	<0.029	0.00	0.01	<0.004	0.00	0.00	<0.00	<0.00	0.67	1.98	<0.00	0.01
MB77aHmPorous-10	0.21	0.02	0.02	0.12	0.01	0.06	0.01	0.04	0.00	0.05	0.01	4.01	3.93	<0.00	0.06
MB77aHmPorous-11	0.02	<0.00	<0.007	0.01	0.00	0.01	<0.0037	0.00	<0.00	<0.00	<0.00	1.81	2.74	0.00	0.04
MB77aHmPorous-12	0.14	0.05	0.01	<0.033	<0.00313	0.03	<0.0032	0.02	<0.00	0.02	0.00	1.10	1.89	0.00	0.01
MB77aHmPorous-13	<0.00	<0.00	<0.0164	<0.0257	0.00	<0.00	<0.00	<0.00	<0.00	<0.00	<0.00	0.02	1.25	<0.00	0.00
MB77aHmPorous-14	<0.021	<0.00	0.00	<0.034	<0.0056	<0.00	<0.00	<0.00	<0.00309	<0.00	0.00	<0.00	<0.064	<0.00	0.04
MB77aHmPorous-15	0.02	<0.00	0.00	<0.038	<0.0036	<0.00	<0.0074	0.00	<0.00	<0.0162	<0.0051	0.16	0.31	<0.00	0.05
MB77aHmPorous-16	<0.00	<0.0266	<0.00	<0.0263	0.00	<0.0146	<0.00	<0.00	<0.0034	<0.00	<0.00	1.27	0.34	<0.00	0.03
MB77aHmPorous-17	0.03	<0.035	0.01	<0.035	<0.00	0.02	<0.00	<0.0103	<0.00	<0.00	<0.0046	6.05	1.53	0.00	0.06
MB77aHmPorous-18	0.01	<0.00	0.01	<0.027	<0.00	0.02	0.00	<0.00	<0.0035	0.01	<0.0051	5.66	1.00	0.00	0.07
MB77aHmPorous-2	0.04	<0.00	0.01	0.03	<0.0061	<0.0145	0.01	<0.0108	0.00	0.01	0.00	6.82	1.24	0.01	0.07
MB77aHmPorous-20	0.04	<0.00	<0.0066	0.02	0.00	0.02	<0.00	0.00	<0.00	<0.00	<0.0034	0.56	1.03	<0.00	0.02
MB77aHmPorous-3	0.03	0.02	0.01	0.02	<0.0035	<0.0144	<0.00	0.02	<0.00	<0.00	<0.0034	0.65	4.10	<0.00	0.01
MB77aHmPorous-4	0.06	0.02	0.01	<0.00	0.00	0.03	0.00	<0.0112	0.00	<0.0162	<0.0036	4.60	1.15	0.01	0.06
MB77aHmPorous-5	0.03	<0.037	<0.0068	<0.037	<0.0035	<0.0252	<0.0051	0.01	<0.00	0.01	<0.00	1.44	0.99	<0.006	0.02

Position	Deposit	Lithology	Sample no.	Analysis no.	Texture	Mg	Al	Si	P	Ca	Sc	Ti	V	Cr	Mn
North	Monarch	BIF	MB77a	MB77aHmPorous-6	porous martite	7.65	74.51	909.90	26.66	<126.94	<0.166	<0.58	0.84	<1.38	23.45
North	Monarch	BIF	MB77a	MB77aHmPorous-7	porous martite	2.52	57.81	386.65	20.32	<97.3	0.36	8.62	2.43	<1.44	9.51
North	Monarch	BIF	MB77a	MB77aHmPorous-8	porous martite	10.87	119.52	456.60	18.05	241.92	<0.181	4.76	1.86	<1.42	31.52
North	Monarch	BIF	MB77a	MB77aHmPorous-9	porous martite	3.83	47.09	<128.58	13.33	<107.91	<0.156	<0.85	0.72	<1.31	12.21
North	Monarch	BIF	MB78	MB78HmPorous-1	porous martite	6.33	773.35	<137	<11.2	<124.59	0.27	152.94	14.30	22.20	10.87
North	Monarch	BIF	MB78	MB78HmPorous-10	porous martite	145.54	808.62	<126.61	22.32	210.43	<0.164	98.96	9.00	<1.51	155.86
North	Monarch	BIF	MB78	MB78HmPorous-11	porous martite	226.87	849.77	912.86	<10.74	259.52	<0.158	95.49	12.19	3.13	312.55
North	Monarch	BIF	MB78	MB78HmPorous-12	porous martite	28.15	977.62	1131.61	46.92	<106.3	0.22	108.65	13.53	2.30	76.39
North	Monarch	BIF	MB78	MB78HmPorous-13	porous martite	239.75	1074.52	419.41	10.27	<95.79	<0.151	145.28	14.79	3.93	43.53
North	Monarch	BIF	MB78	MB78HmPorous-14	porous martite	61.58	850.49	<123.19	15.02	<91.87	<0.167	130.29	16.15	3.07	33.62
North	Monarch	BIF	MB78	MB78HmPorous-15	porous martite	59.53	1092.72	<132.94	13.39	115.51	<0.168	154.09	16.09	3.34	103.82
North	Monarch	BIF	MB78	MB78HmPorous-16	porous martite	72.00	1040.03	292.49	25.22	129.07	0.16	151.05	17.27	1.68	50.11
North	Monarch	BIF	MB78	MB78HmPorous-17	porous martite	12.71	845.86	324.53	29.07	<80.08	0.16	126.92	12.06	<1.39	26.02
North	Monarch	BIF	MB78	MB78HmPorous-18	porous martite	22.17	940.07	639.55	28.69	<105.81	0.19	110.34	13.61	1.50	53.58
North	Monarch	BIF	MB78	MB78HmPorous-19	porous martite	16.49	811.40	201.73	12.52	<95.48	<0.163	121.27	12.76	5.16	36.92
North	Monarch	BIF	MB78	MB78HmPorous-2	porous martite	29.07	988.35	688.43	57.36	159.39	0.21	108.81	14.65	17.56	77.29
North	Monarch	BIF	MB78	MB78HmPorous-20	porous martite	40.16	1079.33	320.40	<11.49	171.27	<0.179	122.52	11.77	<1.49	53.79
North	Monarch	BIF	MB78	MB78HmPorous-3	porous martite	30.34	987.64	337.48	13.28	<125.82	<0.175	133.56	19.50	6.17	41.65
North	Monarch	BIF	MB78	MB78HmPorous-4	porous martite	599.53	831.45	348.30	<12.2	506.27	<0.18	148.33	14.45	4.35	467.06
North	Monarch	BIF	MB78	MB78HmPorous-5	porous martite	110.56	1090.02	<129.33	<10.54	<122.86	0.16	132.09	12.22	12.16	51.50
North	Monarch	BIF	MB78	MB78HmPorous-6	porous martite	519.35	1555.11	1800.55	134.82	<92.79	<0.139	139.76	12.99	<1.35	418.13
North	Monarch	BIF	MB78	MB78HmPorous-7	porous martite	185.60	1377.62	690.66	<11.52	<118.49	<0.158	143.05	13.41	<1.4	57.90
North	Monarch	BIF	MB78	MB78HmPorous-8	porous martite	73.24	994.05	528.38	34.42	<109.39	0.28	83.69	14.08	2.16	101.72
North	Monarch	BIF	MB78	MB78HmPorous-9	porous martite	191.79	1099.47	1134.47	20.68	<96.86	1.02	90.57	14.35	1.41	836.58
Middle	Warrior	CHLORATITE	MB7	MB7Mt-1	magnetite	849.05	647.84	<69.62	<6.28	<41.9	0.72	236.50	16.69	14.04	680.44
Middle	Warrior	CHLORATITE	MB7	MB7Mt-10	magnetite	669.61	484.86	414.76	<5.51	<39.56	0.65	231.36	14.68	2.43	722.49
Middle	Warrior	CHLORATITE	MB7	MB7Mt-11	magnetite	3190.89	2177.89	1751.39	22.82	<50.95	0.67	225.06	16.64	<1.08	2260.04
Middle	Warrior	CHLORATITE	MB7	MB7Mt-12	magnetite	4268.23	3399.15	4826.00	8.81	<46.34	0.77	219.45	28.68	<0.68	550.61
Middle	Warrior	CHLORATITE	MB7	MB7Mt-13	magnetite	2238.47	1813.65	1336.01	<4.99	<42.85	0.91	227.96	18.58	0.69	829.01
Middle	Warrior	CHLORATITE	MB7	MB7Mt-14	magnetite	2137.34	1399.27	1027.72	14.51	<61.67	0.97	251.71	18.48	1.92	1136.89
Middle	Warrior	CHLORATITE	MB7	MB7Mt-15	magnetite	1386.19	962.86	484.20	9.07	75.28	0.84	234.25	18.19	1.51	788.81
Middle	Warrior	CHLORATITE	MB7	MB7Mt-16	magnetite	6365.39	2043.99	2221.76	<5.61	73.33	0.66	238.28	18.14	3.31	2159.58
Middle	Warrior	CHLORATITE	MB7	MB7Mt-17	magnetite	3117.97	2178.04	3499.61	<5.32	<39.01	0.82	256.09	22.56	<0.68	486.45
Middle	Warrior	CHLORATITE	MB7	MB7Mt-18	magnetite	2369.74	1767.61	1601.01	12.68	<50.77	0.88	233.41	16.35	4.64	903.08
Middle	Warrior	CHLORATITE	MB7	MB7Mt-19	magnetite	535.49	531.25	126.29	6.72	<49.3	0.85	238.16	14.70	4.47	435.77
Middle	Warrior	CHLORATITE	MB7	MB7Mt-2	magnetite	737.60	506.87	82.76	<6.4	<50.25	0.48	212.00	13.15	3.73	1997.30
Middle	Warrior	CHLORATITE	MB7	MB7Mt-3	magnetite	806.85	538.31	<65.98	10.11	<45.39	0.97	630.75	45.11	<0.57	1364.34
Middle	Warrior	CHLORATITE	MB7	MB7Mt-4	magnetite	539.72	424.67	221.60	<5.97	47.05	0.90	493.08	28.85	<0.71	454.10
Middle	Warrior	CHLORATITE	MB7	MB7Mt-5	magnetite	2584.78	1694.71	2081.77	10.13	<44.49	0.56	177.07	25.85	9.78	126.04
Middle	Warrior	CHLORATITE	MB7	MB7Mt-6	magnetite	950.81	748.89	232.34	<4.89	53.29	0.80	308.90	19.61	<0.68	712.86
Middle	Warrior	CHLORATITE	MB7	MB7Mt-7	magnetite	754.29	550.03	205.34	8.46	<42.76	1.12	114.75	16.54	<0.6	479.84
Middle	Warrior	CHLORATITE	MB7	MB7Mt-8	magnetite	681.85	613.50	133.11	<6.29	<42.68	0.99	244.08	16.60	12.25	599.97
Middle	Warrior	CHLORATITE	MB7	MB7Mt-9	magnetite	489.81	350.94	7102.23	33.93	382.65	1.46	93.07	29.02	<0.65	462.97

Analysis no.	Co	Ni	Cu	Zn	Ga	As	Sr	Y	Zr	Nb	Mo	Sn	Sb	Ba	La	Ce	Pr
MB77aHmPorous-6	0.23	1.09	2.61	0.47	0.23	19.04	1.16	0.59	0.01	<0.00	<0.042	<0.23	15.43	0.83	0.22	0.24	0.02
MB77aHmPorous-7	0.23	1.10	0.33	2.15	0.08	33.78	0.19	0.02	0.69	0.12	0.23	<0.23	6.37	0.18	0.08	0.03	<0.0062
MB77aHmPorous-8	1.48	3.00	1.01	9.16	0.22	26.39	0.97	0.91	0.19	0.08	0.44	<0.25	7.00	0.59	0.37	0.52	0.08
MB77aHmPorous-9	0.14	1.31	9.81	3.40	0.13	18.63	0.85	0.01	<0.0315	0.02	<0.056	<0.2	2.52	0.58	0.03	0.03	0.00
MB78HmPorous-1	<0.036	0.69	<0.22	7.93	0.93	0.91	0.02	0.01	0.03	0.02	0.07	0.48	0.30	0.09	0.00	0.01	0.00
MB78HmPorous-10	0.31	1.78	<0.28	7.45	0.99	8.49	0.58	0.02	<0.0244	0.02	0.19	0.39	1.45	1.29	0.01	0.01	0.00
MB78HmPorous-11	0.32	2.01	<0.31	11.76	0.95	10.23	0.35	0.06	0.02	0.01	0.31	0.59	5.16	1.02	0.04	0.04	0.00
MB78HmPorous-12	0.73	2.51	1.66	30.90	1.02	32.39	1.47	0.43	1.03	0.08	1.66	0.54	11.03	8.29	0.20	0.28	0.03
MB78HmPorous-13	0.06	2.64	<0.27	6.42	0.85	30.93	1.30	0.06	<0.00	0.08	0.15	0.46	9.16	1.26	0.07	0.04	0.01
MB78HmPorous-14	0.17	1.32	<0.24	8.56	1.08	21.28	0.55	0.57	17.74	0.11	0.05	0.59	4.84	0.84	0.04	0.05	0.00
MB78HmPorous-15	0.14	2.18	<0.33	3.98	0.80	8.98	0.64	0.01	<0.036	0.04	0.02	0.77	0.83	1.63	0.01	0.02	0.01
MB78HmPorous-16	0.25	2.58	<0.29	6.16	1.02	26.77	0.28	0.04	0.03	0.14	0.32	0.75	4.89	1.74	0.02	0.07	0.00
MB78HmPorous-17	0.89	2.33	0.44	9.60	0.88	8.99	0.23	0.04	0.02	0.01	0.09	0.61	2.58	0.31	0.02	0.04	0.01
MB78HmPorous-18	0.89	1.89	5.02	6.83	1.10	10.51	0.24	0.15	0.07	<0.0086	1.09	0.63	3.30	2.97	0.07	0.11	0.02
MB78HmPorous-19	0.51	2.51	0.39	13.37	1.01	28.38	0.33	0.08	0.02	0.04	0.57	1.09	7.71	1.31	0.06	0.07	<0.0041
MB78HmPorous-2	1.39	4.71	<0.32	18.18	1.04	12.71	0.23	0.21	<0.00	0.02	1.31	0.67	2.18	2.35	0.09	0.13	0.02
MB78HmPorous-20	0.35	2.35	<0.35	6.74	1.02	8.78	0.29	<0.0181	<0.00	<0.00	0.04	0.52	4.13	0.70	0.01	0.01	<0.00
MB78HmPorous-3	0.29	1.56	<0.28	5.04	0.93	23.06	0.47	0.09	<0.00	0.04	0.49	0.29	3.94	2.17	0.05	0.09	0.01
MB78HmPorous-4	0.11	1.27	0.79	7.02	1.03	26.56	0.72	0.19	<0.0289	0.09	0.02	0.44	5.74	1.20	0.17	0.24	0.02
MB78HmPorous-5	0.08	2.23	<0.25	4.12	0.83	16.40	0.45	0.05	<0.0256	0.09	<0.08	0.40	2.58	1.17	0.05	0.05	0.01
MB78HmPorous-6	21.35	11.39	1.51	372.25	1.62	8.34	0.25	0.16	0.06	1.83	0.33	0.80	1.36	2.83	0.02	0.06	0.01
MB78HmPorous-7	0.10	2.96	0.39	10.22	0.86	29.59	0.38	0.04	<0.00	0.21	<0.046	0.68	3.47	0.39	0.03	0.05	0.00
MB78HmPorous-8	1.18	1.78	1.31	32.98	0.97	7.77	0.41	0.06	0.06	0.03	0.51	0.59	1.45	2.07	0.01	0.02	0.01
MB78HmPorous-9	1.02	3.82	2.27	17.48	1.06	15.84	0.27	0.35	0.04	0.15	3.09	0.48	3.01	7.44	0.15	0.23	0.04
MB7Mt-1	0.09	1.08	<0.164	70.08	0.89	<0.162	<0.00	0.02	0.02	0.01	<0.00	1.45	<0.037	<0.00	<0.00	<0.0028	0.00
MB7Mt-10	<0.025	1.17	<0.154	55.56	0.85	1.06	0.02	0.02	<0.014	0.09	<0.0238	1.27	0.05	0.11	0.01	0.01	<0.00
MB7Mt-11	<0.019	1.72	<0.19	126.54	0.83	10.53	0.01	0.73	<0.027	1.07	<0.032	1.99	0.27	<0.00	<0.004	0.03	0.00
MB7Mt-12	0.68	1.14	0.19	124.78	1.79	8.42	0.02	0.55	0.07	0.82	<0.033	1.50	0.18	<0.00	0.01	0.04	0.00
MB7Mt-13	0.02	1.01	<0.153	99.70	0.73	7.94	0.05	0.37	0.01	0.70	25.32	1.51	0.27	<0.00	0.01	0.02	0.00
MB7Mt-14	<0.035	0.57	<0.183	95.34	0.68	5.23	<0.00	0.23	0.05	0.43	0.02	1.62	0.15	0.07	0.02	0.05	0.00
MB7Mt-15	0.19	1.85	21.70	84.22	0.95	4.52	0.32	0.21	0.02	0.17	0.04	1.47	0.08	0.32	0.01	0.03	<0.00
MB7Mt-16	<0.036	0.95	<0.177	87.75	0.93	6.00	0.02	0.28	0.05	0.38	<0.035	1.72	0.06	0.17	0.02	0.05	0.00
MB7Mt-17	0.31	1.75	<0.158	86.98	1.72	6.52	0.03	0.35	0.11	0.54	0.01	1.44	0.11	<0.00	0.03	0.07	0.00
MB7Mt-18	0.76	0.93	<0.196	28.59	0.67	2.72	0.08	0.10	0.64	0.02	0.06	1.41	1.59	<0.07	0.01	0.03	0.01
MB7Mt-19	0.04	1.34	<0.176	45.78	0.80	1.53	0.02	0.03	<0.016	0.01	<0.027	1.47	0.23	0.06	0.00	0.01	<0.00
MB7Mt-2	0.09	0.93	<0.144	55.09	0.78	<0.21	0.02	<0.0061	<0.0145	0.01	<0.025	1.43	0.06	<0.00	<0.00	<0.00	<0.00
MB7Mt-3	0.03	0.99	<0.133	71.12	0.76	<0.108	<0.00	0.01	<0.00	0.00	<0.024	1.27	<0.037	<0.00	<0.00	0.00	<0.00
MB7Mt-4	<0.023	0.37	<0.172	48.94	0.81	1.04	0.05	0.03	0.01	0.05	<0.00	1.41	<0.03	0.06	0.00	0.01	0.00
MB7Mt-5	6.90	44.05	44.73	18.36	0.85	27.10	0.10	3.36	0.14	0.02	0.24	0.88	3.04	0.11	2.37	5.64	0.79
MB7Mt-6	<0.0223	0.64	<0.157	56.31	0.93	0.76	0.02	0.02	<0.0126	0.08	<0.00	1.26	<0.00	<0.00	<0.00	<0.0025	<0.00
MB7Mt-7	<0.0244	1.12	<0.119	41.50	0.80	<0.158	<0.00	<0.0082	<0.00	<0.00	0.02	1.17	0.04	<0.00	<0.00	<0.0028	<0.00
MB7Mt-8	<0.028	0.91	<0.192	36.88	0.84	<0.183	0.01	0.03	<0.0225	0.03	0.01	1.27	0.05	0.06	0.01	0.01	0.00
MB7Mt-9	3.50	9.24	6.42	3.81	0.63	11.45	1.71	9.52	0.66	0.21	1.61	0.94	2.06	15.43	6.60	8.06	0.84

Analysis no.	Nd	Sm	Eu	Gd	Tb	Dy	Ho	Er	Tm	Yb	Lu	W	Pb208	Th	U
MB77aHmPorous-6	0.07	0.01	0.02	0.11	0.01	0.05	0.02	0.05	0.01	0.02	0.00	0.05	0.86	<0.00	0.01
MB77aHmPorous-7	0.02	<0.00	<0.00	<0.04	<0.0038	<0.00	0.00	<0.0118	<0.00	<0.00	<0.0038	7.38	0.92	<0.00	0.02
MB77aHmPorous-8	0.23	0.03	0.03	0.12	0.01	0.07	0.01	0.04	0.00	<0.0175	0.01	11.86	4.35	0.02	0.07
MB77aHmPorous-9	0.03	<0.0246	<0.0089	<0.024	<0.0046	<0.00	<0.00	<0.00	<0.00	<0.00	<0.00321	1.55	1.38	<0.00	0.02
MB78HmPorous-1	<0.00	0.01	<0.00	<0.028	<0.00	<0.00	<0.0038	<0.0115	0.00	<0.00	<0.00	0.01	0.55	<0.00	0.00
MB78HmPorous-10	0.02	<0.027	<0.007	<0.038	<0.0036	0.01	<0.0052	0.00	<0.00	<0.00	<0.00	0.01	3.41	0.01	0.03
MB78HmPorous-11	<0.026	0.03	0.01	0.03	0.00	<0.0164	0.00	0.01	<0.00	<0.0177	0.00	0.03	1.87	0.02	0.03
MB78HmPorous-12	0.20	0.04	0.04	0.09	0.01	0.03	0.01	0.03	0.01	0.02	0.00	0.10	15.37	0.11	0.62
MB78HmPorous-13	0.01	0.01	<0.0065	<0.05	0.00	0.01	<0.00	0.01	0.00	<0.00	0.00	0.02	4.65	0.00	0.10
MB78HmPorous-14	0.02	<0.0258	0.01	<0.026	<0.0069	<0.014	0.01	0.03	0.01	0.03	0.01	0.07	3.53	0.02	0.57
MB78HmPorous-15	0.03	<0.028	<0.0073	0.02	<0.00	0.01	<0.0038	<0.00	<0.00	<0.00	<0.00	0.04	1.07	<0.00	0.02
MB78HmPorous-16	0.01	0.01	<0.0065	<0.044	<0.0034	<0.00	<0.00	<0.0104	<0.00	0.02	0.00	0.06	5.64	<0.0058	0.12
MB78HmPorous-17	0.05	0.01	<0.0066	0.01	<0.0049	0.01	0.00	<0.00	<0.00	<0.0153	<0.00	<0.0166	2.96	0.01	0.04
MB78HmPorous-18	0.13	<0.034	0.02	0.04	0.00	0.02	0.01	0.01	0.00	0.02	0.00	0.11	7.47	0.03	0.30
MB78HmPorous-19	0.03	<0.00	0.01	0.01	<0.005	0.01	0.00	<0.00	<0.0034	0.01	0.00	0.08	4.98	0.02	0.06
MB78HmPorous-2	0.15	0.02	0.03	0.07	<0.0034	0.02	0.00	0.01	0.01	<0.022	0.00	0.03	13.25	0.00	0.19
MB78HmPorous-20	<0.00	<0.0301	<0.0078	0.01	<0.0057	<0.00	0.00	<0.00	<0.00	<0.00	<0.0056	<0.0194	0.99	<0.00	0.01
MB78HmPorous-3	0.07	0.02	0.01	<0.04	0.00	<0.00	0.00	<0.016	<0.00	<0.0167	<0.0052	0.15	6.55	<0.00	0.04
MB78HmPorous-4	0.06	0.01	0.02	0.01	0.00	<0.018	0.00	0.02	<0.00	0.01	<0.0042	0.03	3.58	0.01	0.05
MB78HmPorous-5	0.04	<0.028	<0.0073	0.02	<0.0038	<0.00	<0.00	<0.00	<0.00	<0.00	<0.0053	0.06	3.30	0.00	0.06
MB78HmPorous-6	<0.02	0.01	0.01	<0.033	<0.0031	<0.0182	0.00	0.01	0.00	0.02	0.00	0.18	114.86	<0.00	0.11
MB78HmPorous-7	0.01	0.01	<0.00	<0.00	0.00	<0.0156	<0.00	0.00	<0.00	0.01	<0.00	0.08	3.18	0.03	0.08
MB78HmPorous-8	0.06	0.05	<0.0069	<0.037	<0.00	0.01	<0.0051	0.01	0.00	<0.016	<0.0035	0.06	25.63	0.03	0.15
MB78HmPorous-9	0.13	0.03	0.05	0.08	0.00	0.06	0.02	0.02	0.00	0.01	<0.0034	0.12	11.86	0.07	0.07
MB7Mt-1	<0.00	<0.00	<0.0056	<0.022	<0.002	<0.00	<0.00	<0.00	<0.00194	<0.00	<0.002	0.61	0.40	<0.00	0.04
MB7Mt-10	0.01	0.01	<0.00	<0.0151	<0.00202	<0.00	0.00	<0.0062	<0.00192	<0.00	<0.00	0.13	0.10	0.00	<0.00
MB7Mt-11	0.04	0.02	0.01	<0.029	0.01	0.03	0.01	0.04	0.01	0.04	0.02	0.13	0.09	<0.00	0.01
MB7Mt-12	0.02	0.03	0.02	0.04	<0.002	0.03	0.01	0.03	0.00	0.06	0.00	0.55	0.51	0.00	0.01
MB7Mt-13	0.03	0.01	0.01	<0.021	0.01	0.03	0.01	0.05	0.01	0.06	0.01	0.05	<0.02	0.01	<0.002
MB7Mt-14	0.01	0.01	0.01	0.01	0.00	0.01	0.00	0.04	0.00	0.04	0.01	0.40	0.13	<0.00	0.03
MB7Mt-15	0.01	0.01	<0.0042	0.01	<0.0022	<0.0089	<0.00	0.01	0.00	0.01	0.00	0.17	0.04	<0.00	0.00
MB7Mt-16	0.09	<0.0157	0.01	0.03	0.01	0.01	0.00	0.02	<0.002	0.01	0.01	0.15	0.18	<0.00	0.01
MB7Mt-17	0.05	0.01	0.00	<0.0257	<0.002	0.02	0.01	0.02	0.00	0.02	0.00	<0.0098	<0.00	<0.0037	<0.00
MB7Mt-18	0.04	0.01	0.01	0.02	0.00	0.05	0.00	0.02	<0.0023	0.03	0.00	0.01	0.01	<0.00	0.00
MB7Mt-19	0.01	<0.00	0.01	<0.00	<0.00229	<0.0164	0.00	0.01	0.00	0.02	<0.00223	0.01	0.02	0.00	0.00
MB7Mt-2	<0.0137	<0.00	<0.00	<0.027	<0.0021	<0.00	<0.00	<0.00	<0.00	<0.0094	<0.00205	<0.0159	0.01	<0.00	0.00
MB7Mt-3	<0.0187	<0.00	<0.0068	<0.0152	<0.002	<0.00	<0.00	<0.0063	<0.00	<0.0158	<0.00	0.02	0.06	<0.00	0.01
MB7Mt-4	<0.00	<0.00	<0.0045	<0.0172	<0.00	<0.00	0.00	<0.00	<0.00	<0.00	0.00	0.00	<0.0252	<0.00	<0.0026
MB7Mt-5	3.87	1.05	0.75	1.84	0.17	0.87	0.14	0.25	0.02	0.17	0.02	0.00	0.02	<0.00	0.00
MB7Mt-6	<0.00	0.01	<0.0035	<0.019	<0.00182	<0.00	<0.00	<0.0056	<0.00173	<0.0082	0.00	<0.00	0.01	<0.00	0.00
MB7Mt-7	<0.00	<0.00	<0.0039	<0.0149	0.00	<0.00	0.00	<0.00	<0.00	<0.00	<0.00275	0.00	<0.0178	<0.00	<0.00
MB7Mt-8	<0.00	<0.00	<0.0063	<0.017	0.00	0.01	0.00	<0.0071	<0.0022	<0.00	<0.00	0.01	<0.024	<0.00	0.00
MB7Mt-9	3.72	0.82	0.97	1.04	0.16	1.08	0.28	0.86	0.12	0.96	0.16	0.01	0.04	<0.00	<0.0021

Position	Deposit	Lithology	Sample no.	Analysis no.	Texture	Mg	Al	Si	P	Ca	Sc	Ti	V	Cr	Mn
Middle	Warrior	CHLORATITE	MB7	MB7MtPlaty-10	magnetite	353.16	269.80	9312.17	27.26	218.59	2.23	107.61	9.14	<0.6	795.74
Middle	Warrior	CHLORATITE	MB7	MB7MtPlaty-11	magnetite	252.94	223.68	9919.82	49.57	361.31	3.92	34.95	43.48	<0.65	171.21
Middle	Warrior	CHLORATITE	MB7	MB7MtPlaty-12	magnetite	270.03	212.31	9680.44	28.48	473.29	2.38	20.51	3.22	<0.69	253.02
Middle	Warrior	CHLORATITE	MB7	MB7MtPlaty-13	magnetite	855.17	325.47	9851.72	33.97	270.24	3.79	183.42	7.76	<0.59	779.79
Middle	Warrior	CHLORATITE	MB7	MB7MtPlaty-15	magnetite	284.81	260.64	9370.58	28.47	285.83	8.57	164.34	14.37	<0.73	261.80
Middle	Warrior	CHLORATITE	MB7	MB7MtPlaty-16	magnetite	471.08	244.66	6996.82	47.79	69.04	4.60	202.98	9.19	<0.6	231.10
Middle	Warrior	CHLORATITE	MB7	MB7MtPlaty-17	magnetite	379.39	255.33	9288.45	34.54	365.98	14.49	39.85	20.50	<0.83	287.14
Middle	Warrior	CHLORATITE	MB7	MB7MtPlaty-18	magnetite	1112.84	253.38	9490.99	31.37	2629.87	13.11	36.30	19.61	1.37	832.35
Middle	Warrior	CHLORATITE	MB7	MB7MtPlaty-19	magnetite	744.65	323.81	7740.55	28.86	1627.64	11.12	90.20	23.51	<0.84	533.89
Middle	Warrior	CHLORATITE	MB7	MB7MtPlaty-2	magnetite	362.25	222.22	8775.96	24.46	266.40	6.68	60.16	14.03	2.13	492.17
Middle	Warrior	CHLORATITE	MB7	MB7MtPlaty-20	magnetite	587.54	506.57	12430.57	29.54	391.31	12.90	49.05	23.96	<0.76	285.90
Middle	Warrior	CHLORATITE	MB7	MB7MtPlaty-3	magnetite	178.00	163.17	6985.67	19.55	165.19	1.27	14.68	2.08	0.74	161.05
Middle	Warrior	CHLORATITE	MB7	MB7MtPlaty-4	magnetite	2317.22	731.64	9632.17	14.95	3205.84	5.53	103.65	24.11	4.25	1225.76
Middle	Warrior	CHLORATITE	MB7	MB7MtPlaty-5	magnetite	407.42	413.09	9656.53	19.13	249.45	2.46	47.48	18.91	<0.67	253.58
Middle	Warrior	CHLORATITE	MB7	MB7MtPlaty-6	magnetite	220.57	221.17	7944.91	30.93	221.86	2.33	19.73	1.54	<0.63	271.96
Middle	Warrior	CHLORATITE	MB7	MB7MtPlaty-8	magnetite	279.72	276.04	9152.48	30.91	358.84	2.31	77.77	4.20	<0.68	279.76
Middle	Warrior	CHLORATITE	MB7	MB7MtPlaty-9	magnetite	225.36	239.41	8659.51	22.93	485.31	2.40	14.61	3.41	<0.69	250.15
South	Magnet	BIF	MB80a	MB80aMt-1	magnetite	66.91	316.19	316.66	<7.13	<56.64	<0.089	2.86	1.41	<0.63	313.00
South	Magnet	BIF	MB80a	MB80aMt-11	magnetite	99.05	351.29	2786.18	368.34	914.67	<0.082	4.25	2.46	<0.71	314.94
South	Magnet	BIF	MB80a	MB80aMt-13	magnetite	219.66	347.28	6405.92	139.48	763.55	<0.102	3.22	1.82	<0.7	438.98
South	Magnet	BIF	MB80a	MB80aMt-14	magnetite	18.42	211.32	3196.98	<7.26	<47.06	<0.098	2.44	1.57	<0.85	189.48
South	Magnet	BIF	MB80a	MB80aMt-17	magnetite	27.16	234.98	188.68	11.70	<52.88	0.20	3.65	1.59	<0.67	252.19
South	Magnet	BIF	MB80a	MB80aMt-18	magnetite	24.81	276.91	417.38	<7.46	<51.14	<0.113	2.80	1.58	<1.09	288.79
South	Magnet	BIF	MB80a	MB80aMt-19	magnetite	24.35	253.86	624.22	13.58	<71.34	0.10	3.89	1.61	<0.73	279.07
South	Magnet	BIF	MB80a	MB80aMt-2	magnetite	65.81	325.24	627.16	6.58	113.12	0.15	2.89	1.33	<0.69	284.10
South	Magnet	BIF	MB80a	MB80aMt-20	magnetite	25.28	299.24	382.18	23.06	<43.5	<0.099	3.53	1.77	<0.72	319.31
South	Magnet	BIF	MB80a	MB80aMt-21	magnetite	40.24	308.03	1123.84	<6.5	<48.97	0.10	3.21	1.64	1.62	270.23
South	Magnet	BIF	MB80a	MB80aMt-23	magnetite	233.78	256.29	799.37	<6.63	424.57	0.15	3.31	1.59	1.26	325.75
South	Magnet	BIF	MB80a	MB80aMt-24	magnetite	25.22	280.73	671.95	<6.92	<54.55	0.14	2.66	1.37	<0.52	292.58
South	Magnet	BIF	MB80a	MB80aMt-25	magnetite	56.46	335.88	755.39	<7.43	<57.02	0.10	2.96	1.81	<0.89	351.83
South	Magnet	BIF	MB80a	MB80aMt-26	magnetite	442.17	328.46	883.94	<7.2	798.96	0.10	4.67	1.79	<0.71	248.62
South	Magnet	BIF	MB80a	MB80aMt-27	magnetite	44.06	333.08	1275.11	21.19	56.84	0.10	3.06	1.71	<0.7	318.07
South	Magnet	BIF	MB80a	MB80aMt-28	magnetite	16.45	242.81	382.06	<6.78	<51.6	0.15	2.69	1.54	<0.78	195.17
South	Magnet	BIF	MB80a	MB80aMt-29	magnetite	29.21	338.57	1296.31	6.04	<49.25	0.09	2.71	1.61	<0.63	328.22
South	Magnet	BIF	MB80a	MB80aMt-3	magnetite	954.22	322.97	848.57	11.99	2382.04	<0.086	3.87	1.72	<0.63	396.31
South	Magnet	BIF	MB80a	MB80aMt-30	magnetite	25.17	316.58	267.32	<6.49	<46.41	<0.079	3.29	1.41	<0.7	294.32
South	Magnet	BIF	MB80a	MB80aMt-31	magnetite	179.39	221.11	768.13	7.99	61.06	<0.095	2.00	1.73	<0.8	185.56
South	Magnet	BIF	MB80a	MB80aMt-32	magnetite	35.54	338.76	1339.93	<6.58	<48.15	<0.096	2.55	1.70	<0.63	293.21
South	Magnet	BIF	MB80a	MB80aMt-33	magnetite	122.48	303.96	374.79	<6.87	155.30	<0.086	2.03	1.54	1.67	302.74
South	Magnet	BIF	MB80a	MB80aMt-34	magnetite	773.59	309.23	2656.44	<6.94	<61.8	<0.094	3.20	1.94	<0.78	278.15
South	Magnet	BIF	MB80a	MB80aMt-35	magnetite	324.58	432.01	846.42	8.62	<55.56	<0.083	3.69	1.89	<0.64	146.12
South	Magnet	BIF	MB80a	MB80aMt-36	magnetite	24.29	349.99	2732.28	<6.21	<36.75	<0.105	4.07	2.38	1.52	252.11
South	Magnet	BIF	MB80a	MB80aMt-37	magnetite	72.01	320.38	232.35	9.10	314.10	0.12	3.49	2.02	<0.61	263.19

Analysis no.	Co	Ni	Cu	Zn	Ga	As	Sr	Y	Zr	Nb	Mo	Sn	Sb	Ba	La	Ce	Pr
MB7MtPlaty-10	0.66	0.66	150.50	29.97	0.66	4.14	1.86	12.08	0.08	0.20	1.21	1.60	1.49	21.49	7.63	8.16	0.83
MB7MtPlaty-11	0.01	<0.106	<0.155	2.36	0.60	5.58	2.22	6.39	<0.0145	0.92	1.63	2.85	1.00	16.50	7.44	6.71	0.65
MB7MtPlaty-12	<0.0222	<0.128	1.01	6.38	0.69	4.74	2.33	14.41	<0.00	0.22	1.29	0.35	1.74	18.70	8.63	9.64	0.97
MB7MtPlaty-13	0.03	0.29	1.93	10.87	0.83	3.65	2.32	13.90	0.21	0.91	1.40	4.91	1.68	25.54	9.86	11.83	1.20
MB7MtPlaty-15	<0.0247	<0.16	<0.151	2.19	0.82	3.96	1.87	13.66	0.31	1.03	1.52	0.20	1.55	20.93	9.91	11.37	1.18
MB7MtPlaty-16	0.03	0.39	<0.17	3.38	0.55	3.72	1.42	71.16	39.22	1.42	1.77	0.28	0.90	12.71	5.42	5.90	0.61
MB7MtPlaty-17	<0.03	<0.149	<0.202	2.35	0.55	4.68	1.97	15.65	0.08	0.58	1.55	0.37	2.01	23.38	11.72	14.12	1.57
MB7MtPlaty-18	<0.0144	<0.162	<0.173	5.41	0.59	4.57	2.58	16.67	0.08	0.56	1.16	0.16	1.92	20.26	12.17	14.80	1.59
MB7MtPlaty-19	0.09	<0.196	<0.16	3.56	0.83	3.92	1.83	11.54	0.13	0.82	1.81	0.42	1.23	16.56	7.85	10.01	1.02
MB7MtPlaty-2	<0.00	<0.111	<0.172	10.11	0.56	4.38	1.79	15.13	0.11	0.50	1.21	0.29	1.80	19.57	10.75	12.76	1.34
MB7MtPlaty-20	0.08	<0.124	0.24	7.44	0.98	5.18	2.10	15.94	0.09	0.44	1.34	0.27	2.34	23.89	10.80	14.19	1.53
MB7MtPlaty-3	0.02	0.27	<0.155	1.61	0.63	2.37	1.39	9.44	0.03	0.13	1.70	0.17	1.28	15.22	7.13	7.77	0.81
MB7MtPlaty-4	0.24	0.26	0.17	14.25	1.47	3.56	2.13	10.67	0.12	0.52	1.44	0.31	1.85	19.04	7.11	9.10	0.96
MB7MtPlaty-5	0.58	0.94	0.68	5.89	0.95	7.05	2.19	10.67	0.19	0.35	1.43	1.99	1.52	17.05	5.73	6.64	0.69
MB7MtPlaty-6	0.03	<0.195	<0.129	2.02	0.55	3.77	1.55	8.02	0.04	0.20	1.83	0.26	1.07	17.48	3.98	4.48	0.42
MB7MtPlaty-8	0.06	0.39	<0.18	2.80	0.92	4.08	1.88	11.80	0.05	1.15	1.50	0.25	1.74	18.79	5.94	6.71	0.71
MB7MtPlaty-9	<0.0281	<0.122	0.30	2.11	0.70	3.11	1.65	9.75	<0.0193	0.11	1.85	0.35	1.14	18.22	5.45	5.96	0.57
MB80aMt-1	2.60	11.20	<0.176	35.23	0.41	<0.207	0.01	0.01	<0.00	<0.00	0.03	0.33	<0.031	<0.00	0.00	0.00	0.00
MB80aMt-11	2.20	12.07	<0.177	23.37	0.54	0.81	1.71	1.05	0.03	0.00	<0.00	0.30	0.04	0.14	0.55	0.69	0.11
MB80aMt-13	2.91	14.21	<0.19	39.56	0.50	1.48	1.32	1.02	0.20	0.07	0.02	0.41	0.13	0.54	0.63	0.77	0.09
MB80aMt-14	2.85	12.37	0.18	24.04	0.45	<0.153	0.03	0.02	0.04	0.01	0.03	0.49	0.02	<0.00	<0.0033	0.01	0.00
MB80aMt-17	2.63	12.56	<0.186	23.62	0.51	<0.178	0.25	0.04	0.04	<0.00	0.02	0.12	0.04	0.38	0.01	0.01	<0.0029
MB80aMt-18	2.57	12.11	<0.164	22.11	0.57	0.42	0.09	0.06	0.05	0.02	<0.057	0.19	0.05	0.26	0.03	0.06	0.01
MB80aMt-19	2.45	10.57	<0.206	25.14	0.49	<0.22	0.03	0.02	0.04	<0.00	0.02	0.37	<0.025	0.28	0.01	0.02	0.00
MB80aMt-2	2.45	11.27	<0.157	26.14	0.54	0.22	0.22	0.06	0.04	0.01	<0.0264	0.25	0.02	0.15	0.03	0.05	0.01
MB80aMt-20	2.23	12.79	<0.188	24.53	0.42	<0.166	0.02	0.03	<0.017	0.01	<0.03	0.23	<0.033	<0.00	0.01	0.01	0.00
MB80aMt-21	2.67	12.37	0.27	25.75	0.69	0.28	18.11	0.04	0.01	<0.00	0.04	0.24	<0.049	0.09	0.04	0.04	0.01
MB80aMt-23	2.37	12.85	<0.15	31.95	0.60	0.44	0.06	0.03	<0.00	0.03	0.04	0.40	0.03	<0.072	0.00	0.03	0.00
MB80aMt-24	2.69	13.76	<0.196	25.74	0.64	0.22	0.11	0.07	0.05	0.01	0.03	0.28	0.06	0.26	0.06	0.05	0.01
MB80aMt-25	2.69	13.92	<0.217	32.67	0.62	0.21	0.02	0.03	<0.018	0.01	<0.045	0.42	<0.036	0.07	0.04	0.04	0.01
MB80aMt-26	2.55	12.12	2.10	20.72	0.53	0.20	1.43	0.08	0.18	0.02	<0.00	0.46	<0.033	0.16	0.04	0.05	0.01
MB80aMt-27	2.76	12.93	<0.177	33.48	0.58	0.46	0.15	0.18	0.12	0.02	<0.026	0.33	0.10	0.35	0.10	0.12	0.01
MB80aMt-28	2.62	12.06	<0.182	17.74	0.51	<0.25	0.02	0.02	0.03	0.00	<0.042	0.21	<0.034	<0.00	<0.00	0.00	<0.0029
MB80aMt-29	2.41	12.87	<0.148	39.29	0.63	0.19	0.01	0.04	0.06	<0.00	0.04	0.42	<0.0211	<0.00	0.00	0.04	0.00
MB80aMt-3	2.90	15.40	<0.152	27.33	0.51	0.21	0.68	0.85	0.04	0.02	0.02	0.21	<0.03	0.27	0.09	0.28	0.05
MB80aMt-30	2.74	11.03	<0.152	32.19	0.49	0.28	<0.0088	0.04	<0.00	0.00	0.02	0.27	0.06	<0.00	0.04	0.06	0.00
MB80aMt-31	2.66	13.22	<0.214	15.67	0.53	0.15	0.04	0.03	0.06	<0.0071	0.06	0.33	<0.00	0.09	0.00	0.03	0.00
MB80aMt-32	2.59	13.32	<0.181	28.69	0.76	<0.17	0.03	0.05	0.01	0.00	<0.039	0.42	<0.00	<0.00	0.03	0.04	0.00
MB80aMt-33	2.70	11.17	<0.172	33.57	0.62	<0.18	0.11	0.12	0.03	0.00	<0.042	0.46	<0.024	0.13	0.02	0.05	0.01
MB80aMt-34	3.04	17.66	<0.154	27.31	0.51	<0.22	0.04	0.02	0.03	0.00	0.05	0.39	<0.00	0.09	0.02	0.03	0.00
MB80aMt-35	2.54	17.77	0.57	13.43	0.52	0.24	0.10	0.07	0.11	0.01	0.01	0.46	<0.022	<0.00	0.01	0.01	<0.00
MB80aMt-36	2.32	14.71	<0.159	27.98	0.65	<0.15	0.02	0.04	<0.00	<0.0061	0.01	0.37	0.02	0.07	0.03	0.04	0.00
MB80aMt-37	2.02	13.45	<0.161	23.83	0.39	<0.181	<0.011	0.03	<0.0137	<0.00	0.02	0.26	<0.00	<0.00	0.01	0.03	0.00

Analysis no.	Nd	Sm	Eu	Gd	Tb	Dy	Ho	Er	Tm	Yb	Lu	W	Pb208	Th	U
MB7MtPlaty-10	3.29	0.79	1.10	1.24	0.17	1.23	0.29	1.07	0.17	1.37	0.25	<0.0108	0.01	0.00	<0.00
MB7MtPlaty-11	2.62	0.66	0.61	0.81	0.13	0.78	0.18	0.56	0.09	0.73	0.13	0.01	0.08	<0.00	0.00
MB7MtPlaty-12	4.00	0.76	1.26	1.04	0.19	1.44	0.33	1.13	0.20	1.51	0.30	0.00	0.03	0.00	0.00
MB7MtPlaty-13	5.13	1.09	1.55	1.49	0.24	1.39	0.38	1.27	0.19	1.37	0.29	0.03	0.77	0.02	0.02
MB7MtPlaty-15	4.93	1.03	1.40	1.33	0.23	1.62	0.36	1.16	0.19	1.48	0.30	<0.00	<0.025	0.00	<0.00
MB7MtPlaty-16	2.56	0.77	1.70	2.22	0.42	3.71	1.18	4.14	0.62	4.54	0.77	0.05	0.33	<0.00	<0.00215
MB7MtPlaty-17	6.44	1.51	1.90	2.13	0.32	2.02	0.42	1.58	0.22	1.74	0.33	0.00	0.10	0.00	<0.002
MB7MtPlaty-18	6.83	1.57	1.85	2.09	0.35	2.29	0.48	1.61	0.25	1.94	0.37	0.07	0.10	<0.00	0.00
MB7MtPlaty-19	4.79	1.16	1.24	1.48	0.23	1.43	0.35	1.12	0.16	1.33	0.26	<0.00	0.03	<0.00	0.00
MB7MtPlaty-2	6.17	1.28	1.58	1.81	0.27	1.81	0.37	1.30	0.19	1.63	0.28	0.16	0.27	0.00	<0.002
MB7MtPlaty-20	6.79	1.78	1.66	2.29	0.35	2.41	0.48	1.59	0.23	1.89	0.34	0.74	1.95	0.01	0.01
MB7MtPlaty-3	3.00	0.67	1.05	0.93	0.14	0.79	0.21	0.75	0.11	0.94	0.18	0.08	0.17	0.00	<0.00
MB7MtPlaty-4	4.11	1.04	1.09	1.34	0.19	1.41	0.27	0.99	0.15	1.19	0.22	0.08	0.34	<0.00	0.00
MB7MtPlaty-5	2.71	0.70	0.83	0.89	0.14	0.94	0.21	0.86	0.15	1.25	0.22	0.22	0.25	0.00	0.00
MB7MtPlaty-6	1.86	0.41	0.52	0.66	0.11	0.66	0.17	0.63	0.13	0.98	0.17	<0.00	0.01	<0.00	<0.00
MB7MtPlaty-8	3.13	0.67	0.91	1.10	0.14	1.09	0.28	0.98	0.16	1.34	0.27	<0.0103	0.06	<0.00	0.00
MB7MtPlaty-9	2.53	0.47	0.79	0.71	0.12	0.93	0.22	0.75	0.12	1.16	0.21	<0.00	0.03	<0.00	0.00
MB80aMt-1	0.01	<0.0172	0.00	<0.029	0.00	0.01	<0.00	0.00	<0.00	<0.00	<0.0022	0.00	0.05	0.00	<0.00196
MB80aMt-11	0.38	0.14	0.04	0.11	0.01	0.07	0.02	0.05	0.01	0.04	0.01	0.40	0.91	0.00	0.00
MB80aMt-13	0.48	0.07	0.03	0.08	0.02	0.09	0.02	0.07	0.01	0.04	0.01	0.01	0.03	0.00	<0.0028
MB80aMt-14	<0.00	<0.0245	<0.00	<0.00	<0.00	<0.00	<0.00	<0.00	<0.00	<0.00	<0.0022	0.01	0.07	0.00	0.00
MB80aMt-17	0.01	<0.00	<0.00	<0.0182	<0.0024	<0.0101	0.00	<0.00	0.00	0.01	<0.00	0.40	1.03	0.01	0.01
MB80aMt-18	0.01	<0.0208	0.00	<0.029	0.00	0.00	0.00	0.01	<0.0026	<0.0122	0.00	0.11	0.27	<0.00	<0.00
MB80aMt-19	0.03	0.01	<0.005	0.01	<0.00	0.01	<0.0026	0.00	0.00	0.01	<0.00248	0.05	0.33	<0.00	<0.00
MB80aMt-2	0.02	0.02	0.00	<0.023	0.01	<0.0091	0.00	0.01	0.00	0.00	0.00	0.01	0.03	<0.00	0.00
MB80aMt-20	0.01	<0.00	<0.0048	<0.00	<0.00	<0.0101	0.00	<0.0076	0.00	<0.00	<0.00	0.03	0.03	<0.00	0.00
MB80aMt-21	0.03	0.02	<0.0044	0.01	<0.00	0.02	<0.00	0.01	0.00	<0.0101	0.00	0.04	0.19	0.00	0.00
MB80aMt-23	<0.016	<0.00	0.01	0.04	<0.00248	<0.00	<0.00	0.01	<0.00	<0.00	0.00	<0.00	0.03	<0.00	<0.00
MB80aMt-24	0.02	0.02	<0.0067	0.02	<0.00242	0.01	0.00	0.01	<0.00	<0.00	0.00	0.05	6.07	0.00	0.04
MB80aMt-25	0.01	<0.028	0.00	<0.00	<0.00	<0.00	0.00	0.01	0.00	0.00	0.00	0.00	0.04	<0.00	<0.00
MB80aMt-26	0.04	0.02	0.01	<0.025	<0.00241	0.00	0.00	0.01	0.00	0.01	<0.00	<0.00	<0.021	<0.00	<0.00
MB80aMt-27	0.07	0.01	0.01	0.02	<0.0031	0.01	0.00	0.02	0.00	0.01	<0.0021	0.03	0.11	<0.00	0.00
MB80aMt-28	<0.0163	<0.00	<0.00	<0.00	<0.00	0.00	0.00	<0.00	<0.00	<0.00	<0.00	<0.00	<0.021	0.00	<0.0018
MB80aMt-29	0.01	<0.00	<0.00	<0.016	<0.00218	0.00	<0.00	<0.00	0.00	<0.00	<0.00	0.57	0.71	0.00	0.01
MB80aMt-3	0.33	0.29	0.05	0.21	0.03	0.15	0.02	0.06	0.01	0.03	0.00	0.25	0.56	0.00	<0.00
MB80aMt-30	0.02	<0.00	<0.0044	0.02	0.00	0.01	0.00	0.00	<0.00212	<0.00	<0.00	<0.0106	0.02	<0.00	<0.00209
MB80aMt-31	<0.0169	<0.00	0.00	0.01	<0.00	<0.0151	0.01	<0.00	0.00	<0.00	0.00	0.03	0.12	<0.00	0.00
MB80aMt-32	0.01	<0.00	0.01	<0.017	0.00	<0.0136	<0.00	0.00	0.00	<0.00	<0.00	0.61	1.53	<0.0092	<0.0034
MB80aMt-33	0.05	0.03	0.01	0.06	0.00	0.00	0.00	0.01	<0.00	0.01	<0.0024	1.25	0.44	0.00	0.01
MB80aMt-34	0.01	<0.019	<0.00	<0.0184	<0.0043	<0.0102	0.00	0.00	<0.00	<0.00	<0.00	1.00	0.41	0.00	0.01
MB80aMt-35	0.01	0.01	<0.0045	0.01	0.00	0.01	<0.0023	0.01	<0.0022	<0.00	0.00	0.57	0.41	0.00	0.00
MB80aMt-36	0.01	0.01	<0.0044	<0.0166	<0.0022	0.00	0.00	0.00	<0.00	0.00	<0.0022	0.79	0.27	<0.0108	0.01
MB80aMt-37	0.03	0.02	<0.0039	<0.0148	<0.0028	0.01	<0.00202	<0.00	<0.00	0.01	0.00	0.24	0.61	0.01	0.01

Position	Deposit	Lithology	Sample no.	Analysis no.	Texture	Mg	Al	Si	P	Ca	Sc	Ti	V	Cr	Mn
South	Magnet	BIF	MB80a	MB80aMt-38	magnetite	66.01	334.98	1951.05	41.80	103.91	<0.119	4.10	1.68	<0.94	327.24
South	Magnet	BIF	MB80a	MB80aMt-39	magnetite	47.35	359.67	1557.65	14.55	<50.64	<0.114	3.30	1.78	<0.81	330.60
South	Magnet	BIF	MB80a	MB80aMt-4	magnetite	77.42	316.65	2811.97	28.11	105.35	0.16	3.11	1.87	<0.74	312.95
South	Magnet	BIF	MB80a	MB80aMt-40	magnetite	20.77	305.99	424.15	<5.84	<44.77	<0.09	1.90	1.21	<0.64	325.55
South	Magnet	BIF	MB80a	MB80aMt-5	magnetite	34.93	309.98	1244.03	8.44	<52.91	<0.094	2.87	1.75	<0.65	256.14
South	Magnet	BIF	MB80a	MB80aMt-6	magnetite	45.99	332.26	1057.63	<5.87	<54.53	<0.082	3.46	1.64	<0.64	327.79
South	Magnet	BIF	MB80a	MB80aMt-7	magnetite	43.48	311.46	8418.49	<7.17	<51.97	<0.101	3.28	1.72	<0.77	291.34
South	Magnet	BIF	MB80a	MB80aMt-8	magnetite	31.26	310.89	1546.32	9.66	51.47	<0.095	4.10	1.62	<0.75	341.79
South	Magnet	BIF	MB80a	MB80aMt-9	magnetite	34.57	344.77	1095.51	<5.32	<45.53	0.09	2.92	1.77	<0.69	331.36
Middle	Warrior	ORE	MB8	MB8HmPlaty-1	platy hematite	209.56	444.42	525.86	17.14	<101.14	0.44	443.25	15.40	3.68	181.33
Middle	Warrior	ORE	MB8	MB8HmPlaty-10	platy hematite	122.12	502.94	1053.72	11.66	<75.57	0.63	120.29	11.12	5.79	194.74
Middle	Warrior	ORE	MB8	MB8HmPlaty-11	platy hematite	317.69	705.25	3840.39	71.85	287.97	1.52	179.07	5.84	1.94	629.99
Middle	Warrior	ORE	MB8	MB8HmPlaty-13	platy hematite	48.99	275.88	144.43	<7.79	<83.42	0.27	89.21	13.04	<0.98	121.78
Middle	Warrior	ORE	MB8	MB8HmPlaty-14	platy hematite	91.58	184.09	416.82	33.02	221.52	0.91	668.59	24.98	<0.98	92.51
Middle	Warrior	ORE	MB8	MB8HmPlaty-15	platy hematite	122.44	469.58	775.68	12.92	<75.37	0.62	145.14	9.98	3.96	242.59
Middle	Warrior	ORE	MB8	MB8HmPlaty-16	platy hematite	214.26	745.85	249.09	19.63	<75.05	0.35	155.12	8.80	1.89	213.04
Middle	Warrior	ORE	MB8	MB8HmPlaty-17	platy hematite	81.91	324.34	361.48	8.98	137.90	0.28	143.59	10.80	1.38	212.59
Middle	Warrior	ORE	MB8	MB8HmPlaty-18	platy hematite	84.53	309.31	414.62	<7.92	<81.24	0.68	252.75	14.83	1.44	159.04
Middle	Warrior	ORE	MB8	MB8HmPlaty-19	platy hematite	215.94	610.58	861.39	20.76	167.40	0.33	123.83	7.82	2.71	277.73
Middle	Warrior	ORE	MB8	MB8HmPlaty-2	platy hematite	329.29	513.83	7444.38	33.47	<89.36	2.13	18.06	0.91	1.34	599.57
Middle	Warrior	ORE	MB8	MB8HmPlaty-5	platy hematite	70.64	367.11	155.39	13.64	172.16	0.30	136.50	12.18	1.06	162.00
Middle	Warrior	ORE	MB8	MB8HmPlaty-6	platy hematite	150.97	630.41	875.67	<8.37	<82.55	0.39	197.97	6.73	<1	143.21
Middle	Warrior	ORE	MB8	MB8HmPlaty-7	platy hematite	47.43	409.71	536.25	<8.36	<90.63	0.52	168.37	10.88	<0.87	123.86
Middle	Warrior	ORE	MB8	MB8HmPlaty-8	platy hematite	207.59	507.70	5035.56	22.25	<90.25	1.81	118.72	4.31	<1.09	317.34
Middle	Warrior	ORE	MB8	MB8HmPlaty-9	platy hematite	118.12	383.74	360.09	<9.02	<95.3	0.60	266.75	8.56	2.53	199.36
South	Magnet	BIF	MB92a	MB92aMt-1	magnetite	429.11	20.24	1320.53	20.43	266.75	<0.078	5.36	2.44	1.20	220.94
South	Magnet	BIF	MB92a	MB92aMt-10	magnetite	43.99	52.41	256.88	6.28	87.34	0.09	6.42	1.93	1.11	515.65
South	Magnet	BIF	MB92a	MB92aMt-11	magnetite	45.08	52.53	<59.71	6.77	<31.99	<0.067	6.25	2.49	0.57	505.11
South	Magnet	BIF	MB92a	MB92aMt-12	magnetite	15.95	17.58	264.04	4.69	53.23	<0.078	7.28	2.11	<0.68	249.30
South	Magnet	BIF	MB92a	MB92aMt-13	magnetite	33.24	30.86	416.47	7.51	<42.85	<0.086	7.12	2.82	<0.76	175.70
South	Magnet	BIF	MB92a	MB92aMt-14	magnetite	55.11	64.62	123.93	<4.88	<37.67	<0.069	7.73	2.26	<0.5	505.09
South	Magnet	BIF	MB92a	MB92aMt-15	magnetite	56.80	57.71	104.48	7.11	<41.36	<0.061	6.46	2.19	<0.48	386.11
South	Magnet	BIF	MB92a	MB92aMt-16	magnetite	55.23	70.54	177.62	5.66	<46.63	<0.073	6.35	2.21	<0.7	540.35
South	Magnet	BIF	MB92a	MB92aMt-17	magnetite	85.68	32.18	378.56	12.92	296.36	0.11	6.72	2.11	<0.83	303.00
South	Magnet	BIF	MB92a	MB92aMt-18	magnetite	90.89	19.49	439.13	21.06	90.96	<0.081	5.38	2.23	<0.63	251.11
South	Magnet	BIF	MB92a	MB92aMt-19	magnetite	20.73	25.58	255.54	<4.81	<31.16	0.06	5.08	2.14	<0.53	240.16
South	Magnet	BIF	MB92a	MB92aMt-2	magnetite	62.50	79.80	165.93	<5	<46.65	<0.076	7.30	2.29	<0.57	517.45
South	Magnet	BIF	MB92a	MB92aMt-20	magnetite	50.64	56.18	348.93	6.60	89.76	<0.061	5.99	2.08	<0.56	529.41
South	Magnet	BIF	MB92a	MB92aMt-21	magnetite	114.18	48.98	1133.91	6.81	149.85	<0.083	5.82	1.52	0.59	275.93
South	Magnet	BIF	MB92a	MB92aMt-25	magnetite	85.29	39.56	275.00	<5.3	<53.69	<0.084	2.25	0.80	<0.61	434.61
South	Magnet	BIF	MB92a	MB92aMt-26	magnetite	93.42	48.47	196.16	<4.87	<36.69	<0.077	3.15	0.73	<0.52	497.28
South	Magnet	BIF	MB92a	MB92aMt-27	magnetite	56.02	102.77	<54.8	11.81	68.33	<0.067	6.66	1.84	1.13	492.45
South	Magnet	BIF	MB92a	MB92aMt-28	magnetite	152.03	57.23	343.49	16.71	<44.11	<0.063	4.70	1.74	<0.51	526.02

Analysis no.	Co	Ni	Cu	Zn	Ga	As	Sr	Y	Zr	Nb	Mo	Sn	Sb	Ba	La	Ce	Pr
MB80aMt-38	2.35	13.95	<0.237	40.85	0.53	0.50	0.22	0.14	0.09	0.01	0.03	0.25	0.11	<0.00	0.13	0.16	0.01
MB80aMt-39	2.68	12.95	<0.215	34.80	0.58	0.40	0.03	0.08	0.08	0.01	<0.032	0.35	0.05	0.15	0.05	0.07	0.01
MB80aMt-4	2.88	13.28	<0.172	24.62	0.66	0.38	0.12	0.17	0.09	0.01	<0.00	0.35	0.04	<0.00	0.08	0.13	0.02
MB80aMt-40	2.68	10.34	<0.173	27.59	0.54	<0.171	<0.00	0.02	0.05	<0.00	0.03	0.29	<0.02	<0.00	0.01	0.02	0.00
MB80aMt-5	2.32	12.07	<0.2	21.52	0.55	<0.2	0.02	0.05	0.06	0.03	<0.027	0.23	<0.038	<0.00	0.03	0.02	0.00
MB80aMt-6	2.48	13.57	0.30	28.46	0.70	<0.12	0.02	0.03	0.06	<0.00	<0.026	0.21	0.02	<0.00	0.02	0.04	0.00
MB80aMt-7	2.71	16.32	<0.149	27.68	0.62	0.19	<0.0133	0.04	0.09	0.01	0.02	0.23	0.03	<0.00	0.01	0.03	<0.00
MB80aMt-8	3.52	14.03	<0.173	44.13	0.60	0.20	<0.00	0.09	0.04	0.00	0.02	0.25	<0.00	<0.00	0.02	0.05	0.00
MB80aMt-9	2.66	15.37	<0.151	46.77	0.50	0.27	<0.00	0.03	0.06	0.01	<0.034	0.40	<0.019	<0.00	0.02	0.02	0.00
MB8HmPlaty-1	<0.028	0.54	0.46	5.32	0.44	2.71	0.30	0.58	0.66	1.67	0.11	2.70	0.25	0.62	0.30	0.40	0.04
MB8HmPlaty-10	0.07	0.42	0.98	12.41	0.61	1.56	0.31	1.43	0.24	0.17	0.45	1.16	0.40	1.51	0.52	0.77	0.10
MB8HmPlaty-11	0.30	3.02	677.37	84.65	1.09	18.82	2.22	2.99	0.67	0.15	1.44	8.59	2.40	4.95	1.82	2.33	0.24
MB8HmPlaty-13	0.03	<0.00	0.62	2.49	0.52	<0.35	0.04	0.19	0.12	0.15	<0.028	0.82	0.10	1.76	0.12	0.15	0.02
MB8HmPlaty-14	0.14	0.31	2.90	7.79	0.28	13.69	1.24	0.53	2.32	4.60	0.37	1.23	1.27	0.36	0.27	0.42	0.05
MB8HmPlaty-15	0.07	0.28	<0.111	9.30	0.67	1.15	0.22	1.28	0.42	0.27	0.14	0.69	<0.101	1.29	0.58	0.79	0.10
MB8HmPlaty-16	0.11	0.15	3.51	22.46	0.78	0.44	0.14	0.09	0.18	0.11	0.01	1.11	0.11	0.08	0.05	0.09	0.01
MB8HmPlaty-17	0.03	<0.143	0.22	3.74	0.68	1.46	0.20	0.67	1.43	0.75	0.11	0.95	0.18	2.12	0.38	0.62	0.08
MB8HmPlaty-18	0.19	0.36	0.53	4.79	0.27	4.19	0.29	0.27	0.99	0.54	0.14	1.11	0.79	0.79	0.15	0.27	0.03
MB8HmPlaty-19	<0.025	0.31	0.30	9.65	0.69	2.42	0.23	0.89	0.33	0.27	0.02	0.79	0.27	0.98	0.49	0.69	0.09
MB8HmPlaty-2	<0.02	<0.096	<0.114	6.26	0.68	4.00	1.45	6.39	6.28	0.13	1.49	<0.154	0.50	9.90	2.28	2.96	0.32
MB8HmPlaty-5	0.31	<0.206	0.50	16.15	0.66	2.96	0.34	0.39	0.49	0.23	0.05	0.94	0.38	0.83	0.24	0.39	0.04
MB8HmPlaty-6	0.12	0.58	<0.131	23.87	0.76	2.59	0.27	1.22	0.27	0.16	0.03	0.78	0.44	1.12	1.05	1.30	0.13
MB8HmPlaty-7	0.04	0.43	0.50	6.35	0.57	1.32	0.19	0.76	0.71	0.62	0.05	0.77	<0.081	1.33	0.39	0.59	0.08
MB8HmPlaty-8	0.02	<0.119	<0.151	4.47	0.63	5.62	1.33	4.87	0.94	0.31	1.26	0.60	0.81	7.76	2.02	2.62	0.31
MB8HmPlaty-9	0.21	0.31	0.45	17.69	0.41	4.32	0.23	0.84	0.58	0.63	0.18	0.91	0.65	0.48	0.31	0.48	0.07
MB92aMt-1	0.16	1.22	<0.105	5.42	0.10	1.58	0.29	0.79	0.06	0.06	0.22	0.16	0.05	0.81	0.66	0.80	0.06
MB92aMt-10	0.35	1.18	<0.122	9.43	<0.028	0.30	<0.00	0.05	0.03	0.01	0.01	0.18	<0.022	<0.00	0.02	0.01	0.00
MB92aMt-11	0.33	1.97	<0.125	8.89	0.10	0.16	<0.00	0.01	<0.00	<0.0047	0.04	0.15	<0.028	<0.00	0.00	0.00	<0.00
MB92aMt-12	0.40	1.34	0.19	5.45	0.17	0.23	0.03	0.04	0.03	0.01	<0.02	<0.08	0.04	0.05	0.04	0.05	0.00
MB92aMt-13	0.33	1.83	0.37	10.17	0.24	0.89	0.06	0.11	0.07	0.01	0.05	<0.095	0.10	<0.00	0.02	0.04	0.00
MB92aMt-14	0.19	2.48	<0.116	8.74	0.11	0.20	<0.00	0.04	<0.0123	0.01	<0.00	0.14	<0.0229	<0.00	0.02	0.02	0.00
MB92aMt-15	0.10	1.61	<0.107	6.41	0.11	0.81	0.04	0.32	0.02	0.01	0.03	0.14	0.07	0.06	0.18	0.25	0.02
MB92aMt-16	0.05	1.84	<0.126	8.73	0.06	0.75	<0.00	0.26	<0.0124	0.01	0.04	<0.073	<0.033	<0.00	0.12	0.16	0.02
MB92aMt-17	0.11	1.67	<0.164	6.09	0.11	2.79	0.35	1.12	0.04	0.09	0.06	0.16	0.22	0.49	0.75	0.89	0.07
MB92aMt-18	0.17	1.52	<0.13	3.94	0.07	2.03	0.12	0.51	0.09	0.05	0.71	0.09	0.11	0.58	0.76	0.75	0.07
MB92aMt-19	0.15	1.03	<0.122	4.85	0.03	<0.125	0.00	0.05	0.06	0.01	0.26	<0.073	<0.027	<0.00	0.02	0.03	<0.00
MB92aMt-2	0.33	1.16	<0.103	9.32	0.10	<0.097	<0.00	0.01	0.01	<0.00	0.02	<0.072	<0.0152	<0.00	<0.00243	<0.0023	<0.00195
MB92aMt-20	0.23	1.57	<0.113	8.00	0.07	0.55	0.02	0.16	<0.0107	0.01	0.04	<0.069	<0.031	0.33	0.08	0.14	0.01
MB92aMt-21	0.37	2.70	0.12	4.34	0.10	2.10	0.12	0.44	0.09	0.05	0.05	0.18	0.08	0.50	0.31	0.34	0.03
MB92aMt-25	0.77	1.23	<0.135	8.02	0.08	0.19	<0.00	0.02	0.01	0.01	<0.04	0.09	0.03	<0.00	0.00	0.00	<0.00
MB92aMt-26	0.79	1.37	0.20	8.90	0.11	0.42	0.09	0.05	<0.0125	0.00	<0.0212	0.13	<0.033	0.05	0.02	0.04	0.00
MB92aMt-27	0.71	2.43	<0.091	8.63	0.03	<0.119	<0.0062	<0.0057	<0.0111	<0.00	0.05	0.10	<0.0206	0.05	<0.00	<0.0022	<0.00
MB92aMt-28	0.65	2.06	<0.111	8.07	0.12	1.38	0.10	0.50	0.05	0.04	0.05	0.14	0.13	0.56	0.57	0.61	0.06

Analysis no.	Nd	Sm	Eu	Gd	Tb	Dy	Ho	Er	Tm	Yb	Lu	W	Pb208	Th	U
MB80aMt-38	0.09	<0.022	<0.0056	<0.021	<0.0029	<0.0119	0.01	0.00	<0.0027	0.02	<0.0028	0.20	0.64	0.01	0.04
MB80aMt-39	0.03	0.02	0.01	<0.0201	0.00	0.02	<0.0028	0.01	0.00	0.00	<0.00	<0.034	<0.028	<0.00	0.03
MB80aMt-4	0.07	<0.019	0.02	<0.026	0.00	0.02	0.00	<0.0076	0.00	0.01	<0.00	0.57	0.39	<0.0071	0.00
MB80aMt-40	0.01	0.01	0.01	<0.0154	0.00	<0.0085	<0.00	<0.00	<0.00	<0.00	<0.00284	0.37	0.82	0.01	0.02
MB80aMt-5	<0.00	<0.017	0.00	<0.0168	0.00	<0.00	<0.00	<0.00	<0.00	<0.00	<0.00219	0.18	0.48	<0.0054	0.04
MB80aMt-6	0.02	<0.00	<0.0043	<0.0162	0.00	<0.00	0.00	<0.0067	0.00	<0.00	<0.00	0.32	0.62	0.00	<0.0155
MB80aMt-7	0.03	<0.00	<0.0047	<0.036	<0.0041	0.00	0.00	0.02	0.00	0.00	<0.0023	0.24	0.53	0.01	0.01
MB80aMt-8	0.02	<0.017	0.00	<0.024	<0.00	<0.0133	0.00	<0.00	<0.00	0.00	<0.00	0.06	0.42	0.01	0.01
MB80aMt-9	0.04	<0.00	0.00	<0.021	<0.002	<0.00	<0.00	<0.00	<0.00	0.00	<0.00	0.16	0.57	0.01	0.03
MB8HmPlaty-1	0.11	0.08	0.05	0.06	0.02	0.07	0.01	0.07	0.00	0.04	0.00	2.42	3.34	0.11	0.27
MB8HmPlaty-10	0.38	0.13	0.05	0.12	0.02	0.17	0.03	0.08	0.02	0.11	0.02	0.59	1.39	0.04	0.08
MB8HmPlaty-11	1.14	0.27	0.15	0.27	0.05	0.25	0.06	0.24	0.03	0.19	0.04	0.68	36.65	0.12	0.21
MB8HmPlaty-13	0.07	0.03	0.01	0.02	0.00	0.03	0.01	0.02	0.00	0.02	0.01	2.14	0.50	0.03	0.08
MB8HmPlaty-14	0.22	0.06	0.05	0.11	0.02	0.07	0.01	0.06	0.00	0.06	0.00	3.61	16.65	0.35	0.43
MB8HmPlaty-15	0.32	0.06	0.06	0.11	0.02	0.16	0.04	0.12	0.01	0.10	0.02	1.07	0.20	0.07	0.22
MB8HmPlaty-16	0.05	0.01	0.01	0.02	0.00	0.00	<0.00245	0.02	0.00	<0.00	<0.0024	0.17	1.38	0.01	0.10
MB8HmPlaty-17	0.30	0.09	0.04	0.13	0.02	0.07	0.02	0.05	0.01	0.06	0.01	1.19	1.86	0.06	0.33
MB8HmPlaty-18	0.08	0.03	0.01	<0.025	0.01	0.04	0.01	0.01	<0.0023	<0.00	0.00	1.25	5.40	0.11	0.17
MB8HmPlaty-19	0.41	0.11	0.06	0.18	0.03	0.15	0.02	0.07	0.01	0.08	0.01	0.79	0.66	0.06	0.24
MB8HmPlaty-2	1.63	0.25	0.23	0.45	0.07	0.49	0.14	0.36	0.05	0.41	0.08	0.81	1.74	0.06	0.14
MB8HmPlaty-5	0.25	0.05	0.03	0.11	0.01	0.07	0.01	0.05	0.01	0.05	0.01	0.88	5.06	0.07	0.11
MB8HmPlaty-6	0.56	0.13	0.08	0.16	0.02	0.20	0.04	0.15	0.02	0.11	0.02	0.34	2.23	0.07	0.23
MB8HmPlaty-7	0.27	0.07	0.05	0.12	0.01	0.12	0.03	0.10	0.01	0.06	0.01	1.41	0.49	0.08	0.29
MB8HmPlaty-8	1.40	0.22	0.19	0.39	0.05	0.37	0.07	0.31	0.06	0.33	0.07	0.82	5.44	0.05	0.23
MB8HmPlaty-9	0.27	0.10	0.04	0.08	0.01	0.09	0.02	0.07	0.01	0.07	0.01	1.04	5.21	0.12	0.18
MB92aMt-1	0.20	0.03	0.03	0.04	0.01	0.03	0.01	0.06	0.00	0.05	0.01	0.19	0.30	0.01	0.01
MB92aMt-10	0.01	<0.013	0.00	<0.0129	<0.00	0.01	<0.00	0.01	0.00	0.00	0.00	0.02	0.49	0.00	0.22
MB92aMt-11	<0.0115	<0.0133	<0.0048	<0.0186	<0.0018	<0.0073	<0.0018	<0.0055	0.00	0.02	<0.00173	0.07	1.18	0.03	1.19
MB92aMt-12	0.01	<0.00	0.00	<0.018	<0.00171	<0.00	<0.00	0.01	0.00	<0.00	0.00	0.03	0.58	0.01	0.30
MB92aMt-13	0.01	<0.0169	0.00	<0.00	0.00	0.02	0.00	<0.00	<0.00302	0.01	<0.00	0.02	0.27	0.01	0.39
MB92aMt-14	0.01	<0.00	<0.00	0.02	0.00	<0.0074	0.00	0.00	0.00	<0.0081	<0.00176	0.05	0.37	0.01	0.35
MB92aMt-15	0.06	0.02	0.01	0.03	0.00	0.04	0.01	0.02	0.00	0.02	0.00	0.09	0.53	0.03	0.68
MB92aMt-16	0.05	0.01	0.00	<0.023	0.00	0.02	0.01	0.02	0.00	0.01	<0.0031	<0.03	0.24	0.02	0.40
MB92aMt-17	0.29	0.02	0.03	0.03	0.01	0.06	0.02	0.04	0.01	0.09	0.01	0.16	0.29	0.01	0.31
MB92aMt-18	0.22	0.04	0.03	0.03	0.01	0.04	0.02	0.02	0.00	0.03	0.01	0.08	0.26	0.05	0.51
MB92aMt-19	<0.0112	0.01	<0.00	<0.0128	<0.00172	0.00	0.00	0.00	0.00	0.00	<0.00	0.00	0.55	<0.00	<0.00
MB92aMt-2	<0.00	<0.0181	0.00	0.01	0.00	<0.00	<0.00	<0.0053	0.00	<0.0076	0.00	<0.0142	0.05	<0.0052	0.00
MB92aMt-20	0.05	0.01	0.00	0.01	0.00	0.00	0.00	0.01	<0.0015	0.01	0.00	0.02	0.14	<0.00	<0.00
MB92aMt-21	0.13	0.01	0.01	<0.0137	<0.0018	0.02	0.01	0.03	0.00	0.05	0.01	0.05	0.20	0.00	0.02
MB92aMt-25	<0.0129	<0.0149	<0.0038	0.01	0.00	0.00	0.00	0.01	<0.00	0.00	<0.00193	0.04	0.09	<0.00	0.01
MB92aMt-26	0.03	0.01	<0.0035	<0.0136	0.00	<0.0075	<0.00	0.01	0.00	0.01	<0.00178	0.05	0.40	<0.0082	0.01
MB92aMt-27	<0.00	<0.00	<0.00314	<0.017	<0.00	<0.00	<0.00	<0.0071	<0.00	<0.0072	<0.00	0.10	0.85	0.00	0.05
MB92aMt-28	0.20	0.01	0.02	0.04	0.00	0.03	0.01	0.05	0.01	0.03	0.01	0.01	0.11	<0.0056	0.00

Position	Deposit	Lithology	Sample no.	Analysis no.	Texture	Mg	Al	Si	P	Ca	Sc	Ti	V	Cr	Mn
South	Magnet	BIF	MB92a	MB92aMt-3	magnetite	53.08	65.43	<54.23	<4.19	<33.28	<0.067	6.10	2.25	<0.49	520.09
South	Magnet	BIF	MB92a	MB92aMt-30	magnetite	53.49	87.48	60.25	<4.79	<35.58	<0.077	5.23	1.33	<0.48	502.29
South	Magnet	BIF	MB92a	MB92aMt-31	magnetite	93.30	101.29	260.29	8.75	102.62	<0.067	6.54	1.74	<0.55	280.90
South	Magnet	BIF	MB92a	MB92aMt-33	magnetite	101.60	28.79	503.05	10.18	58.75	<0.057	4.94	1.97	<0.57	312.92
South	Magnet	BIF	MB92a	MB92aMt-34	magnetite	189.01	73.64	1422.62	21.55	218.86	<0.074	4.60	1.66	0.88	533.32
South	Magnet	BIF	MB92a	MB92aMt-35	magnetite	176.53	45.60	961.10	37.01	338.14	<0.07	5.51	1.88	0.91	405.09
South	Magnet	BIF	MB92a	MB92aMt-36	magnetite	24.40	40.79	158.96	<5.02	<42.5	<0.073	5.17	1.57	<0.7	257.42
South	Magnet	BIF	MB92a	MB92aMt-37	magnetite	62.31	96.91	110.20	4.74	<29.81	<0.068	4.97	1.46	<0.52	503.99
South	Magnet	BIF	MB92a	MB92aMt-38	magnetite	116.32	63.67	398.86	15.94	48.58	<0.066	5.09	1.71	<0.61	468.26
South	Magnet	BIF	MB92a	MB92aMt-39	magnetite	62.08	21.62	180.64	<4.95	<28.44	<0.068	4.74	1.65	<0.61	286.54
South	Magnet	BIF	MB92a	MB92aMt-4	magnetite	242.74	52.63	2356.03	5.52	109.55	0.10	7.48	2.45	<0.71	353.63
South	Magnet	BIF	MB92a	MB92aMt-40	magnetite	86.50	37.91	282.39	<4.84	<40.35	<0.072	3.00	0.56	<0.55	504.87
South	Magnet	BIF	MB92a	MB92aMt-5	magnetite	116.17	31.54	451.53	32.20	224.97	<0.066	6.96	2.62	<0.64	295.13
South	Magnet	BIF	MB92a	MB92aMt-6	magnetite	81.38	69.46	221.02	<5.07	<49.08	<0.069	7.33	2.51	<0.54	517.94
South	Magnet	BIF	MB92a	MB92aMt-7	magnetite	63.09	50.61	<59.22	<4.6	112.23	<0.082	6.55	2.39	0.55	462.23
South	Magnet	BIF	MB92a	MB92aMt-8	magnetite	60.87	52.65	107.08	4.48	36.36	<0.072	6.77	2.15	<0.59	536.18
South	Magnet	BIF	MB92a	MB92aMt-9	magnetite	52.13	17.45	425.52	<4.57	54.60	0.07	5.69	1.94	<0.61	211.17
South	Magnet	BIF	MB93	MB93Mt-1	magnetite	1791.56	1394.05	379.80	<5.26	52.96	0.26	77.18	4.67	<0.51	878.54
South	Magnet	BIF	MB93	MB93Mt-10	magnetite	1667.57	1736.00	638.30	<3.66	<36.09	0.25	75.66	4.99	0.65	993.89
South	Magnet	BIF	MB93	MB93Mt-11	magnetite	2073.76	1777.78	1040.47	<5.17	<48.65	0.29	85.13	6.86	<0.66	1097.00
South	Magnet	BIF	MB93	MB93Mt-12	magnetite	2056.98	1882.35	957.95	8.03	<42.54	0.35	96.43	6.17	0.67	1220.90
South	Magnet	BIF	MB93	MB93Mt-13	magnetite	1803.41	1786.77	694.53	<4.04	<30.47	0.45	107.72	7.52	<0.46	1037.31
South	Magnet	BIF	MB93	MB93Mt-14	magnetite	2255.45	1734.74	6838.47	<6.32	<53.58	0.35	98.16	4.36	<0.87	610.71
South	Magnet	BIF	MB93	MB93Mt-15	magnetite	1319.62	2294.38	746.56	<5.62	<49.24	0.47	118.90	4.32	<0.64	710.33
South	Magnet	BIF	MB93	MB93Mt-16	magnetite	849.26	1872.25	1207.39	8.14	57.18	0.56	127.44	5.17	<0.66	686.65
South	Magnet	BIF	MB93	MB93Mt-17	magnetite	525.81	1732.60	199.16	16.26	<40.51	0.26	108.34	5.27	<0.47	705.39
South	Magnet	BIF	MB93	MB93Mt-18	magnetite	241.68	1211.95	194.78	<4.42	42.20	0.38	125.32	7.72	2.15	645.71
South	Magnet	BIF	MB93	MB93Mt-19	magnetite	542.51	1284.59	183.16	<4.78	<33.27	0.47	107.62	5.40	2.55	613.98
South	Magnet	BIF	MB93	MB93Mt-2	magnetite	1403.02	1388.41	395.42	7.86	<46.18	0.35	71.45	3.36	<0.45	790.92
South	Magnet	BIF	MB93	MB93Mt-20	magnetite	231.14	1458.81	215.15	<4.33	<31.25	0.47	148.05	8.51	<0.47	647.09
South	Magnet	BIF	MB93	MB93Mt-22	magnetite	827.17	1330.24	1578.50	<4.5	48.24	0.37	127.82	5.31	10.96	633.58
South	Magnet	BIF	MB93	MB93Mt-23	magnetite	569.25	1707.36	258.92	<5.77	<57.56	0.39	129.06	5.08	<0.59	699.54
South	Magnet	BIF	MB93	MB93Mt-24	magnetite	482.21	1784.17	169.17	4.98	74.10	0.50	180.72	4.47	8.08	650.43
South	Magnet	BIF	MB93	MB93Mt-26	magnetite	705.87	1351.20	1762.37	7.02	<53.69	0.31	147.48	8.62	10.75	628.51
South	Magnet	BIF	MB93	MB93Mt-27	magnetite	795.09	1394.74	642.17	12.78	<45.18	0.38	194.33	11.30	8.56	659.93
South	Magnet	BIF	MB93	MB93Mt-29	magnetite	1039.67	2139.88	490.64	8.13	108.04	0.39	211.56	14.35	1.58	886.07
South	Magnet	BIF	MB93	MB93Mt-3	magnetite	2423.05	1278.35	289.37	<4.08	2753.37	0.26	65.13	3.11	0.55	1028.97
South	Magnet	BIF	MB93	MB93Mt-30	magnetite	1401.87	2609.39	346.93	<4.65	<41.53	0.42	219.38	13.15	3.09	1009.54
South	Magnet	BIF	MB93	MB93Mt-31	magnetite	1718.20	1372.79	319.52	7.77	<45.5	0.20	65.79	3.20	1.26	694.68
South	Magnet	BIF	MB93	MB93Mt-32	magnetite	1596.91	1368.48	1174.02	<5.06	<46.15	0.40	70.39	3.21	<0.55	600.42
South	Magnet	BIF	MB93	MB93Mt-33	magnetite	1761.43	1473.54	523.06	6.93	85.31	0.21	110.05	3.25	<0.58	712.32
South	Magnet	BIF	MB93	MB93Mt-34	magnetite	2051.27	1435.62	961.18	4.25	<38.28	0.22	69.49	3.23	0.69	785.98
South	Magnet	BIF	MB93	MB93Mt-35	magnetite	1856.47	1345.04	345.04	4.26	<31.31	0.31	73.30	3.18	<0.45	934.65

Analysis no.	Co	Ni	Cu	Zn	Ga	As	Sr	Y	Zr	Nb	Mo	Sn	Sb	Ba	La	Ce	Pr
MB92aMt-3	0.34	2.25	<0.105	9.85	0.09	0.43	0.01	0.17	<0.0109	0.01	0.05	0.07	<0.0287	0.06	0.09	0.11	0.01
MB92aMt-30	0.53	3.28	<0.126	7.84	0.15	0.23	<0.0065	0.07	<0.0116	0.01	0.05	0.13	0.03	<0.00	0.05	0.07	0.00
MB92aMt-31	0.52	2.59	<0.13	6.16	0.14	0.40	0.02	0.04	0.02	0.01	0.02	<0.071	<0.022	0.11	0.01	0.02	0.00
MB92aMt-33	0.39	3.58	<0.106	5.39	0.06	1.02	0.15	0.34	0.02	0.04	1.41	0.16	0.10	0.53	0.21	0.24	0.03
MB92aMt-34	0.44	2.31	<0.135	10.12	0.09	1.65	0.15	0.47	0.08	0.02	0.09	0.16	0.26	0.78	0.31	0.32	0.04
MB92aMt-35	0.31	2.22	<0.117	7.08	0.15	2.40	0.27	1.47	0.05	0.05	0.19	0.15	0.20	0.59	0.47	0.56	0.05
MB92aMt-36	0.36	3.58	0.14	7.29	0.12	0.26	0.04	0.04	0.04	0.04	0.94	<0.074	<0.029	0.06	0.02	0.02	0.01
MB92aMt-37	0.43	2.38	<0.119	8.89	0.12	<0.153	0.01	0.05	<0.00	0.00	0.06	0.17	<0.025	<0.00	0.02	0.04	0.00
MB92aMt-38	0.55	2.83	<0.121	10.27	0.08	0.91	0.06	0.28	0.02	0.01	0.08	<0.073	0.08	0.08	0.19	0.27	0.02
MB92aMt-39	0.37	2.36	0.18	5.36	0.08	1.10	0.04	0.19	0.02	0.04	0.03	0.12	0.13	0.18	0.16	0.16	0.01
MB92aMt-4	0.34	2.27	<0.114	6.99	0.08	2.01	0.13	0.57	0.07	0.07	<0.031	0.08	0.17	0.41	0.47	0.55	0.05
MB92aMt-40	0.55	0.94	<0.128	9.93	0.09	<0.133	<0.00	0.03	<0.00	0.00	<0.0282	<0.072	0.02	0.17	0.01	0.02	0.00
MB92aMt-5	0.29	1.86	<0.132	6.14	0.05	0.89	0.19	0.79	0.07	0.05	0.03	<0.074	<0.039	0.31	0.59	0.70	0.06
MB92aMt-6	0.40	1.98	<0.117	8.33	0.14	0.15	0.11	0.11	<0.0124	0.00	0.06	0.11	0.04	<0.00	0.03	0.06	0.00
MB92aMt-7	0.31	2.24	<0.109	10.49	0.08	<0.121	0.04	0.10	<0.00	<0.00	0.01	0.10	<0.028	0.06	0.02	0.04	0.00
MB92aMt-8	0.41	1.32	0.18	8.50	0.11	0.40	0.26	0.09	<0.0158	0.00	0.01	<0.074	0.06	1.74	0.03	0.03	0.00
MB92aMt-9	0.25	1.87	<0.089	5.92	0.16	1.04	0.06	0.22	0.03	0.04	0.06	0.08	0.08	0.12	0.29	0.33	0.03
MB93Mt-1	0.85	2.83	<0.109	12.82	1.10	0.87	0.02	0.03	0.03	0.03	0.08	0.70	0.08	<0.00	0.00	0.03	<0.0019
MB93Mt-10	0.77	2.72	<0.065	15.84	1.36	1.38	<0.0053	0.04	0.14	0.06	0.13	0.64	0.04	0.13	0.00	0.08	0.01
MB93Mt-11	0.77	3.04	<0.114	16.61	1.35	2.77	<0.00	0.07	0.13	0.05	0.08	0.76	0.22	0.19	0.01	0.02	0.01
MB93Mt-12	1.03	4.04	<0.126	16.24	1.34	1.56	<0.00	0.06	0.14	0.07	0.06	0.77	0.08	0.34	0.00	0.01	0.00
MB93Mt-13	0.91	3.71	0.11	21.94	1.06	1.44	0.22	0.06	0.15	0.07	0.09	0.79	0.23	0.41	0.04	0.09	0.01
MB93Mt-14	0.60	2.24	0.19	12.71	1.39	0.89	0.16	0.06	0.22	0.14	0.11	0.57	0.03	<0.00	0.02	0.04	0.00
MB93Mt-15	0.65	2.99	<0.109	15.09	1.40	0.28	0.00	0.01	<0.0189	0.01	0.11	0.73	0.01	0.06	0.01	0.02	<0.0023
MB93Mt-16	0.48	2.38	<0.142	7.93	1.19	0.23	0.01	0.01	0.03	0.03	0.10	0.67	<0.032	<0.00	0.01	0.01	<0.00
MB93Mt-17	0.58	3.57	<0.089	13.67	1.33	0.15	0.00	0.01	0.01	0.02	0.10	0.62	0.06	<0.00	0.00	0.01	<0.002
MB93Mt-18	0.47	3.40	<0.105	2.67	1.13	<0.136	0.03	<0.0047	0.03	0.01	0.05	0.21	<0.025	<0.00	<0.00236	0.01	<0.00
MB93Mt-19	0.52	2.94	<0.093	4.69	1.08	<0.133	0.02	0.01	0.02	0.02	0.09	0.32	<0.023	<0.00	0.00	0.02	0.00
MB93Mt-2	0.62	3.33	0.10	13.29	1.43	0.59	0.39	0.03	0.07	0.02	0.05	0.68	0.05	0.42	0.01	0.04	0.01
MB93Mt-20	0.50	2.98	<0.117	10.18	1.10	<0.132	0.01	0.00	0.03	0.02	0.07	0.35	<0.0143	<0.00	<0.00	0.00	<0.00
MB93Mt-22	0.49	2.64	<0.118	4.44	1.22	0.37	0.02	0.01	0.04	0.04	0.09	0.26	0.03	0.71	0.01	0.04	0.00
MB93Mt-23	0.50	2.76	<0.111	5.55	1.32	<0.165	0.01	0.00	<0.00	0.00	0.07	0.63	<0.04	<0.00	0.00	0.00	0.00
MB93Mt-24	0.44	2.92	0.14	11.14	1.27	<0.135	0.01	<0.00	0.01	0.01	0.03	0.60	<0.028	0.05	0.00	0.00	<0.0021
MB93Mt-26	0.54	3.22	<0.119	8.32	1.18	0.69	0.02	0.03	0.10	0.06	0.08	0.35	0.06	0.49	0.02	0.03	0.01
MB93Mt-27	0.63	3.13	0.14	4.20	0.97	1.13	0.01	0.03	<0.0156	0.05	0.09	0.35	<0.021	1.56	0.02	0.03	0.00
MB93Mt-29	0.86	3.21	<0.098	8.82	1.13	0.60	0.20	0.02	0.02	0.10	0.13	0.59	0.27	1.47	0.01	0.02	0.00
MB93Mt-3	0.84	4.82	0.16	5.34	1.17	0.37	0.51	0.16	0.04	0.02	0.14	0.62	0.24	0.29	0.13	0.22	0.03
MB93Mt-30	0.75	3.27	<0.101	24.71	1.18	1.62	0.04	0.07	0.07	0.12	0.09	0.89	0.08	0.52	0.04	0.11	0.02
MB93Mt-31	0.56	3.11	<0.102	11.43	1.30	0.76	0.01	0.02	0.08	0.02	0.13	0.71	<0.029	0.06	0.01	0.03	0.00
MB93Mt-32	0.66	2.98	<0.142	6.66	1.44	0.43	0.01	0.01	<0.0128	0.01	0.08	0.56	<0.029	<0.00	0.01	0.01	0.00
MB93Mt-33	0.59	2.66	<0.111	11.41	1.27	0.86	0.02	0.03	0.07	0.01	0.14	0.56	0.06	0.07	0.01	0.04	0.01
MB93Mt-34	0.53	3.23	<0.114	11.32	1.35	1.41	0.69	0.04	0.10	0.03	0.15	0.59	0.09	1.19	0.02	0.06	0.01
MB93Mt-35	0.64	2.36	<0.112	15.74	1.21	0.59	0.02	0.04	<0.01	0.04	0.07	0.79	0.01	0.18	0.02	0.03	0.00

Analysis no.	Nd	Sm	Eu	Gd	Tb	Dy	Ho	Er	Tm	Yb	Lu	W	Pb208	Th	U
MB92aMt-3	0.04	<0.00	<0.0031	<0.0119	<0.0016	0.02	0.00	0.01	0.00	0.02	<0.0022	0.73	1.05	0.00	0.22
MB92aMt-30	0.02	<0.018	0.00	0.02	0.00	<0.00	0.00	0.00	0.00	0.00	0.00	0.42	0.95	0.01	0.14
MB92aMt-31	<0.00	<0.00	0.00	<0.0127	0.00	<0.0071	<0.00	0.00	<0.00	<0.00	<0.00167	0.59	2.61	0.05	0.23
MB92aMt-33	0.09	0.01	0.01	0.03	0.00	0.01	0.01	0.02	0.00	0.01	0.00	0.30	0.46	0.05	0.06
MB92aMt-34	0.15	0.02	0.01	<0.019	0.00	0.04	0.01	0.02	0.00	0.03	0.00	0.92	0.33	0.01	0.13
MB92aMt-35	0.19	0.02	0.03	0.07	0.01	0.06	0.02	0.05	0.01	0.06	0.01	0.88	1.75	0.03	0.12
MB92aMt-36	0.01	<0.00	0.00	<0.0139	0.00	<0.00	<0.00	<0.0058	<0.00	0.00	<0.0018	0.16	0.88	0.08	0.14
MB92aMt-37	<0.0106	<0.00	0.00	<0.0121	0.00	0.01	0.00	0.01	0.00	<0.0073	0.00	0.01	0.10	<0.0037	0.00
MB92aMt-38	0.09	0.01	0.01	0.01	0.00	<0.0096	0.00	0.01	0.00	0.01	0.00	0.03	0.21	0.00	0.05
MB92aMt-39	0.07	0.02	<0.0048	<0.0131	<0.00	<0.00	0.00	0.01	0.00	0.02	0.00	0.65	0.17	0.01	0.12
MB92aMt-4	0.19	0.03	0.02	0.03	0.01	0.03	0.02	0.06	0.01	0.06	0.01	0.41	0.47	<0.00	0.10
MB92aMt-40	<0.0111	<0.00	<0.0033	<0.00	<0.00171	<0.007	0.00	<0.00	<0.00	0.00	<0.00167	0.76	0.19	<0.00	0.09
MB92aMt-5	0.22	0.04	0.03	0.04	0.01	0.04	0.01	0.03	0.00	0.04	0.00	0.23	0.29	0.01	0.06
MB92aMt-6	0.03	0.01	<0.0035	<0.0192	<0.00182	0.01	<0.0019	0.00	<0.00	0.01	0.00	0.10	1.41	0.01	0.04
MB92aMt-7	0.02	<0.00	<0.00	<0.0133	0.00	0.00	<0.0026	0.01	0.00	<0.008	<0.00	0.29	0.86	0.01	0.05
MB92aMt-8	0.02	0.01	0.00	<0.00	<0.00	0.01	0.00	0.00	0.00	<0.0073	<0.0016	0.18	1.02	0.04	0.06
MB92aMt-9	0.08	<0.0125	0.01	0.01	<0.0029	0.04	0.01	0.01	0.00	0.01	0.01	0.03	17.13	<0.00	0.03
MB93Mt-1	0.04	0.01	0.00	0.01	<0.00168	0.01	<0.00	<0.0052	0.00	<0.0107	<0.00	0.10	0.68	0.01	0.02
MB93Mt-10	0.01	0.01	0.00	0.02	0.00	0.01	<0.00	<0.00	0.00	<0.0064	<0.0014	0.01	0.02	0.00	0.00
MB93Mt-11	0.02	<0.00	<0.0039	<0.0151	<0.002	<0.0084	0.00	0.00	0.00	0.00	0.00	0.01	0.85	0.00	0.00
MB93Mt-12	0.02	0.01	0.01	0.03	0.00	0.00	0.00	0.00	0.00	0.01	0.00	0.00	<0.0126	<0.00	0.00
MB93Mt-13	0.05	0.03	0.00	0.01	<0.00151	0.01	0.00	0.01	0.00	0.01	<0.00	0.57	0.27	0.00	0.02
MB93Mt-14	0.01	0.01	<0.0046	0.02	0.00	0.00	0.00	<0.0074	<0.00	0.00	0.00	0.06	69.84	0.03	0.06
MB93Mt-15	0.00	0.01	<0.0039	0.01	<0.00282	<0.0083	<0.00	<0.00	<0.00	0.00	0.00	0.07	<0.016	<0.0033	0.01
MB93Mt-16	0.01	0.01	<0.0041	<0.0157	<0.0021	<0.0088	0.00	0.00	<0.00	<0.00	0.00	<0.00	0.04	<0.00	<0.00
MB93Mt-17	0.00	<0.0131	<0.0048	0.00	0.00	0.00	0.00	<0.00	<0.00166	0.01	<0.00	0.00	0.16	0.00	0.02
MB93Mt-18	0.01	0.01	<0.0046	<0.0124	<0.00167	<0.00	<0.00	0.00	<0.00	<0.00	<0.00	11.28	29.04	0.29	0.40
MB93Mt-19	0.01	<0.00	<0.0035	0.01	0.00	0.00	0.00	<0.0056	<0.00	<0.00	<0.00178	35.77	10.60	0.07	0.55
MB93Mt-2	0.01	<0.00	0.01	<0.022	<0.00	0.00	0.00	<0.0065	0.00	<0.00	0.00	7.80	7.83	0.10	0.43
MB93Mt-20	0.01	0.01	<0.00313	0.01	<0.0023	0.00	<0.00165	0.00	<0.00154	<0.0073	<0.00	20.24	2.86	0.05	1.37
MB93Mt-22	0.01	<0.00	0.00	0.01	<0.0016	0.01	<0.00	0.00	<0.00	0.01	0.00	13.23	3.40	0.20	0.12
MB93Mt-23	<0.00	<0.00	<0.0039	<0.026	<0.00	<0.00	<0.00	<0.00	<0.00	<0.00	0.00	18.42	8.82	0.19	0.32
MB93Mt-24	<0.0118	0.01	<0.005	<0.00	<0.00	0.00	0.00	<0.00	<0.00	<0.00	0.00	10.92	1.82	0.18	0.18
MB93Mt-26	0.02	0.01	<0.0062	0.01	0.00	0.01	0.00	0.00	0.00	<0.00	<0.00	13.80	2.14	0.40	0.10
MB93Mt-27	0.01	<0.00	<0.00319	0.01	<0.00165	<0.0068	<0.00	0.00	0.00	0.00	<0.0016	13.03	2.61	0.37	0.12
MB93Mt-29	0.02	0.01	<0.0045	0.04	0.00	<0.00	<0.00	<0.00	<0.00156	0.00	<0.00	9.19	3.09	0.22	0.18
MB93Mt-3	0.14	<0.0115	0.03	<0.0161	<0.0015	0.02	0.01	0.02	<0.00146	0.01	0.00	16.55	5.86	0.10	0.15
MB93Mt-30	0.06	0.03	<0.0034	0.02	<0.0025	0.02	0.00	<0.00	0.00	<0.008	0.00	6.84	1.18	0.03	0.12
MB93Mt-31	0.01	<0.0125	<0.00	<0.00	<0.00	0.00	<0.00	<0.00	<0.00	0.00	0.00	15.75	7.51	0.59	0.16
MB93Mt-32	<0.0248	<0.0144	<0.0037	<0.00	0.00	<0.00	<0.00195	0.00	<0.00182	0.01	<0.00	6.46	4.37	0.12	0.47
MB93Mt-33	0.01	<0.00	<0.00324	<0.00	0.00	0.00	0.00	<0.00	<0.00	<0.00	<0.00164	3.57	1.65	0.04	0.36
MB93Mt-34	0.03	<0.00	<0.0031	<0.0166	0.00	0.01	<0.00	0.00	0.00	0.00	<0.00	8.34	10.14	0.30	0.35
MB93Mt-35	0.01	0.01	0.00	<0.00	0.00	<0.0087	<0.00	0.00	<0.00	<0.0067	0.00	5.04	1.82	0.22	0.22

Position	Deposit	Lithology	Sample no.	Analysis no.	Texture	Mg	Al	Si	P	Ca	Sc	Ti	V	Cr	Mn
South	Magnet	BIF	MB93	MB93Mt-36	magnetite	1655.29	1232.98	149.26	10.96	46.38	0.27	74.36	3.30	<0.56	1163.03
South	Magnet	BIF	MB93	MB93Mt-38	magnetite	1710.35	1569.39	285.78	14.41	<38.12	0.10	90.91	4.68	2.34	1039.89
South	Magnet	BIF	MB93	MB93Mt-39	magnetite	1247.08	1464.11	374.93	4.21	<26.3	0.25	92.53	5.14	<0.53	676.79
South	Magnet	BIF	MB93	MB93Mt-4	magnetite	1446.78	1315.61	592.43	5.27	<36.67	0.23	72.64	5.91	5.38	600.21
South	Magnet	BIF	MB93	MB93Mt-40	magnetite	1198.33	1392.59	227.08	11.62	<43.23	0.22	88.06	5.35	1.22	760.54
South	Magnet	BIF	MB93	MB93Mt-5	magnetite	1805.93	1370.23	423.06	<4.15	<36.2	0.15	73.12	5.05	1.64	875.30
South	Magnet	BIF	MB93	MB93Mt-6	magnetite	2567.62	1624.24	1328.50	8.77	<33.26	0.20	73.33	5.84	0.99	969.31
South	Magnet	BIF	MB93	MB93Mt-8	magnetite	1123.56	1631.66	207.11	<4.32	53.74	0.24	83.70	4.53	9.13	727.45
South	Magnet	BIF	MB93	MB93Mt-9	magnetite	1319.90	1567.18	190.61	7.36	<48.74	0.27	75.22	4.03	3.15	644.74
Middle	Warrior	ORE	MB9	MB9Hm-10	porous martite	60.06	161.53	690.37	18.90	<124.94	<0.167	2.09	14.07	<1.17	83.54
Middle	Warrior	ORE	MB9	MB9Hm-11	porous martite	108.23	378.12	713.35	145.02	<85.8	0.76	1.60	15.06	1.87	2290.01
Middle	Warrior	ORE	MB9	MB9Hm-12	porous martite	38.09	141.90	781.25	<11.08	<102.43	<0.167	2.30	9.67	7.16	97.81
Middle	Warrior	ORE	MB9	MB9Hm-13	porous martite	91.73	5611.25	7843.56	82.15	<106.19	0.52	6.20	168.92	14.23	347.36
Middle	Warrior	ORE	MB9	MB9Hm-14	porous martite	60.58	198.41	653.98	<9.05	170.37	<0.146	3.60	23.73	1.70	116.06
Middle	Warrior	ORE	MB9	MB9Hm-15	porous martite	60.89	183.92	761.20	34.86	<87.03	<0.144	1.21	7.99	<1.23	291.77
Middle	Warrior	ORE	MB9	MB9Hm-16	porous martite	20.67	246.23	543.20	129.60	<95.51	0.35	0.81	12.74	<1.17	1034.41
Middle	Warrior	ORE	MB9	MB9Hm-17	porous martite	56.84	123.09	428.96	<9.37	236.37	<0.156	2.24	12.06	<1.32	125.80
Middle	Warrior	ORE	MB9	MB9Hm-18	porous martite	48.76	129.64	619.83	13.19	99.42	<0.147	2.39	16.51	2.09	211.99
Middle	Warrior	ORE	MB9	MB9Hm-19	porous martite	80.82	148.95	761.29	<9.34	<87.31	<0.144	1.69	7.35	<1.14	590.60
Middle	Warrior	ORE	MB9	MB9Hm-2	porous martite	80.56	208.62	835.76	<10.21	<112.04	<0.125	2.66	15.17	<1.01	83.94
Middle	Warrior	ORE	MB9	MB9Hm-20	porous martite	65.00	145.68	524.23	<10.18	332.40	0.17	1.50	5.69	1.55	141.05
Middle	Warrior	ORE	MB9	MB9Hm-3	porous martite	51.10	122.05	397.19	13.10	<111.46	<0.147	4.18	7.00	<1.05	139.24
Middle	Warrior	ORE	MB9	MB9Hm-4	porous martite	44.65	86.58	750.76	11.36	<84.75	<0.128	12.68	10.86	1.04	55.66
Middle	Warrior	ORE	MB9	MB9Hm-5	porous martite	56.09	169.95	619.15	<9.2	<90.88	0.14	1.60	27.63	<0.98	80.43
Middle	Warrior	ORE	MB9	MB9Hm-6	porous martite	49.36	261.98	871.32	80.51	<111.35	0.40	2.72	10.24	<1.11	829.73
Middle	Warrior	ORE	MB9	MB9Hm-7	porous martite	33.50	97.44	584.06	<9.7	<115.78	<0.144	2.28	11.38	<1.23	127.73
Middle	Warrior	ORE	MB9	MB9Hm-8	porous martite	181.18	5886.25	8031.20	196.99	269.56	0.72	5.57	338.06	19.97	699.17
Middle	Warrior	ORE	MB9	MB9Hm-9	porous martite	53.77	136.99	650.47	26.66	<78.72	<0.138	1.37	13.61	2.41	124.69
Middle	Warrior	ORE	MB9	MB9Mg-1	magnetite	15.33	66.90	1548.87	<11.79	<108.41	<0.149	2.41	2.55	<1.2	298.94
Middle	Warrior	ORE	MB9	MB9Mg-10	magnetite	262.04	80.32	1296.39	18.96	289.31	<0.17	2.55	2.70	<1.41	569.09
Middle	Warrior	ORE	MB9	MB9Mg-11	magnetite	27.31	78.04	555.82	<10.3	<98.21	<0.144	2.61	1.90	<1.34	202.66
Middle	Warrior	ORE	MB9	MB9Mg-12	magnetite	39.87	72.26	479.67	14.56	<110.56	<0.148	4.68	1.53	3.49	350.90
Middle	Warrior	ORE	MB9	MB9Mg-13	magnetite	43.74	78.65	1080.71	<10.47	<96.02	<0.155	3.47	1.95	1.59	254.56
Middle	Warrior	ORE	MB9	MB9Mg-14	magnetite	73.16	71.89	417.20	<10.06	<118.1	<0.161	2.72	2.72	<1.22	315.49
Middle	Warrior	ORE	MB9	MB9Mg-15	magnetite	363.84	74.58	276.89	<11.05	<126.77	0.25	1.99	1.65	<1.51	496.00
Middle	Warrior	ORE	MB9	MB9Mg-16	magnetite	80.85	77.97	438.00	<10.27	<94.28	<0.169	3.59	1.74	<1.31	235.06
Middle	Warrior	ORE	MB9	MB9Mg-17	magnetite	63.53	72.44	<176.97	<10.63	<96.36	<0.173	2.72	1.81	<1.43	325.37
Middle	Warrior	ORE	MB9	MB9Mg-18	magnetite	42.43	74.70	798.83	14.89	<78.24	<0.167	3.01	1.71	<1.42	327.15
Middle	Warrior	ORE	MB9	MB9Mg-19	magnetite	20.18	76.79	238.27	<10.44	<98.64	<0.156	4.82	4.75	<1.25	258.25
Middle	Warrior	ORE	MB9	MB9Mg-2	magnetite	219.01	76.14	860.85	<11.82	<130.05	<0.164	2.33	1.55	1.33	612.86
Middle	Warrior	ORE	MB9	MB9Mg-20	magnetite	95.63	94.17	563.02	<11.82	<108.47	<0.187	3.55	21.03	<1.35	274.16
Middle	Warrior	ORE	MB9	MB9Mg-3	magnetite	61.83	72.77	816.21	12.27	<134.07	<0.16	1.72	3.61	1.66	179.94
Middle	Warrior	ORE	MB9	MB9Mg-4	magnetite	241.98	68.94	1895.39	<10.82	<109.52	<0.136	2.35	2.66	<1.15	558.65

Analysis no.	Co	Ni	Cu	Zn	Ga	As	Sr	Y	Zr	Nb	Mo	Sn	Sb	Ba	La	Ce	Pr
MB93Mt-36	0.77	2.99	0.12	18.33	1.37	0.48	<0.00	0.01	0.09	0.04	0.06	0.62	<0.029	0.25	0.01	0.01	0.00
MB93Mt-38	0.66	2.93	0.13	22.40	1.34	1.04	0.18	0.03	0.03	0.04	0.07	0.78	<0.025	0.07	0.02	0.06	0.00
MB93Mt-39	0.56	2.83	<0.095	9.48	1.21	1.26	<0.00	0.03	0.09	0.03	0.12	0.66	0.07	0.31	0.03	0.07	0.01
MB93Mt-4	0.46	2.63	0.11	7.78	1.32	0.85	0.17	0.02	<0.0155	0.04	0.11	0.59	<0.029	0.19	0.01	0.01	<0.0026
MB93Mt-40	0.66	2.93	<0.119	12.32	1.26	0.54	0.01	0.03	0.10	0.03	0.20	0.61	0.06	0.09	0.01	0.04	0.01
MB93Mt-5	0.58	2.99	<0.085	16.11	1.16	0.75	0.01	0.01	0.05	0.05	0.15	0.68	<0.028	0.06	0.01	0.04	0.01
MB93Mt-6	0.86	3.18	<0.121	14.33	1.42	0.65	0.01	0.02	0.13	0.05	0.11	0.74	0.05	0.18	0.01	0.01	0.00
MB93Mt-8	0.46	2.57	<0.077	5.93	1.12	<0.093	<0.00	<0.0034	<0.00	<0.00	0.12	0.77	<0.026	<0.00	<0.00241	<0.00	<0.00194
MB93Mt-9	0.82	4.59	0.80	8.14	1.24	0.39	0.00	<0.0038	0.02	0.00	0.16	0.78	<0.029	<0.00	0.00	0.00	<0.00
MB9Hm-10	0.71	1.34	19.22	57.99	0.19	5.09	0.42	0.82	0.01	0.00	<0.046	<0.214	0.82	1.44	0.22	0.45	0.03
MB9Hm-11	4.75	2.95	9.21	32.75	0.53	26.39	1.92	4.24	<0.00	<0.00	0.19	0.27	<0.058	3.69	1.99	6.90	0.75
MB9Hm-12	1.04	2.15	7.36	37.86	0.13	7.94	0.73	0.88	<0.0257	0.01	0.10	<0.22	1.60	0.53	0.14	0.47	0.06
MB9Hm-13	0.64	5.12	8.91	75.53	0.90	9.51	0.53	1.86	0.10	0.07	0.13	0.47	1.31	2.66	0.58	1.33	0.13
MB9Hm-14	0.45	2.77	10.29	56.51	0.25	9.25	0.90	2.06	0.01	0.02	0.05	0.23	1.60	1.48	0.66	1.38	0.13
MB9Hm-15	0.68	1.34	11.25	47.11	0.32	11.95	0.61	1.39	0.05	<0.00	0.10	<0.178	0.87	1.57	0.44	0.87	0.11
MB9Hm-16	3.04	2.79	4.50	18.10	0.51	18.96	0.51	3.17	0.01	0.00	0.07	0.47	0.30	1.39	1.28	2.49	0.43
MB9Hm-17	0.57	2.28	8.33	43.42	0.37	10.75	0.56	1.93	0.03	0.01	0.09	<0.198	1.43	0.86	0.55	1.02	0.12
MB9Hm-18	0.64	1.77	<0.25	31.23	0.48	8.92	0.36	1.62	0.06	0.01	<0.075	<0.22	1.05	2.34	0.63	0.88	0.08
MB9Hm-19	0.58	1.14	5.89	34.16	0.23	6.23	0.96	2.08	0.10	0.02	0.03	<0.186	1.02	2.22	0.66	0.90	0.13
MB9Hm-2	1.17	1.95	21.65	63.86	0.27	6.56	0.78	0.73	0.08	0.00	0.07	<0.18	0.63	1.71	0.24	0.52	0.05
MB9Hm-20	1.40	1.55	1.86	55.41	0.25	5.61	0.65	0.50	<0.0232	0.00	0.07	0.25	1.00	0.72	0.13	0.30	0.03
MB9Hm-3	0.83	1.63	5.12	30.74	0.31	7.55	0.48	1.08	<0.023	0.02	0.12	<0.19	1.67	1.07	0.33	0.70	0.08
MB9Hm-4	0.30	1.07	0.19	24.27	0.14	3.25	0.47	0.55	0.04	0.00	<0.037	0.22	0.47	0.70	0.21	0.27	0.03
MB9Hm-5	0.86	1.50	7.60	54.75	0.34	5.87	0.75	1.59	0.03	0.00	0.08	<0.183	1.14	0.72	0.44	0.87	0.09
MB9Hm-6	2.07	1.30	11.54	40.37	0.24	17.56	0.53	2.61	<0.0236	<0.00	0.03	<0.191	0.69	2.03	1.02	3.21	0.35
MB9Hm-7	0.79	1.39	1.23	24.17	0.19	6.41	0.50	2.00	0.03	0.01	0.05	<0.217	1.08	0.47	0.60	1.12	0.12
MB9Hm-8	0.82	5.88	15.21	101.11	1.18	13.83	0.88	3.13	0.35	0.07	0.18	0.40	1.82	3.14	0.84	2.05	0.31
MB9Hm-9	2.54	1.14	1.74	53.14	0.20	7.78	0.54	0.91	<0.00	0.01	0.08	<0.19	1.15	0.45	0.25	0.53	0.05
MB9Mg-1	1.59	0.84	0.31	9.10	0.24	1.06	0.07	0.05	<0.043	<0.00	<0.043	<0.192	0.16	<0.00	0.04	0.06	0.01
MB9Mg-10	2.20	0.76	<0.25	8.42	0.24	2.90	0.09	0.23	0.06	0.02	0.03	<0.209	<0.104	0.49	0.16	0.21	0.02
MB9Mg-11	2.56	0.70	<0.22	9.53	0.16	1.20	0.05	0.10	0.02	<0.00	0.03	0.27	<0.094	<0.00	0.04	0.04	0.00
MB9Mg-12	3.01	1.20	<0.21	8.60	0.15	1.10	0.03	0.15	<0.024	<0.00	0.01	0.30	0.17	0.25	0.08	0.12	0.01
MB9Mg-13	3.65	1.06	<0.258	8.46	0.21	1.44	0.03	0.14	0.01	<0.0103	0.04	0.23	<0.084	0.16	0.05	0.06	0.01
MB9Mg-14	2.43	1.02	0.27	11.93	0.34	2.09	0.18	0.20	0.01	<0.00	<0.045	<0.208	0.34	0.40	0.07	0.12	0.01
MB9Mg-15	5.06	2.07	<0.26	8.87	0.23	1.72	0.03	0.23	<0.026	0.01	<0.045	<0.222	<0.101	0.70	0.09	0.16	0.03
MB9Mg-16	1.73	1.43	<0.25	9.51	0.13	1.91	0.04	0.12	0.05	<0.00	<0.044	0.24	<0.087	0.78	0.05	0.09	0.01
MB9Mg-17	3.67	1.42	<0.23	4.66	0.13	0.61	0.02	0.05	0.01	<0.00	0.03	0.26	<0.088	0.40	0.03	0.01	<0.0043
MB9Mg-18	1.61	1.41	<0.236	7.74	0.13	0.82	0.01	0.09	0.08	<0.00	<0.045	<0.222	<0.067	0.14	0.06	0.09	0.01
MB9Mg-19	4.42	1.16	<0.25	12.44	0.24	2.40	0.04	0.37	<0.00	0.00	0.05	<0.217	0.23	0.38	0.15	0.26	0.04
MB9Mg-2	4.86	1.89	<0.25	7.57	0.26	1.40	0.01	0.34	0.08	0.01	0.03	<0.201	<0.076	0.22	0.20	0.41	0.04
MB9Mg-20	3.70	1.21	<0.27	16.52	0.30	3.44	0.11	0.46	0.05	0.02	0.03	<0.24	0.31	0.32	0.18	0.27	0.04
MB9Mg-3	2.23	1.06	<0.25	12.43	0.20	2.31	0.09	0.80	<0.00	0.02	<0.045	<0.199	0.17	0.52	0.17	0.26	0.03
MB9Mg-4	2.74	1.34	<0.223	7.37	0.17	2.43	0.04	0.45	0.04	0.01	<0.042	0.30	0.17	0.87	0.26	0.39	0.03

Analysis no.	Nd	Sm	Eu	Gd	Tb	Dy	Ho	Er	Tm	Yb	Lu	W	Pb208	Th	U
MB93Mt-36	0.02	<0.0122	<0.00	<0.012	0.00	<0.00	<0.00	<0.00	<0.00	<0.00	0.00	6.52	2.26	0.05	0.44
MB93Mt-38	<0.00	<0.00	<0.00314	0.01	0.00	<0.00	0.00	<0.00	0.00	<0.0073	<0.00159	<0.00	0.11	<0.00	<0.00
MB93Mt-39	0.03	0.01	0.00	<0.0111	<0.0026	0.01	0.00	0.00	<0.00	<0.00	<0.00146	0.43	0.30	0.00	0.04
MB93Mt-4	0.01	0.01	<0.0055	<0.0122	<0.00	<0.00	<0.00	0.00	<0.00	0.00	0.00	<0.0099	0.05	<0.0036	0.01
MB93Mt-40	0.01	0.01	0.00	<0.0146	<0.00196	0.01	0.00	0.00	<0.00	0.00	<0.00	0.91	0.61	<0.00	0.05
MB93Mt-5	<0.0101	0.01	<0.00	<0.00	<0.00156	<0.00	<0.00	<0.00	0.00	<0.0122	<0.00154	<0.00	0.04	<0.00	0.00
MB93Mt-6	0.03	<0.0125	0.00	<0.00	0.00	<0.0069	<0.00	<0.00	<0.00	0.00	<0.00	0.01	0.32	0.01	0.26
MB93Mt-8	0.01	<0.0128	<0.0057	<0.0178	0.00	<0.007	<0.00	<0.0053	0.00	<0.0076	0.00	0.02	0.13	<0.00	0.00
MB93Mt-9	<0.00	<0.00	<0.00	<0.00	<0.0027	<0.00	<0.00197	<0.00	<0.00	<0.0087	<0.00	0.03	0.06	<0.00	0.02
MB9Hm-10	0.19	0.06	0.04	0.12	0.01	0.15	0.02	0.09	0.01	0.06	0.02	0.15	11.53	0.00	0.15
MB9Hm-11	3.85	0.95	0.40	1.13	0.16	0.94	0.17	0.56	0.10	0.45	0.06	0.14	42.27	0.01	0.42
MB9Hm-12	0.25	0.07	0.05	0.07	0.01	0.16	0.03	0.09	0.02	0.07	0.01	0.16	12.17	0.01	0.15
MB9Hm-13	0.71	0.22	0.09	0.28	0.05	0.24	0.06	0.18	0.03	0.15	0.03	1.17	18.78	0.02	0.68
MB9Hm-14	0.52	0.21	0.11	0.33	0.03	0.35	0.06	0.16	0.04	0.27	0.03	0.51	15.97	0.01	0.28
MB9Hm-15	0.60	0.15	0.10	0.23	0.04	0.21	0.05	0.13	0.02	0.12	0.02	0.11	17.81	0.00	0.19
MB9Hm-16	2.03	0.46	0.25	0.54	0.11	0.66	0.13	0.34	0.04	0.34	0.04	0.25	28.14	<0.00	0.24
MB9Hm-17	0.49	0.14	0.09	0.22	0.03	0.26	0.06	0.13	0.03	0.19	0.03	0.61	9.50	0.02	0.17
MB9Hm-18	0.46	0.07	0.07	0.20	0.02	0.19	0.04	0.11	0.03	0.18	0.03	0.46	10.30	0.01	0.22
MB9Hm-19	0.61	0.22	0.08	0.19	0.05	0.27	0.06	0.16	0.02	0.14	0.02	1.03	10.81	0.00	0.13
MB9Hm-2	0.26	0.04	0.04	0.06	0.01	0.12	0.01	0.08	0.01	0.10	0.01	0.35	13.01	0.02	0.10
MB9Hm-20	0.10	0.07	0.03	0.06	0.00	0.06	0.01	0.06	0.01	0.08	0.00	0.07	11.13	0.00	0.05
MB9Hm-3	0.39	0.14	0.07	0.13	0.02	0.22	0.05	0.07	0.02	0.09	0.01	0.21	9.69	0.02	0.08
MB9Hm-4	0.17	0.03	0.02	<0.032	0.00	0.05	0.02	0.06	0.01	0.07	0.01	0.22	2.88	0.00	0.06
MB9Hm-5	0.36	0.10	0.08	0.14	0.03	0.18	0.03	0.15	0.02	0.13	0.02	0.17	13.66	0.01	0.24
MB9Hm-6	1.86	0.47	0.18	0.55	0.07	0.61	0.12	0.26	0.05	0.24	0.03	0.17	23.69	0.02	0.26
MB9Hm-7	0.50	0.11	0.08	0.23	0.02	0.21	0.07	0.18	0.02	0.20	0.03	0.31	6.47	0.01	0.12
MB9Hm-8	1.50	0.48	0.18	0.41	0.06	0.55	0.12	0.35	0.06	0.27	0.05	1.59	20.77	0.03	1.44
MB9Hm-9	0.29	0.08	0.07	0.12	0.02	0.22	0.03	0.08	0.01	0.08	0.01	0.21	6.83	0.01	0.13
MB9Mg-1	0.03	0.01	0.00	0.02	<0.0051	0.01	<0.0037	0.00	0.00	0.00	<0.0035	0.13	0.29	0.28	0.00
MB9Mg-10	0.08	0.03	0.01	<0.00	0.00	0.01	0.01	0.02	0.01	0.02	0.00	0.03	0.10	0.00	<0.00
MB9Mg-11	0.03	0.03	0.00	<0.0249	<0.0033	<0.0137	0.00	<0.00	0.00	<0.00	0.00	0.33	0.47	0.00	0.02
MB9Mg-12	0.02	0.03	<0.0097	<0.038	0.00	0.01	<0.0036	0.02	0.00	0.01	0.00	0.04	0.16	0.00	0.00
MB9Mg-13	0.06	<0.00	0.00	0.01	<0.0038	0.01	0.00	0.00	<0.00	0.01	<0.0037	<0.0091	0.11	0.01	0.00
MB9Mg-14	0.10	<0.00	<0.0072	0.02	0.01	0.01	0.01	<0.0115	<0.00	0.01	<0.01	0.00	<0.022	<0.00	0.00
MB9Mg-15	0.07	0.02	0.03	0.03	<0.0065	0.02	0.00	0.02	0.01	<0.0167	0.00	0.00	0.11	<0.004	<0.00204
MB9Mg-16	0.06	<0.0274	0.02	<0.00	0.00	0.01	0.00	0.03	0.00	<0.00	0.00	<0.00	0.01	<0.00	<0.00
MB9Mg-17	<0.00	<0.00	<0.0072	<0.03	<0.00	0.00	0.00	<0.0115	0.00	<0.00	<0.00	0.01	0.02	0.00	0.01
MB9Mg-18	<0.024	0.02	<0.0073	0.02	<0.0038	0.01	0.00	0.01	<0.00	0.00	<0.0037	0.12	0.45	<0.00	0.02
MB9Mg-19	0.16	0.05	0.04	0.07	0.00	0.07	0.01	0.02	0.01	0.03	0.01	0.03	0.13	0.00	0.01
MB9Mg-2	0.15	0.03	0.02	0.06	<0.0035	0.02	0.01	0.02	<0.00	0.01	0.00	0.18	0.30	0.02	0.01
MB9Mg-20	0.17	0.04	0.02	0.03	0.01	0.04	0.01	0.03	0.00	0.06	0.01	0.12	0.65	0.01	0.02
MB9Mg-3	0.16	<0.028	0.03	0.07	0.01	0.04	0.01	0.04	0.01	0.02	0.01	3.15	0.17	0.00	0.00
MB9Mg-4	0.10	0.01	0.03	0.07	0.01	0.04	<0.0035	0.02	0.00	0.01	0.00	0.09	0.34	0.01	0.02

Position	Deposit	Lithology	Sample no.	Analysis no.	Texture	Mg	Al	Si	P	Ca	Sc	Ti	V	Cr	Mn
Middle	Warrior	ORE	MB9	MB9Mg-5	magnetite	99.72	72.95	1038.44	18.74	<95.36	0.19	2.89	3.13	<1.3	397.04
Middle	Warrior	ORE	MB9	MB9Mg-6	magnetite	24.74	61.43	420.11	<10.94	<113.77	<0.162	2.02	2.74	1.87	355.99
Middle	Warrior	ORE	MB9	MB9Mg-7	magnetite	51.44	79.00	187.34	<11.57	365.83	<0.173	2.37	2.21	<1.13	293.35
Middle	Warrior	ORE	MB9	MB9Mg-8	magnetite	25.89	105.70	447.60	<10.87	<103.09	0.16	1.78	39.70	2.49	156.06
Middle	Warrior	ORE	MB9	MB9Mg-9	magnetite	265.55	70.50	996.29	12.56	<99.43	<0.151	1.72	1.35	<1.24	548.06
Middle	Warrior	ORE	MB10	MB10ClastHm-1	clean martite	60.77	165.23	1929.84	127.45	137.45	0.11	2.72	9.74	0.92	310.67
Middle	Warrior	ORE	MB10	MB10ClastHm-2	clean martite	65.30	127.98	1568.59	96.96	<122.73	<0.07	2.55	2.98	0.78	240.62
Middle	Warrior	ORE	MB10	MB10ClastHm-3	clean martite	65.46	161.30	1554.74	88.81	144.88	<0.053	1.78	5.48	<0.53	246.71
Middle	Warrior	ORE	MB10	MB10ClastHm-4	clean martite	57.51	213.17	1472.46	92.79	150.84	<0.101	3.43	12.13	0.79	245.91
Middle	Warrior	ORE	MB10	MB10ClastHm-5	clean martite	189.14	513.87	889.55	17.79	<151.74	0.13	1.43	33.67	1.16	187.77
Middle	Warrior	ORE	MB10	MB10ClastHm-6	clean martite	91.73	576.83	1110.11	18.36	<133.77	0.11	1.06	34.69	1.88	279.05
Middle	Warrior	ORE	MB10	MB10ClastHm-7	clean martite	76.83	432.59	1191.63	16.83	<123.49	<0.081	1.69	37.82	2.14	301.61
Middle	Warrior	ORE	MB10	MB10ClastHm-8	clean martite	46.25	438.99	1024.77	11.07	<105.59	<0.098	1.84	45.23	2.13	339.21
Middle	Warrior	ORE	MB10	MB10Hm-1	clean martite	104.59	296.88	2212.14	49.65	124.03	0.13	5.67	20.74	4.22	268.90
Middle	Warrior	ORE	MB10	MB10Hm-2	clean martite	106.76	402.02	1977.10	30.53	<119.37	<0.091	4.25	30.26	5.11	361.66
Middle	Warrior	ORE	MB10	MB10Hm-3	clean martite	84.71	456.99	1278.55	25.54	132.08	<0.064	3.30	9.99	1.98	183.11
Middle	Warrior	ORE	MB10	MB10Hm-4	clean martite	83.26	438.83	1399.42	42.23	<135.12	0.08	24.43	60.27	1.91	449.54
Middle	Warrior	ORE	MB10	MB10Hm-5	clean martite	120.13	586.21	1731.10	53.54	164.10	0.12	19.34	27.07	7.05	513.35
Middle	Warrior	ORE	MB10	MB10Hm-6	clean martite	39.78	136.33	3337.83	62.27	110.22	<0.075	3.22	5.64	1.10	65.15
Middle	Warrior	ORE	MB10	MB10Hm-7	clean martite	9.54	518.03	2494.61	172.54	148.01	<0.063	0.70	0.54	0.84	26.60
Middle	Warrior	ORE	MB10	MB10Hm-8	clean martite	40.02	121.63	1122.52	425.01	238.09	<0.077	3.47	5.45	0.76	112.13
Middle	Warrior	ORE	MB10	MB10Mt-1	magnetite	71.48	118.33	346.97	7.66	167.85	<0.082	1.93	0.31	0.87	254.67
Middle	Warrior	ORE	MB10	MB10Mt-2	magnetite	52.34	114.61	396.67	9.47	<84.79	<0.101	2.32	0.28	0.65	323.44
Middle	Warrior	ORE	MB10	MB10Mt-3	magnetite	38.39	119.65	355.98	8.13	<120.77	<0.053	2.04	0.42	0.95	303.95
Middle	Warrior	ORE	MB10	MB10Mt-4	magnetite	56.45	118.21	442.58	15.09	<96.03	<0.082	1.36	0.41	0.73	279.54
Middle	Warrior	ORE	MB10	MB10Mt-5	magnetite	46.20	144.14	684.29	32.98	<123.6	<0.087	1.12	1.79	<0.63	262.96
Middle	Warrior	ORE	MB10	MB10Mt-6	magnetite	125.23	120.97	398.96	14.19	<109.57	0.13	2.02	0.47	0.58	194.96
Middle	Warrior	ORE	MB10	MB10Mt-7	magnetite	42.99	120.94	664.62	26.37	135.66	<0.067	1.89	0.96	0.93	282.09
Middle	Camel Hills	BIF	MB13	MB13Hmclean-1	clean martite	16.15	60.19	7411.12	24.53	131.54	0.07	2.75	2.47	<0.24	4.19
Middle	Camel Hills	BIF	MB13	MB13Hmclean-2	clean martite	14.95	53.44	12836.45	58.49	<110.52	0.08	17.72	3.70	0.43	15.76
Middle	Camel Hills	BIF	MB13	MB13Hmclean-3	clean martite	1.43	44.31	9535.31	24.36	<114.61	<0.043	1.64	2.12	<0.25	3.78
Middle	Camel Hills	BIF	MB13	MB13Hmclean-4	clean martite	84.51	223.35	3681.74	138.69	236.47	0.38	6.76	4.77	0.75	48.44
Middle	Camel Hills	BIF	MB13	MB13Hmclean-5	clean martite	4.75	17.94	397.97	25.91	236.37	<0.037	0.87	1.63	0.42	3.49
Middle	Camel Hills	BIF	MB13	MB13Hmclean-6	clean martite	37.00	134.56	2143.06	106.53	163.30	0.10	6.65	3.50	0.61	19.88
Middle	Camel Hills	BIF	MB13	MB13Hmclean-7	clean martite	6.72	12.78	336.78	41.99	412.08	<0.041	1.53	2.21	<0.23	1.78
Middle	Camel Hills	BIF	MB13	MB13Hmclean-8	clean martite	1.17	13.00	323.90	21.55	257.43	<0.037	1.72	1.96	<0.23	2.72
Middle	Camel Hills	BIF	MB13	MB13Hmdirty-1	porous martite	212.44	554.50	19949.11	452.26	343.94	1.03	21.76	17.84	2.21	376.58
Middle	Camel Hills	BIF	MB13	MB13Hmdirty-2	porous martite	66.36	341.99	3540.50	420.58	428.28	0.43	11.65	5.01	1.19	302.44
Middle	Camel Hills	BIF	MB13	MB13Hmdirty-3	porous martite	98.87	609.02	20942.46	289.79	212.50	0.43	11.50	7.62	0.65	387.18
Middle	Camel Hills	BIF	MB13	MB13Hmdirty-4	porous martite	60.63	166.56	4155.70	551.24	399.81	0.28	5.34	4.34	0.80	407.95
Middle	Camel Hills	BIF	MB13	MB13Hmdirty-6	porous martite	52.64	211.84	28515.35	461.91	<159.36	0.50	7.61	6.63	1.11	340.14
Middle	Camel Hills	BIF	MB13	MB13Hmdirty-7	porous martite	68.36	180.69	6223.58	527.81	<156.91	0.36	5.62	5.48	0.66	413.84
Middle	Camel Hills	ORE	MB14	MB14Hm-1	porous martite	420.50	8090.98	2113.76	217.95	<945.23	1.13	7488.51	206.48	212.49	4411.46

Analysis no.	Co	Ni	Cu	Zn	Ga	As	Sr	Y	Zr	Nb	Mo	Sn	Sb	Ba	La	Ce	Pr
MB9Mg-5	5.14	0.69	0.84	9.76	0.14	3.77	0.06	0.33	0.11	0.01	<0.059	0.22	0.15	0.74	0.13	0.21	0.02
MB9Mg-6	2.10	0.69	<0.209	9.31	0.20	1.64	0.03	0.12	0.01	<0.00	<0.043	<0.209	<0.105	0.12	0.06	0.10	0.01
MB9Mg-7	3.75	0.88	<0.28	7.83	0.17	3.38	0.07	0.26	0.04	0.00	<0.045	<0.208	0.23	0.85	0.14	0.26	0.03
MB9Mg-8	2.06	2.33	<0.25	18.81	0.23	2.78	0.29	0.61	0.07	<0.0098	0.05	<0.214	0.79	0.64	0.19	0.34	0.04
MB9Mg-9	2.36	1.70	<0.231	6.30	0.23	1.55	0.03	0.23	0.03	0.02	<0.038	<0.186	<0.095	0.42	0.13	0.19	0.02
MB10ClastHm-1	0.78	2.46	3.15	21.14	0.70	4.72	0.55	4.05	<0.00	0.02	0.26	0.23	2.49	2.30	0.68	0.83	0.07
MB10ClastHm-2	0.53	0.49	0.62	11.90	0.48	2.78	0.56	3.20	0.05	0.03	0.14	0.43	1.57	1.90	0.50	0.64	0.06
MB10ClastHm-3	0.60	1.80	<0.54	20.49	0.72	2.61	0.48	2.86	0.05	0.01	0.08	0.41	1.87	2.69	0.44	0.58	0.06
MB10ClastHm-4	0.76	2.47	0.62	13.02	0.77	5.50	0.59	2.69	0.21	0.09	0.20	0.42	2.51	3.99	0.63	0.86	0.09
MB10ClastHm-5	1.00	3.52	1.05	10.61	0.29	1.88	0.31	0.22	0.23	0.03	0.17	0.40	1.18	4.99	0.13	0.21	0.01
MB10ClastHm-6	1.44	6.95	2.79	21.57	0.61	3.34	0.35	0.48	0.21	0.04	0.15	0.39	1.71	4.37	0.20	0.31	0.02
MB10ClastHm-7	1.05	7.61	3.45	30.64	0.88	6.01	0.58	0.60	0.18	0.01	0.08	0.26	3.65	7.19	0.22	0.43	0.03
MB10ClastHm-8	1.15	7.14	0.59	21.97	0.50	3.54	0.29	0.39	0.24	0.01	0.07	0.32	2.77	8.53	0.18	0.33	0.01
MB10Hm-1	1.18	6.25	<0.44	41.78	0.56	6.80	0.88	0.88	0.41	0.04	0.17	0.71	7.20	4.83	0.26	0.34	0.02
MB10Hm-2	1.98	12.61	<0.49	50.94	0.62	6.57	0.85	0.90	0.41	0.08	0.16	0.79	9.67	6.85	0.20	0.32	0.03
MB10Hm-3	2.16	2.60	6.35	35.28	0.70	7.30	0.68	1.11	0.10	0.01	0.05	0.31	2.75	5.69	0.28	0.50	0.06
MB10Hm-4	1.12	10.97	0.91	37.55	0.59	4.21	0.61	1.84	<0.068	0.03	0.08	0.85	13.17	4.83	0.68	0.76	0.04
MB10Hm-5	1.17	10.27	2.17	45.26	0.58	3.96	0.58	2.27	0.24	0.10	0.23	0.80	7.18	5.90	0.85	1.06	0.05
MB10Hm-6	0.13	0.77	2.95	15.80	0.44	10.15	0.18	3.06	0.16	0.01	0.02	0.47	0.94	0.73	0.23	0.37	0.05
MB10Hm-7	0.44	0.26	2.93	44.80	0.32	4.97	0.08	2.81	<0.00	<0.00	0.01	0.39	0.31	0.41	0.25	0.46	0.04
MB10Hm-8	0.60	1.24	2.26	16.98	0.68	4.71	0.58	1.65	0.07	<0.00	0.03	0.44	1.41	1.28	0.29	0.49	0.06
MB10Mt-1	0.61	0.59	0.72	5.47	0.09	0.62	0.02	<0.0186	<0.00	<0.00	0.02	0.56	<0.31	<0.00	0.04	0.01	<0.00
MB10Mt-2	1.42	0.69	<0.32	17.01	0.12	<0.55	0.05	0.04	<0.00	<0.00	<0.049	0.25	<0.32	<0.00	0.02	0.01	0.00
MB10Mt-3	1.91	0.97	<0.39	3.52	0.30	<0.58	<0.00	0.02	0.03	<0.00	0.05	0.26	<0.27	0.77	0.01	0.02	<0.0069
MB10Mt-4	1.91	0.69	0.42	3.30	0.15	<0.55	<0.00	<0.0132	0.03	0.01	<0.00	0.46	<0.26	<0.00	0.01	0.01	0.01
MB10Mt-5	1.39	1.04	<0.4	8.09	0.38	1.69	0.15	0.26	<0.00	<0.00	0.02	0.19	0.59	2.16	0.11	0.21	0.01
MB10Mt-6	0.37	0.89	<0.39	2.43	0.12	<0.53	<0.00	0.02	<0.00	<0.0162	0.02	0.25	<0.28	<0.00	<0.0096	0.00	<0.00
MB10Mt-7	2.08	0.72	<0.35	10.06	0.33	1.17	0.10	0.96	<0.00	0.01	0.07	0.34	0.54	0.66	0.24	0.32	0.02
MB13Hmclean-1	0.04	0.38	0.19	0.23	0.03	<2.33	0.05	0.08	0.45	0.09	0.46	0.09	8.68	0.08	0.08	0.09	0.02
MB13Hmclean-2	0.04	0.10	0.69	1.56	0.04	<2.59	0.39	0.25	0.79	0.07	0.45	<0.097	6.21	3.70	0.21	0.45	0.05
MB13Hmclean-3	0.01	<0.056	<0.193	1.20	0.01	<2.57	0.06	0.02	0.46	0.05	0.46	<0.082	8.34	<0.00	0.07	0.06	0.01
MB13Hmclean-4	0.21	0.26	11.72	3.94	0.16	<2.34	1.00	0.59	1.60	0.05	0.33	0.20	4.44	1.10	0.36	0.89	0.08
MB13Hmclean-5	0.01	<0.00	0.48	1.10	0.08	<2.2	0.06	0.03	0.22	<0.00	0.28	<0.072	3.65	0.16	0.02	0.05	<0.0038
MB13Hmclean-6	0.24	0.43	45.82	4.04	0.15	2.97	0.70	0.42	1.10	0.10	0.52	0.18	8.96	1.07	0.28	0.60	0.08
MB13Hmclean-7	0.01	<0.00	3.72	0.59	0.02	<2.39	0.21	0.07	0.38	0.05	0.55	<0.071	7.28	<0.00	0.06	0.04	0.00
MB13Hmclean-8	0.02	0.10	0.25	0.21	0.02	<2.31	0.01	<0.0073	0.51	0.08	0.40	0.09	6.93	0.19	0.02	0.02	0.02
MB13Hmdirty-1	1.41	4.26	1.13	13.48	0.20	7.15	4.69	2.87	4.50	0.11	0.48	0.22	5.49	6.63	2.02	4.15	0.52
MB13Hmdirty-2	1.35	1.85	1.38	10.34	0.27	3.77	2.51	1.65	2.27	0.02	0.05	0.12	0.38	11.82	1.08	2.06	0.26
MB13Hmdirty-3	3.02	2.15	1.55	15.40	1.29	<2.62	4.31	1.21	2.09	0.04	0.04	0.25	0.22	56.05	0.92	2.49	0.23
MB13Hmdirty-4	1.40	1.05	0.54	15.91	0.39	5.25	3.05	1.92	1.10	0.02	0.02	0.22	<0.11	20.82	0.86	1.69	0.13
MB13Hmdirty-6	1.21	0.55	3.63	11.68	0.27	3.73	1.79	2.06	1.50	0.06	0.53	0.23	5.45	13.81	0.87	1.68	0.16
MB13Hmdirty-7	1.40	1.29	1.16	13.85	0.19	4.95	2.33	2.23	1.38	0.05	0.13	0.08	0.88	8.89	0.91	1.89	0.19
MB14Hm-1	1.04	10.44	2.49	22.52	10.41	6.91	2.61	0.92	1.83	7.08	0.39	16.43	<0.17	4.42	2.07	1.47	0.68

Analysis no.	Nd	Sm	Eu	Gd	Tb	Dy	Ho	Er	Tm	Yb	Lu	W	Pb208	Th	U
MB9Mg-5	0.08	0.03	<0.0094	<0.04	<0.0035	0.02	0.01	<0.0106	<0.0033	0.01	0.00	0.20	0.39	0.01	0.01
MB9Mg-6	<0.033	0.01	<0.0097	<0.026	0.00	0.01	0.00	0.01	0.00	0.00	0.00	<0.00	0.15	<0.00	<0.0024
MB9Mg-7	0.11	0.02	0.02	0.03	0.01	0.05	0.01	0.02	0.00	0.00	0.01	1.46	0.54	<0.00	0.01
MB9Mg-8	0.21	0.08	0.04	0.07	0.01	0.07	0.02	0.06	0.01	0.04	0.01	0.03	0.18	<0.00	0.00
MB9Mg-9	0.10	0.01	0.01	0.03	0.00	0.00	0.00	0.01	0.00	0.01	0.00	0.14	0.30	0.01	0.01
MB10ClastHm-1	0.49	0.04	0.06	0.27	0.01	0.24	0.06	0.11	0.02	0.24	0.03	0.61	4.73	<0.00	0.03
MB10ClastHm-2	0.32	0.05	0.08	0.22	0.02	0.21	0.05	0.16	0.05	0.06	0.04	0.32	3.92	0.00	0.02
MB10ClastHm-3	0.28	0.12	0.05	0.11	0.03	0.22	0.04	0.14	0.03	0.13	0.02	0.42	3.38	<0.00	0.05
MB10ClastHm-4	0.30	0.07	0.06	0.26	0.03	0.17	0.05	0.12	0.03	0.13	0.03	2.48	6.88	<0.00	0.08
MB10ClastHm-5	0.07	<0.052	0.01	0.02	<0.00	0.01	0.01	0.01	<0.00	0.03	0.01	5.37	3.15	0.00	0.06
MB10ClastHm-6	0.08	0.04	0.02	0.02	<0.0078	0.01	0.01	0.03	0.01	0.04	0.01	2.58	3.77	<0.0096	0.05
MB10ClastHm-7	0.13	<0.05	<0.0125	0.04	0.01	0.01	0.01	0.08	0.00	0.01	0.01	2.18	4.06	0.01	0.02
MB10ClastHm-8	0.06	0.04	0.02	0.02	0.01	<0.00	0.01	0.02	0.00	0.01	0.01	4.11	4.14	0.01	0.04
MB10Hm-1	0.16	0.02	0.02	<0.00	0.02	0.03	0.01	0.05	0.00	0.07	0.01	1.45	3.32	0.02	0.03
MB10Hm-2	0.14	0.07	0.03	0.06	<0.0115	0.03	0.01	0.01	0.01	0.04	0.00	1.54	3.06	<0.00	0.03
MB10Hm-3	0.12	0.04	0.04	0.04	0.02	0.04	0.03	0.05	0.02	0.11	0.02	0.74	4.21	0.01	0.04
MB10Hm-4	0.17	0.03	0.02	0.06	0.00	0.06	0.02	0.08	<0.0088	0.03	0.02	1.29	2.52	0.03	0.04
MB10Hm-5	0.43	0.02	0.07	0.07	0.01	0.09	0.04	0.06	0.03	0.10	0.03	1.82	3.63	0.27	0.05
MB10Hm-6	0.25	0.03	0.09	0.07	0.03	0.22	0.06	0.26	0.04	0.28	0.05	0.55	2.70	<0.00	0.01
MB10Hm-7	0.24	0.08	0.09	0.17	0.02	0.06	0.06	0.21	0.03	0.28	0.03	<0.023	1.93	<0.00	<0.00
MB10Hm-8	0.18	0.03	0.06	<0.072	0.03	0.09	0.03	0.12	0.02	0.07	0.02	0.44	2.88	0.01	0.03
MB10Mt-1	<0.042	<0.00	0.01	<0.00	0.01	0.01	<0.00	<0.00	<0.0134	<0.036	<0.00	0.04	0.04	0.00	0.00
MB10Mt-2	<0.00	<0.00	<0.00	<0.00	<0.00	<0.00	0.00	<0.00	<0.00	<0.00	<0.00	0.06	0.16	0.00	0.02
MB10Mt-3	0.02	<0.00	<0.00	<0.00	<0.00	0.01	0.00	0.01	<0.00	<0.00	<0.00	0.01	0.02	0.00	0.00
MB10Mt-4	<0.00	<0.00	<0.00	<0.00	<0.00	<0.00	0.00	<0.00	0.01	<0.00	0.00	0.02	0.11	0.00	0.01
MB10Mt-5	0.05	0.02	<0.013	<0.00	<0.0084	0.01	<0.0126	0.02	<0.014	<0.00	<0.00	0.04	0.05	<0.00	0.00
MB10Mt-6	0.02	0.02	0.02	<0.056	<0.00	0.01	0.00	<0.00	<0.00	0.01	<0.00	0.01	0.03	<0.00	0.00
MB10Mt-7	0.16	0.08	0.02	0.11	0.01	0.11	<0.0089	0.02	0.01	0.01	0.01	0.16	0.06	0.00	0.00
MB13Hmclean-1	0.04	0.01	0.00	0.02	<0.00	0.01	0.00	0.00	<0.00	0.02	<0.00	8.01	0.34	0.00	0.01
MB13Hmclean-2	0.19	0.01	<0.0241	0.03	0.01	0.05	0.00	0.02	0.00	0.01	0.00	7.87	0.98	0.17	0.01
MB13Hmclean-3	0.01	<0.00	<0.00	<0.00	<0.00	0.01	0.00	0.01	0.00	<0.00	0.01	8.23	0.47	0.01	<0.0033
MB13Hmclean-4	0.40	0.05	0.02	<0.00	0.02	0.03	0.01	0.04	0.01	0.01	0.01	5.18	4.39	0.40	0.04
MB13Hmclean-5	0.01	0.01	0.00	0.02	<0.00	<0.00	<0.00	<0.00	<0.0046	<0.00	<0.00	5.26	0.31	0.00	0.00
MB13Hmclean-6	0.22	0.05	0.01	0.08	0.01	0.04	0.00	0.05	0.01	0.05	0.01	6.68	2.83	0.25	0.02
MB13Hmclean-7	0.02	<0.00	0.01	<0.00	<0.00	0.02	<0.0048	0.01	<0.0049	<0.00	<0.00	5.38	0.06	<0.0097	0.01
MB13Hmclean-8	0.02	<0.00	<0.00	<0.00	0.00	<0.00	<0.00	<0.00	<0.00	<0.00	0.00	5.85	2.46	<0.00	0.00
MB13Hmdirty-1	2.17	0.32	0.14	0.39	0.09	0.43	0.09	0.20	0.03	0.18	0.04	8.87	20.18	1.40	0.12
MB13Hmdirty-2	0.94	0.23	0.05	0.22	0.04	0.19	0.03	0.12	0.03	0.14	0.02	0.30	12.93	0.64	0.06
MB13Hmdirty-3	1.12	0.29	0.04	0.15	0.02	0.20	0.04	0.10	0.01	0.16	0.01	0.42	7.56	0.58	0.06
MB13Hmdirty-4	0.70	0.10	0.05	0.20	0.02	0.12	0.03	0.09	0.03	0.15	0.02	0.12	12.85	0.35	0.04
MB13Hmdirty-6	0.69	0.12	0.06	0.17	0.02	0.22	0.04	0.15	0.01	0.18	0.02	6.57	12.55	0.38	0.04
MB13Hmdirty-7	0.79	0.16	0.06	0.12	0.02	0.19	0.05	0.18	0.01	0.16	0.03	2.05	15.28	0.36	0.06
MB14Hm-1	2.76	0.59	0.16	0.25	0.08	0.53	0.05	0.14	0.03	0.19	<0.03	2.91	31.64	1.19	0.66

Position	Deposit	Lithology	Sample no.	Analysis no.	Texture	Mg	Al	Si	P	Ca	Sc	Ti	V	Cr	Mn
Middle	Camel Hills	ORE	MB14	MB14Hm-10	porous martite	443.27	11142.17	2074.34	266.85	<931.27	2.67	10787.90	264.90	209.49	5339.05
Middle	Camel Hills	ORE	MB14	MB14Hm-11	porous martite	497.61	12044.67	3033.94	226.84	<835.35	2.01	9544.75	185.11	74.24	5059.65
Middle	Camel Hills	ORE	MB14	MB14Hm-2	porous martite	276.16	6346.24	2040.55	224.52	<863.02	0.67	8243.48	223.72	210.18	4677.98
Middle	Camel Hills	ORE	MB14	MB14Hm-3	porous martite	921.32	12328.03	7929.63	452.36	<843.72	2.68	6879.90	198.27	214.16	5384.30
Middle	Camel Hills	ORE	MB14	MB14Hm-4	porous martite	611.47	10377.17	3015.60	232.09	<851.22	1.55	7336.53	217.82	274.17	4423.27
Middle	Camel Hills	ORE	MB14	MB14Hm-5	porous martite	307.26	6076.36	1985.08	190.32	<935.27	1.36	8367.18	236.34	184.14	4592.86
Middle	Camel Hills	ORE	MB14	MB14Hm-6	porous martite	837.66	9845.04	5117.42	287.46	<729.58	1.25	7141.43	211.76	191.41	4400.55
Middle	Camel Hills	ORE	MB14	MB14Hm-7	porous martite	525.15	7588.28	2791.65	197.62	<862.07	1.50	7377.51	197.06	237.97	4180.54
Middle	Camel Hills	ORE	MB14	MB14Hm-8	porous martite	430.49	12866.00	2140.88	212.65	<860.64	1.14	7786.62	205.92	324.95	4285.71
Middle	Camel Hills	ORE	MB14	MB14Hm-9	porous martite	286.89	8100.45	1748.93	185.86	<885.95	1.62	8892.07	212.37	6.74	4352.95
Middle	Camel Hills	BIF	MB16	MB16Hmclean-2	clean martite	2.38	19.19	1820.56	34.98	<1093.77	0.36	9.26	1.90	<1.96	24.30
Middle	Camel Hills	BIF	MB16	MB16Hmclean-4	clean martite	420.92	458.75	1110.07	228.34	<927.31	0.49	7.72	10.80	<1.69	1317.54
Middle	Camel Hills	BIF	MB16	MB16Hmclean-6	clean martite	401.21	100.00	22800.21	32.90	<883.08	<0.24	8.32	3.07	<1.48	110.50
Middle	Camel Hills	BIF	MB16	MB16Hmclean-9	clean martite	11.68	87.80	16129.08	57.60	<1041.38	<0.42	9.01	4.34	<1.73	155.08
Middle	Camel Hills	BIF	MB16	MB16Hmdirty-1	porous martite	206.49	1198.61	9859.85	466.51	<1128.9	0.63	1.54	17.72	<2.1	2332.47
Middle	Camel Hills	BIF	MB16	MB16Hmdirty-2	porous martite	445.47	451.69	7736.99	511.86	1634.40	0.44	6.80	28.54	<2.03	1949.92
Middle	Camel Hills	BIF	MB16	MB16Hmdirty-5	porous martite	167.21	662.99	744.66	341.95	<1138.86	<0.42	373.09	15.38	<2.19	2159.87
Middle	Camel Hills	BIF	MB16	MB16Hmdirty-7	porous martite	162.69	594.09	12681.97	351.37	<1116.23	0.69	<1.82	18.00	<2.13	1873.02
Middle	Camel Hills	BIF	MB16	MB16Hmdirty-8	porous martite	105.87	245.70	16471.69	592.81	<1061.7	<0.45	9.19	15.92	<1.98	868.85
Middle	Camel Hills	BIF	MB18	MB18Mt-3	magnetite	31.94	15.80	368.28	21.39	<158.68	<0.053	6.76	1.14	0.47	837.11
Middle	Camel Hills	BIF	MB18	MB18Mt-4	magnetite	72.70	15.33	354.67	19.14	233.20	<0.061	7.97	1.03	0.45	1055.34
Middle	Camel Hills	BIF	MB18	MB18Mt-5	magnetite	38.19	18.26	943.93	41.35	<149.3	<0.048	3.50	0.94	0.37	850.34
North	Princess	ORE	MB1	MB1-Hm-1	clean martite	21.94	158.61	1363.42	44.36	<156.69	0.47	1.88	2.85	5.45	9.02
North	Princess	ORE	MB1	MB1-Hm-10	clean martite	76.28	130.82	1042.49	54.83	<141.61	0.19	3.21	3.47	5.74	7.97
North	Princess	ORE	MB1	MB1-Hm-12	clean martite	71.51	146.34	880.26	73.46	<188.49	0.22	1.24	3.07	3.83	20.72
North	Princess	ORE	MB1	MB1-Hm-2	clean martite	8.28	125.82	789.77	48.35	<140.81	0.48	2.09	2.97	4.16	8.97
North	Princess	ORE	MB1	MB1-Hm-5	clean martite	11.18	141.89	823.63	32.48	142.90	0.42	1.98	2.89	5.60	7.47
North	Princess	ORE	MB1	MB1-Hm-6	clean martite	12.18	124.48	1264.92	66.78	<156.4	0.38	3.61	2.59	4.07	10.75
North	Princess	ORE	MB1	MB1-Hm-8	clean martite	41.21	137.34	1337.76	104.25	157.94	0.28	1.54	3.21	6.29	15.17
North	Princess	ORE	MB1	MB1-Hm-9	clean martite	95.03	162.70	1401.39	38.84	<169.23	0.17	1.04	3.09	4.21	16.34
South	Duke	ORE	MB20	MB20Hm-1	clean martite	40.88	87.53	787.83	18.08	81.98	<0.044	0.80	0.96	0.64	49.05
South	Duke	ORE	MB20	MB20Hm-10	clean martite	70.31	176.08	1676.53	198.93	<53.24	<0.069	13.01	8.39	3.32	175.11
South	Duke	ORE	MB20	MB20Hm-11	clean martite	666.51	7846.72	11594.89	3175.21	742.25	1.68	169.82	7.47	20.94	707.74
South	Duke	ORE	MB20	MB20Hm-12	clean martite	84.81	80.15	673.30	16.06	<35.63	0.08	1.21	0.67	0.61	41.60
South	Duke	ORE	MB20	MB20Hm-13	clean martite	20.50	76.98	966.85	27.08	<48.55	<0.036	1.00	4.58	0.42	62.03
South	Duke	ORE	MB20	MB20Hm-14	clean martite	29.49	89.61	1789.70	13.90	<35.25	0.05	0.75	0.39	0.79	42.99
South	Duke	ORE	MB20	MB20Hm-15	clean martite	142.07	80.22	1929.49	20.43	<39.31	0.05	0.93	0.54	0.68	36.97
South	Duke	ORE	MB20	MB20Hm-16	clean martite	10.13	85.37	1277.04	21.12	<44.49	<0.055	1.42	0.42	0.77	52.71
South	Duke	ORE	MB20	MB20Hm-2	clean martite	2.66	66.07	2302.30	16.42	<35.01	<0.051	0.33	0.31	0.71	20.90
South	Duke	ORE	MB20	MB20Hm-3	clean martite	26.57	79.93	1963.53	130.55	<37.03	<0.05	1.29	3.10	0.54	71.16
South	Duke	ORE	MB20	MB20Hm-4	clean martite	93.30	114.82	2254.88	199.64	60.34	<0.039	0.55	0.73	0.92	102.59
South	Duke	ORE	MB20	MB20Hm-5	clean martite	108.06	145.63	1053.75	362.37	50.09	<0.042	0.70	2.56	0.60	92.57
South	Duke	ORE	MB20	MB20Hm-6	clean martite	74.16	259.28	2100.05	1046.94	134.92	0.21	11.60	15.66	3.93	287.51

Analysis no.	Co	Ni	Cu	Zn	Ga	As	Sr	Y	Zr	Nb	Mo	Sn	Sb	Ba	La	Ce	Pr
MB14Hm-10	0.92	6.12	1.69	5.44	8.07	2.26	2.46	2.26	97.66	7.99	0.60	16.61	<0.22	5.01	3.58	1.82	1.04
MB14Hm-11	0.62	9.17	3.36	58.82	8.11	3.22	2.02	1.69	0.67	7.47	0.60	15.61	<0.23	2.83	3.46	3.71	0.92
MB14Hm-2	1.09	7.83	1.74	8.06	8.47	2.49	2.26	1.15	0.92	6.75	0.52	17.16	0.29	4.81	3.05	1.78	0.88
MB14Hm-3	1.79	22.13	16.16	217.82	8.32	5.93	2.67	3.23	81.23	7.31	0.49	22.24	0.22	6.57	3.53	4.38	0.97
MB14Hm-4	6.43	37.32	10.04	40.30	8.56	63.60	3.49	1.25	3.47	6.26	0.44	14.63	1.33	8.23	2.32	1.77	0.67
MB14Hm-5	2.08	13.93	3.65	11.57	8.52	17.43	3.53	1.08	0.60	8.09	0.39	18.46	0.62	4.06	2.80	1.47	0.89
MB14Hm-6	24.77	65.03	28.12	81.26	10.21	105.01	4.56	1.50	1.02	6.88	0.63	14.31	2.88	13.05	2.25	2.29	0.71
MB14Hm-7	1.66	9.65	4.95	45.67	10.39	5.79	3.20	1.37	0.59	6.62	0.66	14.03	0.29	6.30	3.37	2.11	1.00
MB14Hm-8	1.07	8.52	2.55	60.91	10.35	2.59	2.83	1.43	18.17	6.35	0.79	14.39	0.43	3.88	3.21	2.27	0.96
MB14Hm-9	0.68	7.70	<0.44	1.66	8.21	2.05	1.86	1.26	0.25	7.05	0.66	14.13	0.18	4.50	3.18	1.62	1.07
MB16Hmclean-2	<0.067	<0.00	<0.44	<0.69	<0.085	2.43	0.37	0.12	0.59	<0.031	0.23	0.32	0.42	0.32	<0.027	0.16	<0.021
MB16Hmclean-4	2.00	9.22	4.60	22.08	0.14	7.00	4.97	3.27	0.63	0.05	0.49	<0.233	<0.23	4.04	1.01	4.93	0.19
MB16Hmclean-6	0.18	<0.168	0.67	4.65	<0.067	2.16	0.52	0.47	0.60	0.05	0.31	<0.23	<0.24	0.52	0.13	0.40	0.06
MB16Hmclean-9	0.19	1.68	0.84	3.31	<0.101	2.18	0.58	0.58	0.50	<0.037	0.55	<0.233	0.32	0.31	0.33	0.96	0.09
MB16Hmdirty-1	3.55	12.70	4.92	33.69	<0.095	8.50	7.83	3.87	<0.00	<0.00	1.67	1.10	<0.191	7.08	0.56	7.19	0.38
MB16Hmdirty-2	6.89	12.02	7.26	49.20	0.16	13.35	7.27	9.66	0.27	0.06	1.82	0.84	0.78	8.80	2.39	4.97	0.90
MB16Hmdirty-5	2.78	13.65	2.06	21.24	0.18	6.99	9.82	3.21	0.14	<0.00	0.61	0.52	<0.223	4.29	0.52	7.12	0.46
MB16Hmdirty-7	2.69	13.26	4.15	30.07	0.14	9.61	8.42	5.60	0.43	0.05	0.91	0.59	<0.28	6.66	1.23	7.02	0.47
MB16Hmdirty-8	1.62	9.15	6.99	53.51	0.13	17.74	3.24	13.97	0.29	0.22	1.75	0.31	0.86	4.12	2.47	8.13	0.60
MB18Mt-3	0.75	0.98	<0.21	14.19	0.19	2.63	0.19	<0.0148	<0.00	<0.00	<0.00	0.08	<0.109	0.66	<0.007	0.15	<0.00
MB18Mt-4	0.75	0.96	0.24	14.78	0.21	<2.4	0.18	0.01	<0.00	0.05	0.02	0.07	0.08	<0.00	0.01	0.03	0.02
MB18Mt-5	0.69	1.00	<0.23	15.51	0.03	<2.57	0.02	0.01	<0.00	<0.00	<0.0255	0.13	<0.099	<0.00	0.00	<0.0051	<0.00
MB1-Hm-1	0.50	7.96	<0.8	2.46	<0.069	<0.00	0.08	0.18	0.10	<0.00	0.85	<0.29	2.39	0.91	0.15	0.16	0.02
MB1-Hm-10	0.40	9.03	<1.04	0.83	0.10	<0.00	0.12	0.28	0.21	0.02	0.75	0.29	2.48	1.64	0.13	0.16	0.03
MB1-Hm-12	2.40	35.11	<1.07	2.36	0.50	<0.00	0.19	0.43	0.08	<0.00	0.49	0.32	5.05	1.52	0.17	0.14	0.03
MB1-Hm-2	0.93	4.45	<0.89	1.57	0.12	<0.00	0.10	1.31	0.27	0.02	0.62	0.49	3.84	0.23	0.15	0.19	0.03
MB1-Hm-5	0.06	3.62	<0.93	0.41	0.12	<0.00	0.10	0.20	0.17	<0.00	0.67	0.47	2.68	2.30	0.08	0.07	0.03
MB1-Hm-6	1.36	4.91	<1.01	1.53	0.15	<0.00	0.32	0.23	0.04	<0.00	0.60	<0.27	3.10	1.22	0.10	0.15	0.01
MB1-Hm-8	1.62	5.01	<0.99	7.71	0.17	<0.00	0.21	0.52	<0.00	0.01	0.96	<0.37	5.24	1.66	0.22	0.30	0.05
MB1-Hm-9	0.40	4.85	1.44	1.17	0.10	<0.00	0.30	0.32	<0.00	<0.00	0.89	<0.3	2.61	1.67	0.23	0.29	0.03
MB20Hm-1	0.47	0.11	8.94	3.17	0.03	0.79	0.16	0.19	<0.00	<0.00	0.05	0.15	0.19	0.21	0.05	0.09	0.01
MB20Hm-10	0.70	2.12	15.46	6.62	0.24	8.82	0.80	1.24	0.18	0.01	1.26	1.47	0.38	12.67	0.54	0.67	0.08
MB20Hm-11	9.27	22.09	217.96	77.48	0.68	6.75	5.10	19.12	0.94	0.37	0.64	57.72	<0.46	7.39	6.29	20.76	1.42
MB20Hm-12	0.55	<0.146	9.23	5.63	0.10	0.59	0.13	0.09	<0.00	0.00	0.07	0.18	<0.104	<0.00	0.03	0.06	0.01
MB20Hm-13	0.54	0.39	<0.87	2.17	0.03	1.09	0.03	0.26	0.03	0.01	0.05	0.13	<0.13	0.08	0.02	0.07	0.01
MB20Hm-14	0.21	0.18	7.31	2.97	0.04	0.50	0.05	0.69	<0.00	<0.011	0.08	0.19	<0.082	0.16	0.06	0.14	0.02
MB20Hm-15	0.31	0.08	5.59	2.84	0.06	1.06	0.13	0.82	0.03	0.02	0.02	0.14	0.14	0.15	0.11	0.16	0.02
MB20Hm-16	0.39	0.21	4.67	2.49	0.08	1.19	0.08	0.39	<0.00	<0.00	<0.024	0.18	<0.102	<0.00	0.06	0.07	0.02
MB20Hm-2	0.31	0.04	2.27	0.99	0.04	1.27	0.06	0.41	0.23	0.00	0.08	0.20	0.13	0.14	0.08	0.09	0.01
MB20Hm-3	0.81	1.34	3.08	13.88	0.06	2.00	0.13	3.31	<0.00	0.01	0.08	0.25	0.23	0.14	0.69	1.18	0.11
MB20Hm-4	0.43	0.16	4.62	3.92	0.16	2.51	0.85	1.16	0.03	<0.00	0.12	0.21	0.21	7.76	0.25	0.32	0.05
MB20Hm-5	1.34	2.34	15.86	10.44	0.07	1.33	0.30	1.55	0.01	0.01	0.11	0.19	<0.125	1.95	0.44	1.21	0.11
MB20Hm-6	2.67	13.43	9.00	23.89	0.35	8.65	0.75	7.46	0.33	0.02	2.19	0.21	0.42	11.82	1.75	2.58	0.35

Analysis no.	Nd	Sm	Eu	Gd	Tb	Dy	Ho	Er	Tm	Yb	Lu	W	Pb208	Th	U
MB14Hm-10	4.83	0.79	0.19	0.65	0.08	0.62	0.12	0.44	0.07	0.42	0.05	3.90	23.00	1.26	0.95
MB14Hm-11	4.25	1.39	0.22	0.59	0.08	0.59	0.08	0.33	0.05	0.35	0.05	4.19	75.63	1.04	0.81
MB14Hm-2	3.81	0.66	0.14	0.61	0.07	0.43	0.08	0.27	0.03	0.24	<0.018	3.50	27.42	1.49	0.62
MB14Hm-3	4.03	1.19	0.24	0.75	0.14	0.78	0.15	0.39	0.04	0.44	0.06	8.58	59.39	2.40	2.24
MB14Hm-4	3.01	0.66	0.12	0.19	0.07	0.26	0.04	0.16	0.04	0.15	<0.03	3.54	60.52	2.28	0.53
MB14Hm-5	3.21	0.57	0.16	0.54	0.07	0.33	0.09	0.17	<0.023	<0.161	0.04	3.46	26.96	1.04	0.65
MB14Hm-6	2.38	0.68	0.08	0.29	0.05	0.22	0.07	0.21	0.03	0.13	0.02	4.76	101.86	0.98	0.61
MB14Hm-7	4.13	0.66	0.19	0.50	0.08	0.61	0.07	0.20	0.03	0.20	0.05	3.41	40.71	0.93	0.64
MB14Hm-8	3.41	0.76	0.29	0.52	0.06	0.45	0.07	0.22	0.04	0.26	0.07	4.05	54.47	7.93	0.69
MB14Hm-9	3.50	1.04	0.20	0.32	0.07	0.43	0.03	0.18	0.04	0.14	<0.024	3.45	17.71	0.89	0.66
MB16Hmclean-2	0.18	<0.168	<0.049	0.09	<0.036	<0.126	<0.021	0.08	<0.00	0.10	<0.033	1.44	<0.18	<0.041	<0.028
MB16Hmclean-4	1.49	0.38	0.09	0.71	0.09	0.61	0.12	0.35	0.07	0.37	<0.055	3.59	2.43	<0.044	0.22
MB16Hmclean-6	0.18	<0.076	<0.031	0.26	<0.057	<0.077	<0.029	0.08	<0.021	0.09	0.03	2.29	0.41	<0.0145	0.05
MB16Hmclean-9	0.34	0.14	0.08	0.10	<0.022	<0.143	<0.035	0.19	<0.033	0.12	<0.0154	1.88	0.83	0.04	0.06
MB16Hmdirty-1	2.43	0.83	0.29	1.01	0.15	0.83	0.25	0.44	0.09	0.64	0.10	0.16	4.27	0.06	0.43
MB16Hmdirty-2	4.83	1.87	0.40	1.89	0.43	1.55	0.35	1.12	0.18	0.82	0.19	1.61	9.43	0.06	0.53
MB16Hmdirty-5	2.12	0.46	0.20	0.95	0.13	0.71	0.16	0.36	0.08	0.14	0.05	0.08	5.20	0.14	0.17
MB16Hmdirty-7	3.05	0.58	0.38	1.51	0.21	0.88	0.25	0.99	0.19	0.50	0.08	5.03	4.54	<0.041	0.36
MB16Hmdirty-8	3.68	1.00	0.49	1.71	0.31	1.59	0.30	1.22	0.13	0.96	0.13	2.09	3.88	<0.017	0.43
MB18Mt-3	<0.00	<0.00	<0.0088	<0.045	0.00	<0.0269	<0.00	<0.00	<0.00	<0.00	<0.00	<0.00	0.02	<0.00	0.01
MB18Mt-4	0.02	0.01	<0.00	<0.043	<0.00	<0.037	0.00	<0.0208	<0.00	<0.00	<0.00	0.06	0.05	<0.00	0.00
MB18Mt-5	<0.00	<0.066	0.00	<0.045	<0.00	<0.00	<0.00	0.01	0.00	0.02	<0.00	0.04	0.03	0.00	0.00
MB1-Hm-1	0.11	<0.00	<0.026	0.03	0.00	<0.048	<0.00	<0.00	<0.00	0.02	0.00	4.05	2.18	0.01	0.13
MB1-Hm-10	0.11	<0.108	0.03	0.03	<0.00	0.03	<0.00	0.01	0.01	0.02	<0.00	2.95	1.52	<0.00	0.15
MB1-Hm-12	0.05	0.03	<0.0205	0.09	0.00	0.05	0.01	0.03	<0.0145	0.04	0.00	3.32	2.14	<0.00	0.57
MB1-Hm-2	0.22	0.03	0.03	0.05	0.02	0.15	0.02	0.17	0.02	0.13	0.02	6.80	1.75	0.01	0.07
MB1-Hm-5	0.04	0.05	0.01	<0.00	<0.00	<0.00	<0.00	0.04	<0.0124	0.04	0.00	4.11	1.29	<0.0191	0.16
MB1-Hm-6	0.12	<0.00	0.01	0.03	0.02	<0.051	<0.0128	0.03	0.01	0.02	<0.0144	3.79	1.80	<0.00	0.18
MB1-Hm-8	0.13	<0.00	0.04	<0.083	0.00	0.07	0.01	<0.039	0.00	0.02	<0.00	3.79	2.22	0.01	0.26
MB1-Hm-9	<0.096	0.03	0.02	0.03	0.00	0.07	<0.0127	0.01	0.00	<0.00	<0.00	3.11	2.56	0.00	0.14
MB20Hm-1	0.03	0.02	0.03	0.03	<0.00	0.01	0.01	0.01	0.00	<0.00	0.00	0.12	0.91	0.00	0.05
MB20Hm-10	0.28	0.05	0.05	0.10	0.01	0.12	0.03	0.08	0.03	0.12	0.01	2.43	4.05	0.01	0.61
MB20Hm-11	6.95	1.67	0.95	1.32	0.18	1.09	0.24	0.89	0.15	0.74	0.14	0.72	12.93	0.21	10.22
MB20Hm-12	0.04	0.01	0.00	0.01	<0.0038	0.02	<0.0041	<0.00	0.01	<0.0164	<0.00	0.02	1.38	<0.00	0.02
MB20Hm-13	0.04	<0.00	0.00	0.01	<0.0068	0.04	0.00	0.00	0.00	0.01	0.00	0.78	0.11	<0.00	0.05
MB20Hm-14	0.15	0.01	0.08	0.01	0.01	0.02	0.02	0.03	0.01	0.06	0.00	0.10	0.95	<0.00	0.03
MB20Hm-15	0.14	<0.034	0.03	0.04	0.00	0.10	0.01	0.06	0.01	0.07	0.01	0.05	0.34	0.00	0.04
MB20Hm-16	0.06	0.02	0.02	<0.027	0.00	0.03	<0.0061	0.01	0.00	0.02	0.00	0.03	0.93	0.00	0.06
MB20Hm-2	0.09	0.01	0.03	0.03	0.00	0.02	0.01	0.02	<0.0039	0.02	0.00	0.01	0.27	<0.0056	0.02
MB20Hm-3	0.62	0.12	0.11	0.25	0.02	0.16	0.05	0.15	0.02	0.10	0.01	0.23	0.63	0.00	0.16
MB20Hm-4	0.17	0.04	0.05	0.15	0.01	0.08	0.03	0.10	0.02	0.07	0.01	0.11	0.70	0.00	0.15
MB20Hm-5	0.46	0.07	0.08	0.12	0.01	0.08	0.01	0.06	0.01	0.02	0.01	0.37	2.09	0.00	0.47
MB20Hm-6	1.58	0.45	0.36	0.57	0.08	0.38	0.14	0.34	0.06	0.37	0.06	3.74	4.49	0.02	0.80

Position	Deposit	Lithology	Sample no.	Analysis no.	Texture	Mg	Al	Si	P	Ca	Sc	Ti	V	Cr	Mn
South	Duke	ORE	MB20	MB20Hm-7	clean martite	49.69	247.76	2246.36	814.87	90.06	0.15	9.60	5.48	1.49	257.24
South	Duke	ORE	MB20	MB20Hm-8	clean martite	40.18	162.33	1304.43	458.42	107.84	<0.076	11.60	5.30	2.34	178.03
South	Duke	ORE	MB20	MB20Hm-9	clean martite	134.24	1665.24	4512.16	2638.60	193.82	0.65	7.96	8.17	3.63	559.87
South	Duke	ORE	MB20	MB20HmBubble-1	clean martite	39.30	98.80	1564.15	70.00	44.26	0.08	2.63	2.58	0.65	75.52
South	Duke	ORE	MB20	MB20HmBubble-2	clean martite	50.80	96.12	1644.78	30.57	27.17	0.05	1.47	2.17	0.66	73.54
South	Duke	ORE	MB20	MB20HmBubble-3	clean martite	61.80	191.68	1250.35	732.93	<49.84	0.06	1.41	5.46	1.02	196.12
South	Duke	ORE	MB20	MB20HmBubble-4	clean martite	45.87	102.76	1339.05	115.97	43.90	<0.041	1.97	3.76	0.92	93.59
South	Knight	ORE	MB22b	MB22bHm-1	clean martite	1357.28	1660.99	3638.47	63.06	<851.81	<0.31	54.88	149.19	<1.17	551.95
South	Knight	ORE	MB22b	MB22bHm-10	clean martite	208.45	1683.22	1445.61	28.08	<899.2	<0.29	55.23	16.42	1.72	434.56
South	Knight	ORE	MB22b	MB22bHm-2	clean martite	1753.14	1777.65	3477.01	<22.36	<899.19	<0.33	61.43	15.52	<1.22	943.89
South	Knight	ORE	MB22b	MB22bHm-3	clean martite	445.38	1027.32	3195.61	54.93	<874.85	<0.33	18.98	310.68	28.26	370.39
South	Knight	ORE	MB22b	MB22bHm-4	clean martite	1284.86	1951.82	3348.94	92.78	<1027.48	<0.36	58.68	190.39	<1.33	741.68
South	Knight	ORE	MB22b	MB22bHm-5	clean martite	18.38	762.97	716.77	64.80	<995.93	0.42	3.05	433.66	<1.27	123.16
South	Knight	ORE	MB22b	MB22bHm-6	clean martite	677.27	653.30	672.12	33.39	2725.80	0.89	9.04	631.25	14.02	726.01
South	Knight	ORE	MB22b	MB22bHm-8	clean martite	623.64	1486.81	2998.58	44.79	<906.59	0.38	96.13	1279.55	16.77	704.12
South	Knight	ORE	MB22b	MB22bHm-9	clean martite	226.51	1695.92	1257.18	<22.7	<890.98	<0.29	65.64	10.03	1.24	509.77
Middle	Count	ORE	MB23	MB23Hm-1	clean martite	73.12	1325.74	3551.41	110.81	182.63	1.46	34.17	119.40	9.35	84.77
Middle	Count	ORE	MB23	MB23Hm-11	clean martite	71.99	490.44	2370.13	30.31	113.01	0.37	12.52	125.44	0.98	91.06
Middle	Count	ORE	MB23	MB23Hm-12	clean martite	33.43	500.47	1702.40	34.93	<82.73	0.47	10.93	54.99	1.13	93.73
Middle	Count	ORE	MB23	MB23Hm-13	clean martite	35.00	2163.83	3623.23	252.61	<104.26	3.09	121.14	371.68	12.59	121.93
Middle	Count	ORE	MB23	MB23Hm-14	clean martite	52.85	301.05	2029.84	44.37	144.69	1.26	10.03	25.36	4.04	24.26
Middle	Count	ORE	MB23	MB23Hm-2	clean martite	40.56	1851.76	3636.71	255.86	<89.53	1.95	22.48	468.99	29.63	180.89
Middle	Count	ORE	MB23	MB23Hm-3	clean martite	34.16	1074.54	2899.60	117.49	93.53	1.41	15.51	103.33	2.67	112.10
Middle	Count	ORE	MB23	MB23Hm-4	clean martite	38.24	1769.95	3808.00	155.32	<90.48	1.69	32.39	271.00	7.31	214.84
Middle	Count	ORE	MB23	MB23Hm-5	clean martite	21.88	521.63	1071.95	56.86	180.11	0.43	16.76	466.67	2.90	59.79
Middle	Count	ORE	MB23	MB23Hm-6	clean martite	37.86	308.54	1312.67	22.24	<85.58	0.34	14.23	50.43	1.06	68.40
Middle	Count	ORE	MB23	MB23Hm-7	clean martite	47.54	1242.74	2397.33	213.28	<88.93	1.73	20.36	254.55	3.74	125.09
Middle	Count	ORE	MB23	MB23Hm-8	clean martite	50.16	1997.71	3578.80	222.16	<91.37	2.07	54.40	522.86	24.97	136.20
Middle	Count	ORE	MB23	MB23Hm-9	clean martite	20.09	305.55	1850.82	25.34	<81.44	0.36	23.69	29.98	3.74	92.81
Middle	Count	ORE	MB23	MB23HmRe-1	clean martite	46.35	1927.79	3471.43	305.28	126.93	2.02	8.77	236.58	2.66	154.57
Middle	Count	ORE	MB23	MB23HmRe-10	clean martite	14.35	284.86	1204.73	39.47	114.38	0.34	19.08	17.38	2.80	105.50
Middle	Count	ORE	MB23	MB23HmRe-11	clean martite	14.33	227.54	950.03	17.34	<61.95	0.19	15.32	32.55	3.53	90.63
Middle	Count	ORE	MB23	MB23HmRe-12	clean martite	31.62	269.84	998.35	30.76	<69.1	0.46	22.22	27.15	3.70	89.53
Middle	Count	ORE	MB23	MB23HmRe-13	clean martite	33.80	1672.18	3694.13	186.93	131.90	1.99	9.13	163.29	14.02	95.93
Middle	Count	ORE	MB23	MB23HmRe-14	clean martite	38.84	1535.27	3805.02	120.38	98.51	1.44	10.01	407.66	11.33	111.42
Middle	Count	ORE	MB23	MB23HmRe-2	clean martite	16.67	250.16	1708.32	28.62	<64.79	0.33	6.58	64.66	0.96	56.14
Middle	Count	ORE	MB23	MB23HmRe-3	clean martite	39.71	2889.67	3500.10	213.72	264.29	1.80	15.80	286.02	2.44	105.30
Middle	Count	ORE	MB23	MB23HmRe-6	clean martite	13.31	528.86	2009.12	56.20	<63.06	1.57	10.05	53.53	4.27	50.60
Middle	Count	ORE	MB23	MB23HmRe-7	clean martite	38.26	896.32	2139.22	104.29	132.76	1.12	14.07	92.70	7.14	79.70
Middle	Count	ORE	MB23	MB23HmRe-8	clean martite	94.90	1048.93	2334.57	46.02	110.63	0.96	40.76	216.56	13.39	138.75
Middle	Count	ORE	MB23	MB23HmRe-9	clean martite	63.82	1938.63	2669.29	333.96	85.75	2.97	69.11	229.89	3.78	186.75
Middle	Cavalier	ORE	MB25	MB25Hm-1	porous martite	389.42	255.56	4124.58	548.19	<93	<0.082	2.84	3.12	1.63	612.42
Middle	Cavalier	ORE	MB25	MB25Hm-10	porous martite	291.96	265.25	6818.41	491.83	<133.66	0.13	2.29	2.70	1.02	693.55

Analysis no.	Co	Ni	Cu	Zn	Ga	As	Sr	Y	Zr	Nb	Mo	Sn	Sb	Ba	La	Ce	Pr
MB20Hm-7	3.13	12.11	26.42	23.59	0.36	12.30	0.70	5.02	0.06	0.01	2.26	0.17	0.17	11.24	1.22	2.81	0.26
MB20Hm-8	2.02	4.53	38.57	27.35	0.15	5.55	0.57	4.19	0.19	0.03	0.30	0.21	0.44	4.56	1.04	1.59	0.23
MB20Hm-9	7.84	25.24	54.06	64.74	0.40	9.63	1.89	17.98	0.18	0.02	1.35	12.25	0.30	8.30	4.59	11.42	0.98
MB20HmBubble-1	0.80	0.83	37.02	16.16	0.16	10.32	0.47	0.96	0.05	0.01	0.09	0.25	<0.19	2.54	0.22	0.38	0.05
MB20HmBubble-2	0.67	0.27	21.69	6.98	0.09	4.68	0.27	0.91	0.04	0.02	0.03	0.29	0.34	1.16	0.28	0.43	0.03
MB20HmBubble-3	2.21	6.38	14.10	20.33	0.22	6.06	0.71	4.19	0.09	0.08	0.09	0.25	<0.14	4.26	0.81	2.28	0.19
MB20HmBubble-4	1.13	1.28	35.83	15.41	0.17	7.64	0.58	1.32	0.01	0.02	0.03	0.22	0.34	3.38	0.35	0.57	0.07
MB22bHm-1	1.06	8.60	1.31	15.96	0.52	17.66	0.93	1.17	0.03	0.10	0.21	1.77	<0.28	18.16	0.66	0.57	0.05
MB22bHm-10	10.34	1.63	2.46	21.70	0.57	5.32	0.66	0.83	0.04	0.02	<0.165	1.92	1.23	22.46	0.20	0.41	<0.026
MB22bHm-2	3.96	1.50	0.96	26.64	0.53	22.79	0.33	0.79	0.03	0.19	<0.11	1.62	0.56	9.92	0.25	0.33	0.05
MB22bHm-3	18.39	12.95	4.30	13.97	1.05	11.93	1.05	2.04	0.11	0.05	0.36	0.43	1.27	31.16	0.61	0.86	0.13
MB22bHm-4	6.55	7.61	1.24	9.48	0.40	5.46	0.27	0.82	0.03	0.26	<0.087	1.64	<0.27	11.54	0.36	0.33	<0.085
MB22bHm-5	1.07	5.11	<0.47	1.59	0.12	2.52	0.27	0.16	0.89	<0.02	1.56	0.52	0.46	3.74	0.15	0.20	0.04
MB22bHm-6	1.10	3.09	<0.48	0.83	0.18	2.74	0.93	1.37	2.00	0.04	0.82	0.91	0.50	2.16	3.18	2.27	0.15
MB22bHm-8	1.11	38.60	1.88	9.00	1.02	4.50	0.86	1.41	0.10	0.08	<0.193	1.52	0.95	31.88	0.69	0.66	0.05
MB22bHm-9	25.06	2.03	10.92	14.80	0.59	3.54	0.81	0.45	0.07	<0.033	<0.172	1.42	0.68	21.49	0.14	0.22	0.04
MB23Hm-1	2.24	4.99	19.14	9.27	0.59	42.55	1.74	0.95	0.72	0.05	0.85	3.57	45.60	2.63	0.56	1.33	0.17
MB23Hm-11	2.93	5.36	1.83	5.89	0.78	32.70	1.30	0.80	0.21	0.05	0.48	0.48	24.96	1.08	0.39	0.94	0.11
MB23Hm-12	3.47	5.97	2.56	5.51	0.57	34.95	1.38	0.85	0.25	0.03	0.48	0.64	23.77	1.08	0.33	0.90	0.09
MB23Hm-13	4.10	9.25	62.06	14.41	1.03	27.93	3.18	0.99	5.93	0.23	0.71	13.01	69.01	4.07	1.70	3.17	0.33
MB23Hm-14	2.27	6.73	16.09	3.75	0.32	47.47	0.51	0.46	0.15	0.02	0.27	0.41	18.36	0.41	0.15	0.42	0.06
MB23Hm-2	4.70	17.49	25.89	14.33	1.25	37.70	8.85	1.65	0.68	0.13	1.46	0.90	55.09	16.92	44.18	17.82	7.64
MB23Hm-3	2.93	5.98	16.07	29.19	0.69	45.07	1.97	1.04	1.19	0.05	2.68	1.02	59.59	1.44	0.46	1.22	0.13
MB23Hm-4	3.18	11.17	21.92	21.20	0.85	45.47	1.96	0.84	1.82	0.12	0.89	0.97	126.20	2.68	0.72	1.78	0.17
MB23Hm-5	2.46	5.42	4.69	3.46	0.78	29.34	0.99	0.63	0.75	0.07	1.27	0.59	24.82	1.40	0.28	0.90	0.08
MB23Hm-6	3.42	6.77	0.67	4.57	0.54	41.93	1.13	0.74	0.20	0.02	0.40	0.47	21.39	1.37	0.30	0.74	0.08
MB23Hm-7	3.73	10.37	17.82	9.64	1.07	27.51	1.80	0.63	1.02	0.04	1.30	0.70	33.58	2.44	5.89	5.10	0.82
MB23Hm-8	4.55	8.49	32.49	18.87	0.88	48.55	3.97	1.05	0.85	0.39	2.34	5.78	63.11	5.07	10.97	7.01	2.18
MB23Hm-9	14.94	5.71	4.88	23.73	0.65	40.02	1.15	1.23	0.54	0.02	1.77	0.51	26.64	1.47	0.77	1.19	0.23
MB23HmRe-1	3.36	11.25	27.76	16.72	1.40	30.26	4.57	1.46	0.48	0.04	1.25	1.06	34.35	13.30	39.35	15.96	9.71
MB23HmRe-10	2.75	4.43	40.61	38.01	0.72	21.94	0.42	1.14	0.19	0.08	0.42	0.42	18.57	0.49	0.56	1.16	0.17
MB23HmRe-11	3.58	4.03	50.66	41.67	0.59	27.26	0.51	1.13	0.23	0.03	0.36	0.35	22.00	0.42	0.41	1.12	0.13
MB23HmRe-12	10.33	7.04	5.08	18.86	0.60	25.63	1.04	1.21	7.51	0.02	0.99	0.53	17.56	0.76	0.28	0.75	0.12
MB23HmRe-13	2.94	6.50	26.15	7.75	0.82	31.03	3.68	1.06	0.95	0.07	1.06	1.96	32.14	5.40	13.26	8.66	2.21
MB23HmRe-14	4.27	15.40	21.05	18.83	0.78	33.98	1.68	0.74	1.21	0.07	0.97	1.00	73.57	3.03	0.80	1.74	0.21
MB23HmRe-2	3.24	5.99	20.69	6.36	0.74	37.84	0.84	0.80	0.08	0.02	0.43	0.43	20.64	0.56	0.26	0.73	0.08
MB23HmRe-3	6.44	17.59	18.56	7.23	1.37	30.66	1.74	0.79	2.56	0.08	1.01	2.50	34.92	3.35	3.98	5.21	0.57
MB23HmRe-6	2.56	7.69	24.36	4.70	0.45	31.44	0.83	0.58	0.12	0.04	0.51	0.66	30.28	2.18	2.57	1.54	0.66
MB23HmRe-7	6.69	9.04	14.61	7.66	1.07	32.58	1.43	0.57	0.78	0.04	0.53	1.12	24.35	1.44	1.23	1.94	0.22
MB23HmRe-8	3.65	3.70	0.79	14.30	0.62	47.55	3.47	1.25	0.15	0.83	2.75	9.60	105.12	4.25	0.52	1.13	0.12
MB23HmRe-9	2.26	3.42	54.81	10.40	1.13	44.91	6.58	1.44	3.08	0.29	3.54	2.12	101.48	13.83	41.58	18.79	7.47
MB25Hm-1	2.75	2.18	1.83	20.04	1.08	1.07	1.29	3.26	0.02	0.05	0.02	<0.111	<0.35	1.70	0.76	1.06	0.16
MB25Hm-10	2.36	1.49	1.08	25.17	0.72	1.02	1.32	2.62	0.08	0.03	<0.00	0.37	<0.2	0.46	0.82	0.96	0.14

Analysis no.	Nd	Sm	Eu	Gd	Tb	Dy	Ho	Er	Tm	Yb	Lu	W	Pb208	Th	U
MB20Hm-7	1.38	0.31	0.29	0.45	0.04	0.41	0.07	0.28	0.04	0.23	0.04	2.12	7.98	<0.0071	1.03
MB20Hm-8	0.95	0.20	0.27	0.48	0.02	0.41	0.08	0.22	0.04	0.14	0.03	0.92	5.37	0.01	0.54
MB20Hm-9	4.97	1.23	0.86	1.40	0.18	0.97	0.24	0.95	0.12	0.60	0.13	1.62	6.57	0.02	4.54
MB20HmBubble-1	0.12	0.08	0.04	0.12	0.02	0.11	0.03	0.04	0.01	0.06	0.02	0.38	3.87	0.00	0.31
MB20HmBubble-2	0.16	0.04	0.03	0.11	0.01	0.06	0.02	0.03	0.01	0.02	0.01	0.80	3.20	0.01	0.23
MB20HmBubble-3	0.96	0.28	0.20	0.41	0.05	0.24	0.07	0.19	0.02	0.16	0.03	0.43	2.67	0.01	1.06
MB20HmBubble-4	0.26	0.10	0.07	0.12	0.02	0.08	0.02	0.09	0.01	0.07	0.01	0.55	3.89	0.01	0.42
MB22bHm-1	0.12	<0.174	<0.039	<0.215	0.04	<0.094	0.03	<0.085	<0.035	<0.103	0.02	0.43	5.68	<0.025	7.96
MB22bHm-10	0.16	<0.173	<0.043	<0.086	0.04	0.08	0.04	<0.085	0.02	0.09	<0.0132	0.18	4.22	0.03	1.64
MB22bHm-2	<0.153	<0.182	0.06	0.11	0.03	0.06	<0.03	0.09	<0.022	<0.092	<0.028	0.55	2.31	<0.031	2.10
MB22bHm-3	0.19	0.13	0.06	0.19	0.07	<0.119	0.06	<0.074	<0.0117	0.09	<0.023	0.75	9.05	0.03	6.91
MB22bHm-4	<0.154	0.03	<0.059	<0.219	0.02	<0.11	<0.0193	0.06	<0.035	0.11	0.01	0.73	3.86	<0.045	5.23
MB22bHm-5	<0.123	<0.119	<0.049	<0.083	<0.021	<0.102	<0.0126	<0.053	<0.023	<0.095	<0.0185	1.11	1.61	<0.035	1.08
MB22bHm-6	0.39	0.20	0.05	<0.149	0.03	<0.092	<0.018	0.11	<0.031	0.09	0.04	2.03	1.35	<0.028	2.67
MB22bHm-8	<0.155	<0.083	<0.048	0.21	0.02	<0.071	<0.0173	0.08	0.03	0.06	<0.018	0.64	10.52	0.07	25.79
MB22bHm-9	<0.135	<0.161	0.05	<0.112	0.02	<0.138	<0.0207	0.03	<0.022	<0.073	<0.017	<0.088	1.93	<0.037	0.65
MB23Hm-1	0.71	0.24	0.05	0.12	0.02	0.21	0.04	0.11	0.01	0.06	0.01	2.23	54.76	0.11	11.13
MB23Hm-11	0.44	0.20	0.02	0.12	0.01	0.14	0.03	0.07	0.01	0.07	0.01	5.99	6.54	<0.0086	4.76
MB23Hm-12	0.46	0.12	0.07	0.12	0.03	0.15	0.03	0.07	0.02	0.02	<0.0038	3.34	27.46	<0.0047	3.49
MB23Hm-13	1.27	0.19	0.09	0.18	0.04	0.21	0.05	0.14	0.01	0.13	0.02	8.19	119.49	1.17	5.79
MB23Hm-14	0.21	0.04	0.02	0.10	0.01	0.09	0.01	0.04	0.01	0.05	0.00	1.01	11.12	0.01	2.23
MB23Hm-2	22.06	2.72	0.66	1.27	0.13	0.57	0.07	0.20	0.02	0.11	0.01	5.75	59.21	0.07	10.33
MB23Hm-3	0.58	0.16	0.07	0.14	0.02	0.20	0.04	0.12	0.02	0.06	0.01	5.08	58.27	0.18	6.48
MB23Hm-4	0.75	0.19	0.06	0.19	0.04	0.20	0.04	0.08	0.01	0.09	0.01	3.82	70.24	0.32	7.15
MB23Hm-5	0.34	0.10	0.02	0.08	0.02	0.14	0.02	0.04	0.00	0.05	0.00	6.48	6.82	0.02	6.06
MB23Hm-6	0.40	0.12	0.03	0.14	0.01	0.13	0.04	0.07	0.02	0.05	0.01	2.47	3.83	0.01	4.27
MB23Hm-7	2.71	0.30	0.09	0.21	0.03	0.10	0.02	0.05	0.01	0.05	0.01	4.86	75.20	0.02	6.23
MB23Hm-8	6.48	1.01	0.13	0.46	0.05	0.23	0.05	0.11	0.01	0.08	0.01	35.46	57.85	0.14	15.38
MB23Hm-9	0.62	0.18	0.07	0.17	0.05	0.27	0.03	0.12	0.01	0.07	0.01	2.20	18.35	0.02	4.20
MB23HmRe-1	19.25	2.56	0.39	0.97	0.12	0.50	0.06	0.15	0.02	0.08	0.01	3.59	44.22	0.03	7.39
MB23HmRe-10	0.73	0.18	0.05	0.16	0.04	0.16	0.04	0.13	0.02	0.06	0.01	3.43	11.70	<0.0059	2.59
MB23HmRe-11	0.67	0.20	0.08	0.28	0.03	0.20	0.05	0.06	0.02	0.10	0.01	3.59	9.46	0.01	2.90
MB23HmRe-12	0.45	0.08	0.05	0.09	0.03	0.15	0.03	0.07	0.01	0.07	0.02	4.94	15.69	0.02	3.07
MB23HmRe-13	5.97	0.79	0.20	0.49	0.06	0.28	0.03	0.13	0.02	0.06	0.02	4.60	68.17	0.08	9.85
MB23HmRe-14	0.88	0.16	0.06	0.17	0.05	0.18	0.03	0.05	0.01	0.03	0.01	4.36	61.48	0.16	9.18
MB23HmRe-2	0.37	0.11	0.06	0.17	0.01	0.13	0.02	0.09	0.01	0.07	0.00	4.38	10.73	<0.0041	4.47
MB23HmRe-3	1.72	0.23	0.06	0.11	0.02	0.15	0.03	0.10	0.01	0.08	<0.0087	8.22	54.57	0.05	9.28
MB23HmRe-6	1.50	0.33	0.07	0.14	0.02	0.10	0.02	0.07	0.01	0.06	0.01	1.69	50.40	0.02	2.03
MB23HmRe-7	0.75	0.15	0.04	0.18	0.02	0.12	0.02	0.07	0.00	0.04	0.00	3.01	38.22	0.07	4.56
MB23HmRe-8	0.48	0.14	0.05	0.27	0.03	0.18	0.06	0.20	0.03	0.09	0.02	124.92	15.45	0.05	16.40
MB23HmRe-9	23.69	2.09	0.74	0.68	0.11	0.38	0.07	0.19	0.02	0.13	0.01	114.30	65.67	0.37	13.49
MB25Hm-1	0.58	0.26	0.11	0.25	0.06	0.21	0.07	0.18	0.06	0.14	0.02	0.03	0.67	0.00	0.02
MB25Hm-10	0.69	0.09	0.06	0.43	0.03	0.38	0.05	0.13	0.02	0.07	<0.00	0.02	0.52	<0.0101	0.02

Position	Deposit	Lithology	Sample no.	Analysis no.	Texture	Mg	Al	Si	P	Ca	Sc	Ti	V	Cr	Mn
Middle	Cavalier	ORE	MB25	MB25Hm-11	porous martite	274.98	181.08	5976.81	446.51	<155.27	<0.098	2.69	2.54	<0.99	564.60
Middle	Cavalier	ORE	MB25	MB25Hm-12	porous martite	130.71	157.98	831.49	349.54	148.62	<0.102	2.70	2.61	<0.98	536.60
Middle	Cavalier	ORE	MB25	MB25Hm-13	porous martite	271.76	300.41	1930.34	652.22	<142.59	0.12	3.71	3.37	0.99	606.67
Middle	Cavalier	ORE	MB25	MB25Hm-14	porous martite	55.15	144.28	558.46	128.37	130.75	0.10	47.52	4.35	1.01	526.37
Middle	Cavalier	ORE	MB25	MB25Hm-15	porous martite	265.59	373.51	5486.98	718.33	<150.67	<0.11	4.90	3.96	1.48	576.00
Middle	Cavalier	ORE	MB25	MB25Hm-16	porous martite	166.55	113.16	675.76	172.98	<160.66	<0.058	1.28	2.02	<0.99	585.29
Middle	Cavalier	ORE	MB25	MB25Hm-17	porous martite	125.93	247.06	1228.32	300.59	<137.48	<0.132	2.64	3.24	<0.88	599.65
Middle	Cavalier	ORE	MB25	MB25Hm-18	porous martite	337.12	366.80	3050.51	762.11	<149.85	<0.101	2.53	4.23	1.96	609.18
Middle	Cavalier	ORE	MB25	MB25Hm-19	porous martite	79.78	112.55	667.67	41.29	<154.48	<0.112	30.21	3.21	1.05	575.08
Middle	Cavalier	ORE	MB25	MB25Hm-2	porous martite	168.72	203.22	982.27	409.32	<94.54	0.10	2.49	2.34	<0.93	604.04
Middle	Cavalier	ORE	MB25	MB25Hm-20	porous martite	306.86	260.05	16630.61	584.30	219.17	0.12	1.79	3.10	1.40	671.30
Middle	Cavalier	ORE	MB25	MB25Hm-21	porous martite	217.33	246.12	1994.65	470.02	<164.06	0.26	94.87	7.05	1.52	736.11
Middle	Cavalier	ORE	MB25	MB25Hm-22	porous martite	197.92	264.43	2041.21	478.54	<170.06	<0.123	2.75	3.03	<0.97	611.65
Middle	Cavalier	ORE	MB25	MB25Hm-23	porous martite	217.67	214.35	933.60	412.74	<173.12	<0.111	1.94	2.95	1.76	594.40
Middle	Cavalier	ORE	MB25	MB25Hm-24	porous martite	243.94	526.06	2712.44	856.12	<140.49	0.26	3.61	4.51	1.18	738.43
Middle	Cavalier	ORE	MB25	MB25Hm-3	porous martite	171.21	185.69	6779.92	416.17	<134.78	0.09	3.00	2.32	<0.97	564.86
Middle	Cavalier	ORE	MB25	MB25Hm-4	porous martite	370.31	220.73	6744.91	691.47	<113.71	0.12	2.94	3.03	1.76	473.30
Middle	Cavalier	ORE	MB25	MB25Hm-5	porous martite	268.33	300.08	9287.46	502.88	182.05	<0.115	2.11	2.53	1.14	644.77
Middle	Cavalier	ORE	MB25	MB25Hm-6	porous martite	339.51	257.94	2261.40	539.30	<132.34	<0.079	1.46	2.47	1.54	564.06
Middle	Cavalier	ORE	MB25	MB25Hm-7	porous martite	171.52	442.95	4119.92	507.79	<127.19	0.18	6.97	7.69	<0.94	680.63
Middle	Cavalier	ORE	MB25	MB25Hm-8	porous martite	630.43	1444.32	5415.16	1679.47	144.85	0.45	32.45	12.98	1.50	2096.44
Middle	Cavalier	ORE	MB25	MB25Hm-9	porous martite	474.51	602.77	4008.09	1129.23	<134.17	0.16	3.15	7.94	<0.92	767.38
Middle	Cavalier	BIF	MB26	MB26Hm-1	clean martite	1014.29	29.74	23404.96	15.53	1489.91	0.34	<0.66	0.01	<1.38	99.21
Middle	Cavalier	BIF	MB26	MB26Hm-5	clean martite	89.44	15.27	6949.61	96.29	1278.61	0.16	1.50	<0.023	<1.34	45.31
Middle	Cavalier	BIF	MB26	MB26Hm-7	clean martite	1464.32	23.69	12009.39	14.93	2083.18	0.18	1.15	<0.0157	<1.27	209.11
Middle	Cavalier	BIF	MB26	MB26Hm-8	clean martite	1571.34	31.19	22833.60	117.57	181.10	0.44	0.67	0.01	<1.24	106.48
Middle	Cavalier	BIF	MB26	MB26Mt-1	magnetite	11.68	334.88	14397.27	45.79	<99.5	0.12	5.31	1.09	<0.85	19.37
Middle	Cavalier	BIF	MB26	MB26Mt-10	magnetite	13.49	77.01	7822.03	97.66	<92.48	0.12	9.61	1.10	<0.78	23.86
Middle	Cavalier	BIF	MB26	MB26Mt-2	magnetite	27.05	452.72	29994.65	124.10	<108.74	0.15	5.43	1.76	<0.88	31.43
Middle	Cavalier	BIF	MB26	MB26Mt-7	magnetite	28.42	501.91	11847.15	102.40	<96.63	0.12	12.35	2.12	1.21	59.06
Middle	Queen	ORE	MB27	MB27HmClean-1	clean martite	85.69	233.67	1944.38	34.66	40.40	<0.067	6.07	1.83	0.67	269.88
Middle	Queen	ORE	MB27	MB27HmClean-10	clean martite	112.65	303.89	713.41	45.72	67.32	0.09	6.43	2.38	0.94	357.02
Middle	Queen	ORE	MB27	MB27HmClean-11	clean martite	55.14	196.68	2926.86	27.66	<58.5	<0.067	4.74	1.76	0.87	199.29
Middle	Queen	ORE	MB27	MB27HmClean-12	clean martite	59.67	204.12	1677.92	25.02	46.18	<0.061	6.84	1.80	0.79	211.83
Middle	Queen	ORE	MB27	MB27HmClean-13	clean martite	53.40	182.34	615.94	17.40	<45.31	<0.065	6.17	1.64	<0.48	161.30
Middle	Queen	ORE	MB27	MB27HmClean-14	clean martite	81.10	203.50	3166.69	25.84	<44.83	<0.076	5.84	1.80	0.69	188.15
Middle	Queen	ORE	MB27	MB27HmClean-15	clean martite	75.01	254.69	944.30	42.08	<49.01	0.09	5.89	1.92	1.36	416.67
Middle	Queen	ORE	MB27	MB27HmClean-2	clean martite	50.14	196.36	2340.21	23.11	<43.66	<0.058	7.41	2.14	1.03	241.86
Middle	Queen	ORE	MB27	MB27HmClean-4	clean martite	196.02	435.33	1077.42	70.86	82.14	0.45	6.32	7.02	1.18	1096.58
Middle	Queen	ORE	MB27	MB27HmClean-5	clean martite	74.70	228.98	912.11	30.94	<61.35	<0.067	4.95	2.52	1.10	350.69
Middle	Queen	ORE	MB27	MB27HmClean-6	clean martite	88.51	251.52	3655.02	35.95	<40.57	0.11	6.04	2.18	0.54	314.31
Middle	Queen	ORE	MB27	MB27HmClean-7	clean martite	191.47	374.73	1005.93	59.47	<43.74	0.12	5.09	4.03	0.88	855.60
Middle	Queen	ORE	MB27	MB27HmClean-8	clean martite	298.04	595.55	1305.74	93.15	60.73	0.25	4.52	2.82	1.32	973.96

Analysis no.	Co	Ni	Cu	Zn	Ga	As	Sr	Y	Zr	Nb	Mo	Sn	Sb	Ba	La	Ce	Pr
MB25Hm-11	1.96	2.43	2.07	18.95	0.57	1.60	0.98	2.42	0.03	0.07	0.02	0.56	<0.29	0.34	0.75	0.85	0.10
MB25Hm-12	1.81	1.26	1.28	21.61	0.53	0.97	0.94	2.14	0.03	0.02	0.04	0.17	0.33	0.65	0.52	0.67	0.08
MB25Hm-13	3.46	4.73	1.79	24.80	0.68	0.90	1.31	3.65	0.03	0.03	0.08	0.20	<0.21	1.70	0.95	1.21	0.16
MB25Hm-14	1.34	1.02	0.49	14.45	0.60	<0.5	0.31	1.42	0.05	0.09	0.02	<0.133	<0.27	0.32	0.49	0.49	0.05
MB25Hm-15	2.87	3.60	2.46	27.06	0.94	1.67	1.57	4.51	0.08	1.29	0.04	0.29	<0.24	0.82	1.30	1.51	0.19
MB25Hm-16	1.19	1.16	<0.39	17.32	0.51	<0.49	0.57	0.93	<0.00	0.02	0.04	0.46	<0.27	<0.00	0.28	0.31	0.04
MB25Hm-17	1.95	3.26	0.93	24.24	0.85	0.58	0.86	3.50	0.05	<0.00	<0.00	0.36	<0.22	1.27	0.66	0.87	0.11
MB25Hm-18	4.22	4.95	8.94	28.16	1.02	1.55	1.44	4.32	0.13	0.03	0.02	0.30	<0.23	0.76	1.11	1.51	0.14
MB25Hm-19	1.02	0.32	<0.36	16.09	0.95	0.95	0.14	0.41	0.03	0.04	0.02	0.16	0.24	0.16	0.17	0.16	0.02
MB25Hm-2	2.34	0.99	1.05	15.26	1.04	0.74	1.08	2.04	0.05	0.01	0.03	0.14	0.32	0.74	0.68	0.71	0.07
MB25Hm-20	2.19	2.87	1.42	24.77	0.95	1.33	1.49	3.15	<0.00	0.02	<0.051	0.27	<0.28	0.67	0.88	1.00	0.19
MB25Hm-21	3.35	3.94	0.89	23.12	0.85	0.91	0.90	5.92	0.29	0.20	0.06	0.30	0.24	0.87	1.35	1.59	0.16
MB25Hm-22	2.49	2.12	1.50	24.39	0.65	1.10	1.38	2.84	0.13	1.08	0.02	0.23	<0.28	0.80	0.89	0.94	0.14
MB25Hm-23	2.44	2.16	0.91	21.09	0.97	1.00	1.24	2.85	<0.00	0.03	<0.00	0.28	<0.21	0.49	0.85	0.93	0.12
MB25Hm-24	4.53	5.60	3.12	34.42	0.90	1.95	1.67	11.57	0.10	0.17	0.05	1.08	<0.3	1.25	1.97	2.74	0.38
MB25Hm-3	1.98	1.34	1.63	16.74	0.58	1.50	1.16	2.39	0.02	0.08	<0.00	<0.088	0.31	0.59	0.72	0.91	0.13
MB25Hm-4	3.00	3.88	1.61	17.25	0.48	0.88	1.41	3.14	0.08	0.03	0.05	<0.126	<0.37	1.42	0.84	0.92	0.12
MB25Hm-5	2.32	2.40	1.14	18.75	0.73	1.03	1.40	2.60	<0.00	0.07	0.02	0.15	<0.32	0.96	0.84	0.99	0.12
MB25Hm-6	2.44	1.92	1.87	18.36	1.06	1.43	1.71	2.72	<0.00	0.08	<0.00	0.29	<0.32	0.33	0.78	0.81	0.11
MB25Hm-7	4.32	3.51	0.99	36.00	0.84	2.29	1.66	11.09	<0.00	0.14	0.02	<0.121	0.31	3.43	2.24	2.83	0.33
MB25Hm-8	14.01	17.25	6.84	56.78	1.21	1.87	2.91	27.02	0.54	0.20	0.07	0.57	<0.23	2.04	4.59	5.87	0.67
MB25Hm-9	5.74	9.35	5.74	33.21	1.04	1.45	1.70	7.98	0.25	0.15	0.07	0.24	<0.25	1.84	1.74	1.94	0.21
MB26Hm-1	0.03	0.16	<0.2	1.10	0.17	3.02	0.39	2.27	<0.085	0.01	0.17	0.52	0.58	1.82	0.38	0.50	0.06
MB26Hm-5	0.07	<0.00	<0.19	2.19	0.03	0.85	0.34	0.88	0.05	<0.00	0.03	0.26	<0.3	<0.00	0.15	0.24	0.02
MB26Hm-7	<0.047	0.09	<0.28	0.62	0.08	2.77	0.42	1.49	<0.00	0.06	0.02	0.86	<0.32	0.56	0.28	0.36	0.02
MB26Hm-8	0.08	<0.00	0.61	2.22	0.21	5.68	0.79	4.39	0.17	0.06	0.50	1.13	0.87	9.49	0.75	1.34	0.13
MB26Mt-1	0.40	1.23	0.50	4.76	0.34	<0.36	0.08	0.50	0.02	0.01	0.03	0.19	<0.219	0.12	0.34	0.38	0.04
MB26Mt-10	0.74	1.36	1.33	6.52	0.04	0.98	0.14	1.55	0.05	0.00	0.07	0.24	<0.15	1.15	0.85	1.09	0.12
MB26Mt-2	0.48	1.12	1.00	6.80	0.46	<0.35	0.17	0.77	<0.00	0.02	0.03	0.21	<0.178	0.26	0.45	0.43	0.05
MB26Mt-7	0.46	1.11	0.89	7.05	0.59	0.65	0.14	2.45	0.02	<0.00	0.01	<0.071	<0.17	0.64	1.20	1.48	0.15
MB27HmClean-1	2.21	2.99	2.72	11.62	1.65	0.63	0.22	0.45	<0.00	0.12	0.19	1.26	<0.23	0.44	0.03	0.12	0.01
MB27HmClean-10	2.88	3.59	5.58	15.55	1.96	0.47	0.45	0.67	<0.00	0.00	0.20	0.93	0.17	0.72	0.08	0.14	0.02
MB27HmClean-11	2.27	1.70	1.09	7.64	2.07	0.59	0.13	0.33	<0.00	0.00	0.37	1.13	<0.141	0.79	0.07	0.13	0.03
MB27HmClean-12	2.38	1.24	<1.04	8.58	1.92	0.88	0.22	0.35	<0.00	0.01	0.31	1.05	0.28	0.91	0.04	0.11	0.02
MB27HmClean-13	1.97	1.49	1.29	6.19	1.88	0.79	0.07	0.16	0.03	<0.00	0.23	0.95	0.22	0.97	0.02	0.09	0.01
MB27HmClean-14	2.87	1.82	<0.99	8.46	2.11	1.67	0.18	0.34	0.01	0.02	0.24	1.04	0.27	0.96	0.05	0.10	0.01
MB27HmClean-15	4.03	2.54	2.38	9.78	2.11	1.53	0.57	1.28	0.06	0.02	0.38	1.03	0.26	1.06	0.19	0.23	0.03
MB27HmClean-2	2.34	1.99	1.70	6.68	1.82	0.55	0.28	0.47	0.04	<0.00	0.24	1.75	0.22	0.50	0.07	0.13	0.02
MB27HmClean-4	5.32	8.01	10.53	20.69	2.26	0.89	3.52	2.61	0.15	0.02	0.81	1.28	0.21	1.96	0.24	0.41	0.06
MB27HmClean-5	3.52	2.16	1.86	10.97	2.04	1.15	0.44	0.61	<0.00	0.03	0.33	1.11	0.21	0.55	0.06	0.12	0.01
MB27HmClean-6	2.24	3.75	5.34	14.22	1.72	0.40	0.50	0.67	0.03	0.01	0.26	1.20	0.16	0.63	0.07	0.09	0.02
MB27HmClean-7	4.04	5.49	9.65	25.43	2.20	1.04	4.12	1.43	0.08	0.01	0.48	1.07	<0.108	1.02	0.16	0.25	0.04
MB27HmClean-8	5.29	6.95	16.78	39.77	2.26	1.27	1.77	2.11	<0.00	0.00	1.04	1.22	0.15	0.75	0.16	0.29	0.05

Analysis no.	Nd	Sm	Eu	Gd	Tb	Dy	Ho	Er	Tm	Yb	Lu	W	Pb208	Th	U
MB25Hm-11	0.63	0.18	0.07	0.22	0.06	0.27	0.05	0.17	0.01	0.13	0.02	0.03	0.59	<0.00	0.03
MB25Hm-12	0.46	0.10	0.01	0.22	0.02	0.24	0.03	0.14	0.03	0.08	0.01	<0.03	0.45	<0.00	0.04
MB25Hm-13	0.76	0.19	0.11	0.29	0.05	0.37	0.07	0.17	0.05	0.13	0.03	0.06	0.36	<0.0106	0.01
MB25Hm-14	0.22	0.08	0.05	0.11	0.01	0.11	0.04	0.06	0.00	0.03	0.02	0.02	0.36	0.05	0.06
MB25Hm-15	0.79	0.32	0.12	0.40	0.07	0.44	0.11	0.31	0.01	0.24	0.03	0.13	1.02	<0.0137	0.09
MB25Hm-16	0.19	0.02	0.02	0.02	0.01	0.12	0.01	<0.041	<0.0099	0.03	0.00	<0.00	0.08	<0.00	0.02
MB25Hm-17	0.67	0.17	0.11	0.37	0.05	0.22	0.08	0.18	0.03	0.19	0.03	0.03	0.35	0.01	0.02
MB25Hm-18	0.93	0.20	0.08	0.43	0.08	0.32	0.09	0.31	0.02	0.24	0.04	0.04	0.61	<0.01	0.04
MB25Hm-19	0.05	<0.00	0.01	0.11	0.01	0.03	<0.0143	0.13	<0.0101	0.03	0.01	0.06	0.19	0.02	0.03
MB25Hm-2	0.43	0.11	0.07	0.14	0.04	0.22	0.04	0.06	0.02	0.05	0.02	0.04	0.48	<0.00	0.01
MB25Hm-20	0.78	0.31	0.08	0.31	0.06	0.13	0.06	0.26	0.02	0.15	0.02	<0.04	0.31	<0.0152	0.01
MB25Hm-21	0.93	0.32	0.15	0.62	0.06	0.62	0.08	0.35	0.06	0.22	0.03	0.07	0.71	0.04	0.05
MB25Hm-22	0.53	0.17	0.10	0.20	0.04	0.23	0.08	0.17	0.03	0.08	0.00	0.07	1.01	0.01	0.03
MB25Hm-23	0.64	0.12	0.07	0.40	0.05	0.28	0.07	0.14	0.02	0.04	0.01	0.03	0.46	<0.00	0.01
MB25Hm-24	2.04	0.64	0.31	1.43	0.22	1.05	0.23	0.63	0.11	0.41	0.09	0.03	0.85	<0.0098	0.04
MB25Hm-3	0.45	0.11	0.08	0.14	0.03	0.13	0.02	0.16	0.02	0.05	0.02	0.06	0.96	<0.00	0.05
MB25Hm-4	0.89	0.19	0.09	0.34	0.06	0.24	0.06	0.18	0.04	0.19	0.02	0.06	0.74	0.01	0.01
MB25Hm-5	0.80	0.14	0.06	0.37	0.03	0.24	0.05	0.13	0.03	0.08	0.02	0.06	0.32	0.01	0.00
MB25Hm-6	0.67	0.12	0.08	0.22	0.04	0.34	0.05	0.10	0.01	0.11	0.01	0.01	0.74	0.00	0.02
MB25Hm-7	1.62	0.43	0.26	0.91	0.16	0.95	0.19	0.68	0.08	0.40	0.11	0.05	1.21	0.01	0.05
MB25Hm-8	3.69	0.94	0.53	1.82	0.27	1.63	0.44	1.43	0.17	0.94	0.14	0.06	0.95	0.04	0.16
MB25Hm-9	1.18	0.41	0.16	0.55	0.12	0.45	0.11	0.49	0.02	0.25	0.04	<0.027	1.18	0.01	0.09
MB26Hm-1	0.26	<0.109	0.05	0.13	0.03	0.13	0.06	0.12	0.01	0.09	0.01	6.39	1.07	0.01	0.28
MB26Hm-5	0.21	<0.00	<0.00	0.04	0.01	<0.038	0.01	0.03	<0.00	<0.00	0.01	0.58	0.04	<0.00	0.00
MB26Hm-7	0.09	0.12	0.04	<0.061	0.01	0.09	0.02	0.07	0.01	0.10	0.01	5.99	0.25	<0.0102	0.13
MB26Hm-8	0.41	0.10	0.09	0.34	0.01	0.33	0.10	0.29	0.04	0.34	0.02	9.71	1.08	0.02	0.38
MB26Mt-1	0.17	0.01	0.04	<0.00	<0.0093	0.03	0.01	<0.00	0.00	0.03	<0.00	<0.012	0.04	<0.00	0.01
MB26Mt-10	0.62	0.08	0.03	0.08	0.02	0.10	0.02	0.06	<0.0064	0.04	0.01	0.23	0.22	<0.0042	0.01
MB26Mt-2	0.17	0.02	0.01	0.03	0.00	0.04	0.02	0.06	0.01	<0.00	<0.0071	0.05	0.06	<0.00	0.01
MB26Mt-7	0.51	0.11	0.06	0.12	0.02	0.16	0.02	0.14	0.01	0.02	0.00	<0.013	0.02	0.00	<0.00
MB27HmClean-1	0.06	0.05	0.01	0.05	0.01	0.04	0.01	0.03	0.01	0.02	<0.0045	0.07	4.37	<0.00	0.14
MB27HmClean-10	0.11	0.07	0.02	0.12	0.02	0.09	0.02	0.08	0.01	0.05	0.01	0.08	6.23	0.00	0.16
MB27HmClean-11	0.10	0.05	0.01	0.11	0.01	0.08	0.02	0.02	0.01	0.04	0.00	0.08	8.63	<0.0065	0.17
MB27HmClean-12	0.09	0.05	0.02	0.10	0.01	0.06	0.01	0.03	0.01	0.01	0.01	0.02	10.71	0.00	0.25
MB27HmClean-13	<0.00	0.04	0.01	0.09	0.02	0.03	0.01	0.02	0.00	<0.0187	0.00	0.01	9.21	0.00	0.18
MB27HmClean-14	0.09	0.11	0.02	0.07	0.01	0.05	0.01	0.02	0.02	0.03	0.00	0.06	14.51	<0.00	0.36
MB27HmClean-15	0.32	0.04	0.05	0.17	0.01	0.12	0.05	0.15	0.00	0.07	0.01	0.20	10.23	<0.0048	0.22
MB27HmClean-2	0.13	0.12	0.03	0.08	0.02	0.12	0.02	0.05	<0.0065	0.03	0.02	0.10	7.00	<0.0045	0.16
MB27HmClean-4	0.34	0.15	0.07	0.37	0.04	0.28	0.08	0.26	0.04	0.21	0.03	0.67	7.64	0.00	0.54
MB27HmClean-5	0.09	0.03	0.02	0.11	0.02	0.11	0.02	0.09	0.01	0.01	0.03	0.44	10.20	0.00	0.26
MB27HmClean-6	0.09	0.04	0.02	0.09	0.02	0.09	0.01	0.06	0.01	0.03	<0.0075	0.10	6.05	0.00	0.20
MB27HmClean-7	0.21	0.09	0.04	0.16	0.02	0.22	0.05	0.16	0.03	0.13	0.02	0.21	6.76	0.00	0.38
MB27HmClean-8	0.18	0.08	0.06	0.31	0.04	0.20	0.10	0.15	0.04	0.15	0.03	0.14	7.84	<0.00	0.27

Position	Deposit	Lithology	Sample no.	Analysis no.	Texture	Mg	Al	Si	P	Ca	Sc	Ti	V	Cr	Mn
Middle	Queen	ORE	MB28	MB28HmAgg-1	clean martite	20.14	148.49	921.84	44.18	<31.93	0.09	6.40	3.08	0.73	69.34
Middle	Queen	ORE	MB28	MB28HmAgg-10	clean martite	12.02	138.66	1332.01	110.14	<51.73	0.12	8.50	3.58	1.34	66.94
Middle	Queen	ORE	MB28	MB28HmAgg-11	clean martite	41.53	171.65	1860.83	92.65	103.23	0.27	8.68	3.33	0.68	88.90
Middle	Queen	ORE	MB28	MB28HmAgg-12	clean martite	13.88	164.09	668.26	51.76	159.23	0.06	10.24	3.94	1.05	53.82
Middle	Queen	ORE	MB28	MB28HmAgg-2	clean martite	20.19	166.83	1381.46	31.42	58.01	0.12	7.47	2.90	1.00	58.51
Middle	Queen	ORE	MB28	MB28HmAgg-3	clean martite	11.02	146.48	1479.68	77.60	58.39	0.18	8.45	4.94	1.06	57.52
Middle	Queen	ORE	MB28	MB28HmAgg-4	clean martite	30.89	168.70	1043.88	96.18	114.49	0.21	6.74	3.48	0.91	117.08
Middle	Queen	ORE	MB28	MB28HmAgg-5	clean martite	14.50	188.13	1896.92	42.87	<44.94	<0.052	6.95	7.73	0.88	67.12
Middle	Queen	ORE	MB28	MB28HmAgg-6	clean martite	11.99	141.77	807.28	30.34	42.05	0.07	8.12	4.08	0.87	45.10
Middle	Queen	ORE	MB28	MB28HmAgg-7	clean martite	9.08	177.88	1512.30	27.93	<49.9	0.10	9.12	2.45	0.67	22.66
Middle	Queen	ORE	MB28	MB28HmAgg-8	clean martite	11.09	145.22	945.26	126.65	<49.03	0.07	9.23	9.37	0.75	56.59
Middle	Queen	ORE	MB28	MB28HmAgg-9	clean martite	9.52	149.92	886.85	148.44	<59.68	0.09	8.82	3.68	0.96	50.66
Middle	Queen	ORE	MB28	MB28HmDirtry-1	clean martite	8.41	180.55	555.05	80.52	105.11	0.14	11.29	5.43	1.29	90.31
Middle	Queen	ORE	MB28	MB28HmDirtry-2	clean martite	16.76	158.14	1010.64	442.78	<59.49	0.22	7.44	21.20	1.78	114.65
Middle	Queen	ORE	MB28	MB28HmDirtry-3	clean martite	14.64	1181.40	895.58	365.13	88.75	0.13	9.31	11.74	1.27	86.75
Middle	Queen	ORE	MB28	MB28HmDirtry-4	clean martite	24.73	202.11	903.25	63.68	145.16	0.33	5.40	58.15	2.21	114.01
Middle	Queen	ORE	MB28	MB28HmDirtry-5	clean martite	15.69	169.47	629.09	381.21	105.83	0.22	8.98	13.02	1.38	98.66
Middle	Queen	ORE	MB28	MB28HmDirtry-6	clean martite	19.88	170.70	1293.74	106.46	87.10	0.13	10.70	5.06	0.90	60.45
Middle	Queen	ORE	MB28	MB28HmLam-1	clean martite	19.67	101.29	990.22	255.88	<67.06	0.11	2.77	8.66	1.30	55.26
Middle	Queen	ORE	MB28	MB28HmLam-2	clean martite	8.26	126.69	986.69	262.26	<52.92	<0.08	2.72	18.54	1.63	39.93
Middle	Queen	ORE	MB28	MB28HmLam-3	clean martite	15.60	140.75	1019.85	129.45	<59.88	0.14	3.07	24.75	1.37	74.84
Middle	Queen	ORE	MB28	MB28HmLam-4	clean martite	11.52	159.96	706.08	219.62	<53.5	0.08	1.73	14.09	1.18	54.17
Middle	Queen	ORE	MB28	MB28HmLam-5	clean martite	15.80	387.89	1020.03	234.34	<75.41	0.16	9.22	29.21	2.38	87.34
Middle	Queen	ORE	MB28	MB28HmLam-6	clean martite	12.92	125.79	978.31	207.77	<57.73	0.16	2.95	13.67	1.10	74.28
North	Princess	BIF	MB2	MB2Hm-1	clean martite	361.25	1494.31	3951.32	31.45	88.87	0.34	757.95	45.45	13.20	102.89
North	Princess	BIF	MB2	MB2Hm-2	clean martite	384.11	1288.10	2141.36	25.45	168.29	0.33	697.38	42.08	12.32	160.05
North	Princess	BIF	MB2	MB2Hm-3	clean martite	609.37	1790.96	2655.25	20.95	126.13	0.39	702.42	43.37	15.54	441.42
North	Princess	BIF	MB2	MB2Hm-4	clean martite	376.72	1440.47	3404.98	24.59	160.26	0.30	799.71	41.42	12.81	80.10
North	Princess	BIF	MB2	MB2Hm-5	clean martite	375.47	1601.63	3171.06	19.49	149.20	0.95	702.93	59.66	294.36	259.64
North	Princess	BIF	MB2	MB2Hm-6	clean martite	207.38	1247.90	2424.36	29.02	118.13	1.06	828.29	52.33	423.46	83.79
North	Princess	BIF	MB2	MB2Hm-7	clean martite	310.56	1552.94	3220.38	25.69	261.31	0.39	645.83	48.69	29.86	213.84
North	Princess	BIF	MB2	MB2Hm-8	clean martite	253.07	1268.00	3499.38	19.40	168.58	0.28	810.07	39.23	10.11	114.08
North	Princess	BIF	MB2	MB2HmVein-3	clean martite	5481.20	8115.43	19951.22	22.83	5663.37	2.67	282.59	24.25	6.68	2778.37
North	Princess	BIF	MB2	MB2HmVein-4	clean martite	1766.73	244.02	4221.85	47.04	5300.34	2.45	44.70	10.52	2.17	4576.68
North	Princess	BIF	MB2	MB2HmVein-6	clean martite	884.50	932.50	2204.67	11.30	2812.21	1.62	264.03	26.26	5.91	1853.30
North	Princess	BIF	MB2	MB2HmVein-7	clean martite	316.32	524.93	3893.73	18.16	2734.00	1.26	180.66	17.87	2.55	409.45
North	Princess	BIF	MB2	MB2HmVein-9	clean martite	2426.59	600.59	1019.33	19.91	4890.20	3.22	56.30	18.27	1.68	8322.28
South	Magnet	BIF	MB34a	MB34aHm-2	clean martite	7485.77	195.75	27726.24	10.04	183.50	0.18	15.94	5.29	1.02	24.88
South	Magnet	BIF	MB34a	MB34aMt-12	magnetite	1138.02	15.83	3304.62	9.58	<145.23	<0.062	2.79	0.32	<0.47	156.49
South	Magnet	BIF	MB34a	MB34aMt-15	magnetite	6064.14	16.15	12373.92	11.17	<173.86	<0.087	1.99	0.19	<0.51	176.93
South	Magnet	BIF	MB34a	MB34aMt-16	magnetite	988.59	114.52	2562.45	42.01	<148.98	<0.12	13.07	5.10	0.71	27.03
South	Magnet	BIF	MB34a	MB34aMt-17	magnetite	7318.91	56.95	16417.49	21.73	303.44	0.11	4.21	1.62	0.59	176.43
South	Magnet	BIF	MB34a	MB34aMt-18	magnetite	16919.53	88.43	36442.30	18.13	505.60	<0.122	3.09	0.26	<0.58	155.10

Analysis no.	Co	Ni	Cu	Zn	Ga	As	Sr	Y	Zr	Nb	Mo	Sn	Sb	Ba	La	Ce	Pr
MB28HmAgg-1	0.82	2.73	9.94	12.78	0.58	2.64	0.14	1.11	0.02	0.01	0.25	0.47	0.27	1.40	0.43	0.57	0.06
MB28HmAgg-10	0.50	2.98	25.67	31.14	0.47	2.42	0.22	1.30	0.05	0.01	0.08	0.56	0.38	1.69	0.45	0.56	0.09
MB28HmAgg-11	1.19	2.34	8.54	10.13	0.59	5.48	0.26	1.85	0.19	0.10	0.28	0.68	0.53	3.72	1.57	2.28	0.15
MB28HmAgg-12	0.42	1.41	25.90	57.96	0.52	1.66	0.22	0.66	0.51	0.02	0.09	0.53	0.24	0.34	0.22	0.46	0.04
MB28HmAgg-2	0.71	2.49	12.03	19.93	0.67	2.33	0.22	0.77	0.02	0.01	0.07	0.61	<0.18	0.47	0.37	0.39	0.05
MB28HmAgg-3	0.40	2.77	10.80	9.77	0.66	3.24	0.33	1.30	0.05	0.02	0.07	0.61	0.39	1.49	0.43	0.58	0.05
MB28HmAgg-4	1.78	2.69	12.08	11.77	0.52	4.12	0.63	1.85	0.15	0.04	0.38	0.64	0.36	2.52	0.68	1.02	0.11
MB28HmAgg-5	0.45	3.31	10.02	12.78	0.47	2.37	0.21	1.07	0.04	0.01	0.09	0.66	0.30	1.67	0.23	0.34	0.03
MB28HmAgg-6	0.53	2.55	7.14	7.41	0.53	2.48	0.12	0.67	0.12	0.00	0.25	0.56	0.21	0.43	0.19	0.29	0.03
MB28HmAgg-7	0.22	2.34	6.38	8.00	0.47	2.30	0.08	0.60	0.11	0.02	1.65	0.69	0.22	0.39	0.19	0.25	0.03
MB28HmAgg-8	0.50	1.91	6.71	9.59	0.61	3.10	0.13	0.85	0.06	0.02	0.24	0.55	0.18	0.48	0.42	0.48	0.04
MB28HmAgg-9	0.28	2.07	12.23	13.07	0.56	2.44	0.24	0.78	0.04	0.09	<0.045	0.67	0.47	0.80	0.26	0.45	0.07
MB28HmDirtry-1	0.58	1.49	60.58	124.28	0.36	1.23	0.48	0.41	<0.00	0.01	0.03	0.86	0.10	2.09	0.17	0.28	0.04
MB28HmDirtry-2	0.35	1.85	21.98	25.99	0.41	2.74	1.01	1.69	0.13	0.00	0.16	0.60	0.17	4.24	0.51	0.95	0.11
MB28HmDirtry-3	0.34	1.31	36.61	60.10	0.42	2.07	0.73	0.89	0.06	0.04	0.18	0.60	0.33	2.20	0.22	0.41	0.05
MB28HmDirtry-4	1.23	4.01	12.36	40.15	0.42	1.37	1.29	1.01	0.47	0.02	0.17	0.69	0.21	12.21	0.30	0.51	0.07
MB28HmDirtry-5	0.31	1.58	28.43	66.29	0.22	2.07	0.55	1.19	0.11	0.03	0.11	0.60	0.22	4.17	0.27	0.55	0.08
MB28HmDirtry-6	0.48	1.23	46.63	75.67	0.53	1.96	0.34	0.45	0.08	0.02	0.06	0.68	0.18	1.27	0.13	0.26	0.05
MB28HmLam-1	0.19	1.70	4.84	7.97	0.39	2.37	0.40	1.26	0.19	0.02	0.07	0.61	0.21	1.39	0.22	0.39	0.04
MB28HmLam-2	0.07	3.01	1.65	4.26	0.33	1.02	0.13	0.70	0.06	0.01	0.18	0.68	0.13	2.03	0.15	0.17	0.03
MB28HmLam-3	0.43	3.03	9.82	37.37	0.51	1.59	0.35	2.14	0.12	0.03	0.20	0.69	0.24	5.15	0.30	0.50	0.10
MB28HmLam-4	0.16	2.15	5.71	8.92	0.37	2.15	0.24	0.85	0.11	0.00	0.13	0.68	0.19	2.41	0.16	0.30	0.02
MB28HmLam-5	0.21	2.15	10.82	10.00	0.40	2.71	0.43	1.04	0.16	0.03	0.19	1.23	0.38	2.69	0.26	0.40	0.04
MB28HmLam-6	0.31	1.91	5.82	9.92	0.35	2.55	0.31	2.67	0.04	0.01	0.18	0.65	0.24	4.26	1.14	1.66	0.18
MB2Hm-1	6.72	16.20	10.52	11.00	3.19	69.70	1.02	0.54	2.15	1.60	1.02	2.18	22.83	2.81	0.42	0.61	0.09
MB2Hm-2	1.83	8.64	7.45	9.21	3.24	59.76	0.98	0.46	0.94	1.54	0.68	1.97	17.85	2.39	0.33	0.56	0.08
MB2Hm-3	5.22	16.89	31.92	15.83	4.17	79.08	1.34	0.57	0.82	1.78	0.71	2.76	27.06	4.37	0.37	0.65	0.06
MB2Hm-4	5.38	16.52	8.58	11.28	3.51	73.84	0.98	0.52	1.90	1.26	0.72	2.56	21.53	3.97	0.49	0.75	0.07
MB2Hm-5	1.23	8.46	2.10	18.05	4.91	98.42	1.42	9.75	182.94	1.29	0.77	1.47	42.76	5.30	0.45	0.75	0.10
MB2Hm-6	1.77	9.86	6.84	9.98	4.11	92.85	1.15	10.25	127.86	2.31	1.16	2.19	34.21	3.69	0.69	1.09	0.09
MB2Hm-7	4.04	10.41	3.82	22.71	5.07	82.34	1.02	0.68	2.11	1.02	0.70	2.34	37.21	6.65	0.35	0.56	0.06
MB2Hm-8	2.76	10.70	21.34	12.94	3.98	72.23	1.25	0.40	0.94	1.10	0.62	1.78	29.25	4.92	0.32	0.49	0.07
MB2HmVein-3	0.46	7.02	0.64	25.05	3.45	7.68	1.34	2.59	1.52	0.75	3.16	1.93	2.36	10.36	2.37	3.11	0.38
MB2HmVein-4	0.18	3.92	<0.29	15.60	0.25	3.98	1.64	6.43	0.65	0.31	2.91	1.42	2.04	4.80	28.68	40.85	4.51
MB2HmVein-6	0.06	2.50	<0.35	13.51	0.45	8.80	0.43	1.99	1.31	1.03	2.27	1.40	2.21	2.57	1.37	1.73	0.18
MB2HmVein-7	0.05	2.65	0.29	2.44	0.41	4.21	1.37	1.79	1.82	0.84	3.39	0.60	1.32	8.76	2.01	2.51	0.26
MB2HmVein-9	0.41	1.90	<0.28	22.07	0.29	5.93	1.16	5.89	1.77	0.32	2.59	1.24	2.82	4.46	3.47	5.34	0.52
MB34aHm-2	0.27	0.09	<0.76	1.44	0.26	0.14	0.26	0.10	0.03	<0.00	0.12	0.48	<0.165	0.17	0.01	0.02	<0.00
MB34aMt-12	0.17	<0.00	<0.62	1.28	<0.00	2.34	0.24	3.82	0.08	0.28	0.97	0.66	0.47	1.41	1.62	1.42	0.16
MB34aMt-15	0.12	0.09	<0.73	2.00	<0.068	2.26	0.19	3.99	0.06	0.24	3.79	0.56	0.64	0.70	1.74	1.51	0.15
MB34aMt-16	0.20	0.27	<0.67	0.66	0.16	0.63	0.12	0.10	<0.00	0.03	0.09	0.38	0.13	<0.00	0.02	0.01	0.01
MB34aMt-17	0.36	0.10	<0.79	1.07	0.08	4.34	0.49	2.22	0.16	0.04	0.26	0.19	0.54	0.77	0.20	0.44	0.08
MB34aMt-18	0.59	<0.29	<0.76	2.28	0.04	2.90	0.58	2.79	0.30	0.05	0.21	0.42	0.99	0.83	0.14	0.30	0.07

Analysis no.	Nd	Sm	Eu	Gd	Tb	Dy	Ho	Er	Tm	Yb	Lu	W	Pb208	Th	U
MB28HmAgg-1	0.37	0.07	0.04	0.13	0.01	0.14	0.02	0.05	0.01	0.11	0.01	0.39	1.69	<0.0041	0.21
MB28HmAgg-10	0.44	0.08	0.07	0.14	0.02	0.15	0.01	0.11	0.01	0.04	0.02	0.45	3.80	0.00	0.31
MB28HmAgg-11	0.74	0.19	0.10	0.19	0.02	0.14	0.04	0.11	0.02	0.14	0.04	1.73	2.41	0.01	0.41
MB28HmAgg-12	0.15	0.13	0.05	0.08	0.01	0.09	0.01	0.03	0.02	0.03	0.01	0.44	3.58	<0.0057	0.18
MB28HmAgg-2	0.22	0.08	0.03	0.09	0.01	0.08	0.02	0.04	0.01	0.05	0.01	0.26	2.02	0.01	0.20
MB28HmAgg-3	0.30	0.11	0.05	0.15	0.02	0.20	0.03	0.08	0.01	0.06	0.01	0.20	2.51	0.01	0.56
MB28HmAgg-4	0.59	0.19	0.11	0.22	0.03	0.19	0.03	0.13	0.02	0.08	0.01	0.68	3.09	0.01	0.78
MB28HmAgg-5	0.24	0.04	0.03	0.08	0.02	0.06	0.02	0.08	0.02	0.05	0.01	0.27	3.19	0.00	0.78
MB28HmAgg-6	0.20	<0.035	0.04	0.10	0.01	0.06	0.01	0.07	0.00	0.04	0.01	0.23	1.10	0.01	0.16
MB28HmAgg-7	0.16	0.08	0.02	0.05	0.01	0.04	0.02	0.03	0.01	0.02	0.01	0.40	1.15	<0.00	0.08
MB28HmAgg-8	0.27	0.08	0.06	0.04	0.02	0.08	0.02	0.05	0.01	0.03	0.02	0.55	1.65	0.00	0.34
MB28HmAgg-9	0.32	0.07	0.05	0.07	0.01	0.07	0.02	0.06	0.00	0.06	0.01	0.22	2.17	0.00	0.24
MB28HmDirtry-1	0.19	0.10	0.05	0.02	0.01	0.06	0.01	0.02	<0.00	0.07	0.01	0.09	9.14	0.00	0.59
MB28HmDirtry-2	0.62	0.19	0.12	0.34	0.03	0.21	0.06	0.13	0.03	0.12	0.01	0.62	6.85	0.03	2.69
MB28HmDirtry-3	0.31	0.12	0.07	0.13	0.02	0.10	0.02	0.05	0.02	0.07	0.01	0.34	6.49	0.00	1.06
MB28HmDirtry-4	0.24	0.04	0.04	0.13	0.01	0.12	0.03	0.09	0.01	0.04	0.01	1.28	17.95	0.01	5.56
MB28HmDirtry-5	0.38	0.14	0.06	0.23	0.02	0.13	0.03	0.09	0.02	0.06	0.01	0.49	6.58	0.02	1.38
MB28HmDirtry-6	0.11	0.04	0.03	0.04	0.01	0.10	0.01	0.04	0.01	0.02	0.01	0.26	7.13	0.01	0.35
MB28HmLam-1	0.25	0.04	0.08	0.18	0.02	0.10	0.02	0.09	0.01	0.10	0.01	0.43	2.99	0.00	1.74
MB28HmLam-2	0.07	0.08	0.04	<0.042	0.01	0.11	0.02	0.06	0.01	0.03	0.01	0.57	3.95	<0.0047	1.75
MB28HmLam-3	0.36	0.11	0.08	0.13	0.02	0.18	0.04	0.15	0.02	0.08	0.01	0.50	7.37	<0.0044	1.83
MB28HmLam-4	0.11	0.05	0.04	0.08	0.02	0.07	0.03	0.05	0.01	0.10	0.01	0.24	3.95	<0.00	1.18
MB28HmLam-5	0.30	0.18	0.06	0.15	0.03	0.12	0.03	0.09	0.01	0.07	0.02	0.60	4.76	0.01	1.68
MB28HmLam-6	0.81	0.20	0.12	0.28	0.04	0.18	0.04	0.18	0.04	0.12	0.03	0.35	4.30	0.00	1.28
MB2Hm-1	0.18	0.09	0.05	0.04	<0.0087	0.10	0.02	0.04	0.00	<0.00	<0.0096	9.87	18.85	0.26	1.75
MB2Hm-2	0.18	0.03	0.02	0.14	0.01	0.16	0.01	0.03	<0.0087	<0.038	0.01	8.73	11.38	0.26	1.48
MB2Hm-3	0.41	0.08	0.01	0.10	0.02	0.12	0.02	0.06	<0.0085	0.12	0.01	11.35	23.50	0.25	1.55
MB2Hm-4	0.22	0.03	0.03	0.04	0.02	0.08	0.03	0.02	0.00	0.08	0.00	9.89	18.30	0.26	1.29
MB2Hm-5	0.44	0.19	0.11	0.50	0.10	0.85	0.21	0.83	0.16	0.96	0.24	13.43	27.47	0.85	5.21
MB2Hm-6	0.53	0.19	0.22	0.63	0.13	1.00	0.26	1.10	0.14	1.39	0.20	10.58	22.95	0.82	4.34
MB2Hm-7	0.27	0.07	0.03	0.18	0.02	0.10	0.02	0.01	0.01	<0.037	0.02	15.23	23.92	0.27	1.41
MB2Hm-8	0.22	0.05	0.01	0.12	0.01	0.08	0.01	0.04	0.00	0.05	0.01	9.53	21.26	0.20	1.38
MB2HmVein-3	1.18	0.46	0.17	0.49	0.09	0.31	0.05	0.23	0.03	0.11	0.03	26.31	5.09	0.28	0.61
MB2HmVein-4	18.22	3.00	0.76	2.54	0.23	1.14	0.16	0.51	0.05	0.16	0.03	27.22	4.73	0.22	0.35
MB2HmVein-6	0.80	0.17	0.14	0.35	0.05	0.37	0.06	0.16	0.03	0.10	0.01	51.06	3.38	0.21	0.46
MB2HmVein-7	1.11	0.14	0.13	0.33	0.06	0.35	0.05	0.22	0.02	0.07	0.02	27.51	4.37	0.12	0.27
MB2HmVein-9	2.27	0.37	0.17	0.87	0.14	0.78	0.15	0.37	0.04	0.30	0.05	16.04	4.41	0.21	1.14
MB34aHm-2	0.02	<0.057	<0.00	<0.00	<0.00	<0.00	<0.0098	<0.00	<0.00	<0.043	0.00	0.11	3.47	0.01	2.12
MB34aMt-12	0.60	0.13	0.06	0.19	0.02	0.19	0.07	0.25	0.05	0.09	0.01	149.41	0.27	0.00	0.00
MB34aMt-15	0.77	0.04	0.10	0.09	0.03	0.23	0.09	0.27	0.02	0.15	0.02	112.81	0.45	<0.00	<0.0086
MB34aMt-16	<0.00	<0.00	0.01	0.02	0.01	<0.00	0.00	0.01	0.00	<0.00	<0.0105	0.46	0.08	0.00	0.01
MB34aMt-17	0.26	<0.00	0.09	0.08	<0.0099	0.15	0.03	0.11	0.04	0.12	0.02	26.27	0.46	<0.0112	<0.00
MB34aMt-18	0.27	0.03	0.06	0.06	0.02	0.13	0.05	0.18	0.04	0.11	0.02	21.22	0.45	0.02	<0.0073

Position	Deposit	Lithology	Sample no.	Analysis no.	Texture	Mg	Al	Si	P	Ca	Sc	Ti	V	Cr	Mn
South	Magnet	BIF	MB34a	MB34aMt-2	magnetite	54.35	173.25	4424.79	28.96	784.84	0.08	3.69	1.59	0.93	29.28
South	Magnet	BIF	MB34a	MB34aMt-22	magnetite	471.82	114.78	2651.39	15.09	<179.47	<0.107	3.54	1.83	<0.58	21.68
South	Magnet	BIF	MB34a	MB34aMt-3	magnetite	701.21	179.36	12340.38	35.72	<52.73	<0.085	3.18	1.43	0.66	25.34
South	Magnet	BIF	MB34a	MB34aMt-4	magnetite	19.10	190.80	2449.41	17.31	156.43	<0.077	5.21	1.62	0.74	24.41
South	Magnet	BIF	MB34a	MB34aMt-5	magnetite	429.39	107.57	2338.30	17.50	286.76	<0.073	3.06	1.55	0.72	23.15
South	Magnet	BIF	MB34a	MB34aMt-6	magnetite	137.28	178.32	3830.43	13.51	156.33	<0.084	5.24	1.34	0.85	24.08
South	Magnet	BIF	MB34a	MB34aMt-7	magnetite	628.13	158.75	7603.07	17.97	<114.23	<0.098	4.74	1.22	1.02	21.00
South	Magnet	BIF	MB34a	MB34aMt-8	magnetite	258.56	209.30	4716.33	26.88	<113.78	<0.074	5.35	1.22	<0.51	23.21
South	Magnet	BIF	MB34a	MB34aMt-9	magnetite	547.84	198.04	10202.32	13.94	242.75	<0.12	5.65	1.30	0.67	22.85
South	Magnet	BIF	MB34b	MB34b-Hm-1	clean martite	10.10	22.65	732.36	31.09	<104.8	0.07	1.00	0.11	0.50	13.60
South	Magnet	BIF	MB34b	MB34b-Hm-10	clean martite	65.38	78.09	2521.07	248.43	<113.5	<0.048	0.68	0.01	0.59	3.62
South	Magnet	BIF	MB34b	MB34b-Hm-11	clean martite	62.76	84.73	9259.36	238.39	103.21	0.08	0.43	0.23	0.69	5.03
South	Magnet	BIF	MB34b	MB34b-Hm-12	clean martite	18.28	5.84	1147.57	38.61	204.25	<0.043	1.14	0.02	1.10	5.98
South	Magnet	BIF	MB34b	MB34b-Hm-2	clean martite	3.86	3.27	510.28	31.40	<99.71	0.08	0.60	0.03	0.83	4.51
South	Magnet	BIF	MB34b	MB34b-Hm-3	clean martite	12.02	5.69	1616.33	15.18	157.19	<0.075	0.99	0.05	<0.36	7.40
South	Magnet	BIF	MB34b	MB34b-Hm-4	clean martite	6.89	11.15	542.78	91.11	<97.74	<0.073	<0.65	0.05	0.86	7.48
South	Magnet	BIF	MB34b	MB34b-Hm-5	clean martite	54.67	89.24	2292.10	319.58	<95.25	<0.078	<0.51	0.09	0.69	4.97
South	Magnet	BIF	MB34b	MB34b-Hm-6	clean martite	19.68	62.58	1070.64	315.15	<112.19	<0.094	<0.56	0.04	0.44	21.56
South	Magnet	BIF	MB34b	MB34b-Hm-7	clean martite	4.51	8.67	494.34	150.16	<98.38	<0.088	1.11	0.03	0.41	7.03
South	Magnet	BIF	MB34b	MB34b-Hm-8	clean martite	8.97	3.57	525.94	133.58	<112.5	0.12	<0.53	0.01	0.59	3.00
South	Magnet	BIF	MB34b	MB34b-Hm-9	clean martite	15.79	174.20	12431.84	195.68	<104.99	0.23	1.38	0.08	0.41	14.28
South	Magnet	BIF	MB34b	MB34b-Mt-1	magnetite	11.72	5.99	770.18	63.05	<76.29	0.07	1.47	0.15	0.75	13.84
South	Magnet	BIF	MB34b	MB34b-Mt-10	magnetite	3.35	7.73	669.91	177.19	183.42	<0.081	<0.43	<0.0127	0.85	4.80
South	Magnet	BIF	MB34b	MB34b-Mt-11	magnetite	8.01	49.39	674.16	190.82	104.11	0.07	0.93	0.02	0.50	16.97
South	Magnet	BIF	MB34b	MB34b-Mt-12	magnetite	20.04	9.57	671.38	20.62	<106.25	<0.066	0.53	0.02	0.68	8.34
South	Magnet	BIF	MB34b	MB34b-Mt-2	magnetite	21.50	72.79	16723.80	240.24	<93.71	<0.067	0.61	<0.026	0.45	4.99
South	Magnet	BIF	MB34b	MB34b-Mt-3	magnetite	5.65	8.39	518.42	101.36	113.78	<0.08	0.84	0.05	0.76	11.98
South	Magnet	BIF	MB34b	MB34b-Mt-4	magnetite	8.08	11.77	2840.60	100.35	<94.95	<0.089	<0.66	<0.013	0.63	12.17
South	Magnet	BIF	MB34b	MB34b-Mt-5	magnetite	4.86	18.15	584.45	69.19	<108.42	0.14	1.40	0.02	0.69	23.31
South	Magnet	BIF	MB34b	MB34b-Mt-6	magnetite	5.09	22.99	563.51	172.56	<101.26	<0.106	1.18	<0.016	0.37	3.45
South	Magnet	BIF	MB34b	MB34b-Mt-7	magnetite	11.24	3.26	452.21	<8.99	<96.36	<0.089	<0.43	0.01	0.63	11.27
South	Magnet	BIF	MB34b	MB34b-Mt-8	magnetite	12.68	69.20	1456.50	270.86	<112.02	0.15	<0.64	0.02	0.92	7.63
South	Magnet	BIF	MB34b	MB34b-Mt-9	magnetite	5.18	3.49	704.64	96.35	115.19	<0.07	<0.37	<0.022	0.73	9.53
South	Magnet	BIF	MB35a	MB35aHm-1	clean martite	56.67	29.77	950.80	20.17	131.39	0.05	5.27	0.71	0.52	462.07
South	Magnet	BIF	MB35a	MB35aHm-2	clean martite	52.94	21.62	448.18	20.18	156.89	0.04	5.55	0.68	0.34	423.06
South	Magnet	BIF	MB35a	MB35aHm-4	clean martite	40.49	27.51	396.12	261.45	302.37	<0.022	2.10	0.57	0.64	466.87
South	Magnet	BIF	MB35a	MB35aHm-5	clean martite	38.96	25.35	463.35	17.37	<80.6	0.02	1.02	0.55	0.53	498.44
South	Magnet	BIF	MB35a	MB35aHm-6	clean martite	594.61	25.58	530.34	22.31	<81.61	<0.031	4.66	0.71	0.65	456.07
South	Magnet	BIF	MB35a	MB35aMt-1	magnetite	132.17	31.59	413.17	21.90	<77.75	<0.03	3.15	0.65	0.54	489.81
South	Magnet	BIF	MB35a	MB35aMt-10	magnetite	52.50	24.94	387.65	15.65	<73.67	0.05	1.23	0.31	0.58	483.84
South	Magnet	BIF	MB35a	MB35aMt-11	magnetite	2575.51	28.28	15585.43	25.08	760.35	0.19	1.75	0.60	0.72	3143.74
South	Magnet	BIF	MB35a	MB35aMt-12	magnetite	701.93	25.93	7932.06	19.39	300.52	0.05	1.56	0.63	0.71	2313.71
South	Magnet	BIF	MB35a	MB35aMt-2	magnetite	45.82	28.41	370.42	9.80	<74.86	0.02	4.95	0.71	0.73	458.69

Analysis no.	Co	Ni	Cu	Zn	Ga	As	Sr	Y	Zr	Nb	Mo	Sn	Sb	Ba	La	Ce	Pr
MB34aMt-2	0.31	0.14	<0.46	0.88	0.17	2.34	1.21	2.20	0.09	0.10	0.11	0.68	0.38	2.22	0.57	0.57	0.07
MB34aMt-22	0.51	0.21	<0.89	0.49	0.25	<0.56	0.20	0.16	<0.00	<0.00	0.21	0.40	<0.15	0.21	0.09	0.07	0.02
MB34aMt-3	0.43	0.30	<0.55	0.50	0.23	<0.44	0.09	0.12	<0.00	0.01	0.15	0.53	<0.23	<0.185	0.00	0.03	<0.0063
MB34aMt-4	0.33	0.38	0.47	1.00	0.17	<0.53	0.32	0.48	0.03	0.02	0.11	0.50	0.25	0.96	0.18	0.19	0.00
MB34aMt-5	0.35	0.15	<0.55	0.70	0.31	0.72	0.23	0.59	<0.00	0.02	0.18	0.40	<0.22	0.45	0.15	0.14	0.02
MB34aMt-6	0.18	<0.21	<0.59	0.65	0.26	0.88	0.16	0.30	0.08	0.01	0.18	0.45	<0.151	1.27	0.08	0.10	0.02
MB34aMt-7	0.27	0.17	<0.68	0.90	0.21	0.59	0.21	0.20	<0.105	0.02	0.20	0.44	<0.147	0.18	0.07	0.05	0.01
MB34aMt-8	0.28	0.43	<0.61	0.72	0.19	<0.47	0.08	0.07	<0.00	0.03	0.12	0.66	<0.159	0.18	0.00	0.00	0.01
MB34aMt-9	0.30	<0.23	<0.65	0.92	0.18	<0.49	0.09	0.16	<0.00	<0.017	0.06	0.62	<0.162	<0.00	<0.0146	<0.0082	<0.0074
MB34b-Hm-1	0.08	0.06	<1	0.49	<0.00	<0.00	0.22	0.05	<0.00	<0.00	<0.00	<0.147	0.93	<0.00	0.02	0.02	0.00
MB34b-Hm-10	0.05	0.16	<0.73	0.15	0.16	<0.00	0.43	0.10	<0.00	<0.00	0.01	<0.147	<0.1	0.56	0.18	0.19	0.02
MB34b-Hm-11	0.04	0.38	<0.81	0.68	0.05	<0.00	0.39	0.11	0.02	<0.00	<0.00	<0.137	0.32	0.46	0.17	0.10	0.01
MB34b-Hm-12	0.63	0.18	<0.69	2.36	0.04	<0.00	0.44	0.03	<0.00	0.02	0.18	<0.117	0.18	0.25	0.02	0.03	0.01
MB34b-Hm-2	0.08	0.06	<0.95	0.39	0.03	<0.00	0.07	0.01	<0.00	<0.00	<0.00	<0.148	0.39	0.24	<0.0078	0.01	<0.0058
MB34b-Hm-3	0.12	<0.00	<0.89	0.96	<0.00	<0.00	0.14	0.03	<0.00	0.00	<0.00	0.17	<0.144	<0.00	0.02	0.01	<0.00
MB34b-Hm-4	0.17	0.11	<0.86	0.42	<0.062	<0.00	0.22	0.02	<0.077	<0.00	0.01	<0.14	0.36	0.12	0.01	0.02	<0.00
MB34b-Hm-5	0.05	0.21	<0.83	0.73	0.02	<0.00	0.34	0.08	0.02	0.00	<0.064	<0.07	<0.103	0.69	0.20	0.21	0.02
MB34b-Hm-6	0.37	0.11	<0.85	3.17	<0.00	<0.00	0.33	0.27	<0.00	<0.00	0.18	<0.12	0.63	0.12	0.88	0.64	0.08
MB34b-Hm-7	<0.045	0.05	<0.76	0.89	0.01	<0.00	0.10	0.02	<0.00	0.00	<0.037	<0.117	0.20	<0.00	0.00	0.00	<0.00
MB34b-Hm-8	0.23	0.50	<0.78	<0.164	<0.037	<0.00	0.12	0.02	<0.00	<0.00	0.04	<0.11	0.12	<0.00	0.02	0.01	0.00
MB34b-Hm-9	0.22	0.11	<0.8	1.21	0.03	<0.00	0.28	0.04	<0.057	0.00	<0.039	0.19	0.41	<0.00	0.03	0.04	0.01
MB34b-Mt-1	0.14	0.59	<0.7	28.51	0.06	<0.00	0.14	0.05	0.02	<0.00	<0.00	<0.115	0.34	0.12	0.04	0.03	0.01
MB34b-Mt-10	0.05	0.12	<1.03	0.40	<0.00	<0.00	0.15	0.03	0.02	0.00	<0.04	0.15	0.13	<0.131	<0.00	<0.0071	0.01
MB34b-Mt-11	<0.00	<0.00	<1.06	0.35	0.03	<0.00	0.16	0.03	<0.00	<0.00	<0.00	0.16	0.30	<0.00	0.02	0.04	0.00
MB34b-Mt-12	0.09	0.06	<0.94	0.56	<0.00	<0.00	0.20	0.02	<0.00	<0.00	<0.00	<0.148	0.27	0.12	0.04	0.03	0.00
MB34b-Mt-2	0.07	0.11	<0.96	0.79	<0.038	<0.00	0.12	0.11	0.02	0.00	<0.00	<0.168	0.13	0.25	0.06	0.17	0.04
MB34b-Mt-3	0.10	0.12	<0.93	0.80	0.01	<0.00	0.15	0.05	<0.00	0.01	0.01	<0.142	0.36	<0.00	0.01	0.02	<0.00
MB34b-Mt-4	0.08	<0.00	<0.89	0.67	<0.00	<0.00	0.10	0.04	0.04	<0.00	<0.00	0.12	0.53	0.12	0.01	0.02	0.00
MB34b-Mt-5	0.09	0.06	<0.82	1.00	0.04	<0.00	0.15	0.10	<0.00	<0.00	<0.00	0.18	0.62	0.39	0.04	0.07	0.01
MB34b-Mt-6	0.10	0.22	<0.81	0.44	0.03	<0.00	0.21	0.02	<0.00	<0.00	<0.00	<0.114	<0.135	<0.00	0.04	0.03	0.00
MB34b-Mt-7	0.16	0.07	<0.99	0.60	0.05	<0.00	0.12	0.09	<0.00	<0.00	0.02	<0.132	0.82	<0.00	0.03	0.04	<0.0094
MB34b-Mt-8	0.09	0.28	<1.04	<0.26	<0.00	<0.00	0.04	0.02	<0.00	0.00	0.04	<0.139	<0.169	<0.00	0.01	0.01	0.00
MB34b-Mt-9	0.22	0.05	<0.91	0.27	0.01	<0.00	0.04	0.06	<0.056	<0.00	<0.037	0.13	0.62	<0.00	0.04	0.04	0.01
MB35aHm-1	0.21	0.52	<0.069	14.07	0.04	<1.69	0.36	0.13	0.06	0.61	0.06	0.27	0.23	0.76	0.16	0.13	0.01
MB35aHm-2	0.29	0.47	0.06	11.96	<0.028	<1.68	0.10	0.02	0.04	0.84	0.03	0.26	0.35	0.17	0.02	0.02	0.00
MB35aHm-4	0.20	0.58	<0.053	12.30	0.05	<1.53	0.58	0.17	0.01	0.17	0.02	0.18	<0.1	0.08	0.17	0.20	0.02
MB35aHm-5	0.25	0.80	<0.086	11.37	0.03	2.20	0.35	<0.0091	0.01	0.06	0.02	0.19	<0.145	<0.00	0.01	0.03	<0.0131
MB35aHm-6	0.17	0.38	<0.038	14.80	0.06	<1.77	0.16	0.05	0.08	0.61	<0.00	0.33	0.20	<0.00	0.03	<0.0162	<0.0058
MB35aMt-1	0.16	0.71	0.09	12.13	0.19	<1.67	0.14	0.01	0.02	0.04	0.11	0.23	0.10	<0.15	<0.0072	0.04	0.00
MB35aMt-10	0.17	0.24	<0.066	9.04	0.14	1.80	0.04	0.04	<0.00	<0.00	<0.024	0.11	<0.074	<0.00	0.02	0.00	<0.0038
MB35aMt-11	1.83	3.37	0.28	14.16	0.05	<2.15	3.47	0.98	<0.00	<0.01	0.13	0.11	0.30	1.92	0.48	0.49	0.03
MB35aMt-12	0.25	0.91	0.21	12.10	0.29	2.10	1.03	1.23	<0.00	0.01	0.27	0.09	0.24	10.07	0.44	0.50	0.03
MB35aMt-2	0.22	0.60	0.39	10.27	0.04	<1.63	0.04	0.02	<0.00	0.00	0.03	<0.109	<0.078	0.19	0.00	0.05	<0.0038

Analysis no.	Nd	Sm	Eu	Gd	Tb	Dy	Ho	Er	Tm	Yb	Lu	W	Pb208	Th	U
MB34aMt-2	0.21	<0.069	0.02	0.06	0.03	0.06	0.02	0.20	0.03	0.09	0.02	2.33	0.60	0.03	0.01
MB34aMt-22	0.06	<0.00	<0.00	0.03	<0.00	<0.00	<0.00	<0.00	<0.00	<0.00	0.01	0.26	0.11	0.00	0.00
MB34aMt-3	<0.00	<0.049	<0.00	<0.00	<0.008	<0.00	0.00	0.01	<0.00	0.01	<0.0088	0.08	0.05	0.01	0.01
MB34aMt-4	0.11	0.06	0.01	<0.00	0.01	0.04	0.00	0.01	0.01	0.01	0.00	0.57	0.23	<0.0095	0.00
MB34aMt-5	0.03	0.02	0.01	0.02	0.00	0.02	0.01	0.02	0.00	0.04	<0.00	0.42	0.24	<0.00	<0.0052
MB34aMt-6	0.08	0.04	0.00	0.02	<0.00	<0.00	0.02	<0.00	0.01	0.06	<0.0094	0.53	0.52	<0.0134	0.01
MB34aMt-7	0.02	<0.056	<0.0132	0.02	<0.00	0.01	<0.00	0.05	<0.0095	0.02	0.00	0.25	0.09	0.00	0.00
MB34aMt-8	0.02	<0.00	0.00	<0.00	<0.00	<0.00	<0.0094	<0.0285	<0.00	<0.041	<0.00	<0.026	<0.049	0.00	<0.0059
MB34aMt-9	<0.046	<0.00	<0.00	<0.063	<0.00	0.01	<0.00	<0.00	<0.00	<0.00	<0.00	0.02	0.04	<0.0104	0.00
MB34b-Hm-1	<0.00	0.01	0.00	<0.00	<0.01	<0.00	<0.00	0.01	<0.0071	<0.03	<0.00	0.08	0.18	0.00	0.00
MB34b-Hm-10	0.06	<0.00	<0.0097	<0.06	0.00	0.01	<0.0096	0.01	<0.0062	0.01	0.00	0.03	0.13	<0.00	0.01
MB34b-Hm-11	0.10	0.05	0.00	<0.00	0.00	0.01	0.00	0.01	<0.00	0.03	<0.00	0.15	0.58	0.00	0.01
MB34b-Hm-12	<0.036	0.02	<0.00	<0.00	<0.00	0.01	0.00	<0.00	<0.0066	<0.00	0.00	0.01	0.12	0.01	0.04
MB34b-Hm-2	<0.00	<0.00	<0.0103	<0.00	0.01	<0.00	0.00	<0.00	<0.00	<0.04	<0.00	<0.00	0.08	<0.0077	<0.00
MB34b-Hm-3	<0.00	0.01	0.01	<0.06	0.00	<0.00	<0.00	0.01	<0.00	<0.039	0.00	0.06	0.14	0.00	<0.0063
MB34b-Hm-4	0.06	0.01	<0.0097	<0.00	<0.00	<0.0262	<0.00	<0.0199	<0.00	<0.027	<0.00	0.23	0.11	0.00	0.00
MB34b-Hm-5	0.04	0.03	0.01	0.03	<0.00	0.04	<0.00	0.03	<0.0062	<0.00	<0.0066	0.05	0.05	0.00	0.01
MB34b-Hm-6	0.26	0.04	0.04	0.04	0.01	0.04	0.00	0.01	0.00	<0.027	0.00	0.04	0.11	<0.00	0.01
MB34b-Hm-7	<0.00	<0.041	<0.00	<0.00	<0.00	<0.0264	<0.00	<0.0201	<0.00	<0.0267	<0.00	0.02	0.07	<0.00	0.00
MB34b-Hm-8	0.01	0.05	<0.00	<0.00	<0.00	0.01	<0.00	<0.00	<0.0064	<0.00	<0.00	<0.0189	0.05	<0.0105	<0.00
MB34b-Hm-9	0.02	0.01	<0.00	0.03	<0.007	<0.00	<0.00	0.01	0.00	<0.00	0.00	0.11	0.13	0.01	0.01
MB34b-Mt-1	<0.034	<0.042	<0.0101	<0.00	<0.00	0.02	0.00	<0.028	<0.00	0.02	<0.007	0.01	0.14	<0.00	0.00
MB34b-Mt-10	0.02	<0.00	0.01	<0.00	<0.00	<0.00	<0.00	<0.02	0.00	<0.00	0.00	<0.031	0.05	0.00	<0.0073
MB34b-Mt-11	0.04	<0.00	<0.012	<0.00	<0.00	<0.00	<0.00	<0.02	0.00	0.01	<0.00	0.01	0.07	<0.01	0.00
MB34b-Mt-12	0.01	<0.00	0.01	<0.00	<0.00	<0.0281	<0.00	0.01	<0.00	0.01	<0.00	<0.0197	0.10	<0.00	0.00
MB34b-Mt-2	0.06	0.03	0.01	<0.063	0.00	<0.028	<0.0072	<0.022	0.00	<0.00	0.00	<0.02	0.06	<0.00	0.00
MB34b-Mt-3	<0.00	<0.00	0.01	0.06	<0.0073	<0.00	0.00	<0.0308	<0.007	<0.029	<0.0074	0.03	0.21	0.00	<0.0067
MB34b-Mt-4	0.02	<0.049	0.01	<0.05	<0.00	<0.032	0.00	0.01	0.00	<0.00	0.00	0.03	0.10	<0.0088	<0.00
MB34b-Mt-5	<0.051	0.02	0.02	0.05	<0.00	0.03	<0.0071	<0.00	<0.0072	0.02	0.01	0.15	0.15	0.01	0.02
MB34b-Mt-6	<0.00	<0.00	0.00	0.01	<0.00	<0.00	0.00	<0.021	0.00	<0.00	<0.00	<0.02	0.03	<0.0112	<0.00
MB34b-Mt-7	0.06	0.05	0.01	0.04	0.00	<0.00	0.00	<0.00	<0.00	<0.047	<0.00	0.01	0.18	<0.00	<0.0053
MB34b-Mt-8	0.01	0.02	0.00	<0.047	<0.011	0.02	<0.00	0.01	<0.0132	<0.00	<0.008	0.01	0.05	<0.00	<0.01
MB34b-Mt-9	0.02	0.01	<0.0102	<0.00	0.00	<0.00	0.00	<0.00	<0.00	<0.04	0.01	0.01	0.15	<0.00	0.00
MB35aHm-1	0.02	<0.027	0.00	<0.00	0.00	0.01	0.01	0.01	<0.0061	0.01	<0.0175	0.13	1.46	0.00	<0.0076
MB35aHm-2	0.01	<0.00	0.00	0.01	<0.0042	<0.00	0.00	<0.00	0.00	<0.00	<0.0043	0.04	1.04	0.01	0.03
MB35aHm-4	0.08	0.03	<0.0112	0.04	0.00	<0.00	0.01	0.01	0.00	0.01	0.00	<0.0199	0.82	<0.0047	0.03
MB35aHm-5	<0.024	<0.00	<0.0129	<0.00	<0.0044	<0.0177	<0.00	<0.00	<0.00	<0.00	<0.0064	<0.0164	0.41	<0.00	<0.005
MB35aHm-6	<0.024	<0.0276	<0.00	<0.00	0.01	<0.0175	<0.0064	0.03	<0.0088	<0.00	<0.00	0.04	0.95	0.00	0.00
MB35aMt-1	<0.023	<0.00	0.00	<0.00	<0.0059	<0.00	<0.0044	<0.0134	<0.00	0.02	<0.00	0.28	1.41	0.01	0.02
MB35aMt-10	0.04	<0.00	0.00	<0.048	<0.00	0.01	<0.0075	0.00	0.00	<0.0182	<0.00	0.02	0.13	<0.00	<0.00
MB35aMt-11	0.06	<0.049	0.01	0.09	<0.0054	0.05	0.01	0.08	0.00	0.05	0.02	<0.00	0.01	<0.00	0.00
MB35aMt-12	0.14	0.02	0.01	0.01	0.00	0.02	0.02	0.04	<0.0045	0.04	0.01	0.28	0.93	0.01	0.01
MB35aMt-2	<0.0312	0.01	0.00	0.01	<0.00	0.01	<0.00	0.01	<0.0041	<0.00	<0.0058	0.02	0.10	<0.00	<0.00156

Position	Deposit	Lithology	Sample no.	Analysis no.	Texture	Mg	Al	Si	P	Ca	Sc	Ti	V	Cr	Mn
South	Magnet	BIF	MB35a	MB35aMt-3	magnetite	92.71	33.55	603.28	13.19	<83.64	<0.024	1.71	0.77	0.52	474.29
South	Magnet	BIF	MB35a	MB35aMt-4	magnetite	210.79	10.45	767.87	17.96	128.99	<0.0247	3.75	0.72	0.35	129.55
South	Magnet	BIF	MB35a	MB35aMt-5	magnetite	129.33	9.27	605.89	14.74	<83.98	<0.0204	2.45	0.57	0.69	162.74
South	Magnet	BIF	MB35a	MB35aMt-6	magnetite	75.41	32.41	343.31	27.70	154.54	0.03	1.45	0.34	0.54	517.17
South	Magnet	BIF	MB35a	MB35aMt-7	magnetite	70.31	23.34	465.12	8.94	<79.91	<0.022	1.61	0.35	0.36	475.35
South	Magnet	BIF	MB35a	MB35aMt-8	magnetite	87.94	32.97	462.58	16.61	<78.53	<0.034	6.90	0.58	0.45	403.06
South	Magnet	BIF	MB35a	MB35aMt-9	magnetite	310.84	13.06	2282.91	18.68	<81.27	0.03	0.92	0.78	1.53	348.14
South	Magnet	BIF	MB35a	MB35aMtVein-1	magnetite	756.87	17.16	3257.83	94.14	385.67	<0.026	2.01	0.71	1.33	489.67
South	Magnet	BIF	MB35a	MB35aMtVein-2	magnetite	665.00	11.02	1204.82	23.28	930.35	<0.029	1.76	0.81	3.36	1208.06
South	Magnet	BIF	MB35a	MB35aMtVein-4	magnetite	580.03	9.65	1035.27	27.45	626.31	0.05	1.64	0.66	4.72	686.96
South	Magnet	BIF	MB35a	MB35aMtVein-5	magnetite	349.42	12.52	1060.18	27.60	484.35	0.10	7.70	0.67	2.63	495.06
South	Magnet	BIF	MB35a	MB35aMtVein-6	magnetite	1855.74	16.42	3613.45	22.40	<88.04	<0.043	1.54	0.76	2.64	510.23
South	Magnet	BIF	MB36b	MB36bMt-1	magnetite	3231.03	27.87	946.31	12.53	7454.02	<0.029	8.93	2.65	0.63	1490.88
South	Magnet	BIF	MB36b	MB36bMt-10	magnetite	6060.18	6.27	360.70	17.52	12913.75	<0.0217	1.38	1.52	0.60	679.20
South	Magnet	BIF	MB36b	MB36bMt-11	magnetite	925.03	10.42	1296.80	15.29	1021.99	<0.0225	3.88	1.70	0.58	292.20
South	Magnet	BIF	MB36b	MB36bMt-12	magnetite	20.93	5.77	376.54	20.63	126.82	<0.03	1.10	1.47	0.49	290.19
South	Magnet	BIF	MB36b	MB36bMt-13	magnetite	9.42	13.06	358.96	16.97	<73.15	0.02	0.96	1.41	0.37	224.74
South	Magnet	BIF	MB36b	MB36bMt-17	magnetite	8.70	5.25	366.44	33.91	<71.08	<0.033	5.28	1.66	0.76	172.39
South	Magnet	BIF	MB36b	MB36bMt-18	magnetite	13.71	16.32	405.25	13.39	<66.06	<0.0156	1.80	10.74	0.62	1915.80
South	Magnet	BIF	MB36b	MB36bMt-19	magnetite	18.62	20.54	458.26	12.27	201.76	<0.029	2.23	2.75	0.48	1400.99
South	Magnet	BIF	MB36b	MB36bMt-20	magnetite	4853.94	9.72	347.68	20.63	1089.41	0.03	4.51	0.53	0.46	1996.34
South	Magnet	BIF	MB36b	MB36bMt-21	magnetite	12073.19	13.43	639.72	16.47	135.16	<0.0264	2.63	3.72	0.61	3164.57
South	Magnet	BIF	MB36b	MB36bMt-22	magnetite	1794.35	4.93	373.09	19.37	163.41	<0.033	0.51	1.60	0.42	697.14
South	Magnet	BIF	MB36b	MB36bMt-22	magnetite	3648.25	11.11	526.47	19.87	5246.27	<0.034	0.71	1.88	0.73	791.97
South	Magnet	BIF	MB36b	MB36bMt-24	magnetite	13.81	23.47	399.87	16.31	143.59	<0.022	1.82	1.88	0.34	1451.08
South	Magnet	BIF	MB36b	MB36bMt-3	magnetite	12978.22	18.58	1217.08	25.81	28355.45	0.10	16.58	5.57	1.03	2093.48
South	Magnet	BIF	MB36b	MB36bMt-4	magnetite	3474.90	19.49	919.69	23.76	7386.15	<0.03	16.70	2.75	0.62	1919.84
South	Magnet	BIF	MB36b	MB36bMt-5	magnetite	3323.46	35.36	5797.16	15.82	1665.75	0.07	17.17	2.98	0.63	1050.69
South	Magnet	BIF	MB36b	MB36bMt-6	magnetite	10.39	5.03	379.45	18.25	<69.67	<0.0194	1.19	1.47	0.42	282.23
South	Magnet	BIF	MB36b	MB36bMt-7	magnetite	9.33	10.35	360.54	27.14	134.68	<0.031	9.69	1.41	0.35	310.41
South	Magnet	BIF	MB36b	MB36bMt-8	magnetite	31.74	16.53	342.19	17.11	<73.22	0.07	3.46	0.46	0.70	594.18
South	Magnet	BIF	MB36b	MB36bMt-9	magnetite	4208.05	14.76	440.31	16.25	8952.97	<0.042	34.54	2.67	0.46	2049.11
Middle	Count	BIF	MB40a	MB40a-Hm-1	clean martite	241.85	207.98	1017.44	111.26	153.45	4.44	1313.87	46.41	59.93	32.14
Middle	Count	BIF	MB40a	MB40a-Hm-10	clean martite	630.27	429.81	1517.40	789.88	751.43	5.49	1734.67	66.38	63.47	157.39
Middle	Count	BIF	MB40a	MB40a-Hm-11	clean martite	153.00	190.95	858.33	142.00	235.28	3.46	882.58	53.01	6.89	42.84
Middle	Count	BIF	MB40a	MB40a-Hm-12	clean martite	100.55	181.51	722.01	93.02	94.84	4.02	977.17	49.42	6.46	36.40
Middle	Count	BIF	MB40a	MB40a-Hm-2	clean martite	109.13	156.77	596.51	49.14	189.64	4.11	1129.74	43.82	32.00	28.09
Middle	Count	BIF	MB40a	MB40a-Hm-3	clean martite	368.82	211.18	1115.22	85.49	239.19	4.25	914.22	44.76	18.88	41.97
Middle	Count	BIF	MB40a	MB40a-Hm-4	clean martite	211.77	322.78	1095.01	57.43	179.73	4.33	1092.60	45.96	32.28	31.25
Middle	Count	BIF	MB40a	MB40a-Hm-5	clean martite	141.91	169.08	748.06	54.99	173.54	4.33	1028.54	45.78	27.31	29.16
Middle	Count	BIF	MB40a	MB40a-Hm-6	clean martite	277.94	176.47	1041.13	66.69	235.02	3.40	867.65	41.36	42.33	34.17
Middle	Count	BIF	MB40a	MB40a-Hm-7	clean martite	254.03	1993.27	3016.85	71.14	159.27	4.06	1257.51	48.70	54.22	51.07
Middle	Count	BIF	MB40a	MB40a-Hm-8	clean martite	278.37	146.14	1108.72	41.08	<77.15	4.51	1409.34	43.04	67.09	20.50

Analysis no.	Co	Ni	Cu	Zn	Ga	As	Sr	Y	Zr	Nb	Mo	Sn	Sb	Ba	La	Ce	Pr
MB35aMt-3	0.22	0.61	<0.058	8.20	0.05	<1.67	<0.00	<0.0062	<0.00	<0.00	<0.051	0.12	<0.099	<0.00	0.00	0.00	0.00
MB35aMt-4	0.28	0.90	0.12	7.51	0.06	<1.71	0.26	0.64	0.08	0.06	0.11	0.15	0.66	1.53	0.49	0.48	0.03
MB35aMt-5	0.21	0.96	0.31	11.58	0.11	<1.84	0.48	0.21	<0.00	0.04	0.36	0.09	0.19	0.37	0.18	0.20	0.01
MB35aMt-6	0.05	0.40	0.35	10.71	0.09	<1.74	0.08	0.23	<0.00	<0.00	<0.037	<0.117	<0.096	0.17	0.13	0.13	0.01
MB35aMt-7	0.11	0.34	0.11	11.27	0.06	<1.76	0.26	0.01	<0.00	<0.00	0.03	0.08	<0.085	<0.00	0.02	0.01	<0.0041
MB35aMt-8	0.07	0.77	0.07	9.51	0.04	<1.8	0.16	0.03	<0.0195	<0.0066	0.08	0.41	<0.096	0.27	0.01	<0.0077	<0.00
MB35aMt-9	0.17	0.39	0.21	10.26	0.09	<1.78	0.38	0.23	<0.028	0.00	0.11	0.15	0.11	0.19	0.04	0.28	0.00
MB35aMtVein-1	0.65	0.79	0.28	11.36	0.07	2.50	0.45	0.48	0.05	0.02	<0.03	0.11	0.33	0.88	0.48	0.35	0.04
MB35aMtVein-2	0.47	0.71	0.22	11.04	0.07	1.80	0.99	0.65	<0.00	0.01	0.03	0.09	<0.114	0.79	0.40	0.35	0.03
MB35aMtVein-4	0.38	0.61	0.31	14.41	0.16	<1.97	0.92	0.58	<0.00	0.01	0.14	0.08	0.39	0.78	0.50	0.39	0.03
MB35aMtVein-5	0.26	0.80	0.35	11.51	0.14	3.20	1.02	0.44	0.05	0.03	0.16	<0.081	0.19	2.85	0.47	0.37	0.02
MB35aMtVein-6	0.43	0.74	<0.086	12.24	0.15	<1.92	0.48	0.17	0.01	<0.00	0.04	<0.073	<0.121	0.50	0.14	0.10	0.01
MB36bMt-1	0.96	0.36	0.09	5.46	0.06	<1.88	1.42	0.42	0.46	0.03	<0.091	0.14	0.82	0.77	0.11	0.17	0.03
MB36bMt-10	0.60	0.72	0.08	1.78	0.07	<2.47	1.90	1.54	0.04	0.01	<0.0253	0.10	0.37	2.23	0.74	0.66	0.09
MB36bMt-11	0.80	0.72	<0.053	2.07	0.07	<2.47	0.61	0.62	0.02	0.01	0.01	0.10	0.17	2.13	0.32	0.35	0.04
MB36bMt-12	0.72	0.35	0.05	2.34	0.06	<2.44	0.42	0.86	0.01	<0.0063	0.03	<0.068	0.17	2.00	0.52	0.36	0.02
MB36bMt-13	0.67	0.70	0.13	2.18	0.06	2.76	0.80	0.52	0.02	0.01	<0.0244	<0.072	0.35	2.32	0.41	0.33	0.03
MB36bMt-17	0.69	0.71	0.05	2.04	<0.0145	<2.94	0.56	0.60	0.07	0.02	0.02	<0.076	0.26	1.83	0.30	0.28	0.02
MB36bMt-18	1.78	0.21	0.64	5.95	0.14	<3.09	0.50	0.26	0.31	0.14	0.12	1.98	2.77	1.05	0.08	0.07	0.01
MB36bMt-19	1.11	0.36	0.31	7.26	0.10	8.51	0.47	0.30	0.20	0.02	0.12	0.14	3.07	0.34	0.09	0.10	0.01
MB36bMt-20	1.20	0.71	<0.057	7.36	0.10	<3.09	0.24	0.14	<0.00	<0.00	0.05	<0.064	0.05	<0.00	0.05	0.06	0.01
MB36bMt-21	1.16	0.58	<0.063	4.26	0.13	<3.69	0.61	0.25	0.13	0.02	0.15	0.10	1.52	1.69	0.03	0.04	0.00
MB36bMt-22	0.84	0.87	<0.043	2.69	0.13	<3.51	0.36	0.45	0.01	<0.0108	<0.00	0.06	0.12	1.49	0.25	0.21	0.02
MB36bMt-22	0.65	0.65	<0.057	2.54	0.17	3.38	2.17	1.39	<0.00	0.01	0.04	<0.07	0.20	2.30	0.52	0.54	0.06
MB36bMt-24	1.31	0.10	<0.038	5.32	0.08	4.17	0.74	0.05	0.01	0.02	0.02	0.16	0.74	0.49	0.00	0.02	<0.0081
MB36bMt-3	1.08	0.54	<0.042	5.22	0.20	<2.32	6.27	4.87	0.51	0.03	0.05	0.10	1.67	2.01	0.70	1.45	0.16
MB36bMt-4	1.25	0.27	<0.027	4.11	0.05	2.21	0.97	0.47	0.82	0.04	0.14	0.06	0.87	<0.22	0.12	0.14	0.02
MB36bMt-5	1.32	0.37	0.14	4.53	0.07	<2.15	0.49	0.23	0.69	0.03	0.15	0.15	0.94	0.26	0.05	0.08	0.02
MB36bMt-6	0.76	0.31	<0.046	2.04	0.10	3.97	0.45	0.67	0.02	0.01	<0.00	<0.067	0.21	2.75	0.49	0.42	0.03
MB36bMt-7	0.65	0.63	0.06	1.77	0.06	3.19	0.58	0.81	0.01	0.01	<0.00	<0.049	0.24	2.63	0.50	0.38	0.04
MB36bMt-8	0.81	0.32	<0.043	7.83	0.03	<2.24	<0.025	<0.0062	<0.00	<0.00	<0.00	<0.064	<0.075	<0.00	0.00	<0.0061	0.01
MB36bMt-9	1.52	0.27	<0.049	3.83	0.10	<3.12	1.90	1.67	0.61	0.05	0.05	<0.105	0.80	1.40	0.35	0.62	0.07
MB40a-Hm-1	0.03	0.14	28.22	<0.19	0.69	<0.00	0.41	1.57	1.13	3.09	1.74	2.19	2.02	0.75	0.90	2.30	0.21
MB40a-Hm-10	0.09	1.87	1.50	1.37	0.72	<0.00	1.61	8.74	11.09	4.45	2.95	3.60	2.41	7.61	3.98	11.43	1.00
MB40a-Hm-11	1.15	1.34	45.24	1.19	0.72	<0.00	0.55	1.95	2.90	3.51	2.04	1.95	2.32	1.38	0.94	3.02	0.24
MB40a-Hm-12	0.21	0.24	52.14	0.48	0.63	<0.00	0.92	1.58	2.82	3.76	2.03	2.12	1.99	0.67	1.23	2.55	0.31
MB40a-Hm-2	0.05	0.09	9.79	<0.142	0.59	<0.00	0.28	0.78	0.87	3.13	1.22	2.37	2.53	0.55	0.54	1.41	0.13
MB40a-Hm-3	0.14	0.14	39.37	0.89	0.69	<0.00	0.52	1.82	1.33	3.94	2.05	2.34	2.53	0.55	0.83	2.18	0.22
MB40a-Hm-4	0.09	0.24	25.77	0.50	0.69	<0.00	0.30	1.25	1.47	3.41	1.76	2.93	2.12	0.68	0.62	1.71	0.15
MB40a-Hm-5	0.08	<0.00	28.07	0.14	0.57	<0.00	0.38	1.65	2.18	3.54	1.74	2.41	2.28	0.77	0.77	2.01	0.21
MB40a-Hm-6	1.05	1.62	28.60	0.34	0.87	<0.00	0.43	2.25	0.95	2.84	1.09	2.20	1.99	0.33	0.68	1.62	0.17
MB40a-Hm-7	0.09	2.01	34.42	0.25	0.90	<0.00	0.47	1.35	1.75	2.89	2.00	2.45	1.90	2.11	0.68	1.62	0.20
MB40a-Hm-8	0.16	0.30	8.74	0.25	0.89	<0.00	0.25	1.56	8.68	2.79	1.42	2.51	2.17	1.39	0.89	2.15	0.22

Analysis no.	Nd	Sm	Eu	Gd	Tb	Dy	Ho	Er	Tm	Yb	Lu	W	Pb208	Th	U
MB35aMt-3	<0.023	<0.00	<0.00	<0.00	0.00	<0.0171	<0.00	0.01	0.00	0.01	<0.0043	<0.00	<0.0182	<0.00	<0.00
MB35aMt-4	0.17	0.07	0.02	0.04	0.01	0.01	0.02	0.05	0.00	0.04	0.01	0.05	0.72	0.00	0.00
MB35aMt-5	0.06	0.01	0.01	0.01	0.00	0.01	<0.007	0.02	0.00	0.02	<0.0067	0.35	1.07	0.01	0.01
MB35aMt-6	0.02	0.01	0.01	0.01	0.01	<0.00	<0.0047	0.01	<0.0044	0.01	0.00	0.32	1.11	0.01	0.01
MB35aMt-7	<0.00	<0.00	<0.00	<0.00	0.00	<0.0181	<0.0047	<0.00	<0.0099	0.01	0.00	0.02	1.24	<0.00	0.04
MB35aMt-8	0.02	0.01	<0.00	0.01	<0.00	0.01	0.00	<0.00	<0.00	<0.019	<0.0043	0.73	0.63	0.01	0.00
MB35aMt-9	0.03	<0.0282	0.01	<0.00	<0.00	0.01	0.00	<0.0135	0.00	0.03	<0.0044	0.00	0.06	<0.00	<0.0018
MB35aMtVein-1	0.11	<0.00	0.02	<0.032	0.01	0.05	0.01	0.03	0.00	<0.03	0.01	0.25	0.93	0.00	0.01
MB35aMtVein-2	0.07	0.02	0.01	0.05	<0.00	0.01	0.01	0.02	0.00	0.03	0.01	0.03	0.31	0.00	0.00
MB35aMtVein-4	0.17	<0.032	0.02	0.01	<0.005	0.02	0.00	<0.015	0.00	0.01	0.01	0.01	0.19	0.01	0.00
MB35aMtVein-5	0.09	0.03	0.01	0.01	0.00	0.02	0.01	0.03	<0.0067	0.01	0.00	0.08	1.04	0.01	0.00
MB35aMtVein-6	0.03	0.02	<0.0116	<0.00	<0.00	<0.0204	<0.00	0.00	0.00	<0.00	<0.0049	0.12	0.75	0.01	0.00
MB36bMt-1	0.10	0.03	0.01	0.03	<0.0042	<0.035	0.02	0.03	0.00	0.02	<0.0067	0.35	1.55	<0.00	0.00
MB36bMt-10	0.23	0.05	0.03	0.07	0.00	0.12	0.03	0.07	0.01	0.09	0.01	0.02	0.14	<0.00	0.00
MB36bMt-11	0.16	0.04	0.01	0.03	0.01	0.02	0.01	0.02	0.01	<0.02	<0.0049	0.02	0.11	<0.00	0.00
MB36bMt-12	0.08	0.02	0.02	<0.049	0.00	0.03	0.01	0.05	0.01	0.03	0.01	0.06	4.07	<0.00	0.00
MB36bMt-13	0.10	0.01	0.00	<0.028	<0.0057	0.02	0.01	0.04	0.00	0.02	<0.0065	0.07	0.74	0.01	0.02
MB36bMt-17	0.05	0.04	0.01	0.02	0.00	0.05	<0.0045	0.03	<0.0048	<0.02	0.00	0.14	0.75	0.00	0.04
MB36bMt-18	0.03	<0.028	0.01	0.02	<0.0042	0.03	0.01	<0.0135	0.00	<0.0198	<0.0049	0.43	0.38	0.01	0.07
MB36bMt-19	0.02	0.01	<0.0074	0.03	<0.006	<0.018	<0.0065	<0.00	0.00	<0.00	<0.0049	0.18	0.21	0.09	0.12
MB36bMt-20	<0.021	0.01	0.01	0.01	0.00	<0.0157	0.01	0.01	0.00	<0.017	<0.0043	0.04	0.02	0.01	0.01
MB36bMt-21	0.05	<0.03	0.00	0.04	<0.00	<0.00	0.01	0.02	<0.00	<0.021	0.01	0.03	0.06	0.01	0.01
MB36bMt-22	0.05	<0.027	0.00	0.02	0.00	0.02	0.00	0.03	0.00	<0.019	0.00	0.03	0.04	0.01	0.02
MB36bMt-22	0.24	0.03	0.03	<0.041	0.00	0.08	0.01	0.05	0.01	0.06	0.01	0.18	0.64	<0.00	0.09
MB36bMt-24	0.02	<0.028	<0.00	0.01	0.00	<0.00	<0.00	<0.00	<0.0049	<0.00	0.00	<0.0081	0.07	0.00	0.05
MB36bMt-3	0.96	0.21	0.12	0.29	0.05	0.27	0.09	0.27	0.05	0.35	0.06	0.02	0.39	0.01	0.00
MB36bMt-4	0.14	0.03	0.02	0.06	0.00	0.07	<0.0047	0.06	<0.0136	0.05	0.01	<0.0073	0.16	0.00	<0.00148
MB36bMt-5	0.02	<0.029	0.01	0.02	0.00	<0.0254	<0.0066	0.01	<0.00	0.03	0.00	0.06	0.67	0.00	0.00
MB36bMt-6	0.12	<0.029	0.00	0.05	<0.0076	0.02	0.01	0.06	0.01	0.01	0.01	0.11	0.52	0.01	0.00
MB36bMt-7	0.11	<0.028	0.01	0.05	<0.0042	0.04	0.01	0.04	0.00	0.02	0.00	0.38	1.26	0.01	0.02
MB36bMt-8	<0.023	<0.00	<0.00	0.01	<0.00	0.01	<0.00	0.02	<0.0046	0.01	<0.00	0.02	0.16	<0.00	0.00
MB36bMt-9	0.34	0.11	0.05	0.08	0.01	0.07	0.02	0.15	0.01	0.06	0.01	0.20	0.69	<0.00	0.00
MB40a-Hm-1	0.88	0.28	0.10	0.38	0.08	0.38	0.04	0.14	0.02	0.18	0.02	3.12	8.54	2.25	7.12
MB40a-Hm-10	4.63	1.45	0.47	2.08	0.38	1.94	0.31	1.00	0.14	0.95	0.13	3.45	60.25	4.86	12.89
MB40a-Hm-11	1.33	0.40	0.11	0.41	0.09	0.57	0.08	0.26	0.04	0.21	0.02	3.00	12.14	2.18	8.24
MB40a-Hm-12	1.21	0.35	0.11	0.43	0.09	0.33	0.09	0.17	0.03	0.19	0.03	3.15	7.56	2.67	6.82
MB40a-Hm-2	0.65	0.29	0.06	0.22	0.06	0.25	0.04	0.12	0.01	0.14	0.01	2.49	3.98	2.40	7.65
MB40a-Hm-3	0.76	0.34	0.08	0.46	0.08	0.35	0.07	0.18	0.02	0.20	0.03	3.18	7.08	2.29	8.06
MB40a-Hm-4	0.77	0.23	0.05	0.40	0.07	0.42	0.05	0.16	0.01	0.16	0.01	2.76	5.79	2.46	7.58
MB40a-Hm-5	0.77	0.19	0.11	0.34	0.05	0.33	0.07	0.14	0.02	0.09	0.02	3.10	5.11	2.73	9.83
MB40a-Hm-6	0.63	0.28	0.06	0.38	0.07	0.35	0.07	0.26	0.02	0.16	0.03	2.37	5.77	2.10	6.34
MB40a-Hm-7	0.72	0.21	0.07	0.25	0.06	0.36	0.05	0.13	0.02	0.08	0.01	2.47	6.45	2.01	6.96
MB40a-Hm-8	0.76	0.36	0.10	0.37	0.05	0.29	0.07	0.21	0.04	0.26	0.05	2.34	3.76	2.45	5.82

Position	Deposit	Lithology	Sample no.	Analysis no.	Texture	Mg	Al	Si	P	Ca	Sc	Ti	V	Cr	Mn
Middle	Count	BIF	MB40a	MB40a-Hm-9	clean martite	242.74	145.41	898.02	119.38	350.52	4.86	1416.09	46.96	47.14	28.13
Middle	Count	BIF	MB40b	MB40bHmClean-1	clean martite	209.90	181.42	733.26	26.17	378.65	3.60	564.79	24.02	5.69	26.45
Middle	Count	BIF	MB40b	MB40bHmClean-2	clean martite	247.53	873.14	1533.75	289.35	301.48	4.64	651.02	25.35	10.43	23.82
Middle	Count	BIF	MB40b	MB40bHmClean-3	clean martite	96.27	258.97	695.76	32.21	351.95	4.24	600.31	23.75	6.38	16.55
Middle	Count	BIF	MB40b	MB40bHmClean-4	clean martite	137.00	275.05	771.97	51.22	386.93	4.55	655.49	25.68	8.09	20.96
Middle	Count	BIF	MB40b	MB40bHmClean-5	clean martite	220.81	275.62	831.24	33.69	234.06	3.54	546.71	24.33	7.27	18.49
Middle	Count	BIF	MB40b	MB40bHmClean-6	clean martite	237.88	274.52	871.06	40.06	178.07	3.96	705.06	25.99	11.48	24.43
Middle	Count	BIF	MB40b	MB40bHmClean-7	clean martite	301.51	173.99	1039.34	356.64	370.14	3.37	380.44	24.92	5.18	23.33
Middle	Count	BIF	MB40b	MB40bHmClean-8	clean martite	444.24	255.30	1412.80	406.85	365.62	4.13	487.65	28.10	9.06	28.26
Middle	Count	BIF	MB40b	MB40bMt-1	magnetite	771.80	76.19	1485.98	42.60	<76.21	0.48	6.93	17.34	4.50	69.04
Middle	Count	BIF	MB40b	MB40bMt-2	magnetite	643.51	649.20	1603.21	466.92	78.92	2.01	13.31	17.67	5.20	66.51
Middle	Count	BIF	MB40b	MB40bMt-3	magnetite	554.80	138.10	1156.79	141.70	91.41	0.50	2.24	17.78	4.46	56.13
Middle	Count	BIF	MB40b	MB40bMt-4	magnetite	802.72	97.78	1671.81	107.17	78.19	1.04	5.14	17.07	4.78	81.54
Middle	Count	BIF	MB40b	MB40bMt-5	magnetite	907.82	91.23	1593.82	75.53	74.34	0.68	11.93	17.38	4.79	79.49
Middle	Count	BIF	MB40b	MB40bMt-6	magnetite	762.59	118.86	1575.06	130.45	94.55	1.03	22.98	16.73	3.92	81.24
Middle	Count	BIF	MB40b	MB40bMt-7	magnetite	216.61	1339.54	2184.35	219.85	102.76	0.57	2.11	14.37	10.81	48.95
Middle	Count	BIF	MB40b	MB40bMt-8	magnetite	173.83	157.28	607.23	146.75	<77.05	0.49	2.04	14.26	7.39	46.53
Middle	Count	BIF	MB40b	MB40bMt-9	magnetite	508.50	277.82	1138.75	188.91	<73.75	0.80	7.15	17.14	4.78	64.47
Middle	Count	BIF	MB40b	MB40bPorousHm-1	porous martite	421.05	891.03	1608.22	878.98	150.08	3.19	3.49	17.48	5.64	44.12
Middle	Count	BIF	MB40b	MB40bPorousHm-2	porous martite	439.47	729.28	1544.16	1006.44	270.68	3.65	4.17	16.66	7.20	51.64
Middle	Count	BIF	MB40b	MB40bPorousHm-3	porous martite	261.88	754.68	1243.42	812.80	171.61	2.53	3.30	17.45	10.41	36.51
Middle	Count	BIF	MB40b	MB40bPorousHm-4	porous martite	219.07	600.40	1121.11	780.60	142.10	2.26	4.00	18.02	6.83	34.88
Middle	Count	BIF	MB40b	MB40bPorousHm-5	porous martite	474.11	956.83	2013.29	824.86	93.75	2.95	3.71	17.47	8.35	39.46
Middle	Count	BIF	MB40b	MB40bPorousHm-6	porous martite	451.90	658.46	1554.74	767.24	92.92	2.90	4.54	17.24	9.41	38.99
Middle	Count	BIF	MB40b	MB40bPorousHm-7	porous martite	469.31	796.37	1637.80	807.78	95.92	3.06	3.67	17.23	7.50	36.00
Middle	Count	BIF	MB41a	MB41aHm-1	clean martite	56.83	258.71	848.75	21.89	115.32	0.12	0.31	1.74	<0.26	58.30
Middle	Count	BIF	MB41a	MB41aHm-10	clean martite	69.97	249.56	1962.59	27.62	95.49	0.20	1.05	3.17	0.39	58.99
Middle	Count	BIF	MB41a	MB41aHm-11	clean martite	147.12	178.34	825.82	38.96	<81.96	0.33	6.79	4.65	0.60	28.94
Middle	Count	BIF	MB41a	MB41aHm-12	clean martite	173.15	183.51	13396.62	36.72	<78.95	0.29	2.56	4.51	0.76	34.57
Middle	Count	BIF	MB41a	MB41aHm-13	clean martite	44.73	300.31	838.92	64.63	<85.61	0.55	15.23	8.98	0.86	36.73
Middle	Count	BIF	MB41a	MB41aHm-14	clean martite	53.68	308.41	1457.09	52.10	130.18	0.69	6.65	17.28	0.74	49.03
Middle	Count	BIF	MB41a	MB41aHm-15	clean martite	18.52	284.42	848.67	39.67	84.78	0.59	8.13	26.49	0.73	80.78
Middle	Count	BIF	MB41a	MB41aHm-16	clean martite	39.72	458.91	1067.70	171.00	278.46	1.29	36.59	39.76	2.24	161.87
Middle	Count	BIF	MB41a	MB41aHm-18	clean martite	859.90	284.38	7229.52	38.91	79.77	0.29	4.08	16.82	1.06	51.12
Middle	Count	BIF	MB41a	MB41aHm-2	clean martite	78.14	204.55	514.17	52.65	77.70	0.23	3.21	4.58	0.51	68.39
Middle	Count	BIF	MB41a	MB41aHm-20	clean martite	324.02	161.75	11829.16	52.28	<80.3	0.16	1.03	2.88	0.53	28.42
Middle	Count	BIF	MB41a	MB41aHm-21	clean martite	390.60	431.15	8161.38	51.28	123.46	0.65	27.41	43.13	3.84	111.33
Middle	Count	BIF	MB41a	MB41aHm-23	clean martite	216.62	198.15	12226.67	31.61	<79.3	0.27	5.41	6.99	0.81	46.66
Middle	Count	BIF	MB41a	MB41aHm-24	clean martite	128.00	272.42	11633.40	25.02	107.48	0.41	19.74	14.88	1.97	73.27
Middle	Count	BIF	MB41a	MB41aHm-3	clean martite	63.89	340.12	3179.66	25.60	124.53	0.16	2.18	1.84	0.46	19.25
Middle	Count	BIF	MB41a	MB41aHm-4	clean martite	83.81	355.79	3113.73	20.45	98.65	0.07	0.20	1.44	<0.26	17.16
Middle	Count	BIF	MB41a	MB41aHm-5	clean martite	75.49	266.53	1580.09	22.54	82.28	0.09	3.75	1.64	0.51	21.35
Middle	Count	BIF	MB41a	MB41aHm-6	clean martite	115.38	168.63	8864.84	26.94	<76.48	0.38	0.88	10.13	0.74	90.89

Analysis no.	Co	Ni	Cu	Zn	Ga	As	Sr	Y	Zr	Nb	Mo	Sn	Sb	Ba	La	Ce	Pr
MB40a-Hm-9	0.27	1.30	51.19	0.55	0.66	<0.00	1.23	2.58	1.34	4.16	1.48	2.51	2.80	1.16	3.21	7.44	0.71
MB40bHmClean-1	0.17	0.28	94.82	0.24	0.57	6.29	1.44	1.08	1.06	1.37	1.41	3.89	1.98	1.18	0.61	1.18	0.14
MB40bHmClean-2	0.38	1.35	65.98	1.50	0.77	5.90	1.72	2.49	1.64	1.24	1.38	3.28	1.38	3.75	1.41	2.49	0.32
MB40bHmClean-3	0.15	0.63	99.61	0.37	0.70	6.85	0.96	1.61	1.18	1.54	1.24	3.14	1.84	1.15	0.61	1.16	0.14
MB40bHmClean-4	0.15	0.29	115.83	0.64	0.81	7.92	1.39	2.07	1.76	1.66	1.36	4.12	1.82	0.85	1.25	2.25	0.24
MB40bHmClean-5	0.08	0.28	68.39	0.21	0.66	6.51	0.72	1.73	1.33	1.45	1.20	3.80	1.87	0.72	0.49	1.31	0.15
MB40bHmClean-6	0.24	0.64	81.38	0.71	0.68	5.97	0.91	1.83	1.42	1.04	1.22	3.70	1.24	1.68	0.70	1.33	0.14
MB40bHmClean-7	0.25	1.08	4.68	0.80	0.59	7.33	0.33	5.20	2.21	1.61	2.29	4.10	1.58	1.36	4.38	9.22	1.18
MB40bHmClean-8	0.06	0.80	4.68	1.72	0.62	7.95	0.52	7.76	2.07	1.56	2.65	3.99	1.21	3.09	5.62	11.21	1.28
MB40bMt-1	8.66	16.28	70.48	10.33	1.56	0.72	0.14	1.33	0.11	0.03	0.04	<0.076	<0.134	0.11	0.04	0.08	0.03
MB40bMt-2	8.64	16.43	9.15	12.41	1.99	1.76	1.02	1.59	0.14	0.04	0.09	<0.079	<0.172	2.00	0.31	0.59	0.09
MB40bMt-3	8.32	17.06	27.94	10.23	1.77	0.44	0.29	0.58	<0.059	0.01	0.03	0.15	0.31	0.23	0.17	0.19	0.04
MB40bMt-4	8.57	14.62	0.43	11.14	1.62	0.65	0.69	0.16	0.02	0.01	0.04	0.10	<0.119	0.47	0.06	0.13	0.02
MB40bMt-5	8.70	16.22	1.84	9.91	1.89	0.41	0.31	0.48	6.24	0.02	0.04	<0.077	0.15	0.18	0.07	0.20	0.03
MB40bMt-6	8.42	15.39	11.11	11.69	1.63	0.99	0.64	0.33	0.14	0.05	0.10	0.16	0.22	0.65	0.10	0.21	0.01
MB40bMt-7	8.61	13.19	1.52	9.59	1.67	0.67	0.44	0.58	0.39	0.01	<0.00	0.14	<0.116	0.10	0.19	0.31	0.05
MB40bMt-8	8.19	13.29	1.06	6.72	1.67	1.76	0.51	0.33	0.17	0.00	0.05	<0.093	0.40	0.60	0.06	0.24	0.02
MB40bMt-9	9.10	14.77	2.00	9.28	1.81	1.07	0.51	0.67	0.27	0.04	0.07	0.10	0.14	0.19	0.18	0.39	0.04
MB40bPorousHm-1	8.56	16.43	11.48	7.82	1.95	2.87	2.54	2.02	1.78	0.03	0.23	0.20	0.68	2.14	0.55	1.14	0.15
MB40bPorousHm-2	8.41	14.36	8.34	7.11	1.97	2.70	4.43	11.42	0.88	0.03	0.18	0.19	0.77	3.87	3.68	7.12	0.80
MB40bPorousHm-3	7.99	15.88	8.53	5.99	1.92	3.21	2.23	2.28	0.61	0.05	0.15	0.12	0.75	4.58	0.71	1.49	0.18
MB40bPorousHm-4	8.60	17.42	10.13	5.93	1.85	2.74	1.81	2.36	3.14	0.01	0.16	0.12	0.91	1.65	0.53	1.09	0.19
MB40bPorousHm-5	8.27	14.75	8.38	6.94	2.26	3.04	2.23	1.70	0.50	0.04	0.19	0.17	0.57	1.18	0.43	1.01	0.11
MB40bPorousHm-6	7.97	17.68	8.46	10.00	1.95	2.45	2.25	2.14	0.28	0.02	0.08	0.13	0.57	2.06	0.73	1.65	0.20
MB40bPorousHm-7	8.86	15.53	8.86	6.46	1.93	2.89	2.29	2.02	1.46	0.03	0.20	<0.077	0.75	1.72	0.38	0.77	0.11
MB41aHm-1	1.01	1.04	32.27	14.24	0.22	7.54	0.20	0.21	0.30	<0.00	0.54	0.11	4.49	0.27	0.10	0.23	0.03
MB41aHm-10	1.21	1.28	33.85	28.33	0.31	16.64	0.65	0.44	0.38	0.01	0.32	0.06	15.41	1.77	0.17	0.46	0.09
MB41aHm-11	0.77	2.14	17.96	8.35	0.22	18.45	0.46	0.43	0.38	0.07	0.23	0.34	11.25	1.25	0.12	0.37	0.05
MB41aHm-12	1.11	2.77	42.13	8.85	0.22	27.94	0.50	0.65	0.16	0.03	0.30	0.32	17.96	1.04	0.19	0.53	0.06
MB41aHm-13	0.53	0.72	1.54	2.13	0.25	13.82	1.62	0.95	0.59	0.17	0.39	1.18	12.23	1.61	0.45	0.97	0.13
MB41aHm-14	0.38	0.34	0.71	2.30	0.22	11.88	0.96	0.93	0.73	0.12	0.22	0.82	22.16	1.51	0.29	0.67	0.07
MB41aHm-15	0.48	0.44	0.89	3.04	0.18	17.17	0.93	0.53	0.78	0.10	0.36	0.70	40.59	1.59	0.26	0.46	0.06
MB41aHm-16	1.32	2.05	2.21	5.60	0.72	30.54	2.22	2.18	1.23	0.12	0.80	1.05	89.94	3.35	1.31	2.71	0.32
MB41aHm-18	2.02	2.60	70.12	10.67	0.43	41.47	1.15	0.98	0.34	0.02	0.30	0.07	48.21	1.42	0.33	0.75	0.12
MB41aHm-2	1.22	0.85	17.19	17.17	0.36	5.53	1.72	0.25	2.12	0.01	0.77	0.21	5.15	0.59	0.20	0.50	0.05
MB41aHm-20	0.52	0.78	3.00	3.79	0.27	16.48	0.81	0.73	0.32	0.04	0.57	0.20	12.96	0.38	0.19	0.39	0.05
MB41aHm-21	1.59	2.10	10.41	13.24	0.47	36.37	1.10	1.04	0.34	0.11	0.43	0.09	125.52	3.34	0.79	1.09	0.15
MB41aHm-23	0.80	1.22	2.60	8.02	0.28	17.51	0.52	0.47	0.25	<0.0063	0.25	0.09	34.53	1.58	0.24	0.62	0.05
MB41aHm-24	1.31	2.44	2.78	12.10	0.26	23.88	0.73	0.65	0.15	0.03	0.25	0.16	74.40	2.37	0.48	0.73	0.08
MB41aHm-3	1.17	1.12	10.18	5.39	0.26	4.28	0.13	1.12	0.40	0.01	0.12	0.19	4.71	0.20	0.16	0.35	0.04
MB41aHm-4	1.27	1.45	7.05	5.24	0.26	2.17	0.09	0.46	0.41	<0.00	0.25	0.13	1.82	0.14	0.20	0.42	0.05
MB41aHm-5	1.36	1.13	8.51	4.39	0.26	2.38	0.08	0.20	0.65	<0.00	0.23	0.06	1.92	<0.00	0.11	0.17	0.03
MB41aHm-6	2.52	1.12	64.81	43.26	0.30	29.71	0.92	0.52	0.10	0.00	0.17	0.14	18.28	0.30	0.19	0.52	0.07

Analysis no.	Nd	Sm	Eu	Gd	Tb	Dy	Ho	Er	Tm	Yb	Lu	W	Pb208	Th	U
MB40a-Hm-9	2.64	0.88	0.18	0.73	0.11	0.62	0.12	0.26	0.05	0.22	0.03	3.26	8.13	3.86	10.18
MB40bHmClean-1	0.53	0.17	0.06	0.32	0.03	0.21	0.04	0.12	0.02	0.08	0.02	6.36	3.70	1.04	6.21
MB40bHmClean-2	1.06	0.31	0.10	0.55	0.10	0.40	0.06	0.22	0.04	0.14	0.02	5.47	4.55	1.19	6.61
MB40bHmClean-3	0.55	0.21	0.06	0.32	0.05	0.31	0.05	0.16	0.02	0.09	0.02	5.23	5.21	0.98	5.43
MB40bHmClean-4	0.78	0.32	0.10	0.63	0.05	0.39	0.08	0.22	0.02	0.20	0.03	7.26	5.15	1.15	6.80
MB40bHmClean-5	0.60	0.31	0.04	0.37	0.05	0.33	0.04	0.22	0.02	0.14	0.02	5.72	4.30	1.07	5.79
MB40bHmClean-6	0.85	0.20	0.06	0.38	0.06	0.39	0.06	0.19	0.03	0.16	0.03	4.53	4.32	0.78	5.01
MB40bHmClean-7	4.34	1.04	0.36	1.46	0.17	0.79	0.21	0.35	0.04	0.34	0.05	5.81	15.33	1.29	8.30
MB40bHmClean-8	5.62	1.32	0.37	1.79	0.23	1.25	0.26	0.79	0.05	0.39	0.11	6.81	19.73	1.27	10.27
MB40bMt-1	0.06	<0.00	0.01	0.03	0.01	0.22	0.06	0.43	0.12	1.05	0.28	0.36	0.32	<0.00	0.02
MB40bMt-2	0.27	0.09	0.05	0.24	0.08	0.23	0.04	0.13	0.01	0.14	0.03	<0.00	0.03	0.00	0.01
MB40bMt-3	0.08	0.04	0.01	0.09	<0.0084	0.08	0.01	0.06	0.01	0.13	0.01	0.15	1.11	0.02	0.05
MB40bMt-4	0.07	<0.031	0.01	0.05	0.00	0.04	0.01	0.02	0.00	<0.023	0.01	0.04	0.77	0.03	0.04
MB40bMt-5	0.15	0.07	0.02	0.06	0.01	0.09	0.02	0.10	0.01	0.09	0.02	0.01	<0.0216	<0.00	<0.00
MB40bMt-6	0.14	0.02	0.01	0.06	0.02	0.07	0.00	0.06	0.00	0.03	0.00	0.00	0.04	0.01	0.01
MB40bMt-7	0.23	0.06	0.03	0.07	0.03	0.08	0.02	0.06	<0.0062	0.05	0.01	0.05	0.08	0.01	0.02
MB40bMt-8	0.07	0.05	0.00	0.07	0.01	0.06	0.01	0.05	0.00	<0.057	0.00	0.03	0.49	0.03	0.05
MB40bMt-9	0.20	0.11	0.01	0.09	0.02	0.13	0.02	0.04	0.01	0.10	0.00	0.13	0.24	0.01	0.01
MB40bPorousHm-1	0.74	0.25	0.05	0.30	0.07	0.41	0.07	0.17	0.02	0.11	0.02	0.16	1.60	0.18	2.94
MB40bPorousHm-2	3.59	0.94	0.39	1.82	0.34	1.85	0.35	0.92	0.14	0.72	0.13	0.09	3.68	0.20	2.58
MB40bPorousHm-3	0.86	0.26	0.09	0.38	0.07	0.31	0.08	0.18	0.03	0.13	0.02	0.08	1.93	0.16	2.98
MB40bPorousHm-4	0.61	0.23	0.09	0.45	0.07	0.28	0.07	0.21	0.04	0.13	0.03	0.11	2.08	0.12	3.08
MB40bPorousHm-5	0.53	0.24	0.08	0.33	0.07	0.34	0.07	0.16	0.02	0.18	0.03	0.06	1.56	0.13	2.27
MB40bPorousHm-6	0.79	0.24	0.09	0.46	0.08	0.37	0.07	0.16	0.01	0.14	0.02	0.12	2.07	0.19	2.32
MB40bPorousHm-7	0.46	0.24	0.05	0.27	0.05	0.20	0.04	0.15	0.03	0.17	0.02	0.06	1.33	0.15	2.23
MB41aHm-1	0.14	0.09	0.00	0.05	0.01	0.05	0.01	0.01	<0.0037	0.02	0.00	5.43	2.50	0.01	0.19
MB41aHm-10	0.32	0.07	0.00	0.09	0.03	0.12	0.02	0.06	0.01	0.06	0.00	3.87	5.37	0.01	0.98
MB41aHm-11	0.23	0.05	0.04	0.10	0.02	0.12	0.01	0.02	0.01	0.04	0.01	2.68	1.94	0.07	0.76
MB41aHm-12	0.39	0.14	0.03	0.14	0.03	0.14	0.02	0.08	0.01	0.03	0.01	1.80	3.63	0.02	1.18
MB41aHm-13	0.54	0.17	0.02	0.24	0.02	0.13	0.02	0.05	0.01	0.04	0.00	5.83	2.02	0.02	2.06
MB41aHm-14	0.36	0.11	0.04	0.13	0.01	0.09	0.02	0.05	0.01	0.04	0.01	8.79	2.02	<0.0188	2.65
MB41aHm-15	0.24	0.10	0.03	0.11	0.02	0.09	0.01	0.07	0.01	0.04	0.01	7.39	2.77	0.05	4.23
MB41aHm-16	1.74	0.33	0.06	0.42	0.07	0.34	0.10	0.26	0.03	0.17	0.03	13.40	7.39	0.09	5.70
MB41aHm-18	0.45	0.13	0.04	0.15	0.04	0.20	0.04	0.16	0.03	0.07	0.01	1.60	6.11	0.04	4.50
MB41aHm-2	0.24	0.07	0.03	0.08	0.01	0.05	<0.0069	0.02	0.00	0.01	<0.0059	18.05	2.12	0.02	0.51
MB41aHm-20	0.28	0.06	0.04	0.13	0.02	0.10	0.01	0.08	0.01	0.04	0.01	6.14	2.88	<0.0068	5.52
MB41aHm-21	0.57	0.15	0.05	0.24	0.03	0.15	0.03	0.18	0.02	0.08	0.01	3.60	7.26	0.05	2.92
MB41aHm-23	0.37	0.08	0.02	0.09	0.02	0.09	0.02	0.03	0.01	0.05	0.00	1.97	2.70	0.01	1.82
MB41aHm-24	0.42	0.10	0.02	0.13	0.01	0.11	0.03	0.08	0.01	0.05	0.01	3.81	4.73	0.01	2.50
MB41aHm-3	0.18	0.05	0.05	0.08	0.01	0.09	0.01	0.03	0.01	0.04	0.00	4.04	6.79	<0.0041	0.19
MB41aHm-4	0.22	0.07	0.05	0.10	0.01	0.06	0.01	0.03	0.01	0.02	<0.0051	10.41	8.43	0.01	0.13
MB41aHm-5	0.11	0.03	0.02	0.08	0.00	0.04	0.01	0.01	0.00	0.03	0.00	4.76	4.44	0.01	0.06
MB41aHm-6	0.29	0.09	0.05	0.14	0.02	0.09	0.02	0.07	0.01	0.05	0.01	3.23	5.14	0.01	2.25

Position	Deposit	Lithology	Sample no.	Analysis no.	Texture	Mg	Al	Si	P	Ca	Sc	Ti	V	Cr	Mn
Middle	Count	BIF	MB41a	MB41aHm-7	clean martite	55.56	236.61	745.99	33.12	<76.76	0.49	1.79	21.66	0.67	60.78
Middle	Count	BIF	MB41a	MB41aHm-8	clean martite	71.78	227.33	8091.90	21.95	78.24	0.58	3.23	32.97	0.93	45.43
Middle	Count	BIF	MB41a	MB41aHm-9	clean martite	85.31	239.56	760.60	26.02	<73.83	0.29	1.17	6.37	0.55	71.44
Middle	Count	BIF	MB41b	MB41bHm-10	clean martite	57.91	102.84	8092.37	483.66	102.93	0.17	4.26	10.34	3.11	127.91
Middle	Count	BIF	MB41b	MB41bHm-12	clean martite	95.19	76.76	9323.82	222.71	187.46	0.16	4.58	5.74	14.28	206.92
Middle	Count	BIF	MB41b	MB41bHm-13	clean martite	81.69	82.22	18805.71	120.64	128.81	0.20	3.72	4.79	3.54	156.18
Middle	Count	BIF	MB41b	MB41bHm-14	clean martite	114.95	117.07	10061.24	65.55	90.85	0.12	2.77	6.95	2.00	185.29
Middle	Count	BIF	MB41b	MB41bHm-16	clean martite	64.98	245.62	7568.74	92.56	91.53	0.50	6.49	36.85	4.84	111.90
Middle	Count	BIF	MB41b	MB41bHm-6	clean martite	93.09	85.90	8087.71	924.80	498.86	0.21	3.68	4.72	1.80	223.28
Middle	Count	BIF	MB41b	MB41bHm-7	clean martite	43.01	93.40	14994.13	752.90	406.29	0.21	4.32	6.91	1.16	187.50
Middle	Count	BIF	MB41b	MB41bHm-8	clean martite	30.73	127.44	9647.35	269.44	225.13	0.21	4.45	11.23	1.29	131.36
Middle	Count	BIF	MB41b	MB41bHmRe-1	clean martite	85.53	104.53	10496.40	65.77	91.80	0.33	5.44	15.28	1.71	137.10
Middle	Count	BIF	MB41b	MB41bHmRe-10	clean martite	97.00	104.44	22010.75	304.78	265.81	0.29	3.86	21.74	2.03	141.92
Middle	Count	BIF	MB41b	MB41bHmRe-12	clean martite	82.35	148.58	19511.79	751.30	395.67	0.19	3.84	14.97	2.92	245.74
Middle	Count	BIF	MB41b	MB41bHmRe-14	clean martite	80.44	126.04	14057.72	1102.58	544.55	0.34	4.30	10.74	1.58	232.56
Middle	Count	BIF	MB41b	MB41bHmRe-16	clean martite	48.00	176.98	21898.33	100.79	165.80	0.27	2.09	18.38	3.20	109.81
Middle	Count	BIF	MB41b	MB41bHmRe-18	clean martite	110.72	102.71	8656.29	938.10	749.33	0.23	3.09	8.79	1.17	223.15
Middle	Count	BIF	MB41b	MB41bHmRe-19	clean martite	47.51	137.70	9246.81	437.18	264.59	0.25	2.46	12.74	1.47	165.25
Middle	Count	BIF	MB41b	MB41bHmRe-22	clean martite	86.10	81.67	9173.54	978.44	466.34	0.23	2.78	5.46	1.99	217.63
Middle	Count	BIF	MB41b	MB41bHmRe-24	clean martite	60.20	242.78	17778.82	855.16	251.82	0.28	2.93	13.91	3.32	182.90
Middle	Count	BIF	MB41b	MB41bHmRe-3	clean martite	67.01	202.01	23589.02	124.34	65.86	0.28	3.00	35.49	1.59	189.73
Middle	Count	BIF	MB41b	MB41bHmRe-6	clean martite	81.91	97.06	8973.46	117.82	117.06	0.13	2.98	7.22	2.87	168.23
Middle	Count	BIF	MB41b	MB41bHmRe-8	clean martite	51.96	157.45	11834.03	119.84	159.73	0.12	3.30	18.56	2.78	78.63
Middle	Count	BIF	MB41b	MB41bHmRe-9	clean martite	84.37	83.39	24402.67	104.94	69.10	0.22	4.23	9.80	1.89	122.29
Middle	Baron	ORE	MB43	MB43Hm-1	clean martite	1283.38	801.97	1603.32	48.39	<73.96	0.76	153.79	80.86	9.48	1517.72
Middle	Baron	ORE	MB43	MB43Hm-10	clean martite	589.43	504.38	482.30	12.47	<74.73	0.50	195.44	9.78	2.21	486.76
Middle	Baron	ORE	MB43	MB43Hm-11	clean martite	1955.62	772.73	1053.08	22.56	123.61	0.68	201.56	18.15	8.24	1670.59
Middle	Baron	ORE	MB43	MB43Hm-12	clean martite	1775.98	721.50	884.26	15.67	<80.1	0.77	212.23	18.09	11.47	1584.51
Middle	Baron	ORE	MB43	MB43Hm-13	clean martite	1667.06	1313.26	1966.14	22.39	<75.5	0.55	190.73	16.92	8.30	1885.49
Middle	Baron	ORE	MB43	MB43Hm-14	clean martite	4683.11	2242.67	3027.14	18.38	87.96	0.80	199.40	10.48	9.43	2347.06
Middle	Baron	ORE	MB43	MB43Hm-15	clean martite	5025.55	2516.54	4077.06	32.40	102.08	0.89	232.01	15.41	1.79	1335.44
Middle	Baron	ORE	MB43	MB43Hm-16	clean martite	4083.01	2831.40	4665.66	42.98	<76.53	0.91	195.61	48.64	1.43	1605.52
Middle	Baron	ORE	MB43	MB43Hm-2	clean martite	4803.66	2688.86	3856.36	25.24	144.11	0.87	175.99	92.48	9.83	1795.45
Middle	Baron	ORE	MB43	MB43Hm-3	clean martite	5351.92	2194.08	4214.05	23.13	<84.26	0.82	204.64	16.34	0.61	300.92
Middle	Baron	ORE	MB43	MB43Hm-4	clean martite	5130.19	2016.39	3659.30	16.47	<78.35	0.81	204.42	9.05	0.51	534.78
Middle	Baron	ORE	MB43	MB43Hm-5	clean martite	3545.55	1288.08	2327.05	15.50	81.43	0.83	210.84	10.00	0.94	1093.01
Middle	Baron	ORE	MB43	MB43Hm-6	clean martite	2020.56	1099.94	1606.34	20.69	152.13	0.66	183.18	42.52	12.81	1922.07
Middle	Baron	ORE	MB43	MB43Hm-7	clean martite	990.57	439.21	518.70	20.30	<74.93	0.61	226.77	13.33	3.29	1441.90
Middle	Baron	ORE	MB43	MB43Hm-8	clean martite	1406.31	616.45	737.75	20.07	82.48	0.59	200.54	20.99	3.06	2433.17
Middle	Baron	ORE	MB43	MB43Hm-9	clean martite	1391.40	694.24	949.15	18.77	98.41	0.64	188.66	31.46	1.86	1565.45
Middle	Baron	ORE	MB44a	MB44aHm-1	clean martite	2443.33	663.27	1361.81	16.83	46.64	0.39	145.04	10.97	8.60	1755.97
Middle	Baron	ORE	MB44a	MB44aHm-10	clean martite	2338.99	483.70	1712.58	15.57	113.55	0.42	37.67	64.57	40.86	1790.08
Middle	Baron	ORE	MB44a	MB44aHm-11	clean martite	1657.12	311.60	1136.09	24.70	<74.38	0.43	96.33	23.61	9.96	2224.21

Analysis no.	Co	Ni	Cu	Zn	Ga	As	Sr	Y	Zr	Nb	Mo	Sn	Sb	Ba	La	Ce	Pr
MB41aHm-7	1.43	1.72	20.92	13.40	0.31	36.56	1.07	0.90	0.25	0.01	0.38	0.16	26.70	3.25	0.26	0.74	0.12
MB41aHm-8	1.50	1.36	34.12	7.70	0.33	31.03	0.65	0.42	0.24	0.00	0.29	0.16	29.01	1.42	0.15	0.38	0.07
MB41aHm-9	2.30	1.17	36.41	17.35	0.33	27.77	0.50	0.85	0.11	0.00	0.67	0.16	21.68	1.52	0.34	0.76	0.09
MB41bHm-10	1.52	1.81	53.48	6.70	0.32	345.42	1.89	2.10	0.08	0.02	1.06	0.87	16.59	1.43	0.43	1.12	0.19
MB41bHm-12	1.48	0.72	28.03	10.68	0.26	107.23	2.85	1.66	0.06	0.01	0.81	1.24	25.90	2.80	1.26	1.97	0.27
MB41bHm-13	2.91	1.00	131.26	19.20	0.22	70.88	3.05	1.55	0.05	0.01	0.39	0.82	55.83	2.23	0.27	0.82	0.11
MB41bHm-14	1.28	1.22	12.22	7.10	0.34	97.74	2.67	1.30	0.11	0.01	1.48	1.01	19.65	2.66	0.78	1.48	0.20
MB41bHm-16	1.24	2.20	16.58	7.33	0.68	41.94	2.21	2.04	0.47	0.05	1.25	1.61	25.38	2.72	0.57	1.62	0.23
MB41bHm-6	0.81	1.29	15.41	8.55	0.36	105.75	4.46	5.60	0.10	0.05	0.74	0.99	25.88	4.58	1.87	3.78	0.49
MB41bHm-7	0.67	1.11	13.69	9.26	0.66	65.37	3.65	4.16	0.16	0.03	0.57	0.86	34.96	24.33	1.10	2.57	0.39
MB41bHm-8	1.24	0.95	25.81	13.27	0.45	61.12	2.49	3.82	0.08	0.04	1.06	0.89	25.66	6.27	1.05	2.37	0.30
MB41bHmRe-1	2.19	2.25	41.35	16.91	0.43	67.74	2.20	0.86	0.14	0.01	0.86	1.28	14.42	2.39	0.26	0.66	0.09
MB41bHmRe-10	4.50	2.75	3.32	10.30	0.43	282.89	5.80	2.31	0.13	0.03	2.79	0.80	22.56	11.63	0.72	1.30	0.18
MB41bHmRe-12	0.83	2.14	5.48	10.59	0.62	64.10	4.14	4.34	0.12	0.03	0.96	0.76	99.75	12.88	0.91	2.19	0.31
MB41bHmRe-14	0.85	2.37	10.36	8.41	2.08	80.85	5.52	11.47	0.18	0.04	0.85	0.98	80.01	94.17	2.85	6.06	0.74
MB41bHmRe-16	1.84	1.62	32.51	8.53	1.10	57.36	5.30	3.48	0.07	0.03	1.19	0.89	23.99	32.88	1.43	3.77	0.42
MB41bHmRe-18	1.12	2.18	37.75	16.67	0.34	80.30	5.50	7.31	0.10	0.01	0.69	1.09	33.48	5.55	1.31	3.52	0.48
MB41bHmRe-19	0.70	1.30	18.22	8.87	0.44	64.45	2.89	3.22	0.15	0.01	1.00	0.98	34.60	5.90	0.75	2.25	0.27
MB41bHmRe-22	1.92	1.48	60.61	16.04	0.16	153.68	4.11	3.44	0.09	0.04	0.95	0.90	28.67	2.13	0.97	2.24	0.27
MB41bHmRe-24	1.95	3.01	20.91	8.49	0.37	109.46	7.43	4.28	0.24	0.02	1.06	0.81	55.31	9.32	5.58	9.01	0.98
MB41bHmRe-3	3.37	8.63	7.15	14.93	0.53	156.03	3.35	1.43	0.13	0.01	2.19	0.71	257.58	3.85	0.40	0.83	0.11
MB41bHmRe-6	1.24	1.13	26.10	8.19	0.28	94.51	2.39	1.83	0.02	<0.00	0.97	0.74	16.03	0.90	0.48	1.31	0.18
MB41bHmRe-8	3.52	5.69	23.62	8.24	0.43	73.39	2.70	1.80	0.05	0.02	0.71	1.10	18.24	4.64	0.91	1.95	0.26
MB41bHmRe-9	3.05	2.07	4.40	7.36	0.21	125.16	2.61	1.82	0.08	0.04	1.65	0.54	26.78	2.11	0.40	0.64	0.11
MB43Hm-1	3.95	9.67	2.37	26.68	0.86	8.10	1.28	0.89	2.69	0.19	0.08	6.56	0.78	7.38	0.44	1.83	0.10
MB43Hm-10	4.31	0.95	1.62	17.37	0.77	3.18	0.18	0.12	0.01	0.01	0.02	7.50	0.38	0.82	0.06	0.11	0.01
MB43Hm-11	1.82	2.80	0.99	33.75	0.98	6.91	0.32	0.47	0.70	0.24	0.01	7.62	0.71	3.68	0.14	0.30	0.03
MB43Hm-12	2.18	2.05	1.12	31.63	0.98	5.03	0.24	0.44	1.88	0.13	0.09	7.28	0.29	2.51	0.13	0.24	0.03
MB43Hm-13	0.81	2.04	2.32	37.18	0.74	2.41	0.28	0.42	0.86	0.12	0.01	7.31	0.61	2.50	0.10	0.26	0.02
MB43Hm-14	0.20	2.93	1.28	43.56	0.66	14.81	0.82	0.72	7.46	0.49	<0.019	7.49	1.21	4.30	0.24	0.33	0.05
MB43Hm-15	5.01	1.99	3.40	26.17	1.07	23.84	0.72	1.83	7.47	1.09	1.04	9.36	3.11	4.45	0.22	0.63	0.09
MB43Hm-16	3.55	4.29	2.95	21.52	1.39	11.61	0.80	1.05	0.13	0.36	<0.036	7.62	1.80	3.88	0.33	0.95	0.08
MB43Hm-2	1.78	8.82	3.25	33.96	0.96	11.71	0.93	1.22	18.79	0.45	0.23	7.67	0.86	9.28	0.33	0.57	0.07
MB43Hm-3	4.44	2.55	1.57	7.38	0.72	10.29	0.17	0.78	0.14	0.62	0.06	7.94	1.11	1.44	0.10	0.25	0.03
MB43Hm-4	0.39	1.13	0.94	6.91	0.87	10.87	0.21	0.53	0.09	0.42	<0.00	8.50	1.29	0.16	0.06	0.14	0.01
MB43Hm-5	1.49	1.44	1.70	18.82	0.64	12.75	0.20	0.43	0.09	0.38	0.08	7.86	1.09	2.52	0.06	0.15	0.03
MB43Hm-6	2.08	5.43	3.00	35.39	0.98	8.09	0.64	0.79	1.47	0.21	0.04	6.70	0.84	6.81	0.24	0.47	0.06
MB43Hm-7	3.29	2.16	1.16	26.03	0.67	6.28	0.27	0.33	0.82	1.50	0.02	13.52	0.44	2.49	0.10	0.24	0.02
MB43Hm-8	0.21	2.38	0.58	45.03	0.61	6.17	0.17	0.24	0.11	1.23	0.03	7.86	0.86	0.60	0.13	0.27	0.03
MB43Hm-9	1.81	6.77	2.22	29.64	0.78	4.45	0.40	0.63	6.08	0.13	0.04	6.89	0.50	4.46	0.17	0.33	0.04
MB44aHm-1	2.01	1.44	3.44	17.55	0.33	10.51	0.31	0.53	3.69	0.32	0.02	2.23	0.37	1.02	0.16	0.28	0.02
MB44aHm-10	1.33	6.38	1.48	14.56	0.77	8.44	0.57	0.46	0.20	0.10	0.24	1.81	0.52	5.45	0.26	0.46	0.12
MB44aHm-11	1.55	2.71	5.66	25.16	0.51	15.07	0.72	0.54	0.07	0.12	0.20	0.85	0.79	8.53	0.23	0.43	0.05

Analysis no.	Nd	Sm	Eu	Gd	Tb	Dy	Ho	Er	Tm	Yb	Lu	W	Pb208	Th	U
MB41aHm-7	0.54	0.13	0.04	0.16	0.03	0.15	0.03	0.10	0.01	0.06	0.01	3.28	3.37	0.04	4.61
MB41aHm-8	0.26	0.08	0.02	0.12	0.02	0.17	0.01	0.07	0.00	0.08	0.00	5.40	3.14	0.02	3.20
MB41aHm-9	0.43	0.13	0.06	0.12	0.03	0.24	0.03	0.08	0.01	0.05	0.02	6.62	4.59	0.01	3.75
MB41bHm-10	0.66	0.24	0.12	0.41	0.07	0.43	0.08	0.16	0.04	0.21	0.03	2.21	7.98	0.01	15.10
MB41bHm-12	1.17	0.39	0.07	0.37	0.09	0.41	0.07	0.13	0.02	0.16	0.01	0.66	7.84	0.00	8.96
MB41bHm-13	0.67	0.39	0.08	0.35	0.05	0.43	0.06	0.19	0.03	0.23	0.02	0.71	7.71	0.00	5.82
MB41bHm-14	0.83	0.23	0.06	0.26	0.06	0.37	0.05	0.16	0.03	0.10	0.02	1.93	6.87	0.02	18.33
MB41bHm-16	0.95	0.42	0.08	0.41	0.05	0.43	0.09	0.33	0.03	0.27	0.03	8.73	4.87	0.05	10.72
MB41bHm-6	2.22	0.75	0.44	0.98	0.14	0.71	0.15	0.42	0.05	0.27	0.04	1.66	8.55	0.01	8.06
MB41bHm-7	1.58	0.59	0.19	0.65	0.16	0.75	0.18	0.39	0.04	0.35	0.04	1.83	5.98	0.03	4.97
MB41bHm-8	1.65	0.37	0.15	0.50	0.14	0.65	0.11	0.35	0.04	0.23	0.06	3.75	6.53	0.01	11.91
MB41bHmRe-1	0.39	0.18	0.03	0.18	0.04	0.20	0.04	0.11	0.03	0.10	0.02	3.08	6.74	0.00	17.13
MB41bHmRe-10	0.63	0.18	0.11	0.28	0.05	0.30	0.08	0.24	0.04	0.13	0.03	1.80	17.53	0.04	31.56
MB41bHmRe-12	1.44	0.54	0.22	0.70	0.12	0.59	0.12	0.28	0.04	0.26	0.06	2.24	7.72	0.01	5.60
MB41bHmRe-14	3.33	1.17	0.74	1.48	0.23	1.62	0.28	0.81	0.09	0.65	0.10	2.89	11.59	0.01	6.07
MB41bHmRe-16	2.31	0.56	0.11	0.68	0.10	0.57	0.11	0.30	0.04	0.26	0.06	5.05	7.30	0.01	15.71
MB41bHmRe-18	2.25	0.78	0.35	0.68	0.17	0.99	0.20	0.59	0.08	0.42	0.07	3.12	10.13	0.01	5.69
MB41bHmRe-19	1.54	0.52	0.14	0.61	0.12	0.72	0.12	0.31	0.05	0.30	0.04	3.08	6.67	0.01	6.65
MB41bHmRe-22	1.26	0.48	0.25	0.53	0.09	0.46	0.11	0.27	0.04	0.25	0.02	1.46	12.39	0.01	14.70
MB41bHmRe-24	3.78	1.01	0.28	0.87	0.15	0.95	0.14	0.38	0.05	0.22	0.05	2.84	9.25	0.04	7.60
MB41bHmRe-3	0.50	0.22	0.04	0.30	0.08	0.33	0.06	0.16	0.04	0.15	0.02	1.45	10.02	0.03	17.07
MB41bHmRe-6	0.74	0.31	0.04	0.28	0.09	0.42	0.08	0.20	0.03	0.12	0.02	1.75	6.90	0.01	17.30
MB41bHmRe-8	0.98	0.30	0.04	0.39	0.07	0.32	0.05	0.20	0.03	0.12	0.02	3.12	7.62	0.01	17.42
MB41bHmRe-9	0.34	0.16	0.06	0.21	0.04	0.27	0.06	0.16	0.03	0.14	0.03	1.20	10.91	0.05	27.24
MB43Hm-1	0.47	0.13	0.08	0.09	0.03	0.13	0.02	0.06	0.01	0.07	0.02	0.67	4.37	0.08	0.21
MB43Hm-10	0.07	0.04	0.01	0.01	<0.00	0.01	<0.0058	0.01	<0.0071	<0.00	<0.00	0.10	1.00	0.01	0.02
MB43Hm-11	0.20	0.05	0.02	0.05	0.01	0.05	0.01	0.06	0.01	0.02	0.01	0.32	2.15	0.03	0.21
MB43Hm-12	0.11	0.02	0.03	0.04	0.01	0.04	0.01	0.04	<0.0061	0.04	0.01	0.13	1.58	0.04	0.16
MB43Hm-13	0.16	0.06	0.03	<0.027	0.00	0.02	0.01	0.03	0.00	0.04	<0.0058	0.16	1.72	0.02	0.12
MB43Hm-14	0.11	0.01	0.02	0.07	0.01	0.06	0.01	0.06	0.01	0.06	0.01	0.80	3.08	0.27	0.65
MB43Hm-15	0.48	0.10	0.05	0.17	0.01	0.16	0.02	0.09	0.02	0.11	0.02	0.68	3.17	0.03	0.53
MB43Hm-16	0.43	0.17	0.04	0.10	0.01	0.12	0.01	0.08	0.01	0.04	0.01	0.44	2.97	0.08	0.27
MB43Hm-2	0.25	0.04	0.04	0.05	0.01	0.11	0.02	0.08	0.01	0.08	0.01	0.40	3.91	0.10	0.45
MB43Hm-3	0.11	0.05	0.00	0.04	<0.004	0.02	0.01	0.06	0.01	0.06	0.01	0.32	1.55	0.01	0.26
MB43Hm-4	0.07	0.05	0.02	0.04	0.01	0.04	0.01	0.01	<0.0059	0.03	0.01	0.26	1.18	0.01	0.15
MB43Hm-5	0.12	0.02	0.01	0.04	0.01	0.05	0.01	0.03	0.01	0.03	0.01	0.29	1.13	0.01	0.18
MB43Hm-6	0.35	0.09	0.03	0.08	0.01	0.10	0.02	0.05	0.01	0.02	0.01	0.61	2.88	0.07	0.18
MB43Hm-7	0.13	0.02	0.01	0.02	0.00	0.02	0.01	0.01	0.00	0.03	0.00	0.06	1.28	0.01	0.21
MB43Hm-8	0.12	0.05	0.02	0.05	0.01	0.05	<0.0042	<0.013	0.01	0.02	0.01	0.28	1.38	0.03	0.21
MB43Hm-9	0.18	0.05	0.02	0.02	0.01	0.05	<0.0042	0.05	0.01	0.04	0.01	0.52	2.22	0.06	0.15
MB44aHm-1	0.17	0.05	0.03	0.06	0.01	0.04	0.01	0.05	0.02	0.05	0.01	0.14	1.27	0.05	0.19
MB44aHm-10	0.20	0.08	0.07	0.11	0.04	0.11	0.02	0.07	0.03	0.09	0.06	0.95	3.62	0.08	0.20
MB44aHm-11	0.26	0.11	0.02	0.05	0.04	0.06	0.02	0.05	0.01	0.05	0.01	0.37	2.89	0.02	0.11

Position	Deposit	Lithology	Sample no.	Analysis no.	Texture	Mg	Al	Si	P	Ca	Sc	Ti	V	Cr	Mn
Middle	Baron	ORE	MB44a	MB44aHm-12	clean martite	11938.92	4110.01	11157.98	20.69	85.18	0.68	73.79	78.96	3.73	2138.43
Middle	Baron	ORE	MB44a	MB44aHm-13	clean martite	2211.48	641.50	1727.14	22.23	96.27	0.49	79.29	94.46	40.37	2552.36
Middle	Baron	ORE	MB44a	MB44aHm-2	clean martite	2299.85	169.65	342.83	17.51	62.84	0.29	144.63	7.90	1.93	3030.62
Middle	Baron	ORE	MB44a	MB44aHm-3	clean martite	1306.06	234.11	820.23	25.34	122.76	0.28	81.19	23.66	8.45	1530.48
Middle	Baron	ORE	MB44a	MB44aHm-4	clean martite	1925.34	246.52	727.51	18.17	262.34	0.23	77.08	13.26	4.99	2460.17
Middle	Baron	ORE	MB44a	MB44aHm-5	clean martite	877.57	358.80	740.82	24.66	<56.47	0.34	84.21	25.15	7.73	1195.04
Middle	Baron	ORE	MB44a	MB44aHm-6	clean martite	3447.01	421.43	969.59	14.99	<59.1	0.45	55.34	13.03	2.71	3889.49
Middle	Baron	ORE	MB44a	MB44aHm-7	clean martite	4427.33	1305.25	4163.30	71.86	342.77	1.10	73.42	10.35	10.11	2261.55
Middle	Baron	ORE	MB44a	MB44aHm-8	clean martite	1735.83	1633.53	3408.00	34.61	228.32	0.80	47.52	81.41	28.06	2259.22
Middle	Baron	ORE	MB44a	MB44aHm-9	clean martite	2615.31	304.90	1254.51	23.61	126.11	0.60	58.51	32.81	24.36	3345.07
Middle	Baron	ORE	MB44a	MB44aHmLam-11	platy hematite	5.73	818.65	458.68	13.02	<69.19	0.48	6.65	566.53	88.58	115.05
Middle	Baron	ORE	MB44a	MB44aHmLam-12	platy hematite	116.50	875.30	1064.23	39.33	<67.59	0.51	5.42	511.14	83.18	213.10
Middle	Baron	ORE	MB44a	MB44aHmLam-2	platy hematite	151.85	855.49	1777.44	34.63	50.96	0.39	15.41	463.41	23.58	422.45
Middle	Baron	ORE	MB44a	MB44aHmLam-3	platy hematite	70.25	2487.18	3657.12	26.83	105.93	0.87	17.50	553.12	47.73	84.42
Middle	Baron	ORE	MB44a	MB44aHmLam-4	platy hematite	26.80	893.03	573.67	22.82	<64.19	0.50	12.06	498.50	42.04	132.90
Middle	Baron	ORE	MB44a	MB44aHmLam-5	platy hematite	667.59	844.58	2731.57	237.35	<53.72	1.03	117.57	174.73	95.01	1101.81
Middle	Baron	ORE	MB44a	MB44aHmLam-6	platy hematite	139.84	11296.66	14014.65	79.48	204.67	1.12	19.31	766.12	58.94	132.32
Middle	Baron	ORE	MB44a	MB44aHmLam-7	platy hematite	9.89	887.32	558.54	15.85	136.21	0.46	7.77	475.28	40.41	102.20
Middle	Baron	ORE	MB44a	MB44aHmLam-8	platy hematite	212.75	958.67	1392.86	26.78	94.87	0.63	11.04	464.97	29.37	341.35
Middle	Baron	ORE	MB44a	MB44aHmLam-9	platy hematite	46.25	1302.88	1618.22	30.85	140.40	0.54	13.78	476.95	236.44	245.38
Middle	Baron	ORE	MB44a	MB44aHmRe-1	clean martite	799.37	552.98	1382.82	34.31	97.96	0.42	28.28	140.88	142.79	1393.12
Middle	Baron	ORE	MB44a	MB44aHmRe-10	clean martite	2761.67	489.47	1513.33	31.80	67.74	0.46	77.05	29.58	130.95	3284.40
Middle	Baron	ORE	MB44a	MB44aHmRe-11	clean martite	3503.40	647.27	1621.89	22.23	105.92	0.40	66.30	20.43	58.97	3628.34
Middle	Baron	ORE	MB44a	MB44aHmRe-12	clean martite	2957.75	898.30	2794.19	38.38	<66.42	0.49	63.33	31.12	204.43	3764.09
Middle	Baron	ORE	MB44a	MB44aHmRe-2	clean martite	1466.69	322.53	685.95	36.08	197.25	0.48	113.40	23.50	18.16	2408.80
Middle	Baron	ORE	MB44a	MB44aHmRe-3	clean martite	1266.17	726.01	2170.62	64.21	<70.9	0.36	23.53	220.90	166.40	1082.24
Middle	Baron	ORE	MB44a	MB44aHmRe-4	clean martite	2633.37	679.50	2353.95	25.96	300.31	0.51	44.35	42.61	14.07	1775.01
Middle	Baron	ORE	MB44a	MB44aHmRe-5	clean martite	712.13	975.97	1996.45	54.58	104.61	0.55	28.40	42.91	74.52	1615.80
Middle	Baron	ORE	MB44a	MB44aHmRe-6	clean martite	1088.50	251.74	538.92	16.41	<70.46	0.31	51.60	5.81	17.28	581.06
Middle	Baron	ORE	MB44a	MB44aHmRe-7	clean martite	2484.85	460.16	1867.75	29.38	<69.97	0.35	60.08	21.22	60.32	3160.52
Middle	Baron	ORE	MB44a	MB44aHmRe-8	clean martite	2077.75	211.60	492.99	12.91	<67.11	0.44	43.06	7.18	3.32	2860.04
Middle	Baron	ORE	MB44a	MB44aHmRe-9	clean martite	3747.96	683.08	1383.57	20.32	<73.34	0.37	54.46	6.28	3.03	2705.27
Middle	Prince	ORE	MB45	MB45-Hm-1	clean martite	75.65	525.97	1054.73	26.49	104.88	0.54	3.60	58.40	11.56	839.97
Middle	Prince	ORE	MB45	MB45-Hm-10	clean martite	106.45	573.76	966.15	25.74	128.45	0.31	6.27	8.89	5.90	420.74
Middle	Prince	ORE	MB45	MB45-Hm-11	clean martite	126.36	553.83	1052.91	13.15	185.65	0.42	3.13	66.95	4.89	413.19
Middle	Prince	ORE	MB45	MB45-Hm-12	clean martite	84.53	819.32	1190.41	23.61	83.10	0.77	3.91	108.72	20.08	1238.84
Middle	Prince	ORE	MB45	MB45-Hm-2	clean martite	82.28	499.43	1003.42	22.82	<83.84	0.29	4.33	26.68	4.35	474.36
Middle	Prince	ORE	MB45	MB45-Hm-3	clean martite	65.57	674.12	1135.60	28.05	<73.4	0.77	3.73	68.01	11.79	840.18
Middle	Prince	ORE	MB45	MB45-Hm-4	clean martite	50.39	494.56	728.11	16.47	116.66	0.24	4.72	16.11	1.37	268.96
Middle	Prince	ORE	MB45	MB45-Hm-5	clean martite	75.39	510.98	855.93	13.28	<92.46	0.35	5.54	12.62	2.25	406.40
Middle	Prince	ORE	MB45	MB45-Hm-6	clean martite	139.99	585.78	983.50	25.25	75.84	0.34	5.47	7.53	5.13	400.09
Middle	Prince	ORE	MB45	MB45-Hm-7	clean martite	71.85	617.19	818.43	25.69	128.95	0.31	4.96	9.25	5.89	444.43
Middle	Prince	ORE	MB45	MB45-Hm-8	clean martite	60.24	489.70	1204.99	22.74	<85.59	<0.08	7.01	9.70	2.37	244.22

Analysis no.	Co	Ni	Cu	Zn	Ga	As	Sr	Y	Zr	Nb	Mo	Sn	Sb	Ba	La	Ce	Pr
MB44aHm-12	3.75	31.08	<1.6	31.21	1.21	9.63	0.33	2.53	96.76	0.10	0.07	1.13	0.44	5.83	0.26	0.37	0.03
MB44aHm-13	7.97	14.23	3.13	23.77	0.57	8.09	0.48	0.67	0.37	0.06	0.10	1.30	0.43	6.29	0.31	0.62	0.07
MB44aHm-2	0.35	0.72	1.80	39.79	0.27	8.03	0.19	0.07	0.01	0.03	0.08	1.87	0.26	1.17	0.05	0.07	0.01
MB44aHm-3	3.81	2.91	2.38	9.26	1.50	10.54	0.47	0.45	0.11	0.13	0.18	2.00	0.71	5.13	0.23	0.43	0.07
MB44aHm-4	0.79	1.14	0.86	19.60	0.55	19.60	1.24	0.52	36.37	0.28	0.22	3.12	0.93	3.38	0.18	0.29	0.03
MB44aHm-5	1.83	1.52	3.32	13.28	0.46	10.61	0.69	0.37	0.35	0.09	0.22	2.05	0.61	3.06	0.17	0.36	0.05
MB44aHm-6	0.48	3.15	<1.17	63.33	0.55	21.91	0.47	0.20	0.04	0.08	0.17	2.12	1.04	2.67	0.14	0.33	0.11
MB44aHm-7	6.96	4.90	2.65	27.98	1.41	17.13	1.86	0.83	10.62	0.77	2.60	7.06	4.86	3.81	0.64	1.52	0.88
MB44aHm-8	3.64	10.42	1.70	24.15	1.96	7.60	1.82	0.93	0.25	0.35	1.58	3.32	2.41	6.96	0.56	1.21	0.57
MB44aHm-9	1.34	4.56	<1.21	48.95	0.79	20.82	0.63	0.58	0.19	0.31	1.17	3.14	2.07	4.33	0.36	1.08	0.30
MB44aHmLam-11	1.02	5.86	1.64	3.46	0.50	0.73	0.11	0.47	1.95	0.07	0.72	0.50	0.55	1.19	1.90	1.88	0.14
MB44aHmLam-12	1.19	12.05	<1.5	3.82	0.52	5.13	0.72	0.71	1.23	0.07	0.44	1.22	0.59	3.17	0.89	1.73	0.11
MB44aHmLam-2	2.58	52.83	0.87	2.73	0.99	6.02	0.59	0.90	1.79	0.19	0.69	0.75	<0.114	23.11	0.71	1.13	0.07
MB44aHmLam-3	1.27	2.97	<1.03	2.15	3.23	5.90	0.50	0.63	1.38	0.21	1.25	1.21	0.83	0.82	2.57	2.41	0.25
MB44aHmLam-4	0.99	10.49	<1.09	7.00	1.70	2.75	0.39	0.27	1.14	0.13	0.75	1.99	1.06	3.00	0.62	0.63	0.24
MB44aHmLam-5	3.37	19.37	17.16	10.70	1.25	37.79	3.10	2.64	0.49	0.12	0.15	1.71	0.92	10.21	1.28	7.40	0.38
MB44aHmLam-6	2.47	14.00	4.32	9.78	4.81	4.97	0.69	0.60	1.16	0.24	3.41	5.02	2.34	4.51	1.03	1.36	0.38
MB44aHmLam-7	1.69	8.46	1.52	1.64	0.41	<0.78	0.13	0.26	1.18	0.06	0.69	1.22	0.21	2.31	0.53	0.59	0.13
MB44aHmLam-8	1.85	27.80	<1.38	2.52	0.85	5.20	0.45	0.68	0.88	0.15	0.63	1.17	0.49	11.52	0.90	1.21	0.19
MB44aHmLam-9	2.28	22.60	<1.36	2.83	1.41	2.81	1.02	0.63	2.03	0.49	1.78	2.32	1.28	12.66	0.82	1.36	0.42
MB44aHmRe-1	5.98	19.49	2.19	9.95	0.52	5.58	0.96	0.65	0.21	0.02	0.10	1.62	0.53	7.63	0.36	0.95	0.07
MB44aHmRe-10	42.00	33.04	6.09	32.96	0.67	9.28	0.88	1.27	0.04	0.11	0.10	0.90	1.25	10.45	1.82	3.34	0.47
MB44aHmRe-11	10.42	14.64	3.29	48.82	0.49	8.91	0.61	0.62	0.14	0.15	0.04	1.34	1.70	7.89	0.34	0.66	0.06
MB44aHmRe-12	45.88	49.56	9.15	50.88	1.12	10.93	1.09	1.63	0.15	0.10	0.06	1.26	1.63	26.21	0.68	1.81	0.14
MB44aHmRe-2	1.06	1.52	1.44	28.90	0.31	10.53	1.13	0.31	0.03	0.10	<0.0314	2.27	0.71	2.35	0.18	0.56	0.05
MB44aHmRe-3	2.37	26.46	5.56	6.32	0.67	5.28	1.02	1.08	0.25	0.08	0.20	1.35	0.39	12.19	0.56	1.90	0.11
MB44aHmRe-4	1.15	5.26	1.97	15.66	0.33	12.01	0.97	0.57	0.19	0.12	0.04	2.07	1.27	4.04	0.36	0.61	0.08
MB44aHmRe-5	1.38	4.74	4.05	10.69	0.62	7.77	0.90	0.77	0.07	0.03	0.06	1.67	0.53	6.66	0.42	1.49	0.13
MB44aHmRe-6	1.83	1.42	0.14	5.65	0.34	<2.53	0.12	0.13	0.01	0.04	0.07	2.03	<0.144	0.08	0.05	0.08	0.01
MB44aHmRe-7	52.73	21.90	10.21	41.85	0.92	9.12	0.92	1.48	<0.00	0.05	0.06	2.17	1.03	23.04	0.58	1.04	0.13
MB44aHmRe-8	1.03	1.63	1.07	38.00	0.24	6.94	0.46	0.28	<0.00	0.04	0.04	2.30	0.73	1.88	0.13	0.31	0.04
MB44aHmRe-9	0.65	1.74	0.59	33.19	0.28	8.11	0.18	0.39	0.21	0.13	0.03	2.23	1.10	1.83	0.11	0.19	0.02
MB45-Hm-1	11.72	15.85	45.32	79.27	1.41	<0.00	0.68	0.35	0.11	0.03	0.16	0.55	0.64	17.19	0.30	1.11	0.04
MB45-Hm-10	18.28	4.07	60.47	76.66	1.93	<0.00	0.75	0.34	0.02	0.03	0.11	0.98	0.81	17.98	0.27	0.93	0.04
MB45-Hm-11	1.76	8.93	1.69	20.50	0.99	<0.00	0.52	0.43	0.13	0.11	0.26	0.77	0.63	6.53	0.26	0.56	0.04
MB45-Hm-12	3.74	24.13	7.30	68.42	1.27	<0.00	0.71	0.52	0.13	0.12	0.32	0.76	1.40	20.02	0.71	1.78	0.08
MB45-Hm-2	2.54	6.43	3.91	34.15	0.89	<0.00	1.08	0.35	0.09	0.01	0.16	0.69	0.82	9.48	0.23	0.66	0.03
MB45-Hm-3	13.78	15.39	44.18	80.90	1.25	<0.00	0.77	0.44	0.12	0.01	0.23	0.54	1.96	22.55	0.33	1.19	0.04
MB45-Hm-4	2.59	2.39	3.70	10.06	1.19	<0.00	0.45	0.16	0.03	0.03	0.03	0.70	0.46	3.05	0.15	0.30	0.03
MB45-Hm-5	1.13	3.23	1.05	15.89	1.16	<0.00	0.85	0.19	0.02	0.04	0.10	0.91	1.05	5.47	0.19	0.44	0.02
MB45-Hm-6	32.33	2.61	85.50	97.43	1.49	<0.00	0.78	0.35	0.02	0.01	0.05	0.86	0.74	20.31	0.31	1.06	0.06
MB45-Hm-7	28.88	3.51	83.71	95.70	1.42	<0.00	0.64	0.38	0.02	<0.0178	0.07	0.87	0.64	17.30	0.29	1.08	0.04
MB45-Hm-8	0.98	3.11	1.15	13.84	0.88	<0.00	0.52	0.16	<0.00	0.03	0.16	0.58	0.77	2.96	0.19	0.50	0.03

Analysis no.	Nd	Sm	Eu	Gd	Tb	Dy	Ho	Er	Tm	Yb	Lu	W	Pb208	Th	U
MB44aHm-12	0.13	0.02	0.03	<0.00	0.02	0.14	0.03	0.19	0.05	0.37	0.09	0.94	2.37	0.14	0.37
MB44aHm-13	0.20	0.11	0.03	0.02	0.02	0.04	0.01	0.05	0.01	0.05	0.01	0.66	2.99	0.02	0.66
MB44aHm-2	<0.0164	<0.00	0.00	<0.00	0.00	0.01	<0.0033	0.00	0.00	0.01	0.01	0.27	1.00	0.01	0.01
MB44aHm-3	0.19	0.05	0.05	0.06	0.04	0.09	0.02	0.04	0.01	0.07	0.01	0.58	3.24	0.04	0.17
MB44aHm-4	0.09	0.05	0.02	<0.026	0.01	0.04	0.02	0.06	<0.006	0.08	0.02	1.82	20.46	0.11	0.51
MB44aHm-5	0.15	0.05	0.03	0.03	0.04	0.06	0.02	0.05	0.02	0.05	0.02	0.26	3.64	0.05	0.18
MB44aHm-6	0.20	0.03	0.03	0.04	0.01	0.03	0.04	0.03	0.05	0.08	0.03	0.54	2.42	0.03	0.13
MB44aHm-7	0.72	0.54	0.64	0.41	0.33	0.38	0.38	0.51	0.39	0.47	0.38	2.09	4.18	0.44	2.44
MB44aHm-8	0.43	0.29	0.38	0.25	0.21	0.37	0.26	0.24	0.22	0.40	0.21	2.02	5.70	0.22	1.27
MB44aHm-9	0.30	0.18	0.23	0.10	0.08	0.17	0.07	0.09	0.15	0.12	0.14	1.13	3.84	0.09	0.48
MB44aHmLam-11	0.22	0.05	0.01	0.05	<0.0065	0.06	0.01	0.04	0.01	0.05	0.00	2.66	1.38	0.04	0.07
MB44aHmLam-12	0.39	0.04	0.02	0.14	0.02	0.14	0.02	0.08	0.02	0.08	0.01	2.04	2.63	0.05	0.12
MB44aHmLam-2	0.29	0.11	0.03	0.07	<0.005	0.10	0.02	0.05	0.00	0.07	0.01	5.40	6.33	0.13	0.07
MB44aHmLam-3	0.56	0.16	0.22	0.09	0.07	0.11	0.11	0.23	0.13	0.27	0.14	1.79	1.16	0.21	0.46
MB44aHmLam-4	0.26	0.05	0.16	0.09	0.07	0.08	0.03	0.07	0.05	0.08	0.04	2.16	1.61	0.12	0.30
MB44aHmLam-5	1.96	0.34	0.14	0.51	0.08	0.48	0.08	0.24	0.04	0.29	0.05	1.35	10.36	0.07	0.45
MB44aHmLam-6	0.50	0.23	0.30	0.22	0.16	0.27	0.18	0.13	0.22	0.16	0.15	5.92	4.27	0.21	1.22
MB44aHmLam-7	0.14	0.11	0.07	0.04	0.04	0.04	0.04	0.10	0.03	0.06	0.03	1.94	0.82	0.05	0.37
MB44aHmLam-8	0.24	0.07	0.03	0.15	0.07	0.11	0.15	0.07	0.15	0.17	0.21	3.38	4.40	0.10	0.21
MB44aHmLam-9	0.38	0.39	0.40	0.29	0.25	0.24	0.22	0.21	0.22	0.24	0.25	4.17	5.60	0.30	1.32
MB44aHmRe-1	0.29	0.07	0.03	0.03	0.01	0.06	0.01	0.05	0.01	0.08	0.01	1.56	3.95	0.01	0.08
MB44aHmRe-10	2.17	0.36	0.12	0.28	0.04	0.15	0.04	0.07	0.03	0.13	0.02	0.59	4.69	0.02	0.11
MB44aHmRe-11	0.19	0.07	0.03	0.04	0.01	0.11	0.02	0.03	0.01	0.05	<0.0038	1.07	2.77	0.03	0.12
MB44aHmRe-12	0.52	0.28	0.08	0.18	0.03	0.18	0.05	0.10	0.01	0.10	0.01	0.56	6.29	0.04	0.14
MB44aHmRe-2	0.18	0.10	0.03	0.06	0.01	0.04	0.01	0.06	0.01	0.04	<0.0069	0.34	3.45	0.04	0.15
MB44aHmRe-3	0.54	0.07	0.04	0.15	0.03	0.14	0.04	0.08	0.01	0.05	0.02	2.43	6.08	0.04	0.17
MB44aHmRe-4	0.32	0.04	0.04	0.06	0.02	0.04	0.01	0.06	<0.0063	0.05	0.01	0.78	4.15	0.04	0.19
MB44aHmRe-5	0.63	0.20	0.06	0.14	0.02	0.08	0.02	0.06	0.01	0.11	0.02	0.25	4.43	0.02	0.15
MB44aHmRe-6	0.03	<0.027	0.00	<0.039	0.00	0.01	0.00	<0.0129	<0.0063	<0.00	0.00	0.05	0.39	0.01	0.04
MB44aHmRe-7	0.47	0.22	0.08	0.15	0.02	0.13	0.03	0.10	0.02	0.10	0.02	0.49	7.31	<0.0047	0.12
MB44aHmRe-8	0.15	0.04	0.03	0.03	0.01	0.02	0.01	0.03	0.00	0.01	<0.00	0.26	0.93	0.02	0.06
MB44aHmRe-9	0.14	<0.037	0.02	0.03	0.00	0.03	0.01	0.03	0.01	0.04	0.00	0.29	1.36	0.03	0.11
MB45-Hm-1	0.11	<0.054	0.02	0.03	0.00	0.03	0.01	0.02	<0.00	0.03	0.01	0.36	6.24	<0.00	0.93
MB45-Hm-10	0.09	0.02	0.01	0.06	0.01	<0.046	0.01	0.05	<0.0094	0.01	<0.00	0.18	5.74	<0.00	0.63
MB45-Hm-11	0.19	0.05	0.01	0.05	<0.00	0.06	0.01	0.03	0.00	0.01	<0.0073	0.43	10.31	0.01	0.60
MB45-Hm-12	0.33	0.07	0.01	<0.043	0.02	0.07	0.01	0.08	0.01	0.04	0.00	0.54	11.04	0.02	1.30
MB45-Hm-2	0.09	0.02	0.02	<0.043	0.01	0.03	<0.0067	0.04	<0.0068	0.06	0.00	0.24	15.90	<0.0078	0.68
MB45-Hm-3	0.07	0.02	0.01	0.06	0.01	0.02	0.01	0.02	0.00	<0.00	0.00	0.34	8.19	<0.00	1.12
MB45-Hm-4	0.05	0.02	<0.00	<0.047	0.00	0.04	<0.00	0.01	<0.00	<0.033	<0.00	0.17	21.86	0.01	0.19
MB45-Hm-5	0.05	0.07	0.01	0.02	<0.00	0.02	0.00	0.02	<0.00	0.02	0.01	0.17	33.74	0.01	0.29
MB45-Hm-6	0.09	0.03	0.00	0.01	0.01	0.05	0.01	0.02	0.00	0.02	<0.0064	<0.017	5.99	<0.00	0.68
MB45-Hm-7	0.19	0.03	0.02	<0.00	0.00	<0.037	0.01	<0.02	0.02	0.06	0.00	0.05	5.88	<0.0075	1.03
MB45-Hm-8	0.11	0.08	<0.0111	0.05	0.01	<0.041	0.01	<0.00	0.01	0.02	0.00	0.08	19.15	0.01	0.28

Position	Deposit	Lithology	Sample no.	Analysis no.	Texture	Mg	Al	Si	P	Ca	Sc	Ti	V	Cr	Mn
Middle	Prince	ORE	MB45	MB45-Hm-9	clean martite	101.78	511.14	1138.79	21.83	<85.74	0.51	5.39	12.01	9.26	477.25
South	Chieftain	ORE	MB4	MB4Hm-1	clean martite	45.84	715.64	1817.33	176.39	<59.68	0.49	71.18	2.66	4.31	452.59
South	Chieftain	ORE	MB4	MB4Hm-10	clean martite	45.09	1624.16	2495.82	245.56	<39.36	0.97	116.88	3.09	6.70	1354.73
South	Chieftain	ORE	MB4	MB4Hm-11	clean martite	41.61	3483.29	4858.61	465.02	<29.65	1.75	97.57	3.51	11.43	927.62
South	Chieftain	ORE	MB4	MB4Hm-12	clean martite	40.53	2532.13	3648.39	268.96	44.74	1.60	164.92	3.43	13.11	584.25
South	Chieftain	ORE	MB4	MB4Hm-13	clean martite	31.40	3666.52	3489.01	329.17	50.91	1.80	127.80	3.00	14.57	774.10
South	Chieftain	ORE	MB4	MB4Hm-14	clean martite	33.22	2152.39	3172.72	237.50	45.12	2.38	106.22	4.31	10.48	1361.14
South	Chieftain	ORE	MB4	MB4Hm-15	clean martite	35.25	935.26	3137.06	257.18	<51.69	0.58	104.01	2.52	5.14	511.69
South	Chieftain	ORE	MB4	MB4Hm-16	clean martite	36.24	1072.57	2641.62	224.40	<48.37	0.73	86.94	2.69	5.09	520.95
South	Chieftain	ORE	MB4	MB4Hm-17	clean martite	29.72	1389.68	3137.31	253.05	<50.61	0.92	128.62	2.72	8.37	626.36
South	Chieftain	ORE	MB4	MB4Hm-2	clean martite	38.02	613.47	2537.56	213.84	62.87	0.70	38.45	1.97	3.69	374.26
South	Chieftain	ORE	MB4	MB4Hm-3	clean martite	22.75	753.55	1760.61	173.23	<45.7	0.59	78.25	2.23	4.51	479.28
South	Chieftain	ORE	MB4	MB4Hm-4	clean martite	39.78	3409.36	3780.48	318.90	<34.67	2.51	122.49	5.22	17.51	2526.70
South	Chieftain	ORE	MB4	MB4Hm-5	clean martite	33.59	585.58	2446.65	193.14	50.83	0.49	63.64	2.26	3.94	342.81
South	Chieftain	ORE	MB4	MB4Hm-6	clean martite	53.80	530.12	2159.48	130.23	<34.59	0.70	65.55	2.01	4.25	440.46
South	Chieftain	ORE	MB4	MB4Hm-7	clean martite	32.49	658.54	2156.53	159.50	<41.94	0.69	88.00	2.84	3.42	661.13
South	Chieftain	ORE	MB4	MB4Hm-8	clean martite	35.17	770.90	2161.94	176.01	<41.82	0.59	75.59	2.50	4.15	395.76
South	Chieftain	ORE	MB4	MB4Hm-9	clean martite	35.53	672.21	2903.66	208.68	120.00	0.71	65.56	2.51	3.89	500.90
Middle	Prince	ORE	MB54	MB54Hm-1	porous martite	13.28	90.13	229.80	15.03	<59.25	0.97	0.85	30.03	1.12	27.98
Middle	Prince	ORE	MB54	MB54Hm-2	porous martite	74.69	199.54	1208.87	42.51	47.75	0.09	2.49	6.39	1.09	194.84
Middle	Prince	ORE	MB54	MB54Hm-3	porous martite	68.17	160.39	1264.40	14.84	<48.71	<0.058	1.86	4.81	0.59	190.29
Middle	Prince	ORE	MB54	MB54Hm-4	porous martite	53.41	163.65	1743.47	45.10	66.81	0.09	2.60	4.90	1.03	188.43
Middle	Prince	ORE	MB54	MB54Hm-5	porous martite	3.27	242.53	289.89	14.16	<64.26	0.57	0.44	17.32	<0.6	60.07
Middle	Prince	ORE	MB54	MB54HmLam-1	platy hematite	49.97	209.61	296.08	17.73	803.47	1.03	2.75	9.46	<0.63	364.73
Middle	Prince	ORE	MB54	MB54HmLam-10	platy hematite	36.39	312.35	1847.20	35.57	117.52	0.12	2.23	9.39	<0.56	223.67
Middle	Prince	ORE	MB54	MB54HmLam-11	platy hematite	46.91	229.59	286.90	23.99	491.90	1.24	0.87	15.17	1.85	327.41
Middle	Prince	ORE	MB54	MB54HmLam-12	platy hematite	25.20	494.94	1164.13	15.91	79.94	0.35	2.90	24.91	0.97	211.22
Middle	Prince	ORE	MB54	MB54HmLam-13	platy hematite	61.50	216.20	2053.74	20.48	60.77	0.05	1.87	5.46	0.70	183.27
Middle	Prince	ORE	MB54	MB54HmLam-14	platy hematite	37.44	374.72	1740.76	30.96	71.87	0.13	2.03	13.41	0.89	232.51
Middle	Prince	ORE	MB54	MB54HmLam-2	platy hematite	47.04	326.25	1557.58	35.56	58.11	0.20	2.18	12.38	0.78	225.55
Middle	Prince	ORE	MB54	MB54HmLam-3	platy hematite	1.60	252.18	227.21	13.12	<61.78	0.80	0.72	17.10	<0.69	38.08
Middle	Prince	ORE	MB54	MB54HmLam-4	platy hematite	11.42	299.51	265.87	13.12	<54.37	1.03	0.44	17.06	1.49	57.44
Middle	Prince	ORE	MB54	MB54HmLam-5	platy hematite	26.66	435.30	1375.11	24.62	89.07	0.38	3.57	15.82	1.18	213.26
Middle	Prince	ORE	MB54	MB54HmLam-6	platy hematite	59.12	161.98	1708.25	31.07	<63.34	<0.06	1.75	4.28	1.23	199.00
Middle	Prince	ORE	MB54	MB54HmLam-7	platy hematite	14.63	376.24	743.56	19.58	<48.97	0.42	1.52	21.61	1.86	144.91
Middle	Prince	ORE	MB54	MB54HmLam-8	platy hematite	37.02	188.79	2067.99	22.32	<56.62	0.11	1.90	6.34	<0.56	184.32
Middle	Prince	ORE	MB54	MB54HmLam-9	platy hematite	39.74	369.78	1312.34	56.82	94.29	0.22	2.74	12.17	1.68	283.46
Middle	Prince	ORE	MB54	MB54HmVuggy-1	porous martite	45.72	415.89	1219.38	132.80	139.89	0.45	2.67	12.25	2.86	320.33
Middle	Prince	ORE	MB54	MB54HmVuggy-2	porous martite	38.37	394.26	1152.07	260.02	74.77	0.43	2.78	12.84	2.43	309.70
Middle	Prince	ORE	MB54	MB54HmVuggy-4	porous martite	45.29	331.76	1314.89	119.27	105.50	0.29	3.16	13.34	5.34	316.70
Middle	Prince	ORE	MB54	MB54HmVuggy-5	porous martite	56.71	344.95	1384.74	366.00	72.08	0.27	4.60	9.81	1.30	322.37
Middle	Prince	ORE	MB54	MB54HmVuggy-6	porous martite	43.20	416.67	1246.32	222.85	91.24	0.39	2.98	14.37	5.64	328.39
Middle	Prince	ORE	MB54	MB54HmVuggy-7	porous martite	47.05	220.59	886.13	370.06	75.34	0.28	2.54	6.96	2.24	286.03

Analysis no.	Co	Ni	Cu	Zn	Ga	As	Sr	Y	Zr	Nb	Mo	Sn	Sb	Ba	La	Ce	Pr
MB45-Hm-9	6.59	5.48	27.74	72.79	1.16	<0.00	0.87	0.44	0.08	0.06	0.09	0.71	0.95	17.55	0.32	1.24	0.05
MB4Hm-1	4.09	4.47	10.72	38.18	0.10	136.61	0.25	0.94	1.97	0.31	1.51	0.46	2.47	0.99	0.88	2.11	0.12
MB4Hm-10	10.44	14.71	26.77	116.47	0.29	197.89	0.25	1.87	3.45	0.48	2.53	0.72	1.76	0.08	2.77	11.17	0.42
MB4Hm-11	12.07	24.64	44.93	237.53	0.58	123.49	0.62	9.00	4.21	0.27	3.61	0.41	0.98	0.41	3.06	6.22	0.56
MB4Hm-12	5.10	10.89	36.41	152.62	0.24	135.41	1.27	2.14	10.86	0.49	2.47	0.48	0.81	0.70	0.90	2.88	0.18
MB4Hm-13	11.24	24.54	41.48	221.08	0.34	141.03	0.20	3.92	4.49	0.40	2.93	0.40	0.72	0.26	1.66	4.04	0.33
MB4Hm-14	8.91	12.92	21.06	244.99	0.41	213.41	1.20	4.96	8.18	0.43	2.53	0.38	0.97	0.59	6.10	25.67	1.06
MB4Hm-15	4.17	5.79	11.71	58.31	0.13	103.06	0.98	3.34	2.17	0.40	2.74	0.69	1.13	0.38	1.05	2.20	0.21
MB4Hm-16	3.72	5.14	15.70	43.78	0.13	140.37	0.60	1.91	2.97	0.49	2.10	0.75	1.53	0.58	0.79	2.31	0.16
MB4Hm-17	4.16	5.62	18.97	55.28	0.14	152.19	0.77	1.92	3.51	0.47	2.54	0.54	1.09	0.31	0.78	2.54	0.17
MB4Hm-2	2.85	3.84	10.22	22.11	0.15	110.44	0.76	1.26	1.66	0.27	1.54	0.50	1.45	0.29	0.85	2.04	0.14
MB4Hm-3	3.21	4.12	12.81	20.27	0.13	136.90	0.16	0.78	2.02	0.29	1.51	0.47	1.90	0.08	0.70	2.14	0.11
MB4Hm-4	13.31	14.44	52.70	285.74	0.72	311.33	0.76	3.51	6.67	0.39	3.10	0.58	1.24	0.53	3.75	15.26	0.60
MB4Hm-5	2.34	2.54	9.08	22.20	0.10	106.37	0.78	1.31	1.62	0.27	1.45	0.61	2.22	0.57	0.87	1.53	0.13
MB4Hm-6	3.88	5.29	41.34	43.57	0.03	189.39	0.42	1.18	1.67	0.35	1.67	0.38	1.64	0.43	2.64	9.04	0.31
MB4Hm-7	5.75	7.49	12.80	67.82	0.10	191.80	0.44	1.68	2.31	0.35	2.25	0.47	2.19	0.54	4.06	14.00	0.51
MB4Hm-8	2.85	4.21	14.60	27.17	0.12	152.41	0.31	1.11	2.42	0.38	1.53	0.42	1.96	0.17	1.27	4.00	0.16
MB4Hm-9	3.46	4.58	12.16	40.74	0.12	124.32	0.96	2.06	2.17	0.31	1.86	0.51	1.31	0.67	2.46	7.12	0.32
MB54Hm-1	0.12	0.21	0.54	1.24	0.14	0.68	0.03	0.03	0.04	0.02	0.07	0.21	<0.093	0.16	0.02	0.03	0.00
MB54Hm-2	1.22	2.40	67.65	31.09	0.97	5.77	0.32	1.69	0.01	<0.00	0.07	0.35	0.14	8.81	0.21	0.38	0.06
MB54Hm-3	0.74	2.46	68.14	22.51	0.53	5.01	0.31	2.05	0.01	0.01	0.03	0.46	0.17	6.28	0.22	0.44	0.08
MB54Hm-4	0.87	1.83	28.27	23.10	0.78	6.93	0.63	2.59	0.02	0.00	0.04	0.38	0.25	12.77	0.34	0.65	0.09
MB54Hm-5	0.46	1.57	0.62	4.67	0.28	1.05	0.09	0.09	0.01	<0.00	0.04	0.14	0.26	0.84	0.07	0.09	0.02
MB54HmLam-1	0.41	0.71	0.30	3.99	0.20	1.09	0.64	0.51	0.04	0.01	0.11	0.14	0.23	1.74	0.15	0.19	0.02
MB54HmLam-10	2.25	5.86	46.87	38.50	0.85	11.27	0.79	2.96	0.05	0.01	0.08	0.35	0.38	19.39	0.47	0.88	0.11
MB54HmLam-11	0.64	1.30	<0.51	9.51	0.37	2.09	0.77	0.52	0.02	<0.00	0.03	0.10	0.26	4.96	0.15	0.14	0.03
MB54HmLam-12	3.10	7.38	16.61	40.88	0.97	9.92	0.38	1.53	0.05	0.01	0.13	0.24	0.22	11.17	0.21	0.35	0.04
MB54HmLam-13	1.54	2.80	41.37	30.40	0.75	9.85	0.43	2.66	0.01	0.01	0.05	0.39	0.36	11.61	0.32	0.61	0.06
MB54HmLam-14	2.44	5.97	22.73	41.18	1.10	13.71	0.82	3.00	0.06	0.01	0.17	0.45	0.55	17.86	0.30	0.66	0.09
MB54HmLam-2	2.51	5.29	25.37	32.89	1.11	11.44	0.64	2.46	<0.053	0.01	0.12	0.36	0.38	12.61	0.31	0.59	0.10
MB54HmLam-3	0.16	0.27	0.41	1.41	0.16	<0.5	0.04	0.05	0.04	<0.00	0.05	<0.096	0.25	0.52	0.05	0.06	0.01
MB54HmLam-4	0.80	1.24	<0.33	6.25	0.33	0.90	0.09	0.08	0.01	0.00	0.11	0.15	0.21	1.91	0.04	0.05	0.01
MB54HmLam-5	2.49	5.79	31.14	39.37	1.02	9.62	0.68	1.80	0.06	0.01	0.16	0.34	0.40	13.29	0.25	0.40	0.06
MB54HmLam-6	0.85	2.03	42.69	22.22	0.56	7.21	0.47	2.81	0.01	0.00	0.02	0.43	0.23	6.77	0.24	0.51	0.07
MB54HmLam-7	1.69	4.27	2.78	31.68	0.63	5.50	0.34	0.79	0.01	0.00	0.14	0.93	0.44	6.99	0.13	0.28	0.03
MB54HmLam-8	1.09	2.60	46.79	26.37	0.60	6.46	0.31	3.42	0.04	<0.0076	0.09	0.50	0.14	8.23	0.37	0.71	0.09
MB54HmLam-9	3.43	5.79	13.82	45.92	1.40	12.73	2.06	2.03	0.07	0.01	0.15	0.30	1.08	35.46	0.39	0.64	0.09
MB54HmVuggy-1	4.84	7.65	8.23	55.97	1.46	11.95	2.09	2.45	0.14	0.01	0.20	0.54	0.89	36.26	0.57	0.94	0.10
MB54HmVuggy-2	4.56	8.19	3.86	53.35	1.23	12.57	1.67	2.56	0.06	0.02	0.26	0.36	0.87	24.76	2.37	3.25	0.37
MB54HmVuggy-4	3.92	6.71	7.67	46.09	1.31	11.53	1.66	3.25	0.06	0.03	0.13	0.68	1.36	29.85	1.79	2.36	0.24
MB54HmVuggy-5	4.16	6.02	1.08	45.87	1.14	10.74	1.99	8.11	0.07	0.01	0.15	0.37	0.78	31.01	6.75	9.06	1.00
MB54HmVuggy-6	4.97	9.00	2.46	55.14	1.34	11.92	1.43	6.18	0.14	0.02	0.25	0.39	1.09	27.05	2.59	3.75	0.37
MB54HmVuggy-7	2.01	3.61	1.19	35.85	0.91	10.63	1.44	6.50	0.03	0.01	0.09	0.31	0.66	22.70	3.26	4.25	0.42

Analysis no.	Nd	Sm	Eu	Gd	Tb	Dy	Ho	Er	Tm	Yb	Lu	W	Pb208	Th	U
MB45-Hm-9	0.21	0.03	0.01	0.09	0.00	0.04	0.01	0.04	0.00	0.01	0.01	0.16	9.88	<0.0077	0.86
MB4Hm-1	0.54	0.09	0.11	0.13	0.01	0.10	0.01	0.10	0.01	0.04	0.02	0.34	87.09	0.61	0.54
MB4Hm-10	1.54	0.26	0.16	0.33	0.04	0.16	0.05	0.13	0.02	0.10	0.02	0.24	105.14	1.01	0.33
MB4Hm-11	2.43	0.45	0.52	0.92	0.10	0.72	0.14	0.50	0.07	0.47	0.10	0.22	65.02	0.67	0.67
MB4Hm-12	0.82	0.18	0.17	0.15	0.03	0.20	0.05	0.19	0.03	0.12	0.02	0.25	97.53	0.92	1.32
MB4Hm-13	1.41	0.32	0.27	0.53	0.06	0.27	0.07	0.28	0.03	0.23	0.03	0.18	91.19	1.01	0.41
MB4Hm-14	3.81	0.75	0.27	0.70	0.09	0.47	0.10	0.37	0.05	0.19	0.08	0.32	189.44	0.82	1.26
MB4Hm-15	0.87	0.16	0.21	0.30	0.03	0.20	0.06	0.25	0.02	0.26	0.05	0.22	87.73	0.60	1.21
MB4Hm-16	0.85	0.12	0.13	0.23	0.04	0.20	0.05	0.15	0.02	0.14	0.03	0.25	104.22	0.70	0.95
MB4Hm-17	0.81	0.12	0.12	0.15	0.03	0.18	0.04	0.11	0.02	0.14	0.04	0.31	147.29	0.87	0.90
MB4Hm-2	0.52	0.06	0.06	0.12	0.01	0.08	0.03	0.08	0.01	0.05	0.01	0.20	73.63	0.45	0.67
MB4Hm-3	0.28	0.11	0.07	0.07	0.02	0.05	0.02	0.05	0.01	0.07	0.01	0.22	89.19	0.67	0.20
MB4Hm-4	2.49	0.49	0.24	0.37	0.08	0.42	0.09	0.22	0.03	0.17	0.03	0.24	126.97	0.83	0.97
MB4Hm-5	0.57	0.14	0.08	0.10	0.02	0.10	0.02	0.08	0.01	0.11	0.01	0.26	74.76	0.56	0.49
MB4Hm-6	1.13	0.22	0.08	0.20	0.02	0.16	0.02	0.09	0.01	0.09	0.02	0.22	74.97	0.51	0.36
MB4Hm-7	1.85	0.21	0.14	0.31	0.02	0.17	0.04	0.09	0.02	0.12	0.01	0.51	88.31	0.57	0.90
MB4Hm-8	0.74	0.14	0.05	0.09	0.01	0.12	0.03	0.05	0.01	0.05	0.01	0.23	90.87	0.87	0.49
MB4Hm-9	1.22	0.16	0.13	0.22	0.03	0.19	0.04	0.13	0.02	0.12	0.02	0.23	63.99	0.54	1.03
MB54Hm-1	<0.024	<0.00	0.00	0.01	<0.0045	0.01	<0.00	0.01	0.00	0.03	<0.00	0.48	0.83	<0.0051	0.56
MB54Hm-2	0.23	0.11	0.08	0.11	0.03	0.15	0.04	0.14	0.01	0.07	0.01	0.07	24.91	0.00	0.16
MB54Hm-3	0.32	0.17	0.13	0.17	0.03	0.19	0.05	0.17	0.02	0.12	0.02	0.03	17.00	0.00	0.09
MB54Hm-4	0.46	0.15	0.10	0.21	0.03	0.32	0.08	0.16	0.03	0.11	0.02	0.09	21.61	<0.0065	0.27
MB54Hm-5	0.05	0.02	0.00	0.02	0.00	0.01	0.00	0.01	0.00	0.01	0.00	2.27	8.98	<0.0044	2.39
MB54HmLam-1	0.06	0.01	0.01	0.06	0.01	0.07	0.01	0.02	0.01	0.04	0.00	1.81	6.99	<0.0041	1.49
MB54HmLam-10	0.60	0.10	0.15	0.31	0.05	0.36	0.08	0.25	0.02	0.14	0.03	0.22	46.30	0.01	0.34
MB54HmLam-11	0.04	0.01	0.01	0.05	0.00	0.05	0.01	0.03	0.01	0.05	0.01	1.05	9.62	0.01	1.25
MB54HmLam-12	0.24	0.07	0.06	0.12	0.02	0.15	0.04	0.12	0.02	0.08	0.02	0.50	53.15	0.01	0.74
MB54HmLam-13	0.45	0.08	0.13	0.17	0.04	0.21	0.04	0.13	0.02	0.13	0.02	0.18	30.03	0.00	0.19
MB54HmLam-14	0.45	0.13	0.12	0.19	0.04	0.27	0.06	0.22	0.04	0.21	0.02	0.21	50.27	0.00	0.45
MB54HmLam-2	0.39	0.12	0.12	0.09	0.05	0.25	0.04	0.18	0.04	0.12	0.02	0.35	38.95	0.00	0.42
MB54HmLam-3	0.04	0.01	0.00	<0.00	0.00	0.01	0.00	0.01	<0.00	0.01	0.00	2.69	3.69	0.00	1.94
MB54HmLam-4	0.06	0.02	<0.00	0.02	<0.00	0.01	0.01	0.01	0.01	0.02	0.00	1.34	5.95	<0.0045	1.49
MB54HmLam-5	0.38	0.15	0.10	0.10	0.03	0.18	0.04	0.11	0.02	0.12	0.02	0.56	44.11	0.01	0.68
MB54HmLam-6	0.47	0.12	0.13	0.15	0.04	0.32	0.06	0.19	0.04	0.16	0.01	0.06	20.38	0.00	0.09
MB54HmLam-7	0.20	0.05	0.07	0.06	0.02	0.06	0.02	0.08	0.01	0.05	0.01	0.95	30.74	0.01	1.38
MB54HmLam-8	0.58	0.23	0.18	0.28	0.06	0.30	0.11	0.28	0.04	0.18	0.02	0.05	21.74	<0.0039	0.14
MB54HmLam-9	0.37	0.15	0.10	0.28	0.04	0.21	0.05	0.10	0.01	0.18	0.03	0.35	49.94	0.00	0.98
MB54HmVuggy-1	0.50	0.19	0.12	0.26	0.03	0.25	0.04	0.19	0.02	0.12	0.02	0.24	60.75	0.01	1.78
MB54HmVuggy-2	1.51	0.30	0.15	0.33	0.05	0.29	0.04	0.15	0.02	0.09	0.01	0.36	54.25	0.00	0.78
MB54HmVuggy-4	1.29	0.30	0.15	0.24	0.03	0.27	0.06	0.20	0.02	0.12	0.02	0.43	40.56	0.01	0.85
MB54HmVuggy-5	4.77	0.68	0.47	0.95	0.10	0.41	0.14	0.38	0.05	0.17	0.03	0.28	48.04	0.01	0.57
MB54HmVuggy-6	1.76	0.29	0.23	0.44	0.05	0.37	0.09	0.23	0.04	0.28	0.05	0.36	50.36	<0.0081	0.90
MB54HmVuggy-7	2.36	0.37	0.29	0.60	0.06	0.40	0.11	0.31	0.03	0.18	0.04	0.26	33.09	0.00	1.14

Position	Deposit	Lithology	Sample no.	Analysis no.	Texture	Mg	Al	Si	P	Ca	Sc	Ti	V	Cr	Mn
Middle	Prince	ORE	MB57b	MB57bHm-1	porous martite	93.71	3222.07	6117.26	92.69	365.02	2.73	66.36	621.20	8.27	572.15
Middle	Prince	ORE	MB57b	MB57bHm-10	porous martite	61.42	2372.65	4456.20	66.68	146.18	2.43	141.83	985.66	7.13	550.75
Middle	Prince	ORE	MB57b	MB57bHm-11	porous martite	60.66	2536.86	4857.76	90.85	203.65	2.71	73.81	608.93	4.14	676.03
Middle	Prince	ORE	MB57b	MB57bHm-12	porous martite	97.75	3266.06	6613.98	93.86	285.47	2.93	41.10	589.59	2.25	748.43
Middle	Prince	ORE	MB57b	MB57bHm-13	porous martite	6234.23	5251.84	11055.13	3886.25	415.45	17.02	7.45	1551.89	230.86	7295.20
Middle	Prince	ORE	MB57b	MB57bHm-2	porous martite	55.78	2391.33	4473.62	74.21	112.97	2.69	152.87	915.14	10.03	588.17
Middle	Prince	ORE	MB57b	MB57bHm-3	porous martite	81.95	2615.66	4976.02	99.76	203.76	3.28	65.05	531.70	4.57	738.28
Middle	Prince	ORE	MB57b	MB57bHm-4	porous martite	56.45	2394.51	4414.51	102.53	140.15	2.18	135.97	782.45	6.04	875.95
Middle	Prince	ORE	MB57b	MB57bHm-5	porous martite	65.38	1991.43	3959.30	80.24	87.13	2.29	58.15	458.11	5.66	615.70
Middle	Prince	ORE	MB57b	MB57bHm-6	porous martite	104.85	3040.45	6122.13	158.75	860.07	3.04	26.85	496.77	2.30	489.94
Middle	Prince	ORE	MB57b	MB57bHm-7	porous martite	92.55	3015.20	5871.64	109.72	108.08	2.77	89.44	786.41	7.23	913.15
Middle	Prince	ORE	MB57b	MB57bHm-8	porous martite	105.76	3198.00	6394.69	94.44	227.67	2.94	47.58	581.51	3.15	724.02
Middle	Prince	ORE	MB57b	MB57bHm-9	porous martite	20.92	305.77	1759.45	20.56	79.77	0.41	14.33	127.58	1.66	134.61
Middle	Prince	ORE	MB57b	MB57bHmRe-1	porous martite	87.48	3121.56	6390.65	100.68	406.94	2.76	41.83	612.88	3.97	614.42
Middle	Prince	ORE	MB57b	MB57bHmRe-10	porous martite	69.64	2845.03	5247.32	87.78	386.18	2.46	81.08	768.33	5.96	514.23
Middle	Prince	ORE	MB57b	MB57bHmRe-11	porous martite	110.68	3811.34	7475.95	120.03	479.78	3.08	37.48	757.90	2.24	623.75
Middle	Prince	ORE	MB57b	MB57bHmRe-12	porous martite	78.21	2722.27	5127.61	88.23	243.43	2.49	76.02	762.53	3.48	637.64
Middle	Prince	ORE	MB57b	MB57bHmRe-2	porous martite	106.69	3480.81	6795.85	111.72	595.65	3.33	37.86	625.25	5.28	602.77
Middle	Prince	ORE	MB57b	MB57bHmRe-3	porous martite	84.47	2609.83	5088.00	86.88	150.05	2.65	55.98	593.43	4.71	889.23
Middle	Prince	ORE	MB57b	MB57bHmRe-4	porous martite	86.66	2740.57	4913.53	102.91	523.58	2.51	72.87	746.26	3.93	560.70
Middle	Prince	ORE	MB57b	MB57bHmRe-5	porous martite	86.56	3090.71	6166.99	94.31	235.71	3.15	50.46	568.33	4.48	805.26
Middle	Prince	ORE	MB57b	MB57bHmRe-6	porous martite	105.84	3722.17	7004.52	94.90	243.65	3.58	40.95	597.04	3.22	696.87
Middle	Prince	ORE	MB57b	MB57bHmRe-7	porous martite	77.38	2570.76	5134.81	99.49	150.11	2.86	72.64	619.19	4.65	771.61
Middle	Prince	ORE	MB57b	MB57bHmRe-8	porous martite	77.06	3030.82	5863.60	96.52	172.18	3.46	62.34	592.98	5.29	808.69
Middle	Prince	ORE	MB57b	MB57bHmRe-9	porous martite	44.80	1945.65	3302.07	65.43	90.78	2.41	173.64	1029.90	7.76	564.39
Middle	Prince	ORE	MB59	MB59aHm-1	platy hematite	14.38	867.51	1259.38	17.99	177.75	0.81	27.06	139.54	1.37	40.33
Middle	Prince	ORE	MB59	MB59aHm-5	platy hematite	49.07	820.67	1059.97	26.98	202.92	0.53	26.19	108.22	2.47	212.16
South	Chieftain	BIF	MB5	MB5Hm-1	clean martite	21.71	60.48	21651.80	385.20	<47.51	0.16	5.30	2.88	<0.5	124.98
South	Chieftain	BIF	MB5	MB5Hm-10	clean martite	28.96	68.63	290.95	49.42	<34.11	<0.079	1.50	1.73	0.63	163.55
South	Chieftain	BIF	MB5	MB5Hm-11	clean martite	23.37	61.12	1245.56	307.01	44.89	<0.053	1.29	1.70	0.90	151.65
South	Chieftain	BIF	MB5	MB5Hm-12	clean martite	33.85	59.13	8736.52	63.93	<41.6	<0.058	1.95	2.03	0.70	162.62
South	Chieftain	BIF	MB5	MB5Hm-2	clean martite	13.25	47.10	5991.71	534.26	<74.09	<0.048	4.98	3.42	0.74	108.83
South	Chieftain	BIF	MB5	MB5Hm-3	clean martite	34.73	46.26	4247.54	472.47	<50.26	0.04	3.63	2.52	1.29	152.95
South	Chieftain	BIF	MB5	MB5Hm-4	clean martite	32.00	48.73	3684.67	171.01	<48.24	0.06	5.20	2.04	0.53	144.08
South	Chieftain	BIF	MB5	MB5Hm-5	clean martite	57.96	63.65	2625.57	57.01	<46.14	<0.056	5.08	1.99	0.99	162.27
South	Chieftain	BIF	MB5	MB5Hm-6	clean martite	69.36	57.31	333.58	14.96	<45.98	<0.054	3.71	2.59	0.65	182.36
South	Chieftain	BIF	MB5	MB5Hm-7	clean martite	146.93	53.48	3196.07	360.70	<47.91	<0.061	3.63	2.60	0.75	128.37
South	Chieftain	BIF	MB5	MB5Hm-8	clean martite	43.18	67.59	1670.13	251.76	<59.37	<0.056	4.72	2.79	0.99	126.75
South	Chieftain	BIF	MB5	MB5Hm-9	clean martite	25.07	47.69	12417.71	23.80	<51.53	0.07	1.42	1.90	<0.45	150.43
South	Chieftan	BIF	MB5	MB5Mt-1	magnetite	28.37	64.26	358.77	22.52	<47.26	<0.064	2.26	1.83	0.63	166.18
South	Chieftan	BIF	MB5	MB5Mt-10	magnetite	414.44	57.09	7624.65	324.23	<54.19	0.12	2.82	2.91	0.79	124.04
South	Chieftan	BIF	MB5	MB5Mt-11	magnetite	103.96	70.69	439.14	31.87	<49.46	<0.047	3.45	2.62	<0.48	162.54

Analysis no.	Co	Ni	Cu	Zn	Ga	As	Sr	Y	Zr	Nb	Mo	Sn	Sb	Ba	La	Ce	Pr
MB57bHm-1	6.70	37.39	319.79	132.45	7.92	45.87	11.51	5.41	1.39	0.22	0.79	0.44	4.02	396.13	1.72	3.95	0.43
MB57bHm-10	5.79	25.67	95.14	117.89	5.74	39.92	5.96	4.00	2.34	0.65	0.55	0.96	3.42	212.59	1.33	2.50	0.28
MB57bHm-11	7.67	27.71	134.37	125.89	4.17	53.24	7.15	4.54	2.14	0.34	0.89	1.03	3.07	151.76	1.46	3.27	0.38
MB57bHm-12	7.77	38.88	150.91	162.98	4.86	52.34	8.61	5.66	1.35	0.18	0.73	0.66	5.24	214.37	1.85	4.13	0.46
MB57bHm-13	99.71	81.79	106.65	3291.36	26.44	1563.61	14.33	45.37	1.26	0.04	0.05	2.36	0.78	281.51	1.29	2.43	0.78
MB57bHm-2	4.92	18.48	32.79	114.05	2.55	41.33	4.96	3.85	2.35	0.71	0.66	0.80	4.04	89.83	1.25	2.72	0.31
MB57bHm-3	5.17	27.73	116.98	129.46	3.60	72.52	7.02	5.45	2.95	0.31	0.80	0.96	3.70	116.96	1.76	3.92	0.46
MB57bHm-4	6.18	21.11	29.39	182.20	1.92	54.68	4.45	4.24	2.18	0.58	0.56	0.93	4.81	68.73	1.30	2.73	0.38
MB57bHm-5	4.80	18.05	41.78	117.39	2.07	56.76	4.86	4.15	1.92	0.23	0.59	0.61	4.28	78.05	1.32	2.84	0.33
MB57bHm-6	10.22	79.98	692.25	116.38	18.26	49.48	25.30	5.87	0.98	0.16	0.91	0.36	4.38	799.95	1.70	3.44	0.40
MB57bHm-7	6.86	27.91	48.77	165.23	4.09	66.52	7.06	5.89	2.35	0.35	0.80	0.97	5.40	143.55	1.66	3.77	0.47
MB57bHm-8	6.91	40.62	205.21	154.03	6.05	54.20	9.88	5.86	1.57	0.20	0.89	0.44	3.92	237.15	1.96	4.06	0.47
MB57bHm-9	14.18	2.63	0.99	19.09	0.38	11.82	1.10	0.99	0.19	0.04	0.22	0.21	0.56	13.74	0.25	0.46	0.07
MB57bHmRe-1	7.61	42.66	247.66	133.89	9.44	50.15	12.71	5.13	1.43	0.21	0.73	0.64	3.92	364.29	1.77	3.61	0.43
MB57bHmRe-10	9.65	30.07	344.79	113.26	6.81	40.68	11.35	4.48	1.28	0.33	0.90	0.75	4.26	275.02	1.35	2.94	0.35
MB57bHmRe-11	10.93	58.34	382.78	156.27	13.14	50.75	19.82	6.22	1.10	0.22	1.05	0.65	4.37	595.61	2.01	4.19	0.47
MB57bHmRe-12	7.94	31.31	193.16	126.64	6.05	44.66	9.34	4.54	1.53	0.39	0.56	0.61	4.49	249.78	1.35	3.01	0.31
MB57bHmRe-2	9.33	45.50	364.25	138.84	12.12	52.92	19.17	6.02	1.33	0.20	0.90	0.52	4.33	527.60	2.01	3.93	0.50
MB57bHmRe-3	5.67	28.53	138.38	192.99	3.22	54.99	7.79	5.15	1.67	0.24	0.74	0.53	4.65	137.14	1.52	3.45	0.42
MB57bHmRe-4	9.08	41.55	321.13	128.46	12.56	50.35	17.46	4.68	1.69	0.41	0.88	0.62	3.70	515.80	1.41	2.96	0.34
MB57bHmRe-5	7.34	36.36	98.55	156.88	3.47	59.90	6.53	5.74	1.61	0.28	0.71	1.09	5.66	122.15	2.01	4.23	0.51
MB57bHmRe-6	8.96	42.08	96.38	143.42	4.31	53.01	7.64	6.70	1.64	0.26	0.78	0.48	3.95	171.43	2.33	4.65	0.57
MB57bHmRe-7	6.25	32.11	83.58	156.96	2.76	68.18	5.51	5.36	1.94	0.37	0.73	0.67	5.47	93.83	1.62	3.50	0.45
MB57bHmRe-8	5.70	28.79	107.79	149.16	3.32	64.22	7.15	5.84	1.93	0.23	0.92	0.74	3.61	122.67	1.81	4.00	0.48
MB57bHmRe-9	5.76	23.29	51.82	101.90	2.46	43.33	5.12	3.22	2.20	0.71	0.61	0.79	3.58	110.33	1.09	2.15	0.26
MB59aHm-1	0.34	1.35	257.56	3.09	0.67	15.08	0.44	0.32	0.36	0.23	1.30	4.53	1.33	1.37	0.20	0.49	0.07
MB59aHm-5	0.35	2.96	1.65	4.93	0.78	8.43	0.62	0.66	0.25	0.09	1.23	0.43	2.46	15.27	1.34	1.51	0.14
MB5Hm-1	0.48	2.22	<0.63	7.59	0.17	2.15	0.08	2.51	0.02	0.02	<0.046	0.22	0.30	0.48	0.54	1.10	0.13
MB5Hm-10	0.14	0.14	<0.62	6.64	0.14	<0.36	<0.00	0.11	<0.00	0.02	<0.00	0.44	<0.104	<0.00	0.02	0.05	0.01
MB5Hm-11	0.42	0.64	<0.64	6.81	0.23	1.86	0.10	1.10	<0.00	0.03	0.01	0.35	0.37	0.46	0.26	0.51	0.07
MB5Hm-12	0.13	0.36	0.74	5.80	0.14	0.77	0.05	0.60	<0.00	<0.00	0.04	0.18	<0.117	<0.00	0.14	0.36	0.04
MB5Hm-2	0.86	3.16	<0.54	8.14	0.20	3.22	0.05	2.55	<0.00	0.03	<0.00	0.25	0.23	0.29	0.39	0.73	0.09
MB5Hm-3	0.33	1.17	<0.55	7.20	0.15	0.76	0.01	1.54	0.02	<0.0108	<0.00	0.25	0.14	0.18	0.17	0.31	0.03
MB5Hm-4	0.50	1.17	<0.52	5.81	0.14	1.53	0.04	0.71	<0.00	0.01	0.01	0.38	0.30	0.18	0.13	0.23	0.03
MB5Hm-5	0.18	0.74	16.05	3.64	0.15	0.43	0.01	0.22	<0.00	<0.00	0.03	0.22	0.16	0.09	0.07	0.11	0.02
MB5Hm-6	0.06	0.60	0.58	7.43	0.19	0.41	0.01	0.01	<0.00	<0.00	0.03	0.41	<0.131	<0.00	0.01	<0.0085	0.00
MB5Hm-7	0.64	1.73	<0.56	6.73	0.13	4.46	0.12	2.17	<0.044	0.09	0.02	0.21	0.50	1.09	1.06	1.23	0.15
MB5Hm-8	0.50	1.24	<0.61	7.34	0.12	1.55	0.04	1.27	0.08	0.03	0.01	0.62	0.14	0.27	0.27	0.54	0.10
MB5Hm-9	0.12	0.49	<0.69	5.39	0.16	0.48	0.05	0.13	0.02	0.01	<0.00	0.37	<0.146	<0.00	0.02	0.04	<0.0042
MB5Mt-1	0.16	0.29	<0.4	6.23	0.28	0.91	0.01	0.11	<0.00	<0.00	<0.00	0.51	<0.25	0.08	0.04	0.06	0.01
MB5Mt-10	0.77	1.26	0.80	7.19	0.18	2.06	0.05	1.80	0.02	0.02	<0.00	0.35	0.21	0.10	0.58	0.86	0.11
MB5Mt-11	0.18	0.60	<0.49	4.10	0.19	<0.38	0.08	0.39	0.03	<0.00	0.04	0.15	<0.174	<0.00	0.04	0.13	0.01

Analysis no.	Nd	Sm	Eu	Gd	Tb	Dy	Ho	Er	Tm	Yb	Lu	W	Pb208	Th	U
MB57bHm-1	1.91	0.80	0.30	0.81	0.13	0.74	0.17	0.48	0.07	0.30	0.06	0.79	89.57	0.21	118.58
MB57bHm-10	1.32	0.51	0.20	0.62	0.08	0.67	0.12	0.31	0.04	0.35	0.06	0.81	66.28	0.23	81.59
MB57bHm-11	1.79	0.56	0.30	0.73	0.12	0.88	0.14	0.51	0.06	0.41	0.08	0.83	80.66	0.25	113.13
MB57bHm-12	2.15	0.67	0.35	0.86	0.13	0.81	0.16	0.61	0.08	0.43	0.10	1.30	91.34	0.26	163.81
MB57bHm-13	5.84	3.16	1.45	6.95	1.44	10.11	2.22	6.37	1.01	6.58	0.94	0.80	127.61	0.05	203.41
MB57bHm-2	1.61	0.57	0.20	0.52	0.08	0.67	0.13	0.28	0.06	0.33	0.08	0.84	47.30	0.33	81.96
MB57bHm-3	2.16	0.78	0.27	1.03	0.14	0.83	0.20	0.64	0.10	0.56	0.09	0.92	81.48	0.35	161.00
MB57bHm-4	1.68	0.55	0.28	1.02	0.11	0.62	0.15	0.51	0.05	0.47	0.07	0.84	54.78	0.29	88.50
MB57bHm-5	1.65	0.68	0.28	0.74	0.13	0.77	0.19	0.38	0.06	0.42	0.07	0.66	51.74	0.22	98.84
MB57bHm-6	1.64	0.55	0.28	0.65	0.13	0.64	0.15	0.44	0.07	0.38	0.09	0.62	121.88	0.16	124.45
MB57bHm-7	1.91	0.73	0.31	0.84	0.16	0.93	0.19	0.58	0.07	0.58	0.09	1.06	69.20	0.32	130.52
MB57bHm-8	2.54	0.56	0.30	0.81	0.13	0.88	0.18	0.68	0.08	0.46	0.09	1.07	97.61	0.22	160.06
MB57bHm-9	0.26	0.13	0.05	0.09	0.01	0.06	0.02	0.03	0.01	0.08	0.01	0.12	22.97	0.02	8.81
MB57bHmRe-1	2.01	0.57	0.30	0.87	0.15	0.79	0.15	0.44	0.07	0.42	0.07	0.90	90.65	0.19	133.23
MB57bHmRe-10	1.63	0.50	0.27	0.53	0.11	0.74	0.14	0.37	0.05	0.40	0.08	0.83	83.89	0.20	84.67
MB57bHmRe-11	2.11	0.62	0.33	0.83	0.16	0.94	0.18	0.55	0.09	0.51	0.08	1.14	121.04	0.19	173.03
MB57bHmRe-12	1.70	0.67	0.27	0.69	0.11	0.77	0.15	0.39	0.06	0.47	0.05	0.87	71.98	0.19	96.30
MB57bHmRe-2	2.23	0.61	0.30	0.79	0.13	0.69	0.19	0.53	0.06	0.41	0.09	0.89	128.10	0.20	147.43
MB57bHmRe-3	2.19	0.65	0.33	0.87	0.13	0.86	0.17	0.44	0.07	0.40	0.08	0.95	92.69	0.31	124.20
MB57bHmRe-4	1.75	0.52	0.24	0.81	0.10	0.67	0.16	0.44	0.06	0.33	0.08	0.75	87.15	0.20	103.27
MB57bHmRe-5	2.36	0.75	0.31	0.91	0.14	0.93	0.19	0.54	0.09	0.50	0.10	1.31	86.67	0.29	164.48
MB57bHmRe-6	2.34	0.80	0.33	0.92	0.12	1.10	0.24	0.63	0.08	0.50	0.11	1.22	93.86	0.27	193.83
MB57bHmRe-7	2.11	0.60	0.33	0.86	0.10	0.90	0.18	0.52	0.08	0.55	0.06	0.93	74.26	0.32	135.56
MB57bHmRe-8	2.16	0.61	0.37	0.99	0.17	0.72	0.17	0.66	0.07	0.37	0.08	1.01	85.74	0.31	156.18
MB57bHmRe-9	1.40	0.45	0.22	0.48	0.07	0.65	0.12	0.44	0.04	0.30	0.05	0.80	42.53	0.34	62.92
MB59aHm-1	0.28	0.04	0.03	0.08	0.00	0.03	0.01	0.06	<0.0042	0.03	0.00	5.10	7.69	0.01	4.45
MB59aHm-5	0.63	0.13	0.04	0.09	0.02	0.12	0.02	0.09	0.01	0.05	0.00	12.04	19.82	0.01	1.57
MB5Hm-1	0.81	0.25	0.15	0.27	0.04	0.35	0.04	0.19	0.04	0.22	0.03	0.02	1.89	<0.00	0.01
MB5Hm-10	0.05	<0.00	0.00	<0.00	<0.00	<0.02	<0.00	<0.0157	<0.00	<0.0234	<0.0055	0.04	0.15	<0.00	<0.0034
MB5Hm-11	0.36	0.10	0.09	0.21	0.02	0.06	0.02	0.08	0.01	0.06	0.00	0.10	0.70	0.00	0.03
MB5Hm-12	0.25	0.07	0.03	0.08	0.01	<0.018	0.01	<0.0141	0.04	0.04	0.00	0.01	0.25	<0.00	<0.0043
MB5Hm-2	0.63	0.16	0.12	0.31	0.03	0.15	0.05	0.22	0.01	0.09	0.02	0.05	2.98	<0.00	0.02
MB5Hm-3	0.19	0.04	0.08	0.11	0.03	0.08	0.03	0.08	0.02	0.11	0.01	0.04	1.61	<0.00	0.01
MB5Hm-4	0.17	0.04	0.02	0.08	0.01	0.07	0.01	0.05	<0.0056	0.03	0.00	0.03	1.87	<0.00	0.01
MB5Hm-5	0.05	0.03	0.00	0.02	0.00	0.01	0.00	0.02	0.00	0.01	<0.00	0.01	0.51	<0.00	0.00
MB5Hm-6	<0.024	<0.00	<0.0069	0.01	<0.00	<0.00	0.00	0.01	<0.00	<0.00	<0.00	<0.0144	0.06	<0.00	0.02
MB5Hm-7	0.55	0.18	0.12	0.18	0.03	0.15	0.03	0.18	0.01	0.13	0.03	0.31	1.53	<0.0073	0.13
MB5Hm-8	0.39	0.16	0.12	0.17	0.02	0.10	0.03	0.15	0.01	<0.035	0.02	0.05	0.94	<0.0058	0.00
MB5Hm-9	0.02	0.02	<0.00	0.01	0.00	0.03	0.00	0.01	0.00	0.02	<0.00	<0.022	0.26	0.01	0.00
MB5Mt-1	0.04	<0.00	0.00	0.03	<0.00	<0.00	0.00	0.03	<0.00	0.01	<0.01	0.15	2.09	0.04	0.04
MB5Mt-10	0.44	0.10	0.11	0.13	0.04	0.13	0.02	0.14	0.02	0.06	0.01	0.05	0.07	<0.0031	0.01
MB5Mt-11	0.13	<0.00	0.03	0.06	0.01	0.04	<0.0075	0.02	0.00	<0.024	<0.00	0.23	0.38	0.02	0.10

Position	Deposit	Lithology	Sample no.	Analysis no.	Texture	Mg	Al	Si	P	Ca	Sc	Ti	V	Cr	Mn
South	Chieftan	BIF	MB5	MB5Mt-12	magnetite	81.48	69.39	3625.38	32.78	<49.79	0.05	3.43	2.54	0.67	160.26
South	Chieftan	BIF	MB5	MB5Mt-2	magnetite	26.01	81.83	571.85	39.15	<52.81	<0.051	2.30	1.81	0.99	161.16
South	Chieftan	BIF	MB5	MB5Mt-3	magnetite	96.90	75.32	5204.64	23.96	<47.11	<0.069	1.63	1.90	0.71	156.03
South	Chieftan	BIF	MB5	MB5Mt-4	magnetite	55.91	74.35	311.55	19.33	<52.45	<0.06	2.18	1.93	0.94	177.97
South	Chieftan	BIF	MB5	MB5Mt-5	magnetite	24.07	64.40	976.03	103.67	78.49	0.06	1.75	1.79	1.15	142.93
South	Chieftan	BIF	MB5	MB5Mt-6	magnetite	35.89	76.07	270.57	15.61	<52.83	<0.031	3.57	1.60	0.82	182.85
South	Chieftan	BIF	MB5	MB5Mt-7	magnetite	32.57	80.33	265.88	34.55	<52.24	<0.063	2.66	1.94	1.11	173.81
South	Chieftan	BIF	MB5	MB5Mt-8	magnetite	65.84	74.84	443.34	10.92	<38.09	<0.057	1.94	1.83	0.65	169.92
South	Chieftan	BIF	MB5	MB5Mt-9	magnetite	140.17	60.52	2366.16	80.03	<46.65	<0.056	3.87	2.82	1.31	139.90
Middle	Prince	ORE	MB60	MB60Hm-1	platy hematite	183.05	1159.89	2418.94	30.88	464.85	0.35	10.84	43.06	6.00	376.14
Middle	Prince	ORE	MB60	MB60Hm-10	platy hematite	322.81	3327.31	5241.96	25.81	1075.35	0.61	6.00	40.42	1.66	494.80
Middle	Prince	ORE	MB60	MB60Hm-11	platy hematite	403.85	904.90	966.66	20.90	1664.59	0.33	12.64	65.88	1.44	722.12
Middle	Prince	ORE	MB60	MB60Hm-12	platy hematite	363.97	659.22	834.88	24.19	954.58	0.17	7.69	50.67	1.11	381.11
Middle	Prince	ORE	MB60	MB60Hm-13	platy hematite	314.62	811.23	811.42	18.82	777.25	0.78	7.33	51.08	1.56	344.52
Middle	Prince	ORE	MB60	MB60Hm-2	platy hematite	474.78	936.82	973.98	23.89	1502.46	0.36	20.85	49.78	1.77	617.74
Middle	Prince	ORE	MB60	MB60Hm-3	platy hematite	164.25	779.00	721.53	23.90	659.64	0.61	16.95	63.22	6.18	268.74
Middle	Prince	ORE	MB60	MB60Hm-4	platy hematite	156.88	1469.85	1686.02	16.46	678.26	1.30	5.24	45.51	2.07	440.64
Middle	Prince	ORE	MB60	MB60Hm-5	platy hematite	443.98	779.86	841.16	164.50	1506.81	0.21	13.77	43.00	2.63	637.17
Middle	Prince	ORE	MB60	MB60Hm-6	platy hematite	509.55	593.71	1192.37	14.64	1029.13	0.18	27.16	35.78	6.02	365.24
Middle	Prince	ORE	MB60	MB60Hm-7	platy hematite	560.23	1039.19	948.25	20.33	1372.76	1.31	3.78	38.56	1.78	419.97
Middle	Prince	ORE	MB60	MB60Hm-8	platy hematite	557.19	706.23	1498.53	156.06	1625.83	0.53	22.50	49.15	5.19	396.88
Middle	Prince	ORE	MB60	MB60Hm-9	platy hematite	434.32	926.21	861.19	21.88	1306.31	0.30	18.98	43.44	4.77	572.87
Middle	Prince	ORE	MB60	MB60Hmlamellar-4	platy hematite	6.93	650.71	570.02	14.42	<118.12	1.67	4.37	222.47	2.36	14.24
North	Princess	ORE	MB68	MB68HmClean-1	porous martite	54.21	74.68	387.37	15.14	<58.4	<0.053	0.93	0.24	0.67	408.16
North	Princess	ORE	MB68	MB68HmClean-3	porous martite	88.81	388.28	1075.52	83.51	112.25	0.17	1.46	0.25	0.64	436.65
North	Princess	ORE	MB68	MB68HmLowerBand-1	porous martite	95.45	280.22	1454.26	484.16	<82.62	0.54	1.07	1.01	0.76	614.99
North	Princess	ORE	MB68	MB68HmLowerBand-2	porous martite	143.44	481.58	1723.74	585.22	<101.96	0.47	0.98	1.25	0.86	783.77
North	Princess	ORE	MB68	MB68HmLowerBand-3	porous martite	73.07	234.10	1679.68	440.15	<116.6	0.49	1.58	0.64	1.07	566.00
North	Princess	ORE	MB68	MB68HmLowerBand-4	porous martite	78.15	258.40	1138.11	492.85	<85.73	0.65	1.57	0.93	0.65	642.67
North	Princess	ORE	MB68	MB68HmLowerBand-5	porous martite	86.90	337.51	1966.35	457.44	391.44	0.34	2.09	1.75	1.04	583.25
North	Princess	ORE	MB68	MB68HmLowerBand-6	porous martite	101.97	300.27	1236.46	505.95	<70.85	0.39	1.04	0.86	0.88	707.73
North	Princess	ORE	MB68	MB68HmLowerBand-7	porous martite	79.69	233.75	1131.96	511.61	141.95	0.48	2.42	1.16	0.74	598.91
North	Princess	ORE	MB68	MB68HmLowerBand-8	porous martite	128.47	307.36	1158.31	392.68	2416.22	0.38	2.08	1.54	0.66	696.21
North	Princess	ORE	MB68	MB68HmMidBand-1	porous martite	93.09	261.76	1412.15	392.83	<73.72	0.62	0.77	0.33	0.92	719.97
North	Princess	ORE	MB68	MB68HmMidBand-2	porous martite	111.29	470.76	1842.96	345.25	<88.42	0.51	1.24	0.46	0.78	668.51
North	Princess	ORE	MB68	MB68HmMidBand-3	porous martite	126.63	495.11	1951.15	447.16	127.36	0.74	1.15	0.45	0.56	749.92
North	Princess	ORE	MB68	MB68HmMidBand-4	porous martite	180.26	422.67	3045.52	435.58	113.29	0.57	0.60	0.34	0.91	665.87
North	Princess	ORE	MB68	MB68HmMidBand-5	porous martite	140.31	417.33	2625.68	299.22	85.04	0.55	1.58	0.36	0.56	658.73
North	Princess	ORE	MB68	MB68HmMidBand-6	porous martite	68.56	404.11	2743.90	229.22	5611.24	0.73	2.16	0.33	1.26	624.28
North	Princess	ORE	MB68	MB68HmMidBand-7	porous martite	154.51	571.22	3601.10	332.63	236.64	0.86	1.69	0.42	0.91	640.05
North	Princess	ORE	MB68	MB68Hmporousarea-1	porous martite	103.33	479.37	1590.43	286.44	<110.32	0.61	1.10	0.31	0.69	745.38
North	Princess	ORE	MB68	MB68Hmporousarea-2	porous martite	419.09	2315.71	5002.21	992.24	<67.72	1.11	2.22	0.74	0.98	1737.10
North	Princess	ORE	MB68	MB68Hmporousarea-3	porous martite	230.34	1239.62	3448.86	628.36	<102.01	0.94	1.36	0.90	0.76	1132.46

Analysis no.	Co	Ni	Cu	Zn	Ga	As	Sr	Y	Zr	Nb	Mo	Sn	Sb	Ba	La	Ce	Pr
MB5Mt-12	0.16	0.63	0.59	4.05	0.26	0.64	0.02	0.14	<0.00	0.00	<0.00	0.23	<0.149	0.18	0.03	0.07	0.01
MB5Mt-2	0.20	0.25	0.79	5.59	0.12	<0.39	0.01	0.11	<0.00	0.01	0.02	0.31	<0.188	<0.00	0.02	0.04	0.01
MB5Mt-3	0.12	0.33	<0.38	4.92	0.15	0.47	0.01	0.07	0.01	0.02	<0.00	0.24	<0.18	0.08	0.01	0.12	<0.00
MB5Mt-4	0.13	0.40	<0.38	5.57	0.10	0.40	0.01	0.12	0.02	<0.00	<0.00	0.34	<0.204	0.09	0.07	0.09	0.01
MB5Mt-5	0.33	0.89	<0.51	5.05	0.07	0.76	0.04	0.33	<0.00	0.01	<0.00	0.15	<0.162	0.18	0.10	0.13	0.03
MB5Mt-6	0.08	0.13	<0.44	6.19	0.17	0.35	<0.00	0.03	<0.00	0.04	<0.025	0.31	<0.173	<0.00	0.02	0.03	0.01
MB5Mt-7	0.14	0.36	<0.43	7.78	0.07	0.49	<0.02	0.06	<0.00	<0.00	0.01	0.28	0.25	<0.00	0.01	0.01	<0.00
MB5Mt-8	0.09	0.14	<0.47	5.35	0.22	<0.35	0.01	0.10	<0.00	0.01	0.02	0.36	<0.16	0.27	0.12	0.11	<0.0058
MB5Mt-9	0.31	0.44	0.74	3.74	0.85	1.32	<0.022	0.47	<0.00	0.02	<0.032	0.25	0.21	0.28	0.09	0.23	0.02
MB60Hm-1	0.47	3.21	3.63	4.44	0.59	9.93	0.65	0.36	0.82	0.05	2.89	2.77	<0.4	2.41	0.25	0.60	0.09
MB60Hm-10	0.38	3.95	1.37	4.89	0.76	7.90	0.41	0.43	2.55	0.03	2.53	<0.1	0.70	1.68	0.31	0.56	0.06
MB60Hm-11	0.35	4.65	<0.215	2.02	0.58	5.75	0.72	0.41	0.94	0.06	2.05	0.17	0.53	1.68	0.25	0.52	0.06
MB60Hm-12	0.28	5.03	<0.23	1.96	0.27	10.96	0.52	0.26	0.96	0.03	1.79	0.21	0.33	1.37	0.25	0.46	0.05
MB60Hm-13	0.41	4.03	0.85	3.43	0.50	7.40	0.45	0.35	0.51	0.04	2.64	<0.097	0.67	2.94	0.22	0.56	0.07
MB60Hm-2	0.54	4.04	0.53	2.55	0.58	10.86	0.54	0.62	0.65	0.08	2.87	0.24	0.38	2.47	0.31	0.80	0.10
MB60Hm-3	0.34	2.41	2.74	4.07	0.79	5.14	0.27	0.30	0.59	0.02	2.06	0.46	0.59	1.14	0.16	0.34	0.03
MB60Hm-4	0.20	0.80	0.70	1.46	0.57	3.34	0.28	0.29	0.44	<0.0077	2.25	0.56	0.26	0.76	0.18	0.50	0.06
MB60Hm-5	0.45	3.81	<0.166	3.05	0.56	5.03	0.60	0.62	0.89	0.03	2.14	1.85	0.39	3.05	0.35	0.69	0.09
MB60Hm-6	0.11	2.11	<0.157	5.31	0.19	<2.68	0.44	0.21	1.26	0.13	0.99	0.20	0.26	2.25	0.11	0.18	0.05
MB60Hm-7	0.34	3.02	1.57	3.40	0.53	8.23	0.79	0.36	0.69	0.02	2.83	0.76	0.44	1.21	0.29	0.57	0.07
MB60Hm-8	0.24	3.44	2.23	10.59	0.40	6.24	0.82	0.48	1.12	0.12	1.46	10.47	0.57	3.23	0.20	0.59	0.05
MB60Hm-9	0.36	3.29	2.66	3.88	0.50	7.60	0.97	0.51	0.54	0.04	1.91	1.01	0.35	2.58	0.27	0.66	0.07
MB60Hmlamellar-4	0.14	0.40	0.70	1.13	0.27	<3	0.06	0.02	0.28	0.04	1.72	0.60	0.23	0.80	0.05	0.12	0.01
MB68HmClean-1	0.46	0.58	<0.29	2.44	<0.062	0.86	0.02	0.20	<0.00	<0.00	0.03	<0.107	<0.35	<0.00	0.14	0.23	0.03
MB68HmClean-3	0.64	1.35	0.57	6.94	0.55	15.35	0.31	0.75	0.07	<0.00	0.05	0.12	<0.27	0.14	0.29	0.41	0.08
MB68HmLowerBand-1	1.78	1.83	1.61	8.33	0.42	40.51	0.33	1.64	0.03	<0.0174	0.28	0.16	<0.27	0.50	1.78	0.71	0.36
MB68HmLowerBand-2	2.07	3.87	1.43	9.82	0.54	60.66	0.38	2.43	<0.00	<0.00	0.29	<0.141	0.25	0.33	2.06	0.93	0.41
MB68HmLowerBand-3	1.62	2.88	0.43	6.56	0.09	38.30	0.32	1.38	<0.077	<0.0174	0.24	<0.155	<0.24	0.33	1.88	0.79	0.34
MB68HmLowerBand-4	1.31	1.40	0.96	7.31	0.28	43.11	0.37	1.60	0.05	<0.00	0.38	0.14	<0.26	0.16	2.09	0.94	0.35
MB68HmLowerBand-5	1.99	2.43	0.75	6.89	0.20	35.59	4.83	1.34	0.15	<0.00	0.33	0.20	<0.28	1.93	1.43	0.96	0.29
MB68HmLowerBand-6	1.51	1.52	0.83	8.27	0.30	40.45	0.35	1.65	<0.00	<0.00	0.33	0.42	<0.154	0.32	1.73	0.79	0.33
MB68HmLowerBand-7	1.58	1.99	0.66	7.22	0.11	44.91	0.36	1.06	0.03	0.01	0.25	0.44	<0.25	0.70	1.68	0.67	0.33
MB68HmLowerBand-8	1.40	1.64	1.67	6.75	0.09	31.98	20.20	1.68	0.03	<0.0176	0.28	0.10	<0.188	1.05	2.27	1.74	0.40
MB68HmMidBand-1	1.11	1.24	0.88	7.33	0.16	38.42	1.76	1.27	<0.00	<0.0174	0.32	0.27	<0.26	1.17	1.85	0.82	0.34
MB68HmMidBand-2	1.73	2.24	1.18	7.06	0.70	32.66	0.46	1.80	0.03	<0.00	0.27	0.17	<0.22	1.52	1.78	0.98	0.32
MB68HmMidBand-3	2.35	1.96	1.63	9.25	0.50	46.94	0.48	2.34	<0.00	<0.00	0.41	0.10	0.21	0.92	1.96	1.13	0.46
MB68HmMidBand-4	2.49	1.41	0.64	8.55	0.15	46.54	6.04	1.70	0.03	<0.00	0.24	<0.127	0.18	1.11	1.52	0.87	0.32
MB68HmMidBand-5	1.22	1.75	0.69	6.99	0.16	28.59	4.94	1.75	<0.00	0.01	0.20	0.24	<0.219	0.17	1.61	1.04	0.35
MB68HmMidBand-6	1.82	1.72	1.00	7.19	0.14	23.33	19.14	1.33	0.06	<0.0176	0.21	<0.121	<0.18	0.52	1.37	1.17	0.33
MB68HmMidBand-7	1.80	1.82	0.56	7.02	0.16	32.35	19.97	1.83	<0.00	<0.00	0.35	<0.14	<0.24	<0.00	1.61	1.23	0.35
MB68Hmporousarea-1	1.67	1.48	1.01	9.16	0.45	34.92	0.66	1.56	<0.00	<0.00	0.26	0.65	<0.184	0.53	1.44	1.27	0.34
MB68Hmporousarea-2	6.86	7.98	5.86	39.84	2.50	141.32	2.13	6.68	0.21	<0.00	0.64	1.09	<0.165	0.15	4.78	2.51	1.05
MB68Hmporousarea-3	4.08	5.89	4.13	24.10	1.52	100.20	0.79	3.69	<0.00	<0.00	0.43	0.97	0.23	0.17	3.12	1.64	0.73

Analysis no.	Nd	Sm	Eu	Gd	Tb	Dy	Ho	Er	Tm	Yb	Lu	W	Pb208	Th	U
MB5Mt-12	0.03	<0.00	0.01	0.04	0.00	<0.029	0.01	0.01	0.00	<0.024	0.01	0.10	1.96	<0.0031	0.05
MB5Mt-2	0.04	<0.0296	0.01	0.01	<0.0049	<0.00	0.00	0.01	<0.00	0.01	<0.0054	0.50	0.23	0.01	0.02
MB5Mt-3	0.05	0.02	0.00	0.01	0.00	0.01	0.00	0.00	<0.00	0.01	0.02	0.26	0.36	<0.00	0.01
MB5Mt-4	0.04	<0.031	0.02	<0.05	0.00	<0.00	0.00	0.01	<0.00	<0.034	<0.00	0.29	0.51	0.03	0.03
MB5Mt-5	0.05	0.05	0.02	0.05	0.01	0.02	0.01	0.02	0.01	<0.00	0.00	0.11	0.20	0.00	0.02
MB5Mt-6	0.04	0.02	<0.00	0.01	<0.0043	<0.00	<0.00	<0.00	<0.00	<0.0196	<0.00	0.05	0.10	<0.0037	0.01
MB5Mt-7	0.01	<0.00	0.02	<0.00	<0.00	<0.00	0.00	<0.0153	0.00	0.01	<0.00	0.06	0.35	<0.00	0.03
MB5Mt-8	0.10	<0.0302	0.01	<0.00	<0.00	0.01	<0.00	0.02	<0.00	<0.00	0.03	0.18	0.41	0.01	0.04
MB5Mt-9	0.17	0.08	0.04	0.06	0.01	0.04	0.01	0.03	0.03	0.03	0.00	0.09	0.29	0.00	0.02
MB60Hm-1	0.34	0.08	0.02	0.08	0.01	0.10	0.01	0.06	<0.0082	0.07	<0.0078	1.91	8.61	0.10	3.71
MB60Hm-10	0.35	0.08	0.03	0.11	0.01	0.08	0.02	0.04	<0.0055	0.01	0.01	1.93	10.16	0.02	3.88
MB60Hm-11	0.27	0.09	0.02	0.10	0.01	0.05	0.01	0.02	0.01	0.03	0.01	2.26	10.81	0.09	4.52
MB60Hm-12	0.23	0.04	0.03	0.03	0.01	0.04	0.01	0.02	<0.00	0.05	0.01	2.81	10.10	0.07	4.42
MB60Hm-13	0.30	0.05	0.03	0.06	0.01	0.03	0.01	0.03	0.01	0.02	0.01	2.39	9.20	0.09	3.42
MB60Hm-2	0.44	0.09	0.03	0.15	0.01	0.08	0.02	0.05	<0.0088	0.06	0.01	1.85	10.07	0.02	4.46
MB60Hm-3	0.14	0.07	0.00	0.06	0.01	0.02	0.01	0.02	0.00	0.03	<0.00	2.40	4.36	0.05	2.07
MB60Hm-4	0.23	0.04	0.02	0.12	0.02	0.03	0.02	0.02	0.01	0.03	0.01	2.58	5.97	0.01	3.23
MB60Hm-5	0.41	0.09	0.04	0.07	0.02	0.04	0.01	0.05	<0.00	0.03	<0.0069	2.36	9.70	0.06	4.47
MB60Hm-6	0.11	<0.025	0.00	0.02	<0.0039	<0.016	<0.0042	0.01	0.00	0.02	0.00	1.42	4.90	0.11	3.13
MB60Hm-7	0.34	0.13	0.03	0.05	<0.0074	0.07	<0.0079	0.05	0.01	0.01	0.01	1.72	8.80	0.04	3.63
MB60Hm-8	0.25	0.11	0.02	0.14	0.01	0.01	0.01	0.05	<0.0075	<0.023	0.01	1.59	8.33	0.05	3.42
MB60Hm-9	0.29	0.04	0.04	0.09	0.01	0.08	0.01	0.06	0.01	0.04	0.01	1.94	9.97	0.10	3.98
MB60Hmlamellar-4	0.09	0.02	0.01	<0.00	<0.0068	0.03	0.00	0.01	0.00	0.02	<0.00	3.61	0.92	0.01	1.70
MB68HmClean-1	0.09	<0.051	0.01	0.02	<0.0085	0.05	<0.00	0.01	<0.00	<0.00	<0.00	<0.033	0.71	0.04	0.05
MB68HmClean-3	0.29	0.04	0.02	0.06	0.01	0.08	0.00	0.09	0.01	0.09	0.01	0.01	0.46	<0.00	0.01
MB68HmLowerBand-1	1.66	0.20	0.10	0.28	0.04	0.25	0.05	0.12	0.02	0.08	0.01	0.01	0.74	0.01	0.01
MB68HmLowerBand-2	1.69	0.32	0.11	0.50	0.07	0.40	0.06	0.16	0.02	0.09	0.05	0.09	0.32	0.01	0.00
MB68HmLowerBand-3	1.48	0.26	0.02	0.28	0.03	0.15	0.06	0.15	0.01	0.11	0.02	0.05	0.74	0.00	0.02
MB68HmLowerBand-4	1.47	0.21	0.05	0.54	0.03	0.19	0.04	0.14	0.02	0.09	0.02	0.01	1.21	0.01	0.05
MB68HmLowerBand-5	1.08	0.31	0.05	0.27	0.05	0.23	0.03	0.10	0.02	0.11	0.01	0.03	0.95	0.04	0.16
MB68HmLowerBand-6	1.38	0.23	0.10	0.18	0.02	0.23	0.07	0.16	0.01	0.12	0.01	0.03	1.18	0.01	0.09
MB68HmLowerBand-7	1.44	0.27	0.05	0.19	0.02	0.13	0.02	0.09	0.04	0.05	0.01	0.08	0.34	0.00	0.01
MB68HmLowerBand-8	1.76	0.35	0.07	0.15	0.04	0.16	0.05	0.09	0.02	0.05	0.02	0.06	0.98	0.17	0.01
MB68HmMidBand-1	1.57	0.24	0.03	0.19	0.03	0.22	0.04	0.14	0.01	0.05	0.01	1.83	0.44	0.00	0.16
MB68HmMidBand-2	1.75	0.30	0.07	0.35	0.04	0.28	0.04	0.21	0.02	0.08	0.03	0.34	0.69	<0.00	0.18
MB68HmMidBand-3	2.00	0.22	0.08	0.51	0.04	0.33	0.07	0.22	0.05	0.15	0.03	0.04	0.48	0.01	0.16
MB68HmMidBand-4	1.06	0.23	0.06	0.20	0.05	0.26	0.04	0.13	0.03	0.10	0.02	0.03	0.26	<0.00	0.15
MB68HmMidBand-5	1.18	0.20	0.04	0.28	0.04	0.25	0.05	0.15	0.02	0.11	0.01	0.05	0.28	0.00	0.13
MB68HmMidBand-6	1.17	0.37	0.04	0.24	0.06	0.26	0.04	0.15	0.01	0.06	0.03	0.12	0.25	0.01	0.11
MB68HmMidBand-7	1.51	0.24	0.09	0.35	0.05	0.26	0.04	0.12	0.03	0.15	0.02	<0.025	0.33	0.00	0.18
MB68Hmporousarea-1	1.35	0.19	0.06	0.22	0.05	0.16	0.04	0.14	0.02	<0.042	0.02	0.10	0.25	<0.00	0.14
MB68Hmporousarea-2	4.67	0.86	0.28	1.13	0.13	0.81	0.21	0.45	0.06	0.38	0.07	0.21	0.48	<0.00	0.60
MB68Hmporousarea-3	3.08	0.60	0.13	0.69	0.09	0.58	0.08	0.25	0.05	0.29	0.04	0.03	0.61	<0.00	0.37

Position	Deposit	Lithology	Sample no.	Analysis no.	Texture	Mg	Al	Si	P	Ca	Sc	Ti	V	Cr	Mn
North	Princess	ORE	MB68	MB68Hmporousarea-4	porous martite	156.09	884.11	2574.31	505.67	147.92	0.68	1.28	0.48	0.64	916.41
North	Monarch	BIF	MB71	MB71aHm-1	clean martite	3.23	36.23	1112.83	39.30	<59.05	0.09	1.61	1.57	1.19	67.43
North	Monarch	BIF	MB71	MB71aHm-10	clean martite	11.42	232.55	416.48	103.85	<64.06	0.08	0.62	4.61	6.30	91.13
North	Monarch	BIF	MB71	MB71aHm-11	clean martite	65.96	62.59	26762.59	49.66	<57.46	0.37	1.59	0.72	0.67	35.31
North	Monarch	BIF	MB71	MB71aHm-12	clean martite	12.62	60.14	2254.99	34.11	<59.2	<0.071	2.25	0.80	0.64	15.38
North	Monarch	BIF	MB71	MB71aHm-14	clean martite	5.22	30.79	19960.91	65.08	<69.81	0.15	4.47	0.67	0.75	22.21
North	Monarch	BIF	MB71	MB71aHm-15	clean martite	4.59	44.60	3029.22	44.56	<68.67	0.06	3.76	0.87	0.82	21.72
North	Monarch	BIF	MB71	MB71aHm-16	clean martite	96.29	61.81	11340.97	43.46	<68.87	0.15	<0.34	1.06	1.33	165.71
North	Monarch	BIF	MB71	MB71aHm-17	clean martite	4.01	38.38	6238.72	178.18	<67.44	<0.049	2.18	0.76	0.96	35.16
North	Monarch	BIF	MB71	MB71aHm-18	clean martite	9.84	34.75	26629.37	124.40	92.91	0.23	2.18	1.65	0.78	24.94
North	Monarch	BIF	MB71	MB71aHm-19	clean martite	10.10	36.89	11625.31	185.84	<78.03	<0.081	1.39	0.72	0.69	44.72
North	Monarch	BIF	MB71	MB71aHm-2	clean martite	51.12	25.56	10796.01	23.85	<69	0.18	1.43	1.30	<0.66	115.05
North	Monarch	BIF	MB71	MB71aHm-20	clean martite	17.94	71.59	5908.28	26.78	<90.37	<0.08	1.97	1.38	0.83	214.26
North	Monarch	BIF	MB71	MB71aHm-21	clean martite	13.50	38.74	25734.64	83.94	<61.31	0.21	1.52	0.82	0.80	24.95
North	Monarch	BIF	MB71	MB71aHm-22	clean martite	7.30	52.84	13189.68	28.91	<64.74	0.17	1.41	1.11	0.68	69.52
North	Monarch	BIF	MB71	MB71aHm-23	clean martite	48.84	124.64	2417.91	40.76	138.24	0.11	1.28	16.77	11.65	168.97
North	Monarch	BIF	MB71	MB71aHm-24	clean martite	43.44	107.05	26338.08	70.49	<79.31	0.36	<0.43	6.76	4.02	97.32
North	Monarch	BIF	MB71	MB71aHm-25	clean martite	37.62	107.22	6402.21	59.86	95.95	0.10	<0.45	6.88	2.86	109.18
North	Monarch	BIF	MB71	MB71aHm-3	clean martite	5.45	45.72	1276.89	32.70	<66.64	<0.068	1.85	1.92	0.69	130.23
North	Monarch	BIF	MB71	MB71aHm-4	clean martite	11.68	33.43	410.58	55.91	<55.72	<0.067	2.21	1.43	0.84	106.05
North	Monarch	BIF	MB71	MB71aHm-5	clean martite	7.34	45.07	492.54	26.65	<65.04	<0.064	1.32	2.34	<0.64	82.48
North	Monarch	BIF	MB71	MB71aHm-6	clean martite	7.70	48.35	770.92	72.19	<56.28	0.08	2.77	2.38	1.25	64.26
North	Monarch	BIF	MB71	MB71aHm-7	clean martite	8.30	55.30	554.87	28.69	<57.66	0.12	2.81	1.11	0.65	88.07
North	Monarch	BIF	MB71	MB71aHm-8	clean martite	16.80	29.36	4181.79	94.02	66.70	<0.065	1.67	1.29	<0.56	136.95
North	Monarch	BIF	MB71	MB71aHm-9	clean martite	9.61	52.12	1063.93	30.26	<66.09	<0.045	1.91	1.48	0.84	112.52
North	Monarch	BIF	MB72	MB72aHm-1	clean martite	127.78	866.02	13772.42	40.01	63.68	0.16	3.51	15.92	2.31	75.49
North	Monarch	BIF	MB72	MB72aHm-10	clean martite	43.24	737.03	1655.21	33.87	<81.05	<0.062	4.52	30.06	2.23	63.04
North	Monarch	BIF	MB72	MB72aHm-2	clean martite	199.85	697.68	1997.26	28.98	598.52	0.19	5.19	8.69	2.16	26.18
North	Monarch	BIF	MB72	MB72aHm-3	clean martite	199.49	791.70	7861.32	34.27	573.92	0.11	3.85	7.14	2.11	28.34
North	Monarch	BIF	MB72	MB72aHm-4	clean martite	152.54	718.41	1173.57	35.44	651.79	<0.096	4.28	8.99	1.82	28.52
North	Monarch	BIF	MB72	MB72aHm-9	clean martite	49.24	717.66	8948.39	28.66	77.40	0.16	3.78	25.98	2.68	69.86
Middle	Warrior	CHLORATITE	MB7	MB7Mt-1	magnetite	3311.98	1906.84	1762.70	15.45	<76.99	0.97	247.85	14.90	<0.67	1962.92
Middle	Warrior	CHLORATITE	MB7	MB7Mt-2	magnetite	3615.68	1732.69	1141.02	19.73	617.23	1.03	251.71	15.15	0.63	2742.21
Middle	Warrior	CHLORATITE	MB7	MB7Mt-3	magnetite	3615.59	2286.57	2174.78	14.41	<71.52	0.97	252.71	15.41	<0.6	2282.17
Middle	Warrior	CHLORATITE	MB7	MB7Mt-4	magnetite	2438.60	1708.91	1117.60	14.90	129.57	0.74	264.98	14.15	0.68	2668.07
Middle	Warrior	CHLORATITE	MB7	MB7Mt-5	magnetite	3088.11	1892.62	1527.36	17.66	73.29	0.96	246.77	14.23	1.61	2351.53
Middle	Warrior	CHLORATITE	MB7	MB7Mt-6	magnetite	5766.32	2776.77	3106.98	15.58	<123.14	0.81	262.77	15.62	1.62	2439.62
Middle	Warrior	CHLORATITE	MB7	MB7Mt-7	magnetite	4077.21	2318.69	2373.49	9.55	<93.23	0.80	246.64	15.46	3.56	1151.96
Middle	Warrior	CHLORATITE	MB7	MB7Mt-8	magnetite	3671.69	2044.68	1776.05	17.15	150.28	0.94	233.79	15.96	5.08	1612.06
South	Knight	ORE	MB98a	MB98aHmBand-1	platy hematite	230.75	682.90	3737.62	215.34	84.66	0.47	31.75	41.99	2.40	373.58
South	Knight	ORE	MB98a	MB98aHmBand-10	platy hematite	38.61	262.27	1182.23	281.57	<65.76	0.51	68.26	35.77	1.80	283.35
South	Knight	ORE	MB98a	MB98aHmBand-11	platy hematite	210.02	116.32	3052.53	24.57	76.71	0.17	28.57	18.03	1.22	215.99
South	Knight	ORE	MB98a	MB98aHmBand-12	platy hematite	281.49	211.38	2707.23	27.40	48.77	0.14	22.70	12.40	1.00	172.66

Analysis no.	Co	Ni	Cu	Zn	Ga	As	Sr	Y	Zr	Nb	Mo	Sn	Sb	Ba	La	Ce	Pr
MB68Hmporousarea-4	2.67	4.27	2.86	15.05	0.81	86.71	0.57	2.91	<0.00	<0.0203	0.47	0.42	<0.16	0.83	2.63	1.58	0.55
MB71aHm-1	1.68	0.26	<1.27	10.18	0.10	7.37	0.17	0.12	0.21	0.01	0.20	0.19	9.01	0.22	0.06	0.07	0.01
MB71aHm-10	0.68	0.44	<1.26	15.78	0.19	3.20	0.19	0.02	<0.04	0.01	0.61	0.18	1.57	1.68	0.01	0.03	0.01
MB71aHm-11	0.58	0.93	6.49	9.74	0.15	9.52	0.23	0.22	0.05	0.01	0.34	0.11	9.19	2.24	0.08	0.10	0.01
MB71aHm-12	0.60	0.35	2.74	10.65	0.04	5.70	0.11	0.19	0.07	0.03	0.36	<0.077	5.46	1.05	0.05	0.10	0.02
MB71aHm-14	0.45	0.49	1.63	9.48	0.04	4.30	0.08	0.28	0.10	0.01	0.15	0.11	5.89	0.47	0.06	0.08	0.01
MB71aHm-15	0.90	0.51	4.05	13.58	0.08	5.81	0.24	0.13	0.15	0.01	0.21	<0.094	5.86	1.35	0.07	0.06	0.01
MB71aHm-16	1.51	1.44	<1.27	13.16	0.29	16.63	0.60	0.61	<0.00	<0.00	0.23	0.11	5.04	5.26	0.29	0.51	0.05
MB71aHm-17	0.71	0.39	4.16	16.82	0.10	4.78	0.15	0.20	0.04	0.01	0.20	<0.081	8.04	0.74	0.08	0.13	0.02
MB71aHm-18	0.80	0.25	4.10	15.36	0.05	5.79	0.30	0.16	0.23	0.01	0.20	0.14	8.88	0.55	0.06	0.09	0.02
MB71aHm-19	0.75	0.43	2.37	14.17	0.08	5.63	0.10	0.45	0.15	0.02	0.19	0.11	5.12	1.71	0.15	0.20	0.03
MB71aHm-2	1.66	0.20	<1.24	5.45	0.06	4.58	0.29	0.10	0.20	0.02	0.15	0.16	5.72	0.23	0.07	0.05	0.04
MB71aHm-20	3.30	0.67	<1.46	12.30	0.17	11.73	0.23	0.44	0.12	0.01	0.41	<0.105	8.97	3.31	0.14	0.20	0.03
MB71aHm-21	0.69	0.35	<1.38	12.23	0.09	4.11	0.15	0.18	0.08	0.00	0.25	<0.098	2.62	0.66	0.09	0.08	0.01
MB71aHm-22	2.32	0.13	<1.35	6.36	0.11	5.61	0.16	0.11	0.16	0.01	0.18	0.09	5.51	0.57	0.05	0.08	0.02
MB71aHm-23	2.40	4.04	<1.48	22.40	0.34	17.95	0.78	0.76	0.03	<0.00	0.37	0.13	5.16	4.95	3.27	3.75	0.34
MB71aHm-24	2.03	1.18	<1.69	9.27	0.12	26.64	0.44	1.26	0.04	0.00	0.70	<0.116	7.26	3.26	0.30	0.63	0.08
MB71aHm-25	2.55	1.45	<1.5	10.78	0.18	24.12	0.43	1.00	0.03	0.02	0.53	0.26	6.40	2.53	0.29	0.62	0.08
MB71aHm-3	1.83	0.39	1.71	5.24	0.18	6.75	0.18	0.10	0.22	0.01	0.20	0.27	5.06	0.92	0.07	0.07	0.01
MB71aHm-4	1.44	0.31	<1.18	6.80	0.06	5.92	0.07	0.11	0.11	0.03	0.26	0.14	5.84	0.32	0.05	0.04	0.02
MB71aHm-5	1.92	0.27	<1.32	6.98	0.13	7.33	0.10	0.14	0.15	0.01	0.27	0.19	6.09	0.99	0.04	0.08	0.00
MB71aHm-6	1.23	0.50	2.64	12.81	0.13	7.47	0.22	0.21	0.14	0.01	0.25	0.18	5.21	1.81	0.09	0.12	0.01
MB71aHm-7	1.55	0.32	<1.35	7.96	0.04	4.37	0.14	0.16	0.11	0.01	0.24	0.25	5.37	0.32	0.07	0.07	0.01
MB71aHm-8	0.93	0.25	2.52	13.20	0.06	9.87	0.32	0.28	0.13	0.02	0.32	0.12	9.55	1.04	0.10	0.13	0.01
MB71aHm-9	3.18	0.49	<1.25	6.35	0.07	5.23	0.18	0.23	0.09	0.00	0.27	0.12	6.78	1.03	0.07	0.11	0.02
MB72aHm-1	4.71	6.55	<1.24	7.57	0.43	10.52	1.92	0.58	0.26	0.01	1.20	0.35	14.72	1.25	0.70	0.93	0.21
MB72aHm-10	4.00	7.71	1.39	8.91	0.42	12.57	1.39	0.77	0.54	0.04	3.68	<0.094	11.65	1.41	1.17	1.34	0.29
MB72aHm-2	4.71	6.20	<1.23	4.35	0.39	9.48	33.50	0.37	0.33	0.03	0.55	0.35	10.26	1.11	0.44	0.59	0.19
MB72aHm-3	3.75	4.91	<1.25	5.07	0.35	10.59	25.14	0.38	0.43	0.06	0.50	0.14	14.36	1.37	0.42	0.50	0.17
MB72aHm-4	3.56	5.03	1.19	6.09	0.44	10.22	38.21	0.40	0.52	0.06	0.53	0.31	12.21	1.28	0.39	0.47	0.19
MB72aHm-9	3.93	7.68	1.73	10.73	0.46	14.64	1.42	0.73	0.28	0.05	4.35	<0.109	14.37	0.62	0.64	0.84	0.20
MB7Mt-1	0.03	0.82	<0.24	95.03	0.97	12.69	0.02	0.65	0.08	1.28	<0.052	3.47	2.02	<0.00	0.02	0.04	0.00
MB7Mt-2	0.04	1.03	<0.2	107.64	0.70	4.66	0.34	0.28	0.05	0.45	0.03	2.97	<0.22	<0.00	0.04	0.05	0.00
MB7Mt-3	0.13	1.18	<0.37	109.23	0.77	13.24	0.37	0.49	0.12	0.99	<0.045	3.51	0.54	<0.00	0.05	0.11	0.02
MB7Mt-4	0.20	0.90	<0.25	106.80	0.93	2.57	<0.00	0.11	0.13	0.26	0.02	3.29	0.37	<0.00	0.01	0.02	0.00
MB7Mt-5	0.08	1.38	<0.35	115.98	0.68	5.42	<0.00	0.24	0.08	0.58	<0.00	3.13	1.00	<0.00	0.02	0.04	0.02
MB7Mt-6	0.02	1.45	0.39	113.84	0.87	12.91	0.28	0.59	0.03	0.98	0.08	4.04	0.46	<0.00	0.02	0.08	0.00
MB7Mt-7	0.43	1.11	<0.37	74.25	1.17	9.17	0.04	0.63	0.79	0.86	<0.00	3.62	0.27	<0.148	0.03	0.07	<0.0072
MB7Mt-8	0.05	1.09	<0.39	46.47	0.83	3.78	0.11	0.15	<0.00	0.26	0.05	2.72	0.21	<0.00	0.24	0.41	0.02
MB98aHmBand-1	0.65	13.69	9.16	5.65	2.11	15.87	2.61	5.41	1.85	0.19	2.43	0.68	0.89	28.68	1.71	2.68	0.29
MB98aHmBand-10	43.67	1.83	3.40	4.18	0.66	24.28	1.28	2.61	2.87	0.36	1.03	1.05	1.41	1.50	1.73	2.36	0.20
MB98aHmBand-11	0.57	16.40	<0.64	1.62	0.58	5.39	0.56	5.58	0.49	0.21	0.75	0.28	0.47	29.71	1.61	1.95	0.22
MB98aHmBand-12	0.62	10.80	<0.71	0.40	0.60	3.23	0.36	4.09	0.41	0.20	0.72	0.33	0.22	21.07	1.15	1.35	0.16

Analysis no.	Nd	Sm	Eu	Gd	Tb	Dy	Ho	Er	Tm	Yb	Lu	W	Pb208	Th	U
MB68Hmporousarea-4	2.53	0.59	0.13	0.55	0.05	0.39	0.09	0.24	0.04	0.20	0.04	0.02	0.15	<0.00	0.30
MB71aHm-1	0.03	0.02	0.01	0.01	0.01	<0.0183	<0.0065	0.01	0.00	0.01	<0.0044	1.68	2.10	0.01	0.18
MB71aHm-10	0.02	0.03	0.03	<0.00	0.00	0.02	<0.00	0.00	<0.0041	0.02	0.00	25.45	8.02	<0.00	0.47
MB71aHm-11	0.04	0.01	0.01	0.01	0.00	0.02	<0.0063	<0.0131	<0.0044	0.01	0.01	2.87	2.37	0.01	0.17
MB71aHm-12	0.06	<0.035	0.01	0.01	<0.0056	0.01	0.00	0.02	0.00	<0.0175	0.00	3.08	1.13	0.01	0.22
MB71aHm-14	0.04	<0.035	0.01	0.05	0.01	0.03	0.01	0.01	<0.00	0.01	0.00	1.18	1.32	<0.0063	0.12
MB71aHm-15	0.07	<0.00	0.01	0.02	0.00	0.01	0.00	<0.0122	0.00	0.01	<0.0041	4.01	1.86	<0.0063	0.15
MB71aHm-16	0.30	0.19	0.04	0.09	0.01	0.12	0.02	0.03	0.00	0.04	0.01	0.21	2.93	0.01	0.59
MB71aHm-17	0.13	0.03	0.00	0.04	0.00	0.02	0.00	<0.0126	<0.00	0.01	<0.0043	2.17	1.70	0.00	0.16
MB71aHm-18	0.05	0.01	0.01	<0.00	0.00	<0.017	0.01	0.02	<0.00	0.01	0.00	1.19	1.54	0.00	0.21
MB71aHm-19	0.09	0.03	0.01	0.04	0.00	0.03	0.01	0.02	0.00	0.02	0.00	1.98	2.47	0.01	0.17
MB71aHm-2	0.02	0.01	0.00	0.01	<0.0064	<0.019	0.00	<0.00	0.00	0.01	0.00	0.64	1.91	<0.00	0.07
MB71aHm-20	0.09	0.06	0.01	0.03	<0.0049	0.04	0.01	0.04	0.01	0.03	0.00	3.89	4.64	0.01	0.39
MB71aHm-21	0.04	<0.036	0.02	0.03	0.00	0.01	<0.006	0.01	<0.00	0.02	0.00	2.06	1.37	0.01	0.14
MB71aHm-22	0.02	0.01	<0.0061	0.02	<0.00	<0.0168	<0.00	0.02	0.01	<0.0177	<0.0043	1.63	2.49	0.01	0.24
MB71aHm-23	0.99	0.24	0.10	0.15	0.02	0.12	0.01	0.04	0.01	0.04	0.01	2.98	7.50	0.01	1.49
MB71aHm-24	0.43	0.18	0.10	0.17	0.02	0.22	0.03	0.12	0.02	0.04	0.01	0.71	5.11	0.00	2.45
MB71aHm-25	0.31	0.22	0.08	0.19	0.02	0.16	0.03	0.07	0.02	0.02	0.01	0.83	5.95	<0.0068	2.14
MB71aHm-3	0.03	0.03	0.00	0.03	<0.00	0.04	<0.0062	0.00	0.00	<0.00	<0.00	1.19	2.55	<0.0095	0.13
MB71aHm-4	0.01	0.03	0.00	0.02	0.00	0.01	0.01	0.01	<0.00	0.01	0.00	1.38	1.54	0.00	0.09
MB71aHm-5	0.03	0.04	<0.0068	<0.00	0.00	0.02	0.00	0.00	<0.0064	<0.00	<0.00	1.70	2.41	0.01	0.18
MB71aHm-6	0.07	0.01	0.01	<0.00	0.00	0.02	0.00	0.00	0.00	0.02	0.00	2.04	3.68	0.00	0.40
MB71aHm-7	0.06	<0.00	<0.0095	0.02	<0.00	0.01	0.01	0.01	0.01	0.01	0.00	2.14	2.52	0.01	0.16
MB71aHm-8	0.08	0.04	0.02	<0.00	0.01	0.04	0.00	0.01	<0.00	0.01	<0.0041	1.68	3.48	<0.0045	0.18
MB71aHm-9	0.07	0.01	0.01	<0.00	0.01	<0.0174	0.00	0.01	0.00	0.01	0.00	2.25	3.96	0.00	0.18
MB72aHm-1	0.77	0.12	0.04	0.20	<0.0065	0.16	0.01	0.05	0.01	0.15	0.02	2.79	2.82	0.01	1.80
MB72aHm-10	1.11	0.30	0.04	0.14	0.02	0.17	0.03	0.12	0.02	0.11	0.03	5.25	3.47	0.01	2.12
MB72aHm-2	1.10	0.31	0.04	0.16	0.03	0.11	0.02	0.07	0.05	0.08	0.01	3.94	1.42	0.02	0.49
MB72aHm-3	0.60	0.22	0.04	0.20	0.02	0.15	0.02	0.06	0.00	0.11	0.02	4.23	1.43	0.00	0.43
MB72aHm-4	0.88	0.25	0.06	0.11	0.04	0.15	0.02	0.07	0.01	0.08	<0.0082	3.89	2.05	0.02	0.57
MB72aHm-9	0.69	0.21	0.04	0.15	0.01	0.15	0.04	0.07	0.01	0.12	0.01	4.58	2.59	<0.0061	1.97
MB7Mt-1	0.03	0.06	<0.0134	<0.083	<0.00	<0.037	0.02	0.03	0.00	<0.039	0.02	0.14	0.35	0.00	0.05
MB7Mt-2	<0.042	<0.00	0.00	<0.054	<0.00	<0.034	<0.009	<0.037	0.00	0.04	0.00	0.10	0.26	0.00	0.01
MB7Mt-3	0.03	<0.00	<0.0164	0.02	0.00	0.05	0.02	0.01	0.01	<0.034	0.01	0.13	0.12	0.01	0.03
MB7Mt-4	0.02	<0.00	0.00	0.02	<0.00	0.01	0.00	<0.00	<0.00	<0.00	<0.00	0.14	0.43	0.00	0.03
MB7Mt-5	0.11	<0.00	0.01	<0.00	0.00	<0.00	0.01	<0.028	0.00	0.01	<0.0138	0.14	0.49	<0.00	0.01
MB7Mt-6	0.05	0.02	0.02	0.09	<0.00	0.03	0.01	0.04	0.02	<0.00	0.01	0.17	2.63	0.01	0.05
MB7Mt-7	0.03	<0.00	0.02	0.02	<0.00	0.04	0.02	0.03	0.02	<0.054	0.02	<0.00	<0.0148	<0.00	<0.00
MB7Mt-8	0.08	0.02	0.01	0.02	<0.0084	0.01	0.00	0.01	0.01	0.01	<0.00	0.04	0.39	<0.00	0.00
MB98aHmBand-1	1.36	0.34	0.27	0.44	0.05	0.34	0.11	0.38	0.06	0.41	0.06	10.54	9.74	0.10	22.92
MB98aHmBand-10	0.87	0.19	0.09	0.22	0.06	0.34	0.05	0.16	0.04	0.19	0.04	12.57	52.22	0.51	8.26
MB98aHmBand-11	1.20	0.25	0.34	0.46	0.07	0.40	0.13	0.37	0.06	0.32	0.08	12.16	2.77	0.16	1.76
MB98aHmBand-12	0.74	0.15	0.20	0.27	0.03	0.35	0.07	0.22	0.04	0.33	0.06	9.91	1.84	0.14	1.26

Position	Deposit	Lithology	Sample no.	Analysis no.	Texture	Mg	Al	Si	P	Ca	Sc	Ti	V	Cr	Mn
South	Knight	ORE	MB98a	MB98aHmBand-13	platy hematite	160.33	162.39	1870.94	23.18	<48.81	0.14	39.27	16.89	0.99	133.34
South	Knight	ORE	MB98a	MB98aHmBand-14	platy hematite	145.30	142.12	3170.98	26.98	152.48	<0.085	41.98	66.29	0.78	272.95
South	Knight	ORE	MB98a	MB98aHmBand-15	platy hematite	145.64	338.17	1837.69	94.44	510.87	0.58	54.16	37.76	3.49	364.92
South	Knight	ORE	MB98a	MB98aHmBand-16	platy hematite	138.10	196.40	1227.49	67.09	<55.54	0.42	276.06	368.86	6.29	519.27
South	Knight	ORE	MB98a	MB98aHmBand-17	platy hematite	149.00	1498.23	3318.13	493.20	115.16	0.54	36.34	54.46	8.52	459.28
South	Knight	ORE	MB98a	MB98aHmBand-18	platy hematite	149.98	626.25	2753.03	159.64	80.77	0.47	31.23	44.63	4.13	298.83
South	Knight	ORE	MB98a	MB98aHmBand-2	platy hematite	206.28	974.06	3450.47	292.51	164.64	0.86	25.86	60.13	2.10	435.90
South	Knight	ORE	MB98a	MB98aHmBand-3	platy hematite	137.27	976.97	2298.13	269.88	113.20	0.62	25.54	50.77	2.77	333.32
South	Knight	ORE	MB98a	MB98aHmBand-4	platy hematite	256.53	1603.51	4449.00	526.16	165.55	0.80	31.62	49.55	2.74	594.54
South	Knight	ORE	MB98a	MB98aHmBand-5	platy hematite	83.42	364.21	1068.06	143.82	144.72	0.45	52.65	28.60	1.60	542.62
South	Knight	ORE	MB98a	MB98aHmBand-6	platy hematite	29.61	124.69	765.09	99.04	65.26	0.46	172.00	44.77	1.43	367.61
South	Knight	ORE	MB98a	MB98aHmBand-7	platy hematite	108.15	140.30	1130.43	107.37	48.76	0.67	73.54	55.51	1.08	519.93
South	Knight	ORE	MB98a	MB98aHmBand-8	platy hematite	73.66	225.25	1121.82	138.10	39.91	0.36	151.47	53.77	1.61	505.20
South	Knight	ORE	MB98a	MB98aHmBand-9	platy hematite	42.03	372.61	1141.63	173.84	43.23	0.41	108.42	39.76	1.43	343.94
South	Knight	ORE	MB98a	MB98aHmClast-1	platy hematite	285.10	224.65	3826.51	68.56	58.38	0.14	23.36	13.27	1.43	234.31
South	Knight	ORE	MB98a	MB98aHmClast-2	platy hematite	173.52	160.63	5131.86	50.54	79.04	0.10	56.16	11.76	1.40	252.70
South	Knight	ORE	MB98a	MB98aHmClast-3	platy hematite	317.72	142.83	7320.68	65.51	83.05	0.25	19.40	10.97	1.06	318.39
South	Knight	ORE	MB98a	MB98aHmClast-4	platy hematite	54.05	280.60	1172.41	155.81	50.61	0.27	24.47	21.63	3.14	219.65
South	Knight	ORE	MB98a	MB98aHmRe-1	platy hematite	117.40	534.04	1874.65	275.04	99.43	1.03	101.30	42.53	1.76	504.19
South	Knight	ORE	MB98a	MB98aHmRe-10	platy hematite	131.09	164.21	3016.86	26.11	67.77	0.24	79.04	65.27	1.14	202.76
South	Knight	ORE	MB98a	MB98aHmRe-11	platy hematite	118.74	199.45	2645.10	23.47	<40.19	0.21	42.27	17.02	0.83	143.48
South	Knight	ORE	MB98a	MB98aHmRe-12	platy hematite	175.67	130.25	3719.79	24.30	<54.44	0.23	73.24	83.44	0.81	212.97
South	Knight	ORE	MB98a	MB98aHmRe-13	platy hematite	207.26	137.32	6363.76	103.61	<53.18	0.31	72.32	12.49	2.72	300.26
South	Knight	ORE	MB98a	MB98aHmRe-14	platy hematite	126.63	415.48	2394.56	28.08	<56.54	0.20	24.83	78.12	1.03	107.45
South	Knight	ORE	MB98a	MB98aHmRe-15	platy hematite	188.24	1065.96	2677.14	332.86	77.35	0.53	27.20	51.90	2.28	298.62
South	Knight	ORE	MB98a	MB98aHmRe-16	platy hematite	203.15	627.49	3913.86	187.14	50.90	0.46	30.73	46.73	2.13	374.17
South	Knight	ORE	MB98a	MB98aHmRe-17	platy hematite	170.33	238.09	2410.57	19.00	<51.3	0.17	10.81	31.93	1.13	141.02
South	Knight	ORE	MB98a	MB98aHmRe-18	platy hematite	164.09	424.99	3250.79	112.90	<75.87	0.45	18.14	74.97	2.27	291.26
South	Knight	ORE	MB98a	MB98aHmRe-19	platy hematite	146.71	639.74	2998.20	165.89	58.17	0.45	16.43	61.19	1.72	321.43
South	Knight	ORE	MB98a	MB98aHmRe-2	platy hematite	146.67	156.80	1371.12	59.76	81.11	0.39	111.69	65.32	1.52	530.42
South	Knight	ORE	MB98a	MB98aHmRe-20	platy hematite	169.80	390.71	2940.26	100.14	69.30	0.32	14.35	67.57	1.28	274.78
South	Knight	ORE	MB98a	MB98aHmRe-21	platy hematite	139.94	462.55	2802.08	135.74	<55.81	0.61	16.62	69.43	1.37	280.53
South	Knight	ORE	MB98a	MB98aHmRe-22	platy hematite	133.92	484.16	2705.08	129.61	61.27	0.42	18.12	69.83	1.38	246.64
South	Knight	ORE	MB98a	MB98aHmRe-23	platy hematite	229.94	1818.67	3653.83	697.95	200.80	1.18	38.53	48.21	4.95	412.28
South	Knight	ORE	MB98a	MB98aHmRe-24	platy hematite	183.08	734.97	3598.43	271.20	89.37	0.72	38.14	56.88	2.08	356.39
South	Knight	ORE	MB98a	MB98aHmRe-3	platy hematite	116.03	315.25	1281.76	128.35	60.63	0.47	98.26	47.79	1.28	497.03
South	Knight	ORE	MB98a	MB98aHmRe-4	platy hematite	122.50	243.03	1302.75	141.90	72.41	0.41	125.02	51.64	1.38	547.01
South	Knight	ORE	MB98a	MB98aHmRe-5	platy hematite	73.61	177.06	934.48	68.67	<39.59	0.53	132.46	53.07	1.06	487.69
South	Knight	ORE	MB98a	MB98aHmRe-6	platy hematite	89.64	218.25	1149.23	97.39	<48.63	0.59	191.58	53.92	1.73	525.23
South	Knight	ORE	MB98a	MB98aHmRe-7	platy hematite	60.63	90.89	909.26	94.40	<52.73	0.52	149.73	49.55	1.93	598.38
South	Knight	ORE	MB98a	MB98aHmRe-8	platy hematite	61.29	284.74	1266.20	187.32	75.75	0.60	133.27	40.48	2.30	304.70
South	Knight	ORE	MB98a	MB98aHmRe-9	platy hematite	134.42	604.48	3065.22	230.74	<54.54	0.51	26.17	47.55	12.20	302.95
Middle	Baron	ORE	MB99	MB99aHm-1	platy hematite	218.53	87.38	761.32	53.37	67.75	<0.071	1.97	0.91	0.86	1.56

Analysis no.	Co	Ni	Cu	Zn	Ga	As	Sr	Y	Zr	Nb	Mo	Sn	Sb	Ba	La	Ce	Pr
MB98aHmBand-13	0.60	11.31	<0.82	0.74	0.39	6.20	0.48	3.86	0.72	0.32	0.81	0.50	0.53	15.95	1.19	1.68	0.21
MB98aHmBand-14	0.79	10.05	<0.86	0.81	0.62	5.25	0.58	6.13	0.50	0.34	1.37	0.48	0.35	34.68	1.74	2.28	0.22
MB98aHmBand-15	0.96	3.85	3.04	2.90	0.85	14.04	1.44	3.16	1.48	0.28	3.48	0.86	0.41	9.44	2.17	2.97	0.31
MB98aHmBand-16	40.80	6.26	1.31	5.82	0.67	21.79	2.38	2.98	2.87	2.07	3.22	1.42	1.25	4.45	0.99	1.59	0.18
MB98aHmBand-17	2.26	8.81	14.60	14.10	3.92	29.43	2.38	4.35	3.40	0.26	5.05	0.56	0.66	12.38	1.92	4.79	0.55
MB98aHmBand-18	0.84	7.75	4.59	3.65	1.60	17.86	0.94	4.44	2.17	0.26	3.49	0.60	0.53	17.83	1.38	2.79	0.29
MB98aHmBand-2	6.00	16.86	7.49	14.89	2.93	21.67	2.00	6.08	2.73	0.19	4.78	0.55	0.97	19.15	2.32	6.14	0.76
MB98aHmBand-3	0.89	7.36	13.14	7.56	3.01	19.78	2.48	3.68	2.52	0.19	4.65	0.59	0.90	9.97	1.46	2.93	0.32
MB98aHmBand-4	9.13	25.33	16.40	25.89	4.73	22.69	2.56	6.83	2.51	0.25	3.08	0.38	0.69	22.42	2.28	7.58	0.95
MB98aHmBand-5	71.59	1.25	3.53	4.43	0.55	15.79	0.85	2.61	4.54	0.35	1.38	0.79	1.08	1.67	2.00	2.43	0.19
MB98aHmBand-6	57.45	0.81	1.54	2.65	0.58	17.10	0.73	2.71	3.54	1.12	0.94	1.21	1.06	0.75	1.10	1.42	0.15
MB98aHmBand-7	19.40	0.80	1.14	3.21	0.63	25.63	1.97	5.95	7.13	0.79	5.37	1.29	1.66	1.99	2.49	3.44	0.32
MB98aHmBand-8	65.99	0.97	1.96	3.28	0.41	18.24	1.40	2.98	4.30	0.81	2.92	1.18	1.51	1.38	1.22	1.85	0.21
MB98aHmBand-9	23.11	1.77	4.25	3.14	0.52	19.00	0.87	2.99	4.51	0.77	1.40	1.13	1.18	3.54	1.27	1.95	0.19
MB98aHmClast-1	2.58	10.79	1.03	1.12	1.02	6.77	0.75	18.26	0.76	0.16	1.12	0.35	0.73	34.61	1.52	2.21	0.24
MB98aHmClast-2	0.52	15.77	<0.56	0.83	1.13	8.68	1.08	11.50	0.77	0.19	1.10	0.23	1.49	53.17	2.90	4.42	0.48
MB98aHmClast-3	0.46	10.65	0.79	1.85	1.17	2.21	0.94	8.90	0.22	0.12	1.49	0.19	0.30	58.01	3.18	3.27	0.38
MB98aHmClast-4	9.51	4.97	0.87	2.57	0.44	17.14	1.04	1.68	1.49	0.15	1.03	0.36	1.35	4.97	0.64	1.15	0.12
MB98aHmRe-1	42.82	1.17	17.51	9.36	1.17	23.47	2.31	3.40	4.39	0.64	3.49	0.82	0.77	2.20	3.34	4.11	0.30
MB98aHmRe-10	0.32	10.52	<0.79	0.40	0.59	3.98	0.42	5.23	0.78	0.47	1.37	0.36	0.15	27.64	1.94	2.60	0.30
MB98aHmRe-11	0.28	4.18	<0.72	0.64	0.56	1.59	0.28	3.07	0.55	0.20	0.78	0.14	0.10	21.17	1.47	1.68	0.17
MB98aHmRe-12	0.28	10.77	<0.7	0.57	0.94	2.89	0.52	6.66	0.35	0.54	1.22	0.43	0.21	39.88	2.43	3.11	0.34
MB98aHmRe-13	0.36	7.06	<0.71	0.78	1.55	9.13	1.32	17.27	1.54	0.22	1.65	0.15	0.70	60.40	91.08	108.51	9.88
MB98aHmRe-14	0.17	2.75	<0.81	0.66	0.45	1.76	0.31	2.43	0.97	0.10	0.37	0.10	0.16	15.68	6.87	7.59	0.74
MB98aHmRe-15	0.97	7.94	11.85	7.04	2.54	22.02	1.80	3.55	2.54	0.14	5.86	0.58	0.56	15.72	1.84	3.22	0.38
MB98aHmRe-16	0.97	13.83	5.94	4.79	2.20	17.18	1.72	5.98	2.63	0.19	3.91	0.41	0.53	32.42	2.11	3.71	0.37
MB98aHmRe-17	0.39	10.59	<0.86	0.25	0.38	2.21	0.39	3.03	0.16	0.16	0.58	0.22	0.28	20.63	0.86	1.14	0.12
MB98aHmRe-18	0.67	11.55	3.29	2.71	1.54	18.75	1.41	5.04	2.38	0.14	5.36	0.60	0.65	21.97	1.70	3.27	0.33
MB98aHmRe-19	0.92	10.68	6.05	4.75	1.99	19.97	1.64	4.52	2.75	0.12	4.99	0.51	0.47	18.20	1.81	3.41	0.35
MB98aHmRe-2	39.02	2.14	0.98	5.55	0.41	19.19	1.58	3.09	3.41	0.73	2.86	0.75	1.11	3.49	1.63	2.26	0.19
MB98aHmRe-20	1.03	10.52	3.80	3.24	0.92	17.42	1.33	4.93	2.30	0.14	4.45	0.50	0.69	21.71	1.65	3.12	0.36
MB98aHmRe-21	0.63	8.53	5.11	3.05	1.07	22.68	1.83	4.58	2.09	0.16	5.42	0.48	0.63	19.90	1.85	3.54	0.38
MB98aHmRe-22	0.78	7.92	6.48	3.13	1.11	19.57	1.62	4.46	2.50	0.16	5.36	0.53	0.68	18.48	1.80	3.25	0.35
MB98aHmRe-23	6.76	13.49	22.11	18.67	3.00	26.52	3.03	4.07	2.75	0.20	1.29	0.30	0.44	16.45	1.77	4.24	0.50
MB98aHmRe-24	1.15	13.13	7.59	5.37	2.23	28.65	2.05	5.93	2.91	0.21	6.30	0.53	0.78	23.51	2.18	4.36	0.43
MB98aHmRe-3	50.99	2.28	5.29	6.40	1.05	19.27	1.64	2.96	3.20	0.71	2.08	0.89	0.83	3.14	1.21	1.97	0.22
MB98aHmRe-4	57.69	2.72	2.75	3.30	0.84	19.07	1.51	2.94	3.89	0.85	2.70	0.92	0.95	2.48	1.54	2.27	0.20
MB98aHmRe-5	81.44	1.46	2.39	3.27	0.49	16.40	1.26	2.63	3.60	1.08	2.17	1.50	0.63	1.89	1.40	1.92	0.14
MB98aHmRe-6	72.71	1.15	1.93	4.42	0.36	18.47	1.39	2.74	3.92	0.85	1.95	1.18	0.76	14.80	1.09	1.71	0.19
MB98aHmRe-7	88.23	1.16	1.15	2.01	0.30	18.48	1.12	2.80	3.52	0.86	2.87	0.59	0.89	1.25	1.87	2.25	0.21
MB98aHmRe-8	16.62	1.19	4.04	6.43	0.65	18.44	1.47	3.98	3.22	1.05	1.43	0.76	0.95	2.64	1.88	2.70	0.37
MB98aHmRe-9	0.76	8.27	6.74	6.88	2.23	20.56	1.66	3.64	1.74	0.20	3.99	0.39	0.40	16.37	1.33	2.62	0.31
MB99aHm-1	<0.024	0.09	<1.82	<0.33	0.36	1.63	0.15	0.05	0.06	0.01	0.03	0.26	<0.116	0.08	0.02	0.05	0.02

Analysis no.	Nd	Sm	Eu	Gd	Tb	Dy	Ho	Er	Tm	Yb	Lu	W	Pb208	Th	U
MB98aHmBand-13	0.85	0.12	0.22	0.35	0.05	0.29	0.10	0.33	0.05	0.24	0.05	14.85	2.07	0.25	2.57
MB98aHmBand-14	1.29	0.39	0.28	0.44	0.05	0.41	0.14	0.36	0.06	0.27	0.06	21.57	2.96	0.18	3.97
MB98aHmBand-15	1.16	0.23	0.17	0.36	0.03	0.38	0.11	0.28	0.05	0.17	0.05	13.08	6.53	0.21	19.86
MB98aHmBand-16	0.83	0.23	0.12	0.25	0.05	0.27	0.07	0.30	0.05	0.23	0.05	13.15	13.87	0.27	56.90
MB98aHmBand-17	2.70	0.57	0.33	0.72	0.10	0.58	0.14	0.40	0.06	0.40	0.07	7.87	26.24	0.20	28.79
MB98aHmBand-18	1.42	0.27	0.21	0.43	0.06	0.44	0.10	0.33	0.04	0.27	0.05	13.93	8.81	0.16	15.76
MB98aHmBand-2	3.38	1.05	0.60	1.01	0.14	0.88	0.15	0.50	0.07	0.56	0.10	11.99	36.71	0.12	25.99
MB98aHmBand-3	1.39	0.24	0.21	0.28	0.05	0.29	0.09	0.36	0.03	0.22	0.04	9.10	11.14	0.19	21.46
MB98aHmBand-4	4.12	1.37	0.62	1.37	0.19	1.37	0.32	0.65	0.10	0.80	0.09	9.49	56.65	0.13	23.75
MB98aHmBand-5	0.73	0.18	0.09	0.25	0.04	0.29	0.06	0.26	0.03	0.28	0.03	10.44	17.83	0.49	19.71
MB98aHmBand-6	0.66	0.20	0.08	0.22	0.04	0.25	0.09	0.26	0.03	0.19	0.04	10.36	15.91	0.24	17.54
MB98aHmBand-7	1.52	0.44	0.19	0.59	0.08	0.54	0.17	0.59	0.09	0.60	0.11	17.21	15.74	0.38	86.11
MB98aHmBand-8	0.75	0.14	0.14	0.24	0.05	0.27	0.07	0.25	0.06	0.22	0.04	9.60	16.64	0.34	53.22
MB98aHmBand-9	0.77	0.25	0.11	0.26	0.04	0.47	0.12	0.31	0.02	0.24	0.04	12.42	21.24	0.44	14.48
MB98aHmClast-1	1.41	0.21	0.51	0.67	0.11	0.93	0.33	0.98	0.16	0.87	0.13	7.79	8.58	0.11	3.78
MB98aHmClast-2	2.25	0.55	0.73	0.78	0.14	0.90	0.22	0.72	0.11	0.56	0.11	12.94	13.13	0.11	4.64
MB98aHmClast-3	1.76	0.40	0.76	0.71	0.10	0.59	0.18	0.47	0.07	0.40	0.07	8.13	10.43	0.02	6.80
MB98aHmClast-4	0.57	0.20	0.07	0.19	0.03	0.19	0.06	0.16	0.04	0.18	0.04	11.33	31.70	0.08	9.04
MB98aHmRe-1	1.24	0.30	0.11	0.42	0.06	0.37	0.08	0.28	0.05	0.35	0.04	7.91	17.46	0.63	45.81
MB98aHmRe-10	1.33	0.33	0.54	0.60	0.06	0.35	0.11	0.30	0.06	0.29	0.06	20.84	4.56	0.10	6.30
MB98aHmRe-11	0.71	0.20	0.33	0.29	0.05	0.26	0.05	0.17	0.05	0.23	0.04	12.46	2.40	0.04	1.38
MB98aHmRe-12	1.64	0.34	0.64	0.69	0.09	0.49	0.13	0.41	0.07	0.42	0.06	20.51	4.99	0.08	3.50
MB98aHmRe-13	39.60	4.54	4.01	3.91	0.37	1.77	0.31	1.04	0.13	0.70	0.10	9.93	10.10	0.46	4.24
MB98aHmRe-14	2.99	0.43	0.43	0.44	0.04	0.14	0.05	0.17	0.03	0.25	0.04	11.51	3.28	0.10	4.56
MB98aHmRe-15	1.41	0.23	0.17	0.25	0.03	0.36	0.06	0.26	0.05	0.36	0.04	11.00	10.15	0.17	22.85
MB98aHmRe-16	1.71	0.32	0.32	0.62	0.08	0.43	0.12	0.37	0.05	0.35	0.07	9.35	7.89	0.14	20.05
MB98aHmRe-17	0.52	0.10	0.15	0.21	0.03	0.25	0.05	0.22	0.03	0.18	0.04	21.37	1.56	0.07	2.93
MB98aHmRe-18	1.61	0.28	0.27	0.41	0.06	0.38	0.11	0.32	0.06	0.32	0.05	17.52	7.49	0.07	23.85
MB98aHmRe-19	1.33	0.34	0.26	0.52	0.03	0.37	0.08	0.25	0.05	0.29	0.06	13.69	9.63	0.11	26.78
MB98aHmRe-2	0.91	0.13	0.08	0.23	0.04	0.30	0.09	0.23	0.05	0.23	0.04	11.89	9.57	0.33	50.73
MB98aHmRe-20	1.31	0.26	0.24	0.37	0.06	0.45	0.09	0.31	0.06	0.25	0.05	17.43	8.58	0.10	21.72
MB98aHmRe-21	1.43	0.28	0.25	0.36	0.07	0.46	0.10	0.38	0.07	0.32	0.05	14.95	8.75	0.09	25.18
MB98aHmRe-22	1.62	0.35	0.32	0.34	0.07	0.33	0.08	0.23	0.04	0.25	0.05	16.10	8.44	0.10	22.30
MB98aHmRe-23	2.25	0.55	0.27	0.64	0.11	0.68	0.13	0.37	0.08	0.35	0.07	15.42	36.83	0.18	19.77
MB98aHmRe-24	1.91	0.56	0.33	0.54	0.07	0.49	0.11	0.36	0.07	0.36	0.05	10.31	14.89	0.13	35.75
MB98aHmRe-3	0.84	0.24	0.07	0.24	0.05	0.29	0.06	0.25	0.04	0.25	0.04	11.48	10.29	0.29	32.21
MB98aHmRe-4	0.94	0.17	0.05	0.31	0.04	0.28	0.09	0.22	0.04	0.26	0.04	14.71	14.22	0.35	40.34
MB98aHmRe-5	0.81	0.19	0.08	0.18	0.04	0.26	0.08	0.28	0.05	0.33	0.06	16.87	9.31	0.34	23.45
MB98aHmRe-6	0.65	0.20	0.10	0.22	0.04	0.24	0.05	0.21	0.04	0.18	0.05	10.26	11.39	0.22	38.33
MB98aHmRe-7	0.91	0.18	0.09	0.24	0.04	0.33	0.06	0.21	0.04	0.16	0.03	13.27	14.76	0.43	58.60
MB98aHmRe-8	1.27	0.22	0.11	0.47	0.06	0.52	0.11	0.33	0.06	0.28	0.05	12.71	14.82	0.54	16.71
MB98aHmRe-9	1.05	0.34	0.21	0.49	0.06	0.32	0.07	0.37	0.05	0.28	0.06	11.34	12.46	0.11	18.80
MB99aHm-1	0.07	<0.00	0.00	<0.00	0.00	<0.00	<0.0046	<0.0189	<0.00	<0.00	0.00	0.21	<0.023	<0.0047	0.01

Position	Deposit	Lithology	Sample no.	Analysis no.	Texture	Mg	Al	Si	P	Ca	Sc	Ti	V	Cr	Mn
Middle	Baron	ORE	MB99	MB99aHm-10	platy hematite	819.57	155.42	1856.61	31.90	<68.39	0.07	3.55	0.90	0.64	3.46
Middle	Baron	ORE	MB99	MB99aHm-2	platy hematite	211.93	92.97	710.82	36.63	<65.2	<0.07	3.23	0.96	0.51	3.66
Middle	Baron	ORE	MB99	MB99aHm-3	platy hematite	72.95	86.81	462.78	20.10	<75.51	<0.074	3.18	0.90	0.69	2.58
Middle	Baron	ORE	MB99	MB99aHm-4	platy hematite	128.30	136.95	607.31	18.39	<66.35	<0.088	2.79	1.47	0.85	7.12
Middle	Baron	ORE	MB99	MB99aHm-5	platy hematite	158.60	244.68	954.64	46.35	87.38	<0.051	4.54	2.48	1.13	47.29
Middle	Baron	ORE	MB99	MB99aHm-6	platy hematite	746.59	121.26	1655.67	23.60	<82.42	<0.065	1.96	0.40	0.70	14.30
Middle	Baron	ORE	MB99	MB99aHm-7	platy hematite	498.71	157.31	1210.93	17.39	<75.85	<0.079	3.36	0.84	0.64	4.07
Middle	Baron	ORE	MB99	MB99aHm-8	platy hematite	181.87	94.08	687.01	44.79	153.10	<0.062	1.91	1.08	0.56	5.81
Middle	Baron	ORE	MB99	MB99aHm-9	platy hematite	235.74	129.15	790.06	22.33	<68.28	0.12	2.66	1.10	0.66	4.88
Middle	Baron	ORE	MB99	MB99aHmLam-1	platy hematite	413.35	35.14	1104.55	52.48	<47.34	0.16	2.40	0.63	0.75	2.19
Middle	Baron	ORE	MB99	MB99aHmLam-10	platy hematite	261.29	118.59	833.53	30.74	88.64	0.08	2.45	0.85	1.07	4.02
Middle	Baron	ORE	MB99	MB99aHmLam-2	platy hematite	428.98	85.66	1059.44	23.68	<53.52	<0.065	2.85	0.93	0.58	2.88
Middle	Baron	ORE	MB99	MB99aHmLam-3	platy hematite	88.35	60.59	465.99	452.65	873.28	<0.063	3.54	0.97	0.77	2.02
Middle	Baron	ORE	MB99	MB99aHmLam-4	platy hematite	965.62	165.83	2131.45	26.65	<50.74	0.10	4.22	0.96	0.80	6.12
Middle	Baron	ORE	MB99	MB99aHmLam-5	platy hematite	769.05	142.72	1690.93	25.58	<54	<0.072	2.67	1.02	0.63	4.34
Middle	Baron	ORE	MB99	MB99aHmLam-6	platy hematite	261.63	136.27	824.79	21.44	<61.14	<0.055	4.17	0.92	0.88	7.24
Middle	Baron	ORE	MB99	MB99aHmLam-7	platy hematite	226.80	22.33	400.15	29.87	249.86	0.53	3.02	0.06	0.89	25.23
Middle	Baron	ORE	MB99	MB99aHmLam-8	platy hematite	98.19	65.74	462.41	17.01	<64.55	<0.072	2.20	1.00	0.51	1.16
Middle	Baron	ORE	MB99	MB99aHmLam-9	platy hematite	372.36	53.84	897.06	34.35	<70.66	0.08	2.07	0.88	<0.47	1.91

Analysis no.	Co	Ni	Cu	Zn	Ga	As	Sr	Y	Zr	Nb	Mo	Sn	Sb	Ba	La	Ce	Pr
MB99aHm-10	0.05	0.26	<1.9	0.28	0.22	2.86	0.06	0.02	<0.00	0.03	0.04	0.20	0.32	<0.00	0.03	0.08	0.01
MB99aHm-2	0.02	0.17	<1.71	0.41	0.33	1.27	0.04	0.03	<0.00	0.02	0.05	0.22	0.29	<0.00	0.03	0.05	0.01
MB99aHm-3	0.03	0.13	<1.99	<0.24	0.22	0.90	0.04	0.05	<0.00	0.01	0.01	0.20	<0.103	<0.00	0.02	0.05	0.00
MB99aHm-4	<0.036	0.27	<1.94	1.16	0.39	2.78	0.12	0.10	0.10	0.02	0.02	0.23	<0.133	0.61	0.04	0.09	0.02
MB99aHm-5	2.51	13.69	14.53	35.82	0.45	5.22	0.12	2.08	0.22	0.08	0.23	0.23	<0.144	0.25	0.54	1.64	0.19
MB99aHm-6	0.07	0.17	<1.89	<0.19	0.28	1.94	0.07	0.05	0.03	0.07	0.03	0.08	<0.117	0.08	0.05	0.07	0.01
MB99aHm-7	0.08	0.13	<1.93	0.25	0.20	2.83	0.07	0.01	<0.00	0.01	<0.029	<0.098	<0.123	0.17	0.04	0.06	0.01
MB99aHm-8	<0.025	0.35	<1.9	0.35	0.38	2.25	0.14	0.09	<0.00	0.02	0.01	0.16	0.13	0.42	0.04	0.14	0.02
MB99aHm-9	0.05	0.23	<1.84	0.26	0.28	2.24	0.06	0.08	0.02	0.03	0.03	0.22	0.12	0.41	0.03	0.06	0.02
MB99aHmLam-1	0.05	0.16	<1.23	0.26	0.20	<0.6	0.12	0.03	0.04	0.02	0.02	0.18	<0.23	<0.00	0.02	0.01	0.01
MB99aHmLam-10	0.09	0.12	<1.71	0.15	0.31	1.42	0.06	0.05	0.01	0.02	0.02	0.24	<0.122	0.08	0.03	0.05	0.02
MB99aHmLam-2	<0.023	0.04	<1.18	0.29	0.28	1.48	0.07	0.00	<0.00	0.02	0.02	0.18	<0.18	0.08	0.00	0.02	<0.00
MB99aHmLam-3	<0.023	0.35	<1.28	0.19	0.26	1.41	0.87	1.38	0.03	0.05	0.05	0.45	<0.168	0.08	0.22	0.47	0.06
MB99aHmLam-4	0.14	0.16	<1.37	0.40	0.22	1.94	0.10	0.00	<0.042	0.05	<0.00	0.09	<0.181	<0.00	0.02	0.05	0.01
MB99aHmLam-5	0.14	0.20	<1.45	0.51	0.31	3.15	0.10	0.03	0.07	0.03	0.06	0.11	<0.144	0.38	0.02	0.05	0.01
MB99aHmLam-6	0.16	0.24	<1.59	0.46	0.33	2.55	0.13	0.02	0.01	0.06	0.01	0.12	<0.154	<0.072	0.04	0.03	0.01
MB99aHmLam-7	0.03	0.21	<1.61	<0.213	0.37	0.57	0.08	0.09	<0.00	<0.00	0.01	0.13	<0.144	<0.00	0.02	0.07	<0.00
MB99aHmLam-8	0.01	0.27	<1.66	<0.225	0.48	2.31	0.02	<0.0136	<0.00	<0.0093	<0.029	0.16	<0.135	<0.00	0.01	0.02	0.01
MB99aHmLam-9	0.03	0.21	<1.77	<0.2	0.35	0.98	0.03	0.01	0.02	0.02	0.19	0.10	0.13	<0.00	0.01	0.01	0.00

Analysis no.	Nd	Sm	Eu	Gd	Tb	Dy	Ho	Er	Tm	Yb	Lu	W	Pb208	Th	U
MB99aHm-10	0.05	0.01	<0.0067	0.01	0.00	<0.00	<0.00	0.01	0.00	0.01	<0.00	0.17	0.04	0.00	0.01
MB99aHm-2	<0.03	<0.00	<0.0061	<0.00	0.00	<0.00	0.00	<0.00	<0.00	<0.0177	0.00	0.26	0.12	0.00	0.02
MB99aHm-3	0.03	<0.00	0.01	<0.00	<0.00	0.01	<0.005	<0.0206	<0.00	<0.00	<0.00	0.10	0.10	<0.00	0.09
MB99aHm-4	0.06	<0.04	0.00	0.05	0.00	0.01	0.00	0.02	0.00	0.02	0.01	0.21	0.06	0.02	0.09
MB99aHm-5	1.02	0.28	0.08	0.23	0.02	0.15	0.05	0.14	0.02	0.12	0.03	0.74	0.28	0.02	1.12
MB99aHm-6	0.03	<0.0269	<0.0065	<0.043	<0.00	<0.0181	0.01	0.00	0.00	<0.00	0.00	0.07	0.14	0.01	0.04
MB99aHm-7	0.07	<0.00	0.00	<0.00	<0.00	0.02	0.00	<0.00	<0.00	0.01	0.00	0.09	0.05	0.00	0.03
MB99aHm-8	0.05	0.01	0.00	<0.031	0.00	0.01	0.01	0.02	0.00	0.01	<0.00	0.08	0.17	0.03	0.06
MB99aHm-9	0.09	0.01	0.00	<0.029	<0.00	<0.024	<0.00	0.02	<0.00	<0.00	<0.0072	0.23	<0.047	0.02	0.07
MB99aHmLam-1	<0.036	<0.00	0.01	<0.00	<0.004	0.01	0.00	0.00	0.00	<0.00	<0.00	0.19	0.09	0.00	0.01
MB99aHmLam-10	0.02	0.03	0.01	0.01	<0.0043	0.02	0.00	<0.00	0.00	0.02	<0.0044	0.11	0.20	0.01	0.09
MB99aHmLam-2	<0.03	<0.00	<0.006	<0.041	0.00	<0.00	<0.00	<0.0127	<0.00	<0.00	0.01	0.17	<0.035	0.00	0.01
MB99aHmLam-3	0.42	0.11	0.08	0.11	0.01	0.07	0.02	0.07	0.02	0.07	0.01	0.19	<0.016	0.00	0.08
MB99aHmLam-4	0.02	0.02	0.00	<0.00	<0.0061	<0.00	<0.00	<0.00	<0.00	<0.00	<0.00	0.23	0.04	0.01	0.01
MB99aHmLam-5	0.04	<0.00	0.00	<0.00	0.00	<0.0186	0.00	0.01	<0.0048	<0.00	0.01	0.28	0.09	<0.0048	0.02
MB99aHmLam-6	0.03	0.02	0.02	0.01	<0.00	<0.0179	<0.00	<0.0187	<0.0065	0.01	0.00	0.17	<0.028	0.00	0.02
MB99aHmLam-7	<0.031	0.01	0.00	<0.00	<0.0042	0.01	<0.00	0.01	0.00	0.01	<0.00	0.00	0.09	0.01	0.01
MB99aHmLam-8	<0.00	<0.0273	0.00	<0.00	0.00	<0.0185	0.00	0.02	<0.0047	0.01	0.00	0.20	0.05	0.01	0.00
MB99aHmLam-9	0.01	0.02	0.01	0.01	0.01	<0.0188	<0.00	<0.0139	<0.00	0.02	<0.00	0.23	0.06	<0.0049	0.01

ELECTRONIC APPENDIX C FOR CHAPTER 3

Electronic Appendix C. Pearson correlation coefficients of trace elements in clean martite, porous martite and platy hematite

clean martite, N = 30

	Mg	Al	Si	P	Sc	Ti	V	Cr	Mn	Co	Ni	Cu	Zn	Ga	As	Sr	Y	Zr	Nb	Mo	Sn	Sb	Ba	W	Pb	Th	U	∑REE
Mg	1.0																											
Al	0.4	1.0																										
Si	0.5	0.2	1.0																									
P	-0.2	0.1	0.3	1.0																								
Sc	0.4	0.6	0.1	0.2	1.0																							
Ti	0.5	0.7	0.1	0.1	0.8	1.0																						
V	0.2	0.8	0.0	0.0	0.5	0.7	1.0																					
Cr	0.4	0.7	0.1	0.2	0.8	0.8	0.7	1.0																				
Mn	0.5	0.4	0.0	-0.1	0.1	0.3	0.3	0.3	1.0																			
Co	0.3	0.7	0.1	0.1	0.2	0.3	0.6	0.5	0.7	1.0																		
Ni	0.2	0.8	0.0	0.2	0.3	0.4	0.7	0.6	0.6	0.8	1.0																	
Cu	0.1	0.6	0.1	0.5	0.7	0.6	0.6	0.6	0.2	0.4	0.5	1.0																
Zn	0.1	0.5	0.0	0.1	-0.1	0.0	0.4	0.2	0.8	0.8	0.7	0.3	1.0															
Ga	0.4	0.8	0.1	0.0	0.5	0.6	0.7	0.7	0.4	0.6	0.6	0.6	0.4	1.0														
As	0.1	0.6	0.3	0.5	0.4	0.3	0.4	0.4	0.3	0.5	0.6	0.5	0.5	0.4	1.0													
Sr	0.4	0.6	0.4	0.2	0.5	0.4	0.5	0.5	0.3	0.6	0.5	0.5	0.3	0.5	0.6	1.0												
Y	0.2	0.6	0.3	0.5	0.6	0.5	0.5	0.5	0.3	0.4	0.5	0.7	0.3	0.6	0.7	0.6	1.0											
Zr	0.2	0.6	0.1	0.3	0.8	0.8	0.5	0.7	0.1	0.2	0.3	0.5	0.0	0.4	0.6	0.5	0.5	1.0										
Nb	0.4	0.5	0.0	0.2	0.7	0.9	0.5	0.7	0.3	0.1	0.3	0.5	0.0	0.4	0.3	0.3	0.4	0.8	1.0									
Mo	0.1	0.5	0.3	0.4	0.7	0.5	0.5	0.6	-0.1	0.3	0.4	0.6	-0.1	0.4	0.6	0.6	0.5	0.8	0.5	1.0								
Sn	0.6	0.7	0.2	0.2	0.7	0.8	0.6	0.7	0.5	0.4	0.4	0.6	0.2	0.8	0.4	0.5	0.6	0.5	0.7	0.3	1.0							
Sb	-0.1	0.5	0.3	0.3	0.4	0.3	0.5	0.5	-0.1	0.3	0.4	0.5	0.1	0.4	0.7	0.5	0.4	0.6	0.3	0.7	0.2	1.0						
Ba	0.4	0.7	0.2	0.1	0.4	0.4	0.7	0.6	0.5	0.6	0.7	0.6	0.5	0.7	0.5	0.6	0.6	0.3	0.3	0.4	0.6	0.5	1.0					
W	0.0	0.3	0.3	0.2	0.5	0.3	0.3	0.4	-0.3	-0.1	0.2	0.4	-0.2	0.3	0.5	0.5	0.5	0.7	0.3	0.7	0.2	0.8	0.4	1.0				
Pb	0.2	0.8	0.2	0.3	0.6	0.6	0.7	0.7	0.3	0.6	0.7	0.8	0.5	0.7	0.6	0.5	0.7	0.5	0.5	0.6	0.6	0.5	0.6	0.4	1.0			
Th	0.3	0.5	0.1	0.3	0.9	0.9	0.5	0.8	0.1	0.1	0.2	0.6	-0.1	0.4	0.4	0.4	0.5	0.9	0.9	0.7	0.6	0.4	0.3	0.5	0.6	1.0		
U	0.4	0.7	0.4	0.3	0.7	0.6	0.7	0.7	0.1	0.5	0.5	0.8	0.1	0.7	0.5	0.7	0.7	0.5	0.4	0.7	0.7	0.5	0.7	0.5	0.8	0.6	1.0	
∑REE	0.1	0.6	0.2	0.6	0.7	0.6	0.5	0.7	0.3	0.4	0.6	0.8	0.2	0.6	0.8	0.7	0.9	0.7	0.6	0.7	0.6	0.6	0.6	0.6	0.7	0.7	0.7	1.0

porous martite; N = 22

	Mg	Al	Si	P	Sc	Ti	V	Cr	Mn	Co	Ni	Cu	Zn	Ga	As	Sr	Y	Zr	Nb	Mo	Sn	Sb	Ba	W	Pb	Th	U	∑REE
Mg	1.0																											
Al	0.6	1.0																										
Si	0.3	0.3	1.0																									
P	0.6	0.4	0.6	1.0																								
Sc	0.5	0.7	0.4	0.6	1.0																							
Ti	0.5	0.8	0.2	0.0	0.4	1.0																						
V	0.5	0.6	0.2	-0.1	0.4	0.7	1.0																					
Cr	0.6	0.8	0.0	0.1	0.6	0.9	0.7	1.0																				
Mn	0.6	0.5	0.5	0.5	0.4	0.4	0.4	0.4	1.0																			
Co	0.6	0.4	0.4	0.6	0.6	0.1	0.4	0.4	0.6	1.0																		
Ni	0.7	0.5	0.2	0.4	0.6	0.4	0.6	0.6	0.5	0.7	1.0																	
Cu	0.5	0.5	0.3	0.4	0.7	0.2	0.6	0.4	0.5	0.8	0.8	1.0																
Zn	0.5	0.3	0.2	0.3	0.3	0.2	0.5	0.3	0.7	0.6	0.6	0.7	1.0															
Ga	0.6	0.8	0.2	0.1	0.6	0.8	0.7	0.9	0.3	0.4	0.6	0.5	0.3	1.0														
As	0.1	0.2	-0.2	-0.1	0.1	0.1	0.1	0.2	0.1	0.2	0.6	0.3	0.4	0.1	1.0													
Sr	0.4	0.6	0.6	0.6	0.8	0.3	0.5	0.4	0.6	0.8	0.5	0.7	0.5	0.4	0.1	1.0												
Y	0.5	0.3	0.7	0.6	0.3	0.1	0.3	0.2	0.6	0.7	0.5	0.6	0.5	0.3	0.0	0.6	1.0											
Zr	0.3	0.6	0.3	0.2	0.6	0.5	0.4	0.6	0.1	0.3	0.5	0.3	0.0	0.5	0.3	0.5	0.2	1.0										
Nb	0.5	0.8	0.2	0.1	0.4	0.9	0.6	0.8	0.3	0.1	0.4	0.2	0.1	0.7	0.2	0.4	0.1	0.6	1.0									
Mo	0.2	0.4	-0.1	0.1	0.3	0.2	0.2	0.3	0.2	0.2	0.6	0.3	0.1	0.1	0.7	0.4	0.1	0.6	0.3	1.0								
Sn	0.6	0.8	0.3	0.2	0.4	0.9	0.7	0.8	0.6	0.2	0.5	0.3	0.4	0.7	0.2	0.4	0.3	0.3	0.8	0.2	1.0							
Sb	-0.2	0.0	-0.5	-0.5	0.0	0.1	0.2	0.2	-0.3	-0.1	0.3	0.1	0.1	0.2	0.6	-0.1	-0.4	0.4	0.2	0.4	-0.1	1.0						
Ba	0.4	0.5	0.4	0.2	0.5	0.4	0.8	0.5	0.4	0.5	0.6	0.7	0.6	0.6	0.2	0.6	0.5	0.4	0.4	0.2	0.5	0.2	1.0					
W	-0.2	0.3	0.1	-0.2	0.3	0.3	0.3	0.3	0.0	-0.1	0.0	0.0	-0.1	0.2	0.1	0.3	-0.1	0.7	0.5	0.4	0.2	0.4	0.2	1.0				
Pb	0.3	0.4	-0.1	0.0	0.4	0.4	0.5	0.5	0.5	0.4	0.7	0.6	0.7	0.3	0.6	0.4	0.2	0.4	0.3	0.5	0.3	0.5	0.5	0.3	1.0			
Th	0.5	0.7	0.5	0.4	0.7	0.7	0.6	0.7	0.4	0.5	0.5	0.4	0.2	0.6	0.2	0.7	0.4	0.8	0.8	0.4	0.6	0.2	0.5	0.5	0.4	1.0		
U	0.2	0.6	0.2	0.2	0.7	0.3	0.6	0.5	0.2	0.6	0.7	0.7	0.3	0.5	0.5	0.6	0.4	0.7	0.4	0.6	0.3	0.4	0.6	0.3	0.6	0.6	1.0	
∑REE	0.5	0.5	0.7	0.7	0.6	0.2	0.3	0.3	0.6	0.6	0.4	0.6	0.4	0.3	0.0	0.8	0.9	0.4	0.3	0.2	0.4	-0.4	0.5	0.2	0.2	0.6	0.4	1.0

platy hematite; N = 11

	Mg	Al	Si	P	Sc	Ti	V	Cr	Mn	Co	Ni	Cu	Zn	Ga	As	Sr	Y	Zr	Nb	Mo	Sn	Sb	Ba	W	Pb	Th	U	∑REE
Mg	1.0																											
Al	0.6	1.0																										
Si	0.1	0.4	1.0																									
P	0.4	0.3	0.6	1.0																								
Sc	0.5	0.9	0.4	0.2	1.0																							
Ti	0.4	0.6	0.4	0.1	0.7	1.0																						
V	0.3	0.9	0.6	0.4	0.8	0.5	1.0																					
Cr	0.4	0.7	0.6	0.3	0.7	0.4	0.8	1.0																				
Mn	0.5	0.7	0.3	0.5	0.8	0.4	0.8	0.5	1.0																			
Co	0.3	0.6	0.6	0.7	0.6	0.2	0.8	0.5	0.7	1.0																		
Ni	0.3	0.8	0.6	0.6	0.6	0.3	0.9	0.7	0.7	1.0	1.0																	
Cu	-0.1	0.4	0.1	0.4	0.5	0.0	0.5	0.1	0.6	0.5	0.4	1.0																
Zn	0.2	0.6	-0.1	0.4	0.6	0.2	0.5	0.2	0.8	0.6	0.6	0.6	1.0															
Ga	0.7	0.9	0.5	0.6	0.9	0.5	0.8	0.7	0.8	0.8	0.8	0.5	0.6	1.0														
As	0.6	0.7	0.4	0.4	0.7	0.4	0.5	0.4	0.5	0.7	0.7	0.3	0.4	0.7	1.0													
Sr	0.6	0.8	0.3	0.6	0.7	0.5	0.7	0.4	0.7	0.8	0.8	0.4	0.7	0.8	0.8	1.0												
Y	0.4	0.7	0.4	0.7	0.7	0.5	0.7	0.4	0.9	0.8	0.7	0.6	0.8	0.8	0.6	0.8	1.0											
Zr	0.2	0.6	0.7	0.1	0.6	0.8	0.6	0.6	0.4	0.3	0.4	-0.1	0.0	0.4	0.3	0.4	0.4	1.0										
Nb	0.3	0.5	0.6	0.1	0.6	0.9	0.5	0.5	0.3	0.2	0.2	0.0	0.0	0.5	0.3	0.3	0.4	0.9	1.0									
Mo	0.2	0.7	0.6	0.2	0.6	0.6	0.8	0.5	0.5	0.5	0.6	0.2	0.2	0.4	0.6	0.5	0.4	0.9	0.6	1.0								
Sn	0.4	0.8	0.5	0.3	0.9	0.7	0.8	0.7	0.7	0.4	0.5	0.5	0.4	0.8	0.4	0.4	0.6	0.6	0.7	0.5	1.0							
Sb	0.1	0.5	0.3	-0.1	0.5	0.5	0.4	0.3	0.2	0.4	0.5	0.1	0.2	0.3	0.8	0.6	0.2	0.4	0.4	0.5	0.2	1.0						
Ba	0.3	0.7	0.5	0.6	0.8	0.4	0.8	0.5	0.9	0.9	0.8	0.7	0.8	0.8	0.6	0.8	0.9	0.4	0.3	0.5	0.6	0.3	1.0					
W	0.2	0.6	0.6	0.3	0.7	0.7	0.7	0.5	0.5	0.6	0.7	0.2	0.2	0.5	0.8	0.7	0.5	0.8	0.7	0.9	0.5	0.8	0.6	1.0				
Pb	0.3	0.7	0.2	0.5	0.7	0.3	0.7	0.3	0.9	0.8	0.8	0.7	0.9	0.7	0.7	0.8	0.9	0.2	0.1	0.5	0.5	0.4	0.9	0.5	1.0			
Th	0.6	0.7	0.6	0.4	0.7	0.8	0.6	0.7	0.6	0.5	0.6	-0.1	0.2	0.7	0.5	0.6	0.6	0.8	0.8	0.7	0.6	0.4	0.5	0.7	0.4	1.0		
U	0.4	0.7	0.5	0.7	0.6	0.5	0.7	0.3	0.8	0.8	0.7	0.6	0.6	0.7	0.6	0.8	0.8	0.5	0.4	0.7	0.5	0.2	0.9	0.7	0.8	0.5	1.0	
∑REE	0.5	0.8	0.6	0.6	0.8	0.7	0.8	0.5	0.7	0.8	0.8	0.3	0.6	0.8	0.7	0.9	0.8	0.6	0.6	0.7	0.6	0.6	0.8	0.8	0.7	0.7	0.8	1.0

SUPPLEMENTARY MATERIAL C

FOR CHAPTER 4 – MULTIVARIATE STATISTICAL ANALYSIS OF TRACE ELEMENTS IN PYRITE: PREDICTION, BIAS AND ARTEFACTS IN DEFINING MINERAL SIGNATURES

APPENDIX A: SUPPLEMENTARY MATERIAL A

APPENDIX B: SUPPLEMENTARY MATERIAL B

APPENDIX C: SUPPLEMENTARY MATERIAL C

ELECTRONIC APPENDIX A FOR CHAPTER 4

Table S1. Sequential binary partitioning used to obtain 17 ilr-coordinates of 18 geochemical variables of N = 4,989 dataset. The procedure of partitioning is based on the hierarchical dendrogram (Fig. 3d). Composite variables within a balance are the geometric mean of all components.

Balance	Binary partition
b1	[Bi, ^{206}Pb, ^{207}Pb, ^{208}Pb | Ni, Te, Co, Re, Au, Cu, Ag, As, ^{204}Pb, Mn, Sn, Zn, Se, Ti]
b2	[Bi | ^{206}Pb, ^{207}Pb, ^{208}Pb]
b3	[^{206}Pb | ^{207}Pb, ^{208}Pb]
b4	[^{207}Pb | ^{208}Pb]
b5	[Ni | Te, Co, Re, Au, Cu, Ag, As, ^{204}Pb, Mn, Sn, Zn, Se, Ti]
b6	[Te | Co, Re, Au, Cu, Ag, As, ^{204}Pb, Mn, Sn, Zn, Se, Ti]
b7	[Co | Re, Au, Cu, Ag, As, ^{204}Pb, Mn, Sn, Zn, Se, Ti]
b8	[Re | Au, Cu, Ag, As, ^{204}Pb, Mn, Sn, Zn, Se, Ti]
b9	[Au, Cu, Ag | As, ^{204}Pb, Mn, Sn, Zn, Se, Ti]
b10	[Au | Cu, Ag]
b11	[Cu | Ag]
b12	[As | ^{204}Pb, Mn, Sn, Zn, Se, Ti]
b13	[^{204}Pb | Mn, Sn, Zn, Se, Ti]
b14	[Mn, Sn, Zn | Se, Ti]
b15	[Mn | Sn, Zn]
b16	[Sn | Zn]
b17	[Se |Ti]

Figure S1. Silhouette widths values (s) within a cluster $k = 3, i = 1,2,3$. Cluster number i, a number of analyses (n_i), average s_i and Jaccard similarity value j_i per cluster are given. Sum of squared errors versus and the number of clusters $k = 1, \ldots, 10$ showing that 3 clusters are sufficient for k-means clustering.

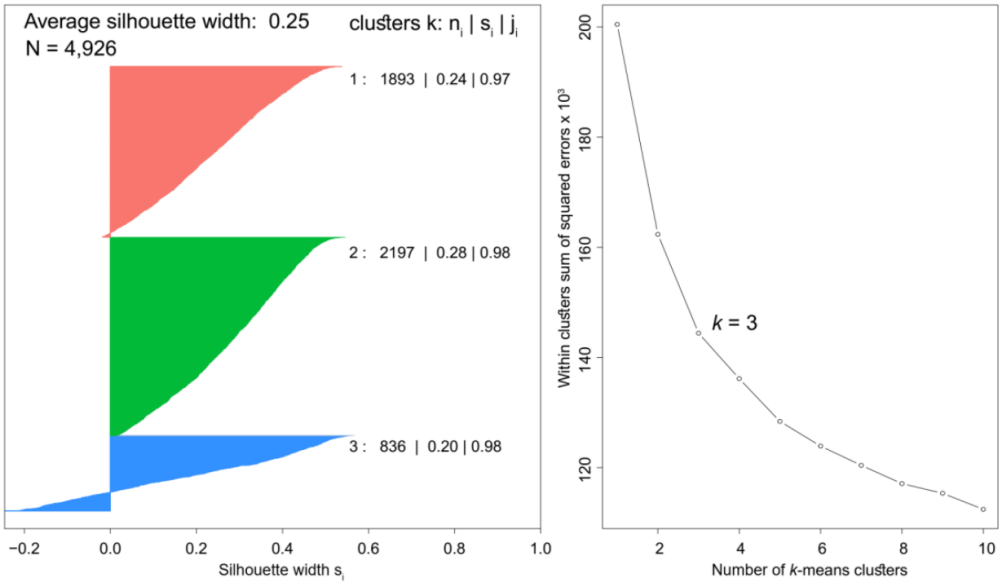


Table S2. Sequential binary partitioning used to obtain 17 ilr-coordinates of 18 geochemical variables of N = 1,501 dataset. The procedure of partitioning is based on the hierarchical dendrogram (Fig. 4d). Composite variables within a balance are the geometric mean of all components.

Balance	Binary partition
b1	[Au, ^{206}Pb, ^{207}Pb, ^{208}Pb, ^{204}Pb, Ag, Bi, Cu | Ni, Co, Re, Te, As, Mn, Se, Ti, Sn, Zn]
b2	[Au | ^{206}Pb, ^{207}Pb, ^{208}Pb, ^{204}Pb, Ag, Bi, Cu]
b3	[^{206}Pb, ^{207}Pb, ^{208}Pb, ^{204}Pb, Ag | Bi, Cu]
b4	[Bi | Cu]
b5	[^{206}Pb, ^{207}Pb, ^{208}Pb | ^{204}Pb, Ag]
b6	[^{206}Pb | ^{207}Pb, ^{208}Pb]
b7	[^{207}Pb | ^{208}Pb]
b8	[^{204}Pb | Ag]
b9	[Ni | Co, Re, Te, As, Mn, Se, Ti, Sn, Zn]
b10	[Co | Re, Te, As, Mn, Se, Ti, Sn, Zn]
b11	[Re | Te, As, Mn, Se, Ti, Sn, Zn]
b12	[Te | As, Mn, Se, Ti, Sn, Zn]
b13	[As | Mn, Se, Ti, Sn, Zn]
b14	[Mn | Se, Ti, Sn, Zn]
b15	[Se, Ti | Sn, Zn]
b16	[Se | Ti]
b17	[Sn | Zn]

Figure S2. Silhouette widths values (s) within a cluster $k = 3, i = 1,2,3$. Cluster number i, a number of analyses (n_i), average s_i and Jaccard similarity value j_i per cluster are given. Sum of squared errors versus and the number of clusters $k = 1, \ldots, 10$ showing that 3 clusters are sufficient for k-means clustering.

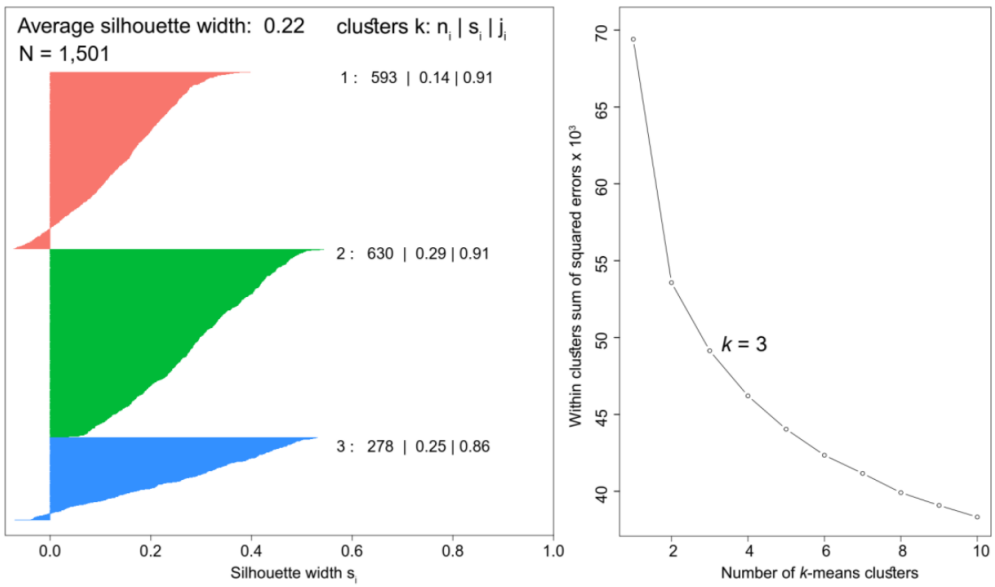
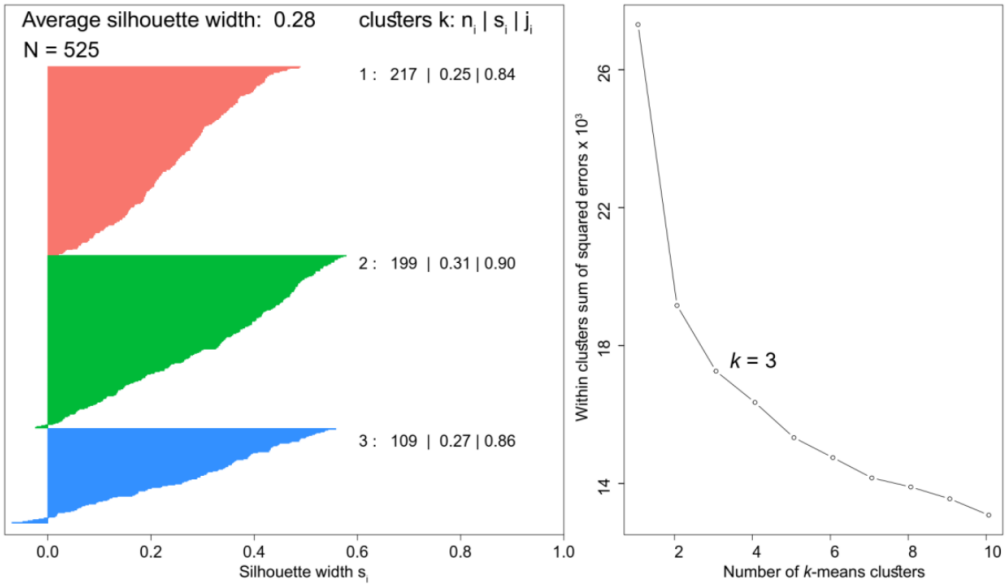


Table S3. Sequential binary partitioning used to obtain 17 ilr-coordinates of 18 geochemical variables of N = 525 dataset. The procedure of partitioning is based on the hierarchical dendrogram (Fig. 5d). Composite variables within a balance are the geometric mean of all components.

Balance	Binary partition
b1	[^{204}Pb, ^{206}Pb, ^{207}Pb, ^{208}Pb, Bi, Ag, Au, Cu | Ni, Re, Co, Mn, Se, Ti, Sn, Zn, As, Te]
b2	[^{204}Pb, ^{206}Pb, ^{207}Pb, ^{208}Pb, Bi, Ag | Au, Cu]
b3	[Au | Cu]
b4	[^{204}Pb, ^{206}Pb, ^{207}Pb, ^{208}Pb | Bi, Ag]
b5	[Bi | Ag]
b6	[^{204}Pb | ^{206}Pb, ^{207}Pb, ^{208}Pb]
b7	[^{206}Pb | ^{207}Pb, ^{208}Pb]
b8	[^{207}Pb | ^{208}Pb]
b9	[Ni, Re | Co, Mn, Se, Ti, Sn, Zn, As, Te]
b10	[Ni | Re]
b11	[Co | Mn, Se, Ti, Sn, Zn, As, Te]
b12	[Mn, Se, Ti, Sn, Zn | As, Te]
b13	[As | Te]
b14	[Mn | Se, Ti, Sn, Zn]
b15	[Se, Ti | Sn, Zn]
b16	[Se | Ti]
b17	[Sn | Zn]

Figure S3. Silhouette widths values (s) within a cluster $k = 3, i = 1,2,3$. Cluster number i, a number of analyses (n_i), average s_i and Jaccard similarity value j_i per cluster are given. Sum of squared errors versus and the number of clusters $k = 1, \ldots, 10$ showing that 3 clusters are sufficient for k-means clustering.



Supplementary Material B

Table S4. Summary statistics (in ppm) for three clusters obtained via k-means algorithm from N = 4,989 dataset

parameters/clusters	1	2	3	1	2	3	1	2	3	1	2	3	1	2	3	1	2	3
	Ag			**As**			**Au**			**Bi**			**Cu**			**Co**		
minimum	0.0016	0.0014	0.0018	0.0969	0.2602	0.2771	0.0003	0.0003	0.0004	0.0003	0.0003	0.0005	0.1017	0.0807	0.1522	0.0192	0.6345	0.2818
geometric mean	0.0068	0.0063	0.1223	14.601	20.342	28.484	0.0026	0.0025	0.0157	0.0036	0.0047	0.5872	0.6145	0.6594	10.169	434.07	450.20	534.80
median	0.0059	0.0057	0.1130	14.601	21.595	26.396	0.0020	0.0018	0.0120	0.0024	0.0029	0.5577	0.4934	0.5014	8.7360	440.73	560.22	604.18
mean	0.0150	0.0342	1.9494	45.254	66.004	97.419	0.0206	0.0190	0.2063	0.0237	0.0399	4.0003	1.7937	2.9092	152.79	2203.9	1329.5	2256.6
standard deviation	0.0882	0.6781	10.791	120.36	311.80	301.36	0.2383	0.1551	0.9227	0.1346	0.1415	11.499	8.3139	31.454	564.82	4996.1	2347.9	5021.0
maximum	2.8356	27.327	223.78	3227.1	8586.3	5087.5	8.4104	3.7857	14.926	3.7275	2.3194	156.85	201.66	1096.4	5468.0	46103	39276	44267
	Mn			**Ni**			**Re**			**Se**			**Sn**			**Te**		
minimum	0.0649	0.0628	0.0637	0.0026	1.8224	0.0047	0.0003	0.0004	0.0004	1.6048	5.6708	4.0150	0.0179	0.0163	0.0222	0.0084	0.0123	0.0091
geometric mean	0.3007	0.2886	0.7378	3.5316	227.02	32.313	0.0050	0.0178	0.0076	86.642	152.91	109.77	0.0509	0.0500	0.0768	0.4373	3.2311	4.1176
median	0.2731	0.2646	0.4537	4.4059	252.65	41.339	0.0039	0.0256	0.0072	99.021	163.20	124.26	0.0427	0.0428	0.0542	0.4019	4.0269	5.2625
mean	0.5138	0.5123	4.5165	13.812	442.05	213.18	0.0172	0.0489	0.0274	107.66	175.08	137.61	0.0631	0.3468	0.4968	4.9304	16.304	18.404
standard deviation	1.4365	1.4515	31.395	28.839	543.25	436.90	0.0368	0.0697	0.0506	62.283	89.386	84.898	0.0662	13.052	5.3147	32.817	45.103	58.792
maximum	34.800	32.777	809.23	402.95	4357.8	3886.4	0.7295	0.8067	0.6624	483.77	1075.5	601.80	1.2688	611.69	122.34	990.14	738.43	815.40
	Ti			**^{204}Pb**			**^{206}Pb**			**^{207}Pb**			**^{208}Pb**			**Zn**		
minimum	0.0550	0.0524	0.0507	0.0447	0.0442	0.0490	0.0010	0.0011	0.0098	0.0009	0.0009	0.0022	0.0007	0.0007	0.0036	0.0915	0.0894	0.1403
geometric mean	0.4439	0.4205	0.4698	0.1895	0.1811	0.7490	0.0162	0.0172	2.8705	0.0133	0.0120	0.7925	0.0106	0.0108	0.6312	0.4116	0.3782	0.7859
median	0.4160	0.4074	0.4346	0.2095	0.2080	0.4427	0.0105	0.0104	2.2892	0.0102	0.0098	0.6278	0.0083	0.0084	0.4942	0.3874	0.3376	0.5902
mean	0.6608	0.6110	0.8149	0.2438	0.2346	5.0604	0.0686	0.0762	21.726	0.0390	0.0309	6.4843	0.0298	0.0297	5.8416	0.5197	0.4677	3.0003
standard deviation	1.0592	0.6901	2.3591	0.3107	0.2465	25.096	0.2556	0.2425	68.016	0.1518	0.0691	28.627	0.0900	0.0831	26.588	0.5560	0.4270	12.823
maximum	33.211	8.4155	56.448	9.0058	4.3204	467.70	4.1881	4.2200	765.87	5.2060	0.8667	490.77	2.5097	2.0863	466.65	11.702	8.4170	167.87
parameters/clusters	1	2	3	1	2	3	1	2	3	1	2	3	1	2	3	1	2	3

Supplementary Material B

Table S5. Summary statistics (in ppm) for three clusters obtained via k-means algorithm from N = 1,501 dataset

parameters/clusters	1	2	3	1	2	3	1	2	3	1	2	3	1	2	3	1	2	3
	Ag			**As**			**Au**			**Bi**			**Cu**			**Co**		
minimum	0.0023	0.0016	0.0016	0.3577	0.3966	0.4527	0.0006	0.0003	0.0004	0.0021	0.0003	0.0005	0.1410	0.0964	0.1312	0.4903	1.1091	0.2818
geometric mean	1.1852	0.0082	0.0373	33.264	23.251	26.473	0.0831	0.0047	0.0061	3.4451	0.0209	0.1756	44.611	1.0384	4.3906	477.36	590.10	640.99
median	1.1851	0.0063	0.0407	31.776	23.089	25.090	0.0934	0.0037	0.0042	3.9807	0.0231	0.1962	32.424	0.8116	4.4170	533.50	665.57	675.18
mean	5.5525	0.0224	0.1899	118.50	89.193	83.139	0.4832	0.0760	0.0640	10.370	0.1041	0.6747	384.75	6.4174	28.202	2165.8	2113.0	2626.7
standard deviation	18.200	0.0970	1.1715	257.42	444.78	309.08	1.4726	0.4746	0.3672	18.032	0.2575	1.7708	907.55	57.951	110.34	5174.4	4190.4	5470.8
maximum	223.78	2.1587	27.327	1910.5	8586.3	5087.5	14.926	8.4104	7.0316	156.85	3.1234	29.130	5468.0	1096.4	1349.2	44267	39276	40589
	Mn			**Ni**			**Re**			**Se**			**Sn**			**Te**		
minimum	0.0744	0.0646	0.0601	0.0181	0.0240	0.0156	0.0004	0.0004	0.0004	4.7775	8.2873	4.0150	0.0212	0.0173	0.0201	0.0146	0.0107	0.0097
geometric mean	0.7986	0.4303	0.7057	24.891	81.507	38.070	0.0058	0.0190	0.0092	105.00	138.61	114.19	0.0898	0.0534	0.0669	6.6221	4.1816	3.1466
median	0.6061	0.2754	0.4162	27.974	129.64	51.749	0.0048	0.0244	0.0109	120.19	148.52	125.64	0.0555	0.0414	0.0476	8.3624	4.8729	3.8349
mean	5.5154	1.2379	3.6276	182.05	311.56	226.35	0.0225	0.0474	0.0313	135.11	161.61	140.63	0.5574	1.0485	0.4449	20.415	14.508	16.306
standard deviation	49.356	3.1460	13.895	386.17	498.38	435.70	0.0468	0.0685	0.0558	85.873	93.331	83.123	3.9023	24.368	5.7204	58.759	32.268	57.406
maximum	809.23	34.800	203.30	3886.4	4357.8	3411.4	0.3900	0.7295	0.6624	418.06	1075.5	506.32	51.924	611.69	122.34	815.40	386.82	814.41
	Ti			**^{204}Pb**			**^{206}Pb**			**^{207}Pb**			**^{208}Pb**			**Zn**		
minimum	0.0499	0.0541	0.0567	0.0650	0.0433	0.0445	0.2012	0.0011	0.0044	0.0141	0.0015	0.0027	0.0036	0.0008	0.0024	0.1396	0.1251	0.1283
geometric mean	0.4673	0.4956	0.4785	3.1297	0.1685	0.3111	18.154	0.0366	0.8561	4.6027	0.0272	0.2354	3.8100	0.0239	0.1962	1.1135	0.4689	0.6385
median	0.4243	0.4726	0.4280	3.3754	0.1828	0.2404	16.053	0.0398	0.8410	4.5920	0.0269	0.2495	3.8676	0.0261	0.1992	0.7588	0.4662	0.5604
mean	0.9964	0.7501	0.8060	13.640	0.2465	0.6824	58.240	0.1003	2.8036	17.673	0.0705	0.7579	15.927	0.0551	0.7049	5.0120	0.6426	1.9260
standard deviation	3.7945	0.7791	1.7411	42.210	0.3345	1.4686	107.61	0.2613	9.1897	47.629	0.1416	2.0816	44.326	0.0854	2.2160	16.117	0.8082	10.374
maximum	56.448	7.6922	33.211	467.70	4.1830	23.348	765.87	4.2200	180.71	490.77	1.6920	39.858	466.65	0.5756	40.895	156.25	8.4170	167.87
parameters/clusters	1	2	3	1	2	3	1	2	3	1	2	3	1	2	3	1	2	3

Supplementary Material B

Table S6. Summary statistics (in ppm) for three clusters obtained via k-means algorithm from N = 525 dataset

parameters/clusters	1	2	3	1	2	3	1	2	3	1	2	3	1	2	3	1	2	3
	Ag			**As**			**Au**			**Bi**			**Cu**			**Co**		
minimum	0.0021	0.0017	0.0143	1.4325	0.8367	0.3600	0.0007	0.0006	0.0007	0.0016	0.0013	0.0025	0.1475	0.1883	0.3473	5.6749	1.4888	0.5547
geometric mean	0.1960	0.0276	2.0358	38.568	32.480	27.545	0.0261	0.0124	0.1465	0.8577	0.1723	6.8781	14.366	5.3476	92.130	823.51	716.24	367.75
median	0.1787	0.0215	2.2949	36.258	33.823	28.775	0.0245	0.0099	0.1839	1.0809	0.2055	9.3740	12.593	4.1904	136.22	746.76	943.91	450.03
mean	2.0119	0.4544	7.4957	95.889	119.11	117.72	0.1629	0.1711	0.5845	3.6045	0.7161	18.088	221.66	38.395	424.57	2804.2	3265.2	2058.0
standard deviation	15.317	3.4956	16.381	175.65	444.61	240.50	0.5014	0.7419	1.6062	8.0654	2.4890	24.296	796.04	141.04	718.18	5681.2	6555.4	4959.8
maximum	223.78	47.780	95.397	1510.9	5087.5	1483.1	4.8422	9.0287	14.926	93.509	29.130	156.85	5468.0	1096.4	4713.2	44267	38047	33546
	Mn			**Ni**			**Re**			**Se**			**Sn**			**Te**		
minimum	0.0745	0.0670	0.0773	0.1642	0.2304	0.0398	0.0004	0.0004	0.0005	6.7453	9.3390	8.2395	0.0191	0.0156	0.0249	0.0384	0.1212	0.0327
geometric mean	1.1354	0.9754	0.8822	62.775	103.34	23.912	0.0114	0.0209	0.0061	128.74	134.85	103.93	0.0834	0.0869	0.1227	5.7910	8.2400	7.9956
median	0.9423	0.8129	0.7744	93.754	131.40	30.644	0.0159	0.0285	0.0059	140.35	141.49	118.90	0.0761	0.0819	0.0814	7.9219	8.9625	9.2850
mean	5.6951	2.9717	3.4227	319.90	336.14	128.96	0.0321	0.0549	0.0219	155.22	156.94	127.09	0.2317	4.1549	1.1668	17.406	20.209	21.160
standard deviation	20.515	5.7017	14.780	545.90	590.84	250.05	0.0476	0.0787	0.0479	88.442	83.387	76.610	1.0309	44.381	6.1762	38.509	37.262	45.127
maximum	203.30	37.916	152.55	3886.4	4357.8	1396.4	0.3334	0.6624	0.3900	469.57	483.77	405.49	14.700	611.69	51.924	393.96	296.31	432.18
	Ti			**^{204}Pb**			**^{206}Pb**			**^{207}Pb**			**^{208}Pb**			**Zn**		
minimum	0.0565	0.0577	0.0488	0.0542	0.0430	1.1962	0.1295	0.0039	5.2471	0.0720	0.0033	1.3729	0.0136	0.0028	1.2403	0.1237	0.1138	0.1610
geometric mean	0.5129	0.5182	0.4552	1.1891	0.1945	13.866	5.5899	0.2176	68.865	1.6316	0.1065	20.284	1.3154	0.0940	17.316	0.9569	0.7015	2.2733
median	0.4233	0.5364	0.4041	1.4210	0.2096	12.615	5.4487	0.2327	68.105	1.7477	0.1150	19.432	1.4592	0.1018	15.780	0.7414	0.6528	1.7079
mean	1.0456	0.7170	1.1657	2.1443	0.2971	31.152	11.477	0.6110	126.32	2.7782	0.1872	40.153	2.3755	0.1713	36.425	3.2469	1.9344	9.7918
standard deviation	2.2733	0.5808	5.4026	2.4102	0.3258	63.642	16.412	1.0157	147.23	3.0128	0.1972	70.482	2.7598	0.2102	65.830	13.026	11.907	23.802
maximum	23.089	2.8503	56.448	15.014	2.4952	467.70	112.10	8.2948	765.87	16.939	1.3251	490.77	16.366	1.6727	466.65	164.11	167.87	156.25
parameters/clusters	1	2	3	1	2	3	1	2	3	1	2	3	1	2	3	1	2	3

Supplementary Material C

Table S7. Results from regression of log [Au] for the ilr-coodinates of the remaining elements; N = 4,926

	Classic Regression						Robust Regression				
	Estimate	**Std. Error**	**t value**	**Pr(>|t|)**	**significance**		**Estimate**	**Std. Error**	**t value**	**Pr(>|t|)**	**significance**
Intercept	-0.59	0.09	-6.61	0.000	***	Intercept	-1.50	0.08	-19.83	0.000	***
As	-0.01	0.01	-1.17	0.243		As	-0.01	0.01	-2.79	0.005	**
Bi	0.07	0.01	12.36	0.000	***	Bi	0.03	0.00	7.39	0.000	***
Cu	0.00	0.01	-0.68	0.498		Cu	0.00	0.01	-0.02	0.987	
Co	-0.01	0.00	-2.11	0.035	*	Co	-0.01	0.00	-2.97	0.003	**
Mn	0.03	0.01	2.70	0.007	**	Mn	0.03	0.01	3.20	0.001	**
Ni	0.01	0.00	3.77	0.000	***	Ni	0.00	0.00	1.23	0.220	
Re	-0.02	0.01	-3.46	0.001	***	Re	0.01	0.00	2.19	0.028	*
Se	-0.22	0.01	-18.47	0.000	***	Se	-0.14	0.01	-13.46	0.000	***
Sn	-0.02	0.01	-1.48	0.140		Sn	-0.12	0.01	-11.61	0.000	***
Te	0.05	0.00	11.25	0.000	***	Te	0.01	0.00	4.26	0.000	***
Ti	0.01	0.01	0.53	0.593		Ti	0.02	0.01	2.94	0.003	**
^{204}Pb	0.03	0.01	2.99	0.003	**	^{204}Pb	0.17	0.01	18.44	0.000	***
^{206}Pb	-0.03	0.01	-3.62	0.000	***	^{206}Pb	-0.01	0.01	-1.66	0.098	.
^{207}Pb	0.02	0.01	1.81	0.070	.	^{207}Pb	0.01	0.01	1.86	0.063	.
^{208}Pb	0.01	0.01	1.68	0.092	.	^{208}Pb	0.01	0.01	1.75	0.080	.
Zn	-0.05	0.01	-4.34	0.000	***	Zn	-0.05	0.01	-4.59	0.000	***
Ag	0.13	0.01	16.76	0	***	Ag	0.06	0.01	8.55	0.000	***
Multiple R-squared: 0.35; Adjusted R-squared 0.34						**Multiple R-squared 0.29; Adjusted R-squared 0.29**					

Table S8. Results from regression of log [Au] for the ilr-coordinates of the remaining elements; N = 1,501

	Classic Regression					Robust Regression					
	Estimate	**Std. Error**	**t value**	**Pr(>|t|)**	**significance**	**Estimate**		**Std. Error**	**t value**	**Pr(>|t|)**	**significance**
Intercept	-0.13	0.19	-0.71	0.479		Intercept	0.11	0.17	0.67	0.505	
As	0.00	0.01	-0.25	0.804		As	0.01	0.01	0.71	0.481	
Bi	0.06	0.01	4.92	0.000	***	Bi	0.05	0.01	4.12	0.000	***
Cu	-0.02	0.01	-1.37	0.172		Cu	-0.02	0.01	-1.57	0.117	
Co	0.00	0.01	-0.05	0.962		Co	-0.02	0.01	-2.01	0.045	*
Mn	-0.01	0.02	-0.59	0.556		Mn	-0.03	0.01	-2.18	0.030	*
Ni	0.02	0.01	1.72	0.087	.	Ni	0.01	0.01	0.75	0.451	
Re	-0.05	0.01	-4.09	0.000	***	Re	0.00	0.01	-0.36	0.719	
Se	-0.32	-0.03	11.89	0.000	***	Se	-0.33	0.02	-13.55	0.000	***
Sn	0.05	0.02	2.46	0.014	*	Sn	0.01	0.02	0.36	0.719	
Te	0.11	0.01	9.27	0.000	***	Te	0.07	0.01	6.61	0.000	***
Ti	-0.01	0.02	-0.30	0.763		Ti	0.00	0.02	0.11	0.911	
^{204}Pb	0.05	0.02	2.24	0.025	*	^{204}Pb	0.10	0.02	5.52	0.000	***
^{206}Pb	-0.05	0.02	-3.02	0.003	**	^{206}Pb	-0.05	0.01	-3.07	0.002	**
^{207}Pb	0.01	0.02	0.24	0.807		^{207}Pb	0.00	0.02	0.15	0.879	
^{208}Pb	0.00	0.02	-0.02	0.982		^{208}Pb	-0.01	0.02	-0.28	0.777	
Zn	-0.01	0.02	-0.61	0.545		Zn	0.00	0.02	0.04	0.968	
Ag	0.18	0.01	13.45	0.000	***	Ag	0.18	0.01	14.63	0.000	***
Multiple R-squared 0.40; Adjusted R-aquared 0.39						**Multiple R-squared 0.46; Adjusted R-squared 0.46**					

Supplementary Material C

Table S9. Results from regression of log [Au] for the ilr-coordinates of the remaining elements; N = 525

	Classic Regression						Robust Regression				
	Estimate	**Std. Error**	**t value**	**Pr(>|t|)**	**significance**		**Estimate**	**Std. Error**	**t value**	**Pr(>|t|)**	**significance**
(Intercept)	-0.26	0.30	-0.87	0.385		Intercept	-0.03	0.28	-0.12	0.902	
As	0.01	0.02	0.60	0.552		As	0.01	0.02	0.38	0.706	
Bi	0.09	0.02	4.14	0.000	***	Bi	0.08	0.02	3.93	0.000	***
Cu	0.00	0.02	-0.21	0.833		Cu	-0.01	0.02	-0.81	0.419	
Co	0.01	0.02	0.49	0.621		Co	-0.02	0.02	-1.42	0.156	
Mn	-0.05	0.03	-1.95	0.052	.	Mn	-0.07	0.02	-2.76	0.006	**
Ni	0.02	0.02	1.17	0.242		Ni	0.03	0.02	1.92	0.056	.
Re	-0.06	0.02	-3.24	0.001	**	Re	-0.07	0.02	-3.65	0.000	***
Se	-0.34	0.04	-7.70	0.000	***	Se	-0.35	0.04	-8.38	0.000	***
Sn	0.04	0.03	1.51	0.131		Sn	0.03	0.03	1.11	0.270	
Te	0.14	0.02	5.86	0.000	***	Te	0.12	0.02	5.60	0.000	***
Ti	0.00	0.03	-0.01	0.992		Ti	0.04	0.03	1.15	0.251	
^{204}Pb	0.00	0.04	-0.05	0.960		^{204}Pb	0.02	0.04	0.56	0.574	
^{206}Pb	-0.01	0.04	-0.17	0.863		^{206}Pb	-0.01	0.04	-0.23	0.817	
^{207}Pb	0.02	0.06	0.31	0.761		^{207}Pb	0.00	0.06	0.04	0.967	
^{208}Pb	-0.05	0.06	-0.93	0.351		^{208}Pb	0.01	0.05	0.21	0.831	
Zn	0.02	0.03	0.66	0.513		Zn	0.07	0.03	2.48	0.013	*
Ag	0.17	0.02	7.80	0.000	***	Ag	0.20	0.02	9.91	0.000	***
Multiple R-squared 0.45; Adjusted R-squared 0.43						**Multiple R-squared 0.52; Adjusted R-squared 0.51**					

SUPPLEMENTARY MATERIAL D

FOR CHAPTER 5 – DEFINING IOCG SIGNATURES THROUGH COMPOSITIONAL DATA ANALYSIS: A CASE STUDY OF LITHOGEOCHEMICAL ZONING FROM THE OLYMPIC DAM DEPOSIT, SOUTH AUSTRALIA

APPENDIX A: THE AITCHISON VARIATION MATRIX

ELECTRONIC APPENDIX A FOR CHAPTER 4

Appendix 1. The variation matrix.

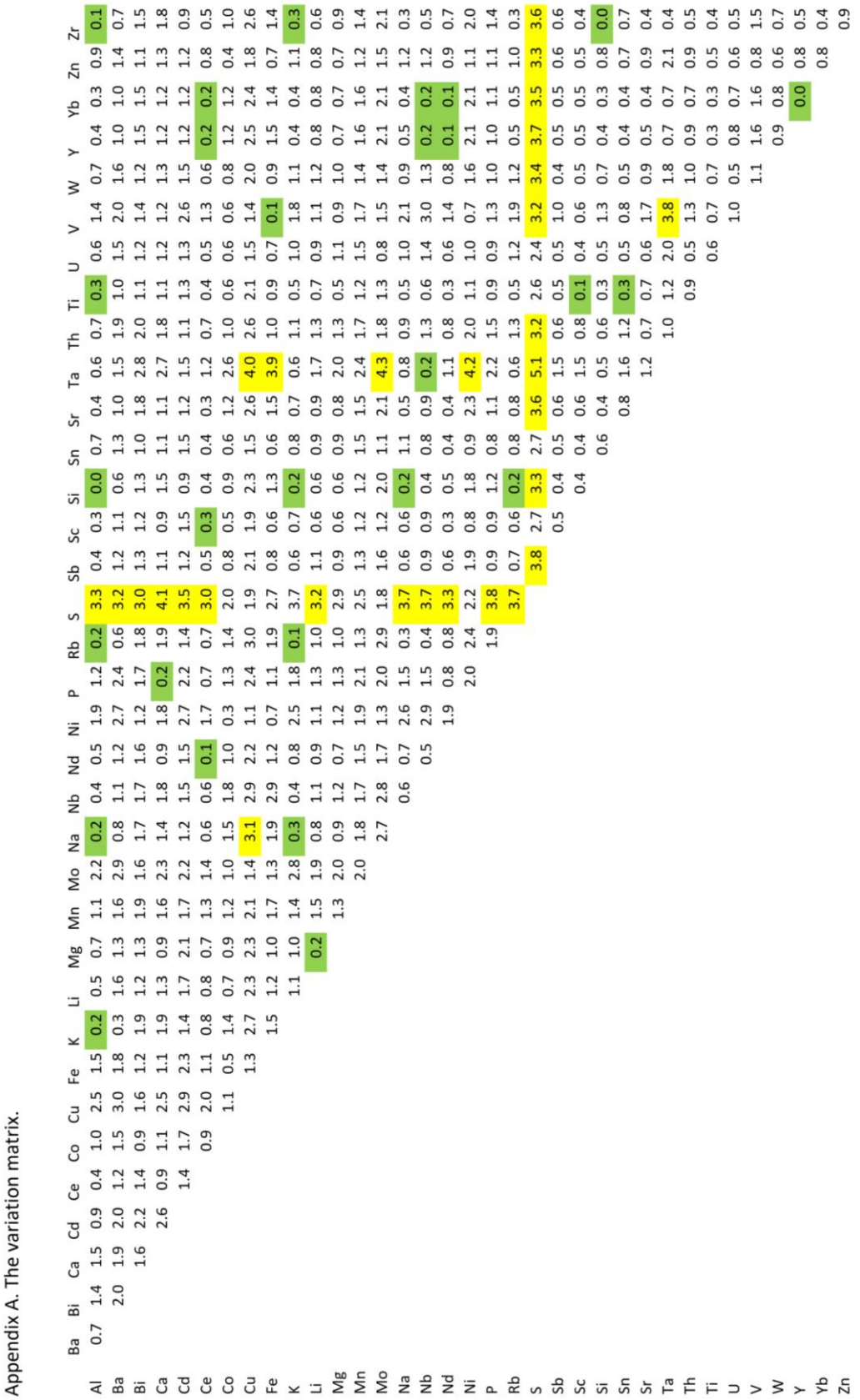
	Ag	Al	Au	As	Ba	Bi	Ca	Ce	Cl	Co	CO_2	Cu	F	Fe	Ga	K	Mg	Mn	Mo	Na	Nb	Nd	Ni	P	S	Sb	Se	Si	Sn	Sr	Ta	Te	Th	Ti	U	W	Y	Zr	Zn
Al	2.6																																					
Au	1.9	4.2																																				
As	2.0	3.7	1.7																																			
Ba	3.1	4.0	3.1	1.4																																		
Bi	1.0	3.1	1.8	1.5	2.5																																	
Ca	1.7	2.9	2.6	2.2	3.0	1.5																																
Ce	0.9	2.2	1.2	1.2	2.0	0.9	1.2																															
Cl	1.8	1.6	3.4	2.4	3.5	2.2	2.3	1.5																														
Co	1.9	2.1	3.0	3.2	4.7	2.0	1.9	1.5	1.6																													
CO_2	4.1	3.7	5.7	5.4	5.9	4.2	3.1	3.6	3.3	2.6																												
Cu	1.7	3.9	2.7	3.8	4.9	1.9	2.3	1.9	3.8	2.1	4.6																											
F	1.6	1.8	2.3	2.2	2.6	1.6	0.7	0.9	2.2	1.8	3.3	2.1																										
Fe	1.2	2.9	1.7	1.0	2.5	1.1	1.5	0.6	1.1	1.3	3.5	2.5	1.7																									
Ga	1.4	0.6	2.5	1.9	2.5	1.7	1.7	0.9	0.7	1.3	3.1	2.9	1.1	1.1																								
K	3.9	0.4	5.8	5.2	5.0	4.4	4.1	3.5	2.9	3.5	4.4	5.0	2.6	4.5	1.5																							
Mg	2.2	1.0	3.8	3.2	4.2	2.8	2.4	2.0	0.8	1.4	3.1	4.0	2.3	1.8	0.7	2.2																						
Mn	3.9	3.0	5.8	5.5	6.3	4.2	3.3	3.6	2.5	2.0	0.9	4.8	3.4	3.1	2.6	3.9	2.1																					
Mo	1.5	3.4	1.3	0.9	1.7	1.2	1.7	0.8	2.3	2.5	4.2	2.5	1.5	0.9	1.7	4.7	3.2	4.5																				
Na	2.2	0.8	4.0	2.8	3.2	2.6	2.4	1.8	0.8	2.1	3.5	4.1	2.0	1.9	0.5	1.7	0.9	2.8	2.7																			
Nb	1.3	2.1	2.1	1.8	3.2	1.6	1.9	0.9	0.9	1.3	3.7	2.8	1.8	0.5	0.7	3.7	1.3	3.0	1.7	1.4																		
Nd	0.9	2.0	1.5	1.3	2.2	0.9	1.2	**0.1**	1.3	1.3	3.3	1.9	0.9	0.6	0.7	3.3	1.7	3.2	1.0	1.6	0.7																	
Ni	2.1	2.1	3.4	2.9	4.5	2.4	2.2	1.9	1.3	0.9	3.2	3.1	2.3	1.3	1.3	3.5	1.2	2.5	2.8	1.8	1.3	1.6																
P	1.3	2.4	1.8	1.5	2.9	1.4	1.6	0.7	1.1	1.1	3.6	2.6	1.7	0.3	0.9	4.0	1.4	3.1	1.5	1.7	0.5	0.6	1.1															
S	1.5	3.6	1.8	2.1	3.0	1.4	1.6	1.0	2.4	1.4	3.6	1.4	1.6	0.9	2.0	5.0	3.0	3.6	1.2	3.1	1.6	1.1	2.1	1.2														
Sb	2.0	3.5	1.9	**0.4**	1.2	1.5	2.0	1.2	2.4	3.2	4.9	3.6	2.0	1.2	1.8	4.8	3.1	5.2	0.8	2.7	1.9	1.3	3.0	1.6	2.1													
Se	2.0	3.7	2.7	3.0	4.9	2.3	2.8	1.9	2.5	1.9	5.0	2.4	2.8	1.6	2.3	5.3	2.9	4.4	2.8	3.3	1.6	1.8	2.2	1.5	1.9	3.3												
Si	2.1	0.4	3.5	2.7	3.0	2.5	2.4	1.7	0.9	1.9	3.3	3.7	1.6	1.9	0.3	1.1	0.9	2.7	2.4	0.5	1.4	1.5	1.8	1.7	2.8	2.5	3.1											
Sn	1.4	2.7	1.9	1.1	2.2	1.4	1.7	0.8	1.5	2.1	4.0	3.1	1.7	0.7	1.1	4.2	2.1	3.8	1.1	1.9	0.9	0.8	2.2	1.0	1.6	1.2	2.5	1.9										
Sr	1.3	2.1	1.5	0.9	1.3	1.2	1.6	0.5	1.6	2.0	3.9	2.6	1.2	0.8	0.8	3.3	2.1	3.9	0.9	1.6	1.0	0.6	2.1	0.8	1.2	1.0	2.3	1.4	0.9									
Ta	1.6	1.0	2.8	2.2	2.9	2.0	2.1	1.2	0.7	1.4	3.3	3.2	1.5	1.2	**0.3**	2.0	0.9	2.6	2.0	0.7	0.7	1.0	1.4	1.1	2.1	2.1	2.3	0.5	1.4	1.1								
Te	1.3	2.9	1.5	1.1	2.0	1.3	1.7	0.7	1.8	2.3	4.3	2.7	1.6	0.9	1.4	4.4	2.5	4.3	0.8	2.3	1.3	0.7	2.4	1.1	1.4	1.1	2.6	2.1	0.8	0.8	1.7							
Th	1.8	0.4	3.2	2.6	3.1	2.2	2.3	1.3	0.8	1.6	3.2	3.3	1.5	1.7	**0.2**	1.2	0.8	2.6	2.3	0.5	1.0	1.1	1.6	1.4	2.5	2.5	2.8	0.2	1.6	1.3	**0.4**	1.9						
Ti	2.2	0.5	3.7	2.6	3.0	2.7	2.5	1.7	1.0	2.1	3.5	4.0	1.8	2.0	0.4	1.1	0.8	2.8	2.5	0.6	1.5	1.6	1.8	1.7	3.0	2.5	3.3	0.2	1.9	1.5	0.6	2.2	0.4					
U	1.0	2.5	1.7	2.2	3.4	1.1	1.4	**0.6**	1.9	1.1	3.4	1.0	1.2	1.0	1.4	3.8	2.2	3.4	1.4	2.4	1.1	**0.6**	1.8	1.0	0.8	2.2	1.6	2.2	1.5	1.2	1.6	1.4	1.7	2.4				
W	1.5	3.8	1.2	**0.8**	1.9	1.3	1.7	0.8	2.4	2.6	4.6	2.8	1.7	0.8	1.9	5.4	3.2	4.8	**0.6**	3.0	1.7	1.0	2.9	1.3	1.4	0.8	2.6	2.9	0.9	1.0	2.2	0.8	2.6	2.9	1.5			
Y	1.1	1.2	2.3	1.9	2.7	1.3	1.3	**0.6**	0.8	1.0	2.9	2.2	1.0	0.8	**0.3**	2.3	1.1	2.6	1.6	1.0	**0.6**	**0.4**	1.2	0.7	1.4	1.8	1.9	0.9	1.0	0.8	**0.6**	1.2	0.6	1.0	**0.8**	1.6		
Zr	2.3	0.4	3.7	2.8	3.0	2.7	2.7	1.8	1.1	2.2	3.5	4.0	1.8	2.2	**0.4**	0.9	1.0	2.8	2.6	0.6	1.7	1.7	2.1	1.9	3.1	2.6	3.5	0.2	2.0	1.6	**0.6**	2.2	0.3	0.2	2.4	3.0	1.0	
Zn	2.0	1.5	3.5	2.5	3.3	2.3	2.4	1.7	1.2	1.8	3.5	3.6	2.0	1.7	0.9	2.5	1.3	2.8	2.5	1.2	1.6	1.5	1.7	1.7	2.7	2.4	3.1	1.1	1.9	1.8	1.1	2.1	1.0	1.2	2.1	2.6	1.1	1.2

SUPPLEMENTARY MATERIAL E

FOR CHAPTER 6 – MINERALIZATION-ALTERATION FOOTPRINTS IN THE OLYMPIC DAM IOCG DISTRICT, SOUTH AUSTRALIA: THE ACROPOLIS PROSPECT

APPENDIX A: THE AITCHISON VARIATION MATRIX

ELECTRONIC APPENDIX A FOR CHAPTER 6



Appendix A. The variation matrix.

SUPPLEMENTARY MATERIAL F

FOR CHAPTER 7 – GEOCHEMICAL DATA

ANALYSIS AND 3D MODELLING OF WIRRDA

WELL PROSPECT, SOUTH AUSTRALIA:

STRUCTURAL CONTROL ON IRON-OXIDE COPPER

GOLD MINERALISATION

APPENDIX A: SEQUENTIAL BINARY PARTITIONING USED TO OBTAIN 51 ILR-COORDINATES OF 52 GEOCHEMICAL VARIABLES

APPENDIX B: THE AITCHISON VARIATION MATRIX

APPENDIX C: RESULTS OF PCA GIVEN AS THE PROPORTIONS OF EXPLAINED VARIANCE BY FIRST, SECOND AND THIRD PRINCIPAL COMPONENTS, WITH LOADINGS

ELECTRONIC APPENDIX A FOR CHAPTER 7

Appendix A. Sequential binary partitioning used to obtain 51 ilr-coordinates of 52 geochemical variables. The procedure of partitioning is based on the hierarchical dendrogram (Fig. 6). Composite variables within a balance are the geometric mean of all components.

Balance	Binary partition
b1	[CO_2, Mn | Ba, Na, Sr, Cs, Tl, K, Rb, Al, Si, Ta, Hf, Zr, Nb, Th, Cd, Cr, Zn, Ti, Li, Mg, Ca, P, Sc, V, Co, Fe, Ni, Sb, Sn, W, As, In, LOI, Ce, Nd, Ge, Se, Lu, Y, Yb, Be, Ga, Cu, S, Bi, Au, Ag, Mo, Te, U]
b2	[CO_2 | Mn]
b3	[Ba, Na, Sr, Cs, Tl, K, Rb, Al, Si, Ta, Hf, Zr, Nb, Th, Cd, Cr, Zn, Ti, Li, Mg, Ca, P, Sc, V, Co, Fe, Ni, Sb, Sn, W, As, In, LOI, Ce, Nd, Ge, Se, Lu, Y, Yb, Be, Ga | Cu, S, Bi, Au, Ag, Mo, Te, U]
b4	[Ba, Na, Sr, Cs, Tl, K, Rb, Al, Si, Ta, Hf, Zr, Nb, Th | Cd, Cr, Zn, Ti, Li, Mg, Ca, P, Sc, V, Co, Fe, Ni, Sb, Sn, W, As, In, LOI, Ce, Nd, Ge, Se, Lu, Y, Yb, Be, Ga]
b5	[Ba, Na, Sr | Cs, Tl, K, Rb, Al, Si, Ta, Hf, Zr, Nb, Th]
b6	[Ba | Na, Sr]
b7	[Na | Sr]
b8	[Cs, Tl, K, Rb, Al, Si, Ta, Hf, Zr | Nb, Th]
b9	[Nb | Th]
b10	[Cs, Tl | K, Rb, Al, Si, Ta, Hf, Zr]
b11	[Cs | Tl]
b12	[K, Rb | Al, Si, Ta, Hf, Zr]
b13	[K | Rb]
b14	[Al, Si | Ta, Hf, Zr]
b15	[Al | Si]
b16	[Ta | Hf, Zr]
b17	[Hf | Zr]
b18	[Cd | Cr, Zn, Ti, Li, Mg, Ca, P, Sc, V, Co, Fe, Ni, Sb, Sn, W, As, In, LOI, Ce, Nd, Ge, Se, Lu, Y, Yb, Be, Ga]
b19	[Cr, Zn, Ti, Li, Mg | Ca, P, Sc, V, Co, Fe, Ni, Sb, Sn, W, As, In, LOI, Ce, Nd, Ge, Se, Lu, Y, Yb, Be, Ga]
b20	[Cr | Zn, Ti, Li, Mg]
b21	[Zn | Ti, Li, Mg]
b22	[Ti | Li, Mg]
b23	[Li | Mg]
b24	[Ca, P, Sc, V, Co, Fe, Ni | Sb, Sn, W, As, In, LOI, Ce, Nd, Ge, Se, Lu, Y, Yb, Be, Ga]
b25	[Ca, P | Sc, V, Co, Fe, Ni]
b26	[Ca | P]
b27	[Sc, V | Co, Fe, Ni]
b28	[Sc | V]
b29	[Co | Fe, Ni]
b30	[Fe | Ni]
b31	[Sb, Sn, W, As, In, LOI | Ce, Nd, Ge, Se, Lu, Y, Yb, Be, Ga]
b32	[Sb, Sn, W | As, In, LOI]
b33	[Sb | Sn, W]
b34	[Sn | W]
b35	[As | In, LOI]

b36	[In | LOI]
b37	[Ce, Nd | Ge, Se, Lu, Y, Yb, Be, Ga]
b38	[Ce | Nd]
b39	[Ge | Se, Lu, Y, Yb, Be, Ga]
b40	[Se | Lu, Y, Yb, Be, Ga]
b41	[Lu, Y, Yb | Be, Ga]
b42	[Lu | Y, Yb]
b43	[Y | Yb]
b44	[Be | Ga]
b45	[Cu, S | Bi, Au, Ag, Mo, Te, U]
b46	[Cu | S]
b47	[Bi | Au, Ag, Mo, Te, U]
b48	[Au | Ag, Mo, Te, U]
b49	[Ag | Mo, Te, U]
b50	[Mo | Te, U]
b51	[Te | U]

ELECTRONIC APPENDIX B FOR CHAPTER 7

Appendix B. The Aitchison variation matrix

	Ag	Al	As	Au	Ba	Be	Bi	CO2	Ca	Cd	Ce	Cu	Co	Cs	Cr	Fe	Ga	Ge	Hf	In	K	Li	Lu	Mg	Mn	Mo	Na	Nb	Nd	Ni	P	Rb	S	Sc	Sb	Se	Si	Sn	Sr	Ta	Te	Th	Ti	Tl	U	V	W	Y	Yb	Zn	Zr	LOI
Al	2.6																																																		
As	1.9	1.4																																																	
Au	2.0	2.8	2.0																																																
Ba	3.4	1.0	2.3	3.5																																														
Be	1.8	0.5	0.9	2.1	1.3																																													
Bi	2.5	2.9	1.8	2.6	4.3	2.9																																													
CO2	6.8	5.2	4.7	6.4	6.9	4.8	5.5																																												
Ca	2.5	1.0	1.1	2.5	1.9	0.6	2.9	3.8																																											
Cd	2.1	1.6	1.7	2.8	2.0	1.0	3.9	5.8	1.5																																										
Ce	1.7	1.0	1.1	1.7	2.1	0.8	2.4	5.1	1.3	1.7																																								
Cu	1.8	3.1	2.4	2.1	4.3	2.7	2.0	6.0	2.7	3.3	2.0																																							
Co	2.1	1.4	0.8	2.1	2.6	0.8	2.3	4.5	0.8	1.8	1.0	2.2																																						
Cs	2.7	0.4	1.9	3.0	1.4	0.6	3.6	6.0	1.4	1.7	1.4	3.7	1.9																																					
Cr	2.7	1.0	1.4	2.7	1.9	0.9	3.1	5.5	1.3	1.9	1.3	3.0	1.4	1.2																																				
Fe	1.6	1.5	0.7	1.8	2.5	0.6	2.4	4.3	0.7	1.3	1.0	2.0	0.5	2.0	1.4																																			
Ga	1.8	0.5	0.8	2.2	1.3	0.1	2.6	4.5	0.5	0.9	0.9	2.6	0.7	0.8	0.9	0.5																																		
Ge	1.9	1.1	1.0	2.1	2.2	0.5	2.9	4.1	0.8	1.3	0.8	2.5	0.8	1.4	1.4	0.5	0.5																																	
Hf	2.9	0.1	1.7	3.1	1.1	0.7	3.2	5.4	1.3	1.7	1.2	3.5	1.7	0.5	1.4	1.9	0.7	1.3																																	
In	1.7	0.9	0.8	1.7	1.7	0.7	2.0	4.2	1.1	1.4	0.9	2.3	1.1	1.1	1.1	0.9	0.6	0.9	1.1																																
K	3.3	0.2	2.2	3.6	1.0	0.9	4.0	6.1	1.6	1.9	1.5	4.1	2.2	0.5	1.4	2.3	0.9	1.7	0.2	1.4																																
Li	2.1	0.3	1.1	2.2	1.4	0.4	2.6	5.3	0.8	1.4	0.7	2.4	0.9	0.6	0.7	1.0	0.4	0.8	0.5	0.8	0.7																														
Lu	1.9	0.4	1.0	2.0	1.2	0.3	2.7	5.0	0.9	1.1	0.7	2.7	1.0	0.7	1.0	0.9	0.3	0.7	0.5	0.7	0.8	0.4																												
Mg	2.3	0.4	1.1	2.3	1.4	0.4	2.8	5.0	0.7	1.5	0.8	2.5	0.8	0.6	0.7	0.9	0.4	0.9	0.6	0.8	0.9	0.1	0.5																												
Mn	4.1	2.4	2.3	3.8	3.8	2.1	3.5	1.6	1.5	2.9	2.4	3.4	1.7	3.1	2.6	1.7	1.8	1.8	2.6	2.0	3.2	2.2	2.2	2.0																												
Mo	1.8	1.8	1.4	2.1	2.8	1.4	2.2	5.7	1.7	2.1	1.2	1.8	1.5	2.3	2.1	1.1	1.3	1.5	2.0	1.5	2.5	1.3	1.5	1.5	3.0																												
Na	2.6	0.4	1.4	2.7	0.8	0.6	3.1	5.6	1.2	1.4	1.4	3.4	1.7	0.6	1.2	1.6	0.5	1.2	0.5	0.9	0.6	0.7	0.6	0.7	2.8	2.0																												
Nb	2.4	0.5	1.4	2.5	1.3	0.6	2.9	5.2	1.2	1.5	1.0	3.0	1.5	0.9	1.5	1.4	0.6	1.1	0.4	1.0	0.7	0.7	0.4	0.8	2.5	1.8	0.6																												
Nd	1.7	0.8	1.0	1.7	1.8	0.6	2.3	4.9	1.1	1.5	0.0	2.1	0.9	1.1	1.2	0.9	0.7	0.7	1.0	0.7	1.3	0.6	0.5	0.6	2.2	1.2	1.1	0.8																												
Ni	2.1	1.3	1.1	2.3	2.3	0.6	3.0	4.5	0.6	1.4	1.1	2.5	0.4	1.7	1.1	0.3	0.5	0.7	1.6	1.2	2.0	0.8	0.9	0.7	1.7	1.6	1.5	1.5	1.0																												
P	2.3	1.0	0.9	2.3	2.0	0.7	2.7	4.1	0.4	1.5	0.8	2.5	0.7	1.5	1.3	0.6	0.5	0.7	1.1	0.9	1.6	0.7	0.8	0.7	1.7	1.4	1.2	1.0	0.7	0.7																												
Rb	3.0	0.2	1.9	3.3	1.1	0.6	3.8	5.8	1.4	1.6	1.3	3.8	1.9	0.4	1.2	1.9	0.7	1.4	0.2	1.2	0.1	0.5	0.6	0.7	2.9	2.3	0.6	0.7	1.1	1.6	1.3																												
S	3.4	3.9	3.1	3.5	5.0	3.1	3.7	5.0	2.6	3.6	2.8	1.9	2.0	4.8	3.8	1.9	2.8	2.5	4.2	3.4	4.9	3.1	3.1	3.2	2.6	2.7	4.5	3.5	2.7	2.0	2.6	4.4																												
Sc	2.0	0.6	0.8	2.3	1.5	0.3	2.7	4.5	0.5	1.1	0.8	2.5	0.6	0.9	0.7	0.5	0.2	0.5	0.8	0.7	1.1	0.3	0.5	0.3	1.7	1.3	0.8	0.9	0.6	0.4	0.5	0.8	2.7																												
Sb	1.7	1.1	0.6	1.9	2.0	0.6	2.1	4.1	0.9	1.4	0.9	2.3	0.8	1.5	1.2	0.5	0.5	0.8	1.4	0.6	1.8	0.9	0.7	0.9	1.8	1.3	1.2	1.1	0.8	0.7	0.8	1.5	2.7	0.6																												
Se	1.7	0.8	1.0	1.9	1.6	0.4	2.6	4.8	0.8	1.1	0.8	2.4	0.8	1.1	1.2	0.7	0.4	0.7	1.0	0.8	1.3	0.6	0.4	0.7	2.2	1.4	0.9	0.8	0.6	0.7	0.7	1.1	2.7	0.5	0.8	0.6																												
Si	2.3	0.1	1.1	2.5	0.9	0.3	2.6	4.9	0.9	1.3	0.9	2.9	1.2	0.4	1.0	1.2	0.3	0.9	0.2	0.7	0.4	0.3	0.3	0.4	2.2	1.6	0.3	0.4	0.7	1.1	0.8	0.3	3.6	0.5	0.6	0.6																												
Sn	1.8	0.8	0.8	1.8	1.6	0.5	2.5	4.7	0.8	1.2	0.7	2.2	0.7	1.3	1.0	0.6	0.4	0.6	1.0	0.7	1.3	0.6	0.4	0.6	1.9	1.4	0.9	0.8	0.6	0.6	0.7	1.0	2.4	0.4	0.5	0.6	0.6																												
Sr	2.7	0.6	1.6	2.6	0.7	1.0	2.8	6.1	1.4	1.9	1.3	3.1	1.9	0.9	1.4	2.0	1.0	1.7	0.7	1.1	0.8	0.8	0.9	0.9	3.3	1.9	0.4	0.9	1.1	2.0	1.2	0.9	4.6	1.1	1.6	1.1	0.5	1.3																												
Ta	2.7	0.2	1.6	2.9	1.1	0.6	3.0	5.4	1.2	1.6	1.2	3.5	1.6	0.5	1.3	1.7	0.6	1.3	0.2	1.1	0.4	0.6	0.4	0.7	2.6	2.0	0.4	0.3	1.0	1.6	1.2	0.4	4.2	0.8	1.2	0.9	0.2	0.9	0.7																												
Te	1.6	2.3	1.3	1.6	3.3	1.4	2.3	4.7	1.6	2.1	1.3	2.1	1.2	2.6	2.2	0.8	1.3	1.2	2.6	1.4	3.2	1.7	1.5	1.8	2.5	1.4	2.3	2.0	1.2	1.3	1.4	2.7	2.4	1.4	1.1	1.3	1.9	1.2	2.7	2.4																												
Th	2.2	0.7	1.5	2.7	1.3	0.6	3.1	5.4	1.3	1.3	1.3	3.4	1.7	0.9	1.7	1.4	0.5	1.1	0.7	1.0	1.0	0.9	0.6	1.1	2.8	1.8	0.5	0.6	1.0	1.6	1.2	0.9	4.1	1.0	1.2	0.8	0.4	1.1	0.9	0.5	2.0																												
Ti	2.4	0.2	1.1	2.5	1.2	0.4	2.9	5.0	0.7	1.4	0.8	2.7	1.0	0.6	0.7	1.1	0.4	0.9	0.4	0.8	0.6	0.2	0.4	0.2	2.1	1.6	0.6	0.7	0.7	0.9	0.7	0.4	3.3	0.3	0.9	0.7	0.3	0.5	0.7	0.5	2.0	1.0																												
Tl	2.5	0.2	1.6	2.9	0.9	0.4	3.6	5.8	1.2	1.3	1.2	3.6	1.7	0.3	1.1	1.6	0.5	1.1	0.4	1.0	0.3	0.5	0.5	0.6	2.8	2.1	0.3	0.6	1.0	1.4	1.2	0.2	4.3	0.7	1.3	0.8	0.2	0.9	0.7	0.3	2.4	0.6	0.5																												
U	1.3	1.8	1.2	1.4	2.7	1.0	2.4	5.4	1.4	1.7	1.0	2.0	1.1	2.0	1.9	0.8	1.1	1.0	2.0	1.1	2.5	1.2	1.0	1.4	2.7	1.3	1.9	1.5	0.9	1.1	1.3	2.2	2.4	1.2	1.0	0.9	1.5	0.9	2.1	1.9	0.9	1.5	1.6	1.8																												
V	2.2	1.3	1.0	2.4	2.2	0.6	3.0	4.6	0.6	1.4	1.1	2.5	0.6	1.6	1.0	0.3	0.5	0.7	1.7	1.1	2.0	0.8	0.9	0.7	1.9	1.5	1.5	1.5	1.0	0.3	0.7	1.6	2.4	0.2	0.7	0.8	1.1	0.6	1.8	1.6	1.4	1.6	0.7	1.3	1.3																												
W	1.9	1.4	0.7	1.8	2.3	0.9	1.9	4.1	1.0	1.7	1.1	2.0	0.7	2.0	1.4	0.6	0.7	0.9	1.7	0.8	2.1	1.1	0.9	1.1	1.8	1.4	1.5	1.3	0.9	0.9	0.8	1.8	2.2	0.7	0.5	0.9	1.1	0.4	1.8	1.5	1.0	1.6	1.1	1.7	1.0	0.8																												
Y	1.9	0.4	0.9	2.0	1.2	0.3	2.5	4.8	0.8	1.1	0.6	2.6	0.9	0.7	1.0	0.8	0.3	0.6	0.5	0.6	0.8	0.4	0.0	0.5	2.1	1.4	0.5	0.4	0.4	0.9	0.6	0.6	3.1	0.4	0.7	0.4	0.3	0.4	0.8	0.4	1.4	0.5	0.4	0.5	1.0	0.9	0.9																												
Yb	1.9	0.4	1.0	2.0	1.2	0.3	2.6	4.9	0.8	1.1	0.7	2.7	1.0	0.7	1.0	0.9	0.3	0.7	0.5	0.6	0.7	0.4	0.0	0.5	2.2	1.5	0.5	0.4	0.5	0.9	0.7	0.6	3.2	0.4	0.7	0.4	0.3	0.4	0.8	0.4	1.5	0.5	0.4	0.4	1.0	0.9	0.9	0.0																												
Zn	2.1	0.9	1.3	2.4	1.6	0.6	3.4	6.2	1.2	1.0	1.2	3.1	1.1	0.9	1.1	1.2	0.7	1.1	1.2	1.1	1.3	0.6	0.8	0.5	2.8	1.9	0.9	1.2	1.0	1.0	1.1	4.0	0.7	1.2	0.9	0.8	0.9	1.2	1.1	2.0	1.2	0.7	0.7	1.6	1.0	1.5	0.8	0.8																												
Zr	2.6	0.1	1.4	2.8	1.0	0.5	3.0	5.1	1.0	1.5	1.0	3.2	1.4	0.5	1.2	1.5	0.5	1.1	0.1	0.9	0.3	0.5	0.4	0.5	2.4	1.8	0.4	0.4	0.8	1.3	0.9	0.3	3.8	0.6	1.1	0.8	0.1	0.8	0.6	0.2	2.2	0.6	0.3	0.3	1.8	1.3	1.4	0.4	0.4	1.0																												
LOI	2.1	0.6	0.8	2.1	1.6	0.4	2.1	3.3	0.5	1.4	0.8	2.1	0.6	1.0	0.9	0.6	0.3	0.6	0.8	0.5	1.2	0.5	0.5	0.4	1.0	1.4	0.9	0.8	0.6	0.6	0.5	1.0	2.3	0.3	0.5	0.6	0.5	0.5	1.1	0.8	1.3	1.0	0.5	0.9	1.2	0.6	0.6	0.5	0.5	1.0	0.7																												

ELECTRONIC APPENDIX C FOR CHAPTER 7

Appendix C. Results of PCA given as the proportions of explained variance by first, second and third principal components, with loadings (coordinates of the elements on the PCs projection; Figs 8a, 9a).

Eigenvalues of PC1 to PC3			
Eigenvalues	PC1	PC2	PC3
λ	3.36	2.45	1.84
λ%	29	15	8
$\sum\lambda$%	29	44	52
Loadings of the elements on PC1-PC3			
Elements	PC1	PC2	PC3
Ag	-0.14	**0.32**	-0.07
Al	**0.15**	-0.05	-0.08
As	-0.09	0.04	-0.01
Au	**-0.16**	**0.26**	**-0.16**
Ba	**0.21**	0.02	-0.06
Be	0.05	0.00	0.11
Bi	**-0.21**	**0.15**	**-0.49**
CO_2	**-0.29**	**-0.67**	**-0.28**
Ca	-0.04	-0.12	0.14
Cd	0.03	0.04	**0.21**
Ce	-0.03	0.09	-0.04
Cu	**-0.26**	**0.22**	**-0.22**
Co	-0.12	-0.01	**0.16**
Cs	**0.19**	0.00	-0.04
Cr	0.05	-0.01	0.10
Fe	**-0.15**	0.02	**0.20**
Ga	0.03	-0.03	0.09
Ge	-0.06	-0.03	0.12
Hf	**0.18**	-0.06	-0.12
In	-0.02	0.01	-0.13
K	**0.24**	-0.06	-0.09
Li	0.07	0.02	0.05
Lu	0.06	0.02	0.00
Mg	0.06	-0.02	0.08
Mn	**-0.18**	**-0.40**	-0.03
Mo	-0.11	**0.16**	-0.07
Na	**0.16**	0.00	-0.08
Nb	0.10	-0.01	-0.10
Nd	-0.02	0.07	-0.03
Ni	-0.09	-0.04	**0.30**
P	-0.04	-0.07	0.10
Rb	**0.20**	-0.05	-0.02
S	**-0.34**	-0.02	0.13
Sc	0.01	-0.04	**0.16**
Sb	-0.07	0.00	0.02
Se	0.00	0.03	0.06
Si	0.12	-0.04	-0.07
Sn	-0.03	0.02	0.08

Sr	**0.16**	0.05	**-0.18**
Ta	**0.17**	-0.04	-0.12
Te	**-0.20**	0.11	0.01
Th	0.11	0.02	-0.08
Ti	0.09	-0.04	0.06
Tl	**0.19**	-0.01	0.02
U	-0.13	**0.17**	0.04
V	-0.07	-0.03	**0.29**
W	-0.13	0.01	0.00
Y	0.06	0.02	-0.01
Yb	0.07	0.01	-0.01
Zn	0.08	0.07	**0.19**
Zr	**0.15**	-0.05	-0.08
LOI	-0.04	-0.11	-0.03

Numbers in bold indicate absolute loadings of the elements with >0.15.

ADDITIONAL MATERIAL G

CO-AUTHORED ARTICLE ABSTRACT:

PETROGRAPHY AND TRACE ELEMENT SIGNATURES OF IRON-OXIDES IN DEPOSITS FROM THE MIDDLEBACK RANGES, SOUTH AUSTRALIA: FROM BANDED IRON FORMATION TO ORE

William Keyser [1], Cristiana L. Ciobanu [1], Nigel J. Cook [1], Geoff Johnson [2], Holly Feltus [2], Steve Johnson [2], **Marija Dmitrijeva** [1], Ehrig [3], Phung T. Nguyen

[1]*School of Chemical Engineering and Advanced Materials, The University of Adelaide, Adelaide, SA 5005, Australia*

[2]*SIMEC Mining, Level 2, 169 Fullarton Road, Dulwich, SA 5065, Australia*

[3]*BHP Olympic Dam, Adelaide, SA 5000, Australia*

Article published in Ore Geology Reviews 93 (2018) 337-360

Ore Geology Reviews 93 (2018) 337–360

Contents lists available at ScienceDirect

Ore Geology Reviews

journal homepage: www.elsevier.com/locate/oregeorev

Petrography and trace element signatures of iron-oxides in deposits from the Middleback Ranges, South Australia: From banded iron formation to ore

William Keyser[a,*], Cristiana L. Ciobanu[a], Nigel J. Cook[a], Geoff Johnson[b], Holly Feltus[b], Steve Johnson[b], Marija Dmitrijeva[a], Kathy Ehrig[c], Phung T. Nguyen[b]

[a] School of Chemical Engineering, The University of Adelaide, Adelaide, SA 5005, Australia
[b] SIMEC Mining, Level 2 169 Fullarton Road, Dulwich, SA 5065, Australia
[c] BHP Olympic Dam, Adelaide, SA 5000, Australia

ARTICLE INFO

Keywords:
Middleback Ranges
Banded iron formation
Fe-oxides
Trace element geochemistry
Hydrothermal overprinting

ABSTRACT

The Middleback Ranges is a major iron ore belt in the southeastern region of the Gawler Craton, South Australia, interpreted to be of BIF origin. Iron ore deposits are hosted within ~2550 Ma metasedimentary rocks of the Middleback Group and occur as a series of N-S trending hills, forming a ~60 km-long magnetic anomaly. A petrographic-geochemical study of iron-oxides from BIFs and iron ores was undertaken on samples from thirteen locations spanning the strike of the belt. Iron-oxides are texturally diverse due to multiple processes accompanying and postdating ore formation. Primary magnetite features preserved in the southern segment of the belt display distinct overprinting features (e.g., increased porosity, reworked grain boundaries) and multiple generations of growth associated with deposition of trace minerals, including native gold. Northwards along strike, this overprint is expressed by the pseudomorphic replacement of magnetite by hematite (martite) and is locally associated with brecciation, the presence of rare earth element (REE)-minerals, and replacement by iron-hydroxides. Whereas evidence of microplaty hematite accompanying martitization and predating iron-hydroxides is observed throughout the belt, distinct iron-oxide generations postdating the iron-hydroxides are inferred based on compositional zoning with respect to Si and intimate relationships between iron-oxides and -hydroxides. Chondrite-normalized fractionation trends obtained from the various iron-oxides and from different BIF types generally display LREE-enrichment and distinct positive Eu- and Y-anomalies. An increasing ΣREY- and LREE-trend accompanies martitization. The presence of specific element groups, e.g., granitophile elements (U, W, Sn, Mo), or transition metals (Cr, Mn, Co, Ni, Ti, V, Nb) within the lattice of iron-oxides suggests their formation in evolving environments associated with the emplacement of felsic and mafic lithologies, respectively. The impact of local setting on iron-oxide formation is highlighted by complex trace element signatures of iron-oxides; the northern segment of the belt is relatively enriched in As and Sb, while the southern segment is enriched in granitophile elements and REY. Further complexity is shown in the local variation of Mn and Zn in iron-oxides in the southern segment of the belt, where the Iron Magnet deposit shows the strongest correlation between the two elements. Various depositional settings for BIFs are inferred based upon Post-Archean Australian Shale-normalized REY fractionation trends of iron-oxides and various water types. These settings include environments where iron-minerals precipitate from mixtures of 1) anoxic seawater and high-temperature hydrothermal fluids, 2) anoxic seawater and low-temperature hydrothermal fluids, and 3) oxygen-richer seawater and low-temperature hydrothermal fluids. A genetic model for ore formation is proposed based upon textural and compositional variations observed in iron-oxides throughout the belt and includes formation resulting from supergene fluids rich in elements leached from local granites penetrating BIF, interaction with granite-derived hydrothermal fluids, and heat generated during emplacement of younger dikes. Recognition of petrographic features linked to changes in composition demonstrates the utility of iron-oxides to trace iron ore formation in a temporal and spatial context, with implications for ore genesis and models of mineral exploration.

* Corresponding author.
E-mail address: william.keyser@adelaide.edu.au (W. Keyser).

https://doi.org/10.1016/j.oregeorev.2018.01.006
Received 9 August 2017; Received in revised form 10 December 2017; Accepted 10 January 2018
Available online 10 January 2018
0169-1368/ © 2018 Elsevier B.V. All rights reserved.

ADDITIONAL MATERIAL H

CO-AUTHORED ARTICLE ABSTRACT:

IRON-OXIDES CONSTRAIN BIF EVOLUTION IN TERRANES WITH PROTRACTED GEOLOGICAL HISTORIES: THE IRON COUNT PROSPECT, MIDDLEBACK RANGES, SOUTH AUSTRALIA

William Keyser [1], Cristiana L. Ciobanu [1], Nigel J. Cook [1], **Marija Dmitrijeva** [1]**,** Liam Courtney-Davies [1], Holly Feltus [2], Sarah Gilbert [3], Geoff Johnson [2], Kathy Ehrig [4]

[1]*School of Chemical Engineering and Advanced Materials, The University of Adelaide, Adelaide, SA 5005, Australia*

[2]*SIMEC Mining, Level 2, 169 Fullarton Road, Dulwich, SA 5065, Australia*

[3]*Adelaide Microscopy, The University of Adelaide, Adelaide, SA 5005, Australia*

[4]*BHP Olympic Dam, Adelaide, SA 5000, Australia*

Article published in Lithos (2019) *324-325*, 20-38.

Lithos 324–325 (2019) 20–38

Contents lists available at ScienceDirect

Lithos

journal homepage: www.elsevier.com/locate/lithos

Iron-oxides constrain BIF evolution in terranes with protracted geological histories: The Iron Count prospect, Middleback Ranges, South Australia

William Keyser [a,*], Cristiana L. Ciobanu [a], Nigel J. Cook [a], Marija Dmitrijeva [a], Liam Courtney-Davies [a], Holly Feltus [b], Sarah Gilbert [c], Geoff Johnson [b], Kathy Ehrig [d]

[a] School of Chemical Engineering, The University of Adelaide, Adelaide, SA 5005, Australia
[b] SIMEC Mining, Level 2, 169 Fullarton Road, Dulwich, SA 5065, Australia
[c] Adelaide Microscopy, The University of Adelaide, Adelaide, SA 5005, Australia
[d] BHP Olympic Dam, Adelaide, SA 5000, Australia

ARTICLE INFO

Article history:
Received 22 March 2018
Accepted 31 October 2018
Available online 03 November 2018

Keywords:
U—Pb hematite geochronology
Banded iron formation
Middleback Ranges
Iron-oxides
Trace element geochemistry

ABSTRACT

When studied at appropriate scales of observation and using complementary methods, the intrinsic textural and geochemical complexity of iron-oxides can provide unparalleled insights into the evolution of iron ore resources from banded iron formation deposition to ore formation. Iron Count is one of >20 deposits and prospects within the Archean Middleback Ranges iron ore belt, South Australia, in which iron-oxides from BIFs and ores display variable textural and trace element signatures. Integrated petrography, iron-oxide laser-ablation mapping and geochemistry, and in-situ dating of BIF-derived ores was undertaken to assess whether features observed in samples from this representative prospect might be attributed to localized and superimposed overprint processes. The prospect consists of a West and East ridge, each characterized by a sequence of overprints expressed as interconversions between iron-(hydr)oxides and accompanying variation in trace element concentrations. Pseudomorphic replacement of early magnetite by hematite (martite), followed by replacement by iron-hydroxides is recognized in samples from the East Ridge. Further overprints are expressed as veining, brecciation and crystallization of (micro)platy hematite rich in granitophile elements (Sn, Mo, W, U). Martitization of early magnetite in the West Ridge is accompanied by enrichment in Zn, Co and Ni in martite. Subsequent recrystallization of martite/iron-hydroxides by granoblastic hematite is marked by enrichment in Ti, Ta, Nb, REE and granitophile elements, and co-crystallization of REE-minerals. This is followed by crystallization of (micro)platy hematite, similarly rich in these elements. Enrichment in Ti and granitophile elements in granoblastic hematite is interpreted to infer crystallization from highly saline fluids generated by interaction between evaporite-bearing sedimentary rocks and granite-derived fluids. Post-Archean Australian Shale-normalized REY fractionation trends of iron-oxides from the East Ridge are consistent with precipitation of iron-rich minerals from a mixture of anoxic seawater and hydrothermal vent fluids. Analogous trends from the West Ridge lack a seawater signature. Contrasts in REY fractionation trends between the two ridges is interpreted as a combination of the loss of primary seawater signature due to severe overprinting in the West Ridge, and to lateral variation in the marine depositional environment. Results validate the hypothesis that variation in iron-oxide trace element signatures seen throughout the Middleback Ranges iron ore belt results from overprinting due to superimposed tectono-magmatic events that have locally affected each deposit. Despite undergoing different sequences of ore-forming stages, as well as possibly distinct depositional environments, the two ridges share a common overprint, dated here at ~1790 Ma using in-situ U—Pb geochronology of co-existing hematite, monazite and xenotime. This age is considered to represent the timing of interaction between granite-derived fluids with ore-hosting rock. Such interpretation is supported by the geochemical signatures of the dated iron-oxides showing enrichment in granitophile elements and coincident ages for the Wertigo Granite and Myola Volcanics, which occur proximal to the prospect and were emplaced/erupted during intracontinental rifting. The approach undertaken here, combining petrography, iron-oxide geochemistry and in-situ dating of BIF-derived ores is generically applicable to other iron resources within the Middleback Ranges or analogous terranes elsewhere.

© 2018 Published by Elsevier B.V.

* Corresponding author.
E-mail address: william.keyser@adelaide.edu.au (W. Keyser).

https://doi.org/10.1016/j.lithos.2018.10.035
0024-4937/© 2018 Published by Elsevier B.V.

ADDITIONAL MATERIAL I

CO-AUTHORED ARTICLE ABSTRACT:

PETROGRAPHIC AND GEOCHRONOLOGICAL CONSTRAINTS ON THE GRANITIC BASEMENT TO THE MIDDLEBACK RANGES, SOUTH AUSTRALIA

William Keyser [1], Cristiana L. Ciobanu [1], Nigel J. Cook [1], Liam Courtney-Davies [1], Allen Kennedy [2], Benjamin P. Wade [3], Kathy Ehrig [4], **Marija Dmitrijeva** [1], Alkiviadis Kontonikas-Charos [1], Holly Feltus [5], Geoff Johnson [5]

[1]*School of Chemical Engineering and Advanced Materials, The University of Adelaide, Adelaide, SA 5005, Australia*

[2]*John de Laeter Centre, Curtin University of Technology, Bentley, WA 6102, Australia*

[3]*Adelaide Microscopy, The University of Adelaide, Adelaide, SA 5005, Australia*

[4]*BHP Olympic Dam, Adelaide, SA 5000, Australia*

[5]*SIMEC Mining, Level 2, 169 Fullarton Road, Dulwich, SA 5065, Australia*

Article published in Precambrian Research (2019) *324*, 170-193.

Precambrian Research 324 (2019) 170–193

Contents lists available at ScienceDirect

Precambrian Research

journal homepage: www.elsevier.com/locate/precamres

Petrographic and geochronological constraints on the granitic basement to the Middleback Ranges, South Australia

William Keyser[a,*], Cristiana L. Ciobanu[a], Nigel J. Cook[a], Liam Courtney-Davies[a], Allen Kennedy[b], Benjamin P. Wade[c], Kathy Ehrig[d], Marija Dmitrijeva[a], Alkiviadis Kontonikas-Charos[a], Holly Feltus[e], Geoff Johnson[e]

[a] School of Chemical Engineering, The University of Adelaide, Adelaide, SA 5005, Australia
[b] John de Laeter Centre, Curtin University of Technology, Bentley, WA 6102, Australia
[c] Adelaide Microscopy, The University of Adelaide, Adelaide, SA 5005, Australia
[d] BHP Olympic Dam, Adelaide, SA 5000, Australia
[e] SIMEC Mining, Level 2, 169 Fullarton Road, Dulwich, SA 5065, Australia

ARTICLE INFO

Keywords:
Middleback Ranges
Archean granites
SHRIMP U-Pb zircon geochronology
Banded iron formation

ABSTRACT

The Middleback Ranges is a 60 km-long BIF-endowed iron ore belt located in the southeastern Gawler Craton and is the largest exploited iron resource in South Australia. The belt is hosted within an Archean- to Paleoproterozoic-aged granitic-gneissic basement terrane. Petrographic and geochronological constraints are given for a suite of granites associated with deposits throughout the Middleback Ranges and compared with other regional granites. Granites from the Middleback Ranges show complex mineralogical and geochemical features indicating multiple overprinting events. Sensitive high-resolution ion microprobe U-Pb zircon ages from all granites across the Middleback Ranges yield Archean ages, suggesting the existence and a more extensive distribution of Mesoarchean crust than previously recognized beneath the entire Middleback Ranges BIF sequence. Grey and pink granites from the central Middleback Ranges (Sultan prospect) produced the oldest $^{207}Pb/^{206}Pb$ weighted mean ages within the sample suite (3241 ± 6 and 3238 ± 9 Ma, respectively). Zircon in the latter granite also features overgrowths dated at ~2.6 Ga and interpreted to be metamorphic. A second group of younger granites from the Iron Monarch deposit and a sample of Cooyerdoo Granite (northern Middleback Ranges) have a minimum crystallization age of 3165 ± 8 Ma and a $^{207}Pb/^{206}Pb$ weighted mean magmatic age of 3134 ± 18 Ma, respectively. The youngest granites analyzed here derive from the Iron Baron deposit in the central part of the belt, which display strong deformation and have a minimum crystallization age of 3089 ± 9 Ma, and from the Iron Magnet deposit in the southern part of the belt ($^{207}Pb/^{206}Pb$ weighted mean age of 3023 ± 33 Ma). Petrographic and geochemical features observed within the sample suite indicate that post-Archean overprinting events led to alteration of the granitic basement and may infer that fluid-rock interaction and granite leaching were important for BIF upgrading processes and iron-oxide formation.

1. Introduction

The Middleback Ranges (MR) is a 60 km-long metallogenetic belt hosting iron ores and located in the Eyre Peninsula, South Australia (Fig. 1). These ores are associated with banded iron formation (BIF) that were initially considered as Paleoproterozoic (~2.0 Ga; Parker et al., 1988) but more recently are recognized as Late Archean (~2.5 Ga; Szpunar et al., 2011). The depositional age of the BIF with lower stratigraphic position relative to the Cook Gap Schist is thus constrained as Neoarchean ("no older than c. 2570 Ma and is likely to have been deposited before 2450 Ma"; Szpunar et al., 2011). Uncertainties nevertheless still exist with respect to the regional correlation of Fe-rich lithologies relative to this horizon along the MR, and to the origin of the basement at the time of BIF deposition.

The MR belt is part of the southeastern Gawler Craton, which comprises magmatic rocks spanning the Archean (Cooyerdoo Granite; ~3.15 Ga, Fraser et al., 2010) to Mesoproterozoic (~1.6 Ga Gawler Range Volcanics and Charleston Granite; Fanning et al., 1988; Creaser and Fanning, 1993) and is crosscut by mafic dikes inferred to be of Gairdner age (~820 Ma; Wingate et al., 1998), but as yet unconfirmed

* Corresponding author.
E-mail address: william.keyser@adelaide.edu.au (W. Keyser).

https://doi.org/10.1016/j.precamres.2019.01.024
Received 26 October 2018; Received in revised form 30 January 2019; Accepted 30 January 2019
Available online 01 February 2019
0301-9268/ © 2019 Elsevier B.V. All rights reserved.

ADDITIONAL MATERIAL J

CO-AUTHORED ARTICLE ABSTRACT:

ZIRCON AT THE NANOSCALE RECORDS METASOMATIC PROCESSES LEADING TO LARGE MAGMATIC–HYDROTHERMAL ORE SYSTEMS

Liam Courtney-Davies [1], Cristiana L. Ciobanu [1], Max R. Verdugo-Ihl [1], Ashley Slattery [2], Nigel J. Cook [1], **Marija Dmitrijeva** [1], William Keyser [1], Benjamin P. Wade [2], Urs I. Domnick [1], Kathy Ehrig [3], Jing Xu [1,4], Alkiviadis Kontonikas-Charos [1]

[1] *School of Chemical Engineering and Advanced Materials, The University of Adelaide, Adelaide, SA 5005, Australia*

[2] *Adelaide Microscopy, The University of Adelaide, Adelaide, SA 5005, Australia*

[3] *BHP Olympic Dam, Adelaide, SA 5000, Australia*

[4] *Key Laboratory of Mineral Resources, Institute of Geology and Geophysics, Chinese Academy of Sciences, Beijing 100029*

Article published in Minerals (2019) *9*, 364.

minerals

MDPI

Article

Zircon at the Nanoscale Records Metasomatic Processes Leading to Large Magmatic–Hydrothermal Ore Systems

Liam Courtney-Davies [1,*], Cristiana L. Ciobanu [1], Max R. Verdugo-Ihl [1], Ashley Slattery [2], Nigel J. Cook [1], Marija Dmitrijeva [1], William Keyser [1], Benjamin P. Wade [2], Urs I. Domnick [1], Kathy Ehrig [3], Jing Xu [1,4] and Alkiviadis Kontonikas-Charos [1]

[1] School of Chemical Engineering and Advanced Materials, The University of Adelaide, Adelaide, SA, 5005, Australia; cristiana.ciobanu@adelaide.edu.au (C.L.C.); max.verdugoihl@adelaide.edu.au (M.R.V.-I.); nigel.cook@adelaide.edu.au (N.J.C.); marija.dmitrijeva@adelaide.edu.au (M.D.); william.keyser@adelaide.edu.au (W.K.); urs.domnick@adelaide.edu.au (U.I.D.); j.xu@adelaide.edu.au (J.X.); alkiviadis.kontonikas-charos@adelaide.edu.au (A.K.-C.)

[2] Adelaide Microscopy, The University of Adelaide, Adelaide, SA 5005, Australia; ashley.slattery@adelaide.edu.au (A.S.); benjamin.wade@adelaide.edu.au (B.P.W.)

[3] BHP Olympic Dam, Adelaide, SA 5000, Australia; kathy.ehrig@bhp.com

[4] Key Laboratory of Mineral Resources, Institute of Geology and Geophysics, Chinese Academy of Sciences, Beijing 100029, China; xujing3800@126.com

* Correspondence: liam.courtney-davies@adelaide.edu.au

Received: 30 April 2019; Accepted: 13 June 2019; Published: 16 June 2019

Abstract: The petrography and geochemistry of zircon offers an exciting opportunity to better understand the genesis of, as well as identify pathfinders for, large magmatic–hydrothermal ore systems. Electron probe microanalysis, laser ablation inductively coupled plasma mass spectrometry, high-angle annular dark-field scanning transmission electron microscopy (HAADF-STEM) imaging, and energy-dispersive X-ray spectrometry STEM mapping/spot analysis were combined to characterize Proterozoic granitic zircon in the eastern Gawler Craton, South Australia. Granites from the ~1.85 Ga Donington Suite and ~1.6 Ga Hiltaba Suite were selected from locations that are either mineralized or not, with the same style of iron-oxide copper gold (IOCG) mineralization. Although Donington Suite granites are host to mineralization in several prospects, only Hiltaba Suite granites are considered "fertile" in that their emplacement at ~1.6 Ga is associated with generation of one of the best metal-endowed IOCG provinces on Earth. Crystal oscillatory zoning with respect to non-formula elements, notably Fe and Cl, are textural and chemical features preserved in zircon, with no evidence for U or Pb accumulation relating to amorphization effects. Bands with Fe and Ca show mottling with respect to chloro–hydroxy–zircon nanoprecipitates. Lattice defects occur along fractures crosscutting such nanoprecipitates indicating fluid infiltration post-mottling. Lattice stretching and screw dislocations leading to expansion of the zircon structure are the only nanoscale structures attributable to self-induced irradiation damage. These features increase in abundance in zircons from granites hosting IOCG mineralization, including from the world-class Olympic Dam Cu–U–Au–Ag deposit. The nano- to micron-scale features documented reflect interaction between magmatic zircon and corrosive Fe–Cl-bearing fluids in an initial metasomatic event that follows magmatic crystallization and immediately precedes deposition of IOCG mineralization. Quantification of α-decay damage that could relate zircon alteration to the first percolation point in zircon gives ~100 Ma, a time interval that cannot be reconciled with the 2–4 Ma period between magmatic crystallization and onset of hydrothermal fluid flow. Crystal oscillatory zoning and nanoprecipitate mottling in zircon intensify with proximity to mineralization and represent a potential pathfinder to locate fertile granites associated with Cu–Au mineralization.

ADDITIONAL MATERIAL K

CO-AUTHORED ARTICLE ABSTRACT:

HEMATITE GEOCHEMISTRY AND GEOCHRONOLOGY RESOLVE GENETIC AND TEMPORAL LINKS AMONG IRON-OXIDE COPPER GOLD SYSTEMS, OLYMPIC DAM DISTRICT, SOUTH AUSTRALIA

Liam Courtney-Davies [1], Cristiana L. Ciobanu [1], Max R. Verdugo-Ihl [1], **Marija Dmitrijeva** [1], Nigel J, Cook [1], Kathy Ehrig [2], Benjamin P. Wade [3]

[1] *School of Chemical Engineering and Advanced Materials, The University of Adelaide, Adelaide, SA 5005, Australia*

[3] *BHP Olympic Dam, Adelaide, SA 5000, Australia*

[2] *Adelaide Microscopy, The University of Adelaide, Adelaide, SA 5005, Australia*

Article published in Precambrian Research (2019) *335*, 105480.

Precambrian Research 335 (2019) 105480

Contents lists available at ScienceDirect

Precambrian Research

journal homepage: www.elsevier.com/locate/precamres

Hematite geochemistry and geochronology resolve genetic and temporal links among iron-oxide copper gold systems, Olympic Dam district, South Australia

Liam Courtney-Davies[a,*], Cristiana.L. Ciobanu[a], Max R. Verdugo-Ihl[a], Marija Dmitrijeva[a], Nigel J. Cook[a], Kathy Ehrig[b], Benjamin P. Wade[c]

[a] School of Chemical Engineering and Advanced Materials, The University of Adelaide, Adelaide, SA 5005, Australia
[b] BHP Olympic Dam, Adelaide, SA 5000, Australia
[c] Adelaide Microscopy, The University of Adelaide, SA 5005, Australia

ARTICLE INFO

Keywords:
Hematite U-Pb dating
IOCG
Wirrda Well
Acropolis
Olympic Cu-Au province

ABSTRACT

The Wirrda Well and Acropolis prospects, ~25 km south from the Olympic Dam deposit, are among several dozen examples of iron-oxide copper gold (IOCG) mineralisation forming a 600 km-long province in the eastern Gawler Craton, South Australia. IOCG systems across the province differ in terms of host lithology, iron-oxide mineral associations, intensity of brecciation, and grade of Cu-(U)-Au mineralisation. Previous efforts to provide a geochronological framework for mineralisation, and correlate this with igneous activity, were inhibited by a lack of clear crosscutting features (particularly in breccia-hosted systems) and a scarcity of reliable hydrothermal mineral geochronometers. The earliest generation of hematite, characterised by enrichment in U-W-Sn-Mo and previously reported from Olympic Dam, provides confident U-Pb dates and insights into hydrothermal fluid signatures. Similar hematite is recognised from Wirrda Well and Acropolis, allowing direct comparison between the three IOCG systems. Relationships between early, silician (Wirrda Well) and titaniferous (Acropolis) magnetite and U-bearing hematite at the two prospects differ. Inferred martitisation of magnetite at Acropolis has generated zoned hematite with U-W-Mo-enrichment at constant Sn concentration, but with a marked loss of REE + Y (REY) and Ti, whereas at Wirrda Well, single-crystal zoned hematite, resembling that from Olympic Dam, retains high REY and Sn concentrations. Although morphologies, textures and compositions of U-bearing hematite at Olympic Dam, Wirrda Well and Acropolis vary significantly, a common U-Pb (laser ablation-inductively coupled plasma-mass spectrometry) age of ~1590 Ma is obtained from the most reliable data ($^{207}Pb/^{206}Pb$: 1598.9 ± 6.3 Ma at Wirrda Well and 1590.6 ± 6.5 Ma at Acropolis). The geochemical signatures of iron-oxides from the two prospects share common trends for U, W, Sn, Mo, high field strength and siderophile elements, comparable with signatures of Fe-oxides from the 'outer shell' of the Olympic Dam deposit. Given that datable iron-oxides would seem to be ubiquitous phases throughout the eastern Gawler Craton, the commonality in geochemistry and age of U-bearing hematite from the Olympic Dam district is significant, as it provides a single, traceable mineral to compare IOCG systems across the province.

1. Introduction

Mesoproterozoic magmatic-hydrothermal ore deposits and prospects occur within a Cu-Au ± U-rich metallogenic province, extending for 600 km along the eastern margin of the Gawler Craton, South Australia (Fig. 1A). Climaxing at ~1.6 Ga, a craton-scale tectonothermal event resulted in emplacement of voluminous, bi-modal intrusive and volcanic rocks of the co-magmatic Gawler Range Volcanics (GRV) and Hiltaba Suite (Drexel et al., 1993, and references therein). Together, these rocks form an intracontinental Large Igneous Province (LIP), which unlike most mantle plume derived LIP's (Ernst, 2014), is dominated by felsic rather than mafic rocks (Allen et al., 2008). The magmatism, and associated metallogenesis in the region, has been temporally correlated with the episodic breakup of the Columbia/Nuna supercontinent (Goldfarb et al., 2010; Groves et al., 2010).

Based on geophysical and geochemical data, lithospheric models for the region acknowledge the important role of mantle-derived components and, moreover, recognise delamination of metasomatised

* Corresponding author.
E-mail address: liam.courtney-davies@adelaide.edu.au (L. Courtney-Davies).

https://doi.org/10.1016/j.precamres.2019.105480
Received 12 June 2019; Received in revised form 4 October 2019; Accepted 4 October 2019
Available online 05 October 2019
0301-9268/ © 2019 Elsevier B.V. All rights reserved.

ADDITIONAL MATERIAL L

CONFERENCE ABSTRACT:

MULTIVARIATE STATISTICAL ANALYSES OF LA-ICP-MS TRACE ELEMENT DATA FOR IRON-OXIDES: EXAMPLES FROM GENETICALLY DISTINCT ORE DEPOSITS FROM SOUTH AUSTRALIA

Marija Dmitrijeva [1], Cristiana L. Ciobanu [1], Andrew V. Metcalfe [2], Nigel J. Cook [1], Max R. Verdugo-Ihl [1], William M. Keyser 1, Kathy Ehrig [3]

[1]*School of Chemical Engineering and Advanced Materials, The University of Adelaide, Adelaide, SA 5005, Australia*

[2] *2School of Mathematical Sciences, The University of Adelaide, Adelaide, SA 5005, Australia*

[3] *BHP Olympic Dam, Adelaide, SA 5000, Australia*

Conference presentation at IAMG 2017, Perth, Australia, September 3rd-9th

18TH ANNUAL CONFERENCE
IAMG2017
2-9 SEPTEMBER • PERTH, AUSTRALIA

69: MULTIVARIATE STATISTICAL ANALYSES OF LA-ICP-MS TRACE ELEMENT DATA FOR IRON-OXIDES: EXAMPLES FROM GENETICALLY DISTINCT ORE DEPOSITS FROM SOUTH AUSTRALIA

Dmitrijeva, M.[1], Ciobanu, C. L.[1], Metcalfe, A. V.[2], Cook, N. J.[1], Verdugo-Ihl, M. R. [1], Keyser, W.M. [1], Ehrig, K.[3]

[1]School of Chemical Engineering, The University of Adelaide, Adelaide, SA 5005, Australia
[2]School of Mathematical Sciences, The University of Adelaide, Adelaide, SA 5005, Australia
[3]BHP Billiton Olympic Dam, Adelaide, SA 5001, Australia

Abstract: Magnetite and hematite are ubiquitous components of banded iron formations (BIF) and iron-oxide copper-gold-type (IOCG) deposits. These minerals can incorporate anomalous concentrations of large number of trace elements, which in turn, are expected to deliver unique geochemical signatures mirroring conditions of mineral formation and superimposed tectonothermal events. In contrast to whole-rock data approach, prone to averaging-out effects, trace element signatures in minerals (TESIM) are governed by crystal structure and the ability to record changes in physical- chemical parameters, and are thus more suitable for fingerprinting distinct stages of mineralization. With improvements in laser-ablation inductively-coupled plasma-mass spectrometry (LA-ICP- MS), present-day TESIM datasets may be very large, yet are often presented without reference to mineral texture or detailed analysis of mineral assemblage, and apart from bi/trivariate visualizations, often lack a numerical approach. The complexity of TESIM data demands statistical formalism, as the full potential of these data cannot be realized without being able to mathematically model dependencies and understand the relationships among elements.

Trace element distributions expose inter/intra-grain variability, along with relative variation conjugated with position of the mineral assemblage within a given ore system. This has potential for development of exploration vectors, particularly for discrimination of distal/proximal positions of mineralization.

We evaluate suitability and limitations of multivariate statistical analyses to describe, and model dependencies within TESIM data, and formalize a general TESIM concept for building geochemical vectors accounting for interdependence of elements for spatial and temporal factors. We present trace element signatures of Fe-oxides from South Australian deposits (the IOCG-type Olympic Dam Cu-U-Au-Ag deposit and BIF-type iron deposits of the Middleback Ranges) and provide recommendations for LA-ICP-MS data treatment, which acknowledge and address issues of inter/intra-grain zoning, censoring, missing data and dependence modelling. The potential of TESIM to become a viable too for deciphering evolution of complex IOCG and BIF-type ore systems is demonstrated.

ADDITIONAL MATERIAL M

CONFERENCE ABSTRACT:

DEFINING IOCG SIGNATURES THROUGH COMPOSITIONAL DATA ANALYSIS: A CASE STUDY OF LITHOGEOCHEMICAL ZONING AT OLYMPIC DAM, SOUTH AUSTRALIA

Marija Dmitrijeva [1], Kathy Ehrig [2], Cristiana L. Ciobanu [1], Nigel J. Cook [1], Max R. Verdugo-Ihl [1], Andrew V. Metcalfe [3],

[1]*School of Chemical Engineering and Advanced Materials, The University of Adelaide, Adelaide, SA 5005, Australia*

[2] *BHP Olympic Dam, Adelaide, SA 5000, Australia*

[3] *School of Mathematical Sciences, The University of Adelaide, Adelaide, SA 5005, Australia*

Conference presentation, 15th Quadrennial IAGOD Symposium, Salta, Argentina, August 28th-31st. Symposium Volume, SEGEMAR, 246-247.

A | 118

DEFINING IOCG SIGNATURES THROUGH COMPOSITIONAL DATA ANALYSIS: A CASE STUDY OF LITHOGEOCHEMICAL ZONING AT OLYMPIC DAM, SOUTH AUSTRALIA

Marija Dmitrijeva[1], Kathy J. Ehrig, Cristiana L. Ciobanu, Nigel J. Cook, Max R. Verdugo-Ihl, Andrew V. Metcalfe

[1]University of Adelaide - marija.dmitrijeva@adelaide.edu.au

BACKGROUND

Iron-oxide–Cu-Au (IOCG) comprises a diverse clan of ore deposits that are found in a wide spectrum of geological settings spanning the Archean to Tertiary (Groves *et al.*, 2010). These deposits are inherently associated with zoned alteration assemblages represented by distal alkali-rich, and proximal hydrolytic alteration, with respect to the main Fe-oxide (±Cu-Au) mineralization (Barton, 2014). This zonation is observed at different scales, from regional down to individual orebodies, and results from the circulation and evolution of hydrothermal fluids. Understanding the spatio-temporal distribution of metals and minerals relative to fluid sources is thus crucial to constrain genetic models and develop exploration strategies.

The Olympic Dam (OD) deposit, South Australia, shows a regional and deposit-scale zoning with respect to alteration assemblages. The sulphide-zonation is roughly concentric, displaying a deeper-to-shallower transition from pyrite-chalcopyrite (Py-Cp) through chalcopyrite-bornite (Cp-Bn) to bornite-chalcocite (Bn-Cc) (Ehrig *et al.*, 2012). The deposit is hosted within the Olympic Dam Breccia Complex (ODBC), itself within the ~1.59 Ga Roxby Downs Granite and is predominantly derived from progressive brecciation and increasing Fe-metasomatism of the host granite. This relatively simple geological setting and mineralogical zonation make OD a prime target to investigate geochemical patterns potentially associated with zoning and concentration gradients relative to metal source(s). As a first step towards constraining zoning within the ODBC, principal component analysis (PCA) was performed to derive lithogeochemical zonation and identify key elements defining IOCG signatures.

METHODS

The whole-rock dataset consists of 10,546 samples from 533 drillholes and forms a dense grid in the south-eastern part of ODBC. Each sample represents a 15 m-long drillhole interval, which was assayed for 39 elements (as on Fig. 1). The PCA was performed on the centred logratio transformed data containing all elements, and the PC1 interpolated in Leapfrog3D software (Fig. 1a).

We present only the first principal component (PC1), which governs the greatest variability (~32%) within the dataset and represents an interpretable geological process. As an example, the NW-SE partial cross-section (Fig. 1b) represents the majority of lithologies/alteration types documented in the ODBC. The combination of multivariate statistics, i.e. PCA/hierarchical clustering, with a large whole-rock dataset, allows a comparison of empirical lithological/alteration and sulphide and gangue mineralogical zonation (obtained from Cu:S ratios and supported by modal mineralogy data), with an IOCG geochemical signature represented as the PC1, and provides data-driven decisions for element groupings.

RESULTS AND DISCUSSION

Relationships among elements within whole-rock geochemical datasets are governed by the mixture of minerals and their stoichiometries. The PCA transforms data into a set of linear combinations of elements or PCs, whereby the dominant PC1 reflects mineralogy and describes geological processes, which are mirrored by a relative increase or decrease of elements. The resulting PC1 and dendrogram shows two main element groups (Fig. 1c), defined as Class 1, and an antithetic association represented by Classes 2, 3 and 4. These two distinct groups represent the inverse relationship between (i) trace elements in host rocks (unmineralized granite, mafic and carbonate units), and (ii) elements typifying an IOCG geochemical signature within the ODBC. Notably, the highest loadings on PC1 are given by Class 3 elements Au-W-As-Mo-Sb (Fig. 1d).

If compared with the lithological/alteration cross-section (Fig. 1b), the distribution of positive PC1 values only partially overlaps with the distribution of >20 wt% Fe hematite breccias and vice versa. This may suggest that: (i) in some areas mineralization may not be associated with the Fe-metasomatism; and (ii) the presence of some Fe-rich lithologies may pre- or postdate IOCG mineralization.

The Cu(-Fe)-sulphide zone interfaces represent a complex but mappable feature. However, when compared to the significant correlation between PC1 and lithological/alteration zones, no pattern can be observed. This mismatch may be attributed to the low-resolution sampling and/or pervasive distribution of abundant Cu(-Fe)-

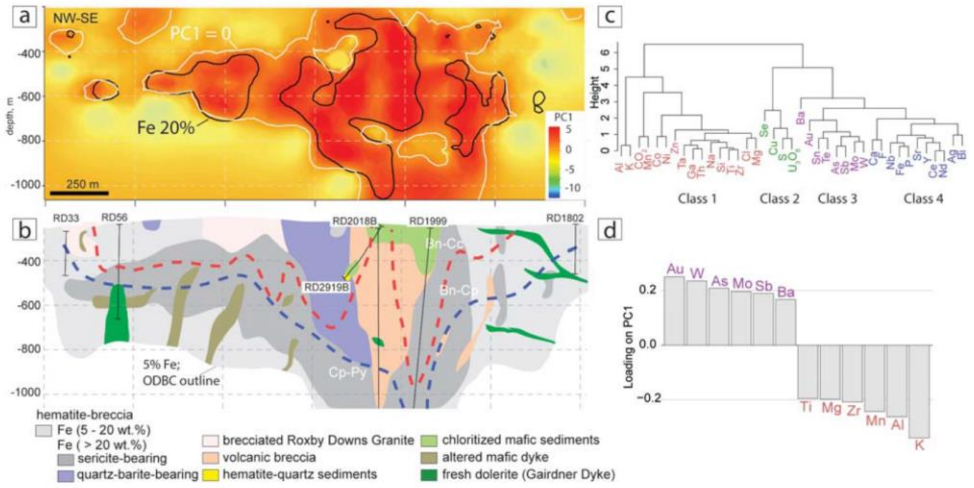


Figure 1. (a) NW-SE cross-section showing interpolated values of PC1 scores; (b) corresponding geological sketch; (c) dendrogram of analysed elements; (d) highest absolute element loadings on PC1.

sulphides and Fe-oxides that host trace elements. The latter stresses the necessity for investigation of individual metal gradients with emphasis on statistically defined classes, such as the Au-W-As-Mo-Sb signature.

CONCLUSIONS

The PCA has implications for delineation of the ODBC from the enclosing granite by deriving groups of elements representing IOCG mineralization. Although PC1 overlaps with Fe- metasomatism, it neither gives solid gradients nor defines zonation. This may signify that data-driven grouping of elements is the next step for further metal zonation investigation with a potential to detect primary/replacement patterns. However, given the complexity of ore assemblages in response to multiple episodes of mineral dissolution and (re)precipitation, trace element signatures in individual minerals (e.g. Cu(-Fe)-sulphides, Fe- oxides) may prove better at constraining the spatiotemporal evolution of the ODBC.

REFERENCES

Groves, D.I., Bierlein, F.P., Meinert, L.D., and Hitzman, M.W., 2010. Iron oxide copper- gold (IOCG) deposits through Earth history: Implications for origin, lithospheric setting, and distinction from other epigenetic iron oxide deposits: Economic Geology, 105, 641–654.

Barton, M.D., 2014. Iron Oxide (–Cu–Au–REE–P–Ag–U–Co) Systems, in: Treatise on Geochemistry. Elsevier, 13, pp. 515–541.

Ehrig, K., McPhie, J., Kamenetsky, V., 2012. Geology and Mineralogical Zonation of the Olympic Dam Iron Oxide Cu-U-Au-Ag Deposit, South Australia, in: Hedenquist, J.W., Harris, M., Camus, F. (Eds.), Geology and Genesis of Major Copper Deposits and Districts of the World: A Tribute to Richard H. Sillitoe. Society of Economic Geologists, Special Publication 16, pp. 237–267.

ADDITIONAL MATERIAL N

CONFERENCE ABSTRACT:

MINERALIZATION SIGNATURES OF THE MAGNETITE-DOMINANT ACROPOLIS PROSPECT, OLYMPIC DAM IOCG DISTRICT, SOUTH AUSTRALIA

Marija Dmitrijeva [1], Cristiana L. Ciobanu [1], Kathy Ehrig [2], Nigel J. Cook [1], Andrew V. Metcalfe [3], Max R. Verdugo-Ihl [1], Jocelyn McPhie

[1]School of Chemical Engineering and Advanced Materials, The University of Adelaide, Adelaide, SA 5005, Australia

[2] BHP Olympic Dam, Adelaide, SA 5000, Australia

[3] School of Mathematical Sciences, The University of Adelaide, Adelaide, SA 5005, Australia

[4] School of Natural Sciences and Centre of Excellence in Ore Deposits (CODES), University of Tasmania, Hobart, Tasmania 7001, Australia

Conference presentation at AEGC 2019, Perth, Australia, September 2nd-5th.

Mineralization signatures of the magnetite-dominant Acropolis prospect, Olympic Dam IOCG district, South Australia

Marija Dmitrijeva
School of Chem. Engineering
The University of Adelaide
marija.dmitrijeva@adelaide.edu.au

Cristiana L. Ciobanu
School of Chem. Engineering
The University of Adelaide
cristiana.ciobanu@adelaide.edu.au

Kathy J. Ehrig
BHP Olympic Dam
Adelaide
kathy.j.ehrig@bhp.com

Nigel J. Cook
School of Chem. Engineering
The University of Adelaide
nigel.cook@adelaide.edu.au

Andrew V. Metcalfe
School of Mathematical Sciences
The University of Adelaide
andrew.metcalfe@adelaide.edu.au

Max R. Verdugo-Ihl
School of Chem. Engineering
The University of Adelaide
max.verdugoihl@adelaide.edu.au

Jocelyn McPhie
CODES
The University of Tasmania
j.mcphie@utas.edu.au

SUMMARY

The Acropolis prospect is a vein-style magnetite (±apatite ±hematite) system located ~20 km southwest from the giant Olympic Dam iron-oxide copper gold (IOCG) deposit, South Australia. A whole rock dataset comprising 4,864 core samples from 14 drillholes was analysed using multivariate statistics to understand and identify geochemical signatures of mineralization at Acropolis. Statistical analyses included principal component analysis, hierarchical and k-means clustering. The results of statistical analyses are overlaid and interpreted relative to a 3D implicit geological model of the prospect, and encompass a projection of mineralization signature as PC1.

The mineralization footprint of Acropolis is multi-element and typified by a distinct 'magnetite' signature of Fe-V-Ni-Co. Such a signature is developed in the western part of the prospect and represents samples containing >60 wt.% Fe. In contrast, the 'hematite' signature displays an association of REE, W, Sn, Sb, U, Th, Ca, and P and is present throughout the prospect. Furthermore, kriged values of Cu (> 200 ppm) demonstrate an offset from Fe-rich veins, thus supporting a genetic model in which (earlier) Cu-Au-deficient veins in which magnetite is the dominant Fe-oxide are subsequently overprinted by Cu-bearing hematite-dominant mineralization.

Results obtained provide insights into the evolution from magnetite- to hematite-dominant IOCG systems and may offer a proxy for exploration and discovery of economically significant IOCG deposits at shallower levels in the eastern Gawler Craton.

Key words: Acropolis, magnetite-dominant IOCG, statistical analysis, implicit modelling

INTRODUCTION

Acropolis is a magnetite-dominant hematite-bearing prospect located ~20 km southwest from the giant Olympic Dam (OD) deposit. Displaying a range of mineralogical-petrological similarities to OD, Acropolis is considered to be broadly cotemporaneous with mineralisation at OD (Mortimer et al., 1988). Nevertheless, unlike the OD deposit, which displays disseminated Cu(-Fe)-sulphides within hematite breccias hosted in Roxby Downs Granite of Hiltaba Suite (HS) affiliation, the Acropolis prospect represents a vein-style mineralization with weakly-developed brecciation (Cross, 1993) within felsic Gawler Range Volcanics (GRV) (Mortimer et al., 1988). Both magmatic suites, HS and GRV, form the Large Igneous Province emplaced at ~ 1.6 Ga in the Gawler Craton, South Australia (Allen et al. 2008).

At Acropolis, the GRV units are comprised of rhyolitic, dacitic and andesitic lavas, as well as minor ignimbrites (McPhie, 2016). Within the area, the basement is composed of Donington Suite granitoids (~1850 Ma; Jagodzinski, 2005) which, also host mineralization. Weakly-brecciated Hiltaba Suite-affiliated granite (drillhole ACD7), is also as a relatively minor host rock for mineralization (McPhie, 2016).

Because of the proximity of Acropolis and evident similarities with the styles of alteration at Olympic Dam (Ehrig et al., 2017), this case study aims at obtaining geochemical signatures of this magnetite-rich end-member of the IOCG clan, using statistical analyses of whole rock data. Multivariate statistical analyses are effectively applied to find structures and patterns within geochemical data which lack pre-defined categorical variables (Caciagli, 2016). Such an approach allows identification of mineralized domains with distinct geochemical characteristics, combining the chemistry of protolith lithologies and superimposed geochemical signatures of the mineralization. Coupled with an implicit 3D geological model of Acropolis, these techniques allow visualization of the associations of key elements and mineralization within 3D space. The results obtained here provide insight into the development of IOCG systems from a magnetite- to hematite-dominant end-member.

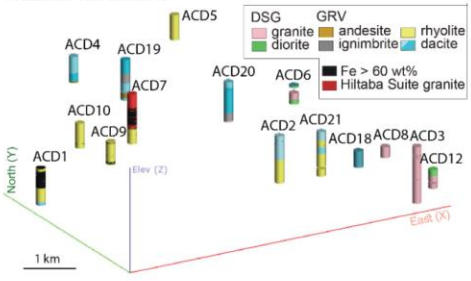


Figure 1. Drillholes and corresponding lithologies at the Acropolis prospect.

METHODS

In this case study, principal component analysis (PCA), hierarchical and k-means clustering are applied to a large multi-element data set (4,864 samples, total of 36 elements), collected from 14 drillholes at the Acropolis prospect (Fig. 1). Hierarchical clustering was applied to a variation matrix containing the variances of log-ratios of every possible element pairs: $\tau_{ij} = var(\ln(x_i/x_j)$ (Eq. 1). The compositional properties of the geochemical data were respected by obtaining isometric log-ratio (ilr) and centred log-ratio (clr) coordinates, which were further utilized for k-means clustering and PCA respectively. In the k-means procedure, the bootstrapping algorithm was used to test the stability of each cluster by calculating a Jaccard similarity value. The optimal number of k clusters was determined as seven based on the sufficient minimal value of the within-cluster sum of squares.

This study incorporates 3D modelling of the major faults, intrusions and lithological groups at the Acropolis prospect using the fault interpretations of McPhie (2016; Fig 2), and careful correlation of felsic GRV units using the Ti/Zr and Ti/Al ratios. Using the 3D model, we are able to overlay the lithologies of Acropolis with the interpolated results of statistical analyses as PC1 scores, the most geochemically meaningful clusters obtained from k-means algorithm and the outlines of 25 wt.% Fe and 200 ppm Cu. Such a holistic approach allows us to understand the extents of mineralization signatures and relate these to the lithologies present within the Acropolis prospect.

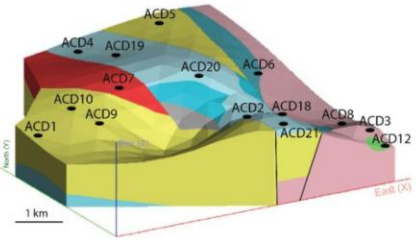


Figure 2. Implicit 3D geological model of the Acropolis prospect based on the 14 drillholes created in Leapfrog Geo software. The legend is as in Figure 1.

RESULTS

The hierarchical dendrogram (Fig. 3) provides a summary of the associations among the elements and suggests four main geochemical groups.

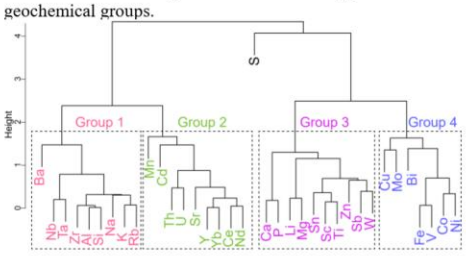


Figure 3. Dendrogram of 36 elements grouped according to their geochemical affinities. The dissimilarity measure was obtained from variation matrix based on Eq. 1.

Group 1, comprising Ba, Zr, Al, Si, Na, K and Rb represents a geochemical signature of granites and GRV felsic units and is also indicative of silicate minerals which are the products of hydrothermal alteration within the host rocks. In contrast, the mineralization signature is typified by Groups 2, 3 and 4, whereby Group 4 is associated with Fe-dominant mineralization, thus reflecting the strong co-dependence among Fe, V, Ni and Co, i.e. 'magnetite' signature, along with sulphide signature of Cu, Mo and Bi. Group 3, which encompasses W, Sb, Zn, Ti, Sc, Mg, Li, Ca and P, is evidently associated with Group 4, and represents a range of indicator and pathfinder elements typically present within a deposit of IOCG *sensu stricto* type (Groves et al., 2010). Combined, Groups 3 and 4 form an indicative IOCG-signature within magnetite-dominant mineralization at Acropolis.

The seven clusters identified by the k-means algorithm are used to define geochemical domains which have direct implication for characterization of data, as they reflect the original lithology along with the superimposed alteration and mineralization (Table 1).

The most geologically significant clusters are Cluster 2, 3 and 6. Cluster 2 represents early sodic alteration within the Donington Suite granite and diorite in the western part of the prospect (Fig. 4). Cluster 6 represents Fe-rich veins, predominantly composed of magnetite. Finally, Cluster 3 is comprised of rhyolites and dacites with relatively higher Fe content of 30 wt.% and is distributed throughout the prospect independently from the Fe-rich veins. The interpolation of Fe 25 wt.% and Cu 200 ppm provides additional comparison with the lithologies and clusters at Acropolis, and indicates a Cu mineralization offset from Fe-rich veins (Fig. 4). A plot of magnetic susceptibility values over clusters also suggest that Cluster 3 is predominantly hematite-bearing (Fig. 5).

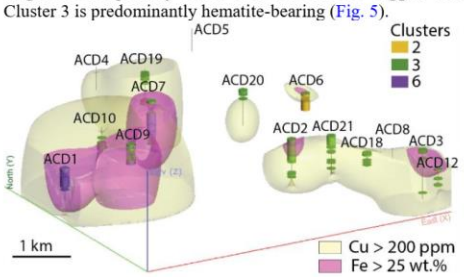


Figure 4. Spatial projection of Clusters 2, 3 and 6 in oblique view, overlaid by the outlines of Cu > 200 ppm and Fe > 25 wt.%.

The projection of 4,864 samples on PC1 and PC2 demonstrate geochemical affinities of Clusters and significantly complements the result of hierarchical and k-means analyses. The PC1-2 projection distinguishes Cluster 6 and its strong association with IOCG-signature elements: Fe-V-Ni-Co and with less pronounced loadings of Ti, Mn and Zn on PC1. (Fig. 6). Similarly, Cluster 3 shows a strong correlation with Group 2 and Group 3 elements, thus likely representing altered and/or partially mineralized/vein samples, i.e. 'hematite' signature rather than the magnetite-dominant mineralization itself.

Finally, the spatial projection of PC1 scores in 3D indicates mineralisation signatures within the western zone of the prospect, namely in drillholes ACD1, ACD9 and ACD7.

Additionally, a mineralization signature is present within the Donington Suite granite in the western zone (Fig. 7).

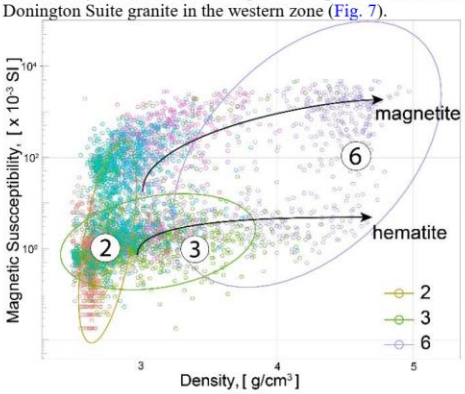


Figure 5. Magnetic susceptibility versus density, colour-coded according to a cluster membership and outlined by 0.95 confidence ellipses for Cluster 2, 3 and 6.

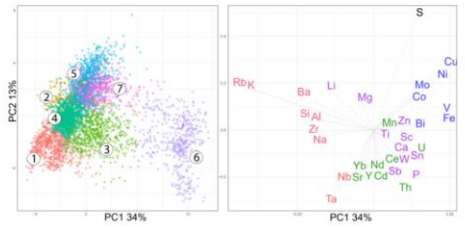


Figure 6. Projection of clr-transformed data demonstrating seven clusters obtained from k-mean algorithm and corresponding element loadings. Each circle represents a single data point. Elements are colour-coded according to the Groups (as in Figure 3).

DISCUSSION

Many magnetite-dominant IOCG systems are known to be deficient with respect to Cu and Au (Barton, 2014). Similarities among alteration types, ore and gangue mineralogy as well as the presence of early magnetite-apatite assemblages within many IOCG deposits has prompted a genetic relation between IOCG and Kiruna-type magnetite-apatite deposits (Hitzman et al., 1992), in spite of the lack of an evident transition between the two. Within the eastern Gawler Craton, and specifically in the immediate proximity of Olympic Dam, magnetite-apatite (± siderite ± chlorite) assemblages correspond to low-grade Cu-U-Au and are regarded as the envelopes of larger IOCG systems (Ehrig et al., 2012).

Analogous to the clan of IOCG systems, which are known to display elevated concentrations of many elements (Groves et al. 2010), the manifestation of the Acropolis IOCG signature is multi-element (Fig. 5). The U-W-Sn-Mo signature in hematite at Olympic Dam (Verdugo-Ihl et al., 2017) is recognised as a distinct W-Mo-Sn subset besides the dominant Fe, Cu, Au association in the IOCG signature obtained from PCA analysis (Dmitrijeva et al., 2019). Although Acropolis is deficient in terms of Au (> 70% of values are below the minimum detection limit) and contains geochemically anomalous, but low concentrations of Cu, it demonstrates a mineralisation signature analogous to that at Olympic Dam, with high loadings of W, Sn, Sb, U, Th and REE (Cluster 3), albeit at trace concentrations.

At Acropolis, sulphide minerals, particularly chalcopyrite, are predominantly associated with hematite-sericite-chlorite assemblages, which replace early magnetite-apatite (Krneta et al., 2017). An analogue mineral assemblage of early sulphide-poor magnetite-apatite overprinted by later sulphur-enriched Fe-oxide-Cu-Au mineralization is recorded at other IOCG systems outside the Gawler Craton (Ernest Henry, Queensland; Mark et al., 2006). The results of statistical analyses demonstrate that although Fe-oxide and Cu(-Fe)-sulphide mineralization are associated, they offset each other in some measure, reaffirming that assemblages observed in petrographic records correspond to patterns within the whole rock data. Cluster 3, which is characterised by Ca-P-Li-Mg-Sc-Ti-Zn-W-Sn-Sb, along with REE, Sr, U and Th is evidently associated with hematite-dominant alteration (Fig. 5), and likely represents its geochemical footprint, overprinting early Cu-deficient magnetite-apatite assemblages. The projection of Cluster 3 in Leapfrog (Fig 4), indicates that such a signature does not form haloes around Fe-rich veins (Cluster 6), but is actually ubiquitous throughout the Acropolis prospect, confirming that a transition from magnetite- to a hematite dominant system involves significant metal endowment.

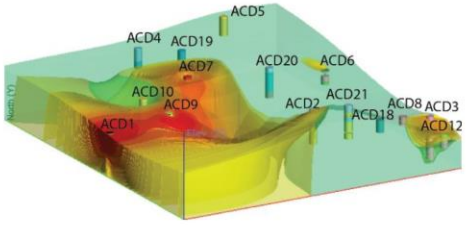


Figure 7. Spatial projection of PC1 scores in oblique view, displaying zones of most intense mineralization at Acropolis.

Overall, these results suggest that recognition of magnetite-dominant members of the IOCG clan are of critical importance in establishing the spatio-temporal model of entire IOCG systems and can facilitate discovery of metal endowed hematite-dominant IOCG deposits. This is particularly relevant in productive mineral districts, such as the Olympic Cu-Au province, where basement and the mineralization contained within is buried beneath a thick, barren sedimentary cover. Therefore, an improved understanding of the genesis and full extent of zonation in IOCG systems is fundamental for effective exploration, both at the local and regional scales.

CONCLUSIONS

Application of statistical analyses combined with implicit 3D geological modelling is an effective way to identify patterns and structures within the data in the absence of detailed petrographic and mineralogical data.

Despite being magnetite-dominant, the Acropolis prospect displays a multi-element mineralisation signature, which is partially similar to that of Olympic Dam, with W, Sn, Mo, and REE distributed throughout the prospect. Within Acropolis, Fe

and Cu mineralization are slightly offset, thus being consistent with observation of Cu-deficient magnetite-apatite veins in the western part of Acropolis and overprinting Cu-endowed hematite-dominant assemblages that extend throughout the prospect area, represented as Cluster 3. This conclusion is supported by the low magnetic susceptibility of Cluster 3 and a range of indicator elements which are typically hosted within a hematite-dominant assemblage: U, Th, REE, W, Sn and Sb. In contrast, magnetite mineralization (Cluster 6) is typified by a Fe-V-Ni-Co signature with less pronounced loadings of Ti, Mn and Zn. The magnetite veins may represent the upper part, or alternatively, the roots of an eroded or undiscovered Cu-Au mineralization, which, although partially coincident, is not centred on the HS granite. The Fe-V-Ni-Co signature is an indicator of relatively early IOCG mineralization and is a significant proxy for exploration of fertile hematite-dominant IOCG deposits at shallower crustal levels.

ACKNOWLEDGMENTS

This work is a contribution to the FOX project 'Trace elements in iron-oxides: deportment, distribution and application in ore genesis, geochronology, exploration and mineral processing', supported by BHP Olympic Dam and the South Australian Mining and Petroleum Services Centre of Excellence. N.J.C. acknowledges additional support from the ARC Research Hub for Australian Copper-Uranium (Grant IH130200033).

REFERENCES

Allen, S.R., McPhie, J., Ferris, G., and Simpson, C., 2008, Evolution and architecture of a large felsic Igneous Province in western Laurentia: the 1.6 Ga Gawler Range Volcanics, South Australia. Journal of Volcanology and Geothermal Research 172, 132–147.

Barton, M.D., 2014, Iron oxide (–Cu–Au–REE–P–Ag–U–Co) systems: In: Holland, H.D., and Turekian, K.K. (Eds.), Treatise on Geochemistry, 2nd ed., Elsevier, Oxford, 515–541.

Caciagli, N., 2016, Multielement geochemical modelling for mine planning: case study from an epithermal gold deposit: In: Martín-Fernández, J.A., and Thió-Henestrosa, S. (Eds.), Compositional Data Analysis. Springer Proceedings in Mathematics & Statistics, 187, 45–61.

Cross, K.C., 1993, Acropolis and Wirrda Well: In: Drexel, J.F., Preiss, W.V., and Parker, A.J. (eds.), The Geology of South Australia. vol. 1, The Precambrian. Geological Survey of South Australia, South Australia, 138 pp.

Dmitrijeva, M., Ehrig, K., Ciobanu, C., Cook, N. Verdugo-Ihl, M., and Metcalfe, A., 2019, Defining IOCG signatures through compositional data analysis: A case study of lithogeochemical zoning from the Olympic Dam deposit, South Australia: Ore Geology Reviews, 105, 86-101.

Ehrig, K., McPhie, J., and Kamenetsky, V., 2012, Geology and mineralogical zonation of the Olympic Dam iron oxide Cu-U-Au-Ag deposit, South Australia: Economic Geology, Special Publication 16, 237-267.

Ehrig, K. Kamenetsky, V.S., McPhie, J. Apukhtina, O., Ciobanu, C., Cook, N., Kontonikas-Charos, A., and Krneta, S. 2017, The IOCG-IOA Olympic Dam Cu-U-Au-Ag deposit and nearby prospects, South Australia: Proceedings, 14th Biennial SGA Meeting 'Mineral Resources to Discover' Québec City, Canada, vol. 3, p. 823-826.

Groves, D.I., Bierlein, F.P., Meinert, L.D., and Hitzman, M.W., 2010, Iron Oxide Copper-Gold (IOCG) deposits through earth history: implications for origin, lithospheric setting, and distinction from other epigenetic iron oxide deposits: Economic Geology, 105, 641–654.

Hitzman, M.W., Oreskes, N., and Einaudi, M.T., 1992, Geological characteristics and tectonic setting of Proterozoic iron oxide (Cu-U-Au-REE) deposits: Precambrian Research, 58, 241–287.

Jagodzinski, E.A., 2005, Compilation of SHRIMP U–Pb geochronological data – Olympic Domain, Gawler Craton, South Australia, 2001–2003: Geoscience Australia Record 2005/20, 197 pp.

Krneta, S., Cook, N.J., Ciobanu, C.L., Ehrig, K.J., and Kontonikas-Charos, A., 2017, The Wirrda Well and Acropolis prospects, Gawler Craton, South Australia: Insights into evolving fluid conditions through apatite chemistry: Journal of Geochemical Exploration, 181, 276-291.

Mark, G., Oliver, N.H.S., and Williams, P.J. 2006, Mineralogical and chemical evolution of the Ernest Henry Fe oxide–Cu–Au ore system, Cloncurry district, northwest Queensland, Australia: Mineralium Deposita 40, 769-801.

McPhie, J., 2016, Acropolis Report (unpublished): BHP Billiton Olympic Dam.

Mortimer, G.E., Cooper, J.A., Paterson, H.L., Cross, K., Hudson, G.R.T., and Uppill, R.K., 1988, Zircon U–Pb Dating in the Vicinity of the Olympic Dam Cu–U–Au Deposit, Roxby Downs, South-Australia: Economic Geology, 83, 694–709.

Verdugo-Ihl, M.R., Ciobanu, C.L., Cook, N.J., Ehrig, K., Courtney-Davies, L., and Gilbert, S., 2017, Textures and U-W-Sn-Mo signatures in hematite from the Cu-U-Au-Ag orebody at Olympic Dam, South Australia: defining the archetype for IOCG deposits: Ore Geology Reviews, 91, 173–195.

Table 1. Characteristics of seven clusters obtained from k-means cluster analysis.

Cluster	*n*, samples	Jaccard similarity value, j_i	Predominant cluster lithology and median values of Fe, K and Cu	Median density, kg/m^3	Median magnetic susceptibility, $\times 10^{-3}$ SI
1	779	0.57	Altered, least-veined rhyolites and minor dacites with 5% Fe, 5-6% K and 35 ppm Cu.	2.6	0.86
2	171	0.74	Altered Donington granite and diorite with pronounced sodic alteration; 8% Fe, 3.5 % K and 85 ppm Cu	2.7	0.94
3	619	0.84	Altered and intensively veined rhyolites and dacites with 30% Fe, 2.7% K and 137 ppm Cu	3.1	1.52
4	1384	0.69	Altered and moderately veined rhyolites, dacites, HS and Donington granite with 10% Fe, 5% K and 180 ppm Cu	2.7	1.91
5	712	0.74	Altered Donington granite and diorite with minor dacites; 20% Fe, 4% K and high Cu content (530 ppm)	2.9	28
6	441	0.93	Fe-rich veins; Fe >60%, K <0.1% and high Cu content (430 ppm)	4.2	306
7	759	0.75	Altered and veined rhyolites, dacites and ignimbrites with Fe 25% and K 2% and 280 ppm Cu	3.1	28

ADDITIONAL MATERIAL O

CONFERENCE ABSTRACT AND POSTER:

COPULA FUNCTIONS AS A TOOL FOR STATISTICAL MODELLING OF TRACE ELEMENT SIGNATURES IN IRON-OXIDES: EXAMPLES FROM SOUTH AUSTRALIAN ORE DEPOSITS

Marija Dmitrijeva [1], Andrew V. Metcalfe [2], Cristiana L. Ciobanu [1], Nigel J. Cook [1], Max R. Verdugo-Ihl [1], William M. Keyser 1, Kathy Ehrig [3]

[1]*School of Chemical Engineering and Advanced Materials, The University of Adelaide, Adelaide, SA 5005, Australia*

[2] *2School of Mathematical Sciences, The University of Adelaide, Adelaide, SA 5005, Australia*

[3] *BHP Olympic Dam, Adelaide, SA 5000, Australia*

Poster presentation at IAMG 2017, Perth, Australia, September 3rd-9th.

18TH ANNUAL CONFERENCE
IAMG2017
2-9 SEPTEMBER • PERTH, AUSTRALIA

70: COPULA FUNCTIONS AS A TOOL FOR STATISTICAL MODELLING OF TRACE ELEMENT SIGNATURES IN IRON-OXIDES: EXAMPLES FROM SOUTH AUSTRALIAN ORE DEPOSITS.

Dmitrijeva, M.[1], Metcalfe, A. V.[2], Ciobanu, C. L.[1], Cook, N. J.[1], Verdugo-Ihl, M. R.[1], Keyser, W. M.[1], Ehrig, K.[3]

[1] School of Chemical Engineering, The University of Adelaide, Adelaide, SA 5005, Australia
[2] School of Mathematical Sciences, The University of Adelaide, Adelaide, SA 5005, Australia
[3] BHP Billiton Olympic Dam, Adelaide, SA 5001, Australia

Trace elements are impurities 'dissolved' in a mineral lattice, and account for a small percentage of the total bulk composition of a given grain. Their concentrations are, implicitly, extremely low by comparison with the major components. Concentrations need, therefore, to be treated as either non-compositional data, or as compositional relative to the sum of the concentrations of all trace elements[1]. These alternatives provide different descriptions of the dataset. The concentrations of trace elements vary over several orders of magnitude, and standard multivariate analysis techniques (typically developed for dealing with samples from multivariate Gaussian distributions) tend to be dominated by outlying values unless the original data are transformed. Various options of transformations are compared. Moreover, large trace element signatures in mineral (TESIM) datasets may comprise multiple sub-populations (related to e.g., different samples or textural types), and analysis should be performed separately for each.
Trace element data is commonly analyzed by computing either Pearson's product-moment or Spearman's rank-order correlation coefficients between pairs of elements. However, correlation coefficients and empirical marginal distributions do not define dependence structure unless a multivariate Gaussian distribution is assumed. Copulas are multivariate distribution functions with one-dimensional uniform margins, and provide a greater flexibility since they can combine various marginal distributions with a variety of copula distributions. Copulas can therefore provide a better fit to data from sub-populations, and offer a powerful method for distinguishing sub-populations in a quantitative manner.
We present, for the first time, successive steps for building copula models for parts-per-million- level trace element concentrations in hematite and magnetite (the main iron-oxides considered here) from different types of deposits in South Australia. We fit various elliptical and Archimedean bivariate copulas to pre-defined textural types and evaluate goodness of fit. Further studies using copulas on larger datasets with extension to pair-copula constructions and spatial modelling are proposed.

Copula function as a tool for dependence modelling of trace element in iron oxides

Marija Dmitrijeva[1], Andrew V. Metcalfe[2], Cristiana L. Ciobanu[1], Nigel J. Cook[1], Max R. Verdugo-Ihl[1], William M. Keyser[1], Kathy J. Ehrig[3]

[1]School of Chemical Engineering, The University of Adelaide, Adelaide, SA 5005, Australia, [2]School of Mathematical Sciences, The University of Adelaide, Adelaide, SA 5005, Australia
[3]BHP Olympic Dam, Adelaide, SA 5001, Australia

Introduction

Iron oxides (Fig. 1 b-d) are the dominant components of banded iron formations (BIFs) and BIF-associated ores, and can incorporate a range of trace elements at measurable concentrations allowing their use as petrogenetic indicators of ore formation throughout space and time.

Trace elements account for a small percentage of the total bulk composition of a given grain. The dependence among trace elements is commonly investigated by computing Pearson's product-moment correlation coefficients between pairs of elements. While correlation coefficient is just one of the tools to describe dependency, the knowledge of correlation coefficient and marginal distributions does not exhibit entire bivariate dependency structure (Boardman & Vann, 2011), especially if data show tail dependence. A copula allows to overcome the limitations of correlation coefficient and offers larger flexibility to model dependence structure given any type of marginal distribution.

The present case study demonstrates fitting a copula to *in-situ* trace element data of hematite (α-Fe_2O_3). The trivariate Gaussian and Student-t copula were fitted to the As, Cu and Zn concentrations in hematite. This case study is a first step towards non-spatial applications of elliptical copulas to trace element data.

Data and Approach

In-situ trace element data, log-transformed concentrations of As_i, Cu_i and Zn_i (i = 1, ..., 1098), is sourced from the hematite of the Middleback Ranges (Dmitrijeva et al. in review). This element association shows a positive relationship (Fig. 1 a) and is potentially inherited from regional emplacement of Hiltaba Intrusive Suite (~1.58).

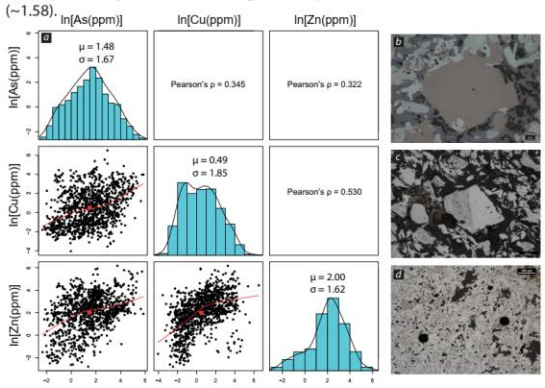


Figure 1 a) A scatterplot matrix of chalcophile elements Zn, Cu and As and the corresponding mean, standard deviation and Pearson's correlation coefficients; photomicrographs of iron oxides showing b) pink euhedral magnetite; c) partial martitization of euhedral magnetite d) interconversions of fine-grained magnetite to martite and two LA-ICP-MS spots. A single spot-analyses corresponds to a point on the scatterplot.

For any n-dimensional joint cumulative distribution function $F(x_1, x_2, \ldots, x_n) = P(X_1 \le x_1, X_2 \le x_2, \ldots, X_n \le x_n)$, and marginal cumulative distribution functions $F_i(x) = P(X_i \le x)$, $i=1,2,\ldots,N$ there is a unique copula C_n such that

$$F(x_1, x_2, \ldots, x_n) = C[F_1(x_1), F_2(x_2), \ldots, F_n(x_n)] = C(u_1, u_2, \ldots, u_n)$$

where $U_i = F_i(X_i)$ so with $U = U_i \sim \text{Uniform}(0,1)$, C is an n-increasing function and dependence structure separated from marginal distributions.

Trivariate Gaussian $C_{Gauss}(As_i, Cu_i, Zn_i | \boldsymbol{\Omega})$ and Student-t copula $C_t(As_i, Cu_i, Zn_i | \boldsymbol{\Omega}, \nu)$ were fitted to the data. The copula parameters, correlation matrix $\boldsymbol{\Omega}$ and degrees of freedom ν, were estimated by maximum likelihood. Given the large number of data, empirical distributions were fitted to the margins. In addition, 10^6 trivariate data values were generated from the theoretical Gaussian and Student-t copula to investigate the tail dependence (Table 1).

Goodness-of-fit

In order to assess the fitted copula, goodness-of-fit tests are performed. The simplest is to graphically compare the observed data with copula density. Another is to assess goodness-of-fit between the empirical copula C_n, evaluated at the observed data (As_i, Cu_i, Zn_i) and the fitted copula (Fig. 2 a, b) (Genest and Favre, 2007). The empirical copula is constructed by transforming observed data to uniform data on [0,1] using probability integral transformations. The uniform data is ranked and used to calculate C_n

$$C_n(u_{1i}, u_{2i}, u_{3i}) = \frac{1}{n}\sum_{i=1}^{n} \mathbf{I}\left(\frac{R_i}{n+1} \le u_{1i}, \frac{S_i}{n+1} \le u_{2i}, \frac{T_i}{n+1} \le u_{3i}\right) \quad (1)$$

where n is a sample size; $\mathbf{I}(A)$ is an indicator variable for the logical expression and is true if $\mathbf{I}(A) = 1$ and false if $\mathbf{I}(A) = 0$; the ranks of i-th observed triple As, Cu, Zn are denoted as R_i, S_i and T_i respectively. The measure of fit is defined by the proximity of points to the line (Fig. 2 a, b).

Results

The Student-t copula has an additional parameter degrees of freedom, and includes the Gaussian as a special case as $\nu \to \infty$. For these data, the maximum likelihood estimate of ν is 15 which represents a significant departure from the Gaussian. The difference between Gaussian and Student-t copula (ν=15) is not apparent from the goodness-of-fit plot (Fig. 2). However, the tail dependence of the Student-t copula is seen if a large number of random trivariate points is drawn from the distribution. The results of simulation are summarized in Table 1.

Table 1 – A number of points per million that have all three components beyond 2 standard deviations below/above the mean

	below 2σ	above 2σ
Gaussian	730	710
Student-t	2800	2410

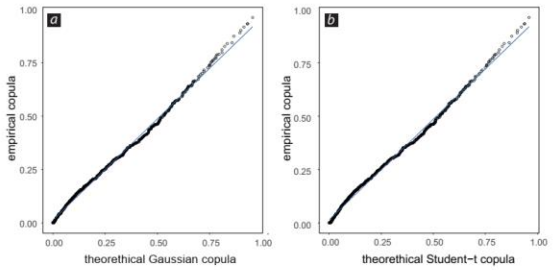


Figure 2 A goodness-of-fit plot of a) Gaussian and b) Student-t copula against empirical copula for log-transformed As_i, Cu_i and Zn_i (i = 1, ..., 1098) as in Eq. (1)

Conclusions

This investigations shows that characterizing linear association between element concentrations using Pearson's correlation coefficient calculated from transformed data, which is equivalent to a Gaussian copula, can be an oversimplification as it ignores the possibility of tail dependence.

Elliptical copulas can be an alternative to other methods of multivariate dependence modelling of trace element data. Future work will focus on application of vine copulas to model dependencies between trace elements.

Acknowledgements

This is a contribution to the 'FOX' project, supported by BHP Olympic Dam and the South Australian Mining and Petroleum Services Centre of Excellence

References

Boardman, R.C. & Vann, J.E., 2011. A review of the application of copulas to improve modelling of non-bigaussian bivariate relationships (with an example using geological data). MODSIM 2011 - 19th International Congress on Modelling and Simulation - Sustaining Our Future: Understanding and Living with Uncertainty, (December), 627–633

Genest, C., & Favre, A.-C., 2007. Everything you always wanted to know about copula modelling but were afraid to ask. Journal of Hydrological Engineering, 12, 347–368

Dmitrijeva, M., Metcalfe, A.V., Ciobanu, C.L., Cook, N.J., Frenzel, M., Keyser, W.M., Johnson, G., Ehrig, K., in review. Discrimination and variance structure of trace elements in hematite: a case study of BIF-mineralization from the Middleback Ranges, South Australia. Mathematical Geosciences.

[1]School of Chemical Engineering, the University of Adelaide, South Australia, 5005 | E-Mail: marija.dmitrijeva@adelaide.edu.au | Tel.: +61 458 823 945

ADDITIONAL MATERIAL P

CONFERENCE ABSTRACT AND POSTER:

'INVISIBLE' AU IN PYRITE FROM OLYMPIC DAM DEPOSIT, SOUTH AUSTRALIA: BRIDGING TEXTURES WITH STATISTICAL ANALYSES

Marija Dmitrijeva [1], Max R. Verdugo-Ihl [1], Kathy Ehrig [2], Cristiana L. Ciobanu [1], Nigel J. Cook [1]

[1]*School of Chemical Engineering and Advanced Materials, The University of Adelaide, Adelaide, SA 5005, Australia*

[2] *BHP Olympic Dam, Adelaide, SA 5000, Australia*

Poster presentation at 2019 TIGeR Conference, September 11th-13th.

'Invisible' Au in pyrite from Olympic Dam deposit, South Australia: bridging textures with statistical analyses

Marija Dmitrijeva[1*], Max R. Verdugho-Ihl[1], Kathy J. Ehrig[2], Cristiana L. Ciobanu[1], Nigel J. Cook[1]

[1]School of Chemical Engineering and Advanced Materials, The University of Adelaide, SA 5005, Australia; *marija.dmitrijeva@adelaide.edu.au; max.verdugoihl@adelaide.edu.au; cristiana.ciobanu@adelaide.edu.au; nigel.cook@adelaide.edu.au

[2]BHP Olympic Dam, Adelaide, SA 5000, Australia; kathy.ehrig@bhp.com

'Invisible' Au in pyrite refers to gold present within the sulphide lattice or as discrete nanoparticle inclusions, making it undetectable by conventional optical and scanning electron microscopy (SEM) (Cook and Chryssoulis 1990). Incorporation of Au into pyrite is often mediated by incorporation of As (Reich et al. 2005). Nevertheless, pore-attached Au-Ag-telluride nanoparticles have been documented within As-free pyrite (Ciobanu et al. 2012) thus representing an alternative mechanism for incorporation of Au into pyrite.

Olympic Dam, is an an archetypal iron-oxide copper gold (IOCG) deposit that contains >100 minerals and displays complex, finely intergrown sulphide assemblages (Ehrig et al. 2012). Of these, pyrite makes up ~0.5 wt% of the orebody. There currently exists a significant knowledge gap with respect to the potential presence of 'invisible' Au within pyrite from such IOCG ores, at Olympic Dam and elsewhere. Identification of the physical and chemical state of Au allows new constraints to be placed on ore genesis and also carries implications for mineral processing.

In a first attempt to address this issue, we combine multivariate statistical analyses of LA-ICP-MS trace element datasets for pyrite from Olympic Dam (OD) with micron-scale characterization. Trace element datasets are often presented with a relatively low-level statistical treatment such as two-three component projections accompanied by summary statistics. However, given the ever-increasing size and complexity of LA-ICP-MS datasets, a data-driven, reproducible and quantitative approach is required for processing (Winderbaum et al. 2012). Sixty-seven pyrite grains with measurable Au content were studied from a single polished block representative of a pyrite-chalcopyrite orezone at OD. Pyrite features oscillatory zoning with respect to As(-Co,-Ni) in individual grains (Fig. 1a) and sub-micron-scale inclusions of Bi- and Au-tellurides, among others (Fig. 1b). Gold-tellurides are also found in As-poor pyrite with no visible compositional zoning (Fig. 1c-d). The LA-ICP-MS dataset shows measurable concentrations of Ag, As, Au, Bi, Cd, Co, Cu, Mn, Mo, Ni, Pb, Se, Sn, Sb, Te, Ti, Tl, Th, ^{238}U, W, and Zn (192 spot analyses). Such elements are likely to be present as lattice-bound as well as inclusion within pyrite. Arsenic concentrations attain up to 3 wt%; mean and median values are 0.64 and 0.72 wt%, respectively.

Principal component analysis (PCA) coupled with construction of hierarchical dendrogram were used to depict geochemical associations among trace elements. Two distinct sub-groups are found: (i) Au-bearing (>10 ppm Au); and (ii) Au-poor pyrite (Fig. 1e-g). These sub-groups are clearly distinguished by different geochemical associations (Fig. 1f-g). In group (i), Au correlates strongly with As and Ag, and to a lesser extent, also with Bi, Sb, Cu, Sn and Pb. This confirms that compositionally zoned pyrite is a host for 'invisible' Au. Group (ii) features the element associations Ni-Co, Te-Se, elements that are easily incorporated in the pyrite structure, and other elements likely to occur as discrete mineral inclusions (Ti, Mn, W, Zn, U and Th). Although Bi-telluride inclusions are observed within As-bearing pyrite (Fig. 1b), PCA results show that Te and As are placed within different clusters. Microscopic observations suggest the presence of Te as telluride inclusions and As-poor pyrite. A possible scenario is that Au is essentially lattice-bond in As-bearing pyrite but present as inclusions of Au-bearing tellurides in As-poor pyrite. This hints at different mechanisms and/or conditions of Au incorporation, consistent with the complex evolution of the ores at Olympic Dam including reworking of primary zoning patterns. Further work includes nanoscale characterization of pyrite which will allow improved discrimination of NPs populations and their formation from lattice-bound elements or by other mechanisms. Statistical analysis could

be an important, novel tool to recognise populations of NPs in pyrite relative to well-defined generations and formation mechanisms e.g., exsolutions from solid solution in grains with crystal zoning, or fluid-assisted brecciation leading to pore-attached NPs.

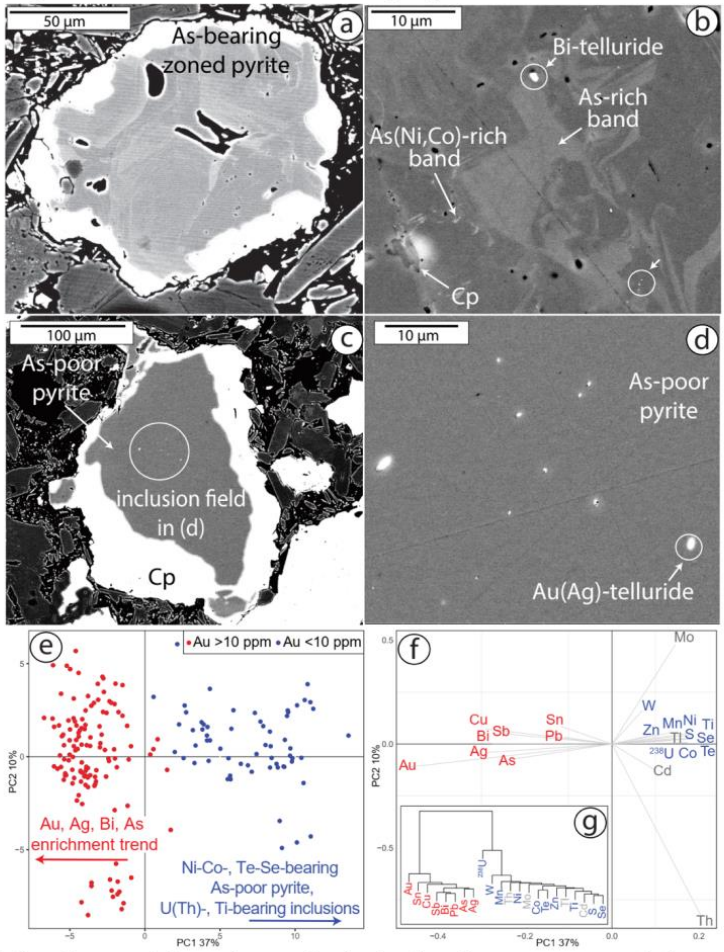


Figure 1. (a-d) Back-scattered electron images of pyrite showing relevant textures as marked. Note presence of sub-micron-sized tellurides. (e) PC scores showing geochemical distinctions among Au-bearing (>10 ppm Au) and Au-poor (<10 ppm Au) pyrite; (f) PC loadings showing geochemical groups associated with distinct pyrite types. Grey colours represent elements with >20% values falling below minimum limits of detection. (g) Hierarchical cluster dendrogram of analysed elements.

References

Ciobanu CL, Cook NJ, Utsunomiya S, Kogagwa M, Green L, Gilbert S, Wade B (2012) Gold-telluride nanoparticles revealed in arsenic-free pyrite, Am. Mineral. 97:1515-1518

Cook NJ, Chryssoulis SL (1990) Concentrations of invisible old in the common sulfides. Can. Mineral. 28: 1-16.

Ehrig K, McPhie J, Kamenetsky V (2012) Geology and mineralogical zonation of the Olympic Dam iron oxide Cu-U-Au-Ag deposit, South Australia. SEG Spec. Publ. 16:237–267

Reich M, Kesler SE, Utsunomiya S, Palenik CS, Chryssoulis SL, Ewing RC (2005) Solubility of gold in arsenian pyrite. Geochim. Cosmochim. Acta 69: 2781-2796

Winderbaum L, Ciobanu CL, Cook NJ, Paul M, Metcalfe A, Gilbert S (2012) Multivariate Analysis of an LA-ICP-MS Trace Element Dataset for Pyrite. Mathem. Geosci. 44: 823-842.

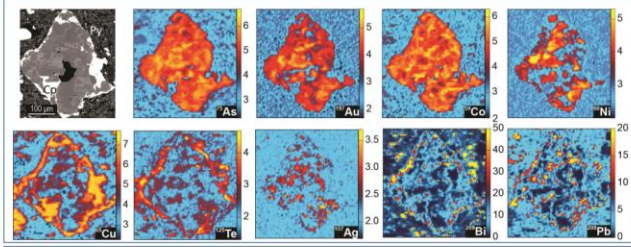
'Invisible' Au in pyrite from Olympic Dam deposit, South Australia: bridging micron- to nanoscale observations with statistical analyses

Marija Dmitrijeva*[1], Max R. Verdugo-Ihl[1], Kathy J. Ehrig[2] Cristiana L. Ciobanu[1], Nigel J. Cook[1]

[1]School of Chemical Engineering and Advanced Materials, The University of Adelaide, Adelaide, SA 5005,
[2]BHP Olympic Dam, Adelaide, SA 5001, Australia

* e-mail: marija.dmitrijeva@adelaide.edu.au

INTRODUCTION: 'Invisible' gold is present either in the pyrite lattice or as discrete Au-nanoparticles (NPs), thus being undetectable by conventional optical and scanning electron microscopy (SEM) [1]. Incorporation of Au into pyrite is often mediated by incorporation of As with a solubility limit defined from empirical analysis of epithermal and Carlin-type Au deposits [2]. Olympic Dam (OD), is an archetypal iron-oxide copper gold (IOCG) deposit that displays finely-intergrown sulphide assemblages [3]. Of these, pyrite makes up ~0.5 wt% of the orebody in one of the main Cu orezones. Despite many studies dedicated to the topic of invisible gold, none has been carried out on IOCG ores. Here we test: (i) the predictability of the Au-As solubility diagram with respect of the physical form of Au incorporated in pyrite; and (ii) the geochemical signatures of these elements using multivariate statistical analysis. Pyrite grains (67) with measurable Au and As content were studied from a polished block representative of the 'pyrite-chalcopyrite' orezone at OD. The study was carried out using LA-ICP-MS analysis, followed by multivariate statistical analysis of the dataset and nanoscale analysis (HAADF-STEM imaging and X-Ray energy-dispersive analysis, STEM-EDS).



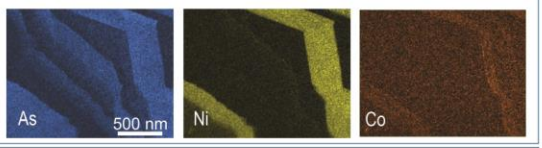


Figure 1. LA-ICP-MS maps (left) of zoned pyrite (Py). Note the overlap between As, Au, Co, partially Ni, and the scatter of other elements including Te, Ag, Bi and Pb. In contrast, the EDS STEM maps (below) resolve the fine scale of the zonation patterns among As, Ni and Co but does not depict the other trace elements due to the much higher threshold of the EDS-STEM detectors. Cp–chalcopyrite

METHODS AND DATA: The LA-ICP-MS dataset obtained from the pyrite grains shows measurable concentrations of Ag, As, Au, Bi, Co, Cu, Mn, Ni, Pb, Se, Sn, Sb, Te, and Zn (238 spot analyses). As concentrations attain up to 3 wt%; mean and median values are 0.64 and 0.72 wt%, respectively. Multivariate statistical analysis of the data included hierarchical and k-means clustering coupled with principal component analysis (PCA; Figure 2). The results correlate with pyrite textures and show two main types of geochemical association among trace elements (Figure 3a). All data plots below the curve of Au solubility in pyrite which is predicted as lattice-bound Au (Figure 3b). Samples for nanoscale analysis were obtained using FIB-SEM methods by cutting across zonation patterns within pyrite representing the three pyrite categories/signatures (PCA in Figure 2b). Nanoscale data show however, the presence of nanoparticles (NPs; Figures 4, 5) throughout all samples including electrum, Au-Ag-tellurides, Pb-Bi-sulphotellurides, Bi-(Ag)-tellurides and cassiterite, albeit with variable distributions relative to the pyrite categories as in Figures 2, 3a.

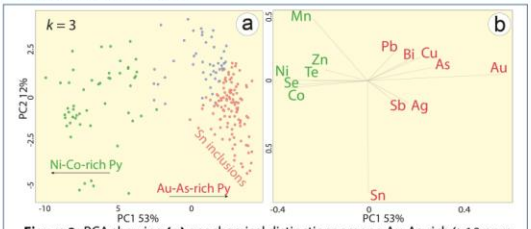


Figure 2: PCA showing **(a)** geochemical distinctions among Au-As-rich (>10 ppm Au) and Ni-Co-rich (<10 ppm Au) pyrite classified into 3 clusters; **(b)** elemental groups associated with distinct pyrite clusters.

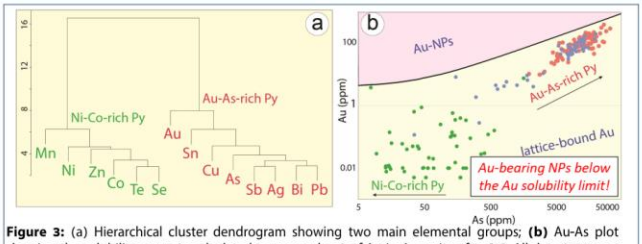


Figure 3: (a) Hierarchical cluster dendrogram showing two main elemental groups; **(b)** Au-As plot showing the solubility curve (recalculated to ppm values) of Au in As-pyrite after [2]. All data (238 spot analyses), including those from grains used for nanoscale study) plot below the solubility curve.

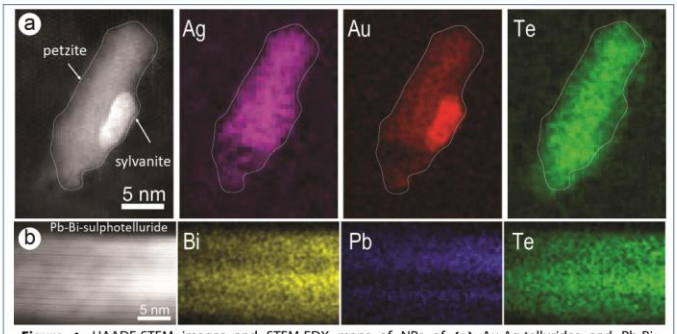


Figure 4. HAADF-STEM images and STEM-EDX maps of NPs of **(a)** Au-Ag-tellurides and Pb-Bi-sulphotellurides from the aleksite series (b). Such inclusions are representative of Au-As-rich pyrite whereas cassiterite NPs are abundant within un-zoned, As-poor pyrite. Tellurium is also associated with cassiterite NPs.

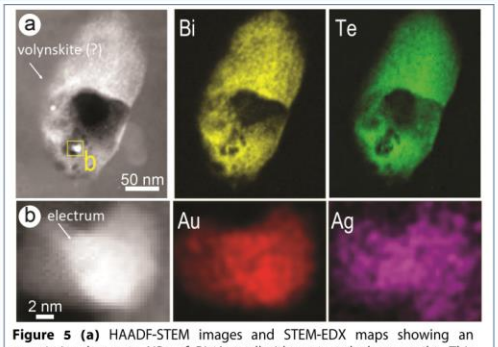


Figure 5 (a) HAADF-STEM images and STEM-EDX maps showing an association between NPs of Bi-(Ag)-tellurides (a) and electrum (b). This correlates with the geochemical association as indicated by the statistical analyses.

Summary: The LA-ICP-MS maps indicate the presence of 'invisible' Au in pyrite at OD, however, the resolution of such maps does not resolve the fine-scale nature of trace element distributions or the physical state of Au. Multivariate statistical analysis of LA-ICP-MS data highlights distinct geochemical clusters attributable to Au-As-rich pyrite, which is characterized by a Au-As-Ag-Cu-Bi-Sb-Pb association. Nanoscale observations reveal numerous Bi-(Pb)-telluride NPs in pyrite. Tellurium, which plots within a different cluster on the PCA diagram, has to also be present in Ni-Co-rich pyrite. The presence of electrum and Au-Ag-telluride NPs contradicts the predictability of Au solubility in As-pyrite since electrum and Au-Ag-tellurides are present in samples that otherwise show data plotting below the solubility limit (Figure 3b). The presence of such Au-bearing NPs hints that brecciation and complex reworking of primary zoning patterns in pyrite results in the formation of Au-NPs, an interpretation fully consistent with the complex evolution of the ores at Olympic Dam and likely in IOCG deposits elsewhere. The association between Au and chalcophile elements, as shown by the statistical analysis, is also revealed by the presence of Bi-(Pb)-tellurides. Here we show that combining statistical analysis with sample characterization that bridges different scales of observation is successful in underpinning the true nature of 'invisible Au' in pyrite.

ACKNOWLEDGEMENTS: This work is supported by BHP Olympic Dam. **REFERENCES:** [1] Cook & Chryssoulis (1990, Can Mineral 28: 1-16); [2] Reich et al. (2005 Geochim Cosmochim Acta 69: 2781-2796); [3] Ehrig et al. (2012, SEG Spec Publ 16:237–267).

ADDITIONAL MATERIAL Q

CO-AUTHORED CONFERENCE ABSTRACT:

WHY DETAILED MINERALOGY IS IMPORTANT: UNDERSTANDING EVOLUTION OF THE OLYMPIC DAM IRON-OXIDE-COPPER-GOLD SYSTEM, SOUTH AUSTRALIA

Nigel Cook[1], Kathy Ehrig[2], Cristiana Ciobanu[1], **Liam Courtney-Davies[1]**, Max Verdugo-Ihl[1], Mark Rollog[1], Danielle Schmandt[1], Nicholas Owen[1], Edeltraud Macmillan[2], Alkiviadis Kontonikas-Charos[1], Sasha Krneta[1], Marija Dmitrijeva[1]

[1]School of Chemical Engineering and Advanced Materials, The University of Adelaide, Adelaide, SA 5005, Australia

[2]BHP Olympic Dam, Adelaide, SA 5000, Australia

Conference presentation, 15th Quadrennial IAGOD Symposium, Salta, Argentina, August 28th-31st. Symposium Volume, SEGEMAR, 371-372.



WHY DETAILED MINERALOGY IS IMPORTANT: UNDERSTANDING EVOLUTION OF THE OLYMPIC DAM IRON-OXIDE COPPER-GOLD SYSTEM, SOUTH AUSTRALIA

Nigel Cook[1], Kathy Ehrig, Cristiana Ciobanu, Liam Courtney-Davies, Max Verdugo-Ihl, Mark Rollog, Danielle Schmandt, Nicholas Owen, Edeltraud Macmillan, Alkiviadis Kontonikas-Charos, Sasha Krneta, Marija Dmitrijeva

[1]*School of Chemical Engineering, University of Adelaide, Australia - nigel.cook@adelaide.edu.au*

Olympic Dam is one of the largest deposits on Earth and a significant producer of copper, uranium, gold and silver (Ehrig, *et al.*, 2013). Uranium-Pb geochronology using undisturbed magmatic and hydrothermal minerals allows interpretation of the initial and major hydrothermal ore- forming event at ~1593 Ma, associated with emplacement of the Gawler Silicic Large Igneous Province. The >10 billion-tonne resource is heterogeneous and contained within a breccia complex, itself confined to the ~1593 Ma Roxby Downs Granite. Ore textures suggest multiple episodes of replacement, remobilization and recrystallization and are supported by (radio) isotope data yielding a range of younger ages. Conceptual models for ore formation, necessary for exploration in the region, and optimised processing of complex fine-grained ores characterised by enrichment in an extraordinarily wide variety of elements are dependent on an exceptionally thorough understanding of mineralogy and geochemistry underpinned by high-quality, high-resolution assay data, extensive MLA datasets, and deportment models for multiple elements.

Micron - to nanoscale studies of feldspars and accessory phases within the alteration envelope, and of Fe-oxides, Cu-(Fe)-sulphides, sulphates, U- and REE-bearing minerals within the deposit all point to common mechanisms involved in formation of the mineral assemblages as observed today, the prevailing Mm-scale mineral textures, and measured variations in mineral compositions. Detailed mineralogical investigation has proven pivotal in establishing a framework for ore evolution.

Each of the 100 minerals in the Olympic Dam deposit has a story to tell. The complex fine- grained, intergrown, heterogeneous assemblages necessitate ultra-careful investigation on multiple representative samples and with compositional data requiring verification by examination at the nanoscale. We therefore use a combination of whole rock assay, optical and scanning electron microscopy, electron probe microanalysis (EPMA), laser-ablation inductively-coupled plasma mass spectrometry, complemented by imaging and nanoscale compositional analysis by transmission electron microscopy (TEM) on foils extracted *in-situ* by focussed ion beam SEM methods.

Investigation of feldspars from within and outside the deposit allows an understanding of the magmatic to hydrothermal transition and early Fe-metasomatism (Kontonikas-Charos, *et al.*, 2017). Nanoscale characterization of feldspars undergoing transformation from early post-magmatic (deuteric) to hydrothermal stages in granites hosting the deposit reveals complex perthitic textures, anomalously Ba, Fe, or REE-rich compositions, and REE-fluorocarbonate+molybdenite assemblages that pseudomorph feldspars (Kontonikas-Charos, *et al.*, 2018). Epitaxial orientations between (igneous) cryptoperthite, (deuteric) patch and albite replacive within vein perthite support interface-mediated reactions between pre-existing alkali-feldspars and pervading fluid, irrespective of micron-scale crystal morphology. Such observations are consistent with coupled dissolution-replacement reactions (CDRR), indicating that albitization enhances rock permeability via the generation of transient pores which facilitate grain-scale element remobilization and trap elements as nanoscale inclusions. These inclusions represent the earliest stage of REE remobilization at the grain-scale, and reflect the significant role feldspar replacement reactions play in concentrating REE during hydrothermal alteration.

Hematite is by far the most abundant hydrothermal mineral and preserves oscillatory and sectorial zoning and incorporation of U, W, Mo, Sn and other trace elements, including REE (Verdugo-Ihl, *et al.*, 2017). The presence of U and Pb allows application of hematite U-Pb geochronology [e.g., Courtney-Davies, *et al.*, 2018]. These primary textures give way to repeated processes of brecciation, fluid-assisted reworking, element redistribution, recrystallization and overprinting. CDRR permits release of trace elements from the lattice to be trapped as nm- to Mm-scale inclusions (e.g., uraninite), or to form discrete minerals (e.g., scheelite molybdenite) in the near vicinity.

EPMA-scale compositional data combined with TEM investigation of chalcocite-group minerals, bornite and chalcopyrite has shown that Cu-Fe-sulphides from different ore zones feature nanoscale intergrowths, lattice defects, superstructure domains and antiphase boundary domains (Ciobanu, *et al.*, 2017). Such features can be interpreted as having originated via a combination of exsolution, coarsening, and phase transformation during cooling from high-T solid solutions (e"400°C) in the system Cu-Fe-S and sub-systems. A scenario of 'exsolution from primary solid-solution, corroborated by the consistency in phase relations within each zone across different scales of observation from deposit- to nanoscale, supports a model of primary hypogene ore precipitation rather than replacement, and

accounts for the observed zoning patterns at OD. Nonetheless, evidence for CDRR, replacement, phase transformation and local (Mm- to tens m-wide) remobilization is evident.

Uraninite, coffinite, brannerite and hematite are the dominant U hosts [Courtney-Davies, *et al.*, 2018, Macmillan, *et al.*, 2016, Macmillan, *et al.,* 2017). Although some uraninite and hematite retain U and daughter isotopes, breakdown and replacement can lead to release, remobilization and redistribution of radionuclides (RN) at scales from nm upwards. New minerals may be formed (late uraninite, coffinite) and U and Pb can also be incorporated into existing minerals (barite, svanbergite-woodhouseite). RN are, however, also concentrated as sub-microscopic particles within pores, microfractures and at grain boundaries in the near vicinity of altered or replaced U-bearing mineral grains (Rollog, *et al.*, 2018) attesting to fluid-mediated processes. Such redistribution carries implications for ore processing and, potentially also for the interpretation of geochronological data.

Three groups of REE-minerals are observed: REE-fluorocarbonates (bastnosite and subordinate synchysite (Schmandt, *et al.*, 2017), which appear paragenetically early; REE-phosphates (dominantly florencite of variable age and association but also minor xenotime, the main carrier of HREE); and Ca-, Sr-, REE-bearing phosphate-sulphates (svanbergite- woodhouseite], which are generally late and replace earlier-formed minerals (Owen, *et al.,* 2018). Minor REE are also contained in apatite, which displays evolving chondrite-normalized REE fractionation trends that can be explained in terms of changes in fluid parameters and speciation of REY in ore-forming fluids (Krneta, *et al.,* 2017). Under hydrothermal conditions typical of iron- oxide copper gold mineralization, a decrease in salinity, pH and temperature is associated with hematite-sericite alteration sufficient to produce a characteristic MREE-enriched apatite. However, anomalous high-pH (~7) fluids at 300 °C may account for high-grade Cu ores as modelled from apatite with strong positive Eu anomalies (Krneta, *et al.,* 2017).

Although primary assemblages are identified, a persistent narrative is offered by multiple episodes of fluid-assisted replacement, phase transition, remobilization, migration, and re- precipitation of all ore components. These processes played a major role in the modification of textural and geochemical patterns in many minerals. However, more refractory minerals, notably hematite, apatite, pyrite, some REE-minerals, and some sub-types of U-minerals, can preserve primary geochemical signatures and can also record and retain evidence of evolving and overprinting fluid signatures. Fluid regimes were likel heterogeneous given observations of texturally and geochemically distinct generations of the same mineral within single samples.

REFERENCES

Ehrig, K., McPhie, J., Kamenetsky, V., 2013. Geology and mineralogical zonation of the Olympic Dam iron oxide Cu-U-Au-Ag deposit, South Australia. In: Hedenquist, J.W., Harris, M., Camus, F. (Eds), Geology and Genesis of Major Copper Deposits and Districts of the World, a Tribute to Richard Sillitoe. SEG Special Publication 16, pp. 237-268.

Kontonikas-Charos, A., Ciobanu, C.L., Cook, N.J., Ehrig, K., Krneta, S., Kamenetsky, V.S., 2017. Feldspar evolution in the Roxby Downs Granite, host to Fe-oxide Cu-Au-(U) mineralization at Olympic Dam, South Australia. Ore Geology Reviews, 80, 838-859.

Kontonikas-Charos, A., Ciobanu, C.L., Cook, N.J., Ehrig, K., Ismail, R., Krneta, S., Basak, A., 2018. Feldspar mineralogy and rare earth element (re)mobilization in iron-oxide copper gold systems from South Australia: a nanoscale study. Mineralogical Magazine 82 (S1), S173–S197.

Verdugo-Ihl, M.R., Ciobanu, C.L., Cook, N.J., Ehrig, K., Courtney-Davies, L., Gilbert, S., 2017. Textures and U-W-Sn-Mo signatures in hematite from the Cu-U-Au-Ag orebody at Olympic Dam, South Australia: defining the archetype for IOCG deposits. Ore Geology Reviews 91, 173–195.

Courtney-Davies, L., Ciobanu, C.L., Tapster, S.R., Cook, N.J., Ehrig, K.J., Kennedy, A.K., Condon, D.J., Verdugo-Ihl, M.R., Wade, B.S., Gilbert, S.E., 2018. The U-Pb systematics of hydrothermal hematite; insights from the IOCG system at Olympic Dam, South Australia. IAGOD Symposium, Salta (this volume).

Ciobanu, C.L., Cook, N.J., Ehrig, K., 2017. Ore minerals down to the nanoscale: Cu-(Fe)- sulphides from the iron oxide copper gold deposit at Olympic Dam, South Australia. Ore Geology Reviews 81, 1218-1235.

Macmillan, E., Cook, N.J., Ciobanu, C.L., Ehrig, E., Pring, A., 2016. Uraninite from the Olympic Dam IOCG-U-Ag deposit: linking textural and compositional variation to temporal evolution. American Mineralogist 101, 1295–1320.

Macmillan, E., Cook, N.J., Ehrig, K., Pring, A., 2017. Chemical and textural interpretation of late-stage coffinite and brannerite from the Olympic Dam IOCG-Ag-U deposit. Mineralogical Magazine 81, 1323-1366.

Rollog, M., Cook, N.J., Gugliardo, P., Ehrig. K., Kilburn, M., 2018. In situ spatial distribution mapping of radionuclides in minerals by nanoSIMS. Geochemistry – Exploration, Environment, Analysis (in press).

Schmandt, D.S., Cook, N.J., Ciobanu, C.L., Ehrig, K., Wade, B.P., Gilbert, S., Kamenetsky, V.S., 2017. Rare earth element fluorocarbonate minerals from the Olympic Dam Cu-U-Au-Ag deposit, South Australia. Minerals 7(10), 202; doi: 10.3390/min7100202.

Owen, N.D., Ciobanu, C.L., Cook, N.J., Slattery, A., Basak, A., 2018. Nanoscale study of clausthalite-bearing symplectites in Cu-Au-(U) ores: Implications for ore genesis. Minerals, 8(2), 67; doi:10.3390/min8020067.

Krneta, S., Ciobanu, C.L., Cook, N.J., Ehrig, K., Kontonikas-Charos, A., 2017. Rare earth element behaviour in apatite from the Olympic Dam Cu-U-Au-Ag deposit, South Australia. Minerals 7(8), 135; doi:10.3390/min7080135.

CHAPTER 10

REFERENCES

Aas, K., Czado, C., Frigessi, A., Bakken, H. 2009. Pair-copula constructions of multiple dependence. Insurance: Mathematics and Economics, 44, 182-198.

Abraitis, P.K., Pattrick, R.A.D., Vaughan, D.J. 2004. Variations in the Compositional, Textural and Electrical Properties of Natural Pyrite: A Review. International Journal of Mineral Processing, 2004, 74, 41-59.

Aitchison, J. 1986. The Statistical Analysis of Compositional Data. Monographs on Statistics and Applied Probability. Chapman and Hall Ltd. (Reprinted 2003 with additional material by The Blackburn Press), London. pp. 416.

Aitchison, J. 1999. Logratios and natural laws in compositional data analysis. Mathematical Geology, 31, 563-580.

Aitchison, J., Barceló-Vidal, C., Pawlowsky-Glahn, V. 2002. Some comments on compositional data analysis in archaeometry, in particular the fallacies in Tangri and Wright's dismissal of logratio analysis. Archaeometry, 44, 295-304.

Akaike, H. 1973. Information theory and an extension of the maximum likelihood principle. In B. N. Petrov and F. Csaki (Eds.), Proceedings of the Second International Symposium on Information Theory Budapest, Akademiai Kiado, pp. 267-281.

Allen, S.R., McPhie, J., Ferris, G., Simpson, C. 2008. Evolution and architecture of a large felsic Igneous Province in western Laurentia: The 1.6 Ga Gawler Range Volcanics, South Australia. Journal of Volcanology and Geothermal Research, 172, 132-147.

Angerer, T., Hagemann, S.G., Danyushevsky, L.V. 2013. High-grade iron ore at Windarling, Yilgarn Craton: a product of syn-orogenic deformation, hypogene hydrothermal alteration and

supergene modification in an Archean BIF-basalt lithostratigraphy. Mineralium Deposita, 48, 697-728.

Apukhtina, O.B., Kamenetsky, V.S., Ehrig, K., Kamenetsky, M.B., Maas, R., Thompson, J., McPhie, J., Ciobanu, C.L., Cook, N.J. 2017. Early, deep magnetite-fluorapatite mineralization at the Olympic Dam Cu-U-Au-Ag deposit, South Australia. Economic Geology, 112, 1531-1542.

Bachmann, K., Menzel, P., Tolosana-Delgado, R., Schmidt, C., Hill., M. Gutzmer, J. 2019. The use of assay data as a foundation for a geometallurgical model-The case of the Thaba Chromite Mine, South Africa: Journal of Geochemical Exploration, 201, 99-112.

Barton, M.D. 2014. Iron Oxide(–Cu–Au–REE–P–Ag–U–Co) Systems, in Holland HD, Turekian KK, eds, Treatise on Geochemistry, 2nd edition Elsevier, Oxford, 515-541.

Bastrakov E., Skirrow, R.G., Davidson, G. J. 2007, Fluid Evolution and Origins of Iron Oxide Cu-Au Prospects in the Olympic Dam District, Gawler Craton, South Australia: Economic Geology, 102, 1415-1440.

Bates, D., Maechler, M., Bolker, B., Walker, S. 2015. Fitting Linear Mixed-Effects Models Using lme4. Journal of Statistical Software, 67, 1-48.

Belissont, R., Boiron, M.C., Luais, B., Cathelinea, M. 2014. LA-ICP-MS analyses of minor and trace elements and bulk Ge isotopes in zoned Ge-rich sphalerites from the Noailhac-Saint-Salvy deposit (France): Insights into incorporation mechanisms and ore deposition processes. Geochimica et Cosmochimica Acta, 126, 518-540.

Berger, B.R., Ayuso, R.A., Wynn, J.C., Seal, R. 2008. Preliminary model of porphyry copper deposits. In: USGS Numbered Series Open-file Report, pp. 55.

Bhattacharya, H.N., Chakraborty, I., Ghosh, K. 2007. Geochemistry of some banded iron formations of the Archean supracrustals, Jharkhand-Orissa region, India. Journal of Earth System Science, 116, 245-259.

BHP. 2019. BHP Annual Report 2019, (https://www.bhp.com/-/media/documents/investors/annual-reports/2019/bhpannualreport2019.pdf)

Bhuiyan, M., Esmaieli, K., Ordóñez-Calderón, J.C. 2019, Application of Data Analytics Techniques to Establish Geometallurgical Relationships to Bond Work Index at the Paracutu Mine, Minas Gerais, Brazil: Minerals, 9, 302.

Blissett, A.H., Creaser, R.A., Daly, S.J., Flint, R.B., Parker, A.J. 1993. Gawler range volcanics. In: Drexel, J.F., Preiss, W.V., Parker, A.J. (Eds.), The Geology of South Australia. vol. 1. The Precambrian, Geological Survey of South Australia, pp. 107–131.

Bookstrom, A. 1977. The Magnetite Deposits of E1 Romeral, Chile, Economic Geology, 72, 1101-1130.

Bowles, J.F.W., Howie, R.A., Vaughan, D.J., Zussman, J. 2011. Non-silicates: volume 5A. In: W.A. Deer, R.A. Howie, J. Zussman (Eds.), Rock-Forming Minerals, Publisher: Geological Society, London, U.K, pp. 920.

Brechmann, E.C. 2010. Truncated and simplified regular vines and their applications. Diploma thesis, Technische Universitaet Muenchen, pp. 227.

Brechmann, E.C., Schepsmeier, U. 2013. CDVine: Modelling Dependence with C- and D-Vine Copulas in R. Journal of Statistical Software, 52, 3.

Breiman, L. 2001. Random Forests. Machine Learning 45, 5-32.

Breiman, L, Friedman, J.H., Olshen, R.A., Stone, C.J. 1984. Classification and Regression Trees. Wadsworth, Belmont pp. 358.

Buddington, A.F., Lindsley, D.H. 1964, Iron-titanium oxide minerals and synthetic equivalents: Journal of Petrology, 5, 310–357.

Caciagli, N. 2016. Multielement geochemical modelling for mine planning: case study from an epithermal gold deposit. In: Martín-Fernández, J.A., Thió-Henestrosa, S. (Eds.), Compositional Data Analysis. Springer Proceedings in Mathematics & Statistics, 187, 45–61.

Carstens, C.W. 1941. Om geokjemiske undersøkelser av malmer. Norsk Geologisk Tidsskrift, 21, 213–221.

Chen, S., Hattori, K., Grunsky, E.C. 2017. Multielement statistical evidence for uraniferous hydrothermal activity in sandstones overlying the Phoenix uranium deposit, Athabasca Basin, Canada. Mineralium Deposita, 53, 493-508.

Cherry, A., Ehrig, K., Kamenetsky, V.S., McPhie, J., Crowley, J. Kamenetsky, M. 2018. Precise geochronological constraints on the origin, setting and incorporation of ca. 1.59 Ga surficial facies into the Olympic Dam Breccia Complex, South Australia. Precambrian Research, 315, 162-168.

Cherry, A.R., Kamenetsky, V.S., McPhie, J., Thompson, J.M., Ehrig, K.J., Meffre, S., Kamenetsky, M.B., Krneta, S. 2018. Tectonothermal events in the Olympic IOCG Province constrained by apatite and REE-phosphate geochronology. Australian Journal of Earth Sciences, 65, 643-659.

Chib, S., Greenberg, E. 1995. Understanding the Metropolis–Hastings algorithm. American Statistician 90, 1313-1321.

Ciobanu, C.L. 2015. Trace element signatures in sulphides at Olympic Dam and satellite prospects: A reconnaissance study for ore vectoring using Cu-(Fe)-sulphides in Iron Oxide Copper Gold Deposits, Unpublished Report, The University of Adelaide.

Ciobanu, C.L., Cook, N.J., Utsunomiya, S., Kogagwa, M., Green, L., Gilbert, S., Wade, B. 2012. Gold-telluride nanoparticles revealed in arsenic-free pyrite. American Mineralogist, 97, 1515-1518.

Ciobanu, C.L., Wade, B.P., Cook, N.J., Schmidt Mumm, A., Giles, D. 2013. Uranium-bearing hematite from the Olympic Dam Cu-U-Au deposit, South Australia: a geochemical tracer and reconnaissance Pb-Pb geochronometer. Precambrian Research, 238, 129-147.

Ciobanu, C.L., Cook, N.J., Maunders, C., Wade, B.P., Ehrig, K. 2016. Focused ion beam and advanced electron microscopy for minerals: insights and outlook from bismuth sulphosalts. Minerals, 6, 112.

Ciobanu, C.L., Cook, N.J., Ehrig, K. 2017. Ore minerals down to the nanoscale: Cu-(Fe)-sulphides from the iron oxide copper gold deposit at Olympic Dam, South Australia. Ore Geology Reviews, 81, 1218-1235.

Ciobanu, C.L., Verdugo-Ihl, M.R., Slattery, A., Cook, N.J., Ehrig, K.J., Courtney-Davies L. 2018, Nanoscale study of silician magnetite from IOCG systems: examples from the Olympic Dam District, South Australia: Quadrennial International Association on the Genesis of Ore Deposits symposium, 15th, Salta, Argentina, 2018, Proceedings, pp. 185–186.

Ciobanu, C.L., Verdugo-Ihl, M.R., Slattery, A., Cook, N.J., Ehrig, K.J., Courtney-Davies, L., Wade, B.P. 2019. Silician magnetite: Si–Fe-nanoprecipitates and other mineral inclusions in magnetite from the Olympic Dam Deposit, South Australia. Minerals 9, 311.

Conor, C., Raymond, O., Baker, T., Teale, G., Say, P., Lowe, G. 2010. Alteration and mineralisation in the Moonta-Wallaroo Cu–Au mining field region, Olympic domain, South Australia. In: Porter, M. (ed.), Hydrothermal Iron Oxide Copper–Gold and Related Deposits: A Global Perspective 3, PGC Publishing, Adelaide, pp. 1-24.

Cook, N.J., Chryssoulis, S.L. 1990. Concentrations of invisible gold in the common sulphides. Canadian Mineralogist, 28, 1-16.

Cook, N.J., Ciobanu, C.L., Mao, J. 2009. Textural control on gold distribution in As-free pyrite from the Dongping, Huangtuliang and Hougou gold deposits, North China Craton (Hebei Province, China). Chemical Geology, 264, 101-121.

Cook, N.J., Ciobanu, C.L. Danyushevsky, L.V., Gilbert, S. 2011. Minor and trace elements in bornite and associated Cu–(Fe)-sulfides: A LA-ICP-MS study. Geochimica et Cosmochimica Acta, 75, 6473-6496.

Cook, N.J., Ciobanu, C.L., Meria, D., Silcock, D., Wade, B.P. 2013. Arsenopyrite-Pyrite Association in an Orogenic Gold Ore: Tracing Mineralization History from Textures and Trace Elements. Economic Geology, 108, 1273-1283.

Cook, N.J., Ciobanu, C.L., George, L., Zhu, Z.-Y., Wade, B., Ehrig, K. 2016. Trace Element Analysis of Minerals in Magmatic-Hydrothermal Ores by Laser Ablation Inductively-Coupled Plasma Mass Spectrometry: Approaches and Opportunities. Minerals, 6, 111.

Cook, N.J., Ciobanu, C.L., Ehrig, K., Slattery, A., Verdugo-Ihl, M.R., Courtney-Davies, L., Gao, W. 2017. Advances and opportunities in ore mineralogy. Minerals 7, 233,

Corbeil, R.R., Searle, S.R. 1976. Restricted Maximum Likelihood (REML) Estimation of Variance Components in the Mixed Model. Technometrics, 18, 31-38.

Corriveau, L. 2005. Iron oxide copper-gold (± Ag ± Nb ± P ± REE ± U) deposits: A Canadian Perspective: Geological Association of Canada, Mineral Deposits Division, Special Publication 5, 2007 pp. 307–328.

Corriveau, L., Montreuil, J.F., Potter, E. 2016. Alteration Facies Linkages Among Iron Oxide Copper-Gold, Iron Oxide-Apatite, and Affiliated Deposits in the Great Bear Magmatic Zone, Northwest Territories, Canada. Economic Geology, 111, 2045-2072.

Courtney-Davies, L., Zhu, Z., Ciobanu, C., Wade, B., Cook, N., Ehrig, K., Cabral, A., Kennedy, A. 2016. Matrix-matched iron-oxide laser ablation ICP-MS U-Pb geochronology using mixed solution standards. Minerals 6, 85.

Courtney-Davies, L., Ciobanu, C., Verdugo-Ihl, M.R., Dmitrijeva, M., Cook, N., Ehrig, K., Wade, B. 2019a. Hematite geochemistry and geochronology resolve genetic and temporal links among iron-oxide copper gold systems, Olympic Dam district, South Australia: Precambrian Research, 335, 105480.

Courtney-Davies, L., Tapster, S., Ciobanu, C., Cook, N.J., Verdugo-Ihl, M.R., Ehrig, K.J., Kennedy, A.K., Gilbert, S.E., Condon, D.J., Wade, B.P. 2019b. A multi-technique evaluation of hydrothermal hematite U-Pb isotope systematics: Implications for ore deposit geochronology. Chemical Geology, 513, 54-72.

Courtney-Davies, L., Ciobanu, C.L., Tapster, S.R., Cook, N.J., Ehrig, K.J., Crowley, J.L., Verdugo-Ihl, M.R., Wade, B.P., and Condon, D.J. in review. Opening the Magmatic-Hydrothermal Window: High-Precision U-Pb High-Precision U-Pb Geochronology of the Mesoproterozoic Olympic Dam Cu-U-Au-Ag Deposit. Economic Geology.

Cracknell, M.J., Reading, A.M. 2014. Geological mapping using remote sensing data: A comparison of five machine learning algorithms, their response to variations in the spatial distribution of training data and the use of explicit spatial information. Computers and Geosciences, 63, 22-33.

Craig, J.R., Vokes, F.M., Solberg, T.N. 1998. Pyrite: physical and chemical textures. Mineralium Deposita, 34, 82-101.

Creaser, R.A. 1989. The geology and petrology of Middle Proterozoic felsic magmatism of the Stuart Shelf, South Australia. Unpublished Ph.D. thesis, La Trobe University, Melbourne, Australia.

Creaser, R.A., Fanning, C.M. 1993. A U-Pb zircon study of the Mesoproterozoic Charleston Granite, Gawler Craton, South Australia. Australian Journal of Earth Sciences, 40, 519-526.

Cross, K.C. 1993. Acropolis and Wirrda Well. In: Drexel JF, Preiss WV, Parker AJ (eds.), The geology of South Australia. vol. 1, The Precambrian. Geological Survey of South Australia, South Australia pp. 138.

Dalstra, H.J., Rosière, C.A. 2008. Structural controls on high-grade iron ores hosted by banded iron formation: a global perspective. Reviews in Economic Geology, 15, 73-106.

Danyushevsky, L.V., Robinson, P., Gilbert, S., Norman, M., Large, R., McGoldrick, P., Shelley, J.M.G. 2011. Routine quantitative multi-element analysis of sulphide minerals by laser ablation ICP-MS: standard development and consideration of matrix effects. Geochemistry: Exploration, Environment, Analysis, 11, 51–60

Dare, S., Barnes, S.-J., Beaudin, G. 2014. Did the massive magnetite "lava flows" of El Laco (Chile) form by magmatic or hydrothermal processes? New constraints from magnetite composition by LA-ICP-MS. Mineralium Deposita, 50, 607-617.

Davies, M.B. 2000. Iron ore in South Australia. Primary Industries and Resources SA. Commodity Review, 8, pp. 35.

Deditius, A.P., Reich, M. 2016. Constraints on the solid solubility of Hg, Tl, and Cd in arsenian pyrite. American Mineralogist, 101, 1451.

Dempster, A.P., Laird, N.M., Rubin, D.B. 1977. Maximum likelihood from incomplete data via the EM algorithm. Journal of the Royal Statistical Society, 39, 1-38.

Dentith, M. 2003. Geophysical signatures of South Australian mineral deposits: Miscellaneous and minor deposits, ASEG Extended Abstracts 3, 257-281.

Di Lascio, F.M.L., Giannerini, S., Reale, A. 2015. Exploring copulas for the imputation of complex dependent data. Statistical Methods and Applications, 24, 159-175.

Dmitrijeva, M., Metcalfe, A.V., Ciobanu, C.L., Cook, N.J., Frenzel, M., Keyser, W.M., Johnson, G., Ehrig, K. 2018. Discrimination and Variance Structure of Trace Element Signatures in Fe-Oxides: A Case Study of BIF-Mineralisation from the Middleback Ranges, South Australia. Mathematical Geosciences, 50, 381-415.

Dmitrijeva, M., Ciobanu, C., Ehrig, K., Cook, N., Metcalfe, A., Verdugo-Ihl, M., McPhie, J. 2019a. Mineralization-alteration footprints in the Olympic Dam IOCG district South Australia: The Acropolis prospect: Journal of Geochemical Exploration, 205, 106333.

Dmitrijeva, M., Ehrig, K., Ciobanu, C., Cook, N. Verdugo-Ihl, M, Metcalfe, A. 2019b. Defining IOCG signatures through compositional data analysis: A case study of lithogeochemical zoning from the Olympic Dam deposit, South Australia. Ore Geology Reviews, 105, 86-101.

Dmitrijeva, M., Cook, N.J., Ehrig, K., Ciobanu, C.L., Metcalfe, A.V., Kamenetsky, M., Kamenetsky, V.S., Gilbert, S., 2020, Multivariate statistical analysis of trace elements in pyrite: prediction, bias and artefacts in defining mineral signature. Minerals, 10, 61.

Dmitrijeva, M., Ciobanu, C.L., Ehrig, K., Cook, N.J., Verdugo-Ihl, M.R., Metcalfe, A.V., Kamenetsky, V.S., McPhie, J. in review, Geochemical data analysis and 3D modelling, Wirrda Well prospect, South Australia: structural control on iron-oxide copper gold mineralisation. Economic Geology.

Dupuis, C., Beaudoin, G. 2011. Discriminant diagrams for iron oxide trace element fingerprinting of mineral deposit types. Mineralium Deposita, 46, 319-335.

Edfelt, A., Martinsson., O. 2003. The Tjårrojåkka Fe-oxide Cu (–Au) occurrence, Kiruna area, northern Sweden. In: Eliopoulos D et al (eds) Mineral Exploration and Sustainable Development. Millpress, Rotterdam, pp. 1069–1072.

Egozcue, J.J., Pawlowsky-Glahn, V. 2005. Groups of parts and their balances in compositional data analysis. Mathematical Geology, 37, 795–828.

Egozcue, J.J., Pawlowsky-Glahn, V., 2006. Simplicial geometry for compositional data. In: Buccianti, A., Mateu-Figueras, G., Pawlowsky-Glahn, V. (Eds.), Compositional Data Analysis in

the Geosciences: From Theory to Practice. Geological Society, London, Special Publications, 264, 145–159.

Egozcue, J.J., Pawlowsky-Glahn, V., Mateu-Figueras, G., and Barceló-Vidal, C. 2003. Isometric logratio transformations for compositional data analysis: Mathematical Geosciences, 3, 279–300.

Ehrig, K. 2013. Geology of the Wirrda Well IOCG deposit. Powerpoint presentation, 10th Annual SA Exploration and Mining Conference, Adelaide. (http://saemc.com.au/archive/2013/13ehrig.pdf)

Ehrig, K., McPhie, J., Kamenetsky, V. 2012. Geology and Mineralogical Zonation of the Olympic Dam Iron Oxide Cu-U-Au-Ag Deposit, South Australia. Society of Economic Geologists Special Publication, 16, 237–267.

Ehrig, K., Kamenetsky, V., McPhie, J., Cook, N.J., Ciobanu, C.L. 2017. Olympic Dam iron-oxide Cu-U-Au-Ag deposit. In G.N. Phillips, ed., Australian Ore Deposits. Australian Institute of Mining and Metallurgy, Melbourne, pp. 601-610.

Ehrig, K. Kamenetsky, V.S., McPhie, J. Apukhtina, O., Ciobanu, C., Cook, N., Kontonikas-Charos, A., Krneta, S. 2017. The IOCG-IOA Olympic Dam Cu-U-Au-Ag deposit and nearby prospects, South Australia. Proceedings, 14th Biennial SGA Meeting 'Mineral Resources to Discover', Québec City, Canada, 3, 823-826.

Filsmozer, P., Hron, K., Templ, M. 2018. Applied Compositional Data Analysis with Worked Examples in R. Publisher: Springer, New York, pp. 280.

Fleischer, M. 1955. Minor elements in some sulphide minerals. In: A.M. Bateman (Ed.), Economic Geology Fiftieth Anniversary, Volume 1905–1955. Economic Geology Publishing Co., Urbana, Ill, pp. 970-1024.

Foster, A.R., Williams, P., Ryan, C. 2007. Distribution of Gold in Hypogene Ore at the Ernest Henry Iron Oxide Copper-Gold Deposit, Cloncurry District, NW Queensland. Exploration and Mining Geology, 16, 125-143.

Frenzel, M., Hirsch, T., Gutzmer, J. 2016. Gallium, germanium, indium, and other trace and minor elements in sphalerite as a function of deposit type - A meta-analysis. Ore Geology Reviews, 76, 52-78.

Frietsch, R. 1978. On the magmatic origin of iron ores of the Kiruna type. Economic Geology, 73, 478-485.

Gabriel, K.R. 1971. The biplot graphical display of matrices with application to principal component analysis. Biometrika 58, 453-467.

Geijer, P. 1931. The iron ores of the Kiruna type: geographical distribution, geological characters, and origin. Sveriges Geologiska Undersökning, pp. 39.

George, L.L., Biagioni, C., D'Orazio, M., Cook. N.J. 2018. Textural and trace element evolution of pyrite during greenschist facies metamorphic recrystallization in the southern Apuan Alps (Tuscany, Italy): Influence on the formation of Tl-rich sulfosalt melt. Ore Geology Reviews, 102, 59-105.

George, L., Biagioni, C., Lepore, G.O., Lacalamita, M., Agrosì, G., Capitani, G.C., Bonaccorsi, E., D'Acapito, F. 2019. The speciation of thallium in (Tl,Sb,As)-rich pyrite. Ore Geology Reviews, 107, 364-380.

Gregory, D.D., Lyons, T.W. 2017. The effects of trace element content on pyrite oxidation rates. In Proceedings of the American Geophysical Union Fall Meeting, New Orleans, Louisiana, December 11-15 2017.

Gregory, D.D., Cracknell, M.J., Large, R.R., McGoldrick, P., Kuhn, S., Maslennikov, V.V., Baker, M.J., Fox, N., Belousov, I., Figueroa, M.C., Steadman J.A., Fabris, A.J., Lyons, T.W. 2019. Distinguishing Ore Deposit Type and Barren Sedimentary Pyrite Using Laser Ablation-Inductively Coupled Plasma-Mass Spectrometry Trace Element Data and Statistical Analysis of Large Data Sets: Economic Geology, 114, 771-786.

Groves, D.I., Bierlein, F.P., Meinert, L.D., Hitzman, M.W. 2010. Iron Oxide Copper-Gold (IOCG) deposits through earth history: implications for origin, lithospheric setting, and distinction from other epigenetic iron oxide deposits. Economic Geology, 105, 641-654.

Grunsky E. 2010. The interpretation of geochemical survey data. Geochemistry: Exploration Environment Analysis. 10, 27-74.

Grunsky, E., Mueller, U.A., Corrigan, D. 2014. A study of the lake sediment geochemistry of the Melville Peninsula using multivariate methods: Applications for predictive geological mapping. Journal of Geochemical Exploration 141, 15-41.

Guilbert, J.M., Park, C.F. 1986. The Geology of Ore Deposits. London: W.H. Freeman and Co, pp. 985

Günther, T., Klemd, R., Zhang, X., Horn, I., Weyer, S. 2017. In-situ trace element and Fe-isotope studies on magnetite of the volcanic-hosted Zhibo and Chagangnuoer iron ore deposits in the Western Tianshan, NW China. Chemical Geology, 453, 111-127.

Hagemann, S.G., Angerer, T., Duuring, P., Rosière, C.A., Figueiredo e Silva, R.C., Lobato, L.M., Hensler, A-S., Walde, D.H.G. 2016. BIF-hosted iron mineral system: A review. Ore Geology Reviews, 76, 317-359.

Hamilton, N. 2018. ggtern: An Extension to 'ggplot2', for the Creation of Ternary Diagrams. R package version 3.0.0.

Hawley, J.E., Nichol, I. 1961. Trace elements in pyrite, pyrrhotite and chalcopyrite of different ores. Economic Geology, 56, 467–487.

Helsel, T. 2005. Nondetects and Data Analysis: Statistics for Censored Environmental Data. John Wiley & Sons, New York, pp. 250.

Helsel, D. 2006. Fabricating data: How substituting values for nondetects can ruin results, and what can be done about it. Chemosphere 65, 2434-2439.

Hennig C. 2018. fpc: Flexible Procedures for Clustering. R package version 2.1-11.1.

Hitzman, M.W., Oreskes, N., Einaudi, M.T. 1992. Geological characteristics and tectonic setting of Proterozoic iron oxide (Cu-U-Au-REE) deposits. Precambrian Research, 58, 241–287.

Hitzman, M.W. 2000. Iron oxide-Cu-Au Deposits: what, where, when, and why T.M. Porter (Ed.), Hydrothermal Iron Oxide Copper-gold & Related Deposits: A Global Perspective, Australian Mineral Foundation, Adelaide, vol. 1 pp. 9-25

Hofert, M., Kojadinovic, I., Maechler, M., Yan, J. 2017. copula: Multivariate Dependence with Copulas. R package version 0.999-18 URL https://CRAN.R-project.org/package=copula

Honaker, J., King, G., Blackwell, M. 2011. Amelia II: A Program for Missing Data. Journal of Statistical Software, 45, 1-47.

Hood, S., Cracknell, M.J., Gazley, M.F. 2018. Linking protolith rocks to altered equivalents by combining unsupervised and supervised machine learning. Journal of Geochemical Exploration, 186, 270-280.

Hood, S., Cracknell, M.J., Gazley, M.F., Reading, A.M. 2019. Element mobility and spatial zonation associated with the Archean Hamlet orogenic Au deposit, Western Australia: Implications for fluid pathways in shear zone. Chemical Geology, 514, 10-26.

Houari, R., Bounceur, A., Tari, A.A.K., Kechadi, M.T. 2014. Handling Missing Data problems with Sampling Methods. International Conference on Advanced Networking Distributed Systems and Applications (INDS), Bejaia, Algeria.

Houari, R., Bounceur, A., Kechadi, M.T., Tari, A.A.K., Euler, R. 2016. Missing Data Analysis Using Multiple Imputation in Relation to Parkinson's Disease. International conference on Big Data and Advanced Wireless, Blagoevgrad, Bulgaria.

Hron, K., Templ, M., Filzmoser, P. 1986. Imputation of missing values for compositional data using classical and robust methods. Computational Statistics and Data Analysis, 54, 3095-3107.

Huang, Q., Kamenetsky, V.S., Ehrig, K., McPhie, J., Kamenetsky, M., Cross, K., Meffre, S., Agangi, A., Chambefort, I., Direen, N.G., Maas, R., Apukhtina, O. 2016. Olivine-phyric basalt in the Mesoproterozoic Gawler silicic large igneous province, South Australia: examples at the

Olympic Dam Iron Oxide Cu–U–Au–Ag deposit and other localities. Precambrian Research, 281, 185-199.

Huang, Q., Kamenetsky, V.S., McPhie, J., Ehrig, K., Meffre, S., Maas, R., Thompson, J., Kamenetsky, M., Chambefort, I., Apukhtina, O., Hu, Y. 2015. Neoproterozoic (ca. 820–830 Ma) mafic dykes at Olympic Dam, South Australia: links with the Gairdner Large Igneous Province. Precambrian Research, 271, 160-172.

Ismail, R., Ciobanu, C.L., Cook, N.J., Teale, G.S., Giles, D., Schmidt Mumm, A., Wade, B. 2014. Rare earths and other trace elements in minerals from skarn assemblages, Hillside iron oxide–copper–gold deposit, Yorke Peninsula, South Australia. Lithos, 184-187, 456-477.

Jagodzinski, E.A. 2005. Compilation of SHRIMP U–Pb geochronological data – Olympic Domain, Gawler Craton, South Australia, 2001–2003. Canberra: Geoscience Australia (Record 2005/20, 197).

Joe, H. 1997. Multivariate Models and Dependence Concepts. Chapman & Hall, London, pp. 424.

Johnson, R., Wichern, D. 2007. Applied Multivariate Statistical Analysis, 6th edition, Springer.

Keyser, W.M., Ciobanu, C.L., Cook, N.J., Courtney-Davies, L., Ehrig, K., Gilbert, S., McPhie, J. 2017. Links between sedimentary protoliths and IOCG-skarn skarn alteration, Island Dam, South Australia. In Proceedings of the 14th SGA Biennial Meeting, Quebec City, QC, Canada, 20–23 August 2017, pp. 935–938.

Keyser, W.M., Ciobanu, C.L., Cook, N.J., Courtney-Davies, L., Ehrig, K., Gilbert, S., McPhie, J. 2017, Links Between Sedimentary Protoliths and IOCG-Skarn Alteration, Island Dam, South Australia: SGA Biennial Meeting, 14^{th,} Quebec City, QC, Canada, 2017, Proceedings, 935–938.

Keyser, K., Ciobanu, C.L., Cook, N.J., Johnson, G., Feltus, H., Johnson, S., Dmitrijeva, M., Ehrig, K., Nguyen, P.T. 2018. Petrography and trace element signatures of iron-oxides in deposits from the Middleback Ranges, South Australia: from banded iron formation to ore, Ore Geology Reviews, 93, 337-360.

Keyser, W., Ciobanu, C.L., Cook, N.J., Feltus, H., Johnson, G., Slattery, A., Wade B.P., Ehrig, K. 2019. Mineralogy of Zirconium in Iron-Oxides: A Micron- to Nanoscale Study of Hematite Ore from Peculiar Knob, South Australia. Minerals, 9, 244.

Knipping, J., Bilenker, J., Simon, A., Reich, M., Barra, F., Deditius, A., Wälle, M., Heinrich, C. Holtz, F., Munizaga, R. 2015. Trace elements in magnetite from massive iron oxide-apatite deposits indicate a combined formation by igneous and magmatic-hydrothermal processes. Geochimica et Cosmochimica Acta, 171, 15–38.

Knipping, J.L., Bilenker, L.D., Simon, A.C., Reich, M., Barra, F., Deditius, A.P., Lundstrom, C., Bindeman, I., Munizaga, R. 2015. Giant Kiruna-type deposits form by efficient flotation of magmatic magnetite suspensions. Geology 43, 591–594.

Kontonikas-Charos, A., Ciobanu, C.L., Cook, N.J. 2014. Albitization and redistribution of REE and Y in IOCG systems: Insights from Moonta-Wallaroo, Yorke Peninsula, South Australia. Lithos, 208–209, 178-201.

Kontonikas-Charos, A., Ciobanu, C.L., Cook, N.J., Ehrig, K., Krneta, S., Kamenetsky, V.S. 2017. Feldspar evolution in the Roxby Downs Granite, host to Fe-oxide Cu-Au-(U) mineralisation at Olympic Dam. South Australia. Ore Geology Reviews, 80, 838-859.

Kontonikas-Charos, A., Ciobanu, C.L., Cook, N.J., Ehrig, K., Krneta, S., Kamenetsky, V.S. 2018a. Rare earth element geochemistry of feldspars: examples from Fe-oxide Cu-Au systems in the Olympic Cu-Au Province, South Australia. Mineralogy and Petrology, 112, 145–172.

Kontonikas-Charos, A., Ciobanu, C.L., Cook, N.J., Ehrig, K., Ismail, R., Krneta, S., Basak, A. 2018b. Feldspar mineralogy and rare earth element (re)mobilization in iron-oxide copper gold systems from South Australia: a nanoscale study. Mineralogical magazine, 82, S173–S197.

Krneta, S., Ciobanu, C.L., Cook, N.J., Ehrig, K., Kontonikas-Charos, A. 2016. Apatite at Olympic Dam, South Australia: A petrogenetic tool. Lithos 262, 470–485.

Krneta, S., Ciobanu, C.L. Cook, N.J., Ehrig, K.J., Kontonikas-Charos, A. 2017a. Rare Earth Element Behaviour in Apatite from the Olympic Dam Cu–U–Au–Ag Deposit, South Australia, Minerals, 7, 135.

Krneta, S., Ciobanu, C.L., Cook, N.J., Ehrig, K., Kontonikas-Charos, A. 2017b. The Wirrda Well and Acropolis prospects Gawler Craton, South Australia: insights into evolving fluid conditions through apatite chemistry. Journal of Geochemical Exploration 181, 276-291.

Kuhn, S., Cracknell1, M.J., Reading, A.M. 2018, Lithologic mapping using Random Forests applied to geophysical and remote-sensing data: A demonstration study from the Eastern Goldfields of Australia: Geophysics, 83, B183-B193.

Large, R.R., Maslennikov, V.V., Robert, V., Danyushevsky, L.V., Chang, Z.S. 2007. Multistage sedimentary and metamorphic origin of pyrite and gold in the giant Sukhoi Log deposit, Lena Gold Province, Russia. Economic Geology, 102, 1233–1267.

Large, R.R., Danyushevsky, L.D., Hollit, C., Maslennikov. V.V., Meffre, S., Gilbert, S., Bull, S., Scott, R., Emsbo, P., Thomas, H., Singh, R., Foster, J. 2009. Gold and trace element zonation in pyrite using a laser imaging technique, implications for the timing of gold in orogenic and Carlin-style sediment-hosted deposits. Economic Geology, 104, 635–668.

Li, R., Chen, H., Xia, X., Yang, Q., Danyushevsky, L.D., Lai, C. 2018. Using integrated in-situ sulphide trace element geochemistry and sulfur isotopes to trace ore-forming fluids: Example from the Mina Justa IOCG deposit (southern Perú). Ore Geology Reviews, 101, 165-179.

Macmillan, E., Cook, N.J., Ehrig, K., Ciobanu, C.L., Pring, A. 2016a. Uraninite from the Olympic Dam IOCG-U-Ag deposit: Linking textural and compositional variation to temporal evolution. American mineralogist, 101, 1295-1320.

Macmillan, E., Ciobanu, Ehrig, K., C.L., Cook, N.J., Pring, A. 2016b. Chemical zoning and lattice distortion in uraninite from Olympic Dam, South Australia. American Mineralogist, 101, 2351-2354.

Macmillan, E., Ciobanu, Ehrig, K., C.L., Cook, N.J., Pring, A. 2016c. Replacement of Uraninite By Bornite Via Coupled Dissolution-Reprecipitation: Evidence from Texture and Microstructure. Canadian Mineralogist, 54, 1369-1383.

Macmillan, E., Cook, N.J., Ehrig, K., Pring, A. 2017. Chemical and textural interpretation of late-stage coffinite and brannerite from the Olympic Dam IOCG-Ag-U deposit. Mineralogical magazine, 81, 1323-1366.

MacQueen, J. 1967. Some methods for classification and analysis of multivariate observations. In: Le Cam, L.M., Neyman, J. (Eds.), Proceedings of the Fifth Berkeley Symposium on Mathematical Statistics and Probability, Berkeley University of California Press, vol 1. 281–297.

Maksaev, V., Gardeweg, M., Ramírez, C.F., Zentilli, M. 1988. Aplicación del método trazas de fisión (fission track) a la datación de cuerpos de magnetita de El Laco e Incahuasi en el Altiplano de la Región de Antofagasta: Congreso Geológico Chileno, 5th, Antofagasta, Actas, vol. 1, p. B1–B23.

Makvandi, S., Ghasemzadeh-Barvarz, M., Beaudoin, G., Grunsky, E.C., McClenaghan, M.B., Duchesne, C., McClenaghan, M.B., Duchesne, C. 2016a. Principal component analysis of magnetite composition from volcanogenic massive sulfide deposits: Case studies from the Izok Lake (Nunavut, Canada) and Halfmile Lake (New Brunswick, Canada) deposits. Ore Geology Reviews, 72, 60-85.

Makvandi, S., Ghasemzadeh-Barvarz, M., Beaudoin, G., Grunsky, E.C., McClenaghan, M.B., Duchesne, C., Boutroy, E. 2016b. Partial least squares-discriminant analysis of trace element compositions of magnetite from various VMS deposit subtypes: Application to mineral exploration. Ore Geology Reviews, 78, 388-408.

Mark, G., Oliver, N.H.S., Williams, P.J. 2006. Mineralogical and chemical evolution of the Ernest Henry Fe-oxide-Cu-Au ore system, Cloncurry district, northwest Queensland, Australia, Mineralium Deposita, 40, 769-801.

Mathieu, L. 2019. Detecting magmatic-derived fluids using pyrite chemistry: Example of the Chibougamau area, Abitibi Subprovince, Québec. Ore Geology Reviews, 114, 103127.

Mauger, A.J., Ehrig, K.J., Kontonikas-Charos, A., Ciobanu, C.L., Cook, N.J., Kamenetsky, V.S. 2016. Alteration at the Olympic Dam IOCG–U deposit: insights into distal to proximal feldspar and phyllosilicate chemistry from infrared reflectance spectroscopy. Australian Journal of Earth Sciences, 63, 959-972.

McAvaney, S. 2012. The Cooyerdoo Granite: Paleo- and Mesoarchean basement of the Gawler Craton. MESA Journal, 65, 31-40.

McIntyre, J.I. 2001. Middleback Ranges Project - South Australia. EL 2763 Annual Report. Helix Resources N.L.

McPhie, J. 2016. Acropolis Report, BHP Billiton Olympic Dam.

McPhie, J., Orth, K., Kamenetsky, V., Kamenetsky, M., Ehrig, K. 2016. Characteristics, origin and significance of Mesoproterozoic bedded clastic facies at the Olympic Dam Cu–U–Au–Ag deposit, South Australia. Precambrian Research, 276, 85-100.

McPhie, J. Ehrig, K., Kamenetsky, M., Crowley, J., Kamenetsky, V.S. 2020. Geology of the Acropolis prospect, South Australia, constrained by high-precision CA-TIMS ages: Australian Journal of Earth Sciences, in press.

Meinert, L. 1997. Application of Skarn Deposit Zonation Models to Mineral Exploration. Exploration and Mining Geology 6, 185-208.

Montreuil, J.-F., Corriveau, L., Grunsky, E.C. 2013. Compositional data analysis of IOCG systems, Great Bear magmatic zone, Canada: To each alteration types its own geochemical signature: Geochemistry: Exploration, Environment, Analysis, 13, 229–247.

Morris, R.C. 2012. Microplaty hematite - its varied nature and genesis. Australian Journal of Earth Sciences, 59, 411-434

Mortimer, G.E., Cooper, J.A., Paterson, H.L., Cross, K., Hudson, G.R.T., Uppill, R.K. 1988. Zircon U–Pb Dating in the Vicinity of the Olympic Dam Cu–U–Au Deposit, Roxby Downs, South-Australia. Economic Geology, 83, 694–709.

Nelsen, R. 2006. An Introduction to Copulas. Springer Science & Business Media, pp. 272

Norris, A., Danyushevsky, L. 2018. Towards Estimating the Complete Uncertainty Budget of Quantified Results Measured by LA-ICP-MS. Goldschmidt, Boston.

Norton, M., Khokhlov, V., Uryasev, S. 2019. Calculating CVaR and bPOE for common probability distributions with application to portfolio optimization and density estimation. Annals of Operations Research, submitted for publication, http://arxiv.org/abs/1811.11301.

O'Brien, J.J., Spry, P.G., Nettleton, D., Xu, R., Teale, G.S. 2015. Using Random Forests to distinguish gahnite compositions as an exploration guide to Broken Hill-type Pb–Zn–Ag deposits in the Broken Hill domain, Australia. Journal of Geochemical Exploration 149, 74–86.

Oliver, N.H.S., Cleverley, J.S., Mark, G., Pollard, P.J., Fu, B., Marshall, L.J., Rubenach, M.J., Williams, P.J., Baker, T. 2004. The role of sodic alteration in the genesis of iron oxide-copper-gold deposits, eastern Mt Isa Block, Australia. Economic Geology, 99, 1145-1176.

Ordóñez-Calderón, J.C., Gelcich, S. 2018. Machine learning strategies for classification and prediction of alteration facies: Examples from the Rosemont Cu-Mo-Ag skarn deposit, SE Tucson Arizona, Journal of Geochemical Exploration, 194, 167-188.

Ordóñez-Calderón, J.C., Gelcich, S., Oliveira, J.F. 2017. Applied data analytics on multielement geochemistry for pre-mining characterization of geological and geometallurgical attributes: examples of the Rosemont Cu-Mo-Ag skarn deposit, Tucson, Arizona. In: CoDaWork 2017 - Abbadia San Salvatore (IT).

Oreskes, N., Einaudi, M.T. 1992. Origin of hydrothermal fluids at Olympic Dam, preliminary results from fluid inclusions and stable isotopes. Economic Geology, 87, 64–90.

Owen, N.D. 2019. The Mineralogical Deportment of Radionuclides in South Australian Cu-Au-(U) Ores. Unpublished PhD Thesis, The University of Adelaide, Australia.

Owen, N.D., Ciobanu, C.L., Cook, N.J., Slattery, A., Basak, A. 2018. Nanoscale study of clausthalite-bearing symplectites in Cu-Au-(U) ores: Implications for ore genesis. Minerals, 8, 67.

Owen, N.D., Cook, N.J., Rollog, M., Ehrig, K.J., Schmandt, D.S.l Ram, R., Brugger, J., Ciobanu, C.L., Wade, B., Guagliardo, P. 2019. REE-, Sr- Ca-aluminum-phosphate-sulfate minerals of the alunite supergroup and their role as hosts for radionuclides. American Mineralogist, in press.

Palarea-Albaladejo, J., Martín-Fernández, J.A. 2013. Values below detection limit in compositional chemical data, Analytca Chimica Acta, 764, 32-43.

Palarea-Albaladejo, J., Martín-Fernández, J.A. 2015. zCompositions—R package for multivariate imputation of left-censored data under a compositional approach. Chemometrics and Intelligent Laboratory Systems, 143, 85-96.

Park, C.F. 1961. A magnetite “flow” in northern Chile. Economic Geology, 56, 431–436.

Parker, A.J. 1993. The geology of South Australia, Volume 1 - The Precambrian. Geological Survey of South Australia, Bulletin, 54.

Parker, A.J. 1990, Gawler Craton and Stuart Shelf - regional geology and mineralization, in Hughes, F.E., ed., Geology of the Mineral Deposits of Australia and Papua New Guinea: Australasian Institute of Mining and Metallurgy, Monograph Series, 14, 999–1008.

Paterson, H. L. 1986. The Acropolis Prospect. In: H. L. C. Paterson (Ed.), Basement geology of the Stuart Shelf region, South Australia (vol. A1 – Olympic Dam/Stuart Shelf Excursion Guide, pp. 17–18). 8th Australian Geological Convention, Adelaide. Sydney, NSW: Geological Society of Australia.

Pawlowsky-Glahn, V., Egozcue, J.J. 2006. Compositional data and their analysis: an introduction. Geological Society, London, Special Publication 264, 1-10.

Pawlowsky-Glahn, V., Egozcue, J.J., Tolosana-Delgado, R. 2015. Modeling and Analysis of Compositional Data. Chichester: Wiley, pp. 272.

Peacock, M. 2016. Structural Geology & High-grade Iron Ore Mineralisation, Middleback Ranges, South Australia, Honours Thesis, The Australian National University.

Pearson, K. 1897. Mathematical contributions to the theory of evolution: on a form of spurious correlation which may arise when indices are used in the measurements of organs. Proceedings of the Royal Society, London 60, 489-498.

Pirajno, F., Hoatson, D.M. 2012. A review of Australia's Large Igneous Provinces and associated mineral systems: implications for mantle dynamics through geological time. Ore Geology Reviews, 48, 2-54.

Putnis, A. 2002. Mineral replacement reactions: from macroscopic observations to microscopic mechanisms. Mineralogical Magazine, 66, 689–708.

R Core Team. 2017. R: A language and environment for statistical computing. R Foundation for Statistical Computing, Vienna, Austria.

Reeve, J.S., Cross, K.C., Smith, R.N., Oreskes, N. 1990. Olympic Dam copper-uranium-gold-silver deposit. In: Hughes, F.E. (Eds.), Geology of the Mineral Deposits of Australia and Papua New Guinea: Australian Institute of Mining and Metallurgy, 14, 1009-1035.

Reich, M., Kesler, S.E., Utsunomiya, S., Palenik, C.S., Chryssoulis, S.L., Ewing, R.C. 2005. Solubility of gold in arsenian pyrite. Geochimica et Cosmochimica Acta, 69, 2781-2796.

Reich, M., Simon, A.C., Deditius, A., Barra, F., Chryssoulis, S., Lagas, G., Tardani, D., Jaayke Knipping, J., Bilenker, L., Sánchez-Alfaro, P., Roberts, M.P., Munizaga, R. 2016. Trace Element Signature of Pyrite from The Los Colorados Iron Oxide-Apatite (IOA) Deposit, Chile: A Missing Link Between Andean IOA And Iron Oxide Copper-Gold Systems? Economic Geology, 111, 743–761.

Reid, A., Hand, M. 2012. Mesoarchean to Mesoproterozoic evolution of the southern Gawler Craton, South Australia. Episodes 35, 216-225.

Richards, J.P., López, G.P., Zhu, J.J., Creaser, R.A., Locock, A.J., Mumin, A.H. 2017. Contrasting Tectonic Settings and Sulfur Contents of Magmas Associated with Cretaceous Porphyry Cu ± Mo ± Au and Intrusion-Related Iron Oxide Cu-Au Deposits in Northern Chile. Economic Geology, 112, 295-318.

Richards, J.P., Mumin, A.H. 2013. Magmatic-hydrothermal processes within an evolving Earth: Iron oxide-copper-gold and porphyry Cu±Mo±Au deposits. Geology 41, 767-770.

Rollog, M., Cook, N.J., Guagliardo, P., Ehrig, K., Ciobanu, C.L., Kilburn, M. 2019. Detection of Trace Elements/Isotopes in Olympic Dam Copper Concentrates by nanoSIMS. Minerals, 9, 336.

Rollog, M., Cook, N.J., Guagliardo, P., Ehrig, K.J., Kilburn, M. 2019. In situ spatial distribution mapping of radionuclides in minerals by nanoSIMS. Geochemistry: Exploration, Environment, Analysis. (in press)

Román, N., Reich, M., Leisen, M., Morata, D., Barra, F., Deditius, A.P. 2019. Geochemical and micro-textural fingerprints of boiling in pyrite. Geochimica et Cosmochimica Acta, 246, 60-85.

Romer, R.L., Martinsson, O. Perdahl, J.-A. 1994. Geochronology of the Kiruna Iron Ores and Hydrothermal Alteration, Economic Geology, 89, 1249-1261.

Rousseeuw, P.J. 1987. Silhouettes: A graphical aid to the interpretation and validation of cluster analysis, Journal of Computational and Applied Mathematics, 20, 53-65.

Ruiz F.C., Ortiz, F., Moraga, A., Aguilar, A. 1968. Genesis of the Chilean iron ore deposits of Mesozoic age. International Geological Congress 7, 323–338.

Rusk, B., Oliver, N., Cleverley, J., Blenkinsop, T., Dexian, Z., Patrick, P., Habermann, P. 2010. Physical and chemical characteristics of the Ernest Henry iron oxide copper gold deposit, Australia, implications for IOGC genesis. In: Porter, T.M., (ed.) Hydrothermal Iron Oxide Copper-Gold & Related Deposits: a global perspective - advances in the understanding of IOCG deposits. Global Perspective Series, 3. PGC Publishing, Linden Park, SA, Australia, pp. 201-218.

Schepsmeier, U., Stoeber, J., Brechmann, E.C., Graeler, B., Nagler, T., Erhardt, T. 2018. VineCopula: Statistical Inference of Vine Copulas. R package version 2.1.8. https://CRAN.R-project.org/package=VineCopula

Schlegel, T.U., Heinrich, C.A. 2015. Alteration and lithology control Cu mineralization at Prominent Hill iron oxide-copper-gold deposit, Gawler craton, South Australia. Economic Geology, 110, 1953–1994.

Schmandt, D.S., Cook, N.J., Ciobanu, C.L., Ehrig, K.J, Wade, B.P., Gilbert, S., Kamenetsky, V.S. 2017. Rare earth element fluorocarbonate minerals from the Olympic Dam Cu-U-Au-Ag deposit, South Australia. Minerals 7, 202.

Schmandt, D.S. 2019. Mineralogical distributions of radionuclides in copper-uranium ores from Olympic Dam, South Australia. Unpublished PhD thesis, The University of Adelaide, Adelaide, Australia.

Skirrow, R.G., Bastrakov, E.N., Barovich, K., Fraser, G.L., Creaser, R.A., Fanning, C.M., Raymond, O.L., Davidson, G.J. 2007. Timing of iron oxide Cu-Au-(U) hydrothermal activity and Nd isotope constraints on metal sources in the Gawler craton, South Australia. Economic Geology, 102, 1441-1470.

Sklar, A. 1959. Fonctions de répartition à n dimensions et leurs marges, Publications de l'Institut Statistique de l'Université de Paris, 8, 229-231.

Sung, Y.H., Brugger, J., Ciobanu, C.L., Pring, A., Skinner, W., Nugus, M. 2009. Invisible gold in arsenian pyrite and arsenopyrite from a multistage Archaean gold deposit: Sunrise Dam, Eastern Goldfields Province, Western Australia. Mineralium Deposita, 44, 765–791.

Szpunar, M., Hand, M., Barovich, K., Jagodzinski, E., Belousova, E. 2011. Isotopic and geochemical constraints on the Paleoproterozoic Hutchison Group, southern Australia: Implications for Paleoproterozoic continental reconstructions. Precambrian Research, 187, 99-126.

Taylor, D., Dalstra, H.J., Harding, A.E., Broadbent, G.C., Barley, M.E. 2001. Genesis of High-Grade Hematite Orebodies of the Hamersley Province, Western Australia. Economic Geology, 96, 837-873.

Templ, M., Hron, K., Filzmoser, P. robCompositions: An R-package for robust statistical analysis of compositional data. 2018. In: V. Pawlowsky-Glahn A. Buccianti, editors, Compositional Data Analysis. Theory and Applications, Publisher: John Wiley & Sons, Chichester (UK), pp. 341-355.

Thomas, H.V., Large, R.R., Bull, S.W., Maslennikov, V., Berry, R.F., Frazer, R., Froud, F., Moye, R. 2011. Pyrite and pyrrhotite textures and composition in sediments, laminated quartz veins, and reefs at Bendigo Gold Mine, Australia: insights for ore genesis. Economic Geology, 106, 1–31.

Thompson, J., Meffre, S., Maas, R., Kamenetsky, V., Kamenetsky, M., Goemann, K., Danyushevsky, L. 2016. Matrix effects in Pb/U measurements during LA-ICP-MS analysis of the mineral apatite: The Journal of Analytical Atomic Spectrometry, 31, 1206–1215.

Van Achterbergh, E., Ryan, C.G., Jackson, S.E., Griffin, W.L. 2001. Data reduction software for LA-ICP-MS. In: Sylvester JP (ed.), Laser-Ablation-ICPMS in the Earth Sciences, Principles and Applications. Mineralogical Association of Canada, Short Course Series 29, 239-243.

van den Boogaart, K.G., Tolosana-Delgado, R. 2013. Analyzing Compositional Data with R. Springer pp. 258.

van den Boogaart, K.G., Tolosana-Delgado, R., Bren, M. 2014. compositions: Compositional Data Analysis. R package version 1.40-1.

Van Tendeloo, G., Bals, S., Van Aert, S., Verbeeck, J., Van Dyck, D. 2012. Advanced electron microscopy for advanced materials. Advanced Materials, 24, 5655-5675.

Vaughan, D.J., Corkhill, C.L. Mineralogy of Sulphides. 2017. Elements, 13, 81-87.

Vella, L. 1997. Interpretation and modelling, based on petrophysical measurements, of the Wirrda Well potential field anomaly, South Australia: Exploration Geophysics, 28, 299-306.

Verdugo-Ihl, M.R., Ciobanu, C.L., Cook, N.J., Ehrig, K., Courtney-Davies, L., Gilbert, S. 2017. Textures and U-W-Sn-Mo signatures in hematite from the Cu-U-Au-Ag orebody at Olympic Dam, South Australia: Defining the archetype for IOCG deposits. Ore Geology Reviews, 91, 173-195.

Verdugo-Ihl, M.R., Ciobanu, C.L., Cook, N.J., Ehrig, K.J., Courtney-Davies, L. 2019. Defining early stages of IOCG systems: evidence from iron-oxides in the outer shell of the Olympic Dam deposit, South Australia, Mineralium Deposita, in press.

Wang, M., Wang, W., Liu, K., Michalak, P.P., Wei, K., Hu, M. 2017. In-situ LA-ICP-MS trace elemental analyzes of magnetite: The Tieshan skarn Fe–Cu deposit, Eastern China. Geochemistry, 77, 169-181.

Wickham, H, ggplot2: Elegant Graphics for Data Analysis. Springer-Verlag New York, 2016.

Williams, P.J., Barton, M.D., Johnson, D.A., Fontboté, L., Haller, A., Mark, G., Oliver, N.H.S., Marschik, R. 2005. Iron-oxide–copper–gold deposits: Geology, space–time distribution, and possible modes of origin. Economic Geology 100th Anniversary Volume, 371–406.

Winderbaum, L., Ciobanu, C.L., Cook, N.J., Paul, M., Metcalfe, A.V., Gilbert, S. 2012. Multivariate analysis of an LA-ICP-MS trace element dataset for pyrite, Mathematical Geosciences, 44, 823-842.

Xu, J., Ciobanu, C.L., Cook, N.J., Slattery, A.D. 2019. Crystals from the Powellite-Scheelite Series at the Nanoscale: A Case Study from the Zhibula Cu Skarn, Gangdese Belt, Tibet. Minerals, 9, 340.

Zhou, Z-J., Tang, H-S., Chen, Y-J., Chen, Z-L. 2017. Trace elements of magnetite and iron isotopes of the Zankan iron deposit, westernmost Kunlun, China: A case study of seafloor hydrothermal iron deposits. Ore Geology Reviews, 80, 1191-1205.